

ISSN: 2249-6645

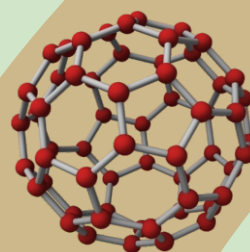


International Journal of Modern Engineering Research (IJMER)

Volume 4

Issue 7

July 2014





International Journal of Modern Engineering Research (IJMER)

Volume : 4 Issue : 7 (Version-1)

ISSN : 2249-6645

July - 2014

Contents :

Pulsation and Vibration Study Of Reciprocating Compressor According To API 618 5th Edition <i>Pradip P. Shejal, Dr. A. D. Desai</i>	01-23
BER Performance for Convalutional Code with Soft & Hard Viterbi Decoding <i>Umesh Kumar Pandey, Prashant Purohit</i>	24-27
Analysis of Conditions in Boundary Lubrications Using Bearing Materials <i>Shinde Sagar Vitthal, Ravindra R. Navthar</i>	28-32
Numerical Analysis of Fin Side Turbulent Flow for Round and Flat Tube Heat Exchangers <i>Mallikarjuna, Dr. V Seshadri, Vijaya Raghu B</i>	33-39
Free Vibration Analysis of Polyproplyne- Nanoclay Composite Beam with Crack <i>Egbe-Ngu Ntui Ogork, Okorie Austine Uche, Augustine Uche Elinwa</i>	40-46
A Review of Issues in Environmentally Conscious Manufacturing and Product Recovery <i>Pisal Mahesh B., Quazi T. Z</i>	47-54
Zigbee Based Wireless Sensor Networks for Smart Campus <i>Prasad P. Netalkar, Yasha Kaushal, Dr. N. Shekar V. Shet</i>	55-62
Experimental Investigation of Performance and Emission Characteristics of Biodiesel from Sterculia Striata <i>K.Balasubramanian, Abhinav Balaji , K.Vignesh</i>	63-73
A Novel Approach of Harmonic Reduction with Transformer Connected 3-Phase Multilevel Inverter <i>Vipul Rastogi, Sudhanshu Tripathi</i>	74-87
Online Intrusion Alert Aggregation with Generative Data Stream Modeling <i>Kothawale Ganesh S., Borhade Sushama R., Prof. B. Raviprasad</i>	88-93

Pulsation and Vibration Study Of Reciprocating Compressor According To API 618 5th Edition

Pradip P. Shejal¹, Dr. A. D. Desai²

¹ (Mechanical Department, P. G. M. College of Engineering / Pune University, India)

² (Mechanical Department, S. R. College of Engineering / Pune University, India)

Abstract: The compressor package contains the reciprocating compressor, pulsation dampers, gas coolers and the connected pipe system which are often the heart of an installation and should be operate smoothly and reliably. The compressor piping vibrations can contribute to fatigue failure of the system or entire package which can lead to unsafe situations for human being as well as environment, loss of capacity and increase in maintenance as well as repair cost and to avoid this situation compressor piping vibration analysis to be carried out at a very early stage of the design of an installation. The pulsation analysis should be carried out before the piping vibration analysis. The guidelines for the pulsation analysis are given in API 618 Approach 2 and the guidelines for the vibration analysis are given in API 618 Approach 3. The original system layout is checked with respect to pulsations with all operating cases that are characterized by steady-state operating conditions. The different gas properties and operation cases are considered with valve unloading cases as operation cases. The measures are proposed to reduce pressure pulsation by installation of orifices. The shaking forces are used in the subsequent vibration study. After the analysis of pulsation results, find out the worst case for the vibration study means we used the shaking forces induced by pressure pulsation excite the mechanical piping system of worst case. The Vibration Study determines the effect on the mechanical piping system and proposes measures to avoid stresses possibly leading to deformation or rupture by fatigue. The finite element program ANSYS is used for modeling of the mechanical system. The model is built of several types of basic piping elements (e.g. pipes, beams, elbows, T-pieces) connected at node points. The modifications are proposed to meet agreed criteria of vibration. This paper demonstrated that by properly analysing the compressor piping vibration in an accurate and economic way using Pulsim and Ansys software. The accuracy of the analytical solution is validated by means of experimental results by using B & K Analyser for the measurement of compressor piping vibration.

Keywords: ANSYS, API 618, APL LANGUGUE, FFT ANALYSER, PULSE, PULSIM

I. INTRODUCTION

The high vibrations were reported at the piping of compressor which was built according to API 618 Standard. This compressor is used to compress Hydrogen gas from 19 bar to 70 bar in two stages for feeding a hydrocracker in a refinery. The flow rate of this compressor is varying from 226 kg/hr to 1136 kg/hr. The compressor rotation speed is 742 RPM. The motor power for this 2 crank compressor is 355 kW.

The objective of this project is to reduce the vibration of piping system of reciprocating compressor. To accomplish this, the following specific objectives are defined and completed.

- Fundamentals of Pulsation and Mechanical Vibration Theory
- Pulsation Analysis as per API 618 5th Edition approach 2 : To reduce the pulsation across the piping system by using orifices at different locations
- Vibration Analysis as per API 618 5th Edition approach 3 : To reduce the Vibration across the piping system by using supports at different locations
- Compare the results with before and after pulsation and vibration analysis plotting graphs in Velocity-Time Domain.

II. LITERATURE OVERVIEW

This literature review summarises, interprets and critically evaluates existing “literature” in order to establish correct knowledge of subject. The many experts present these views about the pulsation and vibration in different literatures. Following are literature review is to go through the main topics of interest.

Shelley Greenfield and Kelly Eberle (2008) summarized an interesting literature overview of the new API standard 618 (5th edition) and its impact on reciprocating compressor package design. The new API 618 5th Edition includes many improvements over the 4th Edition in the specification for engineering studies to minimize pulsation and vibration. This provides the changes of The Pulsation, Vibration, Torsional, Skid and Engineering studies. Also this gives the Summary of API 618 standard and key changes in the 5th edition.

James D. Tison and Kenneth E. Atkins (2008) described the control philosophy for the pulsation and vibration as per new fifth edition of API 618 for reciprocating compressors. This paper provide the user with a working knowledge of good engineering practices for pulsation and vibration control of reciprocating machinery in relatively high mole weight gases as well as an in depth understanding of the postposed changes in API 618 and differing design philosophies. The conclusions for this paper are A) The intent of API 618 at the Third Edition was that Design approach 3 meant effective pulsation control. This usually required that reactive filtering be used in relatively high mole weight systems. B) The Fourth Edition attempted to define the steps required to quality a piping system, in the event that the allowable pulsation levels were exceeded. This created confusion and led to systems being designed with less emphasis on pulsation control, and justified with mechanical response calculations of questionable validity. C) The fifth Edition will clarify the confusion that resulted from the addition of the language concerning mechanical forced response calculations. The User will now be able to determine if the systems mattes Design Approach 3 by the use of the technically sound pulsation and shaking force control philosophy or through the use of the higher risk philosophies based on mechanical forced response calculations.

Paul Alves (2006) studied the acoustical and mechanical Analysis of reciprocating compressor installation as per API 618 4th Edition. This paper gives basic about the Pulsation, Dynamic Forces, Resistive elements, Reactive elements, analysis cycle. Also he explained different clause which are mentioned in API 618 for Pulsation and Vibration analysis. We can easily understand API 618 M3 is applicable for pulsation analysis and API 618 M4 to M8 are applicable for vibration analysis.

Enzo Giacomelli et al. (2006) studied the forced response of cylinder manifold for reciprocating compressor applications by considering Crosshead guides, distance pieces, cylinder flanges, joint, supports etc for the analysis. The study performed frequencies and amplitudes of pulsation induced shaking forces defined by acoustical simulation, internal gas forces in the cylinder, and unbalanced mechanical forces and moments allows a proper forced response analysis of the cylinder manifold system. The study applied these forces to the finite element model to calculate the relevant vibrations and stress amplitudes by performing a harmonic analysis. The paper covered the existing procedures, application experience and recommendations for properly considering the applied loads.

J. C. Wachel and J. D. Tison (1999) investigated a wide variety of vibration and failure problems occur in reciprocating machinery and piping systems. Excessive piping vibration problems usually occur when a mechanical natural frequency of the piping system or compressor manifold system is excited by a pulsation or mechanical excitation source since reciprocating compressors and pumps generate high pulsation forces, vibration and failure problems in these systems are common. As per this paper, whenever high vibrations are encountered in reciprocating compressors, pumps or piping, it is necessary to determine if vibrations and dynamic stresses are acceptable.

W. W. von Nimitz (1982) described pulsation and vibration control requirements in the design of reciprocating compressor and pump installations. The paper provided the basis for evolving improved methods for assuring the reliability of reciprocating compressor and pump installations at the design stage. This contains new methods for sizing surge volumes, maximum allowable pulsation levels at compressor valves and in the piping systems, and improved pressure drop criteria based on performance. The introduction of the paper explained the nature of the problem, previous work, purpose, and the contribution of the paper. The contents of each section may be provided to understand easily about the paper.

III. FUNDAMENTALS OF PULSATION AND MECHANICAL VIBRATION THEORY

In order to understand how to control pulsation and vibration in positive displacement machinery systems, it is imperative that one understands the differences between acoustical and mechanical concepts. In 2.1, the acoustic issues, along with acoustic control techniques, will be addressed. In 3.2, the elements of the mechanical system will be explained along with the concept of acoustic-mechanical coupling and the mechanical techniques for controlling vibration.

Overview of Pulsation Concepts

Pressure variations that result from oscillatory flow of positive displacement machinery are the subject of this section. These variations in pressure are referred to as pulsation. The pulsation occur in systems handling both gases and liquids. High vibration, support degradation and fatigue failures caused by dynamic forces induced by the pulsation are the most common problems resulting from pulsation. In order to reduce the possibility of detrimental pulsation and vibration at the design stage, it is necessary to understand several technical concepts. Excitation mechanisms are first addressed in 2.1.1. Acoustic response is then explained in 2.1.2. In 2.1.3, the most common results of excessive pulsation are reviewed and the concept of acoustic-mechanical coupling is explained.

General Brief about pulsation

Pulsations are the pressure and flow variations in gases and liquids that propagate in the pipe systems and fluid machinery. Every pulsation consists of a pressure pulsation wave and a flow pulsation wave. It found that where the pulsation is high, flow pulsation is low and vice versa. Always pulsation propagate with speed of sound in the gas. Pulsation should be controlled in order to avoid dangerous vibration & fatigue in the pipe system, ensure the integrity of the pipe system, get optimum performance of machinery like compressor and pump, achieve high flow meter accuracy, Control Noise.

Effect of Pulsation

The pulsation that results in high shaking forces can cause excessive vibration in a piping system. However, excessive vibration can occur even in cases where the dynamic forces are low if an excitation frequency is close to, or coincides, with a mechanical natural frequency. In this case, vibration will be amplified, typically a factor of 5 through 10 compared to the off-resonance condition. The amplitude at resonance is limited by the damping of the system. The Pulsation cause pipe vibrations and subsequently failures due to fatigue of the material, reduce compressor efficiency, produce noise, cause errors or inaccuracy in the flow metering, reduce the lifecycle of the compressor valves.

Pulsation Control Methods

The pulsation control in compressor piping systems can be accomplished by application of the basic acoustic elements of acoustical compliance (volume), acoustical inductance (choke tube), and resistance (pressure drop). These elements can be used individually or combined in various manners to achieve pulsation control. The pulsation suppression devices range from single surge volumes (empty bottles) to acoustic filters (bottles with internals or utilizing secondary volumes), often used in conjunction with orifice plates. The user should understand that this discussion is not intended to enable one to design these elements themselves.

Spread of Pressure Wave

Excitation Sources

In systems utilizing positive displacement machinery, the flow of gas or liquid is not steady. Instead, the fluid moves through the piping in a series of flow pulses (dynamic or time varying), which are superimposed upon the steady (average) flow. As an example, the magnitude and shape of the flow pulses through the compressor valves in a reciprocating compressor cylinder are determined by physical, geometrical and mechanical characteristics of the compressor (rotational speed, bore, stroke, loading, compression ratio, etc.). These flow pulses act as excitations which create pressure and flow modulations (acoustic waves) that move through the process fluid as it moves through the piping system. Generally, the predominant pressure and flow modulations generated by a reciprocating compressor are at frequencies which can be modeled as one-dimensional waves. An important part of the acoustic analysis is the development of a compressor model that accurately predicts the dynamic flow excitation (flow versus time) delivered by the compressor. Some simplified examples are shown in Fig.: 3.1, Fig.: 3.2, Fig.: 3.3, and Fig.: 3.4.

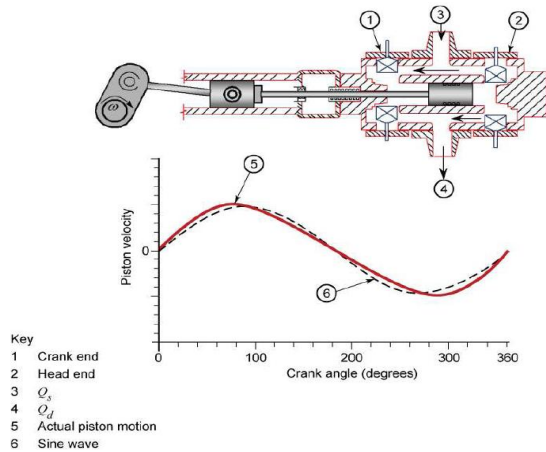


Fig.: 3.1 — Piston Motion and Velocity for a Slider Crank Mechanism

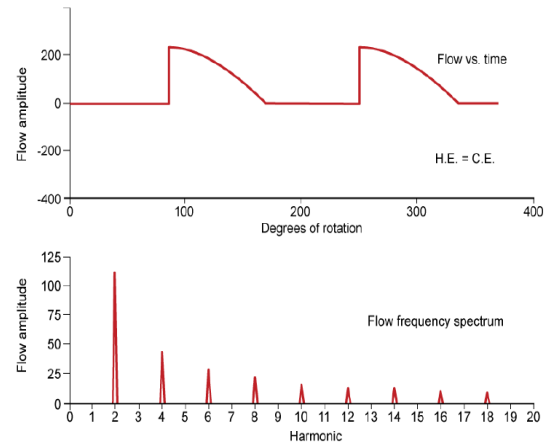


Fig.: 3.3 — Symmetrical, Double Acting Compressor Cylinder with Rod Length/Stroke = ∞ and No Valve Losses

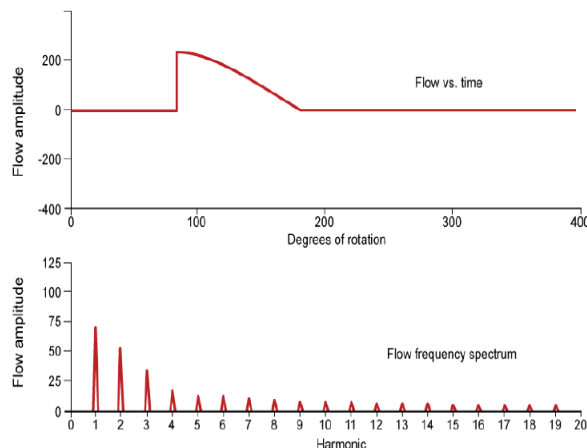


Fig.: 3.2 — Single Acting Compressor Cylinder with Rod Length/Stroke = ∞ and No Valve Losses

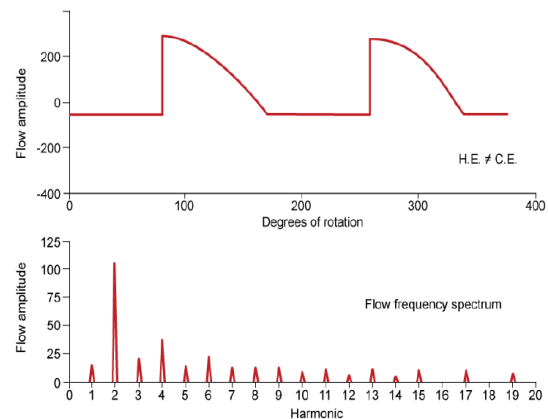


Fig.: 3.4 — Unsymmetrical, Double Acting Compressor Cylinder with Rod Length/Stroke = 5 and No Valve Losses

Acoustic Response and Resonance

The flow pulses caused by the reciprocating action of the compressor or pump create pressure pulses or waves that move through the piping system as shown in Fig.: 5.

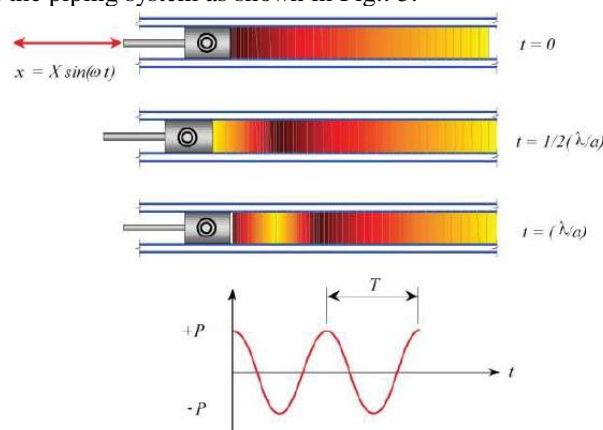


Fig.: 3.5 — Traveling Wave in Infinite Length Pipe

While the flow pulse frequencies generated by the compressor are a function of the mechanical properties of the compressor, the acoustical response in the piping is a function of the mechanical properties of the compressor, the thermo physical properties of the gas, and the acoustical network defined by the attached

piping. When a particular harmonic of running speed is near or coincident with an acoustical natural frequency, the acoustic response (dynamic pressure amplitude) is amplified. These resonances that occur when an excitation frequency coincides with a natural frequency can be simple organ-pipe type resonances or complex modes involving all of the piping. For simple constant diameter lines with open and/or closed boundary conditions, specific pipe lengths determine acoustical natural frequencies. If a line length coincides with integer multiples of one half or one quarter of the wavelength, depending on the combination of open or closed end conditions, an acoustical resonance can be excited. End conditions are defined as either open or closed. For half wave resonances, both end conditions must be the same, i.e. open-open or closed-closed. For quarter wave resonances, the end conditions must be opposite, i.e. one open end and one closed end. Examples of these configurations are shown in Fig.: 6 and Fig.: 7, and are defined by following Equations.

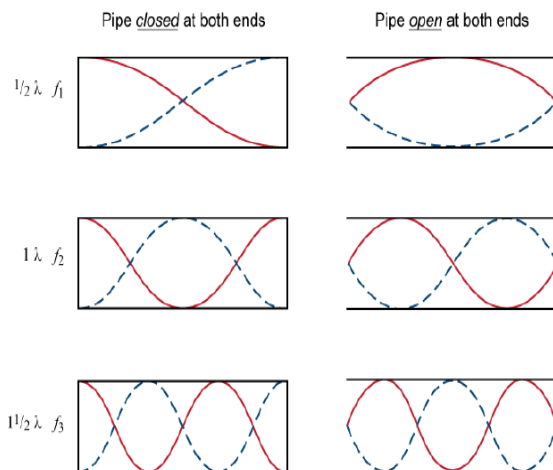


Fig.: 3.6 — Mode Shapes of Half Wave Responses

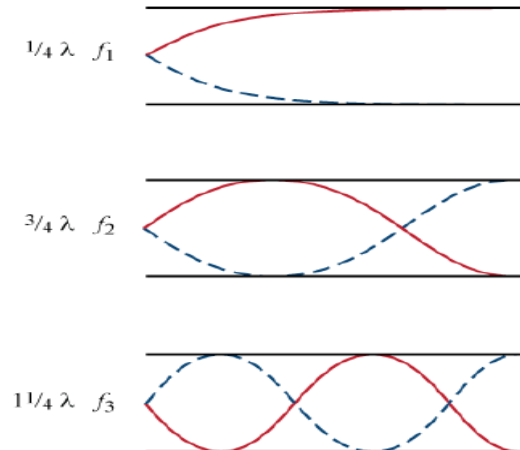


Fig.: 3.7 — Mode Shapes of Quarter Wave Responses

Formula for half wave (closed-closed and open-open acoustic response frequency):

$$f = \frac{na}{2L}$$

Formula for quarter wave (open-closed acoustic response frequency):

$$f = \frac{na}{4L}$$

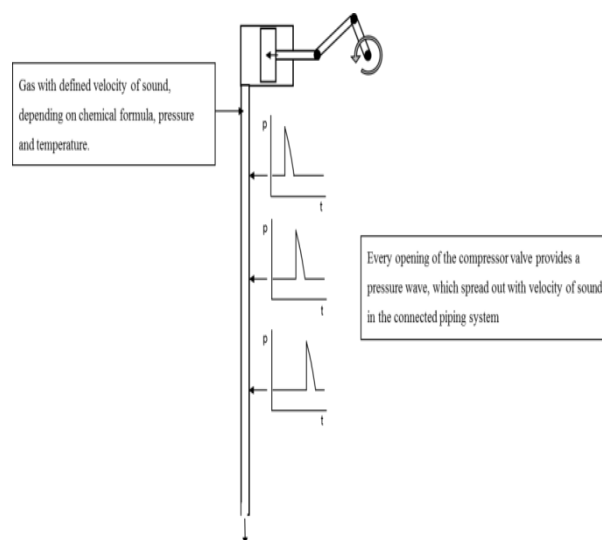


Fig.: 3.8 — Pulsation Wave Form

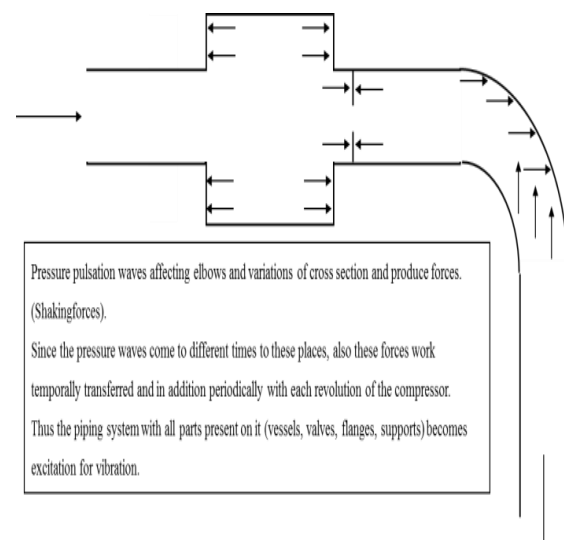


Fig.: 3.9 — Propagation of Pulsation Wave

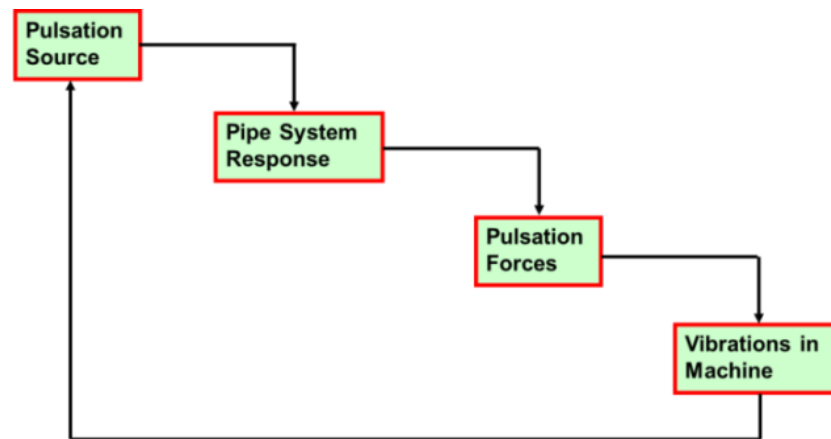


Fig.: 3.10 — Pulsations and Vibrations – the mainline

Pulsation and Vibration Study – The Mainline

Pulsation study

The Pulsations Study defined the height of the pulsations and describes measures to reach the pulsation limits.

The pulsation limits are most according API 618, Approach 2. The calculation program used for this analysis is Pulsim 3.1 which is developed by M/S TNO, Netherland. The more details about this will discuss in chapter III.

Vibration study

Vibrations are mechanical oscillation in a plant, which can occur in pipes, vessels and beam structures. The vibration provides cyclic stress and can lead to fatigue break of the piping system.

In the vibrations study the dynamic behavior of the piping system is investigated and the necessary measures are described to reach the vibration limits. Base of the vibration study is the previous performed Pulsation Study. The Limits are most according API 618, Approach 3. The calculation program used for this analysis is ANSYS. The more details about this will discuss in chapter IV.

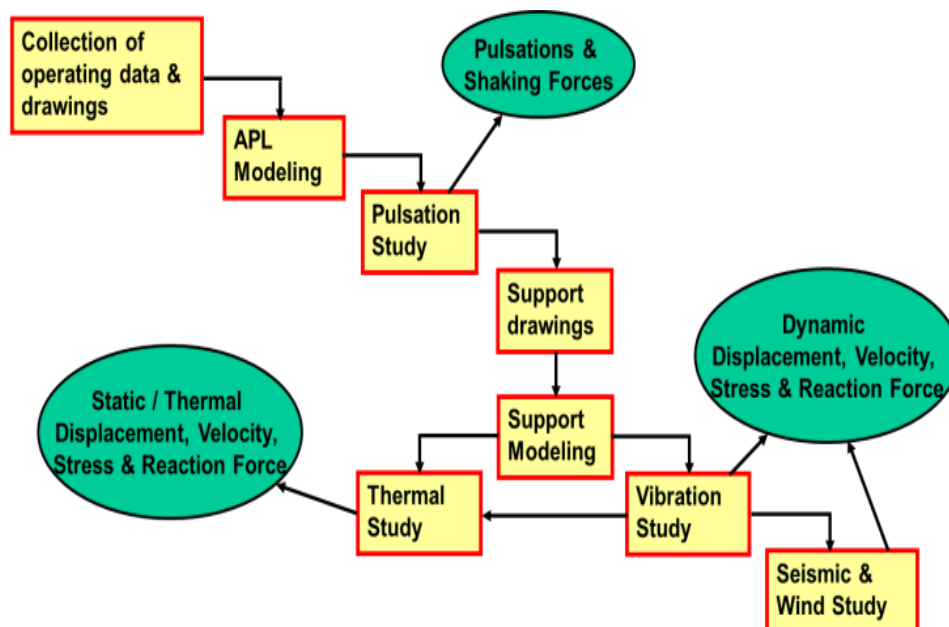


Fig.: 3.11 — Pulsation and Vibration Study – the mainline

IV. STUDY OF PULSATION ACCORDING TO API 618 (ANALYTICAL METHOD)

According Design Approach 2 of API Standard 618 5th edition 2007, an acoustic simulation is required to evaluate and control pulsation in piping systems at reciprocating compressors. The pulsation report contains a summary of the pressure pulsations in the piping system as well as modification proposals to reduce pulsation to the agreed level. The original system layout will be checked with respect to pulsation. All operating cases that are characterized by steady-state operating conditions will be checked, thus transient cases (e.g. start-up-cases) are excluded. Different gas properties and operation cases are considered. Valve unloading cases are considered as operation cases. Measures are proposed to reduce pressure pulsation, e.g. installation of orifices, changes in piping length or diameter. Shaking forces are used in the subsequent vibration study.

Used Documents for Pulsation Study

The exact gas data means gas composition and gas properties like velocity of sound, density, pressure, temperature flow for which compressor is going to use is considered for the pulsation simulation. Also the Isometric drawings of piping and compressors are used for the pulsation simulation.

Table : 4.1 — Gas Properties / Input Data for Pulsation Simulation

Index	Name	Load case:	Unit	1	2	3	4	5	6
				EOR 100%	SOR 100%	Low Purity alt design case	EOR 50%	SOR 50%	Low Purity alt design case 50%
1	1st stage suction	VOS	[m/s]	1358.8	1358.8	876.9	1358.8	1358.8	876.9
		density	[kg/m ³]	1.521	1.521	3.531	1.521	1.521	3.531
		FFF	[-]	0.005	0.005	0.005	0.005	0.005	0.005
		pressure	[bar]	19.8	19.8	19.8	19.8	19.8	19.8
		temperature	[°C]	40	40	40	40	40	40
		flow	[kg/h]	486	487	1136	226	227	530
		wave length	[m]	109.9	109.9	70.9	109.9	109.9	70.9
2	1st stage discharge	VOS	[m/s]	1506.5	1504.4	960.6	1510.8	1508.7	963.4
		density	[kg/m ³]	2.466	2.457	5.831	2.499	2.491	5.923
		FFF	[-]	0.005	0.005	0.005	0.005	0.005	0.005
		pressure	[bar]	39.21	38.98	39.24	39.97	39.73	40.09
		temperature	[°C]	107	106	100	109	108	102
		flow	[kg/h]	486	487	1136	226	227	530
		wave length	[m]	121.8	121.6	77.7	122.2	122.0	77.9
3	Cooler I-2	VOS	[m/s]	1440.9	1439.8	924	1444.5	1443.3	926.2
		density	[kg/m ³]	2.669	2.658	6.260	2.708	2.696	6.365
		FFF	[-]	0.005	0.005	0.005	0.005	0.005	0.005
		pressure	[bar]	38.74	38.515	38.74	39.49	39.255	39.58
		temperature	[°C]	73.5	73	70	75	74.5	71.5
		flow	[kg/h]	486	487	1136	226	227	530
		wave length	[m]	116.5	116.4	74.7	116.8	116.7	74.9
4	2nd stage suction	VOS	[m/s]	1372.2	1372	885.5	1374.8	1374.7	887.2
		density	[kg/m ³]	2.917	2.900	6.772	2.962	2.945	6.895
		FFF	[-]	0.005	0.005	0.005	0.005	0.005	0.005
		pressure	[bar]	38.27	38.05	38.24	39.01	38.78	39.07
		temperature	[°C]	40	40	40	41	41	41
		flow	[kg/h]	486	487	1136	226	227	530
		wave length	[m]	111.0	110.9	71.6	111.2	111.2	71.7
5	2nd stage discharge	VOS	[m/s]	1516.5	1506.9	969.3	1514.6	1505.8	968.1
		density	[kg/m ³]	4.436	4.327	10.465	4.448	4.401	10.494
		FFF	[-]	0.005	0.005	0.005	0.005	0.005	0.005
		pressure	[bar]	70.2	67.68	70.2	70.2	68.68	70.2
		temperature	[°C]	100	96	94	99	95	93
		flow	[kg/h]	486	487	1136	226	227	530
		wave length	[m]	122.6	121.9	78.4	122.5	121.8	78.3

Calculation and Interpretation of Analytical Results

The study of the gas pulsation is carried out with the digital simulation program PULSIM which has been developed by the TNO/TPD Institute in Delft (NL). A system of pipes is built of several complicated parts and elements which must be simplified for calculations. For example volumes of a cylinder casing between valves and connecting flange, heat exchangers, separators, dampers, etc. The data of the gas might also change during operation. In order to take these uncertainties into account, we make several calculations at different velocities of sound. The range of variation is $\pm 12\%$ and it is varied in steps of 2%. The results are presented in tables.

Admissible limits

The main requirements of API618 are as follows:

[API618, section 7.9.4.2.5.2.2.2] "For systems operating at absolute line pressures between 3.5 bar and 350 bar (350-35'000 kPa), the peak-to-peak pulsation level of each individual pulsation component shall be limited to that calculated by (in SI units):"

$$P_1 = \sqrt{\frac{a}{350} \left(\frac{400}{\sqrt{P_L \cdot D_L \cdot f}} \right)}$$

With the following equation for the frequency f

$$f = \frac{rpm \cdot N}{60}$$

For absolute pressures less than 3.5 bar, the peak-to-peak levels of individual pulsation components need only meet the levels calculated for an absolute pressure of 3.5 bar.

Outcome of Pulsation Study for 1st Stage Suction

With the original system layout the pulsations are too high. The dominant order of pulsation is primarily the 1st & 2nd order. The 1st stage suction side showed slightly increased pulsation, the worst case was the EOR 50% regulation of case 4 which reached 4.3% ptp. At the state of realization a change in piping was not practicable; orifices were used to dampen the pulsation to the possible minimum. The residual pulsation is still above the API limit. With orifices the worst case reached values 1.4 times higher than the API Limit. For the calculation of the vibration analysis we use the case with the highest pulsation with its shaking forces. With this procedure we ensure that the increased pulsation does not affect the piping stability. The vibration study however showed throughout acceptable values for the suction system. A reason for this is the relatively small shaking forces due to the relatively low pressure pulsation. No modifications of the piping were made on the suction side. The original system and orifices with only a small pressure drop gives satisfying pulsation results. With the recommended modification no. 5, we achieve satisfied results. The following table shows the highest value of the pulsation at different deviation of velocity of sound for design case at some representative nodes..

Table : 4.2 — A Few Suction Calculation Results for Different Load Cases

Case No.	Case 1	Case 1	Case 4	Case 4	Case 6	Case 6
System No.	1	1	4	4	6	6
Load case	EOR 100%	EOR 100%	EOR 50%	EOR 50%	Low Purity alt design case 50%	Low Purity alt design case 50%
Modification No.	0	5	0	5	0	5
Orifice RO-FAD1-I	No orifice	33.00 mm	No orifice	33.00 mm	No orifice	33.00 mm
Orifice RO-FAD1-O	No orifice	92.00 mm	No orifice	92.00 mm	No orifice	92.00 mm
Node 120	0.54/-	0.34/-	3.0/2.3	1.9/1.4	1.4/+	0.88/+
Node 370	1.5/-	1/-	3.2/1.1	2.1/+	4.2/1.3	2.1/+
Node 810 (Cyl flange)	1.4/-	1.3/-	4.3/+	3.4/-	3.0/-	3.0/-
Recommended		X		X		X

Following are the recommended orifices with locations :

Table : 4.3 — Recommended Orifices for Suction Side

Orifice	Location	Orifice ID (mm)	Line-inner Dia (mm)	Pressure drop [%] Design 100% (EOR 100%)	
RO-FAD1-I	1 st stage Suction Damper FAD1 inlet	33.00	78.00 (3")	0.81%	0.160 bar
RO-FAD1-O	1 st stage Suction Damper FAD1 outlet	92.00	92.00 (4")	0.00%	0.000 bar

Outcome of Pulsation Study for Interstage

With the original system layout the pulsations are too high. The dominant order of pulsation is primarily the 1st & 2nd order. The interstage showed high pulsation, the worst case was the EOR 50% regulation of case 14 which reached 6.0% ptp. At the state of realization a change in piping was not practicable; orifices were used to dampen the pulsation to the possible minimum. For the calculation of the vibration analysis we use the case with the highest pulsation with its shaking forces. With this procedure we ensure that the increased pulsation does not affect the piping stability. The vibration study however showed throughout acceptable values for the interstage system. A reason for this is the relatively small shaking forces due to the relatively low molecular weight. No modifications of the piping were made on the interstage side. The original system and orifices with only a small pressure drop gives satisfying pulsation results. With the recommended modification no. 5, we achieve satisfied results. The following table shows the highest value of the pulsation at different deviation of velocity of sound for design case at some representative nodes.

Table : 4.4 — A Few Interstage Calculation Results for Different Load Cases

Case No.	Case 1	Case 1	Case 4	Case 4	Case 6	Case 6
System No.	11	11	14	14	16	16
Load case	EOR 100%	EOR 100%	EOR 50%	EOR 50%	Low Purity alt design case 50%	Low Purity alt design case 50%
Modification No.	0	5	0	5	0	5
Orifice RO-FAD2-I	No orifice	31.00 mm	No orifice	31.00 mm	No orifice	31.00 mm
Orifice RO-FAD2-O	No orifice	31.00 mm	No orifice	31.00 mm	No orifice	31.00 mm
Orifice RO-FAD3-I	No orifice	35.00 mm	No orifice	35.00 mm	No orifice	35.00 mm
Orifice RO-FAD3-O	No orifice	35.00 mm	No orifice	35.00 mm	No orifice	35.00 mm
Node 2070 (Cyl flange)	3.5/-	3.9/+	6.2/+	4.4/+	3.7/+	5.2/+
Node 2390	3.3/2.6	1.3/+	3.8/1.7	1.6/+	4.0/2.8	1.6/+
Node 3030	1.1/+	0.22/-	1.3/+	0.57/-	0.63/-	0.27/-
Node 3190 (Cyl flange)	3.7/+	1.4/-	2.6/-	2.1/-	3/-	3.1/-
Recommended		X		X		X

Following are the recommended orifices with locations :

Table : 4.5 — Recommended Orifices for Interstage

Orifice	Location	Orifice ID (mm)	Line-inner Dia (mm)	Pressure drop [%] Design 100% (EOR 100%)
RO-FAD2-I	1st stage Discharge Damper FAD2 inlet	31.00	92.00 (4")	0.37%
RO-FAD2-O	1st stage Discharge Damper FAD2 outlet	31.00	67.00 (3")	0.32%
RO-FAD3-I	2 nd stage Suction Damper FAD3 inlet	35.00	67.00 (3")	0.15%
RO-FAD3-O	2 nd stage Suction Damper FAD3 inlet	35.00	67.00 (3")	0.15%

Outcome of Pulsation Study for 2nd Stage Discharge

With the original system layout the pulsations are too high. The dominant order of pulsation is primarily the 1st & 2nd order. The discharge stage showed high pulsation, the worst case was the Low Purity alt design case 50% regulation of case 26 which reached 4.3% ptp. At the state of realization a change in piping was not practicable; orifices were used to dampen the pulsation to the possible minimum. For the calculation of the vibration analysis we use the case with the highest pulsation with its shaking forces. With this procedure we ensure that the increased pulsation does not affect the piping stability. The vibration study however showed throughout acceptable values for the interstage system. A reason for this is the relatively small shaking forces due to the relatively low molecular weight. No modifications of the piping were made on the discharge stage. The original system and orifices with only a small pressure drop gives satisfying pulsation results. With the recommended modification no. 5, we achieve satisfied results.

Table : 4.6 — A Few Discharge Calculation Results for Different Load Cases

Case No.	Case 1	Case 1	Case 4	Case 4	Case 6	Case 6
System No.	21	21	24	24	26	26
Load case	EOR 100%	EOR 100%	EOR 50%	EOR 50%	Low Purity alt design case 50%	Low Purity alt design case 50%
Modification No.	0	5	0	5	0	5
Orifice RO-FAD4-I	No orifice	23.00 mm	No orifice	23.00 mm	No orifice	23.00 mm
Orifice RO-FAD4-O	No orifice	23.00 mm	No orifice	23.00 mm	No orifice	23.00 mm
Node 4070 (Cyl flange)	1.7/-	2.9/-	1.5/-	2.0/-	2.3/-	3.5/-
Node 4170	0.93/-	0.87/-	0.92/-	0.87/-	0.99/-	0.78/-
Node 4490	1.4/1.5	0.61/-	2.2/1.3	0.96/-	3.5/2.5	1.2/+
Node 4640	1.2/+	0.37/-	2.2/1.4	0.83/-	3.4/2.4	1.0/+
Node 4950	1.4/*	0.83/-	2.4/1.6	1.2/+	4.2/2.7	2.0/*
Recommended		X		X		X

Table : 4.7 — Recommended Orifices for Discharge Side

Orifice	Location	Orifice ID (mm)	Line-inner Dia (mm)	Pressure drop [%] Design 100% (EOR 100%)
RO-FAD4-I	2 nd stage Discharge Damper FAD4 inlet	23.00	67.00 (3")	0.36%
RO-FAD4-O	2 nd stage Discharge Damper FAD4 outlet	23.00	49.00 (2")	0.29%

We recommend to install the following orifices:

Sketches of Piping for the Nodes of Pulsation Study

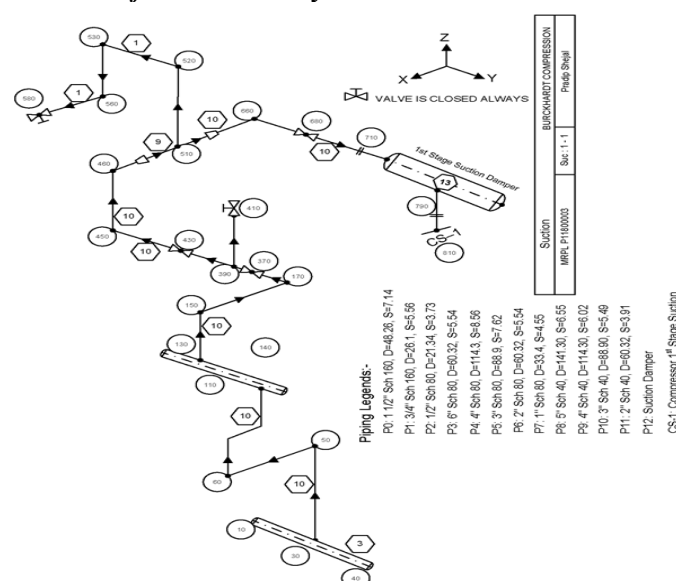


Fig.: 4.1 — Sketch of Suction Piping for Pulsation Study

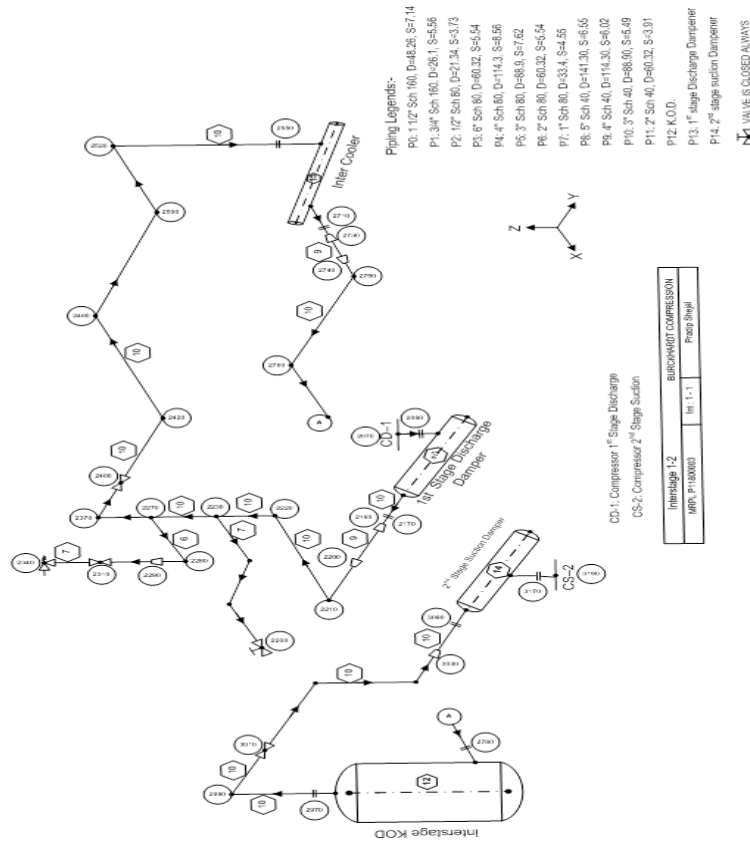


Fig.: 4.2 — Sketch of Interstage Piping for Pulsation Study

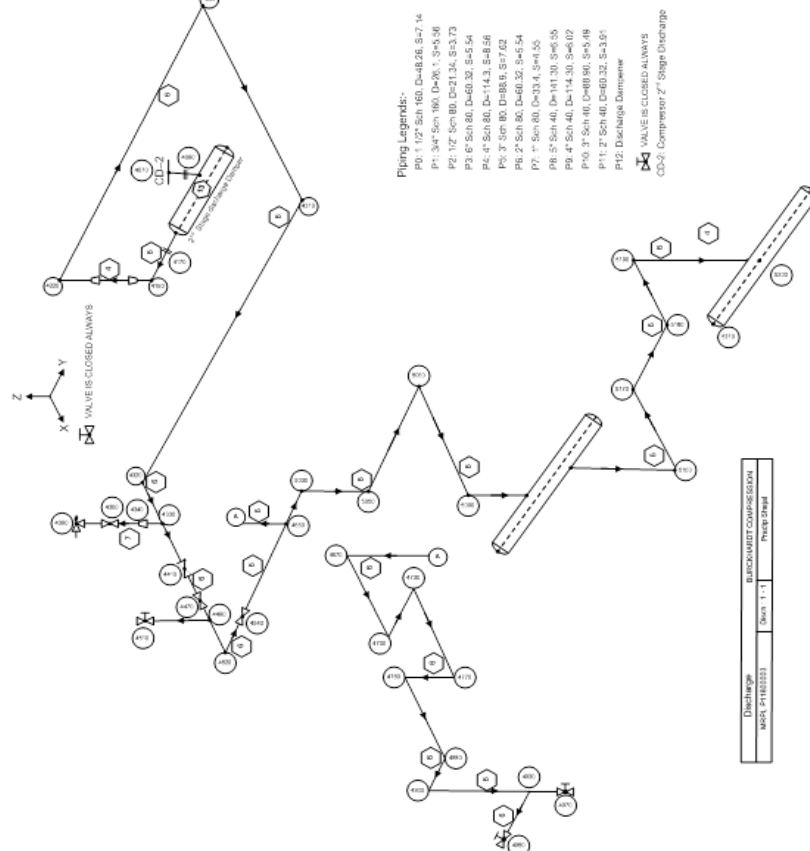


Fig.: 4.3 — Sketch of Discharge Piping for Pulsation Study

V. STUDY OF PIPING VIBRATION ACCORDING TO API 618

In this chapter the results for the vibration study for the compressor type can be found. The vibration study gives an overview of the dynamic behaviour of the piping systems. The natural frequencies and the corresponding modes are determined. In a second step the response of the system towards shaking forces which are caused by the pressure pulsation is calculated. The resulting displacement, velocity and bending stress values should not exceed certain limits.

The most critical case of the pressure pulsation is used for the dynamic analysis. Uncritical parts of the piping are not further investigated.

General Information

Modelling the vibration system

The system is modelled within the Finite Element Program ANSYS. It consists of a piping modelling tool, with several different elements and modelling possibilities. Elements are the connection between different nodes. The vibration study consists in general of the following ANSYS elements:

- BEAM4 : supporting structures
- COMBIN14 : spring supports
- PIPE16 : straight pipes & flanges / valves with specific mass and flexibility factors
- PIPE18 : pipe elbows

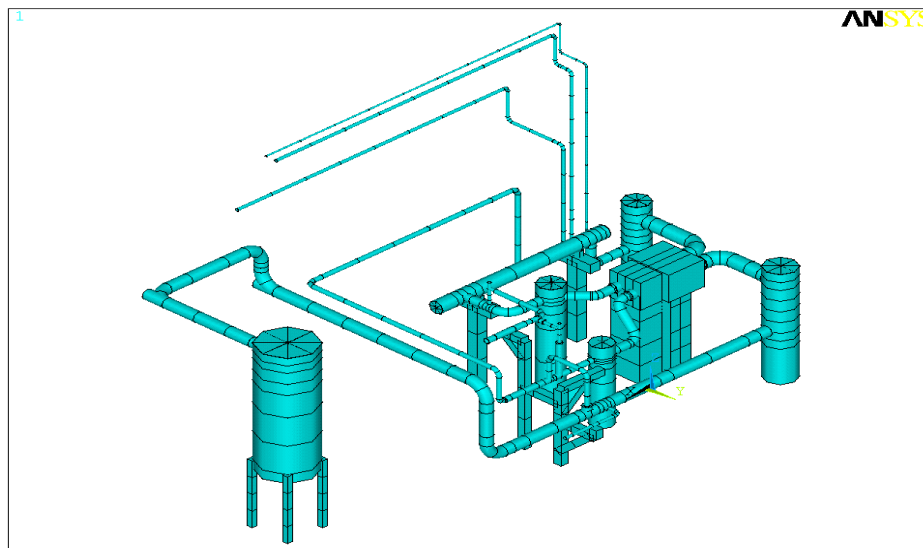


Fig.: 5.1 — Typical Finite Element Model

On the compressor skid our supports are modelled with beam elements, like in fig.: 1. On the customer side of the piping, supports are modelled by restricting at least one degree of freedom of a node. On request we model even the customer piping with supporting structures. Without restriction a node has six degrees of freedom, translations and rotations in each direction. These are the following four typical types of supports:

- Rest Support : restricting only translation in vertical direction
- Directional Guide : restricting translation in vertical and transversal directions
- Fixed Support : restricting translations in all directions
- Anchored Support : restricting translations and rotations in all directions

If friction forces are high enough, a support can possibly restrict an additional direction. For cases with a slight excess in vibration we check if this additional restriction can be furnished by the expected friction. For static thermal analyses, with in general higher force values than for vibration calculations, the friction is neglected.

Calculation procedure

The calculation for the vibration analyses is carried out in two steps.

The first step is the calculation of natural frequencies and mode shapes. This indicates which excitation frequencies will cause resonance effects, and which part of the system will be the most affected. This gives a general overview of the vibration behavior of the system.

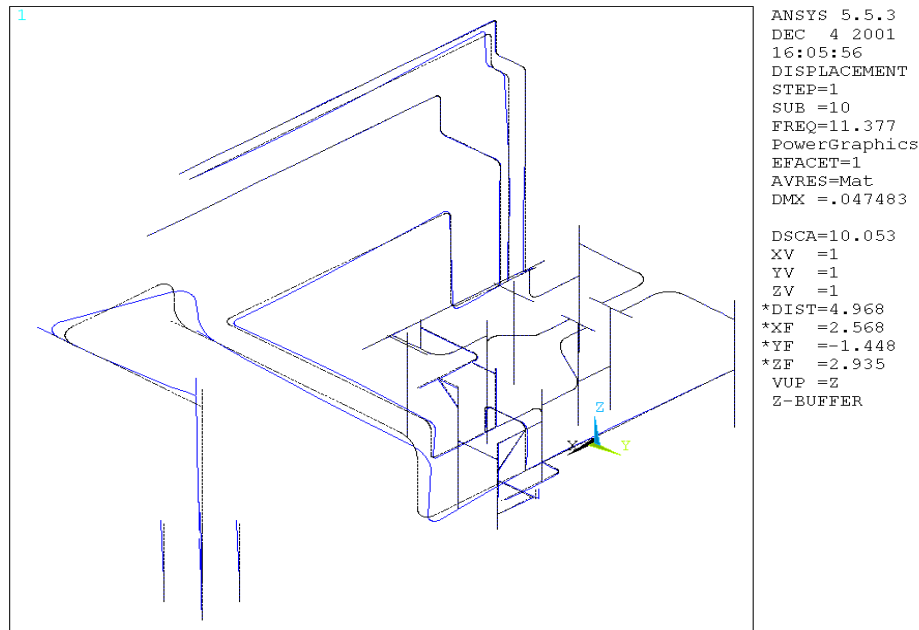


Fig.: 5.2 — Typical Finite Element Model (Wireframe)

In step two we perform a dynamic response analysis. The excitation comes from the shaking forces, which are a result of the pressure pulsation in the piping system. The forces are calculated with the PULSIM program (see pulsation study) and are given as harmonics of the compressor speed for the first twelve orders. Shaking forces occur in case of a change of the flow area or direction (inlet/outlet of a volume, elbows, orifices,...). We use the “worst case” shaking forces that means the forces from the calculated deviation of velocity of sound that delivered overall the highest values.

The results of this calculation are the dynamic displacements, vibration velocities and bending stresses of the pipes as well as the reaction forces on the supports. The peak-to-peak values are given in tables, and for nodes of special interest the time functions are plotted over one crank revolution. The peak-to-peak values are compared to the maximum allowable limit.

Admissible limits

According API 618 5th ed. the stress in the pipes should not exceed the endurance limit of the material used. For steel pipes the peak to peak cyclic stress should be less than 179 N/mm^2 including all stress concentration factors. Normally use a much lower limit of 45 N/mm^2 , because we do not know all locations of stress concentration, especially at welded pipes, and we allow for inaccuracies to a certain degree. Stress intensification factors at pipe elbows and tee pieces are taken into account, according to ANSI B31.1. An additional limit we use, which is not limited by API, is the maximum displacement value of 1 mm. A pipe vibrating at such a high level, may cause problems and will generally leave a bad impression of plant operation, even if stress limits are not exceeded. Moreover, we survey the vibration velocities at all nodes, which should not exceed 30 mm/s, according to our experience. The support loads are given as information only, and have to be checked individually by the customer, if supports could carry the calculated reaction force.

Guide to the Sketches

The node numbers for the following sketches are sorted by the following criterions:

- Node 1 - Node 84 and Node 118 - Node 374 for straight pipes
- Node 85 - Node 117 for the compressor model
- Node 375 - Node 440 for support constructions
- Node 441 - Node 647 for bends
- Node 648 - Node 713 for additional nodes near T connections

The numbers arise in the direction of the flow in the pipes.

Further details are given on the sketches.

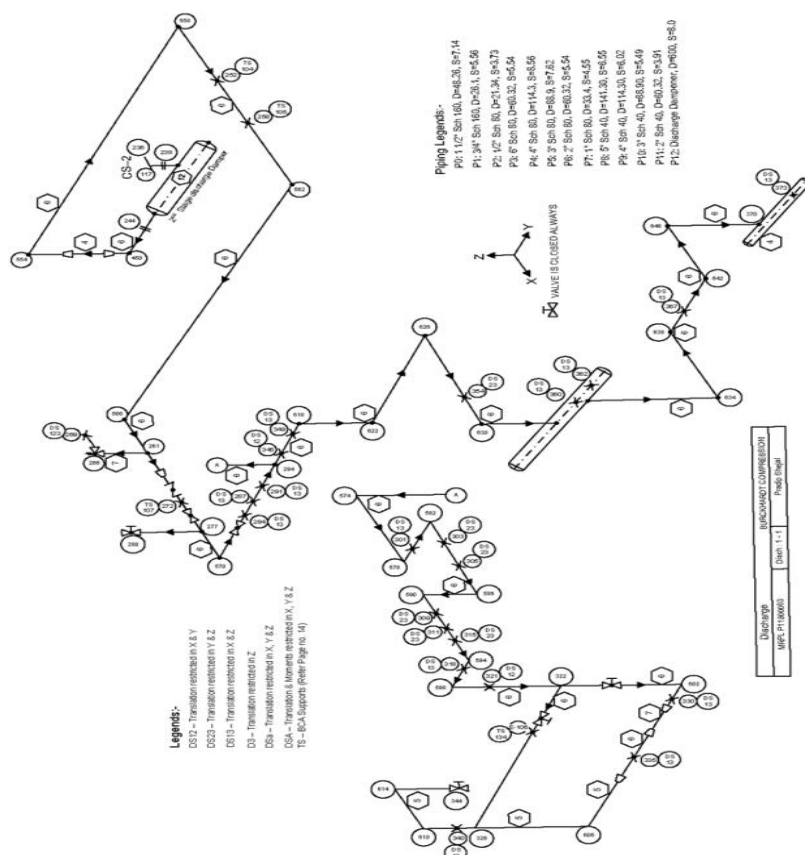


Fig.: 5.5 — Sketches of Discharge Piping for Vibration Study

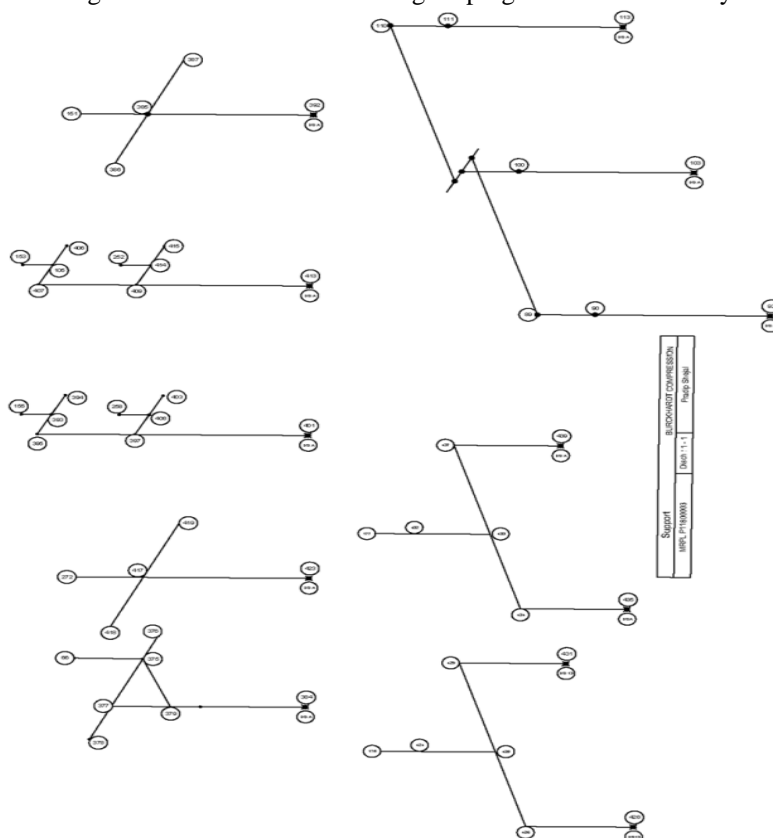


Fig.: 5.6 — Sketches of Support and Compressor

Detailed Results

Summary of Results

The investigation of the piping showed no severe problems with vibrations. One reason for this is the reduced pulsation level which is achieved from the modifications recommended in the pulsation study. The model for this vibration study includes the suction, interstage and discharge side. Therefore natural frequencies could be calculated once for whole system. For the dynamic response analysis we choose deviation of the velocity of sound with the highest pulsations of the worst case. These are the following load cases:

- for suction : Case 4, EOR 50% - Sys 4 Mod 5, variation of velocity of sound +12%
- for Interstage : Case 4, EOR 50% - Sys 14 Mod 5, variation of velocity of sound +12%
- for discharge : Case 6, Low Purity alt design case 50% - Sys 26 Mod 5, variation of velocity of sound +12%

The model contains the suction side starting at 6"-P-551093-B2A1-IT existing header, suction piping, interstage piping with cooler, KOD and PSV line, the discharge side with PSV-line and with the exiting header 4"-P-551107-B4A1-IH40. Relevant sidelines are also included in the calculation.

No change of piping layout is required except orifices which are already discussed for the pulsation study and also following support should be added into the piping layout.

- Support : X & Y at Node 345 : Refer Sketch
- Support : X & Z at Node 367 : Refer Sketch

After several calculations with the support modification all vibration results are within the limits.

The supports with its restricted direction of the last version are indicated in the attached isometrics. At the piping parts it was necessary to implement additional supports to achieve satisfied results. The details of all supports (blocked translations and rotations) in the calculation model can be found in the sketches of the system. These were discussed with the customer, including blocked translations and rotations for all supports.

The highest displacement occurs at the node 145 for the safety valve 554 for interstage piping before the interstage cooler EA-45555. The detailed picture of the displacement for this node (Appendix A4-1) shows influences of the 1st order. The model analysis of the part at node 145 shows resonance for a frequency around 12.942 Hz (16th eigenmode on fig.: 14). This value is close to the compressor frequency of the 1st order (12.37 Hz). All values of displacement at this nodes are within the limit.

The highest velocity occurs at the node 297 in the side line of the main discharge piping around Y-direction. The detailed picture of the displacement for this node (Appendix A4-1) shows influences of the 1st order. The model analysis of the part at node 297 shows resonance for a frequency around 12.882 Hz (15th eigenmode on fig.: 13). This value is close to the compressor frequency of the 1st order (12.37 Hz). All values of velocity at this nodes are within the limit.

The highest stress occurs at the node 140 in the safety valve 554 piping for interstage piping before the interstage cooler EA-45555. The detailed picture of the displacement for this node (Appendix A4-1) shows influences of the 1st order. The model analysis of the part at node 145 shows resonance for a frequency around 12.942 Hz (17th eigenmode on fig.: 14). This value is close to the compressor frequency of the 1st order (12.37 Hz). All values of stress at this nodes are within the limit. The highest reaction force occurs at the node 92 for the 1st stage cylinder support near to the 2nd stage discharge damper Z- direction. The detailed picture of the displacement for this node (Appendix A4-1) shows influences of the 1st order. The model analysis of the part at node 145 shows resonance for a frequency around 12.942 Hz (16th eigenmode on fig.: 14). This value is close to the compressor frequency of the 1st order (12.37 Hz).

An overview of the results is shown in following table 5.1.

Table : 5.1 — Maximum values for the dynamic response analysis

Dynamic response analysis	Operating Case: EOR 50% & Low Purity alt design case 50% (worst deviation for each stage) (with modified supports)	
		Limits
Lowest natural frequency [Hz]	1.6074	-
Max. displacement [mm] (abs value)	0.9685	1
Peak to peak worst case (node)	(145)	
Max. velocity [mm/s]	28.27	30
RMS (node/direction)	(297/Y)	
Max. bending stress [N/mm ²]	16.24	45
Peak to peak (node)	(140)	
Max. reaction force [N]	1216.2	-
Peak to peak (node/direction)	(92/Z)	

Many supports are described to be loose. Therefore the horizontal stiffness is extremely low. In reality the friction between pipe and supports will give an additional stiffness. That means, in reality lower displacements can be expected.

Plot of the model of calculation

Following are the few plots of the compressor package which is modelled in Ansys.

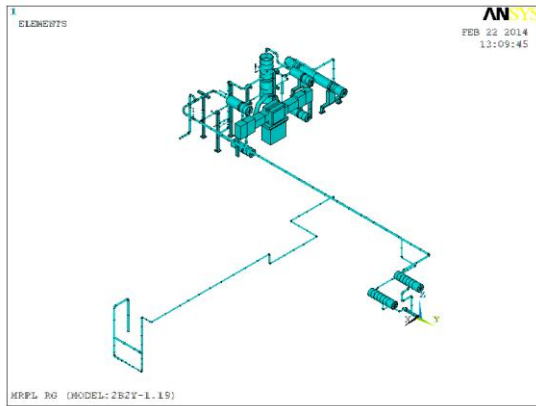


Fig.: 5.7 — Display of Elements for compressor package

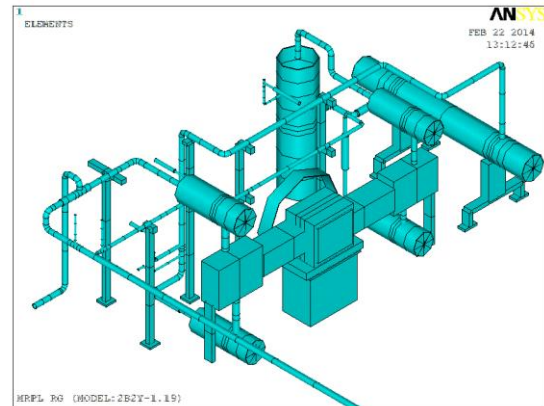


Fig.: 5.8 — Display of Elements for Compressor System

Plot of the model of calculation – Boundary Conditions

Following are the few plots of the compressor package with boundary conditions.

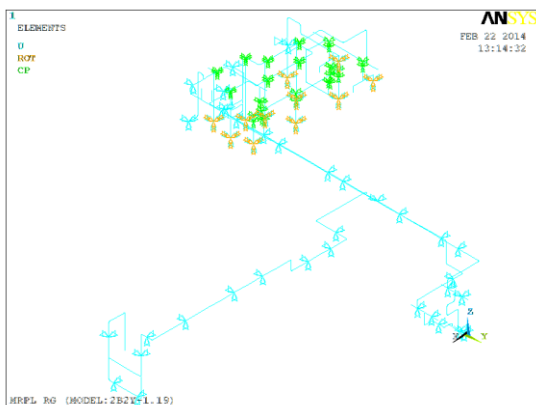


Fig.: 5.9 — Boundary Conditions for compressor package

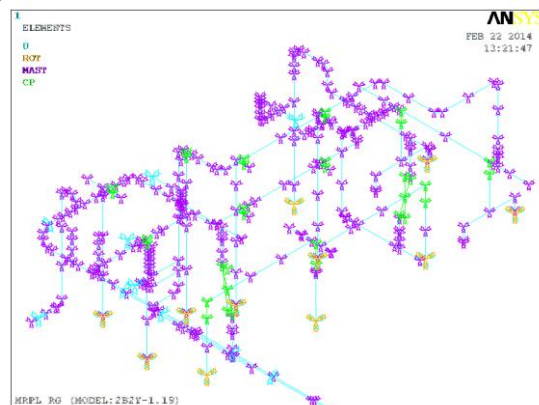


Fig.: 5.11 — Boundary Conditions with Master Nodes for Compressor System

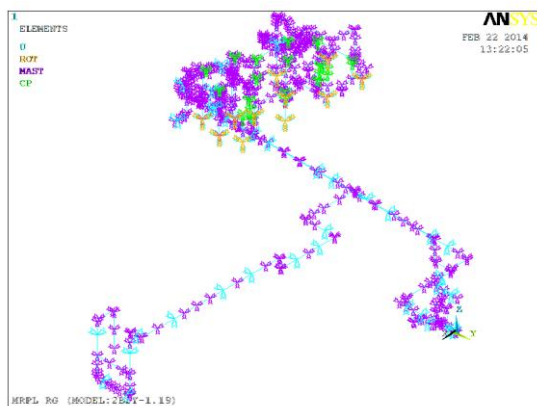


Fig.: 5.10 — Boundary Conditions with Master Nodes for compressor package

Natural frequencies and natural modes of the system

Table : 5.2 — The first 179 eigenmodes (out of 219) of the piping system model

SET	Frequency [Hz]
1	1.6074
2	5.1959
3	5.8717
4	5.9192
5	6.2108
6	6.9121
7	6.9535
8	8.6063
9	8.8348
10	9.5087

The first 10 eigenmodes (out of 219) of the piping system model. The shapes of some Eigenmodes are plotted on the following pages. Some Eigenmodes have to be considered as unrealistic since some boundary conditions are assumed. Therefore only selected Eigenmodes are plotted.

Plot of the mode shapes for the most important frequencies

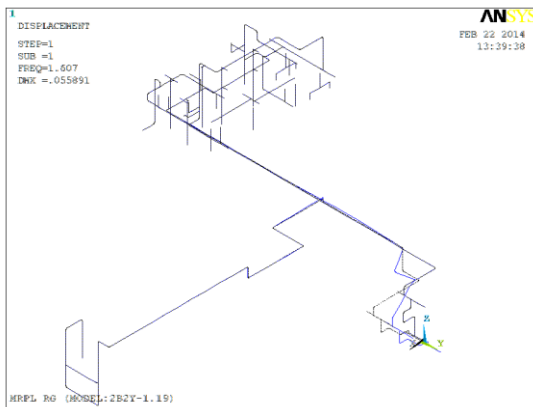


Fig.: 5.12 — Plot of the 1st Eigenmode (1.607 Hz)

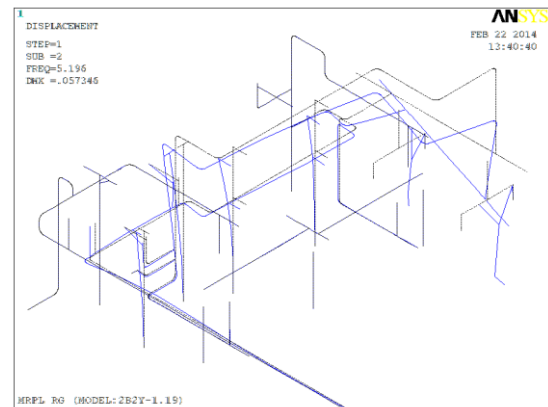


Fig.: 5.13 — Plot of the 2nd Eigenmode (5.196 Hz)

Plot of dynamic responses at selected nodes

Table : 5.3 - Dynamic displacements Peak-to-Peak in mm

Nodes	UX	UY	UZ	ABS
145	0.8888	0.0315	0.3887	0.9706
144	0.788	0.0001	0.3887	0.8786
143	0.6874	0.0295	0.3887	0.7902
142	0.5468	0.062	0.3886	0.6737
297	0.0908	0.61	0.2325	0.6591
298	0.091	0.5822	0.217	0.6279
598	0.3515	0.4971	0.0296	0.6095
577	0.0911	0.5115	0.3093	0.6047
578	0.0931	0.5061	0.3167	0.6043
599	0.3601	0.4822	0.0352	0.6028

Plot of dynamic displacements at selected nodes Peak-to-Peak in mm

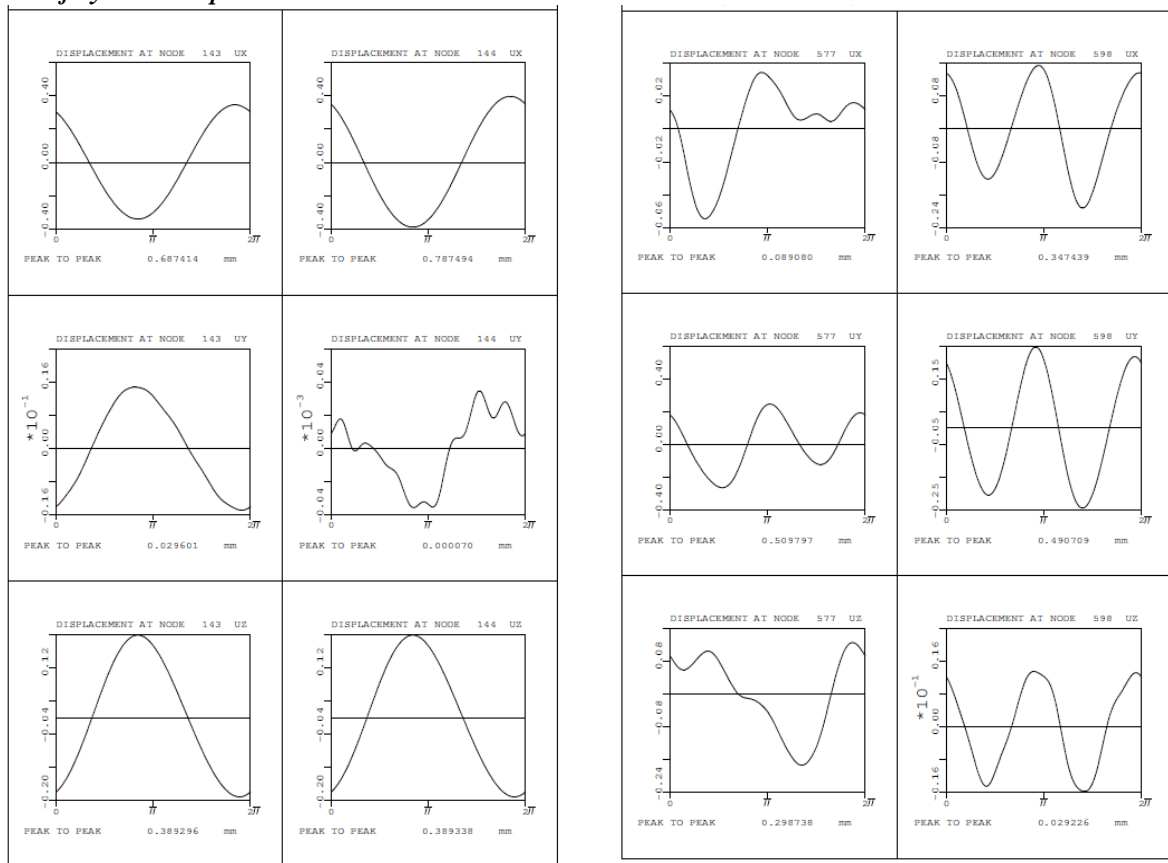


Fig.: 5.14 — Plot of Dynamic Displacements At Selected Nodes Peak-To-Peak in mm

Plot of dynamic responses at selected nodes

Table : 5.5 - Dynamic velocities RMS in mm/s

Nodes	UX	UY	UZ
297	3.37	28.32	7.47
298	3.38	26.38	6.49
595	13.45	25.64	0.98
318	0	25.64	0
597	14.72	25.64	1.19
598	16.98	25.43	1.63
594	15.85	24.7	1.1
599	17.42	24.67	1.91
145	24.56	0.87	10.66
622	23.96	9.28	1.64

Plot of dynamic velocities at selected nodes Peak-to-Peak in mm/s

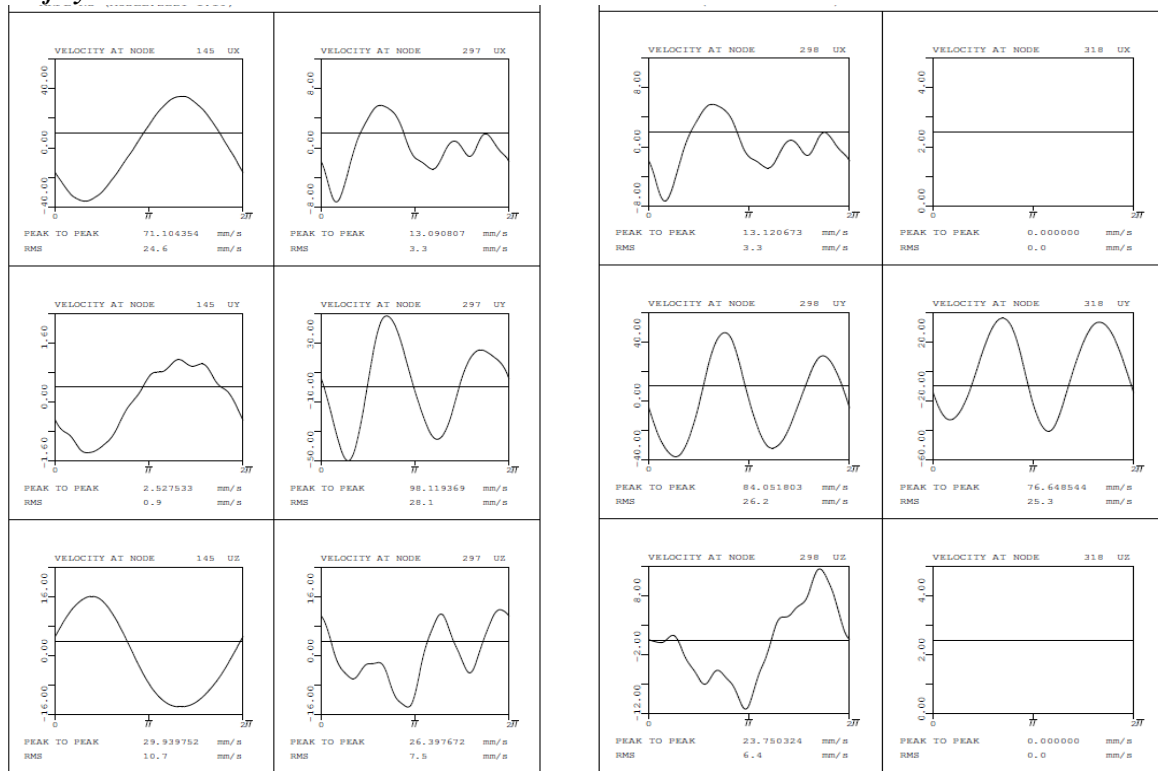


Fig.: 5.15 — Plot of Dynamic Velocities At Selected Nodes Peak-To-Peak in mm/s

Plot of dynamic responses at selected nodes

Table : 5.6 - Dynamic bending stresses Peak-to-Peak in N/mm²

Node	Stress	Element
140	16.29	129
582	13.26	490
141	13.12	129
144	13.01	134
501	12.96	449
583	12.59	490
581	12.5	489
138	11.77	548
593	11.5	495
361	11.38	585

Plot of dynamic bending stresses at selected nodes Peak-to-Peak in N/mm²

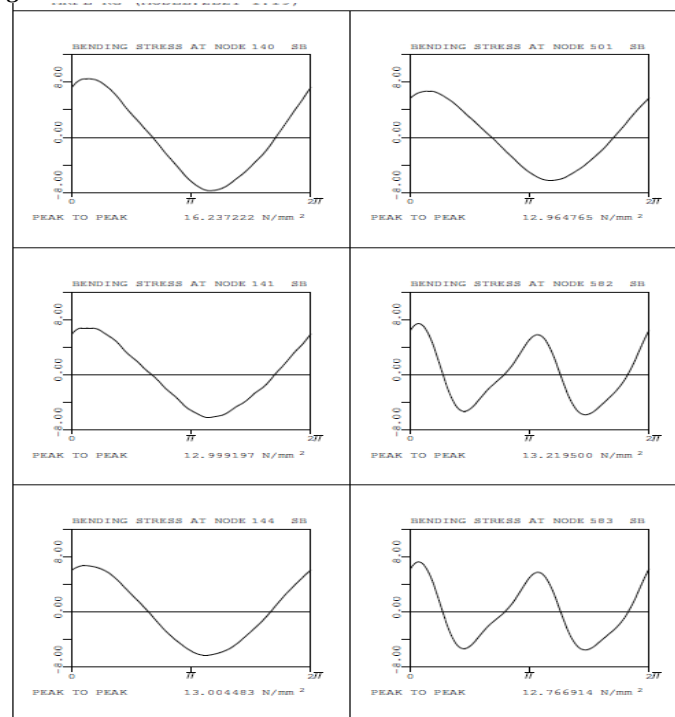


Fig.: 5.16 — Plot of Dynamic Bending Stresses At Selected Nodes Peak-To-Peak in N/mm²

VI. EXPERIMENTATION

Experimental set-up and Instruments

The arrangement of the experimental setup used for the measurements is shown below

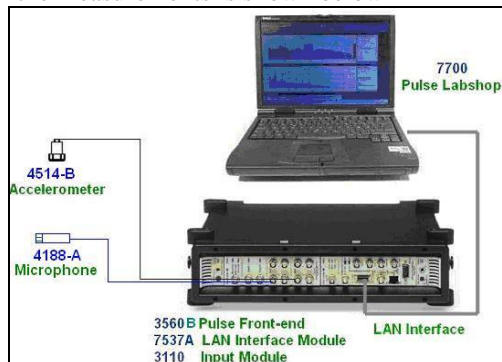


Fig.: 6.1 — Arrangement of Experimental Setup for Vibration Measurements

Table : 6.1 - List of Instruments used

Sr. No.	Instrument / Software	Remarks
1	B & K (Denmark) Make 5 channel PULSE Data Acquisition System (Analyzer) with BNC Connectors – Type 3560B with LAN Interface	Data Acquisition System
2	B & K (Denmark) Make IEPE Accelerometer – Type 4514B	Transducer for Vibration measurement
3	B & K (Denmark) Make Pulse FFT & CPB Analysis Labshop – Type 7700	Vibration & Noise Analysis Software

Experimental Procedure

The vibration measurements were carried out at rated load (EOR case) since EOR case is the design case for this compressor. The Experimental set-up and Instruments details are shown in above chapter VI. The measurements locations at different Nodes for vibration are shown in chapter V Sketches of Piping for Vibration Study.

Vibration Measurements:

Only few nodes 297, 595, 318, 145 and 599 are considered for vibration measurements, which are having very high vibrations. The vibration measured in all three directions (vertical, horizontal & axial) in accelerations for 1/3rd Octave center frequency over a range of 0 Hz to 8 KHz.

Result Analysis and Discussion

Results before Vibration Study (Experimental)

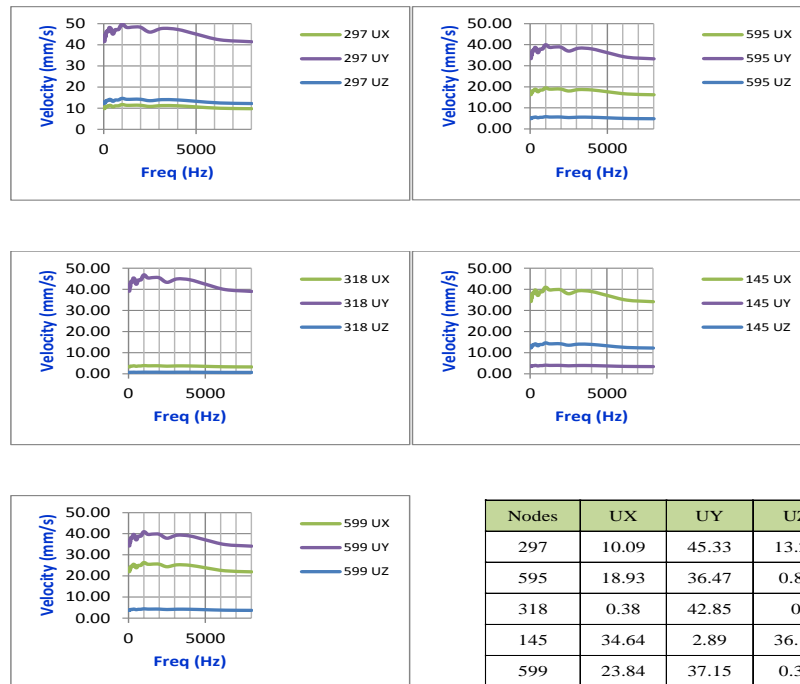


Table : 6.3 – Mean Values Before Vibration Study

The above graphs are the experimental results before Vibration Study means before the modifications into the support. The graphs shown for the five nodes and found that the velocities are the much higher than the specified limit i.e. 30 mm/s in API 618. The above table 6.3 is shown the mean values of the graphs.

Results after Vibration Study (Experimental)

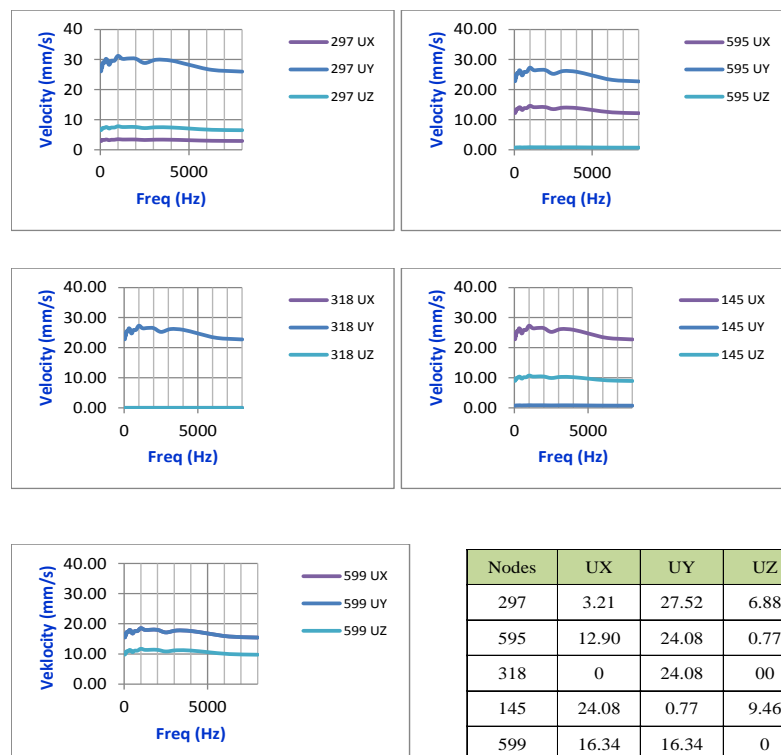


Table : 6.3 – Mean Values after Vibration Study

The above graphs are the experimental results after Vibration Study means after the modifications into the support. The graphs shown for the five nodes and found that the velocities are the much lower than the specified limit i.e. 30 mm/s in API 618. The above table 6.4 is shown the mean values of the graphs.

Results after Vibration Study (Analytical)

Table : 6.4 - List of Nodes with Maximum Velocities RMS in mm/s after Pulsation and Vibration Study (Analytical)

Nodes	UX	UY	UZ
297*	3.26	28.14	7.55
298	3.27	26.24	6.37
595*	13.29	25.29	0.97
318*	0	25.29	0
597	14.54	25.29	1.18
598	16.78	25.08	1.61
145*	24.55	0.87	10.66
594	15.66	24.36	1.09
599*	17.21	24.33	1.89
577	3.28	22.97	10.39

*- nodes are used for comparison with experimental results

The model for this vibration study includes the suction, interstage and discharge side. The model contains the suction side starting at 6"-P-551093-B2A1-IT existing header, suction piping, interstage piping with cooler, KOD and PSV line, the discharge side with PSV-line and with the exiting header 4"-P-551107-B4A1-IH40. Relevant sidelines are also included in the calculation.

The natural frequencies could be calculated once for the whole system. For the dynamic response analysis we choose the deviation of the velocity of sound with the highest pulsations of the worst case. The details about the worst case are mentioned in chapter V. No change of piping layout is required except orifices which are already discussed for the pulsation study and also following support should be added into the piping layout.

- Support : X & Y at Node 345 : Refer Sketch
- Support : X & Z at Node 367 : Refer Sketch

After several calculations with the support modification all vibration results are within the limits. The supports with its restricted direction of the last version are indicated in the attached isometrics. At piping parts it was necessary to implement additional supports to achieve satisfied results. The details of all supports (blocked translations and rotations) in calculation model can be found in the sketches of the system (chapter V).

VII. CONCLUSION

The investigation of the piping showed no severe problems with vibrations. One reason for this is the reduced pulsation level which is achieved from the modifications recommended in the pulsation study. The combination of the acoustic simulation with a mechanical analysis as defined in Design Approach 3 of API 618 is the content of the vibration study. Shaking forces induced by pressure pulsation excite the mechanical piping system. The vibration study determines the effect on the mechanical piping system and proposes measures to avoid stresses possibly leading to deformation or rupture by fatigue.

The finite element program ANSYS is used for modeling of the mechanical system. The model is built of several types of basic elements (e.g. pipes, beams, elbows, T-pieces) connected at node points. Modifications are proposed to meet agreed criteria of vibration as per API 618 5th edition (2007).

Since shaking forces are a result of the previous pulsation calculation, vibration study can only be done in combination with a preceding pulsation study.

Also the accuracy of the analytical solution had been validated by means of experimental results by using B & K Analyser for the measurement of compressor piping vibration.

REFERENCES

- [1.] Shelley Greenfield and Kelly Eberle, New API Standard 618 (5TH ED.) And Its Impact On Reciprocating Compressor Package Design, Compressor Tech^{TWO}, 2008, pp. 55-67.
- [2.] Paul Alves, Acoustical And Mechanical Analysis Of Reciprocating Compressor Installation - API 618, Compressor Tech^{TWO}, 2006, pp. 64-69.
- [3.] James D. Tison and Kenneth E. Atkins, The New Fifth Edition of API 618 for Reciprocating Compressors – Which Pulsation and Vibration Control philosophy should you use?, Engineering Dynamics Incorporated Seminar Manual, San Antonio, Texas, 2008.

- [4.] J. C. Wachel and J. D. Tison, Vibrations In Reciprocating Machinery And Piping Systems, Engineering Dynamics Incorporated Seminar Manual, San Antonio, Texas, 1999.
- [5.] Enzo Giacomelli et al., Forced Response of Cylinder Manifold For Reciprocating Compressor Applications, 8TH Biennial ASME Conference on Engineering Systems Design and Analysis, Torino, Italy, 2006.
- [6.] W. W. von Nimitz , Pulsation And Vibration Control Requirements In The Design Of Reciprocating Compressor And Pump Installations, International Compressor Engineering Conference, Purdue University, Indiana, USA, 1982.
- [7.] Reciprocating Compressors for Petroleum, Chemical, and Gas Industry Services. API Standard 618, Fourth Edition , June 1995.
- [8.] Reciprocating Compressors for Petroleum, Chemical, and Gas Industry Services. API Standard 618, Fifth edition, December 2007
- [9.] <http://www.betamachinery.com/>
- [10.] <http://www.tno.nl/>
- [11.] Ansys Software

BER Performance for Convolutional Code with Soft & Hard Viterbi Decoding

Umesh Kumar Pandey¹, Prashant Purohit²

¹MTECH Schooler, RITS, Bhopal

²HOD, Dept. of EC, RITS, Bhopal

Abstract: Viterbi decoding has a fixed decoding time. It is well suited to hardware decoder. Here we proposed Viterbi algorithm with Decoding rate 1/3. Which dynamically improve performance of the channel.

Keywords: Convolution code, Sova Decoder, Viterbi Decoding, soft & hard viterbi decoding, AWGN channel.

I. INTRODUCTION

In recent years, there has been an increasing demand for efficient and reliable digital data transmission and storage systems. This demand has been accelerated by the emergence of large-scale, high-speed data networks for the exchange, processing, and storage of digital information in the military, governmental, and private spheres. The two key system parameters available to the designer are transmitted signal power and channel bandwidth. These two parameters, together with the power spectral density of receiver noise, determine the signal energy per bit-to-noise power spectral density ratio E_b/N_0 . This ratio uniquely determines the bit error rate for a particular modulation scheme [1]. Practical considerations usually place a limit on the value that we can assign to E_b/N_0 . Accordingly, in practice, one can often arrive at a modulation scheme and find that it is not possible to provide acceptable data quality (i.e., low enough error performance). For a fixed E_b/N_0 , the only practical a prescribed rule, thereby producing encoded data at a higher bit rate. The channel decoder in the receiver exploits the redundancy to decide which message bits were actually transmitted. The combined goal of the channel encoder and decoder is to minimize the effect of channel noise. That is, the number of errors between the channel encoder input (derived from the source) and the channel decoder output (delivered to the user) are minimized.

There are many error-correcting codes, with roots in diverse mathematical disciplines that are used. Historically, these codes have been classified into block codes and convolutional codes. The distinguishing feature for this particular classification is the presence or absence of memory in the encoders for the two coding systems

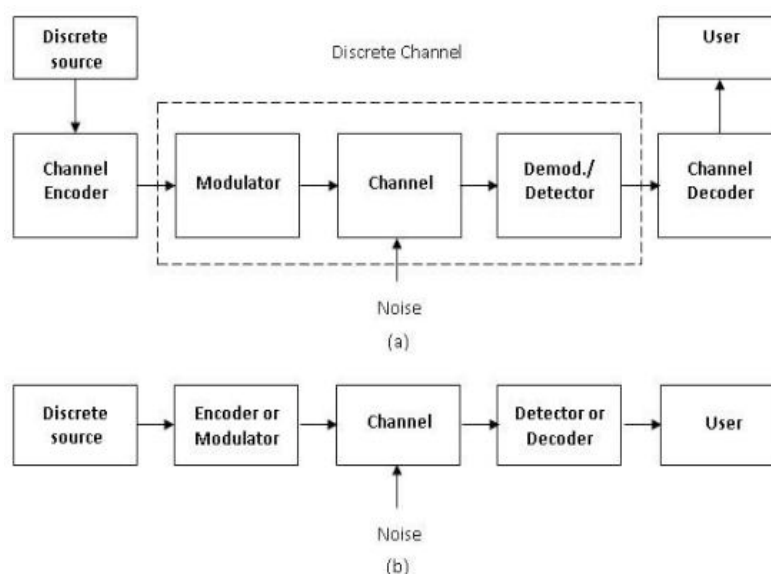


Fig. 1 Simplified models of digital communication system (a) Coding and modulation performed separately. (b) Coding and modulation combined

These Viterbi Decoding has the advantage that it has a fixed decoding time but its computational requirement grow exponentially as a function of the constraint length, so it is usually limitation in practice to constrain lengths of $V=9$ or less. Convolution code with 1/3 Coding Rate in BPSK and AWGN channel.

II. VITERBI ALGORITHM

Viterbi Decoding was developed by Andrew j. Viterbi in 1967 and in the late 1970's become the dominant technique for convolutional codes. The Viterbi algorithm is a dynamic programming algorithm for finding the most likely sequence of hidden states – called the Viterbi path – that results in a sequence of observed events, especially in the context of Markov information sources and hidden Markov models. The terms Viterbi path and Viterbi algorithm are also applied to related dynamic programming algorithms that discover the single most likely explanation for an observation. For example, in statistical parsing a dynamic programming algorithm can be used to discover the single most likely context-free derivation (parse) of a string, which is sometimes called the Viterbi parse.

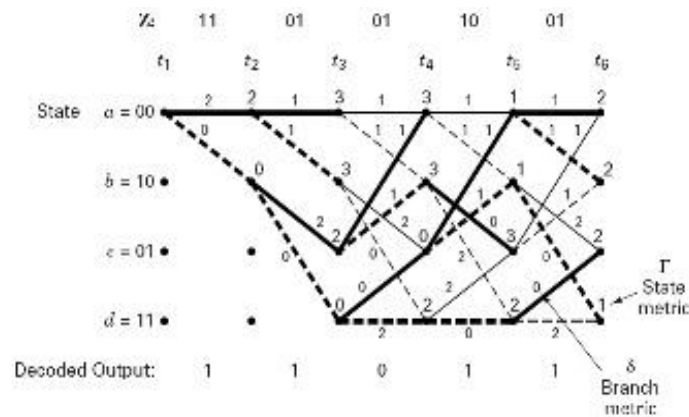


Fig. 2 : Trellis for the convolutional encoder

III. PROBLEM FORMULATION

With Viterbi Decoding the following advantage like:-

- 1) A highly satisfactory bit error performance
- 2) High speed of operation
- 3) Ease of implementation
- 4) Low cost

Most of all parameter I have tried to cover in given simulation.

Simulation Setup

The simulation setup is composed of three distinct parts, namely the encoder, the channel, and the decoder. The simulated convolutional encoder is use modulo-2 adder and shift register or constraint length (K) with code memory, of size m. In the simulation, the Additive White Gaussian Noise (AWGN) channel is used and Viterbi decoder is used as convolutional decoder for hard decision as well as soft decision

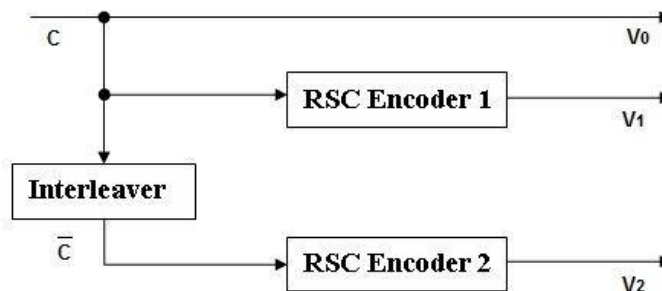


Fig. 3 : Fundamental turbo code encoder

Second, the simulation for the Turbo code encoder is composed of two identical RSC component encoders. These two component encoders are separated by a random interleaver. The random interleaver is a permutation of bit order in a bit stream. This permutation of bit order is stored so that the interleaved bit stream can be deinterleaved at the decoder. The output of the turbo code encoder is described by three streams, one systematic (uncoded) bit stream and two coded bit streams (parity bits), and SOVA decoder.

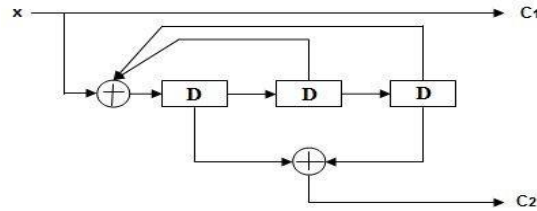


Fig. 4 RSC encoder

However, in many journal papers, the published computer simulations of above codes often use rate 1/2, 1/3, 2/3 and 3/4. This is accomplished by puncturing the coded bit streams of the above code

Comparison Table-

E b/No (dB)	Uncoded (BER)	BPSK (BER)	BER improved over Uncoded
1.5	4.46×10^{-2}	4×10^{-2}	13.8 %
2.5	2.9×10^{-2}	6.1×10^{-2}	79.46 %
3.5	1.7×10^{-2}	3.1×10^{-2}	98.16 %

Table 1. Result of convolutional code with BPSK modulation

E b/No (dB)	Uncoded (BER)	8-PSK (BER)	BER improved over Uncoded
6	2.05×10^{-2}	1.08×10^{-2}	47.11 %
7	1.2×10^{-2}	1.6×10^{-3}	86.34 %
8	6.2×10^{-3}	1.16×10^{-4}	98.11 %

Table 2. Result for Rate- 1/3 soft decision convolutional code

IV. SIMULATON RESULT

Simulation results for a convolutional code are based on bit error rate (BER) performance over a range of E b/ N o. The BER is simply the ratio of incorrect data bits divided by the total number of data bits transmitted. The SNR is computed by di-viding the energy per received data bit Eb by the single-sided noise spectral density no of the channel. For simulation rate 1/3,2/3 and 1/2 convolutional codes and turbo codes rates using two RSC encoder and interleaver is used.

First, the simulation results are shown for convolutional code using different modulation technique (BPSK, QPSK and 8-PSK) with rate 1/2 and different rate (using one modulation technique (BPSK) in AWGN channel. The simulation is carried out on the basis of BER improvement over uncoded BER given by equation:

$$\frac{\text{BER uncoded} - \text{BER coded}}{\text{BER uncoded}} \times 100\%$$

Second, the performance of rate turbo code encoder is shown with RSC encoder and SOVA

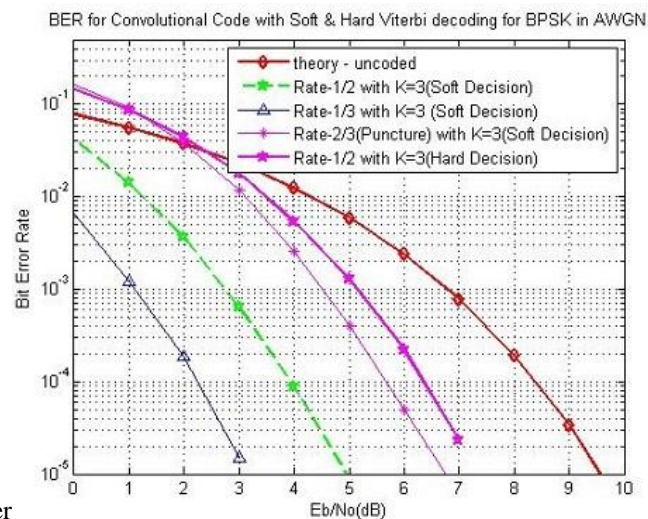


Fig. 5 Convolutional code with Different Coding Rate in BPSK and AWGN channel

V. CONCLUSION

After simulation it is showing that Decoding rate performance best with BPSK. simulations of the convolution codes has been carried out in the MATLAB. Viterbi Decoding is very powerful algorithm for AWGN channel.

REFERENCES

- [1] J. Hagenauer. "Source-controlled channel decoding." IEEE Trans. Commun., vol.43, pp. 2449-2457, 1995.
- [2] K. M. S. Soyjaudah and M. T. Rusool. "Comparative study of turbo codes in awgn channel using map and sova decoding". Department of Electrical and Electronic Engineering, University of Mauritius.2009
- [3] S. Lin J. Chen, M. P. Fossorier and C. Xu. "Bi-directional sova decoding for turbocodes".IEEE Commun. Lett., vol. 4, no. 12, pp. 405-408, 2000.
- [4] Lutz Papke, Patrick Robertson, "Improved Decoding with the SOVA in a Parallel Concatenated (Turbo-code) Scheme". France Telecom, CNET, 38-40 Ave. du General Le Clerc, F-92131 Issy-Les-Moulineaux, France Bhaskaracharya Inst for Space App/Geo-Informatics,2010
- [5] M. K. Gupta, Vishwas Sharma, "To Improve Bit Error Rate Of Turbo Coded Ofdm Transmisalgorithn with soft-decision outputs and its applications. in Proc., IEEE Globecom Conj, pp. 1680-1686, 1989.
- [7] Claude Berrou. "A low complexity soft-output viterbi decoder architecture." IEEE Trans. Commun., pp. 737-745, 1996.

Analysis of Conditions in Boundary Lubrications Using Bearing Materials

Shinde Sagar Vitthal¹, Ravindra R. Navthar²

¹(PG Student, Dept.of Mechanical Engineering, P.D.V.V.P. College, Maharashtra, India)

²(Asst.Prof. Dept.of Mechanical Engineering, P.D.V.V.P. College, Maharashtra, India)

Abstract: In order to clearly establish the tribological potential of these alloys as bearing materials, the tribological parameters of the RAR Zn-Al alloys are compared to parameters of the CuPb15Sn8 lead-tin bronze, as a widely applied conventional bearing material. Existing Bearing of connecting rod is manufactured by using non ferrous materials like Gunmetal, Phosphor Bronze etc.. This paper describes the tribological behavior analysis for the conventional materials i.e. Brass and Gunmetal as well as New non metallic material Cast Nylon. Friction and Wear are the most important parameters to decide the performance of any bearing. In this paper attempt is made to check major tribological parameters for three material and try to suggest better new material compared to conventional existing material. It could help us to minimize the problem of handling materials like Lead, Tin, Zinc etc. After Test on wear machine. Our experimental results are accessing efficient processing in bearing conditions in semantic data representation of extracted related data materials.

Index Terms: Friction, Wear, Cast Nylon, Artificial cooling, engine efficiency, Zn-Al alloys, bronze, tribological.

I. Introduction

The basic motive of such an investigations is of course, of economic nature. Namely, the Zn-Al alloys are characterized by significantly lower price. Besides that, these alloys can successfully be machined by standard casting procedures, like sand casting, centrifugal, permanent and continual casting. Total savings of substitution bronzes with these alloys are estimated up to the level of 35...90%. The concept of application of Zn-Al journal bearings as substitution for the bronze ones is not new. The first experiences are related to the period of the Second World War, when different Zn-Al alloys (before, all with only 30 % Al) were used instead of bronze, primarily due to lack of copper. Besides bearings, the Zn-Al alloys were applied also for other machine elements, like the worm gears, components of hydraulic installations etc.

Special importance in development of Zn-Al alloys during the seventies and eighties has the International Lead and Zinc Research Organization. Based on their investigations and those of other research centers and manufacturers in this area, the Zn-Al alloys for casting were developed, marked as ZA-8, ZA-12 and ZA-27. Realized good carrying capacity and wear resistance enabled application of these alloys, especially for mining equipment and mechanization for tribo-elements, like the sliding radial and journal bearings, various bushings, nuts for the screwed spindles, guides, etc.

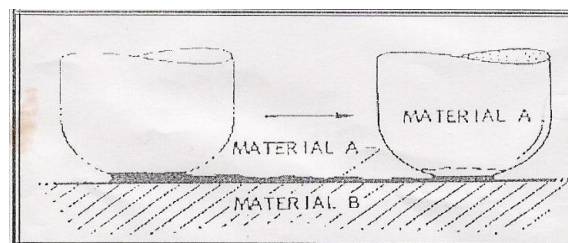


Figure 1: The mechanism illustration of adhesion wear.

There are several theories which were found to explain the phenomenon of adhesion wear, and from that the simple adhesion wear theory. The adhesive wear occurs when two surfaces are moving relatively one over the other, and this relative movement is in one direction or a successive movement under the effect of the load so that the pressure on the adjacent projections is big enough to make a load plastic deformation and adhesion. This adhesion will be at a high grade of efficiency and capability in relative to the clean surfaces, and adhesion will take place between a number of these projections whose sizes will be bigger and the area will be

increased during movement. Wear resistance is one of the most important properties that journal bearings should possess. Several studies and investigations have been made in order to improve the wear resistance. The researchers investigate friction and wear behavior of materials because of the adverse effect observed in the performance and life of machinery components. Much of the research reported in the literature was carried out under the atmospheric conditions. However, some tribological behaviors have been recently investigated under the vacuum conditions. Especially, as a result of some new developments in aeronautic, space, electronic, material, metallurgy, chemistry, coating and manufacturing industrial areas necessitate the machinery components to be investigated under the different conditions.

These conditions are accessed efficient lubricants in semantic data progression in mechanical efficiency in recent year generation. Our experimental results show efficient processing between each bridge connection.

II. Back Ground Work

Wear Apparatus:

The rate of wear will be relatively small in most of the machinery and engineering tool, and mostly the value of the change in dimensions is only few microns every year (Halling, 1976), and for measuring wear they are using some apparatuses and instruments which give results about the rate of wear happening in the tools and machinery. From these apparatus which is used in high pressure contact tests where it is able to get very quick results by applying loads on very small areas of contact and to achieve this test there are some different engineering arrangement as shown in Fig.(2), and for each of these tests, the part (A) is the metal subjected to wear, then the measurement of wear will be known by one of the measurement methods.

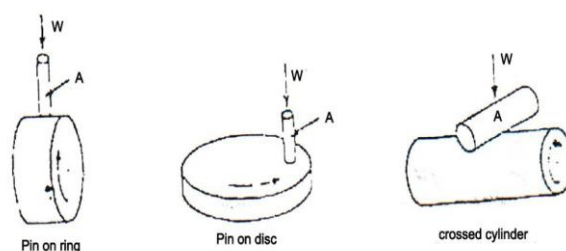


Figure 2: Three common methods to test wear (Halling, 1976).

In the current study the apparatus pin on disc has been used to study the specification of the adhesion wear. **Measurement Methods of wear:** The widely known methods in studying wear, depend on choosing the sliding surfaces, and then measuring, before testing the removal material, and after that, and any change taking place, will be attributed to the resulted wear (Rabinowicz, 1965).

III. Boundary Lubrications

Every surface, however, smoothly appears, it will be rough in the microscopic scale and contains a range of tops and lows, and when two surfaces meet then this contact takes place at these projections which are little and relatively isolated; thus when applying a load on these surfaces, then locally there will be a high pressure and heat which will cause overtaking the elastic limits of one surface or both surfaces and the deformation of the projections in a plastic way, so that, the real contacting areas are increased to a limit to support the applied load. The contacting areas are inclined to be damaged under the effect of the relative movements between the two surfaces. The weariness occurs usually at one surface, because of the resistance of the in between surface to breaking and weariness due to the reaction of strain hardness during the adhesion of projections [18]. The removed substance (due to the shearing of projections) will take the shape of small foils which is usually transferred to the opposite surface or it is found separately between the two surfaces. The improvement of wear and corrosion resistance of RPS Ti-TiN coating by mean of thermal oxidation, and they found that the wear and its rate will be less in the specimens which were painted and oxidized and this will increase in the metals already coated without its oxidization also with the chemical corrosion. In the current research the effect of loads, sliding speeds and times on the wear rate for three different materials were investigated. The modeling of friction and wear is an important engineering problem. In the process of design of machine elements and tools operating in contact conditions, engineers need to know areas of contact, contact stresses, and they need to predict wear of rubbing elements. Friction, wear and contact problems are subjects of numerous experimental and theoretical studies. The very complex nature of tribological phenomena is a reason that many problems of contact mechanics are still not solved. The modeling of friction and wear can be carried out not only with the aid of laboratory tests but using also mathematical models and computer simulations. Due

to computer simulation techniques, physical and mechanical phenomena in real objects can be reconstructed with a high degree of precision.

IV. Experiment Results

4.1. Tested Materials

For the tests there were prepared two types of RAR Zn-Al alloys with commercial marks RAR-12 and RAR-27, cast in ingot mold. RAR-12 and RAR-27 alloys are in accordance with ZA-12 and ZA-27 alloys defined by ASTM B 669-89. In order to provide a comparative evaluation of RAR alloys, lead-tin bronze CuPb15Sn8 was used. Chemical compositions and physical-mechanical properties of these materials are given in tables 1 to 3.

4.2. Wear Test Equipment

Tribometric tests were performed on the computer-supported tribometer (fig. 1). Computer support for the experiment was enabled by application of the Burr-Brown PCI 20000 data acquisition system integrated into PC computer and general-purpose

LABTECH NOTEBOOK software package. Based on requirements to realize the contact and relative motion type similarity on model and real system, for tribological modelling of sliding bearing was chosen (in tribometric practice, the most present) pin-on-disc contact scheme with continuous sliding. As in real tribological system bearing/journal, the tribologically critical contact element is the bearing, on the model, the stationary pin corresponds to it, which is due to a small degree of covering tribologically more critical contact element of the contact pair on the model.

Table 1. Chemical composition of RAR alloys.

Chemical elements, %	RAR-27	RAR-12
Al	26.20	14.4
Cu	2.30	1.3
Mg	0.02	0.018
Zn	Remaining	Remaining

Table 2. Chemical composition of CuPb15Sn8.

Chemical element	Percentage content
Cu	76.0
Sn	7.63
Pb	12.31
Others	Remaining

Table 3. Physical-mechanical properties of alloys.

Physical-mechanical properties	Tested materials		
	RAR-27	RAR-12	CuPb15Sn8
Hardness, HB	115	94	90
Tensile strength, MPa	451	305	188.9
Extension, %	16.7	10.2	7.85
Yield strength $R_{p0.2}$, MPa	353	210	131.7
Elasticity modulus, GPa	137.6	1	110
Density, kg/dm ³	5.0	6.1	8.28

In conducted tests pins of cylindrical form were used, with diameter of 2.5 mm, with flat, ground front (contact) surface (nominal contact area 5 mm²), and made of tested bearings materials. Rotational discs of diameter 100 mm were made of construction Chromium-Nickel-Molybdenum steel C 4732 which was thermally treated, having a hardness of 38 HRC. Contact surfaces were machined by grinding, under the same conditions. The machined contact surfaces quality of pins and discs is characterized by roughness at the level of approximately $Ra = 0.3 \mu\text{m}$. The selected wear specimens were tested in conditions of 0.15 m/s sliding speed, 3, 5 and 7 MPa contact pressure, respectively. These parameters provide “p·v” characteristics of 450, 750 and 1050 [kN/m² (m/s)], that correspond to the typical values of journal bearing applications with boundary lubrication.

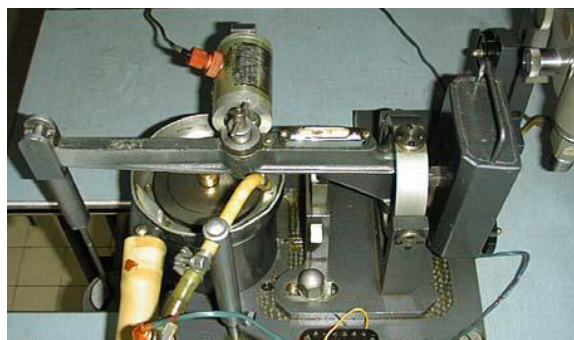


Figure 3: Pin-on-disc testing device.

The tests were performed in conditions of room temperature.

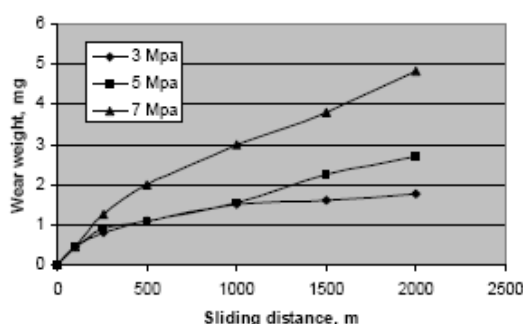


Figure 4: Wear curves of RAR-27 alloy.

The lubricant used for tests was ISO grade 68 hydraulic oil, a multipurpose lubricant recommended for industrial use in plain and antifriction bearings, electric motor bearings, machine tools, chains and gear boxes, as well as high-pressure hydraulic systems. The oil was heated up to 50 °C. Individual tribometric tests for each of combinations of the contact conditions were conducted for 4.5 hours, what corresponds to the friction distance of 3000 m.

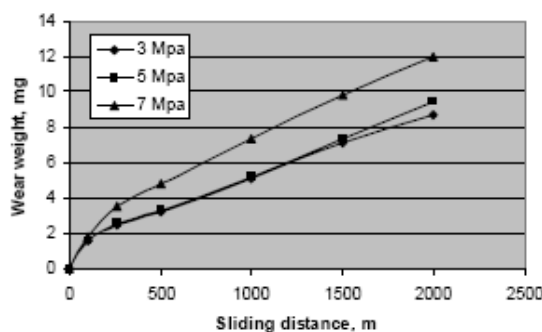


Figure 5: Wear curves of RAR-12 alloy.

The graphical representation of the wear results obtained from the tests for RAR-12, RAR-27 and lead-tin bronze CuPb15Sn8 are shown in figures 4 and 5. The data used for graphs were taken from the average of five measurements. The standard deviation was below 5%. These wear curves represent the functions of the wear

mass loss versus the friction distance for the varied levels of pressure. Results of wear tests of CuPb15Sn8 samples obtained by 7 Map of pressure were not accepted as significant, because of a great dissipation of values.

V. Conclusion

The established level of tribological characteristics, both from aspect of wear and aspect of friction, shows that RAR Zn-Al alloys represent respectable tribological materials. Considering the simulated conditions of tribological interactions, the results nominated these alloys as candidates for bearing's materials for conditions of boundary lubrication, that are characteristic for high loads and low sliding speeds. With respect to bronze they have better antifrictional characteristics, higher resistance to wear and lower price costs. bodies decreases the flow stresses of the rubbing materials to a certain extent, which results in an increase in the plastic zone size in the subsurfaces of the rubbing bodies. Consequently, the friction coefficient as well as wear rate increases with increasing sliding speed when the normal load is over certain levels.

VI. REFERENCES

- [1.] Blok H. Surface temperature under extreme pressure lubricating conditions. Proc. Second World Petr. Cong. 1937, 3, 471-484
- [2.] Block H. Measurement of temperature flashes on gear teeth under extreme pressure conditions. Proc. Instn. Mech. Engrs. 1937, 2, 14-20
- [3.] Jaeger, J.C. Moving sources of heat and the temperatures at sliding contacts. Proc. Roy. Soc. N.S.W. 1942, 26, 203-224
- [4.] Barber, J.R. Distribution of heat between sliding surfaces, Mech. Eng. Sci. 1967. 9, 351-354 5. **Savaskan T., Murphy S.**, 1987, Mechanical properties and lubricated wear of Zn-Al based alloys, Wear, 116, pp. 211-224.
- [5.] **Babic M., Rac A.**, Ninkovic R., 1999, Theory and practice of Zn-Al sliding bearings, Proc. Of. BALKANTRIB'99, Romania, pp. 127-133.
- [6.] **Ninkovic R., Babic M., Rac A.**, 2000, Yugoslav Zn-Al Alloys as Bearing Material, Tribology in Industry, no. 1 & 2, pp. 14-18.
- [7.] **Rac,A., Babi □, M. and Ninkovi □, R.**,2001, Theory and Practice of Zn-Al Sliding Bearings, Journal of the Balkan Tribological Association, 7, 3-4, pp.234-240.
- [8.] **Babic M., Ninkovic R.**, 2004, Zn-Al alloys as tribomaterials, Tribology in industry, Vol. 26, no. 1&2, pp. 3-7.

Numerical Analysis of Fin Side Turbulent Flow for Round and Flat Tube Heat Exchangers

Mallikarjuna¹, Dr. V Seshadri², Vijaya Raghu B³

¹(M.Tech Scholar, Mechanical Engineering, Maharaja Institute of Technology, Mysore, India)

^{2,3}(Professor, Mechanical Engineering, Maharaja Institute of Technology, Mysore, India)

Abstract: Numerical three dimensional simulation of turbulent flow in round and flat tube fin heat exchangers having two rows of staggered arrangement has been carried out to investigate fluid flow and heat transfer characteristics using ANSYS Fluent 14® software. HYPERMESH10® Software has been used for the creation of models as well for meshing. The cases have been simulated for different fin side Reynolds number in turbulent regime to observe the effect of various parameters like fin pitch, tube pitch and fin temperature on Colburn j factor and Friction factor f for both round and flat tubes. Fin side flow has been simulated using various steady flow models in the software for same velocity range. As simulation using k-ε model resulted in close agreement with that of experimental in turbulent regime, it is considered for further analysis. The performance of round tubes is compared with that of flat tubes with same flow area and geometrical parameters. For both round and flat tube domains with all the geometrical configurations simulated in this work Colburn j factor varied inversely with the inlet air velocity. The heat transfer is more with the higher fin spacing for both round and flat tubes following the above said trend. On the other hand, the pressure drop across the tubes is more with the lesser fin spacing in contrast to the heat transfer. Due to lesser turbulent intensity in flat tubes, they exhibit slightly lesser Colburn j factor and considerably lesser pressure drop compared to round tubes. Although flat tubes exhibit slightly lesser Colburn j factor, due to larger exposed tube area increase in the air temperature in the fin side is comparable with that of round tubes. Higher fin temperatures result with lesser Colburn j factor and higher pressure drop across the tubes although the fin temperature affects the pressure drop to lesser extent.

Keywords: Colburn j factor, Extended Surface, Fins, Flat tube, Friction factor, Heat Exchanger, Numerical Analysis, Round Tube.

I. INTRODUCTION

Extensive work has been carried out by many researchers on various configurations of heat exchangers both numerically as well as experimentally. Even though, literature relevant to the field is available in abundance, due to parameters to be observed are too many with varied configurations still the scope exists to research furthermore. In this work performance assessment of heat exchangers by varying the parameters associated has been undertaken for two rows by numerical simulation. This involves building a model of plain fin and tube heat exchangers using HYPERMESH® software for modeling and creation of suitable mesh, selection of solvers and numerical solution methods by using ANSYS FLUENT® software. The presented work is focused on fin side flow and heat transfer characteristics particularly on turbulent flow regime. Colburn J factor and Friction factor f are considered to best suggest the performance characteristics. In this work the effect of parameters such as fin pitch, tube pitch and fin temperature on performance of heat exchangers is studied. Flow in two tube axi-symmetric model is simulated for a range of inlet velocities using various steady flow models available with the used solver software. The simulated results are compared with the experimental results with same flow and geometrical configurations partly as validation of the numerical approach followed and to select most suited model for turbulent regime. Many researchers have worked on flat tubes with same perimeter as of round tubes with different tube arrangements in their comparative study. In the presented work, the performance of plain fin flat tube heat exchanger is compared with that of round tube by keeping the flow area and the pitches as same in respective cases.

The work also includes the study of available literature in related areas as per which many experimental works has been carried out on plate fin and tube heat exchangers. Wang et.al conducted experimental works on plate fin heat exchangers with different geometrical parameters including number of tube rows, fin spacing and fin thickness to study their effect on heat transfer and friction characteristics [1]. Further, Wang along with K Y Chi gave an improved experimental data on plane fin and tube heat exchangers. Study stated that the heat transfer coefficients are strongly dependent on number of tube rows in case of laminar flow

with decrease in fin pitch and increase in tube diameter leads to increase of pressure drops [2]. In parallel, Jang et.al reported that heat transfer practically remains independent of number of tube rows for more than four rows and showed higher Colburn and friction factor for staggered tube arrangement [3]. Yonghan Kim and Yongchan Kim conducted an experiment and found that for the one row heat exchanger fin pitches had negligible effect on heat transfer and increasing fin pitches by increasing the number of tube rows lead to the increase in heat transfer. For the staggered tube alignment with more than 4 tube rows the heat transfer coefficient is independent of number of tube rows [4]. Recently, Gurjeet Singh and Gulshan Sachdeva, conducted CFD simulations for both round and flat tube heat exchangers with same perimeter of the tubes and concluded that in turbulent region the friction factor for round tube was 40 to 45% more than the flat tubes and same Colburn j factor was achieved [5]. Experimental results from Wang et.al have been taken to validate numerically simulated results and to select most suitable model to solve the cases of fin side turbulent flow [1][2].

II. COMPUTATIONAL FLUID DYNAMICS

Computational fluid dynamics or CFD is the analysis of systems involving fluid flow heat transfer associated phenomena such as chemical reactions by means of computer based simulation.

There are three distinct streams of numerical solution techniques which are used by the Solver;

- Finite difference methods
- Finite volume methods
- Spectral methods

Numerical methods that form the basis of the solver perform the following steps.

- Approximation of the unknown flow variables by means of simple functions.
- Discretisation by substitution of the approximations into the governing flow equations and subsequent mathematical manipulations
- Solution of the algebraic equations.

The numerical algorithm consists of the following steps

- Formal integration of the governing equations of fluid flow over all the control volumes of the solution domain.
- Discretisation involves the substitution of a variety of finite difference type approximations for the terms in the integrated equation representing flow processes such as convection, diffusion and sources. This converts the integral equations into a system of algebraic equations.
- Solution of the algebraic equations by an iterative method.

Three mathematical concepts are useful in determining the success: Convergence, consistency and stability

- Convergence is the property of a numerical method to produce a solution which approaches the exact solution as the grid spacing, control volume size or element size is reduced to zero.
- Consistent numerical schemes produce systems of algebraic equations which can be demonstrated to be equivalent to the original governing equation as the grid spacing tends to zero.
- Stability is associated with damping of errors as the numerical method proceeds. If a technique is not stable even round off errors in the initial data can cause wild oscillations or divergence [6].

Governing equations used are:

Continuity equation: $\frac{\partial(\rho u_i)}{\partial x_i} = 0$

Momentum equation: $\frac{\partial}{\partial x_i}(\rho u_i u_j) = \frac{\partial}{\partial x_i}(\mu \frac{\partial u_j}{\partial x_i}) - \frac{\partial p}{\partial x_j}$

Energy equation: $\frac{\partial}{\partial x_i}(\rho u_i T) = \frac{\partial}{\partial x_i}(\frac{k}{C_p} \frac{\partial u_j}{\partial x_i})$

III. COMPUTATIONAL DOMAIN AND BOUNDARY CONDITIONS

The commercial software HYPERMESH is used to create and mesh the computational models. The dimensions of the basic domain are taken from the experimental works [1]. The computational models for round and flat tube with plain fins domains considered for simulation are shown in figure 1 and 2.

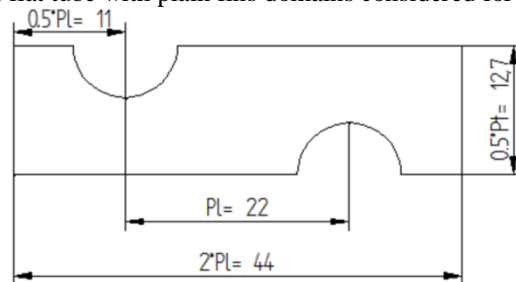


Figure1: Geometric model of round tube and fin heat exchangers

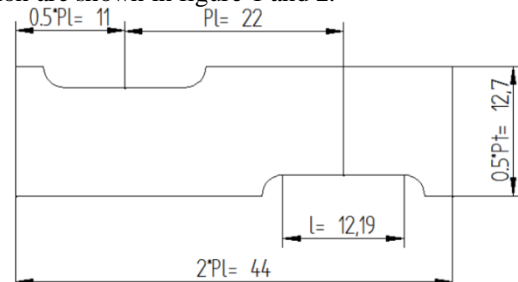


Figure2: Geometric model of flat tube and fin heat exchangers

The geometric details of round tube and fin configuration is listed in table 1 and flat tube and fin heat exchangers is shown in table 2

Geometrical Parameters	Symbol	Dimensions
Fin thickness	T	0.130 mm
Fin pitch	F _p	2.240 mm
Fin collar outside dia	D _c	10.23 mm
Transverse pitch	P _t	25.40 mm
Longitudinal pitch	P _l	22.00 mm
Tube wall thickness	Δ	0.336 mm

Table 1: geometric details of round tube and fin configuration

Geometrical Parameters	Symbol	Dimensions
Fin thickness	T	0.130 mm
Fin pitch	F _p	2.240 mm
Tube outside dia	d	4.14 mm
Transverse pitch	P _t	25.40 mm
Longitudinal pitch	P _l	22.00 mm
Tube wall thickness	Δ	0.336 mm

Table 2: geometric details of flat tube and fin heat exchangers

As it is difficult to conduct CFD simulations for entire heat exchanger with multiple rows and columns, a symmetrical model about both the axes of one channel of air between two fins with the air flowing by two tubes is considered as a geometrical model. Computational models for round and flat tube heat exchangers are shown in figure 3 and 4 respectively. Dimensions of the flat tube have been computed with l/d ratio of 4 maintaining same tube side flow area as of round tube. The gap between the two fins is considered as flow area for air and the model consists of structured hexahedral mesh throughout and the areas around the tubes are densely meshed. Grid independence test has been conducted and results found to be not much sensitive with the further refinement after the number of elements 61750 for round tube domain and 73500 elements for flat tube domain.

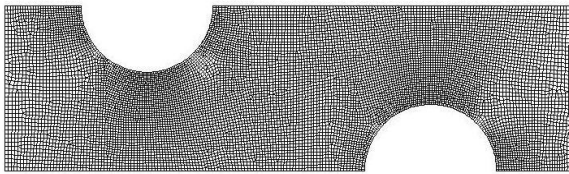


Figure 3: Meshed model for round tube domain

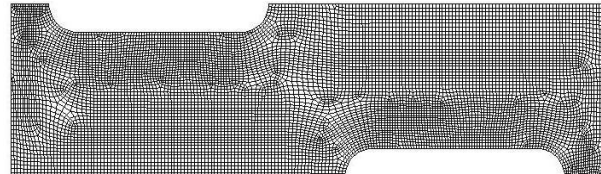


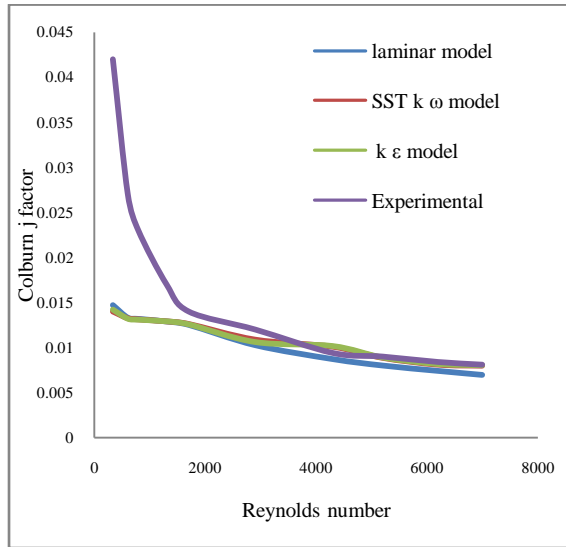
Figure 4: Meshed model for flat tube domain

The fluid is assumed to be incompressible with constant properties and the flow is turbulent and in steady state. All numerical simulations are carried out using a finite-volume method. The boundaries of the computational domain consist of inlet and outlet, symmetry planes and solid walls. Boundary conditions for the domain are applied as tabulated in table 3. A steady state unidirectional uniform velocity at inlet plane and uniform wall temperature of 55°C are applied to simplify the computations. A constant temperature of 5°C is set at the flow inlet to meet the experimental conditions. At the outlet, stream wise gradient (Neumann boundary conditions) for all the variables are set to zero. No-slip boundary condition is used at the fins and the tube surfaces.

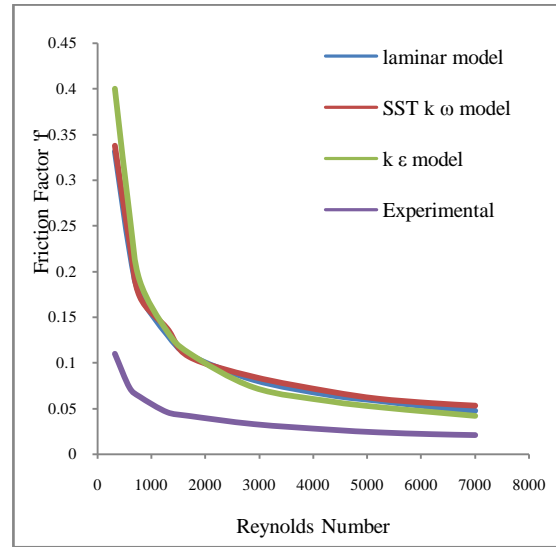
Tube surfaces	Dirichlet boundary condition Air velocity $u = v = w = 0$	$T = T_w = 60^\circ\text{C} = 333\text{K}$
Fins	Dirichlet boundary condition Air velocity $u = v = w = 0$	$T = T_{fw} = 60^\circ\text{C} = 333\text{K}$
Inlet	Dirichlet boundary condition Uniform velocity 'u'	$u = u_{in}$, u_{in} ranging from 3.7 m/s to 6.2 m/s. $T = 5^\circ\text{C} = 278\text{K}$
Outlet	Neumann boundary conditions that is zero gradients of pressure temperatures and velocities	-
Side planes	Symmetry Conditions	$\frac{\partial u}{\partial y} = 0$, $v = 0$, $\frac{\partial w}{\partial y} = 0$, $\frac{\partial T}{\partial y} = 0$

Table 3: Boundary Conditions

For the validation of the numerical approach followed and to select most suitable model for simulation, geometry of round tube domain is maintained same as referred experimental work. The simulation is carried out for the velocities ranging from Reynolds number 330 to 7000 in the mentioned domain is done with all the steady state flow models and compared with the experimental results. As the present work is focused on the turbulent regime, from the graphs 1(a) and 1(b) it is evident that the k-ε model computed most proximate results to the experimental work [1]. Further, same validated numerical approach and model selected is used to simulate rest of the cases in the work.



Graph 1(a): Reynolds Number v/s Colburn j factor



Graph 1(b): Reynolds Number v/s Friction factor f

IV. RESULTS AND DISCUSSIONS

In the present work, round and flat tube domains are simulated for fin side turbulent flow using k-ε model for different fin pitches and fin temperatures. Figure 5(a), 5(b) and 5(c) are simulated contours of pressure, velocity and temperature for round tube domain with fin pitch of 2.24mm for inlet velocity 5.4m/s. Figure 6(a), 6(b) and 6(c) are simulated contours of pressure, velocity and temperature for flat tube domain with fin pitch of 2.24mm for inlet velocity 5.4m/s. As the study is more focused on Colburn j factor and friction factor, above said contours are not discussed in detail.

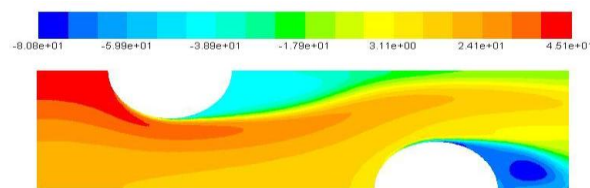


Fig 5(a): Pressure Contour for Round Tube

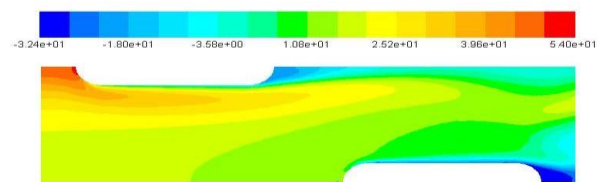


Fig 6(a): Pressure Contour for Flat Tube

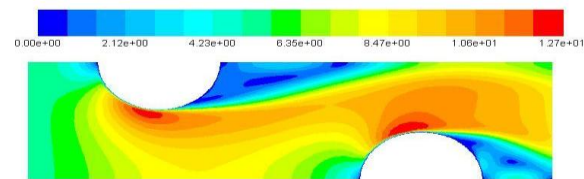


Fig 5(b): Velocity Contour for Round Tube

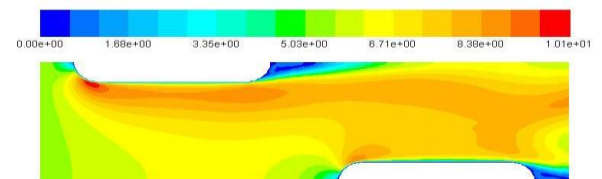


Fig 6(b): Velocity Contour for Flat Tube

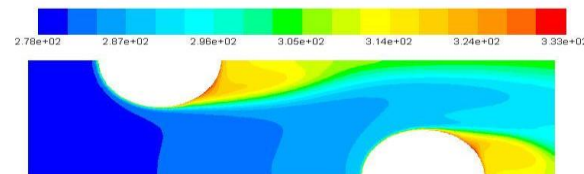


Fig 5(c): Temperature Contour for Round Tube

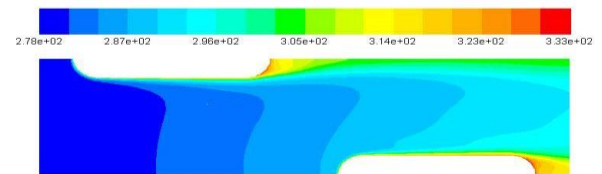
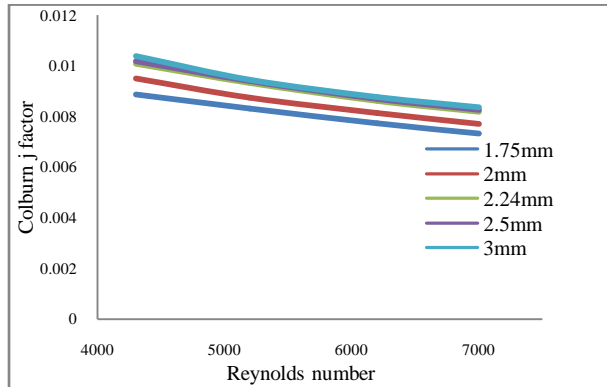
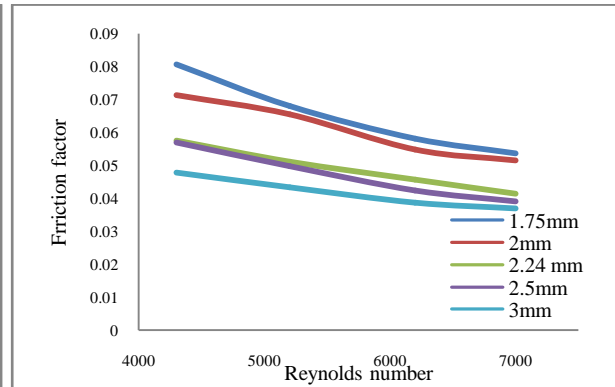


Fig 6(c): Temperature Contour for Flat Tube

The effect of the fin pitch on Colburn j factor and friction factor “f” for different Reynolds number in the turbulence regime is depicted in the graphs 2(a) and 2(b) respectively for the round tube domain. It is evident from the plot that heat transfer varies inversely with the Reynolds number. For the lower Reynolds numbers the air spends more time in the flow area and absorbs the more heat from the fins and tubes. It can also be observed that heat transfer is more with the higher fin spacing. On the other hand, the pressure drop across the tubes is more with the lesser fin spacing in contrast to the heat transfer.

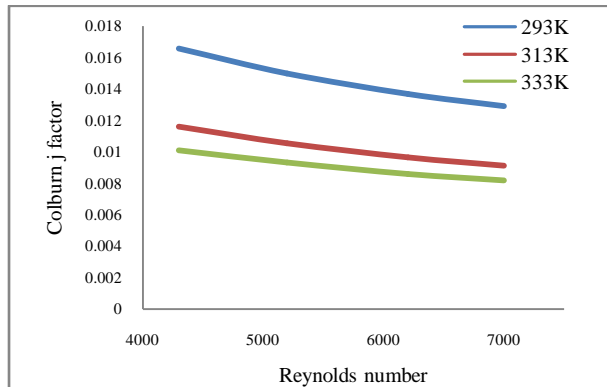


Graph 2(a): Reynolds Number v/s Colburn j factor for round tube

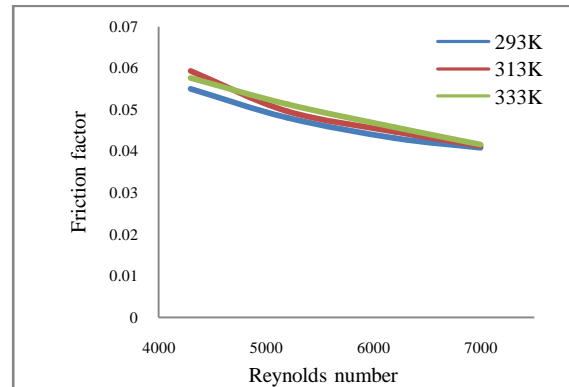


Graph 2(b): Reynolds Number v/s Friction factor f for round tube

The effect of the fin temperature on Colburn j factor and friction factor “f” for different Reynolds number in the turbulence regime is depicted in the graphs 3(a) and 3(b) respectively for the round tube domain. It is evident from the plot that heat transfer varies inversely with the fin temperature and also the variation in heat transfer was considerably larger with initial increase in fin temperature and varied much lesser with later increase in fin temperature. Lower fin temperatures resulted in higher Colburn j factor. On the other hand, it is evident that the fin temperature does not affect the pressure drop across the tubes to a higher extent. Also, it can be seen that increase in fin temperature results in slight decrease in friction factor.

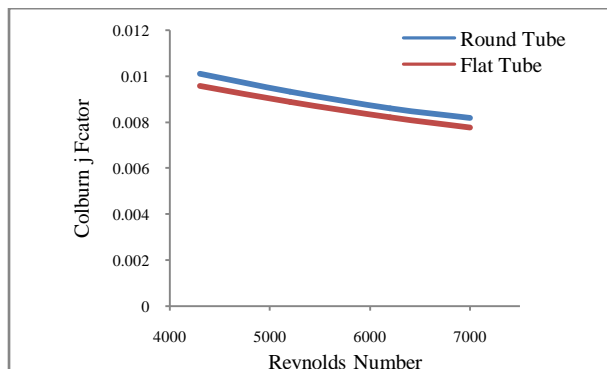


Graph 3(a): Reynolds Number v/s Colburn j factor for round tubes

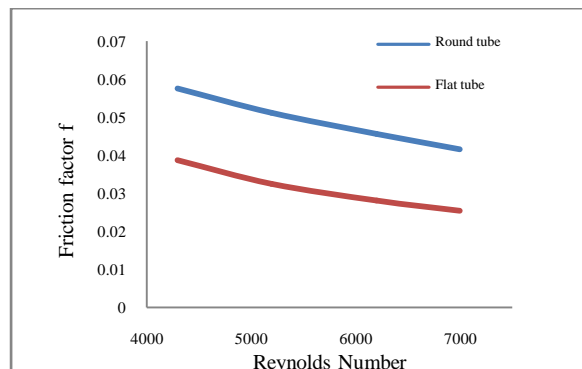


Graph 3(b): Reynolds Number v/s Friction factor f for round tubes

Simulation of fin side turbulent flow is also carried out on flat tube domains with same tube side flow area as that of round tube domain maintaining other geometrical configurations and range of inlet velocities as same. The graphs 4(a) and 4(b) shows the comparisons of Colburn j and friction factors with Reynolds number for round and flat tubes. Similar to round tubes, the flat tubes showed higher heat transfer at lower inlet velocities and higher pressure drops at lower inlet velocities. From the comparisons, it is observed that round tubes exhibited slightly better Colburn j factor but the flat tubes exhibited larger reduction in pressure drop.

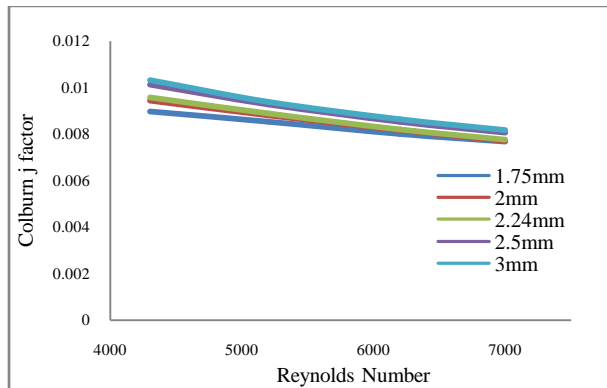


Graph 4(a): Reynolds Number v/s Colburn j factor

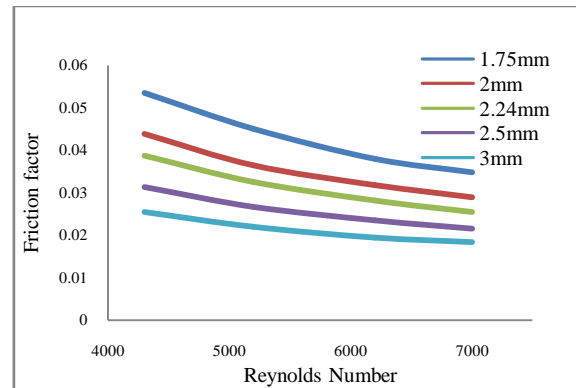


Graph 4(b): Reynolds Number v/s Friction factor f

Graphs 5(a) and 5(b) are plotted to show the variation of Colburn j factor and friction factor for flat tubes with Reynolds number for different fin spacing. Although the plot trends are similar to that of round tubes, flat tubes exhibited very slight variation in heat transfer with fins spacing as compared to that of round tubes. Also, they exhibited considerable reduction in pressure drop when compared to that of round tubes following a similar trend.

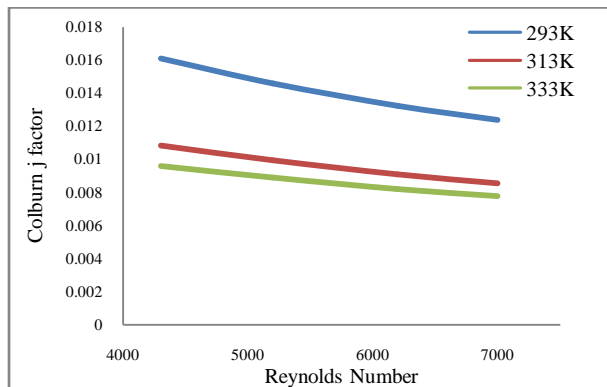


Graph 5(a): Reynolds Number v/s Colburn j factor for flat tubes

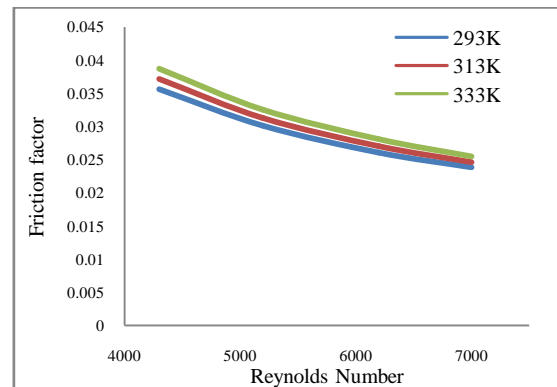


Graph 5(b): Reynolds Number v/s Friction factor f for flat tubes

The variations of Colburn j factor and friction factor for flat tube with Reynolds number at inlet for different fin temperatures are shown in graph 6(a) and 6(b), as per which variations followed a similar trend as that of round tube with almost same heat transfer and considerably better pressure drop.



Graph 6(a): Reynolds Number v/s Colburn j factor for flat tubes



Graph 6(b): Reynolds Number v/s Friction factor f for flat tubes

The increase in air temperature across two staggered tube rows is given in table 4. Although flat tubes exhibited slightly lesser Colburn j factor compared to that of round tubes, numbers tabulated herewith depict that the increase in the air temperature across two staggered rows is higher for flat tubes with lesser fin spacing and round tubes exhibited higher increase in air temperature with larger fin spacing.

Reynolds Number	Fin Pitch 1.75mm		Fin Pitch 2mm		Fin Pitch 2.24mm		Fin Pitch 2.5mm		Fin Pitch 3mm	
	Round Tube	Flat Tubes	Round Tube	Flat Tubes	Round Tube	Flat Tube	Round Tube	Flat Tube	Round Tube	Flat Tubes
4300	36.7	37.38	34.4	33.22	29.22	30.27	28.42	26.84	22.05	21.98
5200	33.4	34.5	31.73	29.97	26.14	26.86	25.23	23.65	19.59	19.35
6200	30.35	31.13	28.40	27.04	23.47	24.21	22.26	21.02	17.73	17.51
7000	28.11	28.88	26.13	24.99	21.44	22.35	20.35	19.31	16.72	16.08

Table 4: Increase in Air temperature across two staggered tube rows

V. CONCLUSION

For both round and flat tube domains with all the geometrical configurations simulated in this work Colburn j factor varied inversely with the inlet air velocity. The heat transfer is more with the higher fin spacing for both round and flat tubes following the above said trend. On the other hand, the pressure drop across the

tubes is more with the lesser fin spacing in contrast to the heat transfer. Due to lesser turbulent intensity in flat tubes, they exhibit slightly lesser Colburn j factor and considerably lesser pressure drop compared to round tubes. Although flat tubes exhibit slightly lesser Colburn j factor, due to larger exposed tube area increase in the air temperature in the fin side is comparable with that of round tubes. Higher fin temperatures result with lesser Colburn j factor and higher pressure drop across the tubes although the fin temperature affects the pressure drop to lesser extent.

REFERENCES

Journal Papers:

- [1] Chi-Chuan Wang and Yu-Juei Chang “Sensible heat and friction characteristics of plate fin-and-tube heat exchangers having plane fins”, International Journal of Refrigeration Vol. 19, No. 4, pp. 223-230, 1996.
- [2] Chi- Chuan Wang and Kuan Yu Chi “Heat transfer and friction characteristics of plain fin-and-tube heat exchangers, part I: new experimental data”, International Journal of Heat and Mass Transfer 43 (2000) pp. 2681-2691.
- [3] Jang et al., 1996. “Numerical and experimental Studies of three-dimensional plate-fin and tube heat exchangers”, International Journal of Heat and Mass Transfer, 39(14), 3057-3066.
- [4] Yonghan Kim and Yongchan Kim “Heat transfer characteristics of flat plate finned-tube heat exchangers with large fin pitch”, International Journal of Refrigeration 28 (2005) 851–858.
- [5] Gurjeet Singh and Gulshan Sachdeva “CFD simulation of round and flat tube fin heat exchanger for laminar and turbulent flow models”, Proceedings of the 37th National & 4th International Conference on Fluid Mechanics and Fluid Power December 16-18, 2010.

Books:

- [6] Versteeg H K., Malalasekera W., 1998 An Introduction to Computational Fluid Dynamics The Finite Volume Method, Second Edition, Pearson Education Limited, Essex, England (2007).

Free Vibration Analysis of Polypropylene- Nanoclay Composite Beam with Crack

Narra. Tilak Ratan¹, Dr. G. Vijay Kumar², M. Rajya Lakshmi³

¹(Dept. of Mechanical Engineering, PVP Siddhartha Institute of Technology, India

²(Professor, Dept. of Mechanical Engineering PVP Siddhartha Institute of Technology, India

³(Asst. Professor, Dept. of Mechanical Engineering, PVP Siddhartha Institute of Technology, India

Abstract: Vibration analysis is one of the most promising techniques to detect the crack. In this paper, Poly Propylene - Nano Clay is analyzed for its free vibration. The proposed composite beam is modeled with crack. Analysis is done by using Finite element package ANSYS-14.5. The Nano Clay in composite is varied from 0 to 15 percentage (0,1,3,5,7,9,11,13,15) and crack depth to width ratios are chosen as, 0,0.25,0.5,0.8. Impact of varying percentage of NC and varying crack depths on natural frequency are analyzed using free vibration analysis.

Keywords: Nano Clay-Poly Propylene composite Cantilever beam, Free vibration Analysis.

I. INTRODUCTION

Fiber Reinforced Plastics (FRP) are commonly used in aerospace, automotive and other engineering applications mainly because of their high strength-to-weight ratio, high stiffness, good resistance to fatigue, and corrosion resistance. Reinforced fibers are usually added in the form of continuous or chopped fibers in a polymer matrix. Each type of these reinforcement fibers has their benefits and limitations in applications. A short fiber reinforced composites can have better processing properties and can be moldable into complex shaped components. Long fiber reinforced composites, on the other hand, provide enhanced strength and stiffness properties as per the desired directions. Various types of synthetic and natural fibers reinforced plastics are presently studied in literature, namely, glass fiber, carbon fiber, boron, alumina, oxide/carbide and sisal/jute based fibers in a polymer matrix. In addition to these fiber reinforced composites, particle reinforced polymer composites are also widely investigated.

In these particle filled composites, various types of nano- and micro-scale particles are used. Nano particle reinforced polymer composites gained special attention due to their superior and improved properties when compared to their corresponding micro-scale particles. Nano clays, carbon nano tubes and alumina/oxide based particles are widely used as nano particle reinforcements in polymer matrices. Polymer-Clay Nano composites (PCN) are a relatively new area of research in particle filled composites, and consists of Nano Clay (NC) as the reinforcement and a polymer serves as the matrix material.

The addition of small amounts of clay (0 to 15% wt) in a polymer matrix leads to improved mechanical, thermal and barrier properties. The addition of nano clays in a polymer matrix may result in the formation of two types of nano composite structures, namely, intercalated and exfoliated nanostructures. In an intercalated structure, the host polymer matrix enters into the interlayer spacing of the nano clay and increases the interlayer spacing but maintains the parallel arrangement of the nano layers of clay in the matrix. If the nano layers of clays are randomly dispersed in the matrix, then the structure is called an exfoliated structure. In practice, exfoliated structures provide enhanced and improved properties due to their excellent dispersions and improved aspect ratio.

The addition of the NC in the Poly Propylene (PP) matrix increases the thermal stability in air medium, increases physical properties (dimensional stability), improves flame retardant properties increased thermal-oxidative stability, and improves mechanical properties, fracture properties and gas barrier properties. Several studies were conducted with various types of clay concentrations and compatibilizers.

The main applications of PP materials are home appliances such as, chairs and toys, clothing, medical, EPP toy air craft. Crack is initiation of the wrecking of material in some cases. Strength plays very key role for crack growth. If material has high strength, crack will grow slowly otherwise, crack will propagate quickly. And frequency analysis is one of the most promising techniques to detect crack depth. If crack depth increases, then, frequency will down in free vibration. In this paper, efforts have been going made through PP-NC composite beam for un-cracked and cracked with different crack to depth ratios.

A -Material Properties

Material properties were extracted from research papers by *J. Yan*[15] and density was calculated from Rule of mixture. Properties of material for different percentages of nano clay with Poly propylene are listed in table 1.

Table 1: Mechanical properties of Poly Propylene - Nano Clay for different % of NC

% of NC	Yong's Modulus (Gpa)	Poissons ratio	Density (Kg/m ³) X 10 ³
0	1.56	0.35	1.45
1	1.7	0.34	1.45
3	1.72	0.28	1.45
5	1.81	0.28	1.46
7	1.92	0.29	1.46
9	1.96	0.31	1.47
11	1.83	0.36	1.47
13	2.26	0.36	1.47
15	2.27	0.33	1.48

B- Steps involved in detecting frequencies of cracked beam main steps involved to detect frequencies of cracked beam are,

- 1) Natural frequencies of un-cracked beam for different composition are determined theoretically.
- 2) Natural frequencies of un-cracked beam for different compositions are estimated in ANSYS 14.5.
- 3) Theoretical results are compared with ANSYS 14.5 Results.
- 4) Natural frequencies of composite beam for different % of NC are estimated using ANSYS 14.5 for different crack depths.

II. THEORETICAL CALCULATIONS

Theoretical calculations are made through the following formulae for four modes of natural frequencies and results are shown in table 2.

$$\text{frequency of first mode } f_1 = \frac{3.52}{2\pi L^2} \sqrt{\frac{EI}{\rho A}}$$

$$\text{frequency of second mode } f_2 = \frac{22}{2\pi L^2} \sqrt{\frac{EI}{\rho A}}$$

$$\text{frequency of third mode } f_3 = \frac{61.7}{2\pi L^2} \sqrt{\frac{EI}{\rho A}}$$

$$\text{frequency of fourth mode } f_4 = \frac{121}{2\pi L^2} \sqrt{\frac{EI}{\rho A}}$$

Where,

L=Length of the beam,

E=Young's modulus of material,

I=Moment of inertia of cross section,

A=Area of cross section,

ρ =Density of material.

Table 2: Variation of frequency with change in NC % with theory

% of NC	frequency of 1 st mode(Hz)	frequency of 2 nd mode(Hz)	frequency of 3 rd mode(Hz)	Frequency of 4 th mode(Hz)
0	1.76	11.0606	31.0199	60.833

1	1.847 4	11.526 2	32.381 8	63.504 1
3	1.857 4	11.608 7	32.557 1	63.847 8
5	1.905 4	11.908 7	33.398 4	65.497 8
7	1.962 4	12.265 5	35.477 5	69.575 8
9	1.981 9	12.386 8	34.739 3	68.127 4
11	1.915 7	12.968 7	33.566 7	65.827 8
13	2.128 2	13.302 5	37.303 9	73.156 8
15	2.131 9	13.324 3	37.368 6	73.283 6

III. FINITE ELEMENT MODELING

The ANSYS 14.5 finite element program was used for free vibration of the cracked beams. A 20-node three-dimensional structural solid element under SOLID 186 was selected to model the beam. The beam was discretized into 1045 elements with 2318 nodes. Geometrical shape of the beam is shown in figure 1. Cantilever boundary condition was considered by constraining all degrees of freedoms of the nodes located on the left end of the beam. The subspace mode extraction method was used to calculate the natural frequencies of the beam and mode shapes are shown in figure 2 and results are in table 3.

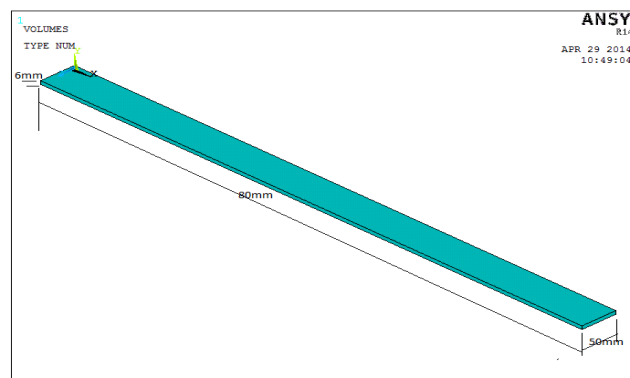
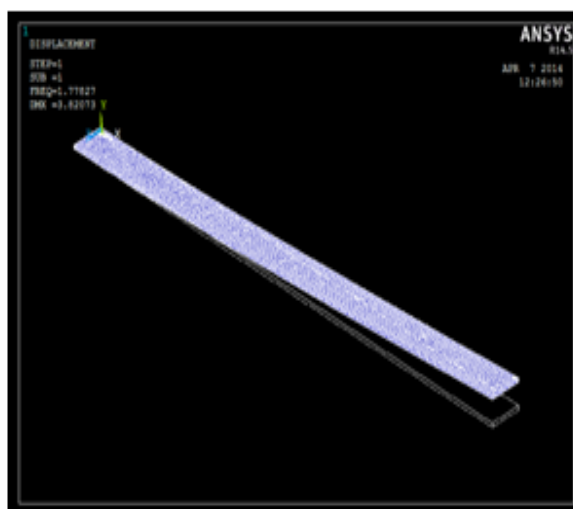
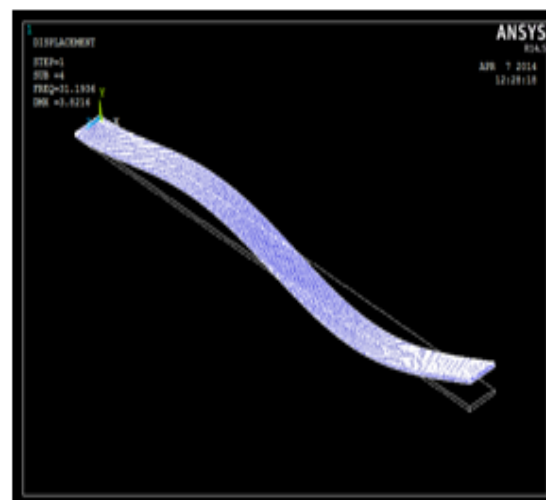


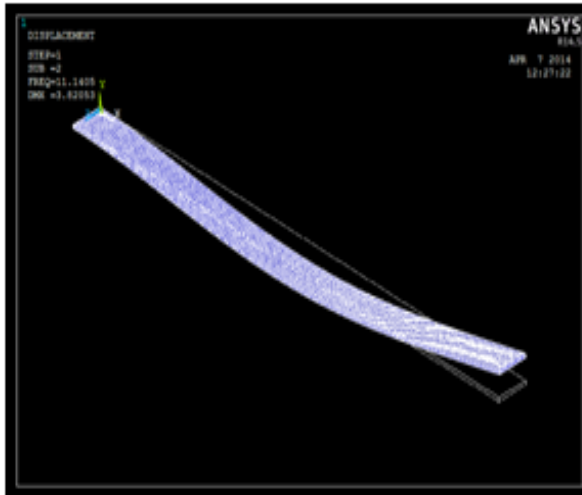
Figure 1 : Geometrical model for un-cracked beam



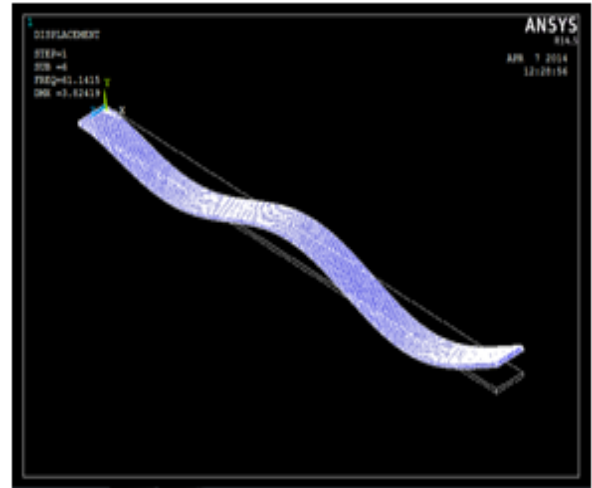
2-a: 1st mode-1.7783Hz frequency



2-b: 2nd mode-11.14Hz frequency



2-c: 3rd mode-31.194Hz frequency



2-d: 4th mode-61.142Hz frequency

Figure 2: Mode Shapes of un-Cracked Beam for 0% Nanoclay

Table 3: Variation of frequency with change in NC % with simulation

% of NC	frequency of 1 st mode(Hz)	frequency of 2 nd mode(Hz)	Frequency of 3 rd mode(Hz)	frequency of 4 th mode(Hz)
0	1.77827	11.1405	31.1936	61.142
1	1.85523	11.623	32.544	63.785
3	1.8621	11.666	32.662	64.004
5	1.9104	11.963	33.509	65.665
7	1.968	12.33	34.52	67.648
9	1.989	12.461	34.889	68.376
11	1.925	12.06	33.768	66.189
13	2.1391	13.401	37.523	73.549
15	2.141	13.413	37.556	73.607

IV. Comparison of results

After comparison of both theoretical and ANSYS-14.5 results, the difference between both results is negligible and comparison of frequency is shown in figure 3. Hence, the analysis of cracked beam is extended in ANSYS-14.5 package.

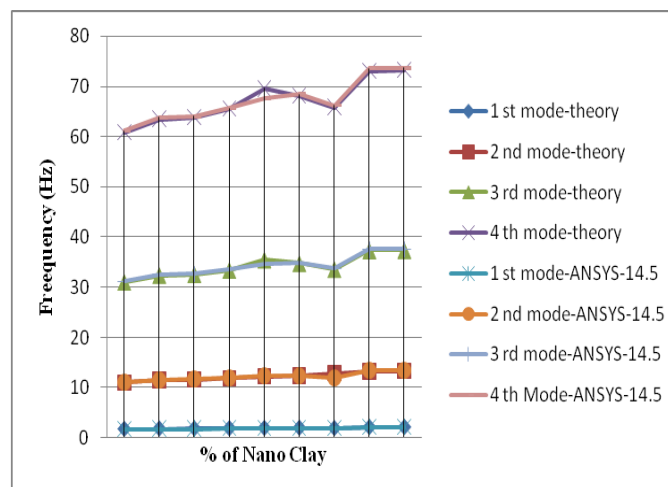


Figure 3: Comparison of theoretical and ANSYS-14.5 results for different % of Nano Clay.

V. Results

After comparison of the both theoretical and ANSYS-14.5 results, Procedure could be verified in ANSYS-14.5 from the journal [19] for Aluminum material. Same results were obtained from that procedure. Hence, the same procedure is adopted for extracting natural frequencies of cracked beam as shown in figure 4 and 5 and obtained results are shown in table 4. The comparisons for different mode frequencies with varying percentage of NC for different crack depth are shown in figures 6 to 9.

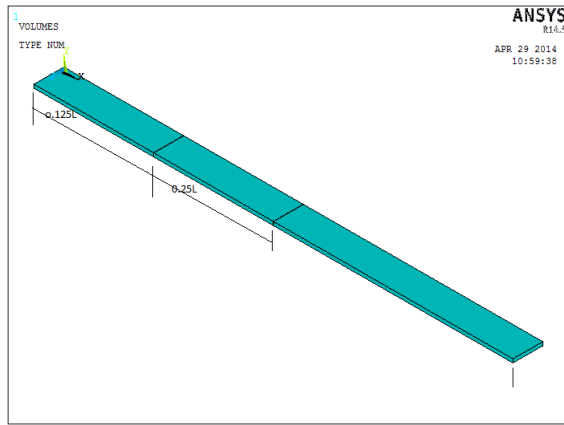


Figure 4: Location of cracks on composite beam

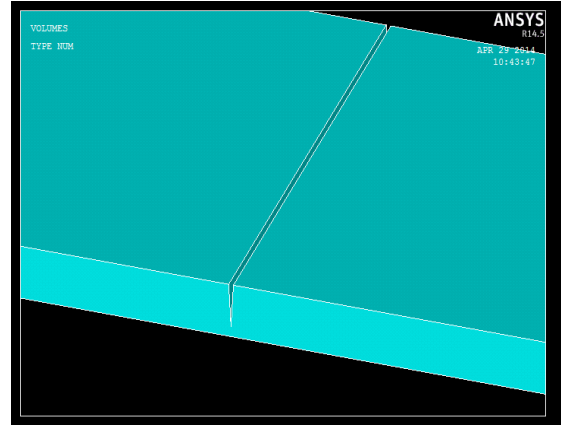


Figure 5: Geometrical model of crack

Table 4: Natural frequencies of Different Cracks

% of NC	Crack Depth to Width Ratio (a/w)	frequency of 1 st mode(Hz)	frequency of 2 nd mode(Hz)	Frequency of 3 rd mode(Hz)	Frequency of 4 th mode(Hz)	% of NC	Crack Depth to Width Ratio (a/w)	frequency of 1 st mode(Hz)	frequency of 2 nd mode(Hz)	Frequency of 3 rd mode(Hz)	Frequency of 4 th mode(Hz)
0	0	1.7783	11.14	31.194	61.142	1	0	1.8553	11.623	32.544	63.785
	0.25	1.7727	11.108	31.135	60.85		0.25	1.8506	11.596	32.502	63.522
	0.5	1.7511	10.977	30.915	59.674		0.5	1.8267	11.452	32.251	62.245
	0.8	1.6253	10.307	29.604	54.129		0.8	1.6947	10.746	30.871	56.429
3	0	1.8621	11.666	32.662	64.004	5	0	1.9104	11.969	33.509	65.665
	0.25	1.8564	11.633	32.603	63.702		0.25	1.9046	11.935	33.449	65.355
	0.5	1.8329	11.49	32.36	62.429		0.5	1.8805	11.789	33.2	64.051
	0.8	1.6983	10.767	30.944	56.518		0.8	1.7424	11.047	31.749	57.989
7	0	1.968	12.33	34.52	67.648	9	0	1.989	12.461	34.889	68.376
	0.25	1.9618	12.293	34.453	67.32		0.25	1.9832	12.427	34.83	68.061
	0.5	1.937	12.143	34.198	65.98		0.5	1.9584	12.277	34.576	66.72
	0.8	1.795	11.381	32.707	59.743		0.8	1.8157	11.513	33.081	60.443
11	0	1.925	12.06	33.768	66.189	13	0	2.1391	13.401	37.523	73.549
	0.25	1.9189	12.025	33.704	65.872		0.25	2.132	13.36	37.446	73.185
	0.5	1.8957	11.884	33.468	64.607		0.5	2.1061	13.203	37.183	71.777
	0.8	1.7602	11.162	32.056	58.628		0.8	1.9554	12.4	35.613	65.129
15	0	2.141	13.413	37.556	73.607	15	0.5	2.1082	13.216	37.221	71.834
	0.25	2.1346	13.376	37.49	73.264		0.8	1.9556	12.401	35.626	65.116

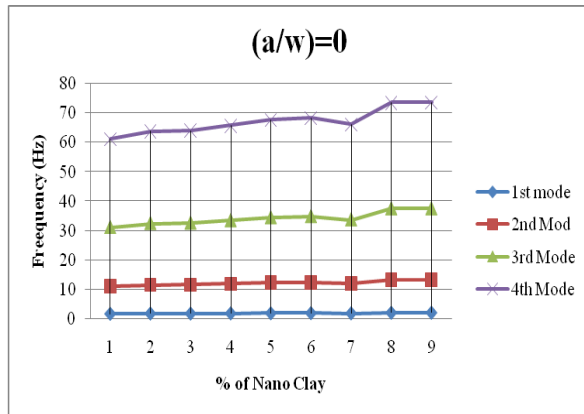


Figure 6: Comparison of Natural Frequency with different % of NC for 0 crack depth to width ratio

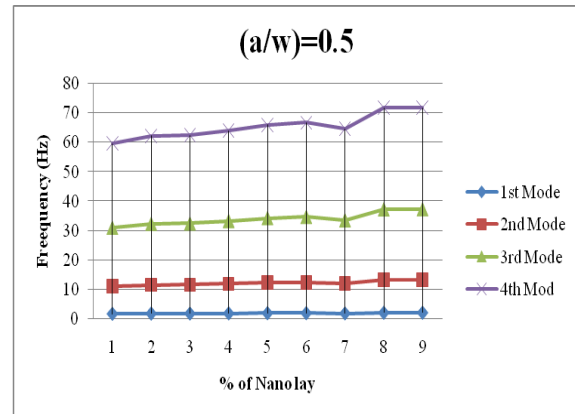


Figure 8: Comparison of Natural Frequency with different % of NC for 0.5 crack depth to width ratio

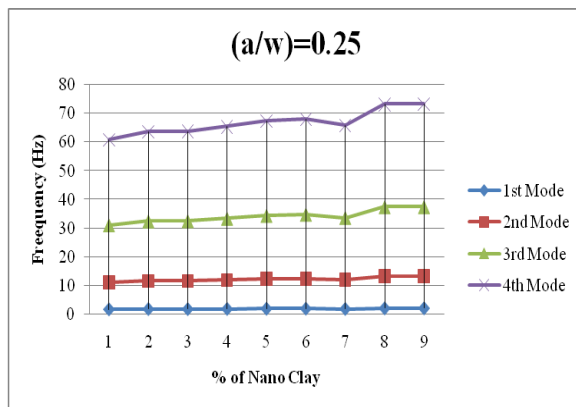


Figure 7: Comparison of Natural Frequency with different % of NC for 0.25 crack depth to width ratio

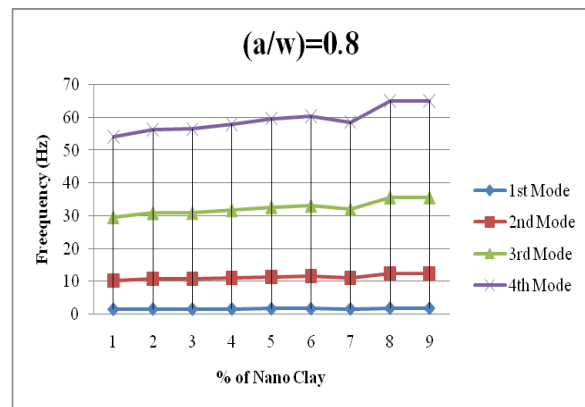


Figure 9: Comparison of Natural Frequency with different % of NC for 0.8 crack depth to width ratio

IV. Conclusions

After studying different compositions of NC in the composite beam with different crack depths, the following conclusions are there.

- Frequency of beam increases with increase in NC %.
- Frequency of beam decreases with increase in crack depth.
- Percentage of change of frequency is almost all negligible for variation of NC at same crack depth.

REFERENCES

- [1] J. Karger-Kocsis, T. Harmia and T. Czigan, "Comparison of the Fracture and Failure Behavior of Polypropylene Nanocomposites Reinforced by Long Glass Fibers and by Glass Mats," *Composites Science and Technology*, Vol. 54, pp. 287-298, No. 3, 1995.
- [2] J. Liakos, B. Wang, R. Cipra and T. Siegmund, "Processing- Microstructure-Property Predictions for Short Fiber Reinforced Composite Structures Based on a Spray Deposition Process," *Composite Structures*, Vol. 61, No. 4, pp. 363-374, 2003.
- [3] G. Ben-Dor, A. Dubinsky and T. Elperin, "An Engineering Approach to Shape Optimization of Impactors against Fiber-Reinforced Plastic Laminates," *Composites Part B: Engineering*, Vol. 40, pp. 181-188, No. 3, 2009.
- [4] M. Bhattacharya and A. K. Bhowmik, "Polymer-Filler Interaction in Nanocomposites: New Interface Area Function to Investigate Swelling Behavior and Young's Modulus," *Polymer*, Vol. 49, pp. 4808- 4818 No. 22, 2008.
- [5] T. A. Rajesh and D. Kumar, "Recent Progress in the Development of Nano-Structured Conducting Polymers Nanocomposites for Sensor Applications," *Sensors and Actuators B: Chemical*, Vol. 136, No. 1, 2009, pp. 275-286.
- [6] L. Kumari, T. Zhang, G. H. Du, W. Z. Li, Q. W. Wang, A. Datye and K. H. Wu, "Thermal Properties of CNT/Alumina Nanocomposites," *Composites Science and Technology*, Vol. 68, No. 9, pp. 2178-2183, 2008.
- [9] D. Sikdar, D. R. Katti, K. S. Katti and R. Bhowmik, "Insight into Molecular Interactions between Constituents in Polymer Clay Nanocomposites," *Polymer*, Vol. 47, No. 14, pp. 5196-5205, 2006.

- [10] J. G. Zhang, D. D. Jiang and C. A. Wilkie, "Polyethylene and Polypropylene Nanocomposites Based upon an Oligomerically Modified Clay," *Thermochimica Acta*, Vol. 430, No. 1-2, pp. 107-113, 2005.
- [11] Y. Dong and D. Bhattacharyya, "Mapping the Real Micro/Nanostructures for the Prediction of Elastic Moduli of Polypropylene/Clay Nanocomposites," *Polymer*, Vol. 51, pp. 816-824, No. 3, 2010.
- [12] L. Cauvin, D. Kondo, M. Brieu and N. Bhatnagar, "Mechanical Properties of Polypropylene Layered Silicate Nanocomposites: Characterization and Micro- Macro Modelling," *Polymer Testing*, Vol. 29, pp. 245-250, No. 2, 2010.
- [13] N. A. Siddiqui, R. S. C. Woo, J.-K. Kim, C. C. K. Leung and A. Munir, "Mode I Interlaminar Fracture Behavior and Mechanical Properties of CFRPs with Nanoclay-Filled Epoxy Matrix," *Composites Part A: Applied Science and Manufacturing*, Vol. 38, pp. 449-460, No. 2, 2007.
- [14] B. Cotterell, J. Y. H. Chia and K. Hbaieb, "Fracture Mechanisms and Fracture Toughness in Semicrystalline Polymer Nanocomposites," *Engineering Fracture Mechanics*, Vol. 74, pp. 1054-1078, No. 7, 2007.
- [15] vibration analysis of cracked cantilever beam with suitable boundary conditions-J. Yan¹ , J. C. Lee², C. W. Lee², D. W. Kang², Y. J. Kang², and S.H. Ahn¹.
- [16] https://www.efunda.com/materials/polymers/properties/polymer_datasheet.cfm?MajorID=P-TP&MinorID=1.
- [17] M. N. Bureau, M.-T. T.-T. and F. Perrin-Sarazin, "Essential Work of Fracture and Failure Mechanisms of Polypropylene-Clay Nanocomposites," *Engineering Fracture Mechanics*, Vol. 73, pp. 2360- 2374, No. 16, 2006.
- [18] <http://en.wikipedia.org/wiki/Polypropylene>
- [19] Vibration Analysis of Cracked beam by Mogal Shyam Prabhakar, Master of Technology In Machine Design and Analysis National Institute of Technology ,Rourkela.

A Review of Issues in Environmentally Conscious Manufacturing and Product Recovery

Pisal Mahesh B.¹, Quazi T. Z.²

^{1, 2} Mechanical Engineering, Saraswati Collage of Engineering, India.

Abstract: Environmentally Conscious Manufacturing and Product Recovery (ECMPRO) has become an obligation to the environment and to the society itself, enforced primarily by governmental regulations and customer perspective on environmental issues. This is mainly driven by the escalating deterioration of the environment, e.g. diminishing raw material resources, over owing waste sites and increasing levels of pollution. ECMPRO involves integrating environmental thinking into new product development including design, material selection, manufacturing processes and delivery of the product to the consumers, plus the end-of-life management of the product after its useful life. ECMPRO related issues have found a large following in industry and academia who aim to find solutions to the problems that arise in this newly emerged research area. Problems are widespread including the ones related to life cycle of products, disassembly, material recovery, and remanufacturing and pollution prevention.

Keywords: Environmentally conscious manufacturing; Product recovery; Recycling; Reuse.

I. Introduction

During the industrial revolution, environmental issues were not addressed when designing and manufacturing products. However, in the last decade or so, Environmentally Conscious Manufacturing and Product Recovery (ECMPRO) has become an obligation to the environment and to the society itself, enforced primarily by governmental regulations and customer perspective on environmental issues. Environmentally conscious manufacturing (ECM) is concerned with developing methods for manufacturing new products from conceptual design to final delivery and ultimately to the end-of-life (EOL) disposal such that the environmental standards and requirements are satisfied ECMPRO is mainly driven by the escalating deterioration of the environment. Today's high-tech society requires thousands of different products which ultimately result in billions of tons of materials discarded, most of which end up in landfills. According to the US Environmental Protection Agency (EPA), in 1990 the amount of waste generated in the USA reached a whopping 196 million ton up from 88 million ton in the 1960s [1]. As a consequence of both fast depletion of the raw materials and an increasing amount of different forms of waste (solid waste, air and water pollution etc.), two commonly accepted primary objectives have been gaining momentum: (1) create environmentally friendly products, (i.e. green products); and (2) develop techniques for product recovery and waste management.

In order to design a product which is environmentally benign, the life cycle of the product should be well understood [2]. Life cycle analysis (LCA) spans over the development, manufacturing, use and disposal stages of the product. These have prompted campaigns such as design for recycling (DFR), design for environment (DFE) and design for disassembly (DFD). Even though LCA may seem to be the most important solution to environmental problems, its immediate effect is in the early stages of new product development. However, the biggest damage to the environment occurs when the product completes its useful life. Thus, understanding and developing techniques for end-of-life management of the products by means of product/material recovery are extremely crucial considering the millions of products that have already been developed without incorporating their undesired effects on the environment. Recoveries of products are usually performed in two ways: recycling and remanufacturing. Recycling aims to recover the material content of retired products by performing the necessary disassembly, sorting and chemical operations. On the other hand, remanufacturing preserves the product's (or the part's) identity and performs the required disassembly, sorting, refurbishing and assembly operations in order to bring the product to a desired level of quality. Disassembly has proven its role in material and product recovery by allowing selective separation of desired parts and materials. Besides being able to recover valuable precious materials by material recovery, good component removal via disassembly could provide parts for discontinued products and reduce the lead times in the assembly of new products [3, 4].

The above raised issues have captured the attention of industries, governments and academia.

II. Background

Our environment has limited resources, i.e. the materials we convert into products, energy, water and air supply and the places where we dispose of old products, are limited. Our society uses these resources to improve the living standard. However, we also need to provide for a sustainable environment for the next generation. To this end, we need to identify the extent of the problem and take corrective action. Many researchers have been doing just that.

2.1. Decreasing earth's resources and increasing environmental problems

Ever since the industrial revolution, the number of manufactured products has increased dramatically. The current state of manufacturing processes requires the use of trillions of tons of different forms of natural resources (raw materials, energy, water, etc.). Wann [5] reports that an average American consumes 20 tons of materials every year. Energy consumption is also at dramatic levels: every day the average American uses the equivalent of twenty-seven years of stored solar energy in the form of fossil fuels [5]. The products originating from renewable and non-renewable natural resources evolve into waste after their useful lives. Waste can be defined as redundant goods, by-products or residues that have no value and must be disposed of at a cost. Different forms of waste (hazardous and non-hazardous) have been generated by both manufacturers and consumers for decades [6].

Bylinsky [7] reports that according to the National Academy of Sciences, 94% of the substance that is pulled out of the earth, enters the waste stream within months. According to the Environmental Protection Agency (EPA), about 12 billion ton of industrial waste is generated annually in the United States and the scary part is, over a third of this amount is hazardous waste. Another estimated figure shows that by the year 2005, every family in the USA will own a computer [7]. That suggests that used computers will enter the waste stream as fast as we produce them. Europe is facing similar problems. The number of landfill sites where we can bury the non-hazardous solid waste is going down with the increasing amount of waste. Since old recycling methods, such as dumping, burying and burning in the open field, are no longer desirable due to tough new environmental laws and increasing consumer concerns [8], new methods have to be explored. For example, the importance of removing hazardous materials from refrigerators, such as Freon (which is a type of gas that has been proven to be destroying the ozone layer of the atmosphere), ABS (Acrylonitrile-Butadiene-Styrene), PVC (Polyvinyl Chloride), BS (Bile Salts) and PUR (Polyurethane) foam, cannot be ignored. Similarly, making responsible end-of-life choices for conventional military munitions is very crucial.

2.2. Response to negative environmental developments the good thing about us as a society is that we learn from our mistakes and experiences.

Wann [5] perfectly emphasizes the interactions between the environmental problems and the future of the society. The society as a whole has developed a heightened environmental awareness in response to numerous environment related problems that have recently surfaced. However, it is crucial to minimize the response time for corrective action to environmental problems as long delays could lead to irreversible damage. The governments, the industries [9] and the public have been very receptive and responsive to the environmental problems. The common goal is to integrate environmentally friendly thinking into daily practices.

One of the reasons for rapid developments in the material recovery and the ECM practices is the changing consumer perspective. Recently, consumers have become aware of their environment and the potential problems that can be created by neglecting it. Therefore, they have started to show more interest in buying products that are environmentally friendly and which will be taken back by their manufacturers at the end of their useful lives for recycling etc. This has become an incentive for the manufacturers to design and market environmentally friendly products (or 'green products') to gain advantage in the marketing platform against their competitors. Therefore, companies have started to analyze the product life cycle in order to insert the environmental component into the product design to produce a product that has a low production cost and is environmentally friendly. The manufacturers and consumers are also forced by many environmental laws and legislation to pay more attention to the environmental issues. In many countries, the environmental protection laws, regulations and tax implications are already in place or in the works [10]. Frosch [11] describes the development of environmental regulations in the USA which has been applied in three stages since Earth Day 1970. The first stage is the 'end-of-pipe regulation' which defines restrictions on the types of materials that can be discarded, as well as where and how they can be discarded. Some of the well-known laws under this stage are the clean Air Act, the Clean Water Act and the Resource Conservation Act. The second stage started with the Pollution Prevention Act of 1990, which focused on reducing pollution within the industrial processes. Finally, in the third stage, the aim is to encourage 'clean production' with the coordination of industry and the Environmental Protection Agency (EPA). The European Community has passed laws prohibiting the disposal of more than 15% of an automotive product by the year 2002 and this percentage drops to 5% in the year 2015 [1]. In Europe, government initiatives to make both manufacturer and user responsible for disposing of the wastes associated with a product are commonly being practiced. Material recycling goals proposed in the law stated

that by 1995, steel, non-ferrous metals, tires, glass and plastics must be recycled to the level of 100, 85, 40, 30 and 20%, respectively. Other European countries have similar measures on their agenda. In addition to making laws that enforce ECMPRO practices, taxation has been used as another weapon in fighting pollution problems. Crognale [10] sees the environmental regulations and laws as the basis for environmental management.

III. Environmentally Conscious Manufacturing (ECM)

ECM involves producing products such that their overall negative environmental effects are minimized [12]. ECM consists of the following two key issues:

1. Understanding the life cycle of the product and its impact on the environment at each of its life stages and
2. Making better decisions during product design and manufacturing so that the environmental attributes of the product and manufacturing process are kept at a desired level.

The first issue is necessary for drawing lines to determine how the product will evolve from the drawing board and how it will affect the environment throughout its life stages. If we fully understand the life cycle of the product, we can then transfer this information onto the actual development of the product (which addresses the second issue of ECM). In addition, understanding the end-of-life stage of the product is critical since one of the largest impact on the environment occurs at that stage.

During the design stage of the product, there are different objectives that the designers may focus on. Depending on the end-of-life strategy of the product, the design of the product can be realized to increase recyclability, manufacturability, disassemblability and to minimize the effect on the environment. When designing a product with environmental features, material selection should also be considered as a key element. Once the design decisions of a product are complete and the materials for its production are identified, the product's environmental attributes are pretty much set. However, in addition to design and materials decisions, issues involving selection of energy source, cooling systems and handling of hazardous byproducts etc. must be controlled during the manufacturing process to achieve a complete ECM concept.

3.1. Environmentally Conscious Design (ECD)

ECD aims to design products with certain environmental considerations. In the literature, both the life cycle analysis (LCA) of the product and the design for environment (DFE) are emphasized.

3.1.1. Life Cycle Analysis or Assessment (LCA)

LCA is a process for assessing and evaluating the environmental, occupational health and resource consequences of a product through all phases of its life, i.e. extracting and processing raw materials, production, transportation and distribution, use, remanufacturing, recycling and final disposal. LCA examines and quantifies the energy and materials used and wasted and assess the impact of the product on the environment. LCA usually facilitates the systematic collection, analysis and presentation of environmentally related data.

The steps involved in LCA, are as follows:

- Identification of the goals and boundaries of LCA,
- Analysis of inventory to achieve a balance between material and energy in the system,
- Evaluation of the system's impact on the environment,
- Assessment of the most promising system improvements to reduce the negative environmental impact.

LCA has applications in many areas. The results of an LCA may provide the basis for the development of environmental laws, taxes and regulations. Industries may use LCA to support product development so that the overall environmental impact of the product is minimized. Qualitative and quantitative characteristics of the product life cycle are taken into account by means of LCA during the conceptual design of each new product. This enables designers to estimate the costs and benefits associated with the design attributes of the product, energy consumption, materials requirement and after-life choices of the product. Many companies make use of LCA to support their public claim of environmental responsibility.

The scope of LCA involves tracking all the materials and energy flows of a product from the retrieval of its raw materials out of the environment to the disposal of the product back into the environment. The complexity of the LCA problem grows when the product structure is large and complex and the number of factors to be considered increases. Utilizing the power of computers for collection, organization and analysis of necessary data can help shorten the time it takes to conclude the LCA related decision process. In practice, however, such a process could be extremely involved if the limits of the system are not clearly defined. Therefore, prior to the execution of LCA, the associated goals and boundaries of the Life Cycle must be defined. Although the goals of LCA are system dependent, the economic issues are valid for all systems.

LCA can be treated as an optimization problem by maximizing the added value and minimizing the resource consumption and waste dispersion activities.

Ishii et al. [13] and Ishii [14] developed software called LINKER (which has been developed using Tool Book under Microsoft Windows) by concentrating on advanced planning for product retirement and

addressing the level to which a product should be disassembled. LINKER allows the user to evaluate a design at various stages of the life cycle. After entering the required data into the software's input stream, LINKER displays the disassembly times for components and fasteners, the compatibility index and the retirement cost breakdown for each clump, including the reprocessing and disassembly cost. These results are used to create better designs to satisfy the measures of the designer. Other computer supported LCA tools have also been developed. Some researchers concentrate on the development of a knowledge-base that can provide understanding of the connections among various elements of life cycle design.

3.1.2. Design for Environment (DFE)

Knowledge gained during LCA needs to be transferred into the initial design of a new product. It is actually possible to focus on a specific stage of the product's life such that the environmental impact is minimized in that stage as well as emphasizing the entire life of the product. Researchers have analyzed different stages of a product's life and developed techniques and logistics to improve the design of the product from an environmental perspective. These techniques, all together, are referred as the design for environment (DFE). Fiksel [15] presents an excellent overview of DFE concepts and practices. Fiksel defines DFE as: a systematic consideration of design performance with respect to environmental, health and safety objectives over the full product and process life cycle." According to the author, DFE can be broken down into many stages, including, manufacturing, consumer use and the end-of-life of the product. Throughout these stages, different forms of design strategies can be envisioned as the pieces of DFE. For example, in order to minimize the effect of the product on the environment at the manufacturing stage, design objectives may include design for energy conservation to reduce the energy use in production and to be able to use renewable forms of energy and design for minimizing the discharge of hazardous byproduct during production. Similar concerns are also valid during the distribution of the product. Finally, during the end-of-life stage of the product, there are design objectives to increase the output of the product recovery. These include design for material and product recovery, design for disassembly, design for waste minimization, design under legislation and regulations, etc.

Design for Recycling (DFR) suggests making better choices for material selection such that the processes of material separation and material recovery become more efficient. Some general characteristics of DFR are as follows:

- Long product life with the minimized use of raw materials (source reduction),
- Fewer number of different materials in a single product while maintaining compatibility with the existing manufacturing infrastructure,
- Fewer components within a given material in an engineered system,
- Increased awareness of life cycle balances and reprocessing expenses,
- Increased number of parts or subsystems those are easily disassembled and reused without refurbishing,
- More adaptable materials for multiple product applications and
- Fewer 'secondary operations' reducing the amount of scrap and simplifying the recovery process.

On the other hand, design for remanufacturing (or part recovery) suggests the use of reusable parts and packaging. Disassembly is used both in recycling and remanufacturing to increase the recovery rate by allowing selective separation of parts and materials. Thus, designing for disassembly (DFD) is important and therefore it has been given special attention. DFD initiatives lead to the correct identification of design specifications to minimize the complexity of the structure of the product by minimizing the number of parts, increasing the use of common materials and choosing the fastener and joint types which are easily removable. DFD is often carried out using software due to the complexity of the problem. Kroll et al. [16] propose a rating scheme that allows the designers to translate properties of a design into quantitative scores and thus provide a means of identifying weaknesses in the design and comparing alternatives.

DFD is just one of the aspects of DFE. However, DFE comes with more than one task. Glantschnig [17] identifies three components of DFE, viz., the challenges faced by product designers and environment specialists, the green design challenges from a company's point of view and the external factors and forces that affect the design decisions. The ultimate goal of green design is to reduce the overall environmental damage when producing goods and providing services. To achieve this goal, in addition to this cooperative work, availability of guidelines, checklists and software-based DFE tools also play a key role. The authors utilize a modified version of the AHP (Analytic Hierarchy Process) model to compare alternative decisions by evaluating the change in the environmental features and the economical performance of the design. According to the authors, the AHP model is the most effective model among multicriteria decision making approaches for comparing different 'green' product development alternatives. The authors note that such a model (1) integrates all the criteria into a single overall score for ranking decision options and (2) particularly appeals to decision makers involved in the evaluation of very complex programs."

Besides DFE approaches, the environmental effect of a product can also be reduced by designing the product for a longer life. The following design considerations may take place in the manufacturing and recovery stage: design for repair, design for assembly, design for minimum tool requirement for disassembly and so on. Some researchers refer to product design improvement efforts as design for 'X' (DFX) where X stands for a design under consideration such as Manufacturability, Testability, Install ability, Compliance, Reliability, Disassembly etc. DFX is an integrated approach to designing products and processes for cost-effective, high quality downstream operations from manufacture through service and maintenance. DFX aims to reduce time to market, lower cost and increase quality of the product.

3.2. Environmentally Conscious Production (ECP)

In addition to environmentally friendly product designs resulting from DFE initiatives, issues involving production must also be addressed to have a complete concept of environmentally conscious manufacturing [15]. These issues include selecting energy sources necessary for production, designing cooling systems and handling hazardous byproducts. Currently, numerous production techniques, material handling systems and energy sources are available. Utilizing some sort of an assessment tool to select among them may be valuable financially as well as improve the environmental features of the production system. Bock [18] develops a tool to come up with a good material and process combination. Similar models have been developed to analyze how the selection of different manufacturing processes effect the environment.

Many companies monitor their waste generation as a result of their manufacturing processes. Several techniques have been proposed for such a monitoring process. For example, weighting methods were proposed to measure the chemical and toxic discharges of different manufacturing methods used. Rupp and Graham [19] evaluate a printed circuit board (PCB) production plant from an environmentally consciousness point of view.

3.3. Industry Examples

The automotive industry leads in research and development activities in response to the negative environmental developments. For example, Chrysler, Ford and GM researchers are trying to improve disassemblability features of their automobiles to take 'ease of destruction' together with 'ease of construction' into consideration. The new European Ford model, Mondeo, is claimed to be 85% recyclable. Another example is the efforts of Mercedes-Benz to implement a total vehicle recycling program with two main elements: vehicle design and vehicle recycling. Billatos and Nevrekar [20] highlight the Benz design efforts which include choosing environmentally compatible and recyclable materials for components, reducing the volume and variety of plastics used, making plastics parts with logos and avoiding composite materials as much as possible. Mercedes Benz started taking scrap cars back in 1991 and has been performing the material recovery process as part of their environmentally friendly production program. The information gathered from the recycling process is transferred as DFE and DFR initiatives to the new product design stage. Mercedes and Swatch have jointly designed a prototype car entirely realized in vegetable fibers (at the expense of metals) and valuable special materials. Another German car company, BMW, recently announced a pilot program in North America to test the feasibility of recycling BMW automobiles; because of the strict German laws the company already recycles cars in Europe. Targeting three US cities, BMW will give owners a \$500 credit towards the purchase of a new or used BMW for turning in a car to a dismantling center. BMW has been using color coding for differing plastic materials for the past 15 yr. The color coding scheme allows development of efficient dismantling and disassembly techniques. BMW transfers the knowledge gained from dismantling and disassembly processes into new product development. Using DFD principles and more recyclable components in the original design, BMW hopes to increase the percentage of recycled car weight from the present 75 to 90% in the future [20]. BMW targets to produce a car out of 100% recycled parts by the year 2000.

Similar efforts are being made by the German manufacturing arm of General Motors (GM), Adam Opel AG, Volkswagen, Nissan Motor Company and Volvo Car Corporation. Volvo has been trying to increase the efficiency of its recycling methods by giving grants to universities and research institutions. The grants have been awarded to projects on life-cycle analysis, dismantling methods, materials recycling, energy recovery, and disposal of environmentally hazardous materials and transportation of materials to/from recycling centers. Consumer electronics and computer industries are also involved in the environmental movement. There are a lot of small and big companies investing into these causes. Digital, Proctor & Gamble and Canon are working to improve the recycleability of their products [21]. Digital uses the 6R approach on their used products (6R means Recycle, Reclaim, Refurbish, Remanufacture, Resell and Reuse).

Xerox Corporation strongly believes that environmentally conscious practices will become a customer requirement in the near future and is taking appropriate actions to prepare by applying life cycle design and DFE on its products. The company's goal is to achieve 0% end-of-pipe parts headed for landfills.

The number of transistors in a Pentium chip is 3.1 million. Increasing the number of transistors in a single chip will result in fewer chips to build and fewer chips to dispose, lowering the resource consumption as well as lowering the generation of waste. Intel has also developed a chip level technology to put PCs in a 'sleep'

mode in which the power consumption is reduced 6 ± 10 fold. One of the world's biggest computer market share holders, IBM, has had a pollution prevention program since 1971. The goal is to achieve continuous improvement in the reduction of hazardous waste generated from IBM's manufacturing processes and its used products. IBM also develops design specifications for its new products to improve product's end-of-life material recovery. Household goods manufacturers are also encouraged by the current environmentally-driven green manufacturing efforts [20].

Another important area related to green production is packaging, since better packaging methods can significantly decrease the use of materials. For example, Colgate [7] has created a very smart design for the packaging of toothpaste. The toothpaste comes in a plastic tube which can stand on its own top. Thus, it does not require a carton box unlike other similar products.

IV. Recovery Of Materials And Products

A recent paper by Fleischmann et al. [22] categorizes recovery simply into material recovery and added value recovery. We also categorize the recovery process into material recovery (recycling) and product recovery (remanufacturing). Material and product recovery are carried out mainly due to three reasons: (1) hidden economic value of solid waste, (2) market requirements and (3) governmental regulations. Material recovery mostly includes disassembly for separation and processing of materials (e.g. carrying out necessary chemical operations) of used products. The main purpose is to minimize the amount of disposal and maximize the amount of the materials returned back into the production cycle. Product recovery includes disassembly, cleaning, sorting, replacing or repairing bad components, reconditioning, testing, reassembling and inspecting. The recovered parts/products are used in repair, remanufacturing of other products and components and for sale to an outsider.

Various forms of the material/product recovery have been around for a long time. Automobile (metal scrap brokers), electronic and paper recycling are the most common examples [22]. Among these, the automobile recycling is most advanced. In the USA, while just 20% of glass, 30% of paper products and 61% of aluminum cans are recycled, 95% of the 10 million cars and trucks that are retired each year go to the recycler and for each of those cars, 75% by weight is recovered for reuse. In Europe, according to the 1994 figures, the recovery rate (in percentage of total consumption) of paper products is relatively higher, about 43% [22]. The recovery rate of electronic consumer products (mostly computer products) is also fast developing.

In order to perform product recovery profitably and according to applicable laws and regulations, collection of retired products must be planned. Collection decisions involve location selection of collection centers (where retired products are collected and stored prior to distribution to recycling or remanufacturing facilities); layout design of collection centers (including material handling and storage); and transportation (designing the transportation networks to bring used products from many origins to a single collection center). The biggest challenge in collection related problems is the level of uncertainty involved in the quality and quantity of products collected.

4.1. Material Recovery or Recycling

Recycling is performed to retrieve the material content of the used and non-functioning products. As previously mentioned it is mainly driven by economic and regulatory factors. The economic value of used products is the reason for several recovery infrastructures. One of the best examples is the US automobile recycling infrastructure [23]. In the USA, for more than half a century, some very well developed automobile recycling centers provided hundreds of jobs and brought millions of tons of materials back into the production cycle. Automobiles arrive at the dismantling facility directly from the end-user or from the auto dealers. The dismantler removes reusable components and particularly valuable materials fractions (e.g. large castings, batteries, etc.). Tires and fluids are also removed to allow the remaining hulk (which is the remaining body and the chassis) to be accepted by the shredding processor downstream. The hulk is flattened for ease of transport to the hulk shredder who buys the hulk from the dismantler. The shredder reduces the hulk into small pieces. Separation into ferrous, nonferrous and non-metallic automobile shredder residue fractions is achieved by the magnetic and density separation techniques. Then the materials are sorted to be sent to the demand points. As a result of this infrastructure, metal recyclers (or scrap 'processors') supply nearly half the USA's iron, steel and copper, 55% of the lead, a third of the aluminum, plus assorted titanium, zinc, molybdenum from over 60 million tons of scrap gathered from an intricate web of suppliers. Encouraged by the success of the automobile and electronic goods recycling in the USA, European companies are also developing ways to increase profitability in their recycling programs.

Economically-driven recovery process finds its application in the consumer electronics industry as well. A typical computer contains gold, silver, palladium and platinum. The amount of precious materials is much higher in earlier manufactured electronics products. Recovery of precious materials from consumer electronic products requires proper equipment and is generally completed in mass. Moyer and Gupta [4] report

that a company in Canada with a specialized copper smelter processed more than 100,000 ton of recyclable materials (one quarter of which consisted of electronics products) in 1993. From this material, the company recovered 34 ton of copper, 123 ton of silver, 7 ton of gold and 5 ton of platinum and palladium.

Besides the recovery of highly valuable materials, other materials such as plastics [10] are being recovered due to environmental concerns. Regulatory electronics recycling is also practiced.

In order to find a balance between the resources invested in a recycling process (i.e. time and money) and value gained from the recovered materials, economic analysis of recycling process is sometimes carried out. The objective, of course, is to continue the recovery process as long as the profitability is maintained.

Johnson and Wang [24] discuss a methodology for carrying out material recovery in an efficient way. The methodology incorporates an initial study to determine the percentage of product which is recoverable, the initial cost/benefit estimates of recovery and the initial goals of material recovery options, identifying the disassembly level which generates a preferred sequence of disassembly which will maximize the value gained from recovery and the implementation stage of strategies developed in the previous levels.

The authors consider design and process attributes as well as the uncertainties that are likely to arise in a recycling system. In order to incorporate these attributes into the proposed approach, the authors utilize fuzzy-set theory and group technology.

4.2. Product Recovery or Remanufacturing

Lund [25] describes remanufacturing as an industrial process in which worn-out products are restored to like-new condition. Through a series of industrial processes in a factory environment, a discarded product is completely disassembled. Usable parts are cleaned, refurbished and put into inventory. Then the product is reassembled from old parts (and where necessary new parts) to produce a unit fully equivalent or sometimes superior in performance and expected lifetime to the original new product." Fleischmann et al. [22] define remanufacturing as a process of bringing the used products back to 'as new' condition by performing the necessary operations such as disassembly, overhaul and replacement. Remanufacturing is also referred as recycling-integrated manufacturing. Industries that apply remanufacturing typically include automobile industry, electronics industry and tire manufacturers. Similar to the conventional production systems, in remanufacturing systems, there are operational, manufacturing, inventory, distribution and marketing related decisions to be made [26,27]. In general, the existing methods for conventional production systems cannot be used for the remanufacturing systems.

V. Conclusion

- Environmental issues are gaining justifiable popularity among society, governments and industry due to negative environmental developments.
- Research shows that the manufacturing of environmentally friendly products is crucial in order to minimize the use of virgin resources. This can be achieved by studying the life cycle of the product from its design stage to its retirement stage and incorporating this information into engineering design and production.
- Reclamation of materials and parts from outdated products is equally crucial in fighting against the environmental degradation. The recovery process reverses the one-way production and helps us move closer to a sustainable system.
- Disassembly is an important component of remanufacturing which is currently labor intensive and expensive. Thus, it is very important to develop automated disassembly systems which may eliminate the drawbacks of manual disassembly, i.e. lengthy disassembly completion time, human exposure to possible hazardous materials and byproducts, expensive labor use, etc.
- For successful implementation of ECM and recovery processes, it is necessary to develop qualitative and quantitative decision tools. The applicability of traditional tools is limited because the objectives, constraints and other characteristics of the traditional systems are different from those for the ECMPRO systems.
- Effort must be made for ECMPRO systems to be profitable so that the incentive for development and planning of these systems continues.
- National environmental laws and regulations must be globalized because our environment is a global issue rather than an individual nation's problem.
- Although the current development in ECMPRO research is encouraging, it is being conducted in clusters. It is, therefore, necessary that interactions between these research efforts be studied in order to develop interrelationships and determine the global effect of this field.
- The ECMPRO research should take advantage of the powerful tools available in Industrial Engineering and Operations Research.

REFERENCES

- [1.] Nasr N. Environmentally conscious manufacturing. In: *Careers and the Engineer*, 1997. p. 26±7.
- [2.] Steinhilper R. Design for recycling and remanufacturing of mechatronic electronic products: challenges, solutions and practical examples from the European viewpoint. In: *ASME Design for Manufacturability Conference*, Chicago, IL, 14±17 March 1994, 1994. p. 65±7.
- [3.] Brennan L, Gupta SM, Taleb KN. Operations planning issues in an assembly/disassembly environment. *International Journal of Operations and Production Management* 1994;14(9):57±67.
- [4.] Moyer LK, Gupta SM. Environmental concerns and recycling/disassembly efforts in the electronics industry. *Journal of Electronics Manufacturing* 1997;7(1):1±22.
- [5.] Wann D. *Deep design: pathways to a livable future*. Washington: Island Press, 1996.
- [6.] Raleigh LH, Knox RC, Canter LW. Proposed nonhazardous-industrial-waste classification scheme. *Journal of Environmental Engineering* 1995;121(5):402±10.
- [7.] Bylinsky G. Manufacturing for reuse. In: *Fortune*, 1995. p. 102±12.
- [8.] Benson A. Engineering cars for recycling. In: *Assembly*, 1996. p. 42±5.
- [9.] Shrivastava P. The role of corporations in achieving ecologically sustainability. *Academy of Management Journal* 1995;20(4):936±60.
- [10.] Crognale G. The next generation of environmental management. In: *Proceedings of the IEEE International Symposium on Electronics and the Environment*, Dallas, TX, 6±8 May 1996, 1996. p. 323±7.
- [11.] Frosch RA. Industrial ecology: adapting technology for a sustainable world. *Environment* 1995;37(10):16±37.
- [12.] Sarkis J. Supply chain management and environmentally conscious design and manufacturing. *International Journal of Environmentally Conscious Design and Manufacturing* 1995;4(2):43±52.
- [13.] Ishii K, Eubanks CF, Di Marco P. Design for product retirement and material life cycle. *Materials & Design* 1994;15(4):225±33.
- [14.] Ishii K. Life-cycle engineering design. *Journal of Mechanical Design* 1995;117B:42±7.
- [15.] Fiksel J. *Design for environment: creating eco-efficient products and processes*. McGraw-Hill, 1996.
- [16.] Kroll E, Beardsley B, Parulian A. A methodology to evaluate ease of disassembly for product recycling. *IEEE Transactions* 1996;28(10):837±45.
- [17.] Glantschnig WJ. Green design: an introduction to issues and challenges. *IEEE Transactions on Components, Packaging and Manufacturing Technology-Part A* 1994;17(4):508±13.
- [18.] Bock L. Material-process selection methodology: design for manufacturing and cost using logic programming. *Cost Engineering* 1991;33(5):9±14.
- [19.] Rupp G, Graham S. Process design and optimization for environmentally conscious printed circuit board assemblies. In: *Proceedings of the IEEE International Symposium on Electronics & the Environment*, Orlando, FL, 1±3 May 1995, 1995. p. 95±9.
- [20.] Billatos SB, Nevrekar VV. Challenges and practical solutions to designing for the environment. In: *ASME Design for Manufacturability Conference*, Chicago, IL, 14±17 March 1994, 1994. p. 49±64.
- [21.] Anonymous. The green designers. In: *Enterprise*, 1994. p. 14±20.
- [22.] Fleischmann M, Boemhof-Ruwaard JM, Dekker R, van der Laan E, van Nunen JAEE, Van Wassenhove LN. Quantitative models for reverse logistics: a review. *European Journal of Operational Research* 1997;103:1±17.
- [23.] Hendrix J, Massey KA, Whitham E, Russel M, Bras BA. Technologies for the identification, separation and recycling of automotive recycling. *International Journal of Environmentally Conscious Design and Manufacturing* 1997;6(2):37±50.
- [24.] Johnson MR, Wang MH. Planning product disassembly for material recovery opportunities. *International Journal of Production Research* 1995;33(11):3119±42.
- [25.] Lund R. *The remanufacturing industry: hidden giant*. Boston, MA: Boston University, 1996.
- [26.] Kopicky RJ, Berg MJ, Legg L, Dasappa V, Maggioni C. *Reuse and recycling: reverse logistics opportunities*. Oak Brook, IL: Council of Logistics Management, 1993.
- [27.] Stock JR. *Reverse Logistics*. Oak Brook, IL: Council of Logistics Management, 1992.

Author Bibliography



Pinal Mahesh B. Research Scholar, Mechanical Engineering, Saraswati College of Engineering Kharghar-Navi Mumbai. Email: mahesh_2007pinal@yahoo.co.in



Quazi T. Z. HEAD OF Department, Automobile Engineering Saraswati College of Engineering Kharghar-Navi Mumbai. Email: kazitaqui@rediffmail.com

Zigbee Based Wireless Sensor Networks for Smart Campus

Prasad P. Netalkar¹, Yasha Kaushal², Dr. N. Shekar V. Shet³

¹(Electronics and Communication, PES Institute of Technology, Bangalore, India)

²(Electronics and Communication, National Institute of Technology, Bhopal, India)

³(Associate Professor, Department of Electronics and Communication, National Institute of Technology, Karnataka, India)

Abstract: A network which connects a bunch of distributed low-power sensor nodes together, with each node dedicated to a predefined operation can be visualized as a Wireless Sensor Network (WSN). The network must have the capability of gathering and transferring the data generated by end nodes efficiently. The major parts of Zigbee based LR-WPAN (Low Range-Wireless Personal Area Network) are-coordinator, routers and end devices. In this paper the authors concentrated on Zigbee based LR-WPAN and analyzed the effect of static and dynamic state of Zigbee PAN Coordinator on the performance of the network. Here the analysis is made on 3 topologies namely- star, mesh and tree with the help of OPNET modeler simulations. Authors suggested that instead of making the end devices dynamic, the coordinator can roam around the network area more easily, giving better global network performance over static coordinator network in terms of throughput and end-to-end delay. For different topologies, different impacts on network parameters are obtained. The main aim of this work is to evaluate, through simulations, the effect of coordinator mobility in a ZigBee/IEEE 802.15.4 based wireless personal area network and allow the people to mould the network topology as per the requirement and performance obtained here.

Keywords: WSN, mobile coordinator, star, mesh and tree topologies, Throughput, End to End delay.

I. INTRODUCTION

Nowadays wireless sensor technology is becoming a popular way to create wireless personal area network (WPAN) due to its low cost, low power consumption applications, convenience of using wireless signals in open areas such as office space or home rather than having to lay out wires and scalability but energy-saving stays a critical design issue. [1] It has applications in environment monitoring, military operation, intelligent home, medical and health and other commercial field. [2], [3], [4]. Devices in a LR-WPAN (Low-range wireless personal area network) can be classified as full function devices (FFDs) and reduced function devices (RFDs). [5] One device is designated as the PAN coordinator (FFD) which is responsible for monitoring the network activities and its devices, it guides and instructs the data flow across the network; others are routers and end nodes (RFDs). A FFD monitors the whole network via control packets and handles security/failure cases. It has the capability of becoming a PAN coordinator or associating with an existing PAN coordinator. A RFD can only relay the data but cannot change the task on its own assigned to it.

Zigbee and IEEE 802.15.4 are not the same. [6],[7] It is a standard base network protocol, widely used for LR-WPAN and supported solely by Zigbee alliance using the transported services of IEEE 802.15.4 network specifications. Zigbee protocol stack has basically 4 layers- application, network and security, MAC layer and physical layer. IEEE defined only latter two for LR-WPAN while former two are provided by Zigbee Alliance. Network and security layer also includes the application framework necessary for application processing. Zigbee networks can support a large number of nodes; approx. 64,000 with dynamic routing and single coordinator. Every node can be configured as a multifunction device with at most 240 applications running at a time. [8] The performance of the network depends on the topology employed which is highly application specific. Here authors tried to simulate via OPNET modeler the impact of various topologies on the global MAC statistics like throughput, global application statistics like end-to-end delay and global network statistics like number of hops which represents average number of hops travelled by application traffic in PAN. Most of the advanced applications of Zigbee Networks like remote location event sensing deploy mobility of the nodes rather than static structure.[9],[10] Authors think that the mobility of the prime node (PAN coordinator) greatly affects the performance of the system.

In section II, authors threw light on the Zigbee specification and its conjunction with IEEE 802.15.4, its protocol architecture and the parameters of each layer that we needed and configured in the study presented. In section III, the three major components of Zigbee based LR-WPAN are briefed and a detailed discussion about each topology of this network is carried out. Section IV demonstrates the simulation scenarios we have taken

along with an example of its application. In section V simulation results in terms of throughput and end-to-end delay are given along with the interpretations.

II. ZIGBEE-802.15.4- OVERVIEW

The growth in wireless technology has lead to an emergence of many standards specifically in the ISM radio band with frequencies: 868 MHz, 915 MHz and 2.4 GHz. The 868 MHz frequency band is used mainly in Europe, the 915 MHz mainly in North America while the 2.4 GHz is used worldwide. There was always a need for a standard communication between sensors with low data rate and low power consumption. As an answer to this plight, many companies forged an alliance to create a standard which could be accepted worldwide. It was the Zigbee Alliance which created **Zigbee**. [11]

ZigBee is a specification based on IEEE 802.15-2006 standard used for high level communication protocols, creating a personal area networks from small and low-powered digital radio system. ZigBee's are capable of transmitting data over long distances by passing data through intermediate devices, reaching more distant ones, thus creating a network. The key components of a Zigbee network are- PAN coordinator, routers and end devices. All of them can be configured to deal with multiple applications as large as 124 simultaneously. ZigBee's are employed in applications which require a lower data rate, longer battery life, and secured networking. It has a defined data rate of 250kb/s. The technologies determined in the ZigBee specification are designed to be simpler and less expensive than other (WPANs) technology.[6]

ZigBee consists of four layers. The top two (Application and Network & security) layer's specifications are provided by the ZigBee Alliance to provide manufacturing standards. The bottom two (MAC and PHY) layer's specifications are provided by the IEEE 802.15.4-2006 standard to ensure coexistence without interference with other wireless protocols, such as Wi-Fi. [12]

2.1 Zigbee stack protocol

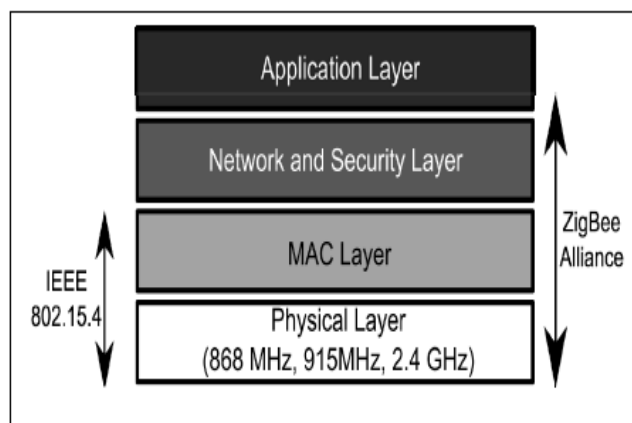


Fig 1: Zigbee Stack Protocol Layers

2.1.1 Physical Layer

Zigbee uses three frequency bands for transmission of data-

- 868 MHz band with a single channel having a data rate of 20 kb/s.
- The 915MHz band with 10 channels, and each channel having a central frequency separated from the adjacent band by 2 MHz and data rate of 40 kb/s. BPSK modulation technique are used in which symbols are transmitted at 1 bit per symbol.
- The 2.4 GHz ISM band having 16 channels, 5 MHz wide offers 250 kb/s of data rate. It uses O-QPSK modulation with 4 bits/symbol transmitted using DSSS with 32 Bit chips. [12]

In our work we took 2.4 GHz transmission band with 0.05 W transmission power.

2.1.2 MAC layer-

The transmission Channel is accessed primarily through Carrier Sense Multiple Access- Collision Avoidance (CSMA-CA) protocol. The MAC layer can take care of transmitting data. The MAC layer decides whether to use slotted or unslotted CSMA-CA. It also takes care of scanning the channel, starting PANs, detecting and resolving PAN ID conflicts, performing device discovery etc [12].In our scenarios we kept channel sensing duration as 0.1 seconds in order to optimize the power consumption with acknowledgements enabled.

2.1.3 Network and Security layer-

The network layer takes control of network startup, device configuration, topology specific routing, and providing security. On each node, the network layer is the part of the stack that does the route calculations, neighbor discovery and reception control. [12] In our work the route discovery time-out is kept as 20 seconds, sufficient for network area of 100 meters range.

2.1.4 Application Support Sub Layer-

It interfaces the network layer and application layer providing a general set of services through two entities, the APS Data Entity and APS Management Entity. These provide services like making application level PDU, group filtering, and managing Object database. [12]

III. ZIGBEE NETWORK TOPOLOGIES-OVERVIEW

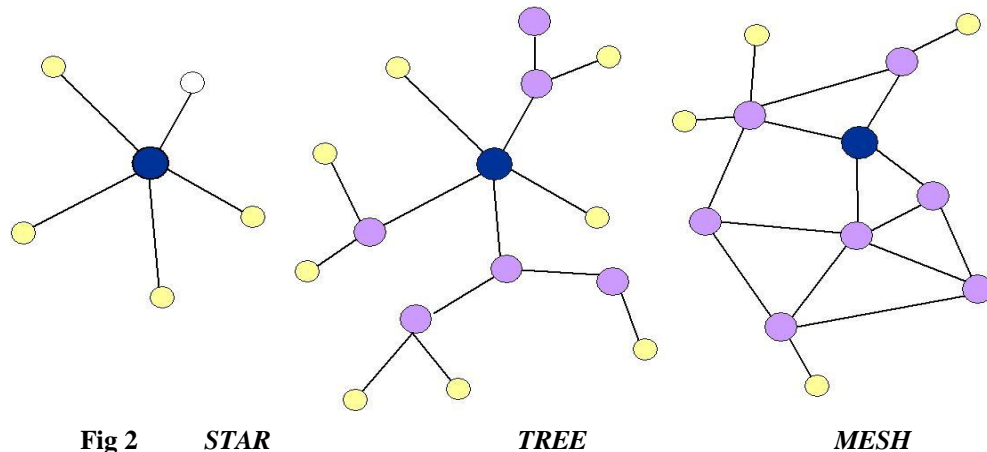


Fig 2 STAR

TREE

MESH

3.1 Zigbee Network Devices:

3.1.1 Zigbee Coordinator (ZC): It is the most capable device which forms the root of the network tree and might bridge to other networks. It collects and stores information about the network.

A **coordinator** has the following characteristics: It

- Allows routers and end devices to join the network
- Assists in routing of the data
- cannot sleep- always on device.

3.1.2 Zigbee Router (ZR): A Zigbee Router can act as an intermediate device, passing on data from other devices as well as running an application function.

3.1.3 Zigbee End devices (ZED): Its job is to communicate with the parent node (either the Coordinator or a Router). It cannot relay data from other devices. This relationship allows the node to be asleep a significant amount of the time thereby giving long battery life. A ZED requires the least amount of memory, and so it is cheaper as compared to ZC or ZR.

3.2 Zigbee Network Topologies:

3.2.1 Star Topology: In star, a coordinator is the prime node and all other devices are directly connected to it. Every data exchange between 2 end devices must pass through the coordinator first. This topology is very much vulnerable to collapses since the whole network goes down if the prime node fails. Employing routers is a waste of energy here as their functionality is never actually used. [13]

3.2.2 Tree Topology: In tree, the prime node would be the root node of the network with hierarchical body. There is a point to point connection between any 2 nodes i.e. a single path exists for reaching a node. Due to the self healing capability of dynamic routing employed, in case of collapses the backup would be prepared from the vicinity instantly (if available). [13]

3.2.3 Mesh Topology: In mesh, data packets can be directly relayed between the routers and then to nodes. They need not pass through the prime node. Such a network has multiple paths for reaching a node and hence a backup can be made easily in failure situations e.g. if a router stops working then any nearby router will tackle the traffic of that router in a very finite time without affecting the performance much. [13]

	Pros	Cons
Star	<ol style="list-style-type: none"> 1. Easy to synchronize 2. Support low power operation 3. Low latency 	<ol style="list-style-type: none"> 1. Small scale
Tree	<ol style="list-style-type: none"> 1. Low routing cost 2. Allow multihop communication 	<ol style="list-style-type: none"> 1. Route reconstruction is costly 2. Latency may be quite long
Mesh	<ol style="list-style-type: none"> 1. Robust multihop communication 2. Network is more flexible 3. Lower latency 	<ol style="list-style-type: none"> 1. Routes discovery is costly 2. Needs storage for routing table

Table 1: Pros and Cons of Topologies

In mesh and tree, if 1 node sends data and in the path if both coordinator and router are available for forwarding the traffic then both will do and the destination will receive from both the same traffic but with some noise and quality degrades slightly. While in star, for such a situation only coordinator will forward the traffic, router won't. Hence the traffic will reach the destination with accuracy.

IV. OPNET- BASED SIMULATION SCENARIOS FOR CAMPUS ENVIRONMENT

OPNET or Optimized Network Engineering Tools is robust tool used to model and simulate sensor networks. The current version support simulation of heterogeneous networks which can be used in various communications protocols. OPNET supports simulation of the network at packet-level to analyze fixed, mobile and satellite networks. The OPNET simulation environment favours the simulation of Zigbee based sensor networks by providing three components.[14],[15],[16].

We have taken a very practical situation of a campus having a dimension of 100m x 100m. The results are then simulated. This practical situation can be used to link various Departments such as in Hospitals, Schools and College etc. Consider a College having six departments and each department is connected to central coordinator. These departments are linked with 3 different network topologies namely star, mesh and tree. Efficiency of each network is evaluated. In the second scenario we have considered mobile Zigbee coordinators. These mobile coordinators are very useful for an industry run application process or may be in battlefield to keep track of enemies.

We are considering two scenarios. First, authors are comparing the three possible topologies (Star, Mesh and Tree) to each other using only *one* ZigBee Coordinator (ZC), *six* ZigBee routers (ZR) and *six* ZigBee End devices (ZED) in each topology. The comparison includes end-to-end delay and global throughput. For the second scenario, we are taking the same three topologies and same Zigbee devices but ZC as mobile.

4.1 Simulation Scenarios

4.1.1 Dynamic Zigbee Coordinator-Star Topology

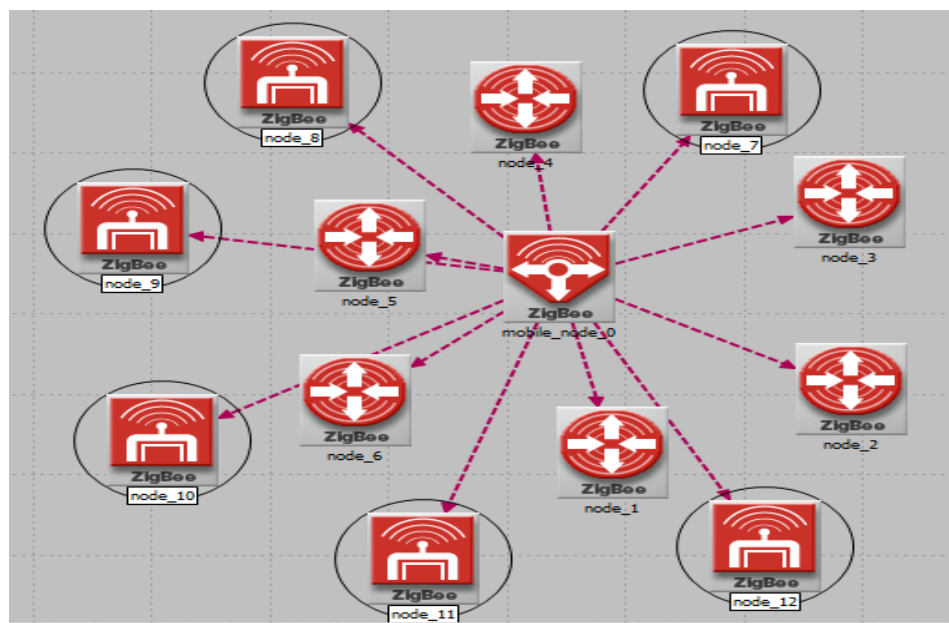


Fig-3

4.1.2 Dynamic Zigbee Coordinator-Mesh Topology

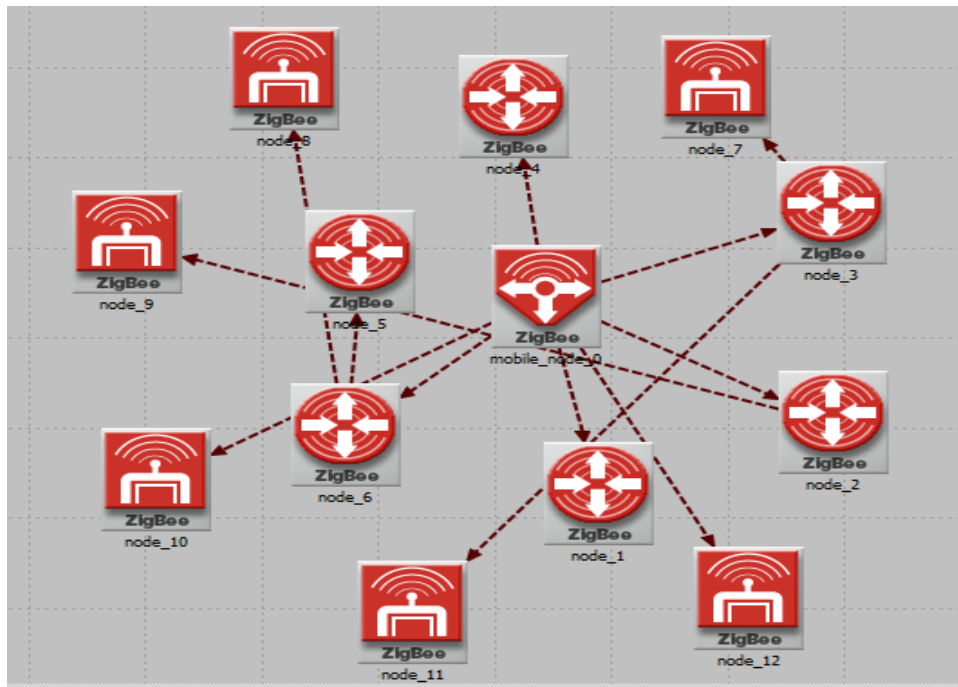


Fig-4

4.1.3 Dynamic Zigbee Coordinator-Tree Topology

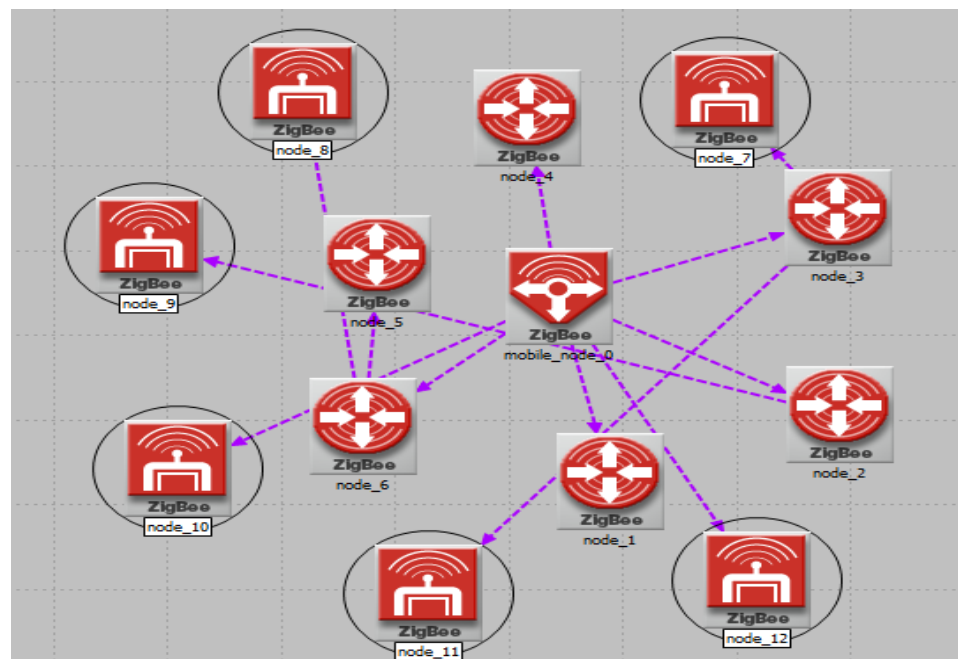


Fig-5

V. SIMULATION RESULTS

We have considered Throughput and End to End delay as the key parameters for comparing efficiency between Star, Mesh and Tree topologies.

5.1 Throughput:

The Throughput or Network throughput is the rate of successful message delivery over a communication channel. This data may be delivered over a physical or logical link, or pass through a certain network node. It is usually measured in bits per second bit/s or bps. During the simulation throughput as a global

statistics has been taken so any object could contribute to its value as it gives a general idea of the overall throughput of the system.[17]

5.1.1 Throughput: Static Zigbee Coordinator

For ZC as Static, throughput is better in the case of Tree Topology with average value of 35500bits/s

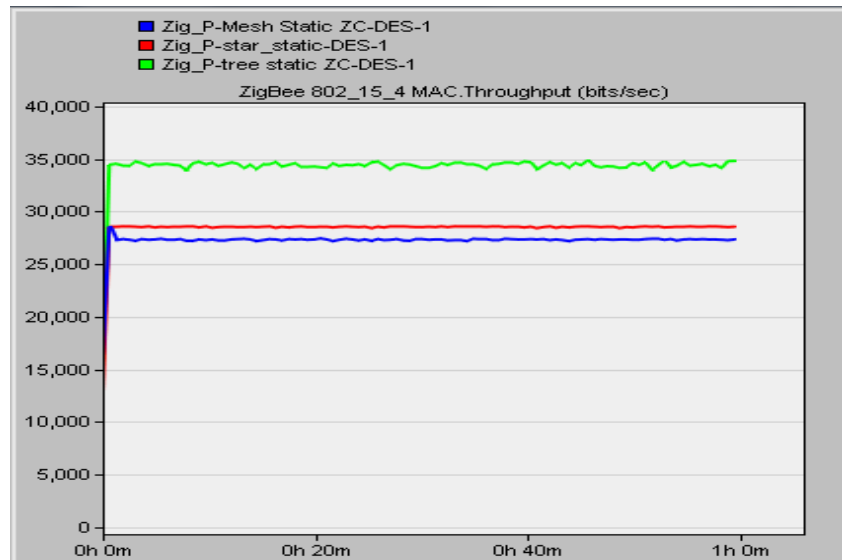


Fig 6

5.1.2 Throughput: Dynamic Zigbee Coordinator

For ZC as Dynamic, Tree topology performs better as compared to Static ZC with throughput slightly more than the former by 1500bits/s.

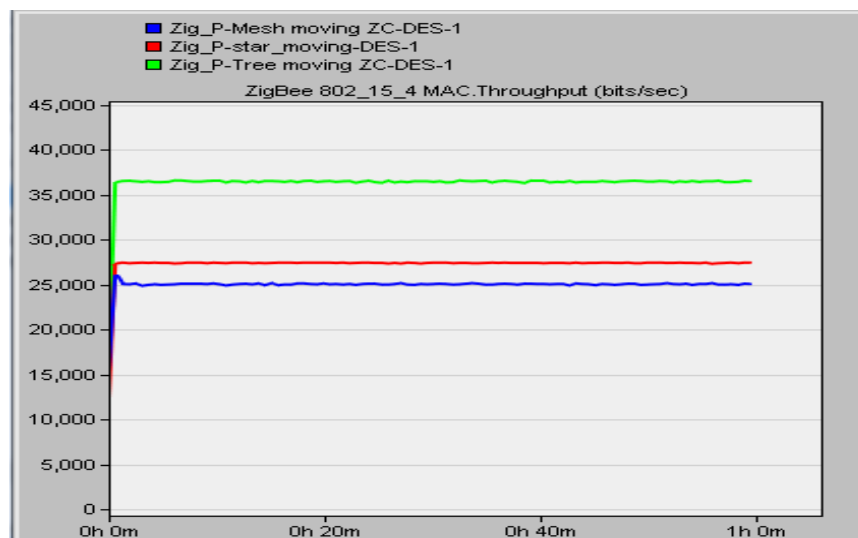


Fig 7

5.2 End To End Delay:

End-to-end delay refers to the time taken for a packet to reach from source to destination in a network.

5.2.1 End to End delay: Static Zigbee Coordinator:

ZC as Static Mesh topology is having least End to End delay of 0.0132s.

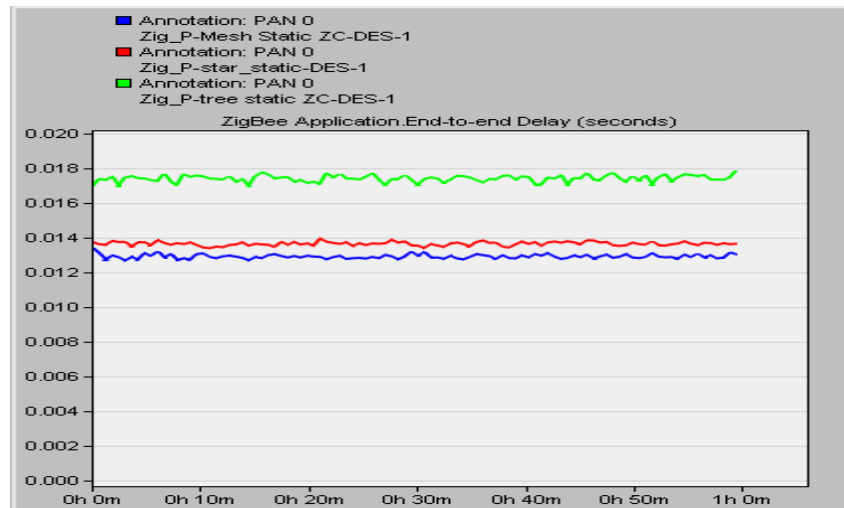


Fig 8

5.2.2 End to End delay: Dynamic Zigbee Coordinator:

ZC as Dynamic, Mesh topology is having least End to End and has a better performance as compared to Static ZC.

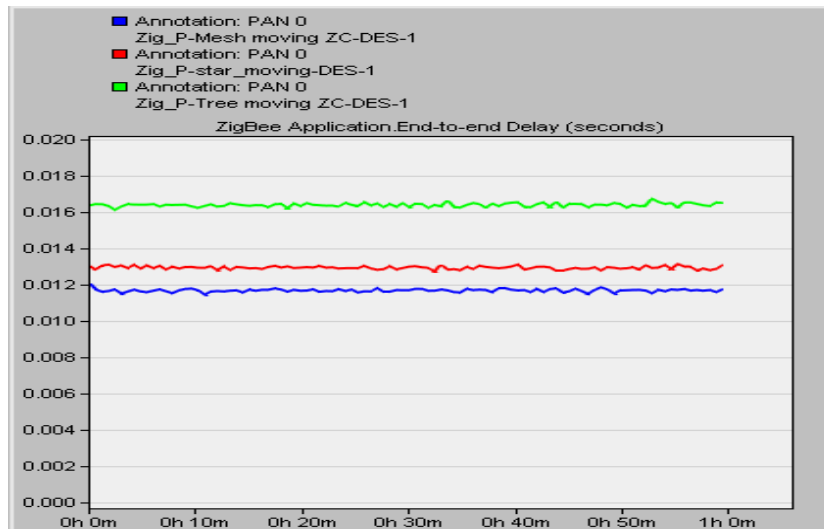


Fig 9

Network Topologies	Throughput	End-End delay
Star	Static ZC-29000bits/s	Static ZC- 0.0142 sec
	Dym ZC- 28000bits/s	Dym ZC- 0.0135 sec
Mesh	Static ZC-28000bits/s	Static ZC- 0.0132 sec
	Dym ZC- 27500bits/s	Dym ZC- 0.0122 sec
Tree	Static ZC-35500bits/s	Static ZC- 0.0178 sec
	Dym ZC- 37000bits/s	Dym ZC- 0.0168 sec

Table 2: Simulation Table

Parameters	Value		
	Star(Default)	Tree(Default)	Mesh(Default)
Max. Children	255	7	7
Max. Routers	0	5	5
Max. Depth	1	5	5
Transmit Band	2.4GHz	2.4GHz	2.4GHz
Transmitted Power	0.05	0.05	0.05
ACK mechanism	Enabled	Enabled	Enabled

Table 3: Zigbee Parameters

Network Size (Campus)	100m*100m
Number of End Devices	6
Number of Routers	6
Number of Coordinators	1
Mobility Model	Random walk- 20m/s
Simulation Duration	3600 s

Table 4: Simulation Parameters

VI. CONCLUSION

In this paper we have gone through several analysis for achieving optimum end to end delay and throughput for smart campus. By making the coordinator as dynamic in Zigbee based LR-WPAN, throughput of tree topology increases considerably as compared to mesh and star topologies. Our OPNET results say that by using dynamic coordinator minimum end-to-end delay is achieved. In dynamic coordinator end to end delay reduces when compared to static, hence when end to end delay reduces automatically energy consumption also reduces. We conclude that our analysis achieved good performance in terms of throughput and end-to-end delay for dynamic tree topology as compared to any other. Further this work can be extended for large scale WSNs.

Acknowledgement

It is our sincere obligation to thank our well-wishers Dr. N.Shekar V Shet, Associate Professor, Dept of Electronics and Communication Engineering and Sarwesh P, PhD student Electronics and Communication Engineering, NITK, Surathkal (Karnataka) India.

REFERENCES

- [1] Lamia Kaddar and Ahmed Mehaoua, 'ESTREL: transmission and reception energy saving model for wireless ad-hoc networks', In proceeding of: Local Computer Networks, 2007. LCN 2007, 32nd IEEE Conference.
- [2] R. Abileah and D. Lewis, "Monitoring high seas fisheries with long range passive acoustic sensors", in proceedings of MTS/IEEE 'Prospects for the 21st century' conference (OCEANS'96), vol.1, pp. 378-382, Fort Lauderdale, Fla, USA, September 1996.
- [3] Norman A. Benjamin and Dr. Suresh S., "Performance of Hierarchical agent based WSMN for patient Health monitoring", World Congress on Nature & Biologically Inspired Computing (NaBIC 2009).
- [4] S.N. Simic and S. Sastry, "Distributed environmental monitoring using sensor networks", in proceedings of the 2nd international workshop on information processing in sensor networks (IPSN'03), April 2003.
- [5] "Wireless sensor network white paper-Tetcos", www.tetcos.com/Enhancing_Throughput_of_WSNs.pdf
- [6] Zigbee-Wikipedia, <http://en.wikipedia.org/wiki/ZigBee>
- [7] IEEE 802.15.4-Wikipedia, http://en.wikipedia.org/wiki/IEEE_802.15.4
- [8] Zigbee white paper- AMX, www.amx.com/assets/whitePapers/AMX.ZigBee.White.Paper.pdf
- [9] A. Willig, K. Matheus, and A. Wolisz, "Wireless technology in industrial networks," Proc. IEEE, vol. 93, no.6, pp. 1130-1151, Jun. 2005.
- [10] J. Lee, C. Chuang, and C. Shen, "Applications of short-range wireless technologies to industrial automation: A Zigbee approach," in Proc. IEEE AICT, 2009, pp. 15
- [11] "Zigbee Overview"- <http://www.engineersgarage.com/articles/what-is-zigbee-technology>
- [12] "Zigbee Stack Protocol"-<http://www.engineersgarage.com/articles/what-is-zigbee-technology?page=3>
- [13] "Zigbee Topologies"-http://wireless.arcada.fi/MOBWI/material/PAN_5_2.html
- [14] C. Marghescu, M. P. Antazica, A. Brodeala and P. Svasta :Simulation of a Wireless Sensor Network Using OPNET –in proceedings of 2011 IEEE 17th International Symposium for Design and Technology in Electronic Packaging (SIITME).
- [15] Fig 1-Harsh Dhaka, Atishay Jain, Karun Verma, Impact of Coordinator Mobility on the throughput in a Zigbee Mesh Networks-in proceedings of 2010 IEEE 2nd International Advance Computing Conference.
- [16] Table 3-Boris Mihajlov and Mitko Bogdanoski., Overview and Analysis of the Performances of ZigBee based Wireless Sensor Networks in proceedings of International Journal of Computer Applications (0975 – 8887) Volume 29– No.12, September 2011
- [17] "Throughput" - <http://en.wikipedia.org/wiki/Throughput>

Experimental Investigation of Performance and Emission Characteristics of Biodiesel from Sterculia Striata

K.Balasubramanian¹, Abhinav Balaji², K.Vignesh³

¹Associate Professor Meenakshi Sundararajan Engineering College ,
^{2,3} 4th Year Mechanical Engineering Meenakshi Sundararajan Engineering College , Chennai, India

Abstract: With this increase in population, industry, transportation the cost of fossil fuels will grow dramatically. There is a need of new technologies for fuel extraction using feed stocks that do not threaten food security, cause minimal or no loss of natural habitat. At the same time, the fuel should be environmental friendly so that environmental pollution should be minimized or eliminated. The search of vegetable oils as the fuels for engine has been developed. This paper presents the characterization, results of investigation of combustion performance and emissions characteristics of diesel engine using Sterculia Striata biodiesel. In this investigation, the blends of varying proportions of Sterculia Striata biodiesel and diesel were prepared, analyzed compared with the performance of diesel fuel, and studied using a single cylinder diesel engine. The brake thermal efficiency, brake-specific fuel consumption, exhaust gas temperatures, CO, HC, NOx, and smoke emissions were analyzed. The emission from the engine exhaust is lesser with the biodiesel compared with that of the neat diesel engine.

Keywords: Sterculia Striata; Characterization of biodiesel; Combustion Parameters; Emission Characteristics

I. Introduction

The concept of using vegetable oil as engine fuel is as old in the engine but the recent research shows renewed interest on biodiesel as fuel in diesel engines. The lower cost of the petroleum diesel has so far attracted the world to use it as fuel in diesel engines until now. But now-a-days due to global political turmoil and other reasons, the cost of petroleum diesel has been increasing exponentially. Moreover, the emission norms are more stringent as ever before. In this context, many biodiesels have been used now-a-days. Sterculia Striata biodiesel is one of the most promising biodiesel among them.

Shrirame et al. 2011 proposed that the biodiesel can be used as 20% blend with petro diesel in existing engines without any modification. Both the edible and non-edible vegetable oils can be used as the raw materials for the biodiesel. Xue et al. 2009 developed a process for the trans-esterification of Jatropha curcas L. seed oil with methanol using artificial zeolites loaded with potassium acetate as a heterogeneous catalyst. The optimum reaction conditions for trans-esterification of J. curcas oil were also investigated. Ueki et al. 2011 synthesized an efficient fibrous catalyst for the biodiesel fuel production by radiation-induced graft polymerization of 4-chloromethylstyrene onto a nonwoven polyethylene (NWPE) fabric followed by lamination with tri-methylamine (TMA) and further treatment with NaOH. Kamimura et al. 2011 analyzed market means in economic terms to various regions of Brazil. Two regions – North and Midwest still display a high degree of poverty for small farmers. The national biodiesel program may represent an interesting economical alternative for them.

II. Sterculia Striata

Sterculia striata is also known as chichá-do-cerrado. It is a tree subfamily of Sterculioideae. The trees are in the height of 8-15 m and trunk diameter of 40 cm. These trees annually produce red fruits that open and contain nuts, which are consumed by man and wildlife. The Dry fruit of sterculia striata is shown in the Figure 1. It is a type of Pioneer plant fast-growing and tolerant of dry and stony land. Sterculia Striata is commonly known as Chicha oil.

Chicha has its origin in India and Malaysia where the seeds are consumed in dried and roasted form (Mangas et al. 2012). It is also available as a source of vegetable oil. This species is also commonly available in the Northeast of Brazil where it grows as a wild tree. The plant starts to produce fruits within 18-24 months from plantation. As an adult tree it can produce about 40kg of seeds per year. The seeds contain up to 60% kernels that contains lipids at concentrations varying from 28 to 32%. Many experimental studies of Sterculia striata biodiesel as a diesel substitute have been done (Aline et al. 2010, Ana et al. 2004, 2005, Aued et al. 2004,

Brito et al. 2004, Dario et al. 2010, Oliveria et al. 2000, Sabria et al. 2004, Silvia et al. 2003, Zeomar et al. 2008). The major properties of Sterculia Striata biodiesel include calorific value, diesel index, flash point, fire point, cloud point, pour point, specific gravity, and kinematic viscosity. The various physicochemical properties of diesel and Sterculia Striata biodiesel are measured and listed in Table 1 for comparison.

It can be noted that the calorific value of Sterculia Striata biodiesel is less than that of diesel. This might be due to the presence of oxygen atoms in the fuel molecule of Sterculia Striata biodiesel. The kinematic viscosity is, respectively, greater in the case of Sterculia Striata biodiesels than that for diesel. The higher viscosity of Sterculia Striata biodiesel could potentially have an impact on the combustion characteristics because the high viscosity affects its atomization quality slightly. The pour and cloud points of Sterculia Striata biodiesel are also favorable. However, the flash point of Sterculia Striata biodiesel is much higher than that of diesel, which makes Sterculia Striata biodiesel safer than diesel from ignition due to accidental fuel spills during handling. It can be seen that the properties of Sterculia Striata biodiesel are found to be within the limits of biodiesel specifications of many countries.

Many researchers investigated the effects of diesel biodiesel blends on performance and emission characteristics in diesel engine and concluded that partial or full replacement of diesel with biodiesel is feasible (alamu et al. 2008, antony et al. 2011, Juhun et al. 2004, kurzin et al. 2007, Thompson, Singh et al. 2010). However, the experimental study of performance and emission characteristics of Sterculia Striata biodiesel on diesel engine is hardly reported. Therefore, such an attempt is made in the present work, to experimentally investigate the performance (brake thermal efficiency, brake-specific fuel consumption, and exhaust gas temperature) and emission (carbon monoxide, unburned hydrocarbon, nitrogen oxides, and smoke) parameters of Sterculia Striata biodiesel and diesel- Sterculia Striata biodiesel blends as fuel in diesel engine.

III. Bio-diesel Processing

Biodiesel is a mono alkyl ester that is derived from vegetable oils or animal fats through trans-esterification. The purpose of trans-esterification is to reduce the viscosity of vegetable oils. All the vegetable oils were trans-esterified with an optimized alkali catalyzed process, which also vary depending on the oil. According to the oil used, the process parameters were adjusted to achieve the maximum ester yield. The process parameters such as alcohol to oil ratio (6:1 molar ratio), catalyst quantity (NaOH, 0.5 wt. %), reaction temperature (65 °C) and reaction time (2 hr) were optimized for a single oil and then subsequently adjusted for other oils. Alkali catalyst was used because of its low cost and also it is easily miscible with methanol. Methanol was used because of its low cost. The biodiesel produced from different oils were washed and dried. Then different biodiesels were blended with different percentage to vary the % of unsaturation. The biodiesel produced were checked for the quality. The important fuel properties were measured as per the ASTM standards and compared with the ASTM limits. It was observed that all the biodiesel fuels have qualified to the ASTM standards.

IV. Experimental Method

Before the present research work was carried out the main technical features of the engine should be studied. The specification of engine and testing conditions are presented in Table 2 and Table 3 respectively. The main objective has been to study the performance and emission characteristics of Sterculia Striata biodiesel as fuel in diesel engine. For conducting the desired set of experiments and to gather required data from the engine, it is essential to get the various instruments mounted at the appropriate location on the experimental setup.

V. Experimental Setup

A single cylinder water-cooled direct injection CI engine developing a power output of 5.2 kW at the rated speed of 1500 rpm was used for the experimental studies. The engine was coupled to an electrical dynamometer. The engine was fitted with all accessories to measure the fuel consumption, air consumption, inlet air temperature, and exhaust gas temperature. The engine was started with neat diesel fuel and warmed up. It was allowed to run for 10 minutes with biodiesel to attain steady condition at its rated speed of 1500 rpm. The engine was gradually loaded to five different load conditions like 20%, 40%, 60%, 80%, and 100% by switching on the load mains. The different biodiesel fuels and their blends were tested in a random order. The speed of the engine was maintained at 1500 rpm and the time taken for 10cc of fuel consumption was measured using a stopwatch. The tests were repeated for five times and the average value of the five readings was taken to eliminate the uncertainty. The in-cylinder pressure, NOX, CO, HC, smoke, and exhaust gas temperature were measured at the entire five loads for different biodiesel fuels blends. The entire experimental work was carried out in the laboratory at room temperature (28.7°C) and atmospheric pressure (1.01325 bar). Before measuring

all the engine exhaust emissions and cylinder gas pressure, the instruments such as gas analyzer and pressure sensor were calibrated and verified with the accuracy levels.

VI. Measurement of Emission

The NO_x, HC, CO emissions were measured by QROTECH, QRO-401 exhaust gas analyzer. Smoke intensity was measured using a Bosch smoke meter. The temperature of the exhaust gas was measured by using K-type (chrome – alumel) thermocouple with digital indicating unit. The probe that was connected to the exhaust gas analyzer was placed inside the exhaust pipe. HC and NO_x were measured in ppm and CO in % by volume and then converted into g/kWh. The smoke intensity was measured in BSU (Bosch Smoke Unit). A “U” tube manometer was used to measure the airflow rate. One end of the manometer was left free to ambient and the other end was connected to the surge tank. The photographic view of test engine is shown in Figure 2 while Figure 3 depicts the pressure and emission measuring setup. The schematic of entire experimental setup is illustrated in Figure 4.

VII. Result and Discussion

The results of experimental investigations are compared to identify the best fuel which has a lower emission and less effect on environment. The performance and the emission characteristics are discussed separately.

VIII. Performance Parameters

Fueling the diesel engine with the biodiesel shows some shift in the performance characteristics. The performance parameters like Exhaust gas Temperature, Brake Specific fuel consumption, Brake specific energy consumption, Brake Thermal Efficiency are discussed.

IX. Exhaust Gas Temperature (EGT)

The relationship between exhaust gas temperature (EGT) and load for different fuel blends and diesel has been shown in Figure 5. The results showed that with the increase in the load increases EGT in all the blends of sterculia striata biodiesel and diesel operation. The increase in EGT with increase in load may be due to the increased cylinder pressure due to improved combustion of fuel as a result of improved atomization at warmed-up condition. The increase in EGT with increase in the proportion of sterculia striata biodiesel may be due to the delayed combustion. This may also be due to the slower combustion characteristics of sterculia striata biodiesel. The exhaust gas temperature of biodiesel is comparable lesser than that of diesel. The percentage of biodiesel blends in the decreases the temperature of the exhaust gas to a greater extent.

X. Brake-Specific Fuel Consumption (BSFC)

Figure 6 shows the comparison of effect of load on brake-specific fuel consumption between diesel and sterculia striata biodiesel for different blend conditions. It is seen that brake-specific fuel consumption increases when the load is increased for all operations of diesel and sterculia striata biodiesel and their blends. It can also be observed that brake specific fuel consumption increases when sterculia striata biodiesel proportion in the blend is increased for any given load. At 100% load the sterculia striata shows the maximum brake specific consumption of 0.294 kg/hr compared to other blends of sterculia striata. Similarly the values of other loads are also tabulated, which results that the B100 has maximum fuel consumption and diesel has the least fuel consumption values.

XI. Brake Specific Energy Consumption (BSEC)

Brake specific energy consumption (BSEC) is the product of the brake specific fuel consumption and calorific value. BSEC depends on the fuel consumption rate and the fuel properties. The important property of the fuel is calorific value. It affects the energy consumption to a greater extent. The comparison of the specific energy consumption of diesel and different blends of sterculia striata is shown in the Figure 7.

XII. Brake Thermal Efficiency (BTE)

Brake Thermal Efficiency characteristics of sterculia striata biodiesel, diesel, and their blends are shown in Figure 8. It is observed that at any given load condition, the brake thermal efficiency of neat sterculia striata biodiesel (B-100) and other blends (B-25, B-50, B-75) is lower than that of diesel operation. It can be seen that as the percentage of sterculia striata biodiesel in the blend increases, there is more decrease in brake thermal efficiency as compared to diesel fuel mode, that is, diesel operation. This lower BTE of sterculia striata biodiesel operation is due to the combined effect of higher viscosity, higher density of sterculia striata biodiesel. The efficiency of the engine depends on the properties of the fuel used. The efficiency of the B100 is

comparable to the efficiency of the diesel engine. The blend of *sterculia striata* B25 has a efficiency of 30.96% which is very near to that of the diesel engine.

XIII. Emissions Parameters

The environmental pollution is mainly due to automobile exhaust. To minimize or eradicate the formation of pollutants, biodiesel are used as a fuel for the diesel engines. The effect of reduction in pollutants from the diesel engine is measured. The major emission parameters are discussed here are Smoke, Carbon Monoxide, Hydrocarbon, Carbon-di-oxide, Oxygen, and Oxides of nitrogen.

XIV. Smoke Density (HSU)

Figure 9 shows variation of smoke density for diesel, *Sterculia Striata* biodiesel, and its blends, respectively, at five various loads. From the figure it follows that smoke density increases with increase in load. It is observed that smoke emissions are higher for diesel and blends compared to bio-diesel *sterculia striata* oil. The smoke is undesirable from the engine exhaust. The smoke density measured for five different load conditions are compared. In 100% load condition the B100 fuel has less smoke density of 43.96 HSU compared to other fuels. Diesel has the maximum smoke release and its percentage decreases by blending it with *sterculia striata* bio-diesel.

XV. Carbon Monoxide (CO)

The effect of load on carbon monoxide (CO) emissions for diesel, neat *sterculia striata* biodiesel, and their blends is shown in Figure 10. It can be seen from the figure that the lowerer CO emissions were obtained with blends of *sterculia striata* biodiesel and diesel and neat *sterculia striata* biodiesel mode of operation. The Co is 0.04, 0.037, 0.034, 0.31, 0.28 % by volume for diesel, B-25, B-50, B-75, and B-100, respectively, at 100% load. CO emissions in the exhaust gas of the engine may be attributed to the polymerization that takes place at the core of the spray; this also caused concentration of the spray core and decreased the penetration rate. Low volatility polymers affected the atomization process and mixing of air and fuel causing locally rich mixture, which leads to difficulty in atomization and vaporization of neat *sterculia striata* biodiesel due to improper spray pattern produced. The CO emission is also undesirable one from the exhaust of the engine. The CO emission of the biodiesel *sterculia striata* and its blends with diesel and the pure diesel fuel is compared to identify the less emission fuel. The B100 has the less CO emission of 0.028% compared to other fuels.

XVI. Unburned Hydrocarbon (UHC)

The effect of load on unburned hydro-carbon (HC) emissions for diesel, neat *sterculia striata* biodiesel and their blends is shown in Figure 11. It can be seen from the figure 11 that the lower HC emissions were obtained with blends of *sterculia striata* biodiesel and neat *sterculia striata* biodiesel. HC emission is 44, 41, 30, 24, 18 ppm for diesel, B-25, B-50, B-75, and B-100, respectively, at 100% load. Lower HC emissions in the exhaust gas of the engine may be attributed to the efficient combustion of *sterculia striata* biodiesel and blends due to the presence of fuel bound oxygen and warmed-up conditions at higher loads. On the comparison biodiesel B100 has the least emission of 18 ppm whereas the diesel has the highest emission of 44ppm which is very dangerous pollutant.

XVII. Carbon Monoxide (CO₂)

The CO₂ emission from a compression ignition engine is the result of better combustion, while HC and CO are of poorer combustion. The CO₂ emission of diesel and different blends of *sterculia striata* biodiesel is shown in the figure 12. The CO₂ emission of the B100 is more compared to other fuel which makes it a desirable fuel for engines. B100 has the 6.9 % of carbon di oxide emission. The diesel has lesser value of 6.3 % by volume.

XVIII. Oxygen (O₂)

O₂ emissions are oxygen particles released into an exhaust system. Oxygen release is required for an engine to work properly, as it supports the combustion process that makes an engine run. Too much oxygen means there is not enough fuel and will cause stress on the engine, which will result in damage to the engine. Too little oxygen means there is too much fuel saturating the engine's cylinders, which will result in bad fuel efficiency and possible loss of horsepower. O₂ emissions are measured and controlled by an O₂ sensor. The oxygen emission of diesel and various blends of *sterculia striata* under different load conditions are shown in the Figure 13. There is no much difference in the oxygen emission. From the figure it is clear that the emission by using the different blends of the biodiesel gives nearly similar values only.

XIX. Oxides of Nitrogen (NOx)

Oxides of Nitrogen (NOx) is generally formed at a temperature higher than 1500°C. High temperature, especially in the regions containing O₂, and time spent at these temperatures are very conducive to NOx formation. The amounts of N₂ and O₂ existing in the region are also factors in NOx formation. Figure 14 shows NOx variations depending on the load of the engine. It was observed that NOx emissions were higher for neat Sterculia striata biodiesel and blends compared to diesel at almost all loads. The increase in NOx emissions with increase in the proportion of Sterculia striata biodiesel may be due to the delayed combustion. Also the higher oxygen content of biodiesels leads to more complete combustion resulting in greater combustion temperature peaks which caused higher NO emissions. However, the higher viscosity and density of biodiesel caused delayed combustion phase which results in the slower combustion characteristics of Sterculia Striata biodiesel. The NOx emission of diesel is less than the biodiesel and its blends. Sterculia striata shows the maximum emission of 676 ppm and the diesel shows the minimum of 625 ppm.

XX. Conclusion

The performance characteristics like brake thermal efficiency, brake specific fuel consumption, and exhaust gas temperature and emission characteristics, carbon monoxide, unburned hydro-carbon, nitrogen oxides, and smoke of a single cylinder four stroke vertical direct injection Kirloskar TV-1 engine using sterculia striata biodiesel and diesel- sterculia striata biodiesel blends as fuels were experimentally investigated. The following conclusions are made based on the experimental results.

1. As the proportion of sterculia striata biodiesel increases in the blend, the brake thermal efficiency decreases. For B-100, the brake thermal efficiency was less than that of diesel at full load. More the proportion of sterculia striata biodiesel in the blend more is the increase in brake specific fuel consumption for any given load.
2. The carbon monoxide emissions are reduced by 30% with neat sterculia striata biodiesel operation when compared to diesel mode at full load condition. HC emissions for sterculia striata biodiesel and blends are quite low compared to diesel. At higher loads, as the quantity of sterculia striata biodiesel in the blend increases HC emissions decrease.
3. The NOx CO₂ and O₂ are higher for neat sterculia striata biodiesel and blends when compared to diesel at almost all loads.
4. The smoke density CO and HC emissions are lesser for neat sterculia striata biodiesel and blends when compared to diesel at almost all loads.

REFERENCES

- [1.] Alamu.O.J, Akintol.T.A, Enweremadu.C.C and Adeleke.A.E. (2008) Characterization of palm-kernel oil biodiesel produced through NaOH - catalyzed trans-esterification process, Scientific Research and Essay Vol.3 (7), pp. 308-311
- [2.] Aline F. Dario, Regina C.M. de Paula, Haroldo C.B. Paula, Judith P.A. Feitosa, Denise F.S. Petri. (2010) Effect of solvent on the adsorption behavior and on the surface properties of Sterculia striata polysaccharide, Carbohydrate Polymers, Volume 81, Issue 2, 11, 284–290
- [3.] Ana Cristina F Brito, Durcilene A Silva, Regina CM de Paula, Judith PA Feitosa. (2004) Sterculia striata exudate polysaccharide: characterization, rheological properties and comparison with Sterculia urens (karaya) polysaccharide. Polymer International, Volume 53, Issue 8, 1025–1032.
- [4.] Ana Cristina F. de Brito, Maria Rita Sierakowski, FanyReicher, Judith P.A. Feitosa, Regina Celia M. de Paula (2005) Dynamic rheological study of Sterculia striata and karaya polysaccharides in aqueous solution, Food Hydrocolloids, Volume 19, Issue 5, Pages 861–867
- [5.] Antony Raja.S, Robinson smart.D.S and Lindon Robert Lee.C. (2011) Biodiesel production from jatropha oil and its characterization, Research Journal of Chemical Sciences, Vol. 1 (1) pp. 81-87
- [6.] Aued-Pimentel, Sabria, Lago, João Henrique Ghilardi, Chaves, Mariana Helena, Kumagai, Edna Emy. (2004) Evaluation of a methylation procedure to determine cyclopropanoids fatty acids from Sterculia striata St Hil. Et Nauds seed oil, Journal of Chromatography A, Volume 1054, p. 235-239.
- [7.] Brito, Ana Cristina F, Silva, Durcilene A, de Paula, Regina CM, Feitosa, Judith PA (2004) Sterculia striata exudate polysaccharide: characterization, rheological properties and comparison with Sterculia urens (karaya) polysaccharide” Polymer International, Volume 53, issue 8, p. 1025 – 1032
- [8.] Dario, A.F. de Paula, R.C.M. Paula, H.C.B. Feitosa, J.P.A. Petri, D.F.S. (2010) Effect of solvent on the adsorption behavior and on the surface properties of Sterculia striata polysaccharide, Carbohydrate Polymers, Volume 81, issue 2, p. 284-290.
- [9.] Juhun Song, Mahabubul Alam and André L. Boehman. (2004) Characterization of diesel and biodiesel Soot, Prepr. Pap.-Am. Chem. Soc., Div. Fuel Chem, 49(2), 767-769
- [10.] Kamimura.A, Oliveira.A and Burani.G. (2011) Brazilian Family Farming Agriculture in the Biodiesel Production: A Portrait of Regional Possibilities, Low Carbon Economy, Vol. 2 No. 1, pp. 7-14.

- [11.] Kurzin A.V, Evdokimov A.N, Pavlova O.S, and Antipina V.B (2007) Synthesis and Characterization of Biodiesel Fuel Based of Esters of Tall Oil Fatty Acids, Chemistry of fossil fuel, ISSN 1070-4272, Russian Journal of Applied Chemistry, Vol. **80**, No. 5, pp. 842-845
- [12.] Mangas.M.B.P, Rocha.F.N, Suarez.P.A.Z, Meneghetti.S.M.P, Barbosa.D.C, dos Santos.R.B, Carvalho.S.H.V, Soletti.J.I. (2012) Characterization of biodiesel and bio-oil from Sterculia striata (chicha) oil, Industrial Crops and Products, Volume **36**, Issue 1, Pages 349–354
- [13.] Oliveira, J.T.A. Vasconcelos, I.M. Bezerra, L.C.N.M. Silveira, S.B. Monteiro, A.C.O. Moreira, R.A.(2000) Composition and nutritional properties of seeds from Pachira aquatica Aubl, Sterculia striata St Hil et Naud and Terminalia catappa Linn, Food Chemistry, Volume **70**, issue 2, p. 185-191.
- [14.] Sabria Aued-Pimentel, Joao Henrique Ghilardi Lago, Mariana Helena Chaves, Edna Emy Kumagai (2004) Evaluation of a methylation procedure to determine cyclopropanoids fatty acids from Sterculia striata St. Hil. Et Nauds seed oil. Journal of Chromatography A, **1054** 235–239
- [15.] Shrirame.H, Panwar.N and Bamniya.B. (2011) Bio Diesel from Castor Oil – A Green Energy Option, Low Carbon Economy, Vol. **2** No. 1, pp. 1-6.
- [16.] Silva, D.A, Brito, A.C.F., de Paula, R.C.M., Feitosa, J.P.A., Paula, H.C.B. (2003) Effect of mono and divalent salts on gelation of native, Na and de acetylated Sterculia striata and Sterculia urens polysaccharide gels, Carbohydrate Polymers, Volume **54**, p. 229-236.
- [17.] Singh.S.P, Dipti Singh. (2010) Biodiesel production through the use of different sources and characterization of oils and their esters as the substitute of diesel: A review, Renewable and Sustainable Energy Reviews **14** 200–216
- [18.] Thompson.J. C, He.B. B, Characterization of crude glycerol from biodiesel production from multiple feed stocks, Applied Engineering in Agriculture, Vol. **22**(2): 261-265
- [19.] Ueki.Y, Mohamed.N, Seko.N and Tamada.M (2011) Rapid Biodiesel Fuel Production Using Novel Fibrous Catalyst Synthesized by Radiation-Induced Graft Polymerization, International Journal of Organic Chemistry, Vol. **1** No. 2, pp. 20-25.
- [20.] Xue, W. , Zhou, Y. , Song, B. , Shi, X. , Wang, J. , Yin, S. , Hu, D. , Jin, L. and Yang, S. (2009) Synthesis of biodiesel from Jatropha curcas L. seed oil using artificial zeolites loaded with CH₃COOK as a heterogeneous catalyst. Natural Science, **1**, 55-62.
- [21.] Zeomar Nitão Diniz, Pushkar Singh Bora, Vicente Queiroga Neto and José Marcelino Oliveira Cavaleiro. (2008) Sterculia striata seed kernel oil: characterization and thermal stability, Grasas Y Aceites, **59** (2), Abril-Junio, 160-165.

Figures



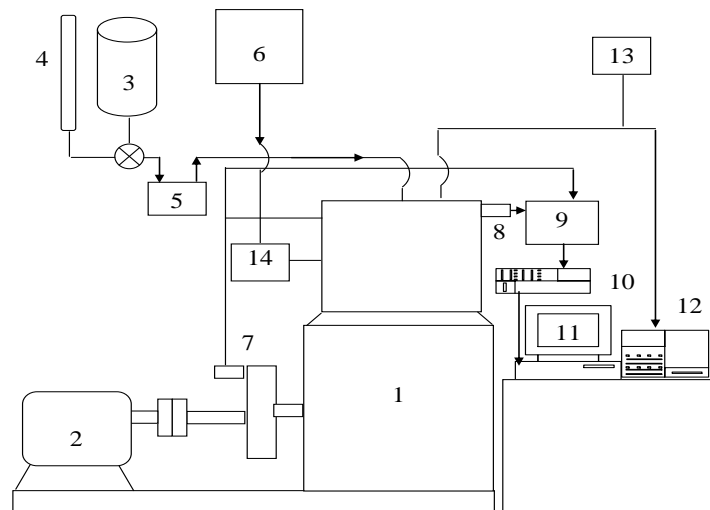
Figure.1. Seeds of Sterculia striata (Chicha oil)



Figure.2. Photographic view of test engine



Figure.3. Photographic view of pressure and emissions measuring setup



1. Test engine	8. Pressure transducer
2. Dynamometer	9. Charge amplifier
3. Biodiesel tank	10. Analog to digital converter
4. Burette	11. Computer
5. Fuel filter	12. Exhaust gas analyzer
6. Air surge tank	13. Exhaust gas temperature indicator
7. TDC pickup	14. Inlet air temperature indicator

Figure.4. Experimental setup

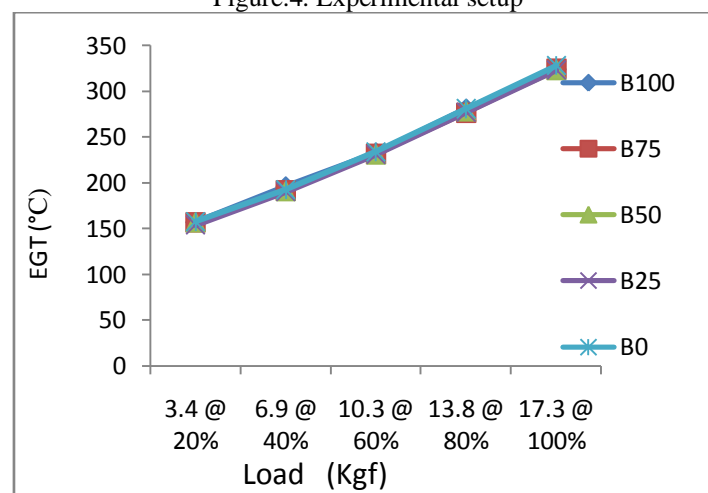


Figure.5. Comparison of EGT of diesel and different blends of sterculia striata

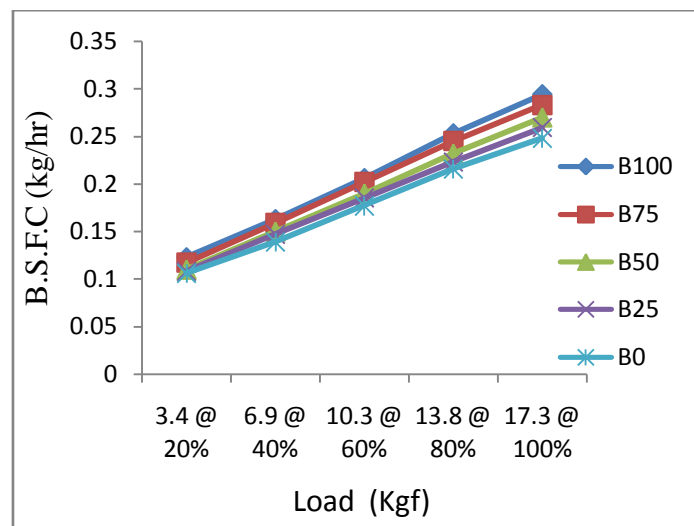


Figure.6. Comparison of B.S.F.C of diesel and four blends of biodiesel (sterculia striata)

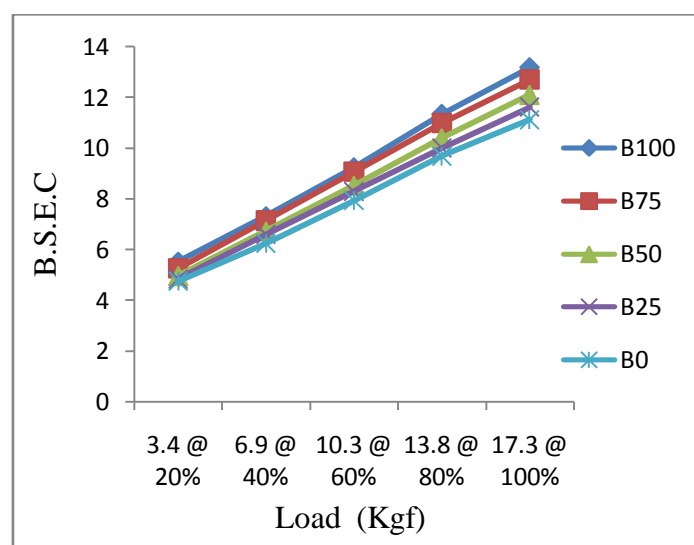


Figure 7 Comparison of B.S.E.C for Diesel and different blends of sterculia striata

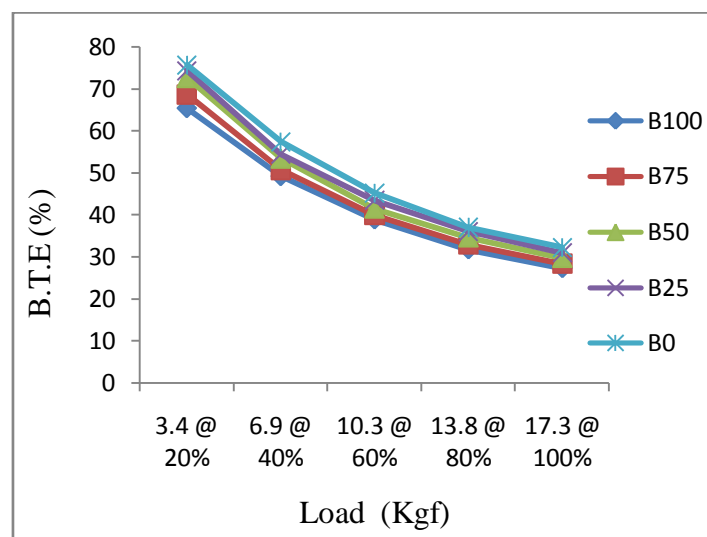


Figure.8. Comparison of BTE of diesel and different blends of sterculia striata

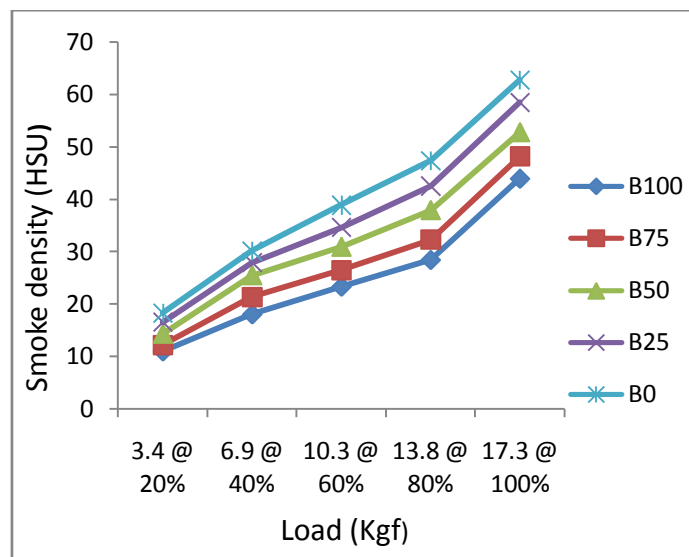


Figure.9. Comparison of smoke density of diesel and different blends of sterculia striata

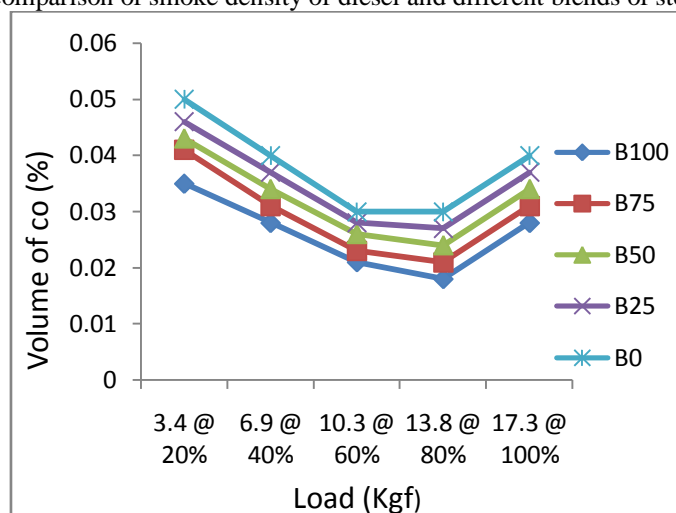


Figure.10. Comparison of CO emissions of diesel and different blends of sterculia striata

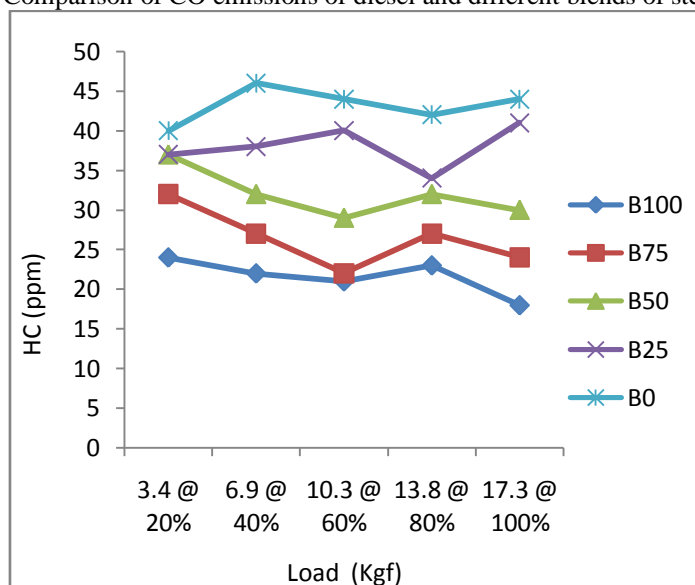


Figure.11. Comparison of HC emissions of diesel and different blends of sterculia striata

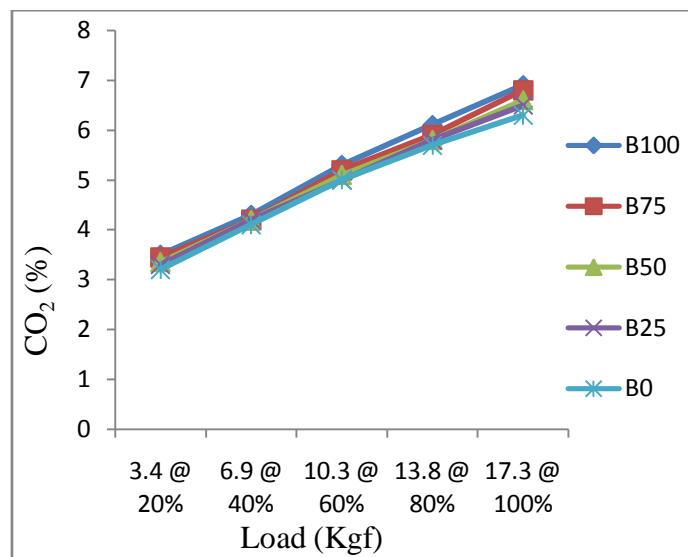


Figure 12 Comparison of CO₂ emissions for Diesel and different blends of sterculia striata

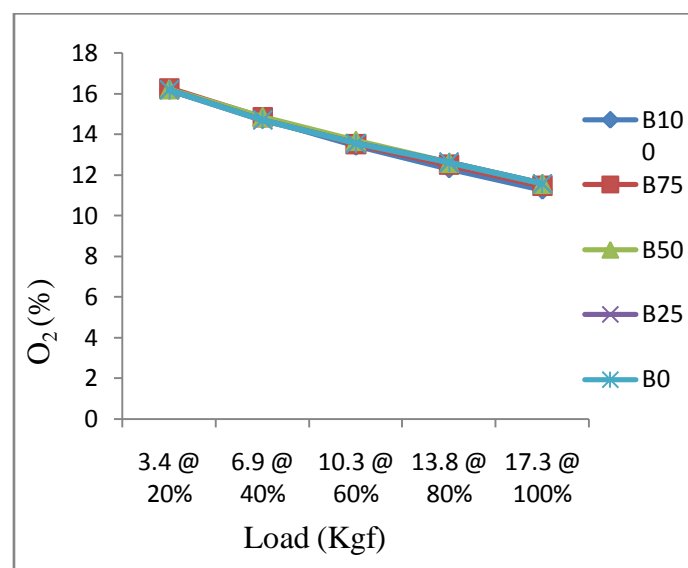


Figure 13 Comparison of O₂ emissions for Diesel and different blends of sterculia striata

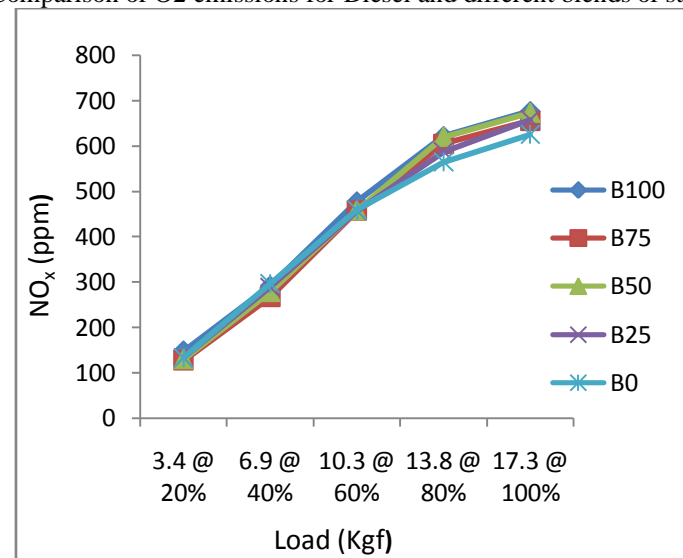


Figure.14. Comparison of NO_x emissions of diesel and different blends of sterculia striata

Tables

Table 1 Comparison of Properties of diesel and different blends of biodiesel

Properties	Diesel	Sterculia Striata
Water Content	0.02	0.96
Density (Kg/m ³) @ 15°C	820	893.1
Kinematic Viscosity (mm ² /s) @ 40°C	2.50	6.31
Conradson Carbon Residue %	-	0.84
Ash Content %	0.01	0.008
Pour Point °C	-16	-10
Flash Point °C	45	56
Acidity (mg of KOH/gm)	-	0.62
Sediments %	-	0.018
Gross Calorific Value (Kcal/Kg)	10,755	10,720
Distillation Range (90% Recovery) °C	330	345
Residue ml	-	3.80

Table.2. Engine Specifications

Type	Kirloskar T.V-1
Cylinder details	Single cylinder, Four Stroke Vertical, Water cooled
Power	7 H.P, 5.2 Kw
Bore	87 mm
Stroke	110 mm
Speed	1500 rpm
Compression ratio	17.5:1
Dynamometer	Eddy Current dynamometer
Model/Srl no	AG-20, 237/2003
Max Kw	20 Kw
Rpm	2450/1000
Dynamometer arm length	0.195 m

Table.3. Engine Load testing conditions

Fuels	Diesel, B100, B75, B50, B25
Compression Ratio	17.5:1
Specific gravity of fuel	0.884
Speed	1500 rpm
Room temperature	28.7°C
Mass flow rate of cooling water	7 Kg/min
Injection pressure	205 kg/cm ²

A Novel Approach of Harmonic Reduction with Transformer Connected 3-Phase Multilevel Inverter

Vipul Rastogi¹, Sudhanshu Tripathi²

M.Tech Scholar, Assistant prof. (Department of Electrical and Electronics Engineering, Sam Higginbottom Institute of Agriculture, Technology & Sciences, India)

Abstract: This paper proposes a multilevel inverter arrangement employing a series connected transformer to suppress 5th, 7th, 11th & 13th order harmonics (generated by non-linear loads). In the proposed scheme sinusoidal pwm signal generation technique is used for three phase multilevel VSI in conjunction with series connected transformer. The proposed model eliminates the need of output filter inductor. With this control strategy harmonic components of output voltage and switching losses can be minimized considerably. Simulation results verify the proposed concept and indicates that the transformer is capable of reducing the harmonics in the line.

Keywords: Multilevel inverter, SHE, Simulation, THD, Three phase transformer.

I. INTRODUCTION

Harmonics are undesirable always whether it is current harmonics or voltage harmonics. With increase dependency on non-linear loads it is necessary to use some arrangement which can suppress, reduce, mitigate or eliminate the harmonics by which power quality and system efficiency could improve. When non-linear loads are considerable part of the total load in the facility (more than 20%) there is a chance of harmonic problem. There are two main affects of harmonic currents on a distribution system. The first is that harmonic currents add to the RMS value of the fundamental. This additional current will increase losses in bus bars, wire and power factor correction capacitors used in the distribution system. The second affect is the additional heating caused by each of the harmonic currents. The higher order harmonics do not contribute to real work done. So these are always undesirable. Harmonics are the by products of modern electronics. They occur frequently when there are a large number of personal computers; uninterrupted power supplies (UPS), variable frequency drive (AC and DC) or any electronic device using solid state power switching.

Large harmonics, poor power factor and high THD in the utility interface are common problems with non-linear loads such as adjustable speed drives induction heating systems, aircraft converter systems, industrial electronic equipment, rectifier, microwave ovens, blenders, TVs, which contains of power semiconductors connected to the electric utility[1]. These power semiconductors are some of the source of harmonics. Large commercial and office buildings are supplied by a three phase utility source. The loads in these buildings are usually fed primarily by single phase power lines connected between one of the three lines and the neutral lines. Both non-linear and linear loads are connected to these single phase distribution system.[2]. Apart from unwanted losses in power systems, harmonics may cause other undesirable effects like flickering of electronic displays, false triggering of power electronic equipment and tripping of circuit breakers. Electronic energy meters may record false reading, loading loss of revenue or related issues like relation between service provider and service consumer. In the long run, harmonics reduces life/efficiency of all electric/electronic equipment

Multilevel power inverter has become extremely popular in recent years considering the advantages over traditional inverters. Amongst the available multilevel topologies the cascaded multilevel has distinct advantages due to compounding effect of the voltage levels. Multilevel voltage source inverter have been paid attention in medium-voltage and high power applications due to low switching losses, low voltage stress on switch devices and low harmonic distortion in output voltage. Therefore, many recent works with different multilevel inverter topologies have widely used in manufacturing factories recently because of their good performance of for the industry applications[3]. According to this when two multilevel inverters are cascaded through the load connection, the result is an operation with an equivalent no. of levels that is the product of the two inverters. Typically each inverter requires an isolated power source. This leads to difficulties in applications where high power density required.

II. INDENTATIONS AND EQUATIONS

2.1 Proposed Transformer Arrangement with Inverter Topology

2.1.1 (General Model)

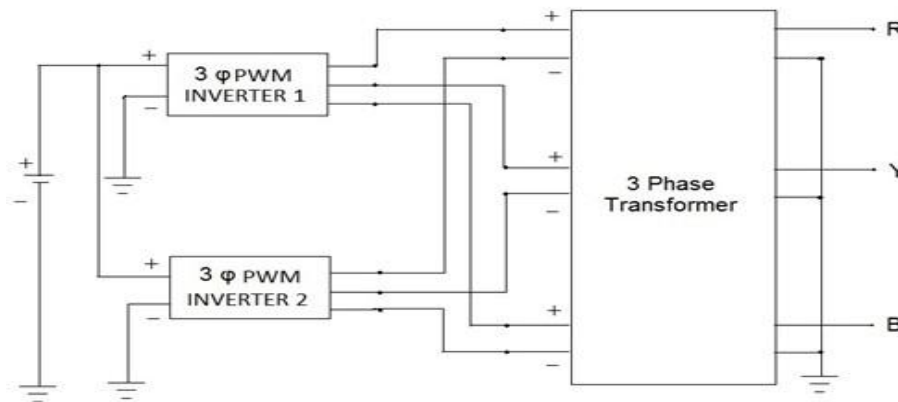


Fig 1: General model of proposed system

2.1.2 General Simulink Model

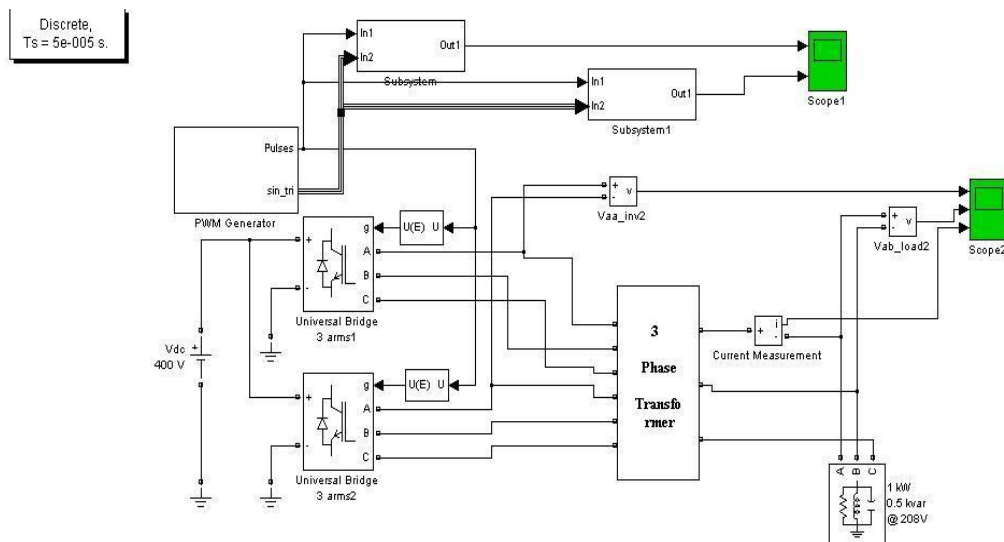


Fig 2: Matlab/Simulink model of system

2.1.3 Circuit Configuration

Fig. 2 shows the circuit configuration of the proposed multilevel inverter for three phase load. It comprises of one single DC input source, two three phase inverters (fed by the same DC source) and one three phase transformer. The output terminals of the transformer are connected with load. As shown in fig.3, SPWM technique is used for switching and corresponding waveform is shown in Fig.3. This scheme provides balanced three phase AC source.

SPWM techniques are characterized by constant amplitude pulses with different duty cycles for each period. The width of these pulses are modulated to obtain inverter output voltage control and to reduce its harmonic content [4]. Sinusoidal pulse width modulation is the mostly used method in motor control and inverter application [5]. In SPWM technique three sine waves and a high frequency triangular carrier wave are used to generate PWM signal [6]. Generally, three sinusoidal waves are used for three phase inverter. The sinusoidal waves are called reference signal and they have 120° phase difference with each other. The frequency of these sinusoidal waves is chosen based on the required inverter output frequency (50/60 Hz). The carrier triangular wave is usually a high frequency (in several KHz) wave. The switching signal is generated by comparing the sinusoidal waves with the triangular wave. The comparator gives out a pulse when sine voltage is greater than the triangular voltage and this pulse is used to trigger the respective inverter switches [7]. In

order to avoid undefined switching states and undefined AC output line voltages in the VSI, the switches of any leg in the inverter cannot be switched off simultaneously. The phase outputs are mutually phase shifted by 120° angles [6]. The ratio between the triangular wave & sine wave must be an integer N , the number of voltage pulses per half-cycle, such that, $2N = f_c/f_s$. SPWM signal waveform for three phase voltage source inverter is shown in Figure 3.

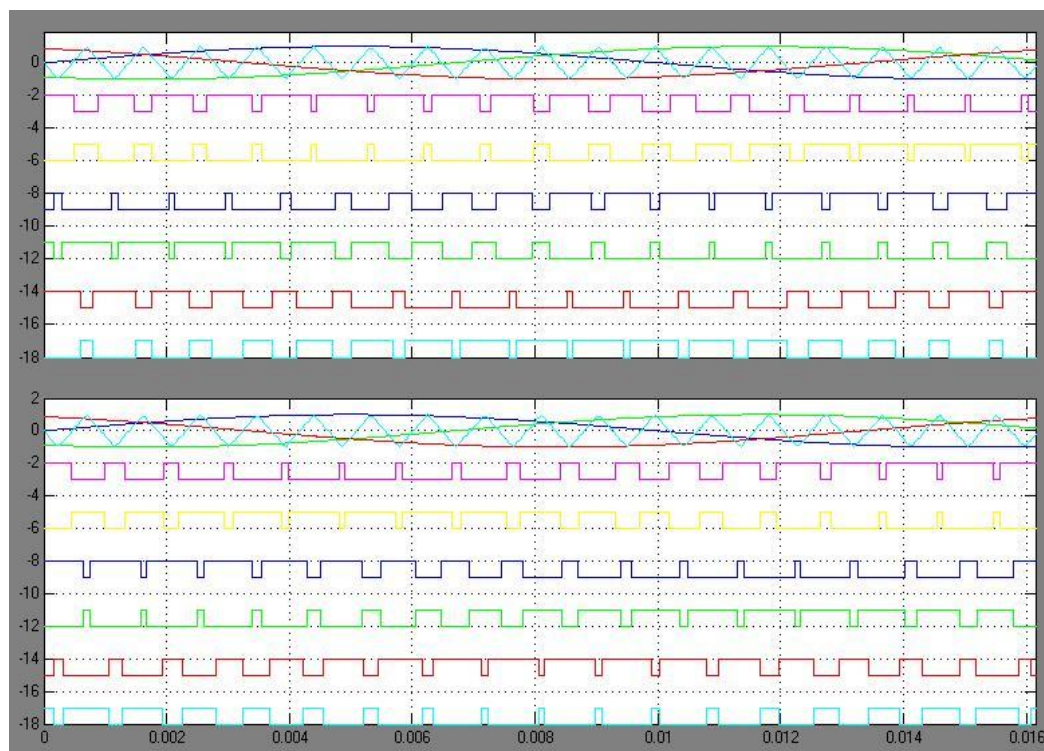


Fig 3: Waveform of SPWM pulse generation for three phase voltage source inverter

In this paper, different internal connections of winding arrangement between primary and secondary, of three phases transformer is proposed for the harmonic reduction. Special connection of windings of the transformer provides immunity from harmonics. Simulation results indicate that THD with select transformer arrangements are within allowable limits.

2.1.4 Transformer as a Harmonic Filter (Basic Concept and Theory)

The clock frequencies and ultrahigh speed operation of today's electronics would seem like science fiction to engineers a few decades ago. But because of the high clock rates associated with modern microprocessors and the high switching frequencies associated with switching power supplies, PCs and other equipment are guilty of generating and kicking back massive amounts of distortion into the line.

Effective noise rejection filters should pass the 50-Hz or 60-Hz fundamental and remove all higher frequencies. However, the line source impedance, combined with the impedance of the actual load, is low (ranging from 1 Ω to 100 Ω at 50 Hz or 60 Hz). Therefore, for optimum attenuation, the impedance of the filter should be low as well. In reality, however, this would require impracticably large and expensive capacitors and inductors. Therefore, there may be some power or performance limitation imposed by current handling capability of the series inductor as it must grow in size, weight and thermal dissipation to accommodate higher power devices. In addition, the high-pass shunt capacitors from line and neutral to ground increase system leakage current to ground. This becomes a significant factor where low levels of leakage current are demanded, such as in medical applications in patient care devices. A more practical approach is to start filtering noise at frequencies above 1 kHz, where most of the unwanted noises are found and where such interference causes malfunction of electronic equipment. The filter should be of the low pass type with second- or higher-order slopes. The internal inductance of the transformer with externally connected capacitors can be used to create the desired filter. Common solutions the installation of an off-the-shelf line filters, which is available in a variety of configurations from various companies.

Leakage inductance between the primary and secondary windings in all transformers already functions as a first order low-pass filter. Its corner frequency is high—20 kHz for EI-transformers and 200 kHz for toroidal transformers (due to the toroid's inherent low leakage inductance).

The two techniques

1. Increasing internal series inductance, and
2. Phase cancellation

Satisfy different attenuation requirements. Simply adding leakage inductance has the affect of inserting a series inductor and removing any current handling limitations. The increased leakage inductance is the prime factor in the performance of the design. The combination of the leakage inductance with the transformed capacitance from secondary to primary (C) and the primary dc-resistance (R) acts as a second-order low-pass filter. The corner frequency of the filter is determined by the combination of the L, C and R elements along with the load impedance Z_L .

2.1.5 Harmonic Cancellation

The non-linear currents from two or more three-phase load panels can be phase-shifted from one another through various types of three-phase transformer connections so that their aggregate distortion is less distorted than each of the original's waveforms. This reduces the distortion of current flowing into the primary power.

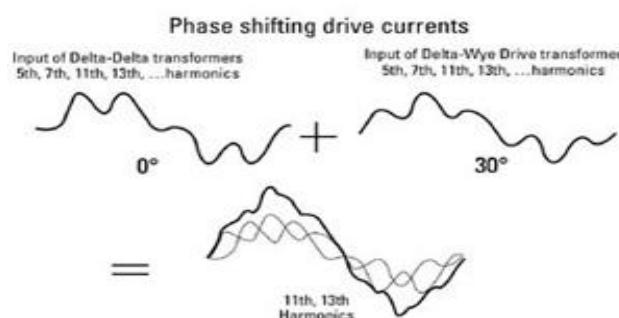


Fig 4: Resultant wave of phase shifting arrangement

In response to the increasing use of adjustable frequency drives in industrial facilities, IEEE 519-1992 has set guidelines for maximum current distortion present at a building service entrance. These guidelines are intended to prevent one factory from affecting the service of another, and to protect utility equipment. The determining factor in meeting IEEE 519-1992 current distortion limits is the percent of the service capacity that is used for serving non-linear loads. Typically, an industrial facility can load up to five percent of its total service capacity with six-pulse variable frequency drives without exceeding recommended limits. Beyond that, some form of harmonic abatement may be necessary. Motor drive current distortion can be reduced using filters, 12-pulse or higher drives, line reactors, drive isolation transformers or harmonic canceling transformers. Both line reactors and drive isolation transformers use reactive harmonic attenuation effects to reduce the actual current distortion at the input terminals to the drives. This practice alone can increase the six-pulse drive load by 20 percent or more of service capacity without exceeding guideline distortions. The effectiveness of reactive harmonic attenuation varies, depending on other system characteristics. Careful system analysis is always a good idea before applying any harmonic abatement solution to ensure the intended results. Harmonic abatement using filtering and/or 12-, 18- or 24-pulse drive technology is becoming increasingly popular, but these are relatively expensive solutions. Using transformers for harmonic cancellation can be an attractive alternative, particularly for users who incorporate isolation transformers for their drives anyway. The simplest cancellation method is to provide Delta-Delta connected transformers for some drive power, and Delta-Wye connected transformers for the remaining drives. If the sum of drive loads on each type of drive isolation transformer is balanced, current distortion into the primary system can be reduced significantly. The largest distortion components by far in six-pulse drive current are 5th and 7th harmonics. Eliminating these can significantly improve point of common-coupling current waveform distortion. The 5th and 7th harmonic cancellation effects brought about by the 30-degree phase shift between Delta-Delta and Delta-Wye connected transformers will depend on load balance. For continuous torque applications, where loads are fairly constant, close load balance is easier to achieve. On the other hand, process control

applications, such as punching, stamping or motion control, make it difficult to maintain consistent balance of multiple drive loads at any given time.

In some cases, Delta-Delta connected drive isolation transformers are undesirable because the secondary cannot be grounded in a balanced way. Ungrounded power can adversely affect the operation of some drives, and can cause drives to trip on surges and impulses coupled from the primary service. For these applications, Delta-Zigzag connected transformers are available. The zero-phase shifting acts like a Wye source for the drive, providing a balanced neutral point for grounding. At the same time, they substitute for Delta-Delta transformers, providing the same harmonic abatement when used in combination with Delta-Wye connected transformers serving other drive loads on the same service, as in Figure 4. Of course, when voltage change is not required, the use of line reactors on half the load along with Delta-Wye connected loads on the other half also can be used. Since standard drive isolation transformers can be effectively used as harmonic canceling transformers, the term 'harmonic canceling transformer' becomes somewhat ill-defined. In general, that special term is attributed to transformer products with special connections that can address 11th, 13th and even higher harmonics in drive loads. These can be single transformers with multiple secondary's, or sets of transformers feeding multiple loads. The basic principles are the same, except that 15-degree phase shift is required to address 11th and 13th harmonics.

The benefits of this additional step in harmonic reduction are dubious, however, because 11th and 13th harmonic components contribute to less than one-fifth of the total distortion in service entrance currents. The difficulties of obtaining precise balance of loads will almost always leave enough residual 5th and 7th harmonic distortion to minimize the benefit of any higher harmonic treatment. Filtering is a much more cost-effective method for addressing upper order (11th and higher) harmonics compared to special 'harmonic cancellation' transformers.

2.1.6 Theory of HMT (Harmonic Mitigating Transformer) or Phase Shifting Transformer

In addition to improved system reliability and reduced maintenance costs, HMTs also have excellent energy-saving characteristics. With the cost of electricity continuing to increase around the world, there is an ever-increasing interest in energy-efficient products. Because HMTs are intended to be installed in systems that contain high levels of nonlinear loads.

HMTs are an economical solution in the battle against the harmful effects of harmonics. Whenever the HMT is energized, it will provide harmonic treatment. Harmonic mitigating transformers are commonly referred to as "phase-shifting" transformers. The HMT has three-wire connected primary windings and four-wire connected secondary windings. The fundamental changes to the orientation of the transformer winding allow a transformer to be designed in a wide variety of different phase-shifts (-15° , 0° , $+15^\circ$, 30°). In standard delta-wye transformers, including K-factor rated transformers, triplen harmonics are passed from the secondary windings, into the primary delta windings, where they flow and cause substantial watt loss. In HMTs, the electromagnetic flux cancellation created by the zigzag winding configuration prevents 3rd and other triplen harmonics from being transmitted into the primary delta winding. Harmonic treatment is provided entirely by electromagnetic flux cancellation; no filters, capacitors, or other such devices are used. It is important to remember that the harmonic currents still flow to the secondary windings.

Phase shifting involves separating the electrical supply into two or more outputs, each output being phase shifted with respect to each other with an appropriate angle for the harmonic pairs to be eliminated. The concept is to displace the harmonic current pairs in order to bring each to a 180° phase shift so that they cancel each other out. Positive sequence currents will act against negative-sequence currents, whereas zero-sequence currents act against each other in a three-phase system. Recall that triplen harmonics are zero-sequence vectors; 5^{th} , 11^{th} and 17^{th} harmonics are negative-sequence vectors, and 7^{th} , 13^{th} and 19^{th} harmonics are positive-sequence vectors. Hence, an angular displacement of: 1) 60° is required between two three-phase outputs to cancel the 3^{rd} harmonic currents; 2) 30° is required between two three-phase outputs to attenuate the 5^{th} and 7^{th} harmonic current pairs; 3) 15° is required between two three-phase outputs to cancel the 11^{th} and 13^{th} harmonic current pairs.[8]

2.1.7 Zig-Zag Transformer

The three-phase four-wire distribution power systems have the problems of harmonic pollution, load unbalance and over-load of neutral conductor. In order to ensure high "Power Quality" for low tension consumers, it is necessary to treat harmonics. So the Zig-Zag transformer's can be used to attenuate the neutral current and zero-sequence harmonic current on the utility sites due to the advantage of low cost, high reliability.[9]. It is an effective way to reduce harmonics by using a zig-zag transformer. A zig-zag transformer cancels the fifth and seventh harmonics as well as triplen (third order) harmonics. The third, fifth and seventh

are the most prevalent harmonics so eliminating them results in a major reduction of the total current distortion. It is important to note that the spectrum of the harmonic distortion created varies depending on the type of nonlinear load. The added benefit of the zig-zag transformer is that it will also reduce the fifth and seventh harmonic as well as reduce the effect voltage distortion on the output caused by the current distortion.[10]

2.1.8 Isolation Transformer

Since input circuit reactance is a major determining factor for the magnitude of harmonics that will be present and flowing to an individual load, isolation transformers can be used effectively to reduce harmonic distortion. The leakage inductance of isolation transformers can offer appropriate values of circuit impedance so that harmonics are attenuated. The typical configuration of isolation transformer, for power quality purposes, is delta primary and wye secondary. Like a reactor, the inductive reactance is low enough at the fundamental frequency to easily pass fundamental current, but increases proportionately for harmonic frequencies and can achieve performance similar to that of a line reactor. Additionally, the isolation transformer can be supplied with an electrostatic shield between the primary and secondary windings. Due to the capacitive coupling between each winding and the shield, a low impedance path is created to attenuate noise, transients and zero sequence currents. The shield helps to mitigate the common mode disturbances to their originating side (primary or secondary) of the transformer. The wye secondary transformer has the capability of providing a new electrical ground for the load circuit. An isolation transformer is a transformer with physically separate primary and secondary windings. These windings are typically separated by an electrostatic shield, which is a sheet of nonmagnetic conducting material (copper or aluminum) connected to ground which acts as a shield to prevent the noise of one system from passing through the transformer to sensitive equipments. Shielded isolation transformers are very popular power-conditioning devices. They isolate sensitive loads from transients and noise caused by the utility. They can also keep harmonics produced by end-user non linear equipments from getting onto the utility's system. They especially eliminate common-mode noise.[11]

2.1.9 Inductive Filtering Connection

The existing new transformer connection, the primary side is wye wiring, and the two group windings of second side adopt delta wiring, which formed the 30° phase differences. Its secondary winding adopts prolonged-delta wiring. The secondary prolonged winding and the common winding of the new converter transformer adopt self-coupling connection, which is similar to the series winding and the common winding of autotransformer. It can realize the goal that once the harmonic current flows into the prolonged winding, the common winding will induct the opposite harmonic current to balance it by the zero impedance design of the common winding.[12].

III. SIMULATION AND RESULTS

In order to verify proposed arrangement simulation analysis (Fig. 5, 11, 17 & 23) was performed with different modulation indices varying from 0.5 to 0.9. Voltage and current waveforms before and after transformer for different suggested connections as well as FFT analysis of proposed system (with modulation index= 0.8) also done and showed in subsequent figures.

CONNECTION A

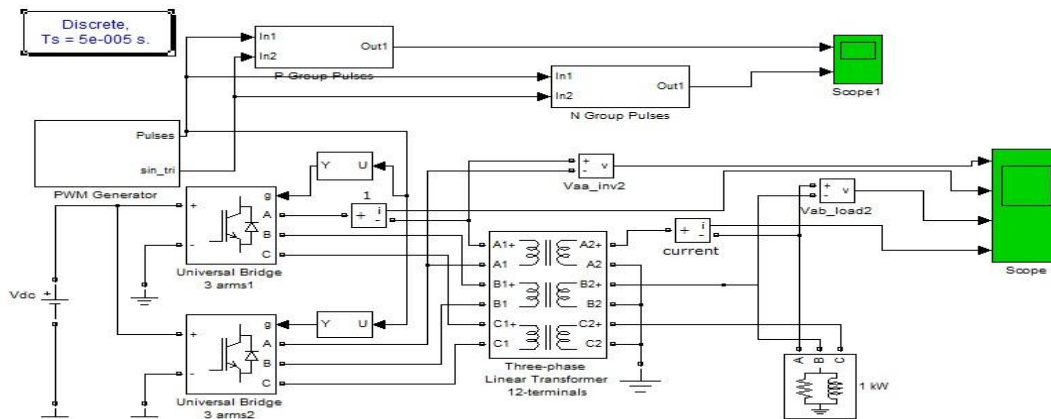


Fig 5:Simulink model of Connection type A

A.1 FFT ANALYSIS OF CONNECTION:

Voltage and current harmonics before transformer

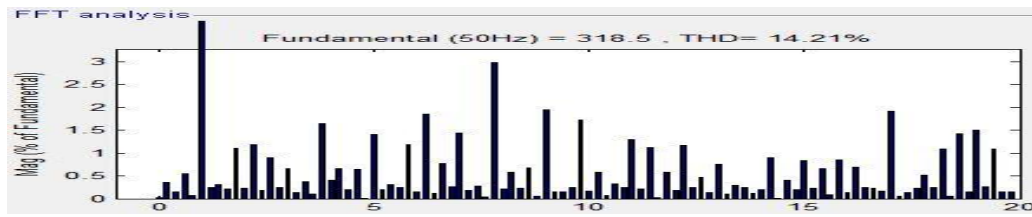


Fig 6: Voltage harmonics before transformer for Connection A

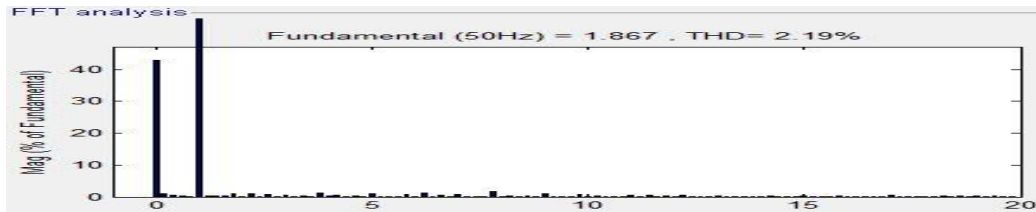


Fig 7: Current harmonics before transformer for Connection A

Voltage and current harmonics after transformer

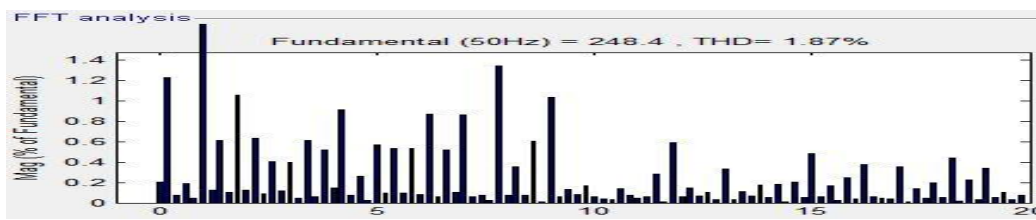


Fig 8: Voltage harmonics after transformer for Connection A

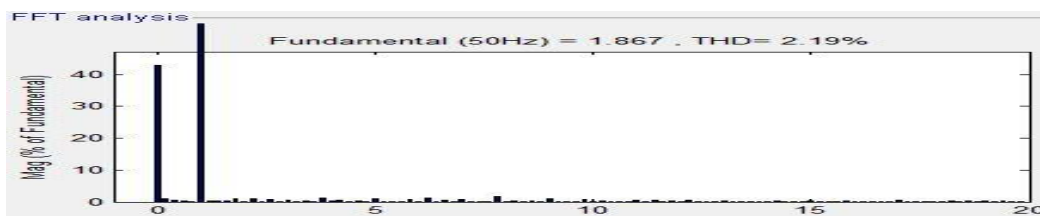


Fig 9: Current harmonics after transformer for Connection A

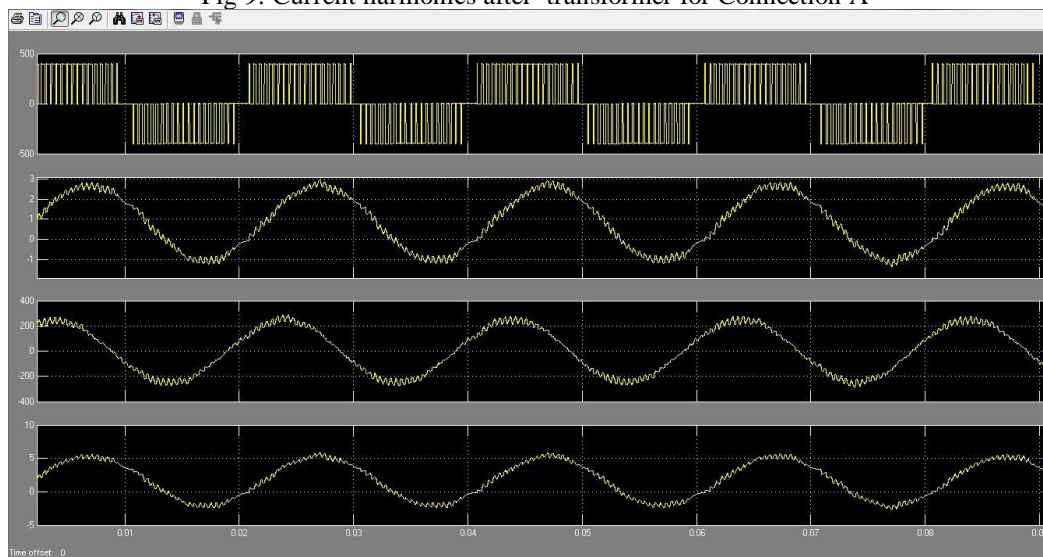


Fig 10: Scope output of connection A

CONNECTION B

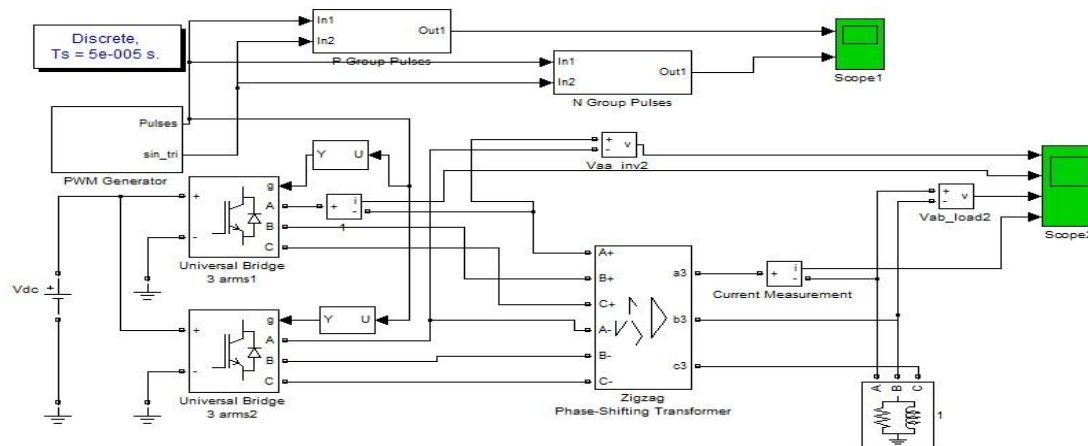


Fig 11: Simulink model of Connection type B

B.1 FFT ANALYSIS OF CONNECTION:

Voltage and current harmonics before transformer

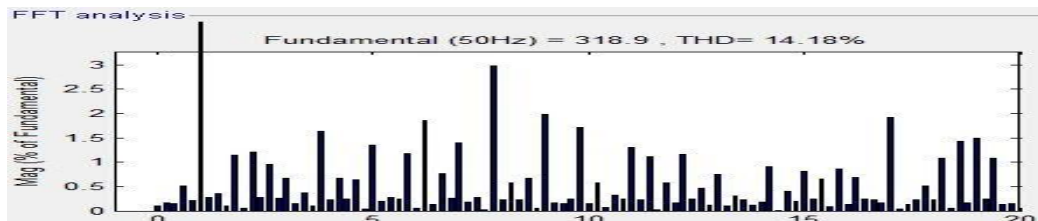


Fig 12: Voltage harmonics before transformer for Connection B

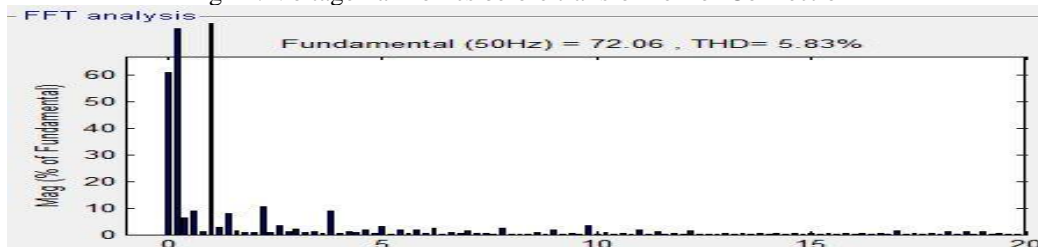


Fig 13: Current harmonics before transformer for Connection B

Voltage and current harmonics after transformer

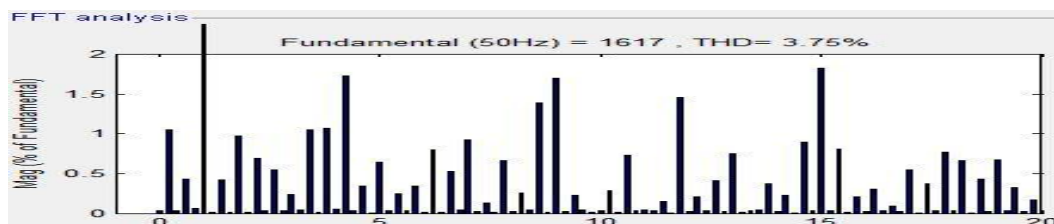


Fig 14: Voltage harmonics after transformer for Connection B



Fig 15: Current harmonics after transformer for Connection B

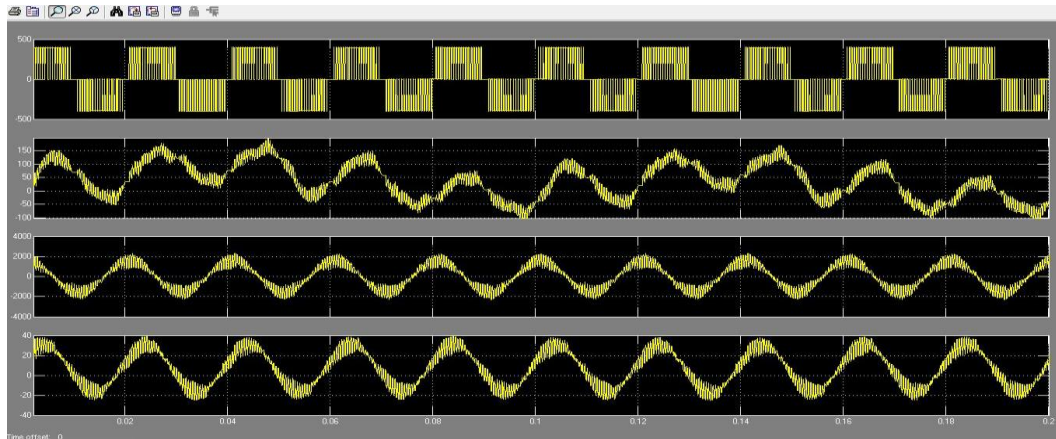


Fig. 16: Scope Output of Connection B

CONNECTION C

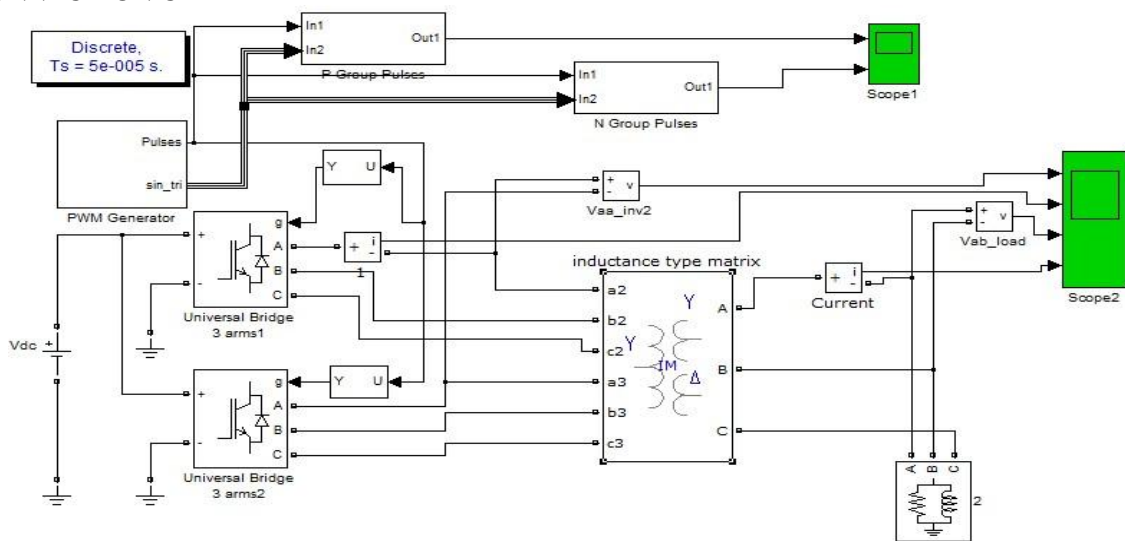


Fig 17: Simulink model of Connection type C

C.1 FFT ANALYSIS OF CONNECTION:

Voltage and current harmonics before transformer

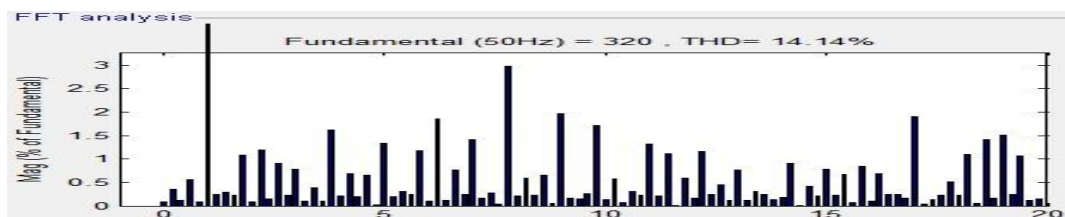


Fig 18: Voltage harmonics before transformer for Connection C



Fig 19: Current harmonics before transformer for Connection C

Voltage and current harmonics after transformer

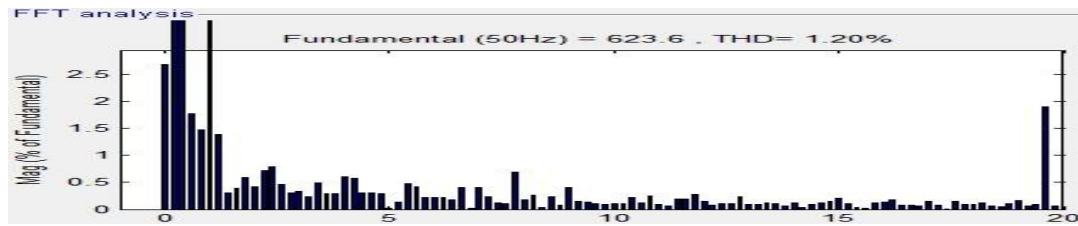


Fig 20: Voltage Harmonics after Transformer For Connection C

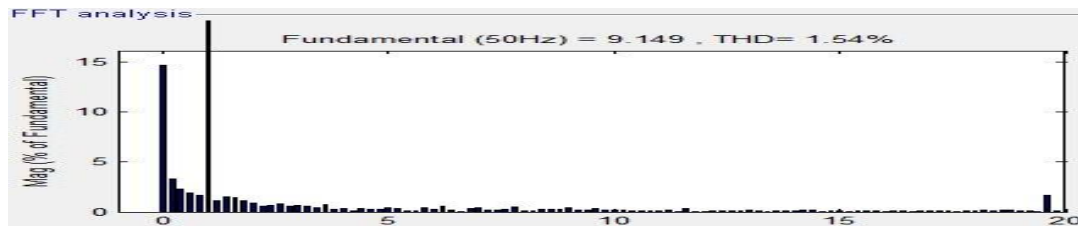


Fig 21: Current harmonics after transformer for Connection C

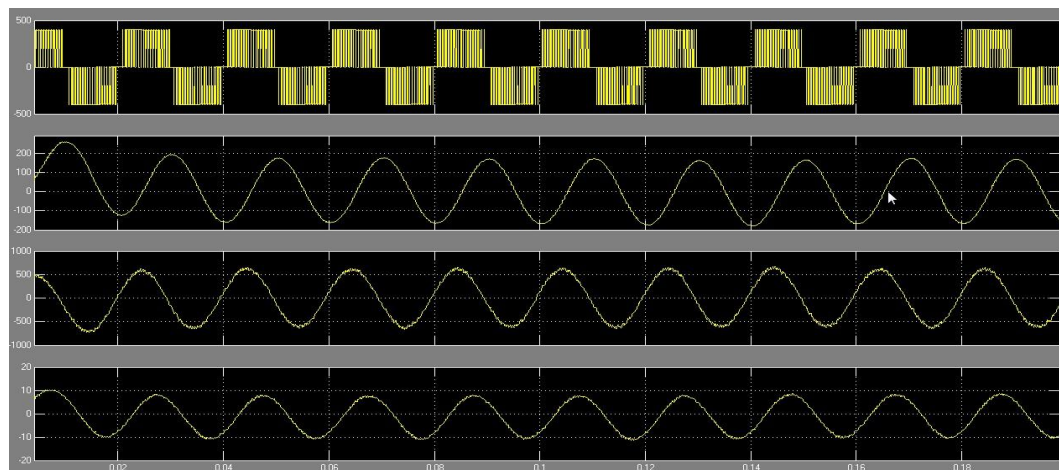


Fig 22: Scope output of Connection C

CONNECTION D

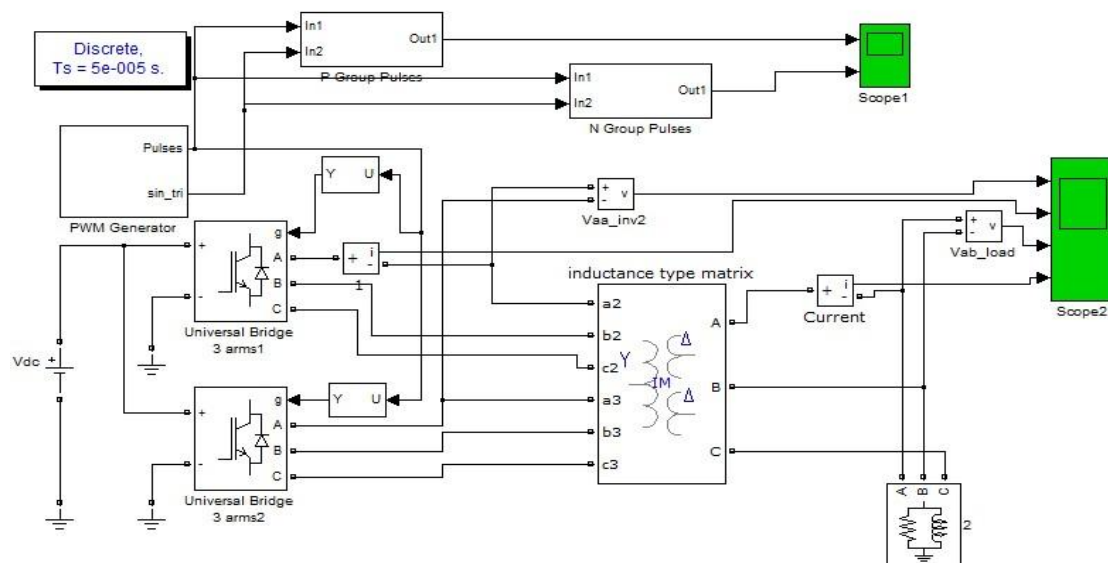


Fig 23: Simulink model of Connection type D

D.1 FFT ANALYSIS OF CONNECTION D:

Voltage and current harmonics before transformer

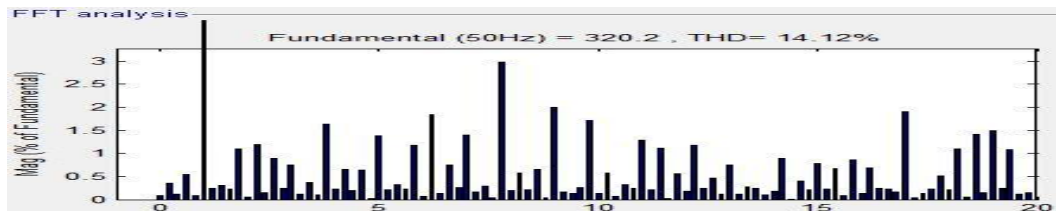


Fig 24: Voltage harmonics before transformer for Connection D

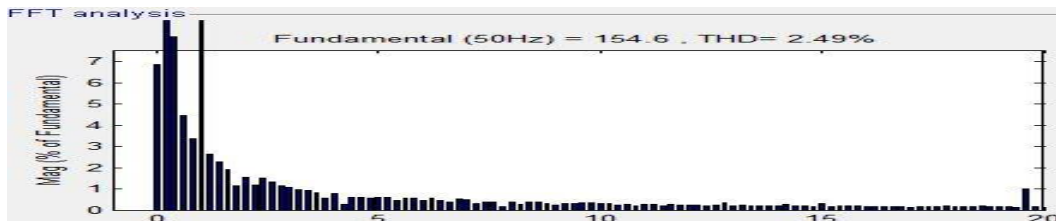


Fig 25: Current harmonics before transformer for Connection D

Voltage and current harmonics after transformer

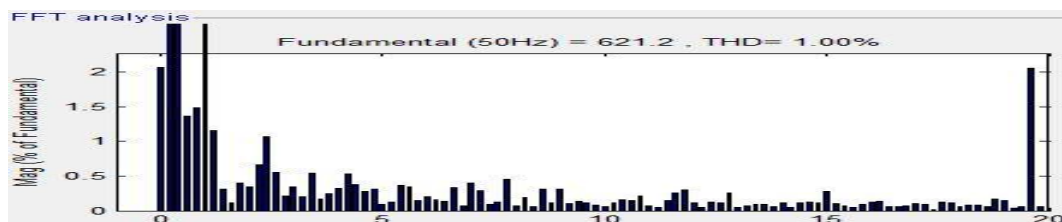


Fig 26: Voltage harmonics after transformer for Connection D

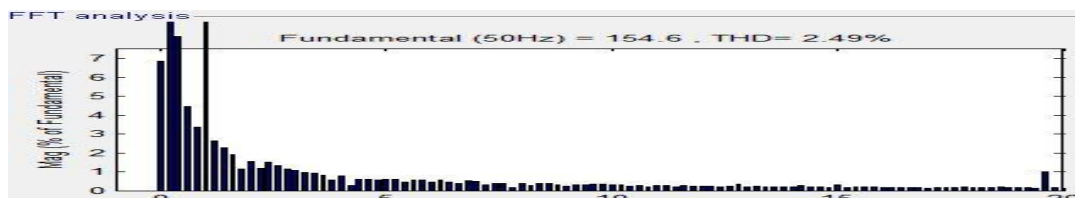


Fig 27: Current harmonics after transformer for Connection D

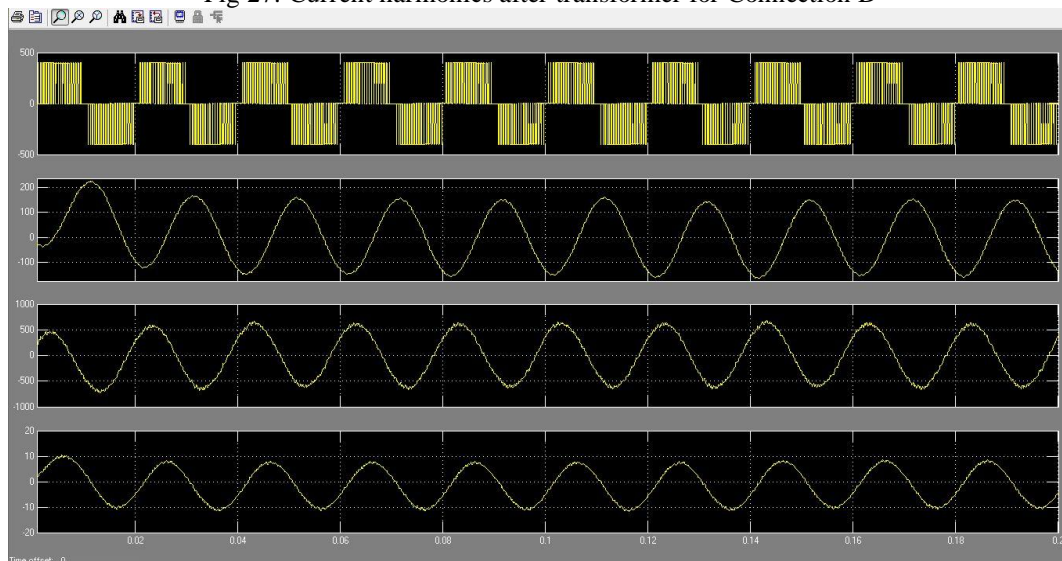


Fig 28: Scope output of Connection D

WITHOUT TRANSFORMER CONNECTION

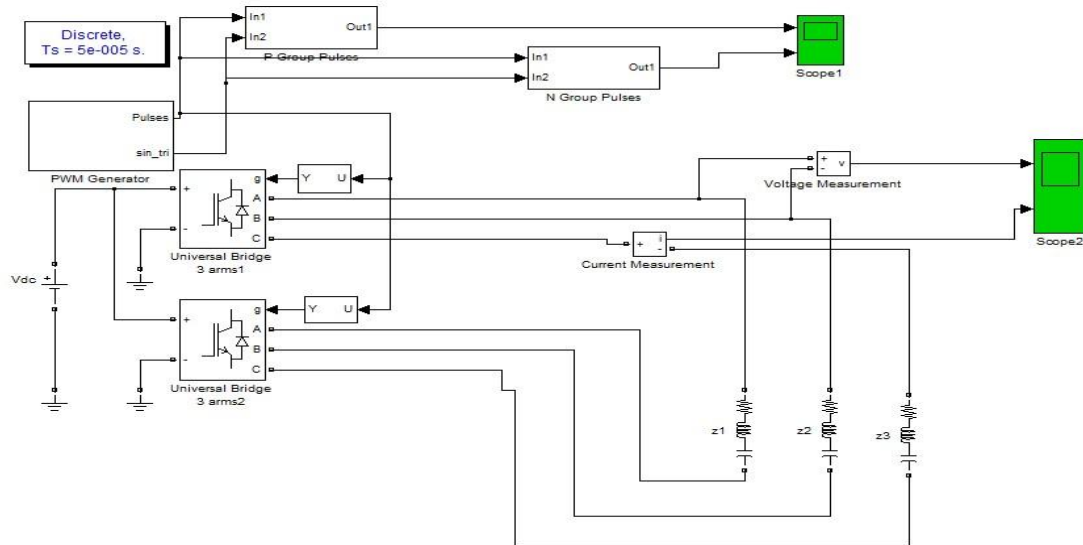


Fig 29: Simulink model without transformer connection

Voltage and current harmonics

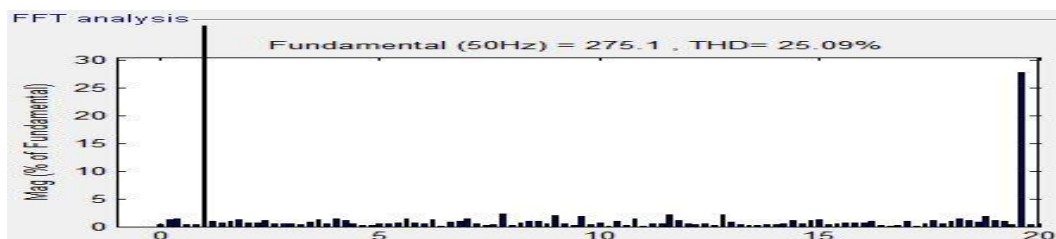


Fig 30: Voltage harmonics for without transformer connection

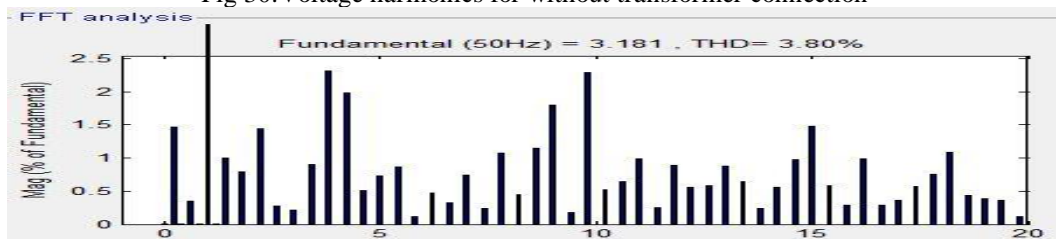


Fig 31: Current harmonics for without transformer connection

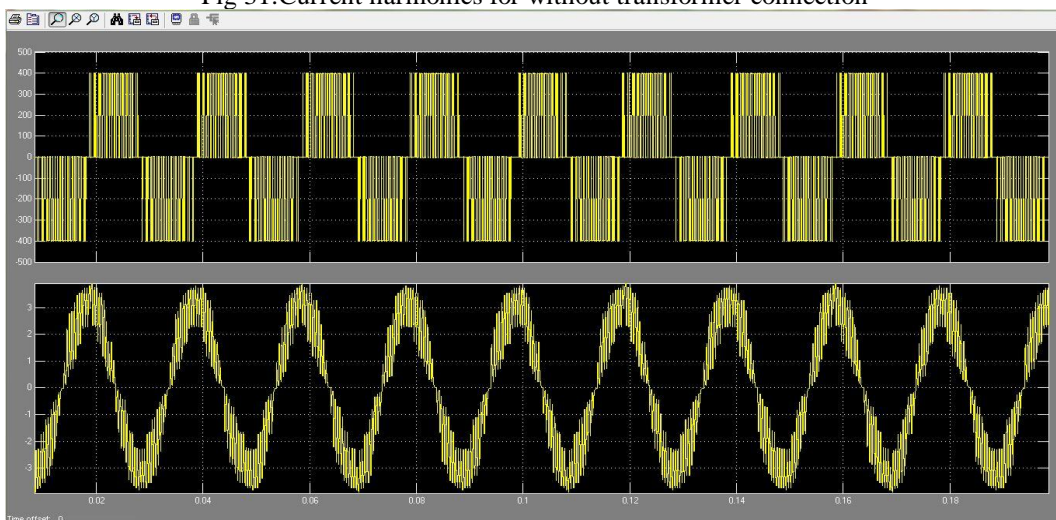


Fig 32: Scope output of without transformer connection

Table -1 Comparison of THD in different connections (for P=1000W $Q_L=500$ VAR)

MI	With out Transf ormer	CONNECTION A (THD V&I) %		CONNECTION B (THD V&I) %		CONNECTION C (THD V&I) %		CONNECTION D (THD V&I) %	
		Before transfor mer	After transfor mer	Before transfor mer	After transfor mer	Before transfor mer	After transfor mer	Before transfor mer	After transfor mer
0.9	19.85 3.22%	13.42%, 2.15%	1.74%, 2.15%	13.40%, 5.35%	3.31%, 3.03%	13.35%, 2.98%	1.02%, 1.42%	13.34%, 2.81%	1.00%, 1.53%
0.8	25.09, 3.80%	14.21%, 2.19%	1.87%, 2.19%	14.18%, 5.83%	3.75%, 3.39%	14.14%, 2.79%	1.20%, 1.54%	14.12%, 2.49%	1.00%, 1.45%
0.7	27.62, 4.32%	16.62%, 1.97%	1.44%, 1.97%	16.58%, 5.88%	3.51%, 3.22%	16.53%, 2.81%	1.23%, 1.35%	16.52%, 2.66%	1.05%, 1.18%
0.6	30.26, 5.19%	18.15%, 1.92%	1.73%, 1.92%	18.12%, 6.34%	5.10%, 4.29%	18.05%, 2.86%	1.32%, 1.43%	18.02%, 2.45%	1.17%, 1.29%
0.5	41.34, 5.52%	23.87%, 2.34%	1.82%, 2.34%	23.80%, 6.20%	5.13%, 4.34%	23.69%, 2.61%	1.19%, 1.67%	23.66%, 2.27%	1.03%, 1.61%

It is observed that THD of all arrangements are in permissible limit which is enviable. It can be observed that the output of transformer has reduced harmonic pollution with practical load attached with transformer. FFT analysis also shows the harmonic spectrum before and after transformer.

Above table shows the THD variation with different connection at different modulation index. From the table it can be deduced that on decreasing the modulation index, THD of system increases with same load with different connections. Performance of Connection C and D is better than A and B. Without transformer connection and performance of FFT analysis also have done and data are shown in table.

IV. CONCLUSION

Based on the analysis and results it can be established that transformer reduces harmonics from a system. Furthermore for the different configurations; Connection C (P- Y/S-Y, Δ) and Connection D (P-Y/S- Δ , Δ) can be judged better in filtering out harmonics effectively. As a common practice Modulation Index is usually kept around 0.8 for which Connection D can be said to be the best option available for the objective of harmonic filtering.

REFERENCES

Journal Papers:

- [1] Sewan Choi., Prasad N. Enjeti, and Ira J. Pitel," Polyphase Transformer Arrangement With Reduced KVA Capacities For Harmonic Current Reduction in Rectifier- type Utility Interface", IEEE Transactions on Power Electronics, Vol. 11, No. 5, September 1996
- [2] M.A Shafie*, H. Singh*, M.Q.A Rahman* , " Harmonic and Neutral to Ground Voltage Reduction Using Isolation Transformer,"International Conference on Power and Energy (PECon2010),Nov29-Dec1,2010 kuala Lumpur, Malaysia.
- [3] Chung-Ming Young, Sheng-Fung Wu ,and Ping-Chun Liao," A New Multilevel Inverter Base on Single DC Input Source and Zig-Zag Connected Transformers,"2011 6th IEEE Conference on Industrial Electronic and Applications.
- [4] PK Sadhu, G Sarkar, A Rakshit," A microcontroller based variable voltage variable frequency sinusoidal power source with a novel PWM generation strategy ,Measurement, 2012 – Elsevier, Volume 45, Issue 1, January 2012, Pages 59-67. (Article).
- [5] B.Ismail, S.T.," Development of a Single Phase SPWM Microcontroller-based Inverter,"(Nov28-29,2006),First International Power and Energy Conference PEC, Putrajaya, Malaysia: IEEE(Conference Paper).
- [6] Miguel Lopez,Luis Moran, Jose Espinoza and Juan Dixon,"Performance Analysis of Hybrid Asymmetric Multilevel Inverter for High Voltage Active Power Filter Applications,"IEEE Industrial Electronics Conference,IECON,2003,Virgina,USA,2003.
- [7] Dehbonei H, Borle L and Nayer C.V.," A Review and Proposal for Optimal Harmonic Mitigation in Single Phase Pulse Width Modulation," Proceedings of 4th IEEE International Conference on Power Electronics and Drive System,2001, Vol.1,2001,pp.408-414.
- [8] Jean-Guy Boudrias, Jeff Bannard, P.Eng," Harmonic Mitigation, Power Factor Correction And Energy Saving With Proper Transformer And Phase Shifting Techniques", CCECE 2004- CCGEI 2004, Niagara Falls, Maylmai 2004IEEE.

- [9] S.Ranjith Kumar, S.Surendhar, Ashish Negi and P.Raja,” Zig Zag Transformer performance analysis on harmonic reduction in distribution load”, International Conference on Electrical, Control and Computer Engineering Pahang, Malaysia, June 21-22, 2011. -1-61284-230-1/11/ 2011 IEEE.
- [10] Mohd Ridhwan B Abdul Rahim, Mohd Najib Mohd Hussain, Ahmad Asri Bin Abd. Samat,” Harmonic Reduction Using Current Injection Based Twelve-Pulse Rectifier”, 2009 IEEE Symposium on Industrial Electronics and Applications (ISIEA 2009), October 4-6, 2009, Kuala Lumpur, Malaysia, 978-1-4244-4683-4/09, 2009 IEEE.
- [11] M.A Shafie*, H. Singh*, M.Q.A Rahman,” Harmonic and Neutral to Ground Voltage Reduction Using Isolation Transformer,”2010 International Conference on Power and Energy(PECon2010),Nov29-Dec1,2010,Kuala Lumpur,Malaysia.978-1-4244-8946-6/10/2010IEEE.
- [12] Shao Pengfei, Luo Longfu, Li Yong, Xu Jiazhu, He Dajiang, Liu Fusheng,” Application Prospect of a New Transformer Inductive Filtering Technology”,DRPT2008 6-9 April 2008 Nanjing China, 978-7-900714-18/08,2008DRPT.



Vipul Rastogi is a research scholar pursuing M. Tech in Power Electronics from Sam Higginbottom Institute of Agriculture Of Technology & Sciences, Allahabad U.P.) India. He secured degree of B. Tech in Engineering from LDC ITS (UPTU) India in 2011.



Sudhanshu Tripathi presently working as Assistant Professor Electrical & Electronics Engineering at Sam Higginbottom Institute of Agriculture Technology & Sciences, Allahabad, (U.P) India. The degree of B. Tech secured in Electrical & Electronics Engineering from U.P TECH University 2004 and M. Tech. in Digital Communication from Maulana Azad National Institute of Technology Bhopal, in 2007.

Online Intrusion Alert Aggregation with Generative Data Stream Modeling

Kothawale Ganesh S.¹, Borhade Sushama R.², Prof. B. Raviprasad³

¹ Student, M.Tech(CSE), R R S College of Engineering & Technology, Muthangi (Vill), Patancheru (Mdl), Andhra Pradesh, India, Pin- 502 300.

² AAEMF's College of Engineering and Management Studies Koregaon Bhima, Tal- Shirur, Dist- Pune, Maharashtra, India PIN- 412216

³ Guide, R R S College of Engineering & Technology, Muthangi (Vill), Patancheru (Mdl), Andhra Pradesh, India, Pin- 502 300.

Abstract: Online intrusion alert aggregation with generative data stream modeling is a approach which uses generative modeling. It also use a method called as probabilistic methods. It can be assume that instances of an attack is similar as a process may be a random process which is producing alerts. This paper aims at collecting and modeling these attacks on some similar parameters, so that attack from beginning to completion can be identified. This collected and modeled alerts is given to security personnel to estimate conclusion and take relative action. With some data sets, we show that it is easy to deduct number of alerts and count of missing meta alerts is also extremely low.

Also we demonstrate that generation of meta alerts having delay of only few seconds even after first alert is produced already.

Keywords: online intrusion detection system, data stream, alert aggregation, IDS, offline alert aggregation, online alert aggregation etc.

I. Introduction

In general, IT system is having huge number of information. This information is always confidential. Providing security to information is essential task in information technology system. To provide information security, emergence of new technologies which are innovative should be happened.

Intrusion Detection System plays an very important role in information security. It can be a device or a software application which is capable to detect outside intrusion as well as monitors inside activities such as unauthorized access. It detects suspicious actions by evaluating TCP/IP connections or LOG files. The working of this IDS is such a way that when it finds some action which is suspicious action then it produces alerts immediately. This alert contains information about source IP address, destination IP address, and possible type of attack. This possible type of attack consist of buffer overflow, denial of service, SQL injection etc. This alert processing is done at very low level of IDS. So it may be possible that single attack instance can have thousands of alerts. It becomes drawback of existing IDS. There are two types of IDS.

1.1 NIDS: NIDS is nothing but Network Based IDS. This IDS is an independent platform. It analyze the traffic on internet. It also monitors many hosts. Network based IDS access network by network tap, network switch, network router etc. In network based IDS sensors are placed, which identifies network traffic and analyze the content. Snort is the example of Network based IDS.

1.2 HIDS: HIDS is Host Based Intrusion Detection System. This IDS is may be dependent or independent platform. Agents are placed in Host based IDS. This agent in Host based IDS analyze log files, system calls and any other activities. Sensors are consists of agents. OSSEC is the example of Host based IDS.

II. Related Work

Existing IDS are having very high accuracy to detect the attacks, but still they have some drawbacks such as alerts are produces at very low level of IDS, thousands of alerts may produce for single attack instances, confusions may happened due to large number of alerts produced in taking appropriate actions while attack is done and so on. Many scientist or publication have done their work to remove these drawbacks. They have provided some direction to do the future enhancement in IDS.

The most suitable way to apply the correlation between different alerts is done in[6]. In this paper reconstruction of alert thread is done. The alerts which are produced by IDS can be aggregated by using some fixed length window. But it can produce duplicates, which should be eliminated for proper working of IDS. So

elimination of these types of duplicates is done in [7] by clustering the alerts online as well as offline. First offline algorithm has been developed to eliminate the duplicates and this offline algorithm had been extended for online algorithm. The situation of current attack is done in [8]. The cluster is used to group same attacks is done in [9]. Instead of using alert clustering, another way to correlate alerts is done in [10]. In this paper the process of combining two alerts is done on the basis of weighted, attribute wise similar operator. But from [11] and [12] this way has one disadvantage that large number of parameters are needed to be set. [13] has same disadvantage as [10]. To overcome this disadvantage [14] uses another clustering algorithm that uses user defined parameters. It uses strict sorting based on source and target i.e. destination IP addresses and ports in alerts. [22] uses fully different and unique way for clustering, AA-NN i.e. auto associator neural network's error is reconstructed and it helps to analyze different alerts. Alerts which produce same reconstruction error are grouped or placed into same cluster. The major advantage of this approach is it can be applied to offline as well as online. Offline training is required to do first of all and that can be extended to online training of AA-NN.

III. Online Intrusion Alert Aggregation Technique

In this section, we will discuss our new alert aggregation approach. As we have already stated that it is probabilistic model of current situation of different types of attacks. First of all we start with architecture of our system. The architecture consists of the diagram showing detailed view and description about the layers in detail. Then we will describe about the process of generation of alerts and the alert format i.e. what are the contents of alerts. After that we discuss about the clustering algorithm for offline alert aggregation and how to extend it to apply it online. At last we prepare result. Analyze it to produce remark for generation of meta alerts. Whatever meta alerts has been produced we will send it to users registered mobile.

3.1 Architecture:

The following figure shows the architecture of proposed system.

3.1.1 Sensor Layer: It is low level layer which acts as an interface between the network and host (agent reside). It captures raw data from both i.e. from network and host, filters it and takes out essential data to create an event. Sensor layer consists of sensors which capture traffic on network

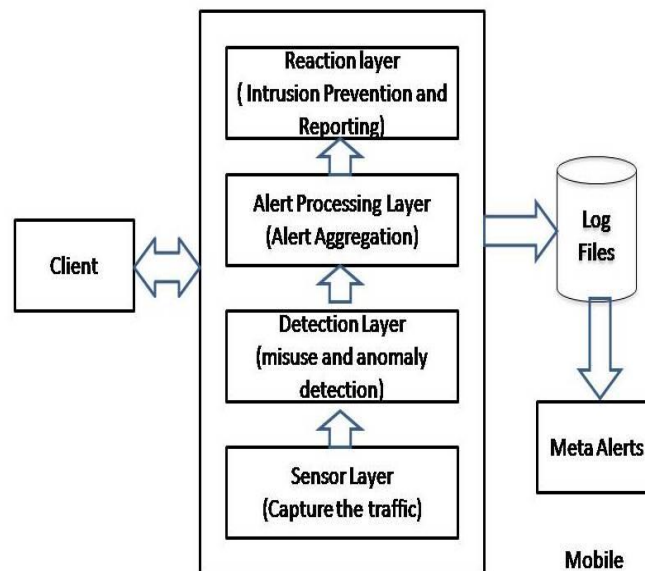


Fig 1. Layered Model of Proposed System

3.1.2 Detection Layer: This layer consists of different types of detectors e.g. Support Vector Machines, Snort. It looks for misuse detection and anomaly detection. If it finds suspicious behaviors, it creates alerts and forwards them to the next layer of our proposed architecture i.e. alert processing layer.

3.1.3 Alert Processing Layer: Whatever alerts have been received from detection layers, alerts are processed at this layer in such a way that meta alerts are generated. This generation of meta alerts is done on the basis of attack instance information which includes source and destination IP address and possible type of attack.

3.1.4 Reaction Layer: It is something like an Intrusion Prevention System which prevents intrusions. Relative and appropriate action is taken for meta alerts produced by the alert processing layer.

3.2 Alert Generation and Format:

We have discussed the functions of each layer in proposed system. Now we will discuss process of generation of alerts in detail. Sensors in sensor layer captures traffic over the internet. It also decides attributes as an input for detector in detection layer. This attribute can be used for differentiation of attack instances. They may be dependent or independent. Attributes generated by the detectors are source IP address, target IP address, and possible type of attack which includes denial of service, buffer overflow and SQL injection etc. The format for alert(A) is as follows:

It has N number of attributes. Out of these N attributes let us suppose that N_m are categorical and remaining i.e. N_{m+1} are continuous.

$A = (A_1, \dots, A_{N_m}, A_{N_m+1}, \dots, A_N)$

Where, A_1, \dots, A_{N_m} are categorical attributes and

A_{N_m+1}, \dots, A_N are continuous attributes.

3.3 Offline Alert Aggregation:

In this section we develop offline alert aggregation which will be extended to data streaming for online alert aggregation. We can show that different attacks are done on TCP/UDP traffic. Some alerts are false positive and some alerts are false negative. All information then get analyzed and finally offline alert can be generated. But they have some drawbacks.

1. Some of false alerts are not identified and they may get assigned to cluster.
2. Wrong assignment of true alerts to cluster may happened.
3. Splitting of cluster may be wrongly done.
4. Many different clusters may get combined wrongly into one single cluster.

Algorithm : Offline alert aggregation

Input : set of alerts (A),

number of components C

Output : $\mu_c, \sigma_c^2, \rho_c$ parameters

Assignment of alerts to components.

1. $\Pi_c = 1/C$
2. Initiate σ_c^2, ρ_c
3. While stopping not done do
// E step : assign alerts to components
4. For all alerts $A^{(p)} \in A$ do
 $C^* := \operatorname{argmax} H(a^{(p)} | \mu_c, \sigma_c^2, \rho_c)$
5. $c \in \{1, \dots, C\}$
6. Assign alert $a^{(p)}$ to C^*
// M step : updating of model parameters.
7. For all component $c \in \{1, \dots, C\}$ do
8. $N_c :=$ No. of alerts assigned to C
9. For all attributes $n \in \{1, \dots, N_m\}$ do
10. $\rho_{cn} := 1 / N_c \quad \square \quad a_n^{(p)}$
11. for all attribute $n \in \{N_{m+1}, \dots, N\}$ do
12. $\mu_{cn} := 1 / N_c \quad \square \quad a_n^{(p)}$
13. $\sigma_{cn}^2 := 1 / N_c \quad \square \quad (a_n^{(p)} - \mu_{cn})^2$

We can conclude from above algorithm that this algorithm performs steps like initialization of model parameters, assignment of alerts to components, updating of model parameters stopping process, coefficient mixing. Next it adds alerts to components slowly.

3.4 Online Alert Aggregation:

The above algorithm is extended to perform online alert aggregation. For this IDS should have component adaption, component creation and component detection. In component adaption attack instances must be identified and should get assigned to proper cluster. In component creation new attack should created and parameters should set. In component detection attack instances should be detected.

Algorithm: online alert aggregation

Input : buffer B, Partition P, cluster number j

Output : $\mu_j, \sigma_j^2, \rho_j$ parameters

Assignment of alerts to components.

1. $B := \Phi$
2. While new alert do

3. If $P := \Phi$ then
4. $P_1 := \{a\}$
5. $P := \{P_1\}$
6. Initiate parameters like μ, σ^2, ρ
7. Else
8. $P' := P$
9. $J^* := \operatorname{argmax} H(\mu_j, \sigma_j^2, \rho_j)$
10. $\rho_j^* := \rho_j \cup \{a\}$
11. $O_j := |C_j^*|$
12. For all attributes $n \in \{1, \dots, N_m\}$ do
13. $\rho_{jn} := 1 / O_{j(n)} \quad \square \quad a^{(p)}$
14. For all attributes $n \in \{N_{m+1}, \dots, N\}$ do
15. $\mu_{jn} := 1 / O_{j(n)} \quad \square \quad a^{(p)}$
16. $\sigma_{jn}^2 := 1 / O_{j(n)} \quad \square \quad (a^{(p)} - \mu_{jn})^2$
17. if $\Omega(p) < \square$
18. $P := P'$
19. $B := B \cup \{a\}$
20. If novelty (a) then
- $P := \text{ALG3}(C, J^*, B)$
- $B := \Phi$
- For $j \in \{1, \dots, |C|\}$ do
- If obsolescence (Pj) then
- $P := P / P_j$

IV. Implementation And Results

We have implemented custom simulator by using java programming language. System requirement to do the implementation is JDK 1.6, Eclipse or Netbeans, JME. The operating system used to do the implementation is Windows XP. We have developed graphical user interface by using swing application programming interface. Following are some user interface of attack simulation.

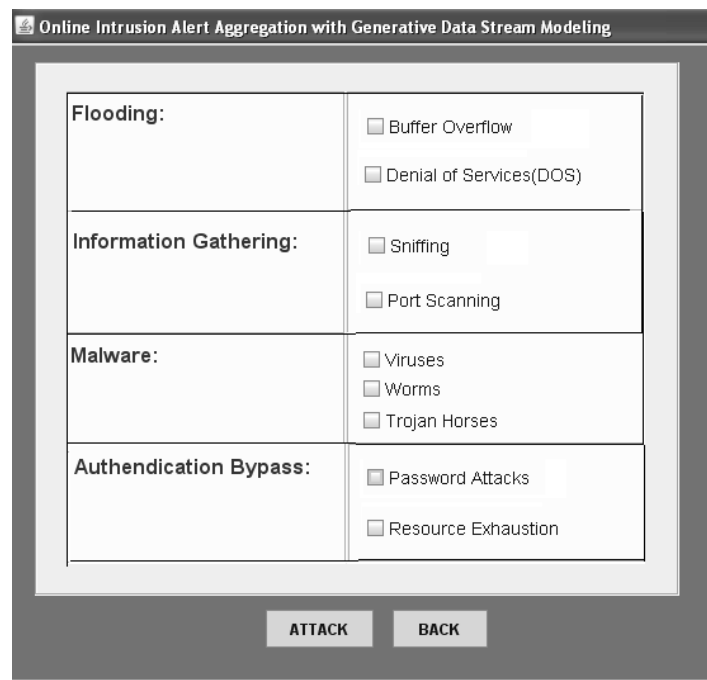


Figure 2. Different Types of Attacks

As shown in figure different attacks can be simulated into information gathering, authentication failure, malwares, and flooding of data. Following is the GUI for alert aggregation



Figure 3 Simulation of Alerts

As shown in above figure there is separate space for each and every layers aggregation messages. When attack is done the relevant or appropriate action or message is displayed as shown in figure

Alerts can be send to users registered mobile as shown in figure.

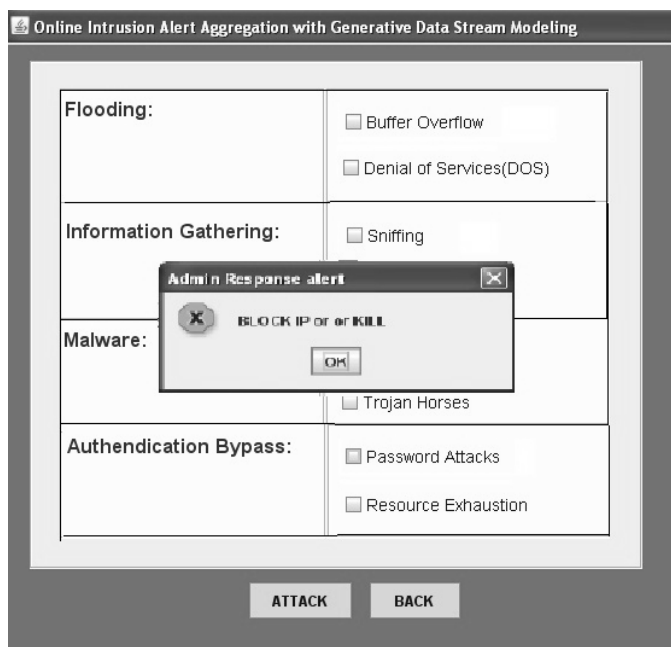


Figure 4. Response when attack is done



Figure 5. GUI of Mobile Alert

V. Conclusion

The proposed way for online alert aggregation generation has been implemented and it found that meta alerts can be generated. Missing false positive rate gets reduced as it uses property of data streaming i.e. it executes a few times only. The experimental result shows that it is very effective and helpful when it gets implemented in real time application. Also IDS accuracy gets increased. More alerts can be detected but compare to number of attacks detected very few false positive alerts gets introduced. So online intrusion alert aggregation with data streaming system is extremely efficient in information technology field to provide security to information.

REFERENCES

- [1] Alexander Hofmann, Bernhard Sick, "Online Intrusion Alert Aggregation with Generative Data Stream Modeling", IEEE transaction on dependable and secure computing, vol 8 No. 2 March-April 2011.
- [2] M. Hanock, K. Srinivas, A. Yaganteeswarudu, "Online Intrusion Alert Aggregation with Generative Data Stream Modeling", International Journal of Electronics and computer Science Engineering, ISSN-2277-1956
- [3] S. Mangesh kumar, K. Mohan, G. Kadirvelu, S. Muruganandam, "Online Intrusion Alert Aggregation Through Mobile", International journal of advancement in Research and Technology, volume 1, issue3, August-2012
- [4] Ravindra Bhat, "Intrusion Detection System with Data Stream Modeling using Conditional Privileges", International journal of computer science and technology, vol.3 no.7 July 2012 ISSN:2299-3345.
- [5] Rupali Shewale, Yugandhar Pandey, Maheshkumar A. Sali, "Distributed Intrusion Alert Aggregation with Data Stream Modeling", International journal of electronics, communication and soft computing science and engineering, ISSN:2277-9477 March-2012.
- [6] V. SrujanarReddy, G. Dileep Kumar, "Online and Offline Intrusion alert aggregation", International Journal of Computer Science and Communication Networks, vol.2(4), 520-525 ISSN:2249-5789
- [7] S. Axelsson, "Intrusion Detection Systems: A Survey and Taxonomy," Technical Report 99-15, Dept. of Computer Eng., Chalmers Univ. of Technology, 2000.
- [8] M.R. Endsley, "Theoretical Underpinnings of Situation Awareness: A Critical Review," Situation Awareness Analysis and Measurement, M.R. Endsley and D.J. Garland, eds., chapter 1, pp. 3-32, Lawrence Erlbaum Assoc., 2000.
- [9] C.M. Bishop, Pattern Recognition and Machine Learning. Springer, 2006.
- [10] M.R. Henzinger, P. Raghavan, and S. Rajagopalan, Computing on Data Streams. Am. Math. Soc., 1999.
- [11] A. Allen, "Intrusion Detection Systems: Perspective," Technical Report DPRO-95367, Gartner, Inc., 2003.
- [12] F. Valeur, G. Vigna, C. Kruegel, and R.A. Kemmerer, "A Comprehensive Approach to Intrusion Detection Alert Correlation," IEEE Trans. Dependable and Secure Computing, vol. 1, no. 3, pp. 146-169, July-Sept. 2004.
- [13] H. Debar and A. Wespi, "Aggregation and Correlation of Intrusion-Detection Alerts," Recent Advances in Intrusion Detection, W. Lee, L. Me, and A. Wespi, eds., pp. 85-103, Springer, 2001.
- [14] D. Li, Z. Li, and J. Ma, "Processing Intrusion Detection Alerts in Large-Scale Network," Proc. Int'l Symp. Electronic Commerce and Security, pp. 545-548, 2008.
- [15] F. Cuppens, "Managing Alerts in a Multi-Intrusion Detection Environment," Proc. 17th Ann. Computer Security Applications Conf. (ACSAC '01), pp. 22-31, 2001.
- [16] A. Valdes and K. Skinner, "Probabilistic Alert Correlation," Recent Advances in Intrusion Detection, W. Lee, L. Me, and A. Wespi, eds. pp. 54-68, Springer, 2001.
- [17] K. Julisch, "Using Root Cause Analysis to Handle Intrusion Detection Alarms," PhD dissertation, Universität Dortmund, 2003.
- [18] T. Pietraszek, "Alert Classification to Reduce False Positives in Intrusion Detection," PhD dissertation, Universität Freiburg, 2006.
- [19] F. Autrel and F. Cuppens, "Using an Intrusion Detection Alert Similarity Operator to Aggregate and Fuse Alerts," Proc. Fourth Conf. Security and Network Architectures, pp. 312-322, 2005.
- [20] G. Giacinto, R. Perdisci, and F. Roli, "Alarm Clustering for Intrusion Detection Systems in Computer Networks," Machine Learning and Data Mining in Pattern Recognition, P. Perner and A. Imiya, eds. pp. 184-193, Springer, 2005.
- [21] O. Dain and R. Cunningham, "Fusing a Heterogeneous Alert Stream into Scenarios," Proc. 2001 ACM Workshop Data Mining for Security Applications, pp. 1-13, 2001.
- [22] P. Ning, Y. Cui, D.S. Reeves, and D. Xu, "Techniques and Tools for Analyzing Intrusion Alerts," ACM Trans. Information Systems Security, vol. 7, no. 2, pp. 274-318, 2004.
- [23] F. Cuppens and R. Ortalo, "LAMBDA: A Language to Model a Database for Detection of Attacks," Recent Advances in Intrusion Detection, H. Debar, L. Me, and S.F. Wu, eds. pp. 197-216, Springer, 2000.
- [24] S.T. Eckmann, G. Vigna, and R.A. Kemmerer, "STATL: An Attack Language for State-Based Intrusion Detection," J. Computer Security, vol. 10, nos. 1/2, pp. 71-103, 2002.
- [25] A. Hofmann, "Alarmaggregation und Interessantheitsbewertung in einem dezentralisierten Angriffserkennungssystem," PhD dissertation, Universität Passau, under review.
- [26] M.S. Shin, H. Moon, K.H. Ryu, K. Kim, and J. Kim, "Applying Data Mining Techniques to Analyze Alert Data," Web Technologies and Applications, X. Zhou, Y. Zhang, and M.E. Orłowska, eds. pp. 193-200, Springer, 2003.
- [27] J. Song, H. Ohba, H. Takakura, Y. Okabe, K. Ohira, and Y. Kwon, "A Comprehensive Approach to Detect Unknown Attacks via Intrusion Detection Alerts," Advances in Computer Science—ASIAN 2007, Computer and Network Security, I. Cervesato, ed., pp. 247-253, Springer, 2008.
- [28] R. Smith, N. Japkowicz, M. Dondo, and P. Mason, "Using Unsupervised Learning for Network Alert Correlation," Advances in Artificial Intelligence, R. Goebel, J. Siekmann, and W. Wahlster, eds. pp. 308-31, Springer, 2008.
- [29] A. Hofmann, D. Fisch, and B. Sick, "Identifying Attack Instances by Alert Clustering," Proc. IEEE Three-Rivers Workshop Soft Computing in Industrial Applications (SMCia '07), pp. 25-31, 2007.
- [30] M. Roesch, "Snort—Lightweight Intrusion Detection for Networks," Proc. 13th USENIX Conf. System Administration (LISA '99), pp. 229-238, 1999.
- [31] O. Buchtala, W. Grass, A. Hofmann, and B. Sick, "A Distributed Intrusion Detection Architecture with Organic Behavior," Proc. First CRIS Int'l Workshop Critical Information Infrastructures (CIWI '05), pp. 47-56, 2005.



International Journal of Modern Engineering Research (IJMER)

Volume : 4 Issue : 7 (Version-2)

ISSN : 2249-6645

July - 2014

Contents :

Time Series Data Analysis for Forecasting – A Literature Review <i>Neelam Mishra, Er. Abhinav Jain</i>	01-05
Design And Analysis Of Precast Load Bearing Walls For Multi Storey Building Using Etabs <i>Pernaty Ramu, S. M. Abdul Mannan Hussain, B. Tharun Kumar</i>	06-13
Analysis of Self Supported Steel Chimney as Per Indian Standard <i>B. Tharun Kumar Reddy, S M Abdul Mannan Hussain, Ramu Parnati</i>	14-17
A Survey on Wireless Sensor Network based Technologies for Precision Agriculture System <i>Omveer, Dr. H.K.Singh, Rishikesh Patankar, Sandeep Bansal, Gaurav Kant Yadav</i>	18-25
Work place stress preventive and curative measures <i>D. Sharon Lily, Dr. V. Tulasi Das</i>	26-29
Strengthening Of RC Beam Using FRP Sheet <i>E. Rakesh Reddy, G. Ramakrishna</i>	30-63
An Asymmetrical Dc-Dc Converter with a High Voltage Gain <i>Sarah Ben Abraham, Ms. Riya Scaria</i>	64-74
Trajectory Control With MPC For A Robot Manipulator Using ANN Model <i>Bekir Cirak</i>	65-83
Effect of V Notch Shape on Fatigue Life in Steel Beam Made of High Carbon Steel A lloy AISI 1078 <i>Qasim Bader, Emad Kadum</i>	84-91
Investigate the Route of Chaos Induced Instabilities in Power System Network <i>Swarnankur Ghosh, Dr. G. K. Panda, Dr. P.K Saha, Avishek Ghose Roy, Indrajit Koley</i>	92-99

Time Series Data Analysis for Forecasting – A Literature Review

Neelam Mishra¹, Er. Abhinav Jain²

¹(Computer Science, C.S.E., GBTU, India)

²(Department of Computer Science, C.S.E., GBTU, India)

Abstract: In today's world there is ample opportunity to clout the numerous sources of time series data available for decision making. This time ordered data can be used to improve decision making if the data is converted to information and then into knowledge which is called knowledge discovery. Data Mining (DM) methods are being increasingly used in prediction with time series data, in addition to traditional statistical approaches. This paper presents a literature review of the use of DM and statistical approaches with time series data, focusing on weather prediction. This is an area that has been attracting a great deal of attention from researchers in the field.

Keywords: Data Mining; Time Series Data Analysis; Knowledge Discovery; Weather Prediction

I. INTRODUCTION

Data Mining (DM) is a challenging field for research and has some practical successful application in several different areas. DM methods are being increasingly used in prediction with time series data, in addition to traditional statistical approaches [1-3].

DM can be presented as one of the phases of the Knowledge Discovery in Databases (KDD) process [4-6], and is identified as “the means by which the patterns are extracted from data” [7]. Nowadays, it can be said that the two terms, DM and KDD, are indistinctly used.

A time series is a collection of data recorded over a period of time—weekly, monthly, quarterly, or yearly. An analysis of history—a time series—can be used by management to make current decisions and plans based on long-term forecasting. One usually assumes that past patterns will continue into the future. Long-term forecasts extend more than 1 year into the future; 5-, 10-, 15-, and 20-year projections are common. Long-range predictions are essential to allow sufficient time for various departments to develop plans for future development.

There are several application domains of DM with time series data, being that one important application domain is weather prediction. This will be the focus of this paper. Rainfall prediction is a sensitive issue and can be considered as an open research issue [9,10]. Intelligent forecasting models have achieved better results than traditional statistical methods. Although intelligent forecasting methods are better, we can still improve the results in terms of accuracy in addition to other factors.

The main contribution of this paper is to provide brief literature survey of the use of statistical methods for time series weather predictions, along with the latest trends in the use of DM for time series forecasting

The paper is organized as follows: a review of literature survey on statistical techniques for time series forecasting is presented in section 2 and a literature review on the use of DM with time series data is presented in Section 3. The paper closes in Section 4, with conclusion and future research directions.

II. STATISTICAL TECHNIQUES FOR TIME SERIES FORECASTING

Various organizations/ employees in India and abroad have done modeling using supported time series data exploitation. The various methodologies viz. statistic decomposition models, Exponential smoothing models, ARIMA models and their variations like seasonal ARIMA models, vector ARIMA models using variable time series, ARMAX models i.e. ARIMA with instructive variables etc has been used.. Many studies have taken place within the analysis of pattern and distribution of rainfall in numerous regions of the globe. Totally different time series methods with different objectives are used to investigate rain information in numerous literatures.

Stringer (1972) reported that a minimum of thirty five quasi-periods with over one year long are discovered in records of pressure, temperature, precipitation, and extreme climatic conditions over the earth

the earth of the world surface. a very common quasi-periodic oscillation is the quasi-biennial oscillation (QBO), during which the environmental condition events recur each two to two.5 years.

Winstanley (1973a, b) reported that monsoon rains from Africa to India decreased by over five hundredth from 1957 to 1970 and expected that the long run monsoon seasonal rain, averaged over five to ten years is probably going to decrease to a minimum around 2030.

Laban (1986) uses time series supported ARIMA and Spectral Analysis of areal annual rain of two same regions in East Africa and counseled ARMA(3,1) because the best appropriate region indice of relative wetness/dryness and dominant quasi-periodic fluctuation around 2.2-2.8 years, 3-3.7 years, 5-6 years and 10-13 years.

Harvey et al., (1987) investigated how patterns of rainfall correlate with general climatic conditions and frequency of the cycles of rain. They used rain information from Brazil for a selected region which frequently suffers from drought to assess the alternate behaviour of rain. They used a model that permits alternate parts to be modeled explicitly. They found that cyclical components are random instead of deterministic, and also the gains achieved from forecast by taking account of the cyclic element are tiny within the case of Brazil.

Kuo and Sun, (1993) used an intervention model for average 10 days stream flow forecast and synthesis that was investigated by to influence the extraordinary phenomena caused by typhoons and alternative serious abnormalities of the weather of the Tanshui river basin in Taiwan.

Chiew et al, (1993) conducted a comparison of six rainfall-runoff modeling approaches to simulate daily, monthly and annual flows in eight unregulated catchments. They concluded that time-series approach will offer adequate estimates of monthly and annual yields within the water resources of the catchments.

Langu, (1993) used statistic analysis to observe changes in rainfall and runoff patterns to go looking for important changes within the parts of variety of rainfall statistic.

Box and Jenkins (1994), in early 1970's, pioneered in evolving methodologies for statistic modeling within the univariate case often referred to as Univariate Box-Jenkins (UBJ) ARIMA modeling.

Carter, M. M. and Elsner, D.J.B., (1997), used results from a factor analysis regionalization of non-tropical storm convective rainfall over the island of Puerto Rico, a statistical methodology is investigated for its potential to forecast rain events over limited areas. Island regionalization is performed on a 15-yr dataset, while the predictive model is derived from 3 yr of surface and rainfall data. The work is an initial attempt at improving objective guidance for operational rainfall forecasting in Puerto Rico. Surface data from two first-order stations are used as input to a partially adaptive classification tree to predict the occurrence of heavy rain. Results from a case study show that the methodology has skill above climatology—the leading contender in such cases. The algorithm also achieves skill over persistence. Comparisons of forecast skill with a linear discriminant analysis suggest that classification trees are an easier and more natural way to handle this kind of forecast problem. Synthesis of results confirms the notion that despite the very local nature of tropical convection, synoptic-scale disturbances are responsible for prepping the environment for rainfall. Generalizations of the findings and a discussion of a more realistic forecast setting in which to apply the technology for improving tropical rainfall forecasts are given.

Makridakis et al. (1998) has given a decent account on exponential smoothing ways.

Al-Ansari et al. (2003) proscribed the applied math analysis of the rainfall measurements for 3 meteorological stations in Jordan: Amman aerodrome (central Jordan), Irbid (northern Jordan) and Mafraq (eastern Jordan). Traditional applied math and power spectrum analyses as well as ARIMA model were performed on the semi-permanent annual rainfall measurements at the 3 stations. The result shows that potential periodicities of the order of 2.3 - 3.45, 2.5 - 3.4 and 2.44-4.1 years for Amman, Irbid and Mafraq stations, respectively, were obtained. A statistic model for every station was adjusted, processed, diagnostically checked and finally an ARIMA model for every station is established with a ninety fifth confidence interval and also the model was used to forecast five years annual rainfall values for Amman, Irbid and Mafraq meteorological stations.

Al-Ansari, A., Al-Shamali B. and Shatnawi A., (2006) used statistical Analysis of rain records at 3 major meteorological stations in Jordan, Al-Mararah University.

Ingsrisawang, L. et.al, (2010), made use of three statistical methods: First-order Markov Chain, Logistic model, and Generalized Estimating Equation (GEE) in modeling the rainfall prediction over the eastern part of Thailand. Two daily datasets during 2004-2008, so-called Meteor and GPCM, were obtained from Thai Meteorological Department (TMD) and Bureau of the Royal Rain Making and Agricultural Aviation (BRRAA). The Meteor observation consists of the average of rain volumes (AVG) from 15 local weather stations, and the observation of the Great Plain Cumulus Model (GPCM) includes 52 variables, for

example, temperature, humidity, pressure, wind, atmospheric stability, seeding potential, rain making operation, and rain occurrence. Merging and matching between the GPCM dataset and Meteor observations, the GPCM+Meteor dataset was generated including 667 records with 66 variables. The first-order Markov chain model was then built using the Meteor dataset to predict two transitional probabilities of a day being wet given the previous day being wet or being dry, $P(W/W)$ and $P(W/D)$, respectively. The odds ratio(OR) was computed from these probabilities and gave the value of 6.85, which indicated that it was about 7 times more likely to be a wet day given the previous day was also wet within the eastern region of Thailand, than that given the previous day was dry. Next, the logistic models were also fitted using the Meteor dataset by taking account of cyclical effect in modeling for the prediction of $P(W/W)$ and $P(W/D)$, respectively. The models showed that the odds ratios of being wet days are not constant over day t during the years 2004-2008. Finally, the GEE method was applied with the GPCM+Meteor dataset to study the effects of weather conditions on the prediction of rainfall estimates on wet days, by taking account of correlation structure among observations. The variables of -15°C isotherm height and K-Index were shown statistically significant for the prediction of rainfall estimates at a 0.05 level. In order to effectively detect the rain conditions and make the right decisions in cloud-seeding operations, the statistical methods presented in this study can help in deriving the useful features from the rain and weather observations and modeling the rain occurrence.

Seyed et al.,(2011) used time series methodology to model weather parameter in Islamic Republic of Iran at Abadeh Station and counseled ARIMA(0,0,1)(1,1,1)₁₂ because the best appropriate monthly rainfall information and ARIMA(2,1,0)(2,1,0)₁₂ for monthly average temperature for Abadeh station.

Seyed, A., Shamsnia, M.,Naeem,S. and Ali, L.,(2011) modelled weather parameter using random methods(ARIMA Model)(Case Study:Abadeh station,Iran).

Mahsin et al. (2012) used Box-Jenkins methodology to create seasonal ARIMA model for monthly rainfall information taken for Dhaka station, Bangladesh, for the amount from 1981-2010. In their paper, ARIMA (0, 0, 1) (0, 1, 1)₁₂ model was found adequate and also the model is employed for forecasting the monthly rain.

III. DATA MINING FORECASTING TECHNIQUES

There are several application domains of DM with time series data, being that one important application domain is time series data analysis for forecasting. Intelligent forecasting models have achieved better results than traditional methods, particularly in time series data analysis for forecasting. Methods based on computational intelligence techniques include such as neural networks (NN) or genetic algorithms (GA). Hybrid methods combining more than one technique are also commonly found in the literature. Computational intelligence methods for time series forecasting generally fall into two major categories: (i) Methods based on NN; and (ii) Methods based on evolutionary computation.

Neural networks are widely applied to model several of nonlinear hydrologic processes like weather forecasting. Additional elaborate discussion concerning the ideas and applications of ANN in geophysical science will be referred to within the 2 technical papers prepared by the ASCE Task Committee on Application of Artificial Neural Networks in geophysical science as appeared within the Journal of Hydrologic Engineering (ASCE, 2000).

Hu(1964) initiated the implementation of ANN, a very important soft computing methodology in weather forecasting. Since the previous few decades, ANN a voluminous development within the application field of ANN has unfolded new avenues to the forecasting task involving environment connected development.

French et al. (1992), took a pioneering work in applying ANN for rain forecasting, that used a neural network to forecast two-dimensional rainfall, 1 h prior to. Their ANN model used present rainfall information, generated by a mathematical rainfall simulation model, as an input data. This work is, however, restricted in a very range of aspects. For instance, there's a trade-off between the interaction and also the training time, that couldn't be simply balanced. The amount of hidden layers and hidden nodes appear short, compared with the amount of input and output nodes, to reserve the upper order relationship required for adequately abstracting the method. Still, it's been thought-about because the 1st contribution to ANN's application and established a brand new trend in understanding and evaluating the roles of ANN in investigating complicated geophysical processes.

Michaelides et al (1995) compared the performance of ANN with multiple linear regressions in estimating missing rainfall information over Cyprus.

Kalogirou et al (1997) enforced ANN to reconstruct the rainfall over the time series over Cyprus.

Monica Adyal and Fred Collopy, (1998) identified eleven guidelines that could be used in evaluating this literature. Using these, they examined applications of NNs to business forecasting and prediction. They

located 48 studies done between 1988 and 1994. For each, they evaluated how effectively the proposed technique was compared with alternatives (effectiveness of validation) and how well the technique was implemented (effectiveness of implementation). It was found that eleven of the studies were both effectively validated and implemented. Another eleven studies were effectively validated and produced positive results, even though there were some problems with respect to the quality of their NN implementations. Of these 22 studies, 18 supported the potential of NNs for forecasting and prediction.

Lee et al (1998) applied ANN in rainfall prediction by rendering the offered information into same subpopulations. Wong et al (1999) made fuzzy rules bases with the help of Kyrgyzstani monetary unit and back-propagation neural networks and so with the assistance of the rule base developed predictive model for rainfall over Switzerland using spatial interpolation.

Koizumi (1999) used an ANN model using microwave radar, satellite and weather-station information along with numerical products generated by the Japan Meteorological Agency (JMA) and also the model was trained using 1-year information. It absolutely was found that the ANN skills were higher than the persistence forecast (after three h), the regression toward the mean forecasts, and also the numerical model precipitation prediction. Because the ANN model was trained with only 1 year information, the results were limited. The author believed that the performance of the neural network would be improved once additional training information became available. It's still unclear to what extent every predictor contributed to the forecast and to what extent recent observations may improve the forecast.

Toth et al. (2000) compared short-time rainfall prediction models for real-time flood forecasting. Completely different structures of auto-regressive moving average (ARMA) models, ANN and Nearest-Neighbors approaches were applied for forecasting storm rainfall occurring within the Sieve river basin, Italy, within the amount 1992- 1996 with lead times variable from 1 to 6 h. The ANN adaptative activity application proved to be stable for lead times longer than three hours, however inadequate for reproducing low rainfall events. Abraham et al. (2001) used an ANN with scaled conjugate gradient algorithmic rule (ANN-SCGA) and evolving fuzzy neural network (EfuNN) for predicting the rainfall time series. In the study, monthly rainfall was used as input data for training model. The authors analyzed eighty seven years of rainfall information in Kerala, a state within the southern a part of the Indian dry land. The empirical results showed that neuro-fuzzy systems were economical in terms of getting higher performance time and lower error rates five compared to the pure neural network approach. nevertheless, rainfall is one in all the twenty most complicated and tough parts of the geophysical science cycle to grasp and to model due to the tremendous range of variation over a wide range of scales both in space and time.

Pucheta Julian A, et. al , (2010), presented a feed-forward NN based NAR model for forecasting time series. The learning rule used to adjust the NN weights is based on the Levenberg-Marquardt method. The approach is tested over five time series obtained from samples of the Mackey-Glass delay differential equations and from monthly cumulative rainfall. Three sets of parameters for MG solution were used, whereas the monthly cumulative rainfall belongs to two different sites and times period, La Perla 1962-1971 and Santa Francisca 200-2010, both located at Córdoba, Argentina. The approach performance presented is shown by forecasting the 18 future values from each time series simulated by a Monte Carlo of 500 trials with fractional Gaussian noise to specify the variance. R. Adhikari and R.K.Agarwal, (2012), in their work comprehensively explores the outstanding ability of Artificial NEURAL network in recognizing and forecasting strong seasonal patterns without removing them from the raw data. Six real world time series data having dominant seasonal fluctuations are used in the present work. The emperical results show that the properly designed ANN;s are remarkably efficient in directly forecasting strong seasonal variation as well as outperform each of the three statistical models for all six time series.

IV. CONCLUSION

This paper presents a literature review of the use of data mining with time series data. This literature review is very useful, since it brings a better understanding of the field of study, and this is an important contribution of this paper.

From the literature review it can be concluded that this subject attracts a great deal of interest by researchers. However, several research issues remain unexplored. One of the ones that were identified during this research is related with the combined use of fundamental and technical issues.

Future research directions include the study of ways to select the best features for DM, with special reference to computational intelligence techniques with time series data analysis. The existence of features with different frequencies is a concern, and methods that will help how to envisage this problem will be made use of for future research work.

REFERENCES

- [1] Box, G.E.P., Jenkins, G.M. and Reinsel, G.C. (1994). Time series analysis : Forecasting and control, Pearson Education, Delhi.
- [2] Makridakis, S., Wheelwright, S.C. and Hyndman, R.J. (1998). Forecasting Methods and Applications, 3rd Edition, John Wiley, New York.
- [3] Chiew, F.H.S., M.J. Stewardson and T.A. McMahon, 1993. Comparison of six rainfall-runoff
- [4] Kuo, J.T. and Y.H. Sun, 1993. An intervention model for average 10 day stream flow forecast and synthesis. J. Hydrol., 151: 35-56.
- [5] Langu, E.M., 1993. Detection of changes in rainfall and runoff patterns. J. Hydrol., 147: 153-167
- [6] M.J.C., Hu, Application of ADALINE system to weather forecasting, Technical Report, Stanford Electron, 1964
- [7] Michaelides, S. C., Neocleous, C. C. & Schizas, C. N. "Artificial neural networks and multiple linear regression in estimating missing rainfall data." In: Proceedings of the DSP95 International Conference on Digital Signal Processing, Limassol, Cyprus. pp 668–673, 1995.
- [8] Kalogirou, S. A., Neocleous, C., Constantinou, C. N., Michaelides, S. C. & Schizas, C. N., "A time series construction of precipitation records using artificial neural networks. In: Proceedings of EUFIT '97 Conference, 8–11 September, Aachen, Germany. pp 2409–2413 1997.
- [9] Lee, S., Cho, S. & Wong, P.M., "Rainfall prediction using artificial neural network.", J. Geog. Inf. Decision Anal. 2, 233–242 1998.
- [10] Wong, K. W., Wong, P. M., Gedeon, T. D. & Fung, C. C. , "Rainfall Prediction Using Neural Fuzzy Technique." 1999
- [11] E.Toth, A.Brath, A.Montanari," Comparison of short-term rainfall prediction models for real-time flood forecasting", Journal of Hydrology 239 (2000) 132–147
- [12] Koizumi, K.: "An objective method to modify numerical model forecasts with newly given weather data using an artificial neural network", Weather Forecast., 14, 109–118, 1999.
- [13] Ajith Abraham, Dan Steinberg and Ninan Sajeeth Philip," Rainfall Forecasting Using Soft Computing Models and Multivariate Adaptive Regression Splines", 2001.
- [14] French, M. N., Krajewski, W. F., and Cuykendall, R. R.: Rainfall forecasting in space and time using neural network, J. Hydrol., 137, 1–31, 1992.
- [15] Koizumi, K.: An objective method to modify numerical model forecasts with newly given weather data using an artificial neural network, Weather Forecast., 14, 109–118, 1999.
- [16] Toth, E., Montanari, A., and Brath, A.: Comparison of short-term rainfall prediction model for real-time flood forecasting, J. Hydrol., 239, 132–147, 2000.
- [17] Maier, R. H. and Dandy, G. C.: The use of artificial neural network for the prediction of water quality parameters, Water Resour. Res., 32(4), 1013–1022, 1996.
- [18] Maier, R. H. and Dandy, G. C.: Comparison of various methods for training feed-forward neural network for salinity forecasting, Water Resour. Res., 35(8), 2591–2596, 1999.
- [19] ASCE: Task Committee on Application of Artificial Neural Networks in Hydrology. I: Preliminary Concepts, J. Hydrol. Eng., 5(2), 115–123, 2000.
- [20] ASCE: Task Committee on Application of Artificial Neural Networks in Hydrology. II: Hydrologic Applications, J. Hydrol. Eng., 5(2), 124–137, 2000
- [21] Pucheta Julian A, et. al , "A Feed-Forward Neural Networks-Based Nonlinear Autoregressive Model for Forecasting Time Series", Computación y Sistemas Vol. 14 No. 4, pp 423-435, 2010.
- [22] Adhikari, R., et. al., "Forecasting strong seasonal time series with Artificial Neural Network", Journal of Scientific and Industrial Research, Vol. 71, pp. 657-666, 2012.
- [23] Adya1, M and Collopy, F., "How Effective are Neural Networks at Forecasting and Prediction? A Review and Evaluation", Journal of Forecasting, J. Forecast. 17, 481±495, 1998.
- [24] Carter, M. M. and Elsner, D.J.B., "A Statistical Method for Forecasting Rainfall over Puerto Rico", American Meteorological Society, vol. 12, pp.515-525, 1997.
- [25] Ingsrisawang, L. et.al., "Applications of Statistical Methods for Rainfall Prediction over the Eastern Thailand", Proceedings of the MultiConference of Engineers and Computer Scientists, vol. III, IMECS 2010, March 17-19, 2010, Hong Kong
- [26] Bhaskaran, S., "Time Series Data Analysis for long term forecasting and scheduling of organizational resources – few cases", International Journal of Computer Applications (0975 – 8887) Volume 41– No.12, March 2012
- [27] Winstanley, D.,(1973a). "Recent rainfall trends in africa, the middle East and India", Nature. 243: 464–465pp.
- [28] Winstanley, D.,(1973b). "Rain Patterns and General atmospheric circulation", Nature. 245: 190–194pp.
- [29] Laban, A.J. and Ogallo, H., (1986), "Stochastic modelling of regional annual rain anomalies in East Africa", Journal of Applied Statistics, Vol.13.
- [30] Harvey, R., Andrew C. and Souza, R.C., (1987), "Assessing and Modeling the alternate Behavior of rainfall in North-East Brazil", Journal of Climate and Applied Meteorology, Vol.26, 1339-1344pp.
- [31] Mahsin, M.D. Yesmin, A. and Monira, B.,(2012). Modeling rain in Dacca (national capital) Division of Bangladesh using Time Series Analysis. Journal of Mathematical Modelling and Application, Vol. 1, No.5, 67-73pp.

Design And Analysis Of Precast Load Bearing Walls For Multi Storey Building Using Etabs

Pernaty Ramu¹, S. M. Abdul Mannan Hussain², B. Tharun Kumar³

¹Student, Department of Civil Engineering (M.Tech Structures), Malla Reddy Engineering college, Hyderabad, Telangana State

²B.E,M.E,(Ph.d) Assistant professor. Department of Civil Engineering Malla Reddy Engineering College, Hyderabad, Telangana state, India.

³Student, Department of Civil Engineering (M.Tech Structures), Malla Reddy Engineering college, Hyderabad, Telangana State,

Abstract: In the present scenario of construction industry, time of construction is very crucial factor. Pre-cast construction is gaining significance in general and urban areas in particular. The precast technology is a viable and alternative technique to reduce the construction time. G+11 storey live project is taken for analysis and design with load bearing walls. Design of precast wall panels and design of precast slabs is carried using Indian codes subjected to gravity and lateral loads (seismic and wind). Connections of wall to wall, wall to slab and foundation beam to wall is designed. The structural system consists of load bearing walls and one-way slabs for gravity and lateral loads have been taken for analysis using ETABS. Various wall forces, displacements and moments have been worked out for different load combinations. Data base is presented for the worst load combination.

Keyword: precast load bearing wall, ETABS, Pier and spandrel labeling, lateral load analysis.

I. Introduction

In this present study, G+11 storey precast load bearing wall structure is taken for analysis. The modeling and analysis has been done in using ETABS. The parametric study has been done to observe the effect of axial compression load, out of plane moments, tensile force, shear force, storey drift, lateral load and storey shear on shear walls. Finally data base is prepared for various storey levels. Although the connection details in the precast construction plays vital role but presently the details of connections not included in the present paper. Hence the emphasis on the analysis of load bearing wall structure.

Now a day, there is an increase in housing requirement with increased population and urbanization. Building sector has gained increasing prominence. However, the fact that the suitable lands for building/construction. Precast load bearing walls provide an economical solution when compared to the conventional column beam in fill wall system for the advantage of speed of construction and elimination of wet trades. In multi-storey buildings, lateral loads that arise as a result of winds and earthquakes are often resisted by a system of shear walls acting as vertical cantilevers. Such walls are usually perforated by vertical bands of openings which are required for doors and windows to form a system of shear walls.

II. Modeling Of Shear Wall Structure

In this present study Ground +11 storey shear wall building is considered for one acre of site with 350 units. Around 400sqft of carpet area per unit is taken with 300 units per floor. The construction Technology is total precast solution with load bearing RCC shear walls and slabs. The modeling is done in ETABS as follows.

1. The structure is divided into distinct shell element. The shell element combines membrane and plate bending behavior, as shown in Figure1. It has six degrees of freedoms in each corner point. It is a simple quadrilateral shell element which has size of 24 x 24 stiffness matrix.
2. Grid lines are made for the x, y and z coordinates and the wall is drawn from scratch.
3. Boundary conditions are assigned to the nodes wherever it is required. Boundary conditions are assigned at the bottom of the wall i.e., at ground level where restraints should be against all movements to imitate the behavior of shear wall.
4. The material properties are defined such as mass, weight, modulus of elasticity, Poisson's ratio, strength characteristics etc. The material properties used in the models are shown in table.
5. The geometric properties of the elements are dimensions for the wall section.
6. Elements are assigned to element type, as shown in Table.2

7. Loads are assigned to the joints as they will be applied in the real structure.
8. The model should be ready to be analyzed forces, stresses and displacements.

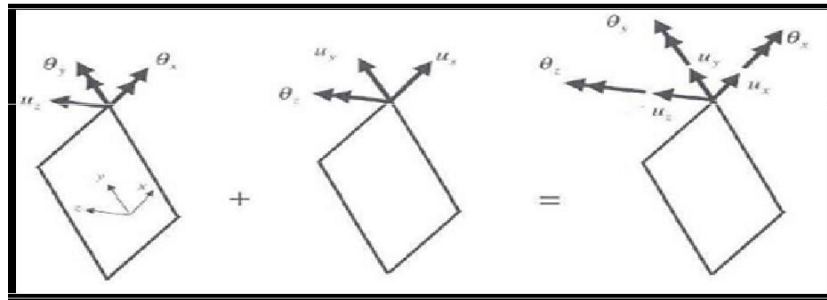


Figure 1: Shell element

Table 1: Material and element property for wall element

Material name	Concrete
Type of material	Isotropic
Mass Per Unit Volume	2.5 kN/m ³
Modulus of elasticity	32 kN/mm ²
Poisson's ratio	0.2
Concrete strength	30 MPa
Section name	Wall
Wall thickness	150 mm

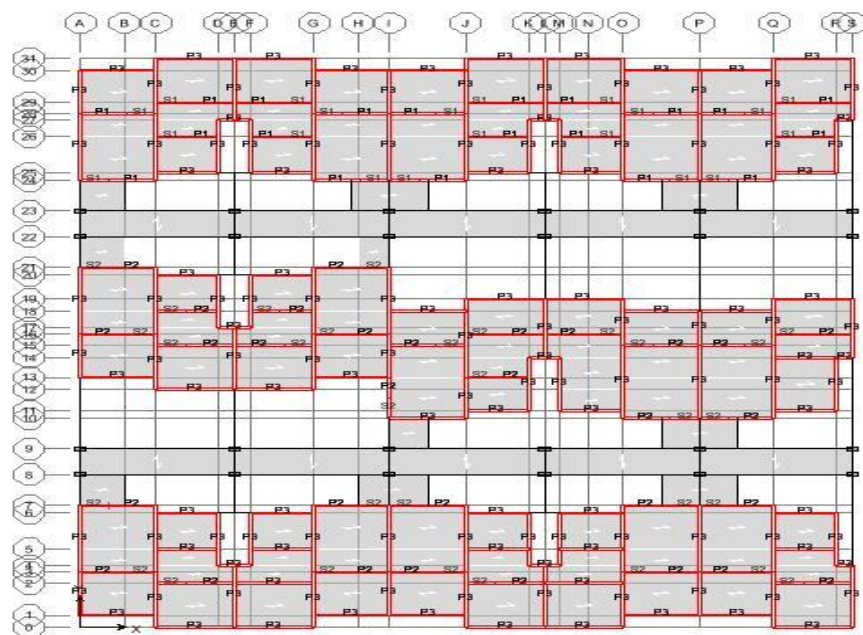
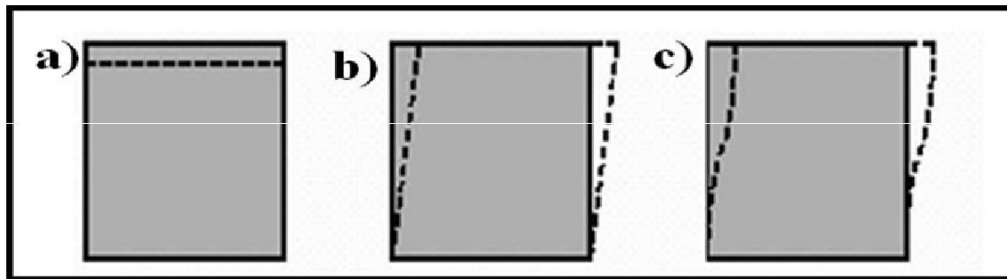


Figure 2: A typical floor plan of structure under consideration

In ETABS single walls are modeled as a pier/spandrel system, that is, the wall is divided into vertical piers and horizontal spandrels. This is a powerful mechanism to obtain design moments, shear forces and normal forces across a wall section. Appropriate meshing and labeling is the key to proper modeling and design. Loads are only transferred to the wall at the corner points of the area objects that make up the wall. Generally the membrane or shell type element should be used to model walls. Here the shell type is used for modeling the wall element. There are three types of deformation that a single shell element can experience axial deformation, shear deformation and bending deformation as shown in Figure3



a) Axial Deformation b) Shear Deformation c) Bending Deformation

Figure 3: Deformation of a shell element

Wall pier forces are output at the top and bottom of wall pier elements and wall spandrel forces are output at the left and right ends of wall spandrel element, see Figure4

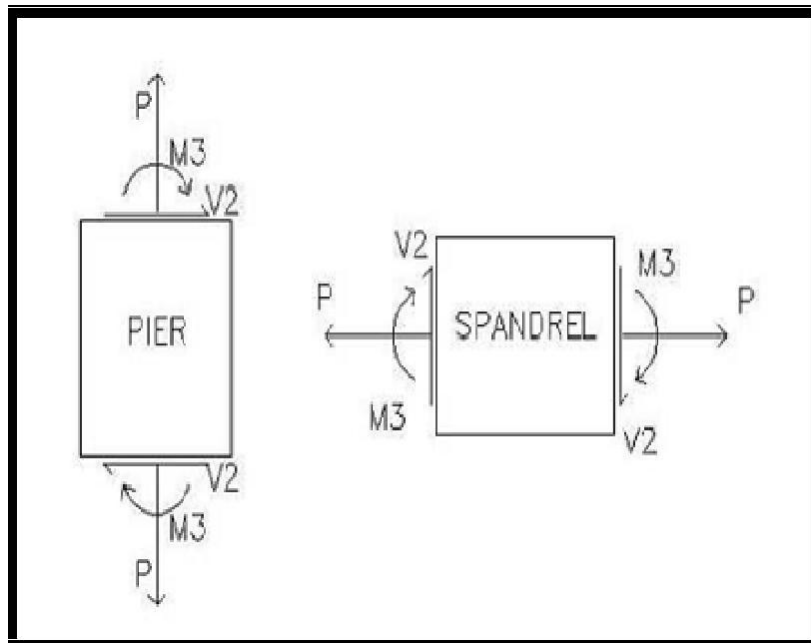


Figure 4: Pier and Spandrel forces in ETABS

At the upper level of this model, pier P1 is defined to extend all the way across the wall above the openings. Pier P2 makes up the wall pier to the left of the top window. P3 occurs between the windows. Spandrel labels are assigned to vertical area objects (walls) in similar fashion to pier labels. The pier and spandrel labels must be assigned to wall element before performing analysis. The lateral load analysis that is seismic and wind analysis requires certain parameters to be assigned in ETABS. These parameters are listed in table.2

Table 2: Seismic and wind parameters

Seismic coefficients AS PER IS: 1893-2000			Wind Coefficients AS PER IS: 875-1987	
Seismic Zone Factor	0.1		Wind speed (Vb)	50m/s
Soil Type	III		Terrain Category	I
Importance Factor (I)	1		Structure Class	B
Response Reduction (R)	3		Risk Coefficient k1 factor	1
			Topography k3 factor	1
			Windward coefficient	0.8
			Leeward coefficient	0.5

III. Results And Discussion

Shear wall structure having G+11 storey is analysed for gravity and lateral loads. The effect of axial force, out of plane moments, lateral loads, shear force, storey drift, storey shear and tensile force are observed for different stories. The analysis is carried out using ETABS and data base is prepared for different storey levels as follows.

Table 3: Axial force and out of plane moments for different storey levels

Storey	Wall location	Axial compression load (KN)	Out of plane moments (KN-M)
12	Top	15.358	20.010
	Bottom	57.277	21.573
11	Top	91.473	-37.385
	Bottom	131.874	34.478
10	Top	170.653	-42.314
	Bottom	209.962	45.532
09	Top	253.931	-46.156
	Bottom	291.969	57.054
08	Top	340.620	-47.442
	Bottom	377.376	68.345
07	Top	430.030	-46.705
	Bottom	465.494	79.316
06	Top	521.423	-46.841
	Bottom	555.598	89.867
05	Top	614.088	-55.166
	Bottom	646.985	100.005
04	Top	707.363	-63.545
	Bottom	739.008	109.844
03	Top	800.846	-71.943
	Bottom	831.300	120.038
02	Top	894.543	-80.360
	Bottom	924.026	132.461
01	Top	994.804	-89.367
	Bottom	1026.764	142.603

Table 4: Shear force and displacements for different storey levels

Storey	Maximum tensile force (kN)	Maximum shear force (kN)	Storey drift (mm)	Lateral load In (kN)	Storey shear (kN)
12	-16156.865	-907.77	0.199	736.67	-608.25
11	-35756.738	-2012.3	0.199	734.36	-598.27
10	-51933.454	-2925.14	0.201	730.37	-1337.36
09	-65018.616	-3664.54	0.2	604.65	-1946.62
08	-75343.36	-4248.75	0.197	494.90	-2436.02
07	-83237.752	-4696.04	0.189	387.14	-2855.50
06	-89030.468	-5024.66	0.177	293.35	-3125.17
05	-93048.654	-5252.87	0.16	217.52	-3334.92
04	-95617.871	-5398.93	0.138	151.66	-3504.71
03	-97062.088	-5481.08	0.11	97.78	-3604.59
02	-97703.854	-5517.6	0.077	55.88	-3634.55
01	-97864.264	-5526.73	0.036	25.94	-3674.50

3.1 Effect of axial force on shear wall

The load bearing wall structure mostly carries axial compression force and transfer on to the foundation. The entire vertical load of all the stories is carried by ground floor load bearing wall. In order to design that wall it is quite essential to understand the variation of axial force in the walls. This force in the shear wall is from worst load combination of gravity and lateral loads. For the worst load combination, the axial force in the wall is plotted on y-axis against at each storey level. From Figure5, it is observed that maximum axial force in storey one is 1026.764 kN. The difference in maximum axial force between storey 11 and 12 is 7.26%. It indicates that the variation in maximum axial force with storey level is linear for worst load combination.

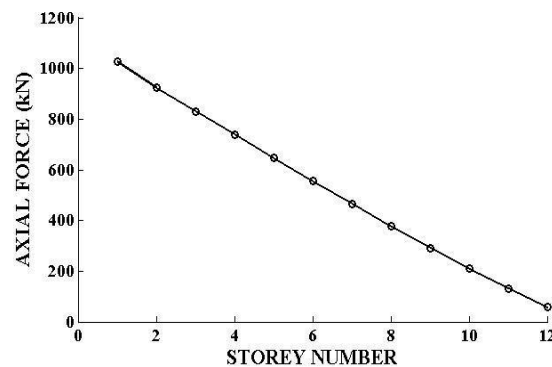


Figure 5: Axial force on shear wall

3.1 Effect of out-of-plane moments on shear walls

Load bearing RCC walls are slender compression elements subjected to in and out-of-plane bending. For the worst load combination, out-of- plane moments in the wall is plotted on y-axis against at each storey level. it is concluded from Figure6 that the maximum out-of- plane moments in walls of storey one is 142.603kN-m. The difference in maximum out of plane moment between storey 11 and 12 is 9.04%. It indicates that the variation in maximum out of plane moment with storey level is linear for worst load combination.

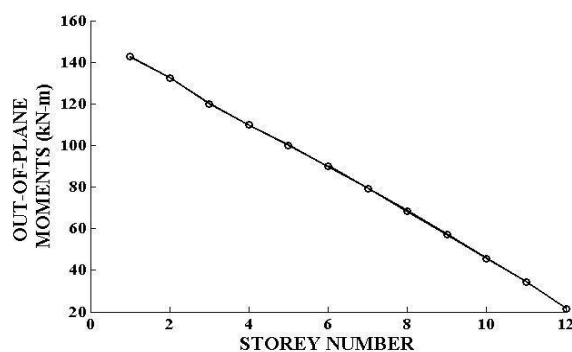


Figure 6: Out of plane moments on shear walls

3.2 Effect of storey lateral load on shear wall

Most lateral loads are live loads whose main component is horizontal force acting on the structure. The intensity of these loads depends upon the building's geographic location, height and shape. For the worst load combination lateral load in the wall is plotted against each storey level. From Figure8, it is observed that maximum lateral load in storey 12 is 736.67 kN. The difference in maximum lateral loads between storey 11 and 12 is 0.54%. It is observed from Figure7 that this is non-linear variation of lateral load.

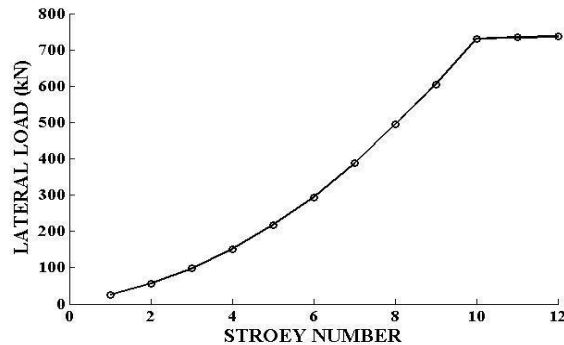


Figure7: Lateral loads on shear walls

3.3 Effect of shear force on shear wall

Shearing forces are unaligned forces pushing one part of a body in one direction, and another part the body in the opposite direction. For the worst load combination shear force in the wall is plotted against at each storey level. From the Figure8, it is observed that maximum lateral load in storey one is 5526.73 kN. The difference in maximum lateral loads between storey 11 and 12 is 19.98%. It indicates that the variation in maximum shear force with storey level is non-linear for worst load combination.

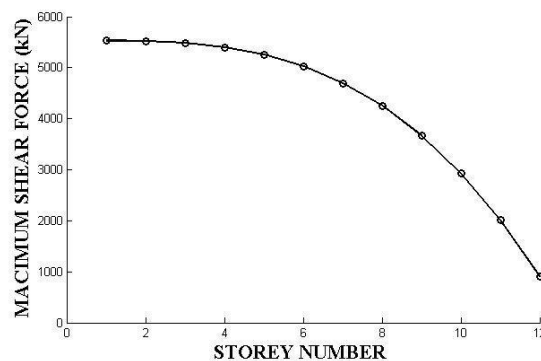


Figure8 Shear force on shear walls

3.4 Effect of storey drift on shear wall

One of the major shortcomings high-rise structures is its increasing lateral displacements arising from lateral forces. For the worst load combination storey drift in the wall is plotted on y-axis against at each storey level. From the Figure9, it is observed that maximum storey drift in between storey 12 is 0.199 mm. It indicates that the variation in maximum storey drift with storey level is non linear for worst load combination.



Figure 9: Storey drifts on shear walls

3.5 Effect of Storey shear on shear wall

For the worst load combination storey shear in the wall is plotted on y-axis against at each storey level. From the Figure10, it is observed that maximum storey shear in storey one is 608.25kN. It indicates that the variation in maximum storey shear with storey level is non linear for worst load combination.

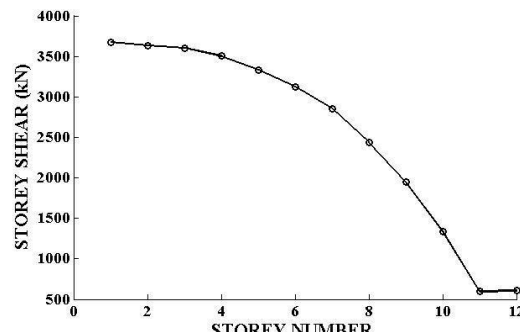


Figure 10: Storey shear on shear walls

3.6 Effect of tensile force on shear wall

The tensile force is the maximum stress that a structure can withstand while being stretched or pulled before failing or breaking. Tensile strength is the opposite of compressive strength and the values can be quite different (Wikipedia, 2013). For the worst load combination tensile force in the wall is plotted against at each storey level. From the figure 11, it is observed that maximum tensile force in storey one is 97864.264 kN. The difference in maximum tensile force between storey 11 and 12 is 20.02% .It indicates that the variation in maximum tensile force with storey level is non-linear for worst load combination

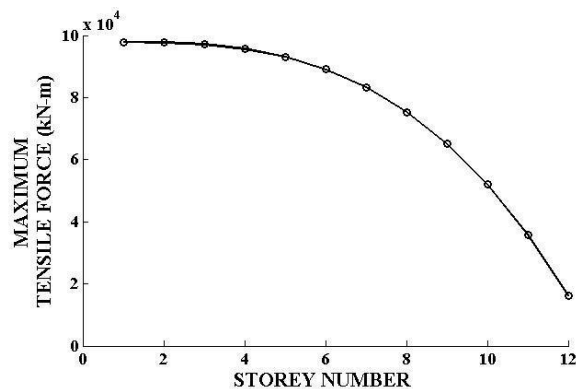


Figure 11: Tensile forces on shear walls

IV. Summary And Conclusion

In this present work ETABS is used to analysis the shear wall structure of G+11 considering the gravity and lateral loads. The following conclusion is drawn from present work.

1. The variation of axial force with stories is linear. The difference in maximum axial force between storey 11 and 12 is 7.26 %.
2. The variation of out-of-plane moment with stories is linear. The difference in maximum out-of-plane moment storey 11 and 12 is 9.04 %.
3. The variation of lateral loads with stories is non-linear. The difference in maximum lateral loads between storey 11 and 12 is 0.54 %.
4. The variation shear force with stories is non-linear. The difference in maximum shear force between storey 11 and 12 is 19.98 %.
5. Variation of storey drift with storey is non-linear. The maximum storey drift in storey 12 is 0.199 mm.
6. Variation of storey shear with storey is non-linear. The maximum storey shear in storey one is 608.25kN.
7. The variation of tensile force with stories is non-linear and the difference in maximum tensile force between storey 11 and 12 is 20.02 %

REFERENCES

- [1.] Wdowicki, J. and Wdowicka, E., (1993), System of programs for analysis of three-dimensional shear wall structures, *The structural design of tall buildings*, 2, pp 295-305.
- [2.] Benjamin J.R., (1968), Variability analysis of shear wall structures, *Earthquake Engineering Research*, 2, pp 45-52.
- [3.] Mazen A.Musmar., (2013), Analysis of shear wall with openings using solid65 element, *Jordan journal of Civil Engineering*, 7(2), pp 164 -173.
- [4.] Thakkar, B.K. (2012), Analysis of shear walls under compression and bending Current trends in technology and science, 1(2), pp 100-104.
- [5.] Hauksdottir B., (2007), Analysis of a reinforced shear wall, Bessason B and Golterman P (eds), DTU.
- [6.] Bozdogan, K.B. and Ozturk, D. (2010), Vibration analysis of asymmetric shear wall structures using the transfer matrix method, *Iranian journal of science and technology, transaction*, 34(B1), pp 1-14.
- [7.] Xiaolei, H., Xuewei, C., Cheang, J., Guiniu, M. and Peifeng, W. (2008), Numerical analysis of cyclic loading test of shear wall based on openSEES” World conference on earthquake engineering, October 12-17, Beijing, China.
- [8.] Carpinteri, A., Corrado, M., Lacidogna, G. and Cammarano, S. “Lateral load effect on tall shear wall structure of different height” *Structural engineering and mechanics*, 41(3), pp 313-337.
- [9.] Biswas, J.K. (1974), Three dimensional analysis of shear wall multi storey building, Open dissertations and theses, In McMaster University.
- [10.] Greeshma S ., Jaya K P ., and Annilet S ., (2011), Analysis of flanged shear wall using Ansys concrete model, *International Journal of Civil and Structural Engineering*, 2(2), pp 454-465.
- [11.] Fahjan, Y.M., Kubin, J. and Tan, M.T., (2010), Nonlinear analysis method for reinforced concrete buildings with shear walls, *ECEE 14*, August 30-november 03, Ohrid.
- [12.] Dar, O.J. (2007), Analysis and design of shear wall-transfer beam structure” boring pengeshan status thesis, Universiti Teknologi Malaysia.
- [13.] Potty N S ., Thanoon W A ., Hamzah H H., and Hamadelnil A M M., (2008), Practical modeling aspects for analysis of shear wall using Finite element method, in proceeding of the Annual Technical Conference-Construction and Building Technology, 2008, pp 89-98. Bookfield, C-08: Construction and Building Technology

Analysis of Self Supported Steel Chimney as Per Indian Standard

B. Tharun Kumar Reddy¹, S M Abdul Mannan Hussain², Ramu Parnati³

¹Student, Department of Civil Engineering, (M.Tech Structures), Malla Reddy Engineering college, Hyderabad, India

²B.E, M.E,(PhD) Assistant professor. Department of Civil Engineering, Malla Reddy Engineering College, Hyderabad, India

³ Student, Department of Civil Engineering , (M.Tech Structures), Malla Reddy Engineering college, Hyderabad,, India

Abstract: Most of the Industrial chimneys are tall structures with circular cross-sections. Such slender, lightly damped structures are prone to wind-excited vibration. Geometry of a self supporting steel chimney plays an important role in its structural behaviour under lateral dynamic loading. This is because geometry is primarily responsible for the stiffness parameters of the chimney. However, basic dimensions of industrial self supporting steel chimney such as height, diameter at exit, etc., are generally derived from the associated environmental conditions. Manholes are provided at the bottom of the chimney for inspection purpose of the chimney. The presence of manhole reduces the cross section area and hence the stiffness of the chimney. In the present study investigates the stresses, deflection and mode shapes of the chimney due to the presence of an inspection manhole. Maximum Von Mises stress, top deflection and mode shapes were calculated using finite element software ANSYS. The results show that, due to the presence of manhole, the stresses are increased by approximately 1.5 times for the chimney and frequency is decreased by approximately 1.12 times.

Key words: steel chimney, Dynamic wind load, Static wind load, Von mises stress, Deflection, Mode

I. Introduction

This paper deals with the analysis of self-supported-steel chimneys. Tall steel chimneys are presently planned in compliance with various codes of practice (IS 6533^{1, 2}, CICIND³ etc.). The chimney is considered as cantilever column with tubular cross section for analysis. Wind loads, temperature loads, seismic loads and dead loads are considered for design purpose. But apart from these loads, wind load is considered as most vital load due to height of the structure. The effect of wind can be divided into two components: (a) along-wind effect (b) across-wind effect. But the across-wind effect is most critical and unpredictable. The bottom portion of the chimney is constructed as conical flare for better stability and for easy entrance of flue gases. Design forces in a chimney is very sensitive to its geometrical parameters such as base and top diameter of the chimney, height of the flare, height of the chimney and thickness of the chimney shell. Height of the chimney is governed by environmental conditions. As per recommendations of the Ministry of Environment and Forests⁵, Govt. of India, height of a self-supporting steel chimney should be as follows:

$$h = \max \begin{cases} 14Q^{0.3} \\ 6m + \text{Tallest Building height in location} \\ 30m \end{cases}$$

Where Q= total SO₂ emission from the plant in kg/hr and h = height of the steel chimney in m.

As per IS-1653 Part-1: 1989¹, height of steel chimney is also a function of environmental conditions as follows:

$$h = \left[\frac{AMFD}{8CV} \right]^{\frac{3}{4}}$$

Where A = coefficient of temperature gradient of atmosphere responsible for horizontal and vertical mixing of plume, M = estimated mass rate of emission of pollutants in g/s, F = dimensionless coefficient of rate of precipitation, C = maximum permissible ground level concentration of pollutant in mg/m³, gases, m³/s, D = diameter of stack at the exit of the chimney in m. V = estimated volume rates of emission of total flume.

Also, inside diameter of the chimney shell at top as per IS 6533 (Part 1): 1989 is given by:

$$D = \sqrt{\frac{4 Q_t}{\pi V_{exit}}}$$

Where D = inside diameter of the chimney at top in m, Q_t = Quantity of the gas in m³/s, and V_{exit} = Velocity of the flue gas at exit point of chimney in m/s. However, the diameter shall be so chosen that velocity of the flue gas at exit point of chimney will not exceed 30m/s, under any circumstances.

As per IS 6533 (Part 2): 19892 there are some limitations for the proportions of the basic dimensions from structural engineering considerations as follows

- Minimum outside diameter of the unlined chimney at the top should be one twentieth of the height of the cylindrical portion of the chimney.
- Minimum outside diameter of the unlined flared chimney at the base should be 1.6 times the outside diameter of the chimney at top

With these parameters, the basic dimensions of the Chimney are

checked to understand the code limitations. A lot of 66 of chimneys are considered for the present study.

II. Analysis Of The Selected Chimneys

2.1 Effect of Geometry

From the discussions in the previous section it is apparent that topto-base diameter ratio and height-to-base diameter ratio are the two essential factors that characterize the geometry of a self-supporting chimney. For the selected Chimneys top-to-base diameter ratio and height-to-base diameter ratio varies with constant thickness and flared base diameter. Fig. 1 presents the different parameters of the selected chimneys according to code limitations. This figure shows that the selected chimneys cover wide range of geometry.

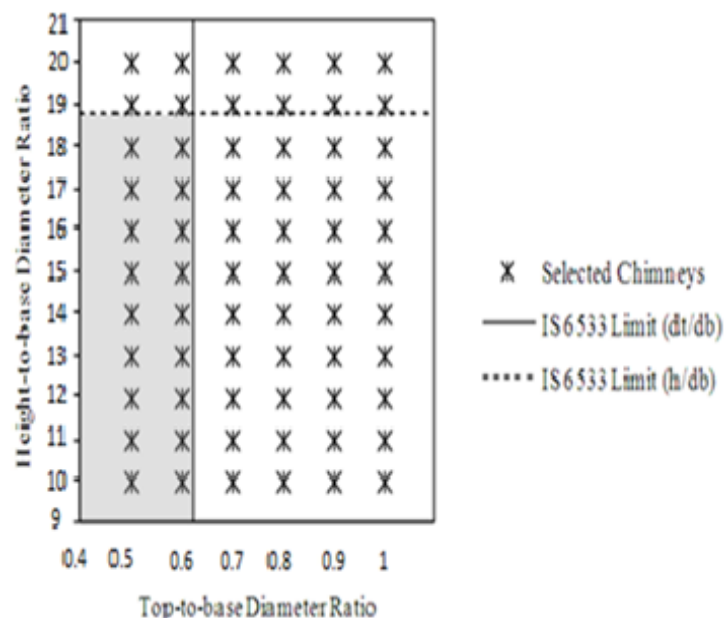


Figure :- Geometrical Parameters Distribution

2.2 Effect of manhole

Manholes are generally provided at the bottom of the chimney for maintenance and inspection purpose. The standard dimension of the manhole is 500mmx800mm according to Indian standard IS 6533 (Part-2):1989. These manholes are at generally located at minimum suitable distance from the base of the chimney. Two chimney models, one with the manhole and other without manhole, are analyzed using finite element software ANSYS for static wind load. Fig 2 (a&b) presents the Von-Mises stress for chimney model with manhole and without it. Fig 3(a&b) presents the displacement response of the two chimneys under static wind force. These two figures show that higher deflection is occurred at the top of the chimney with manhole as compared to chimney without manhole. Fig 4(a&b) presents the fundamental mode shape of the chimney models. Chimney without manhole is found to have higher fundamental frequency compared to the chimney with manhole.

Table-1 represents the difference in the parameters due to the presence of inspection man hole in the chimney.

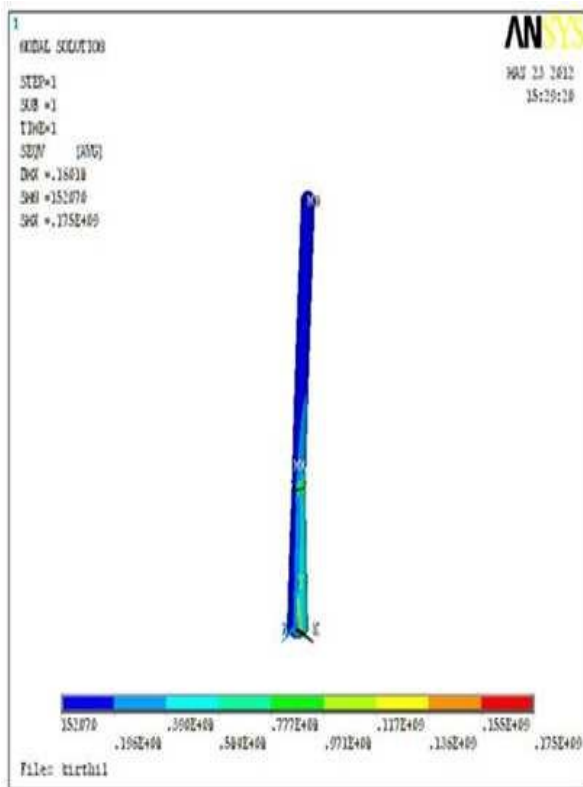


Figure 1

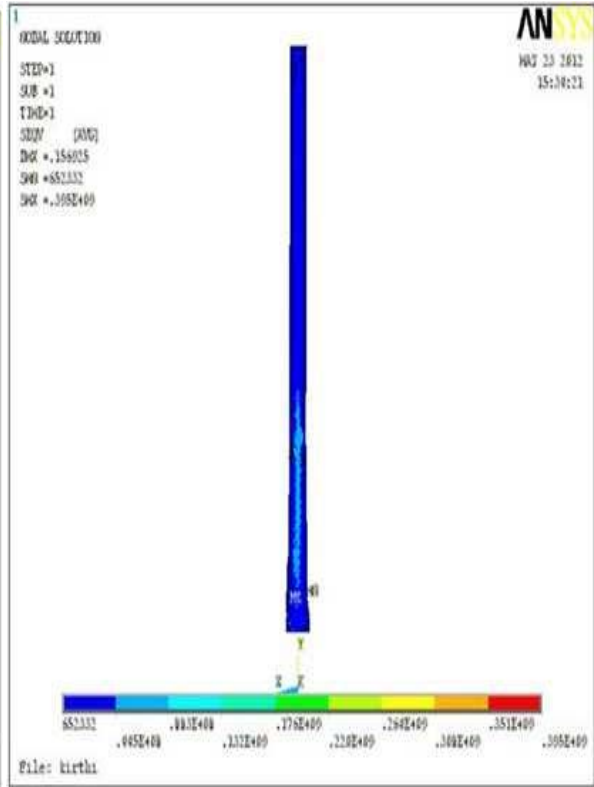


Figure 1

Comparison of Von- Mises Stress
Figure1 without man hole Figure2 With man hole

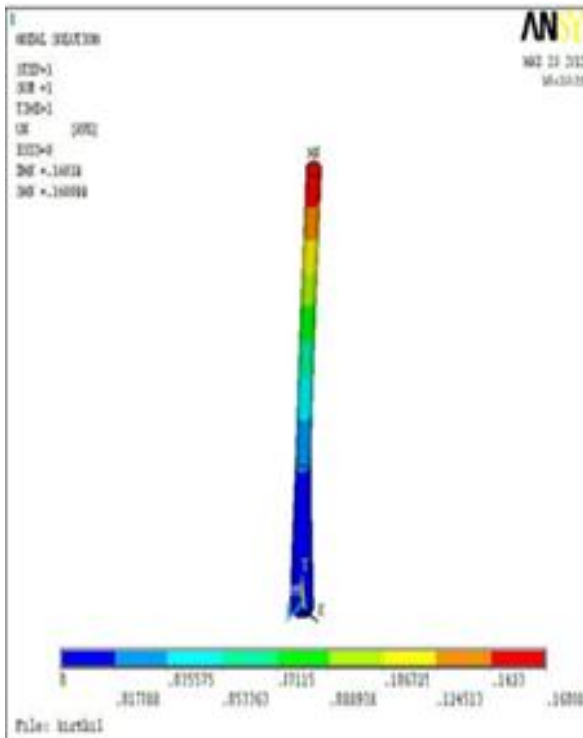


Figure 3

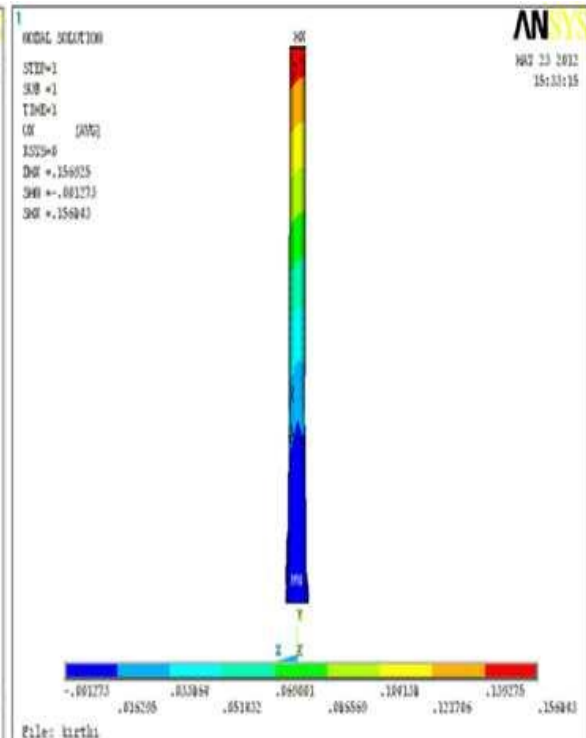


Figure 2

Comparison of top deflection in chimney
Figure3 Without man hole Figure4 With man hole

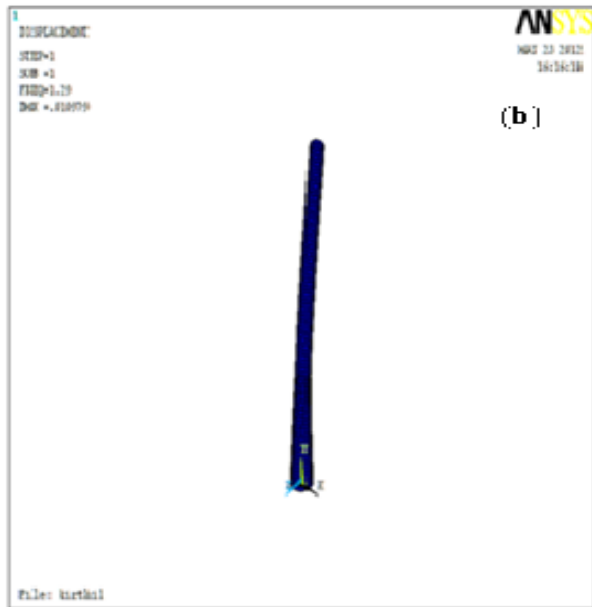


Figure 5

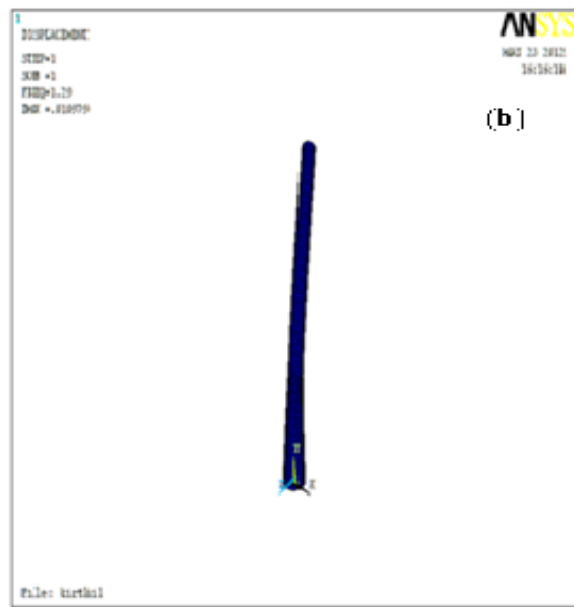


Figure 6

Comparison of mod shape in chimney Figure5 Without man hole Figure6 With man hole

III. Results And Discussions

In fig.1, it shows about the geometrical parameters which affect the design consideration. The shaded portion in the figure represents the region acceptable by the design code IS 6533 (Part 2): 1989. According to code, base diameter should be 1.6 times the top diameter of the chimney. From this relation it is obtained that the maximum limit for top-to-base diameter ratio should be 0.625. Similarly another limitation is minimum top diameter of the chimney should be one twentieth of the height of the cylindrical portion of the chimney. Hence the height-to base diameter ratio as per the code limitation is obtained as 18.75.

TABLE1
COMPARISON OF DESIGN PARAMETERS

	Without man hole	With manhole	% Difference
Top displacement(m)	0.160	0.157	2
Max. von Mises stress(MPa)	175	395	-56
Fundamental frequency(cps)	1.29	1.29	12

IV. Conclusions

The purpose of this paper was to verify the basis of design code limitations with regard to the basic dimensions of self-supporting unlined flared steel chimney and the effect of inspection manhole on the behaviour. It is established from these analyses that maximum moment and the maximum bending stress due to dynamic wind load in a self-supporting steel chimney are continuous functions of the geometry but it does not support the code limitations as mentioned previously. The results show that the maximum stress in the chimney with manhole is increased by 55.6% as compared to the maximum stress in the chimney without manhole. The top deflection is marginally equal. The mode shapes of the chimney are observed to be significantly different due to the presence of manhole. Chimney without manhole is found to have higher fundamental frequency compared to the chimney with manhole. This is because manhole reduces the effective stiffness of a chimney as evident from the modal analysis results.

REFERENCES

- [1.] IS 6533 Part 1; 1989, "Design and Construction of Steel Chimney". Bureau of Indian Standards, New Delhi (2002).
- [2.] IS 6533 Part 1; 1989, "Design and Construction of Steel Chimney: Bureau of Indian Standards, New Delhi (2005).
- [3.] CICIND, Model code for steel chimneys (Revision 1- December 1999), Amendment A-March 2002.
- [4.] Ministry of Environment and Forests, Govt. of India, Notification dated Jul 09, 2002
- [5.] IS 1893 Part 4; 2005, : Criteria for Earthquake Resistant Design of Structures:. Bureau of Indian Standards, New Delhi (2002).
- [6.] STAAD.PRO2006 (Version 11.0). "Integrated Software for 3D model generation, analysis and multi –material design", Inc. Bentley solution centre's (2006).
- [7.] MathCAD, Version14.0, "Parametric Technology Corporation", 2007.

A Survey on Wireless Sensor Network based Technologies for Precision Agriculture System

Omveer¹, Dr. H.K.Singh², Rishikesh Patankar³, Sandeep Bansal⁴,
Gaurav Kant Yadav⁵

¹Jr. Technical Officer, Media Lab Asia, DeitY, Govt of India

²Research Scientist, Media Lab Asia, DeitY, Govt of India

³Sr. Research Scientist, Media Lab Asia, DeitY, Govt of India

⁴Sr. Research Scientist, Media Lab Asia, DeitY, Govt of India

⁵Summer Intern, Media Lab Asia

Abstract: This paper provides the information related to previous work that has been done in the field of agriculture using the wireless sensor network technology over a period of past few years. We also studied the wireless protocols that were used previously. These protocols have limitation of short range which requires multi hopped network as in Zigbee and Bluetooth communication technologies. The multi hopping can be avoided by the use of appropriate long range wireless protocol such as WiMAX, GSM and medium range Wi-Fi protocols.

Over recent years, there have been important advances in several technologies related to wireless communications and networking applications in the agricultural practices. Based on survey results, a more research can be done for providing best technological solution to the common challenges in agriculture. This research would be helpful to develop a device having flexibility, local intelligences and decision power. Hand held device option can be useful in precision agriculture for various commercial crops in Indian scenario.

Keywords: Wireless Sensor Network; Precision Agriculture; Random Topology; Wi-Fi network.

I. INTRODUCTION

Agriculture in the Indian economy has played vital role. It accounted for 15.7% of the GDP in 2009-10, employed 52.1% of the total workforce [1].

Information related to previous work that has been done in the field of Precision Agriculture (PA) is very necessary before going to develop a best solution for precision agriculture. Over a period of past few years, a system which is useful in monitoring as well as controlling the data which provides the flexibility, is realized. The communication and networking technologies that were used previously have limitation of short range which requires multi hopped networks. So this multi hopping can be overcome by the use of appropriate long or medium range wireless protocol such as WiMAX, GSM and Wi-Fi.

Researcher have devoted their time to develop important advances in several technologies related to wireless communications and in network processing, a steady increase of processing capacity, the appearance of mature wireless sensor network (WSN) hardware and software platforms, and the widespread adoption of smart-phones. All these innovations offer a wide set of novel alternatives which could potentially address unsolved problems in PA and offer more convenient alternatives to existing solutions.

II. LITERATURE SURVEY

Santhosh Simon and K Paulose Jacob proposed that the wireless sensor network for crop monitoring in the paddy fields of Kuttanad (India) can be applied because the soil of the paddy fields is salty and is extremely acidic. This acidity of the soil is considered a major problem which retards the production of rice in the area. A best solution to overcome this problem is to regular rinsing of the soil by water which can reduce the acidity and increase the production. So, the pumping of water to and from the field is the major activity from plowing to harvesting. Further, they added that Electro-mechanical sensors in the mesh networking and through ZigBee communication can be automated systems which monitor the water level and regulate the water. It can send messages to the farmers. They suggested Zigbee technology because of its low-cost, low-power consumption, low data-rate, two-way wireless networking standard that is aimed at remote control and sensor applications which is suitable for operation in harsh radio environments and in isolated locations. [2]

Kazunobu and Mitsuho developed a site-specific nitrogen management system “RiceNiSMo” for paddy rice for estimating the appropriate rate of fertilizer nitrogen application. This software can simulate the growth stages, nitrogen uptake, yield and the degree of lodging based on the parameters from soil nitrogen release and the weather. [3]

S.K. Balasundram et al reviewed On-the-go soil sensor technologies and find out that soil sensors can be used to generate real-time soil data, such as pH, electrical conductivity, salinity, dissolved oxygen and nutrient concentration, which are subsequently turned into geo-referenced maps to facilitate site-specific nutrient management. They suggested that numerous ‘on-the-go’ sensors have been manufactured to measure mechanical, physical and chemical soil properties. These sensors have been based on electrical and electromagnetic, optical and radiometric, mechanical, acoustic, pneumatic and electrochemical measurement concepts. [4]

N. G. Shah et al. developed a system for precision irrigation using sensor network mainly aimed for monitoring soil moisture and estimating vaporization by considering soil moisture, soil temperature and relative humidity as the critical parameters for measurement. [5]

A system was developed by Q. Wang et al using microcontroller, universal asynchronous receiver transmitter (UART) interface and sensors while the transmission was done by hourly sampling and buffering the data, transmit it and then checking the status messages. But they find out that its cost and deployment of sensor under the soil which causes attenuation of radio frequency (RF) signals was the major drawbacks. [6]

I. Aziz et al developed a remote monitoring system in agricultural greenhouse using wireless sensor and short message service (SMS). System was divided into four parts namely data acquisition, data communication, data presentation and alert notification which also allowed the reverse communication i.e. from farmer side to the base station. The system was cost effective and reliable. They considered that this system can be made more cost effective by taking other environmental parameters and by using recent technologies such as artificial intelligence, neural network, etc. [7]

A Wi-Fi based smart sensor network for agricultural environment was developed by G. Mendez et al. They considered temperature, humidity, light intensity, air pressure and soil moisture as main parameters. The objectives were to reduce cost and effort of incorporating wiring, to enhance flexibility and mobility for the system. The system was useful for transferring and logging the data from various nodes. [8]

M. Haefke et al. developed a ZigBee based smart sensing platform for monitoring environmental parameters such as temperature, relative humidity, pressure and sunlight with the use of microcontroller which serve as a smart weather station. The research was based on characteristics such as use of low cost equipment, accurate sensors and flexibility in data handling. Use of XBee module provided the wider range and reduced the current consumption of the circuit. [9]

M. Dinesh and P. Saravanam proposed a FPGA based embedded system which could monitor and control microclimatic parameters on regular basis so as to maximize the production of crop with reducing human intervention research. They considered temperature (wet and dry both), humidity and light intensity as their main parameters. The system was low cost, automated and can be made effective by considering other environmental parameters and real time fault detection. [10]

A remote sensing and control irrigation system using distributed wireless sensor network aiming for variable rate irrigation, real time in field sensing, controlling of a site specific precision linear move irrigation system to maximize the productivity with minimal use of water was developed by Y. Kim et al. [11]

M. Dursun and S. Ozden developed a drip irrigation automated system using wireless technology. The objectives were to monitor water content of soil in real time and remove the need for workmanship for flooding irrigation. The designed system has three unit namely base station unit, valve unit and sensing unit which were applied for controlling drip irrigation of 1000 dwarf cherry trees. In this sensors were placed 20cm deep and 50cm away from the trees. The analysis of the system produced the circa linear graph between volumetric water content and time for which system was analysed. It was a low cost and reliable system having advantages such as preventing moisture stress of trees, minimising excessive use of water and ensuring of rapid growing weeds. [12].

Gopala Krishna Moorthy .K et al. developed a monitoring system to measure the water level in agriculture using sensor network which offers precision irrigation. They developed a routing algorithm which provides information related to water level as well as useful in computing threshold values based on transmission range. The algorithm was based on distances of wireless information from source to sink node as well as on minimum angle between source and destination. They also proposed that system can be optimized by the use of algorithms based on genetics and neural network. [13]

T. Pearson proposed “Paprika greenhouse management system” which had WSN environmental sensors and CCTVs at inside/outside of paprika greenhouse. These devices collect the growth-environment related information of paprika. He investigates that Zigbee-based agriculture monitoring system serves is a

reliable and efficient system to monitor the environmental parameters. Wireless monitoring of field not only allows user to reduce the human power, but it also allows user to see accurate changes in it. [14]

Jose I. et al reviewed the principles of biosensor fabrication and operation, their existing and potential applications in the food and agricultural industries, and recent research and future trends. [15]

III. OSERVATION FROM SURVEY

On the basis of survey of the literature, the following findings have been observed.

TABLE 1. FINDINGS FROM ABOVE SURVEY

Agricultural parameters measured by WSN technology	Field capacity during irrigation, dissolved oxygen, nutrient concentration, soil moisture, soil temperature, relative humidity, atmosphere temperature & humidity, light intensity, air pressure etc.
Working principle of sensors used in WSN	Electro-Mechanical, electrical and electromagnetic, optical and radiometric, mechanical, acoustic, pneumatic and electrochemical measurement concepts, Biosensors etc.
Local computation, Networking & Communication techniques in WSN	Mesh networking and Zigbee IEEE standard 802.15.4, Simulation software, artificial intelligence, neural network, Wi-Fi based smart sensor network, FPGA based real time monitoring system, Microcontroller and universal asynchronous receiver transmitter (UART) interface, A remote sensing (GPS enabled) and control irrigation system, genetics and neural network etc.
Benefits of using WSN technology in agriculture	cost effective, low-power consumption and long distance data transmission, two-way wireless networking standard that is aimed at remote control and sensor applications which is suitable for operation in harsh radio environments and in isolated locations, reliability on real time data collection, reduce effort of incorporating wiring, flexibility, mobility, maximise the production & quality of crop with less manual efforts, FPGA based WSN platform is energy efficient and more useful for farmers for decision making.
Challenges in using WSN technology in agriculture	Deployment of sensor under the soil which causes attenuation of radio frequency (RF) signals, power supply, measurement of accurate data in open field, environmental protection issues are the major challenges

TABLE 2. COMPARISON BETWEEN COMMUNICATION TECHNOLOGIES FOR THE FIELD SENSOR NETWORK

Bluetooth	ZigBee	Findings
Protocol IEEE 802.15.1	Protocol IEEE 802.15.4	Zigbee advance in protocol
Frequency Hopping Spread Spectrum (FHSS) modulation technique	Direct Sequence Spread Spectrum (DSSS) modulation technique	DSSS use low power in Zigbee
Protocol stack size 250k byte	Protocol stack size 28k byte	Low size of protocol suites in Zigbee
Intended for frequent recharging	No charging	Long battery life for Zigbee
1M bit/sec network speed	250kbits/sec	High speed for Bluetooth
1-10 meter network range	10-100 meter line of sight range	Long range for Zigbee
3 s network join time	30ms network join time	High selectivity
Bluetooth is more oriented toward user mobility and eliminating short-distance cabling	ZigBee aims more for grand-scale automation and remote control	Remote control in Zigbee

TABLE 3. COMPARISON BETWEEN COMMUNICATION TECHNOLOGIES FOR SENSOR NETWORK TO REMOTE SERVER

Wi-Fi	WiMAX	Findings
Standard: IEEE 802.11x (802.11b, 802.11g, 802.11n)	Standard: IEEE 802.16y (802.16a, 802.16d and 802.16e)	WiMAX is advance in protocol
ISM band	ISM bands or licensed band	For long range, subscriber can pay for license in WiMAX
100metres as it maximum range	80-90kilometers in terms of range	Long range in WiMAX
speeds up to 54mbps	speeds upto 40mbps	Wi-Fi better
channel bandwidth of 20MHz	bandwidth option which ranges from 1.25MHz to 20MHz	Chanel choosing facility in WiMAX
Wi-Fi uses Extensible Authentication Protocol (EAP) Wired Equivalent Privacy (WEP) security algorithms	WiMAX uses X.509 or PKMv2 as authentication algorithms	Both secure

IV. NEW PROPOSED SOLUTION

Considering all above findings, we propose a new solution for agricultural practices which would use WSN technology. Followings are the observations which are considered to use in proposed system.

TABLE 4. COMPONENT WISE OBSERVATIONS

Sr. No.	Components	Observations
1.	Agricultural parameters	Soil nutrients and moisture; atmospheric temperature and sunshine
2.	Working principle of sensors	Electrical conductivity
3.	Computation device	FPGA
4.	Communication techniques	Zigbee and WiMaX
5.	Networking	Random topology
6.	Benefits	Local and real time decision, compatible for any agriculture sites (greenhouse and open filed)

The proposed system would consist of couple of sensors to sense various soil and atmospheric parameters such as nutrients, moisture, temperature and sunshine. The result of sensed parameters would be transmitted via zigbee on a embedded device. The device would be installed at the farmers' premises. In this device, FPGA (Field Programmable Gate Array) may be used to give the system local intelligence power. The device would be able to use the sensor algorithm to accurately predict the health of the crop. This would alert the farmer in the form of textual and audio alarm through local display and alarm system. For public extension system, this device would transmit the signal to centralized server without any interference or interception of signal via WiMAX. In this topology, we may take wireless antenna, router, and gateway and centralized server.

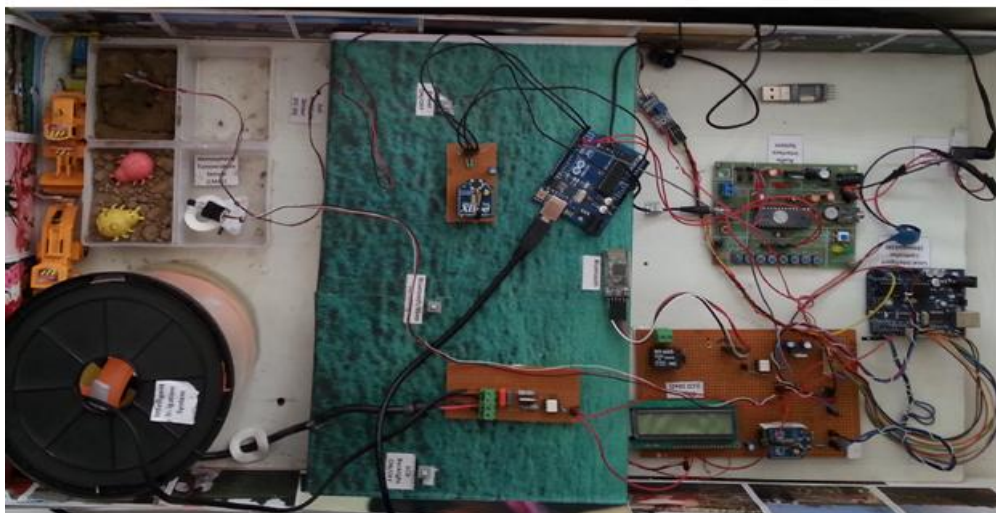


Fig.1. Snapshot of prototype

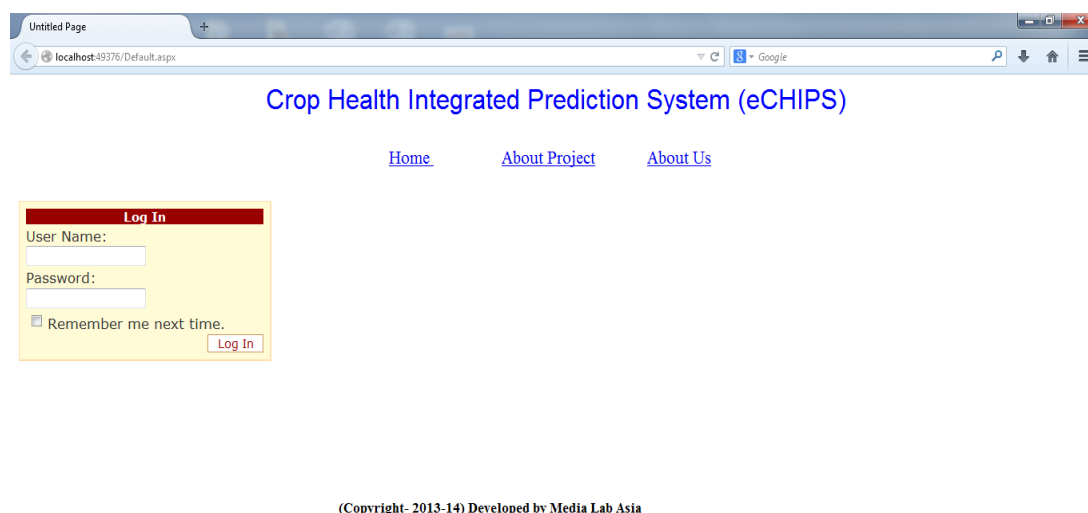


Fig.2. Screenshot of web application for prototype

V. RESULTS

A prototype is developed at Media Lab Asia to prove the proposed concept and experienced results are shown in fig.3 and fig. 4:

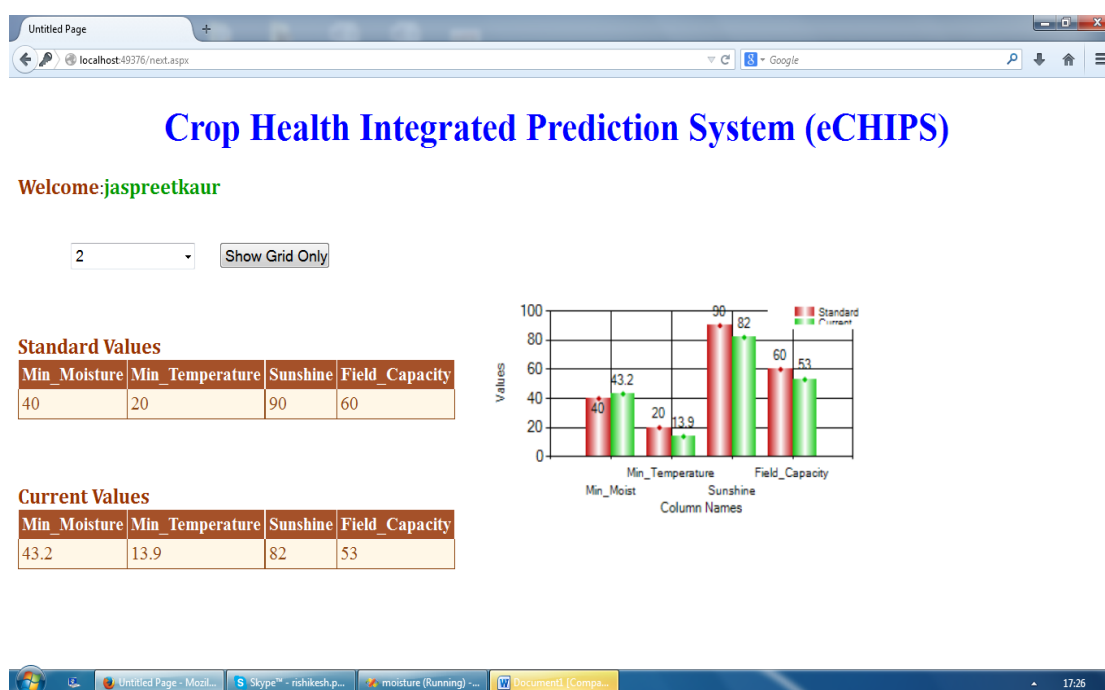


Fig.3 : Screenshot of the results in web application

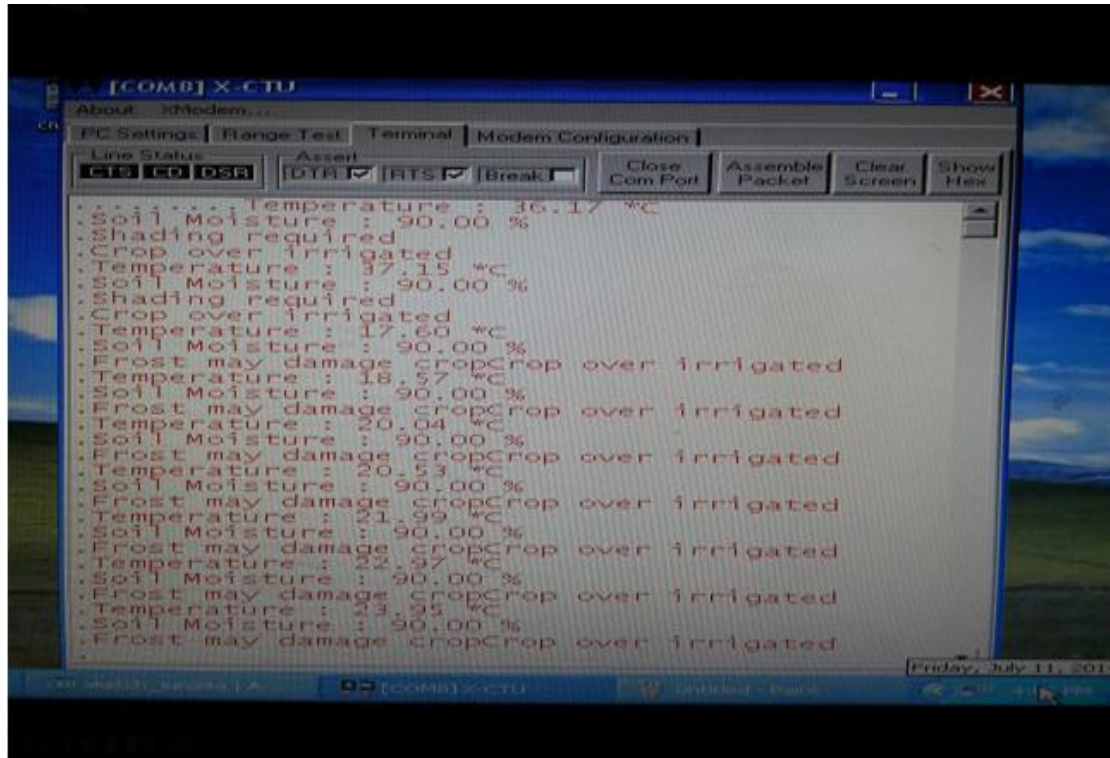


Fig.4: Snapshot of results displayed at remote PC

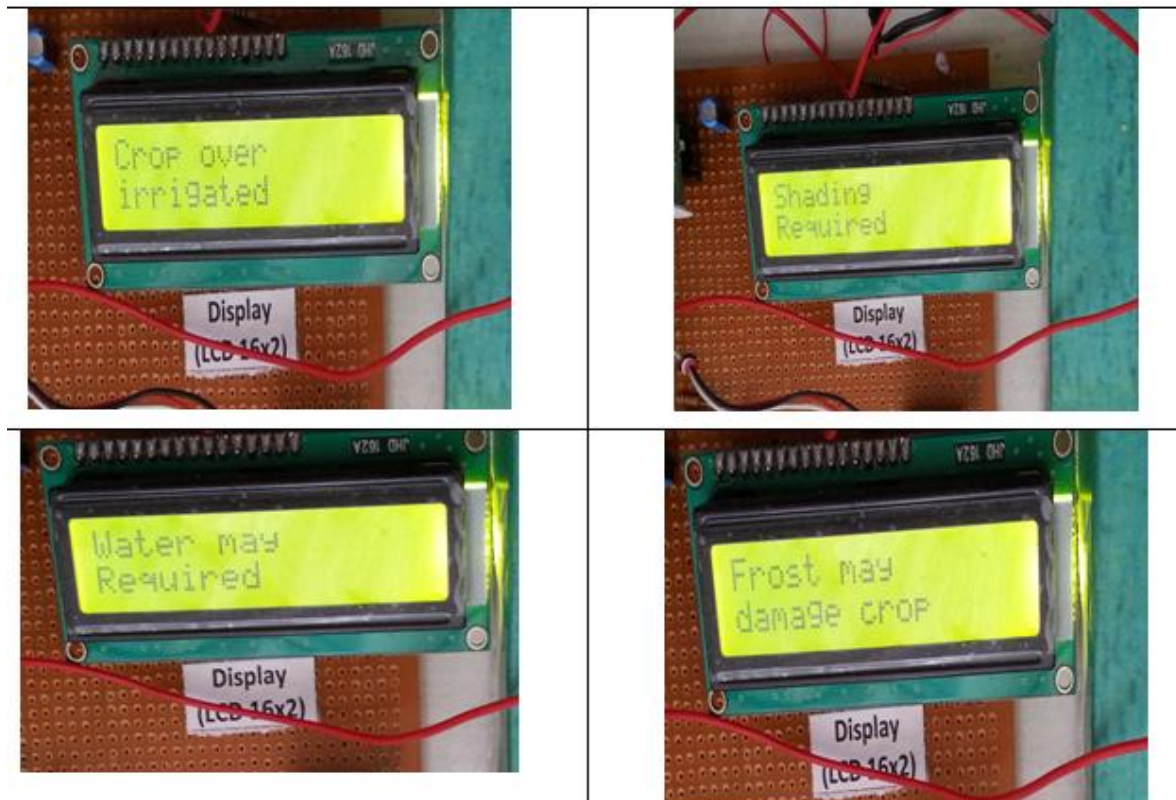


Fig. 5: Snapshot of results displayed at local LCD

VII. CONCLUSION AND FUTURE WORK

Precision agriculture (PA) and WSN applications combined together presents an exciting new area of research that will greatly improve quality in agricultural production especially in area of floriculture where quality is most important because consumer of cut flower are elite group of society. There are potential

applications of Wi-Fi wireless sensor network technology in agricultural systems such as real time field monitoring, automated irrigation control, monitoring, and remote operation.

In this paper, we surveyed the literature available and considering the findings we proposed a new solution in wireless sensor network technology for automatic monitoring and local alarming for the farmers. In our solution, the sensor nodes collect the data such as temperature, soil moisture, sunshine and nutrients from the field. The real-time data is transferred to the FPGA node via zigbee. On the basis of these data, device predicts about crop health. For public extension, this data may be transferred via Wi-Fi/WiMAX to the centralized center which stores and processes the data. Developed prototype gave good results. This would be further extended for the product.

ACKNOWLEDGMENTS

Thankful heart feelings are extended to all those magnanimous persons who stood behind me as an inspiration and rendered their full support throughout my research.

AUTHORS' BIOGRAPHY



Omveer Chaudhary: He received the M.Tech and B.Tech degree with honors in Electronics and Communication engineering from Rajasthan Technical University, Kota, India. He has been working with ITRA & Media Lab Asia, DeitY, Govt. of India since Feb, 2013. As Jr. Technical Officer, he is associated with research, development & deployment in the area of ICT. His papers/articles have been published/accepted in international/national conferences/seminars/journals. His research interests are in image processing, wireless sensor network and the use of information communication technology in societal development.



Dr. Hrishikesh Kumar Singh: He is working as Research Scientist in Media Lab Asia and is having more than 6 years experience in ICT in Agriculture. He is involved in initiating, implementation and monitoring of various ICT in Agriculture based projects eSagu, Gramin Gyan Kendra and ICT based alternate Agri information system. He did his PhD in Agriculture and having lifelong membership of various Scientific Societies.



Rishikesh Patankar: He has more than 12 years of experience in ICT. He has worked in training domain for more than 5 years including stints at top universities in China and India. He holds 3 master degrees in computer science & also NET, CCNA qualified. He has experience of working with ERP projects including training the managers and industry alike. His areas of interest include computer networks, mobile applications and eLearning. He has experience of managing enterprise level systems. He is holding post of Sr. Research Scientist in Media Lab Asia, DeitY, Govt. of India since May 2007. He is involved in initiating, implementation and monitoring of various projects on education and SME domain through premier R&D institutions and other Government organizations and industry.



Mr. Sandeep Bansal: He has more than 9 years of experience in ICT. He holds a M.Tech (I.T.), B.E (Computer Science), CDAC certification in advanced software design & development, EPO & WIPO certification in IP. He is also included in consultant database of EdCIL (a body under MHRD). He has joined Media Lab Asia in September 2004. As a senior research scientist in Media Lab Asia he is associated with research, development & deployment in the area of ICT through involvement at each stage right from formulation, commencement, development, monitoring & steering, protection of IPR involved, promotion / popularization through its presentation in various gatherings, transfer / deployment and formulation of policies for sharing of revenue with development/deployment partners. His papers/articles have been published/accepted in National/International conferences/seminars/journals

REFERENCES

- [1] <http://gradestack.com/An-Introduction-to-Indian-Economy/15521-3151-7088-study-wtw>
- [2] Santhosh Simon, K Paulose Jacob "Wireless Sensor Networks for Paddy Field Crop Monitoring Application in Kuttanad" International Journal of Modern Engineering Research (IJMER), Vol.2, Issue.4, July-Aug 2012 pp-2017-2020.

- [3] Kazunobu TORIYAMA, Mitsuho SUGIMOTO “Development of a Site-Specific Nitrogen Management System for Paddy Rice” JARQ 37 (4), 213 – 218 (2003)
- [4] Bah, A., S.K. Balasundram and M.H.A. Husni “Sensor Technologies for Precision Soil Nutrient Management and Monitoring” American Journal of Agricultural and Biological Sciences 7 (1): 43-49, 2012, ISSN 1557-4989
- [5] N. Shah and I. Das, “Precision Irrigation Sensor Network Based Irrigation”, a book on Problems, Perspectives and Challenges of Agricultural Water Management, IIT Bombay, India, pp. 217–232, April 2008
- [6] Q. Wang, A. Terzis and A. Szalay, “A Novel Soil Measuring Wireless Sensor Network”, IEEE Transactions on Instrumentation and Measurement, pp. 412–415, August 2010.
- [7] I. Aziz, M. Hasan, M. Ismail, M. Mehat and N. Haron, “Remote Monitoring in Agricultural Greenhouse using Wireless Sensor and Short Message Service”, International Journal of Engineering Technology, vol. 9, pp. 1–12, September 2010
- [8] G. R. Mendez, M. A. Yunus and Dr. S. C. Mukhopadhyay, “A Wi-Fi based Smart Wireless Sensor Network for an Agricultural Environment”, Fifth International Conference on Sensing Technology, pp. 405–410, January 2011
- [9] M. Haefke, S. Mukhopadhyay and H. Ewald, “A Zigbee Based Smart Sensing Platform for Monitoring Environmental Parameters”, IEEE Conference on Instrumentation and Measurement Technology, pp. 1–8, May 2011
- [10] M. Dinesh and P. Saravanam, “FPGA Based Real Time Monitoring System for Agricultural Field”, International Journal of Electronics and Computer Science Engineering, pp. 1514–1519, June 2011.
- [11] Y. Kim, R. Evans and W. Iversen, “Remote Sensing and Control of an Irrigation System Using a Distributed Wireless Sensor Network”, IEEE Transactions on Instrumentation and Measurement, pp. 1379–1387, July 2008
- [12] M. Dursun and S. Ozden, “A Wireless Application of Drip Irrigation Automation Supported by Soil Moisture Sensors”, Scientific Research and Essays, pp. 1573–1582, April 2011
- [13] GopalaKrishna Moorthy .K, Dr.C.Yaashuwanth, Venkatesh.K “A Wireless Remote Monitoring Of Agriculture Using Zigbee” International Journal of Engineering and Innovative Technology (IJEIT) Volume 2, Issue 8, February 2013
- [14] T. Pearson, “Hardware-based image processing for high-speed inspection of grains”, Computers and Electronics in Agriculture, vol.69, 2009
- [15] Jose I. Reyes De Corcuera , Ralph P.Cavalieri “Biosensors”, Encyclopedia of Agricultural, Food and Biological Engineering DOI:10.1081/E-EAFE120007212

Work place stress preventive and curative measures

D. Sharon Lily¹, Dr. V. Tulasi Das²

¹ M.A, M.B.A M.Phil,(PhD) Research Scholar, HRM Dept, ANU

² MBA, MHRM. B.G.L, P.G.DPM., M.Phil., PhD, HOD HRM, ANU

Abstract: Stress has been defined in different ways over the years. Originally, it was conceived of as pressure from the environment, then as strain within the person. The generally accepted definition today is one of interaction between the situation and the individual. It is the psychological and physical state that results when the resources of the individual are not sufficient to cope with the demands and pressures of the situation. Thus, stress is more likely in some situations than others and in some individuals than others. Stress can undermine the achievement of goals, both for individuals and for organisations.

I. Introduction

Stress affects an individual's physical and mental health, performance and inter-personal relationships. There are two types of stress, namely, Eustress and Distress. Factors that account for differences in job stress are gender, level of employee in the organization, income, occupation and family situation. Some of the symptoms of stress at workplace are as follows-

- Absenteeism, escaping from work responsibilities, arriving late, leaving early, etc.
- Deterioration in work performance, more of error prone work, memory loss, etc.
- Cribbing, over-reacting, arguing, getting irritated, anxiety, etc.
- Deteriorating health, more of accidents, etc.
- Improper eating habits (over-eating or under-eating), excessive smoking and drinking, sleeplessness, etc.

II. Sources/Causes of Stress

The factors leading to stress among individual are called as stressors. Some of the factors/stressors acting on employees are-

1. Organizational factors- With the growth in organizational stress and complexity, there is increase in organizational factors also which cause stress among employees. Some of such factors are-

- a. Discrimination in pay/salary structure
- b. Strict rules and regulations
- c. Ineffective communication
- d. Peer pressure
- e. Goals conflicts/goals ambiguity
- f. More of centralized and formal organization structure
- g. Less promotional opportunities
- h. Lack of employees participation in decision-making
- i. Excessive control over the employees by the managers

2. Individual factors- There are various expectations which the family members, peer, superior and subordinates have from the employee. Failure to understand such expectations or to convey such expectations lead to role ambiguity/role conflict which in turn causes employee stress. Other individual factors causing stress among employees are inherent personality traits such as being impatient, aggressive, rigid, feeling time pressure always, etc. Similarly, the family issues, personal financial problems, sudden career changes all lead to stress.

3. Job concerning factors- Certain factors related to job which cause stress among employees are as follows-

- j. Monotonous nature of job
- k. Unsafe and unhealthy working conditions
- l. Lack of confidentiality
- m. Crowding

4. Extra-organizational factors- There are certain issues outside the organization which lead to stress among employees. In today's modern and technology savvy world, stress has increased. Inflation, technological change, social responsibilities and rapid social changes are other extra-organizational factors causing stress.

Because April is National Stress Awareness Month, it's the perfect time to make changes in your life to reduce the level of stress you experience, improve your health, and make your life more enjoyable!

The World Health Organization estimates that 15 percent of the world's population will suffer from an anxiety disorder at some point in their lifetime.

III. Preventive Measures Of Workplace Stress

It is thus very essential to have effective stress management strategies in an organization so that the detrimental repercussions of stress on the employees as well as their performance can be reduced and controlled. Stress has a significant effect on job performance and interpersonal relationships among the employees. There is need to establish a staff support Centre at the university, where employees can be offered emotional and psychological support through professional counselling. Relationships can become very stressful if either person feels as if his/her boundaries aren't respected. Hold regular team or group meetings. Encourage participative management, Offer training to employees. Determine the content of each position (analyze positions and tasks).

Conduct an annual evaluation of employees' contribution to Group meetings are a chance to:

- clarify individual roles, responsibilities and powers.
- specify individual expectations, goals and objectives.
- give recognition, social support and feedback.
- stimulate dialogue with supervisors and colleagues.
- assess whether the workload respects employees' limits.

Participative management helps to:

- improve relationships between supervisors and employees.
- increase employees' participation in decisions.
- enhance employees' sense of belonging.

Enables employees to develop new knowledge and skills, which can be seen as a form of recognition and through which they can:

- avoid a qualitative work overload.
- advance their careers.
- Eventually assume more responsibilities. Power and autonomy.

An analysis of each position can:

- determine whether there is a work overload.
- clarify roles, responsibilities and powers related to each position.
- specify expectations, goals and objectives.
- reduce certain risks linked to the work environment and working conditions.

An annual evaluation of employees provides the opportunity to:

- clarify roles, responsibilities and powers.
- specify what is expected of employees, the goals and objectives to be reached.
- provide recognition, social support and feedback.
- communicate career goals and establish a career plan.

The 2001 Canadian Mental Health Survey, found that 51% of respondents felt that work was a major or moderate source. But not all stress is negative; research has shown that individuals function best in a work setting that places reasonable demands on them. One example of positive stress might be preparing for a job interview.

Many employers have instituted programs and policies to reduce stress or help employees deal with stress before it becomes a problem. Indeed, the 1999 Workplace and Employee Survey found that slightly more than one-quarter (26%) of employees [7](#) had access to some type of employee assistance plan.

Leadership columnist Jena McGregor discusses a new study out of Harvard that challenges the common perception that leaders have higher stress levels than non leaders. Researchers tested the stress levels of leaders and non leaders and discovered that leaders had significantly lower levels of cortisol (the stress hormone) and lower reports of anxiety when compared to non leaders. In a second study, they found that leaders who held more powerful positions exhibited lower cortisol levels and reported less anxiety than leaders who held less powerful positions. Most interventions to reduce the risk to health associated with stress in the

workplace involve both individual and organisational approaches. Individual approaches include training and one-to-one psychology services—clinical, occupational, health or counselling. They should aim to change individual skills and resources and help the individual change their situation.

IV. Training Helps Prevent Stress Through

- Becoming aware of the signs of stress, using this to interrupt behaviour patterns when the stress reaction is just beginning. Stress usually builds up gradually. The more stress builds up, the more difficult it is to deal with analysing the situation and developing an active plan to minimise the stressors learning skills of active coping and relaxation, developing a lifestyle that creates a buffer against stress.
- Practising the above in low stress situations first to maximise chances of early success and boost self confidence and motivation to continue.
- A wide variety of training courses may help in developing active coping techniques—for example, assertiveness, communications skills, time management, problem solving, and effective management.

However, there are many sources of stress that the individual is likely to perceive as outside his or her power to change, such as the structure, management style or culture of the organisation. It is important to note that stress management approaches that concentrate on changing the individual without changing the sources of stress are of limited effectiveness, and may be counterproductive by masking these sources. For example, breathing deeply and thinking positively about a situation causing stress may make for a temporary feeling of well being, but will allow a damaging situation to continue, causing persistent stress and, probably, stress to others. The primary aim of the individual approach should be to develop people's skills and confidence to change their situation, not to help them adapt to and accept a stressful situation.

Curative measures of workplace stress:

The prevention and management of workplace stress requires organisational level interventions, because it is the organisation that creates the stress. An approach that is limited to helping those already experiencing stress is analogous to administering sticking plaster on wounds, rather than dealing with the causes of the damage. An alternative analogy is trying to run up an escalator that's going down! Organisational interventions can be of many types, ranging from structural (for example, staffing levels, work schedules, physical environment) to psychological (for example, social support, control over work, participation).

The emphasis on the organisation, rather than the individual, being the problem is well illustrated by the principles used in Scandinavia, where there is an excellent record of creating healthy and safe working environment .

A risk assessment strategy—six stages:

1. **Hazard identification:** Reliably identify the stressors which exist in relation to work and working conditions, for specified groups of employees, and make an assessment of the degree of exposure
2. **Assessment of harm:** Collect evidence that exposure to such stressors is associated with impaired health in the group being assessed or of the wider organisation. This should include a wide range of health-related outcomes, including symptoms of general malaise and specific disorders, and of organisational and health related behaviours such as smoking and drinking, and sickness absence
3. **Identification of likely risk factors:** Explore the associations between exposure to stressors and measures of harm to identify likely risk factors at the group level, and to make some estimate of their size and/or significance
4. **Description of underlying mechanisms:** Understand and describe the possible mechanisms by which exposure to the stressors is associated with damage to the health of the assessment group or to the organisation
5. **Audit existing management control and employee support systems:** Identify and assess all existing management systems both in relation to the control of stressors and the experience of work stress, and in relation to the provision of support for employees experiencing problems.
6. **Recommendations on residual risk:** Take existing management control and employee support systems into proper account, make recommendations on the residual risk associated with the likely risk factors related to work stress.

Increasingly, legislation requires employers to assess and address all risks to employee health and safety, including their mental health (for example, the European Commission's framework directive on the introduction of measures to encourage improvements in the safety and health of workers at work). Creating a safe system of work requires targeting equipment, materials, the environment and people (for example, ensuring sufficient skills for the tasks). It also requires having monitoring and review systems to assess the extent to which prevention and control strategies are effective.

Although associations between workplace factors and psychological ill health and associated sickness absence have been well documented, evidence based interventions to reduce these problems are scarce.

Successful interventions used training and organisational approaches to increase participation in decision making and problem solving, increase support and feedback and improve communication. These studies found that:

- [1.] Those taught skills to mobilise support at work and to participate in problem solving and decision making reported more supportive feedback, feeling more able to cope, and better work team functioning and climate. Among those most at risk of leaving, those undergoing the training reported reduced depression, staff facing organisational change that were taught skills of stress management, how to participate in, and control, their work showed a decrease of stress hormone levels.
- [2.] Staff taught verbal and non-verbal communication and empathy skills demonstrated reduced staff resignations and sick leave
- [3.] Physically inactive employees undergoing stress management training improved their perceived coping ability and those undergoing aerobic exercise improved their feelings of well being and decreased their complaints of muscle pain, but also reported reduced job satisfaction
- [4.] Employees undergoing one of seven training programmes emphasising one or more aspects of stress management—physiological processes, coping with people or interpersonal awareness processes—showed reductions in depression, anxiety, psychological strain, and emotional exhaustion immediately after the programme. There was a further reduction in psychological strain and emotional exhaustion at 9–16 months' follow up

Strengthening Of RC Beam Using FRP Sheet

E. Rakesh Reddy¹, G. Ramakrishna²

Abstract: Strengthening structures via external bonding of advanced fibre reinforced polymer (FRP) composite is becoming very popular worldwide during the past decade because it provides a more economical and technically superior alternative to the traditional techniques in many situations as it offers high strength, low weight, corrosion resistance, high fatigue resistance, easy and rapid installation and minimal change in structural geometry. Although many in-situ RC beams are continuous in construction, there has been very limited research work in the area of FRP strengthening of continuous beams.

In the present study an experimental investigation is carried out to study the behavior of continuous RC beams under static loading. The beams are strengthened with externally bonded glass fibre reinforced polymer (GFRP) sheets. Different scheme of strengthening have been employed. The program consists of fourteen continuous (two-span) beams with overall dimensions equal to (150×200×2300) mm. The beams are grouped into two series labeled S1 and S2 and each series have different percentage of steel reinforcement. One beam from each series (S1 and S2) was not strengthened and was considered as a control beam, whereas all other beams from both the series were strengthened in various patterns with externally bonded GFRP sheets. The present study examines the responses of RC continuous beams, in terms of failure modes, enhancement of load capacity and load deflection analysis. The results indicate that the flexural strength of RC beams can be significantly increased by gluing GFRP sheets to the tension face. In addition, the epoxy bonded sheets improved the cracking behaviour of the beams by delaying the formation of visible cracks and reducing crack widths at higher load levels. The experimental results were validated by using finite element method.

Keywords: continuous beam; flexural strengthening; GFRP; premature failure; debonding failure.

ABBREVIATIONS

ACI	American Concrete Institute
CFRP	Carbon Fibre Reinforced Polymer
BM	Bending Moment
EB	Externally Bonded
FEM	Finite Element Method
FRP	Fibre Reinforced Polymer
FRPC	Fibre Reinforced Polymer Composite
GFRP	Glass Fibre Reinforced plastic
HSC	High Strength Concrete
HYSD	High Yield Strength Deformed
IC	Intermediate Crack
IS	Indian Standards
NSM	Near Surface mounted
PSC	Portland Slag Cement
RC	Reinforced Concrete
RHSC	Reinforced High Strength Concrete

NOTATIONS

D	Overall Depth of the Beam
B	Breadth of the Beam
d	Effective Depth
L	Span Length of the Beam
f_{ck}	Characteristic Cube Compressive Strength of Concrete
f_y	Tensile Strength of the Bar

Pu	Ultimate Load
λ	Load Enhancement Ratio
ϕ	Diameter of the Reinforcement
M	Moment of Resistance
E	Modulus of Elasticity
I	Moment of Inertia
F	Global Nodal Force Vector
K	Stiffness Matrix
U	Global Nodal Displacement Vector
u	Displacement Field
Ni	Interpolation Function
ui	Nodal Displacements

I. Introduction

1.1 General

A structure is designed for a specific period and depending on the nature of the structure, its design life varies. For a domestic building, this design life could be as low as twenty-five years, whereas for a public building, it could be fifty years. Deterioration in concrete structures is a major challenge faced by the infrastructure and bridge industries worldwide. The deterioration can be mainly due to environmental effects, which includes corrosion of steel, gradual loss of strength with ageing, repeated high intensity loading, variation in temperature, freeze-thaw cycles, contact with chemicals and saline water and exposure to ultra-violet radiations. As complete replacement or reconstruction of the structure will be cost effective, strengthening or retrofitting is an effective way to strengthen the same. The most popular techniques for strengthening of RC beams have involved the use of external epoxy-bonded steel plates. It has been found experimentally that flexural strength of a structural member can increase by using this technique. Although steel bonding technique is simple, cost-effective and efficient, it suffers from a serious problem of deterioration of bond at the steel and concrete interphase due to corrosion of steel. Other common strengthening technique involves construction of steel jackets which is quite effective from strength, stiffness and ductility considerations. However, it increases overall cross-sectional dimensions, leading to increase in self-weight of structures and is labour intensive. To eliminate these problems, steel plate was replaced by corrosion resistant and light-weight FRP Composite plates. FRPCs help to increase strength and ductility without excessive increase in stiffness. Further, such material could be designed to meet specific requirements by adjusting placement of fibres. So concrete members can now be easily and effectively strengthened using externally bonded FRP composites. By wrapping FRP sheets, retrofitting of concrete structures provide a more economical and technically superior alternative to the traditional techniques in many situations because it offers high strength, low weight, corrosion resistance, high fatigue resistance, easy and rapid installation and minimal change in structural geometry. FRP systems can also be used in areas with limited access where traditional techniques would be impractical. However, due to lack of the proper knowledge on structural behavior of concrete structures, the use of these materials for retrofitting the existing concrete structures cannot reach up to the expectation. Successful retrofitting of concrete structures with FRP needs a thorough knowledge on the subject and available user-friendly technologies/ unique guidelines.

Beams are the critical structural members subjected to bending, torsion and shear in all type of structures. Similarly, columns are also used as various important elements subjected to axial load combined with/without bending and are used in all type of structures. Therefore, extensive research works are being carried out throughout world on retrofitting of concrete beams and columns with externally bonded FRP composites. Several investigators took up concrete beams and columns retrofitted with carbon fibre reinforced polymer (CFRP)/ glass fibre reinforced polymer (GFRP) composites in order to study the enhancement of strength and ductility, durability, effect of confinement, preparation of design guidelines and experimental investigations of these members.

1.2 Flexural Strengthening of Beams

For flexural strengthening, there are many methods such as: section enlargement, steel plate bonding, external post tensioning method, near-surface mounted (NSM) system and externally bonded (EB) system. While many methods of strengthening structures are available, strengthening structures via external bonding of advanced fibre-reinforced polymer composite (FRP) has become very popular worldwide. During the past decade, their application in this field has been rising due to the well-known advantages of FRP composites over other materials. Consequently, a great quantity of research, both experimental and theoretical, has been conducted on the behaviour of FRP-strengthened reinforced concrete (RC) structures. In this regard, the evolving technology of using carbon-bonded fibre-reinforced polymers (CFRP) for strengthening of RC beams has attracted much attention in recent years.

1.3 Advantages of FRP

Some of the main advantages of FRP can be listed below:

Low weight: The FRP is much less dense and therefore lighter than the equivalent volume of steel. The lower weight of FRP makes installation and handling significantly easier than steel. These properties are particularly important when installation is done in cramped locations. Other works like works on soffits of bridges and building floor slabs are carried out from man-access platforms rather than from full scaffolding. The use of fibre composites does not significantly increase the weight of the structure or the dimensions of the member. And because of their light weight, the transport of FRP materials has minimal environmental impact.

Mechanical strength: FRP can provide a maximum material stiffness to density ratio of 3.5 to 5 times that of aluminium or steel. FRP is so strong and stiff for its weight, it can out-perform the other materials.

Formability: The material can take up irregularities in the shape of the concrete surface. It can be moulded to almost any desired shape. We can create or copy most shapes with ease.

Chemical resistance: FRP is minimally reactive, making it ideal as a protective covering for surfaces where chemical

Joints: Laps and joints are not required.

Corrosion resistance: Unlike metal, FRP does not rust away and it can be used to make long-lasting structures.

Low maintenance: Once FRP is installed, it requires minimal maintenance. The materials fibres and resins are durable if correctly specified, and require little maintenance. If they are damaged in service, it is relatively simple to repair them, by adding an additional layer.

Long life: It has high resistance to fatigue and has shown excellent durability over the last 50 years.

Easy to apply: The application of FRP plate or sheet material is like applying wallpaper; once it has been rolled on carefully to remove entrapped air and excess adhesive it may be left unsupported. Fibre composite materials are available in very long lengths while steel plate is generally limited to 6 m. These various factors in combination lead to a significantly simpler and quicker strengthening process than when using steel plate.

1.4 Suitability of Frp for Uses in Structural Engineering

The strength properties of FRPs collectively make up one of the primary reasons for which civil engineers select them in the design of structures. A material's strength is governed by its ability to sustain a load without excessive deformation or failure. When an FRP specimen is tested in axial tension, the applied force per unit cross-sectional area (stress) is proportional to the ratio of change in a specimen's length to its original length (strain). When the applied load is removed, FRP returns to its original shape or length. In other words, FRP responds linear-elastically to axial stress. The response of FRP to axial compression is reliant on the relative proportion in volume of fibres, the properties of the fibre and resin, and the interface bond strength. FRP composite compression failure occurs when the fibres exhibit extreme (often sudden and dramatic) lateral or sides-way deflection called fibre buckling. FRP's response to transverse tensile stress is very much dependent on the properties of the fibre and matrix, the interaction between the fibre and matrix, and the strength of the fibre-matrix interface. Generally, however, tensile strength in this direction is very poor. Shear stress is induced in the plane of an area when external loads tend to cause two segments of a body to slide over one another. The shear strength of FRP is difficult to quantify. Generally, failure will occur within the matrix material parallel to the fibres. Among FRP's high strength properties, the most relevant features include excellent durability and corrosion resistance. Furthermore, their high strength-to-weight ratio is of significant benefit; a member composed of FRP can support larger live loads since its dead weight does not contribute significantly to the loads that it must bear. Other features include ease of installation, versatility, anti-seismic behaviour, electromagnetic neutrality, excellent fatigue behaviour, and fire resistance. However, like most structural materials, FRPs have a few drawbacks that would create some hesitancy in civil engineers to use it for all applications: high cost, brittle behaviour, susceptibility to deformation under long-term loads, UV degradation, photo-degradation (from exposure to light), temperature and moisture effects, lack of design codes, and most importantly, lack of awareness.

1.5 Applications of Frp Composites in Construction

There are three broad divisions into which applications of FRP in civil engineering can be classified: applications for new construction, repair and rehabilitation applications, and architectural applications. FRPs have been used widely by civil engineers in the design of new construction. Structures such as bridges and columns built completely out of FRP composites have demonstrated exceptional durability, and effective resistance to effects of environmental exposure. Pre-stressing tendons, reinforcing bars, grid reinforcement and dowels are all examples of the many diverse applications of FRP in new structures. One of the most common uses for FRP involves the repair and rehabilitation of damaged or deteriorating structures. Several companies across the world are beginning to wrap damaged bridge piers to prevent collapse and steel-reinforced columns to

improve the structural integrity and to prevent buckling of the reinforcement. Architects have also discovered the many applications for which FRP can be used. These include structures such as siding/cladding, roofing, flooring and partitions.

1.6 Current Research on FRP

A serious matter relating to the use of FRPs in civil applications is the lack of design codes and specifications. For nearly a decade now, researchers from Canada, Europe, and Japan have been collaborating their efforts in hope of developing such documents to provide guidance for engineers designing FRP structures.

1.7 Design Considerations

The development of the advanced composite technology is an engineer's dream for innovative design and application. The characteristics of a composite can be tailored and designed to meet any desired specifications. Most of the information and design data available on composites are in the aerospace applications, but they are protected under the guise of proprietary systems and/or military classified documents. Unlike conventional isotropic materials of steel and concrete, there are no readily available design charts and guidelines to help the structural engineer. When it comes to working with composites as opposed to conventional materials, as the author has discovered, the difference can be as dramatic as night and day.

1.8 Disadvantages of Frp

The main disadvantage of externally strengthening structures with fibre composite materials is the risk of fire, vandalism or accidental damage, unless the strengthening is protected. A particular concern for bridges over roads is the risk of soffit reinforcement being hit by over-height vehicles.

A perceived disadvantage of using FRP for strengthening is the relatively high cost of the materials. However, comparisons should be made on the basis of the complete strengthening exercise; in certain cases the costs can be less than that of steel plate bonding. A disadvantage in the eyes of many clients will be the lack of experience of the techniques and suitably qualified staff to carry out the work. Finally, a significant disadvantage is the lack of accepted design standards.

II. Review Of Literature

2.1 Brief Review

This chapter provides a review of literature on strengthening of RC concrete beams. This review comprises of literature on strengthened beam under two types of support condition i.e. simply supported and continuously supported.

2.1.1 Simply Supported Beam

Grace et al. (1999) investigated the behaviour of RC beams strengthened with CFRP and GFRP sheets and laminates. They studied the influence of the number of layers, epoxy types, and strengthening pattern on the response of the beams. They found that all beams experienced brittle failure, with appreciable enhancement in strength, thus requiring a higher factor of safety in design.

Experimental investigations, theoretical calculations and numerical simulations showed that strengthening the reinforced concrete beams with externally bonded CFRP sheets in the tension zone considerably increased the strength at bending, reduced deflections as well as cracks width (Ross et al., 1999; Sebastian, 2001; Smith & Teng, 2002; Yang et al., 2003; Aiello & Ombres, 2004). It also changed the behaviour of these beams under load and failure pattern. Most often the strengthened beams failed in a brittle way, mainly due to the loss of connection between the composite material and the concrete. The influence of the surface preparation of the concrete, adhesive type, and concrete strength on the overall bond strength is studied as well as characteristics of force transfer from the plate to concrete. They concluded that the surface preparation along with along with soundness of concrete could influence the ultimate bond strength. Thereafter, Study on debonding problems in concrete beams externally strengthened with FRP composites are carried out by many researchers.

Many investigators used externally bonded FRP composites to improve the flexural strength of reinforced concrete members. To evaluate the flexural performance of the strengthened members, it is necessary to study flexural stiffness of FRP strengthened members at different stages, such as pre-cracking, post-cracking and post-yielding. However, only few studies are focused on the reinforced concrete members strengthened under pre-loading or pre-cracking (Arduni & Nanni, 1997).

F. Ceroni(2010) investigated the experimental program on Reinforced Concrete (RC) beams externally strengthened with carbon Fibre Reinforced Plastic (FRP) laminates and Near Surface Mounted (NSM) bars under monotonic and cyclic loads, the latter ones characterized by a low number of cycles in the elastic and post-elastic range. Comparisons between experimental and theoretical failure loads are discussed in detail.

Obaidat et al. (2010) studied the Retrofitting of reinforced concrete beams using composite laminates

and the main variables considered are the internal reinforcement ratio, position of retrofitting and the length of CFRP. The experimental tests were performed to investigate the behaviour of beams designed in such a way that either flexural or shear failure will be expected. The beams were loaded in four-point bending until cracks developed. The beams were then unloaded and retrofitted with CFRP. Finally the beams were loaded until failure. The ABAQUS program was used to develop finite element models for simulation of the behaviour of beams. The concrete was modelled using a plastic damage model and two models, a perfect bond model and a cohesive model, were evaluated for the concrete-CFRP interface. From the analyses the load-deflection relationships until failure, failure modes and crack patterns were obtained and compared to the experimental results. The FEM results agreed well with the experiments when using the cohesive model regarding failure mode and load capacity while the perfect bond model was not able to represent the debonding failure mode. The results showed that when the length of CFRP increases the load capacity of the beam increases both for shear and flexural retrofitting. FEM results also showed that the width and stiffness of CFRP affect the failure mode of retrofitted beams. The maximum load increases with increased width. Increased CFRP stiffness increases the maximum load only up to a certain value of the stiffness, and thereafter it decreases the maximum load.

In another research, Hee Sun Kim (2011) carried on experimental studies of 14 reinforced concrete (RC) beams retrofitted with new hybrid fibre reinforced polymer (FRP) system consisting carbon FRP (CFRP) and glass FRP (GFRP). The objective of this study was to examine effect of hybrid FRPs on structural behavior of retrofitted RC beams and to investigate if different sequences of CFRP and GFRP sheets of the hybrid FRPs have influences on improvement of strengthening RC beams. The beams are loaded with different magnitudes prior to retrofitting in order to investigate the effect of initial loading on the flexural behavior of the retrofitted beam. The main test variables are sequences of attaching hybrid FRP layers and magnitudes of preloads. Under loaded condition, beams are retrofitted with two or three layers of hybrid FRPs, then the load increases until the beams reach failure. Test results conclude that strengthening effects of hybrid FRPs on ductility and stiffness of RC beams depend on orders of FRP layers.

2.1.2 Continuous Beam

Although several research studies have been conducted on the strengthening of simply supported reinforced concrete beams using external plates, there is very less reported work on the behaviour of strengthened continuous beams. Moreover, most design guidelines have been developed for simply supported beams with external FRP laminates. A critical literature review revealed that a minimum amount of research work had been done for addressing the possibility of strengthening the negative moment region of continuous beam using FRP materials. Grace et al., (1999) tested five continuous beams. Four different strengthening systems were examined. The first beam was strengthened only for flexure, while the second beam was strengthened for both flexure and shear. The third beam was strengthened with glass fibre reinforced polymer (GFRP) sheets, and the fourth beam was strengthened by using CFRP plates. The fifth beam was fabricated as control beam. All the beams were loaded and unloaded for at least one loading cycle before failure. The use of FRP laminates to strengthen continuous beams was effective for reducing deflections and for increasing their load carrying capacity. It was also concluded that the beams strengthened with FRP laminates exhibit smaller and better distributed cracks.

Grace et al., (2001) investigated the experimental performance of CFRP strips used for flexural strengthening in the negative moment region of a full-scale reinforced concrete beam. They considered two categories of beams (I and II) for flexural strengthening. Category I beams were designed to fail in shear and Category II beams were designed to fail in flexure. Five full scale concrete beams of each category were tested. It was found that Category I beams failed by diagonal cracking with local debonding at the top of the beams, meanwhile Category II beams failed by delamination at the interface of the CFRP strips and the concrete surface, both with and without concrete-cover failure by means shear/tension delamination. When the beams failed, the CFRP strips were not stressed to their maximum capacity, which led to ductile failures in all the beams. The maximum increase of load-carrying capacity due to strengthening was observed to be 29% for Category I beams, and 40% for Category II beams with respect to corresponding control beams.

On the other hand, Grace et al., (2005) performed another research work where three continuous beams were tested. One of those beam was considered as the reference beam and conventional ductile flexural failure occurred. They strengthened the other two beams along their negative and positive moment regions around the top and bottom face on both sides as a U-wrap. It was concluded that the strengthened beams with the triaxial fabric showed greater ductility than those strengthened with CFRP sheets.

In another research, El-Refaie et al., (2003) examined 11 reinforced concrete (RC) two-span beams strengthened in flexure with external bonded CFRP sheets. According to the arrangement of the internal steel reinforcement, the beams were classified into two groups. Each group included one non-strengthened reference beam. It was noted that, all strengthened beams exhibited less ductility compared with the non-strengthened control beams. An optimum number of CFRP layers were found beyond which there was no further

enhancement in the beam capacity. It was also investigated that extending the CFRP sheet length to cover the entire hogging or sagging zones did not prevent peeling failure of the CFRP sheets, which was the dominant failure mode of tested beams.

More recently, El-Refaie et al., (2003) tested five reinforced concrete continuous beams strengthened in flexure with external CFRP laminates. All beams had the same geometrical dimensions and internal steel reinforcement. The main parameters examined were the position and form of the CFRP laminates. Three of the beams were strengthened using different lay-up arrangements of CFRP reinforcement, and one was strengthened using CFRP sheets. The performance of the CFRP strengthened beams was compared with a non-strengthened reference beam. It was found that, peeling failure was the principal failure mode for all the strengthened tested beams. It was found that the longitudinal elastic shear stresses at the adhesive/concrete interface calculated at beam failure were close to the limiting value recommended in (Concrete Society Technical Report 55, 2000). They also found that, strengthened beams at both sagging and hogging zone produced the highest load capacity.

Ashour et al., (2004) tested 16 reinforced concrete (RC) continuous beams with different arrangements of internal steel bars and external CFRP laminates. All test specimens had the same geometrical dimensions and were classified into three groups according to the amount of internal steel reinforcement. Each group included one non-strengthened control beam designed to fail in flexure. Three failure modes were observed, namely laminate rupture, laminate separation and peeling failure of the concrete cover attached to the composite laminate. The ductility of all strengthened beams was reduced in comparison with their respective reference beam. Additionally, simplified methods for estimating the flexural load capacity and the interface shear stresses between the adhesive and the concrete material were presented. As in previous studies, they observed that increasing the CFRP sheet length in order to cover the entire negative or positive moment zones did not prevent peeling failure of the CFRP laminates.

Aiello et al., (2007) compared the behaviour between continuous RC beams strengthened with of CFRP sheets at negative or positive moment regions and RC beams strengthened at both negative and positive moment regions. All the beams were strengthened with one CFRP sheet layer and with the remark that the beams were not loaded at the middle of span. The control beams underwent a typical flexural and failure of the strengthened beams occurred by debonding of the CFRP sheets, together with concrete crushing. It was found out that when the strengthening was applied to both hogging and sagging regions, the ultimate load capacity of the beams was the highest and about 20% of moment redistribution could be achieved by CFRP sheets externally glued in the sagging region.

Recently, Maghsoudi et al., (2009) examined the flexural behaviour and moment redistribution of reinforced high strength concrete (RHSC) continuous beams strengthened with carbon fibre. They observed that by increasing the number of CFRP layers, the ultimate strength increases, meanwhile ductility, moment redistribution, and ultimate strain of CFRP sheet decrease. Test results also showed that by increasing the number of CFRP sheet layers, there was a change in the failure mode from tensile rupture to IC debonding. End U-straps were effective in limiting end debonding, but not intermediate span debonding.

Again, Akbarzadeh et al., (2010) conducted an experimental program to study the flexural behaviour and moment redistribution of reinforced high strength concrete (RHSC) continuous beams strengthened with CFRP and GFRP sheets. As the previous work, test results showed that by increasing the number of CFRP sheet layers, the ultimate strength increases, while ductility, moment redistribution, and ultimate strain of CFRP sheet decrease. However, by using the GFRP sheets in strengthening the continuous beams, it is possible to reduce the loss in ductility and moment redistribution but a significant increase in the ultimate strength cannot be achieved. The moment enhancement ratio of the strengthened continuous beams was significantly higher than the ultimate load enhancement ratio for the same beam. They also developed an analytical model for moment–curvature and load capacity which they used for the tested continuous beams in this current study and in other similar researches.

Finally, Majid Mohammed Ali Kadhim (2011) focused on the behavior of the high strength concrete continuous beam strengthened with carbon fibre-reinforced polymer (CFRP) sheet with different CFRP sheet lengths. Three full-scale continuous beams are analyzed under two points load, and the data of analysis are compared with the experimental data provided by other researchers. ANSYS program is used and the results obtained from analysis give good agreement with experimental data with respect to load–deflection curve, ultimate strength, and the crack patterns. The length of CFRP sheet is changed in the negative and positive regions and the results showed that the ultimate strength of the beam was reached when the value of $L_{\text{sheet}}/L_{\text{span}}$ reaches 1.0, and when the value decreases, the ultimate strength of beam also decreases a little (1.4%), but when it decreases less than 0.6, the ultimate strength also decreases a lot (15%).

From the above information, it is, thus, clear that there lies a vast scope of research in the field of retrofitting of RC continuous beam. Although a great deal of research has been carried out on simply supported reinforced concrete (RC) beams strengthened with Fibre Reinforced Polymer composites (FRP), a few works has been focused on continuous beams.

2.2 Objective and Scope of the Present Work

The objective of this work is to carry out the investigation of externally bonded RC continuous beams using FRP sheet. In the present work, behavior of RC continuous rectangular beams strengthened with externally bonded GFRP is experimentally studied. The beams are grouped into two series labeled S1 and S2. Each series have different longitudinal and transverse steel reinforcement ratios. All beams have the same geometrical dimensions. These beams are tested up to failure by applying two points loading to evaluate the enhancement of flexural strength due to strengthening. A finite element model has been developed to study the response of strengthened beams.

III. Experimental Study

The experimental study consists of casting of fourteen large scale continuous (two-span) rectangular reinforced concrete beams. All the beams weak in flexure are casted and tested to failure. The beams were grouped into two series labeled S1 and S2. Each series had different longitudinal and transverse steel reinforcement ratios which are mentioned in Table 3.6 and Table 3.7 for S1 and S2 respectively. Beams geometry as well as the loading and support arrangements are illustrated in Figure 3.6. All beams had the same geometrical dimensions: 150 mm wide \times 200 mm deep \times 2300 mm long. One beam from each series (S1 and S2) was not strengthened and was considered as a control beam, whereas all other beams from both the series were strengthened with externally bonded GFRP sheets. Experimental data on load, deflection and failure modes of each of the beams are obtained. The change in load carrying capacity and failure mode of the beams are investigated for different types of strengthening pattern.

3.1 Casting of Specimen

For conducting experiment, the proportion of **1: 1.67: 3.33** is taken for cement, fine aggregate and coarse aggregate. The mixing is done by using concrete mixture. The beams are cured for 28 days. For each beam six concrete cube specimens were made at the time of casting and were kept for curing. The uniaxial compressive tests on produced concrete (150 \times 150 \times 150 mm concrete cube) were performed and the average concrete compressive strength (fcu) after 28 days for each beam is shown in Table 3.6 and Table 3.7.

Table 3.1 Design Mix Proportions

Description	Cement	Sand (Fine Aggregate)	Coarse Aggregate	Water
Mix Proportion (by weight)	1	1.67	3.33	0.55
Quantities of materials (Kg/m ³)	368.42	533.98	1231.147	191.58

3.1.1 Materials for Casting

3.1.1.1 Cement

Portland Slag Cement (PSC) (Brand: Konark) is used for the experiment. It is tested for its physical properties in accordance with Indian Standard specifications. It is having a specific gravity of 2.96.

- (i) Specific gravity : 2.96
- (ii) Normal Consistency : 32%
- (iii) Setting Times : Initial : 105 minutes Final : 535 minutes.
- (iv) Soundness : 2 mm expansion
- (v) Fineness : 1 gm retained in 90 micron sieve

3.1.1.2 Fine Aggregate

The fine aggregate passing through 4.75 mm sieve and having a specific gravity of 2.67 are used. The grading zone of fine aggregate is zone III as per Indian Standard specifications.

3.1.1.3 Coarse Aggregate

The coarse aggregates of two grades are used one retained on 10 mm size sieve and another grade contained aggregates retained on 20 mm sieve. It is having a specific gravity of 2.72.

3.1.1.4 Water

Ordinary tap water is used for concrete mixing in all the mix.

3.1.1.5 Reinforcing Steel

All the beams were grouped into two series labeled S1 and S2. Each series had different longitudinal and transverse steel reinforcement ratios which are mentioned in Table 3.6 and Table 3.7.

Series S1 beams are reinforced with two 8 mm diameter at the bottom, two 12 mm diameter bars as top

reinforcement throughout the length and two 10 mm diameter bars at top tension zone. To strengthen the beam in shear, two different diameter bars is used for stirrups, 10 mm diameter is used in the shear zone of intermediate support and 8mm diameter is used in the zone of end support. The diameter variation is given due to higher shear force in intermediate or continuous support than end support. Series S2 beams were reinforced with two high-yield Strength Deformed bars of 10 mm diameter at the bottom and two 10 mm diameter bars at top tension zone, 6 mm bars were used as hanger bars, closed stirrups of 8 mm diameter high-yield Strength Deformed bars at 100 mm centres were provided to prevent shear failure.

Three bars of each diameter rods were tested in tensile and the measured average yield strength is averaged and shown in Table 3.3. The modulus of elasticity of steel bars was 2×10^5 MPa.

Table 3.2 Tensile Strength of the bars

Diameter of the reinforcement (mm)	Tensile strength (MPa)
8	523
10	429
12	578

3.1.2 Detailing Of Reinforcement

For the same series of continuous reinforced concrete beams, same arrangement for flexure and shear reinforcement is made.

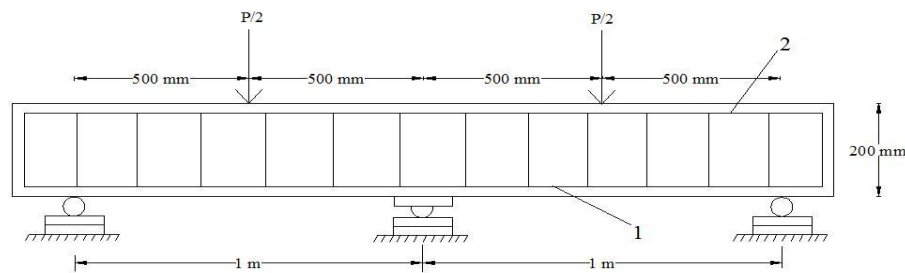


Figure 3.1 Detailing of reinforcement 1, 2 – top and bottom steel reinforcement

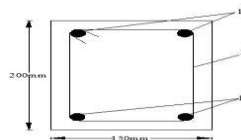


Figure 3.2 Cross section: 1 – Longitudinal rebars, 2 – close stirrups

3.1.3 Form Work



Figure 3.3 Steel Frame Used For Casting of Beam

3.1.4 Mixing Of Concrete

Mixing of concrete is done thoroughly with the help of machine mixer so that a uniform quality of concrete is obtained.

3.1.5 Compaction

Needle vibrator was used for proper Compaction and care is taken to avoid displacement of the reinforcement cage inside the form work. Then the surface of the concrete is leveled and smoothed by metal trowel and wooden float.

3.1.6 Curing Of Concrete

Curing is done to prevent the loss of water which is essential for the process of hydration and hence for hardening. Here curing is done by spraying water on the jute bags spread over the surface for a period of 28 days.

3.2 Strengthening Of Beams

At the time of bonding of fiber, the concrete surface is made rough using a coarse sand paper texture and then cleaned with an air blower to remove all dirt and debris. The fabrics are cut according to the size and after that the epoxy resin is mixed in accordance with manufacturer's instructions. The mixing is carried out in a plastic container (100 parts by weight of Araldite LY 556 to 10 parts by weight of Hardener HY 951). After the uniform mixing, the epoxy resin is applied to the concrete surface. Then the GFRP sheet is placed on top of epoxy resin coating and the resin is squeezed through the roving of the fabric with the roller. Air bubbles entrapped at the epoxy/concrete or epoxy/fabric interface are eliminated. This operation is carried out at room temperature. Concrete beams strengthened with glass fiber fabric are cured for at least 7 days at room temperature before testing.



Figure 3.4 Application of epoxy and hardener on the beam



Figure 3.5 Roller used for the removal of air bubble

3.3 Experimental Setup

The beams are tested in the loading frame of the “Structural Engineering” Laboratory of National Institute of Technology, Rourkela. The testing procedure for all the specimens is the same. The two-point loading arrangement is used for testing of beams. Two-point loading is conveniently provided by the arrangement shown in Figure 3.6.

The load is transmitted through a load cell and spherical seating on to a spreader beam. The spreader beam is installed on rollers seated on steel plates bedded on the test member with cement in order to provide a smooth leveled surface. The test member is supported on roller bearings acting on similar spreader plates. The specimen is placed over the two steel rollers bearing leaving 150 mm from the ends of the beam. The remaining 1000 mm is divided into two equal parts of 500 mm. Two dial gauges are placed just below the center of the mid span of the beam i.e. just below the load point for recording the deflection of the beams.

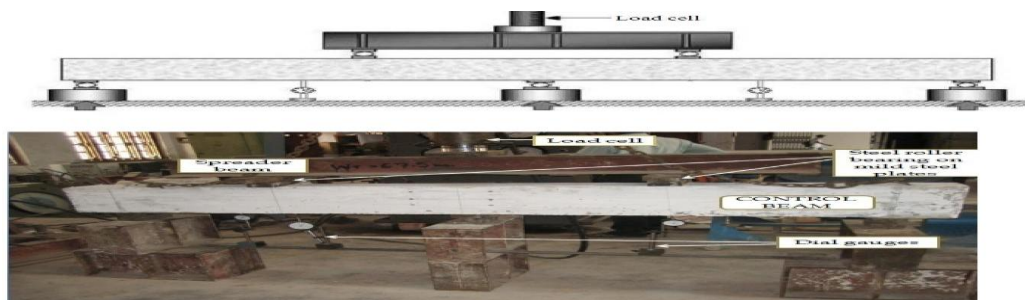


Figure 3.6 Experimental setup

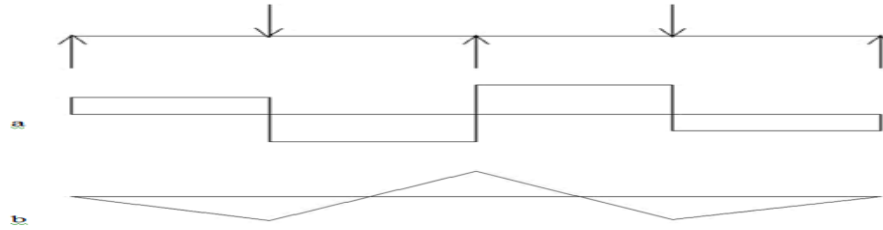


Figure 3.7 Continuous beam (a) Shear Force Diagram (b) Bending Moment Diagram

3.4 Fabrication of GFRP Plate

There are two basic processes for moulding: hand lay-up and spray-up. The hand lay-up process is the oldest and simplest fabrication method. The process is most common in FRP marine construction. In hand lay-up process, liquid resin is placed along with FRP against finished surface. Chemical reaction of the resin hardens the material to a strong light weight product. The resin serves as the matrix for glass fiber as concrete acts for the steel reinforcing rods.

The following constituent materials were used for fabricating plates:

1. Glass Fiber
2. Epoxy as resin
3. Diamine as hardener as (catalyst)
4. Polyvinyl alcohol as a releasing agent

A plastic sheet was kept on the plywood platform and a thin film of polyvinyl alcohol was applied as a releasing agent by the use of spray gun. Laminating starts with the application of a gel coat (epoxy and hardener) deposited in the mould by brush, whose main purpose was to provide a smooth external surface and to protect fibers from direct exposure from the environment. Steel roller was applied to remove the air bubbles. Layers of reinforcement were applied and gel coat was applied by brush. Process of hand lay-up is the continuation of the above process before gel coat is hardened. Again a plastic sheet was applied by applying polyvinyl alcohol inside the sheet as releasing agent. Then a heavy flat metal rigid platform was kept top of the plate for compressing purpose. The plates were left for minimum 48 hours before transported and cut to exact shape for testing.

Plates of 2 layers, 4 layers, 6 layers and 8 layers were casted and six specimens from each thickness were tested.

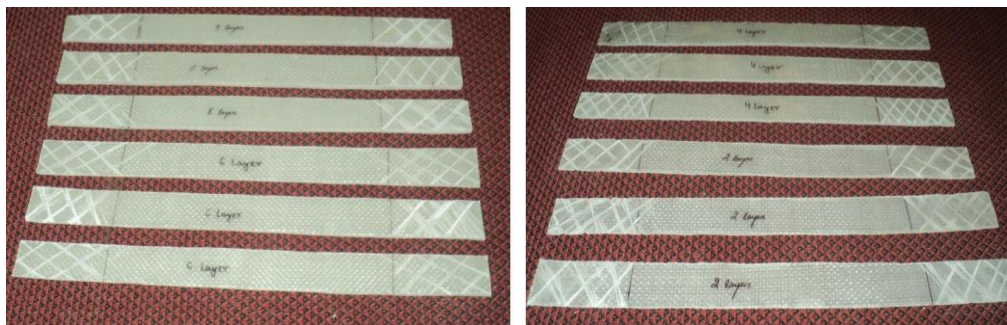


Figure 3.8 Specimens for tensile testing



Figure 3.9 Experimental set up of INSTRON 1195



Figure 3.10 Specimen failure after tensile test

Table 3.3 Size of the specimens for tensile test

No. of layers	Length (cm)	Width (cm)	Thickness (cm)
2	15	2.3	0.1
4	15	2.3	0.25
6	15	2.3	0.3
8	15	2.3	0.45

3.5 Determination of Ultimate Stress, Ultimate Load and Young's Modulus

The ultimate stress, ultimate load and young's modulus was determined experimentally by performing unidirectional tensile test on the specimens cut in longitudinal and transverse direction. The dimensions of the specimens are shown in Table 3.4. The specimens were cut from the plates by diamond cutter or by hex saw. After cutting by hex saw, it was polished in the polishing machine. For measuring the young's modulus, the specimen is loaded in INSTRON 1195 universal tensile test machine to failure with a recommended rate of extension. Specimens were gripped in the upper jaw first and then gripped in the movable lower jaw. Gripping of the specimen should be proper to prevent slippage. Here, it is taken as 50 mm from each side. Initially, the stain is kept zero. The load as well as extension was recorded digitally with the help of the load cell and an extensometer respectively. From these data, stress versus strain graph was plotted, the initial slope of which gives the Young's modulus. The ultimate stress and the ultimate load were obtained at the failure of the specimen. The average value of each layer of the specimens is given in the Table 3.5.

Table 3.4 Result of the specimens

Thickness of the specimen	Ultimate stress (MPa)	Ultimate Load (N)	Young's modulus (MPa)
2 Layers	172.79	6200	6829.9
4 Layers	209.09	9200	7788.5
6 Layers	236.23	12900	7207.4
8 Layers	253.14	26200	7333.14

3.6 Testing Of Beams

All the fourteen beams are tested one by one. All of them are tested in the above arrangement. The gradual increase in load and the deformation in the dial gauge reading are taken throughout the test. The load at which the first visible crack is developed is recorded as cracking load. Then the load is applied till the ultimate failure of the beam. The deflections at midpoint of each span are taken for all beams with and without GFRP and are recorded with respect to increase of load. The data furnished in this chapter have been interpreted and discussed in the next chapter to obtain a conclusion.

Table 3.5 Details of the Test Specimens for Series S1

Designation of Beams	f _{cu} (MPa)	Main Longitudinal steel		Positive moment strengthening		Negative moment strengthening	
		Top	Bottom	No. of layers	Strengthened length (m)	No. of layers	Strengthened length (m)
CB1	22.67	2-12 2-10*	2-8	-	-	-	-
SB1	23.3	2-12 2-10*	2-8	2	0.88m	6	0.88m
SB2	25.82	2-12 2-10*	2-8	1			
SB3	23.85	2-12 2-10*	2-8	2			
SB4	24.46	2-12 2-10*	2-8	3			
SB5	24.68	2-12 2-10*	2-8	4			
SB6	22.86	2-12 2-10*	2-8	4			
SB7	25.3	2-12 2-10*	2-8	2		4	
SB8	25.13	2-12 2-10*	2-8	3		6	
SB9	23.9	2-12 2-10*	2-8	2			

*provided at top tension zone

Table 3.6 Details of the Test Specimens for Series S2

Designation of Beams	f _{cu} (MPa)	Main Longitudinal steel		Positive moment strengthening		Negative moment strengthening	
		Top	Bottom	No. of layers	Strengthened length (m)	No. of layers	Strengthened length (m)
CB2	25.34	2-6, 2-10*	2-10	0	-	0	-
TB1	24.5	2-6, 2-10*	2-10	2	0.88m	6	0.88m
TB2	23.51	2-6, 2-10*	2-10	2			
TB3	25.61	2-6, 2-10*	2-10	4			

*provided at top tension zone

3.6.1 BEAM-1

CONTROL BEAM (CB1)

The control beam, CB1, failed in the RC conventional flexural mode due to yielding of internal tensile steel reinforcement. The wide flexural cracks were occurred at mid-span and central support. These cracks were well extended to the compressive regions.



Figure 3.11 Experimental Setup of the CB1



Figure 3.12 Flexural failure of CB1

3.6.2 BEAM-2

CONTROL BEAM (CB2)

The control beam, CB2 also failed in flexural failure as shown in Figure 3.13.



Figure 3.13 Control Beam, CB2 after failure

3.6.3 BEAM-3

STRENGTHENED BEAM 1 (SB1)

The beam was strengthened by applying two layers of FRP below the beam (width= 150 mm) from support to support and six layers of FRP above the central support (width= 150 mm) between two load points as shown in Figure 3.14. The strengthened beam SB1, showed crack at a load of 110 KN and failed by debonding failure in which the FRP sheet was separated without concrete cover and the ultimate failure occurred at 320KN as shown in Figure 3.15. The rupture of FRP sheet was sudden and accompanied by a loud noise indicating a rapid release of energy and a total loss of load capacity.



Figure 3.14 Experimental Setup of the Beam



Figure 3.15 Debonding failure of FRP



Figure 3.16 Magnified view of the failure of the beam

3.6.4 BEAM-4

STRENGTHENED BEAM 2 (SB2)

Single layer of U-wrap was applied on the beam to prevent flexural failure. Tensile rupture of FRP occurred at the mid section of both left and right span at lower loads and as the load increased, the beam failed in debonding with concrete cover as shown in Figure 3.17 and shear crack was developed below the FRP layer as shown in Figure 3.18.

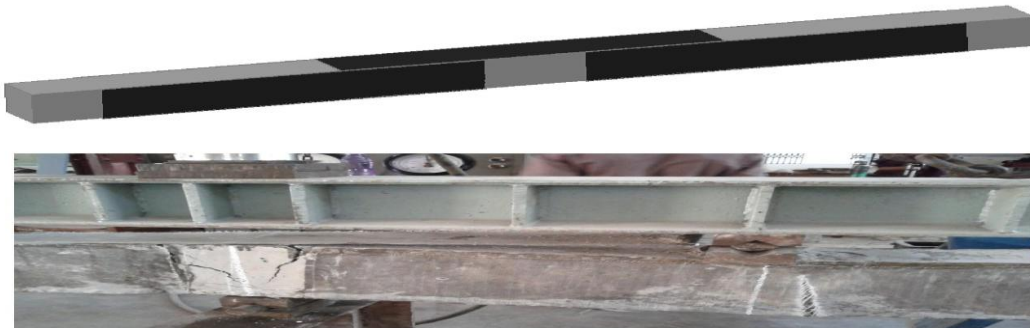


Figure 3.17 Tensile rupture of FRP at mid section of right span at lower value of load



Figure 3.18 Ultimate failure of beam by debonding of FRP with concrete cover

3.6.5 BEAM-5

STRENGTHENED BEAM 3 (SB3)

U- Jacketed double Layered GFRP was applied to enhance the load capacity as shown in the Figure3.19. By strengthening the RC beam using GFRP sheet, the cracking of the beam can be delayed and flexural capacity can be increased. The strengthened beam failed in debonding of FRP sheet (Figure 3.20).

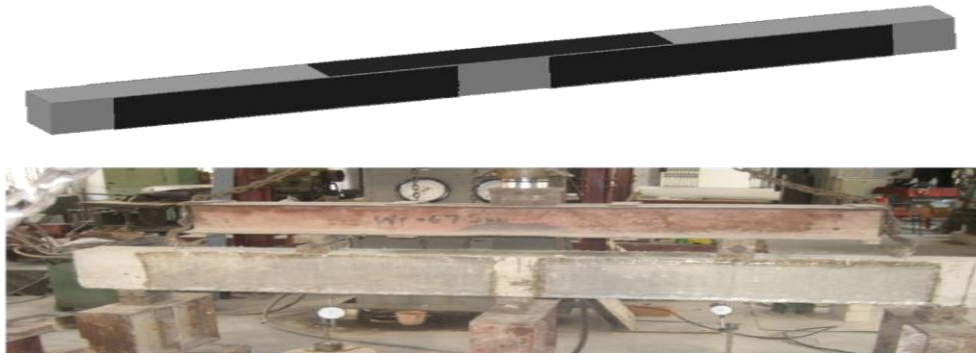


Figure 3.19 U-jacketed GFRP wrapped on the Beam SB3



Figure 3.20 Debonding failure of FRP

3.6.6 BEAM-6

STRENGTHENED BEAM 5 (SB4)

To prevent debonding, one layer of complete U-wrap was provided above the FRP of two layers which was applied at the soffit of the beam (width =150 mm) and one layer of U-strip of width 10 cm was applied over 6 layers FRP above the central support. Complete U-wrap took extra load and prevented the debonding, the failure mode was tensile rupture and as the U-strip could not prevent debonding of upper layer of FRP as it got ruptured at higher load value.



Figure 3.21 Strengthening pattern of beam SB4



Figure 3.22 Crack pattern after initial loading



Figure 3.23 Failure of the beam by tensile rupture

3.6.7 BEAM-7

STRENGTHENED BEAM 5 (SB5)

Same arrangement of FRP was made as SB4 and to enhance the capacity of beam SB4, two layers of complete U-wrap was provided in place of one layer and layers of U-strip of width 10 cm was applied instead of one layer.



Figure 3.24 Cracking pattern at lower load value



Figure 3.25 Rupture of GFRP sheet at mid section of the right span

3.6.8 BEAM-8

STRENGTHENED BEAM 6 (SB6)

Above the U- Jacketed double Layered GFRP, more two layers of FRP but half of the width of the first two layers, was applied at the flexural zone to prevent the flexural failure. In this case, instead of tensile rupture, debonding failure occurred as shown in Figure 3.27.



Figure 3.26 Debonding of FRP and cracking pattern above central support of the beam



Figure 3.27 Debonding failure of Strengthened beam SB6

3.6.9 BEAM-9

STRENGTHENED BEAM 7 (SB7)

The depth of the neutral axis was found out and the GFRP was provided up to the Neutral axis from the tension face. Here, shear crack was found and debonding occurred as shown in Figure 3.29.

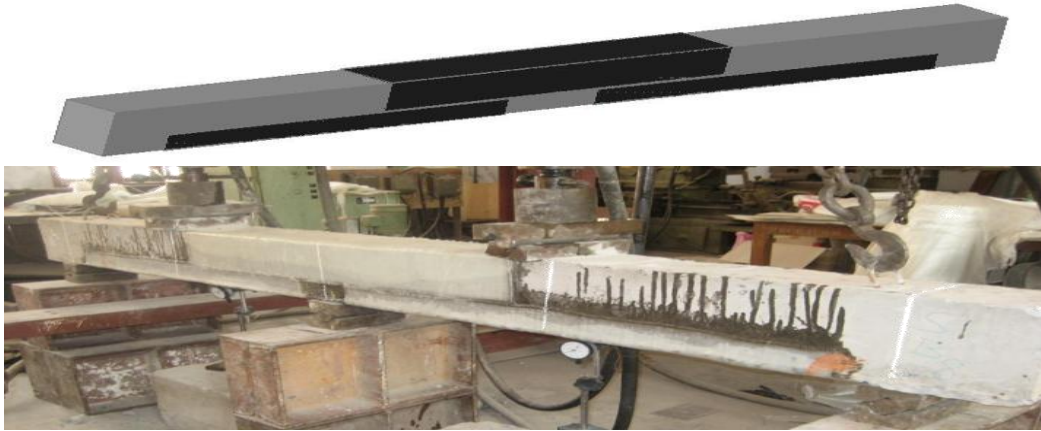


Figure 3.28 Strengthening pattern of SB7



Figure 3.29 Shear crack in the left span



Figure 3.30 Magnified view of shear crack and debonding of GFRP

3.6.10 BEAM-10

STRENGTHENED BEAM 8 (SB8)

The no. of FRP layers was increased here as compared to SB7 to examine the changes in load capacity or the failure pattern. The failure mode of the beam was debonding as shown in Figure 3.32.



Figure 3.31 Strengthening pattern of SB8



Figure 3.32 Failure of SB8 by debonding of GFRP

3.6.11 BEAM-11

STRENGTHENED BEAM 9 (SB9)

To prevent debonding of FRP, steel bolt system was introduced. The holes in the beam were made while casting of the beam and after applying FRP sheet to the beam the steel bolts were inserted into the hole and were tightened after placing the steel plate after the FRP. Anchoring plate, because of high compressive stress got buckled as shown in Figure 3.34.



Figure 3.33 Strengthening and anchoring pattern of SB9



Figure 3.34 Failure pattern of SB9



Figure 3.35 Magnified view of Debonding

3.6.12 BEAM-12

TB1

The strengthened beam showed crack at a load of 110 KN and failed by debonding failure in which the FRP sheet was separated without concrete cover at 224 KN which is shown in Figure 3.37. The rupture of FRP sheet was sudden and accompanied by a loud noise indicating a rapid release of energy and a total loss of load capacity. By strengthening the RC beam using GFRP sheet, the cracking of the beam can be delayed and flexural capacity can be increased.



Figure 3.36 Top FRP of Beam TB1 before Testing



Figure 3.37 FRP sheet separations without concrete

3.6.13 BEAM-13

TB2

Full double layered U-wrap was applied and six layers of FRP above the central support. The ultimate failure load was 298 KN.



Figure 3.38 Experimental set up and strengthening pattern of TB2



Figure 3.39 Failure of the beam by tensile rupture

3.6.14 BEAM-14

TB3

Above the U- Jacketed double Layered GFRP, more two layers of FRP but half of the width of the first two layers, was applied at the flexural crack zone to prevent the flexural failure. In this case, instead of tensile rupture, debonding failure occurred as shown in Figure 3.41 and the failure load was 326 KN.



Figure 3.40 Strengthened beam TB3



Figure 3.41 Failure of beam TB3



Figure 3.42 Shear crack in the left span



Figure 3.43 Failure mode of TB3

IV. Test Results And Discussions

The beams were loaded with a concentrated load at the middle of each span and the obtained experimental results are presented and discussed subsequently in terms of the observed mode of failure and load-deflection curve. The crack patterns and the mode of failure of each beam are also described in this chapter. All the beams are tested for their ultimate strengths and it is observed that the control beam had less load carrying capacity than the strengthened beam. Two sets of beams i.e. S1 and S2 were examined and one beam from each series was tested as un-strengthened control beam and rest beams were strengthened with various patterns of FRP sheets. The different failure modes of the beams were observed for both the series S1

and S2 as shown in Table 4.1 and Table 4.2.

4.1 Experimental Results

4.1.1 Failure Modes

4.1.1.1 Control Beam

The control beam CB1 and CB2 failed completely in flexure. The failure started first at the tension zone and then propagated towards the compression zone and finally failed in flexure.

4.1.1.2 Strengthened Beam

Generally, the rupture of FRP sheet was sudden and accompanied by a loud noise indicating a rapid release of energy and a total loss of load capacity. For all the strengthened beams, the failure modes for Series S1 and S2 are described in Table 4.1 and Table 4.2.

The following failure modes were examined for all the tested beams:

- Flexural failure
- Debonding failure (with or without concrete cover)
- Tensile rupture

Rupture of the FRP laminate is assumed to occur if the strain in the FRP reaches its design rupture strain before the concrete reaches its maximum usable strain. GFRP debonding can occur if the force in the FRP cannot be sustained by the substrate. In order to prevent debonding of the GFRP laminate, a limitation should be placed on the strain level developed in the laminate.

Table 4.1 Experimental Results of the Tested Beams for Series S1

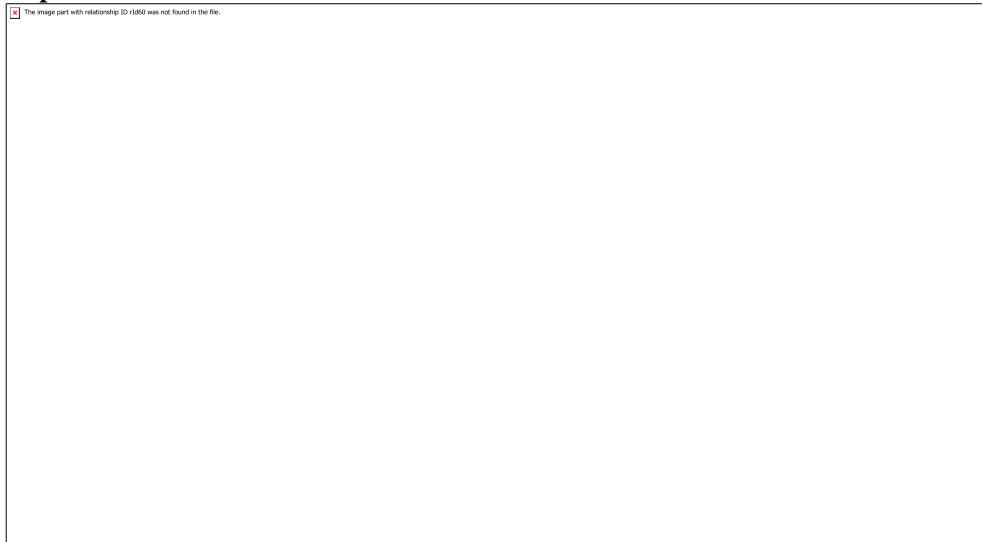


Table 4.2 Experimental Results of the Tested Beams for Series S2

Designation of Beams	Failure Mode	P_u (KN)	$\lambda = \frac{P_u(\text{strengthened beam})}{P_u(\text{Control beam})}$
CB2	Flexural failure	200	1
TB1	Debonding failure	224	1.12
TB2	Tensile rupture	298	1.49
TB3	Debonding of FRP	326	1.68

4.1.2 Load Deflection and Load Carrying Capacity

The GFRP strengthened beams and the control beams are tested to find out their ultimate load carrying capacity. The deflection of each beam under the load point i.e. at the midpoint of each span position is analyzed. Mid-span deflections of each strengthened beam are compared with the control beam. It is noted that the behavior of the flexure deficient beams when bonded with GFRP sheets are better than the control beams. The mid-span deflections of the beams are lower when bonded externally with GFRP sheets. The stiffness of the

strengthened beams was higher than that of the control beams. Increasing the numbers of GFRP layers generally reduced the mid span deflection and increased the beam stiffness for the same value of applied load. The use of GFRP sheet had effect in delaying the growth of crack formation.

The ultimate failure load for all the tested beams are summarized in Table 4.1 and Table 4.2. The ultimate load enhancement ratio (λ), which is the ratio of the ultimate load of the externally strengthened beam to the control beam, is presented in Table 4.1 and Table 4.2. From the two tables it is found that, addition of GFRP layers increased the ultimate load capacity and by introducing the anchoring system, the enhancement of load capacity can be done.

4.1.2.1 Strengthened Beam of S1 Series

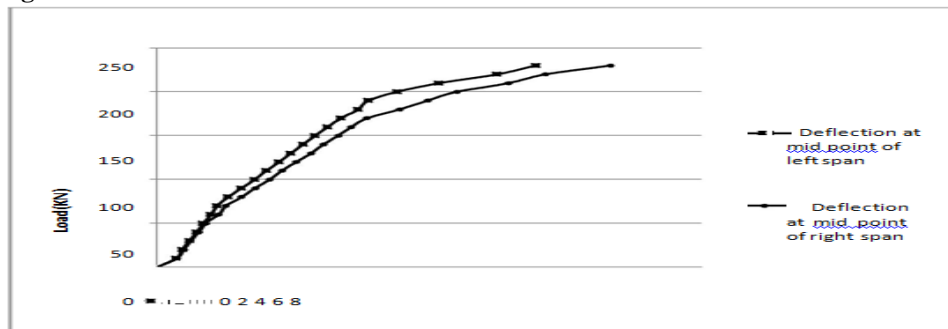


Figure 4.1 Load versus Deflection Curve for CB1

Beam 1 was taken as the control beam (CB1) which is weak in flexure and no strengthening was done to this beam. Two point static loading was applied on the beam and at the each increment of the load, deflection at midpoint of each span were taken with the help of dial gauges. Using this load and deflection data, load vs. deflection curve was plotted. At the load of 70 KN initial hairline cracks appeared. Later with the increase in loading values the crack propagated further. The Beam CB1 failed completely in flexure at the load of 260 KN.

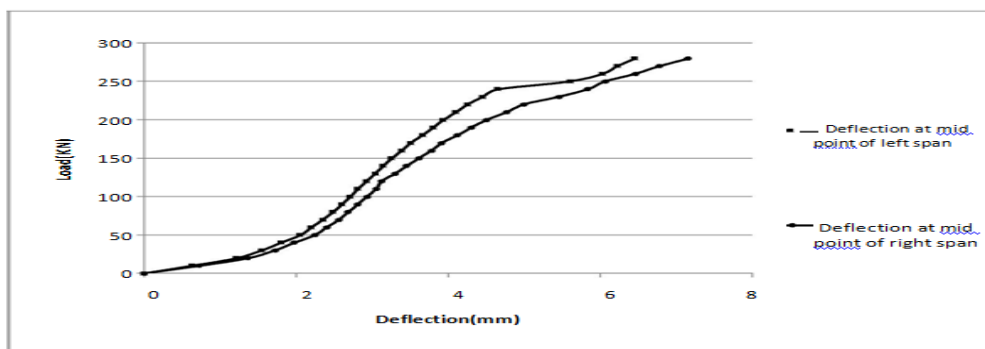


Figure 4.2 Load versus Deflection Curve for SB1

Beam-2, SB1 is strengthened by applying GFRP at the soffit from support to support and at the top between two load points. At the midpoint of each span, deflection values were taken and load versus deflection curve was plotted. The deflection values are less than that of the control beam for the same load value. At the load of 110 KN initial hairline cracks appeared. Later with the increase in loading values the crack propagated further. At lower load, debonding of FRP without concrete cover occurred and SB1 finally failed in concrete crushing with an ultimate load of 320 KN.

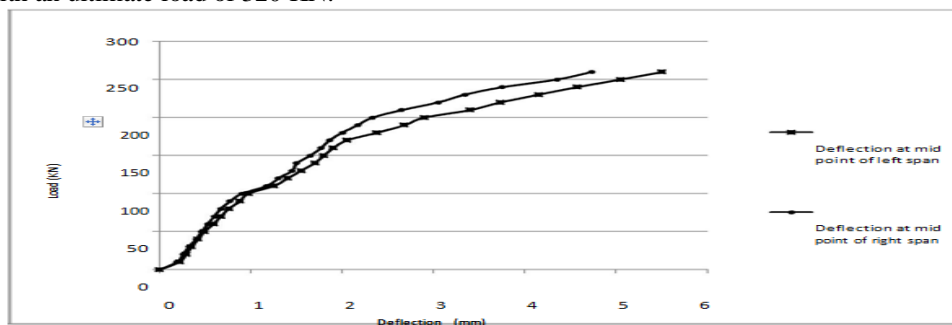


Figure 4.3 Load versus Deflection Curve for SB2

Beam-3, SB2 is strengthened with U-wrap from support to support distance and at the top of the beam between the two load points. The deflection values are less than that of the control beam for the same load value. No initial hairline cracks were visible due to the covering of GFRP. Later with the increase in loading values the crack propagated further under the GFRP. Tensile rupture took place at lower load and as the load increased, debonding of the FRP occurred with concrete cover and finally the beam failed in shear and the failure load was 325 KN.

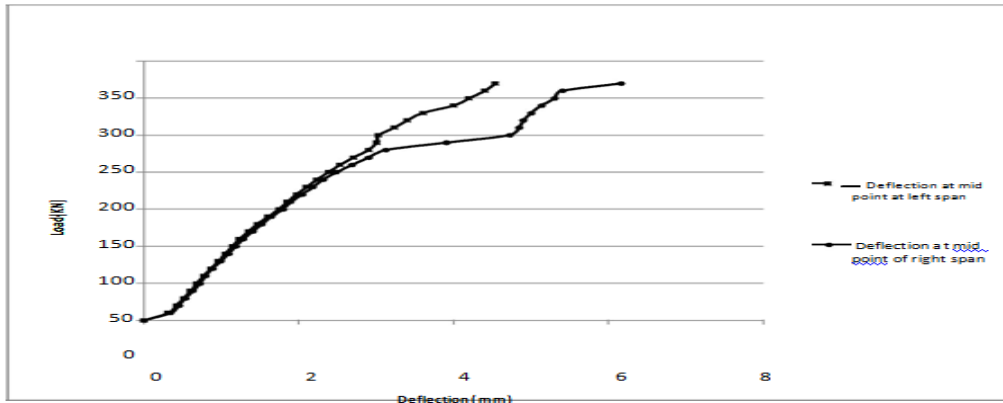


Figure 4.4 Load versus Deflection Curve for SB3

Beam-4, SB3 is strengthened with U-wrap from support to support distance, but the layers were increased and at the top of the beam between the two load points. The beam failed in debonding of FRP without concrete cover. The deflection values are remarkably less than that of the control beam and beam SB1 for the same load value. The cracking load was 120 KN and the failure load was 334 KN.

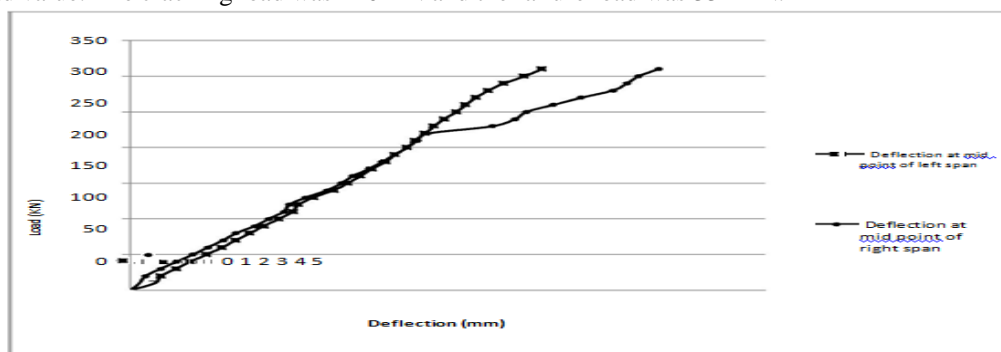


Figure 4.5 Load versus Deflection Curve for SB4

Beam-5, SB4 is strengthened providing FRP at the soffit of the beam from support to support distance and U-wrap above it, and at the top of the beam between the two load points and U-strip above it. Tensile rupture of FRP without concrete cover occurred and later with the increase in loading values the crack propagated further under the GFRP and beam failed in flexure. The failure load of SB4 was 370 KN. The deflection values are again remarkably less than that of the control beam for the same load value.

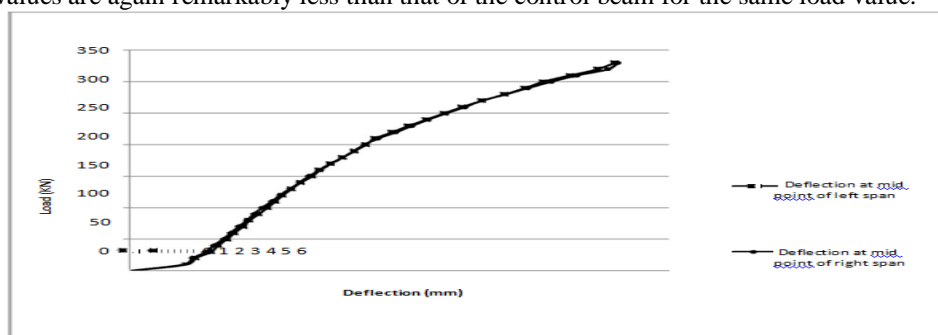


Figure 4.6 Load versus Deflection Curve for SB5

Beam-6, SB5 is strengthened providing FRP at the soffit of the beam from support to support distance and U-wrap above it, and at the top of the beam between the two load points and U-strip above it. Here the

numbers of FRP layers of U-wrap and U-strip were increased. Tensile rupture of FRP without concrete cover occurred at lower load value and later with the increase in loading values the crack propagated further under the GFRP and beam failed in flexure. The deflection values are less than that of the control beam for the same load value. The failure load of SB5 was 380 KN. The ultimate load of this beam was higher than the beam SB4, which was having same pattern of FRP wrapping.

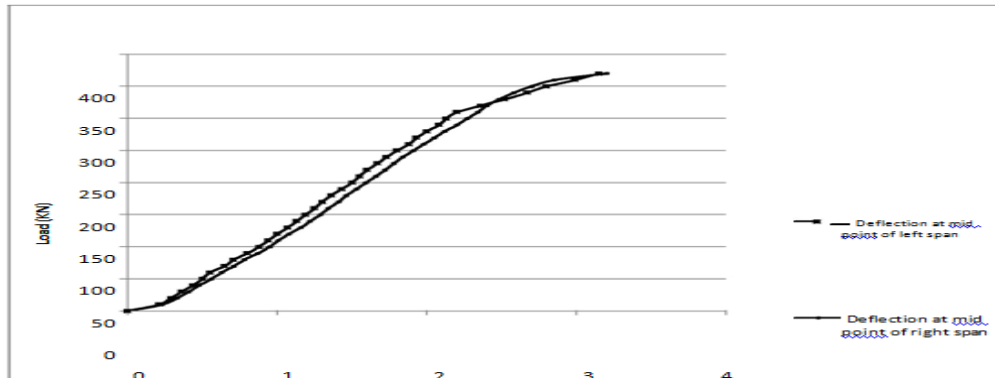


Figure 4.7 Load versus Deflection Curve for SB6

Beam-7, SB6 is strengthened providing U-wrap FRP from support to support distance and U-wrap FRP of half of the width above it, and at the top of the beam between the two load points. Debonding of FRP without concrete cover occurred first and later with the increase in loading values the crack propagated further under the GFRP and beam failed in flexure. The deflection values are quite less than that of the control beam for the same load value. The failure load of SB6 was 415 KN.

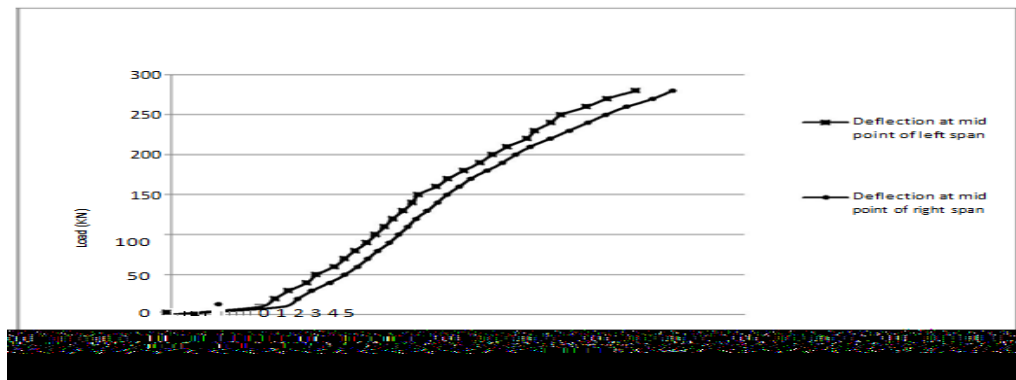


Figure 4.8 Load versus Deflection Curve for SB7

Beam-8, SB7 is strengthened providing U-wrap FRP from support to support distance up to Neutral axis and U-wrap FRP at the top of the beam between the two load points up to Neutral axis. Debonding of FRP without concrete cover occurred, with the increase in loading values the shear crack developed and propagated and beam failed in shear. The deflection values are quite less than that of the control beam for the same load value. The failure load of SB7 was 332 KN.

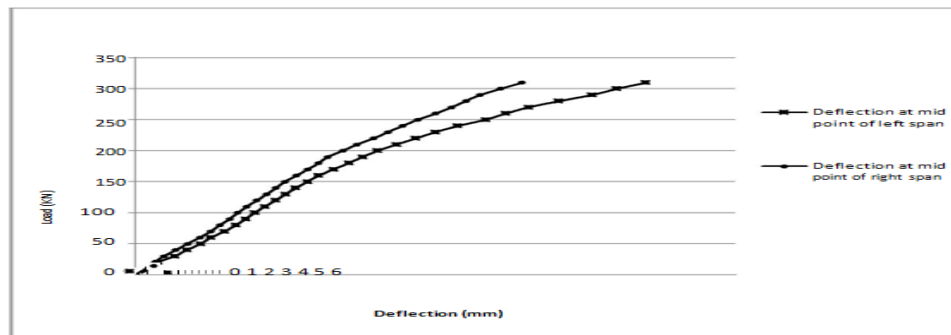


Figure 4.9 Load versus Deflection Curve for SB8

Beam-9, SB8 is strengthened providing U-wrap FRP from support to support distance up to Neutral axis and U-wrap FRP at the top of the beam between the two load points up to Neutral axis. Here the layers of the U-wrap were increased. Beam failed in debonding of FRP without concrete cover. Here also, the deflection

values are quite less than that of the control beam for the same load value. The failure load of SB8 was 345 KN.

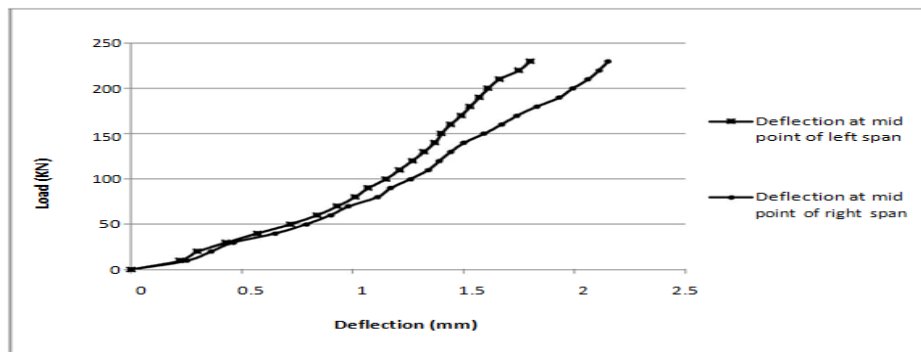
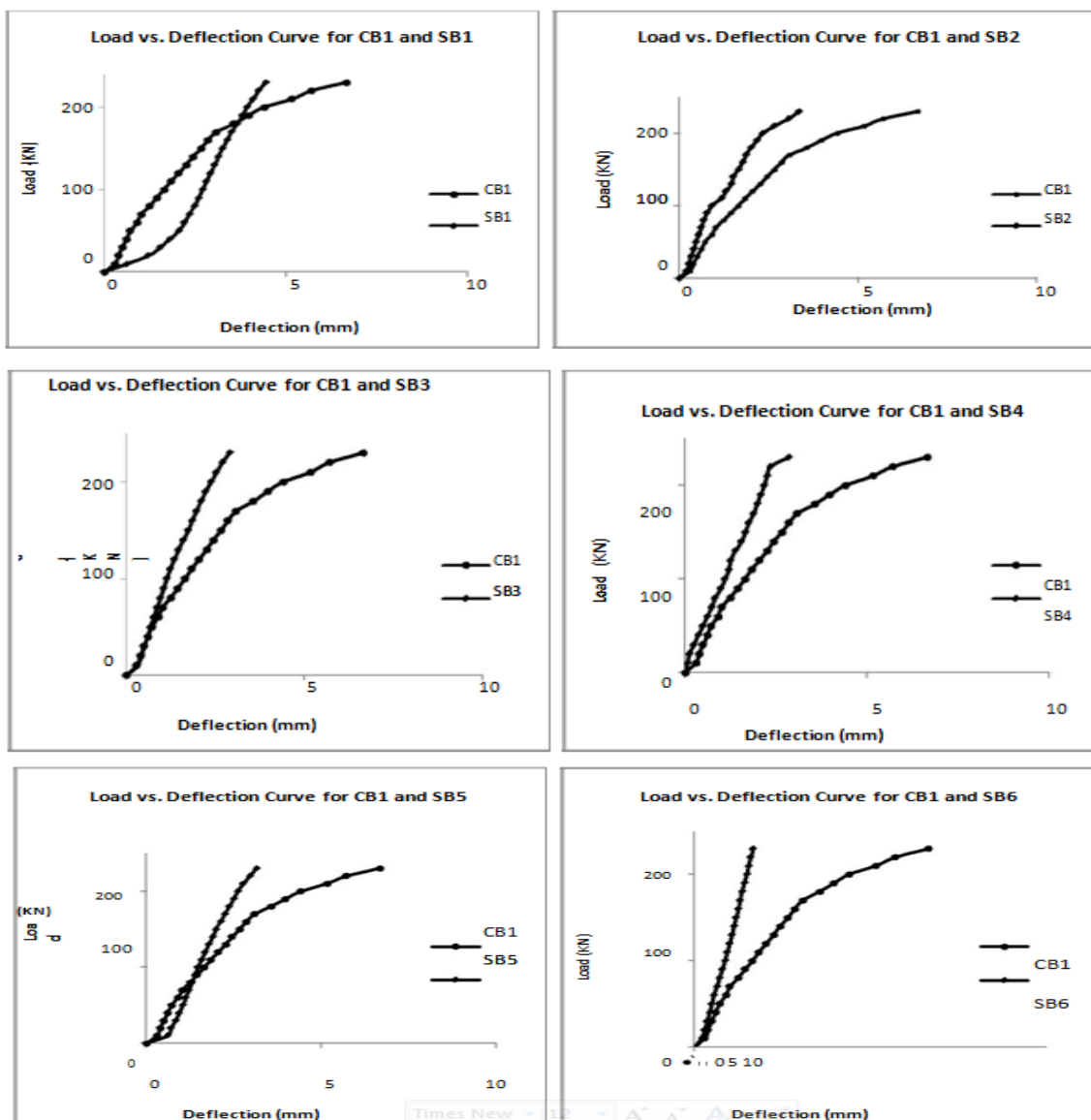


Figure 4.10 Load versus Deflection Curve for SB9

Beam-10, SB9 is strengthened as beam SB6, i.e. U-wrap FRP from support to support distance and U-wrap FRP of half of the width above it, and at the top of the beam between the two load points. Here, to prevent debonding failure anchoring system was introduced. It took more load than the corresponding beam SB6 and up to some load values it prevented the debonding failure. It prevented the debonding failure up to some extent and finally failed in flexure. The deflection values are quite less than that of the control beam for the same load value. The failure load of SB9 was 421 KN.



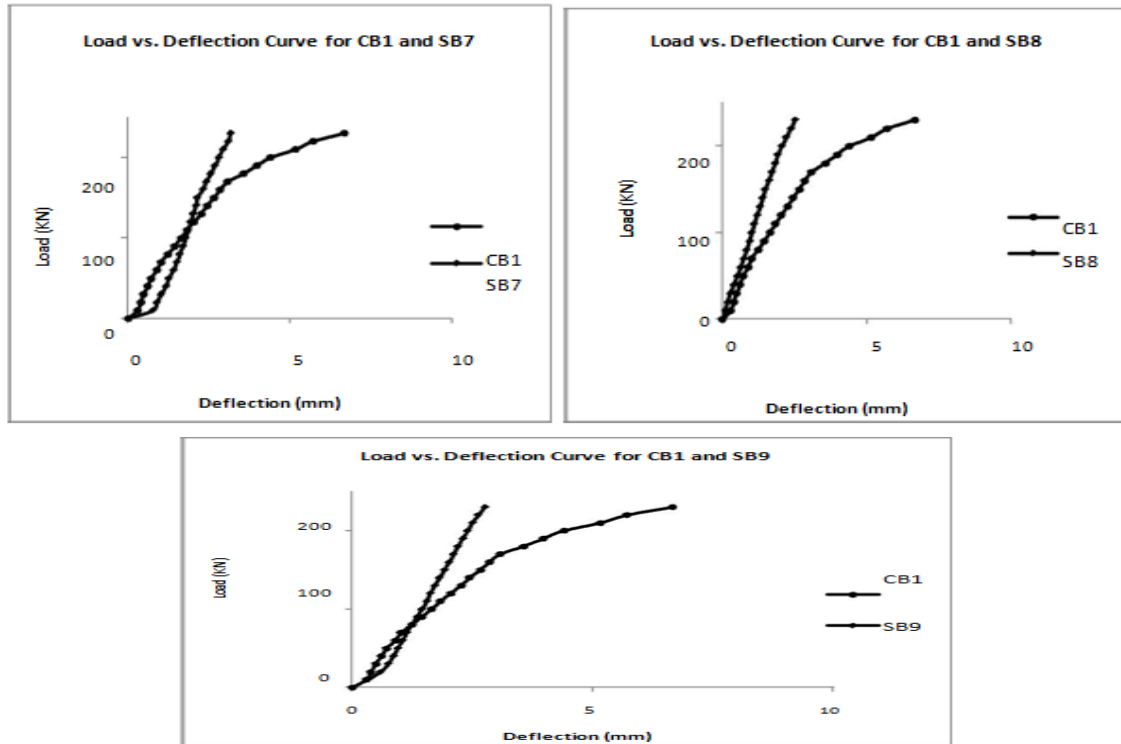


Figure 4.11 Load versus Deflection Curve for Set S1 strengthened beams with CB1

In Figure 4.11, the midpoint deflection values of all the strengthened beams were compared with the control beam CB1 separately and it was found that, by strengthening the beams with GFRP, the stiffness increased and the deflection value reduced up to some extent.

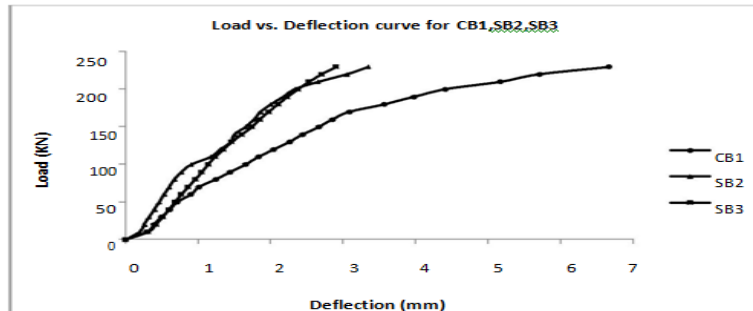


Figure 4.12 Load versus Deflection Curve for CB1, SB2, SB3

In SB2 one layer and in SB3 two layers of U-wrap were provided to strengthen the beams. The midpoint deflections were compared with the control beam and shown in Figure 4.12 from where it can be concluded that the deflection value is decreasing by strengthening the beams and by increasing the layers of GFRP, the stiffness of beam increases slightly.

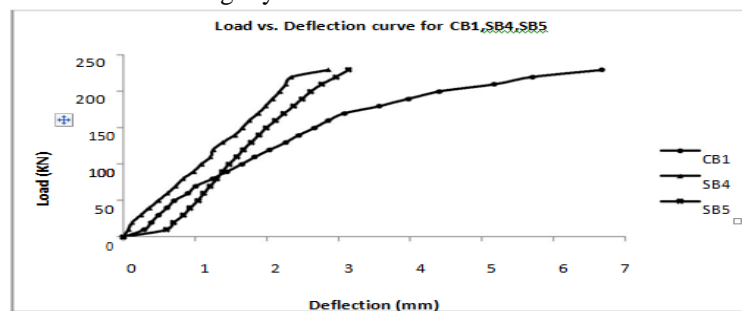


Figure 4.13 Load versus Deflection Curve for CB1, SB4, SB5

In SB4, one layer of U-wrap and U-strip and in SB5, two layers of U-wrap and two layers U-strip was

provided to strengthen the beams. The midpoint deflection was compared with the control beam and shown in Figure 4.13.

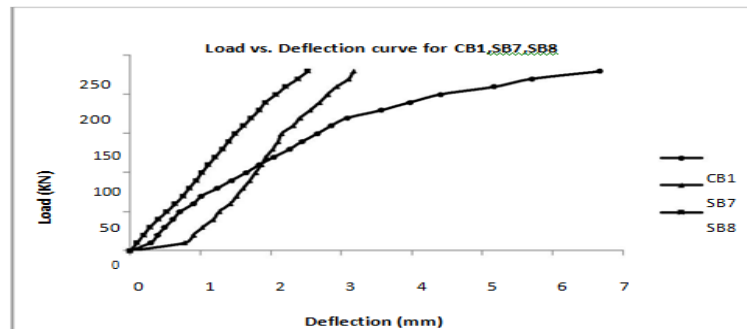


Figure 4.14 Load versus Deflection Curve for CB1, SB7, SB8

In SB7, two and four layers of U-wrap GFRP were provided below and above the Neutral axis respectively and in case of SB8 the GFRP layers were increased to three and six respectively. The midpoint deflections of SB1 and SB8 were compared to CB1 and from the plotted graphs and it is concluded that, by increasing the GFRP layers the stiffness of the beam can be increased.

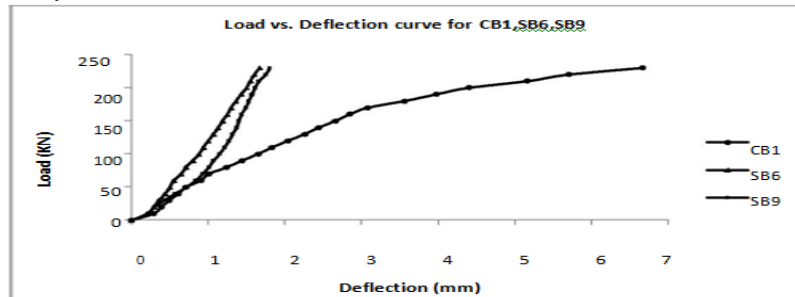


Figure 4.15 Load versus Deflection Curve for CB1, SB6, SB9

In SB9, Steel bolts were used to prevent the debonding failure of FRP. Here, the load capacity of SB9 was higher than SB6, the deflection values were less than CB1 as shown in Figure 4.15.

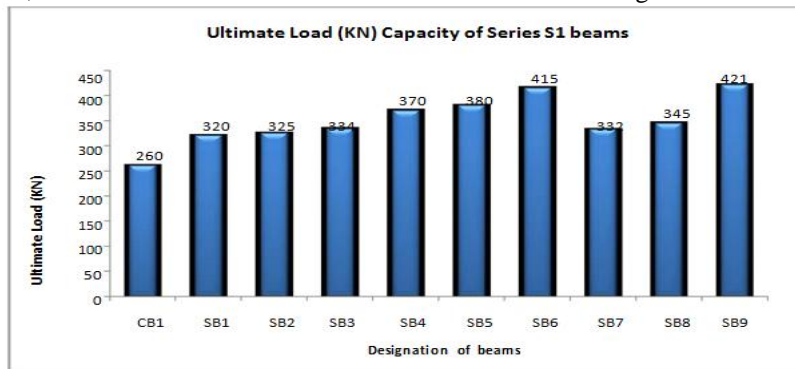


Figure 4.16 Ultimate Load Capacity of Series S1 beams

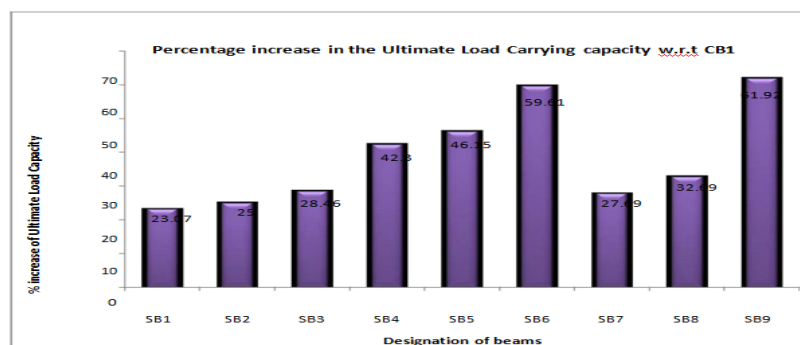


Figure 4.17 Percentage increase in the Ultimate Load Carrying capacity of strengthened beams of S1 w.r.t CB1

From Figure 4.16, it is concluded that the load capacity of SB9 beam is highest and SB6 beam has second highest load capacity among all the strengthened beams of Series S1. The percentage increase of load capacity of all the beams are calculated and are drawn in Figure 4.17 from which it can be concluded that, by application of GFRP to the beams the load capacity can be enhanced. Strengthened beam SB6 and SB9 gives the maximum percentage increase of load capacity.

4.1.2.2 Strengthened Beam of S2 Series

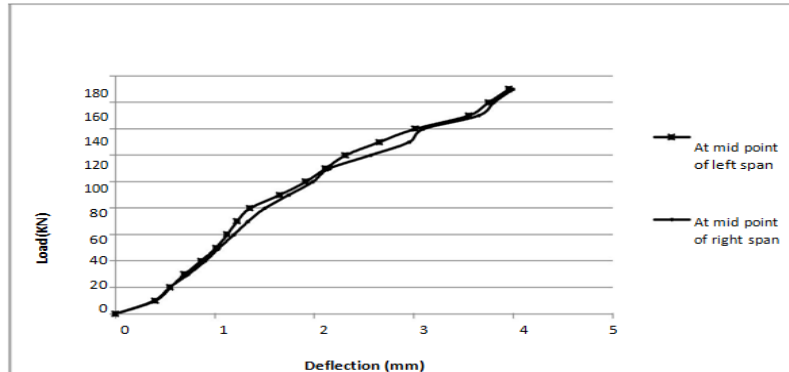


Figure 4.18 Load versus Deflection Curve for CB2

Beam 11, Control Beam for set S2, CB2, to which no external strengthening was provided, two point static loading was applied and at the each increment of the load, deflections at midpoint of each span were taken with the help of dial gauges. Using this load and deflection data, load vs. deflection curve was plotted. At the load of 110 KN initial hairline cracks appeared and the beam failed in flexure with an ultimate load value of 200 KN.

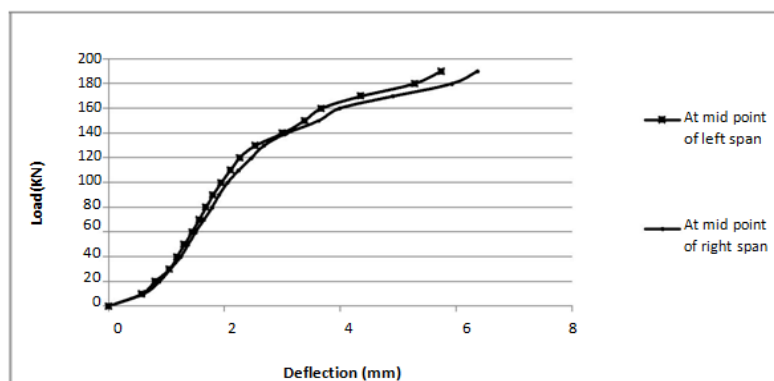


Figure 4.19 Load versus Deflection Curve for TB1

Beam-12, TB1 is strengthened at the soffit from support to support and at the top between two load points. At the midpoint of each span, deflection values were taken and load versus deflection curve was plotted. The deflection values are less than that of the control beam for the same load value. At lower load value, debonding of FRP without concrete cover occurred and TB1 finally failed in concrete crushing. At the load of 120 KN initial hairline cracks appeared. Later with the increase in loading values the cracks propagated further and the beam failed with an ultimate load of 224 KN.

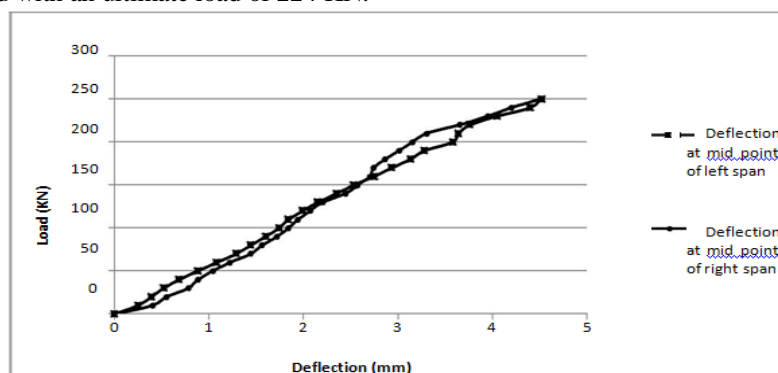


Figure 4.20 Load versus Deflection Curve for TB2

Beam-13, TB2 is strengthened with U-wrap from support to support distance and at the top of the beam between the two load points but the layers of U-wrap was increased here. The deflection values are less than that of the control beam for the same load value. The beam failed in tensile rupture followed by flexural failure. The cracking load was 210 KN and the failure load was 298 KN.

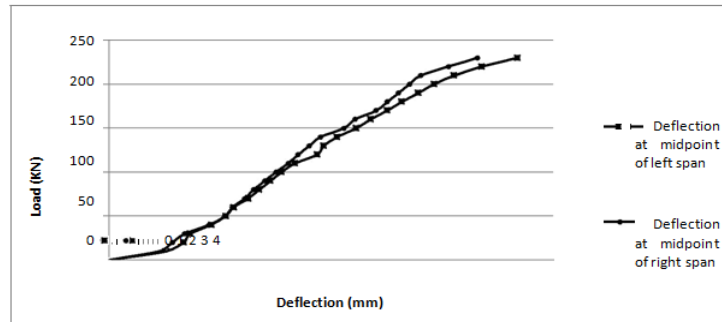


Figure 4.21 Load versus Deflection Curve for TB3

Beam-14, TB3 failed in debonding of FRP without concrete cover followed by shear crack. The deflection values are remarkably less than that of the control beam, CB2 and strengthened beam TB1 for the same load value. The failure load was 326 KN.

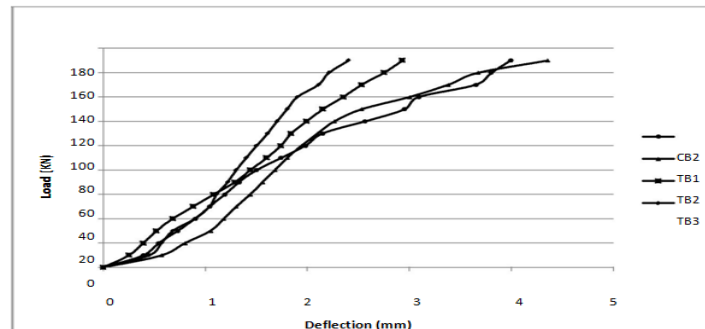


Figure 4.22 Load vs. Deflection Curve for all the Beams of S2

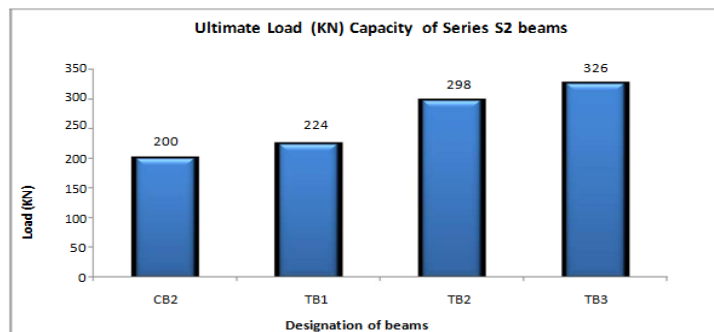


Figure 4.23 Ultimate Load (KN) Capacity of Series S2 beams

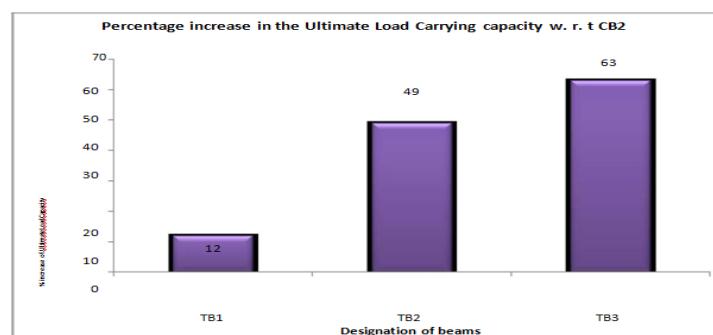


Figure 4.24 Percentage increase in the Ultimate Load Carrying capacity of strengthened beams of S2 w.r.t CB2

The load capacity and the percentage increase of all the strengthened beams of series S2 are discussed here and from Figure 4.23 and Figure 4.24, it is found that beam TB3 has the maximum load capacity and maximum percentage increase of load carrying capacity respectively.

V. Finite Element Analysis

Finite element method (FEM) is a numerical method for solving a differential or integral equation. It has been applied to a number of physical problems, where the governing differential equations are available. The method essentially consists of assuming the piecewise continuous function for the solution and obtaining the parameters of the functions in a manner that reduces the error in the solution.

5.1 Formulation

The governing equation for beam is given in Equation 5.1.

$$M = \frac{d^2 v}{dx^2} EI \quad (5.1)$$

The displacement field $v(x)$ assumed for the beam element should be such that it takes on the values of deflection and the slope at either end as given by the nodal values $v_i, \theta_i, v_j, \theta_j$.

The $v(x)$ can be given by,

$$v(x) = c_0 + c_1 x + c_2 x^2 + c_3 x^3 \quad (5.2)$$

In solving the differential equations through integration, there will be constants of integration that must be evaluated by using the boundary and continuity conditions. The variables whose values are to be determined are approximated by piecewise continuous polynomials. The coefficients of these polynomials are obtained by minimizing the total potential energy of the system. In FEM, usually, these coefficients are expressed in terms of unknown values of primary variables. Thus, if an element has got n nodes, the displacement field u can be approximated as,

$$u = \sum_{i=1}^n N_i u_i \quad (5.3)$$

where u_i are the nodal displacements in x -direction and N_i are the shape functions, which are functions of coordinates. Shape functions or interpolation functions N_i are used in the finite element analysis to interpolate the nodal displacements of any element to any point within each element. The beam element has modulus of elasticity E , moment of inertia I , and length L . Each beam element has two nodes and is assumed to be horizontal as shown in Figure 5.1. The element stiffness matrix is given by the following matrix, assuming axial deformation is neglected.

$$K = \frac{EI}{L^3} \begin{bmatrix} 12 & 6L & -12 & 6L \\ 6L & 4L^2 & -6L & 2L^2 \\ -12 & -6L & 12 & -6L \\ 6L & 2L^2 & -6L & 4L^2 \end{bmatrix} \quad (5.4)$$

It is clear that the beam element has four degrees of freedom: two at each node (a transverse displacement and a rotation). The sign convention used is that the displacement is positive if it points upwards and the rotation is positive if it is counter clockwise. Consequently for a structure with n nodes, the global stiffness matrix K will be of size $2n \times 2n$ (since we have two degrees of freedom at each node). Once the global stiffness matrix K is obtained we have the following structure equation

$$[K] \{U\} = \{F\} \quad (5.5)$$

where U is the global nodal displacement vector and F is the global nodal force vector.

First the boundary conditions are applied manually to the vectors U and F . Then the matrix (5.5) is solved by partitioning and Gaussian elimination. Finally once the unknown displacements and reactions are found, the nodal force vector is obtained for each element as follows:

$$\{f\} = [k] \{u\} \quad (5.6)$$

where $\{f\}$ is the 4×1 nodal force vector in the element and u is the 4×1 element displacement vector. The first and second elements in each vector $\{u\}$ are the transverse displacement and rotation, respectively, at the first node, while the third and fourth elements in each vector $\{u\}$ are the transverse displacement and rotation, respectively, at the second node.

5.2 Validation of Experimental Value

In the experimental work, the tested beams consist of two spans of each 1000 mm as shown in Figure 5.1 is discretized as shown in Figure 5.2.

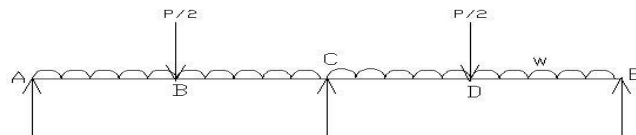


Figure 5.1 Continuous beam

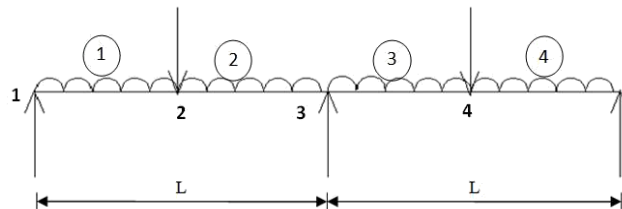


Figure 5.2 Finite element model



Figure 5.3 Beam element forces

The following sign convention is considered for the deflection calculation.

- (a) x is +ve towards right
- (b) y is +ve upwards
- (c) Anticlockwise slopes are +ve
- (d) Sagging BM are +ve

Four element mesh is taken as shown in Figure 5.2. Subdividing the span AC into two elements with a node at the load point has the advantage that, the nodal forces can be specified very easily. The meshing has also ensured that all elements are of uniform size, for easy hand calculation. Following the standard procedure, the global stiffness matrix and force vector is obtained as below,

$$[K]_{10 \times 10} \{U\}_{10 \times 1} = \{F\}_{10 \times 1} \quad (5.7)$$

Since there are five nodes and two d.o.f. per node, the global stiffness matrix is of size (10×10) and $\{F\}$ is a column vector of size (10×1) . The boundary conditions stipulate that the vertical deflection be zero at node 1, 5 and 9. Boundary conditions are the known values of deflection and slope at specified values of x . Here the following boundary conditions are used for the exact analysis of the continuous beam.

At $x = 0$; $y = 0$ At $x = L$; $y = 0$ At $x = 2L$; $y = 0$

Thus reduced set of equations involving unknown nodal d.o.f. is obtained in matrix form as,

$$\{f\}_{7 \times 1} = [k]_{7 \times 7} \{u\}_{7 \times 1} \quad (5.8)$$

Solving the Equation 5.8, the nodal displacement is found out.

The experimental and numerical load-deflection curves obtained for the control beam, CB1 are illustrated in Figure 5.4.

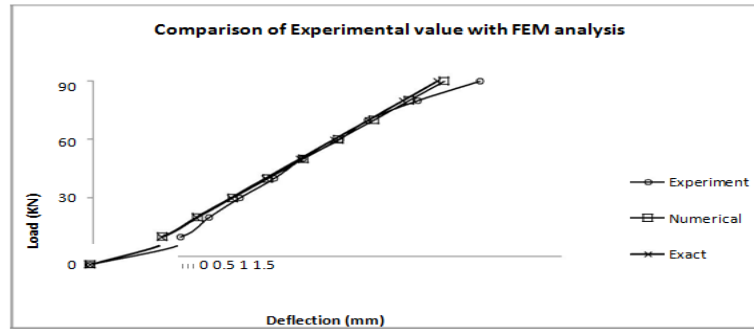


Figure 5.4 Comparison of Experimental value with Numerical and Exact analysis for CB1

The numerical and experimental results for the beam are shown in Figure 5.4. The trend of the loads varying with the deflection presents that the linear elastic state exists in the structure, when the loads are equivalent to about 90 KN.

VI. Conclusions

6.1 Conclusions

The present experimental study is carried out on the flexural behavior of reinforced concrete rectangular beams strengthened by GFRP sheets. Fourteen reinforced concrete (RC) beams weak in flexure having different set of reinforcement detailing are casted and tested. The beams were grouped into two series labeled S1 and S2. Each series had different longitudinal and transverse steel reinforcement ratios. From the test results and calculated strength values, the following conclusions are drawn:

1. The ultimate load carrying capacity of all the strengthen beams is higher when compared to the control beam.
2. The initial cracks in the strengthened beams are formed at higher load compared to control beam.
3. From series S1, beam SB9 which was strengthened by U-wrap and was anchored by using steel plate and bolt system, showed the highest ultimate load value of 415 KN. The percentage increase of the load capacity of SB9 was 61.92 %.
4. The load carrying capacity of beam SB6, which was strengthened by two layers of U-wrap of length 88 cm in positive moment zone and two layers of U-wrap of length 44 cm over first two layers, was 415 KN which was nearer to the load capacity of beam SB9. The percentage increase of load carrying capacity was 59.61 % , from which it can be concluded that applying FRP in the flexure zone is quite effective method to enhance the load carrying capacity.
5. TB3 beam from Series S2, which was strengthened by two layers of U-wrap in positive moment zone and two layers of U-wrap in flexure zone above first two layers, was having maximum ultimate load value of 326 KN, than the other strengthened beams of same category. The percentage increase of this beam was 63 % which was highest among all strengthened beams.
6. Using of steel bolt and plate system is an effective method of anchoring the FRP sheet to prevent the debonding failure.
7. Strengthening of continuous beam by providing U-wrap of FRP sheet is a new and effective way of enhancing the capacity of load carrying.
8. Flexural failure at the intermediate support section can be prevented by application of GFRP sheets.
9. In lower range of load values the deflection obtained using Finite Element models are in good agreement with the experimental results. For higher load values there is a deviation with the experimental results because linear FEM has been adopted.

6.2 Scope Of The Future Work

It promises a great scope for future studies. Following areas are considered for future research:

- a. Experimental study of continuous beams with opening
- b. Non linear analysis of RC continuous beam
- c. FEM modeling of unanchored U-wrap
- d. FEM modeling of anchored U-wrap

REFERENCES

- [1] ACI Committee 440, "Starte-of-the-art report on fiber reinforced plastic reinforcement for concrete structures", Report ACI 440R-96, USA: American Concrete Institute, 1996.
- [2] Aiello MA, Valente L, and Rizzo A, "Moment redistribution in continuous reinforced concrete beams strengthened

- with carbon fiber-reinforced polymer laminates”, *Mechanics of Composite Materials*, vol. 43, pp. 453-466, 2007.
- [3] Aiello MA, and Ombres L, “Cracking and deformability analysis of reinforced concrete beams strengthened with externally bonded carbon fiber reinforced polymer sheet”, *ASCE Journal of Materials in Civil Engineering*, vol. 16, No. 5, pp.292-399,2004.
- [4] Akbarzadeh H, and Maghsoudi AA, “Experimental and analytical investigation of reinforced high strength concrete continuous beams strengthened with fiber reinforced polymer”, *Materials and Design*, vol. 31, pp. 1130-1147, 2010.
- [5] Arduini M, and Nanni A, “Behaviour of pre-cracked R. C. beams strengthened with carbon FRP sheets”, *ASCE Journal of Composites for Construction*, vol. 1, No. 2, pp. 63-70, 1997.
- [6] Ashour AF, El-Refaie SA, and Garrity SW, “Flexural strengthening of RC continuous beams using CFRP laminates”, *Cement and Concrete Composites*, vol. 26, pp. 765-775, 2003.
- [7] Bank LC, and Arora D, “Analysis of RC beams strengthened with mechanically fastened FRP (MF-FRP) strips”, *Composite Structures*, vol. 79, pp. 180–191, 2006.
- [8] Bousselham A and Chaallal O, “Behavior of reinforced concrete T-beams strengthened in shear with carbon fiber reinforced polymer - an experimental study”, *ACI Structural Journal*, vol. 103, pp. 339–347, 2006.
- [9] Brosens K, and Gemert D, “Anchoring stresses between concrete and carbon fiber reinforced laminates”, *Non-metallic (FRP) Reinforcement for Concrete Structures*, Proc.of 3rd International Symposium, Sapporo, Japan, pp. 271–278, 1997.
- [10] Ceroni F, “Experimental performances of RC beams strengthened with FRP materials”, *Construction and Building Materials*, vol. 24, pp. 1547-1559, 2010.
- [11] Chahrouh A, and Soudki K, “Flexural response of reinforced concrete beams strengthened with end-anchored partially bonded carbon fiber-reinforced polymer strips”, *Journal of Composites for Construction ASCE*, vol. 9(2), pp. 170–177, 2005.
- [12] Concrete Society, “Design guidance for strengthening concrete structures using fibre composite materials”, Report No. 55, 71p, 2000.
- [13] El-Refaie SA, Ashour AF, and Garrity SW, “CFRP strengthened continuous concrete beams”, *Proceedings of the ICE - Structures and Buildings*, pp. 395 - 404, 2003.
- [14] El-Refaie SA, Ashour AF, and Garrity SW, “Sagging and hogging strengthening of continuous reinforced concrete beams using carbon fibre-reinforced polymer sheets”, *ACI Structural Journal*, vol. 100, pp. 446-453, 2003.
- [15] El-Refaie SA, Ashour AF, and Garrity SW, “Sagging strengthening of continuous reinforced concrete beams using carbon fibre sheets”, *The 11th BCA Annual Conference on Higher Education and the Concrete Industry*, Manchester, UK, pp. 281–292, 3–4 July 2001.
- [16] El-Refaie SA, Ashour AF, and Garrity SW, “Strengthening of reinforced concrete continuous beams with CFRP composites”, *The International Conference on Structural Engineering, Mechanics and Computation*, Cape Town, South Africa, 2–4. , pp.1591–1598, April 2001.
- [17] El-Refaie SA, Ashour AF, and Garrity SW, “Tests of reinforced concrete continuous beams strengthened with carbon fibre sheets”, *The 10th BCA Annual Conference on Higher Education and the Concrete Industry*, Birmingham, UK, pp. 187–198, Jun 2000.
- [18] Eshwar N, Nanni A, and Ibell TJ, “Performance of two anchor systems of externally bonded fiber-reinforced polymer laminates”, *ACI Materials Journal*, vol. 105(1), pp. 72– 80, 2008.
- [19] Galati D, and De Lorenzis L, “Effect of construction details on the bond performance of NSM FRP bars in concrete”, *Advances in Structural Engineering*, vol. 12(5), pp. 683– 700, 2009.
- [20] Garden HN, and Hollaway LC, “An experimental study of the influence of plate end anchorage of carbon fibre composite plates used to strengthen reinforced concrete beams”, *Composite Structures*, vol. 42, pp. 175–188, 1998.
- [21] Garden HN, and Hollaway LC, “An experimental study of the influence of plate end anchorage of carbon fibre composite plates used to strengthen reinforced concrete beams”, *Composite Structures*, vol. 42, pp. 175–188, 1998.
- [22] Grace NF, “Strengthening of negative moment region of reinforced concrete beams using carbon fiber- reinforced polymer strips”, *ACI Structural Journal*, vol. 98, No. 3, pp. 347-358, 2001.
- [23] Grace NF, Sayed GA, and Saleh KR, “Strengthening of continuous beams using fibre reinforced polymer laminates”, *American Concrete Institute*, Farmington Hills, Mich, pp. 647-657, 1999.
- [24] Grace NF, Wael R, and Sayed AA, “Innovative triaxially braided ductile FRP fabric for strengthening structures”, *7th International Symposium on Fiber Reinforce Polymer for Reinforced Concrete Structures*, ACI, Kansas City, MO, 2005.
- [25] Grace NF, Abdel-Sayed G, Soliman AK, and Saleh KR, Strengthening of reinforced concrete beams using fibre reinforced polymer (FRP) laminates”, *ACI Structural Journal*, vol. 96, No. 5, pp. 865-874, 1999.
- [26] Grace NF, Soliman AK, Abdel-Sayed G, and Saleh KR, “Strengthening of continuous beams using fibre reinforced polymer laminates”, *Proceedings of 4th International Symposium on Fibre Reinforced Polymer Reinforcements for Reinforced Concrete Structures*, SP-188, American Concrete Institute, Farmington Hills, Michigan, USA, pp.647-657, 1999.
- [27] Jumaat MZ, and Alam MA, “Experimental and numerical analysis of end anchored steel plate and CFRP laminate flexurally strengthened R. C. beams”, *International Journal of Physical Sciences*, vol. 5, pp. 132-144, 2010.
- [28] Jumaat MZ, Rahman MM, and Rahman MA, “Review on bonding techniques of CFRP in strengthening concrete structures”, *International Journal of the Physical Sciences*, vol. 6(15), pp. 3567-3575, 4 August. 2011.
- [29] Kadhim, “Effect of CFRP Sheet Length on the Behavior of HSC Continuous Beam”, *Journal of Thermoplastic composite materials*, Vol. 00, 2011.
- [30] Khalifa A, and Nanni A, “Improving shear capacity of existing RC T-section beams using CFRP composites”,

- Cement and Concrete Composites, vol. 22, pp. 165–174, 2000.
- [31] Khalifa A, Tumialan G, Nanni A, and Belarbi A, “Shear Strengthening of Continuous Reinforced Beams Using Externally Bonded Carbon Fiber Reinforced Polymer Sheets”, In: Fourth International Symposium on Fiber Reinforced Polymer Reinforcement for Reinforced Concrete Structures, Baltimore, MD, American Concrete Institute, pp. 995–1008, November 1999.
- [32] Lamanna AJ, Bank LC, and Scott DW, “Flexural strengthening of reinforced concrete beams using fasteners and fiber-reinforced polymer strips”, *ACI Structural Journal*, vol. 98(3), pp. 368–76, 2001.
- [33] Lee TK, and Al-Mahaidi R, “An experimental investigation on shear behaviour of RC T-beams strengthened with CFRP using photogrammetry”, *Composite Structures*, vol. 82, pp. 185–193, 2008.
- [34] Leung CKY, and Cao Q, “Development of strain hardening permanent formwork for durable concrete structures”, *Materials and Structures*, vol. 43(7), pp. 993–1007, 2009.
- [35] Leung CKY, “Delamination failure in concrete beams retrofitted with a bonded plate”, *Journal of Materials in Civil Engineering*, vol. 13, pp. 106–113, 2001.
- [36] Leung CKY, “FRP debonding from a concrete substrate: Some recent findings against conventional belief”, *Cement and Concrete Composites*, vol. 28, pp. 742–748, 2006.
- [37] Maghsoudi AA, and Bengar H, “Moment redistribution and ductility of RHSC continuous beams strengthened with CFRP”, *Turkish Journal of Engineering and Environmental Sciences*, vol. 33, pp. 45–59, 2009.
- [38] Micelli F, Anniah RH, and Nanni A, “Strengthening of short shear span reinforced concrete T joists with fiber reinforced plastic composites”, *Journal of Composites for Construction*, vol. 6, pp. 264–271, 2002.
- [39] Nguyen DM, Chan TK, and Cheong HK, “Brittle failure and bond development length of CFRP-concrete beams”, *Journal of Composites for Construction*, vol. 5(1), pp. 12–17, 2001.
- [40] Niemitz CW, James R, and Beria SF, “Experimental behavior of carbon fiber-reinforced polymer (CFRP) sheets attached to concrete surfaces using CFRP anchors”, *Journal of Composites for Construction*, vol. 12(2), pp. 185–194, 2010.
- [41] Obaidat YT, Susanne H, Ola D, Ghazi A, Yahia A, “Retrofitting of reinforced concrete beams using composite laminates”, *Construction and Building Materials*, vol. 25, pp. 591–597, 2010.
- [42] Oehlers DJ, Liu IST, and Seracino R, “Shear deformation debonding of adhesively bonded plates” *Proc. Institution of Civil Engineers*, vol. 158(1), pp. 77–84, 2005.
- [43] Orton, SL, Jirsa JO, and Beyrak O, “Design considerations of carbon fiber anchors.” *Journal of Composites for Construction*, vol. 12(6), pp. 608–616, 2008.
- [44] Pan JL, and Leung CKY, “Effect of concrete composition on FRP/concrete bond capacity.” *Journal of Composites for Construction*, vol. 11(6), pp. 611–618, 2007.
- [45] Rahimi H, and Hutchinson A, “Concrete beams strengthened with externally bonded FRP plates.” *Journal of Composites for Construction*, vol. 5(1), pp. 44–56, 2001.
- [46] Ritchie PA, Thomas DA, Lu LW, and Connelly GM, “External reinforcement of concrete beams using fiber reinforced plastic”, *ACI Structural Journal*, vol. 88(4), pp. 490–500, 1991.
- [47] Smith ST, and Teng JG, “Debonding failures in FRP-plated RC Beams with or without U strip end anchorage”, *Proc. FRP Composites in Civil Engineering*, vol. 1, pp. 607–615, 2001.
- [48] Panda KC, Bhattacharyya SK, and Barai SV, “Shear behaviour of reinforced concrete T-beams with U-bonded glass fibre reinforced plastic sheet”, *Indian Concrete Journal*, vol. 84, pp. 61–71, 2010.
- [49] Riyadh A, “Coupled flexural retrofitting of RC beams using CFRP straps”, *Composite Structures*, vol. 75, pp. 457–464, 2006.
- [50] Ross CA, Jerome DM, Tedesco JW, and Hughes ML, “Strengthening of reinforced concrete beams with externally bonded composite laminates”, *ACI Structural Journal*, vol. 96. No. 2, pp. 65–71, 1999.
- [51] Sebastian WM, “Significance of mid-span de-bonding failure in FRP-plated concrete beams”, *ASCE Journal of Structural Engineering*, vol. 127, No. 7, pp. 792–798, 2001.
- [52] Sheikh SA, “Performance of concrete structures retrofitted with fibre reinforced polymers”, *Engineering Structures*, vol. 24, pp. 869–879, 2002.
- [53] Smith ST, and Teng JG, “FRP-strengthened RC beams I: Review of debonding strength models”, *Engineering Structures*, vol. 24, No. 4, pp. 385–395, 2002.
- [54] Spadea G, Bencardino F, and Swamy RN, “Structural behaviour of composite RC beams with externally bonded CFRP”, *Journal of Composites for Construction*, ASCE, pp. 132–7, 1998.
- [55] Teng JG, Smith ST, Yao J, and Chen JF, “Intermediate crack-induced debonding in RC beams and slabs”, *Construction and Building Materials*, vol. 17(6–7), pp. 447–462, 2003.
- [56] Yang ZJ, Chen JF, and Proverbs D, “Finite element modelling of concrete cover separation failure in FRP plated R. C. beams”, *Construction and Building Materials*, vol. 17, No.1, pp. 3–13, 2003.
- [57] Yao J, and Teng JG, “Plate end debonding in FRP-plated RC beams—I: Experiments”, *Engineering Structures*, vol. 29(10), pp. 2457–2471, 2007.
- [58] Yao J, Teng, JG, and Lam L, “Experimental study on intermediate crack debonding in FRP-strengthened RC flexural members”, *Advances in Structural Engineering*, vol. 8(4), pp. 365–396, 2005.

An Asymmetrical Dc-Dc Converter with a High Voltage Gain

Sarah Ben Abraham¹, Ms. Riya Scaria²,
^{1,2} Assistant Professor

Abstract: An asymmetrical full bridge converter is proposed in the paper. The proposed converter achieves zero voltage switching of all the power switches. Zero current switching of all the output diodes are also achieved here. This in turn provides a highly efficient operation. The proposed converter can provide a high voltage gain and the voltages across the semi-conductor devices are effectively clamped. The converter can be utilised effectively in high voltage applications as embedded systems, renewable energy systems, fuel cells, mobility applications and uninterrupted power supply.

I. Introduction

The recent growth of battery powered applications and low voltage storage elements are increasing the demand of efficient step-up dc-dc converters. Typical applications are embedded systems, renewable energy systems, fuel cells, mobility applications and uninterrupted power supply. These applications demand high step-up static gain, high efficiency and reduced weight, volume and cost.

Some classical converters with magnetic coupling as flyback or current-fed push-pull converter can easily achieve high step-up voltage gain. However, the power transformer volume is a problem for the development of a compact converter. The energy of the transformer leakage inductance can produce high voltage stress, increases the switching losses and the electromagnetic interference (EMI) problems, reducing the converter be used to reduce the switching losses and the EMI generation. However the voltage stress is higher than in the hard-switching structures and the cost and circuit complexity are increased. Thus, the weight, volume and losses of the power transformer are limiting factors for the isolated dc-dc converters used in embedded applications.

Non-isolated dc-dc converters as the classical boost, can provide high step-up voltage gain, but with the penalty of high voltage and current stress, high duty-cycle operation and limited dynamic response. The diode reverse recovery current can reduce the efficiency when operating with high current and voltage levels. There are some non-isolated dc-dc converters operating with high static gain, as the quadratic boost converter, but additional inductors and filter capacitors must be used and the switch voltage is high.

In order to overcome these problems, an asymmetrical full bridge converter with high-voltage gain is proposed. The limitation of the maximum duty cycle disappears in the proposed topology. The proposed converter features high-voltage gain, fixed switching frequency, soft-switching operations of all power switches and output diodes, and clamped voltages across power switches and output diodes. The reverse recovery problem of the output diodes is significantly alleviated due to an additional inductor at the secondary side. Therefore, the proposed converter shows high efficiency and it is suitable for high-voltage applications.

II. Literature Review

The conventional boost converters are widely employed in power factor correction (PFC) applications due to the simple circuit structure. The conventional single-phase single-switch boost converter is shown in Figure 2.1. In theory, the voltage gain of the boost converter can be infinite when the duty cycle is close to one. However, the switch turn-off period becomes short when the duty cycle increases. The current ripples of the power devices are large, with high-step-up conversion [5], which increases the power device conduction losses and turn-off current. Moreover, the voltage stresses of the switch and the diode are equal to the output voltage, which is large in high output-voltage applications. The cost of the switches with high voltage stress is rather higher than that of the switches with low voltage stress. The switching and reverse-recovery losses are significant due to the hard-switching operation. Furthermore, the power level is limited by the single-phase single-switch solution.

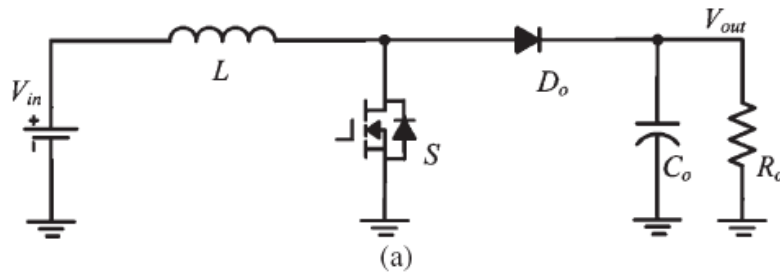


Figure 2.1: Conventional boost converter

The interleaved structure is another effective solution to increase the power level, which can minimize the current ripple, can reduce the passive component size, can improve the transient response, and can realize the thermal distribution. Figure 2.2 shows a two-phase conventional interleaved boost converter. However, the power devices still operate at hard switching [10]. The efficiency is limited because the output diode reverse-recovery problem is still serious in high-output voltage applications.

An active zero current transition (ZCT) interleaved boost converter is derived from the conventional interleaved boost converter by adding a set of auxiliary commutation circuit to each phase [13], which is formed by an active switch, a capacitor, and an inductor. The interleaved boost converter with auxiliary commutation circuits is introduced in Figure 2.3. Turning on of the main switches occurs naturally at zero current, and the output-diode reverse-recovery problem is alleviated due to the critical discontinued current mode (DCM) operation. The auxiliary commutation circuits provide ZCT when the main switch turns off. However, a variable frequency control is mandatory for this converter, which is difficult for the electromagnetic interference (EMI) filter design.

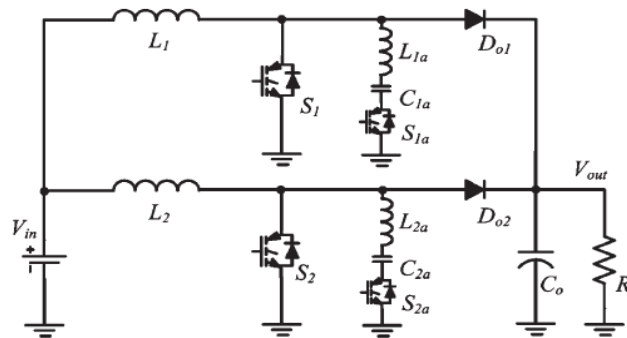


Figure 2.2: Active ZCT interleaved boost converter

The filter inductors of the conventional interleaved boost converter can be integrated into one coupled inductor to reduce the magnetic components. The output-diode reverse recovery problem can be alleviated, and zero current switching (ZCS) turn-on of the switches can be achieved due to the leakage inductance of the coupled inductor.

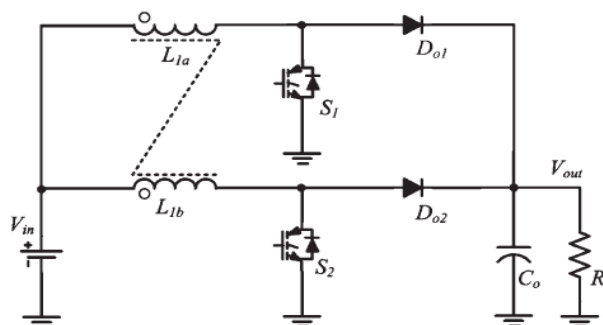


Figure 2.3: Interleaved boost converters with coupled inductor

An active zero-voltage ZCS (ZVZCS) interleaved boost converter with a coupled inductor I shown in Figure 2.5. An auxiliary circuit, which is composed of only a clamp switch and a small capacitor, is inserted into each phase of the interleaved boost converter with coupled inductor. ZCS turn-on and ZVS turn-off are achieved for the main switches. The ZVS soft-switching performance is realized for the auxiliary switches during the

whole switching transition. The leakage inductance of the coupled inductor is used to control the output diode turn-off current falling rate, which alleviates the diode reverse-recovery problem. The converter is symmetrical and suitable for high-power and high-efficiency dc/dc applications.

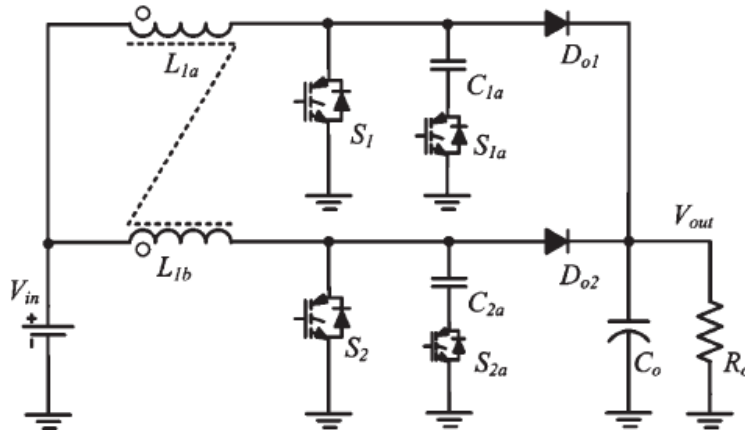


Figure 2.4: Active ZVZCS interleaved boost converter with a coupled inductor

A lot of other active or passive lossless soft-switching solutions are proposed to reduce the switching and reverse-recovery losses that exist in the conventional boost converters. However, most of the improvements are presented for PFC applications. They are not suitable for high-step-up and high efficiency PV grid-connected applications.

The current-fed converters are often used in high step-up applications due to their inherent low input current ripple characteristic and high-voltage gain [11], [12]. However, in the current fed converters, the voltage stresses of the switches are serious. In order to clamp the voltages across the switches and provide zero-voltage switching (ZVS) features, active snubbers are often employed. The snubbers require additional switches and cause additional conduction losses. As a result, the system efficiency decreases. On the other hand, the voltage-fed converters such as phase-shift full-bridge (PSFB) converters, which are widely used, show low-voltage stress of the switching devices. PSFB converters feature fixed switching frequency and ZVS of power switches. However, they have some drawbacks including large conduction loss due to circulating current, duty cycle loss, and the voltage spikes across output rectifiers. The large voltage spikes of the output rectifiers are serious problems especially in high-voltage applications. To remedy these problems, many topologies have been proposed in [13]–[18]. In some of them, auxiliary snubber circuits are employed to suppress the voltage spikes at the secondary side. However, the complexity and the overall cost are increased while the system efficiency decreases due to the additional circuits.

The voltage gain can be extended, and the current ripple can be further reduced to satisfy the high-step-up requirements by employing the cascade structure. Figure 2.6 shows a cascade boost converter. The voltage stress of the first stage is low, and it can be operated with a high switching frequency to improve the power density. The second stage can be worked with a low switching frequency to reduce the switching losses. However, the cascade converter requires two sets of power devices, magnetic cores, and control circuits, which is complex and expensive. The system stability of the cascade structure is another big issue, and the control circuit should be designed carefully. The output-diode reverse-recovery problem of the second stage is severe because a high voltage level should be sustained in the high-output-voltage applications.

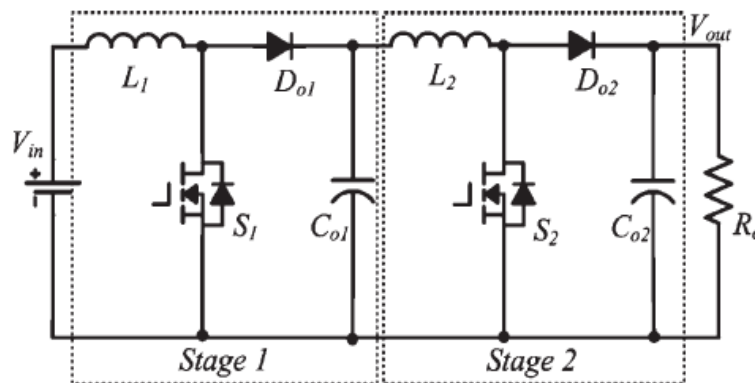


Figure 2.5: Cascade boost converter

The two switches in the cascade boost converter can be integrated into one switch to reduce circuit complexity. The integrated cascade boost converter is shown in Figure 2.7. The inductors L_1 and L_2 operate in the charging mode when switch S turns on. The energy stored in L_1 is transferred to capacitor C_1 through diode D_1 , and the energy stored in L_2 is delivered to the load through diode D_o when switch S turns off. The circuit is simplified, and the instability caused by the cascade structure is avoided, compared with the cascade boost converter.

An integrated cascade boost converter with ZVS soft switching performance is shown in Figure 2.8. The auxiliary circuit is composed of a small inductor L_s , a resonant capacitor C_c , and a power MOSFET S_c , which is used to realize the soft switching for the main and clamp switches. However, the switch voltage stress of the integrated cascade boost converters is equal to the high output voltage, and the current stress is large because the current of the inductors L_1 and L_2 flows through the switch when it turns on. These two factors increase the conduction losses and reduce the circuit efficiency.

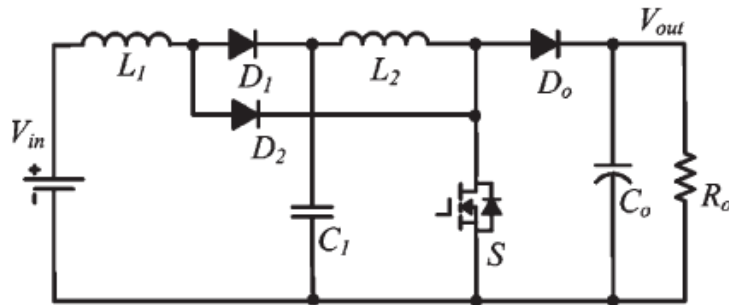


Figure 2.6: Integrated cascade boost converter

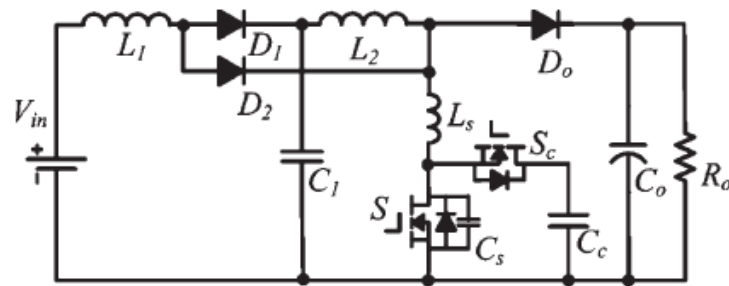


Figure 2.7: Integrated cascade boost converter with ZVS performance

III. Asymmetrical Dc-Dc Converter With High Voltage Gain - Circuit Description

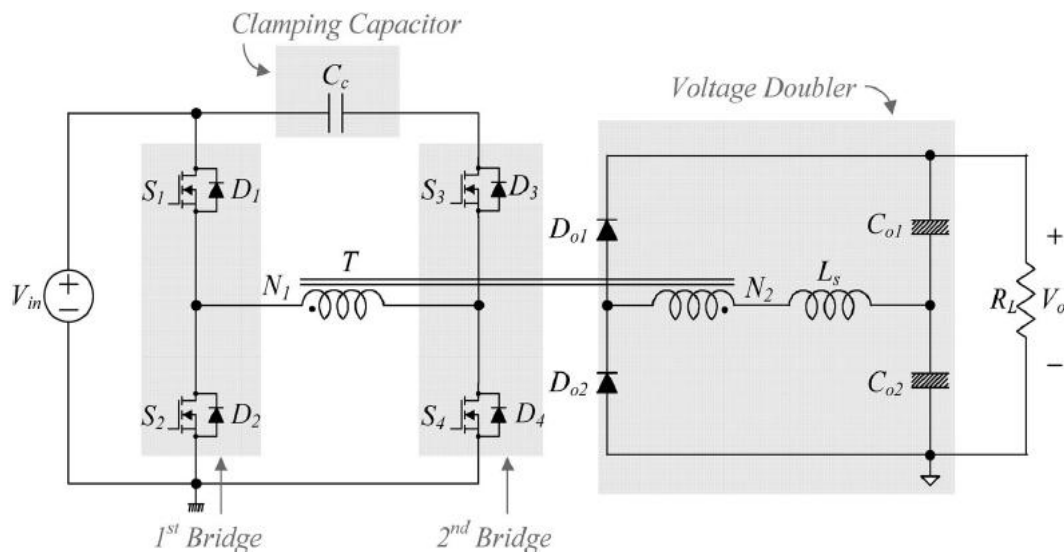


Figure 3.1: Circuit Diagram

The proposed converter has four power switches S_1 through S_4 . There is also the clamping capacitor C_c between top side switches S_1 and S_3 of two switch bridges. The voltages across the switches S_1 and S_2 in the first bridge are confined to the input voltage V_{in} . The clamping capacitor C_c can clamp the voltages across the switches S_3 and S_4 in the second bridge. The output stage of the proposed converter has a voltage doubler structure that consists of the secondary winding N_2 of the transformer T , the serial inductor L_s , the output capacitors C_{o1} and C_{o2} and the output diodes D_{o1} and D_{o2} . According to the voltage doubler structure, the voltage gain increases and the voltage stresses of the output diodes are confined to the output voltage V_o without any auxiliary circuits.

The equivalent circuit of the proposed converter is shown in Fig. 2. The diodes D_1 through D_4 are the intrinsic body diodes of all switches. The capacitors C_1 through C_4 represent their parasitic output capacitances. The transformer T is modeled as the magnetizing inductance L_m and the ideal transformer that has a turn ratio of 1:n ($n = N_2/N_1$). Its leakage inductance is included in the serial inductor L_s . To simplify the analysis, it is assumed that the clamping capacitor C_c has a large value and the voltage across C_c is constant as V_c under a steady state. Similarly, the output capacitor voltages are assumed to be constant as V_{o1} and V_{o2} , respectively.

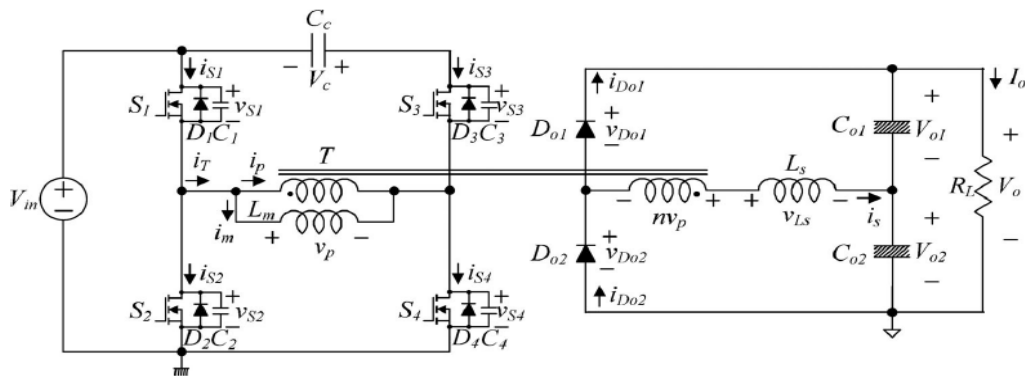
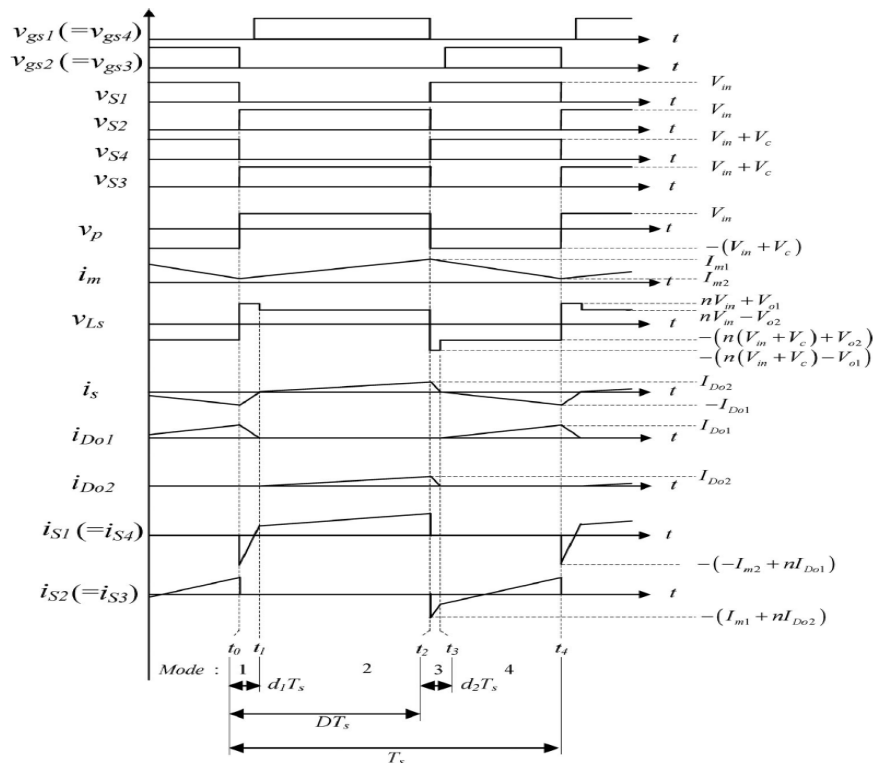


Figure 3.2: Equivalent Circuit

The theoretical waveforms of the proposed converter are shown in Fig. 3. The switch S_1 (S_4) and the switch S_2 (S_3) are operated asymmetrically and the duty cycle D is based on the switch S_1 (S_4). A small delay between driving signals for S_1 (S_4) and S_2 (S_3) is a deadtime for the switches. It prevents cross conduction and allows ZVS.



IV. Modal Analysis

The operation of the proposed converter during a switching period T_s is divided into four modes as shown in Fig. 4. Before t_0 , the switches S_2 and S_3 , and the output diode D_{o1} are conducting. At t_0 , the magnetizing current i_m and the secondary current i_s arrive at their minimum values I_{m2} and $-I_{D_{o1}}$, respectively.

Mode 1 $[t_0, t_1]$: At t_0 , the switches S_2 and S_3 are turned off. Then, the energy stored in the magnetic components starts to charge/discharge the parasitic capacitances C_1 through C_4 . Therefore, the voltages v_{S2} and v_{S3} start to rise from zero. Similarly, the voltage v_{S4} starts to fall from $V_{in} + V_c$ voltage v_{S1} starts to fall from V_{in} . Since all the parasitic output capacitances C_1 through C_4 are very small, this transition time interval is very short and it is ignored in Fig. 3. When the voltages v_{S1} and v_{S4} arrive at zero, their body diodes D_1 and D_4 are turned on. Then, the gate signals are applied to the switches S_1 and S_4 . Since the currents have already flown through D_1 and D_4 and the voltages v_{S1} and v_{S4} are clamped as zero before the switches S_1 and S_4 are turned on, zero-voltage turn-ON of S_1 and S_4 is achieved. With the turn-ON of S_1 and S_4 , the primary voltage v_p across L_m is V_{in} . Then, the magnetizing current i_m increases linearly from its minimum value I_{m2} as follows:

$$i_m(t) = I_{m2} + \frac{V_{in}}{L_m} (t - t_0)$$

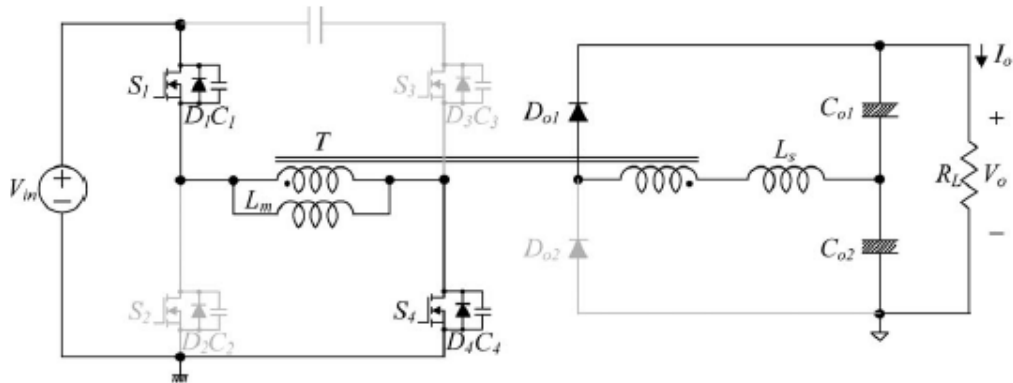


Figure 4.1: Mode 1

Since the voltage V_{L_s} across L_s is $nV_{in} + V_{o1}$, the secondary current is increases from its minimum value $-I_{D_{o1}}$ as follows:

$$i_s(t) = -I_{D_{o1}} + \frac{nV_{in} + V_{o1}}{L_s} (t - t_0)$$

Mode 2 $[t_1, t_2]$: At t_1 , the currents i_s and $i_{D_{o1}}$ arrive at zero and the diode D_{o1} is turned off. Then, the output diode D_{o2} is turned on and its current increases linearly. Since the current changing rate of D_{o1} is controlled by the serial inductor L_s , its reverse-recovery problem is significantly alleviated. Since the voltage v_{L_s} is $(nV_{in} - V_{o2})$ in this mode, the current is are given by:

$$i_s(t) = \frac{nV_{in} - V_{o2}}{L_s} (t - t_1)$$

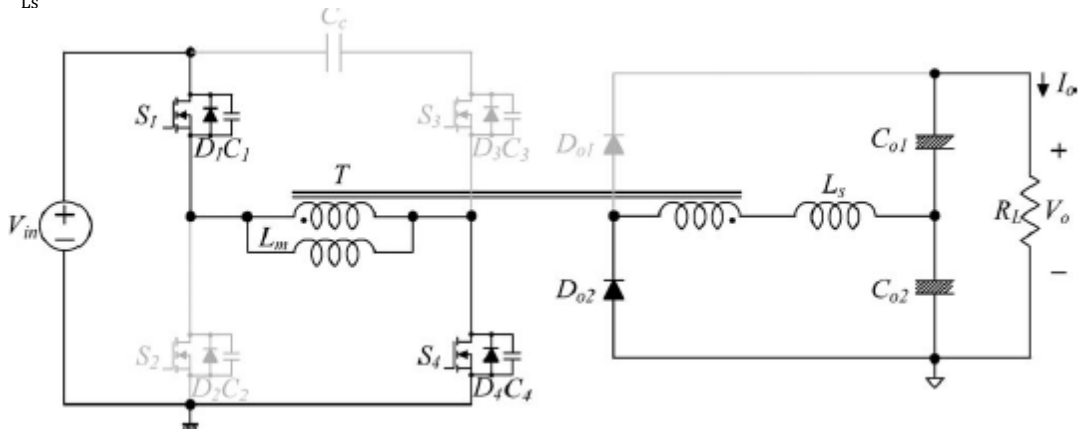


Figure 4.2: Mode 2

At the end of this mode, i_m and i_s arrive at their maximum values I_{m1} and $I_{D_{o2}}$, respectively.

Mode 3 $[t_2, t_3]$: Similar to mode 1, the switches S_1 and S_4 are turned off at t_2 . The parasitic capacitors C_1 and C_4 start to be charged from zero, whereas the parasitic capacitors C_2 and C_3 start to be discharged from V_{in} and $V_{in} + V_c$, respectively. With the same assumption as mode 1, this transition time interval is very short and it is

ignored in Fig. 3. After the parasitic capacitors are fully charged and discharged, the voltages v_{S2} and v_{S3} become zero and the body diodes D_2 and D_3 are turned on. Then, the gate signals are applied to the switches S_2 and S_3 . Since the currents have already flown through D_2 and D_3 and the voltages v_{S2} and v_{S3} are clamped as zero, zero-voltage turn-on of S_2 and S_3 is achieved. With the turn-on of S_2 and S_3 , the voltage v_p across L_m is $-(V_{in}+V_c)$. Then, the current i_m decreases linearly from its maximum value I_{m1} as follows:

$$i_m(t) = I_{m1} - \frac{V_{in}+V_c}{L_m}(t-t_2)$$

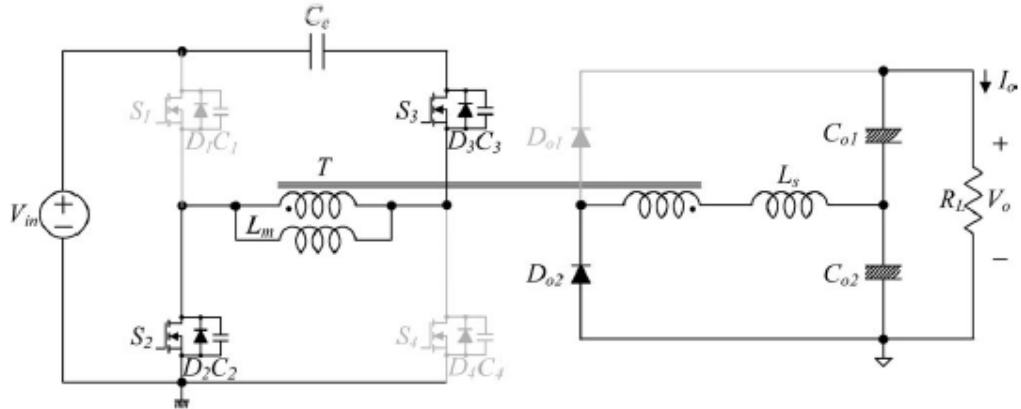


Figure 4.3: Mode 3

Since the voltage v_{Ls} across L_s is $-(n(V_{in}+V_c)+V_{o2})$, the current is decreases from its maximum value $I_{D_{o2}}$ as follows:

$$i_s(t) = I_{D_{o2}} - \frac{n(V_{in}+V_c)+V_{o2}}{L_s}(t-t_2)$$

Mode 4 [t_3 , t_4]: Similar to mode 2, the currents i_s and $i_{D_{o2}}$ arrive at zero and the diode D_{o2} is turned OFF at t_3 . Then, the output diode D_{o1} is turned on and its current increases linearly. Since the current changing rate of D_{o2} is controlled by L_s , its reverse-recovery problem is significantly alleviated. Since the voltage v_{Ls} is $-(n(V_{in}+V_c)-V_{o1})$, the current i_s is given by:

$$i_s(t) = -\frac{n(V_{in}+V_c)-V_{o1}}{L_s}(t-t_3)$$

At the end of this mode, the currents i_m and i_s arrive at I_{m2} and $-I_{D_{o1}}$, respectively.

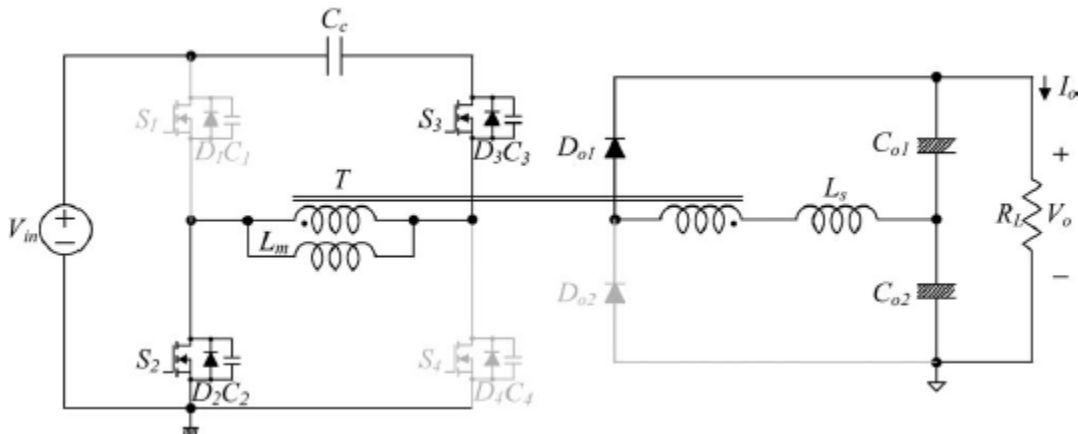


Figure 4.4: Mode 4

IV. Design Parameters

To validate the characteristic of the proposed converter, design procedure is given in this section with the following specifications:

- 1) Input voltage $V_{in} = 48V$.
- 2) Output voltage $V_o = 400V$.
- 3) Maximum output power $P_{o,max} = 150W$.
- 4) Switching frequency $f_s = 74 \text{ kHz}$.

4.1 Selection Dmax and n

The voltage stresses of S3 and S4 depend on D. If they need to be kept below 150V, D should be smaller than 0.75. Therefore, the maximum duty cycle Dmax is determined as 0.7.

Since the required voltage gain is 8.3, the turn ratio n can be calculated as 3 from the following equation:

$$M = \frac{V_0}{V_{in}} = \frac{n(1-2k)D}{(D+(1-2D)k)(1-D-(1-2D)k)}$$

4.2 Selection of Ls

Serial inductor Ls can be determined as follows:

$$L_s = \frac{nD_{max}V_{in}T_s}{8I_{omax}} [1-(1-2k)]^2$$

By using previously selected k* and Dmax, (32) gives Ls = 87.5 μH. Then, Ls is selected as 90 μH.

4.3 Selection of Lm

ID01 is calculated as 2.287 A from the following equation:

$$I_o = \frac{(1-D+d1-d2)IDo1}{2} = \frac{(D-d1+d2)IDo2}{2}$$

Where, $d1 = kD$

$d2 = k(1-D)$

By assuming the output capacitances C1 to C4 of the switches as 500pF, we choose Lm < 136 μH from an inequality which arises since there is current cancellation between ip and im at to. Therefore, for ZVS of S1 and S4, the energy difference between the energies stored in Lm and Ls should be larger than the energy stored in C1 through C4 as follows:

$$-\frac{L_m I_m^2}{2} + \frac{L_s I_o^2}{2} > \frac{(C1+C2)V_{in}^2}{2} = \frac{(C3+C4)(V_{in}+V_c)^2}{2}$$

4.4 Selection of Cc

The switch current is3 flows through Cc. From the current waveform is3 in Fig. 3, the resulting ripple in the voltage across Cc depends on the area under the current waveform. The voltage ripple ΔVc across Cc is approximately given by:

$$\Delta V_c = \frac{(1-D)T_s}{4C_c} (I_{m1} + nIDo2)$$

Where,

$$I_{m1} = I_{in} + \frac{V_{in}DT_s}{2L_m}$$

$$I_{in} = \frac{V_o}{V_{in}}$$

$$IDo2 = \frac{nV_{in} - V_o}{L_s} (D-d1) T_s$$

$$V_o = \frac{D-d1-(D/(1-D))d2}{D-d1+d2} nV_{in}$$

And from the equation for ΔVc, Cc should be larger than 3.49 μF to keep the ripple below 1 V. The value of Cc is selected as 6.6 μF.

4.5 Selection of C01 and C02

The secondary current is flows through C01 and C02 equally. The voltage ripple across C01 is given by:

$$\Delta V_{o1} = \frac{(D-d1+d2)T_s I_{Do2}}{4C_{o1}}$$

And from the above equation, C01 should be larger than 18.75 μF to keep ΔV01 below 0.1 V. The value of C01 is selected as 47 μF. Similarly, C02 is also selected as 47 μF.

V. Simulation Results

The circuit has been simulated using the software, MATLAB/SIMULINK. MATLAB (matrix laboratory) is a numerical computing environment and fourth generation programming language. Developed by Math Works, MATLAB allows matrix manipulations, plotting of functions and data, implementation of algorithms, creation of user interfaces, and interfacing with programs written in other languages, including C, C++, Java and Fortran.

Simulink, developed by Math Works, is a data flow graphical programming language tool for modelling, simulating and analyzing multi-domain dynamic systems. Its primary interface is a graphical block diagramming tool and a customizable set of block libraries. It offers tight integration with the rest of the MATLAB environment and can either drive MATLAB or be scripted from it.

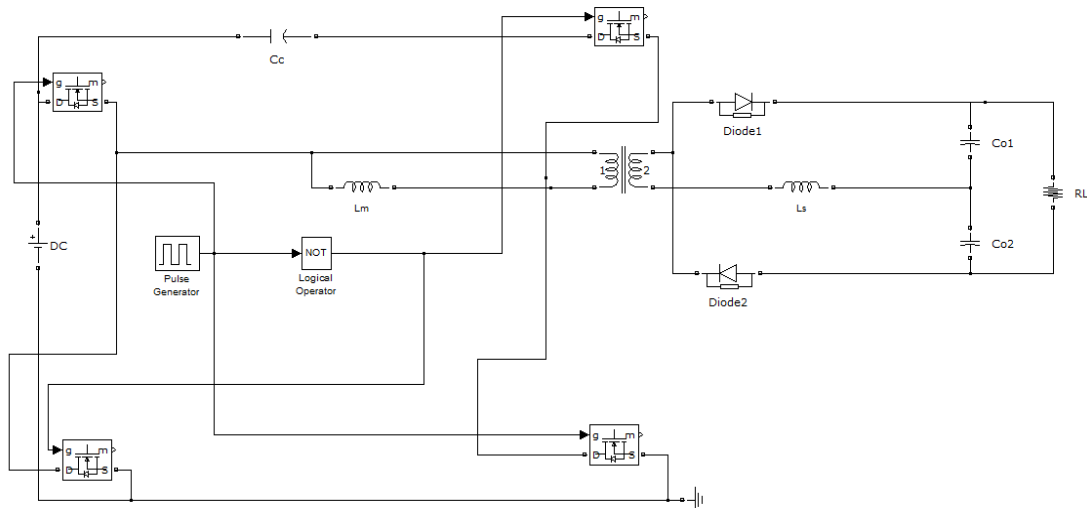


Figure 6.1: MATLAB/SIMULINK model of the circuit

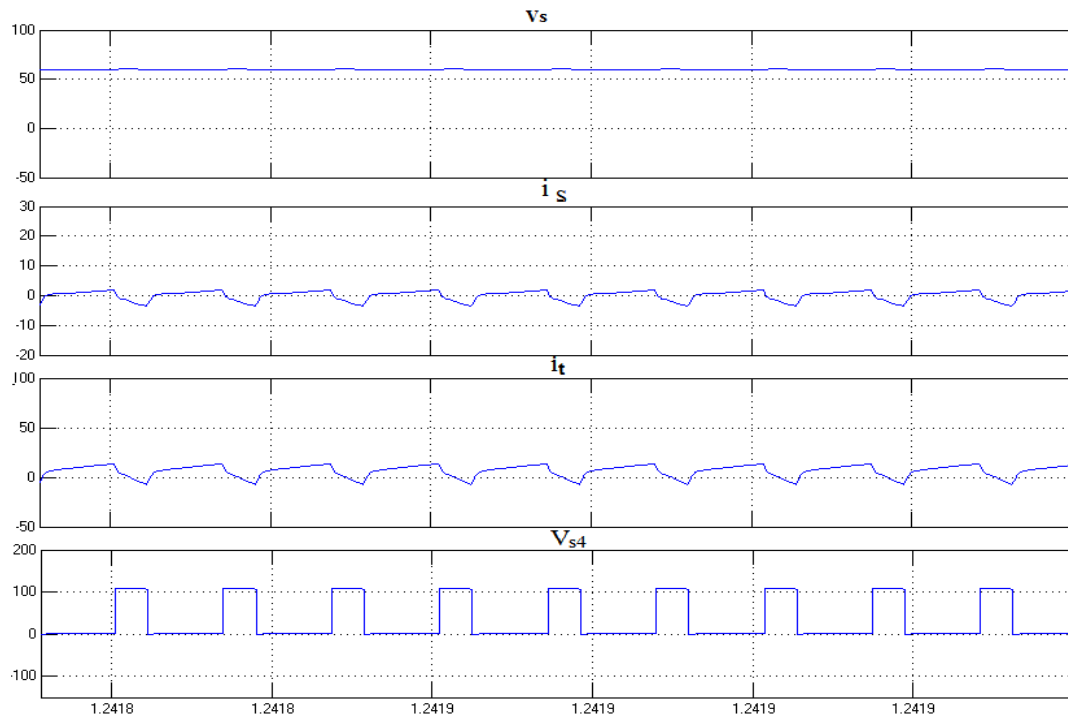


Figure 6.2: Measured Key Waveforms

The figure shows the key waveforms of the proposed converter. It shows the currents i_s and i_t , the clamping capacitor voltage V_c and the switch voltage v_{s2} . According to the equation for C_c , clamping capacitor voltage V_c should be 64 v. It agrees with the experimental result. The measured maximum voltage stress of S4 is around 110v, which agrees with the theoretical analysis.

The ZVS operations of all power switch S4 is shown in the figure 6.3. The voltage across the switches goes to zero before the gate pulses are applied to the switches. Since the switch voltages are clamped to zero before the gate pulses are applied, the ZVS turn on of the switches is achieved. Figure 6.4 shows the ZCS of output diodes. After the diode currents fall to zero, the voltages across the diode rise to output voltage V_o . Therefore, the ZCS turn off of the output diodes is achieved.

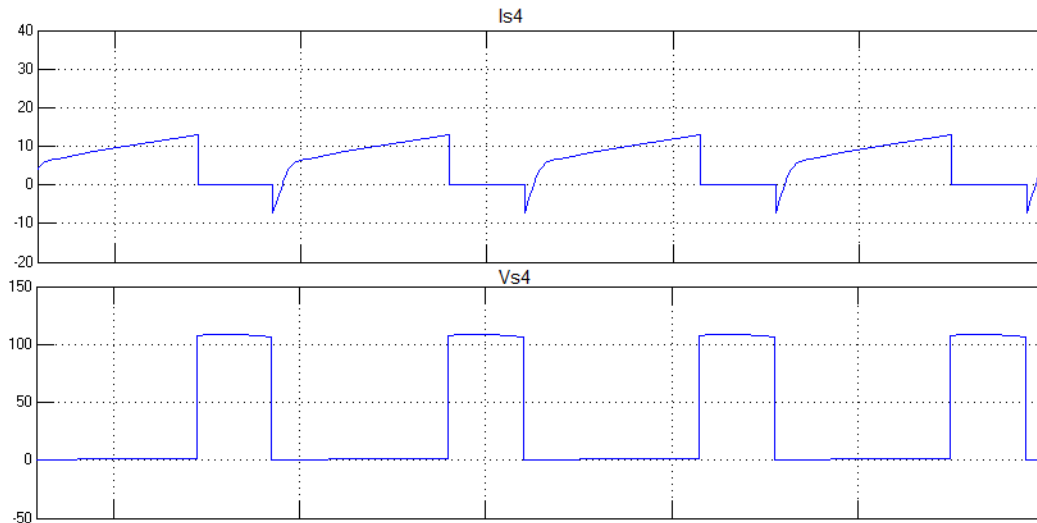


Figure 6.3 ZVS of Switch S4

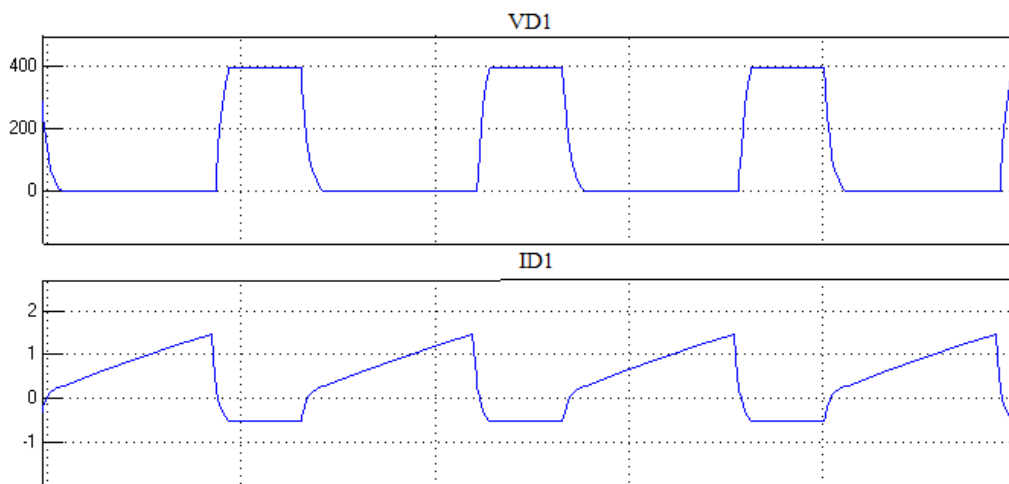


Figure 6.4: ZCS of Diode D1

VI. Conclusion

The limitations of the conventional dc-dc converters in high-step-up, low-cost, and high-efficiency are analyzed. From the aforementioned analysis, the major challenges in applications requiring high voltage gain can be drawn as follows:

- 1) Extension of voltage gain.
- 2) Reduction of switch
- 3) Realization of soft-switching performance to reduce the switching losses.
- 4) Alleviation of the output-diode reverse-recovery problem to reduce the reverse-recovery losses.

In this paper, an asymmetrical full-bridge converter with high voltage gain has been presented. The ZVS of all power switches and ZCS of the output diodes are achieved. The proposed converter is able to provide a high efficiency and high-voltage gain with relatively low transformer turn ratio. Also, without any auxiliary circuits, the voltages across the switches and the output diodes are effectively clamped. Therefore, the proposed converter is suitable for high-voltage applications. A prototype was simulated to verify the performance of the proposed converter. The voltage gain is 8.3 with the transformer turn ratio of 3.

REFERENCES

- [1] R. J. Wai, W. H. Wang, and C. Y. Lin, "High-performance stand-alone photovoltaic generation system," IEEE Trans. Ind. Electron., vol. 55, no. 1, pp. 240–250, Jan. 2008.
- [2] C. Wang and M. H. Nehrir, "Power management of a standalone Wind/photovoltaic/fuel cell energy system," IEEE Trans. Energy Convers., vol. 23, no. 3, pp. 957–967, Sep. 2008.

- [3] R. J. Wai and W. H. Wang, "Grid-connected photovoltaic generation system," *IEEE Trans. Circuits Syst. I, Reg. Papers*, vol. 55, no. 3, pp. 953–964, Apr. 2008.
- [4] M. Prudente, L. L. Pfitscher, G. Emmendoerfer, E. F. Romaneli, and R. Fules, "Voltage multiplier cells applied to non-isolated DC-DC converters," *IEEE Trans. Power Electron.*, vol. 23, no. 2, pp. 871–887, Mar. 2008.
- [5] E. H. Ismail, M. A. Al-Saffar, A. J. Sabzali, and A. A. Fardoun, "A family of single-switch PWM converters with high step-up conversion ratio," *IEEE Trans. Circuit Syst. I*, vol. 55, no. 4, pp. 1159–1171, May 2008.
- [6] Z. Liang, R. Guo, J. Li, and A. Q. Huang, "A high-efficiency PV module integrated DC/DC converter for PV energy harvest in FREEDM systems," *IEEE Trans. Power Electron.*, vol. 26, no. 3, pp. 897–909, Mar. 2011.
- [7] W.-S. Liu, J.-F. Chen, T.-J. Liang, and R.-L. Lin, "Multicascoded sources for a high-efficiency fuel-cell hybrid power system in high-voltage application," *IEEE Trans. Power Electron.*, vol. 26, no. 3, pp. 931–942, Mar. 2011.
- [8] L.-S. Yang, T.-J. Liang, and J.-F. Chen, "Transformerless DC-DC converters with high step-up voltage gain," *IEEE Trans. Ind. Electron.*, vol. 56, no. 8, pp. 3144–3152, Aug. 2009.
- [9] Q. Zhao, F. Tao, Y. Hu, and F. C. Lee, "Active-clamp DC/DC converter using magnetic switches," in *Proc. IEEE Appl. Power Electron. Conf. Expo.*, 2001, pp. 946–952.
- [10] D. A. Grant, Y. Darroman, and J. Suter, "Synthesis of tapped-inductor switched-mode converters," *IEEE Trans. Power Electron.*, vol. 22, no. 5, pp. 1964–1969, Sep. 2007.
- [11] L. Zhu, K. Wang, F. C. Lee, and J. S. Lai, "New start-up schemes for isolated full-bridge boost converters," *IEEE Trans. Power Electron.*, vol. 18, no. 4, pp. 946–951, Jul. 2003.
- [12] E. Adib and H. Farzanehfard, "Zero-voltage transition current-fed fullbridge PWM converter," *IEEE Trans. Power Electron.*, vol. 24, no. 4, pp. 1041–1047, Apr. 2009.
- [13] Y. Jang and M. M. Jovanovic, "A new family of full-bridge ZVS converters," *IEEE Trans. Power Electron.*, vol. 19, no. 3, pp. 701–708, May 2004.
- [14] M. Borage, S. Tiwari, S. Bhardwaj, and S. Kotaiah, "A full-bridge DC-DC converter with zero-voltage-switching over the entire conversion range," *IEEE Trans. Power Electron.*, vol. 23, no. 4, pp. 1743–1750, Jul. 2008.
- [15] Y. Jang and M. M. Jovanovic, "A new PWM ZVS full-bridge ZVS converter," *IEEE Trans. Power Electron.*, vol. 22, no. 3, pp. 987–994, May 2007.

Trajectory Control With MPC For A Robot Manipulator Using ANN Model

Bekir Cirak

Siirt University, Engineering Faculty, Mechanical Engineering Department, Kezer Campus, Siirt-TURKEY

Abstract: In this study, in a computer the dynamic motion modelling of manipulator and control of trajectory with an algorithm this has been tested. First after dynamic motion simulation of manipulator has been made MPC Control. The result in this study we can observe that computed torque method gives better results than MPC methods. So in trajectory control it is approved of using computed torque method. In last part of this study the results are estimated forward development are examined and suggested. The model predictive control (MPC) technique for an articulated robot with n joints is introduced in this paper. The proposed MPC control action is conceptually different with the trajectory robot control methods in that the control action is determined by optimising a performance index over the time horizon. A neural network (NN) is used in this paper as the predictive model.

Keywords: Robot manipulators, Model predictive control (MPC), ANN based model, NMPC, DMPC

I. Introduction

When designing a new process, it is important to exercise some decision making restraint. One critical area to hold back is selecting an advanced process control technology. The choice of PID, model predictive control, or something else should not be decided until the project has been qualified and reasonable objectives have been established. Overlooking this basic principle has caused companies to waste a lot of time and money. When selecting an advanced process control technology, three perspectives are important; process characteristics, process operating objectives and system and application security. Comparing these perspectives to the major process control technologies covered in this series provides a fitting conclusion. An articulated robot with two or more joints is a complex nonlinear time varying MIMO (Multi Input Multi Output) system with dynamic interaction between its inputs and outputs. Up till now, the majority of practical industrial approaches to the robot ann control design treat each joint of the manipulator as a simple linear servomechanism with, for example, a PD or a PID controller. In designing this kind of controllers, the nonlinear, coupled and time varying dynamics of the mechanical part of the robot manipulator have usually been completely ignored, or treated as disturbances [1].

This method generally gives satisfactory performance when properly tuned and drive one joint at a time. However, when the links are moving simultaneously and at high speeds, the nonlinear coupling effects and the interaction forces between the manipulator links may degrade the performance of the overall system badly and hence increase the tracking error.

Theoretically speaking, centralised control strategies, such as the Computed Torque Control Method and adaptive control, can solve above problems. But in practice uncertainties existing in the robot dynamic model may seriously degrade the performance of the both methods. There are two types of uncertainties, structured and unstructured. Structured uncertainty is defined as the case of a correct dynamical model but with parameter uncertainty due to tolerance variations in the manipulator link: properties, unknown loads, inaccuracies in the torque constants of the actuators, and so on. Unstructured uncertainty describes the case of unmodeled dynamics which result from the presence of high frequency modes in the manipulator, neglected time delays, nonlinear friction, and so on. Although adaptive control has the ability to cope with structured uncertainties, it does not solve the problem of unstructured uncertainties[2].

Therefore, trajectory control approaches are not suitable for the occasion where the robot arm moves at higher velocity. In this paper the method of the model predictive control (MPC) for robot trajectory tracking will be investigated. The concept of MPC comes from the area of industrial process control. Its using in robot control has less been reported. The proposed MPC approach is conceptually different with the trajectory robot control methods in that the control action is determined by optimising a performance index, typically the error between the output prediction derived from the model and the desired output, over the time horizon. Then apply the optimal control actions to the system, measure the system outputs over the time horizon and repeat the above steps until the tracking errors are within the pennitted range. The predictive model for a conventional MPC controller is usually either impulse or step response model which is preferred as being more intuitive and

requiring less a prior information for its identification. However, these models are not suitable for such a nonlinear system as a robot. To solve this problem neural networks are proposed to be the predictive model of the robot for the MPC controller, because the neural networks have the ability to map any nonlinear relationships between an input and output set. There have also been many reports on the application of neural network to robot modelling and identification [3].

II. Model Predictive Control

MPC is not a specific control strategy but a wide class of optimal control based algorithms that use an explicit process model to predict the behavior of a plant. There is a wide variety of MPC algorithms that have been developed over past 30 years. For example, the Model Predictive Heuristic Control reported by Richalet et al. in 1976 which is used an impulse response model as its linear model. Model predictive control is a generic term for a group of related algorithms that make an explicit use of a process model to calculate control moves minimizing the objective function. The main ideas of MPC for basic structure of MPC in Figure 1.

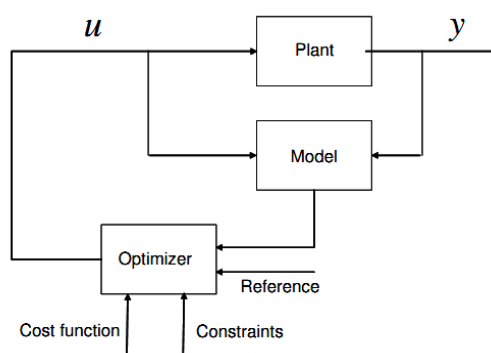


Figure 1. Basic structure of MPC

1. Using an explicit dynamic model of plant to predict the effect of future moves on manipulated variables.
2. Calculating these moves such that they minimize a specific performance criterion while satisfying given operational constraints.
3. Solving this (quadratic) optimization problem in receding horizon manner, using the most recent measurements from the plant to update the prediction. The fundamental framework of MPC algorithms is in common for any kinds of MPC schemes. The basic elements of MPC for MPC strategy are illustrated in Figure 2.

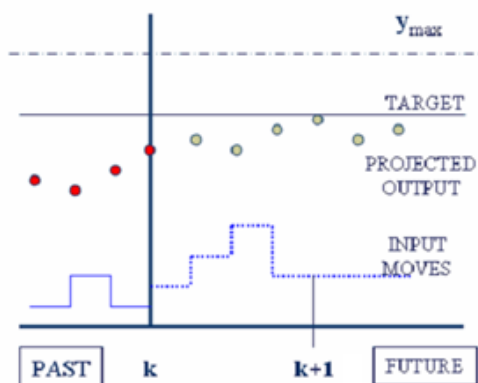


Figure 2. MPC strategy

Model predictive control is especially useful for applications involving constraints on manipulated and/or controlled variables. MPC has been successfully applied in petroleum refineries and extended to numerous other application areas including those found in chemicals, food processing, automotive and aerospace industries. The reason for its popularity is that it addresses the key practical issues often encountered in process control problems including multivariable interactions, constraints, and potentially process nonlinearity all in a single systematic framework [4].

The model predictive control is a strategy that is based on the explicit use of some kind of system model to predict the controlled. Variables over a certain time horizon, the prediction horizon. The control strategy can be described as follows,

1. At each sampling time, the value of the controlled variable $y(t+k)$ is predicted over the prediction horizon $k=l, \dots, N$. This prediction depends on the future values of the control variable $u(t+k)$ within a control horizon $k=l, \dots, NC$,

where $NC \leq N$. If $NC < N$, then $u(t+k)=u(t+NC)$, $k=NC+l, \dots, N$.

2. A reference trajectory $r(t+k)$, $k=l, \dots, N$ is defined which describes the desired system trajectory over the prediction horizon.

3. The vector of future controls $u(t+k)$ is computed such that a cost function, usually. A function of the errors between the reference trajectory and the predicted output of the model is minimised.

4. Once the minimisation is achieved, the first optimised control action is applied to the plant and measurement of the plant states as the initial states of the model to perform the next iteration. Steps 1 to 4 are repeated at each sampling instant; this is called a receding horizon strategy. The above steps can be expressed by the following equations:

$$\text{Min} \left(\sum_{i=1}^p [x_d(k+1) - x(k+1)]^2 \right) \quad (1)$$

subject to

$$U_{\min} < U < U_{\max}, \quad \forall k \quad (2)$$

Where k is the time step, $u(k)$ is the control vector at time k , $x_d(k)$ and $x(k)$ are the desired output (reference) and predicted output vector of the model at time k respectively, p is the prediction time horizon. The block diagram of a model predictive controller is shown in Figure 1.

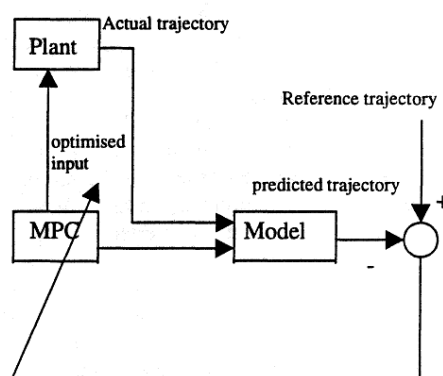


Figure 3. Block diagram of MPC controller

As the control variables in a MPC controller are calculated based on the predicted output, the model thus needs to be able to reflect the dynamic behaviour of the system as accurately as possible, and at least a prior information for the systems identification is required. In the conventional MPC controller, a linear predictive model is used because the theory of the identification of a linear system has well been established. The nonlinear part of the system response is treated as disturbance. But a linear model, no matter how well has it been structured and tuned, may be acceptable only in the case where the system is working around the operating point. If the system is highly nonlinear, such as a robot manipulator, control based on the prediction from a linear model may result in acceptable response. In some cases, remarkable static errors exist, and in other cases, oscillation or even instability may occur. Therefore some kinds of nonlinear models should be used to describe the behaviour of a highly nonlinear system[5].

To overcome the problems produced by using linear models some researchers have tried to extend the MPC to include nonlinear models. The technique Joseph et al used is to obtain a nonlinear model through system analysis to help the control calculation arrive at appropriate action. The predictive methods using such nonlinear models have also been made adaptive by estimating parameters of the model that are most likely to change. This requires the model to be of the correct structure, otherwise steady state offsets from the setpoints may result despite parameter adaptation. Selecting such an accurate structure requires significant analysis. However, due to the complexity of the underlying systems, or lack of knowledge of critical parameters of the models in many cases it is impossible to obtain a suitable physically founded system model through an analytical way.

Since the late 1980's, Artificial Neural Networks (ANN) have found wide applications in the engineering field, because of the development of the error backpropagation algorithm. Most engineering researchers are interested in the following two properties of ANN. The first is ANN universal approximation ability that is, ANN could be used to approximate any nonlinear mapping relationship between the inputs and outputs. The second is ANN learning and parallel processing abilities. Based on above two properties the engineering researchers have successfully applied ANN to pattern recognition, nonlinear system identification, controls and many other engineering areas. All above features naturally allow one to think that ANN may be used as an effective tool for the model predictive control of a nonlinear system[6].

III. Neural Network Model

Neural Networks basically comprised of interconnected simulated neurons. A neuron is the smallest unit in network and is used to receive and send signals. Normally each neuron receives signals from other neurons, sums these signals and transforms this sum by means of an activation function, which is monotonic continuously differentiable, bounded function. Frequent used activation function including logistic sigmoid and hyperbolic tangent functions. In addition, there are weights associated with each connection that scale the input to target and training process is to determine optimal weight. The neuron can be arranged into multi-layers which are normally known as multi layer perceptron. The Figure 4 illustrated the basic structure of a neuron[7].

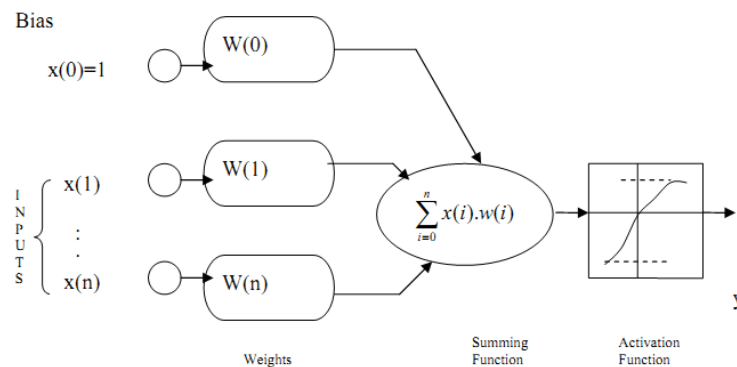


Figure 4. A basic architecture of a neuron

In robotics application to date the most widely used neural network is the Feed forward Neural Network. This is large due its simplicity compared to other networks and its ability to learn the implicit governing relation between the inputs and outputs if sufficient training data is supplied. Feedforward networks is network structure in which the information or signals ill propagates only in one direction on contrary to the recurrent networks in which the delayed time neural net outputs will feed back in to the neural networks as inputs. The Feed forward Neural Network typically consist of three or four layers including input layer, hidden layer and output layer in Figure 5.

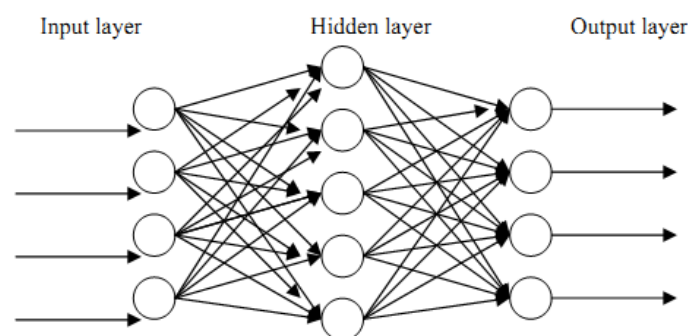


Figure 5. A feedforward artificial neural network structure

For the prediction of the behaviour of the robot forward dynamics, choosen a feedforward neural network with sigmoid activation functions. This kind of neural network is well known and relatively well understood. To set up the neural network predictive model, we can rewrite the robot dynamic equation as

following form since the inertial matrix in the equation is symmetric positive definite, so this inertia matrix is always invertible,

$$\ddot{q} = H^{-1}(q)(t-h(\dot{q}, \ddot{q}) - c(q)\dot{q}) \quad (3)$$

where the vectors \ddot{q} , \dot{q} , q are joint acceleration, joint velocity and joint angle and $H(q)$ is the $n \times n$ symmetric positive definite inertia matrix; $h(\dot{q}, \ddot{q})$ is the $n \times 1$ vector of Coriolis and centrifugal torques; $c(q)$ is $n \times 1$ gravitational torques, f is the $n \times 1$ vector representing Coulomb friction and viscous friction forces. t is the $n \times 1$ vector of joint actuator torques.

The NN model trained using these data will not be accurate. To avoid this we can do numerical differentiation on equation (3). Through Taylor formula we have the first order difference quotient,

$$\dot{q}(t) = \frac{q(t+h) - q(t-h)}{2h} - [\ddot{q}(t_1) + \ddot{q}(t_2)]$$

$$\dot{q}(t) = \frac{q(t+h) - q(t-h)}{2h} - \frac{h^2}{6} + \ddot{q}(t_m) \quad (4)$$

Where $t-h > t_M > t+h$, and second order difference quotient,

$$\ddot{q}(t) = \frac{q(t+h) - 2q(t) + q(t-h)}{h^2} - \frac{h^2}{4!} [q^{(4)}(t_3) + q^{(4)}(t_4)]$$

$$\ddot{q}(t) = \frac{q(t+h) - 2q(t) + q(t-h)}{h^2} - \frac{h^2}{12} q^{(4)}(t_M) \quad (5)$$

where $t-h > t_M > t+h$, Substitute (4) and (5) into (3), after being straightened up we have:

$$\dot{q}(t+h) = F(q(t), \dot{q}(t), \ddot{q}(t-h), t(t)) \quad (6)$$

or

$$q(t+h) = G(q(t), \dot{q}(t-h), t(t)) \quad (7)$$

where t is the time under consideration, h is the numerical differentiation step, F and G are certain function relationships. The accuracy for both (6) and (7) is $O(h^2)$. The above procedure shows that with one step time delay the dynamic system (3) could be expressed by (6) or (7) accurately. Thus the robot dynamic characteristic could be emulated by a FNN model approximating the relationships (6), (7) or both. This FNN model could be easily connected to the MPC controller because both (6) and (7) are in predictive form[8].

3.1. Training

Training is basically a systematic adjustment of weights to get a chosen neural network to predict a desired output data training set and it can be done in either supervised or unsupervised way. The training for FNN is supervised. In the supervised training, the connection weights for each processing element are randomly initialized. As the training begins, the training algorithm will start to compare network predicted outputs to the desired outputs from training data set and any error will be used to correct the network. The correction is done by adjusting the set of connection weights of each processing element neuron and this will continue until the algorithm meets the prespecified convergence criteria. The frequent used criteria including the limit of error and the numbers of iteration.

However, care must be taken to ensure that the network does not overfit or overfamiliarize with the training data set and hence lose its generalization ability. Various approaches can be used to avoid this problem including regularization theory which attempt to smooth the network mapping and cross validation which using as independent test data. To control the simulated robot system the MPC controller is designed by using the neural network predictive model developed in here[8].

$$v = v_{rand} \sin(2\pi f_{rand} t) \quad (8)$$

Where, v is sinusoidal voltage signals, v_{rand} is random magnitude and f_{rand} is random frequency. The frequencies and amplitudes of the signals used to excite the simulated robot system are limited within certain scopes to avoid processing too many data. In this paper the varying ranges of the amplitudes and frequencies of the exciting sinusoidal voltage are within ± 50 volts and 0 to 10 Hz separately. Input voltages v_1 , v_2 and v_3 and corresponding time responses at 10 second interval are then collected. A total of 300 sets of voltage signals are used to excite the robot system and 35,000 data sets are collected.

21 inputs composed of nine displacements. q_1 , q_2 and q_3 at time t and $t-1$ respectively, nine velocities \dot{q}_1 , \dot{q}_2 and \dot{q}_3 at time t and $t-1$ respectively, and three voltages $v_1(t)$, $v_2(t)$ and $v_3(t)$. Hidden layers with 45 neurons respectively. Six outputs representing $q_1(t+1)$, $q_2(t+1)$, $q_3(t+1)$ and $\dot{q}_1(t+1)$, $\dot{q}_2(t+1)$, $\dot{q}_3(t+1)$ respectively. Thus the feedforward neural network has a structure of 21-45-6.

The momentum coefficient (β) and training rate coefficient (α) are set to be 0.90 and 0.004 respectively. The training was terminated after 2 million iterations without further significant reduction being observed. The algorithm used to train the neural network models is the standard backpropagation. Then this neural network model is connected to the MPC controller.

IV. Simulations

4.1 Simulation of robot system

In this study, the inverse kinematics calculations and trajectory planning of a robot arm with three axes has been done. its motion has been obtained and the motion of robot arm has been simulated by a computer. AutoCAD programming was used for the calculations and the 3D simulation of the robot arm. After the image processing detection were done using Matlab R2009 b, the results were transferred to the program written AutoCAD. The robot system to be controlled is simulated by a computer program. The prototype of the simulated robot system is a modified PUMA robot in which the joint motors are voltage controlled. In this study, movement simulation of a three armed robot has been realized by using AutoLISP programming language which is supplied with AutoCAD. Analytical and matrix solution methods have been used in simulation equations. Shows top and front views of PUMA robot made by simulation programme in Figure 2.

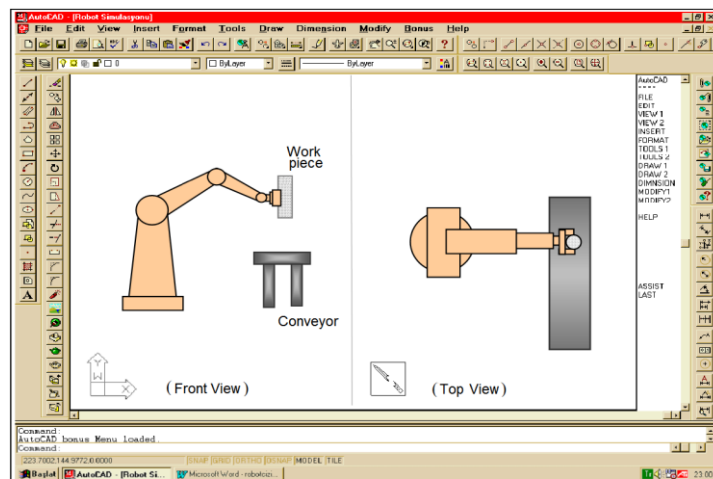


Figure 4. The views of Puma Robots in Simulation Programmes

It is assumed that there are three links with the simulated robot system. The torque produced by a DC motor is used to drive each link through a set of transmission mechanism connecting the motor and load shafts. The DC motor in this paper is simplified as a resistance inductance circuit with voltage source. The voltage source in this circuit is the voltage input to the motor. Back electromotive force produced across the armature is proportional to the angular velocity of the motor shaft. And torque produced by the motor is proportional to the armature current. There is a backlash between the mating gears in the transmission mechanism [9].

The dynamic equation used in the simulated robot system is,

$$\tau_i = H(q_i)\ddot{q}_i + h(q_i, \dot{q}_i) + c(q_i) + f \quad (8)$$

The meaning of all the symbols, used above are similar with those for (3). The friction force, is represented using the following equation,

$$f_i(q_i) = c_i \operatorname{sig}(q_i) + v_i \dot{q}_i \quad (9)$$

where c and v represent the coulomb and viscous friction coefficients, i is the joint number under consideration, $\operatorname{sgn}(x)$ is the sig function[10].

4.2. Simulation of MPC controller

The optimisation problem expressed in equation (1) and (2) is a simple bounded variable nonlinear optimisation problem without constraints. The bounded variables are the control inputs (control torques) of the robot. To solve this optimisation problem, the quadratic nonlinear programming routine NLPQ provided in IMSL is used. This method is chosen because the authors are familiar with this routine. Many other methods may also be used to solve this problem, perhaps in a more efficient way. To test the performance of the proposed model predictive control strategy, the desired trajectories for the simulated robot system to follow are generated by inputting the system a group of sinusoidal excitations, in which the amplitudes and frequencies are within the frequency and amplitude limits used. The desired trajectories to be followed by the robot joints are shown in Figures 5, 6 and 7.

A comparison of the effectiveness of the model predictive control based on the neural network model (NMPC), the model predictive control based on robot model in which the dynamic equations are with nominal parameters (DMPC) is used. Because of the inevitable measurement errors, it is difficult to obtain the accurate values of dynamical parameters for the robot model. In this paper, it is assumed that there are 14 % of measurement errors in the moment of inertia for each link, and the friction terms are neglected. The tracking errors obtained by applying DMPC and NMPC are presented in Figures 8, 9 and 10. The results show that NMPC provides a better performance than DMPC, as predicted. It is clear the performance of the DMPC will improve if the parameters of the nominal model can be obtained more accurately.

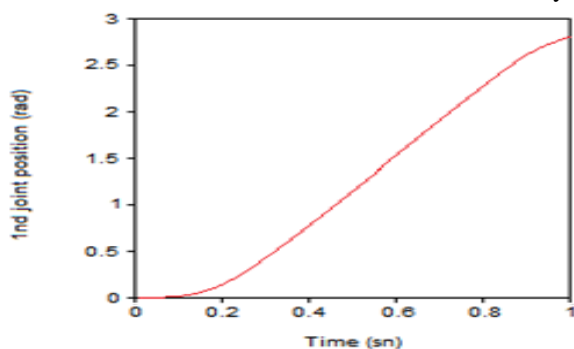


Figure 5. Desired trajectories

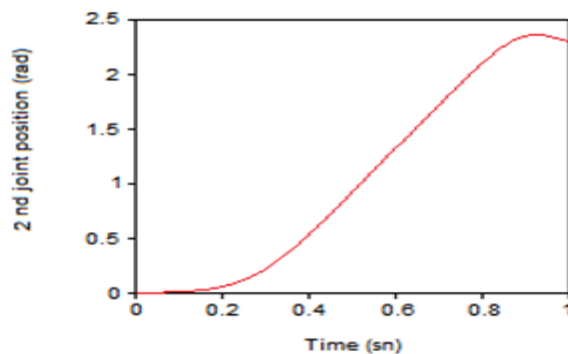


Figure 6. Desired trajectories

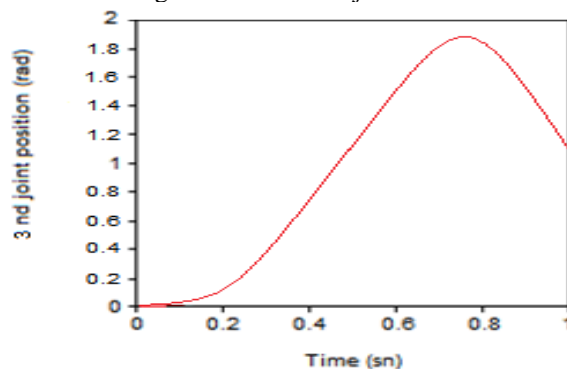


Figure 7. Desired trajectories

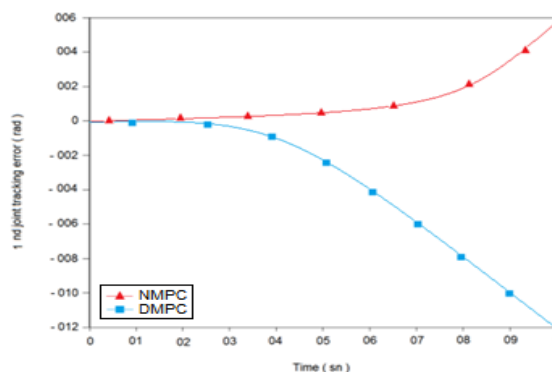


Figure 8. Tracking errors of 1 nd joint

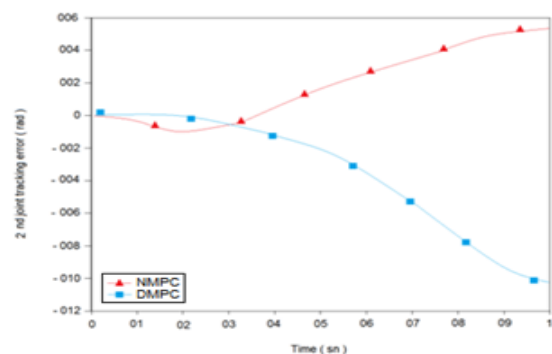


Figure 9. Tracking errors of 2 nd joint

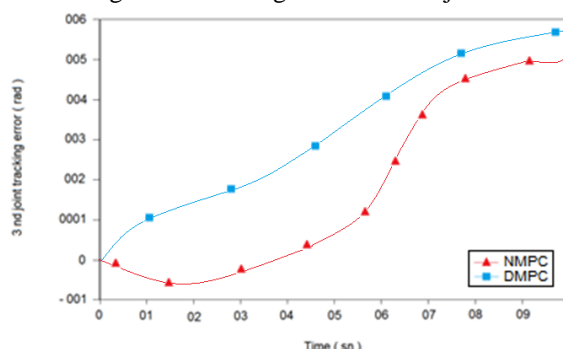


Figure 10. Tracking errors of 3 nd joint

V. Conclusion

The use of DMPC and NMPC to control of trajectory for three joint manipulator, was investigated. An unconstrained, Multi Input Multi Output (MIMO) DMPC and NMPC algorithms were developed using a step response model and two Feedforward Neural Networks respectively. Additionally, the comparison between DMPC and NMPC controller based was conducted. The trajectory tracking results with higher accuracy in this paper are obtained without considering the regulation of the control voltages. the NMPC controller is a potential effective way for robot trajectory tracking. This is not impractical because to obtain a higher tracking accuracy, the frequency of the control voltage may be so high that it is far beyond the frequency response scope of an actual driving motor. Further research on the real time execution of NMPC and the regulation of control voltage is required and is currently being carried out. Comparison of the NMPC and the DMPC controller, both are the industrially popular and successful control strategies in this research had clarify the significant features of NMPC.

REFERENCES

- [1]. Kosmatopoulos E.B., Chassiakos A. And Christodoulo M.A., "Robot Identification using dynamical neural networks." Engineering Systems with Intelligence. Kluwer Academic Publishers. 1991. pp. 187-195.

- [2]. Gupta M. " Robust repetitive model predictive control for systems with Uncertain period-time " Master Thesis of Science in Chemical Engineering Georgia Institute of Technology May, 2004
- [3]. Fu K.S., Gonzalez R. C., Lee C.S.G., Robotics: control, sensing, vision and intelligence. McGraw Hill, New York, 1987
- [4]. Nebot E.M. and Fang G., 'Robot Dynamic Identification using -Neural Networks.'" Proceedings of Mechatronics & Machine Vision in Practice. Toowoomba, Qld., Australia. Sept. 1994. pp. 200-205
- [5]. Boo Chin E., Hong Mei K. ve Amy Tan S. " Formulation of model predictive control algorithm for nonlinear processes "Jabatan Kejuruteraan Kimia Universiti Teknologi Malaysia 2006
- [6]. Seidl D.A., Lam S. Putman J.A. and Lorenz R.D., "Neural Network Compensation of Gear Backlash Hysteresis in Position-Controlled Mechanisms." IEEE Transactions on Industry Applications. Vol. 31, No.6, 1995. pp 1475-1483.
- [7]. Eskandarian A, Bedewi N.E., Kramer B.M. and Barbera A. J., " Dynamics modelling of robotic manipulators using an artificial neural network. "Journal of Robotic Systems. Vol. 11, No.1, 1994. pp.41-56
- [8]. Zhouping W. and Gu F. " Model Predictive Control for Robot Manipulators Using A Neural Network Model " School of Mechatronic, Computer and Electrical Engineering, University of Western Sydney, Nepean, PO Box 10, IGngswood, NSW 2747
- [9]. Garcia C.E., and MorarIM., 'Internal model control. 1. A unifying review and some new results." Ind. Eng. Chern. .Process Des. Dev. Vol. 21, No.2, 1982.pp. 308-323.
- [10]. Joseph, B., Jang, S. and Mukai, H., 'Integrated Model Based Control of Multivariable Non linear Systems." Proceedings IFAC Workshop on Process Model Based Control. Atlanta, 1988.

Effect of V Notch Shape on Fatigue Life in Steel Beam Made of High Carbon Steel Alloy AISI 1078

Qasim Bader¹, Emad Kadum²

^{1,2} (Department Mechanical Engineering, College of Engineering, University of Babylon, Iraq)

Abstract: The present work includes study effect of V notch shape with various angle orientation and depths on fatigue life behavior in steel beam made of High Carbon Steel alloy AISI 1078 which has a wide application in industry. Fatigue life of notched specimens is calculated using the fatigue life obtained from the experiments for smooth specimens (reference) and by use Numerical method (FEA). The fatigue experiments were carried out at room temperature, applying a fully reversed cyclic load with the frequency of 50 Hz and mean stress equal to zero ($R = -1$), on a cantilever rotating-bending fatigue testing machine. The stress ratio was kept constant throughout the experiment. Different instruments have been used in this investigation like Chemical composition analyzer, Tensile universal testing machine, Hardness tester, Fatigue testing machine and Scanning Electron Microscope (SEM). The results show that there is acceptable error between experimental and numerical works.

Keywords: AISI 1078; V Shape Notch; Stress Life approach; Fatigue Life; S-N curve; FEA

I. INTRODUCTION

Fatigue is an important parameter to be considered in the behavior of mechanical components subjected to constant and variable amplitude loading. Mechanical, metallurgical and environmental variables can influence the fatigue resistance of a structural component. Fatigue is the process of a cumulative damage in a benign environment that is caused by repeated fluctuating loads and, in the presence of stress concentrators like notches and fillets.

In cyclic loading, the effect of the notch or the fillet is usually less than predicted by the use of the theoretical factors. The difference depends upon the stress gradient in the region of the stress concentration and on the hardness of the material [1]. A fatigue failure is one that occurs under cyclic or alternating stress of an amplitude that would not cause failure if applied only once. Fatigue is by far the most common cause of mechanical failure in engineering components; the prevention of fatigue failure is a major preoccupation of designers in many industries, such as power generation and

transport [2]. The term "notch" in a broad sense is used to refer to any discontinuity in shape or non-uniformity in material such as the V-shape threads on nut-bolt connections, the square-shape key washer's grooves on shafts, scratches, nonmetallic inclusions and corners, fillets and geometry discontinuities. The failure usually originates in the formation of a crack at a localized point on the notches. Presentation of notches in structural components causes stress intensification in the vicinity of the notch [3]. A. Fatemi, and Z. Zeng, [4] modeled fatigue behavior and life predictions of notched specimens made of QT and forged micro-alloyed steels, they have been used notched circumferentially notched round bar and double-notched flat plate geometries, each with different stress concentration factors. Reference [5], described notch effects in fatigue and fracture and explained that the notch effect in fracture is characterized by the fact the critical gross stress of a notched structure is less than the critical net stress which acts on the remaining alignment under notch tip, the notch effect in fracture is sensitive to structure geometry and the Wohler curve for the notched specimen is below the smooth specimen curve. Reference [6] developed experimental and theoretical life on notched specimens under bending. Fatigue life of notched specimens with various notch geometries and dimensions was investigated by experiment and Manson-Coffin analytical method. An experimental investigation was achieved by [7], this study used cantilever rotating-bending fatigue testing machine to explain the effect of surface roughness on the fatigue life in steel alloy. There are numerous evidences in the literature that the presence of notch can reduce the fatigue life of components dramatically in some circumstances. The fatigue life of V-shape notch specimens under rotating bending by analytical method was examined [8]. Reference [9] also shows failure cycles of notched round specimens under strain controlled cyclic loading by using strain life relations obtained from experiment for plain fatigue round specimens. The maximum strain is computed by appropriate Finite element analysis using the FE software ABAQUS. They obtained that the total strain life curve generated from fatigue test of round specimen can also be used for the prediction of life for notched specimens based on actual strain developed at notch tip, the results show that in most of the cases the predicted life is found to be less compared to experimental values for all the types of notched specimens.

II. FATIGUE METHODOLOGIES

There are three main approaches of fatigue methods which are, Stress life method, Strain life method and Fracture mechanics method. Number of cycles ranging from ($N \leq 10^3$) is considered as low cycle fatigue whereas ($N > 10^3$) cycles is considered as high cycle fatigue. In this work, we consider the Stress life approach to predict the cyclic life of specimens used for the rotational bending machine. This method is often referred to as infinite life design. Material properties from polished specimens are modified for surface conditions and loading conditions being analyzed. Stress concentration factors are used to account for locally high stresses. An effective stress concentration in fatigue loading is computed and an estimate of the fatigue life is determined by use ANSYS Workbench software and comparison between experimental and FEA results for different V shape angles and notch depths has been done.

Basquin's model

The stress-life curve is a graphical representation of fatigue data. It represents the relationship between fatigue life, in cycles, and the applied stress amplitude. Basquin's relation the most commonly used model and provides an analytical expression of the S-N curve, for finite life (low or high cycle fatigue). By use this technique an estimation of life prediction, with little information on the material, can be obtained, see [10].

The simple Basquin's curve is represented by :

$$\sigma_a = a N_f^b \quad (1)$$

Where :

σ_a is the fatigue stress amplitude (MPa),

N_f is the number of cycles to failure (MPa),

The parameters a and b are both constant, depending on the material and on the geometry, respectively. The coefficient a is approximately equal to the tensile strength. The coefficient b is the fatigue strength exponent. These coefficients can be evaluated by use least square method (linearizing the power law in logarithmic form), it is important to mention that the S-N curve is represented in the log-log scale.

The value of Fatigue limit is not clearly obvious on the S-N curve; therefore, the Fatigue limit can be calculated by using the fatigue life estimation equation at 10^6 cycles.

Least Square Method

In many branches of applied mathematics and engineering sciences we come across experiments and problems, which involve two variables. For example, it is known that the Stress amplitude σ_a of a steel specimens in S-N curve varies with the Cycles of failure N according to the Basquin's formula $\sigma_a = aN_f^b$. Here a and b are the constants to be determined. For this purpose we take several sets of readings of stress amplitude and the corresponding Cycles. The problem is to find the best values for a and b using the observed values of σ_a and N , thus, the general problem is to find a suitable relation or law that may exist between the variables x and y from a given set of observed values, (x_i, y_i) , $i = 1, 2, \dots, n$. Such a relation connecting x and y is known as empirical law. For above example, $x = \sigma_a$ and $y = N$.

The process of finding the equation of the curve of best fit, which may be most suitable for predicting the unknown values, is known as curve fitting. Therefore, curve fitting means an exact relationship between two variables by algebraic equations. There are following methods for fitting a curve. The graphical method has the drawback in that the straight line drawn may not be unique but principle of least squares provides a unique set of values to the constants and hence suggests a curve of best fit to the given data. The method of least square is probably the most systematic procedure to fit a unique curve through the given data points.

III. EXPERIMENTAL WORK

The experimental work included assessment of fatigue life specifications by using stress life approach for High Carbon Steel AISI 1078 supplied from the local market with and without notches and the effect of angle orientation, depth of notch on the fatigue limit. The experimental procedure consist of four parts. The first one deals with the selection of materials used and the specimens preparation, the second part deals with different mechanical tests, the third includes details of fatigue test and finally the details of Microscopic inspection. A brief description for the different equipment used in this study had mentioned. For experimental work stages and the specimens distribution have been used in this work, see [11].

3.1 Material Selection

In this work, high carbon steel alloy AISI 1078 treated commercially, was used in this investigation, this type of steel alloy has a wide application in industry. The chemical composition test of the alloy was done by use the device Spectrometer type (ARC. MET 8000), the results found within the standard specification limits as shown in table 1

Table. 1 : Chemical Composition of the AISI 1078

C%	Si%	Mn%	P%	S%	Cr%	Mo%	Ni%	Al%	Cu%	Fe%
0.773	0.236	0.327	0.006	0.012	0.16	0.002	0.069	0.04	0.062	Bal.

3.2 Mechanical Tests Tensile Test

The tensile test is a standard test which was conducted using the microcomputer controlled electronic universal testing machine type (WDW-100E - 100KN). The specifications of the tensile test have been restricted according to the ASTM [12]. Tensile test results are given in table 1. They are presented as the mean value of five identical tests to satisfy an additional accuracy.

Table. 2 :Tensile Test Results of the AISI 1078

Property	Value
Tensile Strength σ_u (MPa)	675
Yield strength σ_y (MPa)	510
Elongation [%]	15
Modula's of Elasticity (Gpa)	206

3.3 Hardness Test

Hardness is the property of a material that enables it to resist plastic deformation, usually by penetration. However, there are two tests have been done in this investigation Brinell's and Vicker's Hardness test. The average value of four readings was recorded ; the results are shown in table 3.

Table 3: Hardness Test Results

Property	Value
Brinell Hardness	200
Vickers Hardness (HV)	220

3.4 Roughness inspection

Surface roughness and surface integrity resulting from manufacturing processes are both important considerations in fatigue design. Fatigue damage on the surface of a component typically develops due to the surface integrity resulting from manufacturing, and the presence of stress concentrations originating from the surface topography. The specimens were first polished with different wet oxide aluminum papers by different degrees ,then followed by polishing with a string cloth soaked in alumina [13] . Once the manufacturing process of the specimens was done the surface roughness was measured by using a portable surface roughness tester type (SADT) and in order to reduce human errors during the measurement, the reading was taken for three times at different points and for all notched and smooth specimen. Then, the average and total surface roughness, R_a and R_t are calculated for both free and notched specimens and given in table 4.

Table 4: Values of surface roughness

Item	R_a [μm]	R_t [μm] max.
Free-Notch Specimen	1.75	3.25
Notched Specimen	1.85	3.31

1. Fatigue Test

a. Fatigue Test of Specimens

Fatigue specimens were machined in suitable dimensions to satisfy the requirement of the machine test that suited cylindrical specimens. Two types of fatigue specimens smooth and notched were prepared according to machine specifications. All the smooth and notched cylindrical fatigue specimens were machined from alloy steel with different content of carbon on a CNC lathe machine adopting standard manufacturing procedure and circumferential V notch shape angle of (30° , 45° & 90°) to a depth of notch was (0.5 & 2) mm respectively [14] with a notch radius as small as possible ($< 0.075\text{mm}$) [15] and was introduced at the portion of maximum bending. The geometry and a schematic view specimen are given in Fig. (2) .

b. Rotating Bending Machine

The fatigue behavior of different materials can be determined from laboratory tests. The type of fatigue testing machine is revolving fatigue testing machine type WP 140, (a single cantilever rotating bending model) with a constant amplitude (fully reversed bending). A rotating sample is clamped which on one side is loaded with a concentrated force with a maximum capacity of (0.3 KN) with constant frequency of (50Hz). A sinusoidal cyclic load with a stress ratio $R = -1$ (minimum load/maximum load) was applied throughout the experiment. As a result, an alternating bending stress is created in the cylindrical sample following a certain number of load cycles, the sample will rupture as a result of material fatigue. Tests were carried out at room temperature (20-24 °C). The experiment was conducted by repeating so many similar procedure tests for all specimens. Bending moment values were used to determine the alternating bending stress, which can be determined directly from equation (6). For constant amplitude load many parameters can be found; for example: stress range, ($\Delta \sigma$), a mean stress, σ_m , an alternating stress or stress amplitude, σ_a , and a stress ratio, R . Below some important relations used in the fatigue life analysis:

$$\text{Stress range: } \Delta \sigma = \sigma_{\max} - \sigma_{\min} \quad (2)$$

$$\text{Mean stress: } \sigma_m = \frac{\sigma_{\max} + \sigma_{\min}}{2} \quad (3)$$

$$\text{Stress amplitude: } \sigma_a = \frac{\Delta \sigma}{2} = \frac{\sigma_{\max} - \sigma_{\min}}{2} \quad (4)$$

$$\text{Stress ratio: } R = \frac{\sigma_{\min}}{\sigma_{\max}} \quad (5)$$

$$M_b = F \cdot a \quad (6)$$

$$W_b = \frac{\pi d^3}{32} \quad (7)$$

By using the section modulus of the sample it is possible to calculate the alternating stress amplitude.

$$\sigma_a = \frac{M_b}{W_b} = \frac{32 F \cdot a}{\pi d^3} \quad (8)$$

$$= 2 F \quad \text{MPa} \quad (9)$$

Where;

σ_a : Stress amplitude which is equal is the maximum alternating stress (MPa)

F: Applied Force (N)

a: bending arm = 106 ± 0.1 mm

d: diameter of the specimen = 8 ± 0.1 mm

M_b : bending moment (N.mm)

W_b : Moment of inertia (for hallow cylinder)

A series of tests was commenced by acting a specimen to the stress cycling, and the number of cycles to failure was counted. This procedure was repeated on other specimens at progressively decreasing stress amplitudes. Data were plotted as stress σ_a versus the logarithm of the number N of cycles to failure for each of the specimens. S-N curves are plotted by using software of Fatigue instrument present in PC which is connected directly to instrument as shown in Fig.(3).

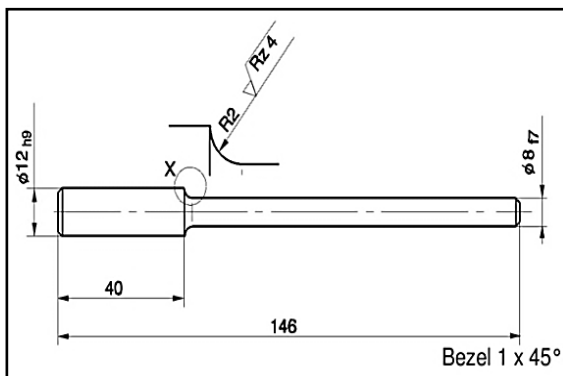


Fig. 2 Fatigue test specimens (mm)

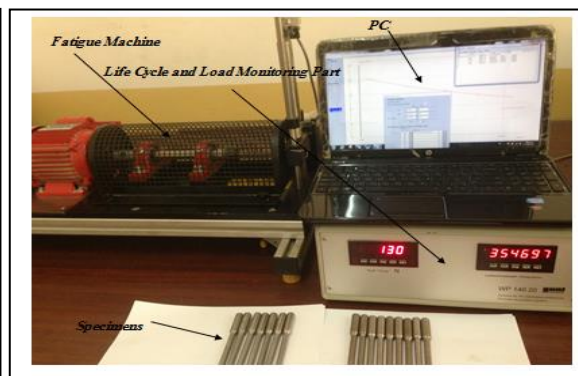


Fig. 3 Fatigue testing machine WP 140

IV. EXAMINATION FRACTURE FATIGUE

The process of achieve test fracture for the different fatigue specimens has been done to check the nature of fracture. Fracture surfaces of failed specimens have been analyzed using Optical Microscope (OM) and Scanning Electron Microscope Zeiss type (EVO 50). Samples for microstructure examination were ground using different grades of wet silicon carbide papers (260, 500, 800, 1200 and 2000), then the samples were polished using two type of alumina (0.5 micron and 0.3 micron). Distilled water and alcohol were used to clean the samples in succession. Etching was carried out with naital (2 % HNO₃) in alcohol followed by washing them with water and alcohol. Fig. (4) illustrates the photo digital system.

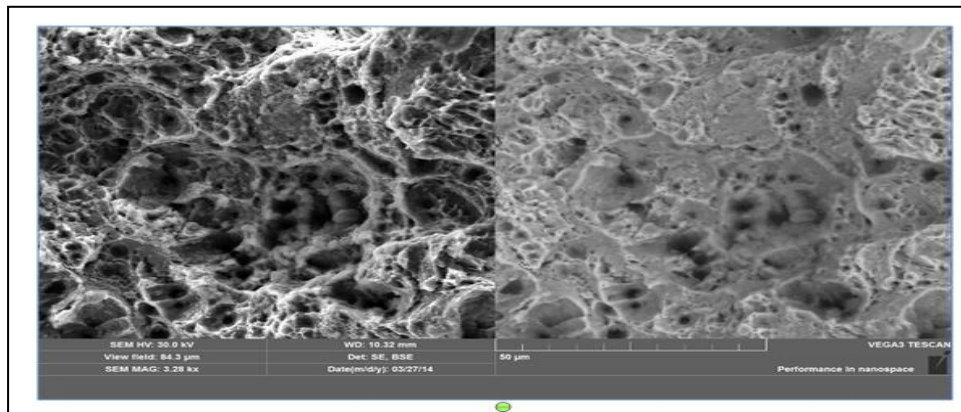


Fig. 4 Fracture surface of a specimen AISI-1078 tested by use SEM

V. NUMERICAL INVESTIGATION

The finite element method (FEM) is a powerful numerical procedure which can be used to obtain the solutions of a large number of engineering problems, especially in the area of solid mechanics [16]. In this work, FEM with the aid of ANSYS Workbench software was utilized for numerical analysis. A frequent tool used to illustrate the effect V notch Geometry on the fatigue performance in a structure element, verify the experimental results and to examine stress distribution at the fracture surface. Smooth and notched fatigue specimens with different notch orientation angles and two depths are modeled, Solid hexahedral elements (solid185), with 8 nodes were considered. Constant amplitude fully reversed loading without any mean stress correction theory was applied to the structure. Also Fatigue analysis through ANSYS show that maximum value of stress occurs at the vicinity of change in cross section of the specimen where a V notch with different geometry present. Fig.(5) explain model with mesh, boundary condition, maximum stresses and biaxiality generated in the model.

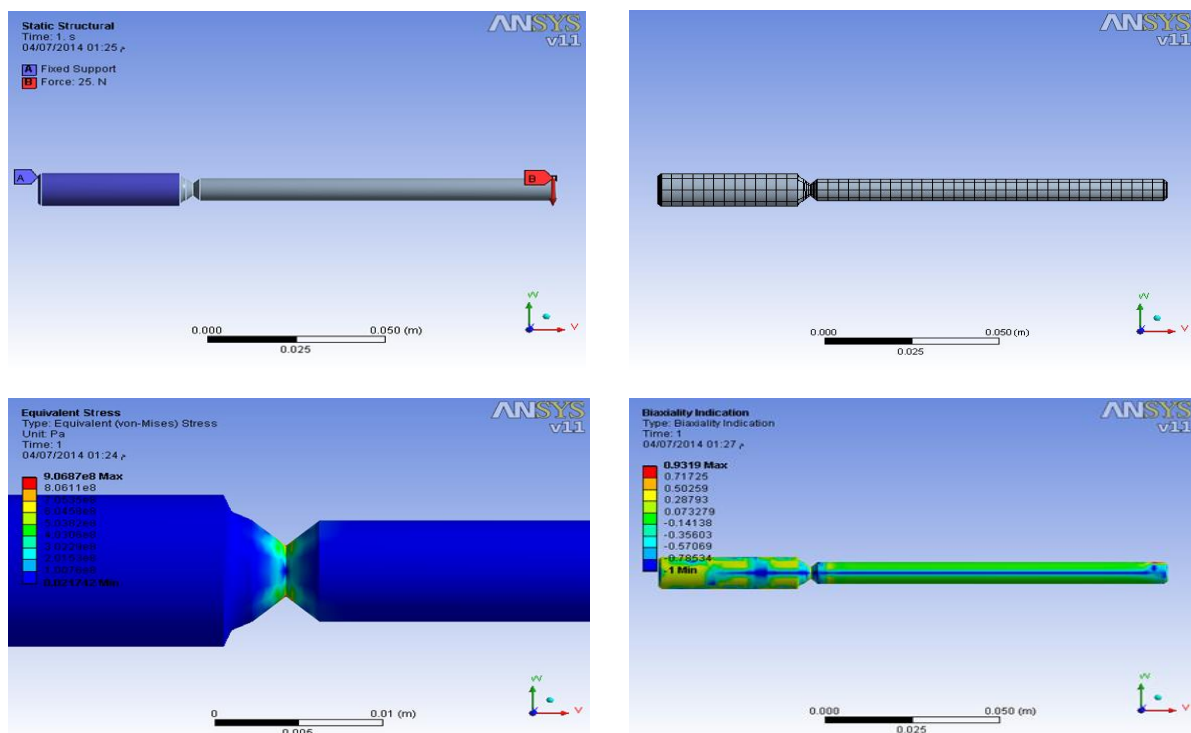


Fig.5 Shows Model with mesh, max. Equivalent stresses and Biaxiality for Notched bar

VI. RESULTS

In this work it is trailed to predict the fatigue life of notched fatigue specimens under effect of cyclic loading using stress life data of smooth fatigue specimen (free-notch) on the basis of maximum stress developed obtained from finite element simulated results of notched specimen under stress controlled cyclic loading . According to the accurate stress concentration factors corresponding bending stress can be found using least square method. Fatigue life equation and coefficients of Basquin's formula values have been found as shown in table 5. The radii of fillet at smooth specimen was found 2 mm ,while for notched specimens ,three angle orientation (30,45&90 degree) with two notch depths (0.5&2) mm were employed corresponding to which stress concentration due to bending (K_t) was found in table 6 , for more details of the procedure for stress concentration determination see [17]. For dynamic loading, we need to calculate Fatigue concentration factor K_f based on the notch sensitivity of the material as in below :

$$K_f = 1 + (K_t - 1) q \quad (10)$$

$$q = \frac{1}{1 + \frac{a}{r}} \quad (11)$$

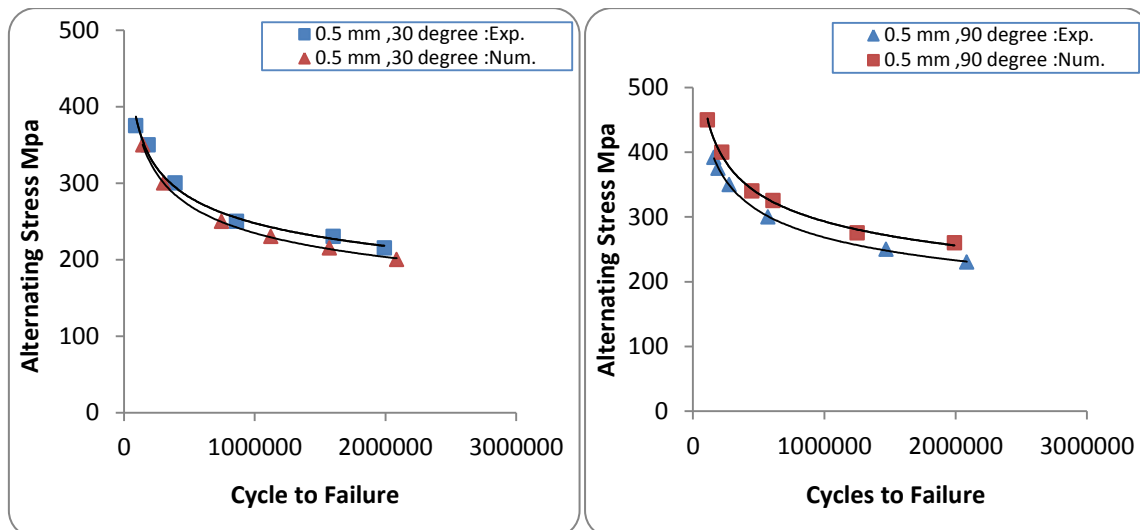
where q is the notch sensitivity it can be defined from the Kunn-Hardarth formula in terms of Neuber's constant (a) and the notch radius (r).

Table 5. Basquin's law parameters and correlation coefficients

Specimen type	σ_f (Mpa)	b	r
Smooth (reference)	5042.13	-0.197	-1
Notched ,h = 0.5 mm ,30°	3189.18	-0.185	-0.99
Notched ,h = 0.5 mm ,45°	4305.41	-0.2	-0.99
Notched ,h = 0.5 mm ,90°	4408.1	-0.196	-0.995
Notched ,h = 2 mm ,30°	2529.8	-0.188	-0.995
Notched ,h = 2 mm ,45°	2197.5	-0.173	-0.99
Notched ,h = 2 mm ,90°	2689.3	-0.183	-0.99

Table 6.: Values of Stress Concentration, fatigue and notch sensitivity factors

α °	h (mm)	r (mm)	K_t	q	K_f
30	0.5	0.07	4.28	0.298	1.98
45	0.5	0.07	4.15	0.301	1.95
90	0.5	0.07	3.47	0.299	1.74
30	2	0.07	3.95	0.301	1.89
45	2	0.07	3.83	0.300	1.85
90	2	0.07	3.23	0.300	1.67



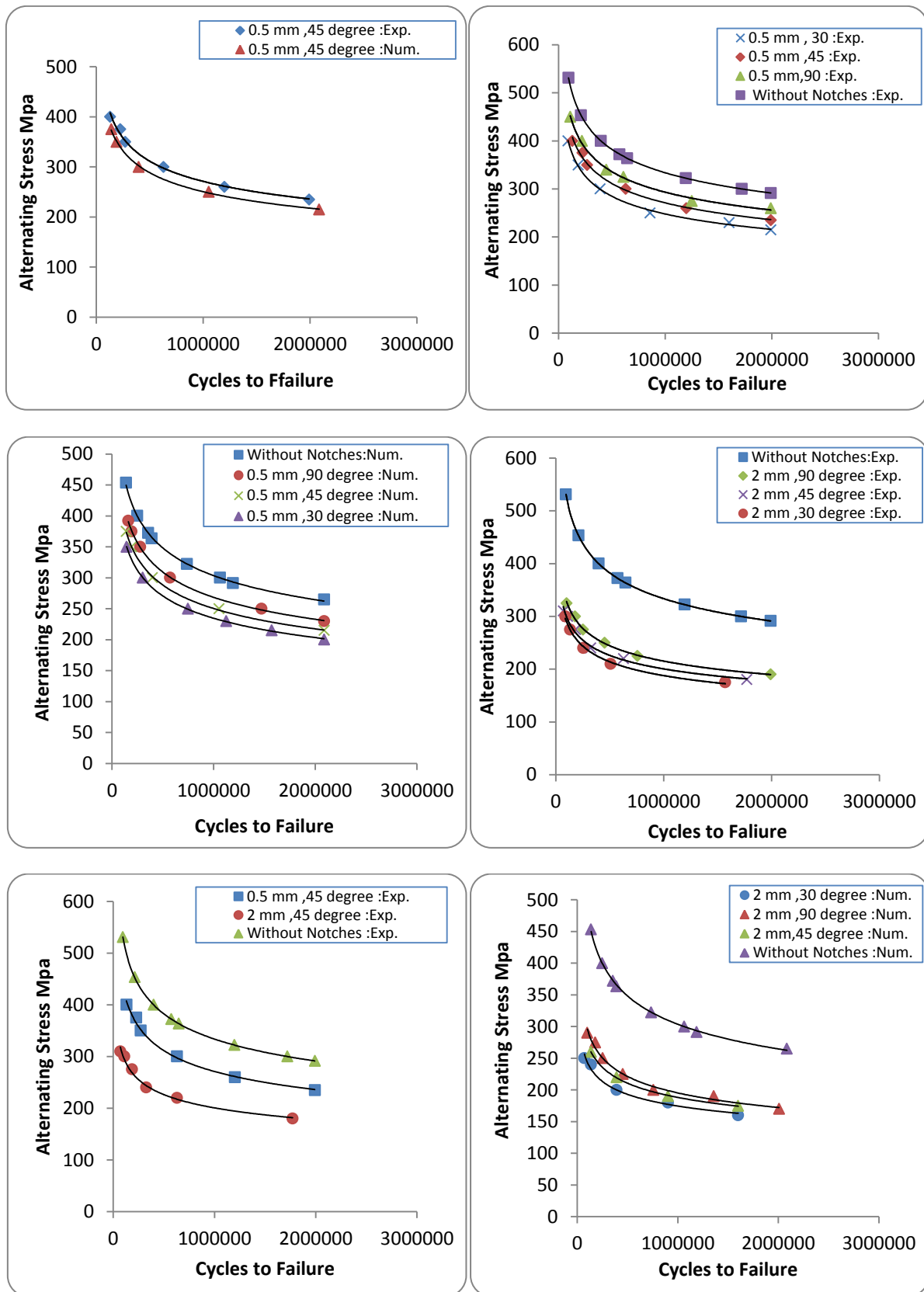


Fig. 6 Numerical and Experimental S-N curves for V notched Specimens with different angle orientation

VII. CONCLUSION

In this work, bending fatigue life of the specimens with V notch geometry of various angle orientation and notch depth was investigated by experiment and by FEA method. The Stress concentration factor is calculated analytically and numerically by use FEM. The results indicate that the FEA method is applicable to the experiments. From the results it is also observed that in most cases the predicted life is found to be less compared to experimental values for all the types of notched specimens. This may be due to the fact that the life has been predicted based on maximum stress in notched section [7]. The accuracy of the predicted life by FEA simulation depends on the selection of appropriate material model and the accuracy of the value of the material parameters used. It is very important to know that the prediction in this method depends on the correctness of the material total S-N curve (simple regression) generated from experimental results of high cycle fatigue data of cylindrical specimens. Good agreement between test and simulation data has been observed, the differences in results remains in range of 13%. The common stress life curve generated from specimens of several notch angles gives a better prediction, which is apparent from the Fig.(6). Stress concentration factor was obtained using finite element method and the results are given in table 6. Also the results show that maximum principle stresses is greater in small angle orientation while the fatigue limit will be more with the increasing of angle orientation.

REFERENCES

- [1] Juli A. Bannantine, Jess J. Comer, James, L. Handrok, Fundamentals of Metal Fatigue Analysis, prentice hall, Englewood Cliffs, New Jersey 07632.
- [2] Yung-Lilee, Jwo pan, Fatigue Testing And Analysis, Elsevier printer, 2002.
- [3] Ralph I. Stephens, Ali Fatemi, Metal Fatigue In Engineering, Second Edition, McGraw Hill, 2001.
- [4] A. Fatemi, Z. Zeng, A. Plaseied, Fatigue behavior and life predictions of notched specimens made of QT and forged microalloyed steels, International Journal of Fatigue 26 (2004) 663–672R.
- [5] Guy Pluvinage and Marenglen Gjonaj, Notch Effects in Fatigue and Fracture, NATO Advanced Research, Kluwer Academic Publishers, 2001.
- [6] Nasim Daemi, Gholam Hossein Majzoobi, Experimental and Theoretical Investigation on Notched Specimens Life Under Bending Loading, International Journal of Mechanical and materials, 2011.
- [7] N.A.Alang, N.A.Razak & A.K.Miskam, Effect of Surface Roughness on Fatigue Life of Notched Carbon Steel, International Journal of Engineering & Technology IJET-IJENS Vol.: 11 No: 01, 2011.
- [8] M. M. Megahed, A. M. Eleiche, N. M. Abd-Allah, Low-cycle fatigue in rotating cantilever under bending III: Experimental investigation on notched specimens, Int. J. Fatigue, 2005, pp. 271-280.
- [9] Bikash Joadder, Jagabandhu Shit, Sanjib Acharyya, Fatigue Failure of Notched Specimen-A Strain-Life Approach, Materials Sciences and Applications, 2011.
- [10] G. Qilafku, Loading mode and Notch Effect in High Cycle Fatigue, NATO Advanced Research, Kluwer Academic Publishers, 2001.
- [11] QASIM BADER & EMAD K. NJIM, Effect of V notch shape on Fatigue Life in Steel beam made of Mild Steel AISI 1020, International Journal of Mechanical and Production Engineering Research and Development (IJMPERD), ISSN(P): 2249-6890; ISSN(E): 2249-8001, Vol. 4, Issue 4, 2014
- [12] Celalettin Karaagac, failure (fracture) of an agitator shaft with a circumferential notch, 2011.
- [13] Annual book of ASTM Standard Section 2, Standards Test Methods and definition for Mechanical Testing of Steel Products, designation A 370-07, 2007.
- [14] Y. Verreman1, H.Guo, Short cracks at notches and fatigue life prediction under mode I and mode III loadings, Nordam Group, Tulsa, OK, USA.
- [15] Atzori, B., Lazzarin, P. and Meneghetti, G., A Unified Treatment of the Mode I Fatigue Limit of Components Containing Notches or Defects, Int. J. Fracture, 133, 61-87 (2005).
- [16] O. Pabut, M. Eerme, M. Pohlak, Design Optimization of Structural Components for fatigue loading”, 7th International Conference "INDUSTRIAL ENGINEERING" 22 - 24 April 2010, Tallinn, Estonia.
- [17] G.H. Majzoobi, N. Daemi, The study of notch geometry on fatigue life using notch sensitivity factor, Transaction of the Indian Institute of Metals Journal. Vol. 63, 2010, pp.547-55.

Investigate the Route of Chaos Induced Instabilities in Power System Network

Swarnankur Ghosh¹, Dr. G. K. Panda², Dr. P.K Saha³, Avishek Ghose Roy⁴,
Indrajit Koley⁵

^{1, 4, 5} Assistant Professor, Electrical Engineering Department, Siliguri Institute of Technology, India

^{2, 3} Professor & Head, Professors, Electrical Engineering Department, Jalpaiguri Govt. Engineering College, India

Abstract: In this paper possible causes of various instability and chances of system break down in a power system network are investigated based on theory of nonlinear dynamics applied to a Power system network. Here a simple three bus power system model is used for the analysis. First the routes to chaotic oscillation through various oscillatory modes are completely determined. Then it is shown that chaotic oscillation eventually leads to system break-down characterized by collapse of system voltage and large deviation in Generator rotor angle (angle divergence), also known as chaos induced instability. It has been shown that chaos and chaos induced instability in Power system take place due to the variation in system parameters and the inherent nonlinear nature of the power system network. The relation between chaotic oscillation and various system instabilities are discussed here. Using the simple power system model, here it is shown that how chaos leads to voltage collapse and angle divergence, taken place simultaneously when the stability condition of the chaotic oscillation are broken. All nonlinear analysis is implemented using MATLAB. It is indicated that there is a maximum loadability point after which the system enters into instability modes. All these studies are helpful to understand the mechanism of various instability modes and to find out effective anti-chaos strategies to prevent power system instability.

Keywords: Angle divergence, bifurcation, chaos, Period Doubling, Power system, Voltage collapse.

I. INTRODUCTION

A power system is inherently of nonlinear nature i.e. the power system dynamics is described by a set of nonlinear equations obtained from system modeling and parameters. To a large extent, this is also due to the fact that most of the major power system breakdowns are caused by problems related to the system dynamic responses. It is believed that new types of instabilities emerge as the system approaches the stability limit which cannot be explain completely or accurately using linear analysis. So, theory of nonlinear dynamics is used to find out the proper explanation of those instabilities. Being an inherently nonlinear system, power system undergoes changes in state either qualitatively or quantitatively with the changes of one or more system parameters. This phenomenon is known as **Bifurcation**. Sometimes variation in parameter may result in complicated behavior which is random and indeterministic, known as chaos. This chaotic oscillation may lead to various instabilities. Most common types of system instabilities, which occur when the system is heavily loaded, are voltage collapse and angle divergence which eventually cause system breakdown.

Voltage collapse in electric power systems has recently received significant attention by researchers. A number of physical mechanisms have been identified which possibly leading to voltage collapse. In several papers [4-10] voltage collapse was viewed as an instability which coincides with the disappearance of the steady state operating point as a system parameter, such as a reactive power demand is quasistatically varied, which is known as fold or saddle node bifurcation of the nominal equilibrium point. Dobson and Chiang [1] first studied and analyzed voltage collapse, and concluded that this phenomenon occurs at a hypothesized static bifurcation of equilibrium points taking place as system loading is increased. The static bifurcation mechanism for voltage collapse postulated in [1] was investigated in [2] and in [3]. It is therefore not surprising that saddle node bifurcation is being studied as a possible route to voltage collapse [4].

Another possibility is that steady state operating point loses stability before the saddle node bifurcation. If this occurs in a given system, stability of the nominal equilibrium point may be lost prior to static/saddle node bifurcation point through a Hopf bifurcation. Study of Hopf bifurcation in power system was done in details in [2, 3, 4, and 5]. Except these, other type's bifurcation occurs in power system like Torus bifurcation [4], cyclic fold bifurcation, period doubling bifurcation [3, 2].

In this paper a complete and detail bifurcation analysis has been done which shows different behavioral changes (Bifurcation) with the slow and gradual variation of load reactive power. It has been shown here how the stable oscillatory behavior of the power system model tends to chaotic instability through period doubling bifurcation. Period doubling bifurcation (PDB) is the most important route to chaos in power system model which is analyzed here with great emphasis. Except continuation method, a detail and explicit picture of PDB has been developed which clearly shows the internal behavior changes of the proposed system which eventually leads to chaos. This paper, for the first time, proposes that Voltage collapse and angle divergence phenomenon which make the system unstable, occurs simultaneously. Also this paper gives an indication on maximum loadability point after which system tends towards instability.

The numerical solution of the basic nonlinear differential equations of the proposed model of power system network and load are implemented using the **MATLAB** environment [16] and assembly language programming.

II. BRIEF REVIEW OF NONLINEAR THEORY [17,18]

A typical nonlinear system with state x can often be expressed as-

$$\dot{x} = f(x, \mu); x \in \mathcal{R}^n, \mu \in \mathcal{R}^p \text{ ----- (2.1)}$$

The corresponding properties of such a system are:

- The solution of (2.1) is called trajectory. With initial condition $x(t_0) = x_0$, the solution is given by $x(t) = \lambda_t(x_0)$.
- Four steady state behaviors are associated with the nonlinear system. Equilibrium points, Periodic solutions, quasi periodic solution and chaos.
- The equilibrium points mean the solutions of the nonlinear equation $f(x, \lambda) = 0$. Alternatively an equilibrium point is a degenerate trajectory which stays in the equilibrium point for all time. It is asymptotically stable if all the Eigen values of its corresponding Jacobian matrix have negative real part. Power system is generally operate on a stable equilibrium point. $\lambda_t(x^*)$ is a periodic solution if $\lambda_t(x^*) = \lambda_{t+T}(x^*)$ for all t and some minimal period $T > 0$. It represents a limit cycle which is a self sustained and bounded oscillation, and, is stable or unstable depending upon its characteristics multiplier..
- Finally, **chaos** is a random, indeterministic phenomenon exhibits stable, bounded but aperiodic behavior. While equilibrium points are zero dimensional and periodic solutions are one-dimensional, chaos is more complex and having fractional dimension.

2.1. Bifurcation Theory:

Bifurcation Theory is used to interpret the way in which qualitative changes occur in the system as one or more parameters are varied. A power system is modeled in the typical form of a nonlinear dynamic system with state x :

$$\dot{x} = f(x, \mu); x \in \mathcal{R}^n, \mu \in \mathcal{R}^p \text{ ----- (2.1.1)}$$

μ represents the vector of the system parameters that can be varied during the analysis.

Bifurcations in dynamical system mean “qualitative” changes of the asymptotic behavior of the system trajectory (2.1.1) which is obtained by varying the μ components.

At a value of $\mu = \mu_c$ the vector field f loses its structural stability, is called the **Bifurcation Point** and μ_c the Bifurcation value. This simply means that the Phase portraits for $\mu < \mu_c$ and for $\mu > \mu_c$ are different. In power system’s nonlinear model there are following types of bifurcations taken place depending upon the Jacobian (3) of the system (2.1.1) –

- **Saddle-node bifurcation (SNB):-** A saddle-node bifurcation is a local bifurcation in which two fixed point (or equilibrium) of a dynamical system collide and annihilate each other, at this point the Jacobian has a zero Eigen value and no other Eigen value with zero real part.
- **Hopf bifurcation (HB):-** A Hopf-bifurcation is a local bifurcation in which a fixed point of a dynamic system loses stability as a pair of the complex conjugate Eigen values of the linearized system around the fixed point cross the imaginary axis of the complex plane. If has 3 a pair of complex conjugate Eigen values on the imaginary axis where all other Eigen values are off the imaginary axis, then Hopf Bifurcation results the emergence of a family of periodic solution in the vicinity of μ_c . If the periodic solution is unstable then it is called “subcritical” and “supercritical” when stable.
- **Period Doubling Bifurcation (PDB):-** During this kind bifurcation with the change in multiplier a new periodic solution or orbit emerges from the previous/existing solution with periodicity approx. Twice that of the previous one. If there is a sequence of such bifurcation which accumulate at a critical value $\mu = \mu_c$, then

period almost becomes infinite, which means we get a aperiodic but bounded solution to the system which is called "Chaos". Actually this is one special type of Hopf **Bifurcation**.

III. POWER SYSTEM MODEL FOR NONLINEAR ANALYSIS

For applying theory of nonlinear dynamics, a simple power system model [1] is considered here. This model is widely used for nonlinear behavior study of power system [2, 3, 4, and 14]. In this power system model generator is represented by classical model. Here the system is represented by a set of four ordinary non linear differential equation. In this paper, classical model is implemented for a three BUS power system network as follows.

A simple 3-BUS power system shown in **fig.1** and its equivalent circuit in **fig.2**, this model consists of an infinite bus on the left, a load bus on the center and a generator bus on the right. $Y_0 \angle (\phi_0 \pm \frac{\pi}{2})$ and $Y_m \angle (\phi_m \pm \frac{\pi}{2})$ are the admittances of the transmission lines. One of the generator buses treated as slack bus and the other is described by swing equation. The concept of an infinite/slack bus refers to a particular node of the system with enough capacity to absorb any mismatch in the power balance equations. Thus, it can be considered as fictitious generator with constant voltage magnitude E_0 and phase ϕ_0 (usually $E_0 = 1$ and $\phi_0 = 0$). On the other hand, the generator has constant voltage magnitude E_m but the angle ϕ_m varies according to the so-called swing equation.

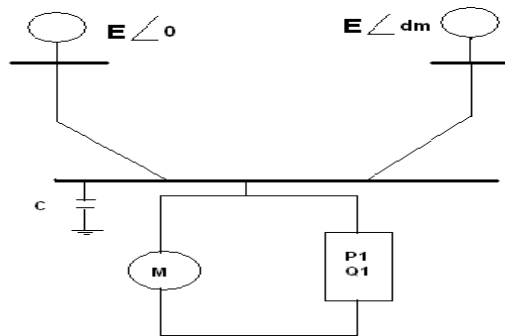


Figure 1: 3-bus power system model

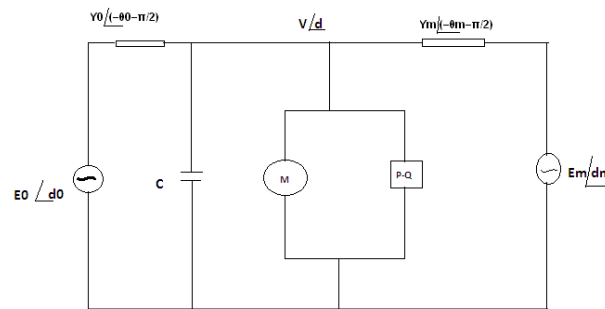


Figure 2: equivalent circuit

So, the set of four dynamic equations is developed for this model as –

$$\dot{\delta}_m = \omega \quad (3.1)$$

$$M \dot{\omega} = -d_m \omega + E_m Y_m \sin(\phi_m) + E_m V Y_m \sin(\phi_0 \pm \phi_m + \phi_m) \quad (3.2)$$

$$k_{qw} \dot{\delta} = k_{qv2} V^2 \pm k_{qv} V \pm Q \pm Q \pm Q(\phi_m, \phi, V) \quad (3.3)$$

$$T k_{qw} k_{qv2} \dot{V} = k_{pw} k_{qv2} V^2 + (k_{pw} k_{qv} \pm k_{qw} k_{pv}) V + k_{qw} [P(\phi_m, \phi, V) \pm P \pm P] \pm k_{pw} [Q(\phi_m, \phi, V) \pm Q_0 \pm Q] \quad (3.4)$$

Where, ϕ_m = Generator rotor angle, ϕ = Generator load angle, ω = Angular frequency, V = Magnitude of Generator load voltage.

The load bus, with voltage magnitude V and phase ϕ consists of an induction motor, a generic load P-Q and a capacitor C. The dynamics of this part is derived from a power balance at the bus. Considering an empirical model for the induction motor [9] and a static load P-Q, the active and reactive power supplied to the load is –

$$P(\varphi_m, \varphi, V) = P_0 + k_{pw}d\varphi + k_{pv}(V + TdV) + P_1 \quad (3.5)$$

$$Q(\varphi_m, \varphi, V) = Q_0 + k_{qw}d\varphi + k_{qv}V + k_{qv2}V^2 + Q_1 \quad (3.6)$$

Where T , k_{pw} , k_{pv} , k_{qw} , k_{qv} and k_{qv2} are constants of the motor, P_0 , Q_0 and P_1 , Q_1 are the static active and reactive power drained by the motor and by the load P-Q, respectively.

Here in this power system network the reactive power demand at the load bus Q_1 is chosen as bifurcation parameter. Therefore the model has the form-

$$\dot{x} = f(x, \varphi)$$

where $x = [\varphi_m, \varphi, V]^T$ is the state vector and $\varphi = [Q_1]^T$ is the bifurcation parameter vector so that increasing Q_1 corresponds to increase in load reactive power.

IV. NUMERICAL SOLUTION- SIMULATION & RESULT

Here the numerical solution of the nonlinear Eqn. (3.1 - 3.4) has been carried out using **MATLAB** simulation, the result of which can be sub divided into following two parts-

1) Bifurcation analysis and Chaos, 2) Chaos induced instability and system collapse.

4.1. Bifurcation and chaos:

In this paper continuous Bifurcation diagram is plotted using **MATLAB** continuation software 'MATCONT' to indicate different types of Bifurcation mentioned in II along with the respective bifurcation values in the proposed Power system model described by Eqns. (3.1-3.6).

Fig.3 shows the complete bifurcation diagram using the continuation method depicting the variation of system voltage V (p.u) with Q_1 . As the power system network is inherently nonlinear system it's dynamic equations are also nonlinear so it's solution exhibits different dynamic behavior with changes in system parameters, which is completely identified in the bifurcation diagram in Fig 3.

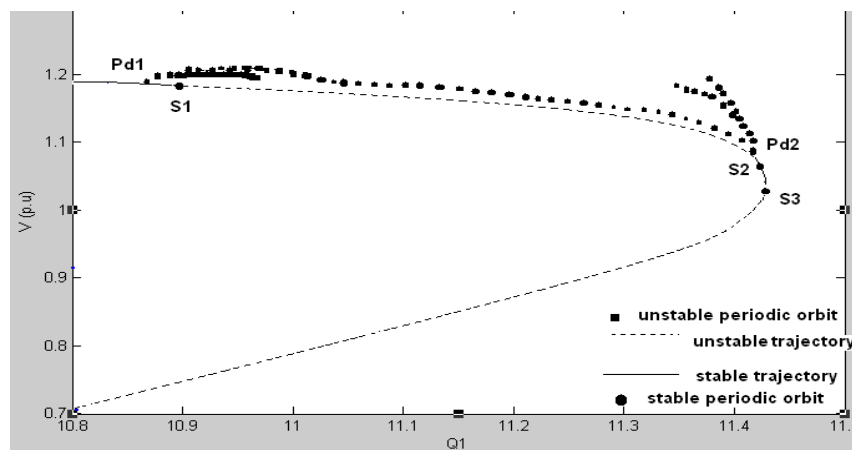


Figure 3: bifurcation diagram using continuous method showing various type of dynamic behavior

Suppose the power system model describe in section 3.1 is operating at a stable equilibrium point. Now Q_1 is slowly increased while other parameter remains fixed. At each parameter step, the system eigen values are calculated. In the course of computing stationary branch, three critical points **S1, S2 & S3** are detected as shown in the Fig.3, at which system changes it's stability. In Fig.3 the solid and dotted lines represent the stable and the unstable stationary trajectory. The stable trajectory becomes unstable at a **subcritical Hopf bifurcation (S1)** for $Q_1=10.868$ and regain stability at **supercritical Hopf bifurcation (S2)** at $Q_1=11.407$. The Eigen values of two critical points **S1** and **S2** are calculated numerically as $(0.0000 \pm j3.4234, -125.2174, -18.2564)$ and $(0.0000 \pm j2.8957, -92.1458, -2.3652)$ respectively i.e. at **S1** and **S2**, a pair of complex conjugate Eigen values cross the imaginary axes. So the real part of the complex conjugate Eigen values of the system becomes positive through **S1** and negative through **S2**. After a short stable region, one real Eigen value becomes positive at **S3**. This last critical point **S3** is called **Saddle node bifurcation** point where one real Eigen value becomes zero. After that system becomes completely unstable.

At point **S1** and **S2**, the possibility of oscillatory dynamic behavior is investigated by applying Hopf bifurcation theory. At this two points periodic branches are calculated. The periodic branch emanating from **S1** up to **Pd1** is unstable because it is subcritical. Then at **Pd1** periodic limit cycle emanates and gains stability. With further increase of Q_1 period doubling bifurcation occurs at **Pd1** where the previous periodic solution is

bifurcate to a new periodic solution or orbit with periodicity approx. twice that of the previous one. If one keep tracing an old periodic orbits, it again passes through the unstable periodic region between **Pd1** and **S2** and reaches **S2**, the **second super critical Hopf bifurcation point**. Now if we decrease the value of Q_1 , it reaches second period doubling point **Pd2**. the periodic orbits gain stability again in the supercritical region between **Pd2** and **S2**. After **Pd2** if we decrease the value of Q_1 , system enters into a series of period doubling bifurcation. All these limit cycles represent periodic oscillation in system behavior with different frequency.

After a short stable region beyond **S2** system become unstable at **S3**. If the reactive power of the load Q_1 is increased beyond this value, the system loses its stability and leading to system collapse.

4.2. Chaos via sequence of Period doubling:

According to bifurcation theory one way to chaotic motion is through a sequence of period doubling bifurcations. Therefore, we give special attention to two Period doubling points **Pd1** and **Pd2**, in this case and tried to show explicitly what happened after these two points with the variation of Q_1 with the detail bifurcation diagram plotted in the neighborhood of these two points. First, consider the period doubling bifurcation point **Pd1** at the left side of main bifurcation diagram of Fig.3. With the further increase of Q_1 a new periodic orbit with periodicity two is emerged, and then the periodic orbit of period four and so on. After a certain value of Q_1 the system finally reaches to a state which is completely indeterministic and having infinite or fractional no of period or become aperiodic but exhibits a bounded oscillation. Dynamic behavior of the power system model at this region is very complex and unpredictable and there is no obvious relation between cause and effect. At this region the power system network shows completely erratic and random behavior. This bounded but random oscillation is known as **Chaos**. It can be termed as **Left side chaos (LSC)** as it occurs left part of continuous Bifurcation diagram of Fig.3. This **Left Side Period doubling Bifurcation** leading to Chaos is shown explicitly in Fig.4.

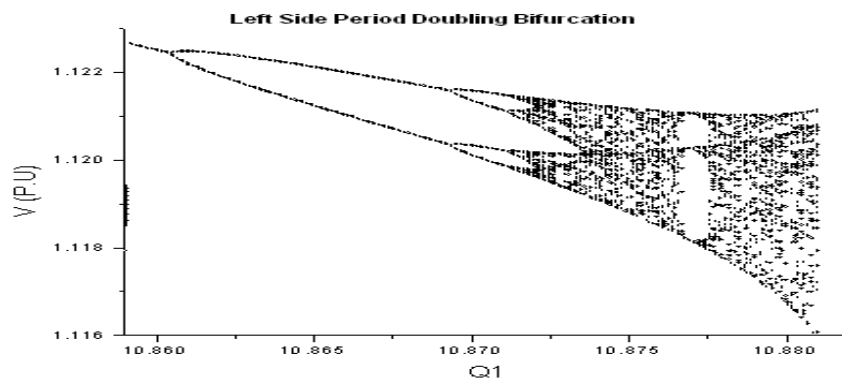


Figure 4: bifurcation diagram showing left side period doubling bifurcation leading to chaos

In the right hand side of the periodic branch, the same phenomenon takes place but here the state enters into period doubling bifurcation at **Pd2** towards the chaos with the decrease of values of Q_1 from its value at **Pd2**. This chaos can be termed as **Right side chaos (RSC)**. This **right Side Period doubling Bifurcation** leading to Chaos is shown explicitly in Fig.5.

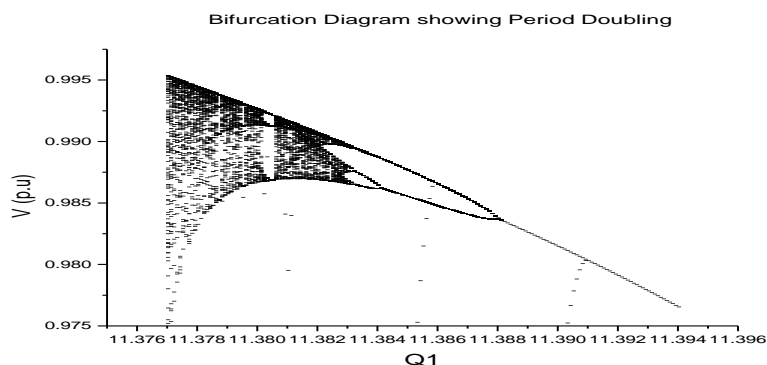


Figure 5: bifurcation diagram showing right side period doubling bifurcation leading to chaos

Table I: values Q_1 (bifurcation parameter) at different bifurcation point

Value of Q_1	Nature of Bifurcation
10.946	Subcritical Hopf Bifurcation (S1)
11.407	Supercritical Hopf Bifurcation (S2)
10.870	Period-1 LHS
10.880	Period-2 LHS
10.883	Period-4 LHS
11.392	Period 1 RHS
11.388	Period 2 RHS
11.384	Period 4 RHS

4.3. Phase Plots and Time plots:

Below the various phase plots are shown which describes the various states of the system dynamics with different values of Q_1 , during PDB leading to chaos through both **Left side PDB** and **Right side PDB**. Also the time plots are shown for different values of Q_1 . These plots are obtained from the numerical solution of the Eqn. (3.1.1-3.1.4) which are numerically integrated with initial condition (0.3, 1.5, 0.2, 0.97) and (0.315, 0.150, 0.150, 0.98) using **Runge-Kutta method**. Here Chaos is observed for $Q_1=10.894$, called **Left side chaos** and $Q_1=11.383$, called **Right side chaos**.

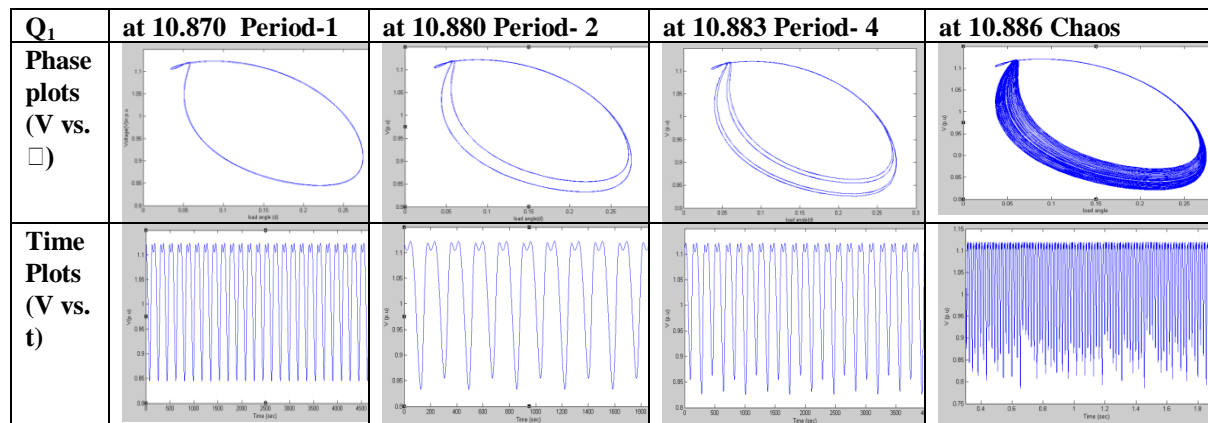


Figure 6: phase plots and time plots showing left side PDB leading to chaos

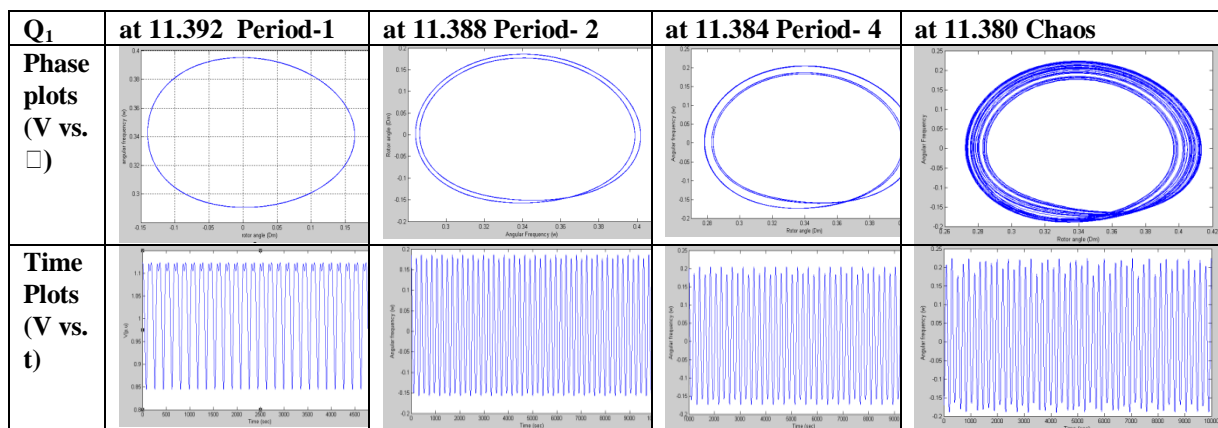


Figure 7: phase plots and time plots showing right side PDB leading to chaos

4.5. Chaos induced instability and system collapse:

Though chaos exhibits aperiodic and random oscillatory behavior and completely indeterministic, it is a bounded and marginally stable region. But Chaos is very sensitive to initial condition and system parameter variation. Any small change to them can break their stable oscillation. Here we discuss what happens after stable chaotic oscillation is broken in power systems. It will be shown that chaos can lead to Voltage collapse and angle divergence simultaneously when value of Q_1 is increased beyond the value corresponds to Left side chaos and decreased below the value corresponds to Right side chaos, which makes a stable system into complete unstable and the system breakdown takes place.

- **Voltage collapse and Angle Divergence:** Many studies have observed this phenomenon [1-11] taking place individually. But in this paper, voltage collapse occurring along with Angle divergence simultaneously is reported for the first time in Power system dynamic stability study. During **Voltage collapse** the system voltage sharply declines to a very low value and possibly brings the blackouts and **Angle Divergence** is the phenomenon when the generator losing synchronism i.e. rotor angle difference is much more than 2π . Here critical point at which voltage collapse and angle divergence phenomena take place simultaneously is $Q_1=10.890$ after **Left side chaos** and $Q_1=11.377$ after **Right side chaos**, using same model, parameter values and same initial condition. These are shown below in Fig 8 & 9 where time plot of load Voltage and Generator angle are given for the above mentioned values of Q_1 . For both the values of Q_1 we get almost same diagram. From the Fig 8 & 9 it is seen that voltage collapse and angle divergence appears after chaos is broken.

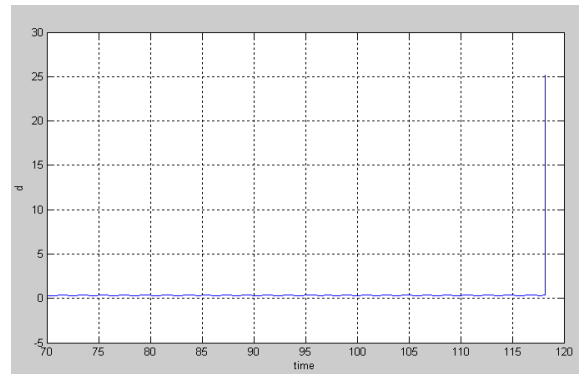
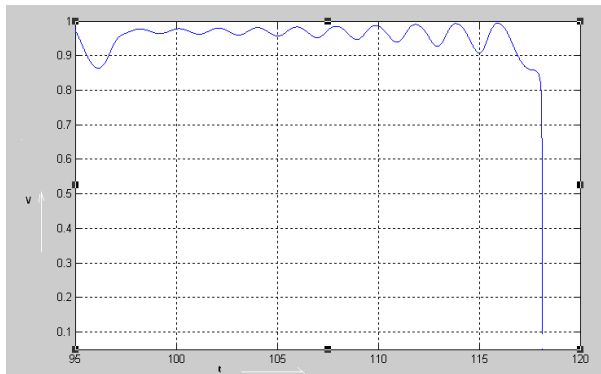


Figure 8: Voltage collapse at $Q_1=10.890$ and $Q_1=11.377$ Figure 9: angle divergence at $Q_1=10.890$ and $Q_1=11.377$

V. CONCLUSION

In this paper various nonlinear dynamical behavior of proposed power system model has been deeply studied using both “Matlab” and Assembly language Programming. Here cascaded period doubling bifurcation which is one of the most important routes to chaos and system instability has been observed in details. All previous studies used continuation method and compact continuation software’s such as **AUTO** [15] for Bifurcation studies in power system network which predicted the occurrence of Period Doubling Bifurcation leading to chaotic phenomenon but were not able to show explicitly and elaborately, the structure of period doubling bifurcation leading to chaos. This limitation is overcome in this paper where bifurcation analysis is done using both MATLAB based continuation software MATCONT to get a continuation Bifurcation diagram and also get an expanded and elaborate diagram of Period doubling bifurcation which clearly shows various state changes of the proposed system with the variation of Q_1 which eventually leads to chaos. This is also described by various phase plots and time plots for different values of Q_1 . The relationship between chaos and major instability modes in power system, such as Voltage collapse and Angle Divergence, has thoroughly been observed. Here it is shown for the first time that Chaos can induce voltage collapse and angle divergence simultaneously when the stability condition of the chaotic oscillation are broken. So it can be concluded that chaos is an intermediate stage of the instability incident when changes in system parameter causes system breakdown. As chaos is very sensitive to initial condition and system parameters, any variation of them can make chaos to be annihilated and breaks into instability. In a real power system all system parameters are fluctuating with changing operating condition and disturbances.

So chaos possibly exists in power system network as in prior stage of instability. When disturbance happens, power system comes into a transient stage. If the disturbance is small, HB may happen and stable oscillatory behavior follows. If the disturbance is prolonged, system may come into chaos. And, when the disturbance becomes larger, the chaos may be broken. Voltage collapse, angle instability or voltage collapse

and angle divergence simultaneously may happen. If the disturbance is very large, system may directly come into the above three instability conditions over the stages of HB, chaos and chaos breaking. Here it is indicated that when there is a large disturbances in system parameter leading to system collapse, chaos is very likely to be an intermediate transient stage between a stable and unstable region a power system. All this studies are helpful in understanding, how various instabilities due to the interaction between system parameter itself take place and the possible routes through which the system moving towards breakdown through various stable and unstable oscillatory modes It also indicated that there is a maximum lodability point after which the system enters into instability modes. All these studies are helpful to understand the mechanism of various instability modes and to find out effective find appropriate measure to prevent nonlinearity induced instability in power system.

REFERENCES

Journal Papers:

- [1] I. Dobson and H.-D. Chiang, "Towards a theory of voltage collapse in electric power systems", Systems and Control Letters, Vol.13, 1989, pp. 253-262.
- [2] E. H. Abed, et al., "Dynamic bifurcations in a power system model exhibiting voltage collapse," Technical Research Report, University of Maryland, pp. 1-15, TR92-26, 25-Feb, 1992.
- [3] H. O. Wang, et al., "Bifurcations, Chaos and Crises in power system Voltage Collapse," Technical Research Report, University of Maryland, pp. 1-23, TR92-72, 25-Feb, 1992.
- [4] E. H. Abed, et al., "On bifurcations in power system models and voltage collapse," in Proc. 29th Conf. Decision and Control, pp. 3014-3015, 1990
- [5] M. M. Begovic and A. G. Phadke, "Analysis of voltage collapse by simulation," Znt. Symp. Circuits and Systems May 1989.
- [6] K. T. Vu and C. C. Liu, "Dynamic mechanisms of voltage collapse", Systems and Control Letters, vol. 15, pp. 329-338, 1990.
- [7] T. Van Cutsem, "A method to compute reactive power margins with respect to voltage collapse," LYEE Trans. Power Systems, vol. 6, pp. 145-156, Feb. 1991.
- [8] H.-D. Chiang, C.-W. Liu, P.P- Varaiya, F.F. Wu and M.G. Lauby, "Chaos in a simple power system", Paper No.92 WM 151-1 PWRs, IEEE Winter Power Meeting, 1992.
- [9] K. Walve, "Modeling of Power System Components at Severe Disturbance", CIGRE paper 38-18, International Conference on Large High Voltage Electrical Systems, 1986.
- [10] K.T. Vu and C.C. Liu "Dynamic mechanisms of voltage collapse," Systems and Control letters, Vol. 15, 1990, pp. 329-338.
- [11] Dobson and H.-D. Chiang, "A model of voltage collapse in electric power systems", IEEE Proceedings of 27th Conference on Control and Decision, Dec.1988, Austin, TX, pp. 2104-2109.
- [12] E. H. Abed and P. P. Varaiya, "Nonlinear Oscillations in power systems"Int. J. Elec. Power and Energy Sys, vol. 6, pp. 3743, 1988.
- [13] C. Rajagopalan , P. W. Saw and M.A. Pai, "Analysis of voltage control systems exhibiting Hopf bifurcation," in Proc 28th IEEE Conf. Dec. Tampa, pp, pp. 332-335, 1989.
- [14] Y Yu, H Jia, P Li and J Su, "Power system instability & chaos", 14th PSC, IEEE conf. Sevilla, 24-28 June, 2002
- [15] E.J. Doedel, "AUTO: A program for the automatic bifurcation analysis of autonomous systems", Cong. Num., Vol.30, pp. 265-284, 1981.

Books:

- [17] Alexander Panfilov, non-linear dynamical systems (Prentice-Hall, 1999)
- [18] D.W Jordan and P. Smith, Nonlinear Ordinary Differential Equations-An introduction for Scientists and Engineers, fourth edition (Oxford Texts in Applied and Engineering Mathematics)
- [16] Matlab Works Inc. Simulink (Dynamic System Simulation for MATLAB)



International Journal of Modern Engineering Research (IJMER)

Volume : 4 Issue : 7 (Version-3)

ISSN : 2249-6645

July - 2014

Contents :

Voltage Support and Reactive Power Control in Micro-grid using DG <i>Nagashree. J. R, Vasantha Kumara. T. M, Narasimhegowda</i>	01-06
Experimental Investigation of Twin Cylinder Diesel Engine Using Diesel & Methanol <i>Dr. Hiregoudar Yerrennagoudaru , Manjunatha K , Chandragowda M, Shivashankara gouda</i>	07-15
Performance & emission of Twin Cylinder Diesel Engine Using Diesel & Ethanol <i>Dr. Hiregoudar Yerrennagoudaru , Manjunatha K, Chandragowda M, Lohit H A</i>	16-23
The Effect of Cryogenic Treatment on the Hardness, Frictionand Wear Resistance of Austenitic Ductile Iron Type D3 Tool Steel <i>K. S. Mahesh Lohith, V. B. Sondur, V. V. Sondur</i>	24-29
A Study on Groundnut Husk Ash (GHA)–Concrete under Acid Attack <i>Egbe-Ngu Ntui Ogork, Okorie Austine Uche, Augustine Uche Elinwa</i>	30-35
Comparing: Routing Protocols on Basis of sleep mode <i>Sukhdeep Kaur, Rohit Kumar, Lokesh Pawar</i>	36-41
Implementation of High Throughput Radix-16 FFT Processor <i>K. Swetha sree, Mr. T. Lakshmi Narayana</i>	42-52
Implementation of UART with Status Register using Multi Bit Flip-Flop <i>P. Rajee Priyanka, S R Sastry Kalavakolanu</i>	53-57
On $\pi g\theta$-Homeomorphisms in Topological Spaces <i>C. Janaki, M. Anandhi</i>	58-65
Optimization of Corynebacterium glutamicum Immobilization on Alginate and <i>Tran Thi Minh Tam, Nguyen Thuy Huong</i>	66-71

Voltage Support and Reactive Power Control in Micro-grid using DG

Nagashree. J. R¹, Vasantha Kumara. T. M², Narasimhegowda³

¹ 4th sem, M.Tech, Power system engineering, Dept. of E&E Engg., Adichunchanagiri Institute of Technology, Chickmagalur, Karnataka

² M.Tech, LMISTE, Asst. Prof., Dept. of E&E Engg., Adichunchanagiri Institute of Technology, Chickmagalur, Karnataka

³ M.Tech, PGDCA, LMISTE Associate Prof., Dept. of E&E Engg., Adichunchanagiri Institute of Technology, Chickmagalur, Karnataka

Abstract: Distribution Generators (DGs) are the renewable energy resource which can be connected to the grid. When it is connected to the grid it should be operated with controlled voltage and reactive power control. And in autonomous mode (i.e. disconnected mode) it should operate in backup generation mode. These DGs are connected towards the micro grid operation. The proposed control system facilitates flexible and robust DG operational characteristics such as active/reactive power (PQ) or active power/voltage (PV) bus operation in the grid-connected mode, regulated power control in autonomous micro-grid mode, smooth transition between autonomous mode and PV or PQ grid connected modes and vice versa, reduced voltage distortion under heavily nonlinear loading conditions, and robust control performance under islanding detection delays. Evaluation results are presented to demonstrate the flexibility and effectiveness of the proposed controller.

Keywords: Distributed generation (DG). flexible control. micro-grids. smart distribution systems.

I. Introduction

The distribution system is an important part of an electric power system. As stated in [1], the capital investment in the distribution system constitutes a significant portion of the total amount spent in the entire power system. Due to the recent market deregulation, this portion may become even larger. Furthermore, since the distribution systems operate at the low voltage levels, the losses are usually higher compared to those in other parts of the system. Thus, the distribution system rates high in economic importance, which makes careful planning and design most worthwhile.

Flexible operation of distributed generation (DG) units is a major objective in future smart power grids. The majority of DG units are interfaced to grid/load via power electronics converters. Current-controlled voltage-sourced inverters (VSIs) are commonly used for grid connection.

Under the smart grid environment, DG units should be included in the system operational control framework, where they can be used to enhance system reliability by providing backup generation in isolated mode, and to provide ancillary services (e.g. voltage support and reactive power control) in the grid-connected mode. These operational control actions are dynamic in nature as they depend on the load/generation profile, demand-side management control, and overall network optimization controllers (e.g., grid reconfiguration and supervisory control actions) [4]. To achieve this vision, the DG interface should offer high flexibility and robustness in meeting

a wide range of control functions, such as seamless transfer between grid-connected operation and islanded mode; seamless transfer between active/reactive power (PQ) and active power/voltage (PV) modes of operation in the grid connected mode; robustness against islanding detection delays; offering minimal control-function switching during mode transition; and maintaining a hierarchical control structure.

Several control system improvements have been made

to the hierarchical control structure to enhance the control performance of DG units either in grid-connected or isolated micro-grid systems [5]–[11]. However, subsequent to an islanding event, changing the controlling strategy from current to voltage control, in a hierarchical control framework, may result in serious voltage deviations especially when the islanding detection is delayed [12].

Fig. 1 shows the micro-grid system under study, which is adapted from the IEEE 1559 standard for low voltage applications. The adopted study system represents a general low voltage distribution system, where different types of loads and different numbers of DG units can be considered to be connected to the main feeder. The DG units can be employed to work either parallel to the utility grid, or in isolated mode to serve sensitive loads connected to the main feeder when the main breaker (BR) is open. Without loss of generality, the performance of the micro-grid system is studied under the presence of two DG units, supplying general types of loads.

Figure 1: Single-line diagram of the study system. The diagram illustrates a power distribution network. At the top, a 'Utility' source (10 KVA, 2.4 kV) is connected to a 'Vgrid,abc' bus. This bus feeds a 'Vfeeder,abc' line through a circuit breaker (BR). The feeder has five buses (B1 to B5). B1 has a 15 KVA transformer (2.4/0.48) and a 0.23+j0.3% impedance. B2 has a 10 KVA transformer (2.4/0.48) and a 10 KVA, 0.95 PF Inductive Load. B3 has a PFC Cap. Bank (2.5 KVAR) and a 0.2+j0.35% impedance. B4 has a 15 KVA transformer (2.4/0.48) and a DG2 (15KVA) connected to it. B5 has a 10 KVA transformer (2.4/0.48) and a Nonlinear Load connected to it. The Nonlinear Load has a 2.3+j0.44% impedance. The system also includes a 'DG1' (15KVA) connected to a 'Source converter and controls' block, which is connected to a 'DG source' block. The 'DG1' block includes a DC link with voltage V_{dc} and a filter with inductor L and resistor R_f . The 'DG source' block includes a 'Source converter and controls' block. The 'Study System' label is at the bottom right.

III. Proposed Control Scheme

The diagram illustrates the control architecture of a VSC-based microgrid. It includes several key components and control loops:

- Real Power Control:** A feedback loop where the reference active power P^* is compared with the measured active power P . The error is processed by a PI controller (represented by m/s) to generate a frequency deviation $\Delta\omega$, which is then integrated ($1/s$) to produce the phase shift δ .
- Reactive Power Control:** A feedback loop where the reference reactive power Q^* is compared with the measured reactive power Q . The error is processed by a PI controller (represented by $k_p/s + k_d$) to generate a voltage deviation ΔV , which is then integrated ($1/s$) to produce the reference voltage magnitude V_o^* .
- Synchronization Controller:** Manages the PLL and internal clock, receiving a synchronization signal and providing a reference phase $\omega^* t$ and a time delay $T/2$.
- Internal Model Based Hierarchical Voltage Control:** Generates the reference voltages $V_{o,a,b}^*$ and $V_{o,c}^*$ based on the phase and magnitude references.
- 3-Ph VSI:** The Voltage Source Inverter that converts the reference voltages into the switching signals for the VSC.
- Power Electronics:** The VSC is connected to the Rest of Micro-grid, which includes a load and a capacitor. The VSC output is filtered by an L-filter.
- Power Calculation:** A block that calculates the active and reactive power from the VSC output and the grid voltage.
- Supervisory Control:** Manages the grid connection and islanding events, receiving signals for Grid Connected/Islanded Mode Transfer Signal, PV or PQ Operation Signal, and Islanding Event in upstream feeder.

In the proposed control scheme the voltage from the feeder is taken and fed to the synchronization controller to synchronize the frequency. If the switch T is connected to islanded mode the voltage is taken from the feeder. If the switch is grid connected the voltage is taken from the micro-grid fed to the 3-Ph dq-PLL with resonant filter. It gives the reference frequency. In this control scheme we have to control the three parameters. i.e., real power, reactive power, and the frequency. In the real power control the reference value of the real

power and measured value of the real power is added. The difference will be fed to the PI/PID controller to produce the change in the frequency. The result is integrated and it will produce the phase angle. This phase angle is added with reference frequency it will produce voltage angle. In the reactive power control the reference signal and the measured signal is added and the difference will be fed to the PI/PID controller. The result from the controller gives the change in the voltage magnitude and is added with the reference voltage magnitude it gives the voltage magnitude. If the switch T is connected to grid connected mode the voltage magnitude is calculated from the above method. If it is islanded the voltage magnitude is directly calculated from the measured reactive power value using the equation

$$|v| = v^* - nQ$$

If the switch S is connected to the PV bus the reference voltage magnitude is directly fed to the reference generator block. If switch S is connected to the PQ bus the reference voltage magnitude is calculated using the reference and measured reactive power value.

The reference value of the phase angle and magnitude of the voltage is fed to the reference generator block. It gives the instantaneous phase- α and phase- β voltage. This voltage is fed to the Internal model based Hierarchical voltage control and is also fed with grid voltage and current and line current and gives the reference inverted voltage. This inverted voltage is fed to the 3-Ph voltage source inverter to produce the three phase inverter voltage. By using the grid voltage and line current the real power and reactive power is calculated.

IV. Simulation Results

Procedure:

Initially with the help of IEEE standard data the system diagram is drawn in MATLAB/SIMULINK software package using the tools. The PI controller is used in the control scheme.

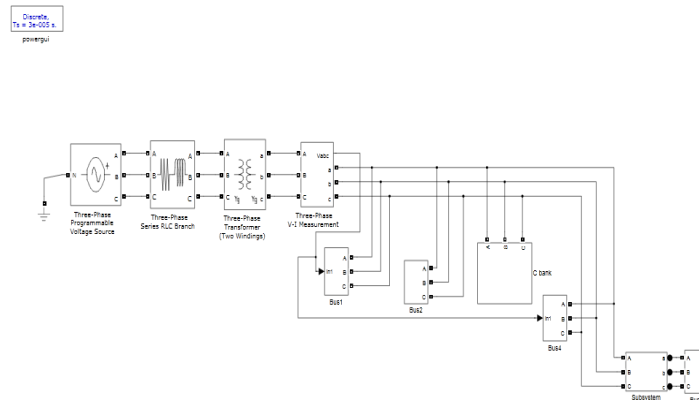


Fig.3.MATLAB circuit for the standard IEEE micro-grid system

To evaluate the performance of the proposed control scheme, the study system depicted in Fig. 1 is implemented for time domain simulation under the Matlab/Simulink environment. The micro-grid system employs two DG units, which can work parallel to the utility grid, or in isolated mode when the grid is not available to serve sensitive loads.

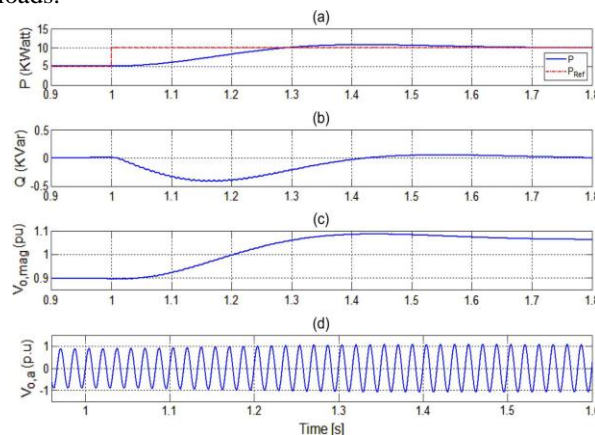


Fig.4. Dynamic response of the system to an active power command step change in grid connected mode and PQ operation. (a) Converter active power. (b) Converter reactive power. (c) Output voltage magnitude. (d) Instantaneous phase-a output voltage.

Fig. 4 shows the control performance under PQ-bus operation mode for one of the DG units. The inductive load and the capacitor bank are activated in this scenario. The reactive power command is set to zero, whereas the active power command experiences a step change from 5 to 10 kW at s. Fig. 4(a) and (b) shows the active and reactive powers generated by the unit. Close active power tracking performance is yielded. On the other hand, the coupling between active and reactive power dynamics is minimal. Fig. 4(c) depicts how the output voltage amplitude changes to maintain the unity power factor condition while increasing the active power injection. Voltage fluctuation in this mode is the natural result of the absence of voltage control at the point of common coupling. The instantaneous phase- output voltage is shown in Fig. 4(d). In addition to active power regulation, the DG unit can contribute to the voltage reliability at the point of common coupling by allowing bus voltage control (i.e., PV mode). This mode can be activated once voltage sags (e.g., due to upstream faults) are detected. Under these conditions, the voltage control mode is activated to inject reactive power during the sag period to provide fault-ride-through performance. Accordingly, the economic operation of the DG unit will not be compromised. On the other hand, in long radial feeders and weak grids, existing DG units can be used for continuous voltage support.

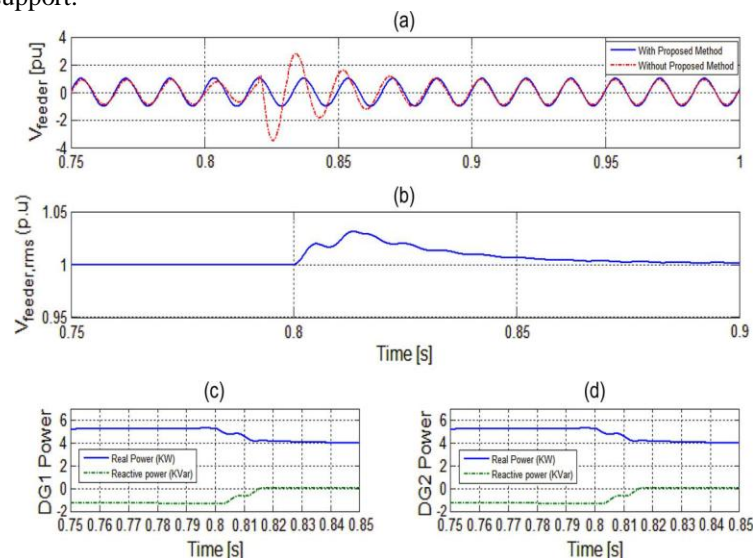


Fig.5. Dynamic response of the two-DG micro-grid system due to an islanding event with DG units acting as PV buses. (a) Instantaneous phase- grid voltage with and without proposed controller. (b) RMS feeder voltage with proposed controller. (c), (d) Active and reactive converter powers of each DG unit.

The transitional performance of the study system under the proposed control scheme from grid connected to islanded mode is evaluated by emulating an islanding event via opening the breaker switch (BR) at the upstream feeder in Fig. 1. Initially, the micro-grid system is connected to the grid and both DG units are working in the PV-bus mode. The study system is islanded at $t=0.8$ s by opening the breaker BR. In this paper, the smart distribution study system is assumed to be equipped with a power line communication-based islanding detection scheme where the islanding event is detected with some communication delays after the upstream feeder breaker goes open and this event is signaled to the supervisory control unit shown in Fig. 2. The detection delay is assumed to be 20 ms; therefore, the islanding event is detected at $t=0.82$ s. Fig. 4 depicts the dynamic response of the system prior to and after the islanding event. DG units utilize the same control structure, which is applied for both grid connected and islanded modes. Reactive power sharing is adopted in the isolated mode. The load voltage waveform and magnitude are shown in Fig. 5(a) and (b), respectively. In Fig. 5(a), the voltage response associated with the conventional method (i.e., switching from current-controlled to voltage-controlled interface) is also shown. As it can be seen, without applying the proposed method, the system is experiencing much higher over voltages due to the internal disturbance generated by switching from current-controlled interface to a voltage-controlled one, and thus implying the effectiveness of the adopted control scheme. Fig. 5 confirms that the proposed controller is well capable of maintaining the load voltage subsequent to an islanding event. The dynamics responses of the active and reactive power components for each DG unit are shown in Fig. 5(c) and (d), where the initial active power generated by each DG is 5 kW, dictated by the power controller in the grid connected mode. However, subsequent to the islanding event, the generated active power is decreased in order to meet the load consumption (i.e., 8.0 kW). The robustness of the proposed controller under micro-grid operation is obvious.

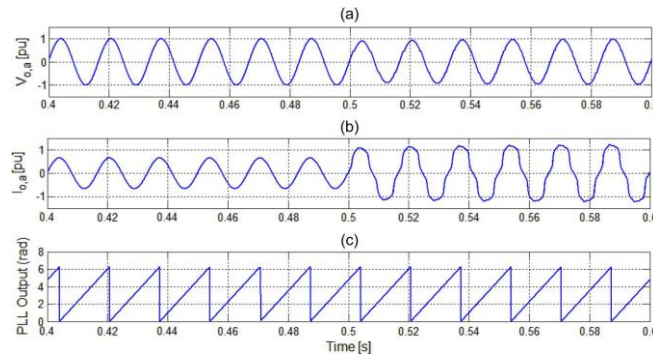


Fig. 6. Dynamic response of the system when a nonlinear load is added in grid connected mode. (a) Phase-output voltage. (b) Phase- load current (c) PLL

Output:

To test the disturbance rejection against loading transients and harmonic loading, the nonlinear load is switched ON at $t=0.82s$. The controller response to the addition of the nonlinear load is shown in Fig. 6. Fig. 6(a) shows the output voltage waveform of phase- , whereas Fig. 6(b) shows the load current. The proposed controller acts fast enough to reject the sudden loading disturbance yielding close voltage regulation at the local ac bus voltage. On the other hand, the harmonic disturbance rejection ability of the proposed controller is obvious. In spite of the heavily distorted load current, the total harmonic distortion (THD) of the phase- voltage is 0.67% and 0.81% before and after adding the nonlinear load, respectively. The PLL output in the presence of harmonics is also shown in Fig. 6(c). Note that the PLL output is robust even after adding the rectifier load to the system. This is because of the resonant filter which provides robust phase tracking in the presence of harmonics. These results confirm the high disturbance rejection performance of the proposed controller.

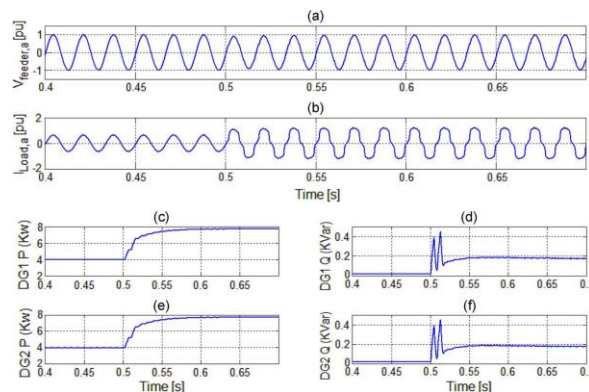


Fig. 7. Dynamic response of the system when a nonlinear load is added in islanded mode. (a) Instantaneous phase-a output voltage. (b) Phase-a load current. Instantaneous phase-a grid current. (c), (d) Active and reactive converter powers for DG1. (e), (f) Active and reactive converter powers for DG2.

Fig. 7 shows the load voltage and current responses of the islanded system when the nonlinear load is added at $t=0.5s$. Fig. 7(a) shows the load voltage, whereas Fig. 7(b) shows the load current. It can be seen that the controller is well capable of maintaining the output voltage quality despite the highly distorted current going through the load. The THD of the load voltage is 2.7%. Fig. 17(c)–(f) shows the active and reactive power profiles of both DG units. Accurate power sharing performance is yielded even in the presence of harmonic loading, which demands reactive power injection by both DG units.

V. Conclusions

An interactive DG interface for flexible micro-grid operation in the smart distribution system environment has been presented in this project. The proposed control scheme utilizes a fixed power–voltage–current cascaded control structure with robust internal model voltage controller to maximize the disturbance rejection performance within the DG interface, and to minimize control function switching. The proposed control scheme has a simple and linear control structure that facilitates flexible DG operation in the grid-connected mode and autonomous micro-grids, yields robust transition between grid-connected and islanded modes either in PQ or PV operational modes, and provides robustness against islanding detection delays due to the fixed control structure under different modes of operation. Therefore, the proposed control scheme enhances the flexibility of micro-grid operation under the dynamic nature of future smart distribution systems. The

proposed control scheme uses the PI and PID controller and compares the results. The results of both will be the same but response time of the PI controller is more compare to the PID controller and also the system will be more stable in the PID controller compare to the PI controller. So the use of PID controller in control scheme is more beneficial than the use of PI controller.

REFERENCES

- [1]. Smart Grid: An Introduction U.S. Department of Energy, 2009.
- [2]. E. M. Lightner and S. E. Widergren, "An orderly transition to a trans-formed electricity systems," IEEE Trans. Smart Grid, vol. 1, no. 1, pp. 3–10, Jun. 2010.
- [3]. K. Moslehi and R. Kumar, "A reliability perspective of smart grid," IEEE Trans. Smart Grid, vol. 1, no. 1, pp. 57–64, Jun. 2010.
- [4]. G. T. Heydt, "The next generation of power distribution systems," IEEE Trans. Smart Grid, vol. 1, no. 3, pp. 225–235, Nov. 2010.
- [5]. A. Timbus, M. Liserre, R. Teodorescu, P. Rodriquez, and F. Blaabjerg, "Evaluation of current controllers for distributed power generation systems," IEEE Trans. Power Electron., vol. 24, no. 3, pp. 654–664, Mar.2009.
- [6]. J. M. Guerrero, J. C. Vasquez, J. Matas, K. Vicuna, and M. Castilla, "Hi-erarchical control of droop-controlled ac and dc microgrids—A general approach towards standardization," IEEE Trans. Ind. Electron., to be published.
- [7]. M. Liserre, R. Teodorescu, and F. Blaabjerg, "Multiple harmonics control for three-phase grid converter systems with the use of PI-RES current controller in a rotating frame," IEEE Trans. Power Electron., vol.21, no. 3, pp. 836–841, May 2006.
- [8]. Y. A.-R. I. Mohamed, "Mitigation of dynamic, unbalanced and harmonic voltage disturbances using grid-connected inverters with LCL filter," IEEE Trans. Ind. Electron., vol. 58, no. 9, pp. 3914–3924, Sep.2011.
- [9]. S. Ahn, "Power-sharing method of multiple distributed generators considering modes and configurations of a microgrid," IEEE Trans. Power Del., vol. 25, no. 3, pp. 2007–2016, Jul. 2010.

Experimental Investigation of Twin Cylinder Diesel Engine Using Diesel & Methanol

Dr. Hiregoudar Yerrennagoudaru¹, Manjunatha K², Chandragowda M³,
Shivashankara gouda⁴

¹Professor and PG Co-ordinator (Thermal Power Engineering), Mechanical Engineering Department, RYMEC Bellary, Karnataka, India

²ASST Professor and PROJECT Co-ordinator (Thermal Power Engineering), Mechanical Engineering Department, RYMEC Bellary, Karnataka, India

³ASST Professor (Thermal Power Engineering), Mechanical Engineering Department, RYMEC Bellary, Karnataka, India

⁴M.Tech (Thermal Power Engineering), Mechanical Engineering Department, RYMEC Bellary, Karnataka, India,

Abstract: In view of increasing pressure on crude oil reserves and environmental degradation as an outcome, fuels like methanol may present a sustainable solution as it can be produced from a wide range of carbon based feedstock. The present investigation evaluates methanol as a diesel engine fuel. The objectives of this report is to analyze the fuel consumption and the emission characteristic of a twin cylinder diesel engine that are using Methanol & compared to usage of ordinary diesel that are available in the market. This report describes the setups and the procedures for the experiment which is to analyze the emission characteristics and fuel consumption of diesel engine due to usage of the both fuels. Detail studies about the experimental setup and components have been done before the experiment started. Data that are required for the analysis is observed from the experiments. Calculations and analysis have been done after all the required data needed for the thesis is obtained. The experiment used diesel engine with no load which means no load exerted on it. A four stroke Twin cylinder diesel engine was adopted to study the brake thermal efficiency, brake specific energy consumption, and emissions at zero load & full load with the fuel of methanol. In this study, the diesel engine was tested using 100% methanol. By the end of the report, the successful of the project have been started which is Diesel engine is able to run with Methanol but the engine needs to run by using diesel fuel first, then followed by methanol and finished with diesel fuel as the last fuel usage before the engine turned off. The performance of the engine using Methanol fuel compared to the performance of engine with diesel fuel. Experimental results of Methanol and Diesel fuel are also compared.

Keywords: Diesel, Methanol, Performance, Emissions.

I. INTRODUCTION

Since the inception of industrial revolution in eighteenth century, the search for portable prime movers to run machines for both industrial and transportation purpose became intense. Steam engines took a lead role in the beginning, but could not pass the test of time as they were bulky, less efficient and required huge quantity of low energy density solid fuels like coal. In the later part of nineteenth century, diesel engine was invented. Since then these engines have become an integral part of modern human civilization and mostly replaced the steam engines which became obsolete. These engines are extensively used worldwide for transportation, decentralized power generation, agricultural applications and industrial sectors because of their high fuel conversion efficiency, ruggedness and relatively easy operation [1,2]. These wide fields of global usage of diesel engines lead to ever increasing demand of petroleum derived fuels. Petroleum fuels are exhaustible sources of energy and hence an over reliability on these fuels is not sustainable in long run. Besides, the rising crude oil prices and increasing pollution due to excessive use of these engines is another grey area. The exhaust emissions of diesel engines, particularly soot, oxides of nitrogen and carbon monoxide are extremely harmful to natural environment and living beings [3]. Projections for the 30-year period from 1990 to 2020 indicate that vehicle travel, and consequently fossil-fuel demand, will almost triple worldwide and the resulting emissions will pose a serious problem [4].

Therefore on a nutshell it can be stated that concerns about long-term availability of petroleum diesel, stringent environmental norms and environmental impacts due to extensive use of diesel engines, have mandated the search for a renewable alternative of diesel fuel [5]. In these context alcoholic fuels as a partial or complete substitute of diesel is an area of interest. Reports on the use of alcohol as a motor fuel were published in 1907 and detailed research was conducted in the 1920s and 1930s. Historically, the level of interest in using alcohol as a motor fuel has followed cycles of fuel shortages and/or low feed-grain prices [6].

Among the alcohols, methanol has the lowest combustion energy. However, it also has the lowest stoichiometric or chemically correct air-fuel ratio. Therefore, an engine burning methanol would produce the maximum power. A lot of research has been done on the prospect of methanol as an alternative fuel. Methanol, CH_3OH , is the simplest of alcohol and originally produced by the destructive distillation of wood. However, methanol can be produced from many fossil and renewable sources which include coal, petroleum, natural gas, biomass, wood landfills and even the ocean [7].

Today it is produced in very large quantities from natural gas by the reformation of the gas into carbon monoxide and hydrogen followed by passing these gases over a suitable catalyst under appropriate conditions of pressure and temperature [8].

In energy deficit countries like India, Methanol can provide a sustainable solution against petroleum crisis due to the following reasons.

- Methanol can be manufactured from a variety of carbon based feedstock such as natural gas, coal and biomass (e.g., wood). As India is rich in all these reduce its dependence on imported petroleum.
- Methanol is much less flammable than the gasoline and results in less severe fires when it does ignite. So far fire safety purpose it is better than petroleum.
- Methanol has a higher laminar flame propagation speed, which may make combustion process finish earlier and thus may improve engine thermal efficiency [9].
- Methanol is a high-octane fuel that offers excellent acceleration and vehicle power [10].
- With economies scale, methanol could be produced, distributed, and sold to consumers at prices competitive with petroleum.

Due to high octane rating and similarities with gasoline. Methanol has always considered as a good SI engine fuel. But bulk of the transport fuel consumed worldwide is diesel. Ironically countries like India hugely subsidized diesel fuel to regulate inflation which in turn reduces Government's ability to fund welfare schemes. Above all major contribution to pollution also comes from diesel engines. Therefore, substitution of diesel by potential fuels like methanol (Which can be produced from locally available raw material by any carry out further study on the effects of methanol, & its fraction on CI engine performance.

1.1 Objectives of the project

- It is proposed to use Methanol Fuel in the diesel engine (CI engine).
- The emissions like CO, HC, CO_2 , NOx, SOx in the exhaust gases are proposed to reduce during the combustion itself.
- To study the performance evaluation of the using Methanol as fuel in the diesel engine.
- Analyze the exhaust emissions and measurement, reduction in the exhaust gas.

Table-1 Properties of Diesel and Methanol			
Sl. No	Properties	Diesel	CH_3O
1	Density(kg/m ³)	850	796.6
2	Calorific value (kJ/kg)	46,500	23,800
3	Kinematic viscosity @ 40C (cst)	3.05	1.04
4	Cetane number	55	4
5	Flash point °C	52	12
6	Fire point °C	56	97.6
7	Specific gravity	0.84	0.79
8	Sulphur content (%)	<0.035	-

1.2 Sources of Methanol

Methanol is a renewable energy source because the energy is generated by using a resource, sunlight, which cannot be depleted. Creation of Methanol starts with photosynthesis causing a feed stock, such as sugar cane or a grain such as maize (corn), to grow. These feed stocks are processed into methanol.

Following are the methods to produce the methanol:-

- Fermentation
- Distillation
- Dehydration

II. EXPERIMENTAL SETUP

The experimental test set up Figure-1 consisted of twin cylinder diesel engine, four stroke, Forced cooling system, crank start. The setup is provided with a resistance load bank, Multi gas analyzer made by testo and Stack monitoring kit for particulate matter & formaldehyde as HCHO...etc for performance and emissions analysis. The engine is cooled using the water jackets on the engine block and cylinder head using a Forced Feed System. While the recommended injection timing given by the manufacturer is 27° BTDC (static), the opening pressure of the nozzle was set at 1800 bar and the engine speed at 1500rpm. There are a number of transducers used in the engine such as piezoelectric pressure transducer flush with the cylinder head surface to measure cylinder pressure. Specifications of engine are shown in Table 2.

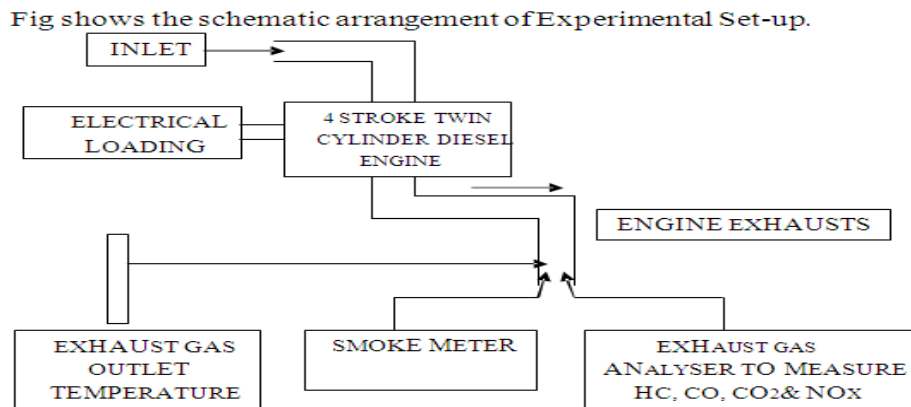


Fig 1: Schematic arrangement of Experimental Set-up



Fig 2: Test engine

Table-2 Test Engine specification	
Engine type	Four stroke Twin cylinder diesel engine
No. of cylinders	02
Stroke	100 mm
Bore Diameter	87 mm
Engine power	19 KW
Compression ratio	17.5:1
RPM	1500
Type of starting	Crank starting
Load type	Electric load bank

Table-3 Load bank specification	
Max. Output	15 KVA / 12.06 KW
Generator type	1 Phase
Amps	63
RPM	1500
PF	0.8
Volts	240

III. PRECAUTION OBSERVED BEFORE STARTING OF THE ENGINE

At the time of starting the engine for each of the tests it was measured that the engine level was in the safe zone and its condition is also good in case the condition was bad, then fresh SAE 40 was introduced into the pump after draining the old. The foundation and mounting bolts were checked periodically as they may go loose due to high speed operations and vibrations.

In the course of experiments the following precautions were observed:

- The ambient temperature variations during the experiment should not be more than 6°C and this was observed as far as possible.
- After each load is applied the engine is allowed to settle before further loads are applied.

Before stopping the engine, it was allowed to run on pure diesel for some time. This is done so that the engine can be restarted easily.

IV. EXPERIMENTAL PROCEDURE

Experiments were initially carried out on the engine using diesel as fuel in order to provide base line data. The methanol was prepared and made to run on the engine.

1st Case:-The engine was started using neat diesel and allowed to run for at least 30 minutes before taking observations. After engine conditions stabilized and reached to steady state, the base line data were taken. Load was varied (Zero load & full load condition) using the alternator load bank and the same was recorded. Gaseous emissions, fuel consumption were also recorded from the respective sensor.

2nd Case:-The engine was started on diesel and when engine became sufficiently heated; the supply of diesel was slowly substituted by 100 % Methanol for which a two way valve was used. After engine conditions stabilized and reached to steady state, the base line data were taken. Load was varied (Zero load & full load condition) using the alternator load bank and the same was recorded. Gaseous emissions, fuel consumption were also recorded from the respective sensor.

V. RESULTS AND DISCUSSION

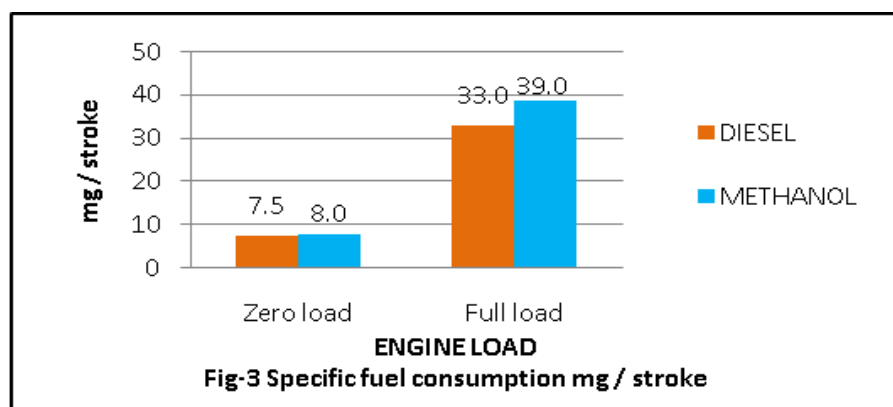
The performance and exhaust emission parameters of the engine with diesel and methanol at zero and full load condition are presented and discussed below.

5.1 Performance parameter

Table-3 Diesel readings							
Load in Kw		LOAD in %	TORQUE in NM	SPEED IN RPM (N)	SFC Mg/stroke	BP in KW	η _{bt} in %
V	I						
230	0	0	8.297	1500	7.5	1.303	16.54
	52	100	76.484	1500	33	12.01	34.67

5.1.1 Specific fuel consumption

Table-4 Methanol readings							
Load in Kw		LOAD in %	TORQUE in NM	SPEED in RPM (N)	SFC Mg/stroke	BP in KW	η_{bth} in %
V	I						
230	0	0	8.297	1500	8.0	1.303	28.7
	52	100	88.517	1500	39	13.90	62.82



At higher temperature the effect of methanol on specific fuel consumption (SFC) are shown in figure3. From that figure-3 it is clear that at different loads the SFC of Methanol is more than the diesel. The reasons behind this results are lower energy value substitute methanol thus engine responds to the load by increasing the fuel flow. Thus SFC decreases with the increase in thermal efficiency.

5.1.2 Brake thermal efficiency

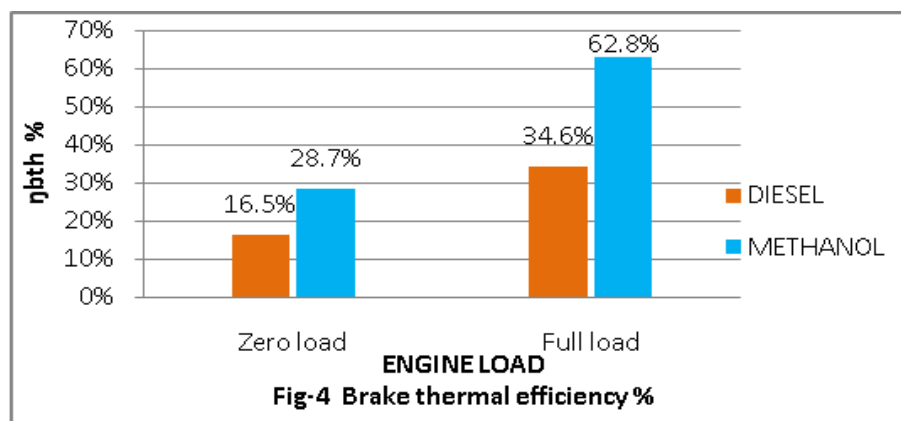
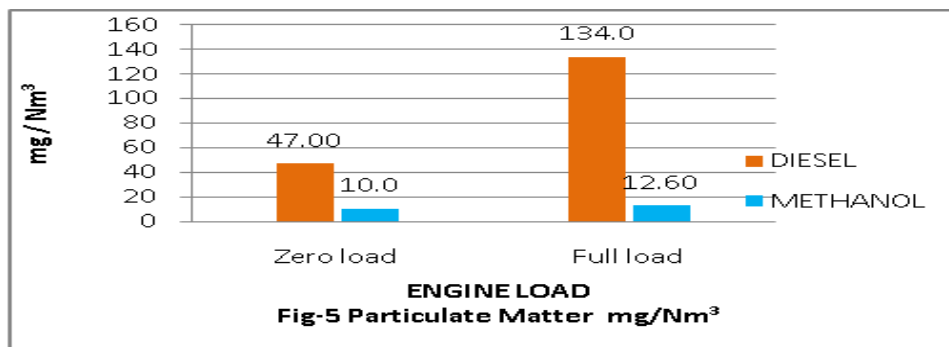


Figure 4, shows the variation of brake thermal efficiency with respect to methanol & Diesel at different loads. From the plot it is observed that as load increases brake thermal efficiency is also increases for diesel as well as Methanol. At full load condition, the brake thermal efficiencies obtained are 34.7% & 62.8% for the diesel & Methanol respectively. Among these two fuels Methanol has maximum BTE i.e 62.8% which is obtained from 100 % Methanol at full load. The BTE using Methanol is increased by 32.1% as compared to the diesel at full load condition. The increment in Brake thermal efficiency is due to low heat value of methanol as compared to diesel & better combustion because of less viscosity of Methanol.

5.2 Emission parameters

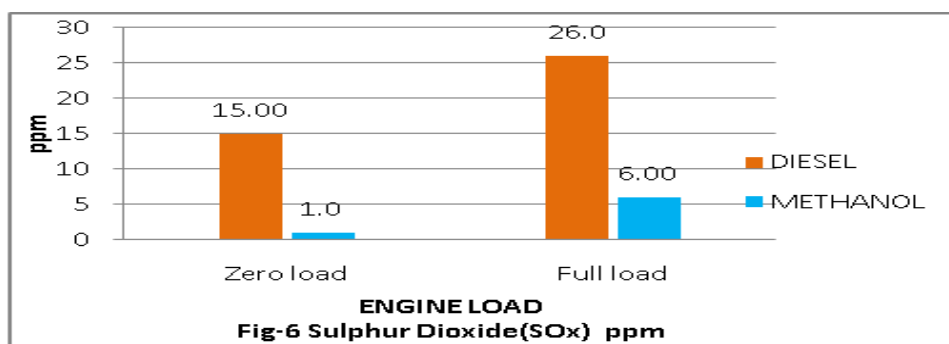
Table-5 Emission parameters of the engine with diesel and methanol at zero and full load					
Parameter	Unit	Diesel Zero load	Diesel full load	Methanol Zero load	Methanol full load
Exhaust gas Temperature	K	375	393	307	310
Particulate Matter	mg/Nm ³	47.00	134.0	10.0	12.60
Sulphur Dioxide(SOX)	ppm	15.00	26.0	1.0	6.00
Nitrogen Dioxide (NOX)	mg/m ³	1986.00	2431.0	859.0	930.00
Carbon monoxide	ppm	38.00	44.0	83.0	98.00
Oxygen(O ₂)	%	14.40	12.3	17.8	15.80
Carbon Dioxide(CO ₂)	%	6.40	8.4	3.4	4.2
Non Methane Hydrocarbon	ppm				
Ethane		<2.00	<2.00	<2.00	<2.00
Propane		<2.00	<2.00	<2.00	<2.00
n _ Butane		<2.00	<2.00	<2.00	<2.00
iso _ Butane		<2.00	<2.00	<2.00	<2.00
Pentane		<2.00	<2.00	<2.00	<2.00
Formaldehyde as HCHO	mg/Nm ³	<0.10	<0.10	<0.10	<0.10

5.2.1 Particulate Matter



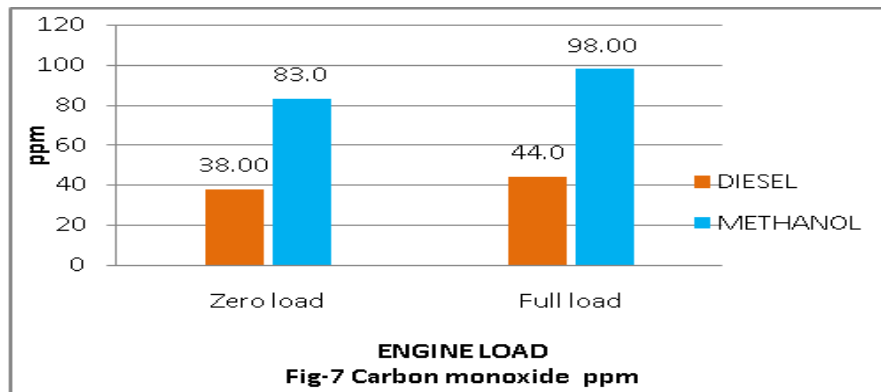
Figures 5, shows the variation of Particulate Matter level with respect to diesel and methanol at different loads. Particulate Matter tends to increase with load, this increase in Particulate Matter is explained by the fact that at low loads, but as the load increases, the temperature also increases which in turn increases the Particulate Matter emissions. Result shows that Particulate Matter is comparatively lower with Methanol. It is found that Particulate Matter emission increases with increase in load in Diesel as fuel but in methanol as fuel minor increase with increase load. 100% Diesel has higher Particulate Matter level when compared to 100% methanol. This is due to rise in exhaust temperature. Particulate Matter is decreased (80 to 90%) when using Methanol as fuel in diesel engine compared to diesel fuel.

5.2.2 SO_x Concentration



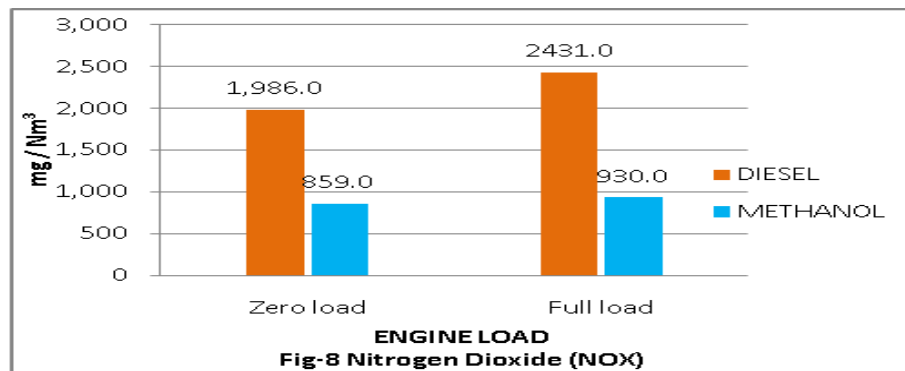
Figures 6, shows the variation of SO_x level with respect to Diesel and methanol at different loads. SO_x tends to increase with load, this increase in SO_x is explained by the fact that at low loads, but as the load increases, the temperature also increases which in turn increases the SO_x emissions. Result shows that SO_x is comparatively higher with Diesel. It is found that SO_x emission increases with increase in load. At full load condition 100% Methanol and 100% Diesel has higher SO_x level when compared to zero load condition. SO_x is decreased (75 to 90%) when using Methanol as fuel in diesel engine compared to diesel fuel. Result shows that SO_x emission is lower with Methanol as fuel.

5.2.3 CO Concentration



Figures 7, shows the variation CO level with respect to Diesel and methanol at different loads. From the graph it is clear that the CO level increases when Methanol has a fuel. This is due to the fact that engine is not optimized to run with Methanol, so there is a large possibility of rich fuel-air mixture in the cylinder and the higher specific fuel consumption resulting in a higher CO level. Carbon monoxide occurs in engine exhaust. It is a product of incomplete combustion due to insufficient amount of air in the air fuel mixture or insufficient time in the cycle for the completion of combustion. CO level is comparatively More when compared to diesel& can be reduce by increasing the compression ratio.

5.2.4 NO_x Concentration

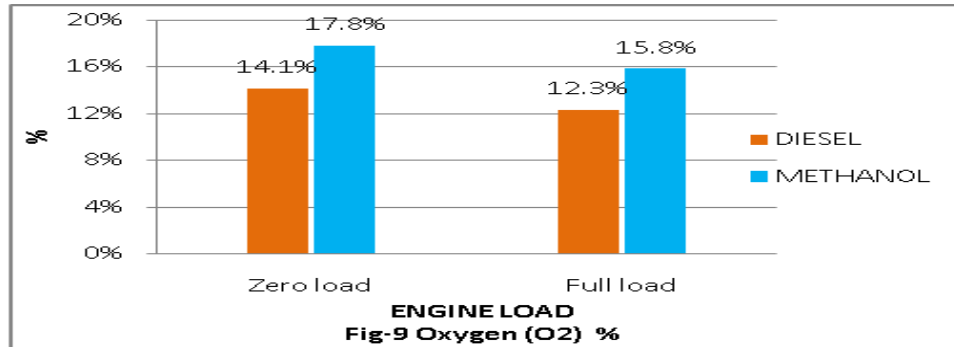


Figures 8, shows the variation of NO_x level with respect to Diesel and methanol at different loads. NO_x tends to increase with load, this increase in NO_x is explained by the fact that at low loads, but as the load increases, the temperature also increases which in turn increases the NO_x emissions. Result shows that NO_x is comparatively higher with Diesel. It is found that NO_x emission increases with increase in load. 100% Diesel has higher NO_x level when compared to 100% methanol. This is due to higher exhaust temperature of Diesel i.e 375 & 393 K. Methanol No_x emission is decreased (55 to 60%) when compared to diesel.

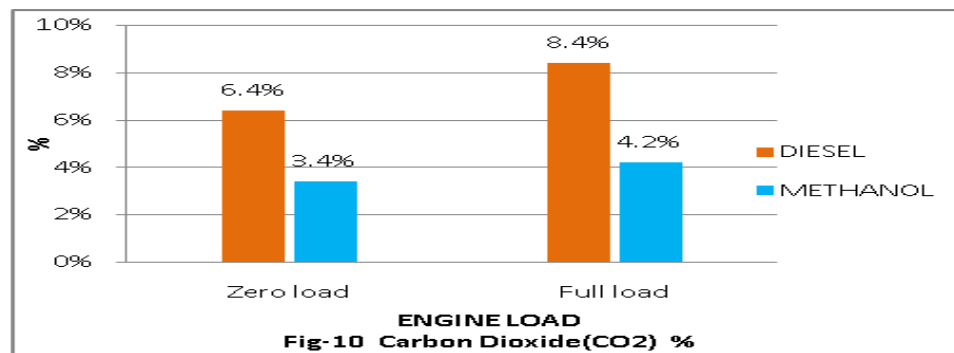
5.2.5 Oxygen (O₂) Concentration

Figures 9, shows the variation of O₂ level with respect to Diesel and methanol at different loads. From the graph it is clear that the O₂ level increases when Methanol has a fuel. This is due to the fact that engine is not optimized to run with Methanol, so there is a large possibility of lean / reach fuel-air mixture in the

cylinder and the lower compression ratio resulting in a higher O_2 level. Oxygen(O_2) occurs in engine exhaust. It is a product of incomplete combustion due to insufficient time in the cycle for the completion of combustion.



5.2.6 Carbon Dioxide (CO_2) Concentration



Figures 10, shows the variation of CO_2 level with respect to Diesel and methanol at different loads. From the graph it is clear that the CO_2 level decreases when Methanol has a fuel. This is due to the fact that engine is not optimized to run with Methanol, so there is a large possibility of lean / rich fuel-air mixture in the cylinder and the lower compression ratio & temperature resulting in a higher CO_2 level. CO_2 occurs in engine exhaust. It is a product of incomplete combustion due to insufficient time in the cycle for the completion of combustion.

VI. CONCLUSION AND FUTURE SCOPE

Based on the performance and emissions of Methanol, it is concluded that the Methanol oil represents a good alternative fuel with closer performance and better emission characteristics to that of a diesel. From the above analysis the Methanol shows better performance compared to the Diesel in the sense of better performance characteristics like Brake thermal efficiency, Specific fuel consumption and decrease in the emission parameters like NO_x , SO_x , Particulate matter, CO_2 but CO , O_2 is little higher than the diesel which can be reduced by increasing the compression ratio. Hence the 100% methanol can be used as a substitute for diesel.

REFERENCES

- [1] Chauhan BS, Kumar N, Cho H.M Cho (2009). Performance and emission studies on an agriculture engine on neat Jatrophia oil. Journal of Mechanical Science and Technology 24 (2) (2010) 529-535.
- [2] Ciniviz M., Köse H., Canli E. and Solmaz O (2011). An experimental investigation on effects of methanol blended diesel fuels to engine performance and emissions of a diesel engine. Scientific Research and Essays Vol. 6(15), pp. 3189-3199, ISSN 1992-2248.
- [3] Yao C, Cheung CS, Chan TL, Lee SC (2008). Effect of diesel/methanol compound combustion on diesel engine combustion and emission. Energy conversion and management. 49:1696-1704.
- [4] Mishra C, Kumar N, Sidharth, Chauhan B. S (2012). Performance and Emission Studies of a Compression Ignition Engine on blends of Calophyllum Oil and Diesel. Journal of biofuels. Volume 3, Issue 1, Online ISSN : 0976-4763.
- [5] Chauhan BS, Kumar N, Pal SS, Jun YD. Experimental studies on fumigation of ethanol in a small capacity diesel engine. Energy 2011; 36:1030-8.
- [6] "Alcohols for motor fuels" by J.L. Smith and J.P. Workman, Colorado State University and U.S. Department of Agriculture. Fact sheet no. 5.010.

- [7] Sayin C (2010). Engine performance and exhaust gas emissions of methanol and ethanol diesel blends. Fuel 89:3410-3415.
- [8] Hydrogen and Methanol: University Kebangsaan Selangor, Malaysia, 1993.
- [9] Liao S.Y., Jiang D.M., Cheng Q., Huang Z.H., Wei Q., Investigation of the cold start combustion characteristics of ethanol-gasoline blends in a constant-volume chamber, Energy and Fuels 19 (2005) 813–819.
- [10] Shenghua L., Clemente E. R., Tiegang H., Yanjv W.(2007), Study of spark ignition engine fuelled with methanol/gasoline fuel blends, Applied Thermal Engineering 27-1904–1910.
- [11]. Q.A. BAKER —Use of alcohols in Diesel Fuel Emulsions and Solutions in a Medium Speed Diesel Engine - SAE 810254.
- [12]. D.HARA GOPALA RAO —Partial Substitution of Alcohols for Diesel Fuel.BHU.
- [13]. H.A.HAVEMANN et al —The Utilization of Pure Alcohol in Combination with Normal and Heavy Fuels in High Speed diesel Engines - Journal of IISc, XXXV, No. 4, 1953.
- [14]. RANGIAH et al —Performance of Ceramic Coated diesel Engines with Methanol – Diesel Mixtures. 9th National Conference in I.C.Engines and Combustion, 1985.
- [15]. B.NAGALINGAM et al—Surface Ignition initiated combustion of Alcohol in Diesel Engines -A New Approach. SAE 800262, SAE TRANS 1980, Vol 89, Section 2,1217-29.
- [16]. M.R.K. RAO and N.SRINIVASA MURTHY —Alcohol as Fuel in Diesel Engines ----Chemical Age of India, Vol – 14, No. 1 Jan 1964.
- [17]. C.M.VARAPRASAD —Performance Evaluation of a High speed light weight diesel engine with Methanol-Diesel mixtures.
- [18] F. PISCHINGES, C. HAVENTH —A New of direct injection of Methanol in a diesel engine —Abstract, Int. Symposium. Alcohol Fuel Tech. May 1979.
- [19] Dr. HiregoudarYerrennagoudar et.al —Oxidation of Aldehydes from the Exhaust Gases of C.I. Engine using Alcohol blends with Diesel in Semi-Adiabatic Air-Gap Copper Crown Piston as Unconventional Catalytic Converter .7th Asia-Pacific Conference on Combustion, National Taiwan University, Taipei, Taiwan ,24-27 May 2009.
- [20]. MurariMohon Roy, Hideyuki Tsunemoto,HiromiIshitani et.al, —Influence of Aldehyde and Hydrocarbon Components in the Exhaust on Exhaust Odor in DI Diesel Engines
- [21]. P. E. Oberdorfer“ the Determination of Aldehydes in Automobile Exhaust Gas” 670123, 1967, doi:10.4271/670123.
- [22] S. Sumiyaet.al "Catalytic Reduction of NOx and Diesel Exhaust," SAE Technical Paper 920853, 1992, doi:10.4271/920853.
- [23] Erlandsson.O "Hydrocarbon (HC) Reduction of Exhaust Gases from a Homogeneous Charge Compression Ignition (HCCI) Engine Using Different Catalytic Mesh-Coatings," SAE. Technical Paper 2000-01-1847, 2000, doi:10.4271/2000-01-1847.
- [24] Magdi K. Khair "Design and Development of Catalytic Converters for Diesels," SAETechnical Paper 921677, 1992, doi:10.4271/921677.
- [25] Kenneth T. Menzies "Comparison of Aldehyde Methods," SAE Technical Paper 820965, 1982, doi:10.4271/82096.

Performance & emission of Twin Cylinder Diesel Engine Using Diesel & Ethanol

Dr. Hiregoudar Yerrennagoudaru ¹, Manjunatha K ² Chandragowda M ³,
Lohit H A ⁴

¹Professor and PG Co-ordinator (Thermal Power Engineering), Mechanical Engineering Department, RYMEC Bellary, Karnataka, India

²ASST Professor and PROJECT Co-ordinator (Thermal Power Engineering), Mechanical Engineering Department, RYMEC Bellary, Karnataka, India

³ASST Professor (Thermal Power Engineering), Mechanical Engineering Department, RYMEC Bellary, Karnataka, India

⁴ M.Tech (Thermal Power Engineering), Mechanical Engineering Department, RYMEC Bellary, Karnataka, India,

Abstract: In view of increasing pressure on crude oil reserves and environmental degradation as an outcome, fuels like ethanol may present a sustainable solution as it can be produced from a wide range of carbon based feedstock. The present investigation evaluates Ethanol as a diesel engine fuel. The objectives of this report is to analyze the fuel consumption and the emission characteristic of a twin cylinder diesel engine that are using Ethanol & compared to usage of ordinary diesel that are available in the market. This report describes the setups and the procedures for the experiment which is to analyze the emission characteristics and fuel consumption of diesel engine due to usage of the both fuels. Detail studies about the experimental setup and components have been done before the experiment started. Data that are required for the analysis is observed from the experiments. Calculations and analysis have been done after all the required data needed for the thesis is obtained. The experiment used diesel engine with no load which means no load exerted on it. A four stroke Twin cylinder diesel engine was adopted to study the brake thermal efficiency, brake specific energy consumption, and emissions at zero load & full load with the fuel of Ethanol. In this study, the diesel engine was tested using 100% Ethanol. By the end of the report, the successful of the project have been started which is Diesel engine is able to run with Ethanol but the engine needs to run by using diesel fuel first, then followed by Ethanol and finished with diesel fuel as the last fuel usage before the engine turned off. The performance of the engine using Ethanol fuel compared to the performance of engine with diesel fuel. Experimental results of Ethanol and Diesel fuel are also compared.

Keywords: Diesel, Ethanol, Performance, Emissions.

I. INTRODUCTION

Rising petroleum prices, increasing threat to the environment from vehicle exhaust emissions and fastly depleting stock of fossil fuels have generated an intense international interest in developing alternative renewable fuels for IC engines. Ethanol is an oxygenated fuel which increases the combustion and makes reduce exhaust emission. It can be produced from crops with high sugar or starch content. Some of these crops include; sugarcane, sorghum, corn, barley, cassava, sugar beets etc. Besides being a biomass based renewable fuel, ethanol has cleaner burning and higher octane rating than the various vegetable oils [1-5]. Jason and Marc (2002) presented the exergetic environmental assessment of lifecycle emissions from M-85, E-85 (used for the gasoline engine) and other alternative fuels[6]. Diesel exhaust is a major contributor to various types of air pollution, including particulate matter (PM), oxides of nitrogen (NO_x), and carbon monoxide (CO) [7]. It has been demonstrated that the formation of these air pollutants can be significantly reduced by incorporating or blending oxygenates into the fossil fuels matrix [8]. Diesel engines are an important part of the public and private transportation sector and their use will continue and grow into the future. But their smoke has become biggest threat to health and environment [9]. Keeping in mind the higher octane number of the ethanol, variable compression ratio engine is a good option in this direction using the ethanol diesel blend as fuel; Shaik et al. (2007) demonstrated VCR engine has great potential for improving part-load thermal efficiency and reducing greenhouse gas emissions [10].

There were many attempts made to use ethanol in compression ignition (CI) engine. Huang et al. (2008) carried out tests to study the performance and emissions of the engine fuelled with the ethanol diesel blends [11]. They found it feasible and applicable for the blends with n-butanol to replace pure diesel as the fuel for diesel engine. Bhattacharya and Mishra (2002) evaluated the feasibility of preparing diesel-ethanol blends using 200° (anhydrous ethanol) and ethanol lower proof [12]. They found that ethanol blends indicated power producing capability of the engine similar to that of diesel. Hansen et al. (2001) found that the properties of ethanol-diesel blends have a significant effect on safety, engine performance, durability and emissions [13]. Wang et al. (2003) analysed that the most noteworthy benefits of E-diesel use lie with petroleum fuel reductions and reductions in urban PM₁₀ and CO emissions by heavy vehicle operations [11]. Ajav and Akingbehin (2002) experimentally determined some fuel properties of local ethanol blended with diesel to establish their suitability for use in compression ignition engines [14]. Eckland et al. (1984) presented, State-of-the-Art Report on the Use of Alcohols in Diesel Engines [15].

Techniques that have been evaluated for concurrent use of diesel and alcohols in a compression-ignition engine include (1) alcohol fumigation, (2) dual injection (3) alcohol/diesel fuel emulsions, and (4) alcohol/diesel fuel solutions. Heisey and Lestz (1981) reported significant reductions in particulate generation; however, NO_x generation increases [16]. Likos et al. (1982) reported increased NO_x and hydrocarbon emissions for diesel-ethanol emulsions [17]. Khan and Gollahalli (1981) reported decreased NO_x and hydrocarbon emissions with increased particulate emissions for diesel-ethanol emulsions [18]. Lawson et al. (1981) reported increased NO_x and decreased particulate emissions with diesel methanol emulsions [19]. This type of inconsistent performance is what has hindered the use of ethanol in diesel. Baker (1981) reported diesel-ethanol emulsions produce similar NO_x, hydrocarbon, and particulate emissions as compared to baseline runs with straight diesel [20]. Ahmed (2001) found Diesel engines are major contributors of various types of air polluting exhaust gasses such as particulate matter (PM), carbon monoxide (CO), oxides of nitrogen (NO_x), sulfur, and other harmful compounds [21]. Ethanol blended diesel (e-diesel) is a cleaner burning alternative to regular diesel for both heavy-duty (HD) and light-duty (LD) compression ignition (CI) engines used in buses, trucks, off-road equipment, and passenger cars. Karabektas and Murat Hosoz (2009) reported the increase of fuel consumption with increase in percentage of ethanol in the blends [22]. Rao et al. (2008) carried out experiment in order to found out optimum compression ratio, experiments were carried out on a single cylinder four stroke variable compression ratio diesel engine [23].

1.1 Objectives of the project

- It is proposed to use Ethanol Fuel in the diesel engine (CI engine).
- The emissions like CO, HC, CO₂, NO_x, SO_x in the exhaust gases are proposed to reduce during the combustion itself.
- To study the performance evaluation of the using Methanol as fuel in the diesel engine.
- Analyze the exhaust emissions and measurement, reduction in the exhaust gas.

Table-1 Properties of Diesel and Methanol			
Sl. No	Properties	Diesel	CH ₄ O
1	Density(kg/m ³)	850	759
2	Calorific value (kJ/kg)	46,500	26,800
3	Kinematic viscosity @ 40C (cst)	3.05	1.4
4	Cetane number	55	8
5	Flash point °C	52	13
6	Fire point °C	56	111
7	Specific gravity	0.84	0.79
8	Sulphur content (%)	<0.035	-

1.2 Sources of Ethanol

Ethanol is a renewable energy source because the energy is generated by using a resource, sunlight, which cannot be depleted. Creation of Ethanol starts with photosynthesis causing a feed stock, such as sugar cane or a grain such as maize (corn), to grow. These feed stocks are processed into Ethanol.

Following are the methods to produce the Ethanol:-

- Fermentation
- Distillation
- Dehydration

II. EXPERIMENTAL SETUP

The experimental test set up Figure-1 consisted of twin cylinder diesel engine, four stroke, Forced cooling system, crank start. The setup is provided with a resistance load bank, Multi gas analyzer made by testo and Stack monitoring kit for particulate matter & formaldehyde as HCHO...etc for performance and emissions analysis. The engine is cooled using the water jackets on the engine block and cylinder head using a Forced Feed System. While the recommended injection timing given by the manufacturer is 27° BTDC (static), the opening pressure of the nozzle was set at 1800 bar and the engine speed at 1500rpm. There are a number of transducers used in the engine such as piezoelectric pressure transducer flush with the cylinder head surface to measure cylinder pressure. Specifications of engine are shown in Table 2.

Fig shows the schematic arrangement of Experimental Set-up.

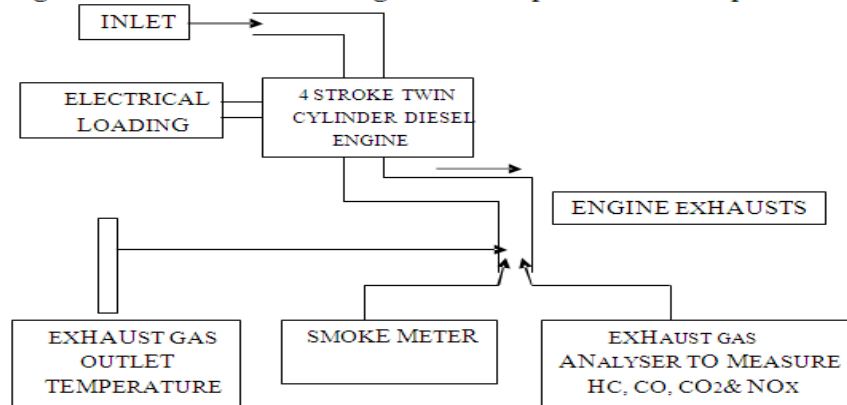


Fig 1: Schematic arrangement of Experimental Set-up



Fig 2: Test engine

Table-2 Test Engine specification	
Engine type	Four stroke Twin cylinder diesel engine
No. of cylinders	02
Stroke	100 mm
Bore Diameter	87 mm
Engine power	19 KW
Compression ratio	17.5:1
RPM	1500
Type of starting	Crank starting
Load type	Electric load bank

Table-3 Load bank specification	
Max. Output	15 KVA / 12.06 KW
Generator type	1 Phase
Amps	63
RPM	1500
PF	0.8
Volts	240

III. PRECAUTION OBSERVED BEFORE STARTING OF THE ENGINE

At the time of starting the engine for each of the tests it was measured that the engine level was in the safe zone and its condition is also good in case the condition was bad, then fresh SAE 40 was introduced into the pump after draining the old. The foundation and mounting bolts were checked periodically as they may go loose due to high speed operations and vibrations.

In the course of experiments the following precautions were observed:

- The ambient temperature variations during the experiment should not be more than 6°C and this was observed as far as possible.
- After each load is applied the engine is allowed to settle before further loads are applied.

Before stopping the engine, it was allowed to run on pure diesel for some time. This is done so that the engine can be restarted easily.

IV. EXPERIMENTAL PROCEDURE

Experiments were initially carried out on the engine using diesel as fuel in order to provide base line data. The methanol was prepared and made to run on the engine.

1st Case:- The engine was started using neat diesel and allowed to run for at least 30 minutes before taking observations. After engine conditions stabilized and reached to steady state, the base line data were taken. Load was varied (Zero load & full load condition) using the alternator load bank and the same was recorded. Gaseous emissions, fuel consumption were also recorded from the respective sensor.

2nd Case:- The engine was started on diesel and when engine became sufficiently heated; the supply of diesel was slowly substituted by 100 % Ethanol for which a two way valve was used. After engine conditions stabilized and reached to steady state, the base line data were taken. Load was varied (Zero load & full load condition) using the alternator load bank and the same was recorded. Gaseous emissions, fuel consumption were also recorded from the respective sensor.

V. RESULTS AND DISCUSSION

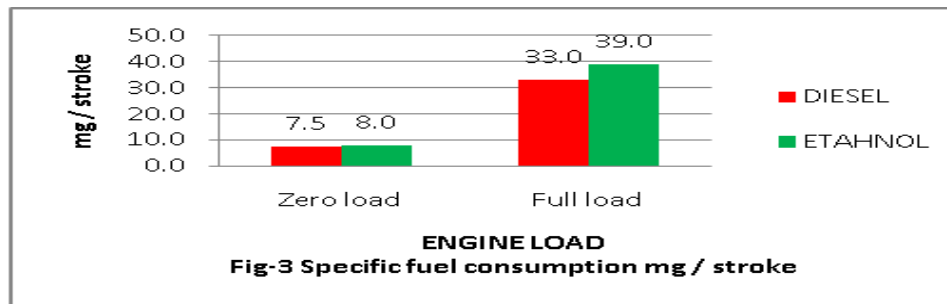
The performance and exhaust emission parameters of the engine with diesel and methanol at zero and full load condition are presented and discussed below.

5.1 Performance parameter

Table-4 Ethanol readings							
Load in Kw		LOAD in %	TORQUE in NM	SPEED in RPM (N)	SFC Mg/stroke	BP in KW	η_{bth} in %
V	I						
230	0	0	8.297	1500	7.5	1.303	24.39
	52	100	120.065	1500	47.5	18.86	55.74

5.1.1 Specific fuel consumption

Table-4 Ethanol readings							
Load in Kw		LOAD in %	TORQUE in NM	SPEED in RPM (N)	SFC Mg/stroke	BP in KW	η_{bth} in %
V	I						
230	0	0	8.297	1500	7.5	1.303	24.39
	52	100	120.065	1500	47.5	18.86	55.74



At higher temperature the effect of Ethanol on specific fuel consumption (SFC) are shown in figure3. From that figure 6.7 it is clear that at different loads the SFC of Ethanol is more than the diesel. The reasons behind this results are lower energy value substitute Ethanol thus engine responds to the load by increasing the fuel flow. Thus SFC decreases with the increase in thermal efficiency.

5.1.2 Brake thermal efficiency

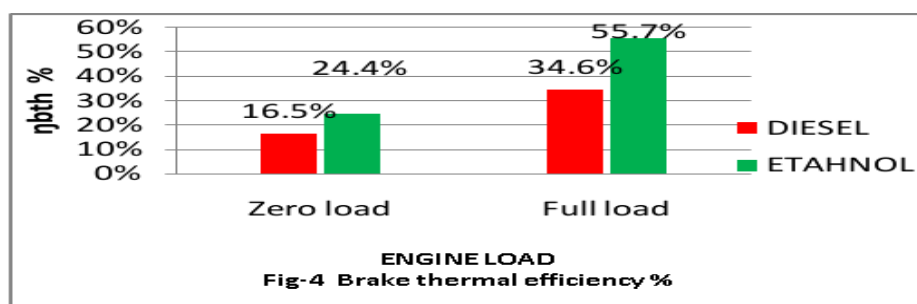
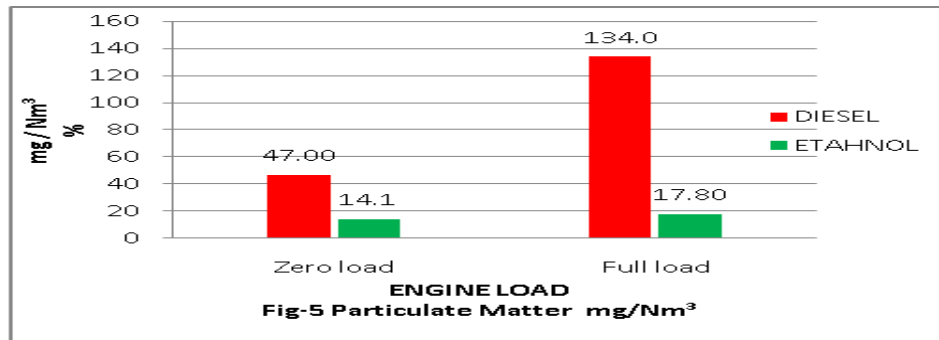


Figure 4, shows the variation of brake thermal efficiency with respect to Ethanol & Diesel at different loads. From the plot it is observed that as load increases brake thermal efficiency is also increases for diesel as well as Ethanol. At full load condition, the brake thermal efficiencies obtained are 34.6% & 55.7% for the diesel & Ethanol respectively. Among these two fuels Ethanol has maximum BTE i.e 55.7% which is obtained from 100 % Ethanol at full load. The BTE using Ethanol is increased by 31.3% as compared to the diesel at full load condition. The increment in Brake thermal efficiency is due to low heat value of Ethanol as compared to diesel & better combustion because of less viscosity of Ethanol.

5.2 Emission parameters

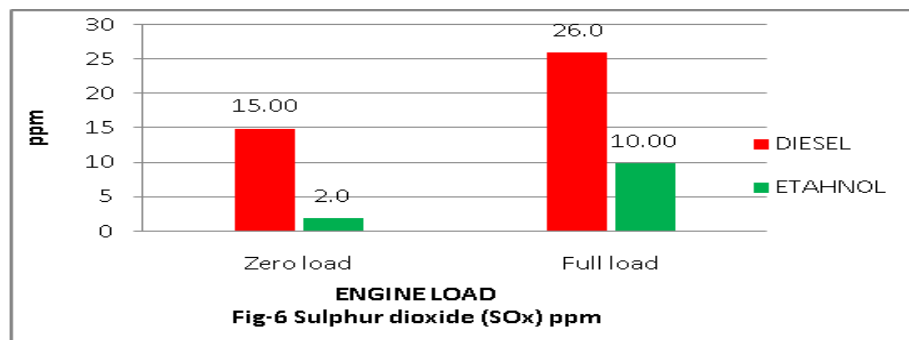
Table-5 Emission parameters of the engine with diesel and Ethanol at zero and full load					
Parameter	Unit	Diesel Zero load	Diesel full load	Ethanol Zero load	Ethanol full load
Exhaust gas Temperature	K	375	393	310	315
Particulate Matter	mg/Nm ³	47.00	134.0	14.10	17.80
Sulphur Dioxide(SOX)	ppm	15.00	26.0	2.0	10.00
Nitrogen Dioxide (NOX)	mg/m ³	1986.00	2431.0	743.0	1048.00
Carbon monoxide	ppm	38.00	44.0	178.0	201.00
Oxygen(O ₂)	%	14.40	12.3	19	18.40
Carbon Dioxide(CO ₂)	%	6.40	8.4	1.20	2.0
Non Methane Hydrocarbon	ppm				
Ethane		<2.00	<2.00	<2.00	<2.00
Propane		<2.00	<2.00	<2.00	<2.00
n Butane		<2.00	<2.00	<2.00	<2.00
iso Butane		<2.00	<2.00	<2.00	<2.00
Pentane		<2.00	<2.00	<2.00	<2.00
Formaldehyde as HCHO	mg/Nm ³	<0.10	<0.10	<0.10	<0.10

5.2.1 Particulate Matter



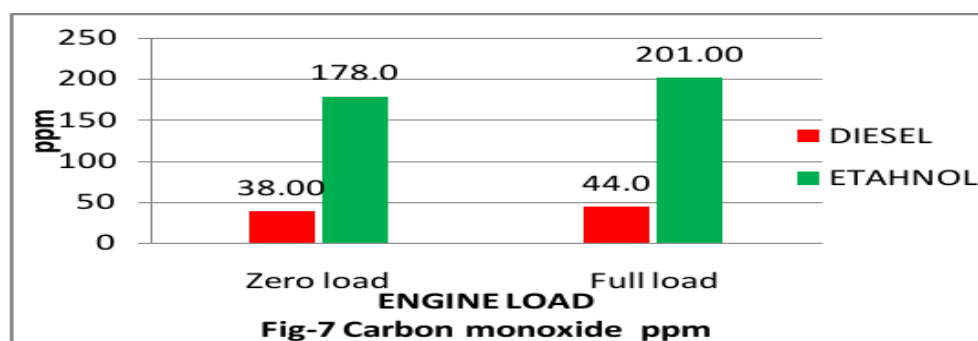
Figures 5, shows the variation of Particulate Matter level with respect to diesel and Ethanol at different loads. Particulate Matter tends to increase with load, this increase in Particulate Matter is explained by the fact that at low loads, but as the load increases, the temperature also increases which in turn increases the Particulate Matter emissions. Result shows that Particulate Matter is comparatively lower with Ethanol. It is found that Particulate Matter emission increases with increase in load in Diesel as fuel but in Ethanol as fuel minor increase with increase load. 100% Diesel has higher Particulate Matter level when compared to 100% Ethanol. This is due to rise in exhaust temperature. Particulate Matter is decreased (80 to 90%) when using Ethanol as fuel in diesel engine compared to diesel fuel.

5.2.2 SOx Concentration



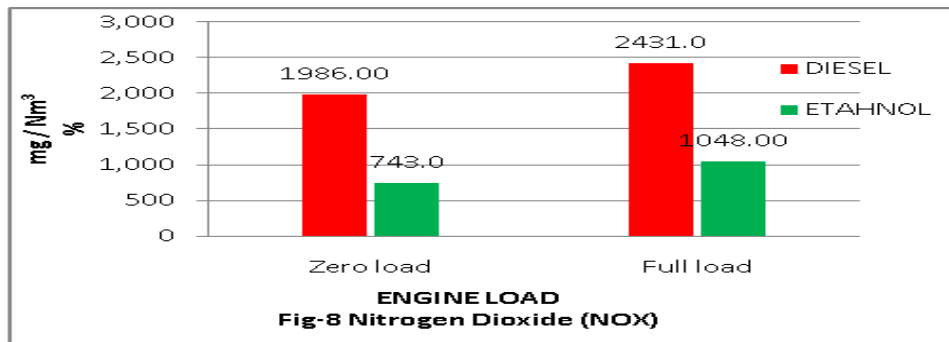
Figures 6, shows the variation of SOx level with respect to Diesel and Ethanol at different loads. SOx tends to increase with load, this increase in SOx is explained by the fact that at low loads, but as the load increases, the temperature also increases which in turn increases the SOx emissions. Result shows that SOx is comparatively higher with Diesel. It is found that SOx emission increases with increase in load. At full load condition 100% Ethanol and 100% Diesel has higher SOx level when compared to zero load condition. SOx is decreased (75 to 90%) when using Ethanol as fuel in diesel engine compared to diesel fuel. Result shows that Sox emission is lower with Ethanol as fuel.

5.2.3 CO Concentration



Figures 7, shows the variation CO level with respect to Diesel and Ethanol at different loads. From the graph it is clear that the CO level increases when Ethanol has a fuel. This is due to the fact that engine is not optimized to run with Ethanol, so there is a large possibility of rich fuel-air mixture in the cylinder and the higher specific fuel consumption resulting in a higher CO level. Carbon monoxide occurs in engine exhaust. It is a product of incomplete combustion due to insufficient amount of air in the air fuel mixture or insufficient time in the cycle for the completion of combustion. CO level is comparatively More when compared to diesel& can be reduce by increasing the compression ratio.

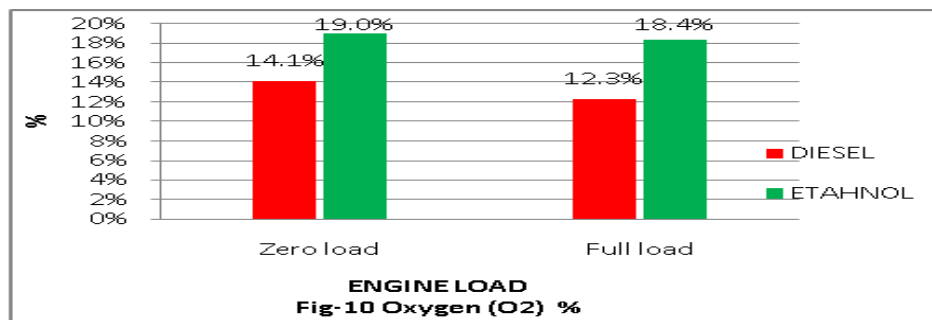
5.2.4 NOx Concentration



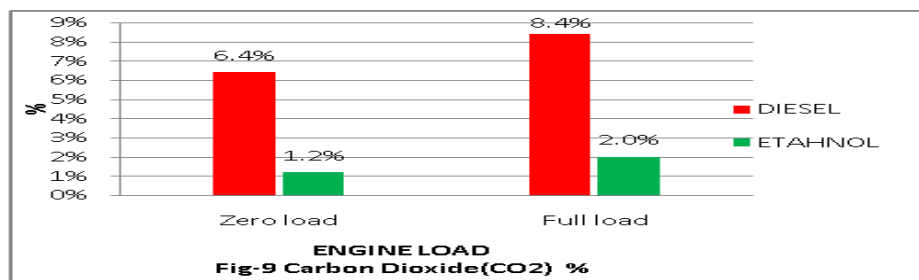
Figures 8, shows the variation of NOx level with respect to Diesel and Ethanol at different loads. NOx tends to increase with load, this increase in NOx is explained by the fact that at low loads, but as the load increases, the temperature also increases which in turn increases the NOx emissions. Result shows that NOx is comparatively higher with Diesel. It is found that NOx emission increases with increase in load. 100% Diesel has higher NOx level when compared to 100% Ethanol. This is due to higher exhaust temperature of Diesel i.e 375 & 393 K. Ethanol Nox emission is decreased (55 to 60%) when compared to diesel.

5.2.5 Oxygen (O₂) Concentration

Figures 9, shows the variation of O₂ level with respect to Diesel and Ethanol at different loads. From the graph it is clear that the O₂ level increases when Ethanol has a fuel. This is due to the fact that engine is not optimized to run with Ethanol, so there is a large possibility of lean / reach fuel-air mixture in the cylinder and the lower compression ratio resulting in a higher O₂ level. Oxygen(O₂)occurs in engine exhaust. It is a product of incomplete combustion due to insufficient time in the cycle for the completion of combustion.



5.2.6 Carbon Dioxide (CO₂) Concentration



Figures 10, shows the variation of CO₂ level with respect to Diesel and Ethanol at different loads. From the graph it is clear that the CO₂ level decreases when Ethanol has a fuel. This is due to the fact that engine is not optimized to run with Ethanol, so there is a large possibility of lean / rich fuel-air mixture in the cylinder and the lower compression ratio & temperature resulting in a higher CO₂ level. CO₂ occurs in engine exhaust. It is a product of incomplete combustion due to insufficient time in the cycle for the completion of combustion.

VI. CONCLUSION AND FUTURE SCOPE

Based on the performance and emissions of Ethanol, it is concluded that the Ethanol oil represents a good alternative fuel with closer performance and better emission characteristics to that of a diesel. From the above analysis the Ethanol shows better performance compared to the Diesel in the sense of better performance characteristics like Brake thermal efficiency, Specific fuel consumption and decrease in the emission parameters like NO_x, Sox, Particulate matter ,CO₂ but CO , O₂ is little higher than the diesel which can be reduced by increasing the compression ratio. Hence the 100% Ethanol can be used as a substitute for diesel.

REFERENCES

- [1.] Alan C. Hansen, Qin Zhang and Peter W. L. Lyne, "Ethanol–diesel fuel blends a review", *Bioresource Technology*, Volume 96, Issue 3, February 2005, Pages 277-285.
- [2.] Hanbey Hazar, "Effects of biodiesel on a low heat loss diesel engine", *Renewable Energy* 34 (2009) 1533–1537.
- [3.] Neven Voca, Boris Varga, Tajana Kricka, Duska Curic, Vanja Jurisic and Ana Matin, "Progress in ethanol production from corn kernel by applying cooking pre-treatment" [*Bioresource Technology* Volume 100, Issue 10, May 2009, Pages 2712-2718.](#)
- [4.] Avinash Kumar Agarwal, "Biofuels (alcohols and biodiesel) applications as fuels for internal combustion engines" *Renewable Energy*, 27 November 2006.
- [5.] Hakan, Bayraktar. "[Experimental and theoretical investigation of using gasoline–ethanol blends in spark-ignition engines](#)", *Renewable Energy*, 2005; Volume 30, Issue 11: pp1733-1747.
- [6.] Jason J, Daniel Marc, Rosen A, "Exergetic Environmental Assessment of Life Cycle Emissions for various Automobiles and Fuels, *Exergy* 2 (2002) 283-294
- [7.] Hwanam Kima, Byungchul Choi, "Effect of ethanol–diesel blend fuels on emission and particle size distribution in a common-rail direct injection diesel engine with warm-up catalytic converter", *Renewable Energy* 33 (2008) 2222–2228.
- [8.] De-gang Li, Huang Zhen, Lu Xingcai, Zhang Wu-gao and Yang Jian-guang, "Physico-chemical properties of ethanol–diesel blend fuel and its effect on performance and emissions of diesel engines", *Renewable Energy* 30 (2005) 967–976.
- [9.] Sehmus Altuna, Husamettin Bulutb and Cengiz Oner, "The comparison of engine performance and exhaust emission characteristics of sesame oil–diesel fuel mixture with diesel fuel in a direct injection diesel engine", *Renewable Energy* 33 (2008) 1791–1795.
- [10.] Amjad Shaik, N Shenbaga Vinayaga Moorthi, and R Rudramoorthy, "Variable compression ratio engine: a future power plant for automobiles an overview," *Proc. IMechE* Vol. 221 Part D April 2007. DOI: 10.1243/09544070JAUTO573.
- [11.] Jincheng Huang, Yaodong Wang, Shuangding Li, Anthony P. Roskilly, Hongdong Yu, Huifen Li, "Experimental Investigation on the Performance and Emissions of a Diesel Engine Fuelled with Ethanol-diesel Blend," *ATE* 2697, 2008.
- [12.] T K Bhattacharya and T N Mishra, "Studies on Feasibility of using Lower Proof Ethanol-diesel Blends as Fuel for Compression Ignition Engines", *IE (I) Journal*–AG 263 145, December 21, 2002
- [13.] Alan C. Hansen, Peter W. L. Lyne, Qin Zhang, "Ethanol-Diesel Blends: A Step towards A Bio-Based Fuel for Diesel Engines", [*American Society of Agricultural and Biological Engineers* \(ASAE\) August 1, 2001.](#)
- [14.] Ajav, E. A. and O. A. Akingbehin, "A Study of some Fuel Properties of Local Ethanol Blended with Diesel Fuel", *Journal of Scientific Research and Development Manuscript* EE 01 003. Vol. IV. March, 2002.
- [15.] Eckland, E. E.; R. L. Bechtold; T. J. Timbario; and P. W. McCallum, "State-of-the-Art Report on the Use of Alcohols in Diesel Engines", SAE Paper No. 840118.
- [16.] Heisey, J. B. and S. S. Lestz, "Aqueous alcohol fumigation of a single-cylinder DI CI engine," SAE Paper No. 811208.
- [17.] Likos, B.; T. J. Callahan; and C. A. Moses, "Performance and Emissions of Ethanol and Ethanol-Diesel Blends in Direct-Injected and Pre-Chamber Diesel Engines", SAE Paper No. 821039.
- [18.] Khan, N and S. R. Gouahalli, "Performance and Emission Characteristics of a Diesel Engine Burning Unstabilized Emulsions of Diesel Fuel with Water, Methanol, and Ethanol", SAE Paper No. 811210.
- [19.] Lawson, A.; A. J. Last; A. S. Desphande; and E. W. Simmons, "Heavy-Duty Truck Diesel Engine Operation on Unstabilized Methanol -Diesel Fuel Emulsions", SAE Paper No. 810346.
- [20.] Baker, Q. A., "Use of Alcohol-in-Diesel Fuel Emulsions and Solutions in a Medium-Speed Diesel Engine", SAE Paper No. 810254.

The Effect of Cryogenic Treatment on the Hardness, Friction and Wear Resistance of Austenitic Ductile Iron Type D3 Tool Steel

K. S. Mahesh Lohith¹, V. B. Sondur², V. V. Sondur³

1 Research Scholar, Research Center, Maratha Mandal Engineering College, Affiliated to Visvesvaraya Technological University, Belgaum, Karnataka, INDIA,

2 Principal & Director, Research Center, Maratha Mandal Engineering College, Affiliated to Visvesvaraya Technological University Belgaum, Karnataka, INDIA

3 Professors, Research Center, Maratha Mandal Engineering College, Affiliated to Visvesvaraya Technological University Belgaum, Karnataka, INDIA

Abstract: Investigations carried out in the recent few decades reveal the advantages of cryogenic treatment as one of the promising techniques to enhance wear resistance in certain tool steels. Thus the cryogenic treatment has significant influence on the tribological performance of tool steels. It is a one time permanent treatment process affecting the entire section of the part, unlike coatings. Enhancing the wear resistance and service life of the steel tools subjected to rubbing condition is of important concern. Literature provides information about the investigations performed on some high-speed steels which reveal remarkable improvement in wear resistance from 92% to 817%. Furthermore, the studies conducted on conventional D3 tool steel reveals the betterment of certain tribo-mechanical properties such as hardness and wear resistance. In the present investigation the effect of cryogenic treatment on austenitic ductile iron type D3 tool steel is studied by sliding the test specimen against the same mating material. The study reveals increase in hardness, reduction in friction coefficient and enhancement in wear resistance.

Keywords: Austenitic ductile iron, Cryogenic treatment, Friction, Wear resistance, Vickers hardness, D3 tool steel, Pin-on-disc tribometer.

I. INTRODUCTION

Techniques like heat treatment and coatings are commonly used to improve the wear resistance of some tool steel components [11-15]. The perfect combination of alloying elements and the domain of heat treatment processes confer materials with excellent hardness and wear resistance properties allied to good toughness [15]. As a result of technological advance a great variety of HSS tools are actually available, including coated and powder metallurgy tools. However, cryogenic treatment has emerged as one of the fruitful techniques for the improvement of tribo-mechanical properties of materials [1,2,5,6].

Investigations carried out over the recent four decades have shown interests in low temperature effects and have been demonstrated particularly during heat treatment cycles of tool steels. Initial studies conducted by Barron on various tool steels show a remarkable improvement in tool life and wear resistance. Barron [2] investigated the effect of cryogenic treatment for several materials including the M2 high speed steel at 84°C. The soaking temperature is maintained at 84 °C for 24 hours. A significant improvement in wear resistance of cryo-treated steels is observed in sliding abrasion tests when compared to tool steels that are conventionally heat treated, quenched and tempered. The reduction in temperature of the cryogenic treatment further to -196°C results in further enhancement in the wear resistance. Literature data indicates that the lives of tools and other steel components increase significantly after being submitted to subzero temperatures. The results are found to be good depending on the application. Improvement in the performance of tool steels from 92% to 817% is observed due to the cryogenic treatment at -196°C.

Barron [1] attributes the improvement in the wear resistance of tool steels to another mechanism besides the transformation of the retained austenite into martensite. The study verifies that tool steels submitted to conventional heat treatment presented only a small amount of retained austenite. Tool steels submitted to cryogenic treatment show even better performance during machining. Barron, thus, attributes this achievement

to transformation of retained austenite to martensite and the presence of both hard and small carbide particles that are well distributed among the larger carbide particles within the martensite matrix.

Paulin [3], in his work, verified the presence of fine precipitated carbide particles and their importance related to the material properties. The precipitated carbides reduce internal tension of the martensite and also micro cracks susceptibility is minimized. The uniform distribution of fine carbides of high hardness enhances the wear resistance. Study conducted by Huang and associates [5] also confirms that the cryogenic treatment not only facilitates the carbide formation, it can also make the carbide distribution more homogeneous.

The study conducted by Yun [4] verifies changes in the micro-structure of M2 high speed steel when the material is subjected to different cycles of cryogenic treatment at -196 °C. The results attribute to the transformation of retained austenite into martensite and precipitation of ultra-fine carbides.

The effect of deep cryogenic treatment (DCT) on the properties of some tool steels is studied by Molinari and others [6]. The investigation is carried out with both field tests and laboratory tests on real tools. The execution of the deep cryogenic treatment on quenched and tempered high speed steel tools increases hardness, reduces tool consumption and down time for the equipment set up, thus leading to cost reductions of about 50%. The laboratory investigation on an AISI M2 and an AISI H13 steel confirms the effectiveness of DCT followed by conventional heat treatment in increasing the wear resistance and toughness.

The mechanical properties such as hardness and wear resistance of the tool and die steel samples treated by conventional tempering and cryogenic quenching with tempering have been evaluated employing Vickers indentation and sliding wear techniques, respectively. The investigation demonstrates deep cryogenic treatment leads to considerable micro-structural changes which results in enhanced tribo-mechanical properties [7].

Study conducted by Dhokey and Nirbhavane [8] describes the effect multiple tempering after cryogenic treatment for D3 tool steel. The hardness, micro structure and wear loss are studied for different kinds of treatments. The treatments are like HT (Hardening and Tempering), HC (Hardening and cryo-treatment), HCT, HCTT, HCTTT (Hardening, cryogenic treatment, tempering and multiple tempering). Wear test is conducted by holding D3 sample pin against the SAE 52100 steel disc of pin on disc tribometer. The study unveils decrease in hardness with multiple tempering of cryo-treated D3 tool steel. The study also reveals the reduction in wear resistance with multiple tempering of the cryo-treated D3 tool steel.

The instrumentation for the measurement of tribo-mechanical properties are of many types and the methods of evaluation of the properties are also of various kinds. There are different forms of tribometers used for the evaluation of tribo-mechanical properties and one of the types, advanced reciprocating tribometer, is studied and published by the author as a co-worker [10]. In the current study pin-on-disc tribometer, conforming with ASTM standards, is used for the evaluation of tribo-mechanical properties of the materials.

II. AUSTENITIC DUCTILE IRON TYPE D3 TOOL STEEL

2.1 COMPOSITION

In the present work, unlike the D3 tool steel used in the study [8], the material selected for the study is austenitic ductile iron (ADI) type D3 tool steel. The composition of austenitic ductile iron is 2.6% of carbon, 2.5-3.5% of chromium, maximum of 1.0% of manganese, 28.0-32.0% of Ni, maximum of 0.08% of phosphorus, maximum of 1.0-2.8% of silicon and iron being the balance percentage of the structure.

2.2 IMPORTANCE OF AUSTENITIC DUCTILE IRON TYPE TOOL STEELS

The study is intended to determine the tribo-mechanical properties of cryo-treated D3 Tool Steel. Since the Pin-On-Disc tribometer could be operated at higher linear speeds when compared to reciprocating tribometer, in the present study an improved version of Pin-On-Disc tribometer with modified pin holding attachment [Fig. 1.] is used to evaluate friction and wear of D3 tool steel. The evaluation of the friction and wear properties is significant and must be done with well defined procedure. Hence The samples are prepared to conform the Pin-On-Disc tribometer specifications.

III. INTRODUCTION TO CRYOGENIC TREATMENT AND ITS INFLUENCE ON SOME TOOL STEELS

Cryogenic treatment process is not a supplement process for heat treatment. Rather, it is an extension of heat treatment process which would be helpful in obtaining improvement in some of the tribo-mechanical properties for some of the materials. The subzero treatment on metals has been extensively employed for many

decades for various applications like stabilizing dimensions of precision machined parts and gauges, removal of internal stresses, improving tool life of cutting tools etc.

When metals are gradually cooled to cryogenic temperatures, soaked for a prolonged period and allowed to warm to room temperature at a predetermined rate, the lattice structure changes due to stresses being relieved during cryogenic treatment cycle. In the case of ferrous metals, the soft, ductile, FCC structured austenite gets converted to strong and harder BCC structured martensite. Apart from this change, a wide precipitation of newly formed carbides into the hard martensite structure induces a dense lattice structure [1,3].

Earlier studies have revealed the fact of newly precipitated carbide particles are largely responsible for the increase in wear resistance characteristics by the process, due to, a denser, uniform and fine micro structure. This results in larger surface area of contact between the tool and metal which reduces friction, heat and wear. Obvious changes have been found in the improvement of tool life of high-speed tool steels.

IV. SAMPLE PREPARATION AND THE PROCESS OF CRYOGENIC TREATMENT

4.1 SAMPLE PREPARATION AND THE PROCESS OF CRYOGENIC TREATMENT

The study is intended to determine the tribo-mechanical properties of cryo-treated D3 Tool Steel. Since the Pin-On-Disc tribometer could be operated at higher linear speeds when compared to reciprocating tribometer, in the present study an improved version of Pin-On-Disc tribometer [Fig. 2.] with modified pin holding attachment [Fig. 1.] is used to evaluate friction and wear of D3 tool steel. The evaluation of the friction and wear properties is significant and must be done with well defined procedure. Hence The samples are prepared to conform the Pin-On-Disc tribometer specifications.

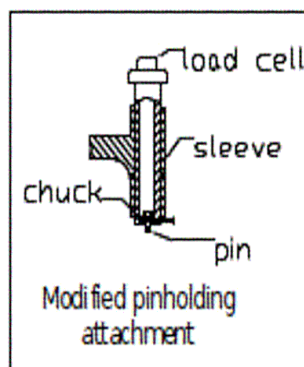


Figure 1. Modified pin holding attachment

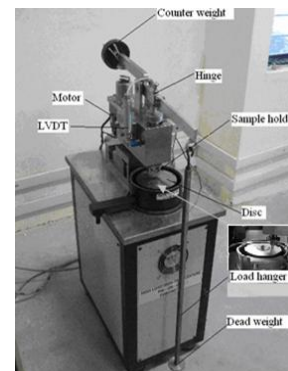


Figure 2. Pin-On-Disc Tribometer

4.2 PREPARATION OF MATERIAL SAMPLES FOR TRIBOLOGY TESTS

It is of interest to test some of the mechanical properties of the selected material. In order to conduct the wear resistance test on the wear testing rig: A disc of D3 tool steel of diameter 110mm having a thickness of 8.1 mm is required. The surface finish of 0.24 micrometer is required for the disc which is accomplished by surface grinding operation. The disc has a central hole of 8.5mm in diameter and an eccentric hole of 4mm in diameter at a distance 11.25mm from the center of the disc. The pins required for wear testing are obtained by cutting and finishing a rod of length 300mm and diameter of 6mm. The length of each pin is 25mm. Square slabs of dimension 50mmx50mmx10mm are fabricated for hardness tests.

4.3 CRYOGENIC TREATMENT FOR THE TEST SAMPLES

Fabricated samples are categorized into two different batches. One batch is taken through a cycle of cryogenic treatment. The hardness specimen, specimen pins and specimen discs are placed inside the cryogenic system Fig. 4. The cryogenic processor system is provided with a container in which liquid nitrogen gets filled. Initially, during the cryo-treatment, the container temperature is maintained at room temperature of 300K. The temperature of the system is gradually reduced to the soaking temperature of 98 K with a cooling rate of 0.417 K/min. This takes about 8 hours to attain the temperature 98 K. The cooling is controlled by a data acquisition system which regulates the liquid flow through the solenoid valve. If the rate of fall in temperature is quick compared to the preset value then the the flow of the liquid nitrogen is stopped so that the temperature drop is maintained at preset value. The amount of liquid required for attaining this temperature is about 250 litre.

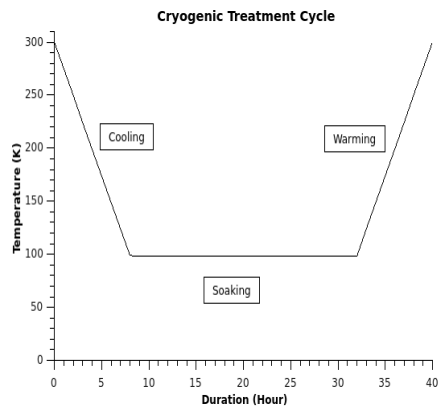


Figure.3. Cryogenic treatment cycle

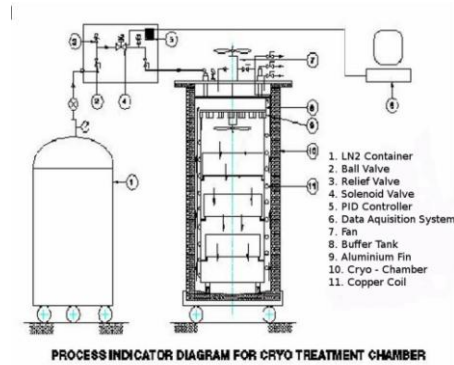


Figure. 4. Schematic Diagram of cryo-processor

Once the specimens are cooled to a temperature of 98 K the temperature is maintained constant for a period of 24 hours [9]. In order to hold the temperature constant for a period of 24 hours it takes about 450 litre of liquid nitrogen. The beneficial changes of the cryogenic treatment occur during this phase of the treatment. After the 24 hours the system is allowed to gradually heat to the room temperature. The warming at rate 2.4 min\K and hence it takes 8 hours for the specimens to attain the room temperature 300K Fig. 3.

V. EXPERIMENTS

The Untreated and cryo-treated samples are fabricated as per the required standards for the Vickers hardness test and conforming to the specifications of the Pin-On-Disc tribometer designed as per ASTM standards.

5.1 DETERMINATION OF VICKERS HARDNESS FOR D3 TOOL STEEL

Hardness measurement is done for both untreated and cryo-treated test specimen. Vickers hardness measurement technique is used to determine the hardness of the selected material specimens. The hardness is determined by taking average of six readings. The average Vickers pyramid number (HV) or Diamond pyramid hardness (DPH) determined using Vickers indentation method is given in the Table. 1.

Sample	F (kg wt)	d(mm)	HV
Untreated	20	0.411	220
Cryo-treated	20	0.379	258

Table. 1. HV – Untreated and Cryo-treated austenitic ductile iron type D3 tool steel.

5.2 FRICTION AND WEAR TESTS

Specifications of the Pin-On-Disc tribometer used for the tribo-mechanical tests are as described below. The loading capacity is from 5N to 250N having the resolution of 1N. The maximum friction force of 100N can be measured with 1N resolution Fig. 2. The resolution of linear variable differential transformer (LVDT) is 1 micron. The Pin-On-Disc tribometer is calibrated using standard specimen for which the tribo-mechanical properties are well defined. Experiments are conducted by sliding D3 pin against D3 Disc, for both untreated and cryo-treated samples, using Pin-On-Disc Tribometer. The idea of making the pin and disc of same material is to study the effect of cryogenic treatment on the material when it is under rubbing condition with identical material. Friction and wear tests were first conducted for untreated D3 pin sliding against untreated D3 disc. In the later part of the experiments friction and wear tests were conducted for the cryo-treated D3 pin sliding against cryo-treated D3 disc. Friction and LVDT Displacement were acquired using data acquisition system for a constant load of 40N and keeping the sliding distance same 1000m. The experiments were conducted for two different sliding speeds of the D3 disc 1m/s and 5m/s. During the tribo-mechanical tests wear debris is not removed from the surface of the disc to simulate practical real time sliding environment.

VI. RESULTS AND DISCUSSION

Vickers hardness measurements are done with six trials and an average value is obtained. The average of the HV is 221 before cryo-treatment. The average of the HV is 258 after cryo-treatment. The results show enhancement by 17% after cryo-treatment. It is evident from the present study that there is appreciable increase in the hardness of the material as a result of cryo-treatment. This is attributed to the transformation from retained austenite to martensite and the formation of carbide particles.

The comparison of co-efficient of friction between untreated and cryo-treated samples conclude the betterment of the performance of the material with lower friction after cryo-treatment. The plots in Fig. 5. reveal the lowering of friction after cryo-treatment, for the sliding speeds 1m/s and 5m/s.

The fluctuations in the values of co-efficient of friction were observed during the experimentation and is due to the lumps of wear particles formed during the three body abrasive wear. It is evident from the visual inspection and the plots that the wear particle size is comparatively high in case of lower speed 1m/s than higher speed 5 m/s

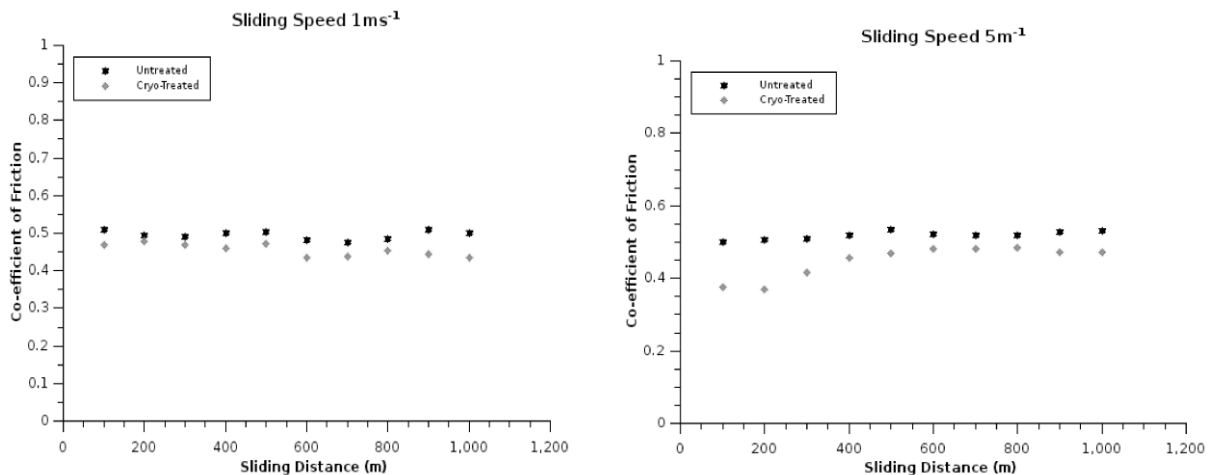


Fig. 5. Variation of friction as a function of sliding distance for linear speeds 1m/s and 5 m/s

Plots of displacement measured by linear variable differential transformer (LVDT) as a function of sliding distance for linear speeds 1m/s and 5m/s are made for both untreated and cryo-treated samples. The plots are as shown in Fig. 6. The plots show appreciable increase in the wear resistance of D3 steel after cryo-treatment. The percentage change in LVDT displacement per kilometer sliding is calculated from trend lines (least square fit). Even though the LVDT displacement does not exactly bring out the precise value of linear wear it represents a value proportional to linear wear since the normal load is constant.

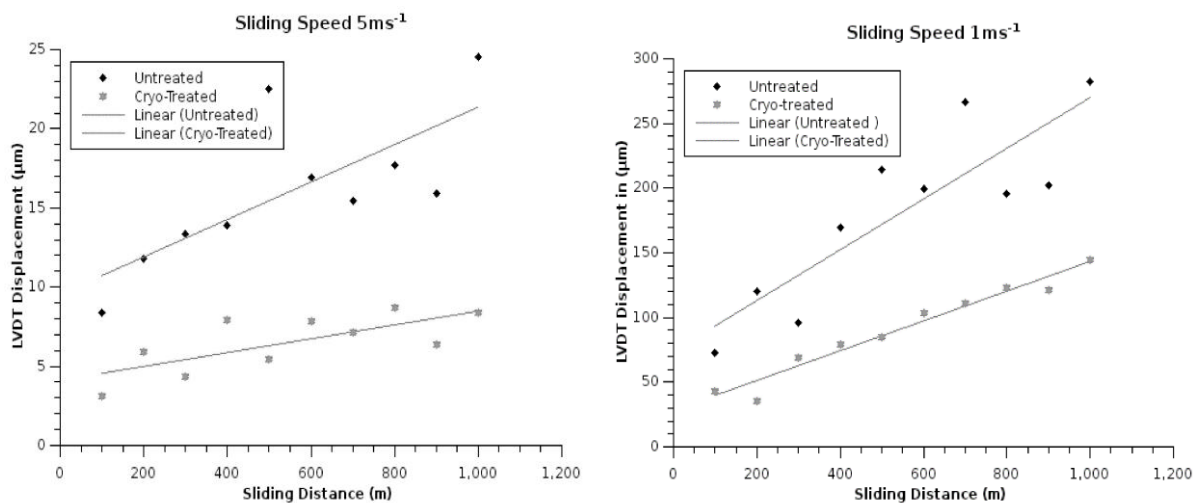


Figure. 6. LVDT displacement function of sliding distance for linear speeds 1m/s and 5 m/s

Wear resistance enhancement in cryo-treated specimen is found to be better by 40% for linear speed 1m/s in comparison with untreated specimen for the same linear speed. Similar plot for the linear speed of 5m/s is made and the plot reveals enhancement in wear resistance better by 80% for cryo-treated specimen in comparison with untreated specimen for the same linear speed.

VII. CONCLUSION

The current investigation reveals the effect of cryo-treatment on austenitic Ductile Iron type D3 Tool steel in terms of increase in hardness and enhancement in the wear resistance of the material. The cryo-treated samples wear out slowly when compared to untreated samples confirming the enhancement in wear resistance there by increasing the tool life. The increase in hardness makes the material better with regard to mechanical properties.

The investigation also confirms cryo-treatment as an efficient onetime process to reduce wear in the austenitic ductile iron type D3 tool steel. The Cryogenic treatment leads to an appreciable increase in wear resistance of the material. It is found that the percentage change in wear is lower for higher speeds thus leading to dependence of wear resistance on speed. The lumps of wear particles formed suggest the initial adhesive wear. Furthermore the wear debris indulge in three body abrasive wear. It can be concluded that the coefficient of friction decreases when austenitic ductile iron type D3 tool Steel is cryo-treated.

ACKNOWLEDGEMENTS

Authors express gratitude to **Dr. Krishna Venkatesh**, CEO, Center for Emerging Technologies, Jain University, for the provision of Pin-On-Disc tribometer. The authors thank Mr. Govindaraju of Magnum Industries, Peenya Industrial Area, Bangalore, for the material samples and fabrication. Authors also thank Mr Suresh Nadig, Indian Institute of Science, Bangalore for the Cryogenic treatment of material samples.

REFERENCES

JOURNAL PAPERS:

- [1] Barron F. R., Yes cryogenic treatments can save you money here is why, *Tapi*, 57(5), 1974, 35-40.
- [2] Barron R. F., Cryogenic treatment of metals to improve the wear resistance, *Cryogenics* 409-413, 1982.
- [3] Paulin P., Frozen gears, *Gear Technol* 26-28, 1993.
- [4] Yun D., Xiaoping L., Hongshen X., Deep cryogenic treatment of high speed steel and its mechanism, *Heat Treat. Met.* 55-59, 1998.
- [5] Huang JY, Zhu YT, Liao XZ, Beyerlein IJ, Bourke MA, Mitchell TE. Microstructure of cryogenic treated M2 tool steel. *Materials Science and Engineering*, A339 241(4), 2003.
- [6] Molinari A., Pellizzari M., Gialanella S., Straffellini S., Stiasny K. H., Effect of Deep cryogenic treatment on the mechanical properties of tool steels, *J. Mater. Process. technol.* 118, 2001, 350-355.
- [7] Mohan Lal D., Renganarayanan S., Kalanidhi A., Cryogenic treatment to augment wear resistance of tool and die steels, *Cryogenics*, 41, 149-155, 2001, 149-155 .
- [8] Dhokey N. B., Nirbhavane S., Dry sliding wear of cryo-treated multiple tempered D-3 tool steel, *Journal of Materials Processing Technology* ,209(3), 2009, 1484-1490.
- [9] Gopal Krishna P. V., Kishore K., Ramadevudu G., Sikandar Ali, Performance evaluation of cryogenic treated tools in turning, *Advances in Production Engineering & Management*, 3, 2012, 187-194 .
- [10] Mohan C. B., Divakar C., Venkatesh K., Gopalakrishna K., Mahesh Lohith K. S., Naveen T. N., Design and development of an linear reciprocating tribometer, *Wear*, 267, 2009, 1111-1116.
- [11] Garcia I., Fransar J., Celis J.P, Electro-deposition and sliding wear resistance of nickel composite coatings containing micron and sub-micron SiC particles *Surface and Coatings Technology*, 148, 2001, 171-178.
- [12] Yuji Chibaa, Toshio Omuraa and Hiroshi Ichimuraa, Wear resistance of arc ion-plated chromium nitride coatings, *Journal of Materials Research*, 8, 1993, 1109-1115.
- [13] Dutta Majumdar J., Galun R., Mordike B. L., Manna I, Effect of laser surface melting on corrosion and wear resistance of a commercial magnesium alloy, *Materials Science and Engineering*, A361, 2003, 119-129.
- [14] Sun Y., Li X., Bell T., Low temperature plasma carburising of austenitic stainless steels for improved wear and corrosion resistance, *Surface Engineering* 15(1), 1999, 49-54.
- [15] Feng B., Weng J., Qu S. X., Leng Y. X., Zhou Z. R., Improving wear resistance by heat treatment in different atmospheres, *key engineering Materials*, 288-289, 2005, 641-644.

A Study on Groundnut Husk Ash (GHA)–Concrete under Acid Attack

Egbe-Ngu Ntui Ogork¹, Okorie Austine Uche², Augustine Uche Elinwa³

^{1,2} Senior Lecturer, Department of Civil Engineering, Bayero University, PMB 3011 Kano, Nigeria.

³ Professor, Civil Engineering Programme, Abubakar Tafawa Belewa University, PMB 0248 Bauchi, Nigeria

Abstract: This paper presents the findings of an investigation on the compressive strength of Groundnut Husk Ash (GHA)-Concrete and its resistance to acid attack. The GHA used was obtained by controlled burning of groundnut husk to a temperature of 600 °C and sieved through 75 µm sieve after allowing cooling. The compressive strength of GHA-Concrete was investigated at replacement levels of 0, 5, 10, 20, 30 and 40 %, respectively by weight of cement. A total of ninety 150 mm cubes of GHA-Concrete grade 20 were tested for compressive strength at 3, 7, 28, 60 and 90 days of curing and the microstructure of GHA-Concrete samples at 0 and 10 % replacements were examined at 28 and 90 days of curing. Also, thirty six 100 mm cubes were subjected to attack from 10 % concentration of diluted solution of sulphuric acid (H₂SO₄) and nitric acid (HNO₃), respectively. The result of the investigations showed that the compressive strength of concrete decreased with increase in GHA content. However 10 % replacement with GHA was considered as optimum for structural concrete. GHA provided a less compact microstructure of concrete at 28 and 90 days curing compared to OPC concrete as a result of low pozzolanic activity. The use of GHA in concrete improved its resistance against sulphuric acid, but not against nitric acid attack. The average weight loss of GHA concrete after 28 days of subjection in sulphuric acid and nitric acid were 16.3 % and 17.3 %, respectively as opposed to 22.4 % and 15.1 %, respectively for plain Portland cement concrete.

Key Words: Groundnut Husk Ash, Concrete, Microstructure, Acid Attack

I. Introduction

The durability of concrete is its ability to resist chemical and physical attacks that lead to deterioration of concrete during its service life. These attacks are leaching, sulphate attack, acid attack, carbonation, alkali-aggregate reaction, freezing-thawing and abrasion [1].

For a long time concrete was considered a very durable material requiring very little or no maintenance. Thus leading to the erection of concrete structures in highly polluted urban and industrial areas, harmful sub-soil water in coastal areas and other hostile conditions where other material of construction have not been found suitable. Though compressive strength of concrete is a measure of durability to a certain extent, but it is not entirely true that strong concrete is always durable, owing to some failures observed of concrete of high compressive strengths due to environmental conditions [2].

In recent years, durability is one of the critical issues to develop concrete technologies and construct reinforced concrete structures with long service life due to some economical and environmental reasons [1].

Supplementary cementitious materials have been identified in literature to be fundamental to advancing low cost construction materials with the main benefits of saving natural resources and energy as well as protecting the environment through the use of the main mineral admixtures [3]. [4] highlighted the effectiveness and durability of natural pozzolanic cement in ancient Greek and Roman structures built about 6th and 7th century BC and still in existence. Several experimental studies have been carried out on variety of pozzolanic materials such as volcanic ash, fly ash, blast furnace slag, silica fume, rice husk ash, sugarcane bagasse ash, sawdust ash, etc. However, there are controversial results about the resistance to acidic attack on pozzolanic cements in technical literature. Acidic attack usually originates from industrial processes, but it can even be due to urban activity. [5] claim that pozzolanic cement has better durability characteristics against acid attacks, while [6] and others claim vice versa. This study has shown that the resistance to acid attack on pozzolanic concrete varies with the acid in consideration. The acidic attack on pozzolanic cement products is affected by the processes of decomposition and leaching of the constituent of cement matrix [7]. Acids react with alkaline components of the binder (calcium hydroxide, calcium silicate hydrates and calcium aluminate hydrates) lowering the degree of alkalinity.

The use of Groundnut Husk Ash (GHA) as a supplementary cementitious material in concrete has been reported in [8] and [9]. They suggested that up to 10 % GHA content could be used as a partial substitute of cement in structural concrete. It is against this background that this research aimed to investigate the resistance of GHA-Concrete subjected to acid attacks.

II. Materials And Methods

2.1 Materials

Ordinary Portland Cement produced in Nigeria (Dangote brand), with a specific gravity of 3.14 was used. The chemical composition analysis of the cement is shown in **Table 1**. Sharp sand collected from River Challawa, Kano, Nigeria, with a specific gravity of 2.62, bulk density of 1899.50 kg/m³, moisture content of 2.50 % was used. The particle size distribution of the sand shown in Figure 1, indicate that the sand used was classified as zone -1 based on [10] grading limits for fine aggregates.

The coarse aggregate is crushed granite of nominal size of 20 mm with a specific gravity of 2.7, moisture content of 1.30 percent and bulk density of 1500.0 kg/m³. The particle size distribution is also shown in Figure 1.

Groundnut husk was sourced from Yakasai village, Kano State, Nigeria. The Groundnut Husk Ash (GHA) was obtained by a two-step burning method [11], where the groundnut husk was burnt to ash and further heating the ash to a temperature of about 600 °C in a kiln and controlling the firing at that temperature for about two hours and the ash was allowed to cool before sieving through 75 µm sieve. The GHA is of specific gravity of 2.12, bulk density of 835 kg/m³, moisture content of 1.60 % and grain size distribution is shown in Figure 1. A chemical composition analysis of the GHA was conducted using X-Ray Fluorescence (XRF) analytical method and shown in **Table 1**.

Table 1: Oxide Composition of OPC (Dangote Brand) and GHA

Oxide	SiO ₂	Al ₂ O ₃	Fe ₂ O ₃	CaO	MgO	K ₂ O	Na ₂ O	SO ₃	TiO ₂	MnO	BaO
OPC	18.0	3.10	4.82	68.37	1.48	0.35	0.32	1.82	0.35	0.03	0.16
GHA	20.03	2.00	4.03	13.19	1.82	38.80	-	1.08	0.68	0.20	0.31
Oxide	V ₂ O ₅	P ₂ O ₅	ZnO	Cr ₂ O ₃	NiO	CuO	SrO	ZrO ₂	Cl	L.o.I	
OPC	0.03	-	-	-	-	-	-	-	-	1.27	
GHA	0.03	1.90	0.08	0.03	0.01	0.10	0.20	0.22	0.26	8.02	

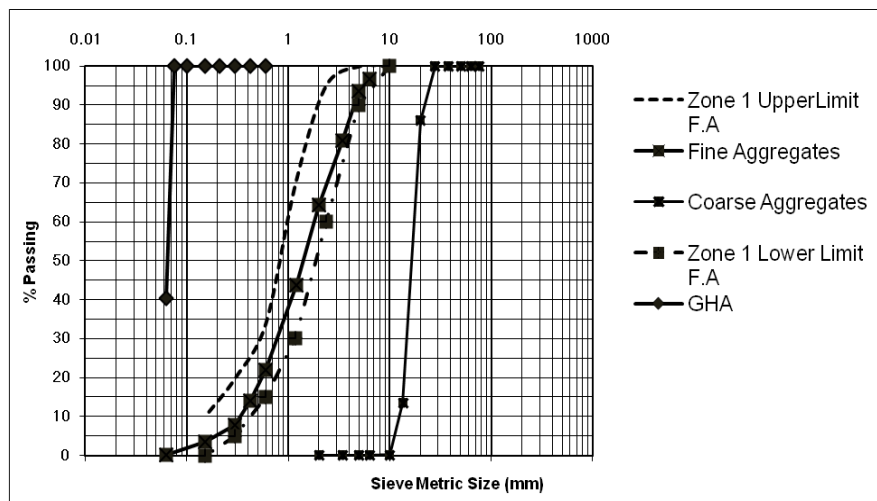


Figure 1: Particle Size Distribution of GHA, River Sand and Crushed Granite

2.2 Methods

2.2.1 Concrete Mix Design

Concrete grade 20 was designed with a target mean strength of 33 N/mm², slump range of 10-30 mm, and a water-cement ratio of 0.55. Six mixes as shown in **Table 2** were used, CM-00 is the control mix and CM-05, CM-10, CM-20, CM-30 and CM-40 are mixes containing GHA at replacement levels of 5, 10, 20, 30, and 40 %, respectively.

Table 2: Mix Proportion for Grade 20 GHA-Concrete

Mix No.	GHA (%)	Cement (kg/m ³)	GHA (kg/m ³)	Aggregates		Water (kg/m ³)	Water/cement ratio
				Fine (kg/m ³)	Coarse (kg/m ³)		
CM-00	0	318.2	0	704.5	1252.4	175.0	0.55
CM-05	5	302.3	15.9	704.5	1252.4	175.0	0.55
CM-10	10	286.4	31.8	704.5	1252.4	175.0	0.55
CM-20	20	254.6	63.6	704.5	1252.4	175.0	0.55
CM-30	30	222.8	95.4	704.5	1252.4	175.0	0.55
CM-40	40	191.0	127.2	704.5	1252.4	175.0	0.55

2.2.2 Compressive Strength Test on Groundnut Husk Ash (GHA)-Concrete

The compressive strength of GHA-Concrete was carried out using the mix proportions in Table 2. Samples were cast in steel cube moulds of 150 mm and cured in water for 3, 7, 28, 60 and 90 days, respectively. A total of ninety (90) cubes were tested and at the end of every curing regime, three samples were crushed in accordance with [12] using the Avery Denison Compression Testing Machine of 2000 kN capacity and at constant rate of 15 kN/s and the average taken. The result of compressive strength is shown in Figure 2.

2.2.3 Microstructure study of GHA-Concrete samples.

Crushed samples of GHA-Concrete from the compressive strength test were labeled and preserved for microstructure study of the concrete on the effect of GHA in concrete. The mixes considered were CM-00 and CM-10 at ages of 28 and 90 days, respectively. The study was carried out using a JOEL JSM 5900 LV Scanning Electron Microscope. The morphology of the concrete samples is shown in Figures 3- 6.

2.2.4 Test of GHA-Concrete in Acids.

The mix proportion of concrete shown in Table 2 was used to determine the effect of acidic media on GHA-Concrete. Six mixes were used, CM-00, CM-05, CM-10, CM-20, CM-30 and CM-40. Concrete was mixed and cast in steel cube moulds of 100 mm during the casting of cubes for compressive strength test. A total of thirty six (36) cubes were cast and cured in water for 28 days. At the end of every curing regime, three samples were air dried, then weighed before immersing in 10 percent concentration of diluted solution of sulphuric acid (H₂SO₄) and nitric acid (HNO₃), respectively. The concrete cubes were weighed after immersion in acid solutions at 7 days interval until the 28th day to determine the weight of the samples after the acid degradation. The result of GHA-Concrete resistance to acidic solutions is shown in Figures 7 and 8.

III. Analysis And Discussion Of Results

3.1 Compressive Strength of GHA-Concrete

Figure 2 is result of compressive strength of GHA-Concrete and shows that compressive strength increased with age of curing but decreased with increase in GHA content at all curing ages. The 28 days compressive strength of GHA-Concrete ranged from 28.2 – 91.1 % of control at GHA content of 5 – 40 %, with least compressive strength occurring at 40 % GHA content. It was however observed that the 28 days compressive strength of concrete with up to 10 % GHA content exceeded the design characteristic strength. The decrease in compressive strength of concrete with increase in GHA content could be due to the fact that partial replacement of cement with GHA caused a reduction in the quantity of cement in the mix available for the hydration process and hence a reduction in the formation of the stable strength producing cementitious compounds, consistent with [13] explanations. The formation of secondary C-S-H gel as a result of pozzolanic reaction of GHA is weaker than that from cement hydration as inferred from [14] working on agroresidual waste in blended cement. Also for constant water/binder ratio, the loss in slump with increase in GHA content reduced the compaction of the concrete which may result in reduction in strength.

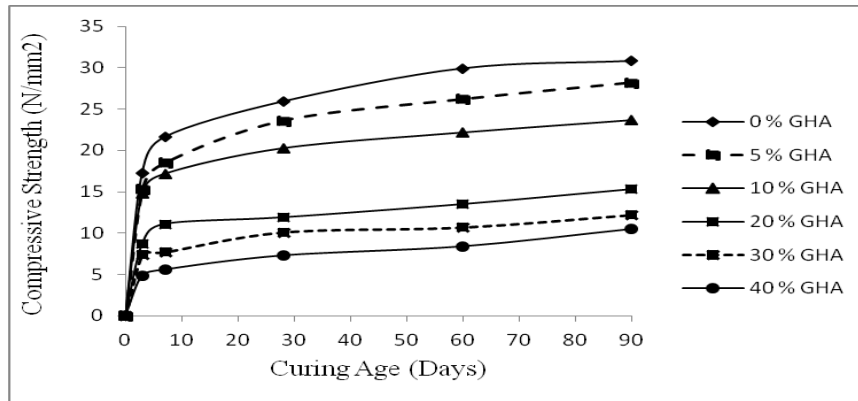


Figure 2: Compressive strength of GHA- Concrete grade 20

3.3 Microstructure of GHA-Concrete Samples

At 28 days of curing, the Scanning Electron Microstructure (SEM) photograph of the plain OPC concrete sample (Fig. 3) showed high content of C-S-H and $\text{Ca}(\text{OH})_2$ as a result of hydration as well as large voids and some anhydrous cement particles. On the other hand, the SEM picture of 10 % GHA-Concrete (Fig. 4) indicated less formation of C-S-H and more large voids as well as more spots of anhydrous cement particles compared to plain OPC concrete. This was due to low pozzolanic reaction of GHA with consequence lower strength of concrete and an increase in porosity of the concrete compared to control.

At 90 days of curing, the SEM photograph of plain OPC concrete (Fig. 5) showed reduction in the voids in the concrete as more compact fibrous C-S-H are formed in the mature concrete as well as smooth platy crystals of $\text{Ca}(\text{OH})_2$ giving a more compact matrix. However, a few bright particles of anhydrous cement were still observed. In the case of 10 % GHA-Concrete, the SEM photograph (Fig. 6) captured less C-S-H, larger voids and plates of $\text{Ca}(\text{OH})_2$ and bright spots of anhydrous cement particles than that of plain concrete. The image however showed a more compacted microstructure than that at 28 days of curing of 10 % GHA-Concrete. This improvement is due to hydration and pozzolanic reaction of GHA.

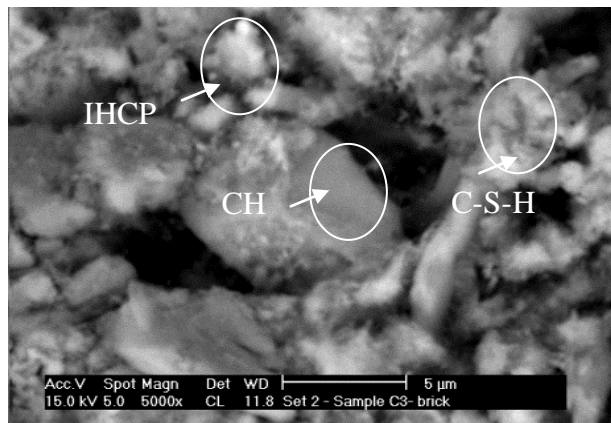


Fig. 3:SEM of OPC Concrete at 28 days,

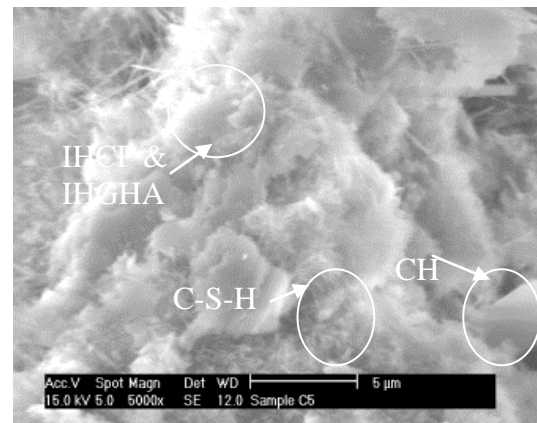


Fig. 4:SEM of 10% GHA-Concrete at 28 days

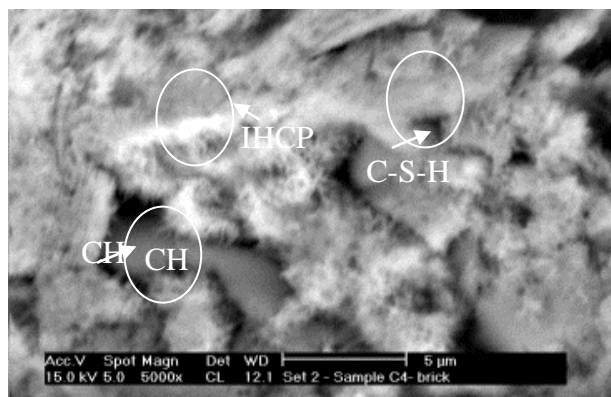


Fig. 5:SEM of OPC Concrete at 90 days,

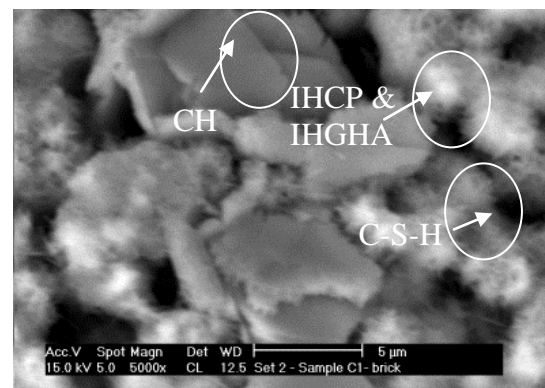


Fig. 6:SEM of 10% GHA-Concrete at 90 days

3.4 Effect of Acids on GHA-Concrete

The effect of 10 % concentration of sulphuric acid (H_2SO_4) and nitric acid, respectively on GHA-Concrete shown in terms of weight retained, in Figures 7 and 8, showed that concrete with GHA offered better resistance to deterioration by H_2SO_4 than Portland cement concrete, while plain Portland cement concrete performed better than GHA concrete in a nitric acid medium. The average weight loss of GHA concrete after 28 days of immersion in sulphuric acid and nitric acid were 16.3 % and 17.3 %, respectively as opposed to 22.4 % and 15.1 %, respectively for plain Portland cement concrete.

The enhanced resistance of GHA-Concrete to Sulphuric acid could be due to depletion in the $\text{Ca}(\text{OH})_2$ content released from the hydration process and consumed in the GHA pozzolanic reaction, with less $\text{Ca}(\text{OH})_2$ left to react with Sulphuric acid or due to less C_3A available to form the more disruptive ettringite in the GHA-Concrete, as well as noted in [15], the calcium sulphate salt formed from the chemical reaction is less soluble in water when compared to calcium nitrate, and this accounts for better resistance of the concrete to Sulphuric acid even though it is a very strong acid. On the other hand, the poor resistance of GHA-Concrete to nitric acid attack when compared with plain OPC concrete could be attributed to incomplete pozzolanic reaction of GHA after 28 days curing in water, as [16] reported that the replacement of OPC by a pozzolanic material usually has beneficial effect on cement durability at ages up to 1.5 years. Also, pozzolanic reaction usually reduces the $\text{Ca}(\text{OH})_2$ available for reaction with acids, but GHA with a high content of CaO (13.19 %) may produce additional $\text{Ca}(\text{OH})_2$ for reaction with HNO_3 to produce aqueous calcium nitrate salt which is deleterious in concrete. The high content of K_2O (38.80 %) in GHA may also be a source of disruption in GHA-Concrete as K_2O react with HNO_3 to produce potassium nitrate salt with adverse effect on the concrete. It was noted that 10 % concentration of solution of Sulphuric and nitric acids were very aggressive media with significant detrimental effect on GHA-Concrete grade 20.

The results have also shown that Sulphuric acid (H_2SO_4) is more aggressive to plain Portland cement concrete than Nitric acid (HNO_3), while GHA-Concrete was more resistant to sulphuric acid than nitric acid.

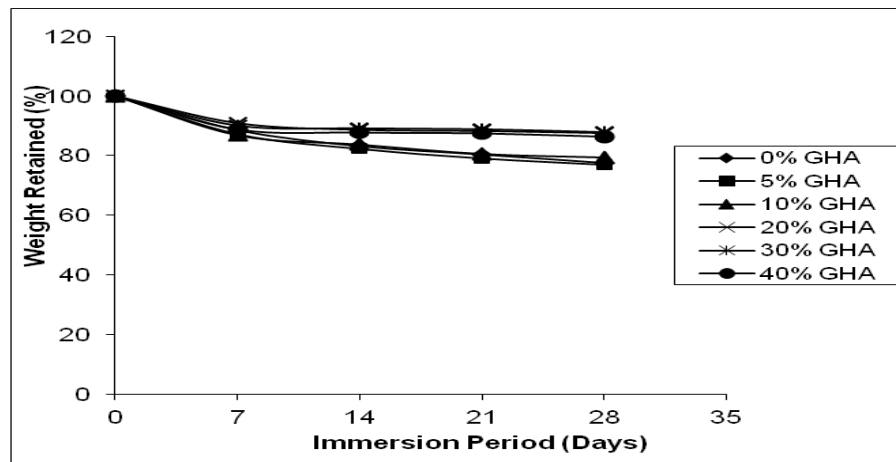


Figure 7: Weight of GHA-Concrete immersed in H_2SO_4 medium.

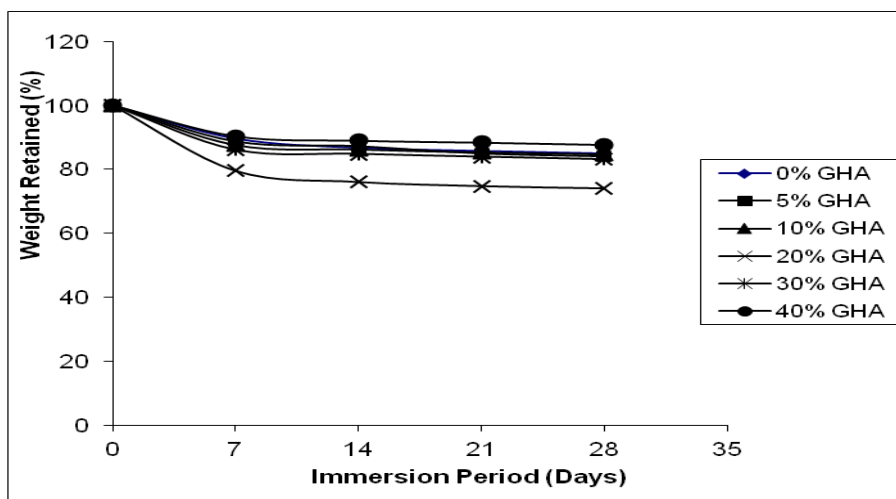


Figure 8: Weight of GHA-Concrete immersed in HNO_3 medium

IV. Conclusions

- i) The compressive strength of concrete decreased with increase in GHA content. However, 10 % would be considered as the optimum percentage replacement to act as a retarder suitable for hot weather concreting, mass concrete and long haulage of ready mixed concrete.
- ii) GHA provided a less compact microstructure of concrete at 28 and 90 days curing compared to OPC concrete as a result of low pozzolanic activity.
- iii) GHA improved the resistance of concrete against sulphuric acid degradation, but concrete containing GHA was more susceptible to nitric acid attack.

REFERENCES

- [1] Yuksel, I; Bilir, T. and Ozkan, O. (2007): Durability of concrete incorporating non-ground blast furnace slag and bottom ash as fine aggregate. *Building and Environment*, 42, 2651-2659. www.sciencedirect.com
- [2] Ogork, E.N; Aboshio, A. and Balami, D.A. (2010): Durability assessment of concrete made with rice husk ash as admixture. *Journal of Engineering and Technology (JET)*, Faculty of Engineering, Bayero University, Kano, Nigeria, 5(1), 90-98
- [3] Elinwa, A.U. and Mahmood, Y.A. (2002): Ash from Timber Waste as Cement Replacement Material. *Cement and Concrete Composites*, 24(2), 219-222.
- [4] Olawuyi, B.J. and Olusola, K.O. (2010): Compressive strength of volcanic ash/ ordinary Portland cement laterized concrete. *Civil Engineering Dimension*, 12(1), 23-28
- [5] Zivica, V. and Bajza, A. (2002): Acid attack of cement based material-A review, part 2, principle of acidic attack. *Construction and Building Materials*, 16, 215-222
- [6] Turkel, S; Felekoglu, B. and Dulluc, S. (2007): Influence of various acids on the physic-chemical properties of pozzolanic cement mortars. *Sadhana*, 32(6), 683-691
- [7] Gutt, W.H. and Harrison, W.H. (1997): Chemical resistance of concrete. *Concrete*, 11(5), 35-37.
- [8] Elinwa, A.U. and Awari, A. (2001): Groundnut-husk ash concrete, *Nigeria journal of Engineering management*, 2(1), 8-15.
- [9] Alabadan, B.A.; Njoku, C.F.; Yusuf, M.O. (2006): The Potentials of Groundnut Shell Ash as Concrete Admixture. *Agricultural Engineering International; The CIGR Ejournal*, VIII, 1-8
- [10] BS 882, Part 2 (1992): Grading limits for fine aggregates. British Standard Institution, London
- [11] Sugita, S. (1993): 'On the Economical Production of large Quantities of Active RHA'. *International Symposium on Innovative World of Concrete*, 2, 3-71
- [12] BS 1881, Part 116 (1983): Method of determination of compressive strength of concrete cubes. British Standard Institution, London
- [13] Prasanphan, S; Sanguanpak, S; Wansom, S. and Panyathanmaporn, T. (2010): Effect of ash content and curing time on compressive strength of cement paste with rice husk ash. *Suranaee Journal of Science and Technology*, 17(3), 293-302.
- [14] Parande, A.K; Stalin, K; Thangarajan, R.K. and Karthikeyan, M.S. (2011): Utilization of Agroresidual waste in effective blending in Portland cement. *International Scholarly Research Network, ISRN Civil Engineering*, 2011, article ID 701862, 1-12
- [15] Zivica, V. and Bajza, A. (2001): Acid attack of cement based material-A review, part 1, principle of acidic attack. *Construction and Building Materials*, 15, 331-340
- [16] Sideris, K. K. and Sarva, A.E. (2001): Resistance of Fly Ash and Natural Pozzolanas Blended Cement Mortars and Concrete to carbonation, sulfate attack and chloride ion penetration, *Special Publication, Material journal*, 199, 275-294.

Comparing: Routing Protocols on Basis of sleep mode

Sukhdeep Kaur¹ Rohit Kumar², Lokesh Pawar³

¹Post Graduate Student, Dept. of Information Technology, Chandigarh University, Mohali, Punjab, 140413

^{2,3}Assistant Professor, Dept. of Computer Science Engineering, Chandigarh University, Mohali, Punjab, 140413

Abstract: The architecture of ad hoc wireless network consists of mobile nodes for communication without the use of fixed-position routers. The communication between them takes place without centralized control. Routing is a very crucial issue, so to deal with this routing algorithms must deliver the packet in significant delay. There are different protocols for handling the mobile environment like AODV, DSR and OLSR. But this paper will focus on performance of AODV and OLSR routing protocols. The performance of these protocols is analyzed on two metrics: time and throughput.

Keywords: WSN, MANET, UDP, TCP, OLSR, AODV.

I. Introduction

Routing means, to choose a suitable path from source to destination. Routing is used in different networks like telephony network, internet network, electronic data network. Routing protocols will help to route the packet from source to destination in correct path. In most of the routing algorithms routing is done through routing tables. When routing is going on there are three main mechanisms i.e. unicast, broadcast and multicast. The wireless networks are classified as Infrastructure or Infrastructure less. In Infrastructure wireless networks, the mobile node can move while communicating, the base stations are fixed and as the node goes out of the range of a base station, it gets into the range of another base station. In Infrastructure less or Ad Hoc wireless network, the mobile node can move while communicating, there are no fixed base stations and all the nodes in the network act as routers. The mobile nodes in the Ad Hoc network dynamically establish routing among themselves to form their own network 'on the fly'.

Mobile Ad Hoc Network is a collection of wireless mobile nodes forming a temporary network without any fixed infrastructure where all nodes are free to move about arbitrarily and where all the nodes configure themselves. In this network, each node acts both as a router and as a host & even the topology of network may also change rapidly. Some of the key challenges in the area of MANET include stable unicast/multicast routing, dynamic network topology, network overhead, scalability, security and power aware Routing. In this research paper, intend is to study the mobility patterns of two prominent MANET routing protocols i.e. DSR and AODV using simulation modeling over varying number of UDP/TCP connections. Rest of the paper is organized as: gives description of routing protocols for MANET, about critique analysis of AODV and DSR, elaborates on mobility metrics, discusses experimental analysis of DSR, AODV using network simulator. At last, concludes the paper and provides an idea to researchers about challenges in the field of ad hoc wireless networks that may be carried out as research work in future.

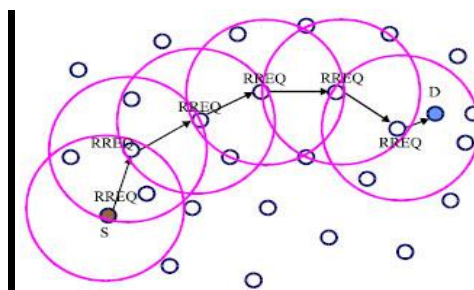


Figure.1 RREQ and RREP messages send in AODV

II. Reactive Routing Protocols

Reactive routing protocols are called on-demand routing protocols so these routing protocols are called when they are needed and the routes are built. These routes can be acquired by sending route requests through the network. Disadvantage of this algorithm is that it offers high latency in searching a network

a) Dynamic Source Routing (DSR)

Dynamic Source Routing (DSR) is a reactive kind of protocol which reacts on-demand. The main feature of DSR is source routing in which the source always knows the complete route from source to destination. It frequently uses source routing and route caching. Route Discovery and Route Maintenance are two main methods used in DSR. It is uncomplicated and efficient protocol. It does not depend on timer-based activities. It allows multiple routes to destination node and routing is loop-free here. Any broken link is notified to the source node with an error message. It works well in large networks where routes change quickly and mobility of routes is higher. In DSR, intermediate nodes do not need to preserve the routing information. Instead the packets themselves contain every routing decision. DSR uses a route discovery process to find a route when a node in the network tries to send a data packet to a destination for which the route is unknown. A route is found by flooding the network with route requests. When a node receives this request, it broadcasts it again until it itself is the destination or it has the route to the destination. This node then replies to the request to the original source. The request and response packets are source routed. Request packet creates the path of traversal. Response packet creates the reverse path to the source by traversing backwards.

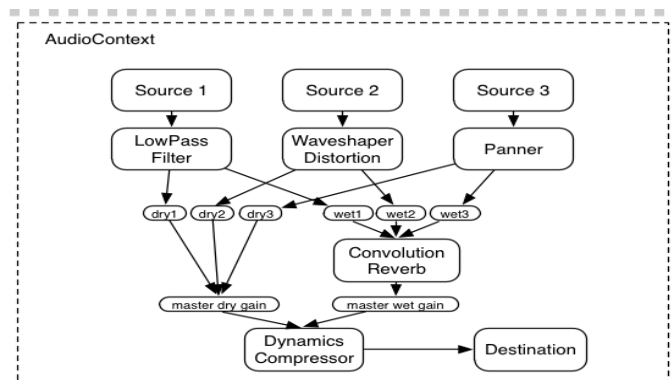


Figure.2 Route discovery procedure in DSR

b) Ad hoc On-Demand Distance Vector Routing (AODV)

AODV is an on-Demand routing protocol which is confluence of DSDV and DSR. Route is calculated on demand, just as it is in DSR via route discovery process. However, AODV maintains a routing table where it maintains one entry per destination unlike the DSR that maintains multiple route cache entries for each destination. AODV provides loop free routes while repairing link breakages but unlike DSDV, it doesn't require global periodic routing advertisements.

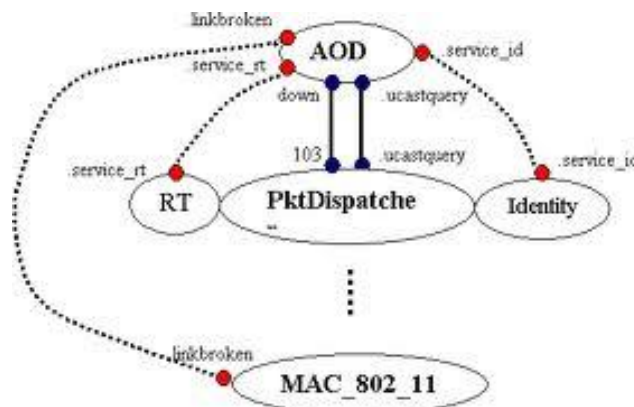


Figure.3 Route discovery procedure in AODV

III. Proactive Routing Protocol

The routing information about all the nodes is build and maintained by the proactive protocols. The proactive routing protocols are independent of whether or not the route is needed. There are many advantages and disadvantages of proactive routing protocols. One of its advantages is that the nodes can easily get routing information, and it easily starts a session. The disadvantages are, too much Performance Analysis of AODV, DSR and OLSR in MANET data kept by the nodes for route maintenance, when there is a particular link failure its reform is too slow.

a. Optimized link –state routing (OLSR)

The Optimized Link State Routing (OLSR) protocol is an optimization of the classical link state algorithm, adapted to the requirements of a MANET ([10]). Because of their quick convergence, link state algorithms are somewhat less prone to routing loops than distance vector algorithms, but they require more CPU power and memory. They can be more expensive to implement and support and are generally more scalable. OLSR operates in a hierarchical way (minimizing the organization and supporting high traffic rates). The key concept used in OLSR is that of multipoint relays (MPRs). MPRs are selected nodes which forward broadcast messages during the flooding process. This technique substantially reduces the message overhead as compared to a classical flooding mechanism (where every node retransmits each message received). This way a mobile host can reduce battery consumption. In OLSR, link state information is generated only by nodes elected as MPRs. An MPR node may choose to report only links between itself and its MPR selectors. Hence, contrarily to the classical link state algorithm, partial link state information is distributed in the network. This information is then used for route calculation. OLSR provides optimal routes. The protocol is particularly suitable for large and dense networks as the technique of MPRs works well in this context.

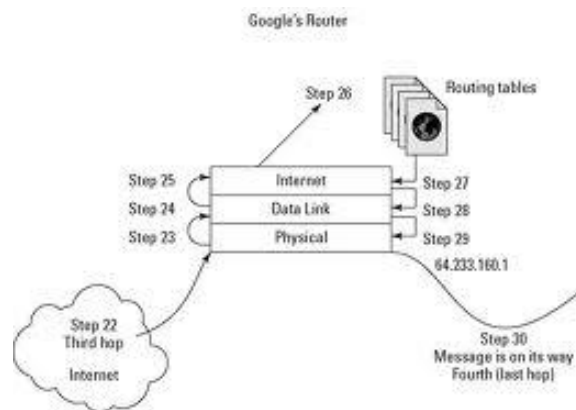


Figure. 4 Routing table of OLSR

Optimized Link State Routing (OLSR) protocol is a table-driven proactive routing protocol for wireless mobile ad hoc networks. This protocol optimizes the flooding process and reduces the control message overheads by marking subset of neighbors as multi-point relays (MPRs). In OLSR, each node periodically broadcasts two types of messages: HELLO messages and Topology Control (TC) messages. A HELLO message contains two lists in which one list includes the addresses of the neighbors to which there exists a valid bi-directional link and the other list includes the addresses of the neighbors from which control traffic has been heard but bidirectional links are not confirmed. Upon receiving HELLO message, a node examines list of addresses, if its own address is in the list, it is confirmed that bidirectional communication has been established with the sender. HELLO messages also allow each node to maintain information describing link between neighbor node and nodes which are two-hop away. The set of nodes among the one-hop neighbors with a bi-directional link are chosen as multipoint relays (MPRs). Only these nodes forward topological information about the network. On the reception of HELLO messages, each node maintains a neighbor table which contains one-hop neighbor information, their link status information and a list of two hop neighbors. Each node also maintains a set of its neighbors which are called the MPR Selectors of the node. When these selectors send a broadcast packet, only its MPR nodes among its entire neighbors forward the packet. The MPR nodes periodically broadcast its selector list throughout the network. The smaller set of multipoint relay provides more optimal routes. The path to the destination consists of a sequence of hops through the multipoint relays from source to destination. A TC message contains the list of neighbors who have selected the sender node as a multipoint relay and is used to diffuse topological information to the entire network. Based on the information contained in the neighbor table and the TC message, each node maintains a routing table which includes destination address, next-hop address, and number of hops to the destination. Fisheye State Routing (FSR) protocol is a proactive (table driven) ad hoc routing protocol and its mechanisms are based on the Link State Routing protocol used in wired networks. FSR is an implicit hierarchical routing protocol. It reduces the routing update overhead in large networks by using a fisheye technique. Fish eye has the ability to see the objects better when they are nearer to its focal point that means each node maintains accurate information about near Nodes and not so accurate about far-away nodes. The scope of fisheye is defined as the set of nodes that can be reached within a given number of hops. The number of levels and the radius of each scope will depend on the size of the network. Entries corresponding to nodes within the smaller scope are propagated to the neighbors with the highest frequency and the exchanges in smaller scopes are more frequent than in larger. That makes the

topology information about near nodes more precise than the information about farther nodes. FSR minimized the consumed bandwidth as the link state update packets that are exchanged only among neighboring nodes and it manages to reduce the message size of the topology information due to removal of topology information concerned far-away nodes. Even if a node doesn't have accurate information about far away nodes, the packets will be routed correctly because the route information becomes more and more accurate as the packet gets closer to the destination. This means that FSR scales well to large mobile ad hoc networks as the overhead is controlled and supports high rates of mobility. The FSR concept originates from Global State Routing (GSR). GSR can be viewed as a special case of FSR, in which there is only one fisheye scope level and the radius is infinite. As a result, the entire topology table is exchanged among neighbors that consume a considerable amount of bandwidth when network size becomes large.

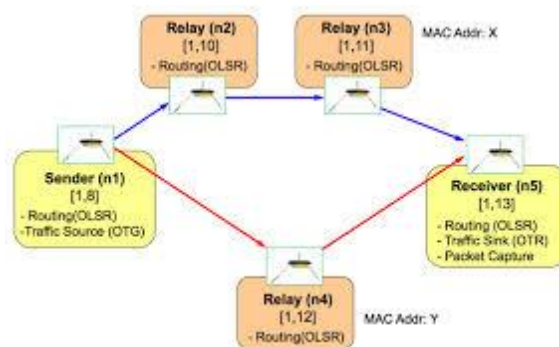


Figure .5 Communication in OLSR

Problem Statement:

Energy conservation is one of most happening and hot issue in the wireless sensor network. Wireless sensor network refers to a network where a lot of nodes share similar network architecture and follow routing algorithms to save energy of the system. There are two different architecture types namely AODV and OLSR. The routing overhead associated with dissemination of routing packets is quite huge.

The aim of the research work is to design a sophisticated protocol which can save maximum amount of energy and can increase the throughput of the system. The proposed routing algorithm is supposed to achieve by combining two algorithms namely AODV and OLSR. The overall aim of this thesis is to design novel energy efficient AODV + OLSR protocol for Wireless Sensor network.

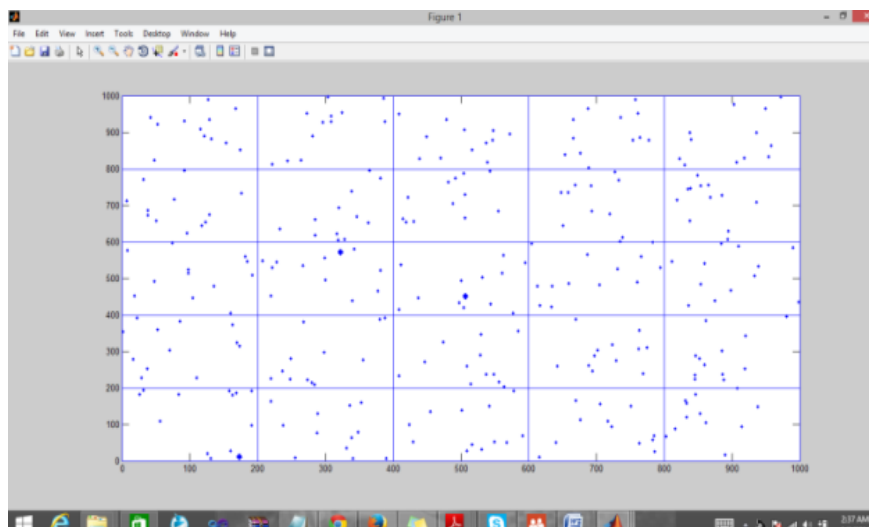
IV. Mobility Metrics

We have selected the energy consumption and accuracy as a metrics during the simulation in order to evaluate the performance of the different protocols.

V. Result and Conclusion

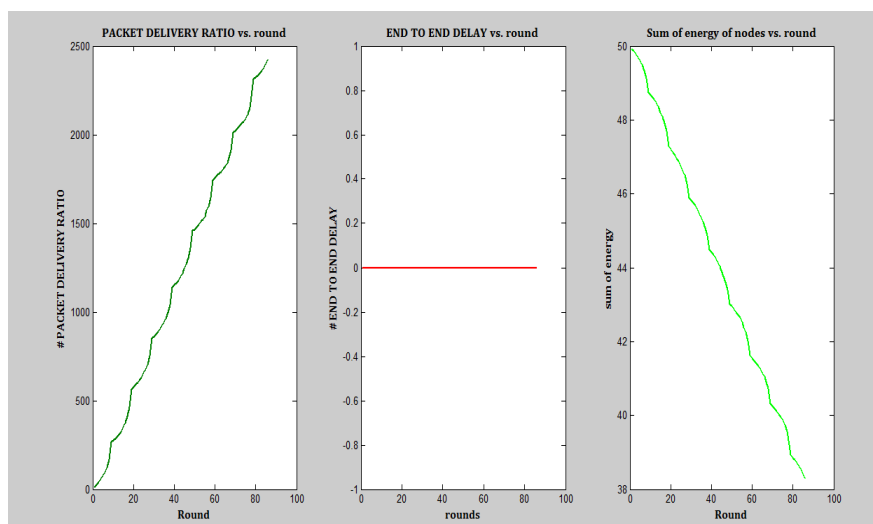
The following figures describe the results of this research work.

Step1:



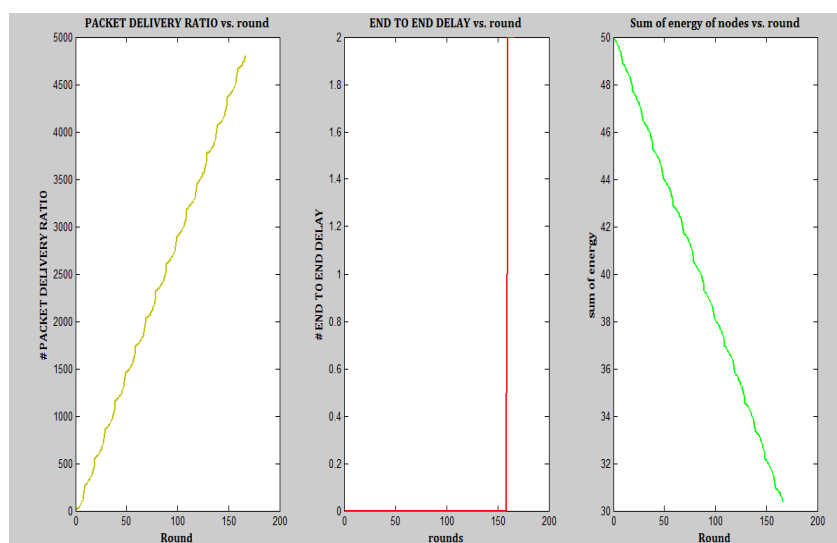
The above figure represents the node movement in the proposed system architecture. When a network node fails, OLSR is called. The till now operation is performed using AODV network topology. Instead of checking for another active node through AODV, the network opt for OLSR.

Step 2:



The above figure represents the end to end delay versus the number of rounds. Till now, no extra dead node is found

Step 3:



The above figure represents the scenario of dead node .When the dead node occurs OLSR is called and the transmission of data continued.

VI. Conclusion

The research work performed concludes that the AODV and OLSR both are optimal protocols for any kind of routing and energy conservation schemes but AODV can be optimized using OLSR protocol if they are combined. The research work has computed its results over different aspects like packet delivery ratio, end to end delay and through put.

VII. Future work

The current research work opens up a lot of possibilities for the future research works like combination of AODV with NEURAL NETWORKS or combination of OLSR with NEURAL NETWORK. The current research work only activates one dead packet or node scenario. It does not deal with multiple node failure system which can become one of the future research works.

REFERENCES

- [1] C.Sivaram murthy, B.S. Manoj, Adhoc wireless networks: Architectures, and protocols, Pearson Education,2004.
- [2] Pankaj Palta and Sonia Goyal , “Comparison of OLSR and TORA routing protocols using OPNET Modeler” in International Journal of Engineering Research and technology Vol. 1 Issue 5, July - 2012 Nehra et al., International Journal of Advanced Research in Computer Science and Software Engineering 3(5), May - 2013, pp. 984-990 © 2013, IJARCSSE All Rights Reserved Page | 990
- [3] C.Parkins, E.B.Royer, S.Das, A hoc On-Demand Distance Vector (AODV) Routing, July 2003, [Online]. Available: <http://www.faqs.org/rfcs/rfc3561.html>. [Accessed: April. 10, 2010]
- [4] Gagangeet singh aujla and Sandeep singh kang “Comparative analysis of AODV, DSR, GRP, OLSR and TORA by varying number of nodes with FTP and HTTP Applications over MANETs” in International Journal of Computer Applications Vol 65 No 2, March 2013.
- [5] Ashish Shrestha and Firat Tekiner, “On MANET Routing Protocols for Mobility and Scalability.” In International Conference on Parallel and Distributed Computing, Applications and Technologies, p.p. 451-456, November 2009. IEEE Computer Society.
- [6] N Vetrivelan and A V Reddy, “Performance Analysis of Three Routing Protocols for Varying MANET Size.” In Proceedings of the International Multi Conference of Engineers and Computer Scientists (IMECS 2008), Vol. II, 19-21 March 2008, Hong Kong.
- [7] Harmanpreet kaur and Jaswinder singh “Performance comparison of OLSR, GRP and TORA using OPNET” in International Journal of Advanced Research in Computer Science and Software Engineering Vol 2 Issue 10 October 2012.
- [8] N. Adam, M.Y. Ismail et al., "Effect of Node density on Performances of Three MANET Routing Protocols." In International Conference on Electronic Devices, Systems and Applications (ICEDSA2010), p.p. 321-325, October 2010.
- [9] R. Al-Ani, “Simulation and performance analysis evaluation for variant MANET routing protocols”, International Journal of Advancements in Computing Technology, Volume 3, Number 1, February 2011
- [10] Mr. L Raja, Capt. Dr. S Santhosh Baboo “Comparative study of reactive routing protocol AODV, DSR, ABR and TORA” in International Journal Of Engineering And Computer Science Vol 2 Issue 3 March 2013 Page No. 707-718

Implementation of High Throughput Radix-16 FFT Processor

K Swetha sree¹, Mr. T. Lakshmi Narayana²

^{1, 2} Department of ECE, Andhra Loyola institute of engineering and technology, India

Abstract: The extension of radix-4 algorithm to radix-16 to achieve the high throughput of 2.59 giga-samples/s for WPAN's. We are also reformulating radix-16 algorithm to achieve low-complexity and low area cost and high performance. Radix -16 FFT is obtained by cascaded the radix -4 butterfly units. It facilitates low-complexity realization of radix-16 butterfly operation and high operation speed due to its optimized pipelined structure. Besides, a new three-stage multiplier for twiddle factor multiplication is also proposed, which has lower area and power consumption than conventional complex multipliers. Equipped with those new performance-boosting techniques, overall the proposed radix-16 FFT processor is area-efficient with high data processing rate and hardware utilization efficiency. The control circuit of the proposed simplified radix-24 FFT SDF architecture is simpler than that of the direct radix-16 FFT SDF structure. The multiplier cost of the proposed FFT architecture is less than that of the previous FFT structures in 256-point FFT applications. The throughput of the proposed FFT processor is one sample per clock. Although the radix-16 FFT algorithm has Less computational complexity, the control circuit of the direct radix-16 SDF architecture for implementing radix-16 FFT is very complex. Thus, the efficient simplified radix-24 SDF structure, which is described in the next section, will be applied to radix-16 FFT algorithm.

Keywords: Fast Fourier transform (FFT), non-conflict memory addressing scheme, OFDM, radix-16 FFT, WPANs.

I. Introduction

SINCE the recent decade, the increasing demand for real time and high-rate multimedia services has been pushing the birth of high-rate wireless communication systems. Ultra wideband (UWB) communication system, for example, can deliver data rates up to 480 Mb/s at a short distance range. However, it is not enough to support high data rate applications of more than 1Gbps such as high-definition (HD) streaming content downloads HD video on demand, home theater, and etc. To meet the application demands, IEEE 802.15.3c-2009 standard for high-rate Wireless Personal Area Networks (WPANs) was ratified recently. In the standard, there are three PHY modes, i.e., Single Carrier mode (SC PHY), High Speed Interface mode (HSI PHY), and Audio/Visual mode (AV PHY). Except SC PHY, both HSI PHY and AV PHY are based on OFDM modulations. As is well known, Fast Fourier transform (FFT) operation is one of the key operations for OFDM-based communication systems. Besides, for SC PHY mode, FFT operations are widely employed for effective channel equalization. Low-cost 256-point FFT SDF design for OFDM systems. The rest of the paper is organized as follows. We begin with the derivation of the radix-16 FFT algorithm. By using the structure of radix-8 FFT algorithm, the radix-16 FFT algorithm is described to guide the depiction of hardware pipelined architectures. Next, the proposed simplified radix-24 SDF pipelined FFT architecture for realization of radix-16 FFT is also shown in this section. A low multiplier cost 256-point FFT architecture with simplified radix-24 SDF structure. The detailed function realizations of the simplified radix-24 SDF structure are also discussed, the proposed simplified radix-24 based FFT processor can reduce the hardware complexity and control circuit complexity.

Another benefit of higher-radix FFT operations over the lower-radix ones is that higher memory access bandwidth can be more conveniently provided in hardware implementations, as the bandwidth is proportional to. An improved radix-16 algorithm is proposed in which can reduce the numbers of twiddle factor operations and lookup-table accesses. A radix-16 algorithm suitable for multiply-and-add instruction is proposed in . However, those algorithms are mainly devised for the execution of general-purpose processors. Owing to the mentioned advantages of a high-radix memory-based FFT design, this work will design a high-performance radix-16 FFT processor which satisfies the mentioned throughput requirement of 802.15.3c applications. However, since generally a radix-16 butterfly unit is more complicated and less flexible than

lower-radix ones, this work reformulates conventional radix-16 FFT algorithm so as to facilitate efficient and optimized pipelined realization of a radix-16 PE with high computing power and speed. Further, several performance-enhancement techniques are applied to the whole FFT processor design, including an efficient multiplier structure for twiddle factor multiplication, schemes of conflict-free memory access and normal-order FFT output generations. The rest of this article is organized as follows. In Section II, design concerns for 802.15.3c FFT processor are examined. In a reformulated radix-16 algorithm and its butterfly structure are analyzed. In Section IV, a high-throughput and high-speed FFT processor architecture is introduced. Also, a three-stage multiplier for twiddle factor multiplication is presented. In a new conflict-free memory addressing scheme is presented. Block-floating point (BFP) operations are designed and implemented to achieve high signal-to-quantization-noise ratio (SQNR).

II. Radix-16 FFT Algorithm And The Simplified Pipelined SDF Architecture

Radix-16 FFT Algorithm

The butterfly structure for computation of the radix-8 FFT algorithm is proposed in [7]. Fig. 1 shows the butterfly structure of the radix-8 FFT algorithm, where replace the k index with the index $k=2k'$ and the index $k=2k'+1$ in radix-8 FFT structure. Thus, the even parts and the odd parts of the radix-16 FFT algorithm can be described in Eq.(1). The radix-16 FFT algorithm listed in Eq.(1) can be summarized to the butterfly structure that is shown in Fig. 2. First, the radix-16 FFT algorithm can be realized with the direct radix-16 SDF architecture, which is shown in Fig. 3. The direct radix-16 SDF structure is constructed by an $N/16$ memory and the radix-16 butterfly processing element (PE). Fig. 4 shows the detailed function block of the radix-16 PE. Although the radix-16 FFT algorithm has less computational complexity, the control circuit of the direct radix-16 SDF architecture for implementing radix-16 FFT is very complex. Thus, the efficient simplified radix-24 SDF structure, which is described in the next section, will be applied to radix-16 FFT algorithm.

$$\begin{aligned}
 X[16k' + a + 2b + 4c + 8d] = & \sum_{n=0}^{N/16-1} \{ \{ [x(n) + (-1)^a \cdot x(n + N/2)] + W^{N(a+2b)/4} \cdot [x(n + N/4) + (-1)^{a+2b} \cdot x(n + 3N/4)] \} \\
 & + W^{N(a+2b+4c)/8} \cdot \{ [x(n + N/8) + (-1)^{a+2b+4c} \cdot x(n + 5N/8)] + W^{N(a+2b)/4} \cdot [x(n + 3N/8) + (-1)^{a+2b+4c} \cdot x(n + 7N/8)] \} \\
 & + \{ [x(n + N/16) + (-1)^{a+2b+4c+8d} \cdot x(n + 9N/16)] + W^{N(a+2b)/4} \cdot [x(n + 5N/16) + (-1)^{a+2b+4c+8d} \cdot x(n + 7N/8)] \} \\
 & + \{ [x(n + 3N/16) + (-1)^{a+2b+4c+8d} \cdot x(n + 11N/16)] + W^{N(a+2b)/4} \cdot [x(n + 7N/16) + (-1)^{a+2b+4c+8d} \cdot x(n + 15N/16)] \} \\
 & \cdot W^{N(a+2b+4c)/8} \} \cdot W^{N(a+2b+4c+8d)/16} \} \cdot W^{(a+2b+4c+8d) \cdot n} \cdot W_{N/16}^{nk'} \quad (1)
 \end{aligned}$$

where a, b, c , and d is 0 or 1, and $k' = 0, 1, \dots, N/16-1$

$$\begin{aligned}
 & X(16k_2 + k_1) \\
 & = \sum_{n_2=0}^{31} \sum_{n_1=0}^{15} x(32n_1 + n_2) W_{512}^{(16k_2+k_1)(32n_1+n_2)} \\
 & = \sum_{n_2=0}^{31} \left\{ \underbrace{\sum_{n_1=0}^{15} x(32n_1 + n_2) W_{16}^{n_1 k_1}}_{16\text{-point DFT of the 1st stage}} \underbrace{W_{512}^{n_2 k_1}}_{\text{twiddle factor of stage 1}} \right\} W_{32}^{n_2 k_2} \quad (\\
 & = \sum_{n_2=0}^{31} \{ BO_{16}^{(1,n_2)}(k_1) \} W_{32}^{n_2 k_2} \quad (
 \end{aligned}$$

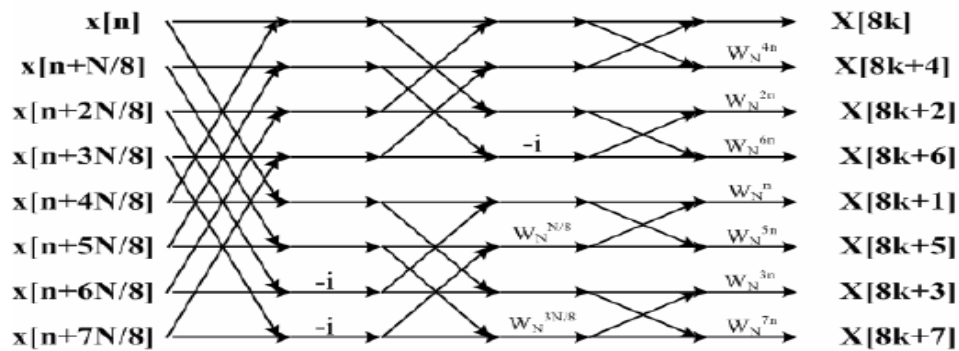


Fig. 1 Butterfly structure of the radix-8 FFT algorithm [7]

2.1 Simplified Radix-2⁴ SDF Pipelined Architecture

In order to simplify the radix-16 control unit, we derive the radix-24 algorithm so that the hardware implementation is performed by cascading four simple radix-2 processing elements. Therefore, the radix-24 architecture is simplified and has the property of high spatial regularity. Subsequently, we use the common factor algorithm (CFA) decomposition method to develop the proposed FFT algorithm, and then the frequency domain indices k and the time domain indices n can be factorized as follows.

$$n = \left\langle \frac{N}{2}n_1 + \frac{N}{4}n_2 + \frac{N}{8}n_3 + \frac{N}{16}n_4 + n_5 \right\rangle_N, \quad (2)$$

where $N=256$, $n_i = 0, 1$ for $i=1, 2, 3$ and 4 , and $n_5 = 0, 1, 2, \dots, N/16 - 1$. And

$$k = \left\langle k_1 + 2k_2 + 4k_3 + 8k_4 + 16k_5 \right\rangle_N, \quad (3)$$

where $k_i = 0, 1$ for $i=1, 2, 3$ and 4 , and $k_5 = 0, 1, 2, \dots, N/16 - 1$.

In Eq.(2) and Eq.(3), the indices n and k are mapped from one dimension to five dimensions linearly. By using Eq.(2) and Eq.(3), the DFT formula is rewritten as the multi-dimension form, which is shown as Eq. (4).

$$X[k_1 + 2k_2 + 4k_3 + 8k_4 + 16k_5] = \sum_{n_5=0}^{N/16-1} \sum_{n_4=0}^1 \sum_{n_3=0}^1 \sum_{n_2=0}^1 \sum_{n_1=0}^1 x\left(\frac{N}{2}n_1 + \frac{N}{4}n_2 + \frac{N}{8}n_3 + \frac{N}{16}n_4 + n_5\right) \cdot W_N^{\left(\frac{N}{2}n_1 + \frac{N}{4}n_2 + \frac{N}{8}n_3 + \frac{N}{16}n_4 + n_5\right)(k_1 + 2k_2 + 4k_3 + 8k_4 + 16k_5)}. \quad (4)$$

Subsequently, we use the period property of the twiddle factor in Eq.(4) and decompose the twiddle factor as follows.

$$W_N^{\left(\frac{N}{2}n_1 + \frac{N}{4}n_2 + \frac{N}{8}n_3 + \frac{N}{16}n_4 + n_5\right)(k_1 + 2k_2 + 4k_3 + 8k_4 + 16k_5)} = W_N^{\frac{N}{2}n_1k_1} \cdot W_N^{\frac{N}{4}n_2(k_1 + 2k_2)} \cdot W_N^{\frac{N}{8}n_3(k_1 + 2k_2 + 4k_3)} \cdot W_N^{\frac{N}{16}n_4(k_1 + 2k_2 + 4k_3 + 8k_4)} \cdot W_N^{n_5(k_1 + 2k_2 + 4k_3 + 8k_4)} \cdot W_N^{n_5k_5}. \quad (5)$$

We expand the dimensional variables n_1, n_2, n_3 , and n_4

In Eq.(4) and Eq.(5), and then the butterfly expressions, which are ranged from the first stage to the fourth stage, are denoted as N

$$A_{N/2}(\frac{N}{4}n_2 + \frac{N}{8}n_3 + \frac{N}{16}n_4 + n_5, k_1) = x(\frac{N}{4}n_2 + \frac{N}{8}n_3 + \frac{N}{16}n_4 + n_5) + (-1)^{k_1} x(\frac{N}{4}n_2 + \frac{N}{8}n_3 + \frac{N}{16}n_4 + n_5), \quad (6)$$

$$B_{N/4}(\frac{N}{8}n_3 + \frac{N}{16}n_4 + n_5, k_1, k_2) = A_{N/2}(\frac{N}{8}n_3 + \frac{N}{16}n_4 + n_5, k_1) + W_N^{\frac{N}{4}(k_1+2k_2)} A_{N/2}(\frac{N}{8}n_3 + \frac{N}{16}n_4 + n_5 + \frac{N}{4}, k_1), \quad (7)$$

$$C_{N/8}(\frac{N}{16}n_4 + n_5, k_1, k_2, k_3) = B_{N/4}(\frac{N}{16}n_4 + n_5, k_1, k_2) + W_N^{\frac{N}{8}(k_1+2k_2+4k_3)} B_{N/4}(\frac{N}{16}n_4 + n_5 + \frac{N}{8}, k_1, k_2), \quad (8)$$

and

$$D_{N/16}(n_5, k_1, k_2, k_3, k_4) = C_{N/8}(n_5, k_1, k_2, k_3) + W_N^{\frac{N}{16}(k_1+2k_2+4k_3+8k_4)} C_{N/8}(n_5 + \frac{N}{16}, k_1, k_2, k_3). \quad (9)$$

/ 2 A , N / 4 B , N / 8 C , and N / 16 D , respectively

2.2 Pallar processing of radix 16 algorithm:

Stages of the proposed SR24SDF structure correspond to the relative 4-stage radix-16 FFT butterfly flow. The architecture of the proposed SR2⁴4SDF is. For the realization of N-point FFT, the SR24SDF architecture needs log₁₆N-1 multipliers, 4log₄N adders, and N-1 registers. The control circuit of SR24SDF is simpler in comparison with the direct radix-16 SDF architecture. The hardware requirements of different pallar SDF FFT architectures

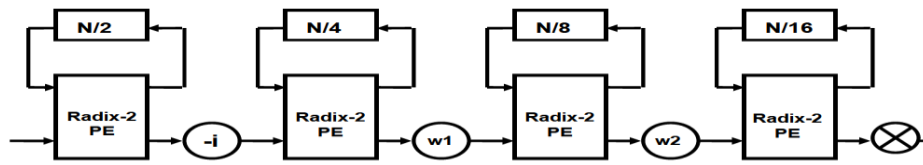


Fig. 5 SR2⁴SDF architecture for FFT

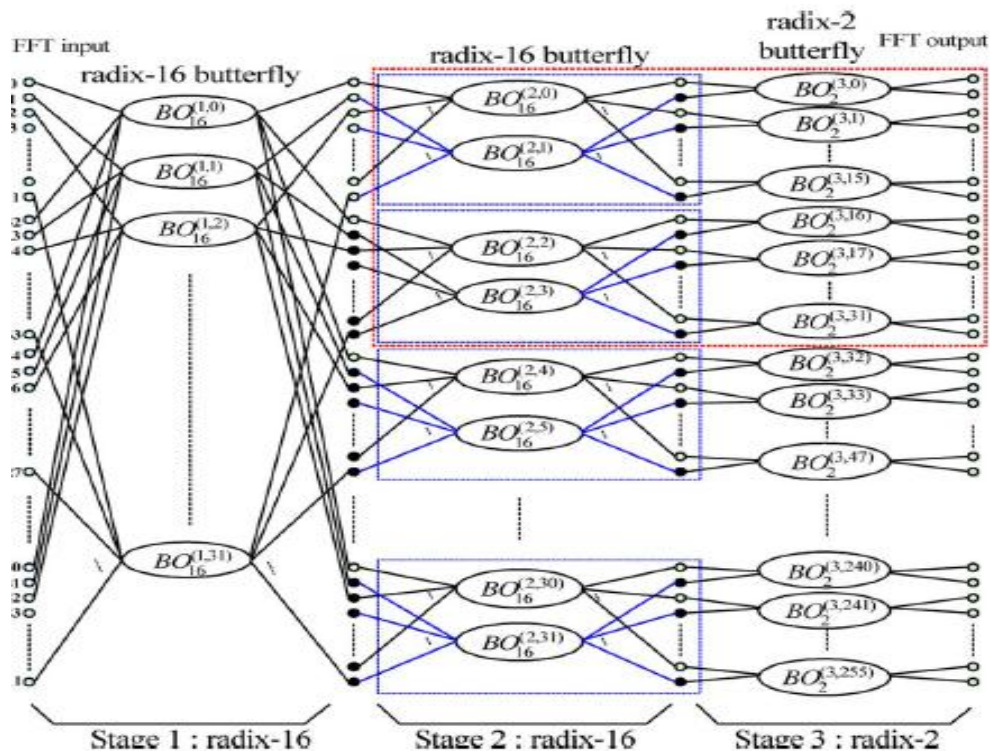
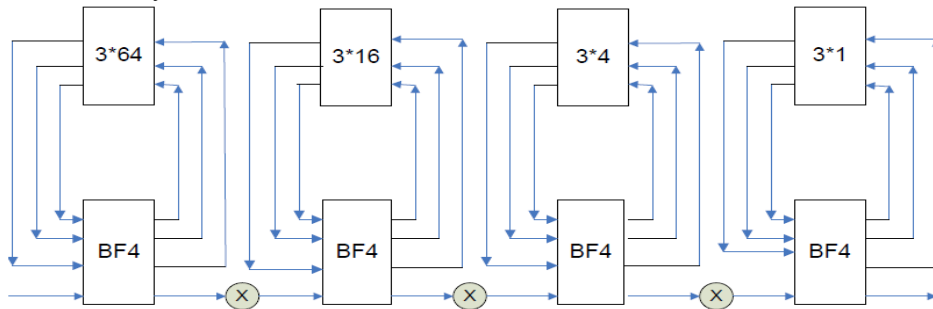


Fig. 2. SFG for radix-16 512-point FFT algorithm.

2.3 Pipelined Radix-16 Algorithm

To improve the performance of the sequential processor, parallelism can be introduced by using a separate arithmetic unit for each stage of the FFT. This increases the throughput by a factor of $\log_2 N$ when the different units are pipelined. This architecture is also known as cascaded FFT architecture and will be used in our proposed design. Pipeline FFTs are a class of parallel algorithms that contain an amount of parallelism equal to $\log_2 N$ where N is the number of points for an FFT and R is the radix. A Pipeline implementation of the FFT was first proposed in [1] which consisted of a series of computational blocks each composed of delay lines, coefficient storage, commutators, multipliers, and adders. Pipeline FFTs can be generally run at high-speeds and the amount of pipelining increased or decreased to meet timing. increased to 75% by storing 3 out of 4 butterfly outputs. However, the utilization of the radix-4 butterfly, which is fairly complicated and contains at least 8 complex adders, is dropped to only 25%. It requires $\log_2 N - 1$ multipliers, $\log_2 N$ full radix-4 butterflies and memory of size $N - 1$ words.



III. A Reformulated Radix-16 FFT Algorithm And Its Butterfly Structures

To fully exploit the advantage of a high-radix FFT algorithm particularly the radix-16 algorithm in this work, conventional FFT algorithm is reformulated in a form suitable for efficient realization of all the function components and overall FFT PE architecture, as will be detailed in the following

3.1 Given an N -point discrete Fourier transform (DFT)

$$X(k) = \sum_{n=0}^{N-1} x(n)W_N^{kn}, \quad k = 0, \dots, N-1$$

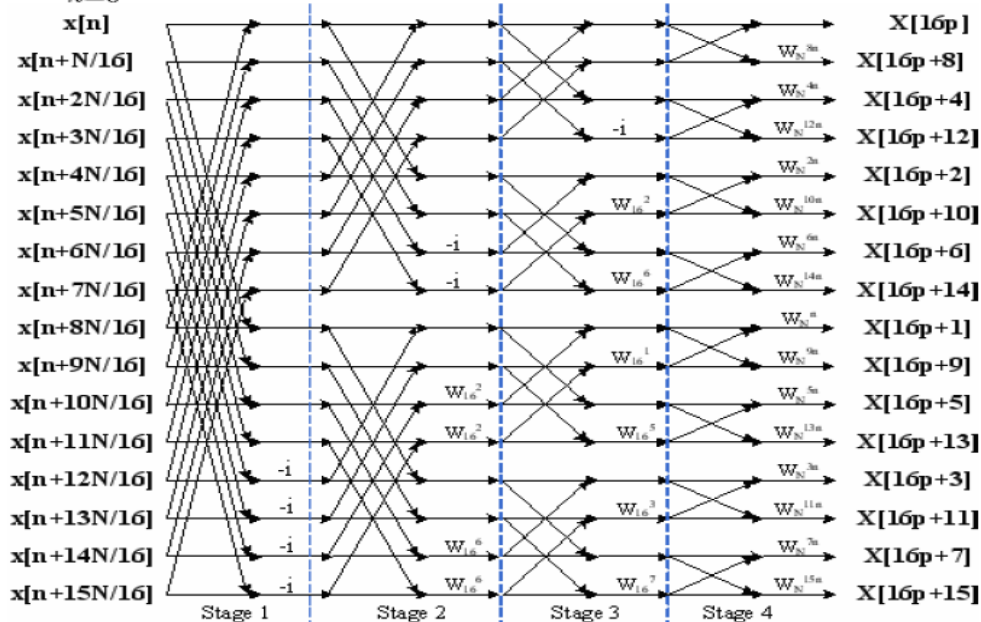


Fig. 2 Butterfly structure of the radix-16 FFT algorithm

where $x(n)$ and $X(k)$ denote the input and output of the DFT respectively, and W_N^{kn} is equal to $e^{-j2\pi kn/N}$. Let

$$N = 512, n = 32n_1 + n_2, k = 16k_2 + k_1, \\ n_1, k_1 = 0, 1, \dots, 15; \quad n_2, k_2 = 0, 1, \dots, 31.$$

A radix-16 decimation-in-frequency (DIF) FFT algorithm can be derived based on the following first-stage decomposition by substituting (3) into (2) as

$$\begin{aligned} X(16k_2 + k_1) &= \sum_{n_2=0}^{31} \sum_{n_1=0}^{15} x(32n_1 + n_2) W_{512}^{(16k_2+k_1)(32n_1+n_2)} \\ &= \sum_{n_2=0}^{31} \left\{ \underbrace{\sum_{n_1=0}^{15} x(32n_1 + n_2) W_{16}^{n_1 k_1}}_{\text{16-point DFT of the 1st stage}} \underbrace{W_{512}^{n_2 k_1}}_{\text{twiddle factor of stage 1}} \right\} W_{32}^{n_2 k_2} \\ &= \sum_{n_2=0}^{31} \left\{ BO_{16}^{(1,n_2)}(k_1) \right\} W_{32}^{n_2 k_2} \end{aligned}$$

3.2 Memory Based Architecture

The combination of the parallel and pipeline process is the memory based architecture it mainly contains following three blocks those are

1. The inputs are given using parallel and pipelined process
2. The mux unit
3. The mixed radix unit

3.3 Implementation of Radix 16 Algorithm

The implementation of this algorithm is done in MATLAB in MATLAB the implementation is done in following steps

1. Radix 16 algorithm for 16 point is calculated
2. Then using the parallel and pipeline process we calculated the radix 16 for N point
3. Then memory based structure is implemented
4. Then radix 16 is extended to radix 32

Implementation radix 16 result:

f =

Columns 1 through 3

0.0000 -0.0000 + 0.0000i 0.0000 - 0.0000i

Columns 4 through 6

0.0000 + 0.0000i -0.0000 + 40.0000i 0.0000 - 0.0000i

Columns 7 through 9

0.0000 + 0.0000i -0.0000 - 0.0000i 0.0000

Columns 10 through 12

$-0.0000 + 0.0000i$ $0.0000 - 0.0000i$ $0.0000 + 0.0000i$

Columns 13 through 15

$-0.0000 - 40.0000i$ $0.0000 - 0.0000i$ $0.0000 + 0.0000i$

Column 16

$-0.0000 - 0.0000i$

twiddle =

1

g = 0000000000000000

Implementation of radix 16 using pallor and pipeline for 256 point:

x =

$1.0e+002 *$

Columns 1 through 3

1.9100 $-0.0500 + 0.0400i$ -0.0500

Columns 4 through 6

$-0.0500 - 0.0400i$ 1.9100 $-0.0500 + 0.0400i$

Columns 7 through 9

-0.0500 $-0.0500 - 0.0400i$ 1.9100

Columns 10 through 12

$-0.0500 + 0.0400i$ -0.0500 $-0.0500 - 0.0400i$

Columns 13 through 15

1.9100 $-0.0500 + 0.0400i$ -0.0500

Columns 16 through 18

$-0.0500 - 0.0400i$ $0.0317 - 1.8129i$ $0.0239 + 0.0273i$

Columns 19 through 21

$0.0031 + 0.0311i$ $-0.0187 + 0.0346i$ $0.0317 - 1.8129i$

Columns 22 through 24

$0.0239 + 0.0273i$ $0.0031 + 0.0311i$ $-0.0187 + 0.0346i$

Columns 25 through 27

$0.0317 - 1.8129i$ $0.0239 + 0.0273i$ $0.0031 + 0.0311i$

Columns 28 through 30

$-0.0187 + 0.0346i$ $0.0317 - 1.8129i$ $0.0239 + 0.0273i$

Columns 31 through 33

$0.0031 + 0.0311i$ $-0.0187 + 0.0346i$ $-1.7028 + 0.1263i$

Columns 34 through 36

$-0.0341 - 0.0380i$ $0.0069 - 0.0420i$ $0.0499 - 0.0463i$

Columns 37 through 39

$-1.7028 + 0.1263i$ $-0.0341 - 0.0380i$ $0.0069 - 0.0420i$

Columns 40 through 42

$0.0499 - 0.0463i$ $-1.7028 + 0.1263i$ $-0.0341 - 0.0380i$

Columns 43 through 45

$0.0069 - 0.0420i$ $0.0499 - 0.0463i$ $-1.7028 + 0.1263i$

Columns 46 through 48

$-0.0341 - 0.0380i$ $0.0069 - 0.0420i$ $0.0499 - 0.0463i$

Columns 49 through 51

$0.3022 + 1.7777i$ $-0.0897 + 0.0683i$ $-0.0879 - 0.0165i$

Columns 52 through 54

$-0.0847 - 0.1096i$ $0.3022 + 1.7777i$ $-0.0897 + 0.0683i$

Columns 55 through 57

-0.0879 - 0.0165i -0.0847 - 0.1096i 0.3022 + 1.7777i
Columns 58 through 60
-0.0897 + 0.0683i -0.0879 - 0.0165i -0.0847 - 0.1096i
Columns 61 through 63
0.3022 + 1.7777i -0.0897 + 0.0683i -0.0879 - 0.0165i
Columns 64 through 66
-0.0847 - 0.1096i 1.8764 - 0.2897i 0.0614 + 0.1159i
Columns 67 through 69
-0.0352 + 0.0985i -0.1426 + 0.0753i 1.8764 - 0.2897i
Columns 70 through 72
0.0614 + 0.1159i -0.0352 + 0.0985i -0.1426 + 0.0753
Columns 73 through 75
1.8764 - 0.2897i 0.0614 + 0.1159i -0.0352 + 0.0985i
Columns 76 through 78
-0.1426 + 0.0753i 1.8764 - 0.2897i 0.0614 + 0.1159i
Columns 79 through 81
-0.0352 + 0.0985i -0.1426 + 0.0753i -0.2397 - 1.7855
Columns 82 through 84
0.0965 - 0.0731i 0.0944 + 0.0185i 0.0888 + 0.1201
Columns 85 through 87
-0.2397 - 1.7855i 0.0965 - 0.0731i 0.0944 + 0.0185i
Columns 88 through 90
0.0888 + 0.1201i -0.2397 - 1.7855i 0.0965 - 0.0731i
Columns 91 through 93
0.0944 + 0.0185i 0.0888 + 0.1201i -0.2397 - 1.7855i
Columns 94 through 96
0.0965 - 0.0731i 0.0944 + 0.0185i 0.0888 + 0.1201i
Columns 97 through 99
-1.6455 + 0.3718i -0.1293 - 0.0882i -0.0174 - 0.1221i
Columns 100 through 102
0.1122 - 0.1615i -1.645 + 0.3718i -0.1293 - 0.0882i
Columns 103 through 105
-0.0174 - 0.1221i 0.1122 - 0.1615i -1.6455 + 0.3718i
Columns 106 through 108
-0.1293 - 0.0882i -0.0174 - 0.1221i 0.1122 - 0.1615i
Columns 109 through 111
-1.6455 + 0.3718i -0.1293 - 0.0882i -0.0174 - 0.1221i
Columns 112 through 114
0.1122 - 0.1615i 0.5563 + 1.6822i -0.1225 + 0.1768
Columns 115 through 117
-0.1699 + 0.0238i -0.2239 - 0.1628i 0.5563 + 1.6822i
Columns 118 through 120
-0.1225 + 0.1768i -0.1699 + 0.0238i -0.2239 - 0.1628
Columns 121 through 123
0.5563 + 1.6822i -0.122 + 0.1768i -0.1699 + 0.0238i
Columns 124 through 126
-0.2239 - 0.1628i 0.5563 + 1.6822i -0.1225 + 0.1768i
Columns 127 through 129
-0.1699 + 0.0238i -0.2239 - 0.1628i 1.7777 - 0.5625i
Columns 130 through 132
0.1789 + 0.1506i 0.0077 + 0.1875i -0.2043 + 0.2244i
Columns 133 through 135
1.7777 - 0.5625i 0.1789 + 0.1506i 0.0077 + 0.1875i
Columns 136 through 138
-0.2043 + 0.2244i 1.7777 - 0.5625i 0.1789 + 0.1506i
Columns 139 through 141

$0.0077 + 0.1875i$ $-0.2043 + 0.2244i$ $1.7777 - 0.5625i$
 Columns 142 through 144
 $0.1789 + 0.1506i$ $0.0077 + 0.1875i$ $-0.2043 + 0.2244i$
 Columns 145 through 147
 $-0.4963 - 1.6972i$ $0.131 - 0.1799i$ $0.1772 - 0.0201i$
 Columns 148 through 150
 $0.2279 + 0.1772i$ $-0.4963 - 1.6972i$ $0.1312 - 0.1799i$
 Columns 151 through 153
 $0.1772 - 0.0201i$ $0.2279 + 0.1772i$ $-0.4963 - 1.6972i$
 Columns 154 through 156
 $0.1312 - 0.1799i$ $0.1772 - 0.0201i$ $0.2279 + 0.1772i$
 Columns 157 through 159
 $-0.4963 - 1.6972i$ $0.1312 - 0.1799i$ $0.1772 - 0.0201i$
 Columns 160 through 162
 $0.2279 + 0.1772i$ $-1.5349 + 0.5960i$ $-0.2251 - 0.1042i$
 Columns 163 through 165
 $-0.0635 - 0.1906i$ $0.1435 - 0.3012i$ $-1.5349 + 0.5960i$
 Columns 166 through 168
 $-0.2251 - 0.1042i$ $-0.0635 - 0.1906i$ $0.1435 - 0.3012i$
 Columns 169 through 171
 $-1.5349 + 0.5960i$ $-0.2251 - 0.1042i$ $-0.0635 - 0.1906i$
 Columns 172 through 174
 $0.1435 - 0.3012i$ $-1.5349 + 0.5960i$ $-0.2251 - 0.1042i$
 Columns 175 through 177
 $-0.0635 - 0.1906i$ $0.1435 - 0.3012i$ $0.7795 + 1.5326i$
 Columns 178 through 180
 $-0.1190 + 0.2795i$ $-0.2351 + 0.0857i$ $-0.3855 - 0.1778i$
 Columns 181 through 183
 $0.7795 + 1.5326i$ $-0.1190 + 0.2795i$ $-0.2351 + 0.0857i$
 Columns 184 through 186
 $-0.3855 - 0.1778i$ $0.7795 + 1.5326i$ $-0.1190 + 0.2795i$
 Columns 187 through 189
 $-0.2351 + 0.0857i$ $-0.3855 - 0.1778i$ $0.7795 + 1.5326i$
 Columns 190 through 192
 $-0.1190 + 0.2795i$ $-0.2351 + 0.0857i$ $-0.3855 - 0.1778i$
 Columns 193 through 195
 $1.6207 - 0.8029i$ $0.2904 + 0.1460i$ $0.0741 + 0.2584i$
 Columns 196 through 198
 $-0.2252 + 0.3985i$ $1.6207 - 0.8029i$ $0.2904 + 0.1460i$
 Columns 199 through 201
 $0.0741 + 0.2584i$ $-0.2252 + 0.3985i$ $1.6207 - 0.8029i$
 Columns 202 through 204
 $0.2904 + 0.1460i$ $0.0741 + 0.2584i$ $-0.2252 + 0.3985i$
 Columns 205 through 207
 $1.6207 - 0.8029i$ $0.2904 + 0.1460i$ $0.0741 + 0.2584i$
 Columns 208 through 210
 $-0.2252 + 0.3985i$ $-0.7233 - 1.5542i$ $0.1297 - 0.2817i$
 Columns 211 through 213
 $0.2435 - 0.0805i$ $0.3902 + 0.1964i$ $-0.7233 - 1.5542i$
 Columns 214 through 216
 $0.1297 - 0.2817i$ $0.2435 - 0.0805i$ $0.3902 + 0.1964i$
 Columns 217 through 219
 $-0.7233 - 1.5542i$ $0.129 - 0.2817i$ $0.2435 - 0.0805i$
 Columns 220 through 222
 $0.3902 + 0.1964i$ $-0.7233 - 1.5542i$ $0.1297 - 0.2817i$
 Columns 223 through 225

0.2435 - 0.0805i 0.3902 + 0.1964i -1.3783 + 0.7865i
Columns 226 through 228
-0.3116 - 0.0890i -0.1265 - 0.2409i 0.1364 - 0.4566i
Columns 229 through 231
-1.3783 + 0.7865i -0.3116 - 0.0890i -0.1265 - 0.2409i
Columns 232 through 234
0.1364 - 0.4566i -1.3783 + 0.7865i -0.3116 - 0.0890i
Columns 235 through 237
-0.1265 - 0.2409i 0.1364 - 0.4566i -1.3783 + 0.7865i
Columns 238 through 240
-0.3116 - 0.0890i -0.1265 - 0.2409i 0.1364 - 0.4566i
Columns 241 through 243
0.9596 + 1.3389i -0.0841 + 0.3665i -0.2773 + 0.1625i
Columns 244 through 246
-0.5582 - 0.1479i 0.9596 + 1.3389i -0.0841 + 0.3665i
Columns 247 through 249
-0.2773 + 0.1625i -0.5582 - 0.1479i 0.9596 + 1.3389i
Columns 250 through 252
-0.0841 + 0.3665i -0.2773 + 0.1625i -0.5582 - 0.1479i
Columns 253 through 255
0.9596 + 1.3389i -0.0841 + 0.3665i -0.2773 + 0.1625i
Column 256
-0.5582 - 0.1479i

Implementation of memory based : DEMO data are calculated as sum of the following components:

- real sinusoid at normalized frequency 0.137, magnitude 2;
- complex exponent at frequency 0.137+1/(4*64), magnitude 1;
- mean value (frequency 0), magnitude 1;
- rectangular pulse in frequency ranges [-0.137 0];
- noise generated by randn function (SNR~30 dB).

Input [1] to select uniformly sampled sequence X1

Input [2] to select nonuniformly sampled sequence X2

Input [3] to select sparse nonuniformly sampled sequence X3

Select input sequence for DEMO:2

Plots True Spectrum [red color], NEDFT [green colour] and DFT [blue colour]. Calculate [F,S]=nedft(X2,tk,fn,1) and ifft(F). Strike any key to continue.

IV. Conclusion

The proposed architecture achieves high throughput rate by employing several performance-enhancement techniques, including a reformulated radix-16 algorithm realized with multiple memory banks and PEs, a novel conflict-free memory addressing scheme, and a new twiddle factor multiplier structure. Also, high operation speed is obtained by devising an efficient pipelined PE structure, while the new twiddle factor multiplier has low hardware complexity and power consumption. Synthesis results show that the proposed FFT processor can provide up to 2.59 GS/

V. Future scope

We can future extend this project by extending the radix or by implementing it in the another method rather than FFT and also we can process for the radix 32 in the same way when we design this paper hardware using this process the control unit will be easy to design

REFERENCES

- [1] IEEE 802.15.3c-2009: Part 15.3: Wireless Medium Access Control (MAC) and Physical Layer (PHY) Specifications for High Rate Wireless Personal Area Networks (WPANs).
- [2] S. Johansson, S. He, and P. Nilsson, "Wordlength optimization of a pipelined FFT processor," in Proc. 42nd Midwest Symp. Circuits Syst., 1999, pp. 501–503.
- [3] S. He and M. Torkelson, "Designing pipeline FFT processor for OFDM (de)modulation," in Proc. URSI Int. Symp. Signals, Syst., Electron., 1998, pp. 257–262.

- [4] Y. N. Chang and K. Parhi, "An efficient pipelined FFT architecture," *IEEE Trans. Circuit Syst. II, Analog Digit. Signal Process.*, vol. 50, no. 6, pp. 322–325, Jun. 2003.
- [5] D. Cohen, "Simplified control scheme of FFT hardware," *IEEE Trans. Signal Process.*, vol. ASSP-24, no. 12, pp. 577–579, Dec. 1976.
- [6] L. G. Johnson, "Conflict free memory addressing for dedicated FFT hardware," *IEEE Trans. Circuit Syst. II, Analog Digit. Signal Process.*, vol. 39, no. 5, pp. 312–316, May 1992.
- [7] Y. Ma, "An effective memory addressing scheme for FFT processors," *IEEE Trans. Signal Process.*, vol. 47, no. 3, pp. 907–911, Mar. 1999.
- [8] Y. Ma and L. Wanhammar, "A hardware efficient control of memory addressing for high-performance FFT processors," *IEEE Trans. Signal Process.*, vol. 48, no. 3, pp. 917–921, Mar. 2000.
- [9] B.M. Bass, "A low-power, high-performance, 1024-point FFT processor," *IEEE J. Solid-State Circuits*, vol. 34, no. 4, pp. 380–387, Mar. 1999.
- [10] J. C. Kuo, C. H. Wen, and A. Y. Wu, "Implementation of a programmable 2048-point FFT/IFFT processor for OFDM-based communication systems," in *Proc. 2003 Int. Symp. Circuit Syst.*, May 2003, pp. 121–124.
- [11] Y. W. Lin, H. Y. Liu, and C. Y. Lee, "A dynamic scaling FFT processor for DVB-T applications," *IEEE J. Solid-State Circuits*, vol. 39, no. 11, pp. 2005–2013, Nov. 2004.

Implementation of UART with Status Register using Multi Bit Flip-Flop

P. Rajee Priyanka¹, S R Sastry Kalavakolanu²

¹(Department of E.C.E, Andhra Loyola Institute of Engineering and Technology, Vijayawada, India)

² (Assistant Professor, Department of E.C.E, Andhra Loyola Institute of Engineering and Technology, Vijayawada, India)

Abstract: A UART (Universal Asynchronous Receiver and Transmitter) is a device allowing the reception and transmission of information, in a serial and asynchronous way. This project focuses on the implementation of UART with status register using multi bit flip-flop. During the reception of data, status register indicates parity error, framing error, overrun error and break error. In modern very large scale integrated circuits, Power reduction and area reduction has become a vital design goal for sophisticated design applications. Multi-bit flip-flop is an effective power saving implementation methodology by merging single bit flip-flops in the design. The underlying idea behind multi-bit flip-flop method is to eliminate total inverter number by sharing the inverters in the flip-flops. Based on the elimination feature of redundant inverters in merging single bit flip-flops into multi bit flip-flops, gives reduction of wired length and this result in reduction of power consumption and area.

Keywords: Clock buffer, Clock network, Multi bit flip-flop, status Register, Single bit flip-flop.

I. Introduction

Universal Asynchronous Receiver Transmitter (UART) is a kind of serial communication protocol. UARTs are used for asynchronous serial data communication by converting data from parallel to serial at transmitter with some extra overhead bits using shift register and vice versa at receiver.

Optimizations in VLSI have been done on three factors: Area, Power and Timing (Speed). The implementation of multi-bit flip-flop is an effective method for clock power consumption reduction. By replacing Flip-Flops with multi-bit Flip-Flops power consumption can be reduced. By using single clock pulse the Multi-bit Flip-flop (MBFF) is designed so that the same functionality like two or more single-bit Flip-flop (SBFF) can be achieved. So in this project multi bit flip-flop is implemented in status register of UART. The timing performance of MBFF can be analyzed by simulating in Xilinx. As a result the Clock network such as clock buffer and gate delay can be reduced. So the total area used for designing is also reduced.

II. UART Concept

UART is a Universal Asynchronous Receiver-Transmitter, which is used to communicate between two devices. Most computers and microcontrollers include one or more serial data ports utilize to communicate with other serial I/O devices, such as keyboards and serial printers. Serial ports are also used to communicate between two computers using a UART in each computer and a crossover cable, which connects the transmitter of one UART to the receiver of the other, and vice versa. Serial communication uses a transmitter to send data, one bit at a time, over a single communication line to a receiver. You can use this method when data transfer rates are low or you must transfer data over long distances. Serial communication is popular because most computers have one or more serial ports, so no extra hardware is needed other than a cable to connect the instrument to the computer or two computers together.

A UART provides the means to send information using a minimum number of wires. The data is sent bit serially, without a clock signal. The main function of a UART is the conversion of parallel-to-serial when transmitting and serial to- parallel when receiving. The fact that a clock signal is not sent with the data complicates the design of a UART. The two systems (transmitter and receiver) contain separate and unsynchronized local clocks. The proposed design of UART, shown in Fig. 2, has LCR, Transmitter and Receiver as its functional units. All these blocks are explained in brief as course of rest of this section.

2.1 Line Control Register (LCR)

The line control register (LCR) is a byte register. It is used for precise specification of frame format and desired baud rate. The parity bits, stop bits, baud rate selection and word length can be changed by writing the appropriate bits in LCR.

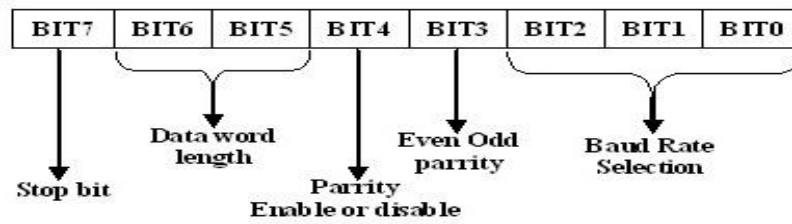


Figure 1: LCR format

2.2 UART Transmitter

The transmitter section accepts parallel data, makes the frame of the data and transmits the data in serial form on the Transmitter Output (TXOUT) terminal. Data is loaded from the inputs TXIN0-TXIN7 into the Transmitter FIFO by applying logic high on the WR (Write) input. If words less than 8 bits are used, only the least significant bits are transmitted. FIFO is 16-byte register. When FIFO contains some data, it will send the signal to Transmitter Hold Register (THR), which is an 8-bit register. At a same time, if THR is empty it will send the signal to FIFO, which indicates that THR is ready to receive data from FIFO. If Transmitter Shift Register (TSR) is empty it will send the signal to THR and it indicates that TSR is ready to receive data from THR. TSR is a 12-bit register in which framing process occurs. In frame start bit, stop bit and parity bit will be added. Now data is transmitted from TSR to TXOUT serially.

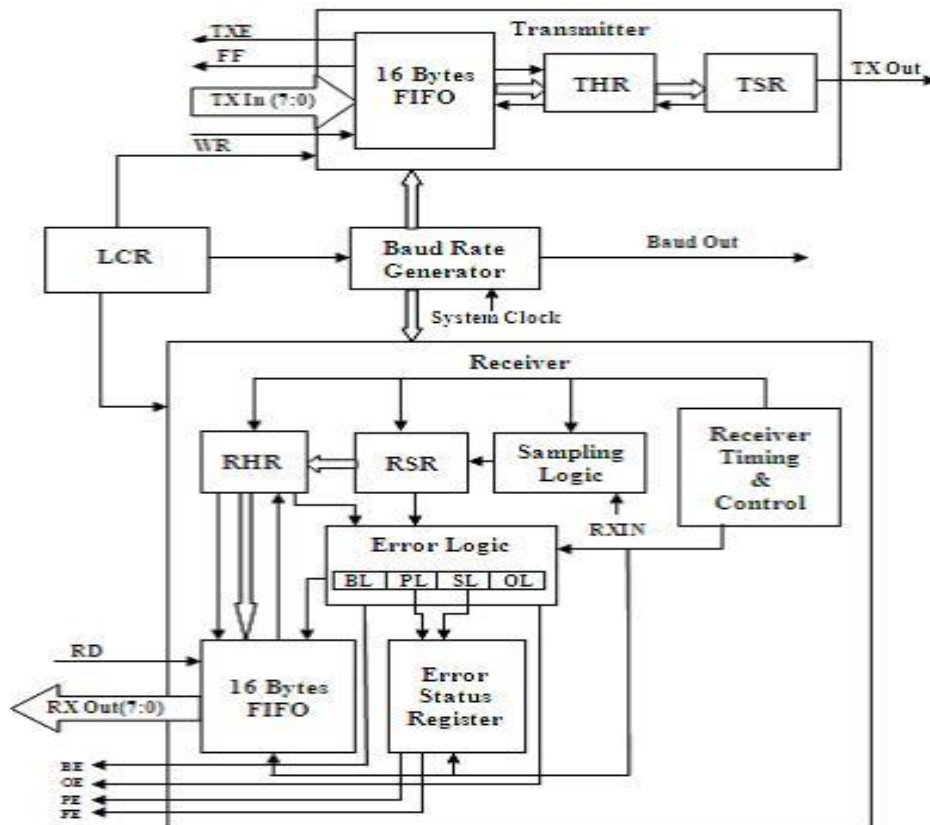


figure 2: UART Architecture

2.3 UART Receiver

The transmitted data from the TXOUT pin is available on the RXIN pin. The received data is applied to the sampling logic block. The receiver timing and control is used for synchronization of clock signal between transmitter and receiver. Initially the logic line is high whenever it goes low sampling and logic block will take 4 samples of that bit and if all four are same it indicates the start of a frame. After that remaining bits are sampled in the same way and all the bits are send to Receiver Shift Register (RSR) one by one where the entire frame is stored. RSR is a 12 bit shift register. Now if the Receiver Hold Register (RHR) is empty it sends signal to RSR so that only the data bits from RSR goes to RHR which is an 8 bit register. The remaining bits in the

RSR are used by the error logic block. Now if receiver FIFO is empty it send the signal to RHR so that the data bits goes to FIFO. When RD signal is asserted the data is available in parallel form on the RXOUT0-RXOUT7 pins. The error logic block handles 4 types of errors: Parity error, Frame error, Overrun error, break error. If the received parity does not match with the parity generated from data bits PL bit will be set which indicates that parity error occurred. If receiver fails to detect correct stop bit or when 4 samples do not match frame error occurs and SL bit is set. If the receiver FIFO is full and other data arrives at the RHR overrun error occurs and OL bit is set. If the RXIN pin is held low for long time than the frame time then there is a break in received data and break error occurs and BL bit is set.

2.4 The UART Standard Data Format

Serial data are contained within frames of 8 data bits, as well as coded information bits. Between successive transmissions, the transmission line is held high. A transmission is initialized by a leading low start bit. Next to the leading low start bit comes 8 bits of data information, beginning with the LSB and afterwards represented at increasing significance order up to the MSB. Next to the 8 data bits comes the parity bit, representing the parity result of the 8 data bits. The parity bit can be encoded true based on even parity or odd parity mode. Next to the parity bit comes a trailing high stop bit indicating the end of a data frame.

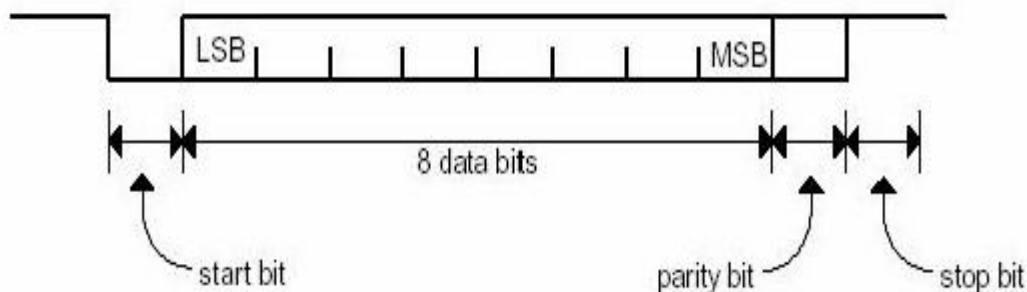


Figure 3: UART data format

III. Multi Bit Flip- Flop Concept

In this section, we will introduce multi-bit flip-flop concept. The proposed method for multi bit flip flop is merging of clock pulse. Before that, we will review single-bit flip-flop. Figure 3 shows an example of single-bit flip-flop. A single-bit flip-flop has two latches (Master latch and slave latch). The latches need "Clk" and "Clk'" signal to perform operations, such as Figure 1 shows.

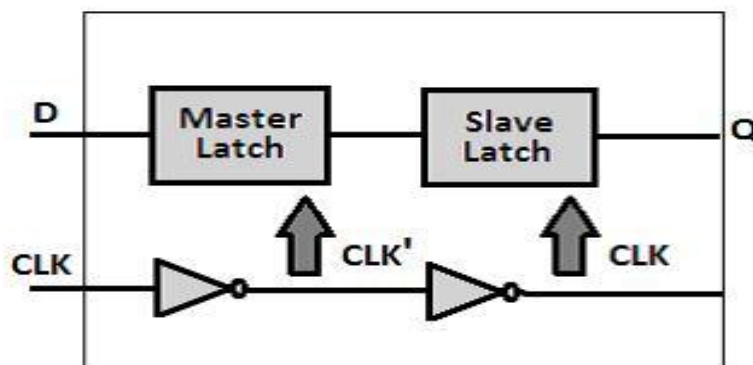


Figure 4: Single-Bit Flip-Flop

In order to have better delay from Clk-> Q, we will regenerate "Clk" from "Clk'". Hence we will have two inverters in the clock path. Figure 4 shows an example of merging two 1-bit flip-flops into one 2-bit flip-flop. Each 1-bit flip-flop contains two inverters, master-latch and slave-latch.

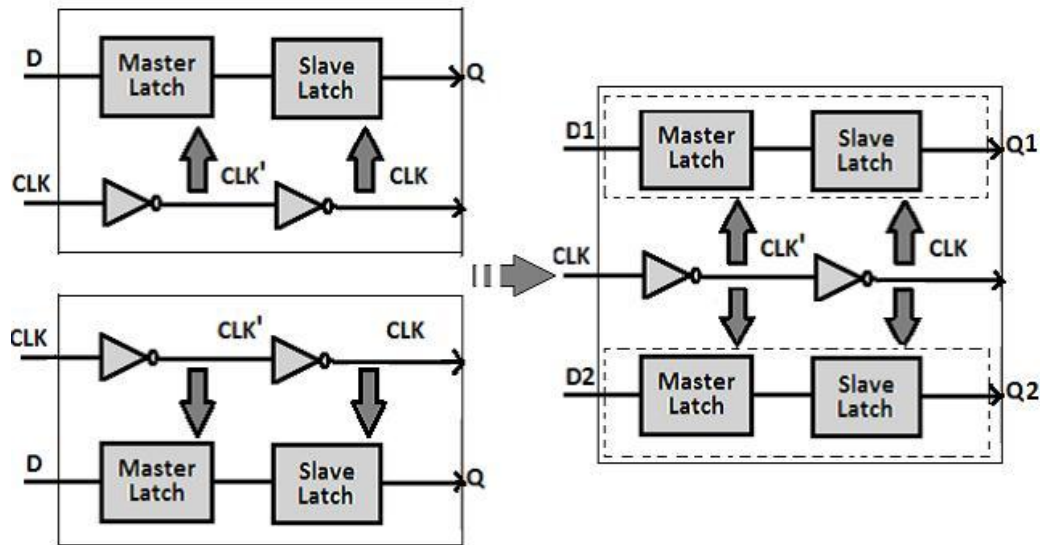


Figure 5: An example of merging two 1-bit flip-flops into one 2-bit flip-flop.

Due to the manufacturing rules, inverters in flip-flops tend to be oversized. As the process technology advances into smaller geometry nodes like 65nm and beyond, the minimum size of clock drivers can drive more than one flip-flop. Merging single-bit flip-flops into one multi-bit flip-flop can avoid duplicate inverters, and lower the total clock dynamic power consumption.

IV. Experimental Results

By implementing the multi bit flip-flop in UART with status register, it is simulated in Xilinx. The total power consumed by clock is 0.00263W. At least 20% of power is reduced when it is compared with normal UART with status register. In synthesis report, we can see only two clock buffers are used in UART with multi bit flip-flop. This indicates that the area is reduced. The simulation result for power and Synthesis report is shown in figure 6 and figure 7.

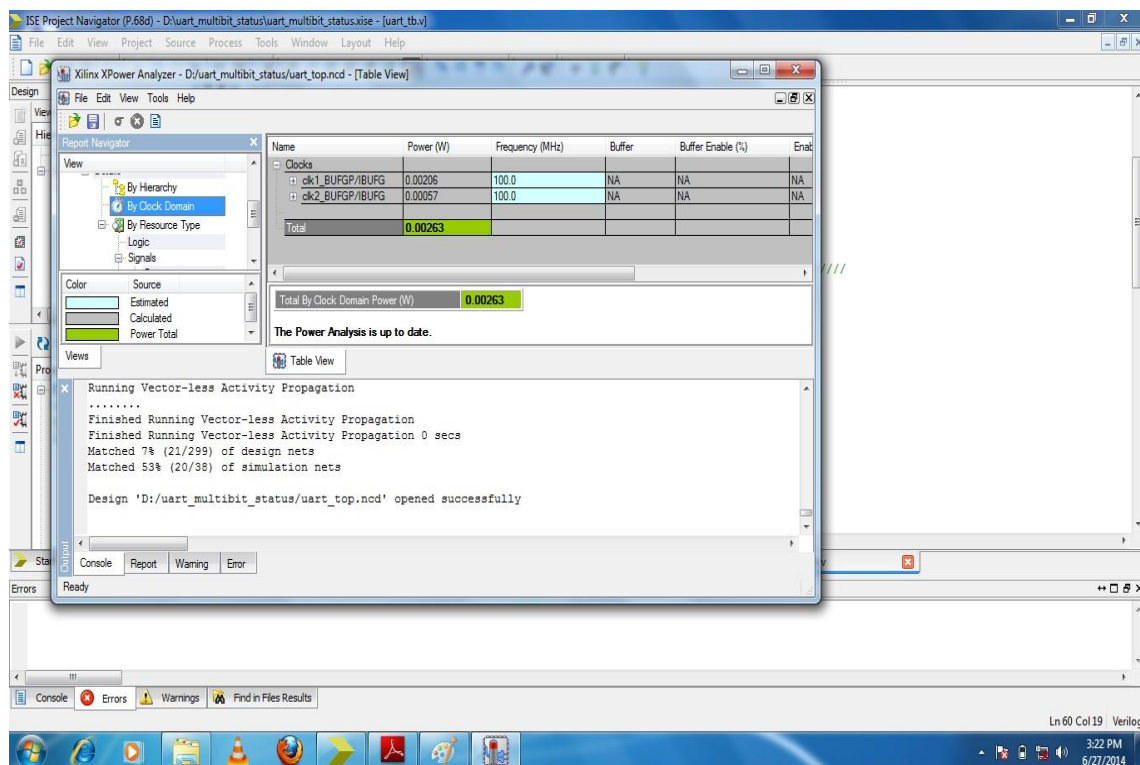


Figure 6: Power report of multi bit flip-flop

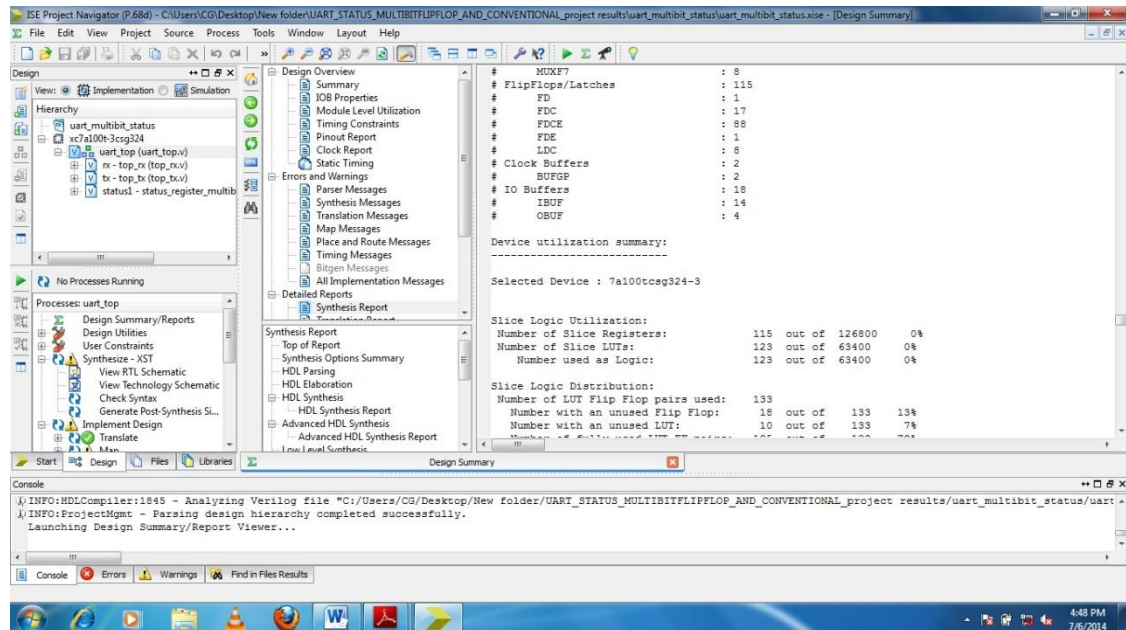


Figure 7: Synthesis report

V. Conclusion

In present VLSI design area is one of the important issues to be addressed. The proposed method is implemented in Xilinx. Experimental results are targeted to number of flip flop usage and power used by clock buffer. Thus this proposed method is more suitable for reduction of hardware.

References

- [1] Zhi-Wei Chen and Jin-Tai Yan, Routability-Driven Flip-Flop Merging Process for Clock Power Reduction, Computer Design (ICCD) IEEE International Conference, 2010
- [2] Ya-Ting Shyu et. Al., Effective and Efficient Approach for Power Reduction by Using Multi-Bit Flip-Flops, IEEE transactions on very large scale integration systems, 2012
- [3] Jin-Tai Yan and Zhi-Wei Chen, Construction of Constrained Multi-Bit Flip-Flops for Clock Power Reduction, Green Circuits and Systems (ICGCS) International Conference, 2010
- [4] Chih-Cheng Hsu, Yao-Tsung Chang and Mark Po-Hung Lin, Crosstalk-Aware Power Optimization with Multi-Bit Flip-Flops, 17th Asia and South Pacific Design Automation Conference, 2012
- [5] Himanshu Patel; Sanjay Trivedi; R. Neelkanthan; V. R. Gujrati; , "A Robust UART Architecture Based on Recursive Running Sum Filter for Better Noise Performance," VLSI Design, 2007. Held jointly with 6th International Conference on Embedded Systems., 20th International Conference on , vol., no., pp.819-823, Jan. 2007.
- [6] Fang Yi-yuan; Chen Xue-jun; , "Design and Simulation of UART Serial Communication Module Based on VHDL," Intelligent Systems and Applications (ISA), 2011 3rd International Workshop on , vol.,no., pp.1-4, 28-29 May 2011
- [7] Idris, M.Y.I.; Yaacob, M.; , "A VHDL implementation of BIST technique in UART design," TENCON 2003. Conference on Convergent Technologies for Asia-Pacific Region , vol.4, no., pp. 1450- 1454 Vol.4, 15-17 Oct. 2003.
- [8] Chun-zhi, He; Yin-shui, Xia; Lun-yao, Wang; , "A universal asynchronous receiver transmitter design," Electronics, Communications and Control (ICECC), 2011 International Conference on , vol., no., pp.691-694, 9-11 Sept. 2011

On $\pi g\theta$ -Homeomorphisms in Topological Spaces

C. Janaki¹, M. Anandhi²

^{1,2}Asst. Professor, Dept. of Mathematics, L.R.G Government Arts College for Women, Tirupur-4, India

Abstract: In this paper, we introduce the concepts of $\pi g\theta$ -closed map, $\pi g\theta$ -open map, $\pi g\theta$ -homeomorphisms and $\pi g\theta c$ -homeomorphisms and study their properties. Also, we discuss its relationship with other types of functions.

Mathematics Subject Classification: 54E55

Key words: $\pi g\theta$ -closed maps, $\pi g\theta$ -M-closed maps, $\pi g\theta$ -homeomorphisms and $\pi g\theta c$ -homeomorphisms.

I. Introduction

Velicko[27] introduced the notions of θ -open sets. Dontchev and Maki [11] alone have explored the concept of θ -generalized closed sets. Regular open sets have been introduced and investigated by Stone[26]. The finite union of regular open sets is π -open and subsequently the complement of π -open set is said to be π -closed, which has been highlighted by Zaitsev[28]. Maki et al[20] introduced generalized homeomorphisms (briefly g-homeomorphisms) and gc-homeomorphisms in topological spaces. Devi et al[9] introduced generalized-semi-homeomorphisms(briefly gs-homeomorphisms) and gsc-homeomorphisms in topological spaces.

In this paper, we first introduce a new class of closed maps called $\pi g\theta$ -closed maps and we study some of the properties of $\pi g\theta$ -homeomorphisms.

II. Preliminaries

Throughout this paper (X, τ) and (Y, σ) represents non-empty topological spaces on which no separation axioms are assumed unless otherwise mentioned. For a subset A of a space (X, τ) , $\text{cl}(A)$ and $\text{int}(A)$ denote the closure of A and the interior of A respectively. (X, τ) and (Y, σ) will be replaced by X and Y if there is no chance of confusion.

Let us recall the following definitions which we shall require later.

Definition 2.1: A subset A of space (X, τ) is called

- (1) a pre- open set[21] if $A \subset \text{int}(\text{cl}(A))$ and a pre closed set if $\text{cl}(\text{int}(A)) \subset A$;
- (2) a semi-open set[4] if $A \subset \text{cl}(\text{int}(A))$ and semi-closed if $\text{int}(\text{cl}(A)) \subset A$;
- (3) a regular open set [15]if $A = \text{int}(\text{cl}(A))$ and a regular closed set if $A = \text{cl}(\text{int}(A))$.

Definition 2.2: A subset A of a space (X, τ) is called

- (1) generalized closed (briefly g-closed) [17] if $\text{cl}(A) \subset U$ whenever $A \subset U$ and U is open in (X, τ) .
- (2) a semi-generalized closed (briefly sg-closed) [6] if $\text{scl}(A) \subset U$ whenever $A \subset U$ and U is semi-open in (X, τ) .
- (3) a generalized semi-closed (briefly gs-closed) [6] if $\text{scl}(A) \subset U$ whenever $A \subset U$ and U is open in (X, τ) .
- (4) a α -generalized closed (briefly αg -closed) [20] if $\alpha \text{cl}(A) \subset U$ whenever $A \subset U$ and U is open in (X, τ) .
- (5) a generalized α -closed (briefly $g\alpha$ -closed) [20] if $\alpha \text{cl}(A) \subset U$ whenever $A \subset U$ and U is α -open in (X, τ) .
- (6) a θ -generalized closed (briefly, θg -closed) [11] if $\text{cl}_\theta(A) \subset U$ whenever $A \subset U$ and U is open in (X, τ) .
- (7) a π generalized closed (briefly πg -closed) [12] if $\text{cl}(A) \subset U$, whenever $A \subset U$ and U is π -open in (X, τ) .
- (8) a π generalized α -closed (briefly $\pi g\alpha$ -closed) [15] if $\alpha \text{cl}(A) \subset U$, whenever $A \subset U$ and U is π -open in (X, τ) .
- (9) a π generalized semi-closed (briefly πgs -closed) [5] if $\text{scl}(A) \subset U$, whenever $A \subset U$ and U is π -open in (X, τ) .
- (10) a π generalized b-closed (briefly πgb -closed) [25] if $\text{bcl}(A) \subset U$, whenever $A \subset U$ and U is π -open in (X, τ) .

- (11) a π generalized pre-closed (briefly πgp -closed)[24] if $\text{pcl}(A) \subset U$, whenever $A \subset U$ and U is π -open in (X, τ) .
 (12) a π generalized θ -closed (briefly $\pi g\theta$ -closed)[24] if $\text{cl}_\theta(A) \subset U$, whenever $A \subset U$ and U is π -open in (X, τ) .

The compliment of g -closed (resp. sg -closed, gs -closed, αg -closed, $g\alpha$ -closed, θg -closed, πg -closed, $\pi g\alpha$ -closed, πgs -closed, πgb -closed, πgp -closed, $\pi g\theta$ -closed) is g -open (resp. sg -open, gs -open, αg -open, $g\alpha$ -open, θg -open, πg -open, $\pi g\alpha$ -open, πgs -open, $\pi g\theta$ -open, πgp -open, $\pi g\theta$ -open).

Definition 2.3 A map $f: (X, \tau) \rightarrow (Y, \sigma)$ is said to be

- (1) generalized-continuous (briefly g -continuous)[7] if $f^{-1}(V)$ is g -closed in (X, τ) for every closed set V in (Y, σ) .
- (2) semi generalized-continuous (briefly sg -continuous)[8] if $f^{-1}(V)$ is sg -closed in (X, τ) for every closed set V in (Y, σ) .
- (3) generalized semi-continuous (briefly gs -continuous)[8] if $f^{-1}(V)$ is gs -closed in (X, τ) for every closed set V in (Y, σ) .
- (4) generalized- α -continuous (briefly $g\alpha$ -continuous) [18] if $f^{-1}(V)$ is $g\alpha$ -closed in (X, τ) for every closed set V in (Y, σ) .
- (5) α -generalized-continuous (briefly αg -continuous)[18] if $f^{-1}(V)$ is αg -closed in (X, τ) for every closed set V in (Y, σ) .
- (6) θ -continuous[11] if $f^{-1}(V)$ is θ -closed in (X, τ) for every closed set V in (Y, σ) .
- (7) θ -generalized-continuous (briefly θg -continuous)[14] if $f^{-1}(V)$ is θg -closed in (X, τ) for every closed set V in (Y, σ) .
- (8) $\pi g\theta$ -open[1] if for each open set V in (X, τ) , $f(V)$ is $\pi g\theta$ -open in (Y, σ) .
- (9) $\pi g\theta$ -closed [1] if for each closed set V in (X, τ) , $f(V)$ is $\pi g\theta$ -closed in (Y, σ) .
- (10) $\pi g\theta$ -continuous[1] if $f^{-1}(V)$ is $\pi g\theta$ -closed in (X, τ) for every closed set V in (Y, σ) .
- (11) $\pi g\theta$ -irresolute[1] if $f^{-1}(V)$ is $\pi g\theta$ -closed in (X, τ) for every $\pi g\theta$ -closed set V in (Y, σ) .
- (12) A space X is called $\pi g\theta$ - $T^{1/2}$ -space[1] if every $\pi g\theta$ -closed set is θ -closed.

Definition 2.4 A bijection $f: (X, \tau) \rightarrow (Y, \sigma)$ is said to be

- (1) g -homeomorphism[20] if f is g -open and g -continuous.
- (2) sg -homeomorphism[20] if f is sg -open and sg -continuous.
- (3) gs -homeomorphism[20] if f is gs -open and gs -continuous.
- (4) $g\alpha$ -homeomorphism[18] if both f and f^{-1} are $g\alpha$ -continuous in (X, τ) .
- (5) αg -homeomorphism[18] if both f and f^{-1} are αg -continuous in (X, τ) .
- (6) θ -homeomorphism[23] if f is both θ -continuous and θ -open.
- (7) θg -homeomorphism[14] if f is both θg -continuous and θg -open.
- (8) πg -homeomorphism[12] if f is both πg -continuous and πg -open.
- (9) πgb -homeomorphism[12] if f is both πgb -continuous and πgb -open.
- (10) $\pi g\alpha$ -homeomorphism[15] if f is both $\pi g\alpha$ -continuous and $\pi g\alpha$ -open.
- (11) πgs -homeomorphism[5] if f is both πgs -continuous and πgs -open.
- (12) πgp -homeomorphism[5] if f is both πgp -continuous and πgp -open.

III. $\pi g\theta$ -Closed Maps

In this section, we introduce the notions of $\pi g\theta$ -closed maps, $\pi g\theta$ -open maps in topological spaces and obtain certain characterizations of these maps.

Definition 3.1 The map $f: (X, \tau) \rightarrow (Y, \sigma)$ is called $\pi g\theta$ -closed if the image of every closed set in (X, τ) is $\pi g\theta$ -closed in (Y, σ) .

Proposition 3.2 If a mapping $f: (X, \tau) \rightarrow (Y, \sigma)$ is $\pi g\theta$ -closed, then $\pi g\theta\text{-cl}(f(A)) \subset f(\text{cl}(A))$ for every subset A of (X, τ) .

Proof: Let $A \subset X$. Since f is $\pi g\theta$ -closed, $f(\text{cl}(A))$ is $\pi g\theta$ -closed in (Y, σ) . Now $f(A) \subset f(\text{cl}(A))$. Also $f(A) \subset \pi g\theta\text{-cl}(f(A))$. By definition, we have $\pi g\theta\text{-cl}(f(A)) \subset f(\text{cl}(A))$.

Remark 3.3 The converse of the proposition 3.2 need not be true as seen in the following example.

Example 3.4 Let $X=Y=\{a,b,c,d\}$. Let $f: (X,\tau) \rightarrow (Y,\sigma)$ be an identity map with $\tau = \{\emptyset, \{a\}, \{c\}, \{a,c\}, \{b,d\}, \{a,b,d\}, \{b,c,d\}, X\}$, $\sigma = \{\emptyset, \{a\}, \{c\}, \{a,c\}, \{a,c,d\}, X\}$ be their topologies. For every subset A of (X,τ) , $\pi g\theta\text{-cl}(f(A)) \subset f(\text{cl}(A))$, but f is not a $\pi g\theta$ -closed map.

Theorem 3.5 A map $f: (X,\tau) \rightarrow (Y,\sigma)$ is $\pi g\theta$ -closed if and only if for each subset S of (Y,σ) and for each open set U containing $f^{-1}(S)$ there exists a $\pi g\theta$ -open set V of (Y,σ) such that $S \subset V$ and $f^{-1}(V) \subset U$.

Proof: Necessity: Suppose that f is a $\pi g\theta$ -closed map. Let $S \subset Y$ and U be an open subset of X such that $f^{-1}(S) \subset U$. Then $V = (f(U^c))^c$ is $\pi g\theta$ -closed set in Y . Therefore $Y - V = Y - f(U^c) = (f(U^c))^c$ is $\pi g\theta$ -open in Y . So $f^{-1}(V) = f^{-1}(Y) - f^{-1}(f(U^c)) = X - U^c = (U^c)^c = U$ such that $f^{-1}(V) \subset U$.

Sufficiency: Let S be a closed set of (X,τ) . Then $f^{-1}((f(S))^c) \subset S^c$ and S^c is open. By assumption, there exists a $\pi g\theta$ -open set V of Y such that $(f(S))^c \subset V$ and $f^{-1}(V) \subset S^c$ and so $S \subset (f^{-1}(V))^c$. Hence $V^c \subset f(S) \subset f(f^{-1}(V))^c \subset V^c$ which implies $f(S) = V^c$. Since V^c is $\pi g\theta$ -closed, $f(S)$ is $\pi g\theta$ -closed and therefore f is $\pi g\theta$ -closed.

The following example shows that the composition of two $\pi g\theta$ -closed maps need not be $\pi g\theta$ -closed.

Example 3.6 Let $X=Y=Z = \{a,b,c,d,e\}$. Let $f: (X,\tau) \rightarrow (Y,\sigma)$ and $g: (Y,\sigma) \rightarrow (Z,\eta)$ be two identity maps with $\tau = \{\emptyset, \{e\}, \{a,b,c,d\}, X\}$, $\sigma = \{\emptyset, \{b\}, \{c\}, \{b,c\}, \{a,b\}, \{a,b,c\}, X\}$ and $\eta = \{\emptyset, \{a,b\}, \{c,d\}, \{a,b,c,d\}, X\}$ be their topologies. Then $(g \circ f) [\{a,b,c,d\}] = \{a,b,c,d\}$ is closed in (X,τ) but not $\pi g\theta$ -closed in (Z,η) .

Proposition 3.7 Let $f: (X,\tau) \rightarrow (Y,\sigma)$ be a closed map and $g: (Y,\sigma) \rightarrow (Z,\eta)$ be $\pi g\theta$ -closed map, then their composition $g \circ f: (X,\tau) \rightarrow (Z,\eta)$ is $\pi g\theta$ -closed.

Proof: Let A be a closed set in X . Since f is closed map, $f(A)$ is closed in Y . Since g is $\pi g\theta$ -closed, $g(f(A))$ is $\pi g\theta$ -closed. Hence $g \circ f$ is a $\pi g\theta$ -closed map.

Remark 3.8 If $f: (X,\tau) \rightarrow (Y,\sigma)$ is a $\pi g\theta$ -closed map and $g: (Y,\sigma) \rightarrow (Z,\eta)$ is a closed map, then their composition need not be closed map as seen from the following example.

Example 3.9 Let $X=Y=Z=\{a,b,c,d\}$. Let $f: (X,\tau) \rightarrow (Y,\sigma)$ and $g: (Y,\sigma) \rightarrow (Z,\eta)$ be two identity maps with $\tau = \{\emptyset, \{a\}, \{b\}, \{c\}, \{a,b\}, \{a,c\}, \{b,c\}, \{a,b,c\}, \{a,c,d\}, X\}$, $\sigma = \{\emptyset, \{a\}, \{c\}, \{a,c\}, \{a,b,c\}, \{a,c,d\}, X\}$ and $\eta = \{\emptyset, \{a\}, \{c\}, \{a,c\}, \{a,b\}, \{a,b,c\}, \{a,c,d\}, X\}$. $f: (X,\tau) \rightarrow (Y,\sigma)$ is a $\pi g\theta$ -closed map and $g: (Y,\sigma) \rightarrow (Z,\eta)$ is a closed map. But $(g \circ f): (X,\tau) \rightarrow (Z,\eta)$ is not a closed map because $(g \circ f)(\{a,d\}) = \{a,d\}$ is not closed in (Z,η) .

Theorem 3.10 Let $f: (X,\tau) \rightarrow (Y,\sigma)$ and $g: (Y,\sigma) \rightarrow (Z,\eta)$ be two mappings such that their composition $g \circ f: (X,\tau) \rightarrow (Z,\eta)$ be a $\pi g\theta$ -closed mapping. Then the following statements are true.

- (i) If f is continuous and surjective, then g is $\pi g\theta$ -closed.
- (ii) If g is $\pi g\theta$ -irresolute and injective, then f is $\pi g\theta$ -closed.

Proof: (i) Let A be a closed set of (Y,σ) . Since f is continuous, $f^{-1}(A)$ is closed in (X,τ) and since $g \circ f$ is $\pi g\theta$ -closed, $(g \circ f)(f^{-1}(A))$ is $\pi g\theta$ -closed in (Z,η) . That is $g(A)$ is $\pi g\theta$ -closed in (Z,η) . Therefore, g is a $\pi g\theta$ -closed map.

(ii) Let B be a closed set of (X,τ) . Since $g \circ f$ is $\pi g\theta$ -closed, $(g \circ f)(B)$ is $\pi g\theta$ -closed in (Z,η) . Since g is $\pi g\theta$ -irresolute, $g^{-1}(g \circ f)(B)$ is $\pi g\theta$ -closed in (Y,σ) . Hence $f(B)$ is $\pi g\theta$ -closed in (Y,σ) . Thus f is a $\pi g\theta$ -closed map.

Analogous to a $\pi g\theta$ -closed map, we define a $\pi g\theta$ -open map as follows:

Definition 3.11 A map $f: (X,\tau) \rightarrow (Y,\sigma)$ is called $\pi g\theta$ -open if the image of every open set in (X,τ) is $\pi g\theta$ -open in (Y,σ) .

Definition 3.12 Let x be a point of (X,τ) and V be a subset of X . Then V is called a $\pi g\theta$ -neighbourhood U of x in (X,τ) if there exists a $\pi g\theta$ -open set U of (X,τ) such that $x \in U \subseteq V$.

By $\pi G\theta O(X)$ we mean the family of all $\pi g\theta$ -open subsets of the space (X,τ) .

Theorem 3.13 : Suppose $\pi G\theta O(X)$ is closed under arbitrary unions. Let $f: (X,\tau) \rightarrow (Y,\sigma)$ be a mapping. Then the following statements are equivalent:

- (i) f is a $\pi g\theta$ -open mapping.
- (ii) For a subset A of (X,τ) , $f(\text{int}(A)) \subset \pi g\theta\text{-int}(f(A))$.

- (iii) For each $x \in X$ and for each neighbourhood U of x in (X, τ) , there exists a $\pi g\theta$ -neighbourhood W of $f(x)$ in (Y, σ) such that $W \subset f(U)$.

Proof. (i) \Rightarrow (ii): Suppose f is $\pi g\theta$ -open. Let $A \subset X$. Since $\text{int}(A)$ is open in (X, τ) , $f(\text{int}(A))$ is $\pi g\theta$ -open in (Y, σ) . Hence $f(\text{int}(A)) \subseteq f(A)$ and we have, $f(\text{int}(A)) \subseteq \pi g\theta\text{-int}(f(A))$.

(ii) \Rightarrow (iii): Suppose (ii) holds. Let $x \in X$ and U be an arbitrary neighbourhood of x in (X, τ) . Then there exists an open set G such that $x \in G \subseteq U$. By assumption, $f(G) = f(\text{int}(G)) \subseteq \pi g\theta\text{-int}(f(G))$. This implies $f(G) = \pi g\theta\text{-int}(f(G))$. Therefore $f(G)$ is $\pi g\theta$ -open in (Y, σ) . Further, $f(x) \in f(G) \subseteq f(U)$ and so (iii) holds, by taking $W = f(G)$.

(iii) \Rightarrow (i): Suppose (iii) holds. Let U be any open set in (X, τ) , $x \in U$ and $f(x) = y$. Then for each $x \in U$, $y \in f(U)$, by assumption there exists a $\pi g\theta$ -neighbourhood W_y of y in (Y, σ) such that $W_y \subset f(U)$. Since W_y is a $\pi g\theta$ -neighbourhood of y , there exists a $\pi g\theta$ -open set V_y of (Y, σ) such that $y \in V_y \subseteq W_y$. therefore, $f(U) = \bigcup \{V_y : y \in f(U)\}$ and $f(U)$ is a $\pi g\theta$ -open set of (Y, σ) . Thus f is $\pi g\theta$ -open mapping.

Theorem 3.14 A function $f: (X, \tau) \rightarrow (Y, \sigma)$ is $\pi g\theta$ -open if and only if for any subset B of (Y, σ) and for any closed set S containing $f^{-1}(B)$, there exists a $\pi g\theta$ -closed set A of (Y, σ) containing B such that $f^{-1}(A) \subseteq S$.

Proof: Similar to Theorem 3.5.

Remark 3.15 A map $f: (X, \tau) \rightarrow (Y, \sigma)$ is $\pi g\theta$ -open if and only if $f^{-1}(\pi g\theta\text{-cl}(B)) \subset \text{cl}(f^{-1}(B))$ for every subset B of (Y, σ) .

Proof: Necessity: Suppose that f is a $\pi g\theta$ -open map. Then for any $B \subset Y$, $f^{-1}(B) \subset \text{cl}(f^{-1}(B))$. By Theorem 3.14, there exists a $\pi g\theta$ -closed set A of (Y, σ) such that $B \subset A$ and $f^{-1}(A) \subset \text{cl}(f^{-1}(B))$. Therefore, $f^{-1}(\pi g\theta\text{-cl}(B)) \subset f^{-1}(A) \subset \text{cl}(f^{-1}(B))$, since A is a $\pi g\theta$ -closed set in (Y, σ) .

Sufficiency: Let S be any subset of (Y, σ) and F be any closed set containing $f^{-1}(S)$. Put $A = \pi g\theta\text{-cl}(S)$. Then A is a $\pi g\theta$ -closed set and $S \subset A$. By assumption, $f^{-1}(A) = f^{-1}(\pi g\theta\text{-cl}(S)) \subset \text{cl}(f^{-1}(S)) \subset F$ and therefore by Theorem 3.14, f is $\pi g\theta$ -open.

Definition 3.16 A map $f: (X, \tau) \rightarrow (Y, \sigma)$ is said to be a M - $\pi g\theta$ -closed map if the image $f(A)$ is $\pi g\theta$ -closed in (Y, σ) for every $\pi g\theta$ -closed set A of (X, τ) .

Remark 3.17 M - $\pi g\theta$ -closed map is independent of a $\pi g\theta$ -closed map as seen in the following examples.

Example 3.18 Let $X = \{a, b, c, d, e\} = Y$. Let $f: (X, \tau) \rightarrow (Y, \sigma)$ be an identity map. Let $\tau = \{\emptyset, \{b\}, \{c\}, \{b, c\}, \{a, b\}, \{a, b, c\}, X\}$ and $\sigma = \{\emptyset, \{a, b\}, \{c, d\}, \{a, b, c, d\}, X\}$ be their topologies. Then f is a $\pi g\theta$ -closed map. But not a M - $\pi g\theta$ -closed map, since $f(\{a, d\}) = \{a, d\}$ is not $\pi g\theta$ -closed in (Y, σ) where $\{a, d\}$ is $\pi g\theta$ -closed in (X, τ) .

Example 3.19 Let $X = \{a, b, c, d, e\} = Y$. Let $f: (X, \tau) \rightarrow (Y, \sigma)$ be an identity map. Let $\tau = \{\emptyset, \{a\}, \{b\}, \{c\}, \{d\}, \{a, b\}, \{a, c\}, \{a, d\}, \{b, c\}, \{b, d\}, \{c, d\}, \{a, b, c\}, \{a, b, d\}, \{a, c, d\}, \{b, c, d\}, \{a, b, c, d\}, \{a, b, c, e\}, X\}$ and $\sigma = \{\emptyset, \{a, b\}, \{c, d\}, \{a, b, c, d\}, X\}$ be their topologies. Then f is not a $\pi g\theta$ -closed map, since $f(\{d\}) = \{d\}$ is not $\pi g\theta$ -closed in (Y, σ) where $\{d\}$ is closed in (X, τ) . However f is a M - $\pi g\theta$ -closed map.

Theorem 3.20 If $f: (X, \tau) \rightarrow (Y, \sigma)$ is a π -irresolute and pre- θ -closed map in X , then $f(A)$ is $\pi g\theta$ -closed in Y for every $\pi g\theta$ -closed set A of X .

Proof: Let A be any $\pi g\theta$ -closed set of X and V be any π -open set of Y containing $f(A)$. Then $A \subset f^{-1}(V)$ where $f^{-1}(V)$ is π -open in X . Since A is $\pi g\theta$ -closed, $\text{cl}_\theta(A) \subset f^{-1}(V)$ and hence $f(\text{cl}_\theta(A)) \subseteq V$. Since f is pre- θ -closed, $\text{cl}_\theta(f(\text{cl}_\theta(A))) \subset V$ and hence we obtain $\text{cl}_\theta(f(A)) \subset V$. Hence $f(A)$ is $\pi g\theta$ -closed in Y .

IV. $\pi g\theta$ -Homeomorphisms

Definition 4.1: A bijection $f: (X, \tau) \rightarrow (Y, \sigma)$ is called $\pi g\theta$ -homeomorphism if f is both $\pi g\theta$ -continuous and $\pi g\theta$ -open map.

Definition 4.2 A bijection $f: (X, \tau) \rightarrow (Y, \sigma)$ is called $\pi g\theta c$ -homeomorphism if both f and f^{-1} are $\pi g\theta$ -irresolute in (X, τ) .

Theorem 4.3

1. Every θ -homeomorphism is $\pi g\theta$ -homeomorphism.
2. Every θg -homeomorphism is $\pi g\theta$ -homeomorphism.
3. Every $\pi g\theta$ -homeomorphism is πg -homeomorphism.
4. Every $\pi g\theta$ -homeomorphism is $\pi g\alpha$ -homeomorphism.
5. Every $\pi g\theta$ -homeomorphism is $\pi g s$ -homeomorphism.
6. Every $\pi g\theta$ -homeomorphism is $\pi g b$ -homeomorphism.
7. Every $\pi g\theta$ -homeomorphism is a $\pi g p$ -homeomorphism.

Proof: Straight forward.

Remark 4.4 The following examples show that the converse of Theorem 4.3 need not be true.

Example 4.5 Let $X=\{a,b,c,d\}=Y$ with topologies $\tau=\{\phi,\{a\},\{b\},\{c\},\{a,b\},\{a,c\},\{b,c\},\{a,b,c\},\{a,c,d\},X\}$, $\sigma=\{\phi,\{a\},\{a,b\},\{a,c\},\{a,b,c\},\{a,c,d\},X\}$ respectively. Let $f:(X,\tau)\rightarrow(Y,\sigma)$ be the identity map. Then f is not a θ -homeomorphism because $f^{-1}(\{b\})=\{b\}$ is not θ -closed in X where $\{b\}$ is closed in Y . However f is a $\pi g\theta$ -homeomorphism.

Example 4.6 Let $X=\{a,b,c,d\}=Y$ with topologies $\tau=\{\phi,\{a\},\{b\},\{c\},\{a,b\},\{a,c\},\{b,c\},\{a,b,c\},\{a,c,d\},X\}$, $\sigma=\{\phi,\{a\},\{a,b\},\{a,c\},\{a,b,c\},\{a,c,d\},X\}$ respectively. Let $f:(X,\tau)\rightarrow(Y,\sigma)$ be the identity map. Then f is not a θg -homeomorphism because $f^{-1}(\{b\})=\{b\}$ is not θg -closed in X where $\{b\}$ is closed in Y . However f is a $\pi g\theta$ -homeomorphism.

Example 4.7 Let $X=\{a,b,c,d\}=Y$ with topologies $\tau=\{\phi,\{a\},\{b\},\{a,b\},\{a,c\},\{a,b,c\},\{a,b,d\},X\}$, $\sigma=\{\phi,\{a\},\{b\},\{a,b\},\{a,b,d\},X\}$ respectively. Let $f:(X,\tau)\rightarrow(Y,\sigma)$ be the identity map. Then f is not a $\pi g\theta$ -homeomorphism because $f^{-1}(\{c\})=\{c\}$ is not $\pi g\theta$ -closed in X , where $\{c\}$ is closed in Y . However f is a πg -homeomorphism.

Example 4.8 Let $X=\{a,b,c,d\}=Y$ with topologies $\tau=\{\phi,\{a\},\{b\},\{c\},\{a,b\},\{a,c\},\{b,c\},\{a,b,c\},\{a,b,d\},X\}$, $\sigma=\{\phi,\{a\},\{b\},\{a,b\},\{a,c\},\{a,b,c\},\{a,b,d\},X\}$ respectively. Let $f:(X,\tau)\rightarrow(Y,\sigma)$ be an identity map. Then f is not a $\pi g\theta$ -homeomorphism because $f^{-1}(\{c\})=\{c\}$ is not $\pi g\theta$ -closed in Y where $\{c\}$ is closed in X . However f is a $\pi g\alpha$ -homeomorphism.

Example 4.9 Let $X=\{a,b,c,d,e\}=Y$ with topologies $\tau=\{\phi,\{a,b\},\{c,d\},\{a,b,c,d\},X\}$, $\sigma=\{\phi,\{a\},\{b\},\{c\},\{d\},\{a,b\},\{a,c\},\{a,d\},\{b,c\},\{b,d\},\{c,d\},\{a,b,c\},\{a,b,d\},\{a,c,d\},\{b,c,d\},\{a,b,c,d\},\{a,b,c,e\},X\}$ respectively. Let $f:(X,\tau)\rightarrow(Y,\sigma)$ be the identity map. Then f is not a $\pi g\theta$ -homeomorphism because $f^{-1}(\{d\})=\{d\}$ is not $\pi g\theta$ -closed in X where $\{d\}$ is closed in Y . However f is a $\pi g s$ -homeomorphism.

Example 4.10 Let $X=\{a,b,c,d\}=Y$ with topologies $\tau=\{\phi,\{a\},\{b\},\{a,b\},\{a,c\},\{a,b,c\},\{a,b,d\},X\}$, $\sigma=\{\phi,\{a\},\{b\},\{a,b\},\{a,b,c\},\{a,b,d\},X\}$ respectively. Let $f:(X,\tau)\rightarrow(Y,\sigma)$ be the identity map. Then f is not a $\pi g\theta$ -homeomorphism because $f^{-1}(\{c\})=\{c\}$ is not $\pi g\theta$ -closed in X where $\{c\}$ is closed in Y . However f is a $\pi g b$ -homeomorphism.

Example 4.11 Let $X=\{a,b,c,d,e\}=Y$ with topologies $\tau=\{\phi,\{a\},\{b\},\{c\},\{a,b\},\{a,c\},\{b,c\},\{d,e\},\{a,b,c\},\{a,d,e\},\{b,d,e\},\{c,d,e\},\{a,b,d,e\},\{a,c,d,e\},\{b,c,d,e\},X\}$, $\sigma=\{\phi,\{a,b\},\{c,d\},\{a,b,c,d\},X\}$ respectively. Let $f:(X,\tau)\rightarrow(Y,\sigma)$ be the identity map. Then f is not a $\pi g\theta$ -closed map, since $f(\{a,b\})=\{a,b\}$ is not $\pi g\theta$ -closed in (Y,σ) , where $\{a,b\}$ is closed in (X,τ) . However f is a $\pi g p$ -homeomorphism.

Remark 4.12 The following examples show that $\pi g\theta$ -homeomorphism is independent of, g -homeomorphism, sg -homeomorphism, gs -homeomorphism, ag -homeomorphism and $g\alpha$ -homeomorphism.

Example 4.13 Let $X=\{a,b,c,d\}=Y$ with topologies $\tau=\{\phi,\{a\},\{b\},\{c\},\{a,b\},\{a,c\},\{b,c\},\{a,b,c\},\{a,c,d\},X\}$, $\sigma=\{\phi,\{a\},\{a,b\},\{a,c\},\{a,b,c\},\{a,c,d\},X\}$ respectively. Let $f:(X,\tau)\rightarrow(Y,\sigma)$ be the identity map. Then $f(\{a,d\})=\{a,d\}$ is not g -closed in (Y,σ) where $\{a,d\}$ is closed in (X,τ) . However f is a $\pi g\theta$ -homeomorphism.

Example 4.14 Let $X=\{a,b,c,d\}=Y$ with topologies $\tau=\{\phi,\{a\},\{c\},\{a,c\},\{a,b\},\{a,b,c\},\{a,c,d\},X\}$, $\sigma=\{\phi,\{a\},\{a,b\},\{a,c\},\{a,b,c\},\{a,c,d\},X\}$ respectively. Let $f:(X,\tau)\rightarrow(Y,\sigma)$ be the identity map. Then $f^{-1}(\{b\})=\{b\}$ is not $\pi g\theta$ -closed in X , where $\{b\}$ is closed in Y . However f is g -homeomorphism.

Example 4.15 Let $X=\{a,b,c,d,e\}=Y$ with topologies $\tau=\{\phi, \{a\}, \{b\}, \{c\}, \{a,b\}, \{a,c\}, \{b,c\}, \{a,b,c\}, \{a,c,e\}, \{a,b,c,d\}, \{a,b,c,e\}, X\}$, $\sigma=\{\phi, \{e\}, \{a,b,c,d\}, X\}$ respectively. Let $f:(X,\tau)\rightarrow(Y,\sigma)$ be the identity map. Then f is neither αg nor $g\alpha$ -homeomorphisms because $f^{-1}(\{a,b,c,d\})=\{a,b,c,d\}$ is neither αg nor $g\alpha$ -closed in X , where $\{a,b,c,d\}$ is closed in Y . However f is a $\pi g\theta$ -homeomorphism.

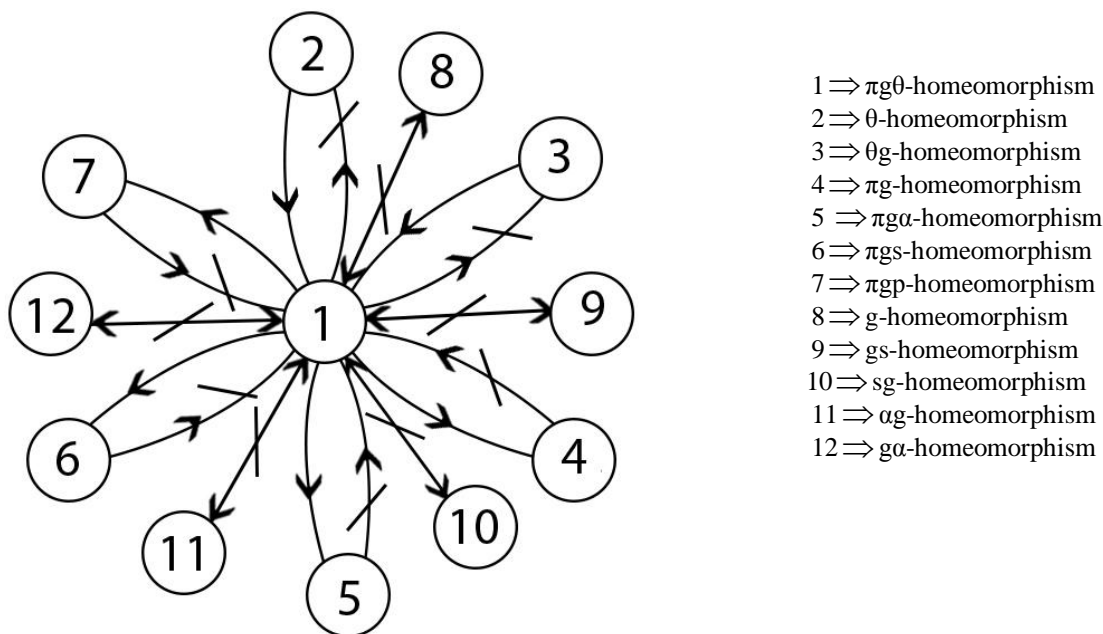
Example 4.16 Let $X=\{a,b,c,d,e\}=Y$ with topologies $\tau=\{\phi, \{a,b\}, \{c,d\}, \{a,b,c,d\}, X\}$, $\sigma=\{\phi, \{e\}, \{a,b,c,d\}, X\}$ respectively. Let $f:(X,\tau)\rightarrow(Y,\sigma)$ be the identity map. Then f is not $\pi g\theta$ -homeomorphism because $f^{-1}(\{a,b,c,d\})=\{a,b,c,d\}$ is not $\pi g\theta$ -closed in X , where $\{a,b,c,d\}$ is closed in Y . However f is a $g\alpha$ -homeomorphism.

Example 4.17 Let $X=\{a,b,c,d\}=Y$ with topologies $\tau=\{\phi, \{a\}, \{b\}, \{c\}, \{a,b\}, \{a,c\}, \{b,c\}, \{a,b,c\}, \{a,b,d\}, X\}$, $\sigma=\{\phi, \{a\}, \{b\}, \{a,b\}, \{a,c\}, \{a,b,c\}, \{a,b,d\}, X\}$ respectively. Let $f:(X,\tau)\rightarrow(Y,\sigma)$ be the identity map. Then f is not $\pi g\theta$ -homeomorphism because $f(\{c\})=\{c\}$ is not $\pi g\theta$ -closed in X , where $\{c\}$ is closed in Y . However f is a αg -homeomorphism.

Example 4.18 Let $X=\{a,b,c,d\}=Y$ with topologies $\tau=\{\phi, \{a\}, \{b\}, \{c\}, \{a,b\}, \{a,c\}, \{b,c\}, \{a,b,c\}, \{a,c,d\}, X\}$, $\sigma=\{\phi, \{a\}, \{a,b\}, \{a,c\}, \{a,b,c\}, \{a,c,d\}, X\}$ respectively. Let $f:(X,\tau)\rightarrow(Y,\sigma)$ be the identity map. Then f is neither sg nor gs -homeomorphism because $f(\{a,d\})=\{a,d\}$ is neither sg nor gs -closed in Y , where $\{a,d\}$ is closed in X . However f is a $\pi g\theta$ -homeomorphism.

Example 4.19 Let $X=\{a,b,c,d\}=Y$ with topologies $\tau=\{\phi, \{a\}, \{b\}, \{c\}, \{a,b\}, \{a,c\}, \{b,c\}, \{a,b,c\}, X\}$, $\sigma=\{\phi, \{a\}, \{b\}, \{c\}, \{a,b\}, \{a,c\}, \{b,c\}, \{a,b,c\}, \{a,c,d\}, X\}$, resp. Let $f:(X,\tau)\rightarrow(Y,\sigma)$ be the identity map. Then f is not a $\pi g\theta$ -homeomorphism because $f^{-1}(\{b\})=\{b\}$ is not $\pi g\theta$ -closed in X , where $\{b\}$ is closed in Y . However f is both sg and gs -homeomorphisms.

Remark 4.20 The above discussions are summarized in the following diagram.



Remark 4.21 Composition of two $\pi g\theta$ -homeomorphism need not be a $\pi g\theta$ -homeomorphism as shown in the following example.

Example 4.22 Let $X=Y=Z=\{a,b,c,d,e\}$. Let $f:(X,\tau)\rightarrow(Y,\sigma)$ and $g:(Y,\sigma)\rightarrow(Z,\eta)$ be two identity maps. $\tau=\{\phi, \{e\}, \{a,b,c,d\}, X\}$, $\sigma=\{\phi, \{b\}, \{c\}, \{b,c\}, \{a,b\}, \{a,b,c\}, X\}$ and $\eta=\{\phi, \{a,b\}, \{c,d\}, \{a,b,c,d\}, X\}$ be their topologies. Then $(g\circ f)[\{e\}]=\{e\}$ is open in X , but not $\pi g\theta$ -open in Z . This implies that $g\circ f$ is not $\pi g\theta$ -open and hence $g\circ f$ is not $\pi g\theta$ -homeomorphism.

Proposition 4.23 For any bijective map $f:(X,\tau)\rightarrow(Y,\sigma)$ the following statements are equivalent.

- (a) $f^{-1}:(Y,\sigma)\rightarrow(X,\tau)$ is $\pi g\theta$ -continuous map.
- (b) f is a $\pi g\theta$ -open map.
- (c) f is a $\pi g\theta$ -closed map.

Proof: (a) \Rightarrow (b): Let U be an open set in (X,τ) . Then $X - U$ is closed in (X,τ) . Since f^{-1} is $\pi g\theta$ -continuous $(f^{-1})^{-1}(X - U)$ is $\pi g\theta$ -closed in (Y,σ) . That is $f(X - U) = Y - f(U)$ is $\pi g\theta$ -closed in (Y,σ) . This implies $f(U)$ is $\pi g\theta$ -open in (Y,σ) . Hence f is $\pi g\theta$ -open map.

(b) \Rightarrow (c): Let V be a closed set in (X,τ) . Then $X - V$ is open in (X,τ) . Since f is $\pi g\theta$ -open, $f(X - V)$ is $\pi g\theta$ -open in (Y,σ) . That is $Y - f(V)$ is $\pi g\theta$ -open in (Y,σ) . This implies $f(V)$ is $\pi g\theta$ -closed in (Y,σ) . Hence f is $\pi g\theta$ -closed map.

(c) \Rightarrow (a): Let U be closed set in (X,τ) . Since f is $\pi g\theta$ -closed map, $f(U)$ is $\pi g\theta$ -closed in (Y,σ) . That is $(f^{-1})^{-1}(U)$ is $\pi g\theta$ -closed in (Y,σ) . Hence f^{-1} is $\pi g\theta$ -continuous.

Proposition 4.24 Let $f:(X,\tau)\rightarrow(Y,\sigma)$ be a bijective and $\pi g\theta$ -continuous map. Then the following statements are equivalent.

- (a) f is a $\pi g\theta$ -open map.
- (b) f is a $\pi g\theta$ -homeomorphism.
- (c) f is a $\pi g\theta$ -closed map.

Proof: Straight forward.

Remark 4.25 $\pi g\theta c$ -homeomorphism is independent of a $\pi g\theta$ -homeomorphism as seen in the following examples.

Example 4.26 Let $X=\{a,b,c,d,e\}=Y$ with topologies $\tau=\{\phi,\{a,b\},\{c,d\},\{a,b,c,d\},X\}$, $\sigma=\{\phi,\{b\},\{c\},\{b,c\},\{a,b\},\{a,b,c\},X\}$ respectively. Let $f:(X,\tau)\rightarrow(Y,\sigma)$ be the identity map. Then f is not $\pi g\theta$ -irresolute, because $f^{-1}(\{d\})=\{d\}$ is not $\pi g\theta$ -closed in X where $\{d\}$ is $\pi g\theta$ -closed in Y . However f is $\pi g\theta$ -homeomorphism.

Example 4.27 Let $X=\{a,b,c,d\}=Y$ with topologies $\tau=\{\phi,\{a\},\{b\},\{c\},\{a,b\},\{a,c\},\{b,c\},\{a,b,c\},X\}$, $\sigma=\{\phi,\{a\},\{b\},\{c\},\{a,b\},\{a,c\},\{b,c\},\{a,d\},\{a,b,c\},\{a,b,d\},\{a,c,d\},X\}$ respectively. Let $f:(X,\tau)\rightarrow(Y,\sigma)$ be the identity map. Then f is not $\pi g\theta$ -continuous, because $f^{-1}(\{b\})=\{b\}$ is not $\pi g\theta$ -closed in Y where $\{d\}$ is closed in Y . However f is $\pi g\theta c$ -homeomorphism.

Proposition 4.28 If $f:(X,\tau)\rightarrow(Y,\sigma)$ and $g:(Y,\sigma)\rightarrow(Z,\eta)$ are $\pi g\theta c$ -homeomorphisms, then $g\circ f:(X,\tau)\rightarrow(Z,\eta)$ is also a $\pi g\theta c$ -homeomorphism.

Proof: Let U be a $\pi g\theta$ -open set in (Z,η) . Now $(g\circ f)^{-1}(U)=f^{-1}(g^{-1}(U))=f^{-1}(V)$ where $g^{-1}(U)=V$. By hypothesis, V is $\pi g\theta$ -open in (Y,σ) and again by hypothesis, $f^{-1}(V)$ is $\pi g\theta$ -open in (X,τ) . Therefore $(g\circ f)$ is $\pi g\theta$ -irresolute. Also for a $\pi g\theta$ -open set A in (X,τ) , we have $(g\circ f)(A)=g(f(A))=g(W)$ where $W=f(A)$. By hypothesis, $f(A)$ is $\pi g\theta$ -open in (Y,σ) and again by hypothesis. Therefore, $g(A)$ is $\pi g\theta$ -open in (Z,η) . Now $(g\circ f)^{-1}$ is $\pi g\theta$ -irresolute. Hence $(g\circ f)$ is a $\pi g\theta c$ -homeomorphism.

Proposition 4.29 The set $\pi g\theta ch(X,\tau)$ is a group.

Proof: Define $\psi:\pi g\theta ch(X,\tau) \times \pi g\theta ch(X,\tau)\rightarrow\pi g\theta ch(X,\tau)$ by $\psi(f,g)=g\circ f$ for every $f,g\in\pi g\theta ch(X,\tau)$. Then by proposition 4.28, $(g\circ f)\in\pi g\theta ch(X,\tau)$. Hence $\pi g\theta ch(X,\tau)$ is closed. We know that the composition of maps is associative. The identity map $i:(X,\tau)\rightarrow(X,\tau)$ is $\pi g\theta c$ -homeomorphism and $i\in\pi g\theta ch(X,\tau)$. Also $iof=foi=f$ for every $f\in\pi g\theta ch(X,\tau)$. For any $f\in\pi g\theta ch(X,\tau)$, $fof^{-1}=i$. Hence inverse exists for each element of $\pi g\theta ch(X,\tau)$. Thus $\pi g\theta ch(X,\tau)$ is a group under composition of maps.

Proposition 4.30 Every $\pi g\theta$ -homeomorphism from a $\pi g\theta$ - $T_{1/2}$ -space into another $\pi g\theta$ - $T_{1/2}$ -space is a θ -homeomorphism.

Proof: Let $f:(X,\tau)\rightarrow(Y,\sigma)$ be a $\pi g\theta$ -homeomorphism. Then f is bijective, $\pi g\theta$ -continuous and $\pi g\theta$ -open. Let U be an open set in X . Since f is $\pi g\theta$ -open, $f(U)$ is $\pi g\theta$ -open in Y . Since (Y,σ) is a $\pi g\theta$ - $T_{1/2}$ -space, $f(U)$ is θ -open in (Y,σ) . This implies f is a θ -open map. Let V be closed in (Y,σ) . Since f is $\pi g\theta$ -continuous and since (X,τ) is a $\pi g\theta$ - $T_{1/2}$ -space, $f^{-1}(V)$ is θ -closed in (X,τ) . Therefore f is θ -continuous. Hence f is a θ -homeomorphism.

Definition 4.31 A space X is called $\pi g\theta$ -space if every $\pi g\theta$ -closed set is closed.

Proposition 4.32 Every $\pi g\theta$ -homeomorphism from a $\pi g\theta$ -space into another $\pi g\theta$ -space is a $\pi g\theta c$ -homeomorphism.

Proof: Let $f: (X, \tau) \rightarrow (Y, \sigma)$ be a $\pi g\theta$ -homeomorphism. Then f is bijective, $\pi g\theta$ -continuous and $\pi g\theta$ -open. Let V be a $\pi g\theta$ -closed set in (Y, σ) . Then V is closed in (Y, σ) . Since f is $\pi g\theta$ -continuous, $f^{-1}(V)$ is $\pi g\theta$ -closed in (X, τ) . Hence f is a $\pi g\theta$ -irresolute map. Let V be $\pi g\theta$ -open in (X, τ) . Then V is open in (X, τ) . Since f is $\pi g\theta$ -open, $f(V)$ is $\pi g\theta$ -open in (Y, σ) . That is $(f^{-1})^{-1}(V)$ is $\pi g\theta$ -open in (Y, σ) and hence f^{-1} is $\pi g\theta$ -irresolute. Thus f is $\pi g\theta c$ -homeomorphism.

V. Conclusion

This paper has attempted to compare $\pi g\theta$ -homeomorphism with the other homeomorphisms in topological spaces. It also states that the several definitions and results in this paper will result in obtaining several characterizations and also enable to study various properties. The future scope of study is the extension of $\pi g\theta$ -closed maps and $\pi g\theta$ -continuous maps in topological spaces.

REFERENCES

- [1] M. Anandhi and C. Janaki: On $\pi g\theta$ -Closed sets in Topological spaces, International Journal of Mathematical Archive-3(11), 2012, 3941-3946.
- [2] D. Andrijevic, Semi preopen sets, Mat. Vesnik 38 (1986), 24-32.
- [3] I. Arockiarani, Studies on Generalizations of Generalized Closed Sets and Maps in topological Spaces, Ph.D thesis, Bharathiar University, Coimbatore (1997).
- [4] S. P. Arya and T. M. Nour, Characteristics of s-normal spaces, Indian J. Pure. Appl. Math., 21(8) (1990), 717-719.
- [5] G. Aslim, A. Caksu Guler and T. Noiri, On $\pi g s$ -closed sets in topological spaces, Acta Math. Hungar., 112 (4) (2006), 275-283.
- [6] P. Bhattacharya and B. K. Lahiri, Semi-generalized closed sets in topology, Indian J. Math., 29 (3) (1987), 375-382.
- [7] K. Balachandran, P. Sundaram, H. Maki, On Generalized continuous maps in topological spaces, Mem. Fac. Sci. Kochi Univ. Ser. A Math., 12(1991), 5-13.
- [8] R. Devi, H. Maki and K. Balachandran: Semi-generalised closed maps and generalized semi-closed maps, Mem. Fac. Sci. Kochi Univ. Ser. A Math., 14(1993), 41-54.
- [9] R. Devi, H. Maki and K. Balachandran: Semi-generalised homeomorphisms and generalized semi-homeomorphisms, Indian J. Pure. Appl. Math., 26(3)(1995), 271-284.
- [10] J. Dontchev, On generalizing semi-pre open sets, Mem. Fac. Sci. Kochi Univ. Ser. A Math. 16 (1995), 35-48.
- [11] J. Dontchev and H. Maki, On θ -generalized closed sets, International J. Math. and Math. Sci. 22(2) (1999) 239-249.
- [12] J. Dontchev and T. Noiri, Quasi Normal Spaces and πg -closed sets, Acta Math. Hungar., 89(3)(2000), 211-219.
- [13] E. Ekici and M. Caldas, Slightly-continuous functions, Bol. Soc. Parana. Mat. (3) 22 (2004), 63-74.
- [14] Govindappa Navalagi and Md. Hanif Page, θ -generalized semi-open and θ -generalized semi-closed functions Proyecciones J. of Math. 28,2,(2009) 111-123.
- [15] C. Janaki, Studies on $\pi g\alpha$ -closed sets in Topology, Ph.D Thesis, Bharathiar University, Coimbatore (2009).
- [16] N. Levine, Semi-open sets and semi-continuity in topological spaces, Amer. Math. Monthly 70 (1963), 36-41.
- [17] N. Levine, Generalized closed sets in topology, Rend. Circ. Mat. Palermo (2) 19 (1970), 89-96.
- [18] H. Maki, R. Devi and K. Balachandran, Associated topologies of generalized α -closed sets and α -generalized closed sets, Mem. Fac. Sci. Kochi Univ. Ser. A Math., 15 (1994), 51-63.
- [19] H. Maki, R. Devi and K. Balachandran: Generalised α -closed maps and α -generalized-closed maps, Indian J. Pure. Appl. Math., 29(1)(1998), 37-49.
- [20] H. Maki, P. Sundaram and K. Balachandran: On Generalized homeomorphisms in topological spaces. Bulletin of Fukuoka Uni. Of Edn. Vol. 40, Part III, (1991), 13-21.
- [21] A. S. Mashhour, M. E. Abd El-Monsef and S. N. El-Deep, On pre continuous and weak pre continuous mappings, Proc. Math. Phys. Soc. Egypt No. 53 (1982), 47-53.
- [22] O. Njastad, On some classes of nearly open sets, Pacific J. Math. 15(1965), 961-970.
- [23] T. Noiri, A note on θ -irresolute functions in the sense of Park, Indian J. Pure Appl. Math. 31 (4) (2000), 449-450.
- [24] J. H. Park, On $\pi g p$ -closed sets in topological spaces, Indian J. Pure. Appl. Math., (To appear).
- [25] D. Sreeja and C. Janaki, On $\pi g b$ -closed sets in Topological Spaces, Inter. J. of Math. Archive, 2(8), (2011), 1314-1320.
- [26] M. H. Stone: Application of the theory of Boolean rings to general topology, Trans. Amer. Math. Soc., 41 (1937), 375-381.
- [27] N. V. Velicko, On H-closed topological spaces, Amer. Math. Soc. Transl., 78, (1968) 103-118.
- [28] V. Zaitsev, On certain classes of topological spaces and their bicompaifications, Dold. Akad. Nauk SSSR, 178 (1968), 778-779.

Optimization of *Corynebacterium glutamicum* Immobilization on Alginate and Investigation into its Storage Conditions

Tran Thi Minh Tam¹, Nguyen Thuy Huong²

^{1,2} Department of Biotechnology, Ho Chi Minh City University of Technology, Vietnam

Abstract: The parameters of the immobilized process of *Corynebacterium glutamicum* VTCC – B – 0632 on alginate were identified by Plackett-Burman matrix, and the experiments were designed by response surface methodology having the central composite designs (RSM-CCD). The maximum yield of cell immobilization on alginate carrier reached at 92.6%. Optimal parameters were the cell density of 89.3 million cells/mL in the 4% sterile alginate with ratio 1:1. This mixture went through the syringe system of the 2M CaCl₂ solution at 20⁰C with the shaking speed of 75 rpm until the gels get in shape. Then, these gels were soaked in the CaCl₂ liquor and shaken for 41 minutes (150 rpm). At last, the particle size of final products was 4mm and the average cell density was 14.75 million cells/gram. This immobile product is maintained under the suitable condition in the CaCl₂ liquor (w/v), pH=7. The cell survival percentage after 72 hours were 98% when it was stored in 4⁰C, 0.5% CaCl₂ and pH of 7.

Keywords: *Corynebacterium glutamicum*, alginate, entrapment, micro-entrapment, Plackett-Burman, Response Surface Methods, Central Composite Designs.

I. INTRODUCTION

Alginate is the natural polysaccharide extracted from the brown alga (*Phaeophyce*) which is discovered in the shallow water in the temperate zones. The viscosity of alginate depends on derivation of the alga, its molecular weight, temperature and pH of the liquor [1]. Under controlled conditions, alginate can create the gels in the liquor containing the II valence cations [2]. The cation Ca²⁺ is often used to immobilize cells because of its low toxicity. The capability of creating gels of alginate mainly relates to acid guluronic. The divalent cations linked with the G mass to make “an egg box” form that it is more solid than the M one [2].

Alginate is used as a carrier in the enzyme immobilization technology and it is developed into the traditional carrier in the cell immobilization technology, especially in the cell of micro-organism one. The cell immobilization in alginate carrier method which is usually used is the entrapment, in micro-encapsulation, creating cross linking [3].

Corynebacterium glutamicum is the viscous membrane bacterium, able to hold on the carrier and together. Therefore, we can use it to study the cell immobilization on some suitable carriers. The *Corynebacterium glutamicum* immobilization process is carried out by the hole trapping technology [4]. L-Lysine is an essential amino acid which cannot be synthesized by human being and animals. The too much amylaceous diets of the agricultural nations lead to the loss of this substance in the body. The L-Lysine is received from *Corynebacterium glutamicum* which can be applied in a few factories all over the world. One of solutions to upgrade the productivity of the L-Lysine is using immobilized *Corynebacterium glutamicum* cells on some carriers. *Corynebacterium glutamicum* is immobilized on alginate by entrapment methods. It is based on the inclusion of cells within a rigid network to prevent the cells from diffusing into the surrounding medium, while still allowing mass transfer of nutrients and metabolites [3]. L-lysine production using immobilized *Corynebacterium glutamicum* cells on alginate in fermentation process seems to be very promising. The advantages of this production process is that time, effort and expense are minimized during preparation period for the breed before fermenting. Consequently, efficiency of the Lysine fermentation is improved. However, application of immobilized *Corynebacterium glutamicum* in L-lysine fermentation still pointed out some disadvantages like physical carriers in fermentation medium or the ability of enzyme activity. It is one of some important reasons to study immobilization of cells [3].

II. THE MATERIALS AND METHODS

2.1 The materials and cultural medium

The micro-organism species: *Corynebacterium glutamicum* VTCC – B – 0632 is provided by the Vietnam Type Culture Collection.

The carrier: the utilized alginate is provided by the producer Sigma – Ahdrich. Alginate is powdery, light brown and its moisture content is below 15%. The 1% alginate solution is prepared and kept at 25°C. Its viscosity is 5-40 Cps and pH is from 5 to 8.

The cultural medium: *Corynebacterium glutamicum* grows in the minimal medium with glucose (20g/L), peptone (10g/L), yeast extract (5g/L), NaCl (5g/L), agar (15g/L), pH ~ 7.2, the temperature at 30°C, the agitation rate of 150 rpm [5].

2.2. Optimizing the *Corynebacterium glutamicum* immobilization process on Alginate

The inoculums were introduced in seed culture and were incubated in a rotary shaker at 120 rpm, 30°C. After 16 hours, the number of the cells was checked and counted and then the necessary breed density was predicted for the immobilization process with 100 mL breed liquor and alginate. Seven factors were examined in the Plackett-Burman matrix with different 12 runs. Determine the immobilization productivity for each validation formula. Analyze the factors that affect the productivity. The main factors had the value of $p < 0.05$. With the selected factors, we carried out the first experiments with the original values (+1, -1). After analyzing the initial experiments, we determined whether the factors having great impacts on the high regression equation suitably or not. Based on that, we conducted the experiments for response surface methodology having the central composite designs (RMS-CCD) and determined function of the polynomial regression accurately to describe relations between the immobilization yield and factors having great impacts on the hole trapping method.

2.3. The survey of the conditions to maintain the immobile *Corynebacterium glutamicum* final products on alginate

The aim is to determine the appropriate conditions to store the immobile *Corynebacterium glutamicum* products. We start to soak the products in some different pH liquors at different temperatures. The major function is the survival percentage of *Corynebacterium glutamicum* after 72 hours storing according to the validation formula laid out (Table 1).

Table 1. Set up the survey experiment of the conditions

Runs	Changeable factors	Fixed factors
1	The liquor to soak (aseptic water-CaCl ₂ (g/L): 0.5 – 1.0 – 2.0 – 3.0)	-The weight of immobile bacterium: 10 gram -The maintaining temperature: 4°C -pH of the liquor: 7
2	pH of the solvent: 4 – 5 – 6 – 7 – 8	-The weight of immobile bacterium: 10 gram -The maintaining temperature: 4°C -The solvent to soak the finished product: chosen in the experiment 1
3	The maintaining temperature (°C): 0 – 4 – 10 – 15 – 20 – 30	-The weight of immobile bacterium: 10 gram -The solvent to soak the finished product: chosen in the experiment 1 -The pH of the liquor: chosen in the experiment 2

2.4 The analyzing method

Analyzing the immobilized finished products: the immobilized *Corynebacterium glutamicum* on alginate is soaked in the sodium citrate in order to break the gels totally, and then release micro-organisms. After diluting the liquid medium, inoculums were spread over surface of culture medium, and then the colonies were counted after 24 hours brewing.

Formula:

$$\text{The immobilization yield: } H = \frac{\text{the immobilized cells in alginate}}{\text{the number of cells added}} \cdot 100 (\%)$$

$$\text{The average cell density: } \frac{\text{the number of immobile cells in alginate}}{\text{the weight of the finished product}} \text{ (millions cells/g)}$$

III. RESULTS

3.1. Optimizing the parameters to immobilize *Corynebacterium glutamicum* on the alginate carrier:

We analyzed the efficiency of the selecting experiments and determine the degree of these factors' impact in the fluctuation range according to different levels (Table 2). The change of the impacted levels of 2 among 7 surveyed factors has a noticeable influence on the immobilization yield of *Corynebacterium glutamicum* on the alginate carrier by the hole trapping method. Those are the density of immobilized cell suspension (X_2) and the soaking duration in CaCl_2 (X_7). The polynomial regression is determined according to the simple function as given below:

$$H = 61.8 - 17.69 x_2 - 13.62 x_7 \quad (3.1)$$

Table 2. The factors in the Plackett-Burman matrix experiments

Names of the factors	Symbols of the factors	The levels			Main effect	The p value
		Low (-1)	Medium(0)	High (+1)		
The weight of particle carriers (%)	X_1	3	4	5	+ 3.53	0.699
The density of biomass (million cells/mL)	X_2	100	200	300	-35.38	0.014
The concentration of CaCl_2 (M)	X_3	1	2	3	-3.56	0.696
The temperature to form gels ($^{\circ}\text{C}$)	X_4	15	20	25	+14.25	0.168
The shaking speed to form particles (rpm)	X_5	50	75	100	-11.46	0.248
The speed when soaking particles (rpm)	X_6	100	150	200	+10.05	0.301
The soaking duration (minutes)	X_7	60	120	180	-27.25	0.032
R-sq = 89.51%; $p < 0.05$ was considered significant						

The two factors, X_2 and X_7 , suit the model of (3.1) 89.51%. This is acceptable. We went on conducting 9 experiments, 4 of them are (-1, 1) ones and 5 are the central ones. ANOVA was carried out to statistically analyze the correlation of immobilization efficiency to the two selected factors. The p-value of Lack-of-fit test was 0.849 and R-sq was 99.67 %. This means that the arrangement of the two big effect factors (Table 2) is far away from the extreme of the aimed function. To define the extreme zone, it is necessary to carry out the path of steepest ascent experiments (Table 3).

Table 3. The Path of steepest ascent extreme zone experiments

Runs	X_1	X_2	X_3	X_4	X_5	X_6	X_7	H (%)
1	4	94.3	2	20	75	150	50	91.23
2	4	88.6	2	20	75	150	40	92.6
3	4	82.9	2	20	75	150	30	89.79
4	4	77.2	2	20	75	150	20	89.29
5	4	71.5	2	20	75	150	10	89.27
6	4	65.8	2	20	75	150	0	88.64

The Path of steepest ascent extreme zone experiments was aimed to define the extreme zone of the yield of cell immobilization. The second experiment was chosen as a central degree. At this, the highest yield of all experiments was obtained. To establish the right relationship between X_2 and X_7 , we analyzed the 13 RMS-CCD experiments showed by the polynomial regression equation 3.2 (R-sq = 85.35%):

$$H = 92.6 - 0.452 x_2 + 0.325 x_7 + 0.355 x_2 x_7 - 1.912 x_2^2 - 1.437 x_7^2 \quad (3.2)$$

The maximum immobilization yield of *Corynebacterium glutamicum* on alginate was 92.65 % when the density of the added cells was 89.3 million cells/ mL, the soaking duration in CaCl_2 was 41 minutes, the concentration of utilized alginate is 4% (w/v), 2M CaCl_2 , the temperature is 20°C , the agitation rate to form gels is 75 rpm, the agitation rate when soaking is 150 rpm. The particle-shaped finished product has the diameter of 4 ± 0.2 mm and the cell density of 14.75 ± 0.053 million cells/g of finished product.

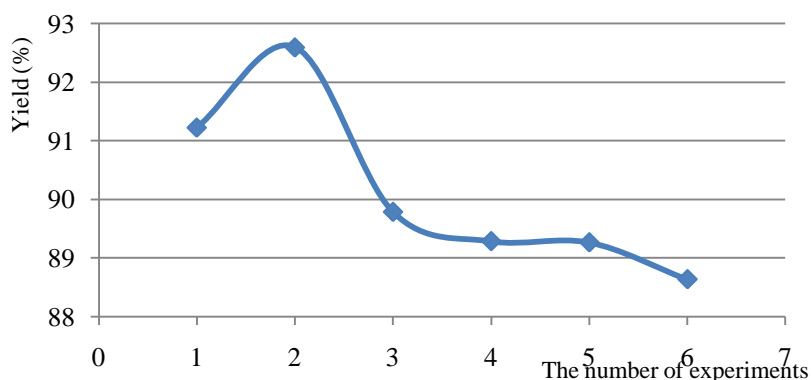


Figure 1. The Path of steepest ascent extreme zone chart

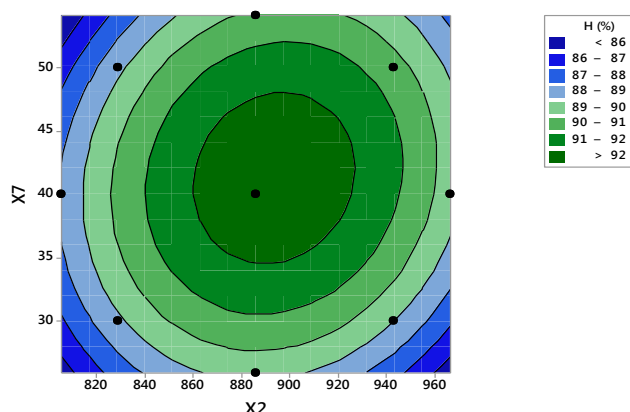


Figure 2. The equation contours (3.2) show the relationship between H (%) and X₂, X₇

3.2. Examination the storage conditions

We chose the round products with no bubbles which are achieved from the optimizing process. We took them to examine. The validation formulas examined use 20 ± 0.2 g of products in 50 mL of solvent.

3.2.1 The influence of the maintaining solvents

We analyzed the finished products of 5 validation formulas to examine the two solvents: water and CaCl₂ liquor (0.5-1.0-2.0-3.0%). We determined the cell survival percentage after 72 hours maintaining under the 4°C condition.

Table 4. The survival percentage of cells at different solvents

The survival cell rate after 72-hour incubation (%)	Sterile water	CaCl ₂ 0.5%	CaCl ₂ 1.0%	CaCl ₂ 2.0%	CaCl ₂ 3.0 %
	67.31 ± 7.87 ^a	94.8 ± 4.64 ^b	90.15 ± 1.05 ^c	83.64 ± 2.35 ^d	68.95 ± 0.45 ^a
	Data presented as mean ± standard deviation The values with the same symbols are not different from the meaning $p < 0.05$; the values with different symbols are different from the meaning of $p < 0.05$				

CaCl₂ was the solvent to maintain the immobile final product *Corynebacterium glutamicum* on alginate better than distilled water. The cell survival percentage after 72 hours was higher 68% and higher than in distilled water (67.3%). Especially, the 0.5% CaCl₂ solution (w/v) had the highest percentage (94.8%). This concentration was used for the next experiments.

3.2.2 The influence of pH

The validation formulas examined the change of pH (4-5-6-7-8) of the 0.5 % CaCl₂ solvent and adjusted by HCl 1N and 25% NH₃ solution, we examined the survival percentage of cells after 72 hours at 4°C.

Table 5. The survival percentage of immobile cells at the different pH

The survival cell rate after 72-hour incubation (%)	pH=4	pH=5	pH=6	pH=7	pH=8
	65.58 ± 2.31 ^a	66.20 ± 2.40 ^a	75.49 ± 2.93 ^b	95.29 ± 3.66 ^c	83.36 ± 3.29 ^d
	Data presented as mean ± standard deviation The values with the same symbols are not different from the meaning $p < 0.05$; the values with different symbols are different from the meaning of $p < 0.05$				

In the limit of pH from 4 to 7, the survival cell rate increases. If we continue to raise the pH to 8, the percentage decreases less 12% than that of pH of 7. At the pH of 7, the survival rate was maximum with the value of 7. The pH of 7 is used to examine the influence of temperature that was used to maintain the finished product.

3.2.3 The influence of temperature

Examine the change of the temperatures that was used to store the final product from 0 to 40°C. Determine the immobilized cell survival percent after 72 hours soaking in 0.5% CaCl₂ solution, pH = 7.

Table 6. The survival cell percent at different maintaining temperatures

The survival cell percentage after 72-hour incubation (%)	0°C	4°C	10°C	20°C	30°C	40°C
	50.37 ± 0.14 ^a	98.31 ± 0.31 ^b	82.24 ± 0.09 ^c	87.91 ± 0.13 ^d	86.09 ± 0.26 ^d	27.35 ± 0.09 ^e
Data presented as mean ± standard deviation The values with the same symbols are not different from the meaning p<0.05; the values with different symbols are different from the meaning of p<0.05						

The cell survival percentage is the lowest one when the temperature is bad for the cells' survival, this percent gets minimum at 40°C (27%). In the limit of 4°C-30°C, the survival percentage is 82% or higher. The percentage is the highest one when we maintain the finished product at 4°C (98%).

IV. DISCUSSION

4.1 The optimizing parameters for the cell *Corynebacterium glutamicum* immobilization on alginate carrier process by entrapment method

The hole trapping technology is also called the outside forming gel. Guisan (2006) assumed that under the Ca²⁺ ion condition, the above surface of alginate immediately caused gels. After that, the Ca²⁺ ions diffused into alginate particles. This made the alginate ones inside become gels and form the network button links [3,6]. The gels were continuously soaked in the Ca²⁺ for a while to make the structures stable before it was used in the fermentation process [3]. According to Gordon F. Bickerstaff (1997), the alginate concentration did not affect the shape and the size of gels but it led solid state. When we increased the alginate concentration, the gel networks in the outside surface became dense. This increased the solid state of gels but decreased the cell metabolism [3]. Moreover, Gordon (1997), Guisan (2006) and Morch (2006) claimed that the gels got more solid when the concentration of Ca²⁺ ions was increased. However, the growth of the cells could be affected by too high concentration [3, 7]. As regards the physical space, the each gel hole had a certain size, so it contained a certain number of cells. Therefore, original suitably adjusted density of cells was able to make the immobilization efficiency maximum. Kourkoutas (2004) claimed that the large density of cells among the mesh fabrics of the linking networks blocked the polymer circuit shrinking and reduce the solid state of the whole gene mass [8].

4.2. The storage condition

The *Corynebacterium glutamicum* immobilized products on alginate has the growth that is nearly same as the *Corynebacterium glutamicum* free cells. The only difference is that disadvantages of the stored condition can be reduced by the assistance of the immobilized carrier. The examination of stored condition is based on the growth limit of *Corynebacterium glutamicum* and the condition to firm the structure of alginate gel. Morch (2006) assumed that Ca²⁺ ions had ability to firm the structure and maintain pH of solvents stably during the store process as well as the fermentation process. Thus, calcium chloride is the chosen solvent that is used to store the final products [7]. Nevertheless, too high concentration of salt in the solvent affects the damage of the membrane of *Corynebacterium glutamicum* [9]. Kourhoutas (2004) recognized that if the pH was not suitable, the solid state of gels would be decreased. However, as mentioned by Eggeling (2003), the gel structure was not affected when pH was in range 4-10, this change affected the existence of *Corynebacterium glutamicum*. He also claimed that these bacteria grew stably at the neutral pH [5]. According to Ohnishi (2003), the suitable limit of temperature for the growth of *Corynebacterium glutamicum* was from 20-40°C [10]. The cells were able to grow within this temperature range. During cell growth, the rapidly increasing number of gels will block the formation of Ca²⁺ and the carboxyl dyads of the alginate molecules in the gel making process. As a result, the stability of gel structures goes down and the cells get out of the easily in store process [3]. Besides, during cell growth, CO₂ is released and break the gel structures [11].

V. CONCLUSION

The maximum yield of the *Corynebacterium glutamicum* immobilization on alginate process is 92.6%. The cells have density of 83.9 million cells/mL mixed in 4g of sterile alginate to get the volume of 100 ml. Let this mixture go through the syringe system of 2M CaCl_2 at 20°C and the agitation rate of 75 rpm until the gel shape is totally created. Continue to soak these gels in CaCl_2 2M in 41 minutes with the agitation rate of 150 rpm. The obtained result is that the final products have particle shape with 4 mm in diameter and the cell density is 14.75 million cells/g. Final product is soaked in 0.5% CaCl_2 solvent (w/v), pH = 7 and then kept at 4°C. After 72h, the percentage of cell survival is 98%. The immobilized *Corynebacterium glutamicum* final product on alginate is used as a method to upgrade the efficiency of ferment to create L-Lysine amino acid.

Acknowledgements

We would like to fully appreciate the help of the teachers/professors in the Chemistry Faculty of Ho Chi Minh City University of Technology in this study.

REFERENCES

- [1] Clayton, H., et al., The effect of capsule composition on the biocompatibility of alginate-poly-L-lysine capsules, *Journal of microencapsulation*, 8(2), 1991, 221-233.
- [2] Smidsrod, O., Molecular basis for some physical properties of alginates in the gel state, *Faraday discussions of the Chemical Society*, 57, 1974, 263-274.
- [3] Guisan, J.M., *Immobilization of enzymes and cells* (Springer, 2006).
- [4] Dautzenberg, H., et al., Development of Cellulose Sulfate-based Polyelectrolyte Complex Microcapsules for Medical Applications, *Annals of the New York Academy of Sciences*, 75(1), 1999, 46-63.
- [5] Eggeling, L. and M. Bott, *Handbook of Corynebacterium glutamicum* (CRC press, 2010).
- [6] Su, Z., Y. Guo, and Z. Peng, Production of intracellular enzyme by *Corynebacterium glutamicum* T6-13 protoplasts immobilized in Ca-alginate gels, *Enzyme and microbial technology*, 15(9), 1993, 791-795.
- [7] Morch, Y.A., et al., Effect of Ca^{2+} , Ba^{2+} , and Sr^{2+} on alginate microbeads, *Biomacromolecules*, 7(5), 2006, 1471-1480.
- [8] Kourkoutas, Y., et al., Immobilization technologies and support materials suitable in alcohol beverages production: a review, *Food Microbiology*, 21(4), 2004, 377-397.
- [9] Bayan, N., et al., Mycomembrane and S-layer: two important structures of *Corynebacterium glutamicum* cell envelope with promising biotechnology applications, *Journal of biotechnology*, 104(1), 2003, 55-67.
- [10] Ohnishi, J., et al., Efficient 40°C fermentation of L-lysine by a new *Corynebacterium glutamicum* mutant developed by genome breeding, *Applied microbiology and biotechnology*, 62(1), 2003, 69-75.
- [11] Rao, B., C.V. Murthy, and A. Swamy, *Studies on Continuous Reactor Kinetics of L-Lysine by Immobilized Corynebacterium glutamicum Cells*, *IUP Journal of Chemical Engineering*, 2011.



International Journal of Modern Engineering Research (IJMER)

Volume : 4 Issue : 7 (Version-4)

ISSN : 2249-6645

July - 2014

Contents :

On Some Integrals of Products of H -Functions <i>Vineeta Malsariya, Yashwant Singh</i>	01-06
Analysis of stiffened plate using FE Approach <i>Anupama B. M, Jayashankar babu B. S</i>	07-12
A review of Carbon Nanotube Reinforced Aluminium Composite and Functionally Graded composites as a Future material for Aerospace <i>Gururaja udupa, S. Shrikantha Rao, K.V. Gangadharan</i>	13-22
An optimised multi value logic cell design with new architecture of many value logic gates <i>Prajiyant Pathak, Puran Gour</i>	23-27
Determination of Stress Intensity Factor for a Crack Emanating From a Rivet Hole and Approaching Another in Curved Sheet <i>Raghavendra. P, Anand. A, S. R. Basavaraddi</i>	28-37
VLSI Design of Fast Addition Using QSD Adder for Better Performance <i>G. Jayaprakash, B. Adinarayana</i>	38-43
Authenticated and unrestricted auditing of big data space on cloud through valid and efficient granular updates <i>Suhas. S, Ramani. S</i>	44-48
A Review of Issues in Photochemical Machining <i>Yadav R. P., Teli S. N</i>	49-53
A Detailed Modeling of a Five Parameters Model for Photovoltaic Modules <i>NouarAoun, Boukheit Nahman, Rachid Chenni, KadaBouchouicha</i>	54-59
Electro Slag Strip Cladding Process <i>Thakare Niraj S, Ram Yadav</i>	60-64

On Some Integrals of Products of \overline{H} -Functions

Vineeta Malsariya¹, Yashwant Singh²

¹ Department of Mathematics, J.J.T. University, Chudela, Jhunjhunu, Rajasthan, India

² Department of Mathematics, Government College, Kaladera, Jaipur, Rajasthan, India

Abstract: The object of the present paper is to evaluate an integral involving products of three \overline{H} -function of different arguments which not only provides us the Laplace transform, Hankel transform ([8], p.3), Meijer's Bessel transform ([8], p.121) and various other integral transforms of the product of two \overline{H} -functions but also generalizes the result given earlier by many writers notably by Bailey ([3], p.38), Meijer ([8], p.422) and Slater ([20], p.54(3.7.2)).

I. Introduction

The \overline{H} -function occurring in the paper will be defined and represented by Inayat-Hussain [12] as follows:

$$\overline{H}_{P,Q}^{M,N}[z] = \overline{H}_{P,Q}^{M,N}\left[z \mid \begin{matrix} (a_j; \alpha_j; A_j)_{1,N}, (a_j; \alpha_j)_{N+1,P} \\ (b_j; \beta_j)_{1,M}, (b_j; \beta_j; B_j)_{M+1,Q} \end{matrix} \right] = \frac{1}{2\pi i} \int_{-i\infty}^{i\infty} \overline{\phi}(\xi) z^\xi d\xi \quad (1.1)$$

$$\text{where } \overline{\phi}(\xi) = \frac{\prod_{j=1}^M \Gamma(b_j - \beta_j \xi) \prod_{j=1}^N \{\Gamma(1 - a_j + \alpha_j \xi)\}^{A_j}}{\prod_{j=M+1}^Q \{\Gamma(1 - b_j + \beta_j \xi)\}^{B_j} \prod_{j=N+1}^P \Gamma(a_j - \alpha_j \xi)} \quad (1.2)$$

Which contains fractional powers of the gamma functions. Here, and throughout the paper $a_j (j = 1, \dots, p)$ and $b_j (j = 1, \dots, Q)$ are complex parameters, $\alpha_j \geq 0 (j = 1, \dots, P)$, $\beta_j \geq 0 (j = 1, \dots, Q)$ (not all zero simultaneously) and exponents $A_j (j = 1, \dots, N)$ and $B_j (j = N + 1, \dots, Q)$ can take on non integer values.

The following sufficient condition for the absolute convergence of the defining integral for the \overline{H} -function given by equation (1.1) have been given by (Buschman and Srivastava[6]).

$$\Omega \equiv \sum_{j=1}^M |\beta_j| + \sum_{j=1}^N |A_j \alpha_j| - \sum_{j=M+1}^Q |\beta_j B_j| - \sum_{j=N+1}^P |\alpha_j| > 0 \quad (1.3)$$

$$\text{and } |\arg(z)| < \frac{1}{2} \pi \Omega \quad (1.4)$$

The behavior of the \overline{H} -function for small values of $|z|$ follows easily from a result recently given by (Rathie [15], p.306, eq.(6.9)).

We have

$$\overline{H}_{P,Q}^{M,N}[z] = O(|z|^\gamma), \gamma = \min_{1 \leq j \leq N} \left[\operatorname{Re} \left(\frac{b_j}{\beta_j} \right) \right], |z| \rightarrow 0 \quad (1.5)$$

If we take $A_j = 1 (j = 1, 2, \dots, N)$, $B_j = 1 (j = M + 1, \dots, Q)$ in (1.1), the function $\overline{H}_{P,Q}^{M,N}[\cdot]$ reduces to the Fox's H -function [9].

The following series representation for the \overline{H} -function will be required in the sequel (see Rathie, [15] pp.305-306, eq.(6.8)):

$$\overline{H}_{P,Q}^{M,N}\left[z \mid \begin{matrix} (a_j, \alpha_j; A_j)_{1,N}, (a_j, \alpha_j)_{N+1,P} \\ (b_j, \beta_j)_{1,M}, (b_j, \beta_j; B_j)_{M+1,Q} \end{matrix} \right] =$$

$$\frac{\sum_{h=1}^M \sum_{r=0}^{\infty} \prod_{\substack{j=1 \\ j \neq h}}^M \Gamma(b_j - \beta_j \xi_{h,r}) \prod_{j=1}^N \left\{ \Gamma(1 - a_j + \alpha_j \xi_{h,r}) \right\}^{A_j} (-1)^r z^{\xi_{h,r}}}{\prod_{j=M+1}^Q \left\{ \Gamma(1 - b_j + \beta_j \xi_{h,r}) \right\}^{B_j} \prod_{j=N+1}^P \Gamma(a_j - \alpha_j \xi_{h,r}) r! \beta_h} \quad (1.6)$$

Where

$$\xi_{h,r} = \frac{(b_h + r)}{\beta_h}.$$

II. The \overline{H} -Function Of Two Variables

The \overline{H} -function of two variables will be defined and represented in the following manner:

$$\begin{aligned} \overline{H}[x, y] &= \overline{H} \left[\begin{matrix} x \\ y \end{matrix} \right] = \overline{H}^{o, n_1; m_2, n_2; m_3, n_2}_{p_1, q_1; p_2, q_2; p_2, q_2} \left[\begin{matrix} x \left| (a_j, \alpha_j; A_j)_{1, p_1}, (c_j, \gamma_j; K_j)_{1, n_2}, (c_j, \gamma_j)_{n_2+1, p_2}, (e_j, E_j; R_j)_{1, n_3}, (e_j, E_j)_{n_3+1, p_3} \right. \\ y \left| (b_j, \beta_j; B_j)_{1, q_1}, (d_j, \delta_j)_{1, m_2}, (d_j, \delta_j; L_j)_{m_2+1, q_2}, (f_j, F_j)_{1, m_3}, (f_j, F_j; S_j)_{m_3+1, q_3} \right. \end{matrix} \right] \\ &= -\frac{1}{4\pi^2} \int_{L_1} \int_{L_2} \phi_1(\xi, \eta) \phi_2(\xi) \phi_3(\eta) x^\xi y^\eta d\xi d\eta \end{aligned} \quad (1.7)$$

Where

$$\phi_1(\xi, \eta) = \frac{\prod_{j=1}^{n_1} \Gamma(1 - a_j + \alpha_j \xi + A_j \eta)}{\prod_{j=n_1+1}^{p_1} \Gamma(a_j - \alpha_j \xi - A_j \eta) \prod_{j=1}^{q_1} \Gamma(1 - b_j + \beta_j \xi + B_j \eta)} \quad (1.8)$$

$$\phi_2(\xi) = \frac{\prod_{j=1}^{n_2} \left\{ \Gamma(1 - c_j + \gamma_j \xi) \right\}^{K_j} \prod_{j=1}^{m_2} \Gamma(d_j - \delta_j \xi)}{\prod_{j=n_2+1}^{p_2} \Gamma(c_j - \gamma_j \xi) \prod_{j=m_2+1}^{q_2} \left\{ \Gamma(1 - d_j + \delta_j \xi) \right\}^{L_j}} \quad (1.9)$$

$$\phi_3(\eta) = \frac{\prod_{j=1}^{n_3} \left\{ \Gamma(1 - e_j + E_j \eta) \right\}^{R_j} \prod_{j=1}^{m_3} \Gamma(f_j - F_j \eta)}{\prod_{j=n_3+1}^{p_3} \Gamma(e_j - E_j \eta) \prod_{j=m_3+1}^{q_3} \left\{ \Gamma(1 - f_j + F_j \eta) \right\}^{S_j}} \quad (1.10)$$

Where x and y are not equal to zero (real or complex), and an empty product is interpreted as unity p_i, q_i, n_i, m_j are non-negative integers such that $0 \leq n_i \leq p_i, 0 \leq m_j \leq q_j (i = 1, 2, 3; j = 2, 3)$. All the $a_j (j = 1, 2, \dots, p_1), b_j (j = 1, 2, \dots, q_1), c_j (j = 1, 2, \dots, p_2), d_j (j = 1, 2, \dots, q_2), e_j (j = 1, 2, \dots, p_3), f_j (j = 1, 2, \dots, q_3)$ are complex parameters. $\gamma_j \geq 0 (j = 1, 2, \dots, p_2), \delta_j \geq 0 (j = 1, 2, \dots, q_2)$ (not all zero simultaneously), similarly $E_j \geq 0 (j = 1, 2, \dots, p_3), F_j \geq 0 (j = 1, 2, \dots, q_3)$ (not all zero simultaneously). The exponents $K_j (j = 1, 2, \dots, n_3), L_j (j = m_2 + 1, \dots, q_2), R_j (j = 1, 2, \dots, n_3), S_j (j = m_3 + 1, \dots, q_3)$ can take on non-negative values.

The contour L_1 is in ξ -plane and runs from $-i\infty$ to $+i\infty$. The poles of $\Gamma(d_j - \delta_j \xi) (j = 1, 2, \dots, m_2)$ lie to the right and the poles of $\Gamma\left\{ (1 - c_j + \gamma_j \xi) \right\}^{K_j} (j = 1, 2, \dots, n_2), \Gamma(1 - a_j + \alpha_j \xi + A_j \eta) (j = 1, 2, \dots, n_1)$ to the left of the contour. For $K_j (j = 1, 2, \dots, n_2)$ not an integer, the poles of gamma functions of the numerator in (1.9) are converted to the branch points.

The contour L_2 is in η -plane and runs from $-i\infty$ to $+i\infty$. The poles of $\Gamma(f_j - F_j\eta)$ ($j=1, 2, \dots, m_3$) lie to the right and the poles of $\Gamma\{(1-e_j + E_j\eta)\}^{R_j}$ ($j=1, 2, \dots, n_3$), $\Gamma(1-a_j + \alpha_j\xi + A_j\eta)$ ($j=1, 2, \dots, n_1$) to the left of the contour. For R_j ($j=1, 2, \dots, n_3$) not an integer, the poles of gamma functions of the numerator in (1.10) are converted to the branch points.

The functions defined in (1.7) is an analytic function of x and y , if

$$U = \sum_{j=1}^{p_1} \alpha_j + \sum_{j=1}^{p_2} \gamma_j - \sum_{j=1}^{q_1} \beta_j - \sum_{j=1}^{q_2} \delta_j < 0 \quad (1.11)$$

$$V = \sum_{j=1}^{p_1} A_j + \sum_{j=1}^{p_3} E_j - \sum_{j=1}^{q_1} B_j - \sum_{j=1}^{q_3} F_j < 0 \quad (1.12)$$

The integral in (1.7) converges under the following set of conditions:

$$\Omega = \sum_{j=1}^{n_1} \alpha_j - \sum_{j=n_1+1}^{p_1} \alpha_j + \sum_{j=1}^{m_2} \delta_j - \sum_{j=m_2+1}^{q_2} \delta_j L_j + \sum_{j=1}^{n_2} \gamma_j K_j - \sum_{j=n_2+1}^{p_2} \gamma_j - \sum_{j=1}^{q_1} \beta_j > 0 \quad (1.13)$$

$$\Lambda = \sum_{j=1}^{n_1} A_j - \sum_{j=n_1+1}^{p_1} A_j + \sum_{j=1}^{m_2} F_j - \sum_{j=m_2+1}^{q_2} F_j S_j + \sum_{j=1}^{n_3} E_j R_j - \sum_{j=n_2+1}^{p_3} E_j - \sum_{j=1}^{q_1} B_j > 0 \quad (1.14)$$

$$|\arg x| < \frac{1}{2} \Omega \pi, |\arg y| < \frac{1}{2} \Lambda \pi \quad (1.15)$$

The behavior of the \overline{H} -function of two variables for small values of $|z|$ follows as:

$$\overline{H}[x, y] = 0(|x|^\alpha |y|^\beta), \max\{|x|, |y|\} \rightarrow 0 \quad (1.16)$$

Where

$$\alpha = \min_{1 \leq j \leq m_2} \left[\operatorname{Re} \left(\frac{d_j}{\delta_j} \right) \right] \quad \beta = \min_{1 \leq j \leq m_2} \left[\operatorname{Re} \left(\frac{f_j}{F_j} \right) \right] \quad (1.17)$$

For large value of $|z|$,

$$\overline{H}[x, y] = 0\{|x|^{\alpha'}, |y|^{\beta'}\}, \min\{|x|, |y|\} \rightarrow 0 \quad (1.18)$$

Where

$$\alpha' = \max_{1 \leq j \leq n_2} \operatorname{Re} \left(K_j \frac{c_j - 1}{\gamma_j} \right), \beta' = \max_{1 \leq j \leq n_3} \operatorname{Re} \left(R_j \frac{e_j - 1}{E_j} \right) \quad (1.19)$$

Provided that $U < 0$ and $V < 0$.

If we take

$$K_j = 1 (j=1, 2, \dots, n_2), L_j = 1 (j=m_2+1, \dots, q_2), R_j = 1 (j=1, 2, \dots, n_3), S_j = 1 (j=m_3+1, \dots, q_3) \text{ in}$$

(1.7), the \overline{H} -function of two variables reduces to H -function of two variables due to [13].

If we set $n_1 = p_1 = q_1 = 0$, the \overline{H} -function of two variables breaks up into a product of two \overline{H} -function of one variable namely

$$\begin{aligned} & \overline{H}_{0,0;m_2,n_2;m_3,n_3}^{0,0;p_2,q_2;p_3,q_3} \left[x \left| \begin{matrix} -(c_j, \gamma_j; K_j)_{1,n_2} (c_j, \gamma_j)_{n+1,p_2} (e_j, E_j; R_j)_{1,n_3} (e_j, E_j)_{n_3+1,p_3} \\ -(d_j, \delta_j)_{1,m_2} (d_j, \delta_j; L_j)_{m_2+1,q_2} (f_j, F_j)_{1,m_3} (f_j, F_j; S_j)_{m_3+1,q_3} \end{matrix} \right. \right] \\ &= \overline{H}_{p_2,q_2}^{m_2,n_2} \left[x \left| \begin{matrix} (c_j, \gamma_j; K_j)_{1,n_2} (c_j, \gamma_j)_{n_2+1,p_2} \\ (d_j, \delta_j)_{1,m_2} (d_j, \delta_j; L_j)_{m_2+1,q_2} \end{matrix} \right. \right] \overline{H}_{p_3,q_3}^{m_3,n_3} \left[y \left| \begin{matrix} (e_j, E_j; R_j)_{1,n_3} (e_j, E_j)_{n_3+1,p_3} \\ (f_j, F_j)_{1,m_3} (f_j, F_j; S_j)_{m_3+1,q_3} \end{matrix} \right. \right] \end{aligned} \quad (1.20)$$

If $\lambda > 0$, we then obtain

$$\lambda^2 \overline{H}_{p_1,q_1;p_2,q_2;p_3,q_3}^{0,n_1;m_2,n_2;m_3,n_3} \left[x^\lambda \left| \begin{matrix} (a_j, \lambda \alpha_j; A_j)_{1,p_1} (c_j, \lambda \gamma_j; K_j)_{1,n_2} (c_j, \lambda \gamma_j)_{n_2+1,p_2} (e_j, \lambda E_j; R_j)_{1,n_3} (e_j, \lambda E_j)_{n_3+1,p_3} \\ (b_j, \lambda \beta_j; B_j)_{1,q_1} (d_j, \lambda \delta_j)_{1,m_2} (d_j, \lambda \delta_j; L_j)_{m_2+1,q_2} (f_j, \lambda F_j)_{1,m_3} (f_j, \lambda F_j; S_j)_{m_3+1,q_3} \end{matrix} \right. \right] y^\lambda$$

$$= \overline{H}_{p_1, q_1; p_2, q_2; p_3, q_3}^{0, n_1; m_2, n_2; m_3, n_3} \left[\begin{matrix} x \left(a_j, \alpha_j; A_j \right)_{1, p_1} (c_j, \gamma_j; K_j)_{1, n_2} (c_j, \gamma_j)_{n_2+1, p_2} (e_j, E_j; R_j)_{1, n_3} (e_j, E_j)_{n_3+1, p_3} \\ y \left(b_j, \beta_j; B_j \right)_{1, q_1} (d_j, \delta_j)_{1, m_2} (d_j, \delta_j; L_j)_{m_2+1, q_2} (f_j, F_j)_{1, m_3} (f_j, F_j; S_j)_{m_3+1, q_3} \end{matrix} \right] \quad (1.21)$$

$$\overline{H}_{p_1, q_1; p_2, q_2; p_3, q_3}^{0, n_1; m_2, n_2; m_3, n_3} \left[\begin{matrix} \frac{1}{x} \left(a_j, \alpha_j; A_j \right)_{1, p_1} (c_j, \gamma_j; K_j)_{1, n_2} (c_j, \gamma_j)_{n_2+1, p_2} (e_j, E_j; R_j)_{1, n_3} (e_j, E_j)_{n_3+1, p_3} \\ \frac{1}{y} \left(b_j, \beta_j; B_j \right)_{1, q_1} (d_j, \delta_j)_{1, m_2} (d_j, \delta_j; L_j)_{m_2+1, q_2} (f_j, F_j)_{1, m_3} (f_j, F_j; S_j)_{m_3+1, q_3} \end{matrix} \right]$$

$$= \overline{H}_{p_1, q_1; p_2, q_2; p_3, q_3}^{0, n_1; m_2, n_2; m_3, n_3} \left[\begin{matrix} x \left(1-b_j, \beta_j; B_j \right)_{1, q_1} (1-d_j, \delta_j)_{1, m_2} (1-d_j, \delta_j; L_j)_{m_2+1, q_2} (1-f_j, F_j)_{1, m_3} (1-f_j, F_j; S_j)_{m_3+1, q_3} \\ y \left(1-a_j, \alpha_j; A_j \right)_{1, p_1} (1-c_j, \gamma_j; K_j)_{1, n_2} (1-c_j, \gamma_j)_{n_2+1, p_2} (1-e_j, E_j; R_j)_{1, n_3} (1-e_j, E_j)_{n_3+1, p_3} \end{matrix} \right] \quad (1.22)$$

III. Main Results

$$c \int_0^\infty \overline{H}_{p_1, q_1}^{m_1, n_1} \left[ax \left(a_j, \alpha_j; A_j \right)_{1, n_1} (a_j, \alpha_j)_{n_1+1, p_1} \right] \overline{H}_{p_2, q_2}^{m_2, n_2} \left[bx \left(c_j, \gamma_j; C_j \right)_{1, n_2} (c_j, \gamma_j)_{n_2+1, p_2} \right]$$

$$\overline{H}_{p_3, q_3}^{0, n_3} \left[cx \left(-e_j, \phi_j \right)_{n_3+1, p_3} (f_j, \theta_j)_{1, m_3} (1-f_j, \theta_j; F_j)_{m_3+1, q_3} \right] dx$$

$$= \overline{H}_{p_1, q_1; p_2, q_2; p_3, q_3}^{m_1, n_1; m_2, n_2; 0, n_3} \left[\begin{matrix} \frac{a}{c} \left(a_j, \alpha_j; A_j \right)_{1, p_1} (c_j, \gamma_j; K_j)_{1, n_2} (c_j, \gamma_j)_{n_2+1, p_2} (1-\phi+e_j, \phi_j)_{n_3+1, p_3} \\ \frac{b}{c} \left(b_j, \beta_j; B_j \right)_{1, q_1} (d_j, \delta_j)_{1, m_2} (d_j, \delta_j; L_j)_{m_2+1, q_2} (f_j, F_j)_{1, m_3} (\theta-f_j, F_j; S_j)_{m_3+1, q_3} \end{matrix} \right] \quad (2.1)$$

Where $\operatorname{Re} \left[\min \frac{b_i}{\beta_i} + \min \frac{d_j}{\delta_j} - \min \frac{e_k}{\theta_k} + 1 \right] > 0; i = 1, 2, \dots, m_1; j = 1, 2, \dots, m_2; k = 1, 2, \dots, m_3$ and

$$\lambda_1, \lambda_2, \lambda_3 > 0, |\arg a| < \frac{\pi \lambda_1}{2}, |\arg b| < \frac{\pi \lambda_2}{2}, |\arg c| < \frac{\pi \lambda_3}{2}, \text{ where}$$

$$\lambda_1 = \sum_1^{m_1} \beta_j - \sum_{m_1+1}^{q_1} B_j \beta_j + \sum_1^{n_1} A_j \alpha_j - \sum_{n_1+1}^{p_1} \alpha_j$$

$$\lambda_2 = \sum_1^{m_2} \delta_j - \sum_{m_2+1}^{q_2} D_j \delta_j + \sum_1^{n_2} C_j \gamma_j - \sum_{n_2+1}^{p_2} \gamma_j$$

$$\lambda_3 = \sum_1^{n_3} E_j \phi_j - \sum_{m_3+1}^{q_3} \theta_j - \sum_{n_3+1}^{p_3} \phi_j$$

Proof: On substituting the value of $\overline{H}_{p_1, q_1}^{m_1, n_1} [ax]$ in terms of Mellin-Barnes integral ([16], p.171) in the integrand of (2.1) and changing the order of integration, the integral transforms into

$$\frac{c}{2\pi i} \int_{-i\infty}^{i\infty} \phi_2(\xi) a^{-\xi} \int_0^\infty \overline{H}_{p_2, q_2}^{m_2, n_2} \left[bx \left(c_j, \gamma_j; C_j \right)_{1, n_2} (c_j, \gamma_j)_{n_2+1, p_2} \right] \overline{H}_{p_3, q_3}^{m_3, 0} \left[cx \left(-e_j, \phi_j \right)_{n_3+1, p_3} (f_j, \theta_j)_{1, m_3} (1-f_j, \theta_j; F_j)_{m_3+1, q_3} \right] dx d\xi$$

The change of the order of integration is readily justified by de la Vallee Poussin's theorem ([2], p.504) in view of the conditions stated earlier.

On evaluating the x -integral by means of ([18], p.1143), it gives us

$$\frac{1}{2\pi i} \int_{-i\infty}^{i\infty} \phi_2(\xi) \left(\frac{c}{a} \right)^\xi \overline{H}_{p_2+p_3, q_2+q_3}^{m_2+m_3, n_2} \left[\frac{b}{c} \left(c_j, \gamma_j; C_j \right)_{1, n_2} (c_j, \gamma_j)_{n_2+1, p_2} (-e_j, \phi_j)_{n_3+1, p_3} \right. \\ \left. \frac{b}{c} \left(d_j, \delta_j \right)_{1, m_2} (d_j, \delta_j; D_j)_{m_2+1, q_2} (f_j, \theta_j)_{1, m_3} (1-f_j, \theta_j; F_j)_{m_3+1, q_3} \right] d\xi$$

$$= \frac{1}{2\pi i} \int_{-i\infty}^{i\infty} \int_{-i\infty}^{i\infty} \phi_2(\xi) \phi_1(\eta) \frac{\prod_1^{n_3} \Gamma(1-\phi_j + e_j + (\xi + \eta)\phi_j)}{\prod_{n_3+1}^{p_3} \Gamma(\phi_j - e_j - (\xi + \eta)\phi_j) \prod_1^{q_3} \Gamma(\theta_j - f_j + (\xi + \eta)\theta_j)} d\xi d\eta$$

On using (1.7), we arrive at the result (2.1).

IV. Particular cases

(i) If we set $n_3 = q_3 = 2, p_3 = 1, \theta_1 = \theta_2 = 1, \phi_1 = 1, f_1 = 2 - k + \rho, e_1 = -\rho - m - \frac{1}{2}$

$e_2 = m - \rho - \frac{1}{2}, K_j = L_j = R_j = S_j = 1$, then on using the identity

$$\overline{H}_{1,2}^{2,0} \left[x \left| \begin{matrix} (1-k+\rho, 1) \\ (\frac{1}{2}+m+\rho, 1) \end{matrix} \right| \left(\frac{1}{2}-m+\rho, 1 \right) \right] = e^{-\frac{1}{2}x} x^\rho \overline{W}_{k,m}(x) \quad (3.1)$$

We find that

$$\begin{aligned} & a^{\rho+1} \int_0^\infty x^\rho e^{-\frac{1}{2}x} \overline{W}_{k,m}(ax) \overline{H}_{p_1, q_1}^{m_1, n_1} \left[bx \left| \begin{matrix} (a_j, \alpha_j; A_j)_{1, p_1}, (a_j, \alpha_j)_{n_1+1, p_1} \\ (b_j, \beta_j)_{1, q_1}, (b_j, \beta_j; B_j)_{m_1+1, q_1} \end{matrix} \right| \overline{H}_{p_2, q_2}^{m_2, n_2} \left[cx \left| \begin{matrix} (c_j, \gamma_j; C_j)_{1, p_2}, (c_j, \gamma_j)_{n_2+1, p_2} \\ (d_j, \delta_j)_{1, q_2}, (d_j, \delta_j; D_j)_{m_2+1, q_2} \end{matrix} \right| \right] dx \\ &= \overline{H}_{p_1, q_1; p_2, q_2; 1, 2}^{m_1, n_1; m_2, n_2; 0, 1} \left[\begin{matrix} \frac{a}{c} \left| \begin{matrix} (a_j, \alpha_j; A_j)_{1, p_1}, (c_j, \gamma_j; K_j)_{1, n_2}, (c_j, \gamma_j)_{n_2+1, p_2}, (k-1+\rho, 1) \\ (b_j, \beta_j; B_j)_{1, q_1}, (d_j, \delta_j)_{1, m_2}, (d_j, \delta_j; L_j)_{m_2+1, q_2}, (f_j, F_j)_{1, m_3}, \left(-\rho-m-\frac{1}{2}, 1\right), \left(-\rho+m-\frac{1}{2}, 1\right) \end{matrix} \right| \end{matrix} \right] \quad (3.2) \end{aligned}$$

Where

$$\operatorname{Re} \left(\rho \pm m + \frac{3}{2} + \min \frac{b_i}{\beta_i} + \min \frac{d_i}{\delta_i} \right) > 0 \text{ for}$$

$$i = 1, 2, \dots, n; j = 1, 2, \dots, m_1; \lambda_1, \lambda_2 > 0, \operatorname{Re}(a) > 0, |\arg b| < \frac{1}{2} \pi \lambda_1, |\arg c| < \frac{1}{2} \pi \lambda_2$$

For $k = 0, m = \frac{1}{2}$, (3.2) gives Laplace transform of the product of two \overline{H} -functions:

$$\begin{aligned} & a^{\rho+1} \int_0^\infty x^\rho \overline{H}_{p_1, q_1}^{m_1, n_1} \left[bx \left| \begin{matrix} (a_j, \alpha_j; A_j)_{1, p_1}, (a_j, \alpha_j)_{n_1+1, p_1} \\ (b_j, \beta_j)_{1, q_1}, (b_j, \beta_j; B_j)_{m_1+1, q_1} \end{matrix} \right| \overline{H}_{p_2, q_2}^{m_2, n_2} \left[cx \left| \begin{matrix} (c_j, \gamma_j; C_j)_{1, p_2}, (c_j, \gamma_j)_{n_2+1, p_2} \\ (d_j, \delta_j)_{1, q_2}, (d_j, \delta_j; D_j)_{m_2+1, q_2} \end{matrix} \right| \right] dx \\ &= a^{-\rho-1} \overline{H}_{p_1, q_1; p_2, q_2; 1, 1}^{m_1, n_1; m_2, n_2; 0, 1} \left[\begin{matrix} \frac{a}{c} \left| \begin{matrix} (a_j, \alpha_j; A_j)_{1, p_1}, (c_j, \gamma_j; K_j)_{1, n_2}, (c_j, \gamma_j)_{n_2+1, p_2}, (-\rho, 1) \\ (b_j, \beta_j; B_j)_{1, q_1}, (d_j, \delta_j)_{1, m_2}, (d_j, \delta_j; L_j)_{m_2+1, q_2}, (f_j, F_j)_{1, m_3}, (-\rho-1, 1), (-\rho, 1) \end{matrix} \right| \end{matrix} \right] \quad (3.3) \end{aligned}$$

Where

$$\operatorname{Re} \left(\rho + 1 + \min \frac{b_i}{\beta_i} + \min \frac{d_i}{\delta_i} \right) > 0 \text{ for}$$

$$i = 1, 2, \dots, n; j = 1, 2, \dots, m_1; \lambda_1, \lambda_2 > 0, \operatorname{Re}(a) > 0, |\arg b| < \frac{1}{2} \pi \lambda_1, |\arg c| < \frac{1}{2} \pi \lambda_2.$$

REFERENCES

- [1]. Agarwal, R.P.; An extension of Meijer's G -function, Proc. Nat. Inst. Sci. India, 3(1965), 536-546.
- [2]. Anandani, P.; On some recurrence formulae for the H -function, Ann. Pol. Math. 21(1969), 113-117.
- [3]. Bailey, W.N.; Some infinite-integrals involving Bessel functions, Proc. London Math. Soc., 40, (1936), 37-48.
- [4]. Braaksma, B.L.J.; Asymptotic expansions and analytic continuations for a class of Barnes-integrals. Compositio Mathematica, 15 (1964), 239-241.
- [5]. Bromwich, T.J.A.; Theory of Infinite Series, Macmillan, London, 1954.
- [6]. Buschman, R.G. and Srivastava, H.M. 1990. The \overline{H} - function associated with a certain class of
- [7]. Feynman integrals, J.Phys.A:Math. Gen. 23, 4707-4710.
- [8]. Erdelyi, A. et. al.; Higher Transcendental Functions, vol.1, McGraw-Hill, New York, 1953.
- [9]. Erdelyi, A. et. al.; Tables of Integral Transforms, vol.2, McGraw-Hill, New York, 1954.
- [10]. Fox, C. 1961. The G and H -function as Fourier kernels. Trans. Amer. Math. Soc. 98:395-429.
- [11]. Fox, C.; A formal solution of certain dual integral equations, Trans. Amer. Math. Soc. 119, (1965), 389-395.
- [12]. Gupta, K.C.; On the H -functions, NN. Soc. Sci. Bruxelles, 79 (1965), 97-106.
- [13]. Inayat-Hussain, A.A.; New properties of hypergeometric series derivable from Feynman integrals :II A generalization of the H -function, J. Phys. A. Math. Gen. 20(1987).

- [14]. Mittal, P.K. and Gupta, K.C.1961. An integral involving generalized function of two variables. *Proc. Indian Acad. Sci. Sect. A*(75):67-73.
- [15]. Munot, P.C. and Kalla, S.L.; On an extension of generalized function of two variables, *Universidad Nac. De Tuc., Rev. Ser. A*, 25 (1971).
- [17]. Rathi, A.K. 1997. A new generalization of generalized hypergeometric functions. *Le Mathematiche Fasc.* II52:297-310.
- [18]. Saxena, R.K. ; A formal solution of certain dual integral equations involving H functions, *Proc. Cambridge Philos. Soc.* 63 (1967), 171-178.
- [19]. Saxena, R.K. and Mathai, A.M.; Applications of Special functions in the characterization of probability distributions, *South Afr. Jour. Statist*, 3 (1969), 27-34.
- [20]. Saxena, R.K. and Mathai, A.M.; Distribution of a product and the structural set up of densities, *Ann. Math. Statistics*, U.S.A., 40, (1969), 1439-1448.
- [21]. Singh, Y. and Mandia, H. 2013. A study of \overline{H} -function of two variables, *International Journal of Innovative research in science, engineering and technology*, Vol.2,(9),4914-4921.
- [22]. Slater, L.J.; *Confluent hypergeometric functions*, Cambridge University Press, 1960.

Analysis of stiffened plate using FE Approach

Anupama B. M¹, Jayashankar babu B. S.²

^{1,2}(Civil Engineering Department, PES College of Engineering, Mandya/ VTU, India)

Abstract: The objective of the present investigation is to study the strengthening effect of the stiffeners on the buckling of unperforated and perforated plate when they are reinforced in longitudinal and transverse directions. The plate is subjected to inplane uniform uniaxial end compression load having simply supported plate boundary condition. The parameters considered are plate aspect ratio, area ratio and types of stiffeners. The analysis has been carried out using ANSYS finite element software. The buckling analysis shows that the influence of transverse stiffener is less when compared to longitudinal stiffener.

Keywords: Buckling load factor, Finite element method, Inplane loads, Stiffened plate.

I. INTRODUCTION

Openings are often provided in plate structures for the purpose of access, services and even aesthetics. Though they are provided to achieve certain structural advantages, when these structures are loaded, the presence of openings will cause change in the buckling characteristics of the plate as well as on the ultimate load capacity of the structure. For the cases, when the opening becomes inevitable for the plates under high working stress, the reduced buckling strength of the perforated plate may be insufficient to meet the requirements of normal serviceability limits and structural safety. A design solution must be devised to increase the structural stability of such perforated plate before it can be used to its best advantage. This always can be accomplished by selecting a thicker plate but the design solution will not be economical in terms of weight of material introduced by an adequate increase in the thickness of the plate. It is possible to design an adequately rigid and economical structural plate element by keeping its thickness as small as possible by introducing reinforcing stiffeners.

A stiffened plate is an assembly of stiffeners welded to the plate. Beam stiffeners on the plates significantly reinforce the structure by relieving some of the stresses and deflections, therefore improve the overall plate's resistance against buckling. Purohit M R [1] investigated the structural instability caused by a plain circular perforation for simply supported square plates under edge compression, and also for those plates reinforced by two symmetric stiffeners in longitudinal and transverse manner based on the principle of minimum potential energy. Shanmugam et al. [2] have used the Finite element method to develop a design formula to determine the ultimate load carrying capacity of axially compressed square plates with centrally located perforations, circular or square. El-Sawy and Nazmy [3] investigated the effect of plate aspect ratio and hole location on elastic buckling of uniaxially loaded rectangular plates with eccentric holes using Finite element method. Ultimate strength of square plate with rectangular opening under axial compression using non-linear finite element analysis was studied by Suneel Kumar et al.[4]. Jeom Kee Paik [5] studied the ultimate strength of perforated steel plate under combined biaxial compression and edge shear loads for the circular cutout located at the centre of the plate by using ANSYS. Bin Cheng and Jincheng Zhao [6] analyzed the buckling behaviors of uniaxially compressed perforated steel plates strengthened by stiffeners. Yucheng Liu and Qingkui [7] investigated the performance of arbitrarily stiffened plates and regularly stiffened plates subjected to biaxial stress. Manoj G Tharian and Nandakumar C G [8] have used ANSYS to quantify the structural advantages of hat shaped stiffeners over the commonly used open section stiffeners. In the literature a great deal of attention has been focused on studying the elastic buckling of perforated plates, but less amount of work appears related to the effect of aspect ratio on stiffened perforated plates. Hence, the main objective of the present study is to contribute to the understanding the buckling behavior of unperforated and perforated plates when subjected to uniform inplane uniaxial compression loading and also to exhibit the importance of providing stiffeners in enhancing the stability of the plate which in turn leads to most economical section. The stiffened plates involved in this study are analysed using ANSYS finite element software.

II. PROMBLEM DEFINITION

The plate has length a , width b , thickness t and a circular hole with diameter d . The plate is subjected to uniform inplane uniaxial compression loading. In the present study three types of rectangular plates are considered. They are, unperforated plate with and without stiffener and also perforated stiffened plate. The stiffeners are placed along longitudinal and along transverse direction. The material of the plate and stiffener are assumed to be homogeneous, isotropic and elastic. Modulus of elasticity and Poisson's ratio are 210924N/mm^2 and 0.3 respectively. In order to correctly assess the effect of aspect ratio, all the remaining parameters that define the plate geometry have been kept constant. The simply supported boundary condition on all the four edges of the plate is considered in this study. Finite element models for the unstiffened and stiffened plates involved in this study are meshed using 8SHELL93 and two node BEAM188 element is used to model the stiffener that is attached to the plate, which are available in ANSYS element library[9].

III. FINITE ELEMENT FORMULATION

The effect of inplane deformations is taken into account in addition to the deformations due to bending. A eight-noded isoparametric element with six degrees of freedom (u , v , w , θ_x , θ_y and θ_z) per node is employed in the present analysis. The element matrices of the stiffened plate element consist of the contribution of the plate and that of the stiffener. The contribution of the stiffener to a particular node depends on the proximity of the stiffener to that node. For a given edge loading and boundary conditions, the static equation, i.e., $[K] \{\Delta\} = \{F\}$ is solved to get the stresses. The geometric stiffness matrix is now constructed with the known stresses. The overall elastic stiffness matrix and geometric stiffness matrix are generated from the assembly of those element matrices and stored in a single array where the variable bandwidth profile storage scheme is used. The elastic stiffness matrix $[K_P]$ and geometric stiffness matrix $[K_{GP}]$ of the plate element may be expressed as follows

$$[K_P] = \int_0^1 \int_0^1 [B_P]^T [D_P] [B_P] J_P d\xi d\eta$$

$$[K_{GP}] = \int_0^1 \int_0^1 [B_{GP}]^T [\sigma_P] [B_{GP}] J_P d\xi d\eta$$

The elastic stiffness matrix $[K_S]$ and geometric stiffness matrix $[K_{GS}]$ of a stiffener element placed anywhere within a plate element and oriented in the direction of x may be expressed, in a manner similar to that of the plate element as follows,

$$[K_S] = \int_0^1 [B_S]^T [D_S] [B_S] J_S d\xi$$

$$[K_{GS}] = \int_0^1 [B_{GS}]^T [\sigma_S] [B_{GS}] J_S d\xi$$

Where,

$$[B_P] = [[B_P]_1 [B_P]_2 \dots [B_P]_r \dots [B_P]_8];$$

$$[B_{GP}] = [[B_{GP}]_1 [B_{GP}]_2 \dots [B_{GP}]_r \dots [B_{GP}]_8]$$

$$[B_S] = [[B_S]_1 [B_S]_2 \dots [B_S]_r \dots [B_S]_8];$$

$$[B_{GS}] = [[B_{GS}]_1 [B_{GS}]_2 \dots [B_{GS}]_r \dots [B_{GS}]_8]$$

and J_S is the Jacobian of the stiffener, which is one-half of its actual length within an element.

The equation of equilibrium for the stiffened plate subjected to inplane loads can be written as,

$$[[K_P] - P [K_G]]/q = 0 \quad (1)$$

Equation (1) can be reduced to the governing equations for buckling problems.

IV. DISCUSSION OF THE RESULTS

The study obtain several values of critical buckling compression for simply supported plate with different aspect ratios, also when a small circular perforation is included there in, and when these perforated plates are reinforced by two stiffeners in longitudinal and transverse direction. These numerical results formulate basis for predicting relative buckling strength of plates with plain circular perforations with or without any stiffeners. Also observed the variation in buckling strength when un-perforated plate reinforce with single stiffener in longitudinal and in transverse directions subjected to inplane uniaxial compression. The

results of static stability behavior of isotropic plates with varying aspect ratios have been detailed. The convergence study shows that a mesh size of 10x10 is sufficient to get a reasonable order of accuracy, the analysis in the subsequent problems is carried out with this mesh size.

4.1 Validation

In Comparison studies of buckling load factor (k) have been carried out for the isotropic solid plates under uniaxial compressive loading by varying aspect ratio for all-round simply supported, (SSSS) boundary condition. The results obtained from the present work have been tabulated with the comparative results in Table 1. From these comparison studies, it can be concluded that results validated the correctness of the formulation.

Table 1

Comparison of buckling load factor (k) of SSSS isotropic unperforated plate for uniaxial compression
($t = 6 \text{ mm}$; $b = 600 \text{ mm}$; $\mu = 0.3$)

Types of plate	Solid plate	Perforated plate	Unperforated stiffened plate		Perforated stiffened plate	
			Longitudinal	Transverse	Longitudinal	Transverse
Present study	3.996	3.8434	17.01	6.29	14.57	10.46
Reference value	4.00(10)	3.896(1)	11.67(10)	6.5(10)	14.26(1)	10.55(1)

4.2 Case studies

The results on the effect of plate aspect ratio(β) and area ratio(δ) on the critical buckling load factor for unperforated and perforated stiffened plates are presented and discussed in this section. Plates with all-round simply supported edges and subjected to inplane uniform uniaxial loading are considered in this study.

4.2.1 Unperforated plate

Fig.1 shows the variation of critical buckling stress (σ_{cr}) versus aspect ratio(β) for unperforated plate. The buckling strength of an unperforated plate is more when $\beta=0.5$, 56%, with respect to $\beta=1$. Also the variation is 8.5% when $\beta=1.5$, but it is almost the same when $\beta>1.5$.

Fig 2 shows the variation of buckling load factor (k) versus area ratio (δ) for different plate aspect ratios (β) having central longitudinal stiffener. The introduction of stiffener causes a linear increase of buckling load with $\delta=0.05$ and this increase is less in magnitude when $\delta>0.1$. The curves are overlapped on each other, indicating the less effect of aspect ratio. The increase in k is 1.72, 3.26, 3.26 and 3.29 with $\beta=0.5$ to 2 and at $\delta=0.1$ and k further increases with respect to unperforated plate without stiffener to 2.07, 3.59, 3.44 and 3.83 for $\beta=0.5$ to 2 and $\delta=0.2$ respectively. The plate with the longitudinal stiffener possessing 4 times higher strength than unstiffened plate.

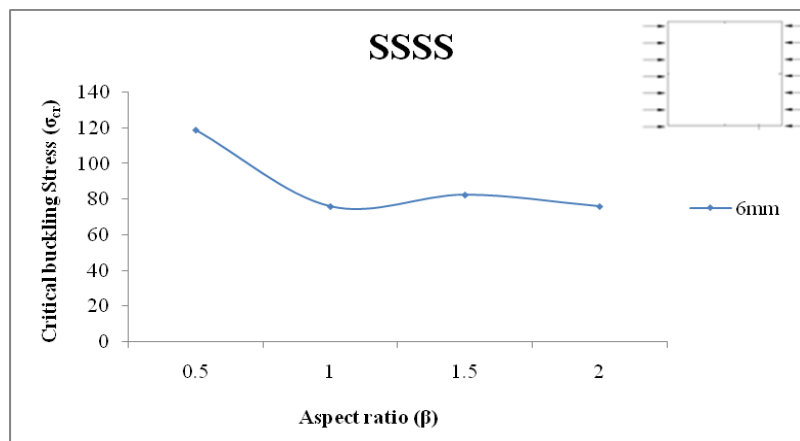


Fig. 1: Variation of σ_{cr} with respect to β for unperforated isotropic plate subjected to inplane uniaxial compression.

The enhancement in buckling load factor is due to the introduction of stiffener exactly at the centre divides the plate to act as two individual plates having larger aspect ratios i.e., when plate having aspect ratio one is provided by one central stiffener it divides the plate into two individual plates of larger aspect ratio which in turn enhances the buckling strength of the stiffened plate compared to unstiffened plate.

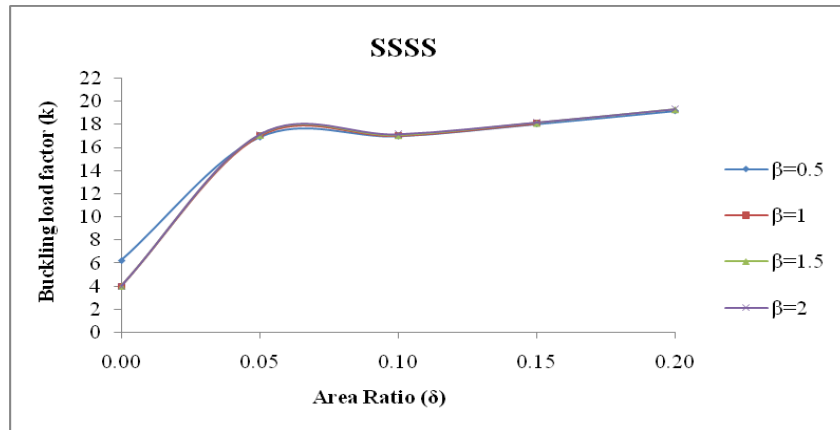


Fig. 2: Variation of k with \square and \square for unperforated plate having central longitudinal stiffener subjected to inplane uniaxial compression

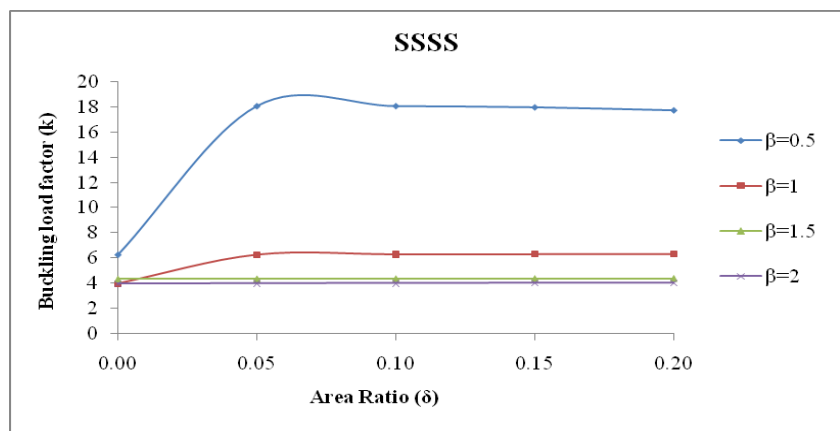


Fig. 3: Variation of k with the \square and \square for unperforated plate having central transverse stiffener subjected to inplane uniaxial compression.

4.2.2 Perforated stiffened plate

Fig 4 shows the variation of buckling load factor (k) versus area ratio (δ) of a perforated plate with central two symmetric longitudinal stiffeners. It is observed that k increases as δ increases. More increment in $\beta=0.5$ and it is 3.65, 3.92, 4.11, 4.48 times higher with respect to perforated plate without stiffener. The same increase in k when $\beta = 1$ is 2.05, 3.13, 3.4, 5.48. But increase is less when $\beta > 1$ with respect to $\delta = 0.05$ to 0.2 respectively. This is due to more stiffening effect of plate having $a \leq b$ than $a > b$.

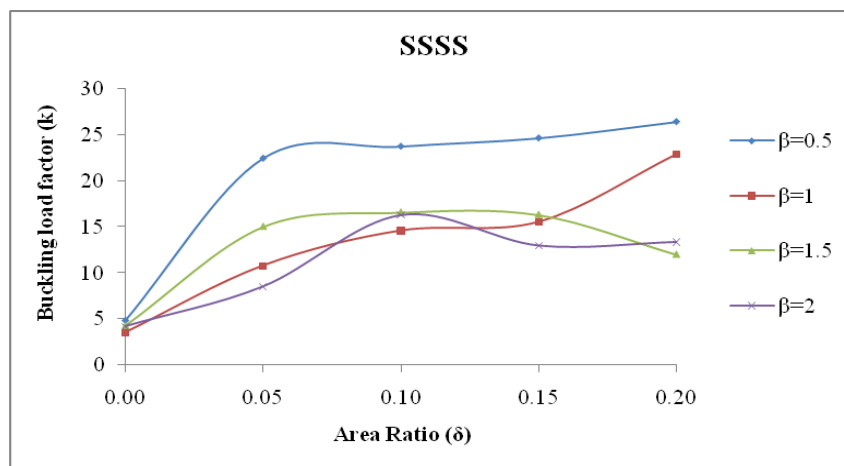


Fig. 4: Variation of k for perforated plate reinforced by two symmetric longitudinal stiffener with respect to \square and \square subjected to inplane uniaxial compression

Fig 5 shows the variation of buckling load factor (k) versus area ratio (δ) of a perforated plate with central two symmetric transverse stiffeners. At $\beta = 0.5$, k increases with respect to δ up to $\delta = 1$ and slight variation is noticed thereafter. The increase is in the order of 3.45, 5.48, 4.56, 5.28 when $\delta = 0.05$ to 0.2 respectively. Less increase of k is noticed compared to longitudinal stiffener for all other cases having $\beta > 0.5$.

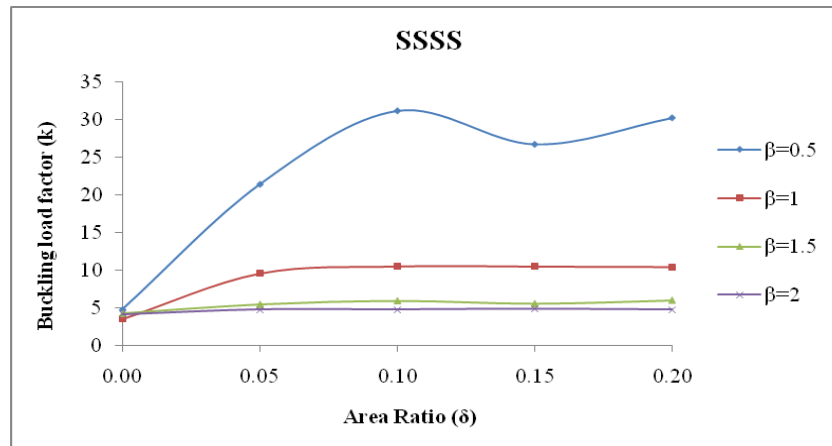


Fig. 5: Variation of k for perforated plate reinforced by two symmetric transverse stiffener with respect to aspect β and δ subjected to inplane uniaxial compression.

V. CONCLUSION

Based on the results obtained in this study, the following conclusions are formulated with regard to buckling of simply supported plates reinforced by two symmetric longitudinal and transverse stiffeners with different plate aspect ratios ($\beta = 0.5$ to 2), and different area ratios ($\delta = 0.05$ to 0.2) and plate having small circular central perforation.

1. The ultimate strength of plate was found to reduce with increasing aspect ratio, remaining practically constant at higher aspect ratios.
2. Unperforated thin plate having more critical buckling stress when $\beta < 1$ and it is observed that 56% compared to $\beta = 1$. Noticed slight increase of 8.5% up to $\beta = 1.5$ but start to decrease then onwards.
3. More increase in strength is observed when $\delta \leq 0.15$ in the case of longitudinal central stiffening of unperforated plate. This indicates the optimization of stiffener proportion with respect to maximum plate strength.
4. The influence of central transverse stiffener on unperforated plate is less when compared to central longitudinal stiffener.
5. The two longitudinal stiffeners on either side of the central circular perforation definitely increase the buckling strength of the perforated plate.
6. The plate with stiffener possessing four times higher strength than unstiffened plate, and lesser increment is observed with respect to the area ratio δ and for $\beta \geq 1$ when stiffeners are placed along longitudinal direction. But the increase in buckling strength is only 50% when the plate is reinforced by central transverse stiffener.
7. The two transverse stiffeners will not participate in carrying the applied compression yet the buckling strength of the perforated plate will be increased to some extent. buckling strength of perforated plate reinforced by longitudinal stiffener is very high when $\beta = 0.5$ and it is 3.66, 3.92, 4.11 and 4.48 times higher when compared to unstiffened perforated plate with respect to area ratio 0.05, 0.1, 0.15 and 0.2 respectively. This increase of k slightly lesser in the stiffened plate having $\beta \geq 1$. The increase in buckling strength is less in transverse stiffened perforated plate.

REFERENCES

- [1] M.R. Purohit, M. Tech Thesis, "Buckling strength of simply supported stiffened plate having a plain circular perforation", Sir George Williams University, Montreal, Canada, 1973.
- [2] N.E. Shanmugam, V. Thevendran, Y.H. Tan, "Design formula for axially compressed perforated plates", Thin-Walled Structures, Vol.34(1), 1999, pp 1–20.
- [3] El-Sawy K.M., Nazmy A.S., Effect of aspect ratio on the elastic buckling of uniaxially loaded plates with eccentric holes, Thin Walled Structures, 39, 2001, 983-998.

- [4] M.P.Suneel Kumar, Alagusundaramoorthy, R.Sundaravadivelu, Ultimate strength of square plate with rectangular opening under axial compression, Journal of Naval Architecture and Marine Engineering, 2007, 15-26.
- [5] Jeom Kee Paik, "Ultimate strength of perforated steel plate under combined biaxial compression and edge shear loads", Thin-Walled Structures, Vol.46, 2008, pp.207–213.
- [6] Bin Cheng and Jincheng Zhao, "Strengthening of perforated plates under uniaxial compression: Buckling analysis", Thin-Walled Structures; Vol.48, 2010, pp.905–914.
- [7] Yucheng Liu, and Qingkui, "Strengthening of arbitrarily stiffened plates and regularly stiffened plates to biaxial stress", Thin-Walled Structures, Vol.68, 2013, pp.85-91
- [8] Manoj G Tharian & Nandakumar, C.G., "Hat stiffened plates for ship building", International Journal of Applied Engineering Research and Development (IJAERD) ISSN 2250-1584, Vol. 3, Issue 1, Mar 2013, pp.1-10
- [9] ANSYS, User Manual, Version 10.0, Ansys Inc
- [10] S.P.Timoshenko, and James M. Gere., "Theory of Elastic Stability", (second ed. McGraw- Hill company, Singapore, 1963) 348-389.

A review of Carbon Nanotube Reinforced Aluminium Composite and Functionally Graded composites as a Future material for Aerospace

Gururaja udupa¹, S. Shrikantha Rao², K.V. Gangadharan³

^{1, 2, 3} Department of Mechanical Engineering, National Institute of Technology, Karnataka, Surathkal, India

Abstract: Material selection is a very critical issue when it comes to aerospace engineering. Materials should have good qualities like light weight, high strength and corrosion resistance with economic viability. Over the period, Aluminium blends of composite are used for variety of applications. Carbon Nanotube reinforced Aluminium composites and Functionally graded composites (FGC) are the new developments in materials engineering. Gradual but continuous variation in composition and structure over volume, results in corresponding changes in the properties of material in contrast to homogeneous mixing of CNT in case of composite. FGM promises to be more suitable in the future. This paper focuses on brief review of CNT reinforced Aluminium composite and FGM application in aerospace.

Keywords: Aerospace, Composites, FGM, CNT

I. INTRODUCTION

A survey of current applications of composite materials and structures in military, transport and general aviation aircraft is presented to assess the maturity of composites technology, and the payoffs are realized[1]. The results of the survey shows that performance requirements and the potential to reduce life cycle costs for military aircraft and direct operating costs for transport aircraft are the main reasons for the selection of composite materials for current aircraft applications. Aluminium/Aluminium alloy is the most usable materials in aerospace structure due to its distinct properties as compared to other metals[2]. Reinforcement of CNT in Aluminium matrix leads to huge changes in physical as well as chemical properties like greater strength, improved stiffness, reduced density(weight), improved high temperature properties, controlled thermal expansion coefficient, thermal/heat management, enhanced and tailored electrical performance, improved abrasion and wear resistance, control of mass (especially in reciprocating applications), improved damping capabilities[3,4,5]. The application of high performance composite materials to military aircraft can be traced back to almost three decades to the F-14 (US Navy) and F-15 (US Air Force) fighters, which uses boron/epoxy skins in their empennages[6,7].

II. COMPOSITE AND FUNCTIONALLY GRADED COMPOSITES MATERIAL

Over the years, research in materials science has geared up with new innovative materials called Functionally graded materials[8]. Especially these materials show new capabilities towards thermal and chemical resistance with application of producing light weight structures. FGM also provides chance to build structures with different functionality as the requirements (needs). These developments are replacing parts of aerospace with FGM components[9,10]. Initial applications of composite materials to aircraft structures were in secondary structures such as fairings, small doors and control surfaces. As the technology developed, the use of composite materials for primary structures such as wings and fuselages has increased[11,12]. A comprehensive list of current aircraft with a significant use of composite materials in the airframe is shown in Table 1. [13,14].

TABLE 1
Composite component of Air Bus

Component	Details
Wing	Box beam skins, box beam sub-structure, winglets, Leading edge flaps/slats, ailerons/flaperons , raps & spoilers, fixed leading edges, fixed trailing edge panels, rap track fairings, actuator fairings.
Empennage	Horizontal stabilizers, skins, sub-structure, elevators, leading edges,fixed trailing edge panels,tips
Vertical stabilizer	Skins ,sub-structure, rudders, leading edges fixed trailing edge panels, ventral fins, tips.
Fuselage	Radome, forward fuselage, canopy frames (helicopters) ,mid fuselage, rear fuselage, speed brakes , tail cone, floor beams, floors rotor-domes, cabin doors (helicopters), lining and partitions, overhead baggage compartment, air ducts.
Helicopter	Main rotor blades, tail rotor blades, rotor drive shafts.
Doors and Fairings	Landing gear doors , landing gear fairings , landing gear pods, Wing-fuselage fairings, stabilizer fairings, equipment access doors.
Propulsion System	Engine fan blades ,engine casing , nozzle flaps, thrust reversers, engine nacelle and cowlings, fan cowls , turbine blade containment rings, pylon fairings, fuel tanks, propeller blades.
Propulsion System	Engine fan blades ,engine casing , nozzle flaps, thrust reversers, engine nacelle and cowlings, fan cowls , turbine blade containment rings, pylon fairings, fuel tanks, propeller blades.

III. MATERIAL FOR AEROSPACE

Materials are classified into the seven broad classes that are shown in figure 1; metals, ceramics, glass, elastomers, polymers, composites and FGM[15,16]. Composites and FGM are the advanced engineering Materials having high specific performance advantages in comparison with the conventional materials. In cases where high moduli of elasticity values are less important, fiberglass is the natural option because of the low cost of material[17,18]. The matrix material used with fiber glass are limited to low temperatures, such as below 121°C. Although it is not a debilitating limitation for the fiber, as its properties can still be used and maintained at temperatures beyond 426 to 482°C. Fiber epoxy composites have been used in aircraft engine to enhance the performance of the system[19]. The pilots' cabin door of aircrafts has also been made with fiber glass resin composites and these are now used in other transport systems. The boron-graphite materials were initially designed for fighter aircraft components and their use in commercial aircraft has been very limited[20,21].However, These are widely used for experimental applications. They are presently limited to secondary structures which can be used in commercial aircraft with considerable safety. The data from such experimentation on the long term effects of loads and stresses on the structure provides an input for design. Both dynamic and static conditions are combined in the turbojet engine and research has always been directed and focused towards replacement of materials[22,23]. Figure 1 shows the evolution of materials from conventional alloys to functionally graded materials used for aerospace structures.

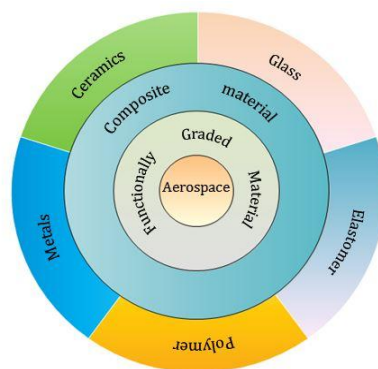


Fig.1. Material advancement for aerospace application

Application of FGM has advantages of light weight and high strength. The weight of the rotors, compressors and bearings are reduced. Initially, turbojet engines were used in fighter aircraft and later in commercial planes[24,25]. The necessity of a commercial plane is durability and higher service life, therefore few turbofan engines are designed to meet the manifold requirements of transport sector. The performance of the engine can be improved by improving the efficiency of propulsion or reducing the weight. The notable stiffness and strengths of composites permit reduction in the number of compressor stages by higher blade loading. The use of composites in rotors, compressors and engine parts are estimated to lead to weight savings[26,27]. Figure 2(a) shows the CNT reinforced composite specimen and Figure 2(b) shows layered CNT reinforced Al functionally graded material specimen.

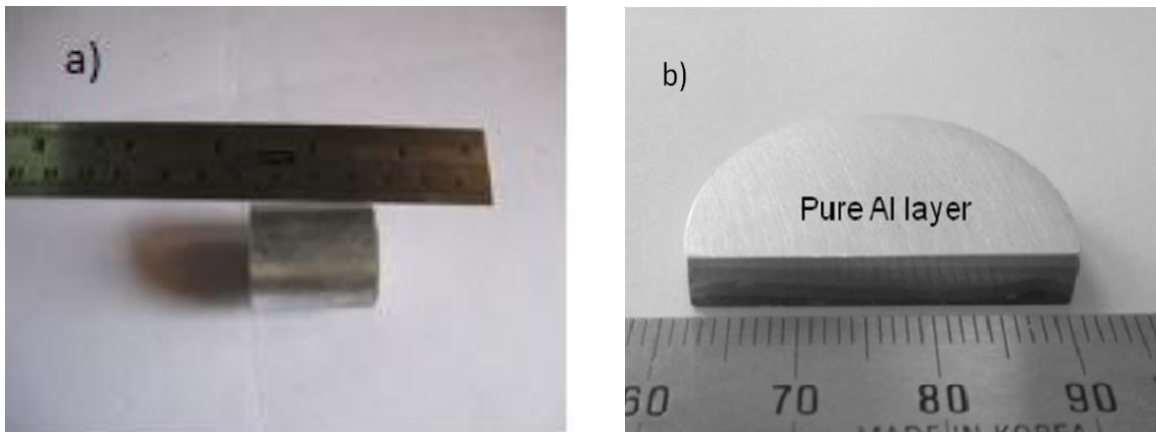


Fig.2 : (a) CNT reinforced Al composite specimen, (b) CNT reinforced Al FGM specimen

Comparison of Composite with FGM was shown in Table 2.

TABLE 2
Comparison of Composite and FGM

CNT reinforced aluminium	FGM
Increased mechanical properties	Increase in mechanical property in a range
Light weight and hard	Light weight, tough and hard
Good chemical resistance	Good chemical resistance and thermal barrier capacity

IV. APPLICATION OF COMPOSITES IN AIRCRAFT INDUSTRY

The use of fiber reinforced composites has become an attractive alternative to the conventional metals for many aircraft components mainly due to their increased strength, durability, corrosion resistance, resistance to fatigue and damage tolerance characteristics[28]. Composites also provide greater flexibility because the material can be tailored to meet the design requirements and they also offer significant weight advantages. Carefully designed individual composite parts, at present, are about 20-30% lighter than their conventional metal counterparts[29]. Although all-composite airplanes are now available in the world market, yet advances in the practical use of composite materials should enable further reduction in the structural weight of airplane. The composite materials used in aircraft industry are generally reinforced fibres or filaments embedded in a resin matrix. The most common fibres are carbon, aramid, glass and their hybrids. Commercial aircraft applications are the most important users of composites[30]. Aircraft, unlike other vehicles, need to lay greater stress on safety and weight. They are achieved by using materials with high specific properties. A modern civil aircraft must be so designed as to meet the numerous criteria of power and safety[31,32]. The composites applications trend over the years in US and European combat aircraft is summarized in table 3.

TABLE 3
Aircraft composite Materials usage

Fighter Aircraft (US)	F-16, F-14, F-18, YF-23, F-22, JSF, UCAV.
Fighter Aircraft (Europe)	Gripen JAS-39, mirage 2000, rafael, eurofighter typhoon, lavi, DASA Mako
Fighter Aircraft (Russia)	MiG-29, su series
Bomber (US)	B-2
Transport (US)	KC-135, C-17
Transport (US- commercial)	B-777, B-767, MD-11
Transport (Airbus, European)	A-320, A-340, A380, Tu-204, ATR42, Falcon 900, A300-600 ST
General aviation	Piaggio, Starship, premier 1
Rotary aircraft	V-22, Eurocopter tiger, comanche, RAH-66, bell/agusta BA-609, EH101, super Lynx 300, S-92.

V. CASE STUDIES

5.1 Civil aircraft applications

Aeronautical engineering comprises of various distinct areas in producing vehicles capable of performing distinct flight programmes. Initially importance was given to weight, speed and power, but other parameters that influence market acceptance of the aircraft should also be considered during design[33]. Airframe design starts with evaluation of flight conditions which the aircraft will encounter. Figure 5 shows the evolution in the use of composite over the years.

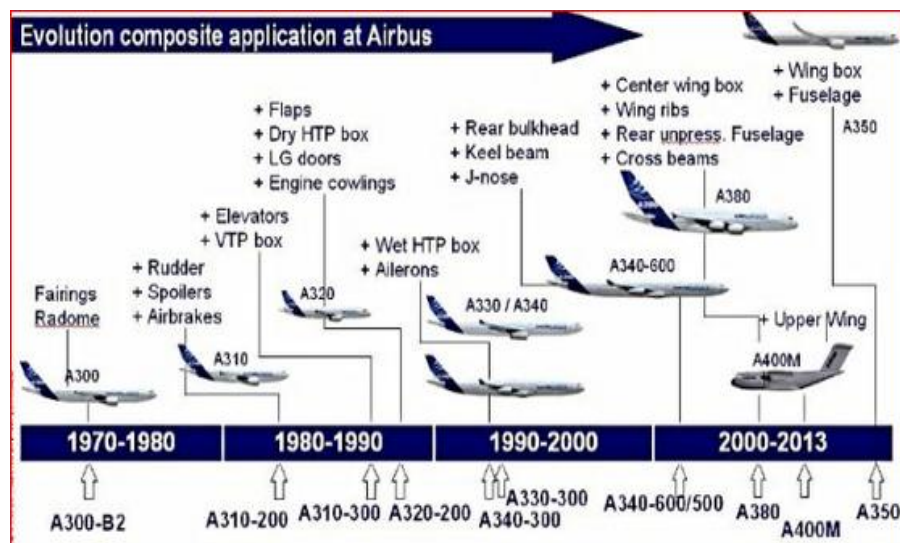


Fig. 5. Evolution in use of composite in Air bus [Courtesy: defenceaviation.com]

In recent designs, wind tunnel tests and analysis are being done to determine the lift and drag forces. Once determined, they are used to compute related factors of structural engineering. The high strength of composites and FGM allows designing of higher aspect ratio wings in aerofoil sections[34]. Figure 6 shows the percentage of forecast of composite structure uses in air bus and predicted huge market in the future grounds.

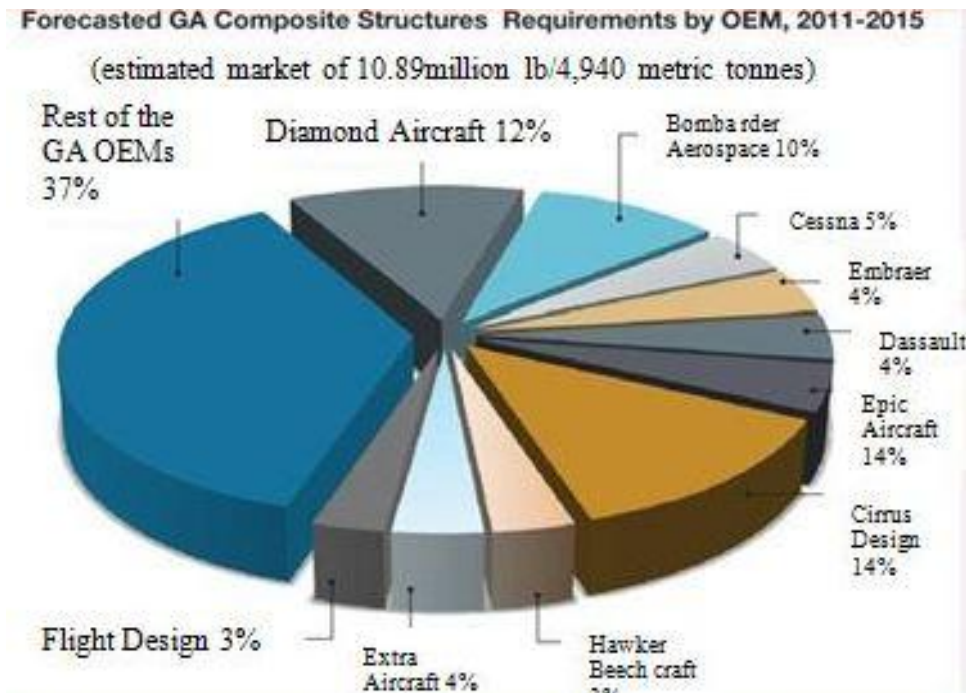


Fig. 6. Forecast of composite structure use in airbus

The selection of material naturally comes into the picture at the early stage of design itself. Airbus Industries used advanced composites on the Airbus A300 aircraft which first flew in 1972. The composite material was used in fin leading edge and other glass fiber fairing panels (as shown in Figure 7)[35]. As shown in the figure 5, the evolution of composite fraction of the structural weight for fighter and airbus aircraft seems to be leveling off at 30 percent. The payoff in combat aircraft is in performance in the form of reduced weight, increased payload and speed. Affordability is also a most important concern since costs associated with aircraft specific structural concept development, production implementation and recurring fabrication of complex composite parts with built in metal fittings and trunnions. Boeing is actively working with its global partners to find applicable best practice guidelines for the 787 program. As the newest member of the Boeing family of airliners, it is an all-new, mid-sized airplane with long range capabilities. The 787 is being made primarily of carbon fiber composite material comprising 50% of the 787's structural weight. This represents a breakthrough from today's airliners that are primarily composed of aluminium. Looking forward, cost reduction strategies for heavily loaded substructure need to be developed[28].

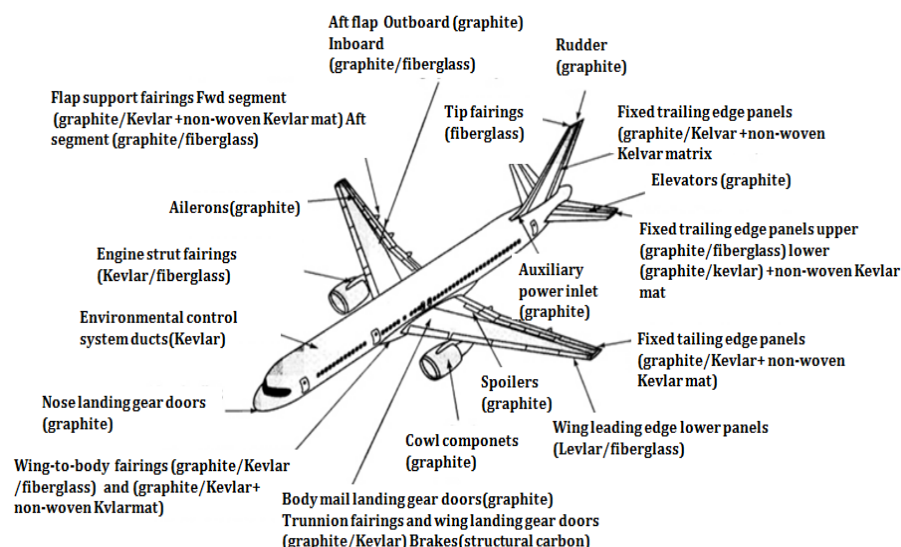


Fig. 7. Use of composite in Air bus [Courtesy: defenceaviation.com]

TABLE 4
The components used on Airbus series

Aircraft Type	Components Made of Composite Materials
Airbus A300B2/B4	Radome, fin leading edge and tip, fin trailing edge panels, cabin and cargo hold furnishings. Fairing -pylon, wing/fuselage rear.
Airbus A310-300	Rudder, elevator, vertical stabilizer, spoilers, cowl (inlet & fan), thrust reverser, main & nose landing gear door of wing leading & trailing edge panels, nacelles. Fairings - Ion, flap track, win fuselage.
Airbus A320/A319 & A321	Aileron, horizontal and vertical stabilizer, elevator, rudder, spoilers, flaps, engine cowl, radome, landing gear doors (main & nose), floor panels, wing panels (leading & trailing edge), other access panels, nacelles, Fairings -flap track, wing/fuselage (forward & rear), and main landing gear leg.
Airbus A330	Ailerons, rudder, flaps, spoilers, elevator, horizontal and vertical stabilizer, wing panels (leading & trailing edge), landing gear doors (main & nose), nacelles, Fairings -flap track, wing/fuselage (forward & rear).
Airbus 340	Ailerons, rudder, flaps, spoilers, elevator, horizontal and vertical stabilizer, wing panels (leading & trailing edge), landing gear doors (main & nose), nacelles, Fairings -flap track, wing/fuselage (forward & rear).

5.2 Military Aircraft Applications

The trends in the use of composite materials for US Fighter aircraft are shown by the examples in Figure 8 . The percentage by weight of composite materials used initially (e.g., F-15E) was small at 2%, but this percentage has since grown to more than 25% for the F-22 which is the designated replacement for the F-15E. The F-22 has demonstrated the feasibility and benefits of introducing processes such as RTM (Resin Transfer Molding) to improve the affordability of composite materials in combat aircraft applications. The use of composite materials in the US Navy's F/A-18E/F equals nearly 20% of its structural weight in flight critical parts as shown in table 5. The choice of composite materials in the F/A-18E/F was dictated by a need to reduce weight and to improve strength, reliability and maintainability in an aircraft carrier environment.

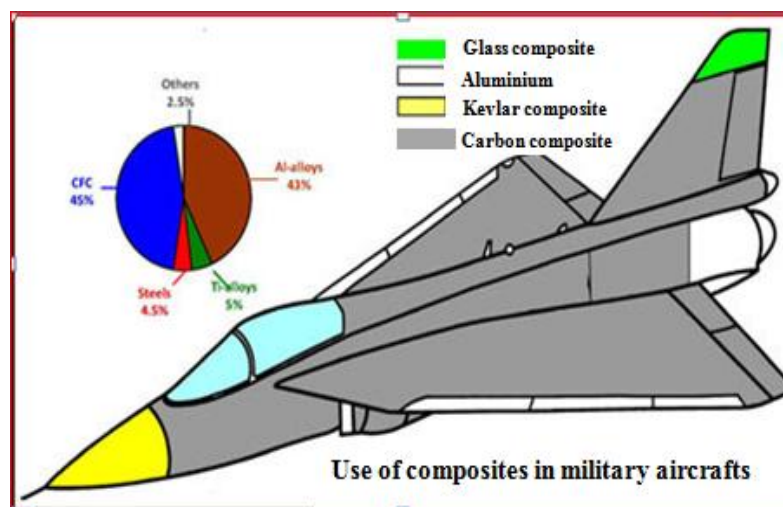


Fig. 8. The composite components used on Military aircraft [Courtesy: defenceaviation.com]

The center and aft fuselage skins and other ancillary structure, such as the speed brake and dorsal covers, are all-carbon/toughened- epoxy construction in the F/A-18E/F. Carbon fibers, such as Hexcel's IM7, with improved strength and stiffness properties are used in the wing and the tail skins. Although composite materials in general are sensitive to impact damage, toughened materials such as Fiberites 977-3 toughened epoxy system are used on the F/A-18E/F have successfully addressed this threat in operations. The AV-8B uses nearly 25% by weight of composite materials in its airframe[29].

TABLE 5
The composite components used on different Military Aircraft

Aircraft type	Components made of composite materials
F-14	Doors, Horizontal tail and fairings
F-15	Rudder, Vertical tail, horizontal tail and speed brake
F-16	Vertical tail and horizontal tail
F-18	Doors, Vertical tail, horizontal tail, wing box, fairings ,speed brake
B-1	Doors, Vertical tail, horizontal tail, Flats and slats
AV-8B	Doors, Vertical tail, horizontal tail, Flats and slats, Aileron, Flaps, Wing box, Body and fairings
TYPHOON	Wing, Fin ,Rudder, In-board aileron, fuselage
LIGHT COMBACT AIRCRAFT(LCA)	Wing, Fin ,Rudder, Control surface, radome

5.3 General aviation application: Helicopter

Composite materials are being used for different helicopter components as shown in figure 9. Use of advanced composites in helicopter application started way back in 1959 with the development of optimum pitch blade for the XCH-47 twin rotor helicopter of Vertol Aircraft Corporation[30].Extensive use of composites has also been made in India's Advanced Light Helicopter (ALH). In ALH, composite material is employed in whole of the secondary structure and several parts of the primary structure. The nose is made of aramid and tail section of carbon fiber reinforced plastic.

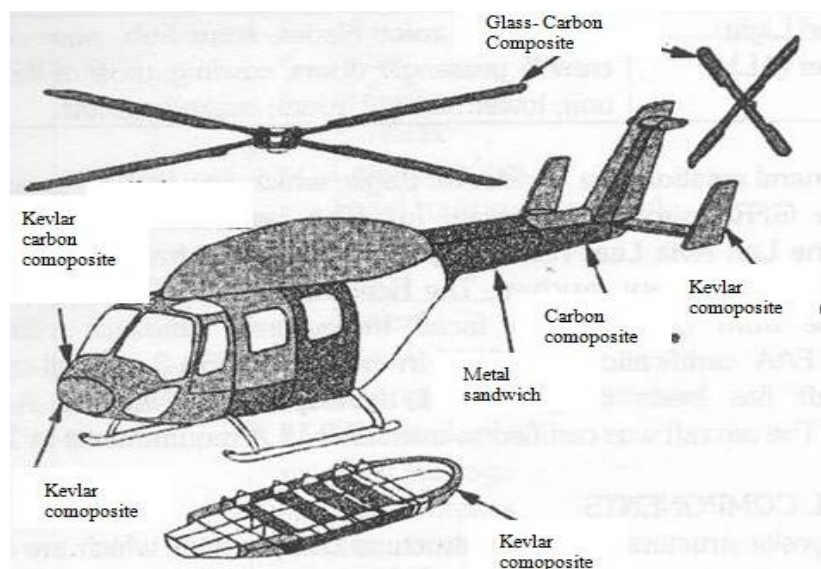


Fig. 9 . Helicopter with composite components [Courtesy: defenceaviation.com]

Rotor hub, main and tail rotor blades are made of composites. Entire cockpit is also made of composite material. The extent of composites used in the structure is about 60% by wetted area and about 29% by weight[31,32].The strength-to-weight ratio advantage of composites is vital to maximize payload in helicopter design. Boeing used composites in rotorcraft fairings in the 1950s and manufactured the first composite rotor blades for the CH-47 helicopter in the 1970s. Composites constitute key structural elements of

the Boeing-Sikorsky Comanche RAH-66 helicopter and the Bell-Boeing tilt rotor V-22 Osprey. The main design driver for these composite applications is weight savings and the listed parts in table 6 [33]. Stiffness tailorability and radar absorbing properties are significant contributors to these savings. The US Army's Advanced Composite Airframe Program (ACAP) and the US Air Force funded DMLCC-BW (Design and Manufacture of Low Cost Composites- Bonded Wing) program have provided major advances in composites technology for helicopters. Development of synthetic foams and bonded assembly technology played a major role in increasing composites usages in helicopters[34].

TABLE 6
The composite components used on Helicopter

Helicopter Type	Components made of composite materials
MBB BK 117	Main rotor blades, tail rotor blades, horizontal stabilizer, vertical stabilizer.
Bell 206L	Vertical stabilizer
Bell 402	Main rotor blades
Dauphin	Main rotor blades, vertical stabilizer.
McDonnell Douglas, MD 520N	Main rotor blades, tail boom
McDonnell Douglas MD 900	Main rotor blades, fuselage mid section, tail boom, canopy frame, internal fuselage, horizontal stabilizer, vertical stabilizer

Composites played a crucial role in the development of the tilt-rotor V-22 due to its weight sensitivity. The V-22 uses composite nacelles, wing, fuselage skins, empennage, side body fairings, and doors as shown in Figure 9. Composites usage in the V-22 is approximately 50 percent of the airframe weight[35,36]. The DMLCC- BW program provided the bonded assembly technology used in the V-22. Bonded assembly virtually eliminates mechanical fastening and allows structural attachments to be integrated into the components. The ACAP program provided advances in manufacturing technology to reduce costs of the composite components. Automated fiber placement technology applications to the fuselage resulted in a 53 percent cost savings since the V-22 aft fuselage skin could be fabricated in one integral piece rather than assembly of 10 skin panels in the original design[37].

Optimise the requirements:

For increased future applications of composites in aircraft structures lowering their costs is essential. Some of the means by which it can be achieved are:

1. Unitize and integrate multiple parts to reduce fabrication costs in the early stages of the design process.
2. Simplify design and apply automation to reduce variable fabrication costs
3. Replace lightly loaded integral stiffeners with syncore sandwich construction
4. Utilize fiber placement, performs, and other innovative material forms to reduce manual lay-up
5. Design for efficient manufacturing processes such as fiber placement and Resin transfer moulding.
6. All aspects of the design and manufacturing processes must be addressed to achieve lower cost composite structures.

VI. CONCLUSION

The Advanced Composites Programme activities have proliferated encompassing number of composite applications and its presence is now being felt across the large geographical canvas of the world as well as diverse user segments. It should be an efficient, successful mechanism in infusing the knowledge component to industrial practices. Effective knowledge among the academia/research institutions, standards & certifying agencies as well as the experts from the actual users has gone a long way in reducing product development cycle time and thus reaching the value-added products to the market in time. Composites are used in peripheral structures of aerodromes. Conventional constructions of composites ought to cost much less in future and will not be a constraint. Automation along with high standard for reinforcement and matrix materials will also decrease fabrication costs, as the rejection on grounds of quality will be less. Performance, reliability and efficiency of operators alone can assure the success of any programme and the space program in particular. The potential for application of high-performance composites and functionally graded composites has revolutionized space structural technology for future needs[36,37].

REFERENCES

- [1] Pindera.M.J, Arnold.S.M, Aboudi.J, Hui.D, Use of Composites in Functionally Graded Materials, Composites Eng. 4, 1994, 1–145.
- [2] Pindera.M.J, Aboudi.J, Arnold.S.M, Jones.W.F, Use of Composites in Multi-Phased and Functionally Graded Materials, Composites Eng., 5, 1995, 743–974.
- [3] Markworth.A.J, Ramesh.K.S, Parks.W.P, Review: Modeling Studies Applied to Functionally Graded Materials, J. Mater. Sci., 30, 1995, 2183–2193.
- [4] IJIMA S. Helical microtubes of graphitic carbon[J]. Nature,354: 1991, 56–58.
- [5] Pindera.M.J, Aboudi.J, Glaeser.A.M, Arnold.S.M, Use of Composites in Multi-Phased and Functionally Graded Materials, Composites, Part B 28,1997, 1–175.
- [6] Suresh.S, Mortensen.A, Fundamentals of Functionally Graded Materials, IOM Communications, London, 1998.
- [7] Miyamoto.Y, Kaysser.W. A, Rabin.B. H, Kawasaki.A, Ford.R.G, Functionally Graded Materials: Design, Processing and Applications, Kluwer Academic, Dordrecht, 1999 .
- [8] Paulino.G.H, Jin.Z. H, Dodds. R. H, Failure of Functionally Graded Materials in Comprehensive Structural Integrity., Elsevier Science, New York, Vol. 2, Chap. 13, 2003, 607–644.
- [9] Noda.N, Thermal Stresses in Functionally Graded Material, J. Therm. Stresses, 22, 1999, 477–512.
- [10] Van der Biest, M. Gasik, Functionally Graded Materials VIII , Proceedings of the Eighth International Symposium on Multifunctional and Functionally Graded Materials, Materials Science Forum, J. Vleugels eds., Trans Tech Publications Ltd, Uetikon-Zuerich, Switzerland, 2004, 492–493.
- [11] Birman.V, Stability of Functionally Graded Hybrid Composite Plates, Composites Eng, 5, 1995, 913–921.
- [12] Birman.V, Stability of Functionally Graded Shape Memory Alloy Sandwich Panels, Smart Mater. Struct., 6, 1997, 278–286.
- [13] Kaysser.W. A, and Ilschner.B, FGM Research Activities in Europe, MRS Bull, 20, 1995, 22–26.
- [14] Cho.J. R,D.Y, Averaging and Finite Element Discretization approaches in the Numerical Analysis of Functionally Graded Materials, Mater. Sci. En., 302, 2001, 187–196.
- [15] Yin. H.M, Paulino.G.H, Buttlar.W.G, Sun. L.Z, Effective Thermal Conductivity of Two-Phase Functionally Graded Particulate Composites, J. Appl. Phys. ,063704, 2005,98-6.
- [16] Liu.G.R, Han.X, Lam.K.Y, Material Characterization of Functionally Graded Materials by Means of Elastic Waves and a Progressive-Learning Neural Network, Compos. Sci. Technol, 61, 2001, 1401– 1411.
- [17] Han.Y, Elliott.J, Molecular dynamics simulations of the elastic properties polymer/carbon Nanotube composites, Comput Mater Sci,39, 2007,315–23.
- [18] Shen.HS, Nonlinear bending of functionally graded carbon nanotubereinforced composite plates in thermal environments, Compos Struct,91, 2009,9–19.
- [19] Halicioglu, Stress Calculations for Carbon Nanotubes, Thin Solid Films, 312, 1998,11-14.
- [20] Hernandez.E, Goze.C, Elastic Properties of Single-Walled Nanotubes, Applied Physics , 68, 1998, 287-292.
- [21] Lu. J. P, Elastic Properties of Carbon Nanotubes and Nanoropes, Physical Review Letters, 79, 1997, 1297-1300.
- [22] Sinnott.S, B.Shenderova.O.A, White.C.T, Brenner.D.W, Mechanical Properties of Nanotubule Fibers and Composites Determined From Theoretical Calculations and Simulations, Carbon, 36, 1998,1-9.
- [23] Treacy. M.J, Ebbeser.W, Exceptionally High Young’s Modulus Observed for Individual Carbon Nanotubes, Nature. 381, 1996, 678.
- [24] Wong.E.W, Sheehan. P. E, Nanobeam Mechanics: Elasticity, Strength, and Toughness of Nanorods and Nanotubes, Science, 277, 1997, 1971-1975.
- [25] Yao. N, Lordi.V, Young’s Modulus of Single Walled Carbon Nanotubes, Journal of Applied Physics, 84, 1998, 1939-1943.
- [26] Yu.M.F, Lourie.O, Dyer.M.J, Moloni.K, Kelly.T. F, Ruoff. R.S, Strength and Breaking Mechanism of Multiwalled Carbon Nanotubes under Tensile Load, Science Magazine, 287,2000,637-640.
- [27] Srivastava.D, Menon.M, Cho.K, Nanoplasticity of Single-Wall Carbon Nanotubes Under Uniaxial Compression, Physical Review Letters, 83, 1999, 2973 .
- [28] Mintmire. J.W, and White. C.T, Electronic and Structural Properties of Carbon Nanotubes, Carbon, 33, 1995, 893.
- [29] Tersoff.J, Ruoff.R.S, Structural Properties of a Carbon-Nanotube Crystal, Physical Review Letters, 73, 1994, 676.
- [30] Talay.T, Cerro, Lepsch.R, Gelhausen.P, Guynn.M, Systems Analysis of Nanotube Technology, published in the Nanotube Technology Assessment, National Aeronautics and Space Administration, Office of AeroSpace Technology, Washington, D. C, August 16, 2000.
- [31] Schiller.C, Siedler.M, Peters.F, Eppel.M, Functionally Graded Materials of Biodegradable Polyesters and Bone-Like Calcium Phosphates for Bone Replacement, Functionally Graded Materials, Proceedings of the Sixth international symposium on Functionally Graded Materials,The American Ceramic Society, Westerville, 97–108, 2000.
- [32] Gururaja Udupa, S.Shrikantha rao, K.V.Gangadharan, Future applications of Carbon Nanotube reinforced Functionally Graded Composite Materials, Proceedings of IEEE-International conference on Advances in Engineering ,Science and Mangagement,E.G.S Pillay Engineering college,Nagapattinam,2012.
- [33] Fukui, Microstructures of Functionally Graded Materials Fabricated by Centrifugal Solid-Particle and in-situ Methods. Metals and Materials International, 11. 5, 391-399, 2005,1598-9623.

- [34] Fukui.Y. Fundamental Investigation of Functionally Gradient Material Manufacturing System using Centrifugal Force. JSME Int. J. Series III, 34, 1, 1991, 144-148, ISSN 0914-8825.
- [35] Inaguma.Y, Sato.H, Miura.Fujiwara.E, A Novel Fabrication Method for Functionally Graded Materials under Centrifugal Force: The Centrifugal Mixed-Powder Method. Materials, 2.4, 2009, 2510-2525.
- [36] Miura.Fujiwara.E, Sato.H, Fabrication of Functionally Graded Materials by Centrifugal Slurry-Pouring Method and Centrifugal Mixed-Powder Method. J. Jpn. Soc. Powder Powder Metallurgy, 57. 5, 2010, 321- 326.
- [37] C.Y. Lin, C.Bathias, H.B.McShane, R.D.Rawlings, Production of silicon carbide Al 2124 alloy functionally graded materials by mechanical powder metallurgy technique, J. Jpn. Soc, Powder Metallurgy, 42, 1999, 129.

An optimised multi value logic cell design with new architecture of many value logic gates

Prajyant Pathak¹, Puran Gour²

^{1,2} Deptt of Electronics Communication, RGPV, INDIA

Abstract: Propose thesis work is a design of a Multi Logic Memory cell of four logic levels which can hold Logic 0, Logic 1, Logic 2 & Logic 3 and also propose an Interface module design between multi logic system with binary systems, thesis work can reduce the no. of wires required to parallel interface with normal memory and also can increase the speed of simple serial data transfer.

I. Introduction

In year 2011 Mrs Fatma Sarica and Mrs. Avni Morgul publish in International conference on Electrical and Electronics Engineering and published in IEEE Journal they discuss in their abstract As Multi-valued logic circuits have been offered as a solution to general interconnection and chip area problem. In this paper they present a new latch and restoration circuit which improves the performance of the previously designed flip-flop circuit. The flip-flop is the usual building block of multilevel sequential circuits and may be used to design sequential circuits such as multilevel counter/dividers and other sequential circuits. In year 2009, Mr. Ben Choi & Mr. Kunal Tipnis entitle 'New Components for Building Fuzzy Logic Circuits in Computer Science & Electrical Engineering' and 'Fuzzy Systems and Knowledge Discovery' paper were published in IEEE Explore. Journal they discuss in their abstract As This Paper Two New design of fuzzy logic circuit components. they designs of a new fuzzy memory cell and a new fuzzy logic gate. Different then a digital memory cell that can only store either a one or a zero, proposed multi logic memory cell store any value ranging from zero to one. Their cell can also be used as a D-type multi logic flip-flop, which is the first design of a D-type multi logic flip-flop.

II. Tools Used

Tanner EDA provides a complete line of software solutions that catalyze innovation for the design, layout and verification of analog and mixed-signal (A/MS) integrated circuits (ICs). Customers are creating breakthrough applications in areas such as power management, displays and imaging, automotive, consumer electronics, life sciences, and RF devices. Tanner EDA is a leading provider of easy-to-use, PC-based electronic design automation (EDA) software solutions for the design, layout and verification of analog/mixed signal ICs and MEMS.

III. Multi Level Digital Logic

Thesis Design is four level logic rather than two level logic (binary logic), physical interpretation is as shown in table 1

Table 1: The Physical Logic Levels of Proposed Multi value logic

Voltage range IN/Out	Multi level logic
0 to 1v	Logic '0'
1 to 3v	Logic '1'
3to 5v	Logic '2'
5 to 6v	Logic '3'

To make computation with four logic, in the thesis work design of four logic AND, four logic OR, four logic NOT & four logic Flip Flop have been done on EDA tool. Our Previous Research paper ref ^[10] already have description and implementation of this Circuits.

IV. Proposed Four Logic D-Flip Flop

Figure shown in below diagram is the design of Flip flop which are been proposed in the paper work. One thing is required to know that the logic GATE's are used in the circuits are also four value logic gates, working of this Gate are explained in Ref [10].

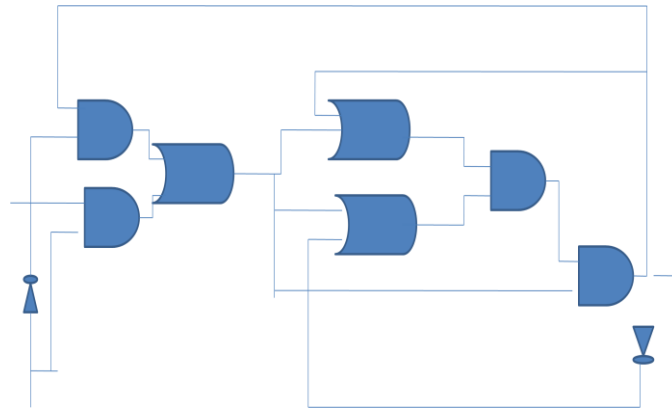


Fig 1: Four value Flip Flop Logical schematic

Four logic Flip flop		
Clock	Input	Output(stored value)
↑	0	0
↑	1	1
↑	2	2
↑	3	3

Table 2: Proposed Flip flop Truth table

As from the table above and from the table 1. The designing done on S-Edit with specified L= 44n and W=440n. NMOS and PMOS is been used and the T-Spice file been generated for the coding and parameter inserting the commands. The simulation time is chosen 600ns and W-edit is been used for generating the waveform. The S-edit schematic is been derived for proposed multi logic NOT, AND & OR logic gates.

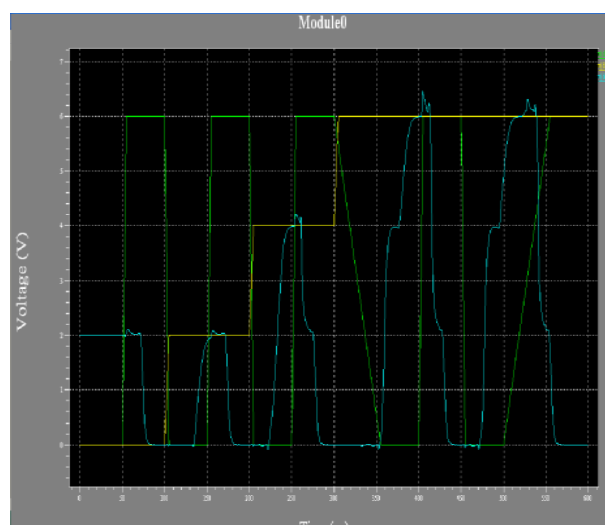


Fig 2 S-Edit Schematic of Proposed four logic F/F

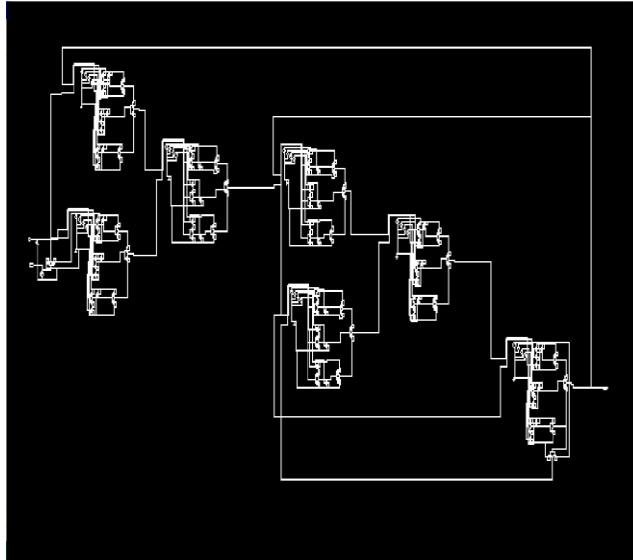


Fig 3 Simulation W-Edit results of four logic F/F

V. Binary To Four Logic Converter

Figure below shows flow of the binary to multi logic conversion proposal. It is required because most of existing digital circuits support binary Boolean logic, and proposed design is four value logic. So this kind of convertor required for make proposed design compatible with existing circuits.

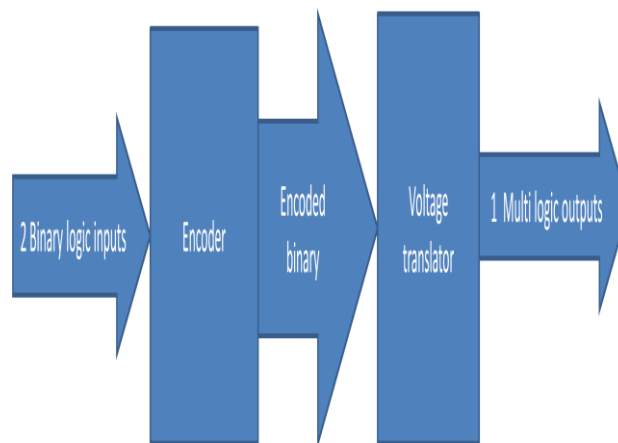


Figure 4 The Dataflow for binary to four logic conversion

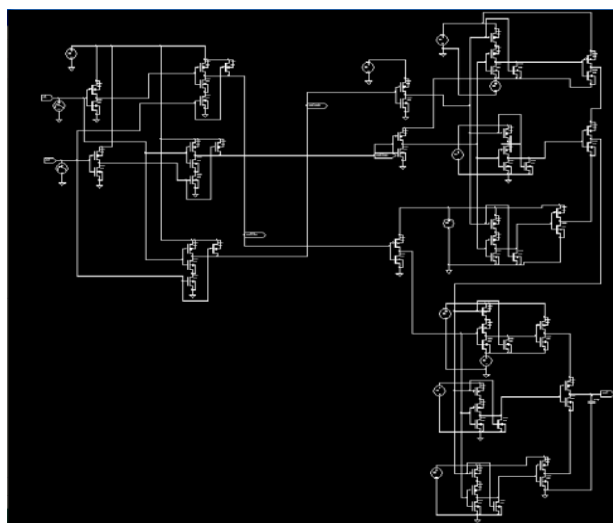


Figure 5: S-Edit Schematic of Converter

Table shows the working of proposed convertor.

Table 3: Voltage level convertor for compatibility

Binary INPUT'S		Multi-logic output
0 (0-0.8 V)	0(0-0.8 V)	0 (0-1 V)
0(0-0.8 V)	1(3-5V)	1(1-3V)
1(3-5V)	0(0-0.8 V)	2(3-5V)
1(3-5V)	1(3-5V)	3(5-6V)

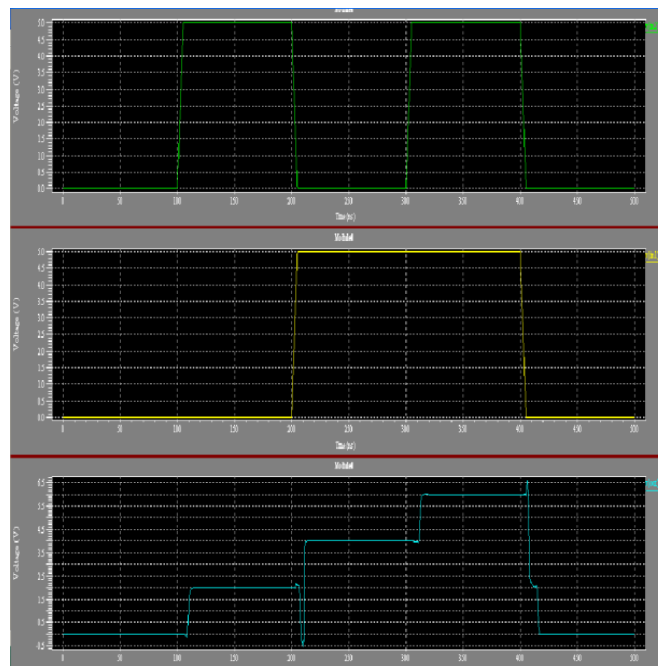


Fig 6 : Wedit Waveform for Proposed convertor

VI. Result

Table 4 Observed Result of each design

Design	MOSFET count	Average power consumed	
Designed four logic NOT	2	1.57 mw	27 ms
Designed four logic AND	18	2.34 mw	40 ms
Designed four logic OR	18	2.21 mw	39 ms
Designed four logic Flip Flop	130	3.95 mw	157 ms
Designed Binary to four logic convertor	58	3.91 mw	54 ms

Result's Analysis Table below shows the comparative analysis of proposed work with other existing design.

Table 5 Performance comparison with previous work

Multi logic Flip flop design			
	Base[1]	Base[2]	Thesis Designed work
No. of MOSFET	133	180	130
Average power consumed	4.15 mw	--	3.95mw

Problems Noise immunity is not significantly reduces as compare to binary logic.

VII. Conclusion

we can conclude that proposed work can be used for existing deign and by that way we can reduce power of data transmission by reducing number of data lines and reduce number of clock cycle by using four logic levels. We can half the number of flip flop using proposed flip flop. All can be achieved because of proposed binary to multi-logic convertor. Future scope of proposed work is that we can use proposed work with good noise margin and design can be further modify by reducing some more MOSFET.

REFERENCES

- [1] Basic Circuits for Multi-Valued Sequential Logic, Fatma Sarica1 and Avni Morgul2, Electrical and Electronics Engineering (ELECO), 2011 7th International Conference , 1-4 Dec. 2011, Page(s): II-66 - II-68,Print ISBN: 978-1-4673-0160-2, IEEE Explore
- [2] New Components for Building Fuzzy Logic Circuits, Ben Choi & Kunal Tipnis, Fourth International Conference on Fuzzy Systems and Knowledge Discovery (FSKD 2007) Vol.2, 24-27 Aug. 2007, pp 586 – 590,ISBN 978-0-7695-2874-8, IEEE Explore
- [3] Array placement for storage size reduction in embedded multimedia systems . Eddey De greef, francky cathoor, hugo de man, Application-Specific Systems, Architectures and Processors, 1997. Proceedings., IEEE International Conference, 14-16 Jul 1997, Page(s): 66 – 75, IEEE Explore
- [4] Modeling and Simulation of Real Defects Using Fuzzy Logic,Amir Attarha, Mehrdad Nourani,Caro Lucas, Design Automation Conference, 2000. Proceedings 2000, 631 – 636, IEEE Explore
- [5] Fuzzy Logic Introduction ,M. Hellmann, Laboratoire Antennes Radar Telecom, Avenue General Leclerc, CS 74205, 35042 Rennes Cedex, France.
- [6] The Concept of Fuzzy Flip-Flop, kaoru hirota, IEEE TRANSACTIONS ON SYSTEMS, MAN, AND CYBERNETICS, VOL. 19, NO. 5, SEPTEMBER/OCTOBER 1989
- [7] SUMMARY OF FUZZY FLIP-FLOP, Kazuhiro OZAWAI, Kaoru HIROTAZ), Laszlo T KOCZY",Witold PEDRYCZ4), Norikazu IKOMA5), 1995 IEEE
- [8] Family of Fuzzy - Flip-Flops Based on Bounded Product, Bounded Sum and Complementation, Lesław Gniewek and Jacek Kluska, IEEE TRANSACTIONS ON SYSTEMS, MAN, AND CYBERNETICS—PART B: CYBERNETICS, VOL. 28, NO. 6, DECEMBER 1998
- [9] Fuzzy Logic and Its Application to Switching Systems, PETER N. MARINOS, IEEE TRANSACTIONS ON COMPUTERS, VOL. C-18, NO. 4, APRIL 1969

Determination of Stress Intensity Factor for a Crack Emanating From a Rivet Hole and Approaching Another in Curved Sheet

Raghavendra. P¹, Anand.A², S. R. Basavaraddi³

1,3 (Department of Mechanical Engineering, KLE Dr M.S.Sheshgiri College of Engineering and Technology, Belgaum, INDIA)

2 (Department of Mechanical Engineering, Vidyavardhaka College of Engineering, Mysore, INDIA)

Abstract: Modern aircraft structures are designed using a damage tolerance philosophy. This design philosophy envisions sufficient strength and structural integrity of the aircraft to sustain major damage and to avoid catastrophic failure. The rivet holes location are one of the stress concentration region in fuselage skin. The current study includes a curved sheet with rivet holes is considered as part of the fuselage skin. During the service life of aircraft fatigue cracks will emanate from rivet holes simultaneously as they experience identical stresses due to internal pressure. In fracture mechanics, Stress Intensity Factor (SIF) is an important criterion to evaluate the impact of crack as the magnitude of SIF determines the propagation of crack. The objective is to investigate the SIF for crack emanating from one rivet hole and approaching another using Displacement Extrapolation Method (DEM) in F.E.M that would aid in the determination of the critical nature of such cracks.

Keywords: Fracture mechanics, stress intensity factor, rivet hole

I. Introduction

Modern aircraft structures are designed using a damage tolerance philosophy. This design philosophy envisions sufficient strength and structural integrity of the aircraft to sustain major damage and to avoid catastrophic failure. However, structural aging of the aircraft may significantly reduce the strength below an acceptable level; this raises many important safety issues.

The most likely places for crack initiating and development are the rivet holes, due to the high stress concentration in this area. Such cracks may grow in time, leading to a loss of strength and the reduction of the lifetime of the fuselage skin as shown in fig 1.

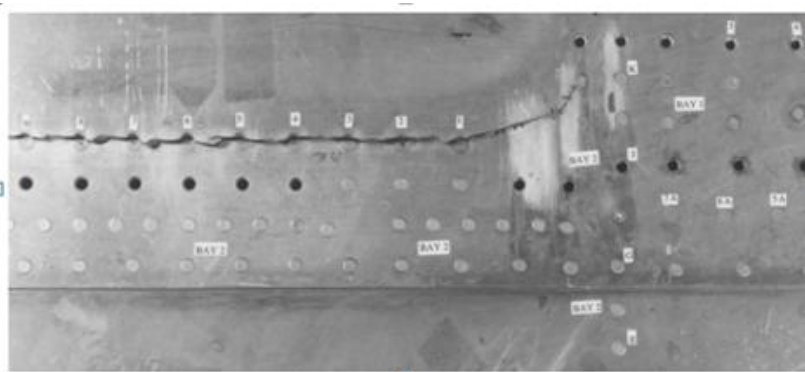


Fig.1. Larger crack formed by the link-up of fatigue cracks at adjacent rivets

The crack behavior must be assessed in order to avoid catastrophic failures. For this, the knowledge of the crack size, service stress, material properties and Stress Intensity Factor is required.

II. FRACTURE MECHANICS

Fracture mechanics involves a study of the presence of the cracks on overall properties and behavior of the engineering component. The process of fracture may be initiated at defect locations like micro-cracks, voids, and the cavities at the grain boundaries. These defects can lead to the formation of a crack due to the rupture and disentanglement of molecules, rupture of atomic bonds or dislocation slip[3]. Cracked body can be subjected to three modes of loads as shown in Figure 2. In some cases, body may experience combination of the three modes.

- 1. Opening mode:** The principal load is applied normal to the crack surfaces, which tends to open the crack. This is also referred as Mode I loading (Figure 2a).
- 2. In-plane shear mode:** This mode corresponds to in plane shear loading which tends to slide One crack Surface with respect to the other. This is also referred as Mode II loading (Figure 2b).
- 3. Out-of-plane shear mode:** This is the tearing and antiplane shear mode where the crack surfaces move relative to one another and parallel to the leading edge of the crack (Figure 2c).

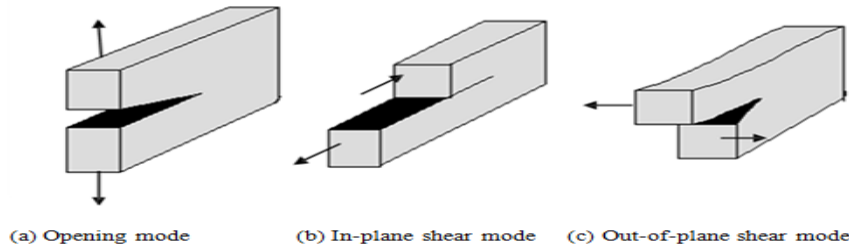


Fig. 2: Three modes of loading that can be applied to a crack

The Stress Intensity Factor (SIF) is one the most important parameters in fracture mechanics analysis. It defines the stress field close to the crack tip and provides fundamental information of how the crack is going to propagate. In this study, a typical and practical point matching technique, called Displacement Extrapolation Method (DEM) is chosen for the numerical analysis method. Plane strain assumption is valid for very thin walled structures; the evaluation of S.I.F (K_I) by Displacement Extrapolation Method (DEM) is as discussed below.

The stress intensity factors at a crack for a linear elastic fracture mechanics analysis may be computed using the KCALC command. The analysis uses a fit of the nodal displacements in the vicinity of the crack. The actual displacements at and near a crack for linear elastic materials are

$$U = +\frac{K_{II}}{2G} \sqrt{\frac{r}{2\pi}} (1 + K) \dots \dots \dots (1)$$

$$V = +\frac{K_I}{4G} \sqrt{\frac{r}{2\pi}} (1 + K) \dots \dots \dots (2)$$

$$W = +\frac{2K_{III}}{G} \sqrt{\frac{r}{2\pi}} \dots \dots \dots (3)$$

Where: u, v, w = displacements in a local Cartesian coordinate system as shown in figure 3r, θ = coordinates in a local cylindrical coordinate system as shown in figure 3

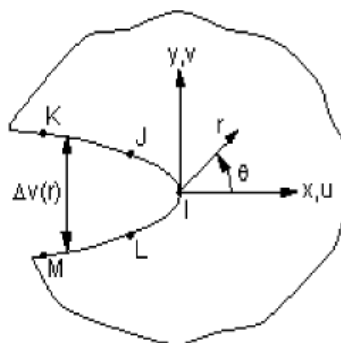


Fig. 3: Nodes Used for the Approximate Crack-Tip Displacements for Full crack Model
G = shear modulus

$$K = \frac{\nu}{1+\nu} \text{In plane stress} \dots \dots \dots (4)$$

$$K = 3 - 4\nu \text{ In plane strain } \dots \dots \dots (5)$$

ν = Poisson's

For mode-I, SIF at crack tip is expressed as

$$K_I = \sqrt{2\pi} \frac{4G}{1+\nu} \frac{|\Delta v|}{\sqrt{r}} \dots \dots \dots (6)$$

Where ΔV , is the motion of one crack face with respect to the other.

At points J and K. if, let r approaches zero

$$\lim_{r \rightarrow 0} \frac{|v|}{\sqrt{r}} = A$$

$$\lim_{r \rightarrow 0} \frac{|u|}{\sqrt{r}} = B \dots \dots \dots (7)$$

$$\lim_{r \rightarrow 0} \frac{|w|}{\sqrt{r}} = C$$

Therefore

$$K_I = \sqrt{2\pi} \frac{4GA}{1+K} \text{ MPa } \sqrt{mm} \dots \dots \dots (8)$$

$$K_{II} = \sqrt{2\pi} \frac{2GB}{1+K} \text{ MPa } \sqrt{mm} \dots \dots \dots (9)$$

$$K_{III} = \sqrt{2\pi} \frac{GC}{2(1+K)} \text{ MPa } \sqrt{mm} \dots \dots \dots (10)$$

III. LOAD CALCULATION AND MODEL DIMENSION FOR CURVED SHEET

The curved sheet considered as a part of the fuselage skin with the rivet holes. The load and model dimensions for the curved sheet are similar to fuselage as given below [5].

- Radius of the fuselage(R) = 1600 mm
- Thickness of the fuselage skin (t) = 1.8mm
- Diameter of the Rivet hole (D) = 4.8mm
- Internal pressurization (P_r) = 0.06695 N/ mm²

All the edges of the curved sheet are subjected to symmetric boundary condition and pressure is applied on the area.

$$\text{Hoop stress} = (P_r * R) / t$$

$$\text{Hoop stress (} \sigma_h \text{)} = (0.06695 * 1600) / 1.8$$

$$\text{Hoop stress (} \sigma_h \text{)} = 59.51 \text{ N/ mm}^2$$

IV. Material Used

Table 1: Material compositions

Component	Weight Percentage
Aluminum	90.7-94.7
Chromium	max 0.1
Copper	3.8-4.9
Ferrous	max 0.5
Magnesium	1.2-1.8
Manganese	0.3-0.9
Titanium	max 0.15
zinc	max 0.25
Other, total	max 0.15

Table 2: Material Properties in Al 2024-T3

Properties	Material Aluminum 2024-T3
Density	27.27 N/ mm ³
Ultimate tensile strength	483 N/ mm ²
Tensile yield strength	362 N/ mm ²
Modulus of elasticity	72000 N/ mm ²
Poisson's ratio	0.33
Fracture toughness	98.90 MPa \sqrt{m}

V. Methodology

The objective of this work is to determine SIF for crack emanating from a rivet hole and approaching another in curved sheet as shown in figure 4. The objective is achieved by developing a model of a curved sheet with rivet hole and a through crack using CATIA V5 software. The CATIA model is imported to ANSYS. The FE model is meshed using 8-node quadrilateral doubly curved SHELL 93 elements in the pre-processor of the ANSYS software. A curved sheet with a crack was meshed using three different mesh densities. Mainly, the area around the imperfection was modeled with a finer mesh.

As a part of the finite element work, a mesh sensitivity study was conducted. Further, the crack tip singular elements were created using KSCON command. For this model there are 36 singular elements around the crack tip and the radius of the first row elements is Δa (Where $\Delta a = a/100$). The model is then solved (Static Analysis)

by subjecting it to an pressure of .06695MPa load with appropriate boundary conditions. Then the SIF is evaluated in general postprocessor by using KCALC command and parametric study is done for different thickness.

The geometry of the meshed test model with crack tip singular elements in ANSYS 12 is as shown in the Figure 5.

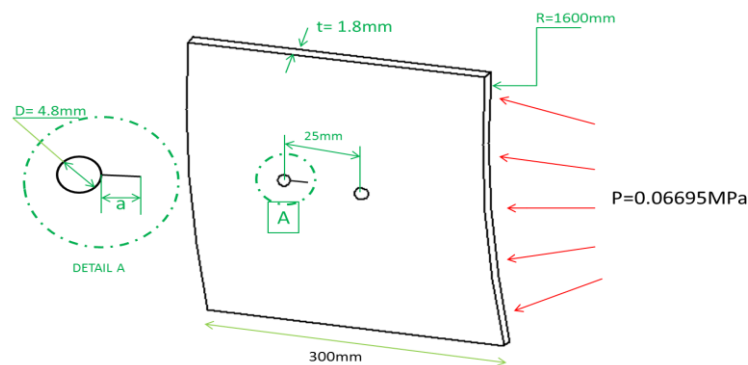


Fig 4: Geometry of model

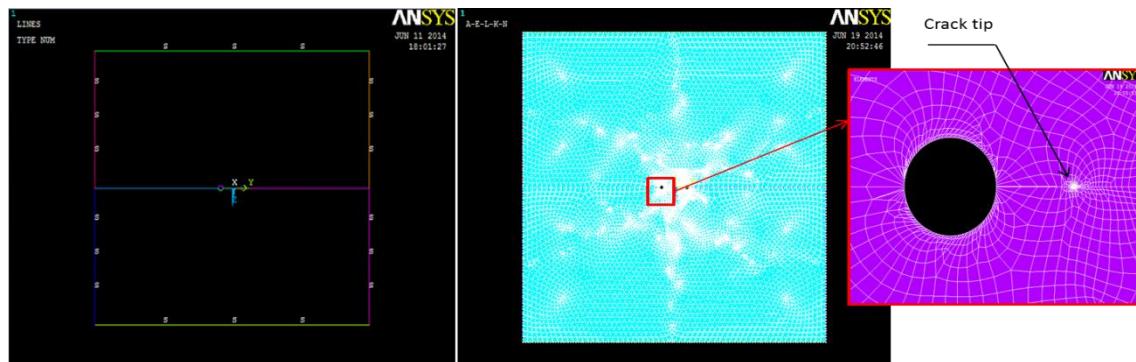


Fig 5: (a) Finite Element Model with Boundary Conditions (b) Meshed Finite Element Model (c) Zoomed View of Crack Tip Singular Elements

VI. Result And Discussion

The Figure 6 shows a pressurized cylindrical shell with varying longitudinal crack length. The theoretical formulae involved in the determination of mode I SIF of the crack is given below [3]. Mode I S.I.F (KI) is given by

$$K_I(\text{Theo}) = \sigma \sqrt{\pi a} f_1(\alpha) \dots \dots \dots (11)$$

Where

$$f_1(\alpha) = \frac{a}{\sqrt{(Rt)}} \sqrt{(1 + .52x + 1.29x^2 - 0.07x^3)}$$

$$x = \frac{a}{\sqrt{(Rt)}}$$

The half crack length was varied from 20mm to 439.53mm .The maximum crack length in a given dimensions of cylindrical shell was determined using curvature parameter β .

$$\beta = \frac{a}{\sqrt{(Rt)}} \sqrt{12(1 - \nu^2)} \dots \dots \dots (12)$$

If $\beta = 8$ for longitudinal cracks, thickness of the cylindrical shell is 10mm and radius of the cylindrical shell is 1000mm then the maximum crack length for given set of cylindrical shell dimension is 439.53mm

The values of mode 1 SIF from the procedure explained in the previous section is also determined for the same problem using FEA in ANSYS. Table 3 shows the values of SIF obtained by the theoretical and FEM.

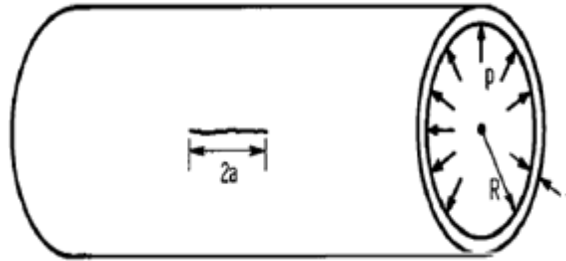


Fig.6: Longitudinal crack in internally pressurized cylinder

Table 3: Mode-1 S.I.F (K_I) Using FEA and theoretical K_I (Theo) for different Half Crack lengths

Half crack length (a) mm	Model-1 S.I.F by FEA MPa \sqrt{mm}	Model-1 S.I.F by analytical MPa \sqrt{mm}	% error
20	816.8	851.322	4.05
60	1837.6	1828.751	0.49
100	2981.4	2931.63	1.69
140	4114.8	4221.655	2.53
220	7166.7	7247.292	1.11
300	10694	10710.546	0.15
380	14644	14471.544	1.19
439.532	17812	17398.911	2.37

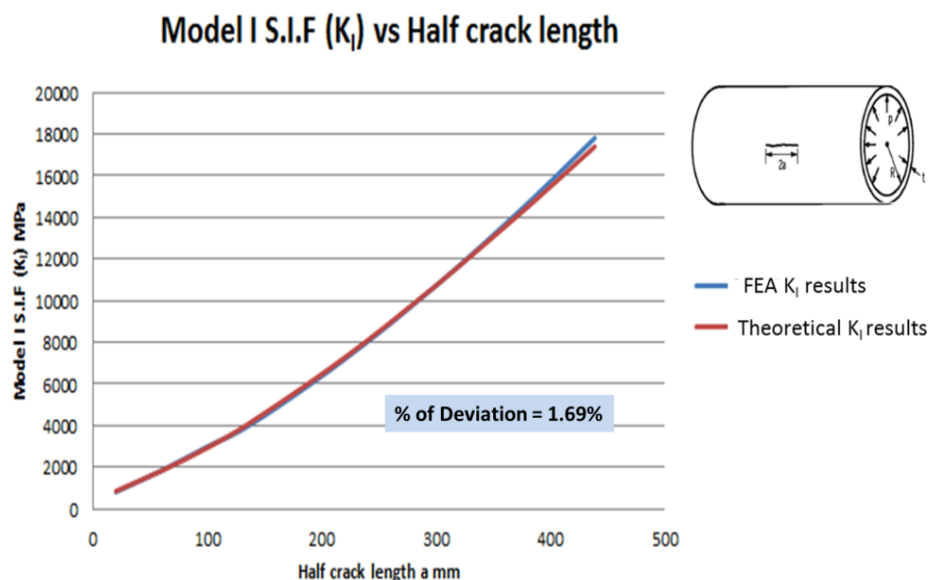


Fig.7: variation of theoretical and FEA values of S.I.F Vs crack length in Pressurized cylinder

Figure 7 shows the variation of theoretical and simulated FEA SIF values for various longitudinal crack length in pressurized cylinder. From the Figure it is indicated that the results which were obtained by using FEM are in good agreement with theoretical equation for a longitudinal through crack emanating in internally pressurized cylinder.

The average percentage of error between the FEA and theoretical SIF values is 1.69%, which is negligible.

Thus the proposed methodology to determine the Mode-I S.I.F for longitudinal cracks in pressurized cylinder is validated against a standard procedure elucidated in literature [3].

The above procedure is used for “Determination of SIF for a Crack Emanating from a rivet hole and approaching another in curved sheet” the test models containing a through crack emanating from a rivet hole is meshed under plane strain condition it is internally pressurized and respective SIF’s are calculated by varying half crack length(a).

$$K_0(\text{Theo}) = \sigma \sqrt{\pi a_{eff}} \text{ MPa } \sqrt{mm}$$

The specimen graphs are plotted to variation of normalized Stress Intensity Factor’s (K_I/K_0), (K_{II}/K_0), (K_{III}/K_0) with respect to (a/D) ratio is as shown in Figure 8(a),8(b),8(c) respectively.

The values of K_I , K_{II} and K_{III} with respect to (a/D) for thickness $t=1.8$ is as shown in table 4. It is observed that as the crack is initiated near the hole, the stress concentration at the hole has a strong influence on the stress intensity factor and makes the crack to propagate at faster rate. When crack approaches another hole there is sudden rise of stress intensity factor. This sudden rise is due to presence of stress concentration at another hole. The specimen graphs 8(a),8(b) and 8(c) shows that the Mode-I S.I.F (K_I) increases steadily as crack grows and rises suddenly when crack is near to another hole. It is clear that mode-I is high value and mode-II and mode-III are negligible. Therefore for crack emanating from on hole and approaching another in a curved sheet mode-I is more influencing for crack propagation. Through comparison it is observed that mode-II and mode-III have very less contribution for crack propagation hence can be ignored.

Table 4: The normalized Stress Intensity Factor (K_I/K_0), (K_{II}/K_0), (K_{III}/K_0) with respect to a/D ratio

a mm	a/D	K_I MPa	K_{II} MPa	K_{III} MPa	K_0 MPa	K_I/K_0	K_{II}/K_0	K_{III}/K_0
6	1.25	278.76	2.364	3.74E-03	245.11	1.1372	9.64E-03	1.52E-05
8	1.67	299.57	0.967	8.94E-03	266.84	1.1226	3.62E-03	3.35E-05
10	2.08	328.24	1.50E-02	1.52E-02	286.93	1.1439	5.22E-05	5.28E-05
12	2.5	360.23	0.78599	1.05E-02	305.7	1.1783	2.57E-03	3.45E-05
14	2.92	387.06	5.10E-01	7.49E-03	323.39	1.1968	1.58E-03	2.32E-05
16	3.33	421.63	0.29899	1.62E-02	340.15	1.2395	8.79E-04	4.77E-05
18	3.75	482.45	2.58E-01	3.58E-02	356.13	1.3547	7.25E-04	1.01E-04
19	3.95	541.35	0.58028	4.32E-02	363.86	1.4877	1.59E-03	1.19E-04

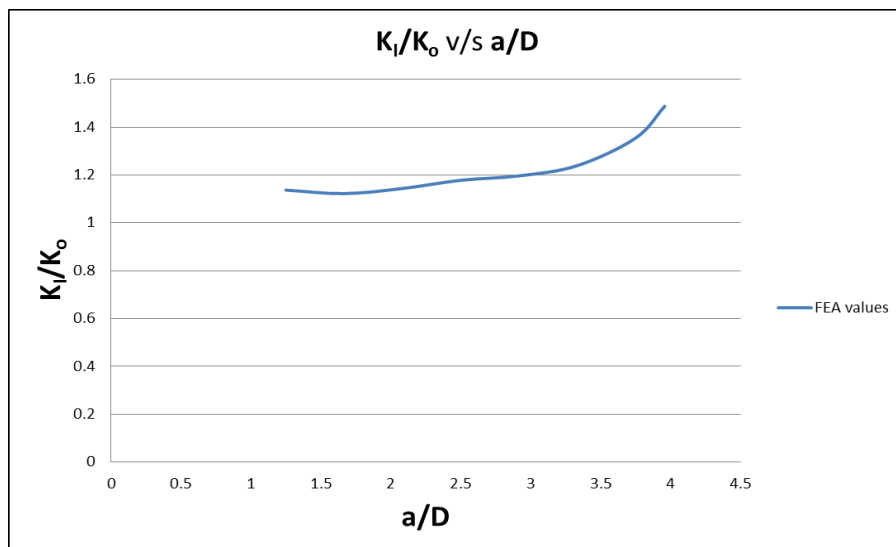


Fig 8(a): Normalized Mode-I SIF Vs a/D ratio by using Finite Element method

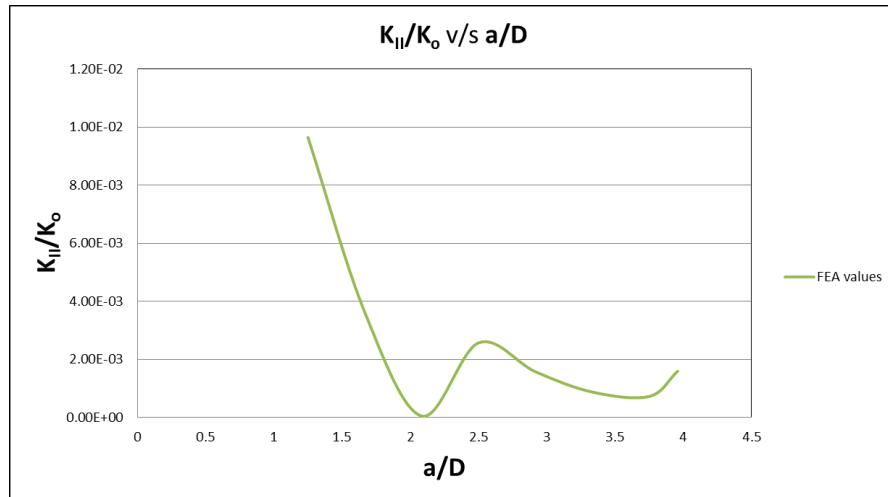


Fig 8(b): Normalized Mode-II SIF Vs a/D ratio by using Finite Element method

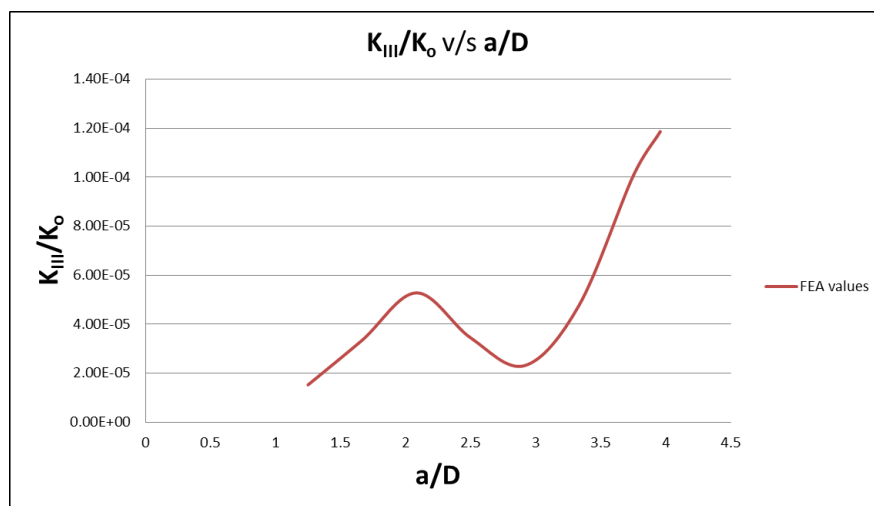


Fig 8(c): Normalized Mode-III SIF Vs a/D ratio by using Finite Element method

The parametric study is done for thickness 1mm, 2mm and 2.5mm, the values of K_I , K_{II} and K_{III} with respect to (a/D) for different thickness is as shown in table 5 and corresponding normalized SIF values for mode-I, mode-II, and mode-III is shown in fig 9(a), 9(b) and 9(c). It is observed that SIF curves in fig 9(a) the normalized stress intensity for mode-I is very high for $t=2.5$ mm compared to thickness 1mm and 2mm and for thickness $t=2$ mm SIF is still lesser than thickness $t=1$ mm, hence for taken dimensional parameter the thickness of the sheet should be nearly equal to 2mm which tends to lower crack propagation.

Table 5: The normalized Stress Intensity Factor (K_I/K_0), (K_{II}/K_0), (K_{III}/K_0) with respect to a/D ratio For $t=1$ mm

a mm	a/D	K_I MPa	K_{II} MPa	K_{III} MPa	K_0 MPa	K_I/K_0	K_{II}/K_0	K_{III}/K_0
6	1.25	504.8	4.2804	2.75E-03	441.21	1.144126	0.009702	6.24E-06
8	1.67	565.89	0.28751	1.53E-02	480.33	1.178128	0.000599	3.18E-05
10	2.08	597.6	2.82E-02	3.79E-02	516.49	1.157041	5.45E-05	7.34E-05
12	2.5	657.91	1.4333	8.36E-03	550.28	1.195591	0.002605	1.52E-05
14	2.92	709.35	0.92056	5.84E-03	582.12	1.218563	0.001581	1.00E-05
16	3.33	775.66	0.5346	1.78E-02	612.3	1.266797	0.000873	2.90E-05
18	3.75	891.55	0.49397	7.38E-02	641.06	1.390743	0.000771	1.15E-04
19	3.95	1003.4	1.0952	1.88E-01	654.97	1.531979	0.001672	2.88E-04

For t=2mm

a mm	a/D	K_I MPa	K_{II} MPa	K_{III} MPa	K_0 MPa	K_I/K_0	K_{II}/K_0	K_{III}/K_0
6	1.25	250.69	2.126	3.64E-03	220.6	1.136401	0.009637	1.65E-05
8	1.67	280.24	0.14227	7.79E-03	240.16	1.166889	0.000592	3.24E-05
10	2.08	294.99	1.34E-02	1.30E-02	258.24	1.142309	5.18E-05	5.03E-05
12	2.5	323.61	0.70628	1.02E-02	275.14	1.176165	0.002567	3.72E-05
14	2.92	347.57	0.45945	7.71E-03	291.06	1.194152	0.001579	2.65E-05
16	3.33	378.42	0.26987	1.52E-02	306.15	1.236061	0.000881	4.95E-05
18	3.75	432.76	0.22975	3.15E-02	320.53	1.350139	0.000717	9.82E-05
19	3.95	485.4	0.51815	3.27E-02	327.48	1.482228	0.001582	9.98E-05

For t=2.5mm

a mm	a/D	K_I MPa	K_{II} MPa	K_{III} MPa	K_0 MPa	K_I/K_0	K_{II}/K_0	K_{III}/K_0
6	1.25	200.28	1.6985	3.32E-03	157.86	1.268719	0.01076	2.11E-05
8	1.67	223.76	0.11356	6.28E-03	171.85	1.302066	0.000661	3.65E-05
10	2.08	235.38	1.06E-02	9.54E-03	184.79	1.27377	5.76E-05	5.16E-05
12	2.5	258.03	0.56333	9.24E-03	196.88	1.310595	0.002861	4.69E-05
14	2.92	276.91	0.367	7.36E-03	208.27	1.329572	0.001762	3.54E-05
16	3.33	301.21	0.21601	1.29E-02	219.07	1.374949	0.000986	5.87E-05
18	3.75	344.09	0.18117	2.40E-02	229.36	1.500218	0.00079	1.05E-04
19	3.95	385.68	0.40964	1.78E-02	234.34	1.645814	0.001748	7.61E-05

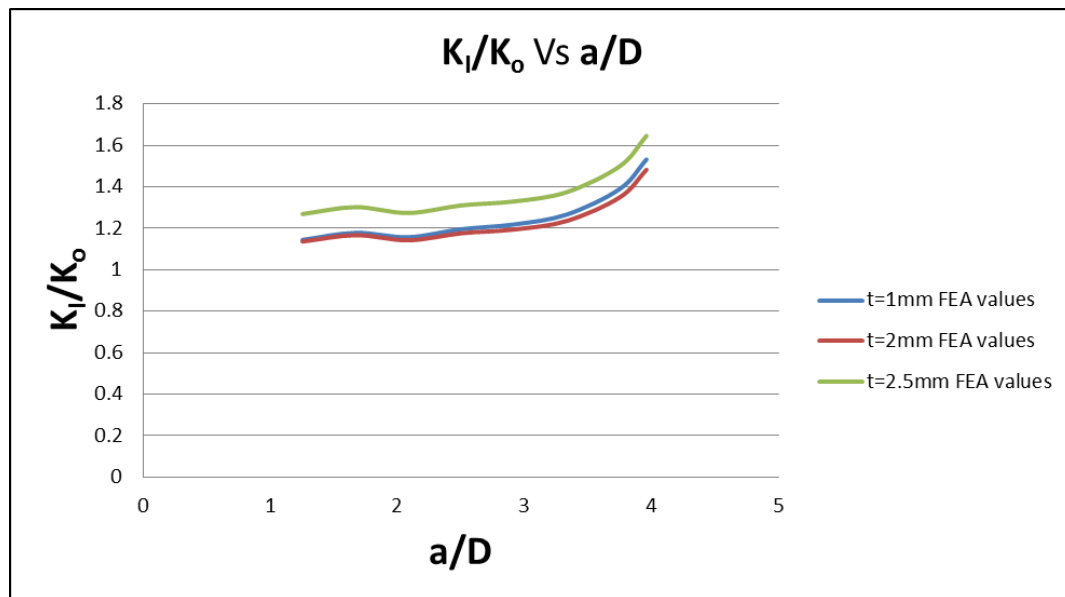


Fig 9(a): Normalized Mode-I SIF Vs a/D for variation of thickness

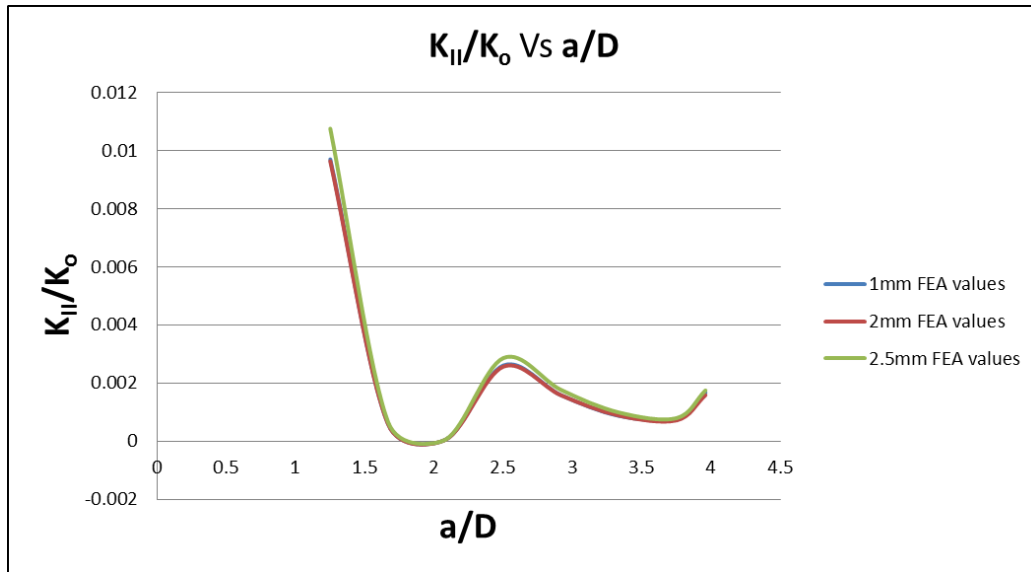


Fig 9(b): Normalized Mode-II SIF Vs a/D for variation of thickness

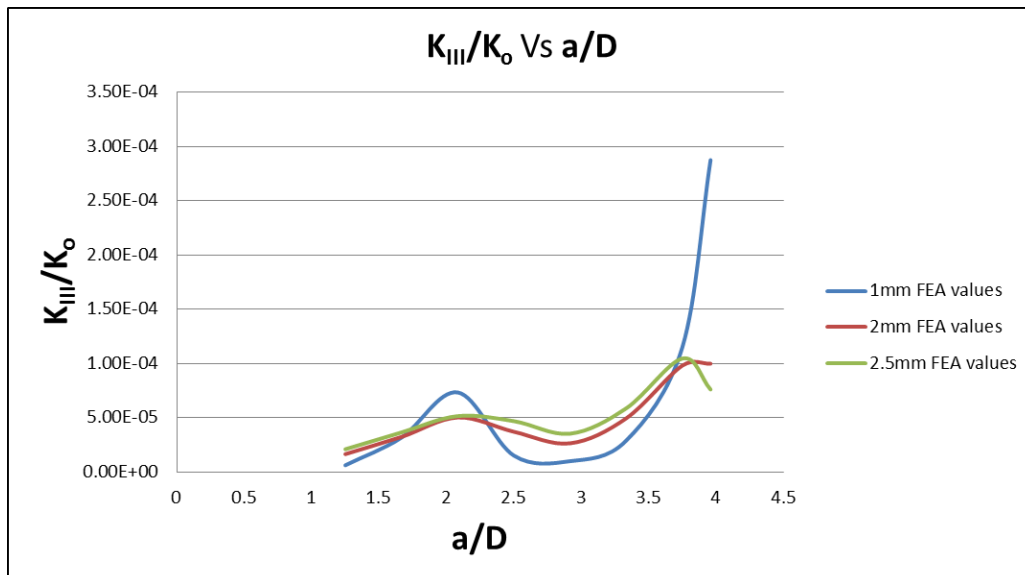


Fig 9(c): Normalized Mode-III SIF Vs a/D for variation of thickness

VII. Conclusion

The problem of determining stress intensity factors for a crack emanating from one rivet hole and approaching another in curved sheet is of prime importance in damage tolerance analysis and has relevance in the structural integrity evaluation of aging transport aircraft due to multisite damage. Fatigue loads due to internal pressurization acting on the fuselage, stress concentration will be high at rivet holes locations of the fuselage joint, which causes the initiation of cracks on all rivet hole edges due to uniform stress acting on the fuselage due to internal pressurization.

Stress Intensity Factor determination in this work which can be considered as a part of a thin sheet with rivet holes used in the aeronautical structures.

Taking all the above points into consideration modeling and finite element analysis for a part of the fuselage skin was carried and from that work, some of the information's are concluded as follows

- The curved is considered as part of the fuselage skin was created using a 3D modeling software tool according to the dimension and the 3D modeled component was imported to ansys tool for pre-processing. The curved sheet was meshed with 8 node SHELL 93 elements and loads and boundary

conditions were applied.

- The material used was Al 2024-T3, which is widely used in aircraft industry for its good fatigue strength and corrosion resistance.
- Stress analysis of the model of the fuselage has been carried out to observe the hoop stress on skin is equal to the analytical value of the hoop stress 59.5 N/mm^2 for $t=1.8\text{mm}$
- Finite element analysis is made for two rivet holes in a curved sheet without crack, it was observed that the rivet holes the stress concentration was maximum and concluded that rivet holes are the initiation of crack.

The method used in this report can be utilized for calculating the stress intensity factor for many other loading cases and many values of the crack length, thus providing important information for subsequent studies, especially for fatigue loads, where stress intensity factor is necessary for the crack growth rate determination.

The problem is intractable by continuum mechanics method. Experimental investigations are prohibitively expensive. Finite Element Modeling for computational fracture mechanics happens to be the right choice. Therefore, there is a real need to adapt computational procedures. The presented stress intensity factors in this paper are essential to predict

- 1) Mixed mode fracture under static, dynamic and sustained loads
- 2) Residual strength
- 3) Crack growth life under cyclic loading conditions.

The results presented in this study conclusively prove that Finite Element Modeling using ANSYS software to be the right choice. The numerical results presented are believed to be quite accurate.

REFERENCES

- [1] Akash.D, Anand.A G.V.Gnanendra reddy "Determination of S.I.F for a Crack Emanating From a Hole in a Pressurized Cylinder using Displacement Extrapolation Method" International Journal of Mechanical Engineering & Technology (IJMET), Vol.4(2),pp. 373-382, March-April (2013)
- [2] A.Anand L.J.Sudev,H.V.Laakshminarayana "Determination of SIF for a Crack Emanating From a Rivet Hole in a Plate using Displacement Extrapolation Method" Journal of Applied Sciences 12(10) 2012,pp 1020-1025
- [3] D.Dinesh Babu, "Theoretical and Finite Element Analysis of High Pressure Components" IOSR Journal of Engineering 3(2)2013,pp 25-34
- [4] T.L.Anderson "Fracture mechanics-Fundamentals and Applications" published by Taylor and Francis group
- [5] Naveen Kumar H S, Prof. B S Suresh, "A Study of Net Section Failure between Two Equal Cracks in an Infinite Plate", International Journal of Modern Engineering Research (IJMER) Vol.2, Issue.4, July-Aug. 2012 pp-2655-2661
- [6] Gustavo V. Guinea, Jaime Planas and Manuel Elices, " K_I Evaluation by the Displacement Extrapolation Technique", Engineering Fracture Mechanics 66 (2000), pp. 243-255.
- [7] Agne Karlsson and Jan Backlund, 1978, "Summary of SIF Design Graphs for Cracks Emanating From Circular Holes" International Journal of Fracture, Vol. 14, No. 6

VLSI Design of Fast Addition Using QSD Adder for Better Performance

G. Jayaprakash¹, B. Adinarayana²

^{1,2} PG Student, Assistant Prof, Santhiram Engineering College, Nandyal.

Abstract: The high speed digital circuits became more prominent with incorporating information processing and computing. Arithmetic circuits play a very critical role in both general-purpose and application specific computational circuits. The modern computers lead to the deterioration in performance of arithmetic operations such as addition, subtraction, multiplication, division, on the aspects of carry propagation delay, large circuit complexity and high power consumption. Designing this adder using QSD number representation allows fast addition/subtraction which is capable of carry free addition and borrows free subtraction because the carry propagation chain are eliminated, hence it reduce the propagation time.

Keywords: QSD, carry/borrow free addition/ subtraction.

I. Introduction

Arithmetic operations are widely used and play important role in various digital systems such as computers and signal processors. Designing this Arithmetic unit using QSD number representation has attracted the interest of many researchers. Additionally, recent advances in technologies for integrated circuits make large scale arithmetic circuits suitable for VLSI implementation. In this paper, we propose a high speed QSD adder which is capable of carry free addition, borrow free subtraction. The QSD addition/subtraction operation employs a fixed number of minterms for any operand size. In QSD number system carry propagation chain are eliminated which reduce the computation time substantially, thus enhancing the speed of the machine. Signed digit number system offers the possibility of carry free addition. QSD Adder / QSD Multiplier circuits are logic circuits designed to perform high-speed arithmetic operations. In QSD number system carry propagation chain are eliminated which reduce the computation time substantially, thus enhancing the speed of the machine.

II. Signed Digit Number

Signed digit representation of number indicates that digits can be prefixed with a – (minus) sign to indicate that they are negative. Signed digit representation can be used to accomplish fast addition of integers because it can eliminate carriers.

$$\begin{aligned}(11\bar{2}2)_2 &= 1 \times 2^3 + 1 \times 2^2 - 2 \times 2^1 + 1 \times 2^0 \\ &= 8 + 4 - 4 + 2 \\ &= 10\end{aligned}$$

III. QSD Number System

QSD numbers are represented using 3-bit 2's complement notation. Each number can be represented by

$$D = \sum x_i 4^i$$

Where x_i can be any value from the set $\{3, 2, 1, 0, 1, 2, 3\}$ for producing an appropriate decimal representation. A QSD negative number is the QSD complement of QSD positive number i.e. $3 = -3$, $2 = -2$, $1 = -1$. For digital implementation, large number of digits such as 64, 128, or more can be implemented with constant delay. A high speed and area effective adders and multipliers can be implemented using this technique. For digital implementation, large number of digits such as 64, 128, or more can be implemented with constant delay. A higher radix based signed digit number system, such as quaternary signed digit (QSD) number system, allows higher information storage density, less complexity, fewer system components and fewer cascaded gates and operations. A high speed and area effective adders and multipliers can be implemented using this technique. Also we can obtain redundant multiple representation of any integer Quantity using this QSD number system. Examples of n digit QSD number are as follows: etc. 3 1021310, 1123, 0112, 0132

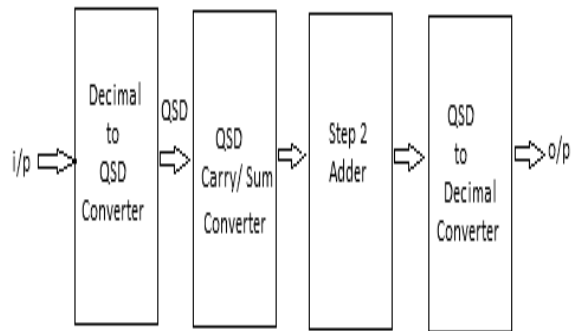
For example:

$$\begin{aligned}(13\bar{3}2)_{QSD} &= 1 \times 4^3 + 3 \times 4^2 - 3 \times 4^1 + 2 \times 4^0 \\ &= 64 + 48 - 12 + 2 \\ &= (102)_{10}\end{aligned}$$

The basic quaternary operators are very similar to binary operators and they are obtained from Boolean algebra.

IV. Basic Concept

For performing any operation in QSD, first convert the binary or any other input into quaternary signed digit



V. Adder/Subs Tractor Design

In arithmetic operation of digital computation addition is the most important operation. A carry-free addition is desirable as the number of digits is large. The carry-free addition can achieve by exploiting redundancy of QSD number and QSD addition. The redundancy allows multiple representations of any integer quantity i.e., $610 = 12QSD = 22QSD$. There are two steps involved in the carry-free addition. The first step generates an intermediate carry and sum from the addend and augends. The second step combines the intermediate sum of the current digit with the carry of the lower significant digit. To prevent carry from further rippling, we define two rules. The first rule states that the magnitude of the intermediate sum must be less than or equal to 2. The second rule states that the magnitude of the carry must be less than or equal to 1. Consequently, the magnitude of the second step output cannot be greater than 3 which can be represented by a single-digit QSD number; hence no further carry is required. In step 1, all possible input pairs of the addend and augends are considered [4]. The output ranges from -6 to 6 as shown in Table 1.

Table 1. The outputs of all possible combinations of a pair of addend (A) and augend (B)

A \ B	-3	-2	-1	0	1	2	3
-3	-6	-5	-4	-3	-2	-1	0
-2	-5	-4	-3	-2	-1	0	1
-1	-4	-3	-2	-1	0	1	2
0	-3	-2	-1	0	1	2	3
1	-2	-1	0	1	2	3	4
2	-1	0	1	2	3	4	5
3	0	1	2	3	4	5	6

The range of the output is from -6 to 6 which can be represented in the intermediate carry and sum in QSD format as show in Table 2. Some numbers have multiple representations, but only those that meet the defined rules are chosen. The chosen intermediate carry and sum are listed in the last column of Table 2. Both inputs and outputs can be encoded in 3-bit 2's complement binary number.

The mapping between the inputs, addend and augends, and the outputs, the intermediate carry and sum are shown in binary format in Table 3. Since the intermediate carry is always between -1 and 1, it requires only a 2-bit binary representation. Finally, five 6-variable Boolean expressions can be extracted. The intermediate carry and sum circuit is shown in Figure 1.

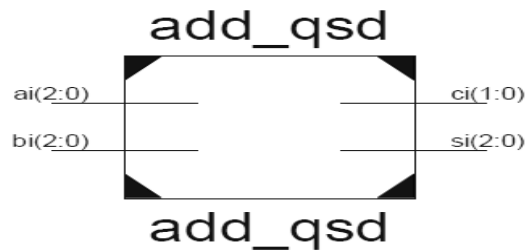


Figure 1. The intermediate carry and sum generator.

THE INTERMEDIATE CARRY AND SUM BETWEEN -6 TO +6

Sum	QSD represented number	QSD coded number
-6	$\bar{2}2, \bar{1}\bar{2}$	$\bar{1}\bar{2}$
-5	$\bar{2}3, \bar{1}\bar{1}$	$\bar{1}\bar{1}$
-4	$\bar{1}0$	$\bar{1}0$
-3	$\bar{1}1, 0\bar{3}$	$\bar{1}1$
-2	$\bar{1}2, 0\bar{2}$	$0\bar{2}$
-1	$\bar{1}3, 0\bar{1}$	$0\bar{1}$
0	00	00
1	01, $1\bar{3}$	01
2	02, $1\bar{2}$	02
3	03, $1\bar{1}$	$1\bar{1}$
4	10	10
5	11, $2\bar{3}$	11
6	12, $2\bar{2}$	12

In step 2, the intermediate carry from the lower significant digit is added to the sum of the current digit to produce the final result. The addition in this step produces no carry because the current digit can always absorb the carry-in from the lower digit. Table-3 shows all possible combinations of the summation between the intermediate carry and the sum.

Example: To perform QSD addition of two numbers A = 107 and B = -233 (One number is positive and one number is negative).

First convert the decimal number to their equivalent QSD representation:

$$\begin{aligned}
 (107)_{10} &= 2 \times 4^3 + \bar{2} \times 4^2 + 3 \times 4^1 + \bar{1} \times 4^0 \\
 &= (2\bar{2}3\bar{1})_{\text{QSD}} \\
 (233)_{10} &= 3 \times 4^3 + 3 \times 4^2 + \bar{2} \times 4^1 + 1 \times 4^0 \\
 &= (33\bar{2}1)_{\text{QSD}}
 \end{aligned}$$

$$\text{Hence, } (-233)_{10} = (\bar{3}\bar{3}2\bar{1})_{\text{QSD}}$$

Now the addition of two QSD numbers can be done as follows:

A = 107	2	$\bar{2}$	3	$\bar{1}$
B = -233	$\bar{3}$	$\bar{3}$	2	$\bar{1}$
Decimal Sum	-1	-5	5	-2
IC	0	$\bar{1}$	1	0
IS	$\bar{1}$	$\bar{1}$	1	$\bar{2}$
S	$\bar{2}$	0	1	$\bar{2}$
C _{out}	0			

The sum output is (2 01 2) QSD which is equivalent to (-126)₁₀ and carry output is 0.

From these examples it is clear that the QSD adder design process will carry two stages for addition. The first stage generates intermediate carry and sum according to the defined rules. In the second stage the intermediate carry from the lower significant digit is added to the intermediate sum of current digit which results in carry free output. In this step the current digit can always absorb the carry-in from the lower digit.

VI. Logic Design And Implementation Using Of Single Digit QSD Adder Unit

There are two steps involved in the carry-free addition. The first step generates an intermediate carry and sum from the addend and augends. The second step combines the intermediate sum of the current digit with the carry of the lower significant digit. To prevent carry from further rippling, two rules are defined. The first rule states that the magnitude of the intermediate sum must be less than or equal to 2. The second rule states that the magnitude of the carry must be less than or equal to 1. Consequently, the magnitude of the second step output cannot be greater than 3 which can be represented by a single-digit QSD number; hence no further carry is required. In step 1, all possible input pairs of the addend and augends are considered.

The range of input numbers can vary from -3 to +3, so the addition result will vary from -6 to +6 which needs two QSD digits. The lower significant digit serves as sum and most significant digit serves as carry. The generation of the carry can be avoided by mapping the two digits into a pair of intermediate sum and intermediate carry such that the n th intermediate sum and the $(n-1)$ th intermediate carry never form any carry generating pair (3,3), (3,2), (3,1), (3, 3), (3, 2), (3,1). If we restrict the representation such that the intermediate carry is limited to a maximum of 1, and the intermediate sum is restricted to be less than 2, then the final addition will become carry free. Both inputs and outputs can be encoded in 3-bit 2's complement binary number. The mapping between the inputs, addend and augends, and the outputs, the intermediate carry and sum are shown in binary format in Table II.

To remove the further carry propagation the redundancy feature of QSD numbers is used. We restrict the representation such that all the intermediate carries are limited to a maximum of 1, and the intermediate sums are restricted to be less than 3, then the final addition will become carry free. The QSD representations according to these rules are shown in Table 4.3 for the range of -6 to +6. As the range of intermediate carry is from -1 to +1, it can be represented in 2 bit binary number but we take the 3 bit representation for the bit compatibility with the intermediate sum. At the input side, the addend A_i is represented by 3 variable input as A_2, A_1, A_0 and the augends B_i is represented by 3 variable input as B_2, B_1, B_0 . At the output side, the intermediate carry IC is represented by IC_2, IC_1, IC_0 and the intermediate sum IS is represented by IS_2, IS_1, IS_0 . The six variable expressions for intermediate carry and intermediate sum in terms of inputs (A_2, A_1, A_0, B_2, B_1 and B_0) can be derived from Table 4.3. So we get the six output expressions for $IC_2, IC_1, IC_0, IS_2, IS_1$ and IS_0 . As the intermediate carry can be represented by only 2 bits, the third appended bit IC_2 is equal to IC_1 so the expression for both outputs will be the same[5].

Using 6 variable K-map, the logic equations specifying a minimal hardware realization for generating the intermediate carry and intermediate sum are derived. The minterms for the intermediate carry (IC_2, IC_1, IC_0) are:

$$IC_2 = a_2 b_2 (\overline{a_0 b_0 a_1 b_1}) + (\overline{a_1 + b_1}) (a_2 \overline{b_0} + b_2 \overline{a_0})$$

$$IC_1 = a_2 b_2 (\overline{a_0 b_0 a_1 b_1}) + (\overline{a_1 + b_1}) (a_2 \overline{b_0} + b_2 \overline{a_0})$$

$$IC_0 = IC_2 + \overline{a_2 b_2} (a_1 b_1 + b_1 b_0 + b_0 a_1 + b_1 a_0 + a_1 a_0)$$

Minterms for intermediate sums are:

$$IS_0 = a_0 \overline{b_0} + \overline{a_0} b_0$$

$$IS_1 = (a_1 \overline{b_1} + \overline{a_1} b_1) \overline{a_0 b_0} + (\overline{a_1 b_1} + \overline{a_1 b_1}) a_0 b_0$$

$$IS_2 = IS_0 (\overline{a_1 b_1} + \overline{a_1 b_1}) + b_2 \overline{a_1 b_0} + a_2 \overline{b_1 a_0} + a_0 b_0 \overline{a_1 b_1} (a_2 +$$

The final sum which is carry free is generated from those outputs i.e. Intermediate carry (IC_2, IC_1 , and IC_0) and Intermediate sum (IS_2, IS_1 , and IS_0). Therefore it has six input and three output bits.

$$S_0 = IC_0 \overline{IS_0} + \overline{IC_0} IS_0$$

$$S_1 = IC_1 \oplus IS_1 \oplus IC_0 IS_0$$

$$S_2 = IC_2 \oplus IS_2 \oplus (IC_1 IS_1 + (IC_1 \oplus IS_1) IC_0 IS_0)$$

Addition operation for higher order digit does not wait for the completion of addition operation of the immediate lower order digit resulting in a parallel addition of each individual pair of digits.

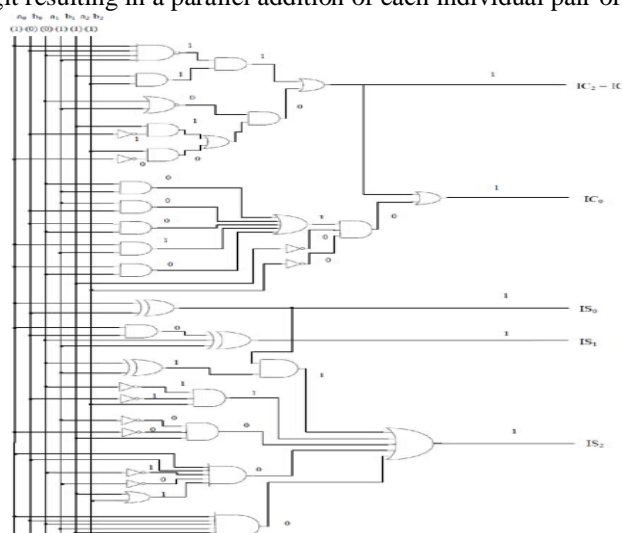


Fig: Data Flow of single digit QSD adder cell.

VII. Simulation Results

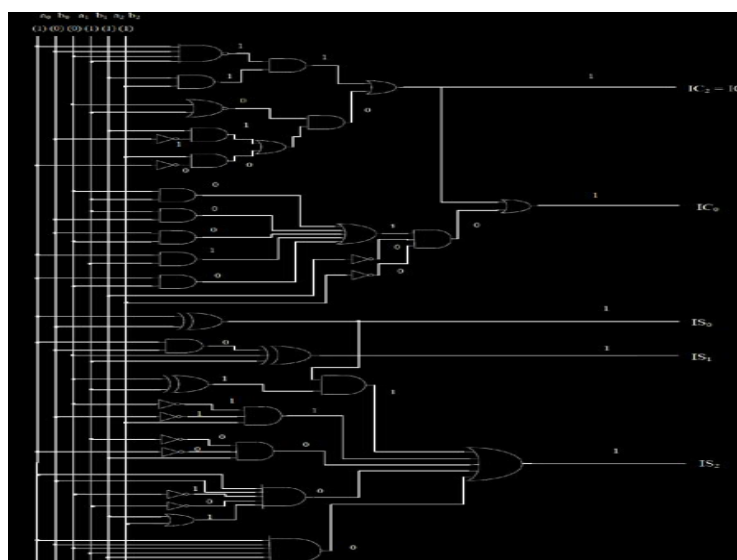


Figure 1: Data Flow of single digit QSD adder cell.

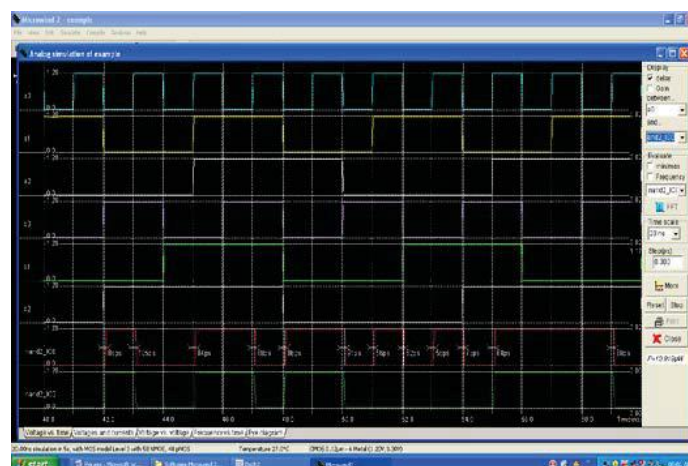


Figure 2: Simulation result of NAND implementation of step1 QSD adder

VIII. Conclusion

In the proposed design of Quaternary Signed Digit adder using NAND-NAND implementation for single digit addition, the dynamic power dissipation is 36.255mW at 5GHz frequency. These circuits consume less energy and less energy and power, and shows better performance power dissipation is obtained using Micro wind.

REFERENCES

- [1] A. Avizinis "signed digit number representation for fast parallel arithmetic", IRE Transactions on Elec. Comp., Vol EC-10, pp 389- 400, sept-1961.
- [2] A.A.S. Awwal and J.U. Ahmed, "fast carry free adder design using QSD number system ,"proceedings of the IEEE 1993 national aerospace and electronic conference, vol 2, pp 1085-1090, 1993.
- [3] Behrooz perhami "generalized signed digit number systems, a unifying frame work for redundant number representation ".IEEE transactions on computers, vol 39, no.1, pp.89-98, January 1990.
- [4] O. Ishizuka, A. Ohta, K. Tannno, Z. Tang, D. Handoko, "VLSI design of a quaternary multiplier with direct generation of partial products," Proceedings of the 27th International Symposium on Multiple-Valued Logic, pp. 169-174, 1997.
- [5] A.A.S Awwal, Syed M. Munir, A.T.M. Shafiqul Khalid, Howard E. Michel and O. N. Garcia, "Multivalued Optical Parallel Computation Using An Optical Programmable Logic Array", Informatica, vol. 24, No. 4, pp. 467-473, 2000.
- [6] F. Kharbash and G. M. Chaudhry, "Reliable Binary Signed Digit Number Adder Design", IEEE Computer Society Annual Symposium on VLSI, pp 479-484, 2007.
- [7] John Moskal, Erdal Oruklu and Jafar Saniie, "Design and Synthesis of a Carry-Free Signed-Digit Decimal Adder", IEEE International symposium on Circuits and Systems, pp 1089-1092, 2007.
- [8] Kai Hwang, "Computer Arithmetic Principles, Architecture and Design", ISBN 0-471-03496-7, John Wiley & Sons, 1979.
- [9] P. K. Dakhole, D.G. Wakde, " Multi Digit Quaternary adder on Programmable Device : Design and verification", International Conference on Electronic Design, pp. 1-4, Dec 2008.
- [10] Behrooz Parhami, "Carry-Free Addition of Recoded Binary Signed- Digit Numbers", IEEE Transactions on Computers, Vol. 37, No. 11, pp. 1470-1476, November 1988.

Authenticated and unrestricted auditing of big data space on cloud through valid and efficient granular updates

Suhas. S¹, Ramani. S²

^{1,2} School of Computer Science and Engineering, Vellore Institute of Technology, Vellore, India

Abstract: Cloud unlocks a different era in Information technology where it has the capability of providing the customers with a variety of scalable and flexible services. Cloud provides these services through a prepaid system, which helps the customers cut down on large investments on IT hardware and other infrastructure. Also according to the Cloud viewpoint, customers don't have control on their respective data. Hence security of data is a big issue of using a Cloud service. Present work shows that the data auditing can be done by any third party agent who is trusted and known as auditor. The auditor can verify the integrity of the data without having the ownership of the actual data. There are many disadvantages for the above approach. One of them is the absence of a required verification procedure among the auditor and service provider which means any person can ask for the verification of the file which puts this auditing at certain risk. Also in the existing scheme the data updates can be done only for coarse granular updates i.e. blocks with the uneven size. And hence resulting in repeated communication and updating of auditor for a whole file block causing higher communication costs and requires more storage space. In this paper, the emphasis is to give a proper breakdown for types of fixed granular updates and put forward a design that will be capable to maintain authenticated and unrestricted auditing. Based on this system, there is also an approach for remarkably decreasing the communication costs for auditing little updates.

Index Terms: Cloud Computing, Big Data, Fine grained updates, Data Security, Authenticated Auditing.

I. Introduction

Cloud Computing is setting the new trend in the present IT field. It is a latest computing framework derived from grid computing, parallel computing, grid computing, virtualization and utility computing [1]. Through virtualization of resources, cloud computing can bring services and resources required to the customers in a pay-per-use mode. Cloud Computing provides services in three ways and they are IaaS-Infrastructure as a Service, PaaS-Platform as a Service, SaaS-Software as a Service [2]. Big Data Analytics is the newly researched in the present IT sector. Big Data usually refers to the term for the set of data that is very huge in volume and also so complex that it is hard to process the data through normal data processing tools [3]. And Cloud Service Storage (CSS) is the largest source of dynamic and traditional Big Data storage. Big Data is usually referred by 3 Vs – high volume, high variety and high velocity. High volume refers to huge amount of datasets. High variety refers to different types of data that make up the dataset. And high velocity refers to constant change or updating of datasets [4]. Hence Cloud and Big data are the newest research fields in the IT sector. Even with all the present development and research of cloud computing is rapid and efficient there is always a debate and uncertainty on the usage. One such concern for the users is of Data Privacy/Security [5, 6]. Contrast to the usual systems, users doesn't have a control on their data.

In this paper, the emphasis is on investigating the various problems of reliability verification for the big data space on cloud. In real world the above problem is commonly known as data auditing or “Auditing As A Service” through a cloud user's point of view and it is done through a verified third party auditing service [7, 8]. In an isolated authentication system, the valid reliability proof cannot be given by the Cloud Storage Server (CSS) to a trusted verifier until all the data is in one piece. And no matter how much secure the data security mechanism provided by the Cloud Service Provider (CSP) it is recommended to use a challenge request for auditing and also that data auditing is to be done on a regular basis for users who have highly varying data from time to time. Also for the users with very high security demands for their data the above process is recommended.

Literature contributions can be outlined as follows:

- 1) In this paper we put forth a formal analysis of various types of fine granular data updates on uneven sized blocks of file dynamically in a data set.
- 2) For an efficient security system, we integrate an extra authentication method. The goal of this system is to remove dangers of unauthenticated auditing requests from illegal third party auditors (TPA's). The above process can concluded into a single term as Authenticated Auditing.
- 3) We also examine how to enhance the effectiveness of validating small updates that are very frequent which form the core of some cloud and big data applications like social networks. Experimental outcomes of proposed system show that it can considerably reduce communication costs as compared to existing methods.

Paper Layout: The remainder of this paper is categorized as follows. Part 2 deals with Literature Survey. Part 3 gives details of existing system and problem statement. Part 4 gives details on the proposed system and also analysis on how to support requests for fine granular updates. Part 5 describes analysis of security for the design. Part 6 deals with the experimental results and part 7 describes conclusion and future enhancements.

II. Literature Survey

Scalable and elasticity are the two main feature of the cloud which can be treated as advantages when compared to traditional systems. Also efficiency in sustaining dynamic data updates is also important. Protection and Privacy of dynamic big data has been a matter to study in the past [9, 10, 12, 15]. Our focus is mainly on frequent and small data updates. This is a important factor since it exists in real world cloud applications like social networks and business transactions. Also sometimes users in the cloud may decide to divide big datasets into smaller datasets for easy management and processing uses. But among all the problems in today's cloud is of security or privacy [5,6,11]. Data privacy and security also the most raised fears about using the cloud since the users does not has a direct control over their data [6,13].

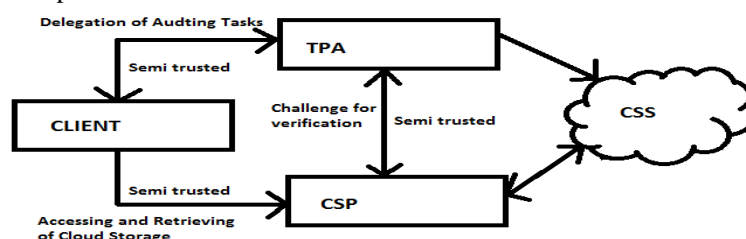
There were many solutions proposed for the above problems of security and small dynamic data updates over a cloud. The first model was Proof Of Verifiability by Jules [15]. But the disadvantage in this scheme is that it can be applied only to static data storage. There were other schemes like Proved data Possession which consists of verifiability tags which computed tags through which authenticator can authenticate the integrity of a part of a file that is outsourced. There was a scheme that used BLS method for public auditing purpose [16]. It had RSA algorithm for encryption and decryption. The production and authentication of validity proofs were same as verifying and signing of BLS signatures. After that both the Proof of verifiability and proved data possession were unified into single model name POR. Since public audit ability and coarse grained updates cannot be supported by default in the above systems there is a need for a new system. The latest one is to divide files into different blocks. But this results in expensive communication difficulties and storage costs. And hence there is need for support for dynamic and frequent small updates.

III. Problem Statement and Analysis

One of the reasons for the cloud to be so popular is that the elasticity feature of it plays a big role in bringing cost-effectiveness to the picture. An example can be considered of a mobile company using cloud platform to provide online video on demand services to customers. The no. of customers watching could drastically vary from millions to a mere hundreds according to the video. To provide for this variation demand the company has to purchase maximum no. of hardwares and other processing units. But even though the overall system is working fine, most of the time some part of the system is idle and does not account to any workload. Hence here is a situation where cloud can save millions of investment capital by providing elastic feature.

Some of the cloud providers are Amazon S3 or EC2, Microsoft Azure and others. Hence we can see that how scalability and elasticity enhance the support of dynamic data updates and are the core feature of cloud computing. A big data application is a collection of related and unrelated data where the datasets are huge in number. One such example of a big data can be given as cloud storage. A lot of big data applications handle datasets which are small and there is a frequent updation of information on the datasets. Hence usually users of the cloud divide this huge amount of datasets into small part of data before uploading to the storage. Only few auditing schemes support small updates over big data and also the security of these schemes is not assured.

The following diagram depicts the role of the entities involved in the scheme



In the above diagram the client has access to the cloud storage via a service provider provided by a Cloud Service Provider. The client does not have complete trust on the service provider. He also does not trust the auditor completely. When the client asks for the third party auditor to do some auditing tasks the auditor has to access the data to be audited through the Cloud server storage through the service provider. The Cloud service provider asks for challenge verification. This challenge verification is based on RSA algorithm and BLS signature scheme and is created in accordance with the client. So that the client can pre determine as to which auditor can be given data without any security concerns for auditing.

Some of the present auditing methods have the capability to support full data dynamics. Only insertion, updations and deletions on same-sized blocks are supported. There is a need for full dynamic support of variable –sized block updates also known as coarse-grained updates. Coarse grained block updates are always more complicated than fine granular updates. For every insert operation there is a new block created by the Cloud Server Storage. But when there are many no. of insertions and updates to be performed, the storage wasted and required is huge. This situation can be fixed if fine granular data updates are supported and hence efficiency is improved. There is always a huge amount of communication overhead involved in verifying large no. of coarse-grained updates. If the fine granular updates are supported it can provide extra flexibility and also improves the efficiency.

The main assumption of this paper is that the Cloud Server Storage will provide honest data query services to all the clients. Also if a user has to retrieve a particular part of his/her data which is stored on the Cloud Server Storage, CSS should not give an incorrect answer. This assumption can be concluded into a single word as Reliability. This is a fundamental service guarantee of Cloud Server Storage.

IV. The Proposed system

We use a data structure called Hashed Rank Merkle Tree. It is same as a binary tree; each node has a max of 2 nodes. It can be considered as a complete binary tree where each non leaf node has 2 child nodes. Info at a node N in a hash tree T can be represented as (h, R_n) in which h is the hash value and R is the rank of that particular node. For leaf node L.N which has data d we can represent as $H=H(di), r_n = S_i$, the parent node can be constructed as $N_p = (h(H1 || H2), (r_{n1} + r_{n2}))$ || is the concatenation operator.

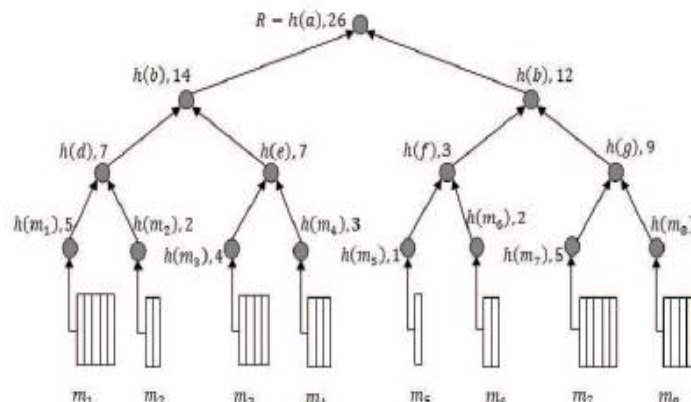


Fig 2. A typical example of Merkle Hash Tree

The leaf contains set of hash values selected from all of its upper levels since the root value can be calculated through (m_i, O) . The update operations defined in our scheme are as follows. Modification is an operation which can be done in two ways- partial and complete. Partial modification deals with a part of a certain block that needs to be updated. And whole modification deals with the situation where a whole block needs to be updated from the tree structure. There is also a operation of insertion if a whole block needs to be inserted on the tree structure for containing new data and split block operation to remove a part of data in a block and is to be replaced with a new block.

The authenticated auditing scheme is carried out using a series of algorithms. Key generation algorithm is used to generate security information like private key, public key and signature for encryption and decryption purposes. This task is carried out by RSA and BLS techniques. The user's data will be stored in the form of a Hashed Merkle tree as metadata. The user will authorize the auditor of his choice by sharing the signature that was generated. File Preprocessing deals with uploading and processing of the file on the Cloud Servicer Storage. The CSS makes that the file has been uploaded by the appropriate user with enough permission.

Challenge algorithm and verifiable update algorithm is done to verify the integrity of the user. After the user uploads the data onto the CSS it completes the update demands through update operation and then user does

update verification to verify whether the CSS has completed the updates on the correct data blocks and their particular authenticators.

Following the above operations in the proposed scheme there is a need to define a fine granular update demand for a file which is divided into n different sized blocks, in which each block consists of segments of a fixed size. If there is a Merkle hash tree that must have updated with operation discussed earlier for CSS to send the root R for the user to validate the integrity of the operation.

After the analysis done above, we can see that a large amount of small updates, be it insert, or deletion or updation. And also for each operation the partial modification is invoked every time and hence this is a big communication overhead. Therefore the emphasis is also on optimizing the partial modification operations and hence making the system efficient.

Even though the proposed system can support the fine granular updates, the user must retrieve the whole file block from the CSS for finishing the authentication work. This means that the user is the only entity who has the private key for authentication. But the user does not have the frequent update factor stored locally. Hence the extra communication overhead will be very expensive for huge no. of frequent updates.

For the split block operation the procedure is same as the basic scheme since there is no new data put into the Merkle hash tree T . hence getting back the whole data block cannot be avoided and is inefficient. For the other operations there is no old data in new blocks and therefore the other procedure remains the same.

The strategy applied here is based on RSA algorithm and can be used for Proved Data Possession which in turn can be used to achieve authenticated auditing and fine granular update requests. This process will be easier since RSA supports coarse grained updates. The auditing also can be applied in batch jobs since there is no change in authenticators and verifiers. This strategy can be used into our system so as to avoid TPA from browsing through the authenticated file segments via sequences of integrity checks for a file block. Also we can reduce the amount of challenges for the same set of file blocks. When there are frequent updates the attack's success rate of authorized access is very low since there is a high chance that challenged blocks are already updated.

V. Analysis of Security

In the verification procedure of the scheme the emphasis is on preventing the CSS cheating the valid TPA about the status of user's data. This is the same concept as Proved Data Possession – PDP. Aside from the new authentication process the only variation in comparison to earlier systems is that of the Merkle Hash Tree and different sized blocks. Also the security of this scheme is enhanced by the use of a signature scheme. Usually the schemes with signatures have a greater efficiency and are also more secure. An invalid or unauthorized TPA is an outside auditor who wants to challenge the client's data stored onto the CSS without the permission of the client. This is not available in the earlier auditing schemes. Hence with the unique authentication process no outside TPA without the user's permission can be able to audit the data without his permission. For even higher security demands the user add a authentication message to make each auditing unique so as to avoid mix up results of auditing work between different auditors. But this enhancement has its own limitations and user has to be online for most of the time.

The second part of the security analysis is to verify the updates over the client's data stored on the CSS. The main analysis to be done here is whether the CSS (partially trusted) has carried out the data updates correctly or not. In the process of updating the data the CSS must be able to honestly provide with the report on updates done on the data correctly. Also the CSS should be able to reduce the communication overhead for this process.

VI. Experiment results

We conducted our experiments on the Amazon S3 cloud, a pay as you go type cloud service provider. The user first has to register onto the cloud and then he can upload the files into a folder called as a bucket. The user uploads his files onto the CSS and subsequently the keys and signatures are generated for encryption and decryption purposes. This information is shared with the TPA of his/her choice. This means that the user has chosen the particular and trusted auditor for auditing tasks over his data hence enhancing security and privacy of the data. After this phase the auditor with the proper credentials challenges the CSS for integrity of the data.

The CSS after confirming the details of the challenging TPA forward the data for auditing tasks. The whole outline of the operation is done with accordance with the user and reports are generated after the auditing tasks.

The results generated show reduction in communication overhead compared to the existing scheme. For each update done on the data the report is generated. The report contains information about the total amount of data retrieved for the existing scheme and proposed scheme.

VII. Conclusion and Future Enhancements

In this paper, the emphasis is to give a proper breakdown for types of fixed granular updates and put forward a design that will be capable to maintain authenticated and unrestricted auditing. Based on this system, there is also an approach for remarkably decreasing the communication costs for auditing small updates. Analysis and experimental results have shown that this scheme can meet high security demands while also providing flexibility and elasticity. Also adding the feature of reducing communication overheads for big data applications through more frequent amount of small updates which can be applied in social networks and business transactions. The future enhancement for this paper can be improving server side security issues while providing confidentiality and data availability. Also the plan is to investigate modifications in authenticated auditing for better security. Also the enhancement on meeting the Quality of service metrics such as data security, storage and computation can be done.

REFERENCES

- [1] Zhang Xin, Lai Song-qing, Liu Nai-wen, "Research on cloud computing data security model based on multi-dimension," Information Technology in Medicine and Education (ITME), 2012 International Symposium on (Volume:2), 3-5 Aug. 2012
- [2] M. Armbrust, A. Fox, R. Griffith, A.D. Joseph, R. Katz, A. Konwinski, G. Lee, D. Patterson, A. Rabkin, I. Stoica and M. Zaharia, "A View of Cloud Computing," Communications of the ACM, vol. 53, no. 4, pp. 50-58, 2010.
- [3] Garlasu D, Sandulescu V, Halcu I, Neculoiu G, Grigoriu O, Marinescu M, Marinescu V, "A big data implementation based on Grid computing," Roedunet International Conference (RoEduNet), 2013 11th .
- [4] Malik P, "Governing Big Data: Principles and practices", IBM Journal of Research and Development (Volume:57 , Issue: 3/4), May-July 2013.
- [5] J. Yao, S. Chen, S. Nepal, D. Levy and J. Zic, "TrustStore: Making Amazon S3 Trustworthy with Services Composition," in Proceedings of the 10th IEEE/ACM International Conference on Cluster, Cloud and Grid Computing (CCGRID '10), pp. 600-605, 2010.
- [6] D. Zissis and D. Lekkas, "Addressing Cloud Computing Security Issues," Future Generation Computer Systems, vol. 28, no. 3, pp. 583-592, 2011.
- [7] Jing Yu, Bin Xu, Yong Shi "The Domain Knowledge Driven Intelligent Data Auditing Model," Web Intelligence and Intelligent Agent Technology (WI-IAT), 2010 IEEE/WIC/ACM International Conference on (Volume:3), Aug. 31 2010-Sept. 3 2010, Page(s): 199 – 202.
- [8] Cong Wang, Qian Wang, Kui Ren, Wenjing Lou "Privacy-Preserving Public Auditing for Data Storage Security in Cloud Computing," INFOCOM, 2010 Proceedings IEEE, 14-19 March 2010, Page(s): 1 - 9
- [9] Q. Wang, C. Wang, K. Ren, W. Lou and J. Li, "Enabling Public Auditability and Data Dynamics for Storage Security in Cloud Computing," IEEE Transactions on Parallel and Distributed Systems, vol. 22, no. 5, pp. 847 - 859, 2011.
- [10] G. Ateniese, R.D. Pietro, L.V. Mancini and G. Tsudik, "Scalable and Efficient Provable Data Possession," in Proceedings of the 4th International Conference on Security and Privacy in Communication Networks (SecureComm '08), pp. 1-10, 2008.
- [11] X. Zhang, L.T. Yang, C. Liu and J. Chen, "A Scalable Two-Phase Top-Down Specialization Approach for Data Anonymization using MapReduce on Cloud," IEEE Transactions on Parallel and Distributed Systems, In Press, 2013.
- [12] C. Erway, A. K  p   , C. Papamanthou and R. Tamassia, "Dynamic Provable Data Possession," in Proceedings of the 16th ACM Conference on Computer and Communications Security (CCS'09), pp. 213-222, 2009.
- [13] S.E. Schmidt, "Security and Privacy in the AWS Cloud," Presentation on Amazon Summit Australia, 17 May 2012, Sydney, 2012,
- [14] Y. He, S. Barman and J.F. Naughton, "Preventing Equivalence Attacks in Updated, Anonymized Data," in Proceedings of the 27th IEEE International Conference on Data Engineering (ICDE '11), pp. 529-540, 2011.
- [15] A. Juels and J. B. S. Kaliski, "PORs: Proofs of Retrievability for Large Files," in Proceedings of the 14th ACM Conference on Computer and Communications Security (CCS '07), pp. 584-597, 2007.
- [16] D. Boneh, H. Shacham and B. Lynn, "Short Signatures from the Weil Pairing," Journal of Cryptology, vol. 17, no. 4, pp. 297-319, 2004.

A Review of Issues in Photochemical Machining

Yadav R. P.¹, Teli S. N.²

^{1,2} Mechanical Engineering, Saraswati Collage of Engineering, India

Abstract: This paper presents the issues in machining of copper using Photochemical Machining (PCM). Twenty-seven experimental runs base on full factorial (3^3) Design of Experiments (DoE) technique can perform. The control parameters can consider the etchant concentration, etching temperature and etching time. The response parameters were Undercut (Uc) and the Surface roughness (Ra). The effects of control parameters on undercut and surface roughness can analyze using Analysis of Variance (ANOVA) technique and their optimal conditions can evaluate. An optimum surface roughness can observe at particular etching temperature, an etching concentration and etchings time. The minimum undercut (Uc) can observe at the particular etching temperature, etching concentration and etching time.

Keywords: PCM, DoE, ANOVA, Surface Roughness, Undercut.

I. Introduction

The photo chemical machining process goes by many names, including photo chemical machining, photo chemical etching, chemical milling, chemical etching, photo etching, even the abbreviation "PCM." All of these names describe the same process. The photo chemical machining process is a means of fabricating thin gauge metal parts. The metal thickness ranges from .001" to .080" depending on the type of metal. In the photo chemical machining process a stencil, called a "photo tool," is used to expose multiple images of the parts to be made on both sides of a sheet of raw material that has been coated with a light sensitive and acid resistant material, called "resist." After the images of the parts have been developed, and the uncured "resist" is washed away, the metal around the part is dissolved using an etching chemistry. The PCM is one of the non-conventional machining processes that produces a burr free and stress free flat complex metal components. The machining takes place using a controlled dissolution of work-piece material by contact of the strong chemical solution. The PCM industry currently plays a vital role in the production of a variety of precision parts viz. micro fluidic channels, silicon integrated circuits, copper printed circuit boards and decorative items. It is mainly used for manufacturing of micro-components in various fields such as electronics, aerospace and medical. It employs chemical etching through a photo-resist stencil as a method of material removal over selected areas. This technique is relatively modern and became established as a manufacturing process. The newly-developed products made from PCM especially relevant to Micro engineering, Micro-fluidics and Microsystems Technology. Copper is an important material for various engineering applications, as because of its excellent electrical and thermal conductivity, easy fabrication, and good strength and fatigue properties. An aqueous solution of ferric chloride (FeCl_3) is the most commonly used etchant.

II. Background

Although the first photo resist was developed in 1826, the start of the photochemical machining industry seemed to coincide with the development of the highly successful KPR family of photo resists marketed by Kodak in the mid- 1950s. These photo resists were propensities and therefore easy to use.

The first PCM companies were formed in North America and the UK but soon the technology was also being applied in mainland Europe and the Far East. Later, the technology spread to Central and South America, Australasia, Central Asia and Southern Africa. The European countries behind the Iron Curtain were active in using PCM as part of their defense industry but, since the fall of the Berlin Wall in 1989, their PCM industry has been greatly contracted, especially in Russia and Bulgaria.

Many of the job-shop (sub-contract) PCM companies were started by entrepreneurs as small spin-off companies intent on manufacturing piece-parts as a rapid and economic alternative to stamping. Some larger companies believed that the PCM process was so critical to their production that it was brought in-house to gain competitive advantage and preserve confidentiality.

In the early days of commercial PCM, process technology was guarded jealously to the point that PCM was regarded as 'Manufacturing's Best Kept Secret'. However, the formation in 1967 of a small, USA-based trade organization, the Chemi Photocl Machining Institute (PCMI), did provide a focus for industrial PCM

companies and that has eventually led to more open discussion of PCM technology and challenges. This organization now has international membership with regional Chapters in the USA and Europe. The Japanese Photo Fabrication Association (JPFA), formed in the late 1970s, provided a similar focus for Japanese PCM companies.

Many PCM companies have also expanded their process capability within the past ten years by installing additional laser cutting, wire-EDM, CNC routing, water jet cutting, forming, electroplating and/or photo electroforming (PEF) processes to form 'one-stop shops'. The business philosophy is to utilize the best technique for both technical and financial benefit.

Research into PCM, outside company laboratories, has been concentrated since the mid-1970s into just a few universities and research institutes based in Europe (e.g. UK, Germany and The Netherlands), Japan and, more recently, China. Since 2000, with the cessation of PCM university research in mainland Europe and to further global pre-competitive research, Canfield University has set up five PCM Research Consortia each of one year's duration.

The Consortia comprise over a dozen rival commercial PCM companies from across the world with the common objective of investigating current industrial PCM challenges. The formation of the consortia constituted the first occasion of PCM multi-collaboration across company and country boundaries.

III. Steps Involved In PCM Process

3.1. Preparation of masters/photo tool

It serves as tool in PCM. It begins with generation of oversize art-work or paper. Art-work is usually generated at some magnification factor to minimize dimensional error. Art-work can be generated by manual drafting or by precision coordination graph plotting or by computer aided drafting. The art-work is photographed with precision reduction camera. In high volume production of parts, multiple image masters are used to expose, develop, etch a number of parts. It results in master film that contains the pattern to be etched. Sets of films are made to facilitate simultaneous exposure from both sides. During master's preparation, provisions are made for reclaiming of parts after etching.

3.2 Selection of metal

Metals should have grain size as fine as possible, because the smoothness of edges of the parts decreases with increase in grain size. A metal that is soluble in etchant should be chosen. A material should be flat and of uniform thickness. Surface finish should be uniform and it should be free from scratches, embedded particles or inclusions.

3.3 Preparation of work piece

To have good adhesion between metal and photo resist metal surface must be free of contaminants. Work piece should be cleared by spraying water on metal surface and determining whether the individual droplet spread out to form thin film of water. Formation of film indicates adequate cleaning. The work piece is then rinsed and dried.

3.4 Masking with photo resists

Photo resists provides photosensitive surface that resists the action etchant. The photo resist can be either positive or negative masking. In positive acting system area that is exposed to light washes away during development. In negative system, exposed areas are made insoluble in the developing solutions. Photo resists can be applied by dipping, whirl coating, or spraying. The resists are dried at room temperature and then baked for 15 minutes at maximum temperature of 120 °C. Exposure of photo resists to ultra-violet light polymerizes exposed areas of light sensitive resin, increasing resistance of these areas to chemicals used as developers.

3.5 Etching

The developed and post baked panel of metal is exposed to heated acid during etching. The acid reacts with exposed metal and oxidizes it to form soluble reaction product. Etching can be done either by immersion in agitated chemical bath or spraying with heated acid. When etching has proceeded to a point at which penetration from each surface has gone half way through the sheet, the break through occurs. Etching machines are made that can withstand corrosion from etchant. Machines have some at the base that contains the etchant. Heating element and cooling coil helps to maintain constant etchant temperature. An etcher with conveyor system allows continuous processing. In batch type machines one sheet at a time is processed.

3.6 Stripping and inspection

After etching, panels are still remain coated with photo resist, removal (stripping) of photo resist is necessary. Photo resist should be removed without staining the metal surface. Handling of parts during stripping is easier when the parts remain attached to metal sheet. Connecting tabs are located such that they do not interfere with function of part. Thickness of etched work piece is inspected. The best method of inspection involves plug gauges and horizontal optical comparator.

IV. Steps For Experiments Designing

4.1 Recognition of and statement of the problem

This may seem to be a rather obvious point, but in practice it is often not simple to realize that problem requiring experimentation exists, nor is it simple to develop a clear and generally accepted statement of this problem. It is necessary to develop all ideas about the objectives of the experiment.

4.2 Choice of factors, levels, and range

When considering the factors that may influence the performance of a process or system, the experimenter usually discovers that these factors can be classified as either potential design factors or nuisance factors. The potential design factors are those factors that the experimenter may wish to vary in the experiment. Some useful classifications are design factors, held-constant factors, and allowed-to-vary factors. Nuisance factors are often classified as controllable, uncontrollable, or noise factors. A controllable nuisance factor is one whose levels may be set by the experimenter. If a nuisance factor is uncontrollable in the experiment, but it can be measured, an analysis procedure called the analysis of covariance.

4.3 Selection of the response variable

In selecting the response variable, the experimenter should be certain that this variable really provides useful information about the process under study. Most often, the average or standard deviation (or both) of the measured characteristic will be the response variable. Multiple responses are not unusual.

4.4 Choice of experimental design

If the pre-experimental planning activities above are done correctly, this step is relatively easy. Choice of design involves the consideration of sample size (number of replicates), the selection of a suitable run order for the experimental trials, and the determination of whether or not blocking or other randomization restrictions are involved.

4.5 Performing the experiment

When running the experiment, it is vital to monitor the process carefully to ensure that everything is being done according to plan. Errors in experimental procedure at this stage will usually destroy experimental validity. Up-front planning is crucial to success. It is easy to underestimate the logistical and planning aspects of running a designed experiment in a complex manufacturing or research and development environment.

4.6 Statistical analysis of the data

Statistical methods should be used to analyze the data so that results and conclusions are objective rather than judgmental in nature. If the experiment has been designed correctly and if it has been performed according to the design, the statistical methods required are not elaborate.

4.7 Conclusions and recommendations

Once the data has been analyzed, the experiments must draw practical conclusions about the results and recommend a course of action. Graphical methods are often useful in this stage, particularly in presenting the results to others. Follow-up runs and confirmation testing should also be performed to validate the conclusions from the experiment.

V. Experimental Setup

During experimentation; temperature, the time of etching and concentration of etchant is necessarily to be changed. For this heating bath is used which varies temperature from 20° C to 125°C. In this heating bath heater is used to change the temperature of water which can be sensed by sensor. In this heated water, four beakers can be placed for experimentation. This instrument is used in place of etching machine as shown in Figures below.



Fig.5.1 PCM lab



Fig. 5.2 Work part preparation

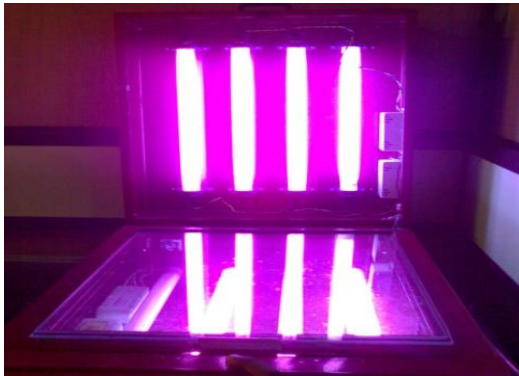


Fig. 5.3 U. V. Exposure



Fig. 5.4 Negative maker



Fig. 5.5 Photo resists coater



Fig. 5.6 Etching machine

VI. Selection Of Pcm Parameters

Many parameters affect the performance of PCM and the setting of these parameters relies strongly on the experience of operator's and the parameter. So the first task is to select a reasonable set of input parameters. On one hand a smaller of parameters might not serve the purpose, but on the other hand a large number of parameters may will make the prediction more difficult. Thus, the choice of input parameters is, to some extent, a compromise. Base on the survey of literature, experience of the operators and some preliminary experiments, input parameter were chosen. These input parameters are called as control parameters. These control parameters were varied in a range during the experiments to study their effect on the performance measure.

- **Control parameters:-** Temperature ($^{\circ}\text{C}$), Concentration (gm/lit), Time (min).
- **Fixed parameters:-** Etchant, Work piece material, Work piece thickness, Workpiece area, Work piece size.
- **Response variables:-** Surface roughness.

VII. CONCLUSION

Cakir (2006) studied that the copper etching with CuCl_2 etchant and a suitable regeneration process of waste etchant simultaneously. This would reduce the overall manufacturing cost and environmentally friendly etching process which ultimately enhances the productivity. David et al. (2004) studied the characterization of aqueous ferric chloride etchant used in industrial photochemical machining. He found that FeCl_3 is most commonly used etchant with a wide variety of grades. Rajkumar et al. (2004) investigated the cost model for PCM which defines standards for industrial etchants and methods to analyze and monitor them. Cakir (2004) stated that the etch rate of FeCl_3 is higher than CuCl_2 but CuCl_2 gives a better surface finish than FeCl_3 during machining of Cu-ETP copper.

The main limitation of PCM is to be found in the characteristics of isotropic etching whereby the etchant will attack not only downwards in to the metal but also sideways beneath the resist stencil layer. The ratio of depth to the undercut is termed the "etch factor". A relatively high level of operator skill is required. Special safety precautions are needed in handling of chemicals; the etchant vapors also very corrosive. Etching equipments must usually be isolated from other plant equipment. Suitable photographic facilities are not always available. Maximum metal thickness that can be blanked is about 1.6 mm. Sharp radii cannot be produced.

It is observed that no statistical study has been reported to analyze the interaction effects of process parameters on etching process of Copper. Till date an accuracy of PCM depends only on the skill and experience of the operator. Work to date an optimal set of process parameters is not calculated. The statistical study is necessary to investigate the performance in different ranges as well as to find the global optimum process parameters. It is also necessary to find out the single optimum process parameters setting to satisfy the requirements of excellent etching quality. In this work, an attempt is made to study the optimum process parameters by using full factorial design method and an ANOVA technique.

REFERENCES

- [1] O. Cakir, 2006, "Copper etching with cupric chloride and regeneration of waste etchant", *Journal of Materials Processing Technology*, 175, 63–68.
- [2] David M. A., 2004, "Photochemical Machining: From Manufacturing's Best Kept secret to a \$6 Billion per annum", *Rapid Manufacturing Process, CIRP Journal of Manufacturing Systems*, 53, 559-573.
- [3] David M. A., Heather, J.A. Heather J.A., 2004, "Characterization of aqueous ferric chloride etchants used in industrial photochemical machining", *Journal of Materials Processing Technology*, 149, 238–245.
- [4] Davis, P.J., Overture, G.E., 1986, "Chemical machining as a precision material removal process", *precision engineering*, 67-71.
- [5] Douglas, C. M., 1997, *Design and Analysis of Experiments*. Fifth Edition, John Wiley and sons, INC.
- [6] Rajkumar, R., Heather J.A., Oscar Zamora., 2004, "Cost of photochemical machining", *Journal of Materials Processing Technology*, 149, 460–465.

A Detailed Modeling of a Five Parameters Model for Photovoltaic Modules

Nouar Aoun¹, Boukheit Nahman², Rachid Chenni³, Kada Bouchouicha⁴

^{1,2} Department of Physics, Constantine 1 University, Algeria

³ MoDERNa Laboratory, Constantine 1 University, Algeria

⁴ Research Unit in Renewables Energies, URER/MS, Development Centre of Renewable Energies, CDER, Adrar, Algeria.

Abstract: In the present paper we interested at the parametric characterization of the five parameters model. However, we reductive the system of the three characteristic points under STC in one equation called f_{R_s} and one unknown parameter (i.e., R_s). Moreover, we vary with a step of 10^{-4} , the ideality factor γ between 0.0 and 4 for each iteration in order to choose the value of γ which gives a minimal relative error of the maximum power point. Finally, when γ is known the other four parameters (i.e., R_s , I_0 , I_{ph} and R_{sh}) are known. The effectiveness of this approach is evaluated through comparison of simulation results to the data provided by product's manufacturer.

Keywords: photovoltaic; nonlinear equation; five parameters model.

I. INTRODUCTION

The modeling of a photovoltaic module (of a cell) implies mainly the estimate of nonlinear curves IV. Preceding researchers [1], [2], [3] and [4] used topological circuits to model the module characteristics when it is subjected to environmental variations such as illumination and the temperature. By far, the simplest approach is the model with a diode, namely a power source simultaneously with a diode [2], [5] and [6]. In the majority of work of the literature, we find mainly the model equivalent to four parameters based on the mathematical modeling of the curve voltage [1], [3].

The model with four parameters utilizes four parameters, namely: I_{ph} (the photo current), I_0 (the saturation current), γ (the factor of the diode ideality) and R_s (resistance series). These parameters are not generally measurable quantities or included in the data of manufacture. Consequently, they must be given starting from an equations system of governing the characteristic IV at various points of operation given by the manufacturer or drawn from the experimental tests.

An extension of the model of only one diode, including an additional resistance shunt R_{sh} is proposed by many authors [7]. While adding resistance shunt, the number of parameters is changed to five.

The performances of the solar cells are normally evaluated under the standard test condition (STC), where an average solar spectrum with 1,5 AM is used and illumination is standardized with 1000 W/m^2 . As it is shown in Fig.1, the model with only one exponential with a parallel resistance R_{sh} described by (1) is nonlinear and implicit; therefore, a solution will be determined by iterative methods (Newton-Raphson, Levenberg Marquardt, ... etc). In our work, the method of Newton-Raphson was used numerically.

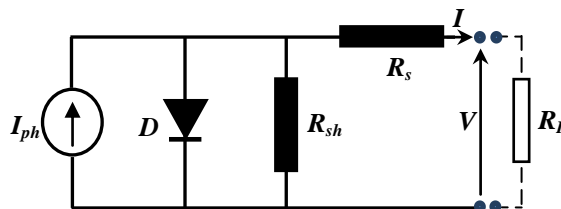


Fig. 1. Circuit equivalent of the five parameters model

The relation current-tension in the conditions ($T=25^\circ\text{C}$, $E=1000 \text{ W/m}^2$) for the equivalent circuit, fig. 1 is expressed in (1).

$$I = I_{ph} - I_0 \left[\exp \left(\frac{q(V + IR_s)}{\gamma k T} \right) - 1 \right] - \frac{V + IR_s}{R_{sh}} \quad (1)$$

Where q the electronic load, K the Boltzmann constant, T the temperature, γ is the ideality factor, I_{ph} the power source, I_0 the reverse current of saturation of the diode, R_s resistance series and R_{sh} resistance shunt.

II. FIVE PARAMETERS MODEL

The five parameters appearing in (1) corresponding to the conditions standards are: γ , I_0 , I_{ph} , R_s , and R_{sh} . These parameters are with starting from the measurement of characteristic I-V for a couple of illumination and reference temperature given to only on nominal database provided by the manufacturer. In general, these five parameters depend on the incidental solar radiation on the cell and on the temperature [8].

Three pairs of parameters of the characteristic voltage are normally provided by the manufacturer (2) to (4): the shortcircuit current I_{sc} , the open circuit voltage V_{oc} and the current and the tension at the maximum powerpoint (i. e., I_{mp} , V_{mp}), respectively. Fourth information results from the assumption that the derivation of the power at the maximum power point is null.

- **Short-circuit Current:**

$$I_{sc} = I_{ph} - I_0 \left[\exp \left(\frac{q R_s I_{sc}}{\gamma k T} \right) - 1 \right] - \left(\frac{R_s I_{sc}}{R_{sh}} \right) \quad (2)$$

- **Open circuit voltage:**

$$0 = I_{ph} - I_0 \left[\exp \left(\frac{q V_{oc}}{\gamma k T} \right) - 1 \right] - \left(\frac{V_{oc}}{R_{sh}} \right) \quad (3)$$

- **Maximum power point:**

$$I_p = I_{ph} - I_0 \left[\exp \left(\frac{q (V_p + R_s I_p)}{\gamma k T} \right) - 1 \right] - \left(\frac{V_p + R_s I_p}{R_{sh}} \right) \quad (4)$$

We obtain the values of four unknown factor I_{ph} , I_0 , R_{sh} and R_s starting from the system of equations as (5), [11]. However, in [11] the ideality factor supposed as a constant parameter.

$$\begin{bmatrix} 0 \\ I_{sc} \\ I_p \end{bmatrix} / \begin{bmatrix} 1 & -C & -V_{oc} \\ 1 & -B & -R_s I_{sc} \\ 1 & -A & -V_p - R_s I_p \end{bmatrix} = \begin{bmatrix} I_{ph} \\ I_0 \\ 1 / R_{sh} \end{bmatrix} \quad (5)$$

Contrary to the various authors who treated the ideality factor as a constant parameter [9], [10] and [11], we vary with a step of 10^{-4} , the ideality factor γ between 0.0 and 4 for each iteration in order to choose the value of γ which gives a minimal relative error of the maximum power point.

Where:

$$A = \exp \left(\frac{q (V_p + R_s I_p)}{\gamma k T} \right) - 1 \quad (6)$$

$$B = \exp \left(\frac{q R_s I_{sc}}{\gamma k T} \right) - 1 \quad (7)$$

$$C = \exp \left(\frac{q V_{oc}}{\gamma k T} \right) - 1 \quad (8)$$

$$I_{ph} = \det^{-1} (V_{oc} I_{sc} A - V_{oc} I_p B - V_p I_{sc} C) \quad (9)$$

$$I_{sc} = \det^{-1} (V_{oc} I_{sc} - V_{oc} I_p - V_p I_{sc}) \quad (10)$$

$$R_{sh}^{-1} = \det^{-1} [I_{sc} A - I_p B - (I_{sc} - I_p) C] \quad (11)$$

The calculation of \det is shown in (12):

$$\det = (V_{oc} - R_s I_{sc}) A + (-V_{oc} + V_p + R_s I_p) B + (-V_p + R_s [I_{sc} - I_p]) C \quad (12)$$

The derivative of the power at the point of maximum power is null:

$$\left. \frac{d(IV)}{dV} \right|_p = I_p - V_p \left. \frac{dI}{dV} \right|_p = 0 \quad (13)$$

With $dI/dV|_p$ is given by the following relation:

$$\left. \frac{dI}{dV} \right|_p = \left\{ \frac{-q I_0}{\gamma k T} \exp \frac{q (V_p + I_p R_s)}{\gamma k T} - \frac{1}{R_{sh}} / 1 + \frac{q I_0 R_s}{\gamma k T} \exp \frac{q (V_p + I_p R_s)}{\gamma k T} + \frac{R_s}{R_{sh}} \right\} \quad (14)$$

The derivative of (1) compared to the voltage can be expressed by:

$$\frac{dI}{dV} = - \left\{ R_s + \left(\frac{q I_0}{\gamma k T} \exp \frac{q (V + R_s I)}{\gamma k T} + \frac{1}{R_{sh}} \right)^{-1} \right\} \quad (15)$$

We introduce (13) in (15), then we define a function f_{Rs} given by:

$$f_{R_s} = I_p - (V_p - R_s I_p) \left(\frac{q I_0}{\gamma k T} \exp \frac{q(V_p + R_s I_p)}{\gamma k T} + \frac{1}{R_{sh}} \right) \quad (16)$$

As I_0 and R_{sh} depend on R_s , the function f_{R_s} is also. The resolution of $f_{R_s}=0$ with the algorithm of Newton-Raphson implies the calculation of its derivative; that is to say:

$$\frac{df_{R_s}}{dR_s} = - \frac{V_T I_p I_{sc} (V_p - R_s I_p) (A - B)}{\det} + \frac{1}{R_{sh}} \left[I_M + \left(\frac{V_p - R_s I_p}{\det} \right) \frac{d_{det}}{dR_s} \right] + V_T I_0 \exp \frac{q(V_p + R_s I_p)}{\gamma k T} \dots$$

$$\left[I_M \left(1 - \frac{q(V_p - R_s I_p)}{\gamma k T} \right) + \left(\frac{V_p - R_s I_p}{\gamma k T} \right) \frac{d_{det}}{dR_s} \right] \quad (17)$$

With:

$$\frac{d_{det}}{dR_s} = (V_T I_p (V_{oc} - R_s I_{sc}) - I_{sc}) A + (V_T I_{sc} (-V_{oc} + V_p + R_s I_p) + I_p) B + (I_{sc} - I_p) C + V_T \dots$$

$$(V_p I_{sc} - V_{oc} (I_{sc} - I_p)) \quad (18)$$

$$V_T = \frac{q}{\gamma k T} \quad (19)$$

III. RESULTS AND DISCUSSIONS

The precision of process of modeling described in this document is validated by the parameters of datasheet of selected photovoltaic modules. Three modules of different technologies are used for the checking; the multi and the single-crystal one like that of thin films type. The characteristics of the modules are summarized in Tab. 1.

TABLE 1. CHARACTERISTICS OF VARIOUS MODULES STUDIED UNDER STC

	BP solar MSX-60	Siemens SM55 <u>multi-crystalline</u>	Shell S36	Shell SP-70 <u>mono-crystalline</u>	Shell ST40 <u>couche mince</u>
I_{sc} (A)	3.8	3.45	2.3	4.7	2.68
V_{oc} (V)	21.1	21.7	21.4	21.4	21.3
I_p (A)	3.5	3.15	2.18	4.25	2.41
V_p (V)	17.1	17.4	16.5	16.5	16.6

We measured the curves voltage and power-voltage of the photovoltaic module for various weather conditions (solar illumination and temperature) and we calculated the statistical parameters in order to estimate the validity of the model used. Tab. 2 shows calculated parameters for the five parameters model.

Fig. 2, show the characteristics power-voltage and current-voltage comparison, respectively, of the five parameters model and the experimental points extracted from the datasheet for the Solarex MSX60 module at various operating temperatures.

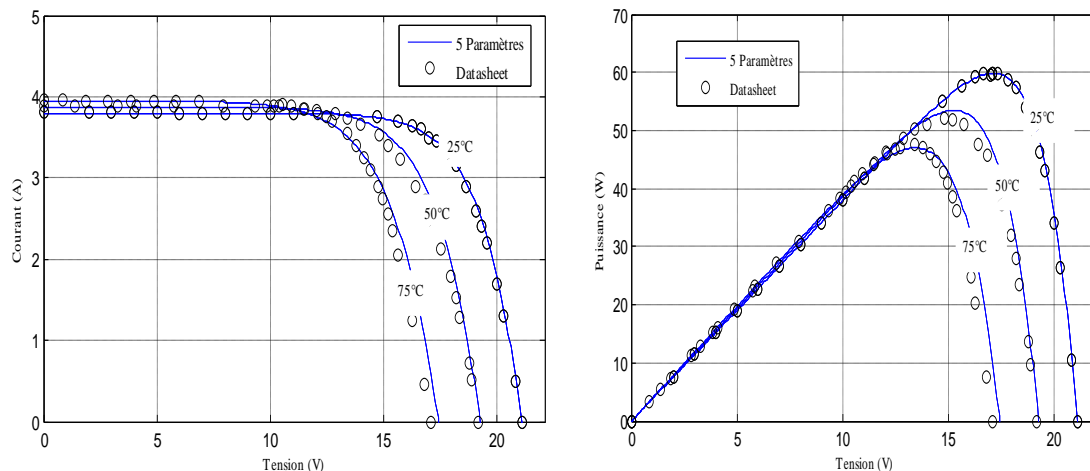


Fig. 2. Curves I-V and P-V of SOLAREX MSX60 Module in Fixed illumination 1KW/m².

Fig. 3, show the characteristics power-voltage and current-voltage comparison, respectively, of the five parameters model and the experimental points extracted from the datasheet for photovoltaic cell Q6LM at various levels of illuminations.

TABLE 2. ELECTRIC PARAMETERS OF THE MODEL PROPOSES

	BP solar MSX-60	Siemens SM55	Shell S36	Shell SP-70	Shell ST40
	<u>multi-crystalline</u>		<u>mono-crystalline</u>		<u>couche mince</u>
γ	1.5	1.7	1.2588	1.7	2.097
I_{ph} (A)	3.8003	3.4503	2.30023	4.7003	2.6804
I_0 (A)	9.4607e-7	3.5065e-6	2.40919e-8	5.7971e-6	1.6315e-5
R_s (m Ω)	0.0034	0.0036	0.01831	0.0078	0.0257
R_{sh} (m Ω)	43.0744	43.7167	179.783	110.6362	215.3892

We observe on Figs 2 to 3 that the two curves appear identical to the points of standard condition of reference. On the other hand, more the temperature and illumination are far away from the standard conditions of reference, more there are divergences in the elbow of the curves and at the point of open circuit voltage.

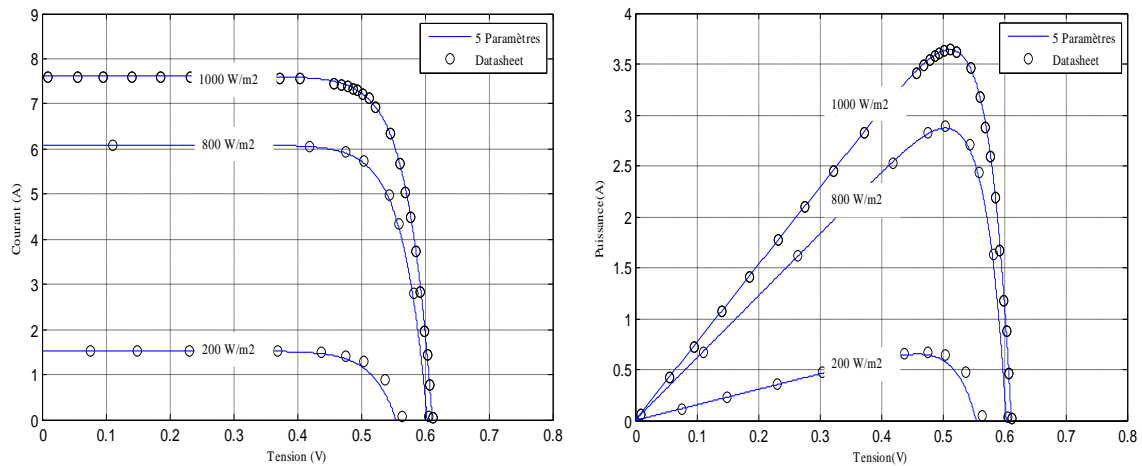


Fig. 3. Curve P-V of Q6LM Cell in Fixe Temperature 25°C

The differences between the data of the datasheet and the computed values occur because of the limitations in the model of the cells themselves, as well as in the calculating methods [12]. Moreover, there are uncertainties inherent in the experimental data. The experimental data points are extracted from datasheet and from [2] and [14].

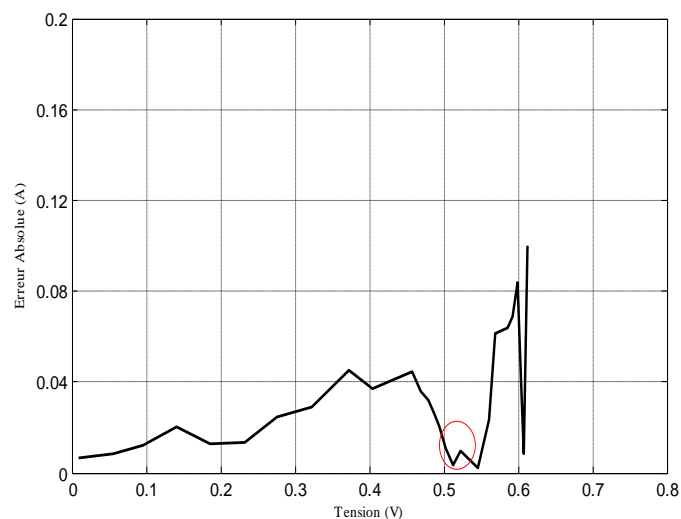


Fig4.. Absolute error For Q6LM Cell in 25 °C, 1000 W/m²

To show the effectiveness of the studied models, the photovoltaic modules: Shell S36, Shell SP70 and Shell ST40 are used of which Tab. 3 to 5 show the relative errors on the maximum power point for different temperature (0°C to 50°C). Figs 4 and 5 show successively the absolute error of the current according to the tension for the Solarex MSX60 module and Q6LM cell.

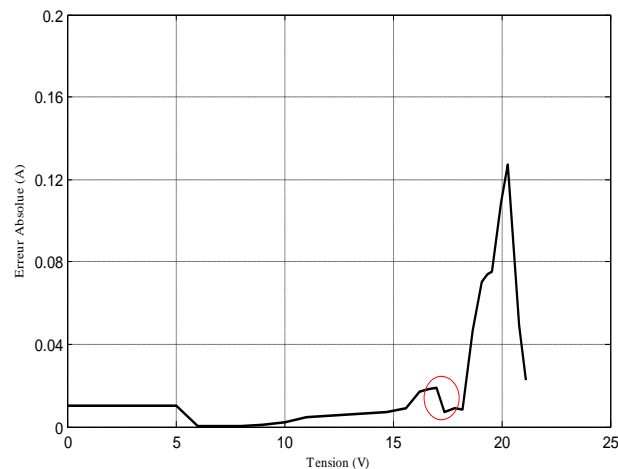


Fig5..Absolute error For the Solarex MSX60 Module in 25 °C, 1000 W/m²

This calculation considers the standard conditions, illumination and temperature STC (25°C, 1000W/m²). The model with five parameters gives incorrect results in the vicinity of the open circuit voltage. It must be provided that our model does not take account of the coefficient of open circuit voltage [1]. The circle represents the zone where normally the point of the maximum power of module. It is observed that this zone represents an absolute error which can be considered negligible (<0.02). Lastly, our model gives a good agreement with the data of datasheet.

TABLE 3.RELATIVE ERRORS OF MULTI-CRYSTALLINE SILICON (SHELL S36)

Temperature	Cinq Paramètres	Datasheet	Erreur -Relative(%)
0° C	39.5228	40.05	1.3164
25° C	36.0317	36	0.0882
50° C	32.3981	31.95	1.4026

TABLE 4.RELATIVE ERRORS OF MONO-CRYSTALLINE SILICON (SHELL Sp70)

Temperature	FiveParameters	Datasheet	Erreur-Relative(%)
0° C	75.1311	77.88	3.5297
25° C	70.0067	70	0.0096
50° C	64.1841	62.13	3.3062

TABLE 5.RELATIVE ERRORS OF THIN-FILM (SHELL St40)

Temperature	Five parameters	Datasheet	Erreur -Relative(%)
0° C	44.4188	46.00	3.4374
25° C	40.0369	40.00	0.0923
50° C	35.6734	34.00	4.9216

IV. CONCLUSION

In this article, a general approach on the photovoltaic modules modeling is presented. The five parameters model uses abundant data only by the manufacturer. The chosen points for the determination of the parameters are the short-circuit current I_{sc} , the open circuit voltage V_{oc} , and the maximum power point (V_p , I_p). The model requires a calculation of these parameters (γ , I_0 , I_{ph} , R_s , and R_{sh}) at the reference conditions STC (25°C, 1000 W/m²). These values are then used in the model to calculate the parameters with real conditions. Three types of photovoltaic modules were modeled and evaluated (CIS, multi-crystalline silicon, and mono-crystalline silicon). We vary the ideality factor γ between 0.0 and 4 with a step of 10^{-4} , for each iteration in order to choose the value of γ which gives a minimal relative error of the maximum power point. The precision of the model is also analyzed by the comparison between the data of the product and the results of simulation. Lastly, our model gives a good agreement with the data of datasheet.

REFERENCES

- [1] R. Chenni, M. Makhlouf, T. kerbach and A. Bouzid, "A detailed modeling method for photovoltaic cells," *Solar Energy*, Vol. 32, pp. 1724-1730, 2007.
- [2] K. Ishaque, Z. Ssalam and T. Hamed, "Simple, fast and accurate two-diode model for photovoltaic modules," *Solar Energy Mater and Solar Cells*, Vol. 95, No. 2, pp.586-594, 2011.
- [3] E. Matagne, R. Chenni and R. El Bachtiri, "A photovoltaic cell model based on nominal data Only," *Proceedings of the international conference on power Engineering Energy and Electrical Drives-Powereng*, Portugal, , pp. 562-565, April 2007.
- [4] M. Rekinge, E. Matagne, R. El Bachtiri and R. Chenni, "Un modèle de cellule photovoltaïque avec effet thermique établi sur base des valeurs nominales," *Conférence EF 2007*, Toulouse, 2007.
- [5] B. Fry, "Simulation of Grid-Tied Building Integrated Photovoltaic Systems," M.S. Thesis, Mechanical Engineering, University of Wisconsin-Madison, 1998.
- [6] D. Sera, R. Teodorescu and P. Rodriguez, "PV panel model based on datasheet values," In: *Proceedings of the IEEE International Symposium on Industrial Electronics (ISIE)*, pp. 2392–2396, 2007.
- [7] V. Lo Brano, A. Orioli, G. Ciulla and A. Di Gangi, "An improved five-parameter model for photovoltaic modules," *Solar Energy Materials and Solar Cells*, Vol. 94, pp. 1358–1370, 2010.
- [8] A. Chouder, S. Silvestre, N. Sadaoui and L. Rahmani, "Modeling and simulation of a grid connected PV system based on the evaluation of main PV module parameters," *Simulation Modelling Practice and Theory*, Vol. 20, pp. 46-58, 2012.
- [9] M.G. Villalva, J.R. Gazoli and E.R. Filho, "Comprehensive approach to modeling and simulation of photovoltaic arrays," *IEEE Trans. power electron*, Vol. 24, pp. 1198–1208, 2009.
- [10] W. De Soto, "Improvement and validation of a model for photovoltaic array performance," M.S. Thesis, Mechanical Engineering, University of Wisconsin-Madison, 2004.
- [11] B. Mustapha, "Modélisation et Simulation d'un Système de Pompe Photovoltaïque," M.S. Thesis. University of Oran, Algérie, 2006.
- [12] W. De Soto, S.A. Klein and W.A. Beckman, "Improvement and validation of a model for photovoltaic array performance," *Solar Energy*, Vol. 80, pp. 78–88, 2006.
- [13] K. Ishaque, Z. Salam, H. Taheri and Syafaruddin, "Modeling and simulation of photovoltaic (PV) system during partial shading based on a two-diode model," *Simulation Modelling Practice and Theory*, Vol. 19, pp. 1613-1626, 2011.
- [14] W. Xiao, W. G. Dunford and A. Capel, "A Novel Modeling Method for Photovoltaic Cells," *35th Annual IEEE Power Electronics Specialists Conference*, Germany, 2004.

Electro Slag Strip Cladding Process

Thakare Niraj S¹, Ram Yadav²

^{1, 2} Mechanical Engineering/ SSJCET College, India

Abstract: The Technological advancements have driven up temperature and pressure serviced in the petroleum, chemical, pulp, and environmental protection. Industries have increased the possibility of severe corrosion and wear in process pressure vessels. The industries must upgrade the corrosion and wear performance of these main important parts. Economic features as a rule will not allow fabricating components from solid high alloyed materials. As a result it is essential to surface non-alloyed or low alloy base materials with high-alloy cladding. The submerged arc welding (SAW) and electroslag welding (ESW) process are appropriate for applying welded deposits over large surface areas by means of strip electrodes. Both processes are using a granular flux material. A strip electrode, fed continuously, is liquefied and fused to the substrate. In contrast with other processes it is very effective in spite of the same equipments used but due to the wide strip used it procures a magnetic flow effect within to rectify it a magnetic steering device is exercised. After the welding to examine the defects NDT's are carried upon it.

Keywords: cladding, electro slag welding, weld overlay.

I. INTRODUCTION

The Welding is “a material joining process used in making welds,” and a weld is “localized coalescence of metals or non-metals produced either by heating the material to a suitable temperature with or without the application of pressure and with or without the use of filler metal. Welding is a fabrication or sculptural process that joins materials, usually metals or thermoplastics, by causing coalescence. This is often done by melting the workpieces and adding a filler material to form a pool of molten material (the weld pool) that cools to become a strong joint, with pressure sometimes used in conjunction with heat, or by itself, to produce the weld. This is in contrast with soldering and brazing, which involve melting a lower-melting-point material between the workpieces to form a bond between them, without melting the workpieces.

Many different energy sources can be used for welding, including a gas flame, an electric arc, a laser, an electron beam, friction, and ultrasound. While often an industrial process, welding may be performed in many different environments, including open air, under water and in outer space. Welding is a potentially hazardous undertaking and precautions are required to avoid burns, electric shock, vision damage, inhalation of poisonous gases and fumes, and exposure to intense ultraviolet radiation.

Until the end of the 19th century, the only welding process was forge welding, which blacksmiths had used for centuries to join iron and steel by heating and hammering. Arc welding and oxyfuel welding were among the first processes to develop late in the century, and electric resistance welding followed soon after. Welding technology advanced quickly during the early 20th century as World War I and World War II drove the demand for reliable and inexpensive joining methods. Following the wars, several modern welding techniques were developed, including manual methods like shielded metal arc welding, now one of the most popular welding methods, as well as semi-automatic and automatic processes such as gas metal arc welding, submerged arc welding, flux-cored arc welding and electroslag welding.

Electro slag strip cladding is an advancement of submerged arc strip cladding, which has speedily established itself as a reliable high deposition rate procedure. ESW is an arc less technique using Joules Effect to liquefy the strip material. The heating is an outcome of current flowing through the strip electrode and a relatively shallow layer of liquid electro conductive slag as shown in figure 1. The penetration is lesser for ESW than for SAW since the molten slag pool is used to liquefy the strip and some of the flux material rather than as an arc between the strip electrode and the flux material. As a rule of thumb, electro slag strip surfacing decreases dilution by up to 50% in contrast with submerged arc strip surfacing for the same heat input with a significantly higher deposition rate.

II. METHODOLOGY

2.1 Cladding

Cladding is the bonding together of dissimilar metals. In many cases, corrosion resistance is required only on the surface of the material and carbon or alloy steel can be clad with a more corrosion resistant alloy. Compared to carbon and alloy steels, all corrosion resistant alloys are expensive. Cladding can save up to 80% of the cost of using solid alloy. Cladding of carbon or low alloy steel can be accomplished in several ways including roll bonding, explosive bonding, weld overlaying and wallpapering. Clad materials are widely used in the chemical process, offshore oil production, oil refining and electric power generation industries. The use of clad steel is not new. Corrosion resistant alloy clad steel has been available for over 40 years. Almost any corrosion resistant stainless steel or nickel alloy can be bonded to steel. The steel can be clad on both sides or on one side only. Hence Strip cladding is a fusion welding technique used to:

- Deposit a strip of weld metal on to a component to achieve the desired dimensions or properties.
- Weld two dissimilar surfaces.
- Providing a wear or corrosion resistant surface.

Weld overlaying technique of cladding is commonly used to clad the surfaces of fabricated steel structures. The actual weld overlay process used depends on many factors including access, welding position, the alloy applied, and economics. In some alloy combinations, dilution of the weld overlay material by the steel requires that more than one weld pass is required. Post weld heat treating to temper the backing steel may be required in some cases. Strip cladding can be a very economical way to provide excellent corrosion resistance for steel structures. Both stainless steels and the more corrosion resistant nickel alloys can be economically applied to steel by Strip cladding. Strip cladding has also been widely used to line interiors of stacks and ducting for flue gas desulfurization units in fossil fuel power plants. One major benefit of weld overlaying is that they can be used to repair or modify existing steel structures.

2.2 Strip Cladding

Strip cladding is a fusion welding technique used to:

Deposit a strip of weld metal on to a component to achieve the desired dimensions or properties.

- Weld two dissimilar surfaces.
- Providing a wear or corrosion resistant surface.

Applications of Strip Cladding:

- The process is usually confined to relatively large and thick components which need to be manipulated to enable welding to be carried out in the flat position.
- The technique finds its widest application in the oil, gas and fertilizer related industries and in the nuclear power generation field.
- Generally used for surfacing the internal surfaces of pressure vessels and large diameter pipe and in the reclamation of steel mill rolls.

2.2.1 Submerged arc Strip Cladding (SASC)

This well-known SAW method has been widely used with strip electrodes since the mid-1960s. There is no fundamental difference between submerged arc welding and cladding. The welding wire is merely replaced with the cladding strip. The equipment is the same, except the head must be adapted to guide the strip. The principle is the same: the energy to melt the strip and the base metal is supplied by the electric arc struck between them. On melting, the agglomerated flux protect the liquid metal and where applicable enriches it with alloying elements. In the SAW process the strip is feed down through the contact jaws at the same time as the flux is feed down on both sides of the strip. The strip generates an arc between itself and the base material, the arc is not uniform and static, it wanders along the width of the strip but is all time sub merged under the molten slag. . It uses a strip, normally with a thickness of 0.5 mm and the width normally varies from 30 to 120 mm, but other width's are available for special applications.

2.2.2 Electro Slag Strip Cladding (ESSC)

The electro slag welding process was patented in USA in February 1940 and is a process that can weld material thicknesses from 25 up to 300 mm . It works in the vertical or very close to vertical position, it is in use for hull welding of ships, it is used for welding heavy wall thickness vessels of different kinds and many more applications. In the early 70's the electro slag concept was adjusted to fit the cladding process with a

metal strip. It can be said to be a development of SAW strip cladding which has quickly established itself as a reliable high deposition process.

- Technological developments have driven temperatures and pressures used in the petroleum, chemical, pulp, and paper, and environmental protection industries, and increased the likelihood of severe corrosion and wear in the process pressure vessels. The industries must improve the corrosion and wear performance of these major components.
- Economic factors as rule will not permit fabricating components from solid high alloyed material. As a consequence, it is necessary to surface non-alloyed or low alloy base material with high alloy cladding. The electro slag welding (ESSC) process is suitable for applying weld deposits over large surface areas using strip electrodes. Both the processes use a granular flux material. A strip electrode, fed continuously, is melted and fused to the substrate.
- In width, which are melted by applying current of appropriate strength; while using an auxiliary magnetic field, which improves the geometry of the bead.

III. MANUFACTURING PROCESS

3.1 Characteristics of ESSC

- Electro slag strip cladding is the modified version of submerged arc strip cladding process.
- The heat generation in the case of ESSC is due to the current flowing through the electro conductive slag.
- Molten weld pool will be visible during welding.
- Radiation only in the visible and infrared spectrum. No ultraviolet radiation because of the absence of the arc.
- Flux fed from front side only.
- Automatic removal of the slag crust.
- Very regular, finely ripped bead, without any slag adherence.

3.2 Process Principle

- In electro slag strip cladding the heat required to melt the base metal and the strip electrode is not generated by an electric arc; the Joule effect is utilized instead.
- The current flows through the strip and into a layer of electrically conductive slag; the resistance of this material generates the heat and keeps the welding process going (slag temperature approximately 2300° C)
- In ESSC process, the arc must be extinguished once it has been ignited and the current flow through the slag. As a consequence, the following must apply:
 $RA \Rightarrow \text{infinity} ; IA = 0$
Where RA is the resistance in the arc and IA is the current in the arc.
- If these conditions are to be satisfactory, the electrical resistance for the slag must be less than that for the arc.
- This presupposes that the electrical conductivity of the liquid slag created during the ignition process will rise with the rising temperature (or, the specific resistance is dependent on the temperature and is going down with rising temperature).
- If the process is to be stable, the thickness of the layer and the surface of the slag pool must be kept constant. This is effected by continuously melting flux, which is fed at one side only.
- To retard the interface resistance; it is important that the strip electrode has a sufficient depth in the slag pool.
- In ESSC process the resistance heating of the slag melts the fillet metal and the base material. Electroslag surfacing is thus classified as a resistance welding technique.

3.3 Welding Parameters

Attitude of the electrode: The electrode is usually located at right angles to the work piece (vertical) and at right angles to the axis of its movement (relative to the work piece). Rotating the electrode around its longitudinal axis is acceptable to a certain extent, but this will produce a narrower, thicker bead.

Spacing of current contact: The distance from the lower edge of the contact jaws to the surface to the work piece is generally about 30 mm. Flux depth: The depth of the flux determines the width of the slag layer obtained. If the flux is not deep enough, the slag pool will be too shallow, causing improved arcing of the strip. If the flux is too deep, the flux will liquefy only in the middle. The slag pool would be cooled by the flux lying on it, causing deterioration in electrical conductivity. At this point, again, the end result will be increased arcing. Normal depth should be 30 mm. Current density: Because of the absence of an arc, the penetration in the ESW procedure is very shallow; this represents that there will be slight mixing of the filler metal with the melted parent material. It is possible, in evaluation with the submerged arc welding (SAW), to use far higher power levels. For thin layers a normal current density of about 33 A/mm², 43 A/mm² for thicker layers. For strip type electrodes calculating 60*0.5 mm this will cause 1000 or 1250 A, respectively. This increased current level will cause penetration, though the here is still at the lower limit of what would be predictable in SAW surfacing using a strip type electrode. Power levels exceeding about 1000 A for 60*0.5 mm strip electrode would require very high welding speed to attain thin layers (below 0.15 in - mm) and the strip electrode would break up either wholly or partially from the front edge of the liquid slag. This would outcome in the increased arcing. When using wider electrode strips -120*0.5 mm, for instance—current of > 2500 A may be necessary.

Welding voltage: The welding voltage influences the specific resistance of the liquid slag and will decide how far the strip electrode is to be submerged in the slag pool. Inadequate immersion in the weld pool will affect the process and turn out the process into unstable one. The welding voltage must be lowered as current ascends. A range of 24 to 26 V when operating at 1250 A, or 22 to 24 V for 2500 A, is normal. The precise value will depend on the properties of the flux and the dimensions of the strip. Arcing may be experienced if the voltage is too high and the electrode is not immersed far enough in the slag pool. The welding process will turn out to be unstable with increased arcing.

Welding travel sound: The travel speed will depend on the desired thickness of the surfacing layer. The greater current density which can be applied along the high melting rate that can be achieved, make it possible to attain higher welding speeds than would be achieved, make it possible to attain higher welding speeds than would be possible with SAW surfacing. A layer of 4mm, is often specified encountered in processing equipment, the welding speed will be between 16 and 20 cm/min. The extent to which the thickness of the cladding can be reduced by increasing the welding speed is limited since, at speed exceeding 20 cm/min, the strip electrode will tend to “run away from “the slag pool. For this reason, lower current densities are used to apply thin layers about 3.5 mm. Not only can the surfacing depth be regulated by adjusting the welding speed; the degree of dilution by the substrate material can also be influenced for two different current levels, in comparison with submerged arc welding.

Supplementary magnetic fields: With the auxiliary steering magnets switched on, the width of the bead will increase by 1 to 2 mm; the depth is reduced accordingly since the filler material will be pulled toward the outer edges. With suitable adjustment of the magnetic fields at the north and south poles of the magnets will make it possible to affect the shape of the bead. The South Pole is always place at the left side in the welding direction. Using additional magnetic fields for steering purposes are not required for 60*0.5 mm electrodes. The geometry of the bead may be unfavorably influenced by welding near the ground connection. The two yokes of the magnet are placed 15 mm to the sides of the electrode strip and 1.5 mm above the surface of the base material. A strong magnetic field at the South Pole (3A: 1A) will pull the liquid filler material against the natural magnetic blow direction, which would be to the left when looking at the rear of the electrode. A strong magnetic field at the North Pole (2 A: 1A) would pull in the opposite direction. This is how we can neutralize the natural magnetic blow effect by accurate correction of the two auxiliary magnetic fields.

IV. ADVANTAGES & APPLICATION

4.1 Advantages of ESSC

Conventional welding procedure being used for overlay such as SMAW, FCAW, SAW, and SASC are all arc welding procedures. This procedure results in high dilution because of concentrated arc forces, which tend to produce a digging action on the parent metal, which is in molten form. This eventually affects the chemistry of the overlay, making it making to deposit more number of layers to attain the desired chemistry's. This problem is not found in ESSC welding procedure. By controlling various interaction parameters of ESSC, dilution can be limited to 7-10%. This gives ESSC a huge advantage over the other overlay procedure in productivity. The further main advantages of ESSC are:

- Lower penetration level (about 0.5mm)
- Lower defect and rework possibilities.
- Better bead characteristics.
- Problem free operation.
- Higher Overall Productivity.
- Simple equipment (similar to SAW equipment)
- Lesser number of layers to attain desired chemistry.

4.2 Applications of ESSC

The process is usually confined to relatively large and thick components which need to be manipulated to enable welding to be carried out in the flat position. The technique finds its widest application in the oil, gas and fertilizer related industries and in the nuclear power generation field. Generally used for surfacing the internal surfaces of pressure vessels and large diameter pipe and in the reclamation of steel mill rolls. Heavy plates, forgings and castings can be butt welded.

Where plates or castings of consistent width are involved or if they taper at a consistent rate, electrosag welding has virtually replaced thermit welding, being much simpler.

Subsequent alloys can be welded:

- Low carbon and medium carbon steels.
- High strength structural steels
- High strength alloy steels such as stainless steel and nickel alloys.
- Longitudinal stiffeners of the upper deck of ships.
- Longitudinal welds in cylindrical pressure vessels.
- Shells for blast furnaces and basic oxygen furnaces.

V. CONCLUSION

Electro slag strip cladding is the most widely used welding procedure in the industry. Electro slag strip cladding is an advancement of submerged arc strip cladding, which has rapidly established itself as a reliable high deposition rate procedure. In ESSC for each application, the efficiency and quality of weld can be controlled by controlling the process variables: attitude of electrode, spacing of current contact, flux depth, current density, welding voltage, welding travel speed, supplementary magnetic fields. There are certain safety measures which are to be taken care of before and during welding. Auto step over technique saves 10 hours of time equivalent to one working shift. It also enhances superior weld quality and very less amount of surface grinding. Thus increasing the productivity of overall activity with better efficiency.

REFERENCES

- [1]. Kuskov, Yu. M., Skorokhodov, V. N., Ryabtsev, I. A., and Sychev I. S. 2001. Electrosag welding and surfacing. Science and Technology, p. 179.
- [2]. YU. M. KUSOV 2001. A New Approach to Electrosag Welding-Welding journal.
- [3]. R.D. Jr. Thomas, 1960. Electrosag Welding- A New Process for Heavy Fabrication, p.111 International journal.
- [4]. George E. Linnert, Welding Metallurgy, 2nd Edition
- [5]. T.W. Eagar W.S. Ricci 1982. A Parametric Study of the Electrosag Welding Process, p.397 Welding journal.
- [6]. B. E. Paton, Electrosag Welding, 2nd Edition
- [7]. F. Eichhorn J. Remmel B. Wubbels 1984. High Speed Electrosag Welding,p.37
- [8]. Y. M. Kuskov 2003. Welding, A New Approach to Electrosag-Welding journal.
- [9]. B. E. Paton 1997. Electrosag Welding: A Status Report -International journal.
- [10]. http://www.soudokay.com/english/646_ENG_HTML.htm
- [11]. http://www.soudokay.com/english/57_ENG_HTML.htm
- [12]. <http://www.freepatentsonline.com/3926788.html>
- [13]. <http://www.welding-advisers.com/Welding-defects.html>
- [14]. <http://www.tech.plym.ac.uk/sme/strc201/wdefects.htm>
- [15]. <http://www.ndt-ed.org/EducationResources/CommunityCollege/MagParticle/Physics/CircularFields.htm>
- [16]. <http://www.ndt-ed.org/GeneralResources/MethodSummary/MethodSummary.htm>
- [17]. <http://www.ndt-ed.org/EducationResources/CommunityCollege/MagParticle/Physics/LongFields.htm>
- [18]. <http://www.ndt-ed.org/EducationResources/CommunityCollege/MagParticle/Physics/Magnetization.htm>



International Journal of Modern Engineering Research (IJMER)

Volume : 4 Issue : 7 (Version-5)

ISSN : 2249-6645

July - 2014

Contents :

Application of Neural Network for Cell Formation in Group Technology <i>Prabhat Kumar Giri , Dr. S. K. Moulick</i>	01-05
Automatic Segmentation of scaling in 2-D psoriasis skin images using a semi supervised algorithm <i>Puneeth G J, Girisha H</i>	06-10
A Comparative Study on Privacy Preserving Datamining Techniques <i>M. Nithya, Dr. T. Sheela</i>	11-14
Review and Comparisons between Multiple Ant Based Routing Algorithms in Mobile Ad Hoc Networks (MANET) <i>Gholamhasan Sajedy-Abkenar, Amirhossein Jozdani, Sahar Aslanzadeh</i>	15-20
A Novel High Performance H-Bridge Converter Topology for 8/6 pole SRM Drive <i>V. V. N. Murthy, S. S. Tulasi Ram, J. Amarnath</i>	21-32
Analysis of Human Behavior Based On Centroid and Treading Track <i>Ms. K. V. Patil, Prof. D. D. Dighe</i>	33-37
To Study the mechanical properties of coconut coir fiber reinforced with epoxy resin AW 106 & HV 953 IN <i>Abdul Nazeer</i>	38-47
Damage Tolerance Evaluation for Wing Structure with Large Cutout <i>Sukeerth D A, Thammaiah Gowda</i>	48-57
Seismic Assessment of Existing Bridge Using OPENSEES <i>Jadhav S. S., Pawar P. M., Kadam Gauri</i>	58-62
Regeneration of Liquid Desiccant in Solar Passive Regenerator with Enhanced Performance <i>J. R. Mehta</i>	63-65

Application of Neural Network for Cell Formation in Group Technology

Prabhat Kumar Giri¹, Dr. S. K. Moulick²

¹Department of Mechanical Engineering, Dr. C.V. Raman University, Bilaspur(Chhattisgarh), India

²Department of Mechanical Engineering, Bhilai Institute of Technology Durg(Chhattisgarh), India

Abstract: Group Technology is a method for increasing productivity of manufacturing quality products. For improving the flexibility in manufacturing systems, cell formation is the main step in group technology. Every manufacturing industry faces problem of productivity and their priority is to deliver product to valuable customer in time. For fulfilling this purpose a proper engineering analysis is needed which can reduce material handling and wait time. This can be done by cell formation. There are various techniques which are available for cell formation and discussed by different researchers but neural network is found the best among them due to its better and fast computation results. Here in this paper Adaptive Resonance Theory ART1 is analyzed and proven a better way to cope up with the manufacturing problems.

Keywords: Cell formation, Adaptive Resonance Theory, Neural network, Group technology

I. INTRODUCTION

Application of Group Technology provides reduction in material handling cost, set-up time, work in progress and many others. The production process requires a variety of machines and often some complex procedures. Frequently, parts have to be moved from one place to another. Due to which not only in machine idle time increases but also wastes the manpower required for the physical movement of the parts. An increasing number of companies are taking small to medium size production orders. With this situation, more setup changes and frequent part or machine movements occur. Group technology (GT) has proven to be a useful way of resolving these problems by creating a more flexible manufacturing process. This can be done by manufacturing similar parts at a particular group of machines which is known as cell or par-machine cell. Cell formation (CF) is the main requirement in GT. It is a method for designing cellular manufacturing systems using the similarities between parts and machines to have part families and machine groups. The parts in the same machine group will be machined in similar way which reduces travel and setup time. The benefit of Group technology can be understood by *Fig-1.1* and *Fig -1.2*.

The products which are having similar design or process may be grouped in to part families' and machines can be grouped as cells. Group technology has been successful due to its positive results in batch type production. Main difficulty in batch manufacturing is more product variety and small manufacturing lot sizes. In cell formation a binary machine/part matrix $m \times p$ is formed where 'm' rows indicate machines and 'p' columns indicate parts. In the binary matrix '1' indicate that pth part is to be machined on mth machine and '0' indicate otherwise. Our aim is to group the similar parts with machine groups on which operations are to be performed.

II. LITERATURE REVIEW

Study of literature has been carried out to identify the findings and directions given by researchers. The contribution and directions of selected research work reported in the literature have been presented below:

The problem was originally identified by Murthy and Srinivasan [1]. They used simulated annealing (SA) and heuristics algorithms (HA) for fractional cell formation. In other research, Srinivasan and Zimmers [2] used a neighborhood search algorithm for fractional cell formation. The architecture of the ART1 is based on the idea of adaptive resonant feedback between two layers of nodes, as developed by Grossberg [3]. The ART1 Model described in Carpenter and Grossberg [4] was designed to cluster binary input patterns. Dagli and Huggahalli [3] and Chen and Park [1] also modified the ART1 in their works to improve its performance in GT cell formation. But their modifications are not suitable for fractional cell formation. Miin-Shen Yang and Jenn-Hwai Yang [4] proposed a modified ART1 neural learning algorithm. In modified ART1, the vigilance parameter can be simply estimated by the data so that it is more efficient and reliable than Dagli and Huggahalli's method for selecting a vigilance value. M. Murugan and Selladurai[5] proposed an Art Modified Single Linkage Clustering approach (ART-MOD-SLC) to solve cell formation problems in Cellular

Manufacturing. In this study, an ART1 network is integrated with Modified Single Linkage Clustering (MOD-SLC) to solve cell formation problems. The Percentage of Exceptional Elements (PE), Machine Utilization (MU), Grouping Efficiency (GE) and Grouping Efficacy (GC) are considered as performance measures. This proposed heuristic ART1 Modified Single Linkage Clustering (ART-MOD-SLC) first constructs a cell formation using an ART1 and then refines the solution using Modified Single Linkage Clustering (MOD-SLC) heuristic. ART1 Modified Single Linkage Clustering has been applied to most popular examples in the literature including a real time manufacturing data. According to P. Venkumar and A. Noorul Haq [6] the GT cell formation by any known algorithm/heuristics results in much intercell movement known as exceptional elements. In such cases, fractional cell formation using reminder cells can be adopted successfully to minimize the number of exceptional elements. The fractional cell formation problem is solved using modified adaptive resonance theory1 network (ART1). The input to the modified ART1 is machine-part incidence matrix comprising of the binary digits 0 and 1. This method is applied to the known benchmarked problems found in the literature and it is found to be equal or superior to other algorithms in terms of minimizing the number of the exceptional elements. The relative merits of using this method with respect to other known algorithms/heuristics in terms of computational speed and consistency are presented. Yong Yina and Kazuhiko Yasudab[7] gave a comprehensive overview and discussion for similarity coefficients developed to date for use in solving the cell formation (CF) problem. Despite previous studies indicated that similarity coefficients based method (SCM) is more flexible than other CF methods, none of the studies has explained the reason why SCM is more flexible. They tried to explain the reason explicitly. They also developed a taxonomy to clarify the definition and usage of various similarity coefficients in designing CM systems. Existing similarity (dissimilarity) coefficients developed so far are mapped onto the taxonomy.

III. GT IMPLEMENTATION WITH NEURAL NETWORK APPROACH

In recent years neural networks is widely used for solving large sized GT problems because of its computational efficiency and consistency. The distinct advantage of using neural network in solving GT problem as compared to other methods is as follows

1. Neural networks can handle large size problem due to greater computational efficiency
2. Neural networks can be designed to solve bottleneck machine problem effectively.
3. Neural networks can be used to solve a wide variety of problems

There are various methods developed to identify part family and their associated machine cells. Generally these methods can be classified as classification and coding procedures or direct analysis of process information. In this paper we are concerned with the 'process information approach'. The machine cells formation problem based on process information is often modeled by a binary machine –part incidence matrix $\{a_{ij}\}$ derived from route card data. This approach is referred to as the matrix formulation of the GT problem. Columns and rows of an incidence matrix represent parts and machines respectively. A matrix element a_{ij} is '1' if machine 'i' is used to process part 'j' and "0" otherwise.

Once the machine and part incidence matrix is constructed from route card data, clustering algorithm is often required to transform the initial matrix into solution matrix to help identify clusters. Numerous algorithms for the construction of machine cells and part families have been developed using a machine part incidence matrix. The grouping of parts and machines can be done simultaneously. There are various methods of cell formation like Rank Order Clustering, Single Linkage Clustering, Direct Clustering Analysis etc. but ART is found best suited for complex problems. ART network is based on unsupervised learning that accepts input vectors and subsequently classifies them according to the stored pattern they most resemble. In an unsupervised learning the network has no knowledge about what the desired or correct output should be. The system learns on its own without external guidance. In cell formation problem, unsupervised learning is more appropriate. This is due to the fact that in practice, no information about the correct group formation is known a priori.

A neural network is a computing system consisting of a large number of simple, highly interconnected processing elements called neurons (nodes), which process information by their dynamic response to external inputs. *Fig. 2.1* shows typical neurons with a number of input and output signals. The topology of a neural network refers to how its nodes are interconnected. *Fig. 2.1* shows a commonly used topology. We form there topologies or architectures, by organizing the nodes into layer connecting them and weighing the interconnections. The network has three layers, one hidden, one input layer and one output layer. Output from each node is fed to all nodes in subsequent layer.

ART1 ALGORITHM

Step 1

Define number of neurons in the input layer . Start top down and bottom up connection weights

Top down connection weights : $t_{ij}(0) = 1$

Bottom up connection weights : $B_{ij} = 1/(1+N)$

For all input nodes $i = 0, 1, 2, \dots, (N-1)$

and output nodes $j = 0, 1, 2, 3, \dots, (M-1)$

Select a value for vigilance threshold between Zero and One

$$0 \leq \rho \leq 1$$

Step 2

Apply new input vector X consisting of zero/one elements x_i then it is treated as the member of the first group.

Step 3

Compute matching scores

The output μ_j of every output node j equals

$$\mu_j = \sum_i b_{ij}(t) x_i$$

Step4

Select best matching exemplar i.e node with maximum output

$$\mu_\theta = \max_j \{ \mu_j \}$$

Output of other neurons are suppressed (lateral inhibition)

In case of tie choose neurons with lower j

Step5

Vigilance test (i.e test for similarity with best matching exemplar)

$$\|T, X\| = \sum_i t_{i\theta} x_i$$

Number of perfectly matching '1's between input vector and best matching exemplar

$$\|X\| = \sum_i x_i$$

Number of '1's in input vector represents the new class

If similarity $\frac{\|T, X\|}{\|X\|} > \rho$ go to step 7, else go to step 6

Step 6

Disable best matching exemplar temporarily.

Output of the best matching node selected in step 4 is temporarily set to zero

Other output has a inhibition

Then go to step3

In step3, a new neuron in the output layer gets selected to represent the new class.

Step7

Update best matching exemplar temporarily

$$b_{i\theta}(t+1) = \frac{t_{i\theta}(t)x_i}{0.5 + \sum_i t_{i\theta}(t)x_i}$$

Step8

Repeat ,Go to step 2 , after enabling any nodes disabled in step6

IV. ADVANTAGES OF GT

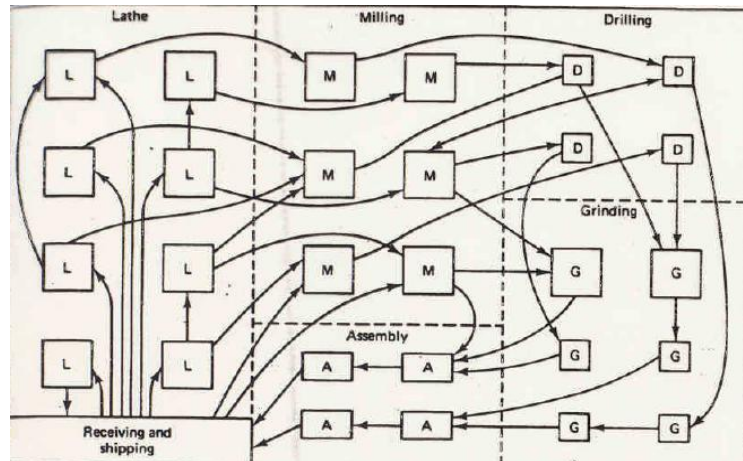


Fig -1.1 FUNCTIONAL (PROCESS) TYPE LAYOUT

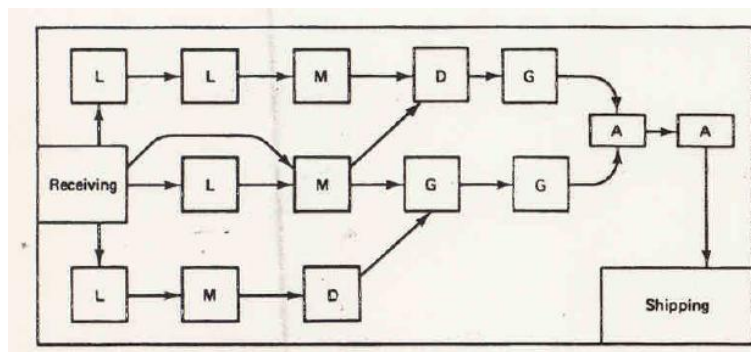
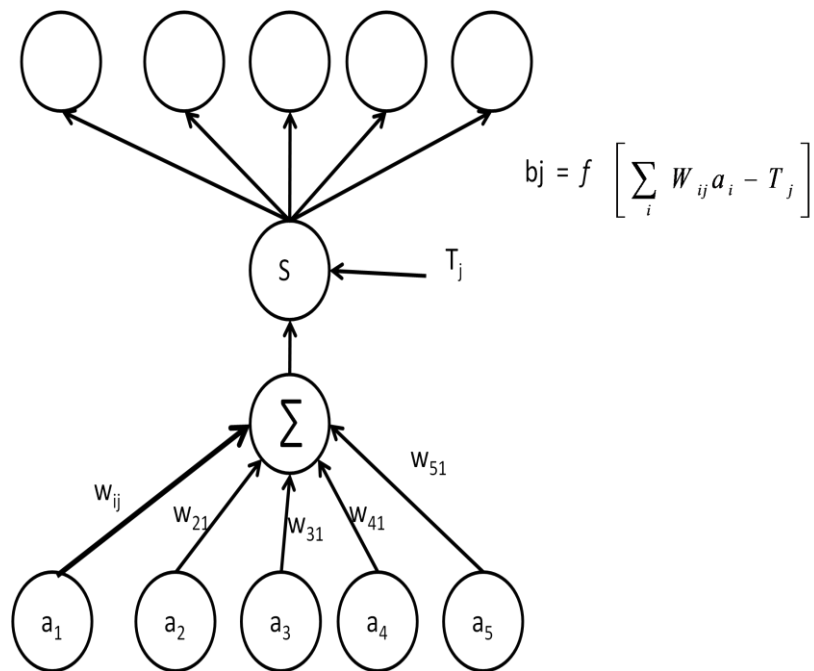


Fig-1.2 CELLULAR MANUFACTURING (GROUP TECHNOLOGY) LAYOUT



NODE ANATOMY

Fig- 2.1

V. CASE STUDY

A case study has been carried out in a manufacturing company, producing varieties of components. The submersible pump under consideration has two main sub-assemblies, namely motor and pump. The pump has 30 parts and the motor has 32 parts. Out of 62 parts, only 14 parts are manufactured in house, and others are purchased from other suppliers. The methodology was applied to the submersible pump-manufacturing factory that uses job shop layout, consisting of 15 different machine types. Out of the 62 parts, the same machines manufacture only 14 parts, and a part is processed through 5–10 steps before it is finished.

VI. CONCLUSION

The neural network based on the adaptive resonance theory (ART1) can be efficiently used for machine- component group formatting contained on the route sheet of the components. Hereby it is found that material handling and cost of manufacturing reduces considerably if the cluster formation is being carried out with the help of neural network model for solution. Grouping efficiency will increase and percentage of exceptional elements will reduce

REFERENCES

Journal Papers:

- [1] Murthy CVR, Srinivasan G (1995) Fractional Cell formation in group technology. *International Journal of Production Research* 33(5):1323–1337.
- [2] Srinivasan G, Zimmers EW Jr (1998) Fractional cell formation – issues and approaches. *International Journal of Industrial Engineering –Theory and Application Practice* 5:257–264.
- [3] Grossberg S (1976) Adaptive pattern classification an universal recording: parallel development and coding of neural feature detectors. *Biol Cybern* 23:187–202.
- [4] Miin-Shen Yang and Jenn- Hwai Yang Machine-part cell formation in group technology using a modified ART1 method *European Journal of Operational Research* 188 (2008) 140–152.
- [5] M. Murugan and Selladurai(2011)vol. 5,3: 199-212 *Jordon Journal of Mechanical and Industrial Engineering*.
- [6] P. Venkumar and A. Noorul Haq Fractional cell formation in group technology using modified ART1 neural networks , *International Journal of Advanced Manufacturing Technology* (2006) 28: 761–765.
- [7] Yong Yina and Kazuhiko Yasudab Similarity coefficient methods applied to the cell formation problem: A taxonomy and review *Int. J. Production Economics* 101 (2006) 329–352.

Books:

- 1. Introduction to Artificial Neural System - Jacek M. Zurada, 2006, Jaico Publishing House.
- 2. Neural Network and Fuzzy System – Bart Kosko, 2008, Printice Hall India Pvt. Ltd. New Delhi.

Automatic Segmentation of scaling in 2-D psoriasis skin images using a semi supervised algorithm

Puneeth G J¹, Girisha H²

¹Computer Science and Engineering, Rao Bahadur Y. Mahabaleswarappa college of engg, India)

²Computer science and engineering, vesvisvarya Technological University, India

Abstract: Psoriasis is a chronic inflammatory skin disease that affects over 3% of the population. Various methods are currently used to evaluate psoriasis severity and to monitor therapeutic response. The PASI system of scoring is widely used for evaluating psoriasis severity. It employs a visual analogue scale to score the thickness, redness (erythema), and scaling of psoriasis lesions. However, PASI scores are subjective and suffer from poor inter- and intra-observer concordance. As an integral part of developing a reliable evaluation method for psoriasis, an algorithm is presented for segmenting scaling in 2-D digital images. The algorithm is believed to be the first to localize scaling directly in 2-D digital images. The scaling segmentation problem is treated as a classification and parameter estimation problem. A Markov random field (MRF) is used to smooth a pixel-wise classification from a support vector machine (SVM) that utilizes a features pace derived from image color and scaling texture. The training sets for the SVM are collected directly from the image being analyzed giving the algorithm more resilience to variations in lighting and skin type. The algorithm is shown to give reliable segmentation results when evaluated with images with different lighting conditions, skin types, and psoriasis types.

Index Terms— Feature extraction, Image segmentation, Markov random field(MRF), Support vector machine(SVM) , Psoriasis.

I. Introduction

PSORIASIS is a chronic skin disease that affects an estimated 125 million people worldwide[1], which manifests as red and scaly patches of itchy skin. The scaling results from an enhanced rate of epidermal cell production manifesting anywhere from a few spots to a large area of plaque, typically found on erythema, or red inflamed skin [2].

At present there is no known cure for psoriasis and, as a consequence, much effort has been expended on treatments to control the symptoms of psoriasis. However, there is no accepted treatment for psoriasis symptoms and different physicians will treat the same symptoms differently[3]. A key factor in the improvement of psoriasis treatment is the ability to compare the efficacy of treatments across a broad range of conditions[4]. To be meaningful, such comparisons must be reliable requiring that the assessment of psoriasis severity is also reliable. Reliable tests are important to dermatologists for assessing treatments and to companies who want to improve their treatment.

Reliable and reproducible severity scores are essential for comparing psoriasis treatments and furthering psoriasis treatment research. Most, if not all [4]–[7], psoriasis assessment methods rely on a visual estimation of the area and severity of the main psoriatic symptoms of erythema and scaling. Consequently, any computer based analysis method for assessing psoriasis severity using 2D digital images must identify erythema and scaling as a precursor to further analysis.

The paper presents what I believe to be the first algorithm to automatically segment scaling directly from skin and erythema in 2-D digital images. The approach is to reduce the problem of segmenting scaling to a binary classification problem by removing erythema from consideration and then classifying the remaining pixels as either skin pixels or scaling pixels. The feature space used in the classification is derived from the color contrast between scaling and erythema, and the image texture describing the roughness of scaling which is determined by the aggregated result from a bank of Gabor filters. Our evaluation indicates that our combination of Markov random fields(MRFs) with support vector machines using an appropriate feature space can solve a wide range of scaling segmentation problems that include variations in lighting conditions, variations in skin type and variations in the types of psoriatic lesions.

II. Feature Space For Detecting Scaling In 2-D Digital Psoriasis Images

2.1 A Scaling Contrast Map

A scaling contrast map is developed to enhance the contrast of scaling from erythema. The map aims to enhance the contrast of scaling especially in situations where scaling is scattered in erythema and is hard to discern visually. $L^*a^*b^*$ Color space is used to develop a pair of multiscale center-surround filters that increase the contrast between scaling and erythema.

The L^* dimension specifies lightness where an L^* value of 0 is black and an L^* value of 100 is a diffuse white. The a^* dimension is the red–green dimension, where a positive value of a^* is red and a negative value green, and the b^* dimension is the blue–yellow dimension, where a positive value of b^* is blue and a negative value is yellow.

A scaling contrast map can be defined as follows:

$$S_{x,y} = J(L^*_{x,y}) + J(inv(a^*_{x,y}))$$

2.2 Texture Analysis with Gabor Filters

Gabor filters have long been used in the analysis of texture in images. Briefly, given a Gaussian distribution function $\exp(-\frac{x'^2 + \gamma^2 y'^2}{2\sigma^2})$ called the envelope, with standard deviation and spatial aspect ratio, and a complex sinusoidal $\exp(i(\frac{2\pi x'}{\lambda} + \phi))$ called the carrier, with spatial frequency $1/\lambda$ and phase shift ϕ the Gabor filter is defined by

$$g(x, y; \gamma', \sigma, \lambda, \phi) = \exp(-x'^2 + \gamma^2 y'^2 / 2\sigma^2) \exp(iy(\frac{2\pi x'}{\lambda} + \phi))$$

The response is highest when the image intensity frequency is close to the Gabor filter. For smooth normal skin the image intensity is relatively homogeneous and is not sensitive to Gabor filters. For rougher scaly skin, the change of intensity is relatively high. Further, the choice of the standard deviation σ of the Gaussian envelope depends on the spatial frequency $1/\lambda$, $\sigma = 0.56\lambda$.

2.3 Semi-Supervised Scaling Segmentation Algorithm

The second stage of the algorithm segments scaling from 2-D skin images through a semi-supervised algorithm to ensure the invariance of segmentation to scaling and skin changes from different patients. This part of the algorithm implements a tri- step process.

- **First:** The scaling contrast map is applied to the image and the resulting image is processed to threshold out all dark pixels representing darker pigments in the skin and including erythema, hair, moles, and other blemishes.
- **Second:** A training set for the scaling classifier is extracted from the image where the training set is composed of pixels that are highly likely to be scaling and pixels that are highly likely to be normal skin.
- **Third:** The pixels are classified using a SVM defined by the training set and the resulting image smoothed using a MRF.

2.4 Removing Erythema and Other Dark Pixels

The first step is to threshold out the dark pixels representing erythema, hair, moles and other blemishes using the scaling contrast map S . Scaling and normal skin pixels remain in consideration after the application of the contrast map because they result in a significantly high value of S . We define a binary image M by

$$M_{x,y} = \begin{cases} 1, & \text{if } S_{x,y} \geq t_s \\ 0, & \text{otherwise} \end{cases}$$

Where t_s is the threshold for dark pixels. Pixels labeled with 1 are retained for further analysis while pixels labeled with 0 denote darker pigments and are removed from further consideration.

2.5 Collecting Training Data for the Scaling Segmentation

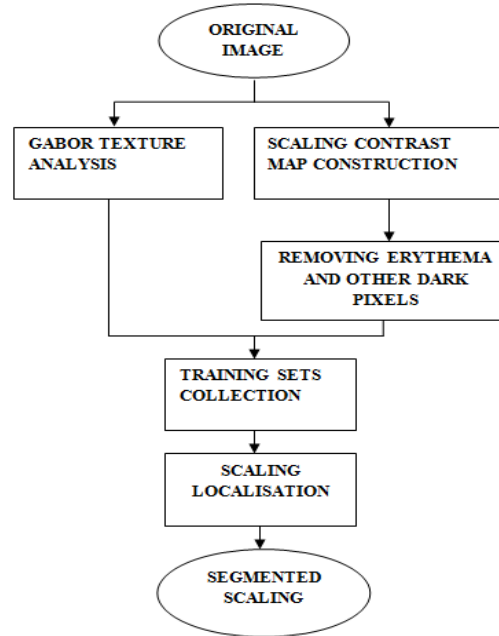
The removal of erythema and darker pixels using simplifies the problem of detecting scaling to a binary classification problem that of distinguishing scaling from normal skin. The classifier used is defined as a MRF in which the likelihood function is derived from the distance of a pixel to the hyperplane of a SVM. The parameters defining the placement of the hyperplane in feature space need to be derived using carefully chosen training data. There is a great deal of variation in skin colors and psoriasis lesions. A hyperplane using parameters derived from a generic set of training data gathered over a wide range of images is unlikely to yield good classification results. Our algorithm gathers the training data needed to place the SVM hyperplane directly from the image being analyzed. Training data is collected by identifying regions of scaling and normal skin using the position of the previously located erythema, which is often found between scaling and normal skin.

Collecting training data proceeds by first locating erythema and then using a soft-constrained -means clustering to identify candidate regions of scaling and normal skin.

III. Proposed Algorithm

The proposed algorithm uses a bank of 24 Gabor filters designed to respond well in a variety of skin and scaling texture conditions.

3.1 Proposed System Block Diagram



3.2 Algorithm: An algorithm to extract a sample of scaling pixels and a sample of normal skin pixels from an image.

Input: The initial location of the erythema and image.

Output: Regions of candidate scaling pixels $L_{scaling}$ and regions of candidate skin L_{skin} pixels.

```

1:  $n \leftarrow 0$ 
2: repeat
3:  $X \leftarrow X \oplus U$ 
4:  $n \leftarrow n + 1$ 
5: if an enclosed region is formed in X then
6:  $X \leftarrow FloodFill(X)$ 
7: end if
8: until no more enclosed region is formed
9:  $L_{scaling} \leftarrow M_{x,y} \cap X_{x,y} \ominus nU$ 
10:  $L_{skin} \leftarrow M_{x,y} \cap X_{x,y}^c$ 
11: return  $L_{scaling}, L_{skin}$ 
    
```

IV. Experiments And Results

Figure 1:

Scaling contrast map construction.(a) Original image. (b) Contrast map derived from L^* (c) Contrast map derived from a^* (d) Scaling contrast map.

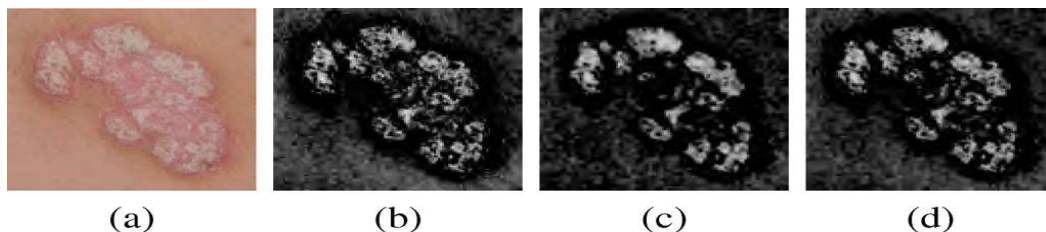
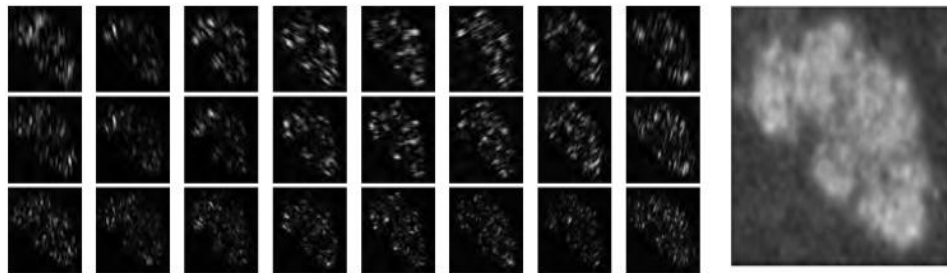


Figure 2:

Texture examination corresponding to the original image in Fig .Gabor filtering responses from a bank of Gabor filters(the spatial frequency changes along the row and the rotation angle changes along the column).
(b) The final Gabor feature image.



V. Conclusion

The result indicates that this algorithm makes progress towards the aim of automatic scaling segmentation. Scaling localization is implemented by a semi-supervised classification in this study. Two features are used: one is the scaling contrast map, which enhances the conspicuousness of scaling against erythema, and the other is a Gabor feature, which differentiates between scaling and normal skin based on image texture. Training sets for the classification are collected by a soft constrained K-means to avoid the human interference. The proposed algorithm shows good performance as is presented in the specificity and dice evaluation. Even though the sensitivity analysis is weaker, the total accuracy from the dice evaluation is always stronger. Moreover, when we compare the algorithm to manually collected training sets, the proposed method presents a slightly weaker sensitivity to the SVM and the MRF. However, better specificity and dice evaluation are achieved when compared to the SVM and the MRF. Notice that the specificity and dice measurements of our method are very close to the case for training sets that are manually selected. This result validates the performance of the soft-constrained k-means, through which the training sets, are automatically collected.

Acknowledgement

I Puneeth GJ would like to thank my guide Mr.Girisha.H,(HOD) who supported me in making this paper.

REFERENCES

- [1]. K. Busse and M. John Koo, "Residents' reports: Goeckerman combination therapy with low dose acitretin for HCV-associated psoriasis," *Practical Dermatol.*, pp. 25–26, Apr. 2010.
- [2]. M.Meier and P.B. Sheth, "Clinical spectrum and severity of psoriasis," *Curr. Probl. Dermatol.*, vol. 38, pp. 1–20, 2009.
- [3]. P. V. de Kerkhof and K. Kragballe, "Psoriasis: Severity assessment in clinical practice. Conclusions from workshop discussions and a prospective multicentre survey of psoriasis severity," *Eur. J. Dermatol.*, vol. 16, no. 2, pp. 167–171, Mar. 2006.
- [4]. 4.C. Paul, P.-A. Gourraud, V. Bronsard, S. Prey, E. Puzenat, S. Aractingi, F. Aubin, M. Bagot, B. Cribier, P. Joly, D. Jullien, M. Le Maitre, M.-A. Richard-Lallemand, and J.-P. Ortonne, "Evidence-based recommendations to assess psoriasis severity: Systematic literature review and expert opinion of a panel of dermatologists," *J. Eur. Acad. Dermatol. Venereol.*, vol. 24, pp. 2–9, 2010.
- [5]. E. Puzenat, V. Bronsard, S. Prey, P. Gourraud, S. Aractingi, M. Bagot, B. Cribier, P. Joly, D. Jullien, M. Le Maitre, C. Paul, M. Richard-Lallemand, J. Ortonne, and F. Aubin, "What are the best outcome measures for assessing plaque psoriasis severity? A systematic review of the literature," *J. Eur. Acad. Dermatol. Venereol.*, vol. 2, pp. 10–16, Apr. 2010.
- [6]. L. Naldi and D. Gambini, "The clinical spectrum of psoriasis," *Clin. Dermatol.*, vol. 25, no. 6, pp. 510–518, 2007.
- [7]. J. Röing, R. Jacques, and J. Kontinen, "Area assessment of psoriatic lesions based on variable thresholding and subimage classification," in *Vis. Interface '99*, May 1999, pp. 303–311.
- [8]. D. D.Gómez, B. K. Ersbøll, and J.M.Carstensen, "S.H.A.R.P: A smart hierarchical algorithm to register psoriasis," in *Int.Wkshp Syst., Signals Image Process.*, Sep. 2004, pp. 43–46.
- [9]. J. Taur, G. Lee, C. Tao, C. Chen, and C. Yang, "Segmentation of psoriasis vulgaris images using multiresolution-based orthogonal subspace techniques," *IEEE Trans. Syst., Man, Cybernet., Part B: Cybernet.*, vol. 36, no. 2, pp. 390–402, Apr. 2006.
- [10]. D. Delgado, B. Ersboll, and J.M. Carstensen, "An image based system to automatically and objectively score the degree of redness and scaling in psoriasis lesions," in *Proc. 13th Danish Conf. Image Anal. Pattern Recognit.*, 2004, pp. 130–137.
- [11]. R. Achanta, F. J. Estrada, P. Wils, and S. Süsstrunk, "Salient region detection and segmentation," in *Proc. Int. Conf. Comput. Vis. Syst.*, 2008, pp. 66–75.

- [12]. S. E. Grigorescu, N. Petkov, and P. Kruizinga, "Comparison of texture features based on Gabor filters," IEEE Trans. Image Process., vol. 11, no. 10, pp. 1160–1167, Oct. 2002.
- [13]. L. Ma and R. C. Staunton, "Optimum Gabor filter design and local binary patterns for texture segmentation," Pattern Recognit. Lett., vol. 29, pp. 664–672, 2008.
- [14]. Z. Kato and T. chuen Pong, "A Markov random field image segmentation model for color textured images," Image Vis. Comput., vol. 24, pp. 1103–1114, 2006.
- [15]. M.-C. Su and C.-H. Chou, "A modified version of the k-means algorithm with a distance based on cluster symmetry," IEEE Trans. Pattern Anal. Mach. Intell., vol. 23, no. 6, pp. 674–680, Jun. 2001.

A Comparative Study on Privacy Preserving Datamining Techniques

M. Nithya¹, Dr. T. Sheela²,

¹ Research scholar, Sathyabama University, Chennai & Assistant professor-II,
Sri sairam engineering college, chennai

² Professor, SriSairam engineering college, Chennai

Abstract: Privacy protection is very important in the recent years for the reason of increasing in the ability to store data. In particular, recent advances in the data mining field have lead to increased concerns about privacy. Data in its original form, however, typically contains sensitive information about individuals, and publishing such data will violate individual privacy. The current practice in data publishing based on that what type of data can be released and use of that data. Recently, PPDM has received immersed attention in research communities, and many approaches have been proposed for different data publishing scenarios. In this comparative study we will systematically summarize and evaluate different approaches for PPDM, study the challenges ,differences and requirements that distinguish PPDM from other related problems, and propose future research directions.

Keywords: PPDM, Privacy-preserving; randomization; k-anonymity;

I. INTRODUCTION

Data mining successfully extracts knowledge to support a variety of domains —marketing, weather forecasting, medical diagnosis, and national security —but it is still a challenge to mine certain kinds of data without violating the data owners' privacy.¹ For example, how to mine patients' private data is an ongoing problem in health care applications. As data mining becomes more pervasive, such concerns are increasing. Online data collection systems are an example of new applications that threaten individual privacy. Already companies are sharing data mining models to obtain a richer set of data about mutual customers and their buying habits. A number of techniques such as classification, k-anonymity, association rule mining, clustering have been suggested in recent years in order to perform privacy preserving data mining. Furthermore, the problem has been discussed in multiple communities such as the database community, the statistical disclosure control community and the cryptography community. We analysis recent work on these topics, presenting general frameworks that we use to compare and contrast different approaches. We begin with the problem of focusing on different techniques of privacy preserving in section II,. In section III, we put rept attention to compare those methods and contrasted and finally we end up with conclusion and future work in subsequent sections.

II. PRIVACY PRESERVING TECHNIQUES

2.1 Anonymization Technique

When releasing micro data for research purpose, one needs to limit disclosure risks to an acceptable level while maximizing data utility. To limit disclosure risk, Samarati et al. [1]; Sweeney [2] introduced the k -anonymity privacy requirement, which requires each record in an anonymized table to be indistinguishable with at least k -other records within the dataset, with respect to a set of quasi-identifier attributes. To achieve the k -anonymity requirement, they used both generalization and suppression for data anonymization. Unlike traditional privacy protection techniques such as data swapping and adding noise, information in a k -anonymous table through generalization and suppression remains truthful. In particular, a table is k -anonymous if the QI values of each tuple are identical, to those of at least k other tuples. Table 3 shows an example of 2-anonymous generalization for Table. With the help of table 1 and table 2 adversary can find the persons and their salary. In this case if we go for annonymization technique its somewhat difficult. If the adversary know the age and zipcode then easily he can find the salary of Alice and Carl with the help of tuple 1 and 3 in table 3.

In general, k anonymity guarantees that an individual can be associated with his real tuple with a probability at most $1/k$.

TABLE 1 MICRODATA

Sex	Zip Code	Age	Salary
F	40178	26	8000
F	40277	30	12000
M	40176	32	8000
F	40175	51	9000
F	40385	28	20000
M	40485	43	23000
M	40286	50	8000

TABLE2 POPULATION CENSUS

Name	Sex	ZipCode	Age
Alice	F	40178	26
Betty	F	40277	30
Carl	M	40276	32
Diana	F	40175	51
Ella	F	40385	28
Finch	M	40485	43
Gavin	M	40286	50

TABLE 3 A 2-ANONYMOUS TABLE

Sex	ZipCode	Age	Salary
*	4017-	26-32	8000
*	4027-	26-32	12000
*	4017-	26-32	8000
*	4017-	35-55	9000
*	4038-	26-32	20000
*	4048-	35-53	23000
*	4028-	35-53	8000

Even k-anonymity protects against identity disclosure, it does not provide sufficient protection against attribute disclosure. There are two attacks: the homogeneity attack and the background knowledge attack.

2.2. Data perturbation approach

In this approach data will be modified so that it no longer represents the real world. Randomization and data swapping methods are two techniques which comes under this approach. Since this method does not reconstruct the original data values but only distributions, new algorithms need to be developed which use these reconstructed distribution in order to perform mining of the underlying data. This means that for each individual data problem such as classification, clustering, or association rule mining, a new distribution based data mining algorithm needs to be developed. For example, Agrawal [3] develops a new distribution-based data mining algorithm for the classification problem, whereas the techniques in Vaidya and Clifton and Rizvi and Haritsa[4] develop methods for privacy-preserving association rule mining. While some clever approaches have been developed for distribution-based mining of data for particular problems such as association rules and classification, it is clear that using distributions instead of original records restricts the range of algorithmic techniques that can be used on the data [5].

In randomisation technique the noise will be added to the original data in randomly so that original record values cannot be guessed from the distorted data. Disadvantage in this method, it treats all records equally irrespective of their local density. Therefore, outlier records are more susceptible to adversarial attacks as compared to records in more dense regions in the data. For an example using this method, randomly adding 50 with age attributes (instead of 26, 26+50=72, 80, 82, etc), easily the adversary know that some of the noise added in that particular attribute. Second method in data perturbation method is data swapping, in this method data values between attributes are randomly swapped. Using this method adversary can easily get the original records.

2.3 Cryptographic technique

Cryptographic technique is also used to provide privacy preserving data mining. This method became hugely popular [6] for two main reasons: Firstly, cryptography is a well-defined model for providing privacy, which includes methodologies for confirming and enumerating it. Secondly, there exists a vast toolset of cryptographic algorithms and constructs to implement privacy-preserving data mining algorithms. However, recent work [7] has pointed that cryptography does not protect the output of a computation. Instead, it prevents privacy leaks in the process of computation. So this method is not useful for provide the complete security for sensitive data in data mining.

2.4 Secure Multiparty Computation

This method reveals nothing except the results between two parties who does not want to reveal their data sources using this we can prevent our sensitive attribute. Anyhow this approach contains miniature drawbacks such as Trusted Third Party Model, Semi-honest Model. In Third party model data will be shared through the third party, so the third party comes to know the data sources. In Semi-honest Model, Consider a secure sum functionality which simply outputs the sum of the local input of the participants. With two parties, the output reveals the input of the other party.

III. Several challenges with PPDM

Iyengar [8] demonstrated that data can be transformed in such a way as to protect individual identity. He suggests that random data can replace any individually identifiable information. The author's argument is that there is a tradeoff between privacy and information loss with this method. Thuraisingham [9] first suggested that privacy issues occur in data mining and that this is a generalization of the inference problem. The inference problem refers to an issue when a user can infer new knowledge by executing successive queries against a database. He also noted that this may cause ethical issues based on how the information is going to be used. Du and Zhan [10] proposed a randomized response technique to perturb data so that users cannot tell whether the data contains truthful information or false information. They used a decision-tree classifier along with randomization methods to perturb the data so that aggregate results still show some degree of accuracy, while at the same time maintain individual privacy. One drawback with this approach is that it only focused on Boolean data types to test their technique. Du and Zhan also neglected to define exactly what tolerances are acceptable during data mining with privacy preservation. Narayanan and Shmatikov [11] demonstrated that data can be encrypted in such a way that users can still use the information contained within it. Their study used provably secure techniques while permitting certain types of queries to be generated. A limitation to their study was that they only examined its use on small databases, not for larger databases. In order for their approach to work, they developed a new query language. Their approach may also be impractical if a user wanted to use widely available databases such as Microsoft SQL Server or Oracle. Generalization for k-anonymity losses considerable amount of information, especially for high-dimensional data due to the curse of dimensionality. In order for generalization to be effective, records in the same bucket must be close to each other so that generalizing the records would not lose too much information. Bucketization does not prevent membership disclosure. Because bucketization publishes the QI values in their original forms, an adversary can find out whether an individual has a record in the published data or not. Also bucketization requires a clear separation between QIs and SAs. However, in many data sets, it is unclear which attributes are QIs and which are SAs. By separating the sensitive attribute from the QI attributes, bucketization breaks the attribute correlations between the QIs and the SAs. To improve the attribute correlation slicing[12] technique has been introduced. Using slicing techniques can improve attribute correlation but it does not achieve 100 percent but it is better than k anonymity and l-diversity approaches.

IV. Merits and Demerits of PPDM techniques

PPDM Techniques	Merits	Demerits
Anonymization technique	This technique is used to protect user identities while releasing information. While <i>k</i> -anonymity protects against identity disclosure, it does not provide sufficient protection against sensitive attribute. 100% accuracy can achieve.	There are two attacks: The homogeneity attack and the background knowledge attack.
Data perturbation approach	Independently the noise can add to the attributes	This method does not reconstruct the original data values ,to reconstruct the original data distribution, new algorithms have been developed . RANDOMIZED RESPONSE : Randomly the noise will be added and swapping technique have been used.

Cryptographic	Cryptography offers a well-defined model for privacy, which includes methodologies for proving and quantifying it. There exists a vast toolset of cryptographic algorithms and constructs to implement privacy preserving data mining algorithms.	This approach is especially difficult to scale when more than a few parties are involved. Also, it does not address the question of whether the disclosure of the final data mining result may breach the privacy of individual records.
Slicing	More efficient and better data utility compare to anonymity and l diversity method	Randomly generate the associations between column values of a Bucket. This may lose data utility. Random data transmission have been used.

V. Conclusion

With the development of data analysis and processing technique, the privacy disclosure problem about individual or company is inevitably exposed when releasing or sharing data to mine useful decision information and knowledge, then give the birth to the research field on privacy preserving data mining. In this paper, we presented different issues and reiterate privacy preserving methods to distribute ones and the methods for handling horizontally and vertically partitioned data. While all the purposed methods are only approximate to our goal of privacy preservation, we need to further perfect those approaches or develop some efficient methods. To address these issues, following problem should be widely studied.

1. In distributed privacy preserving data mining areas, efficiency is an important issue. We should try to develop more efficient algorithms and attain a balance between disclosure cost, computation cost
2. Privacy and accuracy is a pair of contradiction; improving one usually incurs a cost in the other. How to apply various optimizations to achieve a trade-off should be deeply researched.
3. Side-effects are inevitable in data cleansing process. How to reduce their negative impact on privacy preserving needs to be considered carefully. We also need to define some metrics for measuring the side-effects resulted from data processing.

REFERENCES

- [1] J. Han and M. Kamber, Data Mining Concepts and Techniques, Morgan Kaufmann, 2001.
- [2] P. Samarati,(2001). Protecting respondent's privacy in micro data release. In IEEE Transaction on knowledge and Data Engineering,pp.010-027.
- [3] L. Sweeney, (2002)."k-anonymity: a model for protecting privacy ", International Journal on Uncertainty, Fuzziness and Knowledge based Systems, pp. 557-570.
- [4] Evfimievski, A.Srikant, R.Agrawal, and Gehrke J(2002),"Privacy preserving mining of association rules". In Proc.KDD02, pp. 217-228.
- [5] Hong, J.I. and J.A. Landay,(2004).Architecture for Privacy Sensitive Ubiquitous Computing", In Mobisys04, pp. 177- 189.
- [6] Laur, H. Lipmaa, and T. Mieli' ainen,(2006)."Cryptographically private support vector machines". In Twelfth ACM SIGKDD International Conference on Knowledge Discovery and Data Mining, pp. 618-624.
- [7] Ke Wang, Benjamin C. M. Fung1 and Philip S. Yu, (2005) "Template based privacy preservation in classification problems", InICDM, pp. 466-473.
- [8] Iyengar, V. (2002). Transforming data to satisfy privacy constraints. Proceedings of the 8th ACM SIGKDD International Conference on Knowledge Discovery in Data Mining, 279-288.
- [9] Verykios, V., Bertino, E., Fovino, I., Provenza, L., Saygin, Y., & Theodoridis, Y. (2004). State of- the-art in privacy preserving data mining. ACM SIGMOD Record, 33(1), 50-57.
- [10] Du, W., & Zhan, Z. (2003). Using randomized response techniques for privacy-preserving data mining. Proceedings of the 9th ACM SIGKDD International Conference on Knowledge Discovery and Data Mining, 505-510.
- [11] Narayanan, A., & Shmatikov, V. (2005). Obfuscated databases and group privacy. Paper presented at the Proceedings of the 12th ACM Conference on Computer and Communications Security, Alexandria, VA.
- [12] "Slicing: A New Approach for Privacy Preserving Data Publishing" - Tiancheng Li, Ninghui Li, Senior Member, IEEE, Jian Zhang, Member, IEEE, and Ian Molloy IEEE TRANSACTIONS ON KNOWLEDGE AND DATA ENGINEERING, VOL. 24, NO. 3, MARCH 2012

Review and Comparisons between Multiple Ant Based Routing Algorithms in Mobile Ad Hoc Networks (MANET)

Gholamhasan Sajedy-Abkenar¹, Amirhossein Jozdani², Sahar Aslanzadeh³

¹ (Islamic Azad University/ Pardis Branch

^{2,3} (Islamic Azad University, Pardis Branch)

Abstract: Along with an increase in the use and development of various types of mobile ad hoc and wireless sensor networks the necessity for presenting optimum routing in these networks is a topic yet to be discussed and new algorithms are presented. Using ant colony optimization algorithm or ACO as a routing method because of its structural similarities to these networks' model, has had acceptable results regarding different parameters especially quality of service (QoS). Considering the fact that many articles have suggested and presented various models for ant based routing, the need for studying and comparing them can be felt. There are about 17 applied ant based routings, this article studies and compares the most important ant based algorithms so as to indicate the quality and importance of each of them under different conditions.

Keywords: Quality of Service(QoS), Mobile Ad Hoc Network (MANET), Ant-Based Routing.

I. INTRODUCTION

The importance of mobile ad hoc networks (MANET) and wireless sensors is quite obvious under critical conditions due to lack of its infrastructure and its self-organizing feature. Therefore the ever-growing use of it is quite expected. Along with this growth, the related and relevant topics develop and experience innovation as well. One of these topics is routing which in actuality has a decisive role in the quality of the whole network. The effects of various parameters such as traffic, bandwidth, interference, node mobility, energy and a lot of other parameters have made this mode complex.

Numerous topics have been presented so far in order to promote the routing quality of MANETs networks [1] and each one has improved one or more parameters. Ant colony optimization is one of the relatively new optimization algorithms [2] which its use in ad hoc networks has led to different types of ARA (Ant Routing Algorithm) routing [3] through various methods.

In 2010, Vasundhara Uchhula and Brijesh Bhatt [4] compared a number of ant routing algorithms which in addition to being short it did not point out the specific disadvantages and advantages in order to select the algorithm under suitable conditions. This article compares the most common ant-based routing algorithms which have been mentioned so far in ad hoc networks, in addition the problems and advantages of each and the ease of algorithm selection will be studied. Following that in section 2 a general view of different types of routing will be presented. Section 3 states the most important ant-based routing algorithms. Section 4 presents the results of the study and section 5 presents a summary.

II. TYPES OF ROUTING ALGORITHMS

The entire network routings can be divided into three common areas: proactive, reactive or on demand, and hybrid.

2-1. Proactive Protocols

The nodes' tables and networks are constantly updated in these protocols and this is done through sending control packet information, therefore they are called "Table Driven" as well. DSDV [7], GSR [5] and FSR [6] protocols are samples of this group. The problem with this type of routing is that it requires a lot of control packets and it occupies the network bandwidth in the peak of activity.

2-2. Reactive Protocols

Only when routing is demanded the source node starts sending control packets and routing in this model. AODV [7], SSA [7] and ARA [3] protocols are among these protocols. Delay in routing is the problem with this kind of protocol.

2-3. Hybrid Protocols

An interaction between the two mentioned methods leads to the creation of these types of protocols. Depending on topology conditions of the network the network information is updated periodically and also after the request a limited number of control packets are sent. Some instances of it are ZHLS [6] and HOPNET [8] protocols.

III. ANT-BASED ROUTING ALGORITHM

As indicated in figure 1 the natural process of ants routing is based on the spread of a substance named pheromone. Ants which reach the food sooner spatter more pheromone in their path and the following ants select this path due to higher amounts of pheromone. Network routing models the mentioned method in three stages through using forward ants (FANT), backward ants (BANT) and also a target function in selecting the path. In the searching stage, the ants are first sent for routing they find the rout and send the suitable controlling messages. The source begins sending data in the sending stage. In the rout maintenance and investigation in case the connection is interrupted between the two nodes, the information and if necessary routing will be updated.

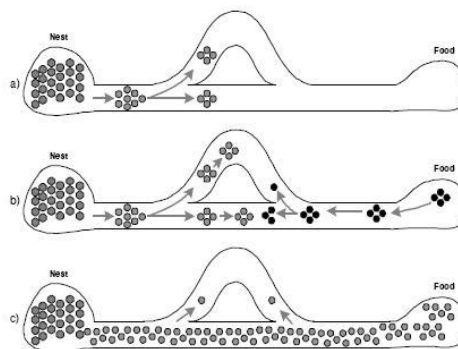


Figure1: Ants Routing Method

3-1. Ant-Based Routing in MANETs (first version)

Mesut Gunes and his colleagues [9] presented one of the first versions of ant-based routing in 2002. Based on their algorithm which was an “on demand” type or reactive, a G graph is first modeled with n nodes and its related connective links. Then the ants start moving forward in the network while routing and selecting the next node after the current node i is done based on the amount of pheromone which was first randomly initialized on the basis of formula (1). The backward ants are formed and sent to the source after finding the destination or a node which has access to it. Updating Pheromone (ϕ) is done in the returning path in the transit nodes based on formula (2) as well.

$$P_{i,j} = \begin{cases} 1 & , \text{if } \phi_{i,j} = \max_{k \in N_i} \{ \phi_{i,k} \} \\ 0 & , \text{else} \end{cases} \quad (1)$$

$$\phi_{i,j} = \phi_{i,j} + \Delta\phi \quad (2)$$

N_i presents the sum of neighboring nodes (j) in formula (1) and $\Delta\phi$ is the constant amount of pheromone increase in case of the ant passing through or the control packet.

One of the benefits of using this method is its dynamic topology, multi-path routing and etc. But the large number of sent control packets, lack of continuous pheromone increase and other issues are its shortcomings. We will name the above-mentioned method “ant routing” in order to prevent confusion due to the similarity between the name of this algorithm and the following algorithms.

3-2. Ant-Based Routing in Mobile Ad Hoc Networks (MANETs) (revised version)

This algorithm which is the revised form of the previous model is specifically known as ARAA [10]. The probability function in formula (3) is used in this model instead of using pheromone dynamics (ϕ in the previous model). And of course pheromone continuously decreases and also increases while sending data (formula 4). A memory buffer is also considered for each group so that the routing packages can be controlled regarding volume and number.

$$p_{i,j} = \begin{cases} \frac{\varphi_{i,j}}{\sum_{k \in N_i} \varphi_{i,k}} & , \text{if } j \in N_i \\ 0 & , \text{if } j \notin N_i \end{cases} \quad (3)$$

$$\varphi_{i,j} = (1-q)\varphi_{i,j} + \Delta\varphi \quad (4)$$

q is a number smaller than 1 and indicates the vaporized pheromone in the route. The above reforms in the new version have led to advantages such as homogeneous load distribution among nodes, preventing sending extra useless packages but it is not suitable for huge routing demands and large number of nodes.

3-3. Probable Routing for Managing the Resources in MANETs

In addition to forward and backward ants there are also destination trail ants in this type of routing which is named ARAMA [11] which are used around the destination node in order to increase pheromone and convergence. Each node has a pheromone table and one probable routing which formula (5) shows its probable function.

$$p(D,i,j) = \begin{cases} \frac{Fun(\tau_{D,i,j}, \eta_{i,j})}{\sum_{j \in N_i} Fun(\tau_{D,i,j}, \eta_{i,j})} & , \text{if } i \in N_i \\ 0 & , \text{if } i \notin N_i \end{cases} \quad (5)$$

$\tau_{D,i,j}$ is the proper amount of pheromone with regard to the j^{th} neighbor of the i node, $\eta_{i,j}$ is heuristic amount of the link or the data of the next node such as traffic and energy. The used function can be any sort of combination of parameters and its simplest type is $Fun(\tau_{D,i,j}, \eta_{i,j}) = \tau_{D,i,j} \times \eta_{i,j}$. After the forward ants reach the destination in routing they are assigned a score or $0 < \rho \leq 1$ value conforming to the parameters which influence the rout updating according to formula (6).

$$\tau_{D,i,j}(n) = f(\rho_{D,j})\tau_{D,i,j}(n-1) + g(\rho_{D,j}) \quad (6)$$

f is the vaporization function and it is as $f(\rho) = 1 - \rho$. $g(\rho)$ is known as Enforcement Function which increases the speed of responding to new data and $g(\rho) = \rho^k$ is one of them. n is also the number of backward ants received. Among the advantages of this proactive and reactive method is the existence and proportional distribution of energy but it is not very efficient in high volumes of packets due to a lot of switching. For more information on this algorithm refer to [11].

3-4. Ant-Based Fuzzy Routing in MANETs (FACO)

FACO [12] applies three parameters of the remaining energy of the node (little, medium, and a lot), buffer amount (full, half full, and empty) and the intensity of the received signal (strong, mediocre, and weak) in order to make better decisions to a fuzzy system. The fuzzy system output called Fuzzy Cost is also considered in five fuzzy levels from very little to a lot and is eventually defuzzified through center-of-gravity method and plays its role in routing. Like other algorithms, in this algorithm also after requesting rout the forward ants spread from the source to the adjacent nodes. Meaning the possibility to select neighboring j for destination d in node i is as formula (7).

$$p_{j,d}^i = \frac{\Phi_{j,d}^i(t)}{\sum_L \Phi_{j,d}^i(t)} \quad (7)$$

L is the neighboring nodes and ϕ is the pheromone amount. Of course each ant saves the essential data and fuzzy cost up to the time it reaches the destination. Backward ants are formed in the destination and sent to the source and update the rout. The rout value (formula 8) and the updated pheromone (formula 9) determine the rout selected by the source for sending purposes.

$$Rout_Cost(t)_{j,d}^i = \sum_{L=1}^t Fuzzy_cost_{L,L+1}^i \quad (8)$$

t is the number of links travelled and $Fuzzy_cost_{L,L+1}^i$ is the fuzzy value link of the neighboring nodes.

$$\Phi_{j,d}^i(t) = (1 - \rho)\Phi_{j,d}^i(t-1) + \rho\Phi_{j,d}^i \quad (9)$$

ρ is the learning rate. Note that the updated pheromone updates probability function. The backward ants are destroyed after they reach the destination and carry out the above-mentioned stages.

In case of error message, maintaining the rout and updating the tables are also carried out like other algorithms.

3-5. Energy Aware Ant Routing Algorithm in MANETs

It specifically focus on the total energy of the network through using CMMBCR algorithm [14] in addition to using ant-based routing process in this model which is called EAAR [13].

The process of the algorithm includes: the forward ants are sent to all neighboring nodes in case there is no route to the destination in the routing table of source node. The intermediate nodes which check the energy parameters and the number of steps also avoid accepting repetitive ants. Also ant parameters for instance the number of steps must not be λ ($1 < \lambda < 2$) times worse than the best state saved in the memory of node. If M will be the number of steps of the best received ant by the intermediate node when an ant enters with N steps formula (10) must be true for the ant to be accepted and after storing the important data, the ant is sent to the next nodes.

$$N \leq \lambda M \quad (10)$$

After reaching the destination node the end-to-end delay of the ant is calculated and in a fraction of this time the received forward ants turn into backward ants and sent towards the source. Also along the path the data of the nodes' routing tables are updated proportionate to the minimum battery charge left from the nodes along the path to (MBR) node and the number of steps (H) (formula 11).

$$T_{n,d}^i = \frac{MBR}{H} \quad (11)$$

$T_{n,d}^i$ is the amount which the data packet checks when sending to the destination. When the source node receives the ants it starts sending data packets based on the possibility formed after the data was updated (formula 12).

$$P_{n,d} = \frac{(T_{n,d}^i)^\beta}{\sum (T_{j,d}^i)^\beta} \quad (12)$$

β is a number used in order to prevent extreme shrinking of the possibility and it somehow normalizes it. Maintaining the route is also done while sending data through an increase in the amount of pheromone caused by the ever-growing passing of information packets through a path and a decrease in pheromone levels in lesser used paths just as it is in other algorithms mentioned in the previous sections.

In general because of optimum and appropriate use of ARA, multi-path routing, maintaining and carefully controlling the routs regarding energy management is a good algorithm. But not evaluating delay and investigating when the number of nodes is large, is amongst its relative shortcomings.

IV. EVALUATION AND COMPARISON

As you can see the evaluation results along with the specifications and conditions of each algorithm in table 1, In Ant Routing formation of tables merely on the basis of pheromone does not require a large number of control packets in ant routing so it is natural for the overhead to be little but the packets are not well controlled.

The control over the networks has increased with the interference of more parameters in ARA and ARAMA but despite the improvement in load distribution, it has lost its efficiency in large networks and large number of data.

Evaluating on the basis of fuzzy calculations leads to high overhead in calculations in FACO and has no consequences except for limiting the efficiency development of the network and of course energy consumption also increases which has not been attended to.

EAAR algorithm focuses more on energy therefore the life span of the network and the energy consumed in each node and also the entire network has improved but are end-to-end delay and network efficiency in large sizes suitable? which has not been studied and compared in the above mentioned algorithm.

Table 1: comparing different types of ant- based routing in Mobile Ad Hoc Networks (MANETs)

Advantages	Shortcomings	Improved parameter	Energy algorithm	Tables' structure	Factor types	Routing and Data transfer structure	Routing type	Presented year	Algorithm
Dynamic topology, being multi-routed	Lack of control on sent packets	Overhead	-	Pheromone density, next step, IP destinations	Forward and backward ants	Based on pheromone density	On demand	2002	Ant Routing [9]
Load distribution, controlling the number of packets and	Low efficiency in large sizes and a large number of	Delivery rate and accuracy of optimal route	Nodes entering sleeping state under special conditions	Pheromone density, next step, IP destinations and buffer	Forward and backward ants	Based on probable function from pheromone	On demand	2003	ARA [10]
Suitable for controlling energy distribution and simultaneous control of parameters	Delivery decrease due to a lot of switching	Homogeneous energy distribution, minimum step in small-number nodes	Lucent wave LAN PC and 2.4 GH	Pheromone density, next step, IP destinations and buffer	Forward and backward ants and destination trail ants	Based on probable function from pheromone and network parameters (Heuristic)	Hybrid	2005	ARAMA [11]
The possibility to select a better route through the source node after routing	A lot of calculations in low-numbered nodes and overlooking the total energy of the network	Delivery rate, delay and number of routing discovery	Applying the remaining battery in fuzzy data	Pheromone density, destination possibility, fuzzy data, IP destinations and intermediate node	Forward and backward ants	Based on pheromone amount and Fuzzy Cost	Hybrid	2009	FACO [12]
Multi- routed, higher efficiency with large-sized packets	Not evaluating delay and investigating when there is a large number of nodes	Total energy consumption reduction of each node and destroyed packets	Conditional Max- min battery capacity routing (CMMBCR)	Pheromone probability, number of steps and the amount of remaining energy from the nodes	Forward and backward and control ants	Sending control packets to neighboring nodes and transferring data based on probability	Hybrid	2010	EAAR [13]

V. CONCLUSION AND FUTURE WORKS

What is quite obvious here is that using ant-based routing in MANET networks can bring about good results and widely using it in combination with various other algorithms and methods is still attended to and shows better outcomes. Also for numerical evaluation a number of parameters such as the number of delivered packages, the energy consumed by the entire network and the ratio of control packets to all packets or overheads are compared in table 2 under similar condition (30 nodes, the size being 1000× 1000 square meters and IEEE802.11 protocol MAC layer). The comparison is made among the mentioned algorithms except for Ant Routing which ARA is the revised version of it and an algorithm known outside this area (DSDV).

Table 2: numerical comparison between some parameters in the algorithms

Parameter	ARA	ARAMA	FACO	EAAR	DSDV
Delivered packages	220	192	228	236	210
Energy consumption by (Kj) network	55	58	60	52	71
overhead	0.32	0.37	0.4	0.39	0.52

As seen in table 2 the ant-based routing algorithms come to better results in comparison with algorithms outside this set (DSDV as a sample) which proves the conclusion of this article based on the necessity to recognize different types of this routing model and the ability to compare them in presenting new methods and using each one in accordance to the situation, we have studied a number of the most important ones in this article.

What we are intending for the future and working on currently is designing and simulating an intelligent algorithm which can change the type of its ant-based routing algorithm according to its usage under different situation in accordance with the network topology.

REFERENCES

- [1] Mehran Abolhasan, Tadeusz Wysocki, Eryk Dutkiewicz, "A review of routing protocols for mobile ad hoc networks," Ad Hoc Networks, Volume 2, Issue 1, January 2004, Pages 1-22
- [2] M. Dorigo, G. Di Caro, L. Gambardella, "Ant colony optimization: a new meta-heuristic," Proc. Congress on Evolutionary Computation, vol. 2, IEEE Press, Washington, DC, 1999, pp. 1470–1477.
- [3] O. Hussein, T. Saadawi, and M. Lee, "Ant routing algorithm for mobile ad hoc networks," Proc. ARL CTAC2003, Apr. 2003, pp. 141–145.
- [4] Vasundhara Uchhula, Brijesh Bhatt, "Comparison of different Ant Colony Based Routing Algorithms," IJCA Journal, Number 2 - Article 8, 2010.
- [5] Johnson, B., Maltz, D.A., Hu, Y.-C., Jetcheva, J.G., "The Dynamic Source Routing for Mobile Ad Hoc Wireless Networks," IETF Internet Draft, Nov 2001.
- [6] M. Abolhasan, T. Wysocki, E. Dutkiewicz, "A review of routing protocols for mobile ad hoc networks," Ad Hoc Networks 2 pp. 1-22, 2004.
- [7] John du Plessis, Ant Colony Optimization Distance Vector Routing In Ad Hoc Network, University of Oretoria, November 2005.
- [8] Jianping Wang, Eseosa Osagie, Parimala Thulasiraman, Ruppa K. Thulasiram, "A hybrid ant colony optimization routing algorithm for mobile ad hoc network," Ad Hoc Networks 7 pp. 690–705, 2009.
- [9] Mesut Gunes, Udo Sorges, and Imed Bouazizi. "ARA - The Ant-Colony Based Routing Algorithm for MANETs," Proceedings of the 2002 ICPP Workshop on Ad Hoc Networks (IWAHN 2002), pages 79-85. IEEE Computer Society Press, August 2002.
- [10] M. Gunes, M. Kahmer, Imed Bouazizi, "Ant-Routing-Algorithm (ARA) For Mobile Multi-Hop Ad Hoc Networks New Features and Results", Proc. of the Med-Hoc Net 2003 Workshop Mahdia, Tunisia 25-27 June, 2003
- [11] Osama H. Hussein et al. "Probability Routing Algorithm for Mobile Ad Hoc Networks' Resources Management", IEEE Journal on Selected Areas In Communication, Vol. 23, No. 12, december 2005.
- [12] M.M. Goswami et al., "Fuzzy Ant Colony Based Routing Protocol For Mobile Ad Hoc Network," Proc. Int. Conf. on Computer Engineering and Technology. 22-24 Jan. 2009.
- [13] Sudip Misra et al. "An ant swarm-inspired energy-aware routing protocol for wireless ad-hoc networks," Journal of Systems and Software, Vol. 83, pp. 2188–2199, June 2010.

A Novel High Performance H-Bridge Converter Topology for 8/6 pole SRM Drive

V. V. N. Murthy¹, S. S. Tulasi Ram², J. Amarnath³

1, (Department of Electrical and Electronics Engineering, University College of Engineering, JNTU Kakinada, Andhra Pradesh, India)

2, 3 (Department of Electrical and Electronics Engineering, University College of Engineering, JNTU Hyderabad, Andhra Pradesh, India)

Abstract: *Despite of the fact that obviously less complex, the SRM drives are these days more expensive than their formal AC drive systems. This is, all things considered brought about by the absence of an optimal power electronic converter for SRM drives, which would be accessible as a single module. Various endeavors were hence made lately to create novel power electronic converter structures for SRM drives, in light of the usage of a Four-phased voltage source inverter (VSI), it is promptly accessible as a single module. This paper takes after this line of thought and presents a novel power switching device for SRM drive, which is totally focused around the use of standard inverter legs, have their own particular favorable circumstances and weakness. The determination of a converter, in the majority of the cases, relies on the application & consistency. To encourage the choice a relative comparative analysis is intended in this paper. An arrangement of SRM formal converter topologies with a definite evaluation of proposed topology fed four phased 8/6 SRM drive worked as open circuit & closed circuit controlling scheme is executed in Matlab/Simulink software package and the relating results are introduced.*

Keywords: *Switched Reluctance Motor Drives, Asymmetric Converter topology, Proposed H-Bridge Converter Topology.*

I. INTRODUCTION

Switched Reluctance Drives have been in the center of research exertion for more than two decades [1]-[3]. These principally vary as for the amount of phases utilized, stator/rotor poles number set-up's, and the concept of torque creation. In spite of the fact that the torque is constantly produced by the doubly-salient structure of the machine, its inception may be two-fold. Torque may be created entirely because of the variation of the winding self-inductance with rotor position (nothing but short pitched SRM's). On the other hand, mutual coupling between phases (i.e. position-dependence on variety of mutual inductances) could be utilized to enhance the torque density. Contingent upon the winding distribution, two types of SRM's may come about, fully pitched and partially pitched SRM's. In fully pitched SRM's there is an unimportant variety in phase self inductance toward oneself with rotor position and torque production comes about because of variety of the mutual inductance in between neighbouring phases. As far as this subdivision, this paper focuses on the short pitched SRM's.

Various power semiconductor topologies have been created throughout the years exclusively for utilization of conjunction with SRM Drives. On a basic level, the quest has been dependably for a converter with a minimized number of switches [4]. An excellent review of various power electronic converter designs for SRM drives is accessible in [5], while some exceptionally insightful comparisons of different commonly utilized topologies might be found in [6]-[8]. Be that as it may, regardless to all the advancements in the SRM drives area, switched reluctance machine have not yet found expansive acceptance.

The low cost feasible design of switched reluctance motor, with its features of fault tolerance and capability to withstand high temperatures makes its very imperative for the automotive application. One of the principle aspects of the research in switched reluctance motor drives has been the converter design [9]-[12]. The execution and the expense of the drive are exceedingly influenced by performance of the converters. The phase independence and unipolar current necessity have produced a wide variety of converter topologies for SRM drives. Numerous diverse topologies have risen with minimized number of active switched and faster commutation time through proceeded research. There has been dependably a trade-off between gaining some of the advantages and losing some with every new topology. The decision of converter for a certain application is an essential issue [13].

The switched reluctance motor is a pivoting electric machine where both, stator & rotor have remarkable poles. The stator comprises of simple concentric windings. There are neither windings or bar wires on the rotor. Stator windings on oppositely inverse poles are connected in arrangement structure to a single phase. At the point when the stator pole pair is energized by the phase winding, the closest rotor pole pair is attracted in around the position, where the attractive magnetic path has the minimum reluctance [14]. Accordingly, by energizing the consecutive stator phases in sequence, it is conceivable to develop a torque in either direction of rotation. The fundamental working principle of the SRM is truly simple; as current is passed through one of the stator windings, torque is created by the tendency of the rotor to adjust with the energized stator pole. The direction of torque generated is a capacity of the rotor position with concerning the energized phase, and is autonomous of the direction of current flow through the phase winding. Continuous torque might be delivered by intelligently synchronizing each phase's excitation with the rotor position. By changing the number of phases, the amount of stator poles, & the amount of rotor poles, numerous diverse SRM geometrics might be realized it out. Normally, expanding the number of SRM phases diminishes the torque ripples, however at the cost of requiring more electronics with which to operate the SRM. At least two phases are obliged to guarantee starting, and least four phases are obliged to insure the starting direction.

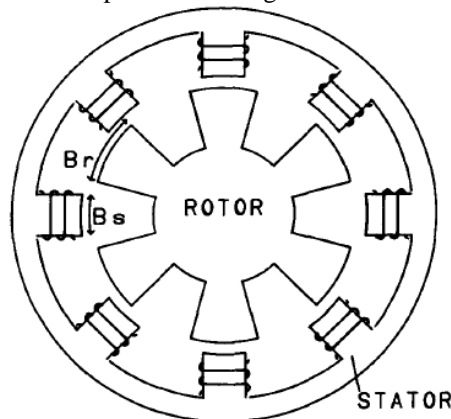


Fig.1 Basic Schematic Diagram of Four Phased 8/6 SRM

The number of rotor poles and stator poles should likewise contrast to insure starting. The accompanying Fig.1 shows the basic four phase 8/6 switched reluctance drive. It has been realized that the reluctance motors requires just unipolar currents and this offers ascent to the possibility of working with only one switching device arrangement for every phase, rather than two in series in each phase leg of an ac or BLDC drive system. The torque is directly proportional to the square of the current; henceforth the current could be unipolar to deliver unidirectional torque. Note that this is truly in spite of the case for ac machines. This unipolar currents necessity has a unique advantage in that one and only power switch is needed for control of current in a phase winding. Such a feature enormously minimizes the number of power switches in the converter and consequently makes the drive economical. A few inverter power circuits are suitable for switched reluctance motor devices are investigated and are contrasted and one another. The correlation is focused around power switches, free-wheeling diodes, size & peak appraisals of DC link components. Since converter decision depends upon motor design, converter design & analysis, determination is ruined for high speed applications [15]-[17]. This paper highlights the operation of proposed converter with minimized number of active devices & finally similarity analysis is carried out and dynamic assessment of formal asymmetrical converter & proposed H-bridge topology by using Matlab/Simulink platform.

II. CONVERTER TOPOLOGIES AND SPEED CONTROL OF SRM

The operation of SRM is very simple on account of its capacity to work efficiently from unidirectional winding currents, thus only one switch for every phase is sufficient yielding an extremely economical brushless drive, however in ac machine drives no less than two switches for every phase are needed. Moreover, phase winding arrangements with a switch in the SRM but the windings are not in arrangement with switches in ac drives that prompt irreparable damage in shoot through faults. This is valid for all SR converter circuits in light of the fact that there ids dependably a motor winding in series with switch with every main power switching device. Second, there is a more prominent level of independence between the phases than is conceivable in formal ac or BLDC rives [18]. A fault in one phase (whether in the motor or in the converter) normally effects that phase; other phases can keep on operating independently [19], [20].

A. Conventional Asymmetric Converter Topology

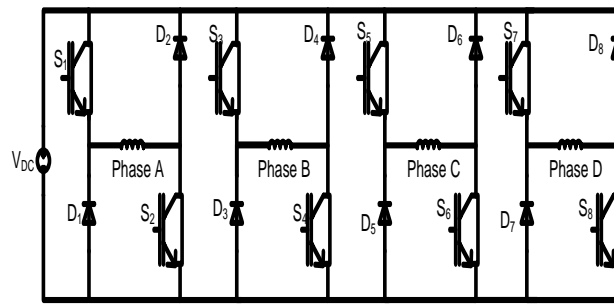


Fig.2 Asymmetrical bridge converter for four phased 8/6 pole SRM Drive system

When switches S1 & S2 are turned ON, the phase A is energized which is shown in Fig.3.

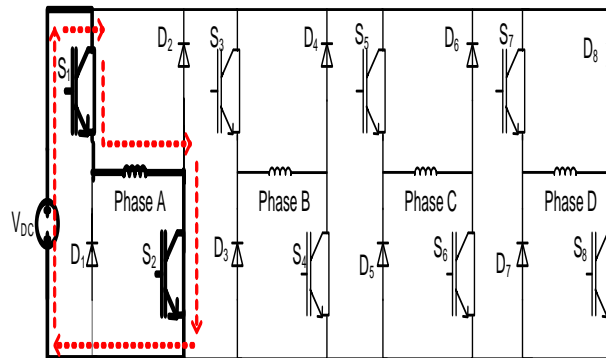


Fig 3. Current path when phase A is energized

When switches S1 & S2 are turned OFF, the diodes D1 & D2 are forward biased. In this case phase A is denenergized, which is shown in Fig.4.

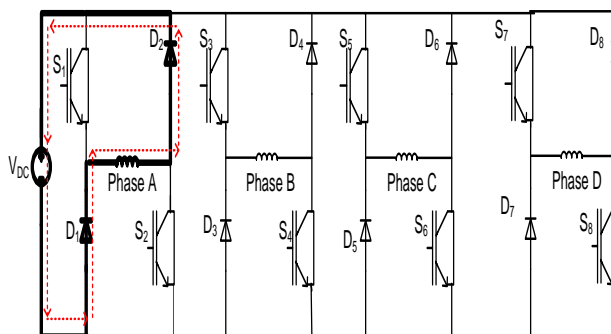


Fig 4. Current path when phase A is denenergized

B. Proposed H-Bridge Converter Topology

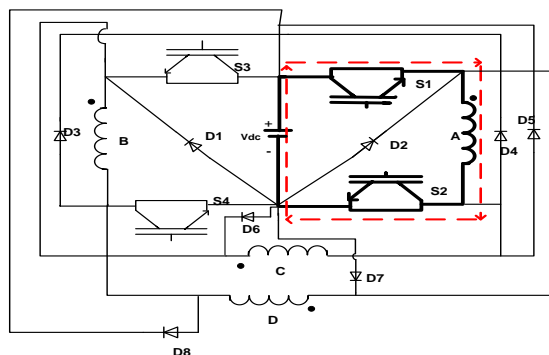


Fig.5 Proposed H-Bridge Converter Topology for Four Phased 8/6 SR Drive (Phase-A Energization)

Fig.5 shows the proposed H-bridge converter topology for 4-phase 8/6 SR drive (Ph-A Energization Mode) represents the inductor current path in phase-A excitation when the switches S1 & S2 will be conducted with respect to diode D2.

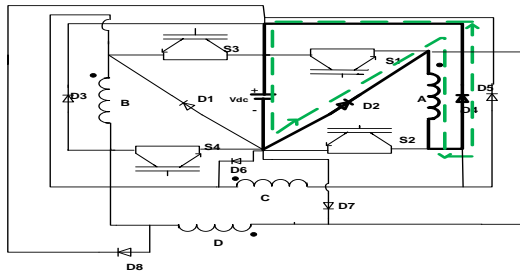


Fig.6 Proposed H-Bridge Converter Topology for a Four Phased 8/6 SR Drive (Ph-A Free-wheeling Path)

Fig.6 shows the proposed H-Bridge converter topology for Four phase 8/6 SR drive (Ph-A Freewheeling Path) represents the inductor current freewheeling path in phase-A, excitation when the switches S1 & S2 will be non-conducted with respect to diode D2 & D4 conducted and achieve the freewheeling action.

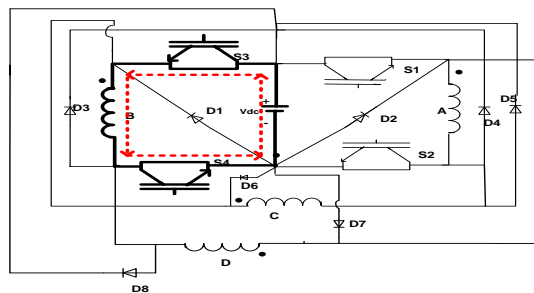


Fig.7 Proposed H-Bridge Converter Topology for Four Phased 8/6 SR Drive (Ph-B Energization)

Fig.7 shows the proposed H-Bridge Converter Topology for Four phased 8/6 SR Drive (Ph-B energization Mode) represents the inductor current path in phase-B excitation when the Switches S3 & S4 will be conducted with respect to Diode D1.

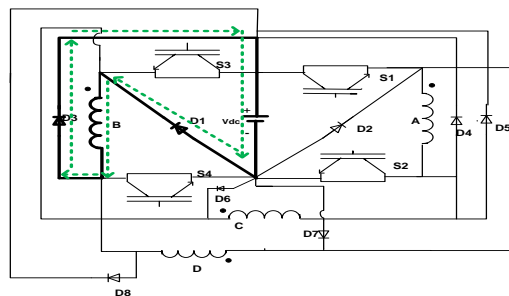


Fig.8 Proposed H-Bridge Converter Topology for Four Phased 8/6 SR Drive (Ph-B Freewheeling Path)

Fig.8 shows the proposed H-Bridge converter topology for four phase 8/6 drive (Ph-B Freewheeling path) represents the inductor current freewheeling path in ph-B excitation when the switches S3 & S4 will be non-conducted with respect to diode D1 & D3 conducted and achieve the freewheeling action.

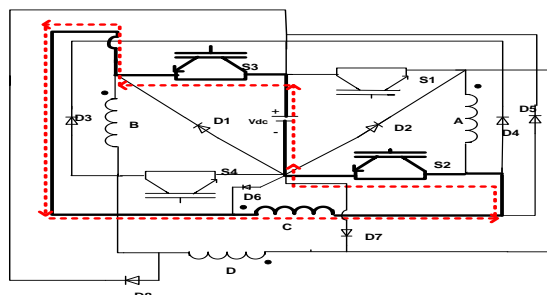


Fig.9 Proposed H-Bridge Converter Topology for Four Phased 8/6 SR Drive (Phase-C Energization)

Fig.9 shows the proposed H-Bridge converter topology for four phased 8/6 SR Drive (Ph-C Energization Mode) represents the inductor current path in phase C excitation when the switches S3 & S2 will be conducted.

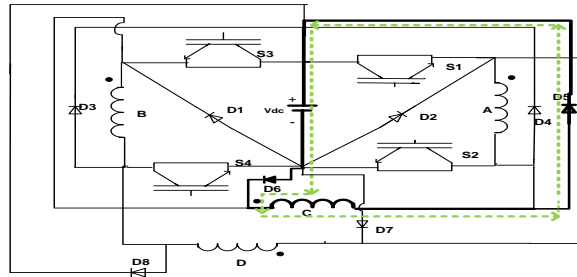


Fig.10 Proposed H-Bridge Converter topology for Four Phased 8/6 SR Drive (Phase-C Freewheeling Path)

Fig.10 shows the proposed H-Bridge converter topology for four phase 8/6 SR drive (Ph-C freewheeling path) represents the inductor current freewheeling path in ph-C excitation when the switches S3 & S2 will be conducted with Diode D5 & D6 conducted & achieved the freewheeling action.

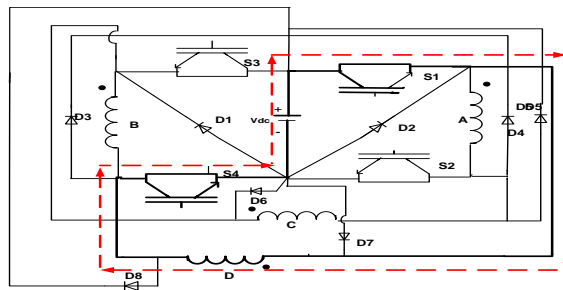


Fig.11 Proposed H-Bridge Converter Topology for Four-Phased 8/6 SR Drive (Ph-D Energization)

Fig.11 shows the proposed H-Bridge Converter Topology for Four phase 8/6 SR drive (Phase-D Energization Mode) represents the inductor current path in phase-D excitation when the switches S1 & S4 will be turns ON condition.

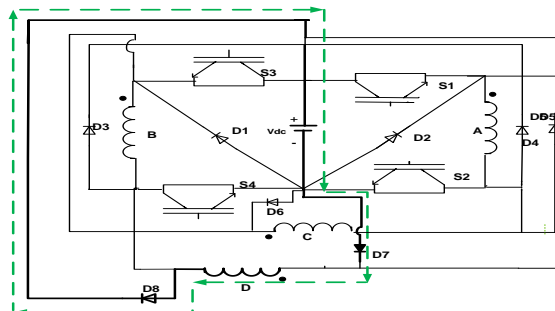


Fig.12 Proposed H-Bridge Converter Topology for Four Phased 8/6 SR Drive (Phase-D Freewheeling path)

Fig.12 shows the proposed H-Bridge converter topology for four phase 8/6 SR drive (Phase-D Freewheeling Path) represents the inductor current freewheeling path in phase D excitation when the switches S1 & S4 will be non-conducted with respect to diode D7 & D8 conducted and achieve the freewheeling action.

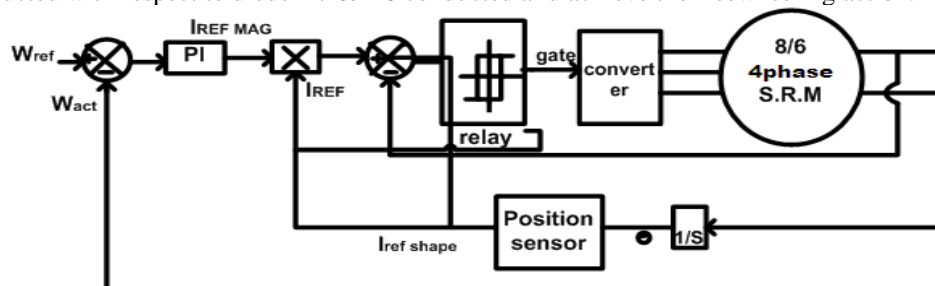


Fig. 13: Closed Loop Control of SRM Drive System

The above Fig.13 shows the closed loop control execution of SRM drive framework for getting quick transient response, the overall drive system is executed in closed manner. The actual speed of the motor is compared with the reference speed give the speed error. The speed error is connected to PI controller creates the reference current which produces the obligated gate pulses for driving the motor [20].

III. MATLAB/SIMULINK MODELLING AND SIMULATION RESULTS

Here simulation is carried out in different cases, in that

- 1). Conventional Asymmetrical Topology for Open Loop & Closed Loop Control of 8/6 SRM Drive.
- 2) Proposed H-Bridge Topology for Open Loop & Closed Loop Control of 8/6 SRM Drive.

Case 1: Conventional Asymmetrical Topology for Open Loop & Closed Loop Control of 8/6 SRM Drive

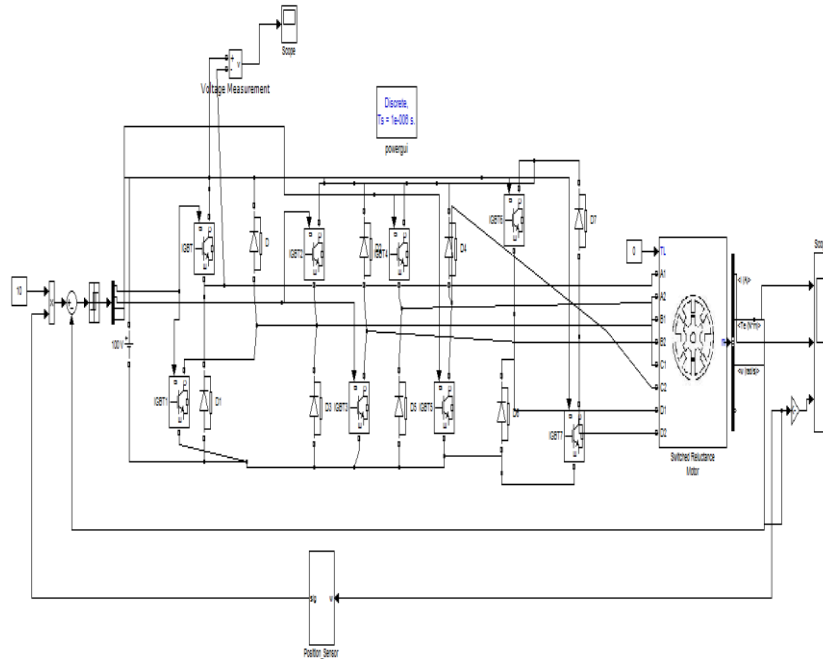
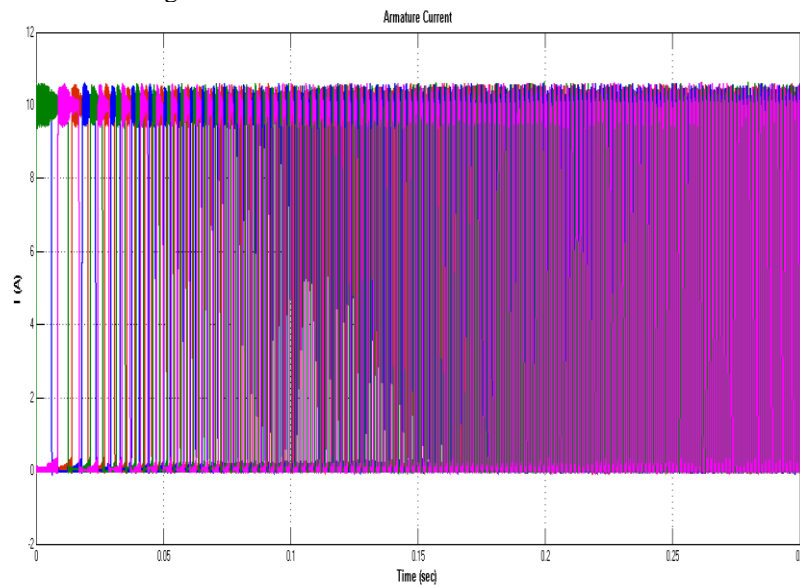
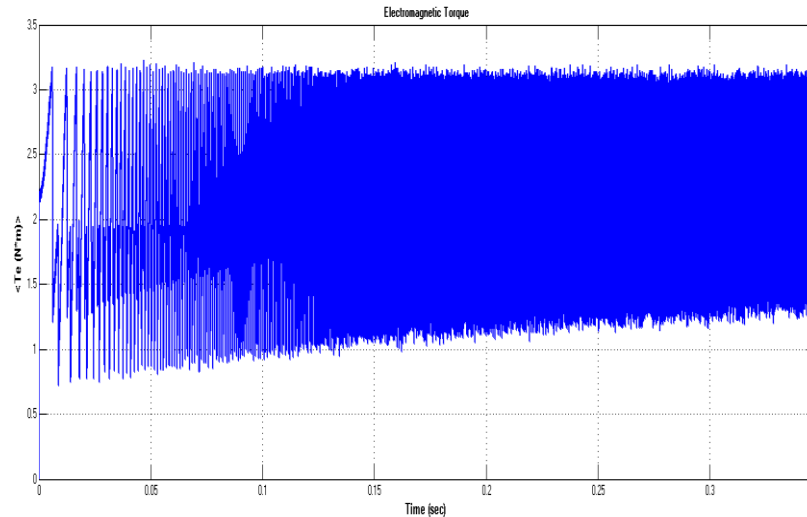


Fig.14 Matlab/Simulink Model of Conventional Open Loop Model of 8/6 SRM Drive Configuration

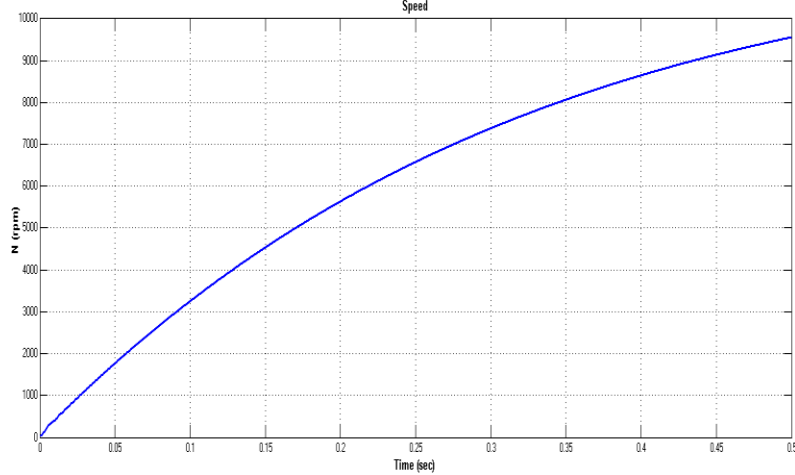
Fig.14 Matlab/Simulink Model of Conventional Open Loop Model of 8/6 SRM Drive Configuration using Matlab/Simulink Software Package.



(a) Current



(b) Electromagnetic Torque



(c) Speed

Fig.15 Current, Electromagnetic Torque, Speed of Conventional Open Loop Model of 8/6 SRM Drive Configuration.

Fig.15 shows the Current, Electromagnetic Torque, and Speed of Conventional Open Loop Model of 8/6 SRM Drive Configuration, due to open loop circuit somewhat delay to achieve steady state.

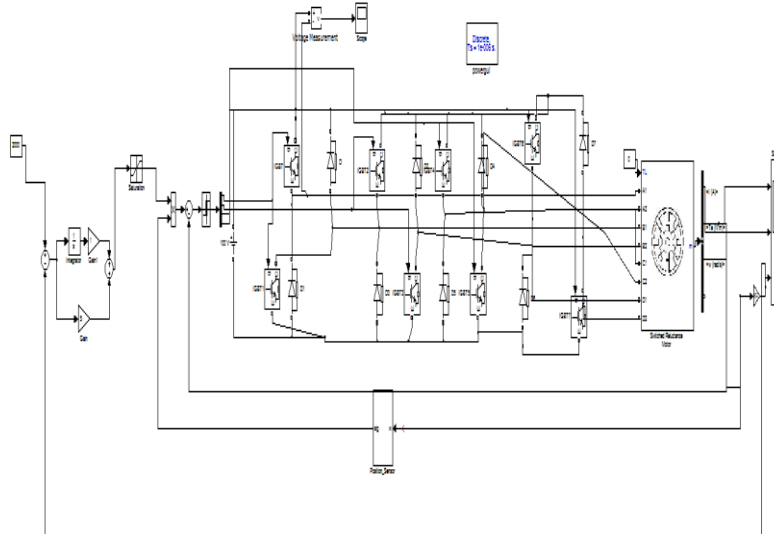


Fig.16 Matlab/Simulink Model of Conventional Closed Loop Model of 8/6 SRM Drive Configuration

Fig.16 Matlab/Simulink Model of Conventional Closed Loop Model of 8/6 SRM Drive Configuration using Matlab/Simulink Software Package.

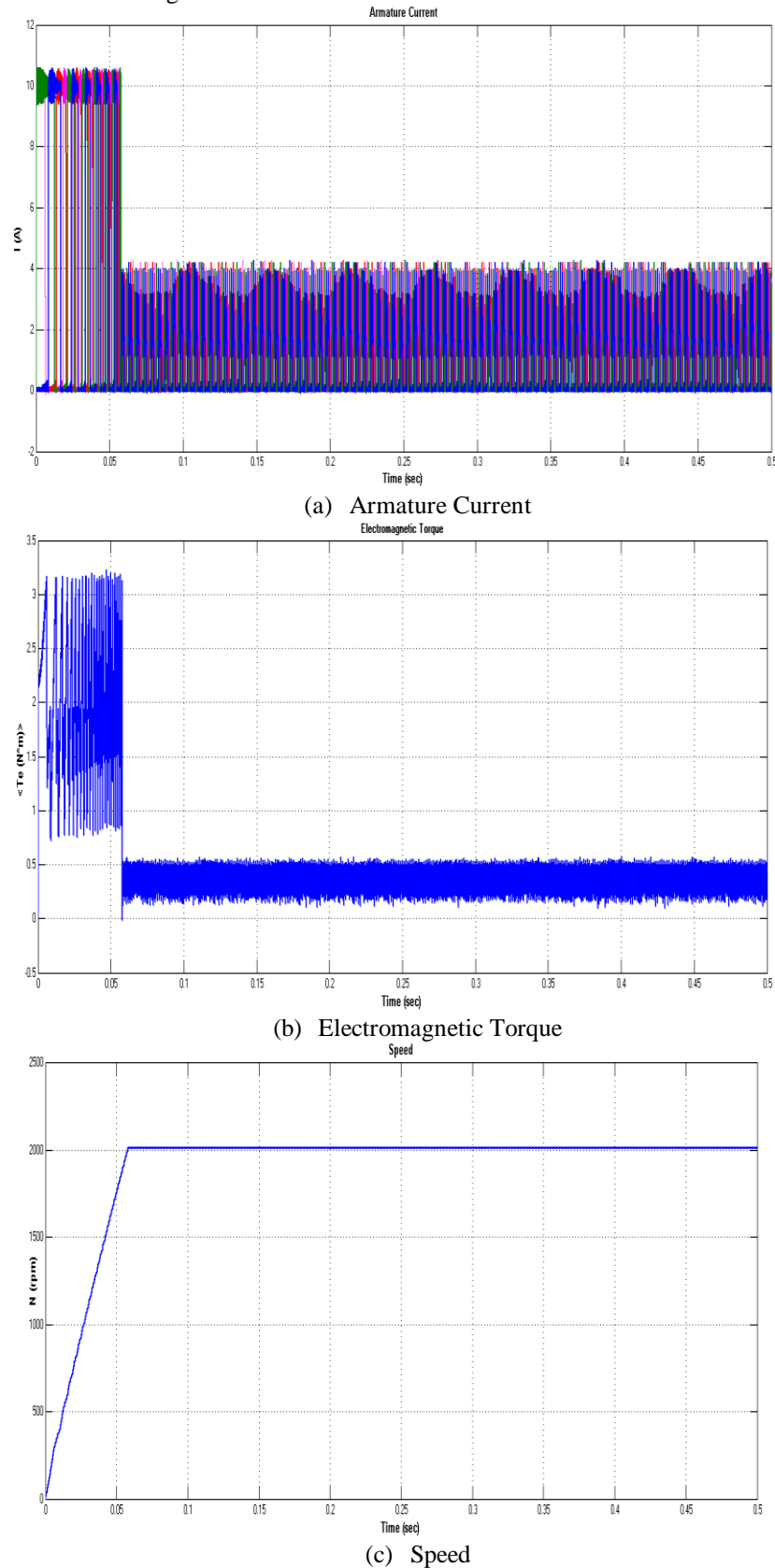


Fig.17 Current, Electromagnetic Torque, Speed of Conventional Closed Loop Model of 8/6 SRM Drive Configuration.

Fig.17 shows the Current, Electromagnetic Torque, and Speed of Conventional Closed Loop Model of 8/6 SRM Drive Configuration, due to closed loop circuit achieve fast response with low steady state error.
Case 2: Proposed H-Bridge Topology for Open Loop & Closed Loop Control of 8/6 SRM Drive.

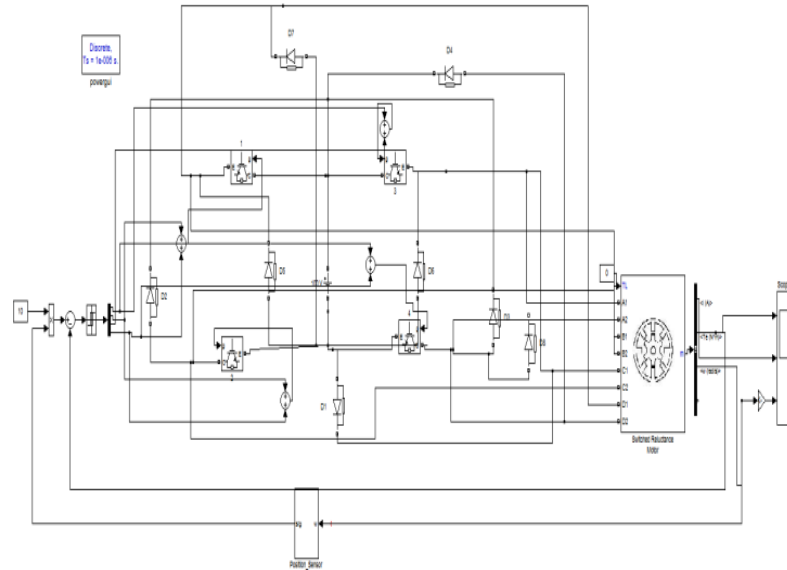
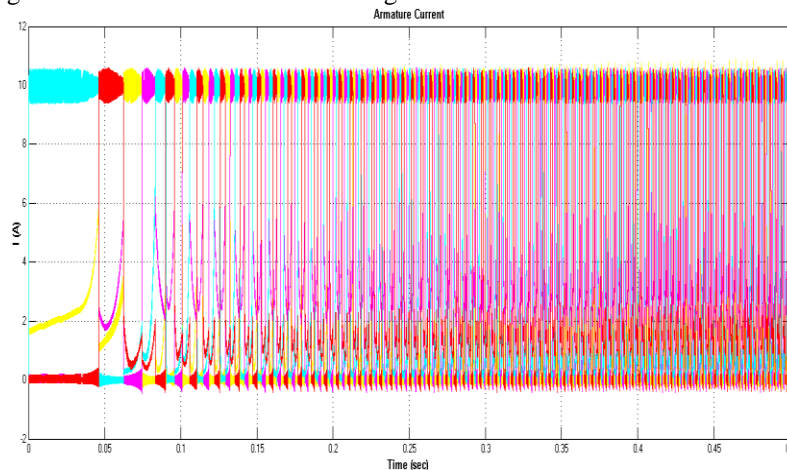
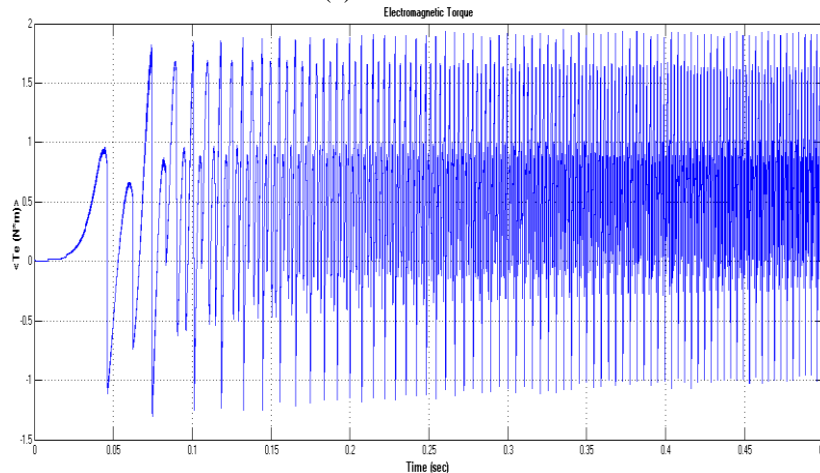


Fig.18 Matlab/Simulink Model of Proposed H-Bridge Topology based Open Loop Model of 8/6 SRM Drive Configuration

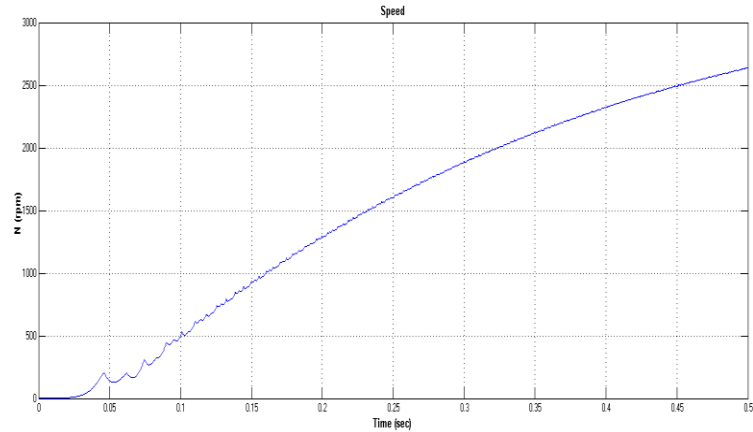
Fig.18 Matlab/Simulink Model of Proposed H-Bridge Topology based Open Loop Model of 8/6 SRM Drive Configuration using Matlab/Simulink Software Package.



(a) Armature Current



(b) Electromagnetic Torque



(c) Speed

Fig.19 Current, Electromagnetic Torque, Speed of Proposed H-Bridge Topology based Open Loop Model of 8/6 SRM Drive Configuration.

Fig.19 shows the Current, Electromagnetic Torque, and Speed of Proposed H-Bridge Topology based Open Loop Model of 8/6 SRM Drive Configuration, due to open loop circuit somewhat delay to achieve steady state.

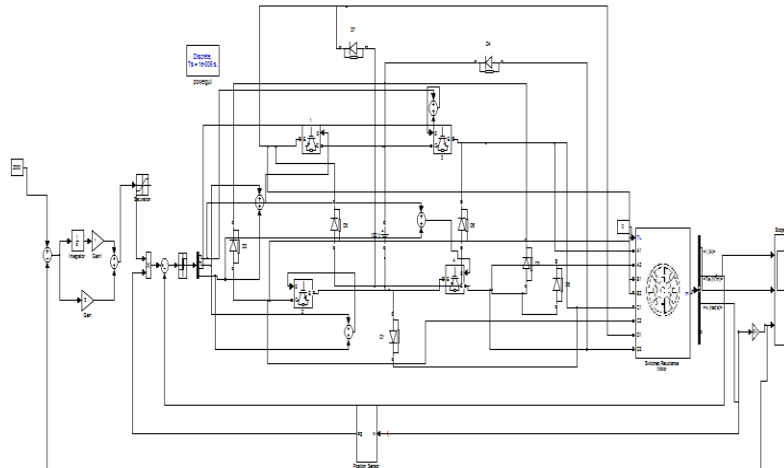
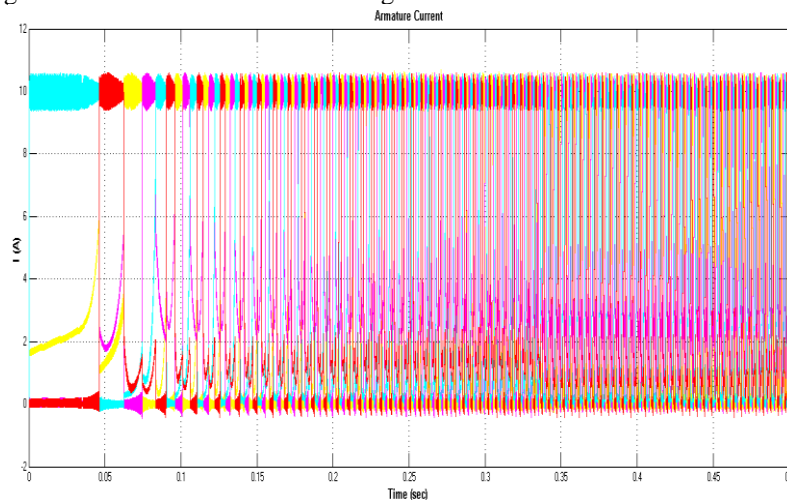
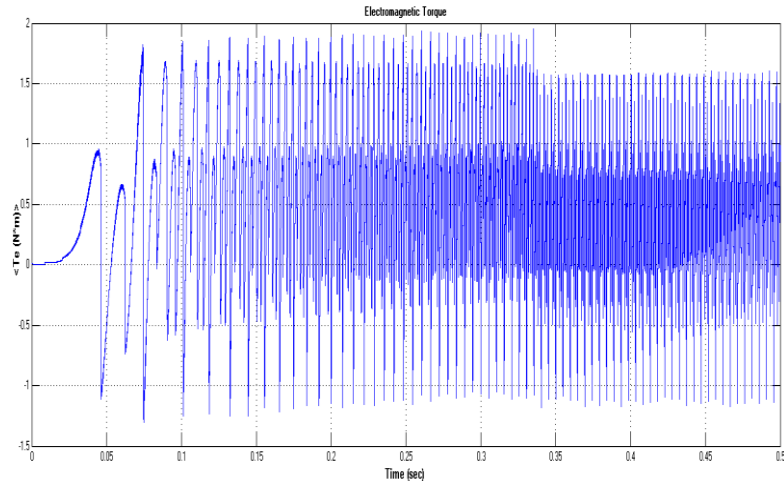


Fig.20 Matlab/Simulink Model of Proposed H-Bridge Topology based Closed Loop Model of 8/6 SRM Drive Configuration

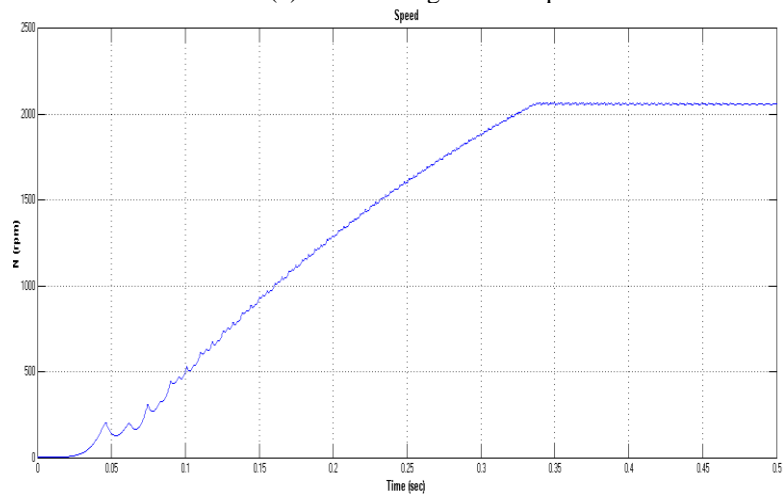
Fig.20 Matlab/Simulink Model of Proposed H-Bridge Topology based Closed Loop Model of 8/6 SRM Drive Configuration using Matlab/Simulink Software Package.



(a) Armature Current



(b) Electromagnetic Torque



(c) Speed

Fig.21 Current, Electromagnetic Torque, Speed of Proposed H-Bridge Topology based Closed Loop Model of 8/6 SRM Drive Configuration.

Fig.21 shows the Current, Electromagnetic Torque, and Speed of Proposed H-bridge Topology based Closed Loop Model of 8/6 SRM Drive Configuration, due to closed loop circuit achieve fast response with low steady state error.

Table I Comparison of Various Converter Topologies to drive Switched Reluctance Motor

S. No	Type of the Converter	Switching Devices	Active Diodes
01	Conventional Asymmetrical Converter Topology	08 Switches	08 Diodes
02	Proposed H-Bridge Topology	06 Switches	06 Diodes

Table I represents the number of switching devices & diodes required to drive the switched reluctance motor with comparison of conventional topology as well as proposed H-bridge topology requires low switches & low diodes which makes system to be required low space, low cost, low complex to design, low switching loss and high efficiency.

IV. CONCLUSION

Switched Reluctance Motor has gained momentum in the exceptionally aggressive market of adjustable speed motor drives. Basic structure and low cost are the most imperative reasons behind this frame. Despite the fact that various converters have developed through the years for SRM drives. All converters have their own disadvantages & some drawbacks. Among the disadvantages are various switching devices & diodes, high voltage ratings, necessities of auxiliary windings, low effectiveness and complicated control schemes. From the formal converter to proposed H-bridge topology has better features, reduction of active switching

device, low complexity, low cost, respectively as well as voltage drops for every phase have been accomplished at the expense of the complication in the control. This paper intends the open loop & closed loop control of four phased 8/6 pole switched reluctance motor (SRM) drive. Finally a novel closed loop controller for 8/6 SRM drive is implemented in Matlab/Simulink Platform, as well as presented the results and used in many industrial applications.

REFERENCES

- [1] T. Wichert, "Design and construction modifications of switched reluctance machines," Ph.D. thesis, Warsaw University of Technology, 2008.
- [2] Y Hasegawa, K. Nakamura, and O. Ichinokura, "Development of a switched reluctance motor made of permendur," in Proc. 2nd Int. Symp. on Advanced Magnetic Materials and Applications, Journal of Physics, 2011.
- [3] M. T. Lamchich, Torque Control, InTech Publisher, February 10 2011, ch. 8.
- [4] R. D. Doncker, D. W. J. Pulle, and A. Veltman, Advanced Electrical Drives: Analysis, Modeling, Control, Springer Press, 2011, ch. 10.
- [5] E. S. Elwakil and M. K. Darwish, "Critical review of converter topologies for switched reluctance motor drives," International Review of Electrical Engineering, vol. 2, no. 1, January-February 2011.
- [6] J. W. Ahn, J. Liang, and D. H. Lee, "Classification and analysis of switched reluctance converters," Journal of Electrical Engineering & Technology, vol. 5, no. 4, pp. 571-579, 2010.
- [7] Ž. Grbo, S. Vukosavić, and E. Levi, "A novel power inverter for switched reluctance motor drives," FACTA Universitatis (NIS), Elec. Eng., vol. 18, no. 3, pp. 453-465, December 2005.
- [8] S.A. Nasar, "DC Switched Reluctance Motor", Proceedings of the Institution of Electrical Engineers, vol.166, no.6, June, 1996, pp.1048-1049.
- [9] J.V. Byrne, et al., "A High Performance Variable Reluctance Drive: A New Brushless Servo", Motor Control Proceedings, Oct. 1985, pp.147-160.
- [10] P.French and A.H. Williams, "A New Electric Propulsion Motor", Proceedings of AIAA Third Propulsion Joint Specialist Conference, Washington, D.C., July, 1967.
- [11] L.E. Unnewehr and H.W. Koch, "An Axial Air-Gap Reluctance motor for Variable Speed Application", IEEE Transactions on Power Apparatus and Systems, vol.PAS-93, no.1, January, 1974, pp.367-376.
- [12] P.J. Lawrenson, "Switched Reluctance Motor Drives", Electronics and Power, 1983, pp.144-147.
- [13] R. Krishnan, "Switched Reluctance Motor Drives: Modeling, Simulation, Analysis, Design, and Applications", CRC Press, 2001.
- [14] T. J. E. Miller. "Electronic control of switched reluctance motors". Newnes Power Engineering Series Oxford, UK, 2001.
- [15] S. Vukosavić and V. R. Stefanović, "SRM inverter topologies: A comparative evaluation," IEEE Transactions on Industry Applications, vol. 27, no. 6, pp. 1034-1047, November/December 1991.
- [16] M. Ahmad, High Performance AC Drives: Modelling Analysis and Control; Springer Press, 2010, ch. 6.
- [17] E. Elwakil, "A new converter topology for high speed high starting torque three-phase switched reluctance motor drive system," Ph.D. thesis, Brunel University London, UK, January 2009.
- [18] D. H. Lee, J. Liang, T. H. Kim, and J. W. Ahn, "Novel passive boost power converter for SR drive with high demagnetization voltage," Dept. of Electrical and Mechatronics Engineering, Kyungshung University, Korea, 2006.
- [19] M. Asgar, E. Afjei, A. Siadatan, and A. Zakerolhosseini, "A new modified asymmetric bridge drive circuit switched reluctance motor," in Proc. European Conference Circuit Theory and Design, Aug 2009, pp. 539-542, 23-27.
- [20] M. Barnes and C. Pollock, "Power electronic converters for switched reluctance drives," IEEE Transactions on Power Electronics, vol. 13, no. 6, pp. 1100-1111, November 1998.

Analysis of Human Behavior Based On Centroid and Treading Track

Ms. K. V. Patil¹, Prof. D. D. Dighe²

^{1,2} Matoshri College of Engineering and Research Centre, Department of E&TC, Pune University, Nashik

Abstract: Human body motion analysis is an important technology which modern bio-mechanics combines with computer vision and has been widely used in intelligent control, human computer interaction, motion analysis, and virtual reality and other fields. In which the moving human body detection is the most important part of the human body motion analysis, the purpose is to detect the moving human body with its behavior from the background image in video sequences, and for the follow-up treatment such as the target classification, the human body tracking and behavior understanding, its effective detection plays a very important role.

Index Terms: Human motion detection, object detection, Classification, Subtraction method, Tread tracking system.

I. Introduction

Real time object detection is critical issue in embedded applications such as security surveillance and visual tracking operations. Image processing is one of the major key specification in real time applications for detecting normal and abnormal behavior of each user in video streaming. In this scenario the main challenge is to detect objects in convenient time interval without using any special hardware specifications in image processing and consuming a lot resources for development of this detection mechanism efficiently. One of the major effective techniques is background subtraction technique.

When a new image is captured, the difference between the image and background model is computed for moving object detection. In this paper we introduce to develop a new video surveillance system model for detecting human categorization effectively. Moving object detection is widely used in real time application development used in surveillance process generation such as transportation with security systems and video monitoring systems efficiently. Moving object detection is the main challenge in real time visualization system applications. The overall performance of these techniques can be discussed in experimental setup and proposed process generation in real time applications for detecting moving objects. Existing technologies of moving object detections does not give a normal and abnormal behavior of the users in realistic data event generation. Our experimental result show efficient process in moving object categorization in video surveillance.

The automatic approach to analyze and detect suspicious behavior will help to quickly and efficiently detect any such abnormal activity and may even provide warning before the occurrence of any big casualty. This is motivation behind implementation of new system. In this paper first introduction given about motion detection of object. Then after that discussed previous work about different method used for motion detection of object. Then explained how effective background subtraction method used for motion detection. After that the demerits of old surveillance system overcome in implemented surveillance system. Then discussed experimental result with algorithm and observation table of centroid movement with treading track and finally explored conclusion along with future scope.

II. Previous Work

2.1 Frame Subtraction Method

In the frame difference, or Frame Subtraction method detect moving objects by calculating the differences between pixels in consecutive frames of a video sequence, as well as extracts the motion regions by the threshold of time difference in adjacent frames pixels. Although frame Subtraction approaches are adaptive to environments with sudden illumination change, some relevant pixels cannot be extracted, this results in holes inside moving entities. The advantages of this method are the insensitive to the change of light, fast background update, good adaptive performance, its calculation is simple and easy to implement. For a variety of dynamic environments, it has a strong adaptability.

2.2 Optical Flow Method

In Optical flow method, firstly it will calculate the image optical flow field, and according to the optical flow distribution characteristics of image it will do clustering processing. It suits for the static as well as dynamic background. This method can get the absolute motion information and detect the moving object from the background better. It usually uses characteristics of flow-vectors over time to indicate moving regions in a video sequence. However, flow-vectors of moving objects only can be applied to illustrate streams of moving objects, thus detecting a sparse form of object regions.

2.3 Drawbacks of Existing Methods

- The Frame Subtraction is generally difficult to obtain a complete outline of moving object, responsible to appear the empty phenomenon; as a result the detection of moving object is not accurate.
- In Optical Flow method, a large quantity of calculation, sensitivity to noise, poor anti-noise performance, makes it not suitable for real-time demanding occasions. If used then special hardware is needed in real time processing.

III. Object Detection Using Background Subtraction

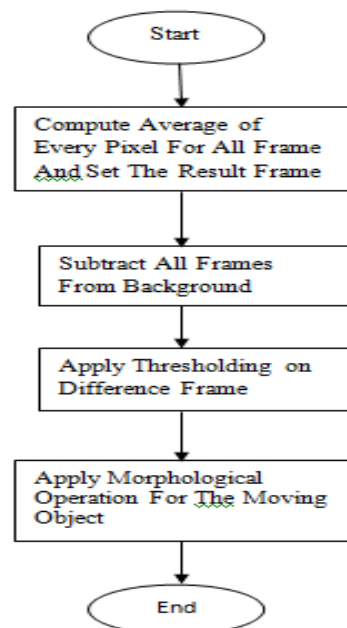


Fig.1 algorithm for background modeling method

Background subtraction method includes all the frames for computation. In this method all the pixel intensities for each and every frame are computed to get background frame. It takes difference between reference image and current image so accurate and sensitive. In this paper, we discuss a new surveillance system model for detecting moving object based on background subtraction method. This method is more accurate and sensitive than other two methods[1].

There are many challenges in developing a good background subtraction algorithm. First, it must be robust against changes in illumination. Second, it should avoid detecting non-stationary background objects and shadows cast by moving objects. A good background model should also react quickly to changes in background and adapt itself to accommodate changes occurring in the background.

IV. Video Surveillance System

This system is able to distinguish moving and stopped foreground objects from the static background scene, track the objects and detect the unusual activity. The first step is to separate foreground objects from stationary background. It use an adaptive background subtraction method and post-processing methods to make a foreground pixel representation at every frame[4]. Then do the grouping of connected regions in the foreground pixel map and object features such as bounding box and center of mass are calculated. Tracking is the next step after background subtraction. An object level tracking Algorithm is used in our video surveillance system. It can't track the object parts such as limbs of human, but track the object as a whole from frame to

frame. Final step is the unusual activity (abandoned object / human fall / person hiding) detection. This system uses a single camera view and unusual activity is detected using the background subtraction and object tracking result[6].

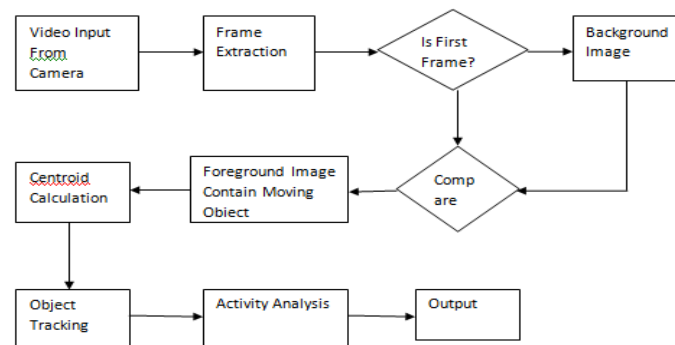


Fig.2 video surveillance system procedure for detecting object categorization

V. Experimental Results

5.1. Extracting Object Feature

5.1.1 Centroid

After segmentation of foreground regions, extracted the features of corresponding objects from the current image scene. These features are the size (S_i) and center of mass (C_e) of the object. In order to estimate the size of the object just calculate the number of pixels of foreground and to calculate the center of mass $C_e = (x_{Ci}, y_{Ci})$ of an object O , use the equation given in (1)[9].

$$x_{Ci} = \sum_{i=1}^k x_i / k, \quad y_{Ci} = \sum_{i=1}^k y_i / k \quad (1)$$

Where,

x_i is the location of white pixel on x Co-ordinate,

y_i is the location of white pixel on y Co-ordinate.

5.1.2 Treading Track

This system can use the background subtraction method to detect contour of person successfully, meanwhile, it can process irregular behavior recognition based on type of track which followed according to centroid movement of person accurately i.e. continuously changes or stable[10].

5.2 Activity Detection

5.2.1 Algorithm 1: Steps for detecting moving object analysis

Input: Video Streaming

Output: Object Tracking process when abnormal behavior accessing.

Step1: Read first frame as background image from recorded video.

Step 2: Convert it into gray.

Step 3: Assign previous_centroid= current_centroid.

Step 4: Read next frames from video.

Step 5: Convert it into gray.

Step 6: Find difference between background and current frame.

Step 7: Apply canny edge detection video.

Step 8: Apply dilation followed by holes filling operation on image.

Step 9: Label different isolated regions of image.

Step 10: Remove isolated areas which are lesser than area A.

Step 11: If two persons are found then copy only those 2 persons in separate image.

Step 12: Find centroid of both the persons.

Step 13: Track the centroid. If continuous change in centroid location is found then display message 'safe'.

Step 14: If irregular or abrupt translation of centroid is found then display message abnormal behavior'.

Step 15: Go to step 3.

5.2.2 Results of abandoning of bag by a person

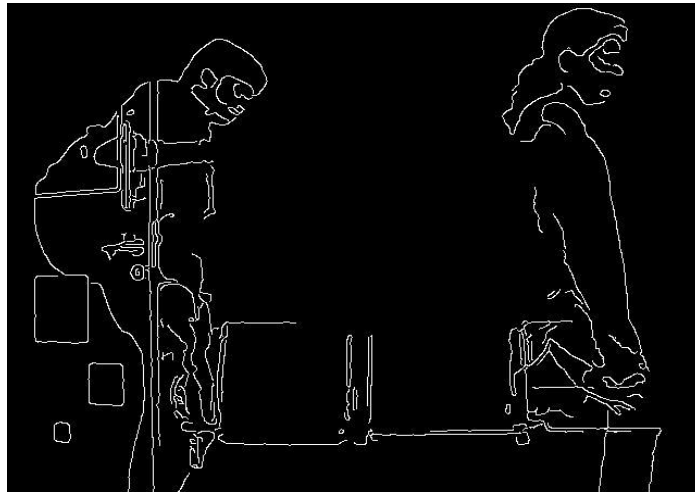


Fig.3 result of edge detected image



Fig.4 result of filled image



Fig. 5 result of final image

The abandoned or carried object detection process uses the output of the tracking model and features extraction as the input for each frame, and determines if they are abandoned or carried. The output of tracking step contains the number of objects, their identities. If the distance between the location of the centroid of the abandoned object or carried object and the person is greater than fixed value and increases continuously then unusual activity is detected.

From the observation of graph and Table1 frame no 50-75 we observe abnormal detection as difference for two corresponding frame is less than considered magnitude so that less difference count increases

and persons observed stable or doing some different from standard i.e. graph not changes continuously it was stable line which is irregular detection. Our method detects people in the target posture with a very low error rate. The few false positives still correspond to people but at some what inaccurate scales or orientations.

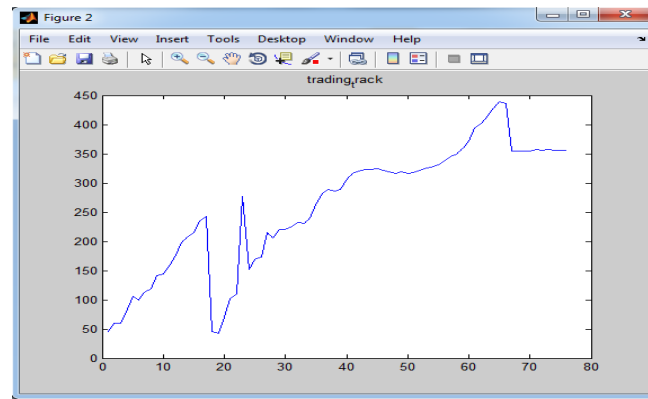


Fig.6 result of treading track image

Table.1 Result of activity detection

Frame No.	Centroid Variation	Observation	Result
58	317.104	0	Safe
59	320.7904	0	Safe
60	322.6346	0	Safe
61	323.3333	0	Safe
62	324.0833	1	Abnormal
63	321.4795	1	Abnormal
64	319.7225	1	Abnormal
65	317.0629	1	Abnormal
66	318.6056	1	Abnormal

VI. Conclusion

This method has also a very good effect on the elimination of noise and shadow, and be able to extract the complete and accurate picture of moving human body. In this proposed work static background considered but in future it can be improved for non-static background. System can be developed to distinguish human activities also human or nonhuman objects also face identification of human can be done.

REFERENCES

- [1] Lijing Zhang and Yingli Liang, "Motion human detection based on background Subtraction," Second International Workshop on Education Technology and Computer Science, IEEE Computer Science, vol.1, pp.284-287, Mar 2010.
- [2] Xiaofei Ji and Honghai Liu, "Advances in view-invariant human motion analysis: a review," IEEE Transactions on SMC PART C, vol.40, pp.13-24, Jan 2010.
- [3] Fan-chieh cheng, Shih-chia Huang, and Shanq- jang Ruan, "Illumination-sensitive background Modeling approach for accurate moving object detection," IEEE Transactions on Broadcasting, vol. 57, no. 4, pp.794-801, Dec 2011.
- [4] Jin-Bin Yang, Min Shi, and Qing-Ming Yi, "A New Method for Motion Target Detection by Background Subtraction and Update," International Conference on Medical Physics and Biomedical Engineering, 2012.
- [5] Shengyong chen, Jianhua Zhang, Youfu Li, and Jianwei Zhang, "A hierarchical model incorporating segmented regions and pixel descriptors for video background subtraction," IEEE Transactions on Industrial Informatics, vol.8, no. 1, pp.118-127, Feb 2012.
- [6] Prithviraj Banerjee and Somnath Sengupta, "Human Motion Detection and Tracking for Video Surveillance," pp.1-6, Apr 2008.
- [7] Sreedevi M, Yaswanth kumar Avulapati, Anjan babu G, and Sendhil kumar R, "Real Time Movement Detection for Human Recognition," WCECS, pp. 24-26, Oct 2012.
- [8] Eyup Gedikli and Murat Ekinci, "Human Motion Detection, Tracking and Analysis For Automated Surveillance," vol. 89, no. 10, Jan 2001.
- [9] R. Manikandan and R. Ramakrishnan, "Human Object Detection and Tracking using Background Subtraction for Sports Applications," International Journal of Advanced Research in Computer and Communication Engineering Vol.2, Issue 10, October 2013.
- [10] Ye Zhang and Zhi-Jing Liu, "Irregular Behavior Recognition Based On Treading Track," Proceedings of the 2007 International Conference on Wavelet Analysis and Pattern Recognition, vol.3, pp.1322-1326, Nov 2007.

To Study the mechanical properties of coconut coir fiber reinforced with epoxy resin AW 106 & HV 953 IN

Abdul Nazeer¹

Assistant Professor, Department of Mechanical Engineering, SECAB Institute of engineering and technology
Bijapur(Karnataka), INDIA

Abstract: In this study the Mechanical Properties of Coconut coir Fiber is reinforced with epoxy resin of different lengths (5mm,10mm,15mm) and coir fibers by treating the fiber with NaOH by fraction of 5 % are studied here. All samples were made using hand layup technique and specimens were prepared as per ASTM standard D3039. The samples were tested according to ASTM D3039 standard using Universal testing machine (UTM). The significant findings of the research showed that NaOH treatment improved the tensile properties, ductility and hardness of the composite further Increase in length of fibers was found to increase the tensile strength. The maximum tensile strength was found for 15 mm length of coir fibers.

Keywords: Coconut fiber, Composites, Sodium hydroxide treatment, Mechanical properties, mechanical testing

I. Introduction

Over a past few decade a lot research is going on composite material for replacement of existing engineering materials. The composite materials have grown rapidly to very high extent and replace almost all engineering materials. Today composite materials consist of many materials in day to day use and also being used in sophisticated applications while composites have already proven their worth as weight saving materials the current challenge is to make them durable in tough conditions to replace other materials and also to make them cost effective. Due to its light weight and low cost composite has given a way to industries.

Green coconuts, harvested after about twelve months on the plant, contain pliable white fibres. Brown fiber is obtained by harvesting fully mature coconuts when the nutritious layer surrounding the seed is ready to be processed into copra and desiccated coconut. Coconut trees are tall – commonly 25 meters high – and this fibrous layer around the seedpod is a strong shock-absorbing mesh that protects the seed from damage.

Composites: A definition A composite material is made by combining two or more materials to give a unique combination of properties, one of which is made up of stiff, long fibers and the other, a binder or 'matrix' which holds the fibers in place

Composites Properties: Natural fibres are now considered as a suitable alternative to glass fiber, due to their advantages, which include low cost, high strength-to-weight ratio, and recyclability. Combining natural fibres with glass fiber also decreases the usage of glass fiber. In this investigation, hybrid glass-/sisal-fiber composites were fabricated using the hand lay-up method.

Epoxy resins: Epoxy resins are characterized by the presence of more than one 1, 2- epoxide groups per molecule. Cross-linking is achieved by introducing curatives that react with epoxy and hydroxyl groups situated on adjacent chains

Reinforcement: The objective of the reinforcement in a composite material is to enhance the mechanical properties of the resin system. All of the distinct fibers that are used in composites have distinct properties and so affect the properties of the composite.

II. Experimental

The Coconut fiber (coir) and epoxy resin were selected for this project and fabricated according to the ASTM standard (D3039). As per the dimension the Coconut fiber and epoxy composite is manufactured with different lengths of fiber. The prepared specimens were tested by using Universal Testing Machine (UTM).

III. Materials

Preparation of the fiber: The Coconut Husk was dried under sunlight and fibers were extracted manually from the coconut husk. To ensure proper interaction between fiber and matrix material, the outer most wax layer of the coir was removed by soaking the coir in hot water.

Table 1: Physical Properties of Coir Fibres

Material Property	Values
Density	1.2g/cm ³
Elongation at break	30%
Youngs modulus	4-6 Gpa

Methods of preparation: There are two method one by treating the fibers with NaoH solution and another is directly using the coir fiber The prepared coir fibers were cut into short length fibers of about 5mm, 10mm, 15mm and divided into separate portions. One portion was chemically pretreated with alkali (NaOH). 5% NaOH was used to treat the fibers in a beaker for 24 hours. The fibers, were then washed in distilled water and finally dried. This was used to prepare the composite.

The second portion of the fibers was untreated, with different lengths of fibers(5mm,10mm &15mm).

Formulations According to ASTM Standards, we are making the mould box of 250×110×3 mm dimension. The mould box was made using Thermopolis as a base surface and plywood as the side boundary. Using Tape, the surface of the mould box was covered to prevent the leakage of the epoxy resin. The mould box is shown below



Fig 1:Mould Box fibers and resin mixture

Sample preparations

There are two types of methods we have used, they are

1. Treated Fibers

The solution of 5% aq. NaOH and 95% of water was prepared (100g NaOH and 2litre water). Fibers of 30g are soaked in the solution for 24 hours.



Fig 2:100g of NaoH



Fig 3:Fibers soaked in solution

After 24 hours, fibers were removed from solution and washed with distilled water 2 to 3 times to remove waste particles. These fibers were dried under the sunlight for 24 hours.



Fig 4:Dried Fibers

The fibers were then cut in different dimensions of 5, 10 and 15 mm in length. Here Epoxy Resin (Araldite AW 106 and Hardener HV 953 IN) was used. The mixture of Araldite and Hardener was prepared (91g Araldite and 39g Hardener). The fibers of 5 mm in length and weight 5g are added to the mixture and mixed well. The mixture was then poured into the mould box. The mixture was properly spread all over the mould box and proper surface finish was given. The mould box was kept at room temperature for 1 day to dry the mixture. After that, the specimen was removed from the mould box.

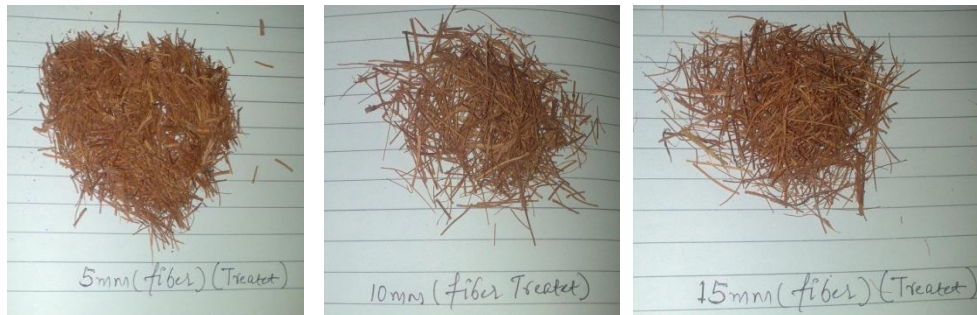


Fig 5: Different lengths of treated fibers



Fig 6:-Epoxy Resin and Hardener



Fig 7: Mould Box with treated fibers and resin mixture

After removing the specimen from mould box, it was cut as per the ASTM Standard D3039, that is 250×25×3 mm. From this mould box 4 specimen of 250×25×3 mm dimension were obtained as shown in figure below for each length of fiber for testing of all specimen and taking average value.

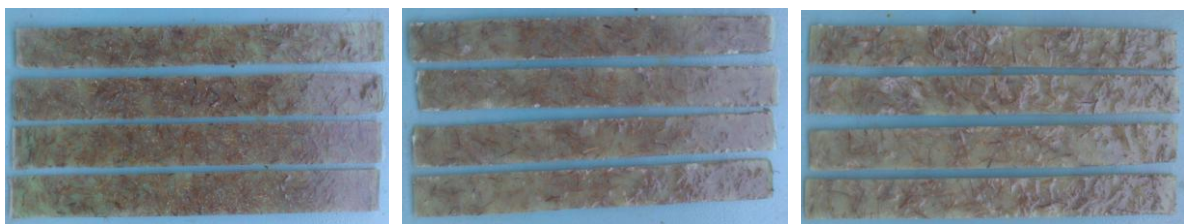


Fig 8: Specimens Treated fibers

2. Un-Treated Fibers

The fibers were directly extracted from coconut husk which are already dried. According to the ASTM Standard D3039, a mould box was prepared of dimension 250×110×3 mm. The fiber length of 5, 10 and 15 mm cut and mixed with Epoxy resin and Hardener. The mixture was then poured inside the mould box and spread. The mixture in the mould box was dried for 24 hours and then the specimen was removed. The specimen was further cut as per ASTM Standard D3039. 4 specimens were obtained of dimension 250×25×3 mm.



Fig 9: Mould Box with Un-Treated fibers and resin mixture



Fig 10: Specimens of 5 mm length



Fig 11: Specimens of 10 mm length



Fig 12: Specimens of 15 mm length

Testing

The prepared specimen were fixed in the UTM machine for tensile test. After fixing the specimen in the UTM, load was applied on the specimen. The load is applied gradually on the specimen. For every 5 division (0.2 kN), note down the corresponding deflection until the specimen breaks.



Fig 13: Testing of Specimen

IV. Result And Discussion

Treated Fibers

The table below shows the deflection of composite specimen for different lengths of fibers, and its the variation of deflection with respect to different loads.

Table:1 Different loads and deflection readings for treated fibers

5mm length of fiber		10 mm length of fiber		15 mm length of fiber	
LOAD kN	Deflection (mm)	LOAD kN	Deflection (mm)	LOAD kN	Deflection (mm)
0.2	0.5	0.2	0.5	0.2	0.5
0.4	0.75	0.4	0.75	0.4	0.75
0.6	1	0.6	1	0.6	1
0.8	1.9	0.8	3.25	0.8	3.19
1	2.9	1	3.65	1	4
1.2	3.75	1.2	4.25	1.2	5.25
1.4	4.4	1.4	5.65	1.4	6.25
1.6	5	1.6	6.5	1.6	6.8
1.8	5.3	1.8	7.5	1.8	7.4
2	5.65	2	8.25	2	8
2.2	6.4	2.2	8.65	2.2	8.55
2.4	7.13	2.4	9.15	2.4	9
		2.6	9.65	2.6	9.75
				2.8	10.25
				3	10.79

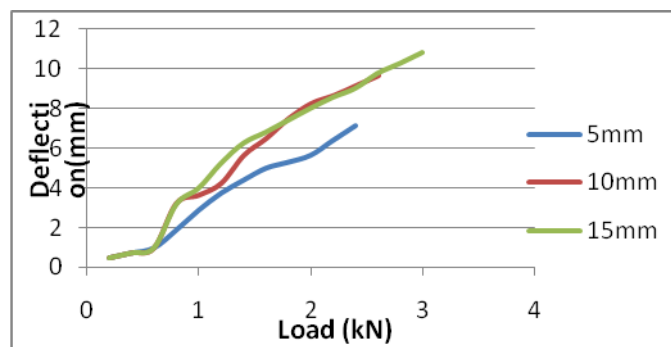


Fig 14: The graph of load versus deflection of the corresponding table

The graph shows the comparison of deflection with different lengths of fiber. It is observed that initially between the load of 0.2kN to 0.6 kN the deflection remains same for all three lengths of fiber. Further increase in load the deflection increases with respect to increase in length of fiber. It is observed that the maximum deflection occur at fiber length of 15mm. the deflection also increases until the break point of specimen is reached. As shown in graph, as we increase the length of fibers in the composite (5-15 mm), deflection also increases.

For 5 mm length of fibers in the composite, the ultimate load was 2.4 kN and the corresponding deflection was 7.13 mm. For 10 mm length of fibers in the composite, the ultimate load was 2.6 kN and the corresponding deflection was 9.65 mm. For 15 mm length of fibers in the composite, the ultimate load was 3 kN and the corresponding deflection was 10.79 mm. With this it is concluded that with increasing the length of fiber the deflection also increases.

Table 2: Table below shows the tensile strength of composite for different length of fibers are

5 mm length of fibers	10 mm length of fibers	15 mm length of fibers
Tensile Strength	Tensile Strength	Tensile Strength
3.2	3.2	3.2
6.4	6.4	6.4
9.6	9.6	9.6
12.8	12.8	12.8
16	16	16
19.2	19.2	19.2
22.4	22.4	22.4
25.6	25.6	25.6
28.8	28.8	28.8
32	32	32
35.2	35.2	35.2
38.4	38.4	38.4
	41.6	41.6
		44.8
		48

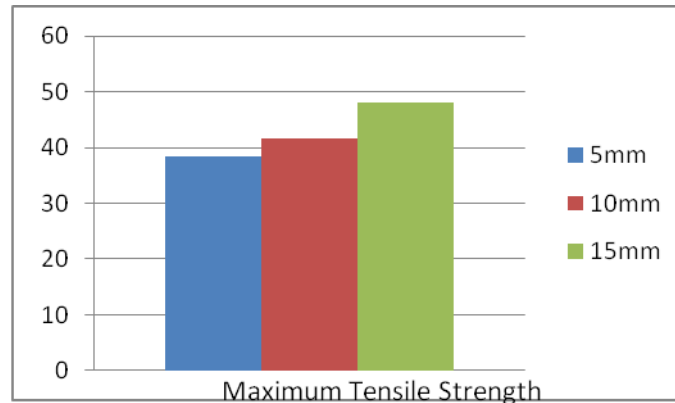


Fig 15: Figure shows the compression of tensile strength by varying the length of fiber

From the figure it can be seen as the length of fiber increases the tensile strength of the composite material is also increases.

Untreated Fibers

The fibres were directly extracted from coconut husk which are already dried. According to the ASTM Standard D3039, a mould box was prepared of dimension 250×110×3 mm. The fibre length of 5, 10 and 15 mm cut and mixed with Epoxy resin and Hardener, also mixed well. The mixture was then poured inside the mould box and spread. The mixture in the mould box was dried for 24 hours and then the specimen was removed. The specimen was further cut as per ASTM Standard D3039. 4 specimens were obtained of dimension 250×25×3 mm.

Table 3: Table shows Different loads and deflection readings for Un-Treated fibers

5mm length of fibers		10 mm length of fibers		15 mm length of fibers	
LOAD kN	Deflection (mm)	LOAD kN	Deflection (mm)	LOAD kN	Deflection (mm)
0.2	0.5	0.2	0.5	0.2	0.5
0.4	1	0.4	0.75	0.4	0.75
0.6	1.75	0.6	1	0.6	1
0.8	2.5	0.8	2.15	0.8	2.5
1	3.25	1	3.5	1	3.5
1.2	3.75	1.2	4.75	1.2	4.25
1.4	4.25	1.4	5.25	1.4	4.75
1.6	4.75	1.6	6	1.6	5.25
1.8	5.25	1.8	6.65	1.8	5.65
2	6	2	7.25	2	6.1
2.2	6.3	2.2	8	2.2	6.5
2.4	6.8	2.4	8.3	2.4	7.25
		2.6	8.8	2.6	7.9
				2.8	8.5
				3	9

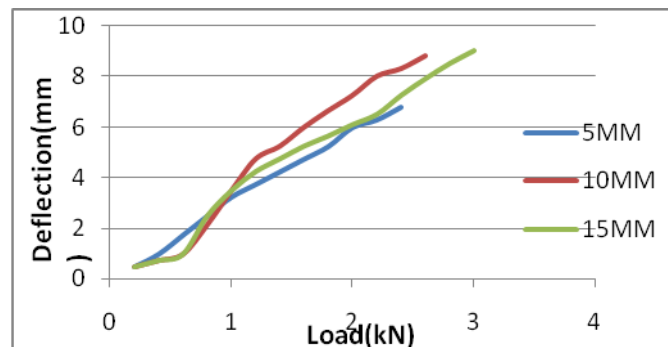


Fig 16: It shows the load versus deflection for different lengths of fiber

From the graph it is observed that the deflection of untreated fiber is same as treated fiber. The graph shows the comparison of deflection with different lengths of fiber. It is observed that initially at the load of

0.2kN the deflection remains same for all three lengths of fiber. Further increase in load the deflection increases with respect to increase in length of fiber. It is observed that the maximum deflection occur at fiber length of 15mm. For 5 mm length of fibers in the composite, the ultimate load was 2.4 kN and the corresponding deflection was 6.8 mm. For 10 mm length of fibers in the composite, the ultimate load was 2.6 kN and the corresponding deflection was 8.8 mm. For 15 mm length of fibers in the composite, the ultimate load was 3 kN and the corresponding deflection was 9 mm. With this it is concluded that the deflection is more for treated fiber than untreated fiber. As it is treated with NaoH the ductility of fiber increases which increases the deflection.

Table 4: Table shows the tensile strength for different lengths of Un-Treated fibers

5 mm length of fibres	10 mm length of fibres	15 mm length of fibres
Tensile Strength	Tensile Strength	Tensile Strength
3.2	3.2	3.2
6.4	6.4	6.4
9.6	9.6	9.6
12.8	12.8	12.8
16	16	16
19.2	19.2	19.2
22.4	22.4	22.4
25.6	25.6	25.6
28.8	28.8	28.8
32	32	32
35.2	35.2	35.2
38.4	38.4	38.4
	41.6	41.6
		44.8
		48

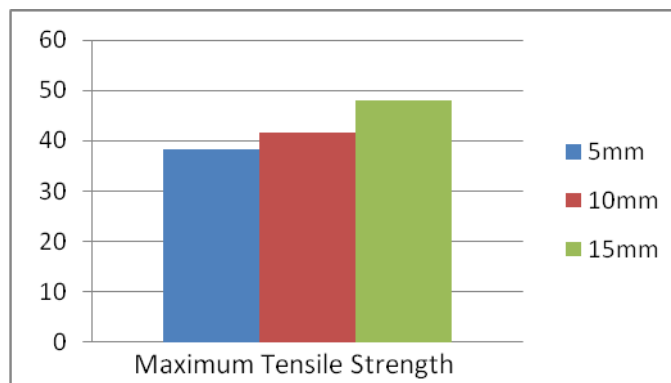


Fig17: Figure shows the compression of tensile strength by varying the length of fiber

Table 5: Comparison between Treated and Un-Treated Fiber Composite

	5mm				10mm				15mm		
Load	Treated	Untreated		Load	Treated	Untreated		Load	Treated	Untreated	
0.2	0.5	0.5		0.2	0.5	0.5		0.2	0.5	0.5	
0.4	0.75	1		0.4	0.75	0.75		0.4	0.75	0.75	
0.6	1	1.75		0.6	1	1		0.6	1	1	
0.8	1.9	2.5		0.8	3.25	2.15		0.8	3.19	2.5	
1	2.9	3.25		1	3.65	3.5		1	4	3.5	
1.2	3.75	3.75		1.2	4.25	4.75		1.2	5.25	4.25	
1.4	4.4	4.25		1.4	5.65	5.25		1.4	6.25	4.75	
1.6	5	4.75		1.6	6.5	6		1.6	6.8	5.25	
1.8	5.3	5.25		1.8	7.5	6.65		1.8	7.4	5.65	
2	5.65	6		2	8.25	7.25		2	8	6.1	
2.2	6.4	6.3		2.2	8.65	8		2.2	8.55	6.5	
2.4	7.13	6.8		2.4	9.15	8.3		2.4	9	7.25	
				2.6	9.65	8.8		2.6	9.75	7.9	
								2.8	10.25	8.5	
								3	10.79	9	

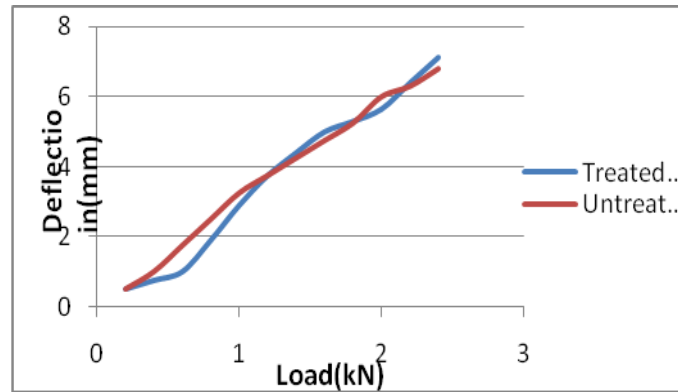


Fig 18: figure shows the compression for load versus deflection for treated and untreated 5mm length of fiber

From the above Figure we observe that, As we increase the load, deflection also increases. The blue line in the graph represents the treated fibers of length 5 mm and the red line in the graph represents the untreated fibers of length 5mm. The deflection obtained from treated fibers specimen was 7.13 mm, while the deflection from untreated fibers specimen was 6.8 mm.

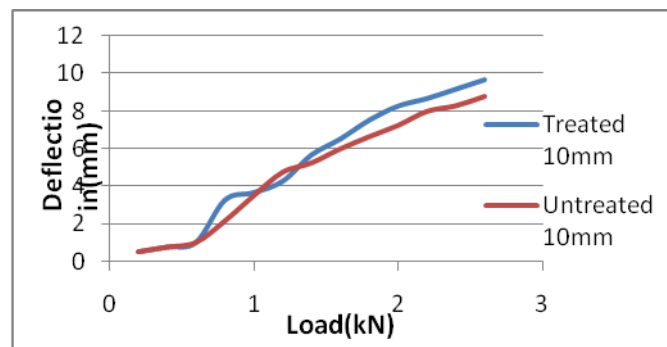


Fig 19 Comparison between Treated and Un-Treated Fiber Composite (10 mm)

From the above Figure we observe that, As we increase the load, deflection also increases. The blue line in the graph represents the treated fibers of length 10 mm and the red line in the graph represents the untreated fibers of length 10 mm. The deflection obtained from treated fibers specimen was 9.65 mm, while the deflection from untreated fibers specimen was 8.8 mm. which indicates that the ductility of fiber is increased when it is treated with NaoH solution.

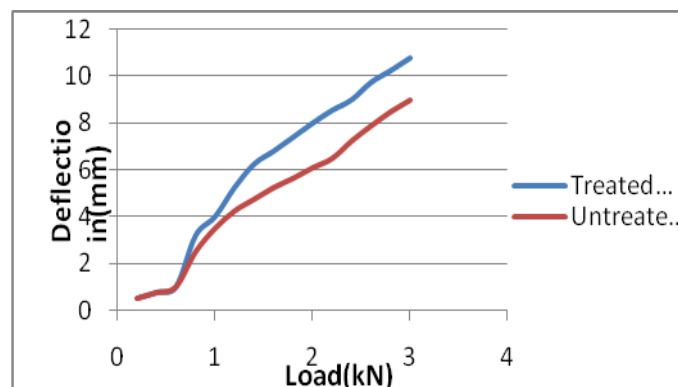


Fig 20: Comparison between Treated and Un-Treated Fiber Composite (15 mm)

From the above Figure we observe that, As we increase the load, deflection also increases. The blue line in the graph represents the treated fibers of length 15 mm and the red line in the graph represents the untreated fibers of length 15 mm. The deflection obtained from treated fibers specimen was 10.79 mm, while the deflection from untreated fibers specimen was 9 mm.

Table 6 Properties of composite for various length of treated fibers

Treated				
Sl.No	Property	5mm	10mm	15mm
1	Density(kg/m ³)	1557.7	2048	1934.8
2	Tensile Strength(Mpa)	38.4	41.6	48
3	Youngs Modulus(Mpa)	1346.4	1077.7	1112.4
4	Tensile Strain at break	0.02852	0.0386	0.04316
5	Extension at break(mm)	7.13	9.65	10.79
6	Load at Break(N)	2400	2600	3000

Table 7 Properties of composite for various length of un-treated fibers

UNTreated				
Sl.No	Property	5mm	10mm	15mm
1	Density(kg/m ³)	13953.2	1446.4	1779.2
2	Tensile Strength(Mpa)	38.4	41.6	48
3	Youngs Modulus(Mpa)	1411.765	1181.818	1333.333
4	Tensile Strain at break	0.0272	0.0352	0.036
5	Extension at break(mm)	6.8	8.8	9
6	Load at Break(N)	2400	2600	3000

The above two tables shown gives the mechanical properties of the composite like Density, Tensile strength, Young's modulus, Tensile strain at break, Extension at break and load at break for treated and un-treated coir fibers.

V. Conclusion

- The mechanical properties of polyester composites reinforced with coir fiber have been studied and discussed here. The following conclusions can be drawn from the present study. Here, we have used randomly discontinuous fiber layout in the composite, so that the ratio of fibers in the composite is high.
- This investigation shows that increase in length of fiber increases the tensile strength.
- The NaOH treatment on coir fiber would remove the impurity and rougher fiber surface may result after treatment. This would increase the adhesive ability of the coir fiber with the matrix in the fabricated composite resulting in good tensile strength.
- The treated fiber have better reinforcing property than un-treated fiber.
- It is observed that the tensile strain at break for treated fibers is more than un-treated fibers, which shows deflection of treated fibers is more than un-treated fibers, which conclude that by treating the fibers with NaOH increase the property of ductility.
- It is observed that by changing the length of fibers the mechanical property of the composite changes increase in length of fiber increase the mechanical property.
- The investigation resulted that if the fibers are treated, then the extension of composite at break is more than un-treated fibers and extension of composite increases with increase in fiber length.
- The load at break increases with increase in fiber length

Acknowledgements

Authors wish to acknowledge the Thanks to Mohammed Yaseen, Khatri G. Ahmed, Khatri G. Mohammed, Lakdawala Amir Hamza for there help in extracting fibers and performing the experimental tests.

REFERENCES

- [1]. **Aireddy, H., Mishra, S.C.**, Tribological behaviour and mechanical properties of bio waste reinforced polymer Matrix composites, J. metal. And Mater. Sci., 53(2) (2011) 139-152.
- [2]. **Jia Yao, Yingchang Hu, Wen lu**, Performance Research On Coir Fiber And Wood Debris Hybrid Boards. *BioRes.* 7 (3)(2012) 4262-4272.
- [3]. **Mazan, S., Zaidi, A.M., Ahmad, Arsat N., Hatta, M.N.M, Ghazali, M.I**, Study on sound absorption properties of coconut coir fiber composite with added recycled rubber, *Inter. J. of integ. engg.* 2(1) (2010) 29-34.
- [4]. **Slate, F. O. (1976)**. "Coconut Fibers In Concrete." *Eng J Singapore*, 3(1), 51-54.
- [5]. **Geethamma, V.G, Kalprasad, G, Thomas Sabu**, dynamic mechanical behaviour of short coir fiber reinforces natural rubber composite, *Elseveir compos. part A* ,36(11) (2005) 1495-1506.
- [6]. **Reis, J. M. L. (2006)**. "Fracture and flexural characterization of natural fiber-reinforced polymer concrete." *Construction and Building Materials*, 20(9), 673-678.
- [7]. **Misra, R. K., Kumar, S., Misra, A.**, some experimental and theoretical investigation on fire retardant coir/ epoxy micro-composites. *J. thermoplas. Compos. Mater.* 21(1) (2007) 1-32.
- [8]. **Almeida, J.R.M.D, Monterio, S.N, Terrones, L.A.H**, Mechanical properties of coir/polyester composites, *Elseveir Polym. Test.*, 27 (5) (2008) 591–595.
- [9]. **Bujang, I.Z., Awang, M.K, Ismail, A.E**, study on dynamic characteristics of coconut fiber reinforced composites, *Regional Conference on Engineering Mathematics, Mechanics, Manufacturing & Architecture*, (2007) 185-202.
- [10]. **Li Z, Wang L, Wang X**, Flexural characteristics of coir fiber reinforced cementitious composites. *Fibers Polym.*, 7(3) (2006) 286-294.

Damage Tolerance Evaluation for Wing Structure with Large Cutout

Sukeerth D A¹, Thammaiah Gowda²

¹(PG student Department of mechanical engineering, AIT, Chikmagalur, VTU, Karnataka, India)

²(Professor Department of mechanical engineering, AIT, Chikmagalur, VTU, Karnataka, India)

Abstract: Damage tolerance evaluation of a wing box with large cutout in the bottom skin is carried out in steps. Stress analysis is first carried out to identify the critical location for fatigue crack initiation. A local analysis is carried out to obtain more accurate stress value and the distribution of stress. Finite element method is adopted for stress analysis and damage tolerance evaluation. Damage tolerance evaluation includes the stress intensity factor calculations at crack tip. This is carried out by simulation of the crack in the finite element model. Stress intensity factor (SIF) at different crack lengths is calculated using Modified Virtual Crack Closure Integral (MVCCI) method.

Keywords: Damage Tolerance Evaluation, Finite Element Method, Wing box, SIF, MVCCI method.

I. INTRODUCTION

Wings are the lift generating components in the airframe structure. Wings are also used as fuel tanks in the transport aircraft. Cutouts are provided in the bottom skin of the wing to permit entry into the airplane fuel tanks for inspection or component repair. Bottom skin is under tension stress field during flight. Cutouts in the bottom skin will act as stress risers due to stress concentration effect. The high tensile stress locations are the most probable locations of fatigue cracking in the structure. The damage tolerance design philosophy says that cracks are allowed in the structure, but the cracks should not lead to catastrophic failure of the structure. The damage-tolerance evaluation of structure is intended to ensure that should fatigue, corrosion, or accidental damage occur within the LOV (Limit of validity) of the airplane, the remaining structure can withstand reasonable loads without failure or excessive structural deformation until the damage is detected [1].

In the damage tolerance design philosophy the safety is ensured by inspection. Identification of the critical locations in the structure is most important to ensure the safety of the structure throughout the service life of the structure. Aircraft designer needs to ensure the structural integrity of the airframe without compromising on the safety of the structure. This would be possible only by adopting the damage tolerance design principles. The current project includes the stress analysis of a wing box of a medium size transport aircraft having large cutout in the bottom skin to identify the critical location for fatigue crack initiation. The aircraft under consideration is a conceptual Light Transport Aircraft. A local analysis is followed to obtain more accurate stress value and the distribution of stress. Aluminium alloy 2024-T351 Material is used for the wing box. Finite element method is adopted for stress analysis of the structural components. MSC NASTRAN and MSC PATRAN FEM packages are used to carry out the analysis. The maximum stress location is found from the wing box FE model (Global analysis). Damage tolerance evaluation includes the stress intensity factor calculations at crack tip. This is carried out by simulation of the crack in the finite element model of the bottom skin of the wing (Local analysis). Stress intensity factor (SIF) at different crack lengths is calculated using Modified Virtual Crack Closure Integral (MVCCI) method. The SIF calculated at every crack length is compared with the fracture toughness of the material. Variation of SIF as a function of crack length is plotted.

II. LITERATURE SURVEY

Damage tolerance philosophy is a refinement of the fail-safe philosophy. It assumes that cracks will exist, caused either by processing or by fatigue, and uses fracture mechanics analyses and tests to determine whether such cracks will grow large enough to produce failures before they are detected by periodic inspection. Three key items are needed for successful damage-tolerant design: residual strength, fatigue crack growth behaviour, and crack detection involving non-destructive inspection. Of course, environmental conditions, load history, statistical aspects, and safety factors must be incorporated in this methodology.[2]

The recent Air Force requirement to apply linear elastic fracture mechanics approach in damage tolerance design of aircraft structures, warrants the critical review of various approaches. Pir M. Toor [3] has critically reviewed some damage tolerance design approaches and their application to aircraft structures. The

paper consists of three main sections: The first section reviews the residual strength analysis methodology, assumptions and limitations of each method are discussed through a simple example. The second part surveys the various crack propagation laws, including linear and non-linear ranges and spectrum loading effects. In the third and last section, fracture mechanics methodology is applied to several types of built-up structural components under spectrum loading conditions. The comparison of test results and analysis of complex structures indicate that simple methods of fracture mechanics can be applied to find the damage tolerant strength and rate of crack growth.

The measurement of energy release rates using virtual crack extensions was made using finite element techniques by T.K. Hellen [4]. Finite element techniques were presented for the accurate determination of stress intensity factors for brittle materials, and for estimating the direction of crack propagation in multi-mode loading systems. The techniques utilized energy differences over small changes in crack length, and used in conjunction with high order elements and special crack tip elements gave very accurate results. Alternatively, to obtain results of engineering accuracy, much coarser finite element meshes can be used than previously, reducing computer costs and data manipulation time. The method also enhanced the feasibility of three-dimensional analysis, where traditional methods required such mesh refinements along crack profiles as to be prohibitive under the computer limitations in 1970's.

An efficient technique for evaluating stress intensity factors using the Finite Element approach is presented by E. F. Rybicki and M. F. Kanninen [5]. The method, based on the crack closure integral, can be used with a constant strain finite element stress analysis and a coarse grid. The technique also permits evaluation of both Mode I and Mode II stress intensity factors from the results of a single analysis. In their work example computations are performed for a double cantilever beam test specimen, a finite width strip with a central crack, and a pin loaded circular hole with radial cracks. Close agreement between numerical results given by this approach and reference solutions were found in all cases.

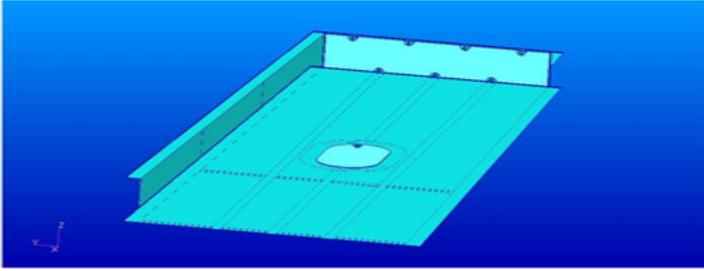
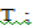


The methodologies for damage tolerant evaluation of stiffened panels under fatigue loading are presented by A Rama Chandra Murthy et al. [6]. The two major objectives of damage tolerant evaluation, namely, the remaining life prediction and residual strength evaluation of stiffened panels have been discussed in the paper. Concentric and eccentric stiffeners have been considered. MVCCI method is adopted for SIF calculations. From the studies, it has been observed that the predicted life is significantly higher with concentric and eccentric stiffener cases compared to the respective unstiffened cases. The percentage increase in life is relatively more in the case of concentric stiffener compared to that of eccentric stiffener case for the same stiffener size and moment of inertia.

Case studies on finite element based computation of strain energy release rate by modified crack closure integral were presented by R. Sethuraman and S.K. Maiti [7]. A modified crack closure integral method with square-root stress singularity elements is given for calculation of strain energy release rate for an in-plane extension of a crack. Case studies were presented to illustrate the improvement in accuracy. Results of case studies on a centre crack, an edge crack and a kinked crack were given to illustrate the effectiveness of the scheme.

III. ANALYSIS OF WING BOX

The wing box under consideration has a capsule shaped Fuel Access cutout in the bottom skin. The total span of the wing is 19330mm. The wings of the aircraft are attached at the bottom of the fuselage making it a Low-wing aircraft. Length of one whole wing is 9665mm. The wing box considered for analysis is 2388mm long and 2400mm away from the wing root. The wing box consists of 2 spars, 4 ribs, 3 stringers in the bottom skin and 4 stringers in the top skin.

Table1. Geometrical details of wing box

 <p align="center">Fig. 3.1 Wing box (global model)</p>	<p>Wing box length = 2882mm. Width of skin near at the root end= 1800mm. Width of skin near the free end = 1200mm. Thickness of bottom skin = 2.5mm. Cross-section of stringers-  Thickness = 1.5mm. Cross-section of ribs -  Thickness = 1.5mm. Cross-section of spar -  Thickness tapered - 2.75mm to 2mm from root end to free end. Rivets used dia- 5mm; Material used Al 2024 T351 alloy.</p>
---	---

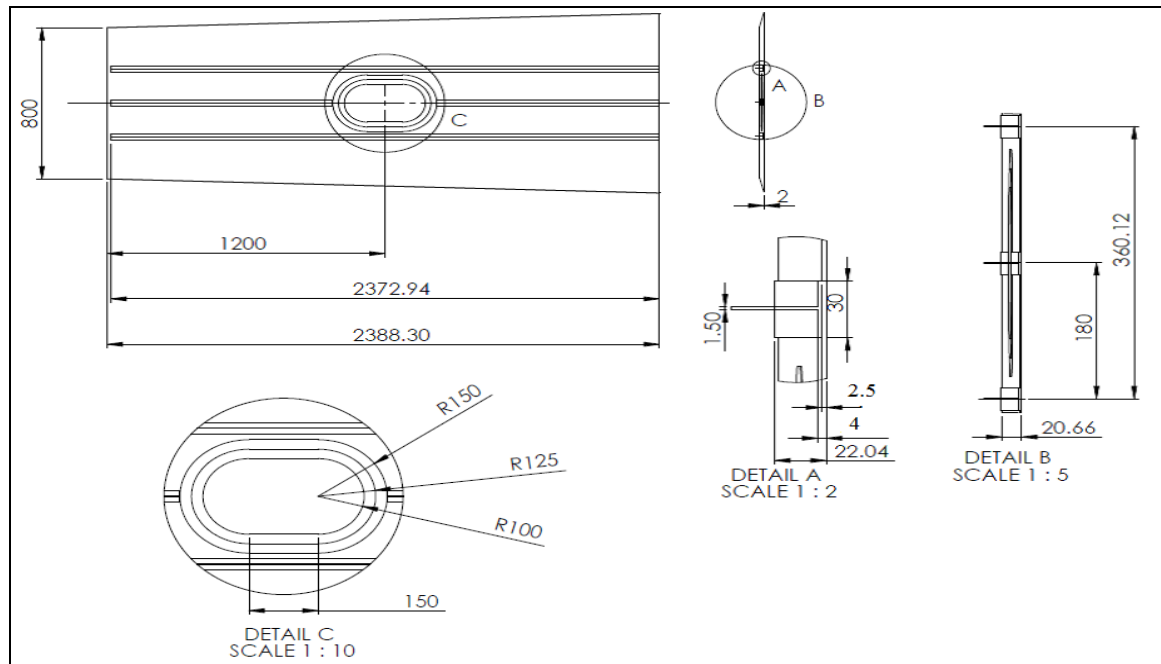


Fig.3.2 Bottom skin of wing box

3.1 Meshing

The CATIA model is imported and meshed in MSC PATRAN. The components other than rivets are meshed using 2D SHELL elements. The rivets are created using 1D BEAM elements. The quality of mesh is maintained so as to get the accurate value of stress. The meshed model of the wing box is shown in fig.3.3.

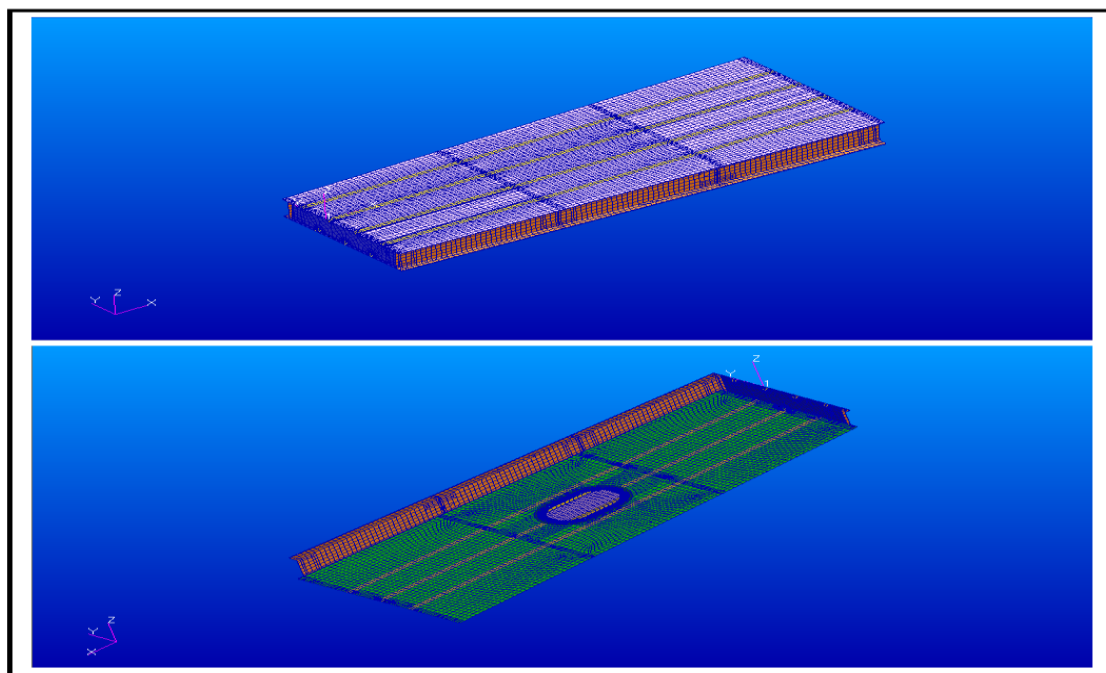


Fig.3.3 Meshed model of the wing box (global model)

3.2 Boundary Conditions (Wing box)

The wing can be treated as a cantilever beam with a tip load. The wing box root end can be considered as fixed end and the wing box tip end can be considered as free end. All six degrees-of-freedom of the free nodes at the wing box root end are constrained making it the fixed end. The aircraft is designed for 3g conditions to withstand loads thrice its weight. For 3g condition the aircraft is designed to withstand 10000kgf or 98100N. 80% of the lift load is taken by the wings. Hence one wing takes 40% of the lift load. In this case

40% of lift load is 40% of 10000, i.e., 4000kg or 39240N. The tip load is deduced using aerodynamic data called span factor and load factor. The tip load for the wing box is found to be 2384.109kgf or 23388.109N. This tip load is uniformly distributed over the perimeter of the wing box. The perimeter of wing box at the tip being 1730mm, the resultant tip load is converted to equivalent 'edge loads' (for application of load in PATRAN) by dividing the resultant tip load by the perimeter of the tip of wing box. The resulting edge load that is applied throughout the perimeter of the free end of wing box in PATRAN is 1.378kg/mm or 13.519N/mm.

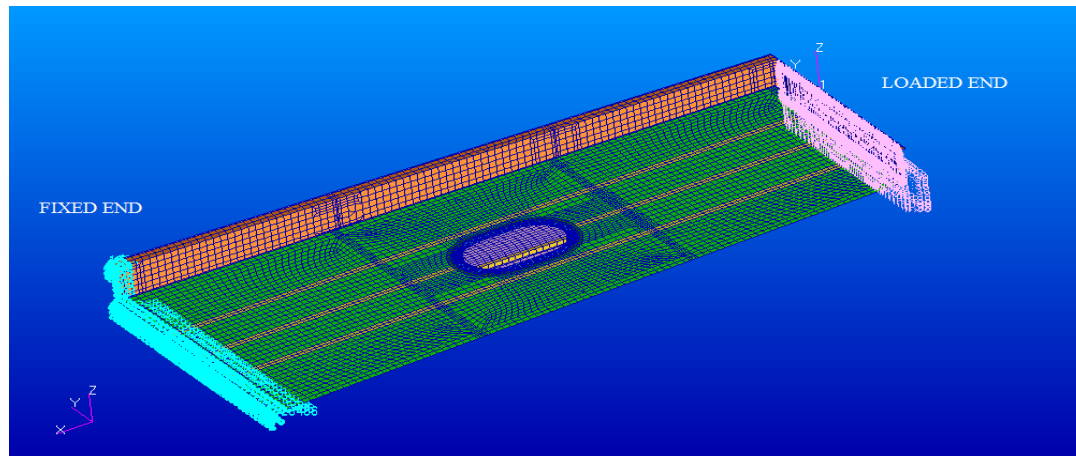


Fig.3.4 Boundary conditions of wing box (global model)

3.3 Maximum Stress in wing box

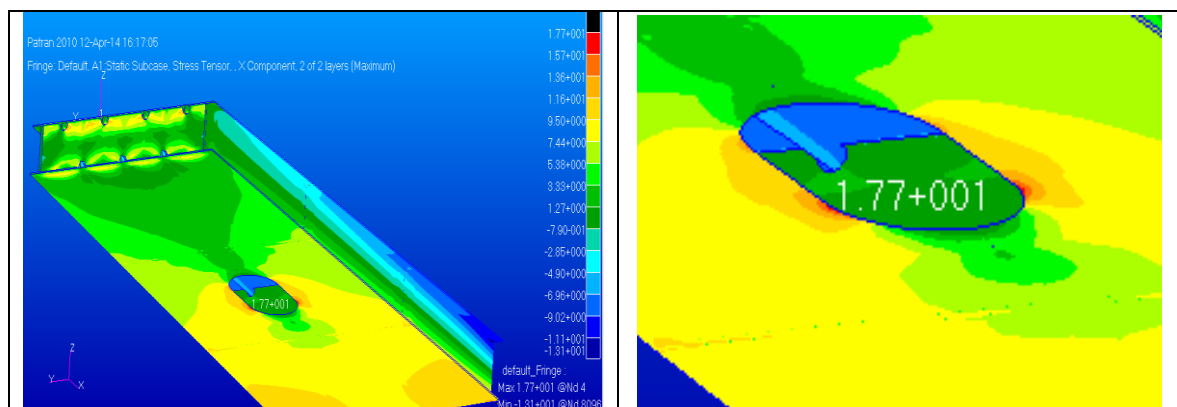


Fig.3.5 Maximum stress in wing box (global model)

The location of maximum stress in the wing box is marked in red fringes in figure. The stress is maximum in the bottom skin near the cutout. The value of stress is 17.7kg/mm² or 173.637N/mm².

3.4 Local Model

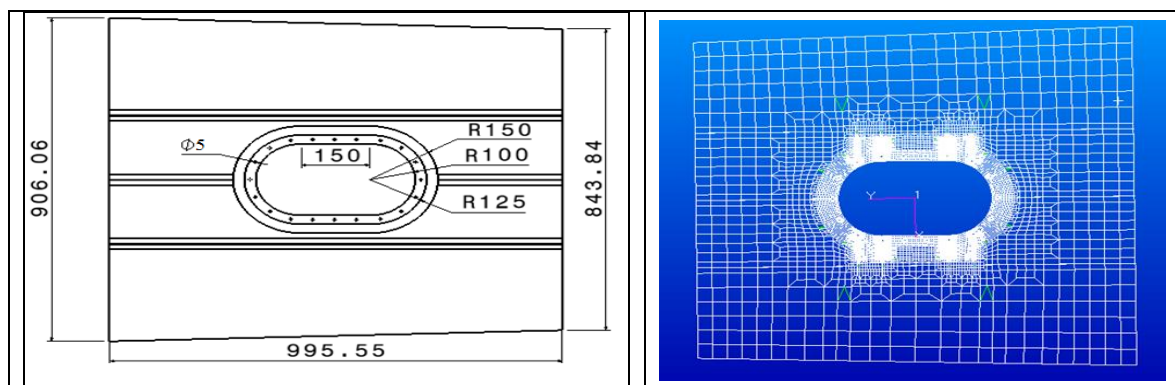


Fig.3.6 Geometry of local model; FE Model of local model

3.5 Boundary Conditions (Local model)

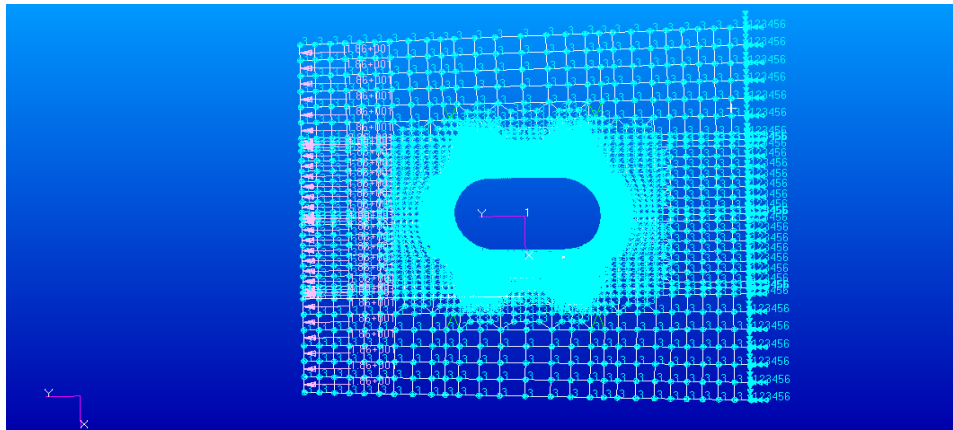


Fig.3.7 Boundary conditions of local model

The boundary conditions for the local model which is a segment of the bottom skin of the wing box can be deduced from the cantilever beam analogy. It is a well-known fact that when a cantilever beam is subjected to a tip load in the upward direction, the fibers in the bottom of the beam, i.e, the fibers below the neutral axis is under tension. The bottom most fibers experience the maximum tensile stresses whereas the top most fibers are under compression. The wing box can be considered as a cantilever beam with an upward load at the free end. Thus the bottom skin is under tension and the top skin is under compression. Hence the boundary condition for the local model can be considered as fixed at one end (near wing root) and tensile load acting on the other end (wingtip end). Also the translation in 'z' direction is constrained in order to ensure the application of pure tensile load. The loads can be summarized as follows:

Edge load on skin = 18.606 kg/mm = 182.52N/mm

Edge load on stringer's flange = 18.606 + 9.997 = 28.603 kg/mm= 280.60 N/mm

Edge load on stringer's web = 9.997 kg/mm = 98.07N/mm

3.6 Maximum stress in local model

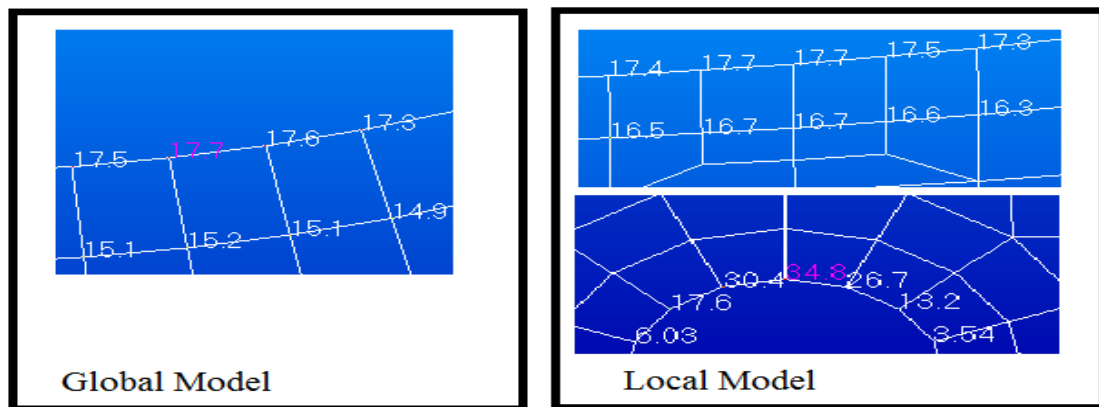


Fig.3.8 Comparison of stress values from global and local model

The figure 3.8 shows the Maximum stress induced in the global model (17.7 kg/mm²) with a different colour in the global model box. The stress is replicated in the local model as we can see in the local model box at the same location in capsule cutout (top picture in local model box). The local model box in the figure also shows the maximum stress induced in the rivet hole. Thus the maximum stress in the local model is 34.8 kg/mm² i.e, 341.388 N/mm² (MPa). The location of this maximum stress is in a rivet hole near to the fixed end. Precisely at the rivet hole near the point, where the curvature of the semi-circle portion of the capsule cutout changes to zero. In other words, the point where the semi-circular curvature of the capsule cutout starts becoming a straight line. This is location where the initiation of a fatigue crack is most imminent.

3.7 MVCCI

Modified Virtual Crack Closure Integral (MVCCI) is a finite element based computation of strain energy release rate. By knowing the strain energy release rate we can calculate the Stress Intensity Factor (SIF). Using the MVCCI method, the SIF is calculated as follows:

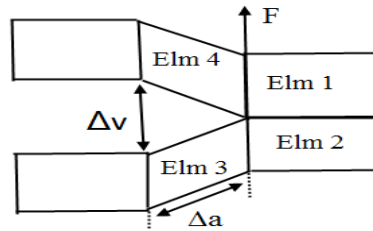


Fig.3.9 Nomenclature for MVCCI method

Stress Intensity Factor (SIF) $K = \sqrt{G \times E}$

Where,

G is the strain energy release rate, E is the Young's modulus

The strain energy release rate, 'G' is calculated by the formula:

$$G = \frac{1}{2 \Delta a} \times \Delta v \times \frac{F}{t}$$

Where,

G = Strain energy release rate, Δa = elemental edge length at crack tip, Δv = differential displacement of opening node, F = grid point force at crack tip, t = thickness of plate at crack tip

3.8 SIF calculations

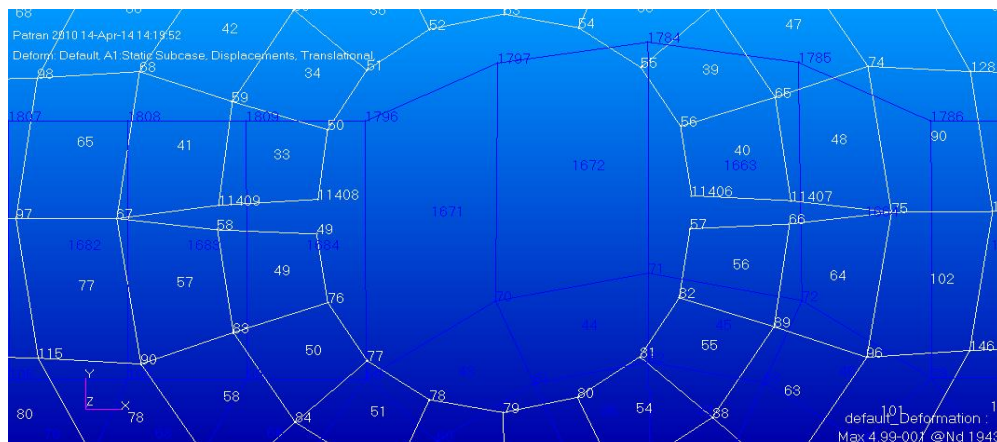


Fig.3.10 A simulated 5mm crack near the rivet hole

Table 2 FE data for SIF calculation for 5mm crack

5 mm Crack					
Displaced nodes	Displacement of displaced nodes T2	Differential Displacement Δv	GP Force at node and Elements		Total Force F
			node	Element	
	mm	mm			kg
66	0.42808260	0.02452010	75	48	53.57285
11407	0.45260270			90	89.37
					142.94

Element edge length is maintained at 1.25mm and the thickness at the tip of this crack is 3.5mm

$F = 142.94 \text{ kg}$

SIF calculations in S.I. units:

$F = 142.94 \times 9.81 = 1402.241 \text{ N}$

$$G = \frac{1}{2 \Delta a} \times \Delta v \times \frac{F}{t}$$

$$G = \frac{1}{2 \times 1.25 \times 10^{-3}} \times 0.025 \times 10^{-3} \times \frac{1402.241}{3.5 \times 10^{-3}}$$

$$G = 3926.27 \text{ N/m}$$

$$K = \sqrt{G \times E}$$

The Young's modulus of Aluminium 2024- T351 is 72.4 GPa ($72.4 \times 10^9 \text{ N/m}^2$)

$$K = \sqrt{3926.27 \times 72 \times 10^9} = 16.87 \text{ MPa}\sqrt{\text{m}}$$

Therefore the Stress Intensity Factor (SIF) in the presence of 5mm crack is **16.87 MPa√m**

Similarly the SIF calculations of the incremental crack lengths can be calculated.

IV. RESULTS AND DISCUSSIONS

SIF for all lengths of crack is tabulated below:

Table 3 SIF for all lengths of cracks

Crack length h mm	Thickness 't' mm	Elemental Edge Length 'Δa' mm	Differential Displacement 'Δv' mm	Grid Point Force Total 'F' N	Strain Energy Release Rate 'G' J/m ²	Stress Intensity Factor 'K' MPa√m
5	3.5	1.25	0.02452010	1402.24	3929.49	16.87
10	3.5	1.25	0.03079650	1737.15	6114.07	21.04
15	3.5	1.25	0.03802010	2110.92	9172.27	25.77
20	3.5	1.25	0.06213050	3153.33	22390.63	40.26
25	3.0	1.25	0.06652280	3082.99	27345.22	44.49
30	3.0	1.25	0.06912730	3199.63	29490.90	46.21
35	3.0	1.25	0.07167760	3315.98	31690.87	47.90
40	3.0	1.25	0.07431560	3435.46	34041.10	49.64
45	3.0	1.25	0.07943630	3399.95	36010.59	51.06
50	2.5	1.25	0.08055130	3102.71	39988.37	53.81
55	2.5	1.25	0.07874510	3029.13	38164.66	52.57
56.25	2.5	1.25	0.07788460	2992.93	37296.50	51.96
57.50	2.5	1.25	0.07641850	2922.40	35732.07	50.86
58.75	2.5	1.25	0.07316050	2780.06	32542.49	48.54
60	4.0	1.25	0.07058100	3922.33	27684.20	44.77

Fig. 4.1 Variation of SIF as a function of crack length

Table 4 Comparison of SIF with Fracture Toughness

Crack length mm	Thickness 't' mm	Fracture Toughness 'K _{IC} ' MPa√m	Stress Intensity Factor 'K' MPa√m
5	3.5	95	16.87
10	3.5	95	21.04
15	3.5	95	25.77
20	3.5	95	40.26

25	3.0	97	44.49
30	3.0	97	46.21
35	3.0	97	47.90
40	3.0	97	49.64
45	3.0	97	51.06
50	2.5	98	53.81
55	2.5	98	52.57
56.25	2.5	98	51.96
57.50	2.5	98	50.86
58.75	2.5	98	48.54
60	4.0	93	44.77

It can be noted from the table that the SIF at any crack length does not exceed the fracture toughness. Thus the structure is safe. However maintenance must be carried out once the crack tip reaches the stringer (stiffener). This is to avoid the damage to stringer.

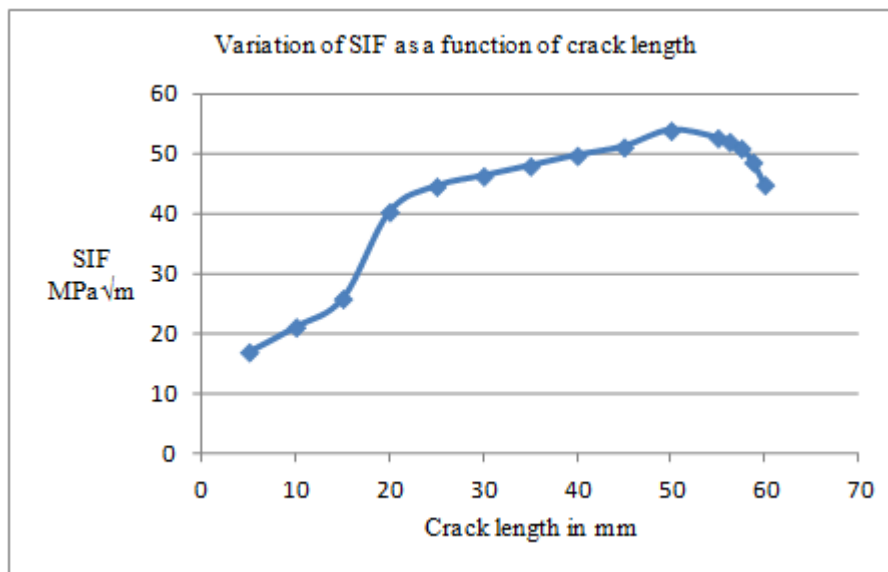


Fig 4.2 Variation of SIF as a function of crack length

The variation of SIF (Stress Intensity Factor) as a function of crack length is shown in figure. From that curvature of the graph it is evident that the SIF initially increases with the increasing length of the crack. The highest SIF value observed is 53.81 MPa√m corresponding to a crack length of 50mm. When the crack extends beyond 50mm the SIF starts decreasing. This is because of the presence of stiffener (stringer) in the crack path. The stringer in the bottom skin is placed 60mm away from the cutout. Hence when the crack extends beyond 50mm, the crack tip is getting closer to the stiffener (stringer). The displacement at crack tip reduces near the stiffener, which results in decrease in strain energy release rate. Thus the SIF starts decreasing as the crack tip approaches the stringer.

Calculation of Residual strength:

The residual strength capability is defined as the amount of static strength available at any time during the service exposure period considering that damage is initially present and grows as a function of service exposure time. Residual strength is the load or force that a damaged structure or material can still carry without failing. Residual strength is calculated as follows:

$$\sigma_{\text{residual}} = \frac{K_{IC}}{K} \times \sigma_{\text{remote}}$$

Where,

σ_{residual} = Residual Strength

σ_{remote} = Remotely applied Tensile stress

K_{IC} = Fracture Toughness

K = Stress Intensity Factor

$$\sigma_{\text{remote}} = \frac{15704.3}{844 \times 2.5} = 7.44 \text{ kg/mm}^2$$

$$\sigma_{\text{remote}} = 72.99 \text{ N/mm}^2$$

For 5mm crack:

$$\sigma_{\text{residual}} = \frac{95}{16.87} \times 72.99 = 411.03 \text{ N/mm}^2$$

Similarly for other crack lengths residual strength is calculated and plotted in fig 4.3

It is evident from the figure that the residual strength decreases with increase in crack length. The residual strength slightly increases near the stiffener. Moreover it interrupts the decreasing trend of the residual strength. If the stringers are not provided, the crack propagates rapidly, the residual strength keeps decreasing and results in catastrophic failure of the wing. Thus the use of stringers is an effective means of increasing the residual strength of damaged panels.

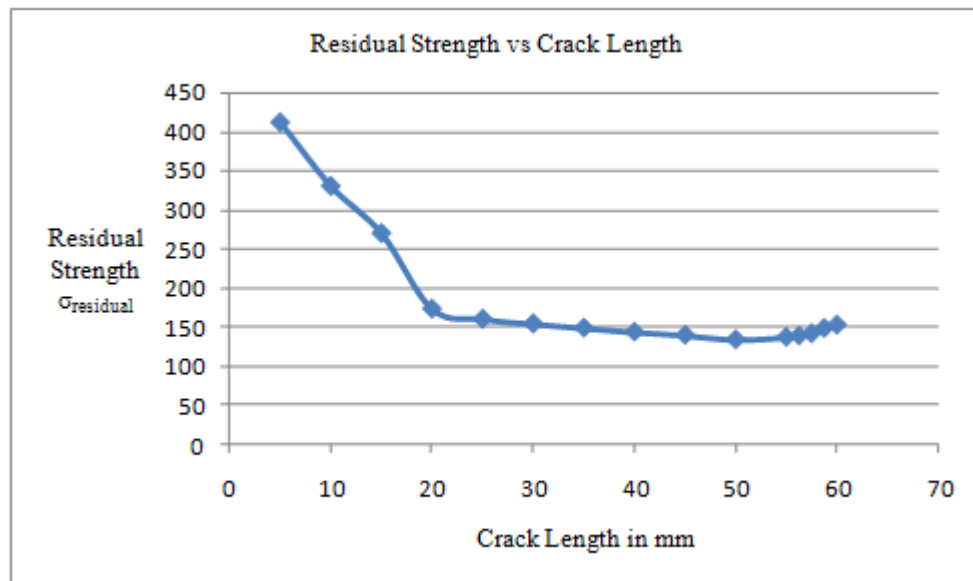


Fig 4.3 Variation of residual strength as a function of crack length

The effectiveness of MVCCI method is illustrated by comparing the SIFs obtained from MVCCI method with the SIFs obtained from the conventional (analytical) method for a plate with centre crack. A plate of length 600mm and breadth 400mm is considered for MVCCI method. Its Young's modulus is considered to be 70GPa. It is subjected to a tensile load of 9810N. The thickness of plate is 2mm. By conventional approach the value of SIF for a various crack lengths is calculated and compared with values from MVCCI method as follows:

Table 5 Comparison of SIF from analytical method with SIF from FE method

Crack Length mm	Stress Intensity Factor (Analytical) 'K _I '	Stress Intensity Factor (FEA) MVCCI 'K'
20	2.17	2.14
30	2.66	2.65
40	3.08	3.08
50	3.46	3.47
60	3.80	3.82

V. CONCLUSIONS

In this work, the damage tolerance evaluation of wing box of a medium size transport aircraft having a large cutout in the bottom skin has been carried out. Finite element method was adopted for stress analysis of the structural components. MSC NASTRAN and MSC PATRAN FEM packages were used to carry out the analysis. The damage tolerance evaluation was carried out in steps. The stress analysis of the entire wing box under the 3g lift load condition was first carried out to identify the critical location for fatigue crack initiation. The critical location was found to be in the bottom skin of the wing. A local analysis was followed to obtain more accurate stress value and the distribution of stress. The maximum stress from the global model was simulated in the local model and at the same location as in the global model. The anomalies in the simulation could be neglected since the maximum stress and its location from global model was replicated in the local model. Hence it was considered sufficient that, only the portion where maximum stress from global model was replicated be considered for analysis. The rest was neglected using the “Plot-Erase” option.

The maximum stress in the local model was found near a rivet hole, close to the fixed end of the wing box. The stress in the rivet hole was found to be 341.388 N/mm^2 (MPa). Since it is lesser than the tensile yield strength (The tensile yield strength of Aluminium 2024- T351 it is 345 MPa) the wing box can be considered safe for static strength under 3g loading conditions. The damage tolerance evaluation includes stress intensity factor and residual strength calculations for various crack lengths. The cracks of incremental length were simulated in the local model. The SIF was calculated for each crack length using Modified Virtual Crack Closure Integral (MVCCI) method which uses FE data like nodal displacements and grid point forces. The SIFs so calculated was compared with fracture toughness.

The SIF initially increased with the increasing length of the crack. When the crack extended beyond 50mm the SIF started decreasing. This is because of the presence of stiffener (stringer) in the crack path. The stringer in the bottom skin is placed 60mm away from the cutout. Hence when the crack extends beyond 50mm, the crack tip is getting closer to the stiffener (stringer). The displacement at crack tip reduces near the stiffener, which results in decrease in strain energy release rate. Thus the SIF starts decreasing as the crack tip approaches the stringer. For all lengths of crack the SIF remained below the fracture toughness. Thus the structure is safe. However maintenance must be carried out once the crack tip extends nearer to the stringer (for 58.75mm). This is to avoid the damage to stringer.

The residual strength calculations revealed that the residual strength decreases with increase in crack length. The residual strength slightly increases near the stiffener. Moreover it interrupts the decreasing trend of the residual strength. If the stringers are not provided, the crack may propagate rapidly, thus the residual strength keeps decreasing and results in catastrophic failure of the wing. Thus the use of stringers is an effective means of increasing the residual strength of damaged panels. Also it is shown that for a rectangular plate there is a close agreement between the SIF values from analytical method and the SIF values from MVCCI (Finite Element) method. Thus MVCCI method is effective for determination of Stress Intensity Factors of cracked structures. Hence it can be concluded that the results obtained from the MVCCI method for the wing box is in close agreement with the actual SIF.

REFERENCES

- [1] Federal Aviation Administration, Advisory Circular, AC No: 25.571-1D, U.S. Department of Transportation, FAA.
- [2] Ralph I Stephens, Metal fatigue in engineering (second edition, John Wiley and sons Inc.)
- [3] Pir M. Toor, Review of some damage tolerance design approaches for aircraft structures, Engineering fracture mechanics, 1973, Vol. 5, pp 837-880, Pergamon press.
- [4] T. K. Hellen, On the method of virtual crack extensions, International journal for numerical methods in engineering, Vol. 9, 187-207 (1975).
- [5] E. F. Rybicki and M. F. Kanninen, A finite element calculation of stress intensity factors by a modified crack closure integral, Engg. fracture mechanics, 1977, Vol. 9, pp 931-938, Pergamon press.
- [6] A Rama Chandra Murthy et al, Damage tolerant evaluation of cracked stiffened panels under fatigue loading, Sadhana Vol. 37, Part 1, February 2012, pp. 171–186.
- [7] R. Sethuraman and S.K. Maiti, Finite element based computation of strain energy release rate by modified crack closure integral, Engineering fracture mechanics, 1988, Vol. 30 No.2, pp 227-231, Pergamon press.

Seismic Assessment of Existing Bridge Using OPENSEES

Jadhav S. S.¹, Pawar P. M.², Kadam Gauri³

1(PG Student ME Civil (Structures),SVERI's C.O.Engg., Pandharpur, Solapur University, India)

2 (Professor, Department of Civil Engineering, C.O.Engg.,Pandharpur, Solapur University, India)

3(Technical Officer, CAE Group, Centre for Development of Advanced Computing, Pune, India)

Abstract: The task of this paper is to determine if the response of existing bridge near village Korti in the vicinity of Pandharpur, designed using the Indian Standard Specifications would meet performance requirements when subjected to the moderate seismic hazard. This paper will provide an analysis of designed bridge behavior in Korti near Pandharpur, and determine if this behavior is acceptable for bridges classified as critical or essential. Analysis of this bridge is carried out using software framework OPENSEES.

Keywords: bridge, nonlinear analysis, opensees, simulation.

I. INTRODUCTION

A large number of bridges were designed and constructed at a time when bridge codes were insufficient according to current standards. The deficiencies in highway bridges designed prior period result in excessive seismic displacements and large force demands that were substantially underestimated. The existing bridge inventory designed to previous provisions is thus likely to suffer damage when subjected to seismic scenarios comparable to those observed in severe earthquakes.

This performance-based evaluation approach requires bridges to satisfy different performance criteria for different levels of ground motion. For instance, the bridge may suffer minor damage but should be operational under frequent earthquakes with low intensity. Under infrequent earthquakes with large intensity, the bridge should provide an acceptable level of life-safety. Quantifying the level of risk associated with anticipated earthquake scenarios enables taking rational decisions to retrofit, replace or accept the risk.

II. DESCRIPTION AND MODLLING

2.1 Description of two span bridges at Korti

This bridge carries the two lanes of state road from Pandharpur to Satara having span length of 25 m each. The two spans support the 300mm thick concrete deck with four T-shaped concrete girders having total depth of 1.35m. Each of these girders rests upon 500mm X 300mm X 64mm neoprene bearing pads. The coefficient of friction for these bearing pads is 0.3. Two spans are supported by pier 1.22m diameter with 75mm of concrete cover. The columns are reinforced longitudinally with 24 -16mm bars and transversely with 8mm bars uniformly spaced at 250mm from bottom of the hinge zone to top of foundation, and spaced at 150mm inside the hinge zone. The total column length is 12.27 and length above grade is 6.71m. The size of deck is 11.9m in width with thickness of 0.3m supported on four T-girders (Web size 1.35m X 0.3m). Embankment length is 25m and its depth 0.5m with total weight of about 30000KN.

2.2 Nonlinear Fiber Section [1]

The nonlinear Fiber section for the column- Nonlinear beam-column elements with fiber section (Fig.2.1) are used to simulate the column. Forced-based beamcolumn elements (nonlinearBeamColumn, Mazzoni et al. 2009) are used for the column (1 element, number of integration points = 5) as well as the pile shaft below grade (number of integration points = 3).

The Steel02 material in OpenSees (Mazzoni et al. 2009) is employed to simulate the steel bars and Concrete02 material is used for the concrete (core and cover). Steel02 is a uniaxial Giuffré-Menegotto-Pinto material that allows for isotropic strain hardening. Concrete02 is a uniaxial material with linear tension softening. The default values for the material properties of the Fiber section are listed in Table 2 for Steel02 and Table 3 for Concrete02 (core and cover). The Concrete02 material parameters were obtained from the Mander (1988) constitutive relationships for confined and unconfined concrete. More details on the derivation of the default values and the OpenSees uniaxialMaterial definitions used for each material.

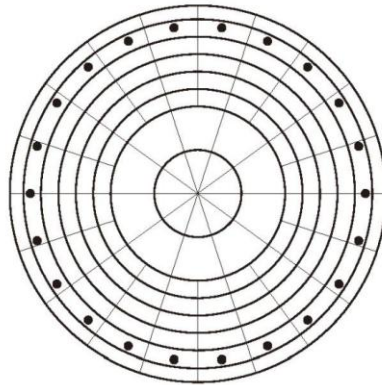


Fig. 2.1 Column fibre section (based on PEER best modelling practices report, Berry and Eberhard, 2007)

Table 4.1 Values for Column Reinforced Concrete (RC) Section Properties	Table 4.2. Values for Steel02 Material Properties
Parameter Value	Parameter Value Typical range
Longitudinal bar size 16	Steel yield strength (kPa) 460,000 345,000-470,000
Longitudinal steel % 2	Young's modulus (MPa) 200,000 -
Transverse bar size 8	Strain-hardening ratio* 0.01 0.005-0.025
Transverse steel % 1.6	Controlling parameter R0** 15 10-20
Steel unit weight (kN/m3) 77	Controlling parameter cR1** 0.925 --
Steel yield strength (kPa) 460,000	Controlling parameter cR2** 0.15 --
Concrete unit weight (kN/m3) 22.8	
Concrete unconfined strength (kPa) 27,600	

*The strain-hardening ratio is the ratio between the post-yield stiffness and the initial elastic stiffness.

**The constants R0, cR1 and cR2 are parameters to control the transition from elastic to plastic branches.

Table 4.3. Values for Concrete02 Material Properties	Table 4. 4. Values for Bridge Deck
Parameter Core Cover	Bridge Deck Parameters
Elastic modulus (MPa) 25,312 25,312	Parameter Value
Compressive strength (kPa) -46,457 -27,600	Deck length (m) 50.0
Strain at maximum strength -0.00367 -0.002	Deck width (m) 11.9
Crushing strength (kPa) -44,9790	Deck depth (m) 1.35
Strain at crushing strength -0.036 -0.006	
Ratio between unloading slope 0.1 0.1	
Tensile strength (kPa) 6504 3864	
Tensile softening stiffness (kPa) 1,771,820 1,932,000	

Table 4.5. Values for Deck Material Properties
Parameter Value
Elastic modulus (MPa) 28,000
Shear modulus (MPa) 11,500
Cross-section area (m2) 5.72
Moment of inertia @ transverse axis (m4) 2.81
Moment of inertia @ vertical axis (m4) 53.9
Weight per unit length (kN/m) 130.3

2.3 Abutment Model-Simplified Model (SDC 2004) [1]

The simplified model of the embankment-abutment system provides several nonlinear springs to better represent abutment-bridge interaction that is neglected with the elastic or roller abutment models. The general scheme of the simplified model is presented in Fig. . It consists of a rigid element of length dw (superstructure width), connected through a rigid joint to the superstructure centerline, with defined longitudinal, transverse and vertical nonlinear response at each end.

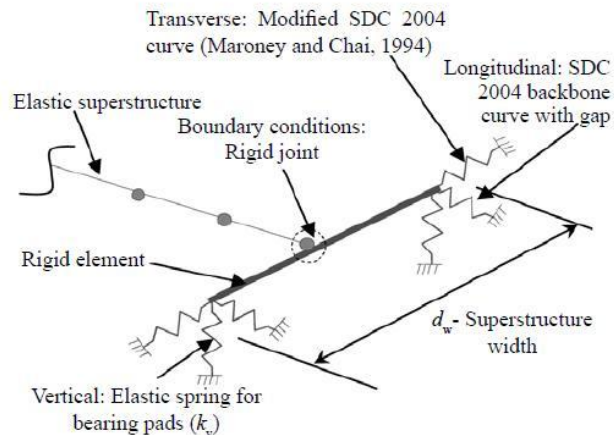


Fig. 2.2 General scheme of the Simplified abutment model [2]

2.4 Specifications of Performance Based Earthquake Engineering Input Motions:

To conduct a PBEE analysis, input motions must be defined. Following ground motions are used for this project.

Table 2.1

Input Motions (10 Records in Total; 1 Records Selected)					Display Intensity Measures	
Record#	Bin	Motion	#Points	Timestep (Sec)	Duration (Sec)	
<input checked="" type="checkbox"/> 1	LMLR	BORREGO/A-ELC	2000	0.0200	40.0000	
<input checked="" type="checkbox"/> 2	LMLR	LOMAP/A2E	1998	0.0200	39.9600	

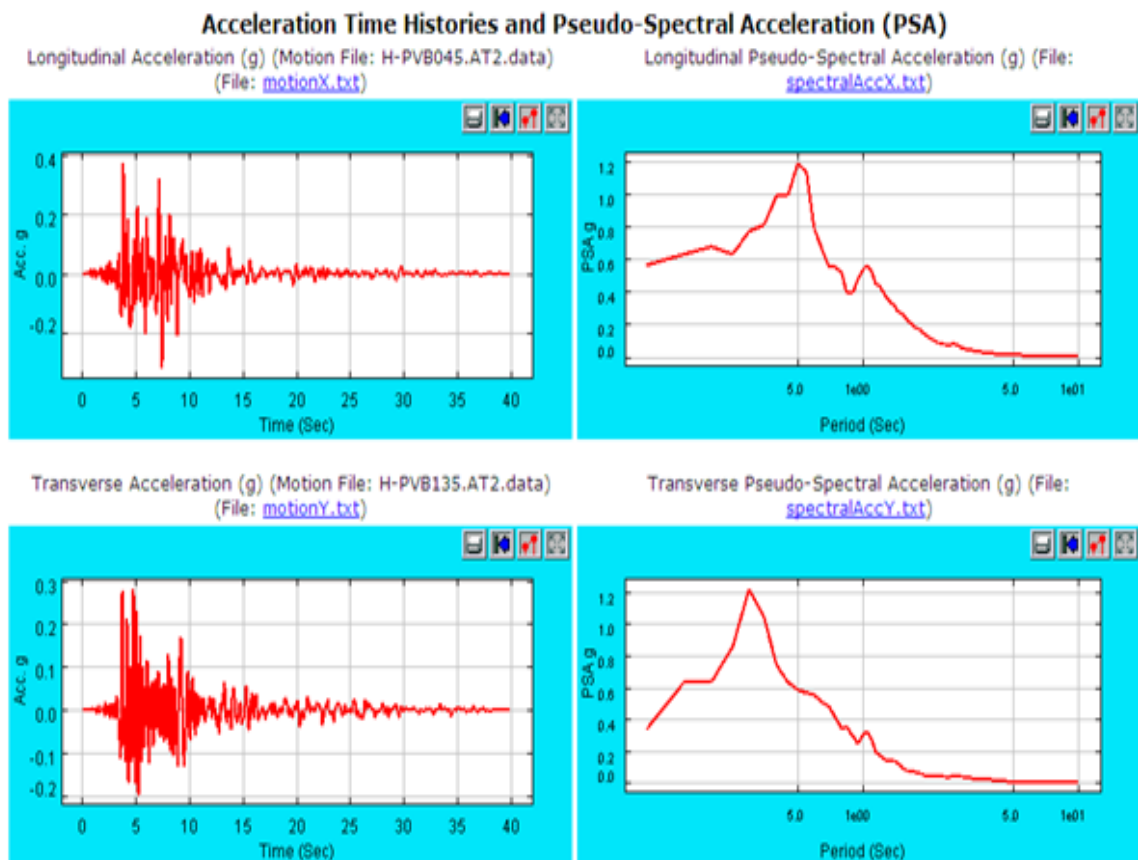


Fig. 2.3 Time histories and response spectra of individual record

III. Results

3.1 SRSS Responses for Each Performance Group

PG1: Max tangential drift ratio SRSS (col)
 PG2: Residual tangential drift ratio SRSS (col)
 PG3: Max long relative deck-end/abut disp (left)
 PG4: Max long relative deck-end/abut disp (right)
 PG5: Max absolute bearing disp (left abut)
 PG6: Max absolute bearing disp (right abut)
 PG7: Residual vertical disp (left abut)
 PG8: Residual vertical disp (right abut)
 PG9: Residual pile cap disp SRSS (left abut)
 PG10: Residual pile cap disp SRSS (right abut)
 PG11: Residual pile cap disp SRSS (col)

Table 3.1

Re c.	PG1 (%)	PG2 (%)	PG3 (m)	PG4 (m)	PG5 (m)	PG6 (m)	PG7 (m)	PG8 (m)
1	0.1127	0.00032	0.01018	0.0092	0.0104	0.0104	0.0079 4	0.0079 4
2	0.4584	0.00066	0.03344	0.0396	0.0339	0.03397	0.0680 8	0.0070 9

PG9 (m)	PG10 (m)	PG11 (m)
0.00025	0.00026	9.4e-6
1.6048	2.1e-04	2.7e-05

3.2 Intensity Measures (Free-field Response)

The intensity measures include:

- ☐ PGA (Peak Ground Acceleration)
- ☐ PGV (Peak Ground Velocity)
- ☐ PGD (Peak Ground Displacement)
- ☐ D5-95 (Strong Motion Duration)
- ☐ CAV (Cumulative Absolute Velocity)
- ☐ Arias Intensity
- ☐ SA (Spectral Acceleration; assuming 1 second period)
- ☐ SV (Spectral Velocity), SD (Spectral Displacement)
- ☐ PSA (Pseudo-spectral Acceleration)
- ☐ PSV (Pseudo-spectral Velocity)

The strong motion duration (D5-95) is defined according to the time domain bounded by the 5% and 95% cumulative Arias intensity of the record. All of the spectral intensity measures are defined at an effective viscous damping of 5%.

Table 3.2 Longitudinal direction

R ec .	PGA (g)	PGV (cm/sec)	PGD (cm)	D(5- 95) (sec)	CAV (cm/sec)	Arias Brack eted (cm/se c)	SA (g)	SV (cm/s ec)	SD (cm)	PSA (g)	PSV (cm/sec)
1	0.139	26.491	12.94	37.7	488.64	20.68	0.182	22.31	4.515	0.1817	28.36
2	0.199	13.756	3.875	37.1	665.82	47.17	0.256	45.45	6.349	0.2556	39.89

Table 3.3 Transverse direction

R ec .	PGA (g)	PGV (cm/sec)	PGD (cm)	D(5- 95) (sec)	CAV (cm/sec)	Arias Brack eted (cm/se c)	SA (g)	SV (cm/s ec)	SD (cm)	PSA (g)	PSV (cm/sec)
1	0.057	13.194	10.16	37.5	414.87	12.28	0.133	20.46	3.291	0.1325	20.68
2	0.154	11.864	5.605	36.5	555.25	32.70	0.177	26.01	4.402	0.1772	27.65

Table 3.4 Horizontal SRSS

R ec .	PGA (g)	PGV (cm/sec)	PGD (cm)	D(5- 95) (sec)	CAV (cm/sec)	Arias Brack eted (cm/se c)	SA (g)	SV (cm/s ec)	SD (cm)	PSA (g)	PSV (cm/sec)
1	0.139	26.491	12.94	37.7	716.99	33.02	0.0988	10.49	2.447	0.0985	15.38
2	0.210	17.251	5.713	36.8	961.41	79.89	0.1434	12.01	3.550	0.1429	22.30

IV. Conclusion

This project presents highlights to assess the seismic response of a two span bridge. The focus is on describing the methodology adopted to idealize the bridge and its foundation system, while only summary of results from the extensive elastic and inelastic analyses under the effect of input ground motions are presented. The demands corresponding to the ground motions are well within the collapse limit state and the capacity of bridge components. Under the ground motions, the response of the bridge was acceptable.

The presented assessment study confirmed there is no need to retrofit different bridge components to mitigate potential seismic risk.

Acknowledgements

I am extremely thankful and pay gratitude to Mr. Asvija (C-DAC Bangalore, GRID GARUDA) for their valuable support and cooperation.

REFERENCES

Book:

- [1] Jinchi Lu et al., Bridge PBEE: Open Sees 3D Pushover and Earthquake Analysis of Single-Column 2-span Bridges By PEER Berkeley Dec.2011 13-23.

Report:

- [2] Aviram et al., Guidelines for Nonlinear Analysis of Bridge Structures in California, PEER Report 2008/03 Pacific Earthquake Engineering Research Center College of Engineering University of California, Berkeley August 2008, 46.

Regeneration of Liquid Desiccant in Solar Passive Regenerator with Enhanced Performance

J. R. Mehta

Mechanical Engineering Department, The Maharaja Sayajirao University of Baroda, India

Abstract: Demand for air conditioning is growing, which many times strains the electricity grid. It is desirable to use technologies like liquid desiccant based air conditioning, which can use waste heat or solar thermal energy. Solar regeneration has challenges like numerous components, higher parasitic power and low efficiency. In this work, a solar passive regenerator is developed and used, which has nominal power consumption for its operation. Its efficiency can be improved significantly by enhanced glass cooling as demonstrated in this work. The moisture removal rate could be improved by more than 100% with this method. The effect of concentration and solar insolation on moisture removal rate was also studied in this work.

Keywords: Air conditioning, Liquid desiccant, Regeneration, Solar energy.

I. INTRODUCTION

Per capita energy consumption of a country is many times considered the indicator to growth of economy. But energy consumption is also related with pollution and climate change concerns. Demand for air conditioning is growing as economy and comfort expectations grow. It would be preferable to use renewable energy source or waste heat source for providing air conditioning rather than depending only on vapour compression refrigeration system, which needs electrical energy. Liquid desiccant (LD) based air conditioning or air dehumidification (LDAD) systems can use solar thermal energy for regeneration of LD. Various methods of regeneration using solar energy, like hot air from solar air heater, hot water from solar water heater, two stage regeneration with in-situ regeneration in evacuated tube collector etc. are reported in literature [1-4].

In-situ regeneration of LD in solar collector would help to reduce system components and parasitic power consumption. Mullick and Gupta preferred flat plate collector for this purpose compared to solar still used by Hollands to improve efficiency [5, 6]. Heavy dependence on weather conditions and dust contamination are limitations of this system. Though efficiency of solar still, which may be called solar passive regenerator, when used for LD regeneration, is less; it has other advantages like nominal power consumption and no dust contamination. Mehta and Gandhi presented simulation as well as experimental results for regeneration of aqueous potassium formate solution in such regenerator [7]. An effort has been done in this work to enhance efficiency of this device and make it a good potential candidate for LD regeneration using solar energy.

II. EXPERIMENTAL SET-UP, PROCEDURE AND INSTRUMENTATION

A fibre reinforced plastic (FRP) solar still with 1 m² area available in market was used as a raw device. LD regeneration involves higher temperatures, which can lead to higher losses in such device. So, the device was modified by providing additional thermocol insulation contained in a wooden box. Calcium chloride is a low price and readily available chemical, so aqueous solution of calcium chloride was used as LD in this work. A cooling system with low flow rate of water was developed to cool the solar regenerator glass (Fig.1). This water need not be taken from outside, but the water condensed in process of regeneration can itself be used for this purpose.

The cooling system consists of a source water tank, a diaphragm type of pump with 14 W rating, plastic tubes and small openings for cooling water distribution over the glass cover. Water was pumped at a rate of around 4 kg/h, excess water was collected and recirculated. Two solar passive regenerators, one with cooling and another without cooling were tested by putting them side by side. Experiment started at 9:30 am in morning and ended at 5:30 pm, in the month of June. Concentration of LD was 40% in one such experiment. Another set of experiment was done, taking two difference concentrations of LD in the regenerator and finding the effect of concentration on regeneration rate of LD.



Figure 1: Experiment scheme for solar passive regenerator, with and without glass cooling

The flow rate of water was measured by collecting the water for 5 min in a container and weighing the its mass. Temperature of LD was measured with K type thermocouple whose junction were submerged in LD pool. Surface temperature of glass was also measured with a contact thermometer, K type with digital display. Ambient conditions were measured using humidity and temperature sensor, which were connected with a datalogger.

III. RESULTS AND DISCUSSIONS

Fig. 2 shows variation of LD temperature and glass temperature for solar passive regenerator with and without glass cooling. Experiment was performed in the month of June and concentration of LD was 40% in this case. Solar insolation was 5.645 kW/m^2 over the day as measured at Vallabh Vidyanagar, a town near Vadodara. It is seen that glass temperature for the system with cooling remains around 10°C lower than that without cooling. Lower glass temperature should help higher heat transfer and thus moisture removal rate. It is seen in Fig. 3 that moisture removal rate from LD is much higher for glass cooled solar passive regenerator. It is seen that regeneration in glass-cooled regenerator started much earlier as compared to the other. Total condensate collected in case of glass-cooled regenerator was 1331 ml as compared to 661 ml for the non-glass-cooled regenerator. Thus, regeneration rate got enhanced by more than 100% due to glass cooling. It is seen that LD temperature also remains lower in glass-cooled regenerator. This is due to higher amount of heat and moisture transfer occurring from LD to glass, which provides higher cooling rate for LD. As LD remains at lower temperature, heat losses to ambient reduce and efficiency would increase.

In another experiment, concentration of LD was taken 37% instead of 40% and solar insolation was 5.916 kW/m^2 on that day. Moisture removal rates were 2014 and 1238 ml with and without glass cooling in regenerator respectively. The increased water removal rate is due to higher water vapour pressure exerted by LD at lower concentration. In addition to that, from higher solar insolation also contributed to higher output in this case. To study the effect of only concentration on regeneration rate, another experiment was conducted testing two glass-cooled solar regenerators simultaneously, one with LD concentration equal to 37% and the other with 42%. Moisture removal rates were 1816 and 1409 ml respectively. Thus, 5% rise in concentration reduced the moisture removal rate by 22%.

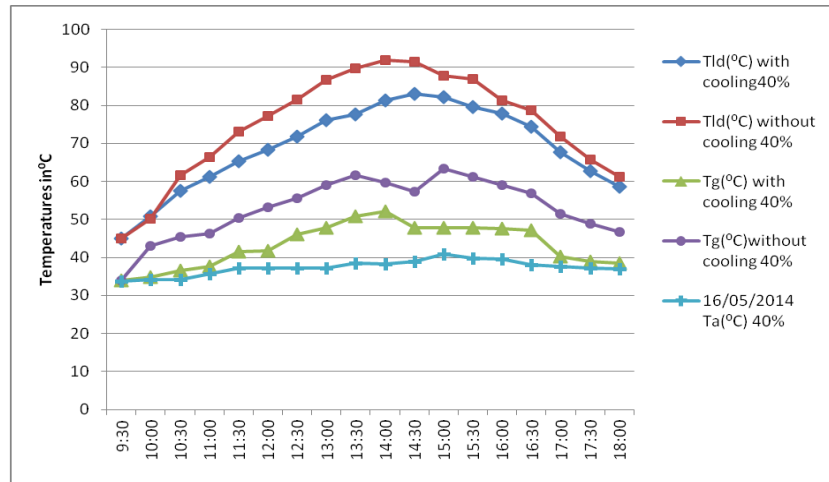


Figure 2: Variation of various parameters for regenerator over the day (T_{ld} : liquid desiccant temperature, T_g : glass temperature, T_a : ambient temperature)

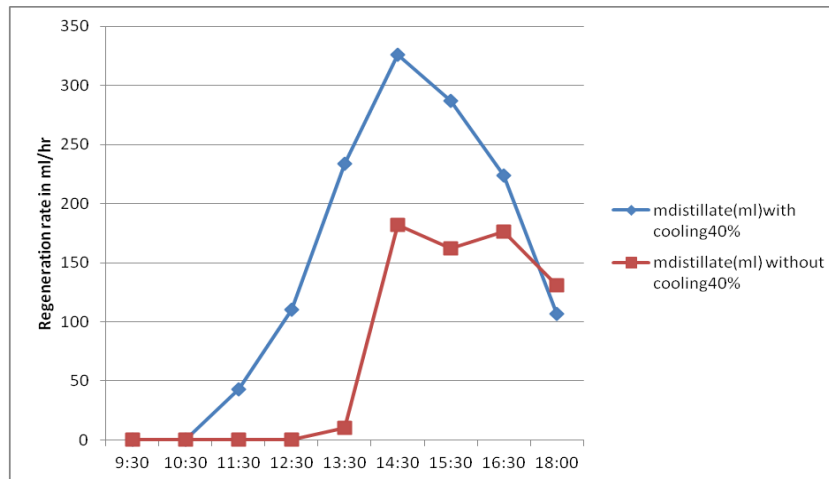


Figure 3: Water removal rate for regenerator over the day ($m_{\text{distillate}}$: mass of distillate or water removed from liquid desiccant)

IV. CONCLUSION

A solar passive regenerator with enhanced efficiency due to glass cooling was demonstrated in this work. Glass cooling helped to increase moisture removal rate by more than 100% for 40% concentration solution of calcium chloride. Moisture removal rate as high as 2014 ml per day was achieved using the regenerator with enhanced performance. Along with other advantages like non-contamination of LD and low parasitic power consumption, this solar passive regenerator seems a good potential candidate for LD regeneration. The work has also demonstrated that solar insolation and concentration of LD has significant effect on moisture removal rate from a solar regenerator.

REFERENCES

- [1] G. O. G. Lof, Cooling with solar energy, World Symposium on Applied Solar Energy, Phoenix, Arizona, 1995.
- [2] K. Gommed, and G. Grossman, Experimental investigation of a liquid desiccant system for solar cooling and dehumidification, Solar Energy, 81, 2007, 131-138.
- [3] J. R. Mehta, and M. V. Rane, Liquid desiccant based solar air conditioning system with novel evacuated tube collector as regenerator, Procedia Engineering, 51, 2013, 688-693.
- [4] J. R. Mehta, Regeneration of liquid desiccant using solar energy - A brief review of the technology for solar air conditioning, 1st International Conference on Non Conventional Energy (ICONCE), Kalyani, India, 2014.
- [5] S. C. Mullick, and M. C. Gupta, Solar desorption of absorbent solutions, Solar Energy, 16, 1974, 19-24.
- [6] K. G. T. Hollands, The regeneration of lithium chloride brine in a solar still, Solar Energy, 7(2), 1965, 39-43.
- [7] J. R. Mehta, and S. M. Gandhi, Investigation of solar still as liquid desiccant regenerator, Nirma University International Conference on Engineering (NUICONE), Ahmedabad, India, 2013.



International Journal of Modern Engineering Research (IJMER)

Volume : 4 Issue : 7 (Version-6)

ISSN : 2249-6645

July - 2014

Contents :

Studies on Al8081-B4C Metal Matrix Composites Fabricated by Stir Casting Method <i>Kumar Lingaraj Patil, Mousil Ali, Madeva Nagaral</i>	01-04
Advanced Automation System in Industrial Applications Using PIC Microcontroller and GSM <i>K. Siva Prasad, B. Kumuda, U. Shantha Kumar, M. Ashok Kumar</i>	05-10
Simulation of MPPT Algorithm Based Hybrid Wind-Solar-Fuel Cell Energy System <i>Kalpana. P, Venkata Pradeep. G</i>	11-18
Applications of Artificial Neural Network and Wavelet Transform For Condition Monitoring of the Combined Faults of Unbalance and Bearing Clearance <i>H. K. Srinivas, Shamanth. S. Holla, Karthik. B. S, Niroop.S, Chiranjeevi. D</i>	19-28
Tensile and Flexural Properties of Sisal/Jute Hybrid Natural Fiber Composites <i>Sudhir.A, Madhukiran. J, Dr. S. Srinivasa Rao, Dr.S.Madhusudan</i>	29-35
Growth and Development of FDI on Indian Economy <i>J. Rama Devi, Prof. B. Ramachandra Reddy</i>	36-40
Modeling and Reduction of Root Fillet Stress in Spur Gear Using Stress Relieving Feature <i>Deep Singh Vishwakarma, Dr. Rohit Rajvaidya</i>	41-48
Introduction to the selection of corridor and requirements, implementation of IVHS (Intelligent Vehicle Highway System) In Hyderabad <i>Maddali Sai Satya Goutham, Bhanu Kireeti Chanda</i>	49-54
Experimentation of Jute Fiber Supplemented with E-Glass in Various Layers Alignment <i>Rahul Komma, K.Prudhvi Raj, Dinesh Souda</i>	55-62
Performance & emission characteristics of Two Cylinder Diesel Engine Using Diesel & Pine oil <i>Dr. Hiregoudar Yerrennagoudaru , Chandragowda. M , Manjunath. K, Manjunath. k. J</i>	63-69

Studies on Al8081-B₄C Metal Matrix Composites Fabricated by Stir Casting Method

Kumar Lingaraj Patil¹, Mousil Ali², Madeva Nagaral³

¹PG Student, Gousia College of Engineering, Ramanagar-562159

²Department of Mechanical Engineering, Gousia College of Engineering, Ramanagar-562159

³Design Engineer, ARDC, HAL-Bangalore-560037

Abstract: Aluminium MMCs are preferred in the fields of aerospace, military, automotive, marine and in many other domestic applications. In the present work, an attempt has been made to develop and study the, Mechanical properties of Al-8081/B₄C reinforced aluminium metal matrix composites. The composite was prepared by using Liquid Metallurgy Route (Stir Casting Technique). Liquid state has some important advantages such as better matrix particle bonding, easier control of matrix structure, simplicity, low cost of processing, nearer to net shape and wide selection of material. Al-8081 alloy was taken as the base matrix to which B₄C particulates are used as reinforcements. Al8081-B₄C composites were prepared by varying weight percentage of B₄C i.e 0 to 6 %, in steps of two. The objective is to study the effect of B₄C particulates on mechanical properties such as ultimate tensile strength, yield strength and hardness of Al8081 alloy composites. The results of this study revealed that, as the B₄C content was increased, there were significant increases in the ultimate tensile strength, yield strength and hardness in the composites as compared to the base matrix.

Key words: Al-8081Alloy, B₄C, Stir Casting, Mechanical Properties, Metal Matrix Composites.

I. Introduction

A composite material is a 'material system' composed of a combination of two or more micro or macro constituents that differ in form, chemical composition and which are essentially insoluble in each other. One constituent is called as Matrix Phase and the other is called reinforcing phase. Reinforcing phase is embedded in the matrix to give the desired characteristic [1].

Metal Matrix Composites (MMCs) have emerged as an important class of materials and are increasingly utilized in various engineering applications, such as aerospace, marine, automobile and turbine compressor engineering, which require materials offering a combination of light weight with considerably accelerated mechanical and physical properties such as strength, toughness, stiffness and resistance to high temperature [2-4].

Particle reinforced metal matrix composite represent a group of materials where the hardness, resistance of the reinforcements is combined with the ductility and toughness of matrix materials [5]. Aluminium is the most frequently use matrix material due to its low density. Because of its extreme hardness and temperature resistant properties, SiC, Al₂O₃ ceramic particles are often used as reinforcement within the aluminium matrix. This type of composite is more frequently used in the automotive industry today, particularly in various engine components as well as brakes and rotors [6-7].

The combined attributes of metal matrix composites, together with the costs of fabrication, vary widely with the nature of the material, the processing quality of the product. In engineering, the type of composite used and its application vary significantly, as do the attributes that drive the choice of metal matrix composites in design. For example, high specific modulus, low cost, and high weld ability of extruded aluminium oxide particle-reinforced aluminium are the properties desirable for bicycle frames. High wear resistance, low weight, low cost, improved high temperature properties, and the possibility for incorporation in a large part of unreinforced aluminium are the considerations for design engine pistons [8-9].

Many researchers exploited the different reinforcement particles with different form to fabricate the aluminum composites and used different fabrication routes to achieve required properties. B₄C are the suitable reinforcement materials to improve tribological properties of a matrix material [10].

As revealed in the so far performed research, the particulate B₄C increases wear resistance and also contribute to improvement of mechanical properties, also at elevated temperatures. The presence of B₄C could effectively prevent the matrix deformation, to carry the load and lock the micro cracks that often develop along the friction direction.

Investigation of mechanical behaviour of aluminium alloys reinforced by micro hard particles such as B₄C is an interesting area of research. Therefore, the aim of this study is to investigate the effect of B₄C content on the hardness and tensile strength behaviour of Al8081 – B₄C composites, made by stir casting method.

II. Experimental Details

2.1 Materials

Metal matrix composites containing 2, 4 and 6 weight percentages of B₄C particles were produced by liquid metallurgy route. For the production of MMCs, an Al8081 alloy was used as the matrix material while B₄C particles with an average size of 80-90µm were used as the reinforcements. Al8081 alloy having chemical composition as per the ASTM ingot specification is given in Table 1 [11].

Table 1: Chemical composition of Al8081 alloy

Si	Fe	Sn	Cu	Mn	Zn	Al
0.7	0.7	18-22	0.7-1.3	0.1	0.05	Bal

2.2 Preparation of composites

In stir casting method before the casting reinforcements, stirrer, permanent mould preheated to 300°C to remove moisture and gases from the surface of the reinforcements, and equipments before casting. Now the required amount of Al8081 is weighed and placed in the graphite crucible and heated to 730°C using resistance furnace then the degassing tablet is added to minimize the coating film defects by expelling the volatile components present in the melt during casting. The tablet helps in the removal of entrapped air in the melt and thus prevents casting defects like porosity and blow holes. Then the matrix Al8081 is reinforced with B₄C particulates with different weight percentages (2, 4&6). The micro particle of B₄C was added at the temperature of 710°C and a constant rigorous stirring was done for 15mins until a clear vortex is formed.

Before the addition of reinforcements the cover flux and magnesium were added to decrease the surface tension and viscosity of the melt. At the pouring temperature of 710°C the molten mixture was poured into the cast iron mould and allowed to solidify for few minutes.

2.3 Testing of Composites

All tests were conducted in accordance with ASTM standards. Tensile tests were conducted at room temperature using a universal testing machine (UTM) in accordance with ASTM standard E8-M82. The tensile test specimens of diameter 9mm and gauge length 45mm were machined from the cast composites with the gauge length of the specimens parallel to the longitudinal axis of the castings. For each composite, three tensile test specimens were tested and the average values of the ultimate tensile strength and yield strength were measured. The Micro-Vickers hardness values of the samples were measured on the polished samples using diamond cone indenter with a load of 100gms and 10 seconds as a holding time. Hardness value reported is the average value of 100 readings taken at different locations on the polished specimen. For tensile results, test was repeated three times to obtain a precise average value.

III. Results And Discussions

3.1 Hardness Measurement

The Vickers micro-hardness of cast Al8081 and Al8081- B₄C composites are evaluated using diamond indenter at an applied load of 100grms at 50X optical zoom with dwell time 10 secs for each sample at different locations. The plot of Vickers Hardness Number (VHN) with a variation in B₄C wt percentages in metal matrix composite has been presented in figure 1 and Table 2. The measured mean values of VHN were plotted as a function of weight percentage of B₄C. From the study it can be observed that as the reinforcement content was increased, there was an increase in the hardness. The increase in the hardness is probably attributed to the fact that the hard B₄C particulates acts as barrier to the movement of the dislocations within the matrix. Various other researchers have also reported that the addition of hard ceramic particulates to metal alloys could lead to improved strength, wear resistance and hardness. A similar effect was observed by Serajul et al. [12] for SiC reinforced aluminium alloy MMCs. They found that the hardness linearly increases with increasing volume percentage of SiC. Boron Carbide, being hard exhibit a greater resistance to indentation by the hardness tester and hence enhanced hardness.

Table 2: Micro-Hardness Test Results of Different Composition.

SL NO	Composition Material	Mean Micro Hardness No (VHN)
1	Al8081 Alloy	64.1
2	Al8081- 2 wt% B ₄ C	76.4
3	Al8081- 4 wt% B ₄ C	89.6
4	Al8081- 6 wt% B ₄ C	108.3

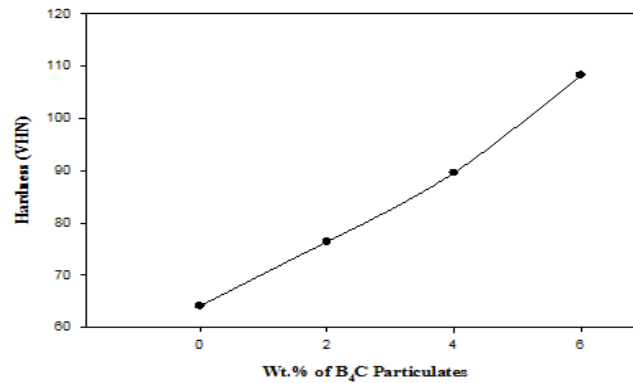


Figure 1: Micro-Hardness Test Results for Different Composition.

3.2 Evaluation of Tensile Strength

The graph of Ultimate Tensile Strength (UTS) and yield strength with a variation of B₄C in metal matrix composite has been presented in figure 2 and 3 respectively. The measured mean values of UTS and yield strength were plotted as a function of weight percentage of B₄C particulates. From the study it can be observed that within the scope of this investigation as the B₄C content was increased, there was an increase in the UTS and yield strength. The increase in ultimate tensile strength is attributed to the presence of hard B₄C particles, which imparts strength to the matrix alloy, thereby providing enhanced tensile strength.

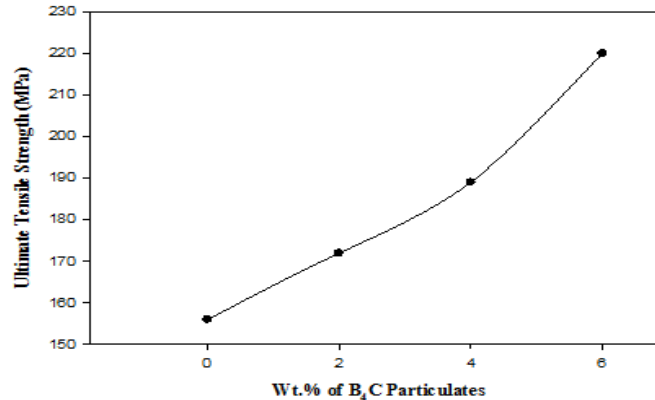


Figure 2: Tensile Test Results of Different Specimens

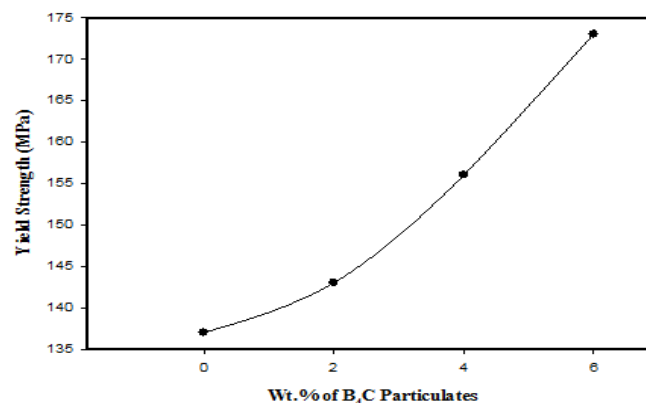


Figure 3: Tensile Test Results of Different Specimens

IV. Conclusions

The present work on processing of Al8081 reinforced with 2, 4 and 6wt% of B₄C particulate composite via melt stirring method has lead to the following conclusions.

1. Al8081 alloy reinforced with B₄C particulate composites were successfully produced by melt stirring method.
2. The addition of B₄C particulate to the Al8081 alloy has led to improved hardness when compared to the matrix alone.
3. The addition of B₄C reinforcement to the Al matrix has improved mechanical properties like ultimate tensile strength and yield strength. The extent of improvements obtained in Yield Stress and Ultimate Tensile Stress were respectively.

REFERENCES

- [1] J. Hasim, L. Looney, M. S. J. Hashmi. Metal matrix composites production by the stir casting method. *Journal of Materials Processing Technology*, 1999, 92-93, 1-7.
- [2] A. Banerji, S. V. Prasad, M. K. Surappa, P. K. Rohatgi. Abrasive wear of cast aluminium alloy zircon particle composites. *Wear*, 1982, 82, 141-151.
- [3] Y. Sahin. Preparation and some properties of SiC particle reinforced aluminium alloy composites. *Materials and Design*, 2003, 24,671-679.
- [4] K. H. W. Seah, S. C. Sharma, B. M. Girish, S. C. Lim. Wear characteristics of as cast ZA-27/Graphite particulate composites. *Materials and Design*, 1996, Vol.17, No. 2, 63-67.
- [5] S. Amirkhanlou, B. Niroumand. Synthesis and characterization of 356-SiC composites by stir casting and compocasting methods. *Trans. Nonferrous Met.Soc., China*, 2010, 20, 788-793.
- [6] A Martin, M. A. Martinez, J. Llorca. Wear of SiC reinforced Al matrix composites in the temperature range 20-200 degree Celsius. *Wear*, 1996,193, 169-179.
- [7] V. Auradi, Madeva Nagaral, Bharath V., Effect of Al₂O₃ particles on mechanical and wear properties of Al6061 alloy metal matrix composites. *J. Material Sci. Eng.* 2:1, 2013.
- [8] S. Tahamtan, A. Halvae, M. Emamy, M. S. Zabihi, Fabrication of Al/A206-Al₂O₃ nano/micro composite by combining ball milling and stir casting technology. *Materials and Design* 49, 347-359, 2013.
- [9] U. T. S. Pillai, R. K. Pandey, P. K. Rohatgi, Effect of volume fraction and size of graphite particulates on fracture behavior of Al graphite composites. *Engineering Fracture Mechanics* Vol.28, No.4, pp.461-477, 1987.
- [10] N. P. Cheng, S. M. Zeng, Z. Y. Liu, Preparation, microstructures and deformation behavior of SiCp/6066Al composites produced by PM route. *Journal of Materials Processing Technology* 202, 27-40,2008.
- [11] Aluminium and aluminium alloys, ASM Specialty Handbook, Edited by J. R. Davis
- [12] Serajul Haque. Mechanical and machining properties analysis of Al6061-Cu-Reinforced SiCp metal matrix composite. *JMMCE*, 2014, 2, 54-60.

Advanced Automation System in Industrial Applications Using PIC Microcontroller and GSM

K. Siva Prasad¹, B. Kumuda², U. Shantha Kumar³, M. Ashok Kumar⁴

^{1,4} Asst Professor, Dept. of EEE, CBIT, Prodhuturu, Andhra Pradesh, India

^{2,3} Asst Professor, Dept. of EEE, RYM Engineering college, Bellary

Abstract: The main aim of this paper is to design and develop an advanced automation system in the industries. In this technique we are using the GSM modem which have the SIM card present in it, the user can send message on the 10 digit SIM number using the cell phone from any part of the world. The micro controller is programmed using the embedded C. when the user will send the message to a particular device that particular device will be on or we can also off the device. Example if the motor is in over voltage, under voltage, over current in that time the microcontroller will trip the circuit and give the message feedback to the user. The micro controller will read the temp from the sensor and it will display the same on the LCD when the incoming temp crosses the set limit the micro controller will turn OFF the device and will send the message to owner using the SIM card present in the GSM modem. We can also check the continuous status of the device.

Key words: IVRS, PIC Micro controller, GSM Module.

I. Introduction

An embedded system is a combination of software and hardware which is designed for one specific application in a time domain constraint. Now-a-days the meaning of the embedded system was changed because, it was not designed only for one specific application but, many applications can run with a single embedded system. The best example of an embedded system is a mobile phone which performs the communication, along with the communication one can surf the internet, access the social network sites, play the games and even global positioning system is deployed into such a small device.

The main aim of the paper is to design and develop an Advanced Automation system in Industries Using GSM system in the industries.

In this technology we are using the GSM modem which have the SIM card present in it, the user can call on the 10 digit SIM number using the cell phone or the land line from any part of the world. The micro controller is programmed using the embedded C. When the caller calls this SIM number, the micro controller will get to know the ring and it will pick up the call and the caller can control any of the devices using the keypad present in the cell phone or the land line. The micro controller will read the temp from the sensor and it will display the same on the LCD when the incoming temp crosses the set limit the micro controller will turn OFF the device and will call the owner using the SIM card present in the GSM modem, when the owner picks the call the micro controller will activate the speech IC and the message will be played to the owner telling that the temp has crossed the limit and the system is turned OFF and this can be told in any of the language whichever the owner chooses.

Despite it's relatively old age, the 8051 / PIC is one of the most popular Microcontroller in use today. Many derivatives Microcontroller have since been developed that are based on--and compatible with--the 8051 / PIC. Thus, the ability to program an 8051 / PIC is an important skill for anyone who plans to develop products that will take advantage of Microcontroller. Using these in built peripherals the designing of GSM [1] Based Industrial Device Control achieves its portability. Other peripherals like GSM modem voltage Current and temperature sensor, LCD and PMDC motor are used in this system.

II. Block Diagram And Explanation

2.1 Hardware requirement

PIC Micro Controller, LCD, GSM Module, Power supply Unit, Voltage sensor, current sensor, temperature sensor and Relay Driver

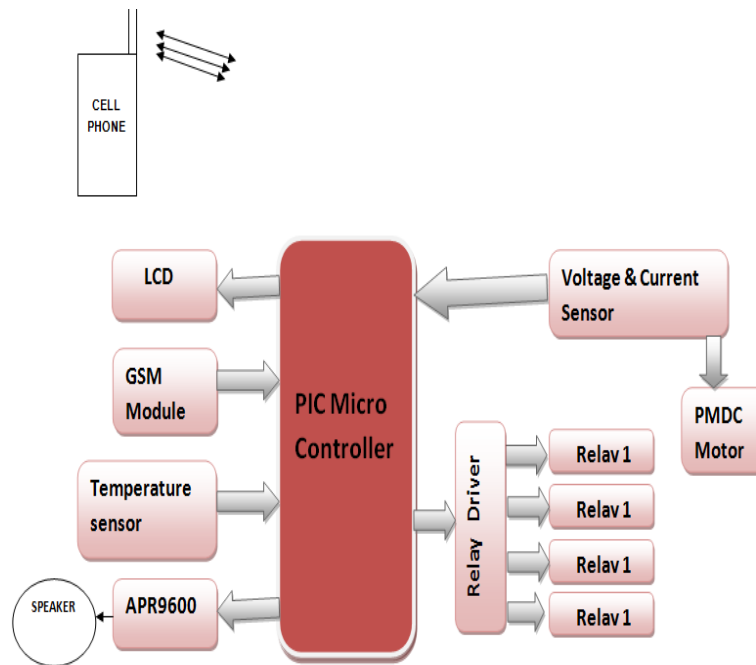


Fig.1. Block Diagram

2.2 Micro Controllers

Micro Controllers are the Heart of the Circuit. In this circuit we are going to use the 8051 MCU. Microcontrollers are used in automatically controlled products and devices, such as automobile engine control systems, implantable medical devices, remote controls, office machines, appliances, power tools, toys and other embedded systems.

2.3 LCD (Liquid Crystal Display)

LCD (Liquid Crystal Display) screen is an electronic display module and find a wide range of applications. A 16x2 LCD display is very basic module and is very commonly used in various devices and circuits. These modules are preferred over even segments and other multi segment LEDs. The reasons being: LCDs are Economical; easily programmable; have no limitation of displaying special & even custom characters (unlike in seven segments), animations and so on.

2.4 Relay Driver IC

Relay Driver IC is a high voltage and high current Darlington array IC. It contains open collector Darlington pairs with common emitters. A Darlington pair is an arrangement of two bipolar transistors. Recommended for high-side switching applications that benefit from separate logic and load grounds, these devices encompass load supply voltages to 50 V and output currents to -500 mA. These 8-channel source drivers are useful for interfacing between low-level logic and high-current loads.

2.5 GSM modem

The GSM modem used by cell phones that provides low cost, long range, wireless communication channel for applications that need connectivity rather than high data rates. The interface between GSM and MUC controller is a textual protocol called Hayes AT- Commands. This particular application connects an ARM controller and Siemens M65 cellular phone using a RS232 based data cable.

2.6 Voltage and Current sensor

VI sensors are use in the project to get voltage and current values for connected load. Sensor is build/designed using resistor network logic.

2.7 Temperature sensor

Temperature sensors are used for getting temperature in the system. Which is countiuonesly monitored, if the temperature goes above predefine value then system will shutdown, which indicates there is fire in the system.

2.8 Voice recorder IC

The APR9600 device offers true single-chip voice recording, -volatile storage and playback capability for 40 to 60 seconds the device supports both random and sequential access of multiple messages. Sample rates are user-selectable, allowing designers to customize their design for unique equality and storage time needs. Integrated output amplifier, microphone amplifier, and AGC circuits greatly simplify system design. The device is ideal for use in portable voice recorders, toys, and many other consumer and industrial applications.

III. Working

The design and implementation of MUC based GSM based devices control system was effectively carried out with the advantages of low cost, low power consumption, high portability and minimum peripheral interfaces.

To start the system first we need to send the SMS for trip setting for device 1 which is in turn connected to motor. SMS sending format is UV=<value>; OV=<value>; OC=<Value>. For ex: UV=18; OV=24; OC=01. After sending sms as above format we need to send one more sms to ON the device, which will in turn on the relays respectively. Suppose to one device1 sms send to send as! DEV1 1 and to off the device1! DEV1 0. Similarly by sending different sms as above format 4 devices can be made on and off. Status of device is also shown in LCD as well as feedback sms for given on which is pre-programmed while coding and speech sound of devices status is also given for any changes in devices status. Like device 1 on, device 1 off etc. which done using IC APV 600 Voices recorder IC.

As soon as device1 gets ON ADC gets activated and immediately voltage and current information's are seen on LCD[2]. If the voltage or current get exceed pre-defined values which is setted before starting the device1, motor will be turned off and sms is send to a number regarding status of motor.

Temperature sensors are used to sense if any fire in the system. If temperature goes beyond the limit then all the devices get shutdown and immediately sms is sent to a person.

IV. Components

4.1 PIC microcontroller

The PIC microcontroller was developed by General Instruments in 1975. PIC was developed when Microelectronics Division of General Instruments was testing its 16-bit CPU CP1600. Although the CP1600 was a good CPU but it had low I/O performance. The PIC controller was used to offload the I/O the tasks from CPU to improve the overall performance of the system.

In 1985, General Instruments converted their Microelectronics Division to Microchip Technology. PIC stands for Peripheral Interface Controller. The General Instruments used the acronyms Programmable Interface Controller and Programmable Intelligent Computer for the initial PICs (PIC1640 and PIC1650).

In 1993, Microchip Technology launched the 8-bit PIC16C84 with EEPROM which could be programmed using serial programming method. The improved version of PIC16C84 with flash memory (PIC18F84 and PIC18F84A) hit the market in 1998.

4.2 PIC Microcontroller Development

Since 1998, Microchip Technology continuously developed new high performance microcontrollers with new complex architecture and enhanced in-built peripherals. PIC microcontroller is based on Harvard architecture. At present PIC microcontrollers are widely used for industrial purpose due to its high performance ability at low power consumption. It is also very famous among hobbyists due to moderate cost and easy availability of its supporting software and hardware tools like compilers, simulators, debuggers etc. The 8-bit PIC microcontroller is divided into following four categories on the basis of internal architecture:

- Base Line PIC
- Mid-Range PIC
- Enhanced Mid-Range PIC
- PIC18

4.3 Base Line PIC

Base Line PICs are the least complex **PIC microcontrollers**. These microcontrollers work on 12-bit instruction architecture which means that the word size of instruction sets are of 12 bits for these controllers. These are smallest and cheapest PICs, available with 6 to 40 pin packaging. The small size and low cost of Base Line PIC replaced the traditional ICs like 555, logic gates etc. in industries.

4.4. Mid-Range PIC

Mid-Range PICs are based on 14-bit instruction architecture and are able to work up to 20 MHz speed. These controllers are available with 8 to 64 pin packaging. These microcontrollers are available with different peripherals like ADC, PWM, Op-Amps and different communication protocols like USART, SPI, I2C (TWI), etc. which make them widely usable microcontrollers not only for industry but for hobbyists as well.

4.5 Enhanced Mid-Range PIC

These controllers are enhanced version of Mid-Range core. This range of controllers provides additional performance, greater flash memory and high speed at very low power consumption. This range of PIC also includes multiple peripherals and supports protocols like USART, SPI, I2C and so on.

4.6 PIC18

PIC18 range is based on 16-bit instruction architecture incorporating advanced RISC[3] architecture which makes it highest performer among the all 8-bit PIC families. The PIC18 range is integrated with new age communication protocols like USB, CAN, LIN, Ethernet (TCP/IP protocol) to communicate with local and/or internet based networks. This range also supports the connectivity of Human Interface Devices like touch panels etc.

4.7 LCD

LCD (Liquid Crystal Display) screen is an electronic display module and find a wide range of applications. A 16x2 LCD display is very basic module and is very commonly used in various devices and circuits. These modules are preferred over seven segments and other multi segment LEDs. The reasons being: LCDs are economical; easily programmable; have no limitation of displaying special & even custom characters (unlike in seven segments), animations and so on.

A 16x2 LCD means it can display 16 characters per line and there are 2 such lines. In this LCD each character is displayed in 5x7 pixel matrix. This LCD has two registers, namely, Command and Data.

The command register stores the command instructions given to the LCD. A command is an instruction given to LCD to do a predefined task like initializing it, clearing its screen, setting the cursor position, controlling display etc. The data register stores the data to be displayed on the LCD. The data is the ASCII value of the character to be displayed on the LCD. Click to learn more about internal structure of a LCD.

4.8 Relay

Relay is an electromagnetic device which is used to isolate two circuits electrically and connect them magnetically. They are very useful devices and allow one circuit to switch another one while they are completely separate. They are often used to interface an electronic circuit (working at a low voltage) to an electrical circuit which works at very high voltage. For example, a relay can make a 5V DC battery circuit to switch a 230V AC mains circuit. Thus a small sensor circuit can drive, say, a fan or an electric bulb. A relay switch can be divided into two parts: input and output. The input section has a coil which generates magnetic field when a small voltage from an electronic circuit is applied to it. This voltage is called the operating voltage. Commonly used relays are available in different configuration of operating voltages like 6V, 9V, 12V, 24V etc. The output section consists of contactors which connect or disconnect mechanically. In a basic relay there are three contactors: normally open (NO), normally closed (NC) and common (COM). At no input state, the COM is connected to NC. When the operating voltage is applied the relay coil gets energized and the COM changes contact to NO. Different relay configurations are available like SPST, SPDT, and DPDT etc, which have different number of changeover contacts. By using proper combination of contactors, the electrical circuit can be switched on and off. Get inner details about structure of a relay switch.

4.9 Regulator IC

7805 is a voltage regulator integrated circuit. It is a member of 78xx series of fixed linear voltage regulator ICs. The voltage source in a circuit may have fluctuations and would not give the fixed voltage output. The voltage regulator IC maintains the output voltage at a constant value. The xx in 78xx indicates the fixed output voltage it is designed to provide. 7805 provides +5V regulated power supply. Capacitors of suitable values can be connected at input and output pins depending upon the respective voltage levels.

4.10 Voltage and current Sensor

ADC module of PIC Microcontroller converts the Signals on its analog pin to 10 bit binary data and it has software selectable high and low voltage reference input to some combination of VDD, VSS, RA2 and RA3. The analog input to PIC is limited to VSS and VDD voltages (0 – 5V) of PIC this circuit is designed to measure 0 to 30V. So we will map 0 to 30V to 0 to 5V by using a voltage divider. Current through a circuit can be

measured by introducing a 1 ohm resistor and measuring the voltage across it. To minimize the path resistance we will use .47 ohm special resistor with and current is calculated. Voltage and Current Sampling circuit is shown below.

When the Input voltage is 30V (max) the voltage across 20K ohm resistor becomes 5V which is feedback to the analog pin RA2 of the PIC Microcontroller. The voltage across .47 ohm resistor is also feedback to the analog pin RA3 via 100K ohm resistor. 5.1V Zener Diode is added in parallel to these analog input pins to protect PIC from over voltages. The ADC module of PIC converts analog input to 10 bit digital number. We want to convert this digital to corresponding voltage n decimal.

V. Software Requirement

5.1 Kiel Compiler

Embedded system means some combination of computer hardware and programmable software which is specially designed for a particular task like displaying message on LCD[4]. If you are still wondering about an embedded system, just take a look at these circuit applications using 8051/PIC microcontroller. You can call these applications embedded systems as it involves hardware (8051/PIC microcontroller) and software (the code written in assembly language).

Some real life examples of embedded systems may involve ticketing machines, vending machines, temperature controlling unit in air conditioners etc. Microcontrollers are nothing without a Program in it.

One of the important part in making an embedded system is loading the software/program we develop into the microcontroller. Usually it is called “*burning software*” into the controller. Before “burning a program” into a controller, we must do certain prerequisite operations with the program. This includes writing the program in assembly language or C language in a text editor like notepad, compiling the program in a compiler and finally generating the hex code from the compiled program. Earlier people used different soft wares/applications for all these 3 tasks. Writing was done in a text editor like notepad/word pad, compiling was done using separate software (probably a dedicated compiler for a particular controller like 8051), converting the assembly code to hex code was done using another software etc. It takes lot of time and work to do all these separately, especially when the task involves lots of error debugging and reworking on the source code.

Kiel Micro Vision is free software which solves many of the pain points for an embedded program developer. This software is an integrated development environment (IDE), which integrated a text editor to write programs, a compiler and it will convert your source code to hex files too.

5.2 How to Burn a Micro Controller

Programming or burning a microcontroller means to transfer the program from the compiler to the memory of the microcontroller. A compiler is software which provides an environment to write, test and debug a program for the microcontroller. The program for a microcontroller is generally written in C or assembly language. Finally the compiler generates a hex file which contains the machine language instruction understandable by a microcontroller. It is the content of this hex file which is transferred to the memory of the microcontroller. Once a program is transferred or written in the memory of the microcontroller, it then works in accordance with the program.

In order to know how to program a microcontroller, we need a device called a burner/programmer. A programmer is a hardware device with dedicated software which reads the content of the hex file stored on the PC or the laptop and transfers it to the microcontroller to be burned. It reads the data of the hex file by connecting itself to the PC via a serial or USB cable and transfers the data to the memory of the microcontroller to be programmed in accordance with the protocols as described by the manufacturer in the datasheet.

The programmer and the compiler differ for microcontrollers from different companies. In some cases the compiler has programmer software inbuilt in it. You simply need to connect the programmer hardware and the microcontroller can be programmed from the compiler itself.

VI. Steps Followed In Designing The System

Three general steps can be followed to appropriately select the control system:

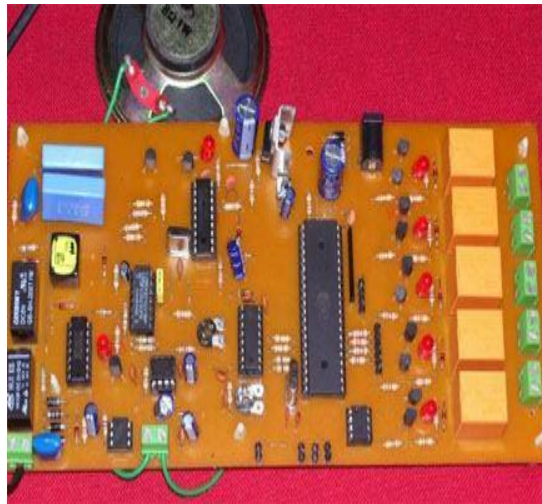
Step # 1: Identify measurable variables important to production. It is very important to correctly identify the parameters that are going to be measured by the controller’s data acquisition interface, and how they are to be measured.

Step # 2: Investigate the control strategies. An important element in considering a control system is the control strategy that is to be followed. The simplest strategy is to use threshold sensors that directly affect actuation of devices.

Step # 3: Identify the software and the hardware to be used. Hardware must always follow the selection of software, with the hardware required being supported by the software selected. In addition to functional

capabilities, the selection of the control hardware should include factors such as reliability, support, previous experiences with the equipment (successes and failures), and cost.

VII. Result Analasis



VIII. Conclusion

Advanced automation system can be used in organization to know about various departments, mode working and levels of control. Hardware circuitry of automation system is very compact .by the wide spread internet it is possible to information from anywhere in the world with advanced features of automation System.

It has been the latest technology for industrial application .this provides the foundation for providing service for industrial process application as well as reduced cost, improved man power satisfaction.

A message interface gives user more flexible navigation outputs. That is less complex and more rigidly hierarchical.

REFERENCES

- [1]. Jain. AnSingh.S "Modified Programming Language Framework for IVRS Accessibility of Graphical User Interfaces," Ubi-Media Computing (U-Media), 2011 4th International Conference on Digital Object Identifier: 10.1109/U-MEDIA.2011.44.
- [2]. Ansari, A.M, Nehal, M.F, Qadeer M.A.e," SIP-based Interactive Voice Response System using Free Switch EPBX " Wireless and Optical Communications Networks (WOCN), 2013 Tenth International Conference on Digital Object Identifier: 10.1109/WOCN.2013.6616224.
- [3]. Soujanya.M, ,Kumar.S. "Personalized IVR system in contact center," Electronics and Information Engineering (ICEIE), 2010 International Conference OnVolume:1 Digital Object Identifier: 10.1109/ICEIE.2010.5559673.
- [4]. Hashizume.K, Tuan Phung-Duc Kasahara.S, Takahashi.Y "Queueing analysis of internet-based call centers withinteractive voice response and redial " Computer Aided Modeling and Design of Communication LinksandNetworks (CAMAD), 2012 IEEE 17th International Workshop on Digital Object Identifier: 1109/CAMAD. 2012.6335371.

Simulation of MPPT Algorithm Based Hybrid Wind-Solar-Fuel Cell Energy System

Kalpana. P¹, Venkata Pradeep. G²

^{1,2} Department of Electrical and Electronics Engineering, JNTU Anantapur

Abstract: This paper presents a new system configuration of the front-end rectifier stage for a hybrid wind/photovoltaic energy system. This configuration allows the two sources to supply the load separately or simultaneously depending on the availability of the energy sources. The inherent nature of this Cuk-SEPIC fused converter, additional input filters are not necessary to filter out high frequency harmonics. Harmonic content is detrimental for the generator lifespan, heating issues, and efficiency. The fused multiinput rectifier stage also allows Maximum Power Point Tracking (MPPT) to be used to extract maximum power from the wind and sun when it is available. An adaptive MPPT algorithm will be used for the wind system and a standard perturb and observe method will be used for the PV system. Operational analysis of the proposed system will be discussed in this paper. Simulation results are given to highlight the merits of the proposed circuit.

I. Introduction

When a source is unavailable or insufficient in meeting the load demands, the other energy source can compensate for the difference. Several hybrid wind/PV power systems with MPPT control have been proposed and discussed in works [1]- [5]. Most of the systems in literature use a separate DC/DC boost converter connected in parallel in the rectifier stage as shown in Figure 1 to perform the MPPT control for each the renewable energy power sources [1]-[4]. A simpler multiinput structure has been suggested by [5] that combine the sources from the DC-end while still achieving MPPT for each renewable source. The structure proposed by [5] is a fusion of the buck and buck-boost converter. The systems in literature require passive input filters to remove the high frequency current harmonics injected into wind turbine generators [6]. The harmonic content in the generator current decreases its lifespan and increases the power loss due to heating [6]. In this paper, an alternative multi-input rectifier structure is proposed for hybrid wind/solar energy systems. The proposed design is a fusion of the Cuk and SEPIC converters. The features of the proposed topology are: 1) the inherent nature of these two converters eliminates the need for separate input filters for PFC [7]-[8]; 2) it can support step up/down operations for each renewable source (can support wide ranges of PV and wind input); 3) MPPT can be realized for each source; 4) individual and simultaneous operation is supported.

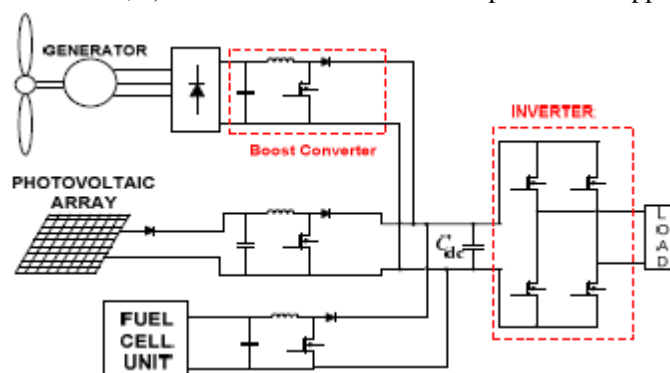


Figure 1: Hybrid system with multi-connected boost converter

II. Proposed Multi-Input Rectifier Stage

A system diagram of the proposed rectifier stage of a hybrid energy system is shown in Figure 2, where one of the inputs is connected to the output of the PV array and the other input connected to the output of a generator. The fusion of the two converters is achieved by reconfiguring the two existing diodes from each converter and the shared utilization of the Cuk output inductor by the SEPIC converter. This configuration

allows each converter to operate normally individually in the event that one source is unavailable. Figure 3 illustrates the case when only the wind source is available. In this case, $D1$ turns off and $D2$ turns on; the proposed circuit becomes a SEPIC converter and the input to output voltage relationship is given by (1). On the other hand, if only the P source is available, then $D2$ turns off and $D1$ will always be on and the circuit becomes a Cuk converter as shown in Figure 4. The input to output voltage relationship is given by (2). In both cases, both converters have step-up/down capability, which provide more design flexibility in the system if duty ratio control is utilized to perform MPPT control.

$$\frac{V_{dc}}{V_W} = \frac{d_2}{1-d_2} \quad (1)$$

$$\frac{V_{dc}}{V_{pv}} = \frac{d_1}{1-d_1} \quad (2)$$

Figure 5 illustrates the various switching states of the proposed converter. If the turn on duration of $M1$ is longer than $M2$, then the switching states will be state I, II, IV. Similarly, the switching states will be state I, III, IV if the switch conduction periods are vice versa. To provide a better explanation, the inductor current waveforms of each switching state are given as follows assuming that $d_2 > d_1$; hence only states I, III, IV are discussed in this example. In the following, $I_{i,PV}$ is the average input current from the PV source; $I_{i,W}$ is the RMS input current after the rectifier (wind case); and I_{dc} is the average system output current. The key waveforms that illustrate the switching states in this example are shown in Figure 6. The mathematical expression that relates the total output voltage and the two input sources will be illustrated in the next section.

State I ($M1$ on, $M2$ on):

$$i_{L1} = I_{i,PV} + \frac{V_{PV}}{L_1} t \quad 0 < t < d_1 T_s$$

$$i_{L2} = I_{dc} + \left(\frac{v_{c1} + v_{c2}}{L_2} \right) t \quad 0 < t < d_1 T_s$$

$$i_{L3} = I_{i,W} + \frac{V_W}{L_3} t \quad 0 < t < d_1 T_s$$

State III ($M1$ off, $M2$ on):

$$i_{L1} = I_{i,PV} + \left(\frac{V_{PV} - v_{c1}}{L_1} \right) t \quad d_1 T_s < t < d_2 T_s$$

$$i_{L2} = I_{dc} + \frac{v_{c2}}{L_2} t \quad d_1 T_s < t < d_2 T_s$$

$$i_{L3} = I_{i,W} + \frac{V_W}{L_3} t \quad d_1 T_s < t < d_2 T_s$$

State IV ($M1$ off, $M2$ off):

$$i_{L1} = I_{i,PV} + \left(\frac{V_{PV} - v_{c1}}{L_1} \right) t \quad d_2 T_s < t < T_s$$

$$i_{L2} = I_{dc} - \frac{V_{dc}}{L_2} t \quad d_2 T_s < t < T_s$$

$$i_{L3} = I_{i,W} + \left(\frac{V_W - v_{c2} - V_{dc}}{L_3} \right) t \quad d_2 T_s < t < T_s$$

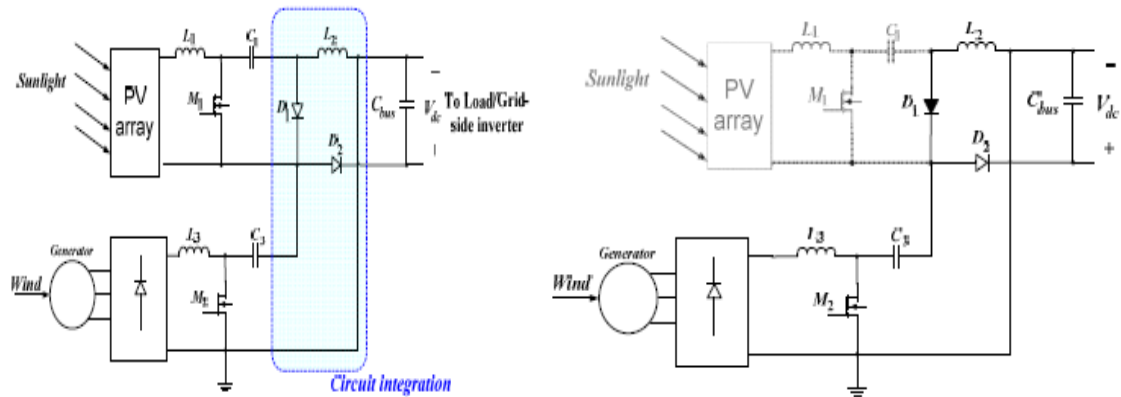


Figure 2: Proposed rectifier stage for a Hybrid wind/PV system, Figure 3: Only wind source is operational (SEPIC)

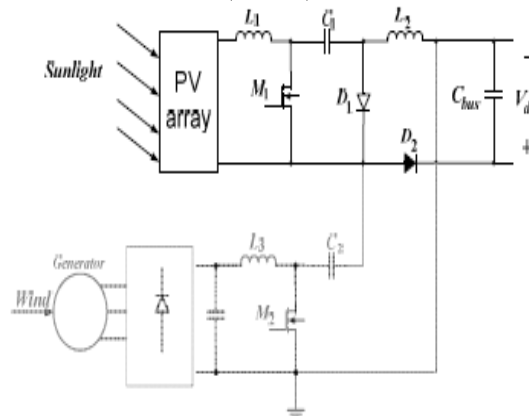


Figure 4: Only PV source is operation (Cuk)

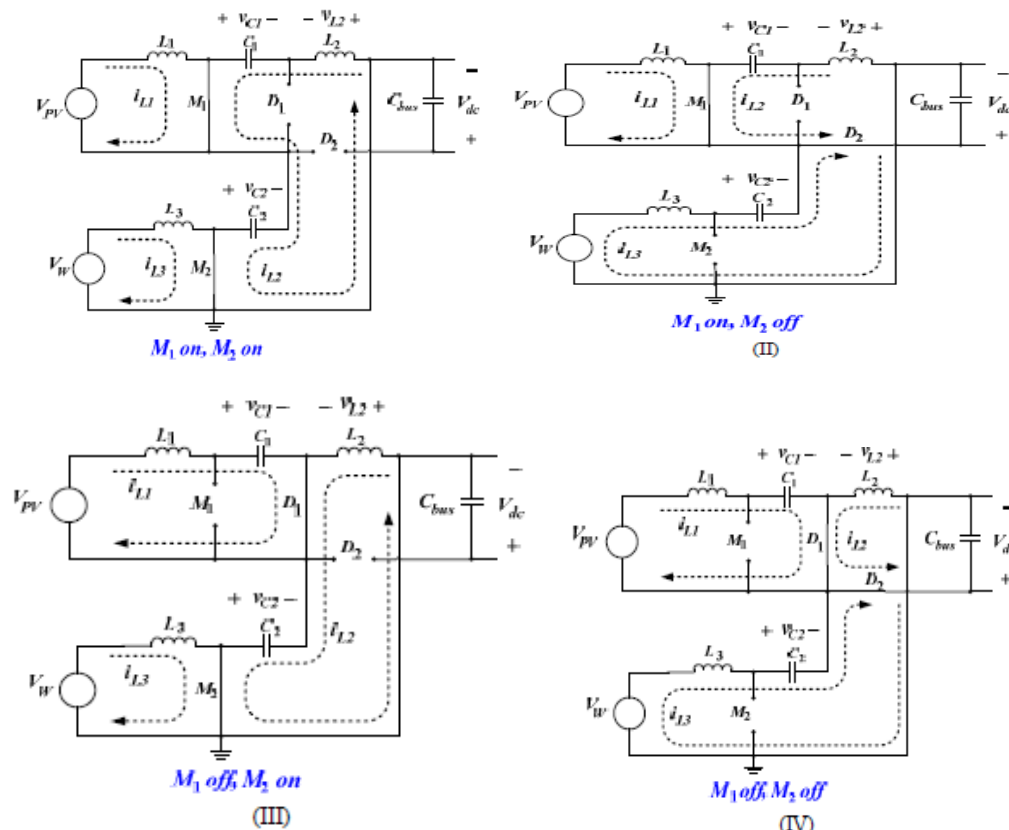


Figure 5 (I-IV): switching states within a switching cycle

III. Analysis Of Proposed Circuit

To find an expression for the output DC bus voltage, V_{dc} , the volt-balance of the output inductor, L_2 , is examined according to Figure 6 with $d_2 > d_1$. Since the net change in the voltage of L_2 is zero, applying volt-balance to L_2 results in (3). The expression that relates the average output DC voltage (V_{dc}) to the capacitor voltages (v_{c1} and v_{c2}) is then obtained as shown in (4), where v_{c1} and v_{c2} can then be obtained by applying volt-balance to L_1 and L_3 [9]. The final expression that relates the average output voltage and the two input sources (V_W and V_{PV}) is then given by (5). It is observed that V_{dc} is simply the sum of the two output voltages of the Cuk and SEPIC converter. This further implies that V_{dc} can be controlled by d_1 and d_2 individually or simultaneously.

$$(v_{c1} + v_{c2})d_1T_s + (V_{c2})(d_2 - d_1)T_s + (1 - d_2)(-v_{dc})T_s = 0 \quad (3)$$

$$v_{dc} = \left(\frac{d_1}{1-d_2}\right)v_{c1} + \left(\frac{d_2}{1-d_2}\right)v_{c2} \quad (4)$$

$$v_{dc} = \left(\frac{d_1}{1-d_1}\right)v_{pv} + \left(\frac{d_2}{1-d_2}\right)v_w \quad (5)$$

The switches voltage and current characteristics are also provided in this section. The voltage stress is given by (6) and (7) respectively. As for the current stress, it is observed from Figure 6 that the peak current always occurs at the end of the on-time of the MOSFET. Both the Cuk and SEPIC MOSFET current consists of both the input current and the capacitors (C_1 or C_2) current. The peak current stress of M_1 and M_2 are given by (8) and (10) respectively. L_{eq1} and L_{eq2} , given by (9) and (11), represent the equivalent inductance of Cuk and SEPIC converter respectively. The PV output current, which is also equal to the average input current of the Cuk converter is given in (12). It can be observed that the average inductor current is a function of its respective duty cycle (d_1). Therefore by adjusting the respective duty cycles for each energy source, maximum power point tracking can be achieved.

$$V_{ds1} = V_{pv} \left(1 + \frac{d_1}{1-d_1}\right) \quad (6)$$

$$V_{ds2} = V_w \left(1 + \frac{d_2}{1-d_2}\right) \quad (7)$$

$$i_{ds1,pk} = I_{i,pv} + I_{dc,avg} + \frac{V_{pv}d_1T_s}{2L_{eq1}} \quad (8)$$

$$L_{eq1} = \frac{L_1L_2}{L_1+L_2} \quad (9)$$

$$i_{ds2,pk} = I_{i,pv} + I_{dc,avg} + \frac{V_{pv}d_2T_s}{2L_{eq1}} \quad (10)$$

$$L_{eq2} = \frac{L_3L_2}{L_3+L_2} \quad (11)$$

$$I_{i,pv} = \frac{P_0}{V_{dc}} \frac{d_1}{1-d_1} \quad (12)$$

IV. Mppt Control Of Proposed Circuit

A common inherent drawback of wind and PV systems is the intermittent nature of their energy sources. Wind energy is capable of supplying large amounts of power but its presence is highly unpredictable as it can be here one moment and gone in another. Solar energy is present throughout the day, but the solar irradiation levels vary due to sun intensity and unpredictable shadows cast by clouds, birds, trees, etc. These drawbacks tend to make these renewable systems inefficient. However, by incorporating maximum power point tracking (MPPT) algorithms, the systems' power transfer efficiency can be improved significantly. To describe a wind turbine's power characteristic, equation (13) describes the mechanical power that is generated by the wind.

$$p_m = 0.5\rho AC_p(\lambda, \beta)v_w^3$$

Where

P=air density,

A=rotor swept area,

$c_p(\lambda, \beta)$ = power coefficient function,

λ =tip speed ratio,

β =pitch angle,

v_w = wind speed

The power coefficient (C_p) is a nonlinear function that represents the efficiency of the wind turbine to convert wind energy into mechanical energy. It is dependent on two variables, the tip speed ratio (TSR) and the pitch angle. The TSR, λ , refers to a ratio of the turbine angular speed over the wind speed. The mathematical representation of the TSR is given by (14) [10]. The pitch angle, β , refers to the angle in which the turbine blades are aligned with respect to its longitudinal axis.

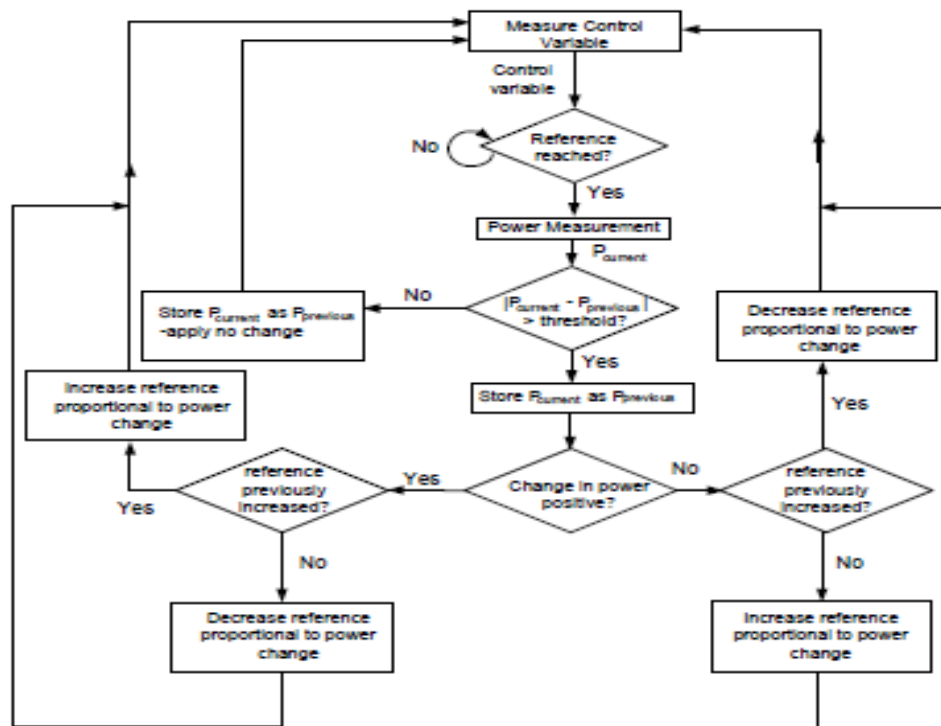


Figure 6: General MPPT Flow Chart for wind and PV

V. Simulation Results

In this section, simulation results from MATLAB 7.8 is given to verify that proposed multi-input rectifier stage can support individual as well as simultaneous operation. The specifications for the design example are given in TABLE I. Figure 10 illustrates the system under the condition where the wind source has failed and only the PV source (Cuk converter mode) is supplying power to the load. Figure 11 illustrates the system where only the wind turbine generates power to the load (SEPIC converter mode). Finally, Figure 12 illustrates the simultaneous operation (Cuk-SEPIC fusion mode) of the two sources where M2 has a longer conduction cycle (converter states I, IV and III—see Figure 5).

TABLE I. Design Specifications

Output power(W)	3Kw
Output voltage	500V
Switching frequency	20kHz

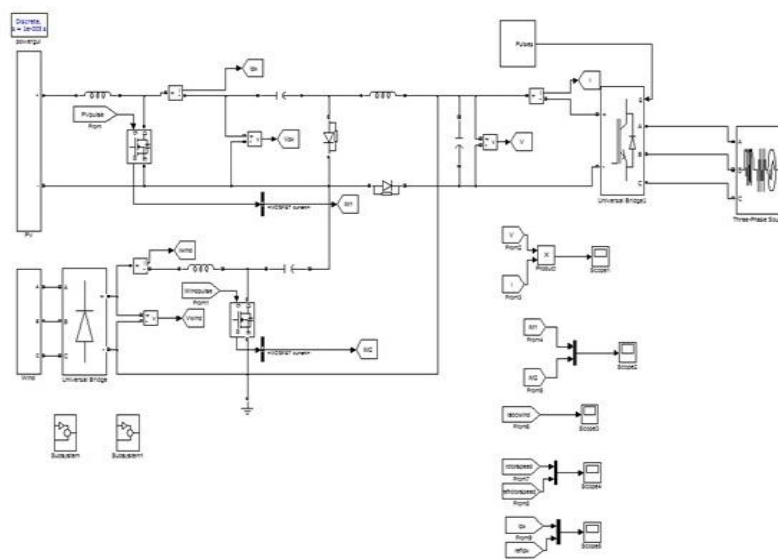


Fig 7: Hybrid solar wind

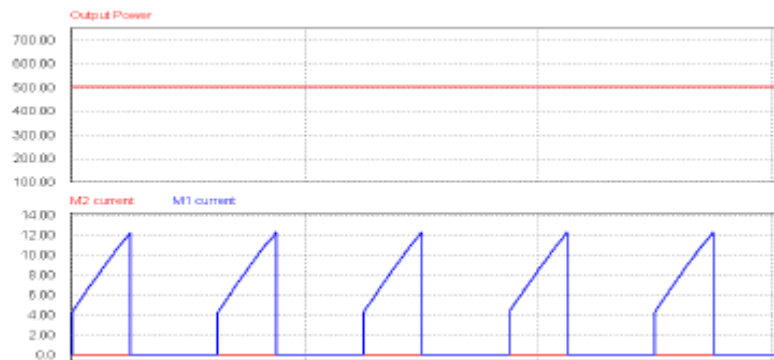


Figure 8 : Individual operation with only PV source (Cuk operation) Top: Output power, Bottom: Switch currents (M1 and M2)

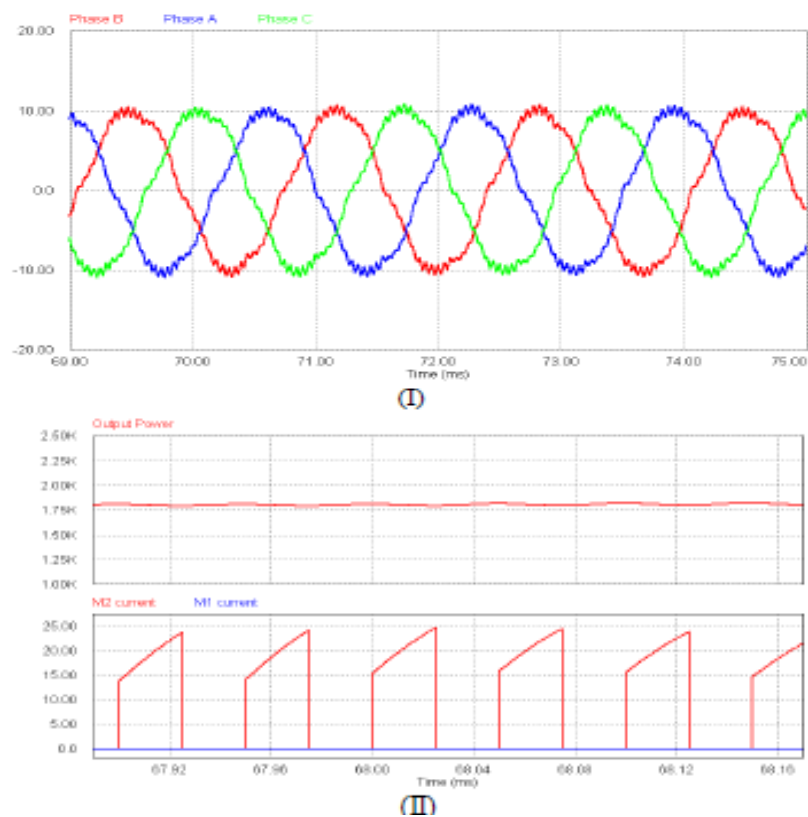
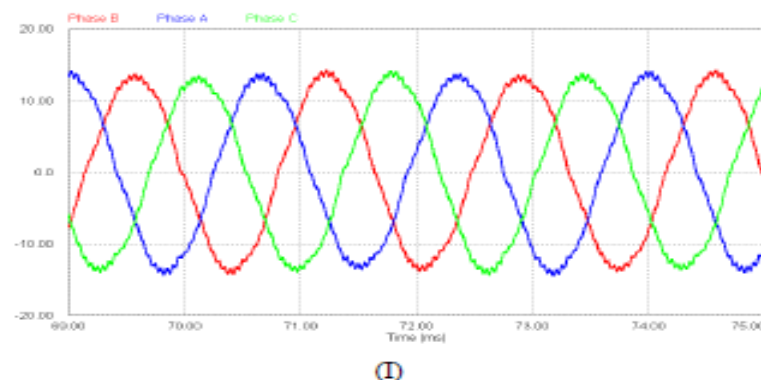


Figure 9 : Individual operation with only wind source (SEPIC operation) (I) The injected three phase generator current; (II) Top: Output power, Bottom: Switch currents (M1 and M2)



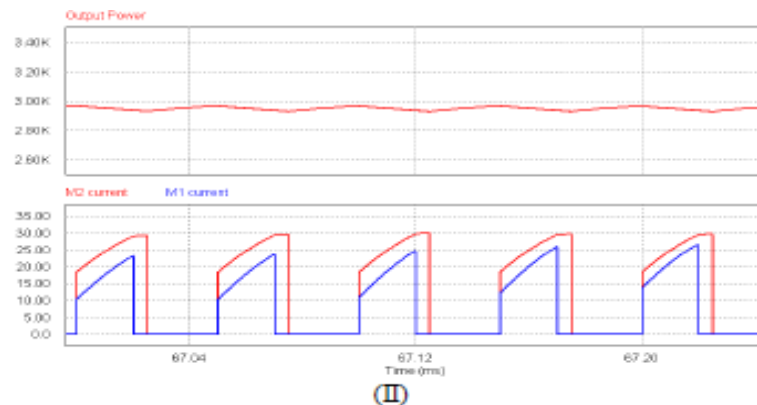


Figure 10 : Simultaneous operation with both wind and PV source (Fusion mode with Cuk and SEPIC)(I) The injected three phase generator current; (II) Top: Output power, Bottom: Switch currents (M1 and M2)

Figure 11 and 12 illustrates the MPPT operation of the PV component of the system (Cuk operation) and the Wind component of the system (SEPIC operation) respectively.

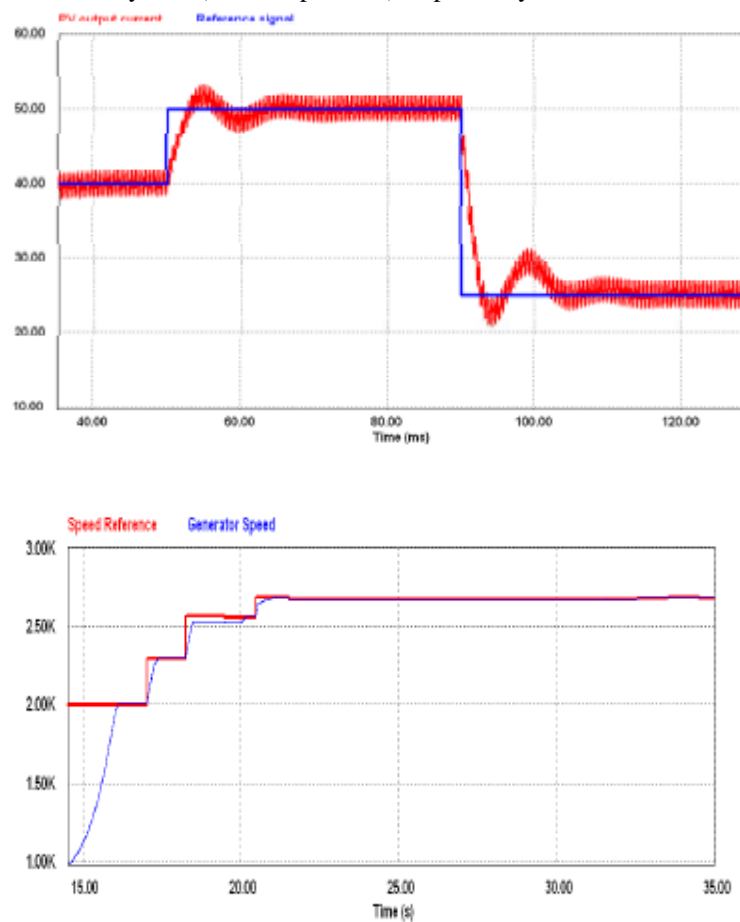


Figure 11 : Solar MPPT – PV output current andReference current signal (Cuk operation)Figure 12 : Wind MPPT –Generator speed and reference speed signal (SEPIC operation)

VI. Conclusion

In this paper a new multi-input Cuk-SEPIC rectifier stage for hybrid wind/solar energy systems has been presented. The features of this circuit are: 1) additional input filters are not necessary to filter out high frequency harmonics; 2) both renewable sources can be stepped up/down (supports wide ranges of PV and wind input); 3) MPPT can be realized for each source; 4) individual and simultaneous operation is supported. Simulation results have been presented to verify the features of the proposed topology.

REFERENCES

- [1] S.K. Kim, J.H. Jeon, C.H. Cho, J.B. Ahn, and S.H. Kwon, "Dynamic Modeling and Control of a Grid-Connected Hybrid Generation System with Versatile Power Transfer," *IEEE Transactions on Industrial Electronics*, vol. 55, pp. 1677-1688, April 2008.
- [2] D. Das, R. Esmaili, L. Xu, D. Nichols, "An Optimal Design of a Grid Connected Hybrid Wind/Photovoltaic/Fuel Cell System for Distributed Energy Production," in *Proc. IEEE Industrial Electronics Conference*, pp. 2499-2504, Nov. 2005.
- [3] N. A. Ahmed, M. Miyatake, and A. K. Al-Othman, "Power fluctuations suppression of stand-alone hybrid generation combining solar photovoltaic/wind turbine and fuel cell systems," in *Proc. Of Energy Conversion and Management*, Vol. 49, pp. 2711-2719, October 2008.
- [4] S. Jain, and V. Agarwal, "An Integrated Hybrid Power Supply for Distributed Generation Applications Fed by Nonconventional Energy Sources," *IEEE Transactions on Energy Conversion*, vol. 23, June
- [5] Y.M. Chen, Y.C. Liu, S.C. Hung, and C.S. Cheng, "Multi-Input Inverter for Grid-Connected Hybrid PV/Wind Power System," *IEEE Transactions on Power Electronics*, vol. 22, May 2007.
- [6] dos Reis, F.S., Tan, K. and Islam, S., "Using PFC for harmonic mitigation in wind turbine energy conversion systems" in *Proc. of the IECON 2004 Conference*, pp. 3100- 3105, Nov. 2004
- [7] R. W. Erickson, "Some Topologies of High Quality Rectifiers" in the *Proc. of the First International Conference on Energy, Power, and Motion Control*, May 1997.
- [8] D. S. L. Simonetti, J. Sebasti'an, and J. Uceda, "The Discontinuous Conduction Mode Sepic and 'Cuk Power Factor Preregulators: Analysis and Design" *IEEE Trans. On Industrial Electronics*, vol. 44, no. 5, 1997
- [9] N. Mohan, T. Undeland, and W. Robbins, "Power Electronics: Converters, Applications, and Design," John Wiley & Sons, Inc., 2003.
- [10] J. Marques, H. Pinheiro, H. Grundling, J. Pinheiro, and H. Hey, "A Survey on Variable-Speed Wind Turbine System," *Proceedings of Brazilian Conference of Electronics of Power*, vol. 1, pp. 732-738, 2003.
- [11] F. Lassier and T. G. Ang, "Photovoltaic Engineering Handbook" 1990
- [12] Global Wind Energy Council (GWEC), "Global wind 2008 report," June 2009.
- [13] L. Pang, H. Wang, Y. Li, J. Wang, and Z. Wang, "Analysis of Photovoltaic Charging System Based on MPPT," *Proceedings of Pacific-Asia Workshop on Computational Intelligence and Industrial Application 2008 (PACIIA '08)*, Dec 2008, pp. 498-501.

Applications of Artificial Neural Network and Wavelet Transform For Condition Monitoring of the Combined Faults of Unbalance and Bearing Clearance

H. K. Srinivas¹, Shamanth. S. Holla², Karthik. B. S³, Niroop.S⁴, Chiranjeevi. D⁵

¹ (Head, Department of Mechanical Engineering, YDIT, Bangalore, Karnataka, India)
^{2,3,4,5} (Students, Department of Mechanical Engineering, YDIT, Bangalore, Karnataka, India)

Abstract: The vibration analysis of rotating machinery indicates of the condition of potential faults such as unbalance, bent shaft, shaft crack, bearing clearance, rotor rub, misalignment, looseness, oil whirl and whip and other malfunctions. More than one fault can occur in a rotor. This paper describes the application of Artificial Neural Network (ANN) and Wavelet Transform (WT) for the prediction of the effect of the combined faults of unbalance and bearing clearance on the frequency components of vibration signature of the rotating machinery. The experimental data of frequency components and corresponding Root Mean Square (RMS) velocity (amplitude) data are used as inputs to train the ANN, which consists of a three-layered network. The ANN is trained using an improved multilayer feed forward back propagation Levenberg-Marquardt algorithm. In particular, an overall success rates achieved were 99.78% for unbalance, 99.81% bearing clearance, and 99.45% for the combined faults of unbalance and bearing clearance. The wavelet transform approach enables instant to instant observation of different frequency components over the full spectrum. A new technique combining the WT with ANN performs three general tasks data acquisition, feature extraction and fault identification. This method is tested successfully for individual and combined faults of unbalance and bearing clearance at a success rate of 99.99%.

Keywords: Artificial Neural Networks, Rotor faults, Rotor test rig, Unbalance and bearing clearance, Vibration analysis and Wavelet.

I. INTRODUCTION

In order to avoid the failure of various types of rotating machinery, including mechanical and electrical ones, using sophisticated instrumentation to monitor the condition of various machine signatures has been found to be of considerable use. Vibration measurement and analysis has been applied with success [1] to machines such as steam and gas turbines, pumps, Compressors and induction motors. Faults such as unbalance, misalignment, looseness, rub and cracks generate vibration signals. In the present work, an experimental study has been carried out for a steady state response (constant speed of 1500 rpm) of the rotor for different unbalance masses and bearing clearance on the rotor test rig. The vibration frequency components recorded in the horizontal, vertical and axial directions for the analysis are applied. The experimental study has also been carried out to discover the difference in vibration characteristics due to the combined faults of unbalance and bearing clearance. The monitoring of the vibration of rotating machines has been reported as being a useful technique for the analysis of their condition [2] [3] [4] [5]. Vibration condition monitoring as an aid to fault diagnosis is examined by Taylor (1995), Smalley and colleagues (1996) present a method of assessing the severity of vibrations in terms of the probability of damage by analyzing the vibration signals. Though the measured vibration signatures of frequency domain features are adequate to identify the faults, there is a need for reliable, fast and automated procedure of diagnostics [6]. Unbalance is an important cause of vibration in rotating machinery, and the reduction of such vibration by balancing needs attention. In this paper the experimental studies are presented in the dynamic balancing of flexible shaft using the four run method (FRM) (Mallik & Basu). The vibration frequency of rotor unbalance is synchronous, i.e., one time the shaft rotation speed (1X rpm Rotor unbalance has been reported to appear occasionally in the frequency domain as a series of harmonics of the shaft running speed, i.e., 1Xrpm, 2Xrpm, 3Xrpm, 4Xrpm, etc. [7].

1.1. Artificial Neural Networks

The neural network techniques are used in conjunction with signal analysis techniques for classification and quantification of faults [8] in some applications. Kaminski [9] has developed neural networks to identify the approximate location of damage due to cracks through the analysis of changes in the neural frequencies. McCormick and Nandi [10] have used neural network method for automatically classifying the machine condition from the vibration time series. Vyas and Satish Kumar [11] have carried out experimental studies to generate data for rotating machinery faults such as mass unbalance, bearing cap loose. Srinivasan [12] carried out extensive studies on faults like parallel misalignment, angular misalignment, unbalance, crack, light and heavy rubs, looseness and bearing clearance.

The Fig-1 shows a simple network consisting of three layers with one input layer, one hidden layer and one output layer. There are no connections between nodes in the same layer and no connection that bridge the layers. Such networks with only one hidden layer can uniformly approximate any continuous function and therefore provide a theoretical basis for the use of this type of network. The input-output relationship of each node is determined by a set of connection weights W_i , a threshold parameter b_i and a node activation function $A(.)$ such that-

$$Y = A(W_i X_i + b_i) \quad (1)$$

Where Y is the output of the node and X_i are the inputs. The activation function $A(.)$ defines the output of a neuron in terms of activity level at its input. The sigmoid function is the most common activation function used in neural networks. It is defined as a strictly increasing function that exhibits smoothness and asymptotic properties. The Tan-sigmoid activation function is used in the hidden layer. The purelin activation function is used in the output layer.

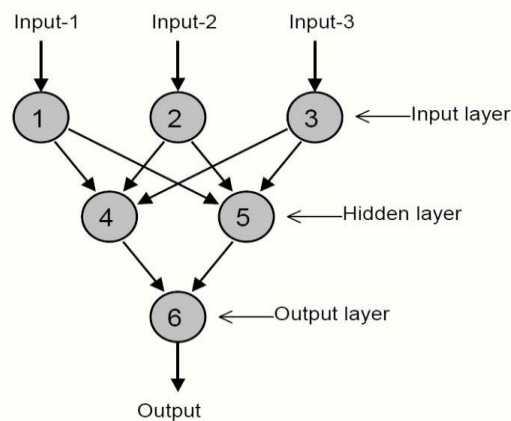


Fig-1 Three- layers network

In the present work, improved back propagation neural network has been applied for the diagnosis of combined faults of unbalance and bearing clearance. It attempts to minimize the square of the error between the output of the network and the desired outputs by changing the connection weights that use some form of gradient descent. The back propagation method has used gradient descent techniques, which are simply the techniques, where parameters such as weights and biases are moved in the opposite direction towards the error gradient. The Levenberg-Marquardt algorithm has the best convergence speeds for small and medium size networks [13, 14]. This optimization technique is more accurate and faster than gradient descent method. The Levenberg-Marquardt update rule is-

$$\Delta W = (J^T J + \Delta \mu I) J T e \quad (2)$$

Where ΔW = Small change in weight. J is the n by m Jacobian matrix $J^T J$ to keep function N rows of J linearly independent and μ is a small positive constant chosen to ensure $(J^T J + \mu I)$ is positive for all ' n ' values. If μ is very large the above expression approximates gradient descent; if it is small, the above expression becomes the Gauss-Newton method. The Gauss-Newton method is faster, more accurate and near to an error minimum. Training continues until the error goal is met, the minimum error gradient occurs, the maximum value of μ occurs, or the maximum number of epochs has been finished. The MAT LAB Neural Network toolbox has been applied for diagnosing the rotating machinery faults.

1.2. Wavelet transform

The wavelet transform acts as a “Mathematical microscope” in which one can observe different paths of the signal by “adjusting the focus”. A frequency component of the RMS velocity indicates the health of a particular machine. The wavelet transform approach allows the detection of short-lived frequency component in the signals. The method is logical since high frequency components (such as short bursts) need high frequency resolution as compared with low-frequency components, which require low- frequency resolution. This paper also describes the use of wavelet transform to decompose the vibration signal into several frequency ranges at different level of resolution. The strength (RMS) of the selected decomposed signals is then calculated under combined faults of unbalance mass and bearing clearance conditions. The neural network is then trained with the generated database to automate the fault diagnostic process.

II. Description Of The Test Rig

The experimental operator is shown in Fig.2. The experimental rotor system used in this work consisted of a motor, which was connected by a flexible coupling and a single disk rotor. The rotor shaft was supported by two identical brass bush bearings and had a length of 250 mm. The diameter of the rotor shaft was 15 mm. It has a disk of 116 mm in diameter, 22 mm in thickness and a disk of mass 1.65 kg which were mounted on the rotor shaft mid-way between the bearing supports. The disk was fixed on the rotor shaft by radial screws. There were 36 tapped holes symmetrically placed on each side of the disk flat faces at a radius of 45 mm in order to attach any desired amount of unbalance mass. The bearing pedestals are provided in order to fix the sensors and measure the dynamic vibration level in the horizontal, vertical and axial directions. The rotor shaft was driven by a 0.37 kW ac/dc variable speed motor. A constant operating speed of 1500 rpm was maintained, though motor speeds ranged from 0-8000 rpm. The natural frequency of the rotor was 4.45Hz in the lateral mode. The critical speed was 267 rpm.

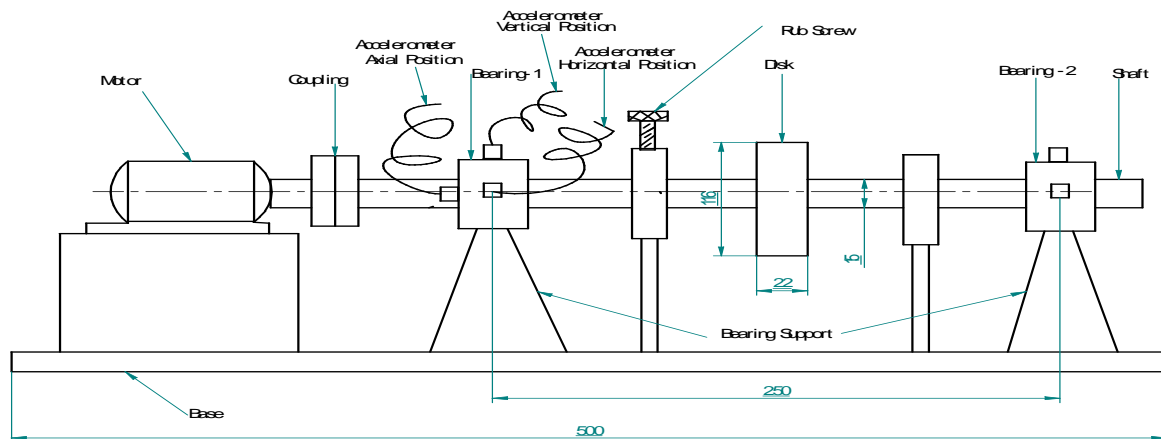


Fig - 2. Rotor Test-Rig

The piezoelectric accelerometers (Bruel & Kjaer, type 4370 piezoelectric accelerometer, Charge Sensitivity 9.99 Picocolumbs/ms²) were attached in three directions for measurement of RMS velocity in mm/s. The frequency analysis was carried out using a FFT analyzer (pulse lite, Basic 2-Channel, Max 12K points up to 1000 Hz in put frequency). An accelerometer enables measurement of the vibration level in the horizontal, vertical and axial directions. The output of the accelerometer was connected to the FFT analyzer for frequency analysis. Three special fixtures attached tightly to the bearing pedestal were used to hold the accelerometer at the desired locations. The signal was transmitted to a transducer and pre-amplifier. The output of the pre-amplifier signal was transmitted to the FFT analyzer.

III. Frequency Spectrum Analysis On Effects Of Combined Faults of Unbalance and Bearing Clearance

In this experiment, combination of mass unbalance and bearing clearance are both introduced simultaneously in the rotor test rig. The unbalance mass ranging from 6.5 g to 18.5g and bearing clearance ranging from 0.02 to 0.08 mm, with a combination of unbalance and bearing clearance were used. In order to investigate the vibration characteristics due to combined unbalance and bearing clearance faults were simulated in the rotor test rig. Initially, the brass bush of bearing clearance of 0.02 mm is used in the rotor test

rig. The unbalance of 6.5 g, 10.5 g, 14.5 g and 18.5 g were created by fixing the unbalance masses at a radius of 45 mm on the periphery of the rotor. The rotor is run at 1500 rpm. The vibration signatures were recorded in horizontal, vertical and axial direction. The frequency analysis has been carried out. The experiments also have been carried out for the bearing clearance of 0.04 mm, 0.06 mm and 0.08 mm by varying the unbalance masses. The frequency components are shown in the Table 1. The graphs of frequency components of RMS velocities are shown in Figure 3(a) to 3(d).

The unbalance mass range was from 6.5 g to 18.5 g with a combination of unbalance and bearing clearance. The machine was run at 1500 rpm. It is observed that the first harmonic in the horizontal direction 1X component has increased from 0.421mm/s to 0.874mm/s. The second harmonic 2X has also increased from 0.029mm/s to 0.147mm/s. There is an increase in the level of 1X frequency component of vibration from 0.234 to 0.346mm/s in vertical direction. The 2X frequency component of vibration has also shown an increasing trend from 0.029 mm/s to 0.159mm/s in the vertical direction. It has been observed from Fig. 3(a) to 3(d) that 1X frequency component of vibration is to be seen predominant in the horizontal direction ranging from 0.421mm/sec to 0.978mm/sec for the bearing clearance ranging from 0.02 mm to 0.08 mm and unbalance ranging from 6.5g to 18.5g corresponding to a speed of 1500 rpm, phase angle of 48 degrees. The increase in the vibration level is the highest with 1X frequency components in the horizontal direction is 0.978 mm/sec.

Table 1: Values of frequency components of RMS vibration velocity (mm/s) for various unbalance mass ranging from 6.5 to 18.5 g and bearing clearance 0.08 mm were obtained at a rotor speed of 1500 rpm.

Frequency components	Unbalance mass in (g) and bearing clearance in (mm)			
	Training set		Testing set	
	6.5+0.08	10.5+0.08	14.5+0.08	18.5+0.08
1XH	0.544	0.622	0.902	0.978
2XH	0.056	0.052	0.134	0.182
3XH	0.036	0.034	0.124	0.166
4XH	0.028	0.028	0.068	0.078
1X V	0.342	0.382	0.462	0.524
2X V	0.046	0.072	0.158	0.198
3X V	0.034	0.041	0.148	0.154
4X V	0.026	0.036	0.084	0.084
1X A	0.072	0.089	0.096	0.098
2X A	0.058	0.066	0.088	0.082
3X A	0.042	0.058	0.066	0.036
4X A	0.036	0.042	0.054	0.054

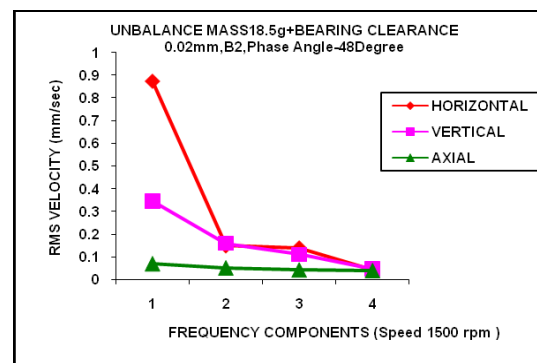
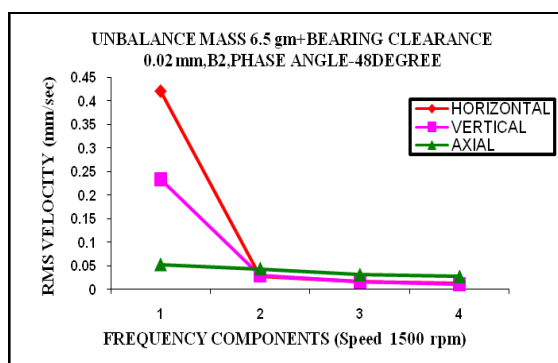


Fig. 3(a). Frequency components of RMS velocity for unbalance mass 6.5g & bearing clearance 0.02mm (L).

Fig. 3(b). Frequency components of RMS Velocity for unbalance mass 18.5g & bearing clearance 0.02mm (R).

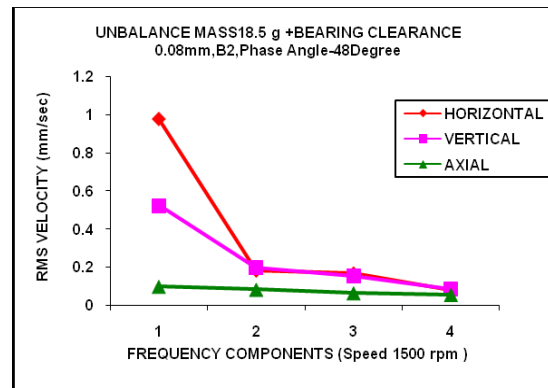
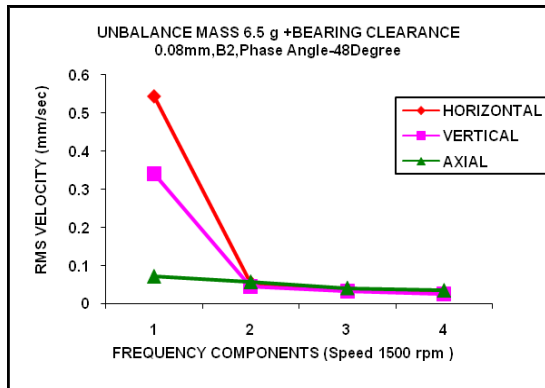


Fig. 3(c). Frequency components of RMS Velocity for unbalance mass 6.5g & bearing clearance 0.08mm (L).
Fig. 3(d). Frequency components of RMS Velocity for unbalance mass 18.5g & bearing clearance 0.08 mm (R).

IV. Applications of A.N.N. For Fault Diagnosis

The neural network used for rotor fault diagnosis consisted of one hidden layer and one output layer. Tan-sigmoid activation function was used in the hidden layer. The output layer used a purelin transfer function. The input vectors for training the network were the RMS velocity (mm/s) frequency components of the vibration signatures measured in the horizontal, vertical and an axial direction for faults such as unbalance and bearing clearance. The network performance is called generalization, which is the ratio of actual output to the desired output expressed in a percentage. The network was trained and tested with different neuron combination with different error goals for the above faults.

4.1. Network training and testing of combined faults of unbalance and bearing clearance data

The training and test data of the present study were generated on a rotor test rig (shown in Fig.2). Table-1 shows the training data and test data of RMS velocity for various unbalance masses and bearing clearance in the horizontal, vertical and axial directions. The values of frequency components in the horizontal, vertical and axial directions for unbalance ranging from 6.5g to 18.5g are noted. The ANN was trained by using MAT LAB Neural Network Tool Box. The ANN is said to be trained when the epochs are maximum, learning rate μ is maximum and error is minimum. The training was carried out using of error goals from 0.01 to 0.0001, with different number of neurons. Since there is no specific method to decide the exact number of neurons in the hidden layer, an empirical geometrical pyramid rule will be discussed [3]. Number of hidden neurons = \sqrt{mn} , Where m = number of output neurons, n = number of input neurons. In this case the value of $m = 3$, and $n = 12$. According to the empirical rule the number of hidden neurons will be 6. The network was trained using 6 neurons with error goal combinations of 0.0001. The testing was carried out using the test set given in the last column of Table 1. From Table 1, with error goal of 0.0001 and 6 neurons, it is seen that in training number 2, the epochs and (μ) remaining constant the sum squared error becomes minimized, which leads to a good generalization. After successful training, the network is tested for simulation with a separate set of untrained data. It is observed that the neural network is able to detect the corresponding unbalance of 18.4909g and bearing clearance of 0.0798mm for epochs of 4 and an error of 4.69917e-006 for an error goal of 0.0001. The experimental value of unbalance is 18.5g and the value of bearing clearance is 0.08mm. The ANN has identified the value of unbalance to an accuracy of 99.95% and bearing clearance of 99.75%. This is in close correlation with the experimental values. This data is shown in Table 2.

Table 2: Quantification of unbalance mass and bearing clearance, error goal 0.0001 and hidden neurons 6

Serial no.	Experimental values of unbalance mass (g) + bearing clearance (mm)	Epochs	MSE	ANN Quantification values	Percentage
1	6.5 0.02	4	0.00108642	6.4458 0.0198	99.16 99.00
2	18.5 0.02	5	5.97176 e-006	18.4259 0.01970	99.60 98.50
3	6.5 0.08	12	8.84591e-008	6.4953 0.0796	99.93 98.50
4	18.5 0.08	4	4.69917e-006	18.4909 0.0798	99.95 99.75

V. Wavelet Analysis

Wavelet transform is a mathematical tool with a powerful structure and enormous freedom to decompose a given signal into several scales at different levels of resolution. Figure 5 (a) shows the multi-resolution signal decomposition algorithm used for implementation of discrete wavelet transform. In this figure, $s^l(n)$ is the sampled signal of $f(t)$, sampled at the rate of " fs " Hz. The digitized signal $s(n)$ is then first decomposed into $a_1(n)$ and $d_1(n)$ using low pass filter $h_1(n)$, and high pass filter $g_1(n)$, respectively, where, $d_1(n)$ is called the detail function containing higher frequency terms, and $a_1(n)$ is called the approximation signal containing low frequency terms. This is called first- scale decomposition. The second scale decomposition is now based on the signal $a_1(n)$ which gives $a_2(n)$ and $d_2(n)$. The next higher scale decomposition is now based on $a_2(n)$ and so on. At any level " f " the approximation signal $a_f(n)$ will be composed of frequencies 0 to f_c Hz. Similarly the detail signal $d_f(n)$ at any level " f " will contain frequencies of range f_c to $2f_c$ Hz. The cut-off frequency " f_c " of approximation signal $a_f(n)$ for a given level f is found by-

$$f_c = fs/2^{f+1} \quad (3)$$

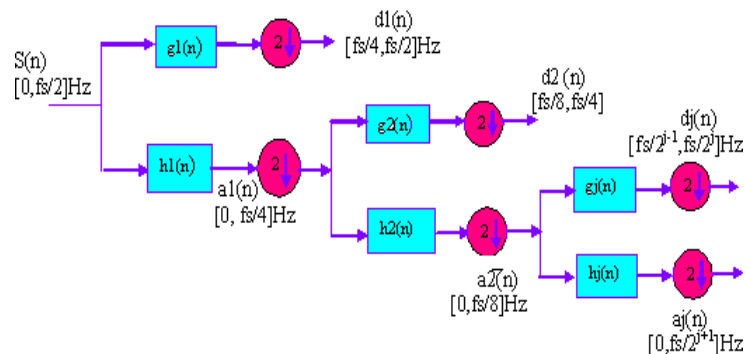


Figure.5 (a). Multi-resolution signal decomposition

Also, the number of points in the decomposed detail and approximation signals decreases gradually through successive decimation. Thus, to compute the Discrete Wavelet Transform (DWT) all that is needed are filters. The signal is convolved with these filters. In contrast to the Short Time Fourier Transforms (STFT), the time resolution becomes arbitrarily fine at high frequency, while the frequency resolution becomes arbitrarily fine at low frequencies. In the present work attempt is made to use wavelet transform for identification of rotor fault, which does not depend on a single frequency, but on a band of frequencies

5.1. Feature Extraction

The aim of the feature extraction is to apply the transformation that extracts the signal features hidden in the original frequently domain. Corresponding to different characteristics of the signal, transformation should be properly selected so that the specific signal structure can be enhanced in its transformed domain. The fault identification techniques are those, which compares current data with that of the known cases to reach the final diagnosis. A multi-resolution property of the discrete wavelet transform (DWT) is used to analyze the vibration signal under different fault conditions. The Daubechies wavelet was selected for the signal analysis because it provides a much more effective wavelet than that obtained with the other wavelets (Haar, Coifman, etc.). When vibration signals collected under different conditions are decomposed via the wavelet, the appreciable differences between the corresponding wavelet coefficients, as shown in Figures. 5(b), (c), (d), and (e), can be seen. However, conducting a direct assessment from all wavelet coefficients turns out to be tedious job. Therefore, the wavelet node power e_j at " f " level decomposition is defined as $e_j = 1/N_j$

Here, N_j is the number of coefficients at level " f " $w_{j,k}$ is the k^{th} coefficient calculated for j^{th} level, e_j is the RMS (root mean square) value of the decomposed signal at a level " f ". It measures the signal power contained in the specified frequency band indexed by the parameter " f ". In order to relate the RMS value of the wavelet decomposition signals with different rotor faults. For each case four sets of data are recorded

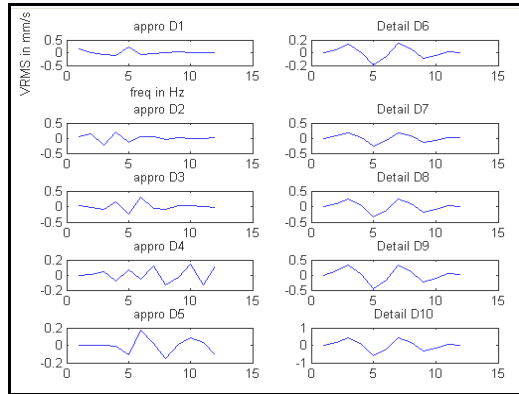


Fig. 5(b) Wavelet decomposition corresponding to unbalance mass 6.5g + bearing clearance 0.08 mm

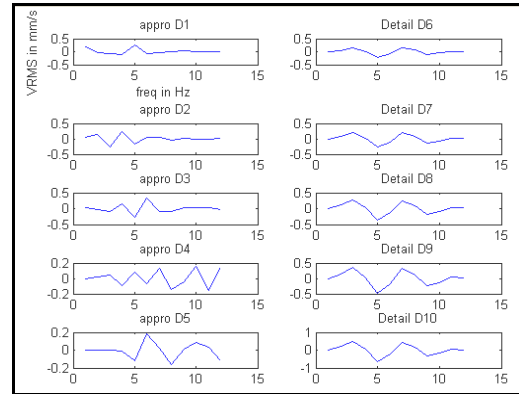


Fig. 5(c) Wavelet decomposition corresponding to unbalance mass 10.5g + bearing clearance 0.08 mm

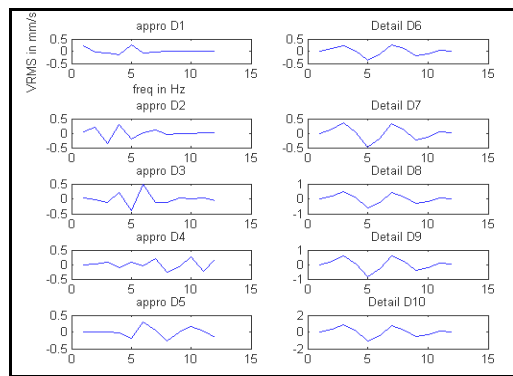


Fig.5 (d) Wavelet decomposition corresponding to unbalance mass 14.5g + bearing clearance 0.08 mm

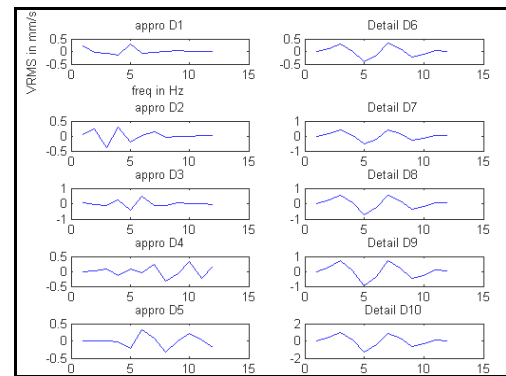


Fig.5 (e) Wavelet decomposition corresponding to unbalance mass 18.5g + bearing clearance 0.08 mm

The vibration in RMS value of first ten decomposition for one segment from each case is shown in Table 3 the similar values are obtained for other vibration segments. From Table 1, it is clearly observed that the bearing clearance is kept constant at 0.08 mm and the unbalance mass is varies from 6.5g to 18.5g in order to study the vibration characteristics due to combination of unbalance and bearing clearance. Due to increase of unbalance mass with constant bearing clearance the 1X frequency component of RMS velocity is predominant in the horizontal direction.

Table 3: RMS value of vibration signal and its ten detailed coefficient wavelet decompositions

Unbalance Mass (g) + Bearing Clearance (mm)	Original RMS	D1	D2	D3	D4	D5
Unbalance Mass 6.5g + Bearing Clearance 0.08 mm	0.1252	0.0278	0.0405	0.0541	0.0301	0.0240
Unbalance Mass 10.5 g + Bearing Clearance 0.08 mm	0.1625	0.0351	0.0549	0.0710	0.0388	0.0284
Unbalance Mass 14.5 g + Bearing Clearance 0.08 mm	0.3635	0.0444	0.0943	0.1393	0.0877	0.0762
Unbalance Mass 18.5 g + Bearing Clearance 0.08 mm	0.4016	0.0523	0.1031	0.1575	0.1141	0.1019

Unbalance Mass (g) + Bearing Clearance (mm)	D6	D7	D8	D9	D10
Unbalance Mass 6.5g + Bearing Clearance 0.08 mm	0.0283	0.0493	0.0899	0.1545	0.2738
Unbalance Mass 10.5 g + Bearing Clearance 0.08 mm	0.0326	0.0569	0.1040	0.1784	0.3163
Unbalance Mass 14.5 g + Bearing Clearance 0.08 mm	0.0970	0.1704	0.3067	0.5302	0.9376
Unbalance Mass 18.5 g + Bearing Clearance 0.08 mm	0.1335	0.2347	0.4207	0.7287	1.2877

5.2. Data Normalization

During training of the neural network, input variables of higher values may tend to suppress the influence of the smaller one. To overcome this problem and in order to make neural network perform well, the data must be well processed and properly scaled before input into the ANN. All the components of feature vector are normalized using the following equation-

$$x_n = \left\lfloor \frac{x}{1.5 \times x_{\max}} \right\rfloor 0.8 + 0.1 \quad (4)$$

Where, x is actual data, x_{\max} is the maximum value of the data and x_n is the normalized data. The maximum value is obtained from the faulty data set. The maximum value is multiplied by the factor 1.5 so that if the fault severity is more than what is consider until now, the same neural network can be useful for fault identification. Table 4 shows the normalized value of RMS level given in Table 3 by using equation 3. The neural network tool box of MATLAB has been used to simulate the desired network. The “newff” function of MATLAB has been used to create three- layered back propagation network. In the training process, the network is trained according to Levenberg-Marquardt optimization technique until the mean square error is found below 0.0001 or the maximum number of epoch's (300) is reached.

Table 4: Normalized training data set

Sl. No	Unbalance Mass + Bearing Clearance	Input									
		W1	W2	W3	W4	W5	W6	W7	W8	W9	W10
1	Unbalance Mass 6.5g + Bearing Clearance 0.08 mm	0.1115	0.167	0.1224	0.1124	0.1099	0.1118	0.1204	0.1372	0.1639	0.2134
2	Unbalance Mass 10.5g+Bearing Clearance 0.08mm	0.1145	0.1227	0.1294	0.1160	0.1117	0.1135	0.1235	0.1430	0.1734	0.2310
3	Unbalance Mass 14.5g + Bearing Clearance 0.08mm	0.1183	0.1390	0.1576	0.1363	0.13125	0.1401	0.1705	0.2270	0.3195	0.4883
4	Unbalance Mass 18.5g + Bearing Clearance 0.08mm	0.1216	0.427	0.1652	0.1472	0.1422	0.1552	0.1972	0.2742	0.4018	0.6333

Table 5: Quantification of combined faults of unbalance and bearing clearance using combined form of ANN and Wavelet transform, error goal of 0.0001 and hidden neurons 6

Serial no.	Experimental values of combined faults of unbalance (g) and Bearing clearance (mm)	Epochs	MSE	ANN Quantification values	Percentage
1	6.5 0.08	5	3.84119e-006	6.4997 0.0799	99.99 99.87
2	10.5 0.08	9	0.000434118	10.4989 0.0797	99.98 99.62
3	14.5 0.08	3	0.00041011	14.4999 0.0798	99.99 99.75
4	18.5 0.08	6	2.89854e-005	18.4998 0.0799	99.99 99.87

Table 4 shows the normalized values of wavelets of combined faults of unbalance and bearing clearance. The first three rows of data [(6.5g+0.08mm) to (14.5g+0.08mm)] have been used for training the network and the last row of data (18.5g to 0.08mm) is test data. The network has used 6 neurons with error goal of 0.0001. The testing set has been shown in the last row of Table 4. After sum squared error has decreased and μ has increased it yielded good generalization. 99.99 % and 99.87 % of the experimental value. The result as shown in Table 5.

VI. Conclusions

The amplitude of vibration of a rotor bearing system, which is measured in the horizontal, vertical and axial directions, is used to study the effects of vibration characteristics of a combination of unbalance and bearing clearance. The experiments are carried out by creating crack depth ranging from 1.5mm to 6.0mm by varying the unbalance mass. It is recorded that the 1X frequency component of vibration has predominantly increased in the horizontal direction in all the cases. To quantify these faults one promising approach is to use the artificial neural network of multilayer feed forward back propagation algorithm. It has been seen by training of network with data that was obtained experimentally and by testing the same data. Further work needs to be done by using other types of networks and algorithm. Removing arbitrariness in the choice of the network parameters is another area where more work must be done. The ANN is used for diagnosing and quantifying of faults. The success rates, based upon each fault, have been reported. In particular, overall success rates of unbalance of 99.78 % unbalance, 99.81% bearing clearance, and 99.45 % for the combined faults of unbalance and bearing clearance have been achieved. This paper has also investigated the feasibility of applying discrete wavelet transform to identify the combined faults of unbalance mass and bearing clearance. To alleviate the frequency-invariant characteristics of the wavelet coefficients and to reduce the dimensionality of the input to the neural network, the RMS value at selected decomposition levels are used as a feature measure of the signal. The features obtained by the proposed method yields nearly 99.99% quantification when used as input to a Neural Network.

REFERENCES

- [1] Dutt, J. K. and Nakra, B. C., Stability of Rotor System with Viscoelastic Support, Journal of Sound and Vibration, 153 (1), (1993), 89–96.
- [2] Genta, G. and De Bona, F. Unbalance Response of Rotors; A Modal Approach with Some Extensions to Damped natural Systems, Journal of Sound and Vibration, 140 (1), (1990), 129–153.
- [3] S. Edwards, A. W. Lees, and M. I. Friswell. Fault Diagnosis of Rotating Machinery, The Shock and Vibration Digest, 30 (1), (1998), 4-13.
- [4] Gasch, R., A survey of the dynamic Behavior of a Simple Rotating Shaft with a Transverse Crack, Journal of Sound and Vibration, 160 (2), (1993), 313-332.
- [5] Meng, G. and Hahn, E. J., Dynamic Response of Cracked Rotor With some Comments on Crack Detection, Journal of Eng. Gas Turbines and Power, 119 (2), (1997), 447–455.
- [6] Isermann, R., Supervision, Fault detection and Fault-Diagnosis methods, Control Eng. Practice, 5(5), (1997), 639–652,
- [7] A.W. Lees and M. I. Friswell, The Evaluation of Rotor Imbalance in Flexibly Mounted Machines, Journal of Sound and Vibration, 208(5), (1997), 671-683.

- [8] D. L. Hall, R. J. Hansen and D. C. Lang , The Negative Information Problem in Mechanical Diagnostics , Journal of Eng. for Gas Turbines and Power, 119,(1997) , 370-377.
- [9] K. S. Srinivasa, Fault Diagnosis in Rotating Machines Using Vibration Monitoring and Artificial Neural Networks, Ph. D Thesis, ITMMEC, Indian Institute of Technology Delhi, (2003).
- [10] K. S. Srinivasan and Umesh K. N., Study of effects of Misalignment on vibration Signatures of Rotating Machinery, National Conf. README-05, PACE, Mangalore,(2005).
- [11] A. C. McCormick and A. K. Nandi, A Comparison of Artificial Neural networks and other statistical methods for rotating machine condition classification, IEE, savoy London, (1996), 2(1)-2(6).
- [12] A. C. McCormick and A. K. Nandi, Classification of the rotating machine condition using artificial neural networks, Proceedings Instrumentation Mechanical Engineers, 211, Part-C, (1997) , 439-450.
- [13] Nalinaksh S.Vyas and D. Sathish kumar, Artificial Neural Network Design for Fault identification in Rotor-Bearing System, 36, Mechanism and Machine Theory, (2001), 157-175.
- [14] M. Kalkat and S.Yildirim and I. Uzmay , Rotor Dynamics Analysis of Rotating Machine Systems using Artificial Neural Networks, International Journal of Rotating Machinery, 9, (2003), 255-262.
- [15] Nahvi and M. Esfahanian, Fault identification in rotating machine condition using artificial neural networks, Proceedings Instrumentation Mechanical Engineering Science, 219, (2004), 141-158.
- [16] Jeong Soo Ryu, Doo Byang Yoon and Jong sup wu, Development of a HANARO Vibration Monitoring System for Rotating Machinery, Proceedings of the Internal Symposium on Research Reactor and Neutron Science, (2005).
- [17] T. S. W. Chow and L. T. Jaw, city polytechnic of Hong Kong, Rotating machines Fault identification using Back-Propagation Artificial Neural Network, 405-412.
- [18] G. G. Yen and Kuo-Chung Lin, Wavelet Packet Feature Extraction for Vibration Monitoring, IEEE Transactions on Industrial Electronics, 47, no 3, (2000), 650-666.
- [19] D. Boras, M. Castila, N. Moreno and J. C. Montano, Wavelet and Neural Structure; A New Tool for Diagnostic of Power System Disturbances, IEEE, Transactions on Industry Applications, 30, no 1 (2001), 184-190.
- [20] Xie FL, Flowers G. T., Feng L. and Lawrence C., Steady State Dynamic Behavior of Flexible Rotor with Auxiliary Support from Clearance Bearing, Journal of Vibration and Acoustics, Vol. 121/79, 1999, 78-83.
- [21] D. Muller, A.G. Sheard., S. Mozumdar., and E. Lohann., Capacitive measurement of compressor and turbine blade tip to casing running clearance, Journal of engineering for gas turbines and power , Vol. 119, Oct 1997, 877-884.
- [22] Sang-Kyu Choi, and Sherif T. Noah., Mode locking and chaos in a Jeffcott rotor with bearing clearances, Journal of applied mechanics, vol. 61, Mar. 1994, 131-138.

Tensile and Flexural Properties of Sisal/Jute Hybrid Natural Fiber Composites

Sudhir.A¹, Madhukiran.J², Dr. S. Srinivasa Rao³, Dr.S.Madhusudan⁴

^{1&3}Department of Mechanical Engineering M.V.G.R. College of Engineering, JNTUK Vizianagaram-535005, A.P.

²Department of Mechanical Engineering A.K.R.G. College of Engineering, JNTUK Nallajerla - 534112, A.P.

⁴Department of Mechanical Engineering Sir.C.R.Reddy College of Engineering, Andhra University Eluru - 534 007.

Abstract: During the last two decades using natural fiber as reinforcement in polymers has increased drastically. The present research work has been carried out to make use of sisal/jute natural fibers. The aim of this paper is to describe the development and characterization of new set of hybrid natural fiber composites. It is made by reinforcing sisal/ jute fibers with epoxy resin in matrix by using hand layup technique. The natural fibers were extracted by retting and combing process manually. Hybrid composites were prepared using sisal/jute fibers of 0/40, 10/30, 20/20, 30/10, 40/0 weight fraction ratios while overall fiber weight fraction was fixed as 0.4 weight fraction. The tensile and flexural properties were carried out using hybrid composite samples. The results indicated that addition of sisal fiber in jute/epoxy composites up to 50% weight fraction results increasing the mechanical properties.

Keywords: Sisal & jute fibers, Hybrid composites, tensile properties and flexural properties.

I. Introduction

Composite materials are consisting of two or more chemically distinct constituents, on a macro-scale, having a distinct interface separating them. One or more discontinuous phases therefore, are embedded in a continuous phase to form a composite. The discontinuous phase is usually harder and stronger than the continuous phase and is called the reinforcement, whereas, the continuous phase is termed the matrix [1–3]. The matrix material can be metallic, polymeric or ceramic. A metal matrix composite consist of a matrix of metals or alloys reinforced with metal fibers such as boron and carbon. When the matrix is a polymer, the composite is called polymer matrix composite (PMC). The reinforcing phase can either be fibrous or non-fibrous (particulates) in nature and if the fibers are derived from plants or some other living species, they are called natural-fibers. The fiber reinforced polymers (FRPs) consist of fibers of high strength and modulus embedded in or bonded to a matrix with a distinct interface between them. In this form, both fibers and matrix retain their physical and chemical identities. In general, fibers are the principal load carrying members, while the matrix keeps them at the desired location and orientation, act as a load transfer medium between them, and protect them from environmental damage [4–8].

Hybrid composite materials are which are made by combining two or more different types of fibers in a common matrix. Hybrid of short fibers having same length and different diameter offer some advantage over the use of one type of fibers alone in a polymer matrix. The natural fibers like jute, sisal, hemp, kenaf, and banana are renewable, non-abrasive and can be incinerated for energy recovery. They possess a good calorific value and cause little concern in terms of health and safety during handling. In addition, they exhibit excellent mechanical properties, have low density and are inexpensive.

Pervaiz and Sain [9] examined the energy consumption of glass and natural fibers, and they found that by using vegetal fibers in place of glass fibers, energy could be saved at a rate of 60% per ton of product. Jute, a natural fiber in polymer composites would be suitable for the primary structural applications, such as indoor elements in housing, temporary outdoor applications like low-cost housing for defense and rehabilitation and transportation. The insulating characteristics of jute may find applications in automotive door/ceiling panels and panel separating the engine and passenger compartments [10]. The use of natural fiber like jute not only help us in ecological balance but can also provide employment to the rural people in countries like India and Bangladesh where jute is abundantly available. S.M. Sapuan et al [11] investigated the tensile and flexural properties of banana fiber reinforced with epoxy. The statistical analysis carried out, showed an increase in mechanical properties. Maries Idicula et al [12] Dynamic studies on mechanical properties of randomly mixed sisal and banana fibers were carried out and it is observed that the flexural and tensile modulus shows improvement in results. The damping behavior also improved for sisal polyester composites. M. Ramesh et

al[13] in their paper hybrid glass/sisal fiber reinforced epoxy composites. The performance of these natural fiber composites is lower than that of the GFRP it has been used in many application which requires medium strength. In this present investigation is to the potential utilization of sisal/jute fiber as reinforcement in polymer matrix composites. Fabricate and evaluate their mechanical properties.

II. Materials and Methods

1. Natural fiber:

Natural fibers such as fiber extraction from sisal, jute, coir, flax, hemp, pineapple and banana for making a new environment friendly and biodegradable composite materials (somehow these composites are called 'Green Composites'). Recent studies in natural fiber composites offer significant improvement in materials from renewable sources with enhanced support for global sustainability. These natural fiber composites possess high/moderate strength, thermal stability when they are recyclable, but the problems of using pure biodegradable polymers are their low strength and transition temperature.

2. Sisal fiber:

Sisal fibers are extracted from the leaves of sisal plant. The fibers are extracted through hand extraction machine composed of either serrated or non serrated knives. The peel is clamped between the wood plank and knife and hand-pulled through, removing the resinous material. The extracted fibers are sun-dried which whitens the fiber. Once dried, the fibers are ready for knotting. A bunch of fibers are mounted or clamped on a stick to facilitate segregation. Each fiber is separated according to fiber sizes and grouped accordingly. To knot the fiber, each fiber is separated and knotted to the end of another fiber manually. The separation and knotting is repeated until bunches of unknotted fibers are finished to form a long continuous strand. This Sisal fiber can be used for making variety of products.

3. Jute fiber:

Jute take nearly 3 months, to grow to a height of 12–15 ft, during season and then cut & bundled and kept immersed in water for "Retting" process, where the inner stem and outer, gets separated and the outer plant gets 'individualized', to form a Fiber. Then the plant get separated and washed to remove dust from the plant. The fiber after drying is taken to Jute mills, for getting converted to Jute yarn and Hessian. From the Jute, various lifestyle products are being produced and diversified into various forms, due to R&D support and also due the support by Government Organizations.

4. Weight fraction of the fiber:

The weight of the matrix was calculated by multiplying density of the matrix and the volume (volume in the mould). Corresponding to the weight of the matrix the specified weight percentage of fibers is taken. For hybrid combination the corresponding weight of fiber obtained is shared by two fibers.



Fig. 1 - Sisal and Jute fibers

5. Preparation of epoxy and hardener:

Epoxy LY556 of density 1.15–1.20 g/cm³, mixed with hardener HY951 of density 0.97–0.99 g/cm³ is used to prepare the composite plate. The weight ratio of mixing epoxy and hardener is 10:1. This has a viscosity of 10-20 poise at 250°C. Hardeners include anhydrides (acids), amines, polyamides, dicyandiamide etc.

6. Mould Preparation:

Mould used in this work is made of well-seasoned teak wood of 200 mm X 200 mm X 3 mm dimension with five beadings. The fabrication of the composite material was carried out through the hand lay-up technique. The top, bottom surfaces of the mould and the walls are coated with remover and allowed to dry. The functions of top and bottom plates are to cover, compress the fiber after the epoxy is applied, and also to avoid the debris from entering into the composite parts during the curing time.

7. Composite fabrication:

The moulds are cleaned and dried before applying epoxy. The fibers were laid uniformly over the mould before applying any releasing agent or epoxy. After arranging the fibers uniformly, they were compressed for a few minutes in the mould. Then the compressed form of fibers (sisal/jute) is removed from the mould. This was followed by applying the releasing agent on the mould, after which a coat of epoxy was applied. The compressed fiber was laid over the coat of epoxy, ensuring uniform distribution of fibers. The epoxy mixture is then poured over the fiber uniformly and compressed for a curing time of 24 h, with load of 5kg. Composites are prepared by changing the weight fractions of both sisal and jute fibers. Individual composites with sisal and jute as reinforcement are also prepared under similar processing conditions for comparison purpose. Laid over the coat of epoxy, ensuring uniform distribution of fibers. The epoxy mixture is then poured over the fiber uniformly and compressed for a curing time of 24 h, with load of 5kg. Composites are prepared by changing the weight fractions of both sisal and jute fibers. Individual composites with sisal and jute as reinforcement are also prepared under similar processing conditions for comparison purpose [14].

III. Testing Of Composites

1. Tensile Test:

The hybrid composite material fabricated is cut into required dimension using a jig saw cutter and the edges finished by using emery paper for mechanical testing. The tensile test specimen is prepared according to the ASTM D638 standard. The dimensions, gauge length and cross-head speeds are chosen according to the ASTM D638 standard. [15] A tensile test involves mounting the specimen in a machine and subjected to the tension. The testing process involves placing the test specimen in the testing machine and applying tension to it until it fractures. The tensile force is recorded as a function of the increase in gauge length. During the application of tension, the elongation of the gauge section is recorded against the applied force. The tensile test is performed on the Universal Testing Machine (UTM). There are five different kinds of specimens are prepared according to the fibers used. The first specimen consists of (0/40) pure sisal. The second specimen consists of (10/30) jute/sisal. The third specimen consists of (20/20) jute/sisal. Fourth specimen consists of (30/10) jute/sisal and fifth specimen is consists of (0/40) pure jute. The fabricated specimen for tensile test is presented in Fig. 2. The experiments are repeated for several times and the average values are used for discussion.



Fig: 2 Tensile test specimens

2. Flexural Test:

The flexural specimens are prepared as per the ASTM D790 standards [16]. The 3-point flexure test is the most common flexural test for composite materials. Specimen deflection is measured by the crosshead position. Test results include flexural strength and displacement. The testing process involves placing the test specimen in the universal testing machine and applying force to it until it fractures and breaks. The specimen used for conducting the flexural test is presented in Fig. 3.



Fig: 3 Flexural test specimens

IV. Results and Discussion

1. Tensile Strength:

Table1. Tensile Properties of Different Composite Samples.

Composites	% Weight fraction	Tensile Strength (MPa)	Tensile Modulus (MPa)
Pure sisal	0/40	38.93	1585.2
Jute/sisal	10/30	37.61	1468.25
Jute/sisal	20/20	39.93	1597.28
Jute/sisal	30/10	31.31	1246.89
Pure jute	40/0	36.93	1457.2

The load with respect to the displacement for different combination of composite specimen is presented in Fig. 4. The results indicated that (20/20) 39.93 MPa, (jute/sisal) specimen gives better tensile strength then the other four types of composites. The ultimate tensile strength of the pure sisal and pure jute composites are 38.93 MPa and 36.93 MPa respectively. Hybrid combination of fibers jute/sisal (10/30) and (30/10) composite values were observed to be low as compared to pure composites. The effect of hybridization is found to be negligible for the above two composites. This behavior can be correlated to hybridization effect as both fibers contributed higher tensile strength to the composite.

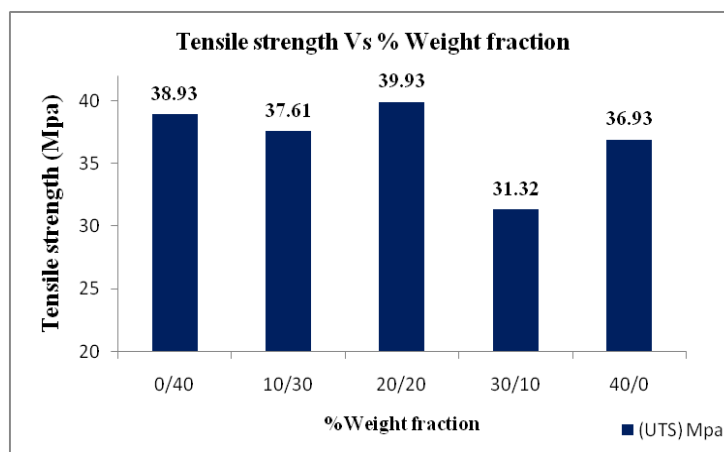


Fig: 4 Tensile Strength Vs Weight Fraction

The tensile modulus of sisal/jute fiber hybrid composites values presented in table 1. Fig 5, the results indicated that the (jute/sisal) (20/20) hybrid composite exhibits higher tensile modulus, than the other fiber reinforced composites. The jute/sisal hybrid composite tensile modulus values for w/f (10/30) and (30/10) are 1468.25 MPa and 1246.25 MPa respectively. But it is lower than the pure composites.

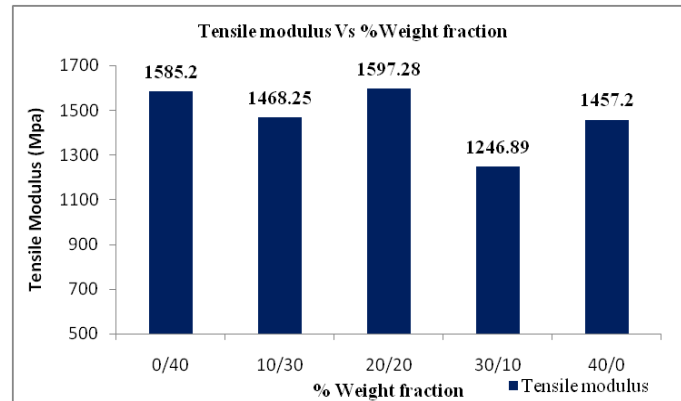


Fig: 5 Tensile Modulus Vs Weight Fraction

Flexural strength:

Table 2. Flexural Properties of Different Composite Samples

Composites	% Weight fraction	Flexural strength (MPa)	Flexural modulus (MPa)	Elongation
Pure sisal	0/40	87.15	3486	4.25
Jute/sisal	10/30	84.35	3374	3.86
Jute/sisal	20/20	88.33	3533	4.72
Jute/sisal	30/10	82.26	3482	1.72
Pure jute	40/0	87.05	3330	2.74

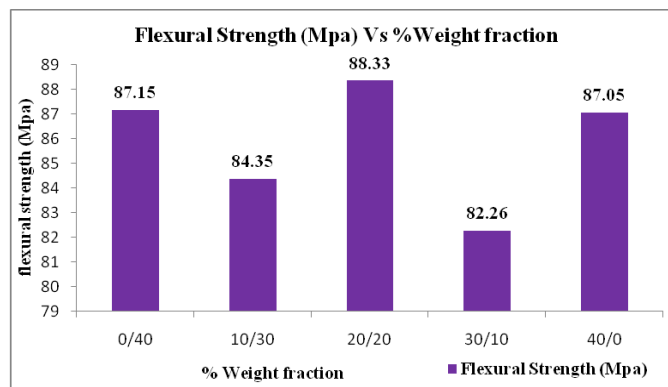


Fig: 6 Flexural Strength vs Weight Fraction

Fig: 6 show that jute/sisal (20/20) hybrid composite exhibits better results among the others. It has been observed that pure sisal and pure jute composite values are 87.15 MPa and 87.05 MPa, these composites performing well when compared to other hybrid composites. The hybrid composites of jute/sisal (10/30) and (30/10) values are compared to low as pure composites. The increase of flexural strength is due to the increased area of bonding at the interfacial region of the matrix and fiber.

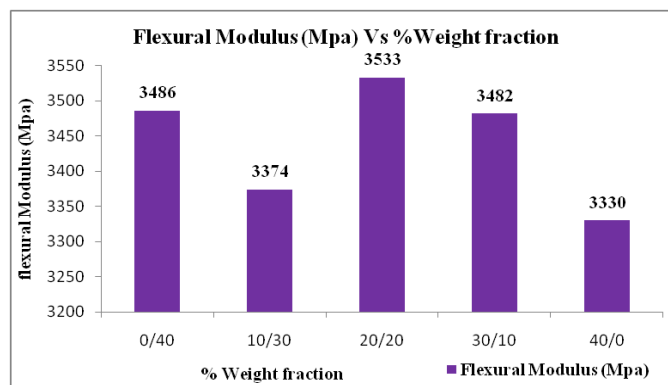


Fig: 7 Flexural Modulus vs Weight Fraction

Sisal/jute hybrid composites is considerable increase of flexural modulus as the percentage adds jute/sisal fiber increases to maximum value of (20/20) 3533 MPa as shown in Fig 7. The flexural modulus were observed pure sisal and pure jute values are 3486 MPa and 3330MPa respectively. The hybrid combination of jute/sisal (10/30) and (30/10) flexural modulus values are very low, when compared to pure composites.

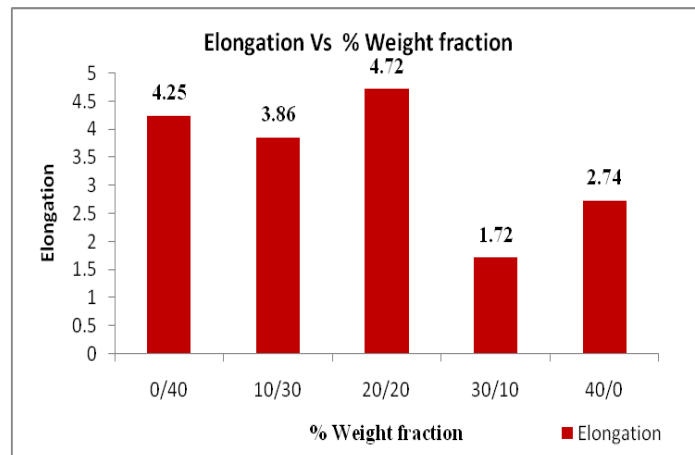


Fig: 8 Elongation vs % Weight fraction

Fig8, the results indicated that elongation of sisal/jute hybrid composite (20/20) value is 4.72MPa. It is evident that the highest tensile strength and highest elongation was found. This can be attributed that hybridization effect as both fibers contributed higher strength and elongation of the hybrid composite.

V. Conclusions

After determining the material properties of natural fiber reinforced epoxy hybrid composites with five different weight fractions of the materials, the following conclusions can be made.

1. Successful fabrication of the hybrid composite using sisal/jute fiber reinforced epoxy has been done by the hand layup technique.
2. It can be observed that jute /sisal (20/20) weight fraction hybrid composite samples possess good tensile strength and can with stand the strength up to 39.93 MPa.
3. The jute /sisal (20/20) weight fraction hybrid composite samples maximum flexural strength 88.33MPa.
4. Now a day's most of automobile manufacture company's try to replace synthetic fibers with natural fibers but it is not comparable in properties. While fabricating hybrid composite by the combination of two natural fibers given them advantage to replace synthetic fibers.
5. This work also demonstrates the potential of the hybrid natural fiber composites can be regarded as a useful material in light weight applications.

REFERENCES

- [1]. K. John, S. Venkata Naidu, "Chemical resistance studies of sisal/glass, fiber hybrid composites", Journal of Reinforced. Plastic Composites. 26(4) (2007) 373–376.
- [2]. H. P. S. Abdul Khalil, S. Hanida, C. W. Kang, N.A. Nikfuaad, Agro hybrid composite, "The effects on mechanical and physical properties of oil palm fiber (efb)/glass hybrid reinforced polyester composites", Journal of Reinforced Plastic Composites. 26(2) (2007) 203–218.
- [3]. Oksman K, Skrivars M, Selin JF, "Natural fibers as reinforcement in polylactic acid (PLA) composites". Composites Science and Technology 2003; 63(9):1317–24.
- [4]. Sreekalaa MS, George Jayamol, Kumaran MG, Thomas Sabu, "The mechanical performance of hybrid phenol–formaldehyde-based composites reinforced with glass and oil palm fibers", Composites Science and Technology 2002.
- [5]. Mishra S, Mohanty AK, Drzal LT, Misra M, Parijag S, Nayak SK, "Studies on mechanical performance of bio fiber/glass reinforced polyester hybrid composites", Composites Science and Technology 2003.
- [6]. Jacob Maya, Thomas Sabu, Varghese KT, "Mechanical properties of sisal/oil palm hybrid fiber reinforced natural rubber composites", Composites Science and Technology 2004.
- [7]. Esfandiari Amirhossein, "Mechanical properties of PP/Jute Glass fiber composites – a statistical investigation", Journal of Applied Sciences 2007.
- [8]. M. Boopalan, M. Niranjanaa, M.J. Umamathy, "Study on the mechanical properties and thermal properties of jute and banana fiber reinforced epoxy hybrid composites", Composites: Part B 51 (2013) 54–57.

- [9] Pervaiz M., Sain M.M.,” Carbon storage potential in natural fibre composites”, *Resources Conservation and Recycling* 39(4), p.325 -2013.
- [10] Khondker O. A., Ishiaku U S., Nakai A., Hamada H.,” Fabrication and Mechanical Properties of Unidirectional Jute/PP Composites Using Jute Yarns by Film Stacking Method”, *Journal of Polymers and the Environment*, 13(2) , p. 11-2005.
- [11]. S. M. Sapuan, Leenie A, Harimi M, Beng YK, “Mechanical properties of woven banana fiber reinforced, epoxy composites”, *Materials and Design* 2006; 27(8):689–93.
- [12]. Maries Idicula, S.K.Malhotra, Kuruvilla Joseph, Sabu Thomas, “Dynamic mechanical analysis of randomly oriented intimately mixed short banana/sisal hybrid fiber reinforced polyester composites”. *Composites Science and Technology* 65 (2005) 1077–1087
- [13] M. Ramesh, K. Palanikumar, K. Hemachandra Reddy. Mechanical property evaluation of sisal–jute–glass fiber reinforced polyester composites. *Composites: Part B* 48 (2012) 1–9
- [14] J. Madhukiran, Dr. S. Srinivasa Rao, Madhusudan.S, Fabrication and Testing of Natural Fiber Reinforced Hybrid Composites Banana/Pineapple, *International Journal of Modern Engineering Research (IJMER)* 2013
- [15] ASTM D638-03, Standard test method for testing tensile properties of plastics.
- [16] ASTM D790-07, Standard tests method for testing flexural properties of unreinforced and reinforced plastics and electrical insulating material.

Growth and Development of FDI on Indian Economy

J. Rama Devi¹, Prof. B. Ramachandra Reddy²

¹ Ph.D. Research Scholar, S. V. University, Tirupati, India

² Professor, Department of Commerce, S. V. University, Tirupati, India

Abstract: India has been attracting substantial of foreign direct investment since last few decades, highly in services sector, telecommunications, software products, real estate etc. FDI are highly promoting manufacturing sector of India's exports & attracting more number of earnings on Foreign exchange, Institutional Investments, MNCs and speeding up our economic growth through Technology transfer, Employment generation and improved access to managerial expertise, global capital, product markets and distribution network. FDI bring out the generation-wise innovation, hidden technology, spending more on research & development to retain our strength in the globalised competitor products. Indian economy is going to over track the developed and developing countries. Recently, due to the recession most of the countries have not able to run their investment as well, but India has been managed better then developed country without elevated struggling. This paper analyzes the growth and development of FDI and it discussed the Indian economic growth through FDI. In addition it explains and showed the various sector-wise FDI performances in India.

Key Words: FDI, Indian Economy, Exports, Service Sector.

I. Introduction

Foreign Direct Investment is one of the main key factors for the development of countries economic growth in the 21st century globalised world. Because, MNCs have able to make it is a long-term management control as opposed to direct investment in buildings and equipment still accounts for a vast majority of FDI activity. Liberalized policy of today world is welcoming investment from other countries and searching for huge capital resources. Further it focusing on new markets where there is availability for abundant labours, product scope, high profits etc. Therefore FDI has become a battle ground of emerging markets, behind allowing FDI is to complement and supplement domestic investment, for achieving a higher level of economic development and providing opportunities to technological up gradation, plus access to global managerial skills and practices(ICA). Initially there were open door policies in South Asian country except India, after 1991 India implemented the liberalized policies during congress government period before that it followed conservative policy of Industrial protection.

II. Objectives

- To identify the various determinants of FDI
- To study the FDI inflows in India

III. What Is FDI?

Foreign Investment refer to long term participation by country. It usually involves participation in management, joint venture, transfer of technology and expertise. It made to serve the business interests of the investor of the company, which is in a different nation direct from the investor's country of origin. It may be individual/ group/incorporate/ unincorporated/enterprise group/government body/estate/trust/social institution/combination of the above.

3.1 Determinants of FDI

One of the most important determinants of foreign direct investment is the size as well as the growth prospects of the economy of the country where the foreign direct investment is being made;

- It is normally assumed that if the country has a big market, it can grow quickly from an economic point of view and it is concluded that the investors would be able to make the most of theory investment in that country.
- One country population plays an important role in attracting foreign direct investors to a country. In such cases the investors are lured by the prospects of a huge customer base.
- If the country has a high per capita income or if the citizens have reasonably good spending capabilities then it would offer the foreign investors with the scope of excellent performances.
- The status of the human resources in a country also helps in attracting FDI from overseas.
- If a country has plenty of natural resources it always finds investors willing to put their money in them.
- Inexpensive labour force is also an important determinant of attracting FDI.
- Infrastructural factors such as the status of telecommunication and railways play an important role in having the foreign direct investors come into a particular country.

IV. FDI Inflows In India

After independence in India 1947, FDI gained attention of the policy makers for acquiring advanced technology and to mobilize foreign exchange resources. In order to boost the FDI inflows in the country Indian government allowing frequent equity participation to foreign enterprises apart from provides many incentives such as tax concessions, simplification of licensing procedures and de-reserving some industries like drugs, fertilizers, aluminium etc. But due to significant outflow of foreign reserve in the form of remittances of dividends, profits, royalties etc in 1973 government of India set up Foreign Investment Board and enacted Foreign Exchange Regulation Act in order to regulate flow of FDI to India. Further Government of India set up Foreign Investment Promotion Board (FIPB) for processing of FDI proposals in India. The Board is the apex inter-ministerial body of the Central Government that deals with proposals relating to FDI into India for projects or sectors that do not qualify for automatic approval by the Reserve Bank of India (RBI) or are outside the parameters of the existing FDI policy.

Table-1: FDI inflows in India (from 1948-2010)

Amount of FDI	Mid 1948	March 1964	March 1974	March 1980	March 1990	March 2000	March 2010
In crores	256	565.5	916	933.2	2705	18486	123378

It could be observed that there has been a steady build up in the actual FDI inflows in the pre-liberalization period in table-1. But measures introduced by the government to liberalize provisions relating to FDI in 1991 increased FDI Rs.2705 crores in 1990 to Rs.123378 crores in 2010. The list of investing countries to India reached to 150 in 2010 as compared to 29 countries in 1991. Nevertheless, still a lion's share of FDI comes from only a few countries.

Fig. 1: FDI Inflows in India (1948-2010)

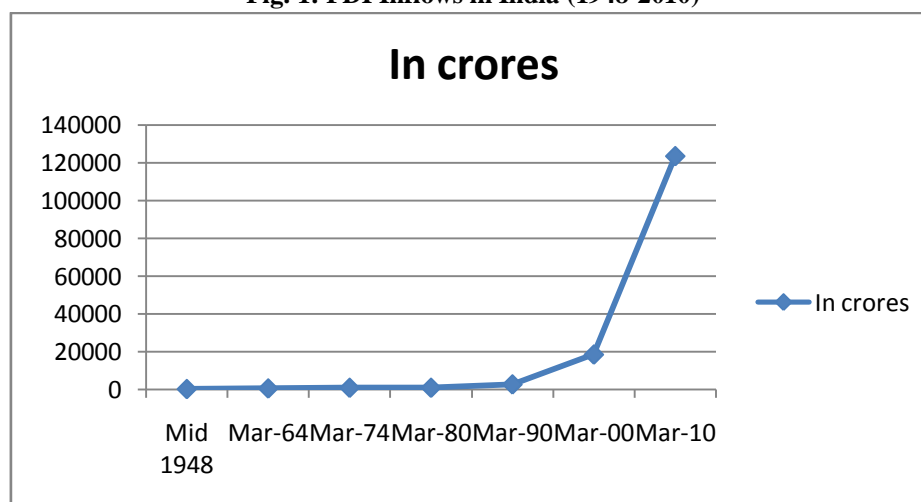


Table-2: Share of Top Ten Investing Countries in FDI Inflows (Financial Year Wise)**(Rs. in Millions)**

Ranks	Country	2008-09 (April-March)	2009-10 (April-March)	2010-11 (April-March)	2011-2012 (April-March)	2012-13 (April-March)
1.	Mauritius	10,165	9,801	5,616	8,142	8,059
2.	Singapore	3,360	2,218	1,540	3,306	1,605
3.	U.S.A	1,236	2,212	1,071	994	478
4.	U.K	690	643	538	2760	1,022
5.	Netherlands	682	804	1,417	1,289	1,700
6.	Japan	266	971	1,256	2,089	1,340
7.	Cyprus	1,211	1,623	571	1568	415
8.	Germany	611	602	163	368	467
9.	France	437	283	486	589	547
10.	U.A.E	234	373	188	346	173
Total FDI Inflows		18,892	19,530	12,846	21,451	15,806

Source: DIPP

Table-2 shows the actual investment flows of top ten countries during the period of 2008-09 to 2012-13. The FDI inflows increased from Rs.18892 million in the year 2008-09 to Rs.21,451 millions in the year 2011-2012, further decreased to Rs. 15,806 millions in 2012-2013 among the Top Ten investing countries in FDI inflows during the year 2012-2013 Mauritius occupied first place and U.A.E is in the last place.

V. Impact On Indian Economy

FDI have helped India to attain a financial stability and economic growth with the help of investments in different sectors. FDI has boosted the economic life of India and on the other hand there are critics who have blamed the government for ousting the domestic inflows. After liberalization of Trade policies in India, there has been a positive GDP growth rate in Indian economy.

Foreign direct investments helps in developing the economy by generating employment to the unemployed, Generating revenues in the form of tax and incomes, Financial stability to the government, development of infrastructure, backward and forward linkages to the domestic firms for the requirements of raw materials, tools, business infrastructure, and act as support for financial system. Forward and back ward linkages are developed to support the foreign firm with supply of raw and other requirements. It helps in generation of employment and also helps poverty eradication. There are many businesses or individuals who would earn their lively hood through the foreign investments. There are legal and financial consultants who also guide in the early stage of establishment of firm.

VI. Need For FDI In India

As India is a developing country, capital has been one of the scare resources that are usually required for economic development. Capital is limited and there are many issues such as Health, poverty, employment, education, research and development, technology obsolesce, global competition. The flow of FDI in India from across the world will help in acquiring the funds at cheaper cost, better technology, employment generation, and upgraded technology transfer, scope for more trade, linkages and pullovers to domestic firms. The following arguments are advanced in favour of foreign capital.

- ❖ **Sustaining a high level of Investment:** As all the under-developed and the developing countries want to industrialize and develop themselves, therefore it becomes necessary to raise the level to investment substantially. Due to poverty and low GDP the saving are low. Therefore there is a need to fill the gap between income and savings through foreign direct investments.
- ❖ **Technological Gap:** In Indian scenario we need technical assistance from foreign source for provision of expert services, training of Indian personnel and educational, research and training institutions in the industry. It only comes through private foreign investment or foreign collaborations.
- ❖ **Exploitation of Natural Resources:** in India we have abundant natural resources such as coal, iron and steel but to extract the resources we require foreign collaboration.

- ❖ **Understanding the Initial Risk:** In developing countries as capital is a scarce resource, the risk of investments in new ventures or projects for industrialization is high. Therefore foreign capital helps in these investments which require high risk.
- ❖ **Development of Basic Economic Infrastructure:** In the recent years foreign financial institutions and government of advanced countries have made substantial capital available to the under developed countries. FDI will help in developing the infrastructure by establishing firm's different parts of the country. There are special economic zones which have been developed by government for improving the industrial growth.
- ❖ **Improvement in the Balance of Payments Position:** The inflow FDI will help in improving the balance of payment. Firms which feel that the goods produced in India will have a low cost, will produce the goods and export the same to other country. This helps in increasing the exports.
- ❖ **Foreign Firm's Helps In Increasing The Competition:** Foreign firms have always come up with better technology, process, and innovations comparing with the domestic firms. They develop a competition in which the domestic firms will perform better it survive in the market.

VII. Measures Of FDI

India, post liberalization, has not only opened its doors to foreign investors but also made investing easier for them by implementing the following measures:

- Foreign exchange controls have been eased on the account of trade.
- Companies can raise funds from overseas securities markets and now have considerable freedom to invest abroad for expanding global operations.
- Foreign investors can remit earnings from Indian operations.
- Foreign trade is largely free from regulations, and tariff levels have come down sharply in the last two years.
- While most Foreign Investments in India (up to 51 %) are allowed in most industries, foreign equity up to 100 % is encouraged in export-oriented units, depending on the merit of the proposal. In certain specified industries reserved for the small scale sector, foreign equity up to 24 % is being permitted now.

As the industry progresses, opportunities abound in India, which has the world's largest middle class population of over 300 million, is attracting **foreign investors** by assuring them good returns. The scope for **foreign investment in India** is unlimited.

VIII. Conclusion

Foreign Direct Investment (FDI) as a strategic component of investment is needed by India for its sustained economic growth and development through creation of jobs, expansion of existing manufacturing industries, short and long term project in the field of healthcare, education, research and development (R & D) etc.

Government should design the FDI policy such a way where FDI inflow can be utilized as means of enhancing domestic production, savings and exports through the equitable distribution among states by providing much freedom to states, so that they can attract FDI inflows at their own level. FDI can help to raise the output, productivity and export at the sectoral level of the Indian economy. However, it can be observed the result of sectoral level output, productivity and export is minimal due to the low flow of FDI into India both at the macro level as well as at the sectoral level. Therefore for further opening up of the Indian economy, it is advisable to open up the export oriented sectors and higher growth of the economy could be achieved through the growth of these sectors.

REFERENCES

- [1]. Basu P., Nayak N.C. and Vani A., Foreign Direct Investment in India: Emerging Horizon, Indian Economic review, **25**, 255-266, (2007)
- [2]. Department of Industrial Policy & Promotion, Ministry of Commerce and Industry
- [3]. Ministry of Finance, Report of the economic survey, Government of India, New Delhi (2011-12)
- [4]. Mishra, S.K and Puri, V.K (2006), Indian Economy, 24th Revised Edition.

- [5]. Nayak D.N., Canadian Foreign Direct Investment in India: Some observations, Political Economy Journal of India, **8**, 51-56 (**1999**)
- [6]. Srivastava S., What is the true level of FDI flows to India?, Economic and Political Weekly, **19**, 1201-1209 (**2003**)
- [7]. Economy Watch, <http://www.economywatch.com/foriegn-direct-investment/>
- [8]. Weisskof T.E., The impact of foreign capital inflow on domestic savings in underdeveloped countries, Journal of International Economics, **2**, 25-38 (**1972**)
- [9]. www.indiastate.com

Modeling and Reduction of Root Fillet Stress in Spur Gear Using Stress Relieving Feature

Deep Singh Vishwakarma¹, Dr. Rohit Rajvaidya²

¹PD, Department of Mechanical Engineering, BUIT Bhopal

²Assistant Professor Mechanical Engineering Department BUIT, B.U. Bhopal, Guide

Abstract: A gear is a component within a transmission device that transmits rotational forces. Gears are commonly used for transmitting power. Gear teeth failure due to fatigue is a common fact observed. Even a small reduction in the root tensile stress results in great raise in the fatigue life of a gear. They develop high stress concentration at the root and the point of contact. The repeated stressing on the fillets causes the fatigue failure of gear tooth. For many years, gear design has been improved by using better material, hardening surfaces with carburization and heat treatment, and shot penning to improve surface finish etc. Few more hard work have been made to improve the durability and strength by changing the pressure angle, using the asymmetric teeth, varying the geometry of root fillet curve and so on. The majority of the above systems don't ensure the compatibility of the current rigging frameworks. This work presents the possibilities of utilizing the stress redistribution techniques by introducing the Stress relieving features in the stressed zone to the advantage of reduction of root fillet stress in spur gear.

I. Introduction

A gear is a toothed wheel that works with others to alter the relation between the speed of a driving mechanism (such as the engine of a vehicle) and the speed of the driven parts (the wheels). Gears have always been of high importance in power transmission. The efficiency of any machine depends on the amount of power loss in the process. One of the best methods of transmitting power between two shafts is gears. Gears are mostly used to transmit torque and angular velocity. Gears are the most common means of transmitting power. Gears change the rate of rotation of shaft and also the axis of rotation. For high speed machinery, they are the optimal medium for low energy loss and high accuracy. Their function is to convert input provided by prime mover into an output with lower speed and corresponding higher torque. The gear materials used for the manufacture of gears depend upon the strength and service conditions like wear and noise etc. The gears can be manufactured from metallic or non-metallic materials. The cast iron and steel are commonly used for the manufacture of gears due to its good wearing properties, excellent machine ability and ease of producing complicated shapes by casting method. The non-metallic materials like wood, rawhide, compressed paper and plastic like Nylon, Acrylic and Polycarbonate etc are used for gears, especially for reducing weight and noise. Gear analyses in the past were performed utilizing analytical methods, which required a number of postulations and simplifications. In general, gear analyses are multidisciplinary, including cognate related to the tooth stresses and the failures. In this work first the solid model of the spur gear is made with relations and equations modeling option in Pro Engineer. After the modeling of spur gear the Segment of three teeth is considered for analysis, then the 3-D model is imported in AUTODESK INVENTOR the program reads the IGES file out from the pro engineering. Static analysis of a 3-D model has been performed by using AUTODESK INVENTOR.



Fig 1. Fatigue failure of gear tooth. (www.google.com)

The surface failures happening mostly because of contact fatigue are pitting and scoring. It is a phenomenon in which little particles are removed from the surface of the tooth because of the high contact stresses that are present between mating teeth. Pitting is really the fatigue failure of the tooth surface. Hardness is the essential property of the gear tooth that gives imperviousness to pitting. In other words, pitting is a surface fatigue failure because of numerous redundancies of high contact stress, which happens on gear tooth surfaces when a couple of teeth is transmitting power. Gear teeth failure due to contact fatigue is a typical marvel watched. Even a slight reduction in the stress at root brings about incredible expand in the fatigue life of a gear.

II. Literature Review

M.S.Hebbel, V.B.Math and B.G.Sheeparamatti [1] utilized elliptical and circular holes as a stress relieving feature. Analysis uncovered that, combo of elliptical and circular stress relieving features at particular, locations are beneficial than single elliptical, single circular, two circular or two elliptical stress relieving features. Ashwini Joshi, Vijay Kumar Karma [2] did a work which deals with the effect on gear strength with variation of root fillet design utilizing FEA. Circular root fillet outline is considered for analysis. The load application is done at the highest point of single tooth contact (HPSTC). Nidal H. Abu-Hamdeh and Mohammad A. Alharthy [3] did a work which deals with the effect of root fillet stress in spur gear by creating stress relieving holes in the gear body and face profile of the gear teeth. The results obtained showed that increasing the diameter size of hole/holes resulted in higher percentage of stress reductions compared to the pilot case. Furthermore, increasing the number of holes resulted in higher percentage of stress reductions compared to the pilot case, however gear rigidity in this case was highly affected. Dhavale A.S., Abhay Utpat [4] did a research study which deals with the effect of root fillet stress in spur gear by introducing stress relief features at stress zone. Analysis revealed that introduction of more than one stress relieving feature has added advantages in one of the most beneficial location principal stresses in the gear segment with a combination of two circular stress relieving features. Prof Vijaykumar Chalwa, Mr. Nagesh Kamanna, Asst Prof Prasad Nayak [5] used an Empirical relation to predict the probable percentage of reduction in root fillet stress in spur gear with circular stress relief feature. This work presents the possibilities of percentage of reduction in the root fillet stress of spur gear by introducing circular stress relieving feature of various sizes at different locations. Vivek Singh, Sandeep Chauhan, Ajay kumar [6] used a circular stress relieving feature in the stressed zone to the reduction of root fillet stress in spur gear. In this work stress relieving feature of various diameters are introduced in gear teeth. Analysis revealed that circular stress relieving feature at specific location is beneficial. Vivek Singh, Sandeep Chauhan [7] used a circular stress relieving feature in the stressed zone to the reduction of root fillet stress in spur gear. Analysis revealed that introduction of a circular hole below the root circle diameter between two teeth reduces the stress levels by a very high percentage about 42%. So by optimizing the diameter and position of the stress relief hole we can reduce the stress value in a gear tooth by a considerable amount without affecting the functioning of the gear. Mahesh. Badithe, Srithanthula Srikanth, Jithendra Bodapalli [8] the main objective of this study is to add different shaped holes to reduce stress concentration. A finite element model of Spur gear with a segment of three teeth is considered for analysis and stress concentration reducing holes of various sizes are introduced on gear teeth at various locations. Analysis revealed that aero-fin shaped hole introduced along the stress flow direction yielded better results. In this study, the best result is obtained by introducing aero-fin hole at (38.7653, 65.4083, and 0) and having scaling factor of 0.6. The result displayed a stress reduction by 50.23% and displacement reduction by 45.34%.

III. Modelling Of Involute Gear

The spur gear model is designed in Pro Engineer design modeller, which are having the following parameters. . Please note that this is the same gear geometry used by Mahesh. Badithe, Srithanthula Srikanth, Jithendra Bodapalli [8] Module (m) = 2 Pitch circle dia (d) = 50mm No. of teeth (N) = 25 Tooth thickness (t) = 3.14mm Root fillet = 0.628mm Addendum dia (Da) = 54mm Dedendum dia (Dd) = 45mm Base circle dia (Db) = 46.984mm Material used: Steel Properties of Steel: Young's modulus = 21000 MPa Poisson's ratio = 0.3 Part parameters are the necessary parameters defining the gear. These part parameters decide all the other parameters that define the gear tooth profile by utilizing the Tools/Relation menu. Figure 2 viewing the part parameters.

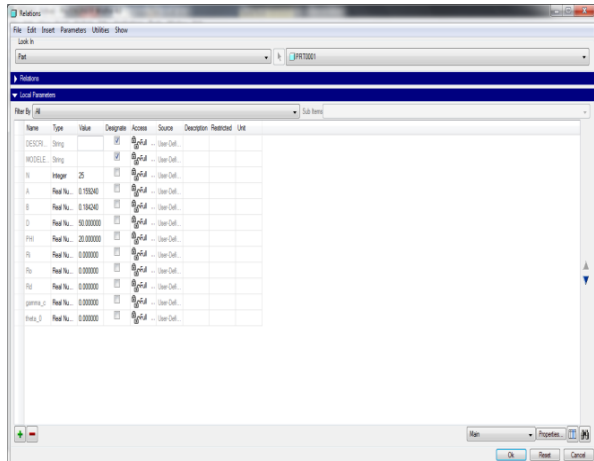


Fig. 2. Part Parameters

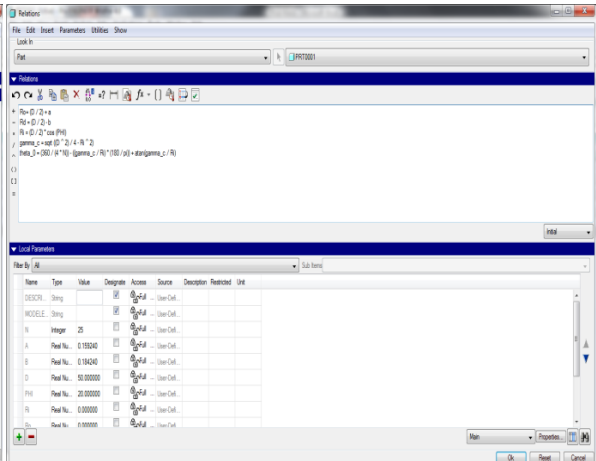


Fig. 3. Tools / Relations menu

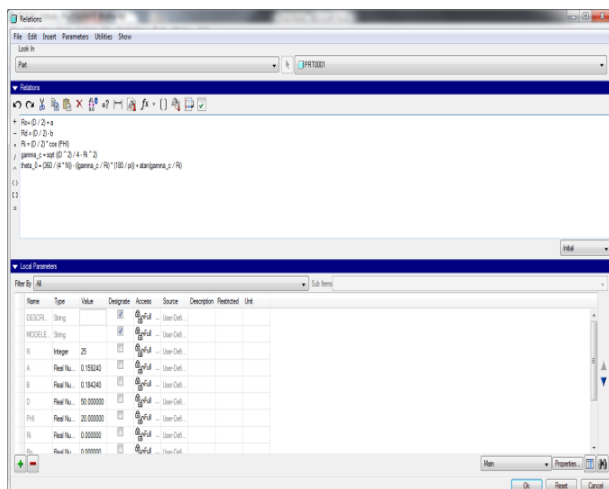


Fig. 4. Part Relations



Fig. 5. Datum Curve Relations

Drawing the circle focused on the sketch references for the extrusion profile and taking the expulsion profundity equivalents to the thickness of gear. By utilizing the Tools/ Relations Menu we characterize relations between the sketch dimension and the part parameters. Figure 3 is demonstrating the Tools/ Relations Menu. In the wake of characterizing these relations, the circle should have the diameter equivalents to the measurement of the addendum diameter of the gear blank. Figure 4 is demonstrating the part relations for getting the addendum diameter.

Selecting From Equation from the Insert/ Model Datum/ Curve Menu. We take “PRT_CSYS_DEF” as a default coordinate system. Taking coordinate system cylindrical type. In this condition a Notepad window will pop up where we can enter all mathematical equations for the datum bend. As demonstrated in the Figure 5. Review after passage of every last one of parameters will demonstrate the involute bend over the gear blank as shown in the Figure 6. Presently we have an involute curve at one side of the gear blank, by mirroring the bend about the axis we get the C shaped profile made up of two involute profiles. In next step heading off to the Tools/ Relations menu and setting the inner arc to the value of parameter Rd. In the wake of extruding the C shaped profile through the entire depth of the gear blank at long last we get the space between the two gear teeth. Figure 8 is demonstrating the space between the two gear teeth.

From the newest extruded feature in the model tree and selecting the pattern, in the top dashboard we select the following parameters;

1. Pattern type: Axis pattern
 2. Axis for pattern: A-1 at the centre of the gear.
 3. Number of copies: Equals to the number of teeth here 25.
- Included angle of the pattern: 360°

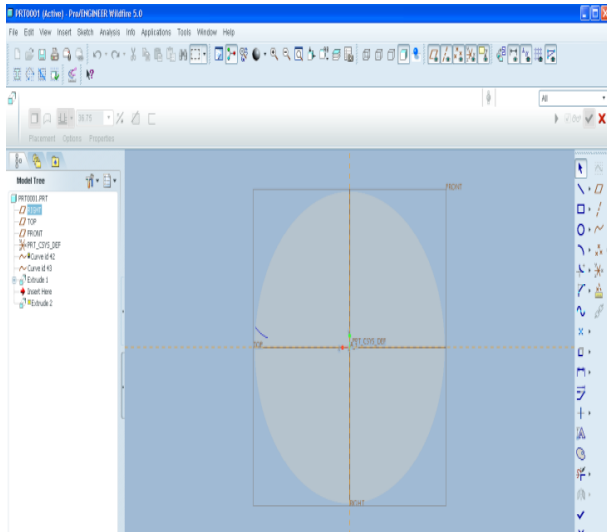


Fig. 6. Involute Profile over the Surface of Gear Blank

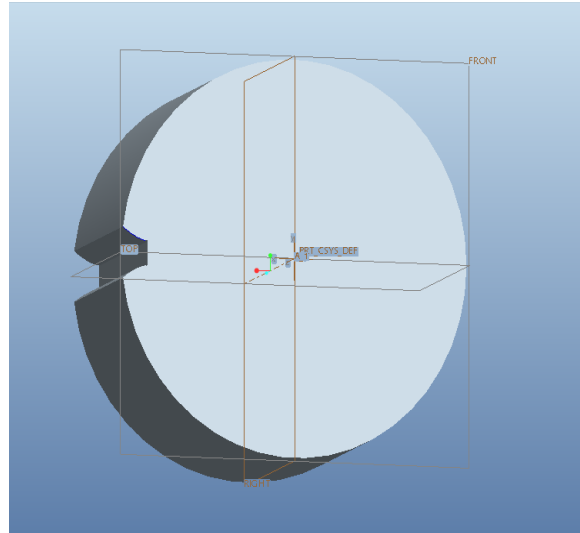


Fig. 7. Gear Blank with Tooth Space

After accepting the settings we get the involute gear with the desired number of the teeth. As shown Figure 8.

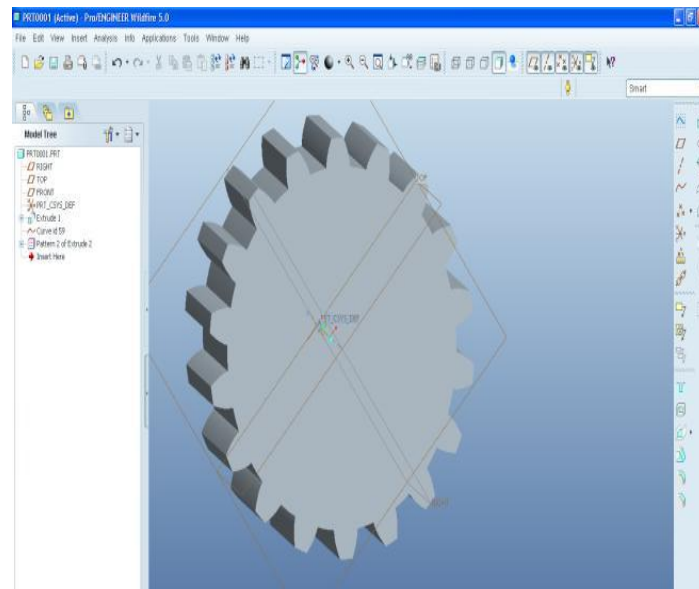


Fig. 8. Gear Model

IV. Finite Element Mesh Generation

A finite element mesh is a situating of a given subset of the three-dimensional space by basic geometrical components of different shapes. The mesh generation is performed in the base up stream i.e., lines are discretized first; the grid of the lines is then used to mesh the surfaces; then the mesh of the surfaces is utilized to mesh the volumes.

V. Problem Definition

A gear having specifications of Module (M) = 2, No. of teeth (N) = 25 to study and experiment is chosen from our reference paper. A load of 89MPa as given in paper is applied at the highest point of contact of gear teeth. The stress at root fillet region is of the value 61.48MPa and displacement is 0.0000746mm. The stress relieving features used in the gear till date are circular holes or the combination of circular and elliptical holes. Here we have tried an oval shape hole in the path of stress flow analogy and the results are analysed. A segment of three teeth is considered for analysis and stress relieving features of various sizes are introduced on gear teeth at various locations.

Laminar flow analogy

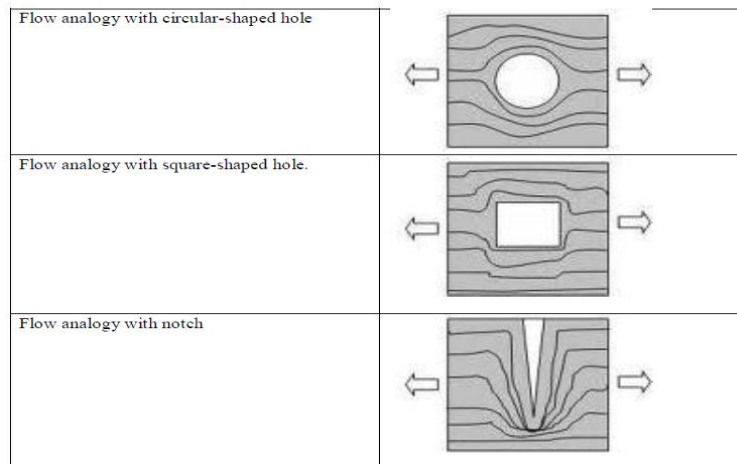


Fig.9. Laminar flow analogy (www.google.com)

The flow analogy is utilized to imagine the stress focus. It provides for us a physical picture of why and where stress focus exists and it might be used as a tool to diminishing stress fixation. The way of flow analogy in gear begins from highest point of application of load and ends at the root fillet of the tooth. This shows that lines of force travel from contact point to root fillet, with continuous decrease in width of the flow pattern.

Significance of oval shape hole

The shape of oval selected for this study is such that it changes the stress flow into a smoother way, i.e., smoother flow of stress is accomplished best by an oval type of design because the curvy nature of this helps stress flow lines of stress to find a fluent path without any interruptions, the shape becomes narrowed towards the end which will help the stress lines to flow smoothly to the fillet without increasing stresses.

Stresses & Displacements of analyzed gears

The gear without hole is examined to determine the maximum stress at the fillet and then the oval shape hole is introduced to gear. The position and size of the oval hole can be varied by changing input values of center of one of the arcs of hole. Now, the gear is experimented with different modifications done to the oval hole by varying the parameters mentioned above. The stresses and displacements are calculated and analyzed so that the maximum stress at the fillet is reduced which is the main aim of this project. The Fig illustrates the coordinates of a focus point. It is considered as the center of oval hole which is used for transformation of entire hole.

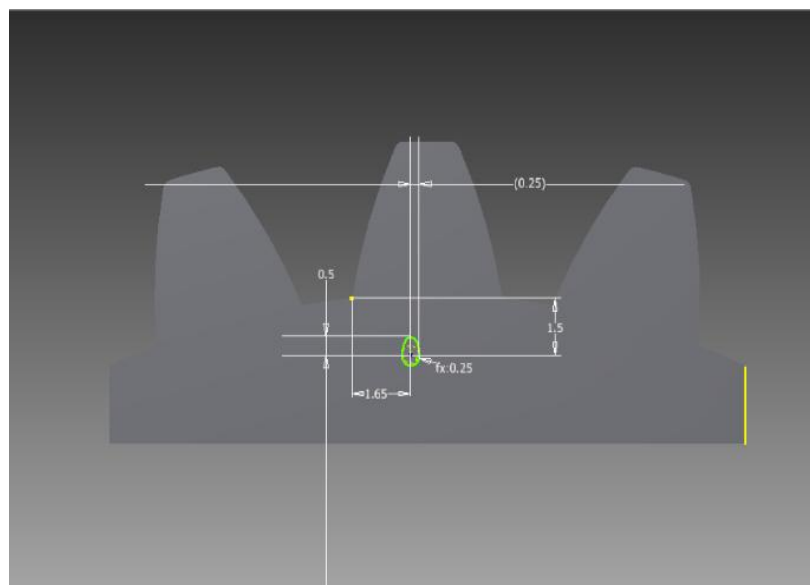


Fig.10. Centre of oval hole

Stress and displacement in Normal Gear

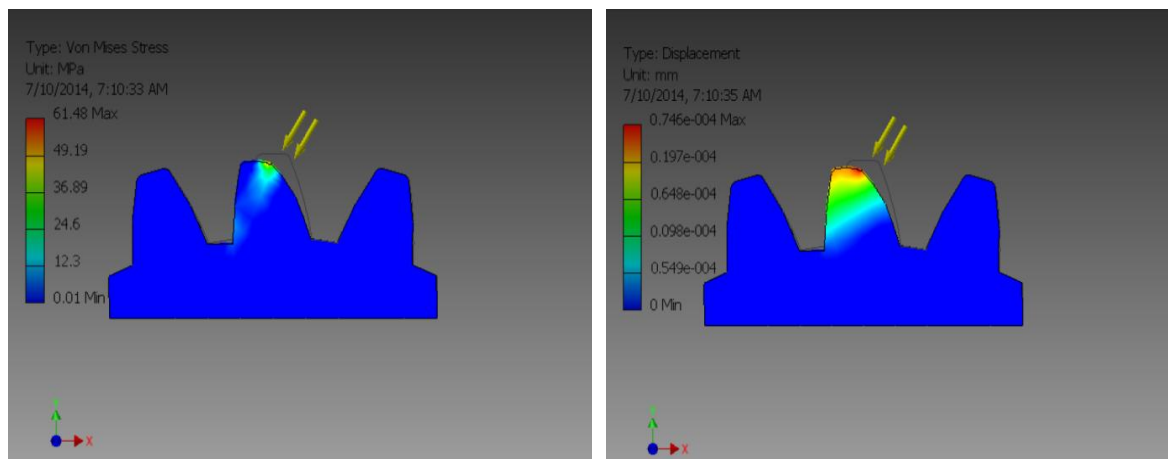


Fig.11. stress and displacement of normal gear

The maximum stress at the fillet is 61.48 Mpa and displacement is 0.0000746mm.

Stress and displacement in gear with oval shape hole (1st position)

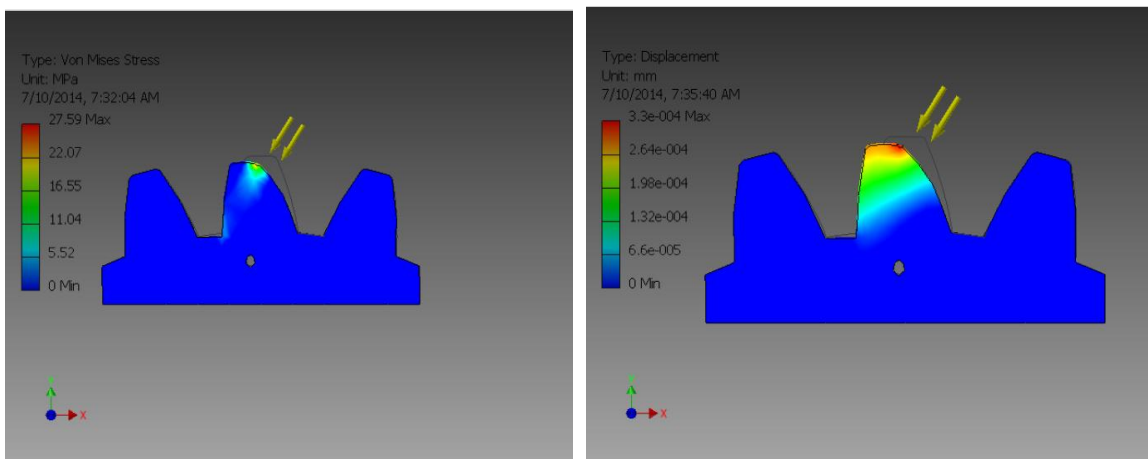


Fig.12 . Stress and displacement in gear with oval shape hole (1st position)

The maximum stress at the fillet is 27.59 Mpa and displacement is 0.000329998 after introducing oval shape hole.

Stress and displacement in gear with oval shape hole (2nd position)

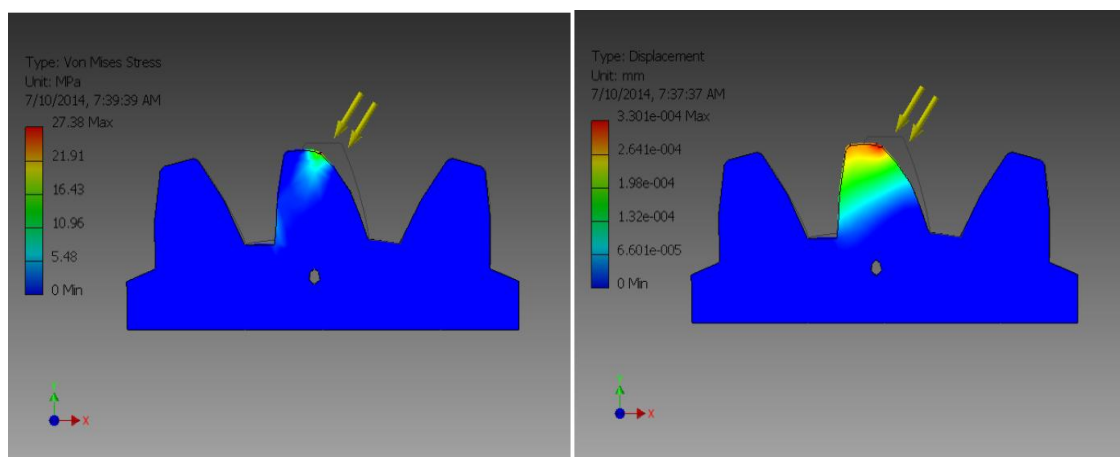


Fig.13. Stress and displacement in gear with oval shape hole (2nd position)

The maximum stress at the fillet is 27.38 Mpa and displacement is 0.000330067 after shifting oval shape hole.

Stress and displacement in gear with oval shape hole (3rd position)

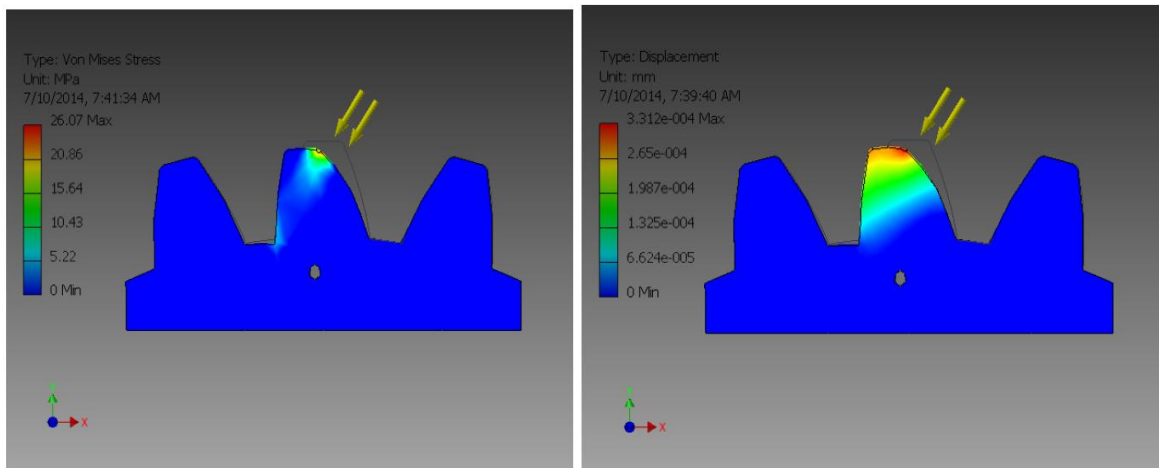


Fig.14. Stress and displacement in gear with oval shape hole (3rd position)

The maximum stress at the fillet is 26.07 Mpa and displacement is 0.00033119 after shifting oval shape hole.

Stress and displacement in gear with oval shape hole (4th position)

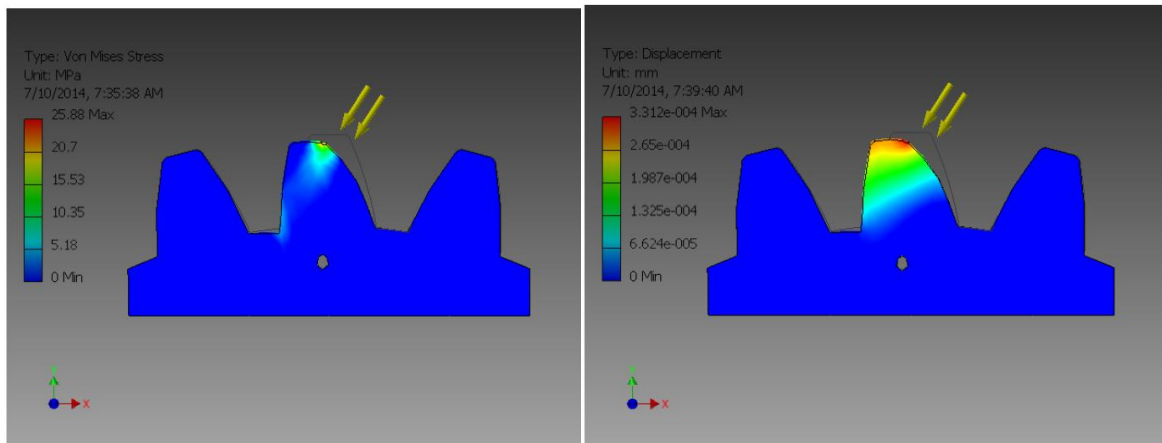


Fig.15. Stress and displacement in gear with oval shape hole (4th position)

The maximum stress at the fillet is 25.88 Mpa and displacement is 0.000332257 after shifting oval shape hole.

Stress and displacement in gear with oval shape hole (5th position)

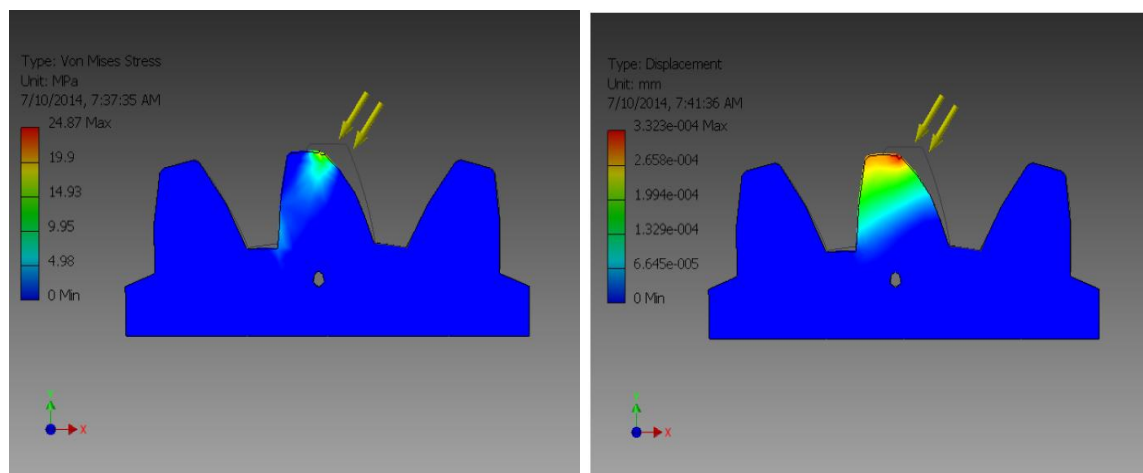


Fig.16. Stress and displacement in gear with oval shape hole (5th position)

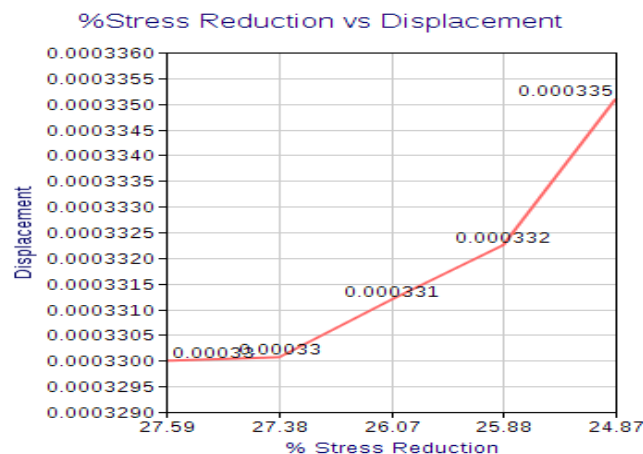
The maximum stress at the fillet is 24.87 Mpa and displacement is 0.000335102 after shifting oval shape hole.

VI. Results Of The Analysed Gears Are Tabulated Below

Positions of oval	Coordinates of oval centre(mm)		Maximum Stress (Mpa)	% Reduction in stress	Safety factor Maximum (ul)	Displacement (mm)
	x	y				
1	1.65	1.5	27.59	55.15	15	0.000329998
2	1.75	1.6	27.38	55.46	15	0.000330067
3	1.75	1.4	26.07	57.59	15	0.00033119
4	1.85	1.5	25.88	57.9	15	0.000332257
5	1.75	1.5	24.87	59.54	15	0.000335102

According to the results tabulated above, the decrease in stress is 59.54%, whereas in the reference paper [8] stress is reduced by 50.23%. From this it can be inferred that oval shape hole serves better as a stress relieving feature compared to other stress relief feature.

Graph



From the above graph it can be concluded that as the % Stress Reduction Increased, displacement also increased.

VII. Conclusion

The main aim of the above study is to relieve stress from the maximum value to as least as could be allowed. So the highest point of contact of teeth is selected as pressure application point which causes highest stress. Stress relieving feature having a shape of oval is used in the path of stress flow which helped to regulate stress flow by redistributing the lines of force. This additionally yielded better results when compared to elliptical, circular and aerodynamic holes.

REFERENCES

- [1]. M.S. Hebbal¹, V. B. Math², B.G. Sheeparamatti³ "The Reduction of Root Fillet Stress in Spur Gear Using Circular and Elliptical Stress Relieving Feature"
- [2]. Ashwini Joshi, Vijay Kumar Karma "Effect on Strength of Involute Spur Gear by Changing the Fillet Radius Using FEA" International Journal Of Scientific & Engineering Research Volume 2, Issue 9, September-2011 1 ISSN 2229-5518
- [3]. Nidal H. Abu-Hamdeh and Mohammad A. Alharthy "A Study on the Influence of using Stress
- [4]. Relieving Feature on Reducing the Root Fillet Stress in Spur Gear" Proceedings of the 2014 International Conference on Mathematical Methods, Mathematical Models and Simulation in Science and Engineering
- [5]. Dhavale A.S. Abhay Utpat "Study of Stress Relief Features at Root of Teeth of Spur Gear" International Journal of Engineering Research and Applications (IJERA) ISSN: 2248-9622 www.ijera.com Vol. 3, Issue 3, May-Jun 2013, pp.895-899
- [6]. Prof Vijaykumar Chalwa, Mr.Nagesh Kamanna, Asst Prof Prasad Nayak "Empirical relations to predict the probable percentage of reduction in root fillet stress in spur gear with circular stress relief feature" International Journal of Innovative Research in Science, Engineering and Technology Vol. 2, Issue 7, July 2013
- [7]. Vivek Singh, Sandeep chauhan, Ajay kumar "Finite element analysis of a spur gear tooth using ansys and stress reduction by stress relief hole"
- [8]. Vivek Singh, sandeep chauhan "FINITE ELEMENT ANALYSIS OF A SPUR GEAR TOOTH USING SOLIDWORKS SIMULATION AND STRESS REDUCTION BY STRESS RELIEF HOLE" International journal of advanced scientific and technical research Issue 2 volume 5, October 2012
- [9]. Mahesh. Badithe, Srimanthula Srikanth, Jithendra Bodapalli "Stress and Reduction Analysis of a Spur Gear Tooth" International Journal of Emerging Technology and Advanced Engineering Website: www.ijetae.com (ISSN 2250-2459, ISO 9001:2008 Certified Journal, Volume 4, Issue 3, March 2014).

Introduction to the selection of corridor and requirements, implementation of IVHS (Intelligent Vehicle Highway System) In Hyderabad

Maddali Sai Satya Goutham¹, Bhanu Kireeti Chanda²

1,2,(Department of civil engineering, St. Martin's Engineering College/ JNTU H, AP, India)

Abstract: Intelligent highway vehicle system is an advanced system which enhances the transportation systems, reduces the congestion and minimizes the environmental impact. To meet needs of future transportation, the present system must follow some strategies like build new capacity, manage travel demand, increase operational efficiency and advanced new technology. The most important part of system is wireless communication like GPS, fiber optic technology, satellite communication. Considering fiber optic technology, the cost of installation is more and the area of coverage is less. Hence researchers are finding alternate ways and selected WIMAX technology for wireless communication. This paper describes an overview of basic requirements for the implementation of IVHS in Hyderabad (India).

Keyword: GPS, IVHS, AVIS, ATMS, CVO, ATIS, PCU.

I. Introduction

Intelligent vehicle highway system (IVHS) is an integrative program which includes information technology, advanced technologies with transportation system. Basically the congestions, traffic jams and road accidents occur due to lack of knowledge or information. So, to avoid the incidents and maintain the life span of highways IVHS is implemented. The principle behind the system is to exchange the information to and from^[1]. This can be achieved by the wireless communication system and specialized sensors which may be non-intrusive sensors or intrusive sensors. Intrusive sensors include weigh in motion sensors and non-intrusive sensors include infrared detectors, microwave radar detectors, laser detectors etc. The data obtained by the sensor will be sent to center and it will be passed to travelers.

II. Implementation

India is the home to ancient Indus valley civilization and a region of historic trade routes and vast empires. The Indian subcontinent was its commercial and cultural wealth for much of its long history. India is a federal constitutional republic governed under parliamentary system consisting of 29 states and 7 Union Territories^[2]. Among the 29 States, there are different metropolitan cities in the country.

They are Delhi, Mumbai, Kolkata, Hyderabad, Chennai, Bangalore, Ahmedabad, Pune, Surat, Jaipur and Kochi. Amongst the above cities, the transportation and traffic situations in Hyderabad are comparatively chaotic. The traffic levels are accelerating faster than the road capacity. Traffic congestion is more than an irritant and it is one of the leading problems being faced today. It could get worse unless we find better ways of using highways system and transit infrastructure.

III. Selection Of Corridor And Strategies

The answer for the traffic congestion lies in using the technology to steer traffic in the right direction. When coming to India, IVHS is completely a new concept to implement. It is successfully implemented in North America and South America and Europe.

IV. How IVHS Is Applicable To Hyderabad?

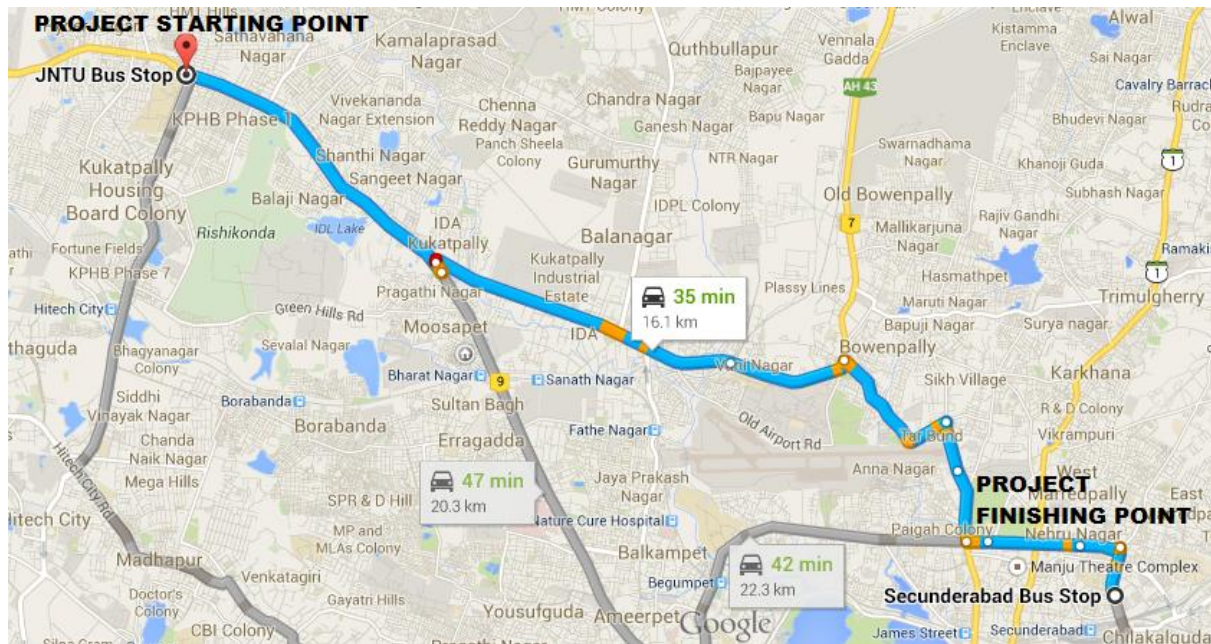
The road network in Hyderabad is radially configured with 3 National Highways (NH) passing through centre of the city. They are (i) NH-7 (National Highway 7 : North to south), (ii) NH-9 (National Highway 9 : Northwest to southwest), (iii) NH-202 (National Highway 202 : towards Northeast). While looking into condition of roads a gradual deterioration is noticed due to heavy flow of traffic. This causes uneven loadings, lack of material properties and composition lead to a low quality road that degrades faster and leads to accidents. To resolve the traffic related issues, the present system would prove to be a plausible solution. An upgradation to the current system is required to solve the traffic congestion, traffic jams, accidents and response time to

accident sites. The only option is IVHS, which will track the traffic information with help of computers using Closed Circuit TV Visuals (CCTV), Global Positioning System (GPS), satellite information and the other technologies.

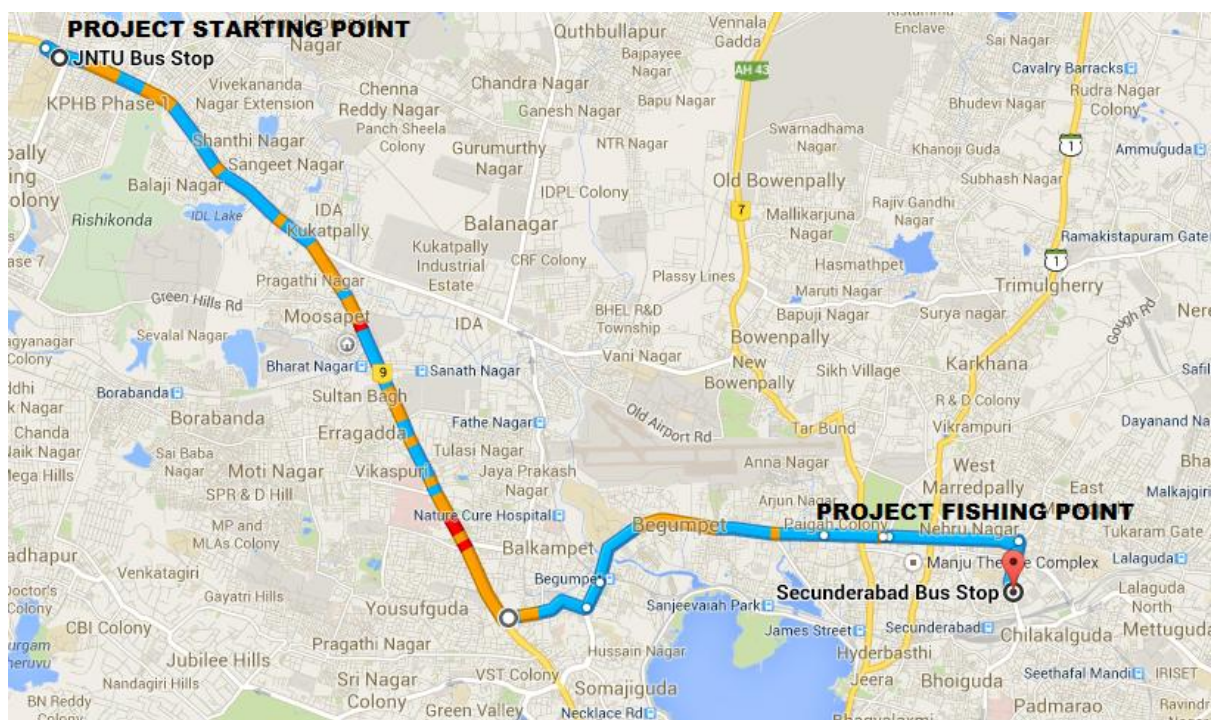
Surveys and studies are done in the corridor to get a clear idea for the implementation of IVHS. The corridor is from JNTU to Secunderabad via Bowenpally and via begumpet. This specific corridor is selected because of the traffic conditions and traffic flow in the corridor. The distance from JNTU to Secunderabad is 17.04KM via Begumpet and the distance between JNTU to Secunderabad is 15.8KM via Bowenpally.

The corridor consists of Educational hubs like JNTU, Kukatpally, S.R. Nagar, Business centres like Patny, Balanagar, Paradise, Ameerpet and the Residential areas like KPHB, Bharathnagar, Moosapet, Erragada, Begumpet, Prashantnagar. The corridor has around 10 junctions in each stretch.

Firstly, the reconnaissance survey was done to get a coarse assessment of corridor.



The above stretch ^[2] is from JNTU to Secunderabad via Bowenpally.



They above stretch ^[3] is from JNTU to Secunderabad via Ameerpet.

For the sake of convenience let the stretch of the corridor via Bowenpally is termed as S1 with the same aspect the stretch of the corridor via Ameerpet is termed as S2. We know that the Intelligent Vehicle Highway System will heavily rely on technology. Let us take a corridor in to consideration, for the basic installation of IVHS technological application like weigh in motion, GPS, detector technology, satellite communication, CCTV, Infrared, Radar technology etc. The reason behind the use of advance technology is to gather the information and pass it on in fraction of seconds.

To setup IVHS in this particular corridor, adoption of data receiving and transmitting system is required. Approximately the corridor covers the distance about 28.5kms. So, setting up the communication room may or may not be in the corridor but it must have an entire visual cover on the corridor.

Intelligent Vehicle Highway System is supported by different interactive elements. By linking them to the installation in this corridor we come to a conclusion that following equipment and implementation procedure are necessary^[4]. They are:

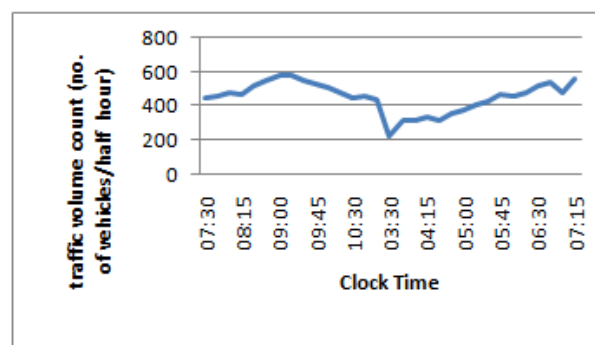
- i. Advanced Traffic Management System (ATMS) ,
- ii. Advanced Traffic Information System (ATIS) ,
- iii. Advanced Public Transportation System (APTS) ,
- iv. Commercial Vehicles Operations (CVO) and ,
- v. Advanced Vehicle Information System (AVIS).

V. Advanced Traffic Management System (ATMS):

This element will monitor, control and manage area with wide operations and serve as the communication link between road way, vehicles and travellers. ATMS gets the information in operation from the traffic management centre, signals, detector technology, parking areas, police emergency and vehicles. The information acquired from here will be used to identify the traffic congestion and optimise the traffic signal timings. There is a limitation in this corridor i.e, the connection of vehicles with source for information is done by updating the vehicles with GPS technology and provides a user interface for the vehicle to operate smoothly. But so far now these sort of vehicles are hardly few. And the visual surveillance could be limited to traffic signals. For better efficiency the application of cameras must be provided in public places, parking areas etc. The detector technology is in the developing stages in the country, once developed it will differentiate between type of vehicles and the average vehicle velocity. At the signals fixed cameras arranged throughout the corridor. If the swinging cameras are arranged that will cover good amount of information than the fixed cameras. When coming to police emergency, the delay on response timing is reduced as the IVHS main concept is to integrate every agency and acquire information and transmit to the travellers, vehicles and commuters. Linking the police emergency to IVHS, the corridor consists of police stations in Kukatpally, SR Nagar, Begumpet, Bowenpally and Secunderabad. By maintaining the good coordination the delay in incident response time would be reduced.

VI. Advanced Traffic Information System (ATIS):

This element provides travellers with trip and traffic information with safety and warning messages related to environmental conditions. The travellers can get the pre-travelling information through different sources. Actually, the information given by the ATIS can be used as real time traffic information. If the IVHS is implemented the traveller can use the pathfinder in the event of doubt in the route. This operation is done by using the Global Positioning System for the identification of routes and to know where the vehicle is exactly located. The another mode of information from the ATIS is related to traffic congestion information. Through this the traveller can select the safest route which saves time and other resources. The real time traffic information can be received by the people by radios and internet etc. If a route is selected a person heading to Secunderabad from JNTU, using traffic information he can chose the route without traffic congestion or else can divert the route. Generally the route S1 will be with heavy traffic flow near Balanagar junction at peak hour time.



The above graph (taking the interval of 30 minutes in the peak hour time) show the traffic volume in the Balanagar junction in the peak hour timing in April 2014.

Due to heavy rush of traffic flow in the corridor and lack of information as well as lack of efficient management, the major traffic jams are becoming common. This traffic jams and congestions are degrading the quality of roads and eventually the life span of the pavement has gone down drastically. The strength of the pavement can be determined using level of service.

Level of service is defined as the qualitative measure describing the operational conditions within a traffic stream, and their perception by drivers/ passengers. Level of service generally describes the factors such as speed and travel time, freedom to manoeuvre, traffic interruptions, comfort, convenience and safety.

A level of service chart taken from IRC: 106-1990 is given in Fig.1.

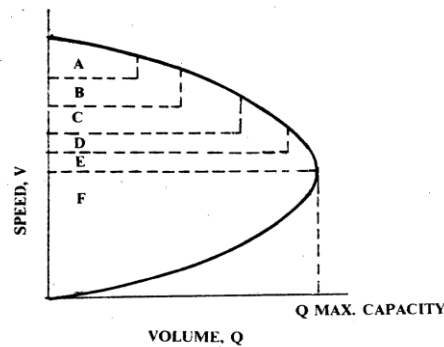


Figure1: Level of Service

Commonly six levels of service are recognized, designated from A to F, with level of service “A” representing the best operating condition (i.e., free flow) and Level of Service “F” the worst (i.e., forced or break down flow). The calculation of LOS is done by taking the junction points at different distances in the corridor in two stretches S1 and S2. These calculations are done by taking the passenger car unit PCU values at the section points which are considered as mid blocks for the corridor.

Level of service at section 1 (Kukatpally) Over all PCU values at mid block 1 = 2889 PCU/hour

Total design service volume = 2900

$2889/2900 = 0.996 \Rightarrow 99.6\%$ (which is greater than 95%)

So, level of service for mid block 1 falls under category ‘F’.

Level of service at section 2 (Erragadda)

Over all PCU values at mid block 2 = 2788 PCU/hour

Total design service volume = 2900

$2698/2900 = 0.903 \Rightarrow 90.03\%$ (which is greater than 85%)

So, level of service for mid block 2 falls under category ‘E’.

Level of service at section 3 (Ameerpet)

Over all PCU values at mid block 3 = 2877 PCU/hour

Total design service volume = 2900

$2877/2900 = 0.992 \Rightarrow 99.2\%$ (which is greater than 95%)

So, level of service for mid block 13 falls under category ‘F’.

Level of service at section 4 (patny)

Over all PCU values at mid block 4 = 2700 PCU/hour

Total design service volume = 2900

$2700/2900 = 0.931 \Rightarrow 93.1\%$ (which is greater than 80%)

So, level of service for mid block 4 falls under category ‘E’.

Level of service at section 5 (Balanagar)

Over all PCU values at mid block 5 = 2687 PCU/hour

Total design service volume = 2900

$2687/2900 = 0.926 \Rightarrow 92.6\%$ (which is greater than 80%)

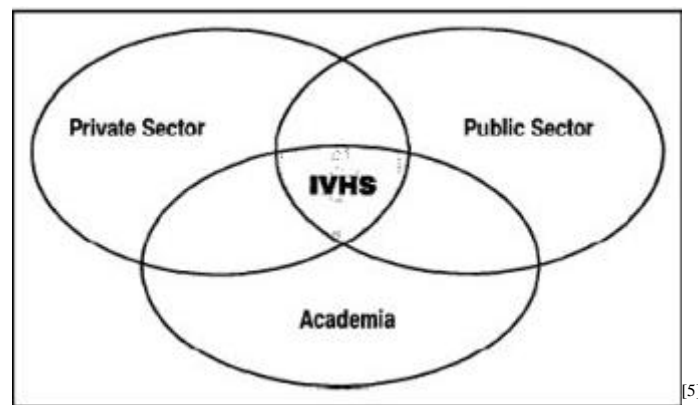
So, level of service for mid block 5 falls under category ‘E’.

Level of service at section 6 (Bowenpally)
Over all PCU values at mid block 6 = 2557 PCU/hour
Total design service volume = 2900
 $2557/2900 = 0.881 \Rightarrow 88.1\%$ (which is greater than 80%)
So, level of service for mid block 6 falls under category 'E'.

The values of level of service explain the condition of pavement. Therefore, boosting the current transportation system is necessary at least now.

VII. Advanced Public Transportation System (APTS):

Another element behind the strategy of efficient IVHS is APTS. This particular system uses the advanced technology to make public transportation more attractive. This enhances number of customer utilizing the service in turn improves the profit. Therefore, intelligent vehicle highway system is a smart way to invest. This system provides a customer interface to obtain information related to fares from one stop to another stop, availability of buses, frequency of buses etc. The best example is Bus Rapid Transit System. When coming to the corridor and taking S1 in to consideration, it consists of 14 bus stops (from project starting point to finishing point). Taking S2 in to consideration, it consists of 10 bus stops (from project starting point to finishing point). The advanced public transportation system can be used smoothly by digitalization of bus stops. By that a commuter can acquire the information related the travel. These bus stops (in the corridor) will get the information from the traffic management centre. Hence it will track the buses by satellite communications and detectors etc. The implementation of intelligent vehicle highway system will be preferred by all levels of government offices, the private sector and the academia.



VIII. Commercial Vehicles Operations (CVO):

This element will enhance the efficiency of motor carrier industry. Highways and roads are critical for everyday life. Traffic congestion, traffic jams, and truck overloading generates tremendous damages to highway system (pavements especially). Overloading trucks and other vehicles accelerates the deterioration of transportation infrastructure. The important way to reduce the damage is to control traffic loads. This will be analyzed by weigh-in-motion system. It will calculate the measurement of gross and axle weights of commercial vehicles and this calculation can be done by weigh in motion sensors. The sensors located on highways weigh trucks at high speed and the vehicles with no over loading will continue on their way. Potential offenders are diverted for inspection. Weigh in motion protect investment and ensures useful life. It also decreases CO2 emission and increases user satisfaction. Taking the corridor in to consideration the application of commercial vehicle operation consists of WIM sensors at particular areas where the commercial vehicles will have more frequency than other. The placement of sensors at Prashanthnagar, Balanagar, Bowenpally and the areas at Moosapet, Bharathnagar, Ameerpet and Secunderabad will helps to identify the heavily loaded vehicles and help to divert them for inspection.

IX. Advanced Vehicle Information System (Avis):

This element will help the drivers to perform various vehicle functions. It warns the presence of the obstacles and vehicles in “driver blind” spots at night times and at the poor weather conditions. Basically this system will involve Infrared technology for the proper vision at dark. Whichever corridor is used this type of technology will help the drivers to drive safe at darks times that eventually reduces accidents.

X. Conclusion

Adapting and installing system described in the paper will upgrade the transportation in Hyderabad. The most important thing is updating the vehicles with user interface and installing with global positioning system. As the level of service for the roads is degrading, IVHS is a better way for investing in advanced technologies.

REFERENCES

- [1]. http://itlaw.wikia.com/wiki/Intelligent_Vehicle_Highway_System
- [2]. <http://en.wikipedia.org/wiki/India>
- [3]. <http://www.Google.com/maps>
- [4]. Houston smart commuter IVHS demonstration project. The Texas transportation institute, The Texas A&M University system college station, TX 77843.
- [5]. <http://www.Google.com/images>

Experimentation of Jute Fiber Supplemented with E-Glass in Various Layers Alignment

Rahul Komma¹, K.Prudhvi Raj², Dinesh Souda³

¹Mechanical Department, RGUKT, India)

² Mechanical Department, MGIT, JNTUH, India

³Mechanical Department, Christu Jyothi Institute of technology, Janagoan, India

Abstract: Composites fiber are moving into the crucial stream of the automobile industry, with manufacturers and suppliers finding different blends of bio composites, glass fibers and places to use them. It has been observed that natural fibers such as flax, hemp, kneaf, jute and sisal help reducing in weight, cost, and CO₂, less dependence on other oil sources, and reusability. Also Fibers like flax, hemp or jute are cheap, have better stiffness per unit weight, corrosion resistance, electrical insulation, reduction in tooling and assembly costs, low thermal expansion, higher stiffness and strength, fatigue resistance and have a lower impact on the environment. [1]

The present study/research focuses on exploring the possibility of using jute fiber, E-Glass and embedding these in a biopolymer matrix system – epoxy – the task of which is to hold the fibers together. This epoxy stabilizes the shape of the composite structure, transmits the shear forces between the mechanically high-quality fibers, and protects them against radiation and other aggressive media. The component is conditioned and prepared for testing and subjected to tensile, compression, hardness and bending test calculating the element results with ANSYS by using the test results. Promising results have been observed and this study enables for future study in the field of natural fiber composite materials. Main aim of this paper is to reduce the impact on the environment, by using recyclable natural fibers[6] [7].

Keywords: ANSYS, Composites, E-glass, Fibers, Jute

I. INTRODUCTION

India enriched with huge source of natural fiber such as Jute, Coir, Bamboo, Sisal, Banana, Pineapple etc. has focused on the improvement of natural fiber composites firstly to explore value-added applications in industries. The material scientists all over the world focused their attention on natural composites strengthened with Sisal, Pineapple, Coir, Jute etc. mainly to cut down the cost of raw materials. Reinforced composites are mostly used in industrial applications due to their inherent high specific strength and stiffness. In this type composite the second phase is in the form of fibers dispersed in the matrix which could be either plastic or metal. The volume fraction (V_f) varies from a few percentage to as high as 70%. Usually the fiber reinforcement is done to obtain high strength and high modulus. For that it is necessary for the fibers to have higher modulus than the matrix material, such that the load is passed on to the fiber from the matrix more efficiently. E-Glass was actually developed for standoff insulators for electrical wiring. Later it was found to possess excellent fiber forming abilities and is now used almost exclusively as the reinforcing phase in the material commonly known as fiberglass[2] [5] [8] [9].

In this paper four layered and three layered jute glass specimen is compared theoretically using ANSYS and practically on material testing machines. Their properties such as inter laminar shear stresses, bending stresses, Tensile and compressive strength of both specimens are compared.

II. PREPARATION OF SPECIMEN

The manner in which the warp and weft threads are interlaced is known as the weave style. Plain weave is the most basic type of textile weaves. The warp and weft are aligned so they form a simple crisscross pattern. In balanced plain weaves the warp and weft are made of threads of the same weight (size) and the same number of ends per inch. Plain weave with 1/1 layer is selected.

For preparation of composite first a rectangular frame of 250mmx250mm with a height of 25mm is prepared then a GI sheet with same dimension prepared. Fiber mat also prepared with respective dimension.

Wax is applied to frame and as well as to GI sheet. Then GI sheet is placed in the frame and resin is mixed with hardener with required proportions. Have to apply the adhesive to the GI sheet and fiber mat is placed over it and again adhesive is applied with help of brushes. When the adhesive applied properly place another layer of fiber over before one and apply adhesive. Similarly we can do this whenever there is need for more layers. This increases the thickness of the composite material. Now another GI sheet with wax applied is placed over this need to keep small load to avoid voids in the composite material. After the soaking period composite material is obtained. 4 bending and 4 tensile specimens are prepared. Bending with 20mmx140mm and for tensile specimen as per the standards is prepared.

Specimen type : Flat

- Specimen width mm : 15.11
- Specimen thickness mm : 5.44
- C/S Area mm² : 82.198
- Original Gauge Length mm : 50
- Final Gauge Length mm : 51.72

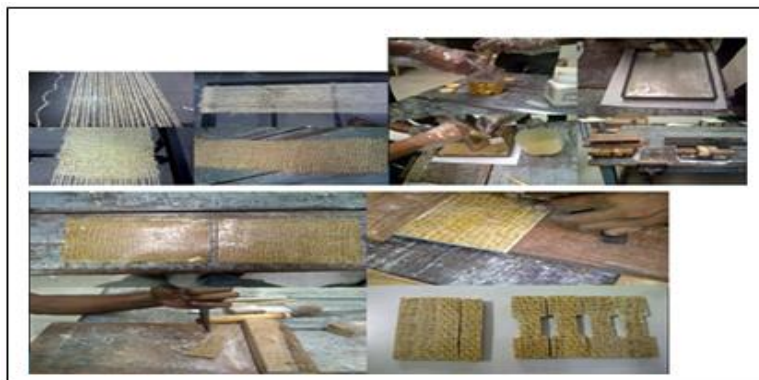


Fig1: Preparation of Specimen

Material Properties of Natural Fiber Jute [4]

- Density gm/cm³ : 1.45
- Youngs Modulus GPa : 55
- Poissons ratio : 0.38
- Shear Modulus GPa : 7.24
- E glass and k12 epoxy resin used

III. FINITE ELEMENT METHOD

The analysis in Ansys is done using the shell 99 element which is used for layered applications. Shell99 element lacks nonlinear capabilities of shell 91 and has shorter formulation time. It allows up to 250 layers. For an analysis requiring more than 250 layers a user input constitutive matrix is shown available. It has six degrees of freedom at each node i.e. 3 translations and rotations at each node. [10] [11].

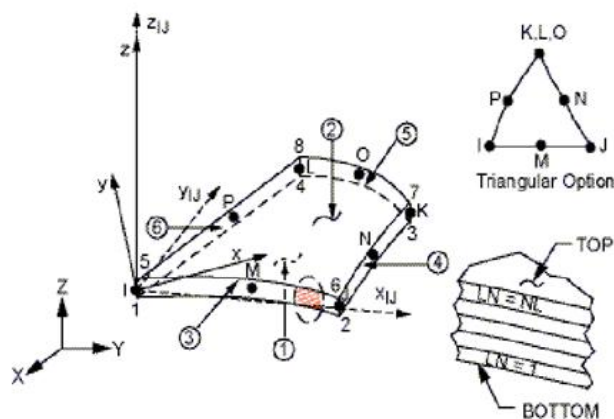


Fig2: SHELL99 element Geometry [3]

x_{ij} = Element x-axis if ESYS is not supplied.

x = Element x-axis if ESYS is supplied.

LN = Layer Number

NL = Total Number of Layers

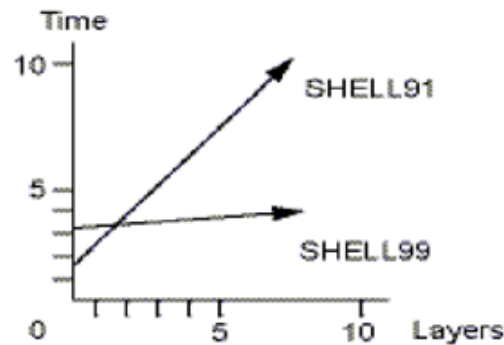


Fig3: Stress recovery time as a function of the number of layers [3]

IV. EXPERIMENTATION RESULTS

The specimen is considered in the form of three layers and four layers. In three layered specimen has two categories. In the first, layers are made in the series of “**Jute-Glass-Jute**” and other in series “**Glass-Jute-Glass**” similarly in the four layered specimen has two categories. In the first, layers are made in the series of “**Jute-Glass-Glass-Jute**” and other in series “**Glass-Jute-Jute-Glass**”. Results are obtained both practically and through Finite Element Method. In practical method by using universal testing machine all the four kinds of specimens are considered and load versus deformation graphs are obtained in the machine. In Finite Element Method also all four cases are considered. Von-Mises stresses in bending and Tensile Tests are obtained.



Fig4: Experimentation showing UTM with Specimen

Tensile Results:

S. No	No.of layers	Specimen	Ultimate Load(N)	Ultimate Tensile Strength (N/mm ²)	Elongation %
1	3	Glass-Jute-Glass	1960	23.844	3.440
2	3	Jute-Glass-Jute	1880	20.678	3.380
3	4	Glass-Jute-Jute-Glass	2840	28.434	5.680
4	4	Jute-Glass-Glass-Jute	1520	13.006	1.800

The below graphs depict the variation of load with respect to deformation in all above four cases obtained from the Universal Testing Machine

Case 1(3 layered GJG):



Fig5: variation of load with respect to deformation in 3 layered Glass-Jute-Glass specimen

Case 2 (3 layered JGJ):

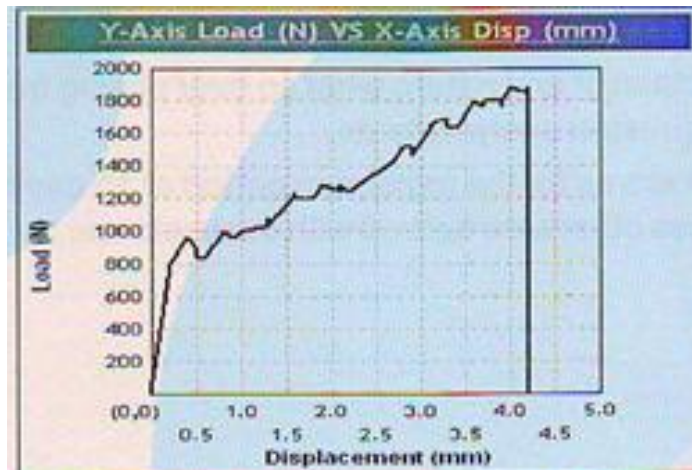


Fig6: Variation of load with respect to deformation in 3 layered Jute-Glass-Jute specimen.

Case 3 (4 layered G2JG):

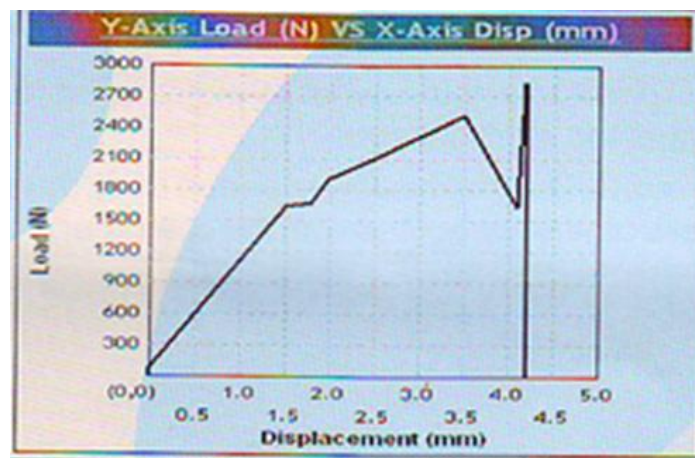


Fig7: variation of load with respect to deformation in 4 layered Glass-Jute-Jute-Glass specimen

Case 4 (4 layered J2GJ):

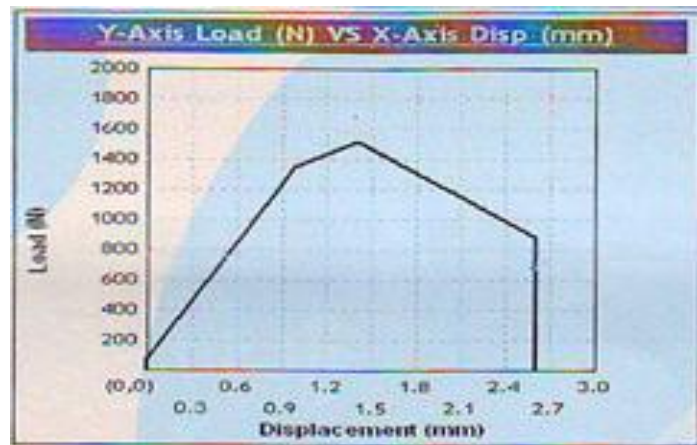


Fig8: variation of load with respect to deformation in 4 layered Jute-Glass-Glass-Jute specimen

Von Mises Stresses In Tensile Test:

Nodal stress distribution of the object in von mises direction. The below images shows the displacement of all layer composite tensile specimens.

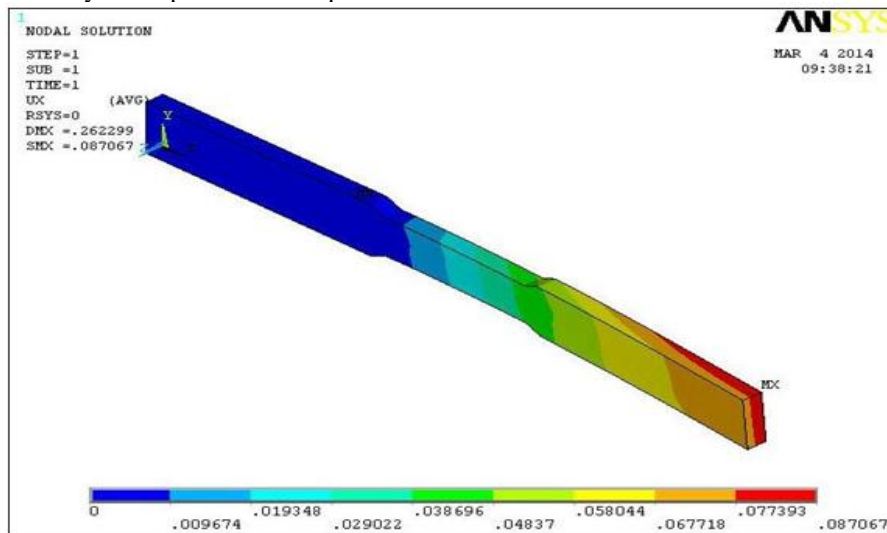


Fig9: Von mises stress of Glas-jute-jute-Glass layer specimen

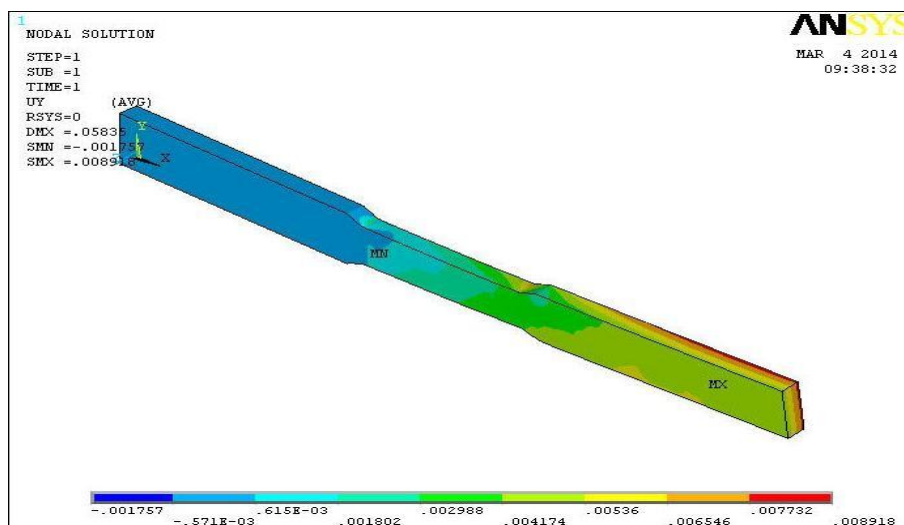


Fig10: Von mises stress of jute- Glas- Glas-jute layer specimen

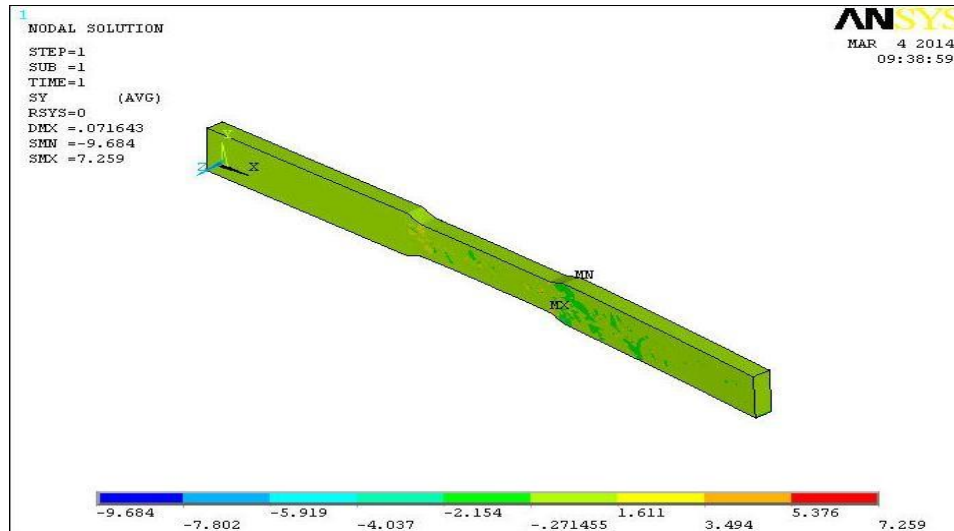


Fig11: Von mises stress of Glas- jute-Glas layer specimen

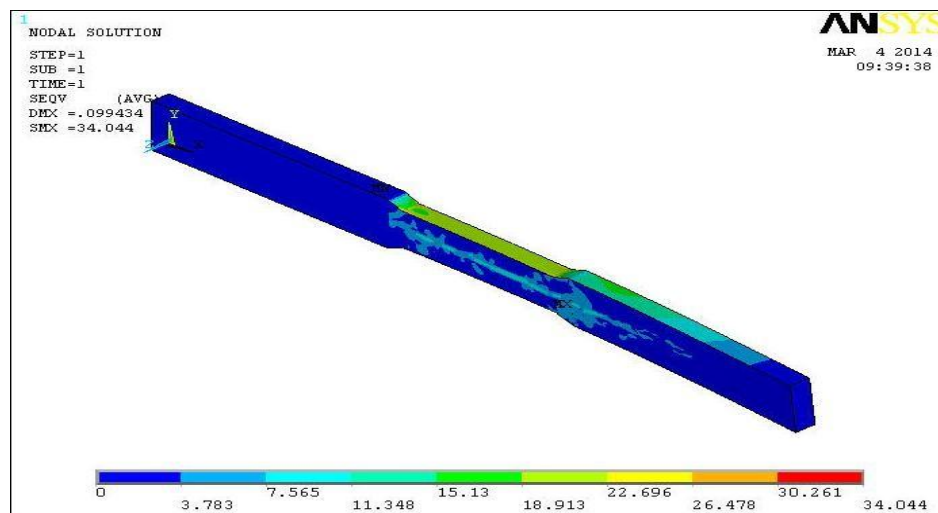


Fig12: Von mises stress of jute-Glas-jute layer specimen

Von Mises Stresses In Bending Test:

Now we get nodal stress of the object in von mises conditions. The below images shows the von mises stress of all layers Bending specimen.

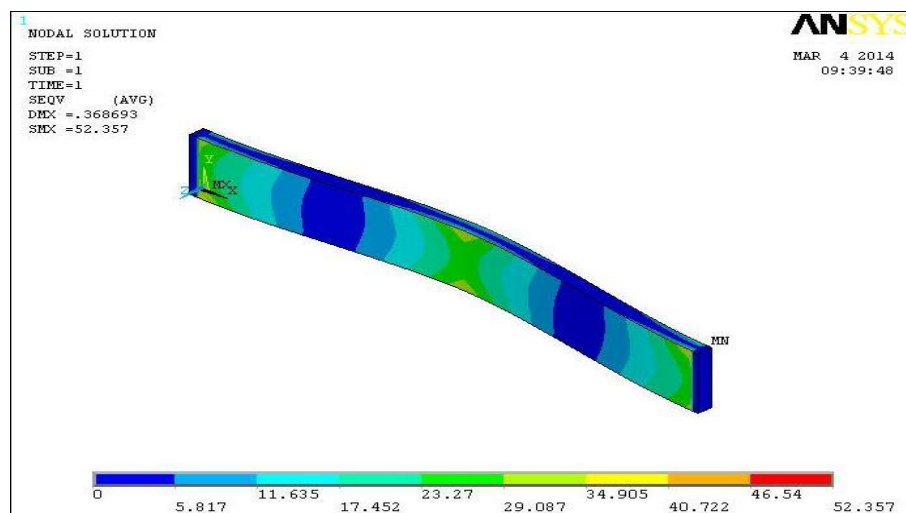


Fig13: Von mises stress of Glas-jute-jute-Glas layer specimen

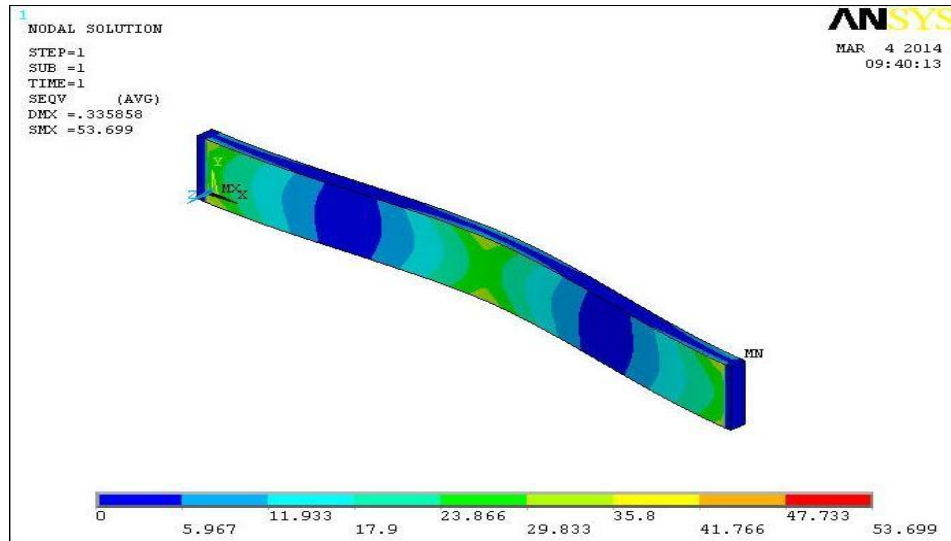


Fig14: Von mises stress of jute- Glas-Glas-jute layer specimen

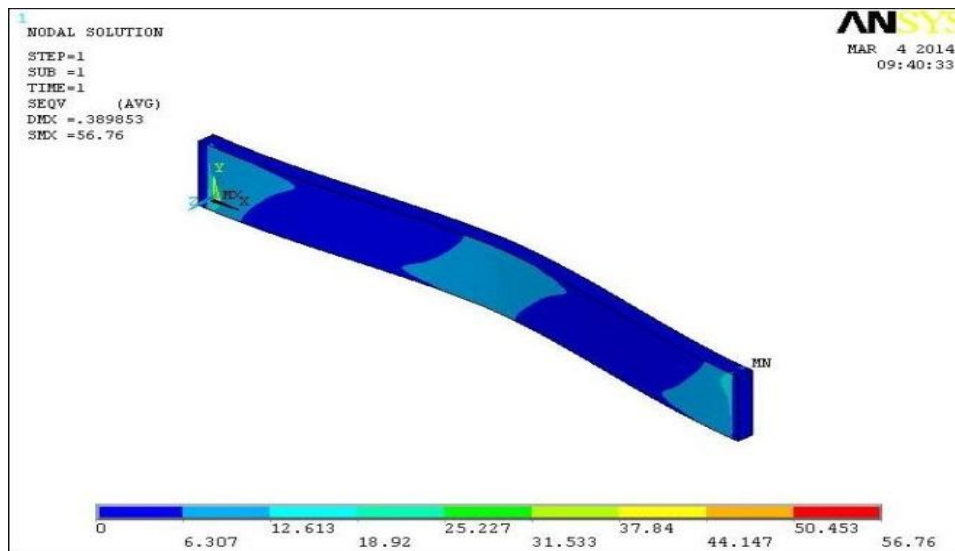


Fig15: Von mises stress of Glas-jute-Glass layer specimen

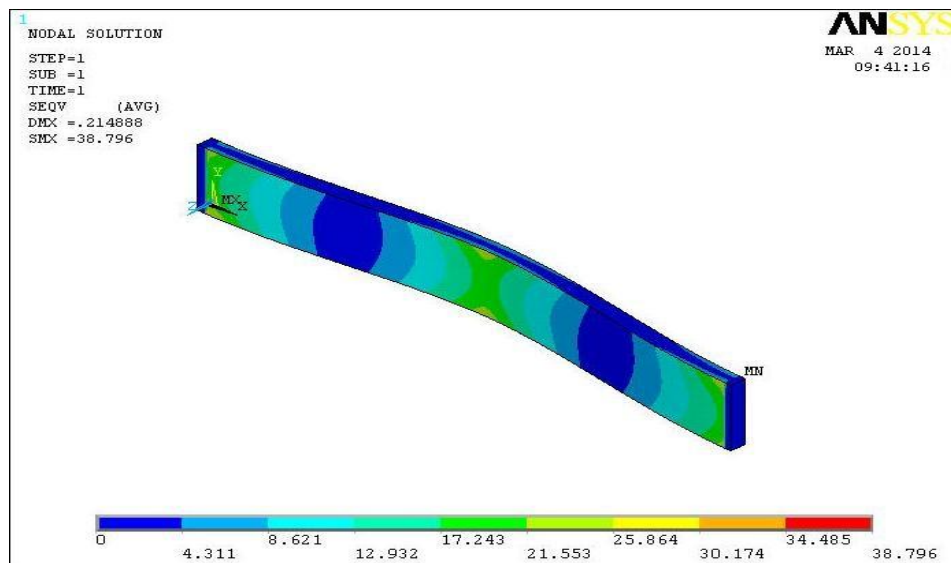


Fig16: Von mises stress of jute-Glas-jute layer specimen

V. CONCLUSION

The following conclusions are drawn from the present work

- The 4 layered Glass-jute-jute-Glass specimen is more stiffer than 3 layered Glass-Jute- Glass specimen because the variation of percentage in deflection is 39.43, and also it is 19.25% more hard enough than 3 layered one.
- The Bending shear stresses are 8.40% more in 3 layered one than the 4 layered Glass-Jute-Glass specimen.
- The 3 layered Jute-Glass-Jute specimen is more stiffer than 4 layered Jute-Glass-Glass-Jute specimen because then variation of percentage in deflection is 65.08, and also it is 58.98% more hard enough than 4 layered one.
- The Bending shear stresses in 38.41% more in 4 layered one than the 3 layered jute glass jute specimen.

REFERENCES

- [1] R. S. Lavate, A. T. Patil, A. M. Patil, N.V. Hargude. "Dynamic Response Analysis of Fiber Reinforced Composite Beam" IOSR Journal of Mechanical and Civil Engineering (IOSR-JMCE); ISSN: 2278-1684, PP: 38-47
- [2] James Holbery, Dan Houston "Natural-fiber-reinforced polymer composites in automotive applications" November 2006, Volume 58, Issue 11, pp 80-86
- [3] Documentation for ANSYS 11.0
- [4] D.nabi Saheb, j.p jog Materials properties Natural-fiber polymer composites a review, Advances in Polymer Technology, Volume 18, Issue 4, pages 351–363, Winter 1999
- [5] Natural fibres - International Year of Natural Fibres 2009 www.naturalfibres2009.org/en/fibres/index.htm
- [6]. International Year of Natural Fibres 2009 www.naturalfibres2009.org/
- [7]. A boron-free E & E-CR glass reinforcement composites.owenscorning.com/aboutAdvantex.aspx
- [8]. Glass fiber - Wikipedia, the free encyclopedia en.wikipedia.org/wiki/Glass_fiber
- [9] E-Glass Fibre www.azom.com/article.aspx?ArticleID=764
- [10]. Finite element method - Wikipedia, the free encyclopedia [en.wikipedia.org/wiki/Finite element method](http://en.wikipedia.org/wiki/Finite_element_method)
- [11] finite element method: an introduction - Indian Institute of technology of madras www.iitg.ernet.in/engfac/rtiwari/resume/usdixit.pdf
- [12] The use of natural fibres in nonwoven structures for applications www.ienica.net/usefulreports/auto.pdf

Performance & emission characteristics of Two Cylinder Diesel Engine Using Diesel & Pine oil

Dr. Hiregoudar Yerrennagoudaru¹, Chandragowda M², Manjunath K³,
Manjunath k J⁴

¹Professor and PG Co-ordinator (Thermal Power Engineering), Mechanical Engineering Department, RYMEC Bellary, Karnataka, India

²ASST Professor and PROJECT Co-ordinator (Thermal Power Engineering), Mechanical Engineering Department, RYMEC Bellary, Karnataka, India

³ASST Professor (Thermal Power Engineering), Mechanical Engineering Department, RYMEC Bellary, Karnataka, India

⁴M.Tech (Thermal Power Engineering), Mechanical Engineering Department, RYMEC Bellary, Karnataka, India,

Abstract: With modernization and increase in the number of automobiles worldwide, the consumption of diesel and gasoline has enormously increased. As petroleum is non renewable source of energy and the petroleum reserves are scarce nowadays, there is a need to search for alternative fuels for automobiles. Work has been done in using a lot of bio-fuels, the fuels obtained from plant to be used in IC engines which have an even added advantage of lower emissions compared to that of diesel and gasoline. In the present investigation Pine has been experimented in a direct injection diesel engine under homogeneous charge compression ignition compression combustion mode

The engine chosen to experiment is a single cylinder Direct ignition diesel engine and modified in such a way to, ignite Pine in a diesel engine under HCCI mode As the Pine has a higher self ignition temperature the ignition of Pine in regular diesel engines with auto-ignition is not possible. Hence, suitable modification is made in the engine to ignite Pine in a diesel engine like diesel fuel. The modified engine has Engine control module controlled fuel spray and an air pre-heater in the suction side of the engine. The combined effort of adiabatic compression and supply of preheated air ignites pine by auto-ignition and its timing of ignition is precisely controlled by changing intake air temperature .Pine oil has been used in direct injection Compression ignition engine as an alternate fuel has similar properties as that of diesel. This investigation revealed that the engine operated with pine performed well with little loss of brake thermal efficiency. Thereafter, the properties of the pine oil obtained are studied and represented in a graphical form.

Keywords: Diesel, Pine oil, Performance, Emissions.

I. INTRODUCTION

Since the inception of industrial revolution in eighteenth century, the search for portable prime movers to run machines for both industrial and transportation purpose became intense. Steam engines took a lead role in the beginning, but could not pass the test of time as they were bulky, less efficient and required huge quantity of low energy density solid fuels like coal. In the later part of nineteenth century, diesel engine was invented. Since then these engines have become an integral part of modern human civilization and mostly replaced the steam engines which became obsolete. These engines are extensively used worldwide for transportation, decentralized power generation, agricultural applications and industrial sectors because of their high fuel conversion efficiency, ruggedness and relatively easy operation [1,2].

These wide fields of global usage of diesel engines lead to ever increasing demand of petroleum derived fuels. Petroleum fuels are exhaustible sources of energy and hence an over reliability on these fuels is not sustainable in long run. Besides, the rising crude oil prices and increasing pollution due to excessive use of these engines is another grey area. The exhaust emissions of diesel engines, particularly soot, oxides of nitrogen and carbon monoxide are extremely harmful to natural environment and living beings [3]. Projections for the 30-year period from 1990 to 2020 indicate that vehicle travel, and consequently fossil-fuel demand, will almost triple worldwide and the resulting emissions will pose a serious problem [4].

The engine chosen to experiment is a single cylinder DI (Direct ignition) diesel engine and modified in such a way to, ignite pine oil in a diesel engine under HCCI mode. As the pine oil has a higher self ignition temperature the ignition of pine oil in regular diesel engines with auto-ignition is not possible. Hence, suitable modification is made in the engine to ignite pine oil in a diesel engine like diesel fuel. The modified engine has ECM (Engine control module) controlled fuel spray and an air pre-heater in the suction side of the engine. The combined effort of adiabatic compression and supply of preheated air ignites pine oil by auto-ignition and its timing of ignition is precisely controlled by changing intake air temperature. Pine oil has been used in direct injection CI (Compression ignition) engine as an alternate fuel has similar properties as that of diesel. This investigation revealed that the engine operated with pine oil performed well with little loss of brake thermal efficiency. Thereafter, the properties of the pine oil obtained are studied and represented in a graphical form.

Pine oil was used in early engines without any modification. The abundant availability of petro-fuels had stopped the usage of pine oil in I.C. engines. But the increasing cost of petro-fuel prevailing today reopens the utility of pine oil in I.C. engine. Pine oil can be used in diesel engine as pine oil and diesel blend or dual fuel mode. Using pine oil in dual fuel mode in diesel engine the CO and UHBC emissions are slightly higher than diesel base line and NO_x emission is found to be almost same. The gaseous fuels are used in dual fuel mode in IC engines. Since gaseous fuels have high auto-ignition temperature, they can't be used directly in CI engines easily. Hence they are normally used in DF mode. The dual fuel engine is the modified diesel engine in which usually a gaseous fuel called the primary fuel is inducted with air. The gaseous fuel-air mixture is then compressed but doesn't auto-ignite as it has a high self-ignition temperature.

A small amount of diesel usually called the pilot, is injected as in a normal diesel engine, near the end of the compression stroke. The pilot diesel fuel auto ignites and acts as a spark or source for the ignition of the primary fuel-air mixture. The combustion of gaseous fuel occurs due to the flame that propagates through. Thus the dual fuel mode combines the feature of CI and SI engine. Fuel injection is the part of CI engine and the compression of charge and propagation of flame is the part of SI engine. In the present work we are designing an apparatus for pine oil which can be inducted into the direct injection CI engine. After that, the properties of the pine oil obtained are represented on graph.

II. LITERATURE SURVEY

Jalpit B. Prajapati et al [16K] conducted the experiment on single cylinder four-stroke compression ignition engine to evaluate the engine performance and emission characteristics of

Diesel-biodiesel (palm) blends i.e. B0, B10, B20, B30, with load variation from no load to full load and compared with diesel as a fuel with fixed compression ratio i.e. 18. They concluded that B20 is best in performance compared to other blends but NO_x formation is also little higher in B20.

S.N. Harikrishnan et al [17K] paper presents performance and emission characteristics on single cylinder, four stroke, constant speed, water cooled, direct injection diesel engine using rubber seed oil (RSO) as a fuel. The experimental data for various parameters such as thermal efficiency, brake specific fuel consumptions are analyzed and acceptable thermal efficiencies of the engine were obtained with blends containing up to 75% of rubber seed oil biodiesel blend compared to 25%, 50% and 100%.

M.Prabhakar et al [18K] This paper presents the performance and emission characteristics of a single cylinder constant speed direct injection diesel engine using neat Pine methyl ester and its diesel blends (PME) such as B20 and B100 at different load conditions. The results showed that the brake thermal efficiency decreased and BSFC increased slightly for Pine methyl ester blends as compared with diesel fuel and also seen that CO and smoke emissions were reduced by about 34% and 25% respectively for B20 at full load but NO_x emission was increased about 8.5% for B20 blend. Finally to be Concluding 20% of Pine methyl ester can be used as diesel fuel without any engine modifications.

Table-1 Properties			
Sl. No	Properties	Diesel	Pine oil (C ₁₁ H ₁₀ BrN ₅)
1	Density(kg/m ³)	850	950
2	Calorific value (kJ/kg)	46,500	43404.03
3	Kinematic viscosity @ 40 ⁰ C (cst)	3.05	1.04
4	Cetane number	55	4
5	Flash point °C	52	65
6	Fire point °C	56	97.6
7	Specific gravity	0.86	0.91
8	Sulphur content (%)	<0.035	-

III. Objective Of The Project

- To study the performance and emissions characteristics of a diesel engine with Pine oil as fuel and it is compared with the base engine.
- To study the performance and emissions characteristics of modified piston diesel engine with Pine oil as fuel and it is compared with the base engine.
- To measure the level of CO, HC and smoke in the exhaust emissions in the above said engine.
- To reduce the CO, HC and smoke level in the exhaust emissions by modifying the piston.
To analyze the exhaust emission.

IV. Methodology

- The engine used for the experiment is started using diesel fuel and then its performance and emission readings are observed under various load condition.
- Selecting suitable Pine oil for double cylinder diesel engine and development of an experimental set-up with necessary instruments to study the performance and emission characteristics.
- The admission of Pine oil along with diesel fuel makes the engine run under dual fuel Mode.
- Conducting same trail for Pine oil and diesel fuel from zero to full load condition for modified piston diesel engine.
- Compare the performance and emission parameters for diesel and Pine oil for both base engine and modified piston diesel engine.

V. Experimental Setup and Engine Specification

The experimental test set up as shown in fig 1 and 2 consists of four stroke, constant speed and multi cylinder diesel engine. The engine is oil cooled. The injection timing given by the manufacturer is 27° BTDC, the operating pressure of the fuel injector was set at 1800 bar and the engine speed is 1500rpm. There are number of sensor are used in the engine to measure the fuel and engine parameter and the engine is loaded with water loading as shown in fig 3. Engine specifications as shown in table 2 and table 3 show load bank specification.

Fig- 1: Schematic arrangement of Experimental Set-up

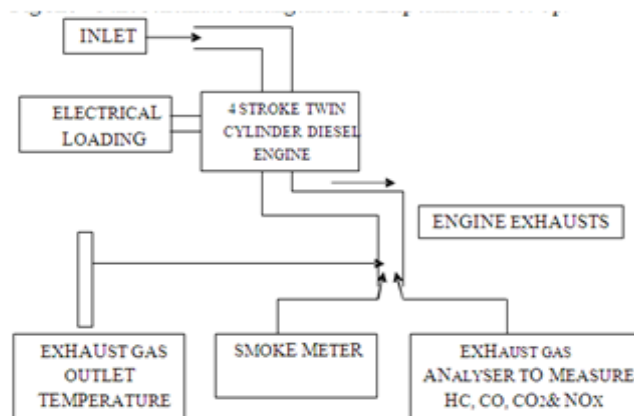




Fig -2: Test engine



Fig- 3: Water loading

Engine type	Four stroke Two cylinder diesel engine
No. of cylinders	02
Stroke	100 mm
Bore Diameter	87 mm
Engine power	15 KV
Compression ratio	17.5:1
NRPM	1500
Type of starting	Crank starting
Load type	Water loading

Table-2 Test Engine specification

Max. Output	15 KV
Generator type	1 Phase
Amps	63
RPM	1500
PF	0.8
Volts	240

Table-3 Load bank specification

VI. Experimental Procedure

- Experiments were initially carried out on the engine using diesel as fuel in order to provide base line data.
- Initially the engine was started using diesel fuel and allowed to run for few minutes until to reach steady state; the base line data were taken. Load was varied from zero loads to full load condition using the water loading and Emissions, smoke and fuel consumption reading were recorded.
- The engine was started on dual fuel mode, when engine became sufficiently heated; the supply of diesel was slowly substituted by 100 % Pine oil for which a two way valve was used. Once the engine reaches steady state, the emission, fuel consumption and smoke reading were taken. The same procedure is carried from zero to full load condition. Similarly same procedures were carried for modified piston diesel engine

VII. Results and Discussion

a) Carbon Monoxide

Figures 4, shows the variation CO level with respect to diesel and Pine oil at different loads. From the graph it is clear that the CO level decreases for conventional pine oil engine and keep on increases for modified engine

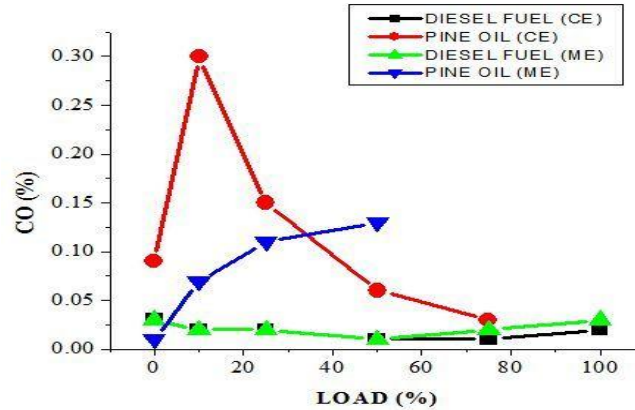


Figure- 4: Comparison of Carbon monoxide vs Load

b) Brake thermal efficiency

Figure 5, shows the variation of brake thermal efficiency with respect to Pine oil & diesel at different loads. From the graph it is observed that as load increases brake thermal efficiency increases for conventional pine oil and diesel oil engine up to 50% of load and decreases for modified Pine oil engine.

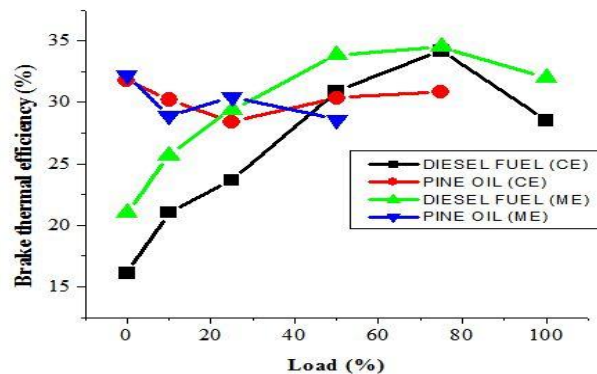


Figure- 5: Comparison of Brake thermal efficiency vs Load

c) Specific fuel consumption

From figure-6 it is clear that as the load increases specific fuel consumption decreases up to 50% load and the SFC of Pine oil is less than the diesel for both conventional and modified upto 50% engine load.

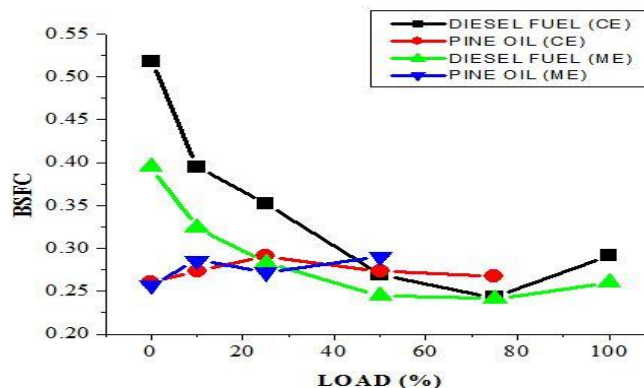


Figure- 6: Comparison of Brake specific fuel consumption vs Load

d)Hydrocarbon

The variation of Hydrocarbon of the engine with diesel & Pine oil is shown in figure 7. It can be seen that there is a higher Hydrocarbon emissions for conventional and modified Pine oil engine at lower loads and emissions keep on decreasing as the engine load increases.

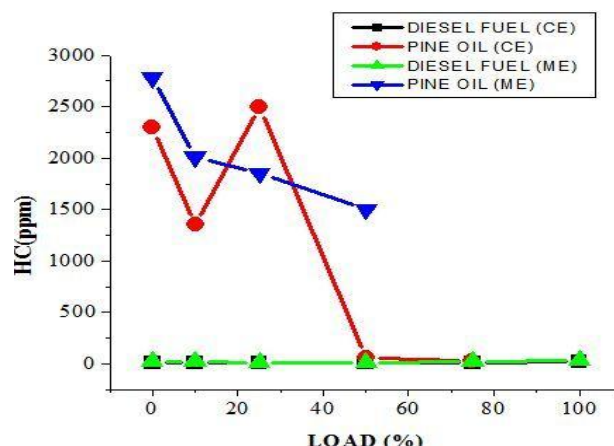


Figure- 7: Comparison of HC vs Load

VIII. Conclusion and Future Scope

Based on the performance and emissions characteristics of Pine oil, it is concluded that the Pine oil shows a good alternative fuel with closer performance and better emission characteristics to that of a diesel. From the above results it is concluded that the Pine oil shows better performance characteristics like Brake thermal efficiency, and decrease in the emission parameters like CO, HC. Hence the 100% Pine oil can be substitute for diesel. The future research directions for scientists or researcher can be done with different engine modification.

REFERENCES

- [1] R K Tripathi, Deepak Kumar and Ajay Kumar (2014).Performance and Emission Evaluation of Indirect Injection Diesel Engines Fuelled with Jatropha Oil.International Journal of Current Engineering and Technology.
- [2]. Q.A. BAKER —Use of alcohols in Diesel Fuel Emulsions and Solutions in a Medium Speed Diesel Engine|| - SAE 810254.
- [3] Erlandsson.O "Hydrocarbon (HC) Reduction of Exhaust Gases from a Homogeneous Charge Compression Ignition (HCCI) Engine Using Different Catalytic Mesh-Coatings," SAE. Technical Paper 2000-01-1847, 2000, doi:10.4271/2000-01-1847.
- [4] Magdi K. Khair "Design and Development of Catalytic Converters for Diesels," SAETechnical Paper 921677, 1992, doi:10.4271/921677.
- [5] Kenneth T. Menzies "Comparison of Aldehyde Methods," SAE Technical Paper 820965, 1982, doi:10.4271/820965
- [6] A.S.Ramadhass, S.Jayaraj, C.Muraleedharan (2004), Characterization and effect of using Pine oil As fuel in the compression ignition engines, Renewable Energy 30 (2005) 795–803
- [7] Kulachate Pianthong and Prachasanti Thaiyasuit (2009), Production of Biodiesel from Pine Oil and Its Effects to Engine Performances, International Conference on Energy Security and Climate Change.
- [8] S.N.Harikrishnan and R.Sabarish (2014). Experimental Analysis of Direct Injection Diesel Engine Using Pine Oil, Middle-East Journal of Scientific Research 20 (6): 709-714, 2014.
- [9] S.Mahalingam and B.R.RameshBapu (2014). Emission analysis of di-diesel engine at different injection pressures using jatropha and Pine oil blended with diesel, Golden Research Thoughts ISSN 2231-5063.
- [10] Gaurav Sharma, DevendraDandotiya, S.K.Agrawal (2013),Experimental Investigation of Performance Parameters of Single Cylinder IC Engine Using Mustard Oil, International Journal of Modern Engineering Research (IJMER).
- [11] N.Shrivastava, S.N.Varma and M.Pandey (2012), Experimental Study on the Production of Karanja Oil Methyl Ester and Its Effect on Diesel Engine.
- [12] Narasiman V, Jeyakumar S, Mani M and Guttu Ofgaa 2012, Effect of Neat Sardine Oil with Varies Blends on the Performance and Emission Characteristics of Diesel Engine, ISSN: 2226-7522(Print) and 2305-3327 Science, Technology, and Arts Research Journal
- [13] Dr.G.R.K.Sastry, K.Venkateswarlu, Dr. Syed Yousufuddin, Dr.B.S.R Murthy 2012, performance, vibration and emission analysis of diesel engine fuelled with fish oil bio diesel blends, International Journal of Advanced Engineering Technology E-ISSN 0976-3945.

- [14] Bhabani Prasanna Pattanaik, Basanta Kumar Nanda and Probir Kumar Bose 2012, performance & emission studies on a single cylinder di diesel engine fueled with diesel and rice bran oil methyl ester blends, International Journal of Advances in Engineering & Technology, ISSN: 2231-1963
- [15] E. M. Shahid 1 and Y. Jamal 2011, Performance Evaluation of a Diesel Engine Using Biodiesel, Pak. J. Engg. & Appl. Sci. Vol. 9, Jul., 2011 (p. 68-75)
- [16] M.Prabhahar, R.Murali Manohar, S.Sendilvelan 2012, performance and emission studies of a diesel engine with Pine methyl ester at different load conditions, International Journal of Engineering Research and Applications (IJERA) ISSN: 2248-9622 Vol. 2, Issue 3, May-Jun 2012, pp.2707-2713.
- [17] K. Harshavardhan Reddy, N.Balajiganesh 2012, Experimental Investigation on Four Stroke Diesel Engine using Diesel –Orange oil Blends, Undergraduate Academic Research Journal (UARJ), ISSN: 2278 – 1129, Volume-1, Issue-2, 2012.